frontiers | Research Topics

Colour and light in the ocean, volume II

Edited by
Shubha Sathyendranath, Gemma Kulk, Astrid Bracher, Jamie Shutler, Victor Martinez-Vicente, Tiit Kutser, Javier A. Concha, Marie-Helene Rio and Heather Bouman

Published in
Frontiers in Marine Science



FRONTIERS EBOOK COPYRIGHT STATEMENT

The copyright in the text of individual articles in this ebook is the property of their respective authors or their respective institutions or funders. The copyright in graphics and images within each article may be subject to copyright of other parties. In both cases this is subject to a license granted to Frontiers.

The compilation of articles constituting this ebook is the property of Frontiers.

Each article within this ebook, and the ebook itself, are published under the most recent version of the Creative Commons CC-BY licence. The version current at the date of publication of this ebook is CC-BY 4.0. If the CC-BY licence is updated, the licence granted by Frontiers is automatically updated to the new version.

When exercising any right under the CC-BY licence, Frontiers must be attributed as the original publisher of the article or ebook, as applicable.

Authors have the responsibility of ensuring that any graphics or other materials which are the property of others may be included in the CC-BY licence, but this should be checked before relying on the CC-BY licence to reproduce those materials. Any copyright notices relating to those materials must be complied with.

Copyright and source acknowledgement notices may not be removed and must be displayed in any copy, derivative work or partial copy which includes the elements in question.

All copyright, and all rights therein, are protected by national and international copyright laws. The above represents a summary only. For further information please read Frontiers' Conditions for Website Use and Copyright Statement, and the applicable CC-BY licence.

ISSN 1664-8714
ISBN 978-2-8325-5672-6
DOI 10.3389/978-2-8325-5672-6

About Frontiers

Frontiers is more than just an open access publisher of scholarly articles: it is a pioneering approach to the world of academia, radically improving the way scholarly research is managed. The grand vision of Frontiers is a world where all people have an equal opportunity to seek, share and generate knowledge. Frontiers provides immediate and permanent online open access to all its publications, but this alone is not enough to realize our grand goals.

Frontiers journal series

The Frontiers journal series is a multi-tier and interdisciplinary set of open-access, online journals, promising a paradigm shift from the current review, selection and dissemination processes in academic publishing. All Frontiers journals are driven by researchers for researchers; therefore, they constitute a service to the scholarly community. At the same time, the *Frontiers journal series* operates on a revolutionary invention, the tiered publishing system, initially addressing specific communities of scholars, and gradually climbing up to broader public understanding, thus serving the interests of the lay society, too.

Dedication to quality

Each Frontiers article is a landmark of the highest quality, thanks to genuinely collaborative interactions between authors and review editors, who include some of the world's best academicians. Research must be certified by peers before entering a stream of knowledge that may eventually reach the public - and shape society; therefore, Frontiers only applies the most rigorous and unbiased reviews. Frontiers revolutionizes research publishing by freely delivering the most outstanding research, evaluated with no bias from both the academic and social point of view. By applying the most advanced information technologies, Frontiers is catapulting scholarly publishing into a new generation.

What are Frontiers Research Topics?

Frontiers Research Topics are very popular trademarks of the *Frontiers journals series*: they are collections of at least ten articles, all centered on a particular subject. With their unique mix of varied contributions from Original Research to Review Articles, Frontiers Research Topics unify the most influential researchers, the latest key findings and historical advances in a hot research area.

Find out more on how to host your own Frontiers Research Topic or contribute to one as an author by contacting the Frontiers editorial office: frontiersin.org/about/contact

Colour and light in the ocean, volume II

Topic editors

Shubha Sathyendranath — Plymouth Marine Laboratory, United Kingdom
Gemma Kulk — Plymouth Marine Laboratory, United Kingdom
Astrid Bracher — Alfred Wegener Institute Helmholtz Centre for Polar and Marine Research (AWI), Germany
Jamie Shutler — University of Exeter, United Kingdom
Victor Martinez-Vicente — Plymouth Marine Laboratory, United Kingdom
Tiit Kutser — University of Tartu, Estonia
Javier A. Concha — European Space Research Institute (ESRIN), Italy
Marie-Helene Rio — European Space Agency (ESA), France
Heather Bouman — University of Oxford, United Kingdom

Citation

Sathyendranath, S., Kulk, G., Bracher, A., Shutler, J., Martinez-Vicente, V., Kutser, T., Concha, J. A., Rio, M.-H., Bouman, H., eds. (2024). *Colour and light in the ocean, volume II*. Lausanne: Frontiers Media SA. doi: 10.3389/978-2-8325-5672-6

Table of contents

06 Fragility of marine photosynthesis
Žarko Kovač and Shubha Sathyendranath

22 Concentration and distribution of phytoplankton nitrogen and carbon in the Northwest Atlantic and Indian Ocean: A simple model with applications in satellite remote sensing
Giuseppe Maniaci, Robert J. W. Brewin and Shubha Sathyendranath

35 Environmental niches and seasonal succession of phytoplankton assemblages in a subarctic coastal bay: Applications to remote sensing estimates
Carlos A. S. Araújo, Claude Belzile, Jean-Éric Tremblay and Simon Bélanger

58 Absorption-based algorithm for satellite estimating the particulate organic carbon concentration in the global surface ocean
Qiang Li, Lingling Jiang, Yanlong Chen, Junwu Tang and Siwen Gao

75 A new merged dataset of global ocean chlorophyll-a concentration for better trend detection
Shujie Yu, Yan Bai, Xianqiang He, Fang Gong and Teng Li

88 Primary production in the North Atlantic estimated from *in situ* water column data observed by Argo floats and remote sensing
Jørgen Bendtsen, Clara R. Vives and Katherine Richardson

101 Chlorophyll and POC in polar regions derived from spaceborne lidar
Zhenhua Zhang, Peng Chen, Chunyi Zhong, Congshuang Xie, Miao Sun, Siqi Zhang, Su Chen and Danchen Wu

115 Bahamian seagrass extent and blue carbon accounting using Earth Observation
Alina Blume, Avi Putri Pertiwi, Chengfa Benjamin Lee and Dimosthenis Traganos

125 Seasonal variability of satellite-derived primary production in the South China Sea from an absorption-based model
Hang Lv, Guifen Wang, Wenlong Xu, Yinxue Zhang and Long Jiang

139 MODIS-derived green *Noctiluca* blooms in the upper Gulf of Thailand: Algorithm development and seasonal variation mapping
Jutarak Luang-on, Joji Ishizaka, Anukul Buranapratheprat, Jitraporn Phaksopa, Joaquim I. Goes, Elígio de Raús Maúre, Eko Siswanto, Yuanli Zhu, Qian Xu, Phattaranakorn Nakornsantiphap, Hiroshi Kobayashi and Satsuki Matsumura

155 Variations of phytoplankton chlorophyll in the Bay of Bengal: Impact of climate changes and nutrients from different sources
Eko Siswanto, Md. Latifur Rahman Sarker, Benny N. Peter, Toshihiko Takemura, Takanori Horii, Kazuhiko Matsumoto, Fumikazu Taketani and Makio C. Honda

172 Optical remote sensing (Sentinel-3 OLCI) used to monitor dissolved organic carbon in the Lena River, Russia
Jan El Kassar, Bennet Juhls, Martin Hieronymi, Rene Preusker, Anne Morgenstern, Jürgen Fischer and Pier Paul Overduin

186 Parameters for the depth of the ocean's productive layer
John F. Marra, W. Sean Chamberlin, Carol A. Knudson, W. Joseph Rhea and Cheng Ho

193 Global ocean colour trends in biogeochemical provinces
Marit van Oostende, Martin Hieronymi, Hajo Krasemann and Burkard Baschek

206 Bio-geo-optical modelling of natural waters
Shun Bi, Martin Hieronymi and Rüdiger Röttgers

231 Phytoplankton pigment *in situ* measurements uncertainty evaluation: an HPLC interlaboratory comparison with a European-scale dataset
Elisabetta Canuti

248 Ocean color atmospheric correction methods in view of usability for different optical water types
Martin Hieronymi, Shun Bi, Dagmar Müller, Eike M. Schütt, Daniel Behr, Carsten Brockmann, Carole Lebreton, François Steinmetz, Kerstin Stelzer and Quinten Vanhellemont

271 Corrigendum: Ocean color atmospheric correction methods in view of usability for different optical water types
Martin Hieronymi, Shun Bi, Dagmar Müller, Eike M. Schütt, Daniel Behr, Carsten Brockmann, Carole Lebreton, François Steinmetz, Kerstin Stelzer and Quinten Vanhellemont

273 Review of algorithms estimating export production from satellite derived properties
Bror F. Jönsson, Gemma Kulk and Shubha Sathyendranath

291 Remote sensing of phytoplankton community composition in the northern Benguela upwelling system
Tebatso M. Moloto, Sandy J. Thomalla, Marie E. Smith, Bettina Martin, Deon C. Louw and Rolf Koppelmann

314 Estimation of primary production from the light absorption of phytoplankton and photosynthetically active radiation in the South China Sea
Hongwuyi Zhao, Wenxi Cao, Lin Deng, Jianzu Liao, Kai Zeng, Wendi Zheng, Yuanfang Zhang, Jie Xu and Wen Zhou

328 Improved multivariable algorithms for estimating oceanic particulate organic carbon concentration from optical backscattering and chlorophyll-a measurements
Daniel Koestner, Dariusz Stramski and Rick A. Reynolds

352 Assessment of ocean color atmospheric correction methods and development of a regional ocean color operational dataset for the Baltic Sea based on Sentinel-3 OLCI
Luis González Vilas, Vittorio Ernesto Brando, Annalisa Di Cicco, Simone Colella, Davide D'Alimonte, Tamito Kajiyama, Jenni Attila and Thomas Schroeder

377 Deconstructing co-occurring marine heatwave and phytoplankton bloom events in the Arkona Sea in 2018
Bronwyn Cahill, Evridiki Chrysagi, Rahel Vortmeyer-Kley and Ulf Gräwe

397 Comparison of ocean-colour algorithms for particulate organic carbon in global ocean
Christina Eunjin Kong, Shubha Sathyendranath, Thomas Jackson, Dariusz Stramski, Robert J. W. Brewin, Gemma Kulk, Bror F. Jönsson, Hubert Loisel, Martí Galí and Chengfeng Le

411 A machine learning model-based satellite data record of dissolved organic carbon concentration in surface waters of the global open ocean
Marko Laine, Gemma Kulk, Bror F. Jönsson and Shubha Sathyendranath

422 Detecting centennial changes in the clarity and colour of the Red and Eastern Mediterranean Seas by retracting the "Pola" expeditions
Jonathan R. Heath, Robert J. W. Brewin, Jaime Pitarch and Dionysios E. Raitsos

frontiers | Frontiers in Marine Science

TYPE Original Research
PUBLISHED 13 September 2022
DOI 10.3389/fmars.2022.963395

Check for updates

OPEN ACCESS

EDITED BY
Thomas Malone,
University of Maryland, United States

REVIEWED BY
Francesco Mattei,
UMR7093 Laboratoire d'océanographie de Villefranche (LOV), France
Jochen Wollschläger,
University of Oldenburg, Germany

*CORRESPONDENCE
Žarko Kovač
zkovac@pmfst.hr

SPECIALTY SECTION
This article was submitted to Ocean Observation, a section of the journal Frontiers in Marine Science

RECEIVED 07 June 2022
ACCEPTED 05 August 2022
PUBLISHED 13 September 2022

CITATION
Kovač Ž and Sathyendranath S (2022) Fragility of marine photosynthesis. *Front. Mar. Sci.* 9:963395. doi: 10.3389/fmars.2022.963395

COPYRIGHT
© 2022 Kovač and Sathyendranath. This is an open-access article distributed under the terms of the Creative Commons Attribution License (CC BY). The use, distribution or reproduction in other forums is permitted, provided the original author(s) and the copyright owner(s) are credited and that the original publication in this journal is cited, in accordance with accepted academic practice. No use, distribution or reproduction is permitted which does not comply with these terms.

Fragility of marine photosynthesis

Žarko Kovač[1]* and Shubha Sathyendranath[2]

[1]Faculty of Science, University of Split, Split, Croatia, [2]National Centre for Earth Observations, Plymouth Marine Laboratory, Plymouth, United Kingdom

Ecosystem fragility is an often used term in oceanography yet to this day it lacks a precise and widely accepted definition. Defining and subsequently quantifying fragility would be of great value, for such measures could be used to objectively ascertain the level of risk marine ecosystems face. Risk assessments could further be used to define the level of protection a given ocean region requires from economic activity, such as fisheries. With this aim we introduce to the oceanographic literature the concepts of marginal production and fragility, which we define for marine photosynthesis, the base of the oceanic food web. We demonstrate that marine photosynthesis is always fragile with respect to light, implying variability in surface irradiance acts unfavourably on biomass. We also demonstrate that marine photosynthesis can be both fragile and antifragile with respect to the mixed-layer depth, implying variability in mixed-layer depth can act both favourably and unfavourably on biomass. Quantification of marginal production and fragility is presented on data from two open ocean stations: Hawaii Ocean Time Series and Bermuda Atlantic Time-Series Study. Seasonal cycle of biomass is modelled and the effects of primary production fragility are analysed. A new tipping point for marine phytoplankton is identified in the form of a depth horizon. Using the new definitions presented here a rich archive of data can be used straightforwardly to quantify primary production fragility. The definitions can also be used to predict when primary production enters the fragile state during the seasonal cycle.

KEYWORDS

ocean ecosystem stability, tipping point, marginal production, fragility, antifragility

1 Introduction

Historically, the study of ocean primary production relied on laboratory and field measurements coupled with mathematical models representing photosynthetic processes (Platt and Sathyendranath, 1991; Regaudie-de Gioux et al., 2014), with the goal of capturing the spatial and temporal variability in its magnitude, with increasing use of satellite ocean-colour data in recent decades to capture basin- and global-scale variability (Platt and Sathyendranath, 1988; Longhurst et al., 1995; Sathyedranath et al., 1995; Kulk

et al., 2021). These models used radiative transfer and light transmission models to capture the spectrally- and angularly-resolved light field in the ocean, coupled with physiological models of photosynthetic response of phytoplankton to available light.

Another long-standing interest in the oceanographic community has been the role of ocean dynamics in controlling the supply of nutrients into the surface layer of the ocean, and the mixing in the layer, thereby controlling phytoplankton growth and formation of blooms (Sverdrup, 1953; Platt et al., 1991; Sathyendranath et al., 2015; Kovač et al., 2021). There has also been considerable investment of effort in embedding primary production models into large-scale simulation models of marine ecosystems, which in turn are embedded in general circulation models of the ocean (Laufkötter et al., 2015).

In recent years, stability and resilience of primary production have emerged as novel themes in the study of the pelagic ecosystem using analytical models (Kovač et al., 2020). At their core both terms attempt to quantify how sustainable primary production is: a topic of paramount interest due to climate change. Unfortunately, easily measurable and practically quantifiable definitions of both have proven to be rather elusive thus far in case of primary production. While stability, fragility, resilience and tipping points are of general interest in today's context of a changing climate, phytoplankton primary production is of particular interest: it is, arguably, one of the oldest productive systems on Earth; and though it is known to have undergone long-term changes in regional magnitude over geological time scales, it is not known to have collapsed at any time, to make room for another type of productive system in the pelagic ocean. Efforts to forecast likely changes in primary production over the next century using simulation models have yielded results with large uncertainties (Frölicher et al., 2016; Kwiatkowski et al., 2020), which have been attributed, among other factors, to "incomplete understanding of fundamental processes". Recent studies of time series of satellite data to extract trends in primary production admittedly suffer from the short length of the time series (Watson and Rouusseaux, 2019; Kulk et al., 2021).

Here we follow an alternative approach, combining marine primary-production models with the rich literature in economics on production theory (Acemoglu, 2009; Perman et al., 2011; Richmond et al., 2013). The two disciplines have not communicated well up to now, and the cross-disciplinary flux of ideas has been virtually non-existent, testifying to the chasm between the two fields, in contrast to other ecological fields where the transfer of knowledge did occur, for example, in fisheries (Clark and Munro, 1975; Munro, 1992).

Of major concern in the context of climate change is the response of primary production to changing surface ocean stratification and consequently mixed-layer depth, which exert a strong control on both phytoplankton blooms and primary production (Da et al., 2021). In Climate Model Intercomparison Project 6 (CMIP6), the surface warming is expected to increase stratification, contributing to shallower mixed layer, a reduction in the supply of nitrogen into the surface layer and a decrease in the ventilation of sub-surface oxygen (Kwiatkowski et al., 2020). For oceanic primary production, variability in the mixed-layer depth presents a strong disturbance, controlling the average light levels in the mixed-layer as well as the supply of nutrients into the layer (Platt et al., 2003b). Mixed-layer shallowing favours phytoplankton growth, as it increases the average light conditions in the mixed layer, whereas mixed-layer deepening decreases it. However, there is an asymmetry in the response of mixed layer production to deepening, in contrast to shallowing. This asymmetry is caused by the exponential light attenuation with depth and the response of production to light, both being nonlinear. In relative terms, shallowing can cause a greater increase in mixed-layer production, than the reduction caused by a mixed-layer deepening of the same magnitude. This asymmetry calls for a re-examination of the notions of stability and resilience in aquatic primary production.

2 Theory

2.1 Photosynthesis irradiance function

Let the rate of carbon assimilation by phytoplankton per unit biomass P^B be given by a photosynthesis irradiance function p^B of the form:

$$P^B = p^B(I), \tag{1}$$

where irradiance is given as I (Figure 1). In the literature there are numerous examples of photosynthesis irradiance functions (Platt and Jassby, 1976; Jones et al., 2014; Kovač et al., 2017) and the exact mathematical expression for the dependence of production on light varies amongst these functions. However, all exhibit a linear response to light at low irradiance:

$$\lim_{I\to 0} p^B(I) = \alpha^B I \tag{2}$$

and a decline in the rate of response with increasing irradiance, which leads to production saturation at high irradiance:

$$\lim_{I\to \infty} p^B(I) = P_m^B \tag{3}$$

where α^B is the initial slope and P_m^B is the assimilation number, which setts the rate of carbon assimilation per unit biomass at saturation (Platt and Jassby, 1976; Jassby and Platt, 1976). Mathematically, we say the photosynthesis irradiance function is curved with respect to light (Jones et al., 2014). We should stress that here we do not consider photoinhibition, a phenomenon in which production declines at sufficiently high irradiance (Platt et al., 1980).

The observed decline in the rate of response has consequences for oceanic primary production as it eventually

sets an upper limit on how productive the ocean can be. A more subtle consequence of the curvature is manifested in the dynamical response of primary production to perturbations in the light field. In the ocean these perturbations arise naturally over a wide range of temporal and spatial scales. To precisely quantify the effect of irradiance variability on primary production we introduce to the oceanographic literature the notions of marginal production and fragility, inspired by the economic concepts from Taleb (2012). In economics, marginal production quantifies the change in output due to a unit change in input, whereas fragility is a more subtle concept. As investigated by Taleb (2012), fragility and closely related antifragiltiy, arise due to nonlinearities in the response of an output to a change in input. These nonlinear responses may make the system decrease/increase output under stochastic variability of the input, in which case we would say the system is fragile/antifragile. To be mathematically precise and to avoid ambiguity in applying these concepts in the oceanographic literature, we proceed as follows.

First, we define marginal production M:

$$M = \frac{dp^B(I)}{dI} \tag{4}$$

As is well known, increasing irradiance leads to increasing production, therefore marginal production is positive (Figure 1):

$$M > 0 \tag{5}$$

Marginal production itself is a function of irradiance $M{=}M(I)$. To describe how M behaves as a function of I we define fragility as:

$$F = \frac{d^2p^B(I)}{dI^2} \tag{6}$$

It is also well known that the rate of increase in production, now termed marginal production, declines with increasing irradiance making fragility negative:

$$F < 0 \tag{7}$$

We say the photosynthesis irradiance function is fragile with respect to variability in irradiance. Fragility imples that under variable light conditions average photosynthesis will be lower than it would otherwise be under constant irradiance.

These definitions apply to the photosynthesis irradiance function and as such describe the response of phytoplankton photosynthesis to light at known irradiance. Typically such functions are determined in experiments under controlled and predetermined light conditions (Platt and Jassby, 1976; Jones et al., 2014). However, in the real ocean phytoplankton are distributed over a light gradient. Therefore, a continuum of light intensities, from the surface to the bottom of the euphotic zone (or the sea bed, whichever comes first), needs to be considered when quantifying marginal watercolumn production and watercolumn production fragility. We now proceed to do that.

2.2 Watercolumn production

Consider a water column with uniform biomass B exposed to sinusoidally varying surface irradiance $I_0(t) = I_0^m \sin(\pi t/D)$ attenuated with depth according to the Beer-Lambert law, such that irradiance at depth equals:

$$I(z,t) = I_0^m \sin(\pi t/D)\exp(-Kz) \tag{8}$$

where $I_0(t)$ is surface irradiance, I_0^m noon irradiance, D is daylength and K is the diffuse attenuation coefficient of downwelling irradiance (Kirk, 2011). Time is continuous and

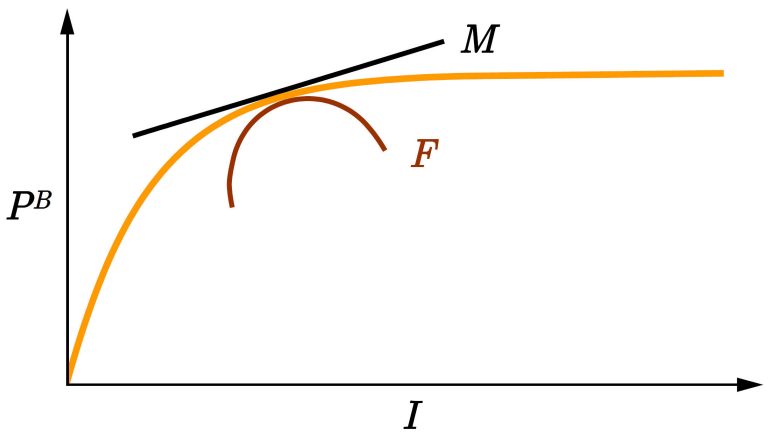


FIGURE 1
Graphical representation of marginal production M (first derivative, black) and fragility F (second derivative, red) for the photosynthesis irradiance function (orange curve), where production per unit biomass P^B is given asa function of irradiance I.

equals zero at sunrise. To quantify production at depth we use the Platt et al. (1980) photosynthesis irradiance function:

$$p^B(I) = P_m^B(1 - \exp(-\alpha^B I/P_m^B)) \quad (9)$$

Inserting $I(z,t)$ in $p^B[I(z,t)]$ and integrating over depth (from surface till infinity) and daylength yields the canonical solution for watercolumn production $P_{Z,T}$ (Platt et al., 1990):

$$P_{Z,T} = \frac{BP_m^B D}{K} f(I_\star^m) \quad (10)$$

where $I_\star^m = \alpha^B I_0^m / P_m^B$ is the scaled noon irradiance (dimensionless) and $f(I_\star^m)$ is a known function (Figure 2). Modification of this solution for a finite depth watercolumn is straightforward (Platt et al., 1991).

Following (4) we define marginal watercolumn production as:

$$M_I = \frac{dP_{Z,T}}{dI_0^m} \quad (11)$$

which is measured in ($mgCW^{-1}$). Here noon irradiance is taken as representative of the watercolumn light conditions. To derive an exact expression for M_I we begin with a prior result from Platt et al. (2017) (their equation 10):

$$\frac{dP_{Z,T}}{dI_\star^m} = \frac{BP_m^B}{KI_\star^m} \int_0^D (1 - \exp(-I_\star^m g(t)))dt \quad (12)$$

which gives the change in watercolumn production $P_{Z,T}$ with respect to $I_\star^m$. By setting $g(t)=sin\ (\pi t/D)$, as used in our model, we get:

$$\frac{dP_{Z,T}}{dI_\star^m} = \frac{BP_m^B}{KI_\star^m} \int_0^D (1 - \exp(-I_\star^m \sin\ (\pi t/D)))dt \quad (13)$$

The integral on the right hand side is recognized as surface production and is given by the analytical solution for the production profile:

$$P_T(0) = BP_m^B D f_z(I_\star^m) \quad (14)$$

where $P_T(z)$ is the daily production at depth z and $f_z(I_\star^m e^{-Kz})$ is a known function (Kovač et al., 2016a). Taking this solution into account transforms (13) into:

$$\frac{dP_{Z,T}}{dI_\star^m} = \frac{BP_m^B D}{KI_\star^m} f_z(I_\star^m) \quad (15)$$

By noting $dI_0^m = I_k\, dI_\star^m$ the previous expression becomes:

$$\frac{dP_{Z,T}}{dI_0^m} = \frac{P_T(0)}{KI_0^m} \quad (16)$$

and following (11) we recognize the result as marginal watercolumn production:

$$M_I = \frac{P_T(0)}{KI_0^m} \quad (17)$$

Therefore, marginal watercolumn production M_I is proportional to surface production divided by the product of K and I_0^m . Given that all the quantities on the right hand side are positive, marginal watercolumn production M_I is positive (Figure 2):

$$M_I > 0 \quad (18)$$

Following (6) we define watercolumn production fragility:

$$F_I = \frac{dM_I}{dI_0^m} \quad (19)$$

which is measured in (mg C m^{-2} W^{-2}). *To calculate* F_I we take the derivative of (17) to get:

$$F_I = \frac{1}{I_0^m}\left(\frac{1}{K}\frac{dP_T(0)}{dI_0^m} - M_I\right) \quad (20)$$

which is negative (Figure 2):

$$F_I < 0 \quad (21)$$

implying watercolumn primary production is fragile with respect to surface irradiance.

Fragility being negative implies that fluctuations in surface irradiance will act to reduce mean primary production from what would otherwise result under steady surface irradiance. This further implies there is a lower limit on marginal watercolumn production:

$$M_I > \frac{1}{K}\frac{dP_T(0)}{dI_0^m} \quad (22)$$

Visual interpretation of (18) and (21) is straightforward. In Figure 2 marginal production equals the first derivative of $f(I_\star^m)$ with respect to $I_\star^m$ and fragility equals the second derivative of $f(I_\star^m)$ with respect to $I_\star^m$. Ecological interpretation is also straightforward. As surface irradiance increases, light penetrates deeper into the watercolumn and production increases, but the rate of increase declines due to light saturation.

2.3 Mixed-layer production

Surface irradiance is not the only controlling factor of underwater light climate and consequently primary production. Typically, surface layer of the ocean has uniform properties up to a certain depth, termed the mixed-layer depth. In this layer phytoplankton are actively mixed (Franks, 2015) and experience uniform production, which is determined by surface irradiance and mixed-layer depth (Jackson et al., 2017). Therefore, mixed-layer depth variability has to be considered in a discussion of marginal production and fragility.

Let the depth of the mixed layer be given by Z_m and let P_{Z_m},T mark average mixed layer production (Figure 3), which following Kovač et al. (2020) equals:

$$\langle P\rangle_{Z_m,T} = \frac{BP_m^B D}{KZ_m}\left[f(I_*^m) - f(I_*^m e^{-KZ_m})\right] \quad (23)$$

We define marginal mixed-layer production as:

$$M_Z = \frac{d\langle P\rangle_{Z_m,T}}{dZ_m} \quad (24)$$

which quantifies the change in average mixed layer production caused by a change in mixed layer depth and is measured in in ($mgCm^{-4}$). Following Kovač et al. (2020), due to light attenuation with depth, marginal mixed-layer production is lees than zero:

$$M_Z < 0 \quad (25)$$

Simply stated, average mixed-layer production decreases with increasing mixed-layer depth (Figure 3). Further following Kovač et al. (2020) (their equation 71) we have:

$$M_Z = \frac{1}{Z_m}\left[P_T(Z_m) - \langle P_T(z)\rangle\right] \quad (26)$$

where $P_T(Z_m)$ is the production at the mixed-layer base and $\langle P_T(z)\rangle$ is the average mixed layer production.

Having defined and expressed M_Z we now define mixed-layer production fragility F_Z as:

$$F_Z = \frac{dM_Z}{dZ_m} \quad (27)$$

which is measured in ($mgCm^{-5}$). Fragility due to mixed-layer depth variability quantifies the change in marginal production caused by a change in mixed-layer depth. Graphically, M_Z is the derivative of average mixed-layer production with depth and F_Z is the second derivative of average mixed-layer production with depth (Figure 3). Taking the derivative of (26) with respect to Z_m we get:

$$F_Z = \frac{1}{Z_m}\left(\left.\frac{dP_T(z)}{dz}\right|_{Z_m} - 2M_Z\right) \quad (28)$$

Since $dP_T(z)/dz<0$ (Kovač et al., 2016a) and $M_Z<0$ (25) the sign of F_Z can be positive, implying mixed-layer production could display antifragility, with variability in mixed-layer depth Z_m acting favourably on average mixed-layer production.

We term mixed-layer production fragile when mixed-layer deepening leads to a greater loss in average production, than the gain in production due to shallowing of the same magnitude. Mathematically we have:

$$F_Z < 0 \quad (29)$$

We term mixed-layer production antifragile when mixed-layer deepening leads to a lesser loss in average production, than the gain in production due to shallowing of the same magnitude. Mathematically we have:

$$F_Z > 0 \quad (30)$$

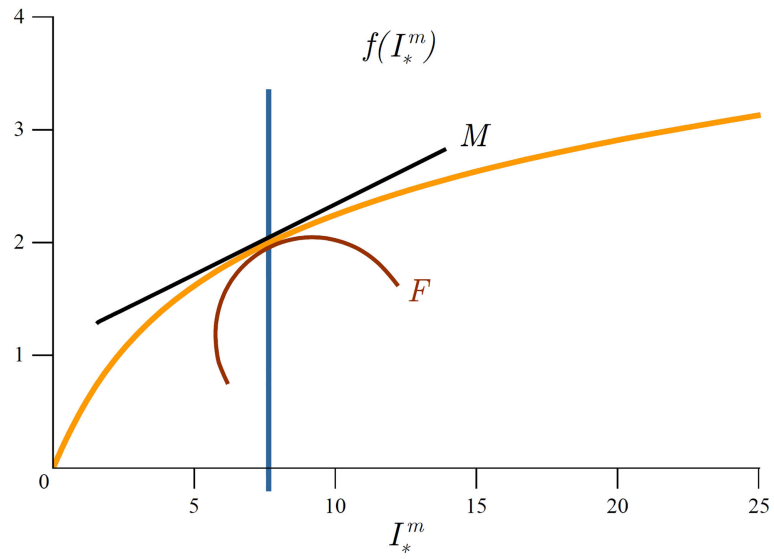


FIGURE 2
Graphical representation of marginal watercolumn production and watercolumn production fragility. The orange curve is the $f(I_*^m)$function (ordinate, dimensionless) from the canonical solution (10) for watercolumn production (Platt et al., 1990). Marginal watercolumn production M_I equals the first derivative of $f(I_*^m)$with respect to I_*^m (black line). Watercolumn production fragility F_I equals the second derivative of $f(I_*^m)$ with respect to I_*^m (red curve). I_*^m is the scaled noon irradiance (dimensionless). As I_*^m increases M_I declines and we say watercolumn production is fragile with respect to irradiance $F_I< 0$.

In contrast to watercolumn production fragility, mixed-layer production can be either fragile or antifragile. By considering F_Z=0 from (28) we get:

$$\left.\frac{dP_T(z)}{dz}\right|_Z = 2M_Z \tag{31}$$

We term the depth at which this condition holds as the fragility depth Z_f as it represents the tipping point for primary production. Since fragility equals the first derivative of marginal production, zero fragility corresponds to an inflexion point of average mixed-layer production (Figure 3). At this depth marginal mixed-layer production has a minimum. If the mixed-layer depth is deeper than the fragility depth $Z_m > Z_f$, then mixed-layer variability acts favourably on primary production, whereas if the opposite holds ($Z_m < Z_f$) mixed-layer variability acts unfavourably on primary production.

3 Measurements

Here we use the available data from the Bermuda Atlantic Time-Series Study (BATS) and the Hawaii Ocean Time Series (HOT) to quantify marginal production and fragility. Both marginal production and fragility can be estimated directly from *in situ* measurements routinely done at these stations, which are comprised of: chlorophyll profile, production profile, attenuation coefficient and surface irradiance, all measured on a monthly basis. Complementary to these measurements, marginal production and fragility require information on the photosynthesis parameters. Following the methodology of Kovač et al. (2016b) these parameters were estimated from the aforementioned measurements, both at HOT (Kovač et al., 2016a) and BATS (Kovač et al., 2018) stations. More details on HOT data set can be found in Section 5 of Kovač et al. (2016a), whereas more details on the BATS data set can be found in Kovač et al. (2018).

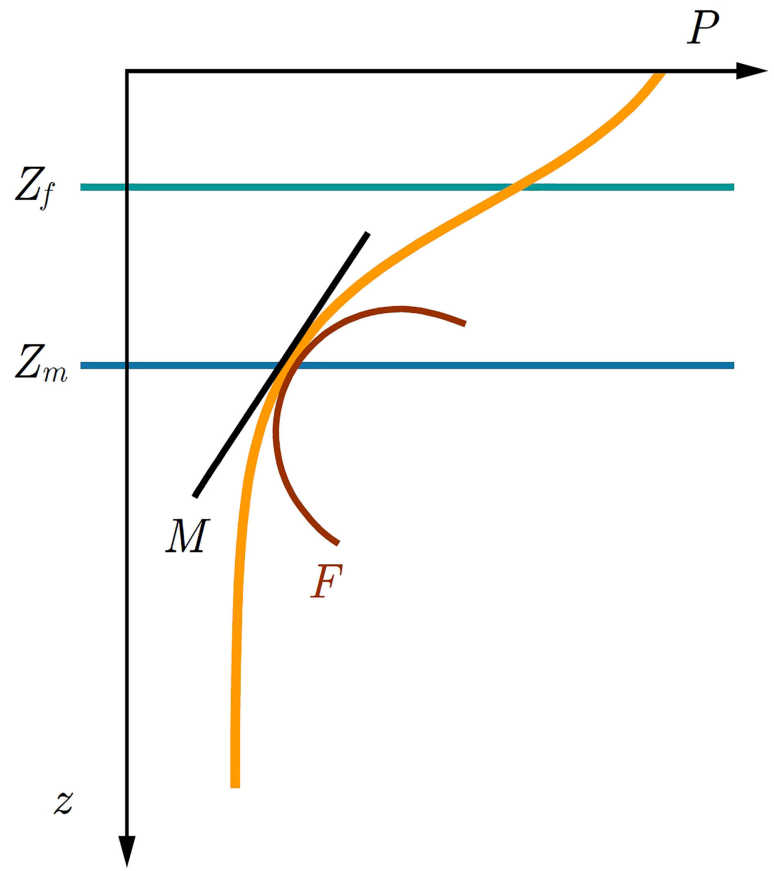


FIGURE 3
Graphical representation of marginal mixed-layer production and mixed-layer production fragility. Orange curve represents average mixed-layer production $\langle P\rangle_{Z_m,T}$ as a function of depth (23). For a given mixed-layer depth Z_m (blue line) marginal production M_Z equals the first derivative of $\langle P\rangle_{Z_m,T}$ with respect to Z_m and is indicated by the tangent (black line) and fragility is indicated by the curvature (red curve). Above Z_f (green line) the system is fragile, whereas below it the system is antifragile. Graphically, Z_f corresponds to the inflexion point and satisfies condition (31).

We first quantified marginal watercolumn production M_I and watercolumn production fragility F_I, as derived in (17) and (20), respectively. The obtained values of M_I and F_I are shown in Figure 4 for both HOT and BATS. As expected, marginal watercolumn production is positive, whereas watercolumn fragility is negative. We then fitted the obtained values of F_I as a function of M_I. For HOT we obtained F_I=2.02−7.7M_I and for BATS F_I=2.05−9.1M_I. These relations help to quantify fragility from the knowledge of marginal production, which, following (17), can be computed from measurements of surface production, surface irradiance and the attenuation coefficient. Therefore, watercolumn fragility, as defined in (19), can be estimated from routine measurements for stations with a rich data archive, such as HOT and BATS.

The estimated values of marginal mixed-layer production M_Z and mixed-layer production fragility F_Z, as derived in (26) and (28), are shown in Figure 5 for both HOT and BATS. As expected, following (25), marginal mixed-layer production is negative, whereas mixed-layer production fragility can be both negative or positive. This implies that at both stations primary production crosses the fragility tipping point as defined in (31). Histograms of Z_f are also shown in Figure 5. For HOT average Z_f equals 65 m with the standard deviation of 18 m. For BATS average Z_f equals 54 m with the standard deviation of 18 m. However, estimating marginal production and fragility from data only provides an insight into the instantaneous state of the system at the time of measurement. In order to provide a broader dynamical picture we now proceed to discuss how these concepts fit into a dynamical framework.

4 Dynamics

In order to demonstrate the effect of fragility on phytoplankton dynamics we place it in a dynamical context. Consider phytoplankton biomass in the mixed layer governed by the following equation (Platt et al., 2003a):

$$B(t+1) = B(t) + \frac{1}{\chi}\langle P\rangle_{Z_m,T} - L^B B(t) \tag{32}$$

where χ is the carbon-to-chlorophyll ratio and L^B is a generalized loss term. Time is discrete and $B(t)$ marks biomass on day t=1,2,…N, where N is the simulation run time. We also include the effect of shading on the attenuation coefficient:

$$K(t) = K_w + k_B B(t) \tag{33}$$

where K_w is the attenuation coefficient of sea water and k_B is the specific attenuation coefficient of phytoplankton (Kirk, 2011). *Via* (33) a bio-optical feedback is in effect, whereby increased biomass reduces light penetration, affecting mixed-layer production (23) and vice versa. Full list of parameters, their respective units and values used is provided in Table 1. We note that these values are not representative of HOT and BATS, but are based on previous literature values (Platt et al., 2003b; Edwards et al., 2004; Kovač et al., 2020) and serve to demonstrate the dynamical consequences of the introduced concepts *via* simulations. The code provided in the Supplementary material can be used to change parameter values and further explore the parameter space.

The solution to this equation is either a trivial steady state biomass B^*=0, when the loss term dominates, or a non-trivial steady state biomass B^*>0, when the bio-optical feedback limits phytoplankton growth (Platt et al., 2003a; Edwards et al., 2004). At the non-trivial steady state production equals losses and therefore the critical depth, which by definition is the depth at which vertically integrated production equals losses (Sverdrup, 1953; Kovač et al., 2021), equals the mixed-layer depth. Upon mixed-layer depth change, the critical depth starts converging to the new mixed-layer depth, accompanied with a corresponding change in biomass, which now converges to the new steady state (Platt et al., 2003a; Edwards et al., 2004; Kovač et al., 2020).

However, this holds in a scenario where it is assumed that surface irradiance and mixed-layer depth are slowly varying in comparison to the growth rate of phytoplankton. Under these assumptions the phytoplankton have time to adjust to the new state after being perturbed, a condition that is hardly ever fulfilled in the real ocean, where variability in surface irradiance and mixed-layer depth is ever present. To take into account this variability, we model both surface irradiance and mixed-layer depth as random variables with a well-defined mean and normally distributed fluctuations. By doing so we explore the extent to which the notion of fragility is useful in explaining the response to rapid fluctuations. We expect that irradiance variability will induce unfavourable effects for phytoplankton biomass due to fragility (21). We also expect that mixed-layer variability could induce both favourable and unfavourable effects due to fragility and antifragility, indicated by (29) and (30).

4.1 Surface irradiance

To demonstrate these effects let us first consider surface irradiance of the form:

$$I_0^m(t) = I_0^m + \delta I_0^m \tag{34}$$

where $I_0^m$is the average surface noon irradiance and $\delta I_0^m$is a normally distributed random variable with zero mean and standard deviation σ_I. Mixed-layer depth is held constant in order to first study the effect of surface irradiance variability. By integrating surface irradiance over time we get the average total received energy at the surface as:

$$E = I_0^m T \tag{35}$$

TABLE 1 Parameters and their typical values used in simulations.

Parameter	Symbol	Range	Unit
Average surface noon irradiance	$\langle I_0^m \rangle$	200 - 350	W m^{-2}
Standard deviation of noon irradiance	σ_I	0 - 100	W m^{-2}
Average mixed-layer depth	$\langle Z_m \rangle$	10 - 300	m
Standard deviation of mixed-layer depth	σ_Z	0 - 100	m
Attenuation coefficient	K	0.04	m^{-1}
Specific attenuation by chlorophyll	k_B	0.015	m^2 (mg Chl)$^{-1}$
Initial slope	a^B	0.05 - 0.5	mg C m^2 (mg ChlW h)$^{-1}$
Assimilation number	P_m^B	1 - 10	mg C (mg Chl h)$^{-1}$
Loss rate	L^B	0.05 - 0.25	h^{-1}
Half-saturation constant	N_k	1 - 10	mg N m^{-3}
Deep water nutrient concentration	N_0	50	mg N m^{-3}
Carbon-to-chlorophyll ratio	χ	50-150	mg C (mg Chl)$^{-1}$
Nitrogen-to-chlorophyll ratio	ν	8	mg C (mg Chl)$^{-1}$

where T is the interval of integration. Considering that the average total received energy is independent of the variability in surface irradiance one would naturally assume that the total realized production and therefore biomass would also be independent of the variably in surface irradiance. However, this is not the case.

Due to the non linear response of production to light, variability in surface irradiance acts to reduce the average realized biomass in the mixed layer, from what would otherwise result due to constant surface irradiance. In Figure 6 we provide an example model run to demonstrate this effect. Therefore, although on average the total received energy is the same, the realized biomass is not, demonstrating that primary production is indeed fragile with respect to surface irradiance (21). As the variability in surface irradiance σ_I increases, biomass declines still further.

4.2 Mixed-layer depth

We now proceed to investigate fragility due to mixed-layer variability. In contrast to fragility due to irradiance variability, there are two possibilities: the system may be fragile or antifragile. We first provide an idealized case where deepening does not dilute mixed layer biomass. This is a reasonable assumption for the regions of the ocean with a deep chlorophyll maximum. Following the same procedure as for exploring the effect of the surface irradiance, we consider mixed-layer depth of the form:

$$Z_m(t) = Z_m + \delta Z_m \tag{36}$$

where Z_m is the average mixed-layer depth and δZ_m is a normally distributed random variable with zero mean and standard deviation σ_Z . Surface irradiance is kept constant. In Figure 6 we provide an example model run where the average mixed-layer depth is greater than the fragility depth $Z_m > Z_f$ (red histogram in Figure 6), therefore the system is in the antifragile state. As expected we notice an increase in biomass, from what would otherwise be obtained under constant mixed-layer depth.

To further explore the effect mixed-layer fragility has on biomass dynamics we extend equation (32) to include dilution as a consequence of mixed-layer deepening:

$$B(t+1) = \left[B(t) + \frac{1}{\chi} P_{Z_m,T} - L^B B(t) \right] \frac{Z_m(t)}{Z_m(t+1)} \tag{37}$$

Dilution takes place in regions of the ocean where biomass is low below the mixed-layer. Here we set it equal to zero, to represent unfavourable growth conditions, a common assumption in the models of mixed layer dynamics (Edwards et al., 2004; Behrenfeld and Boss, 2014). Therefore, equation (32) holds for mixed-layer shallowing, whereas equation (37) holds for mixed-layer deepening. As the mixed-layer depth varies over time the system description alternates between these two equations.

During deepening there are two effects which work in unison to reduce biomass: dilution and production reduction due to reduced irradiance (caused by deepening under constant surface irradiance). During shallowing the production increase (due to increased average irradiance) acts to counterbalance the prior two effects. Results from an example model run are provided in Figure 6. In the figure we observe a biomass drop from a steady state value it would have otherwise achieved under constant or variable mixed-layer depth.

4.3 Nutrient concentration

To further investigate the dynamical effects of fragility on biomass and production we explicitly model the dependence of production on nutrients. Average mixed-layer production now becomes:

$$\langle P\rangle_{Z_m,T} = \frac{N}{N+N_k}\frac{BP_m^B D}{KZ_m}\left[f(I_0^m) - f(I_\star^m e^{-KZ_m})\right] \quad (38)$$

where N stands for nutrients and N_k is the half-saturation constant for nutrient limitation (Kovač et al., 2020).We also explicitly model nutrient concentration $N(t)$ during shallowing as:

$$N(t+1) = N(t) - \frac{\nu}{\chi}\langle P\rangle_{Z_m,T} \quad (39)$$

where ν is the nitrogen-to-chlorophyll ratio. During deepening, mixed-layer nutrient concentration increases due to entrainment and we have:

$$N(t+1) = N(t) - \frac{\nu}{\chi}\langle P\rangle_{Z_m,T}\frac{Z_m(t)}{Z_m(t+1)} + (N_0 - N(t))\left(1 - \frac{Z_m(t)}{Z_m(t+1)}\right) \quad (40)$$

where N_0 is the deep water nutrient pool. Therefore when $Z_m(t+1)<Z_m(t)$ we employ (32) and (39), whereas when $Z_m(t+1)>Z_m(t)$ we employ (37) and (40).

In Figure 6 we provide results from an example model run where the effects of biomass dilution and nutrient enrichment due to mixed-layer deepening are both taken into account. Now, deepening has an additional effect on average mixed-layer production: potential increase in production due to increased nutrients. This effect will manifest itself if the mixed-layer system is in a nutrient-limited state. In Figure 6 we observe an increase in biomass from what is observed under no nutrient limitation.

4.4 Seasonal cycle

So far we have analysed the response to variability in surface irradiance and mixed-layer depth, modelled by (34) and (36) around fixed mean values for both quantities. We next explore the effect of a seasonal cycle. We wish to investigate the change in dynamics resulting from crossing the fragility depth Z_f, which may occur sometime during the seasonal cycle. To model the crossing of Z_f we assume an annual cycle of mixed-layer depth with superimposed stochastic variability, of the form:

$$Z_m(t) = Z_m^0 + Z_m^a\cos(2\pi t/365) + \delta Z_m(t) \quad (41)$$

where now $Z_m^a$is the amplitude of the mixed-layer seasonal cycle. All other variables are the same as in (36). Likewise, for surface irradiance we assume:

$$I_0^m(t) = I_0^m + I_0^a\cos(2\pi t/365) + \delta I_m^0 \quad (42)$$

where now $I_0^a$is the amplitude of the surface irradiance seasonal cycle. Again, all other variables are the same as in (34).

A series of simulations of the seasonal cycle were performed. The model was run for up to 100 seasonal cycles. A typical result is provided in Figure 7, whereas longer model runs are provided in the Supplement. After the start of the simulation biomass quickly becomes phase locked to the seasonal cycle, dictated by mixed-layer depth and surface irradiance.,

However, the seasonal cycle in biomass becomes distorted as soon as the mixed-layer depth crosses the fragility depth (red arrow in Figure 7). The system entered the fragile regime at this point. The distortion is noticed as a drop in biomass over time (black arrow in Figure 7), which lasts until the system exits the fragile regime, which occurs when the mixed-layer depth becomes deeper than the fragility depth once again (orange arrow in Figure 7). The red and orange arrows only indicate the first and final times when F_z is negative and should not be confused with exact timing of the changes in system state due to stochastic variability in the variables. Although the variability in mixed-layer depth is constant over time it is amplified during the fragile regime, which is manifested in higher biomass variability. Mixed-layer fragility F_Z, defined in (27), correctly predicts the timing of this change in dynamics, namely by changing sign (Figure 7), highlighting that fragility is a good measure for quantifying these changes.

We also observe that nutrient concentration remains high, but production and subsequently biomass decline (see Supplement), highlighting that the system naturally tends to a high nutrient low chlorophyll state, something that was also observed prior by Platt et al. (2003a) and Edwards et al. (2004). The production cycle also becomes distorted and acquires multiple seasonal peaks (see Supplement).

We wish to stress that during the whole model run the critical depth criterion is met, yet we notice a decline in biomass as a response to mixed-layer depth variability. This is a manifestation of fragility. In the beginning of the simulation mixed-layer depth is deeper than the fragility depth and the system is in an antifragile state with respect to mixed-layer variability. Therefore, after shallowing the relative gain in biomass can compensate the loss due to dilution from prior deepening and consequently biomass increases over time. Once the mixed-layer depth comes close to, or shallower than the fragility depth, the relative gain from shallowing can no longer compensate the loss from deepening and consequently biomass declines over time. The system entered the fragile state. Perhaps counter-intuitively, whilst the critical depth criterion is met the biomass can still decline due to fragility.

5 Discussion

The ocean ecosystem provides numerous societal services which are now under threat due to climate change (Henson et al., 2021). The socioeconomic value of the ocean ecosystem rests largely on the shoulders of phytoplankton primary production, the basis of the oceanic food web, which at present is estimated at 50 giga tons of carbon per year globally

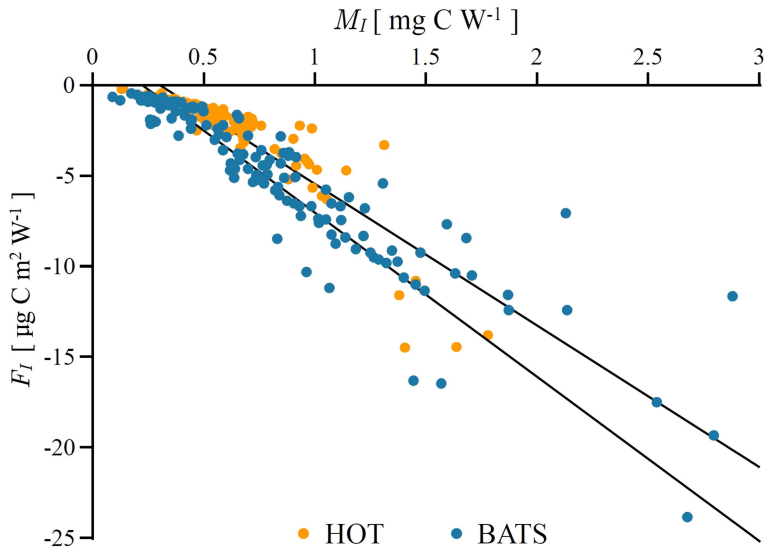


FIGURE 4
Marginal watercolumn production M_I and watercolumn production fragility F_I, as defined in (11) and (19), estimated from *in situ* data at Bermuda Atlantic Time-Series Study (blue dots) and Hawaii Ocean Time Series (orange dots). Black lines give a linear fit of F_I as a function of M_I for each station. All points are fragile implying variability in surface irradiance acts to suppresses biomass and production.

(Kulk et al., 2020; Kulk et al., 2021). The carbon assimilated in photosynthesis is transferred up the food chain, supporting fisheries, which consequently support the ever growing human population with food.

A sobering reminder that the consequences of changes in ecosystem functioning are not limited to the biological component of ecosystems alone and have socio-economical repercussions, are the crashes of Peruvian anchoveta and cod in Canada, which serve as stark reminders of the interplay between the ocean and the economy (Pauly et al., 2002). Arguably, if we are to build a sustainable blue economy, that keeps providing welfare to society, we should venture into thinking about phytoplankton as a productive system in an economic way and use the available economic theory to our advantage. As demonstrated in this work, using the economic concept of fragility enabled us to pinpoint a previously unknown tipping point for primary production.

At present, it is considered that one of the biggest threats ocean ecosystems face is posed by climate tipping points, critical thresholds after which perturbations irreversibly alter the dynamics of the system (Lenton et al., 2008; Lenton et al., 2019). Whereas physical tipping points in the ocean have been explored theoretically for some time now (Stommel, 1961; Weijer et al., 2019), the theoretical basis for tipping points in phytoplankton photosynthesis has not been well developed thus far. The stability of phytoplankton photosynthesis as a productive system has not been questioned on a theoretical basis, although numerous studies on climate change and phytoplankton have been published: Hays et al. (2005); Falkowski and Oliver (2007); Boyce et al. (2010), to name a few. Foremost, the tipping elements themselves have not been identified for phytoplankton prior to this work.

As we have demonstrated here, primary production is fragile with respect to surface irradiance (21) and both fragile and antifragile with respect to mixed-layer depth (29, 30). Fragility with respect to surface irradiance means that for the same amount of light energy received the average realized biomass in the mixed-layer is higher when surface irradiance is constant. For variable irradiance the realized biomass is lower. This highlights the significance of the fragility concept, as it grasps this asymmetry easily. Whereas the diurnal variability in surface irradiance under clear-sky conditions is fixed for a given location and day of year, and insensitive to climate change, the light available to phytoplankton could change with changes in clouds and to a lesser extent with storms and sea-surface roughness, which are indeed likely to be modified with climate change.

Similarly, for variable mixed-layer depth the realized biomass can be both higher or lower than the biomass corresponding to the constant mixed-layer depth. Higher than average biomass is associated with antifragility and lower with fragility. Antifragility is associated with deeper mixed layers and fragility with shallower mixed layers. Therefore, we demonstrated that variability acts favourably for biomass in deeper mixed layers and unfavourably for biomass in shallower mixed layers. Again, this may seem

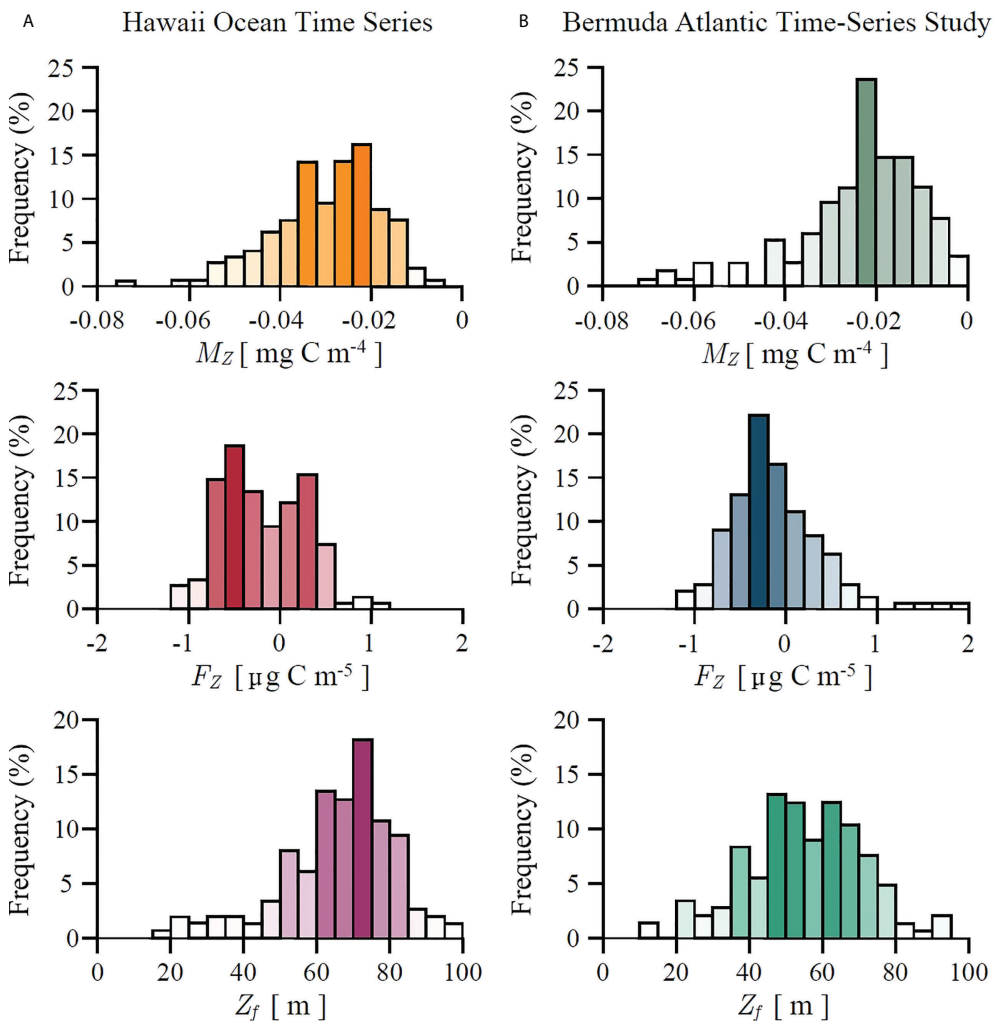


FIGURE 5
Histograms of marginal mixed-layer production M_Z, mixed-layer production fragility F_Z and fragility depth Z_f, as defined in (24), (27) and (31) respectively, estimated from *in situ* data at: **(A)** Hawaii Ocean Time Series and **(B)** Bermuda Atlantic Time-Series Study. At both stations marginal production M_Z is negative. Positive F_Z corresponds to antifragile states for which variability in mixed-layer depth acts favourably on biomass and production. Negative F_Z corresponds to fragile states for which variability in mixed-layer depth acts unfavourably on biomass and production. When the mixed-layer is shallower than Z_f the system is in a fragile state. When it is deeper than Z_f the system is in an antifragile state.

counter-intuitive, as one would expect phytoplankton to be more fragile in average low light due to greater mixed-layer depth. However, at low light any increase in light intensity is more favourable than at high light (as at low light, the photosynthetic response of phytoplankton to light available is a linear one). In economy this is the well known law of diminishing returns. Thought of it in this way the first photon is the most valuable, the second one less so, and so on.

It is important to note that although the concepts of fragility and antifragility did not come from the physical sphere, but rather from the economic one (Taleb, 2012), they were easily transferable to the biophysical models of primary production. Historically, the economic theory of capital has largely been incorporated into fisheries models for some time now (Schaefer, 1957; Clark, 1976; Clark et al., 1979). This is to be expected, since fisheries provide food and economic benefits for society. Unfortunately, the same line of reasoning has not been extended down the food web and economic theory of production has not yet been incorporated into marine primary production models. Here we have to distinguish the term primary production as used in oceanography, where it refers to carbon assimilation in phytoplankton photosynthesis, from the term production in fisheries economics, where it refers to the rate of harvesting.

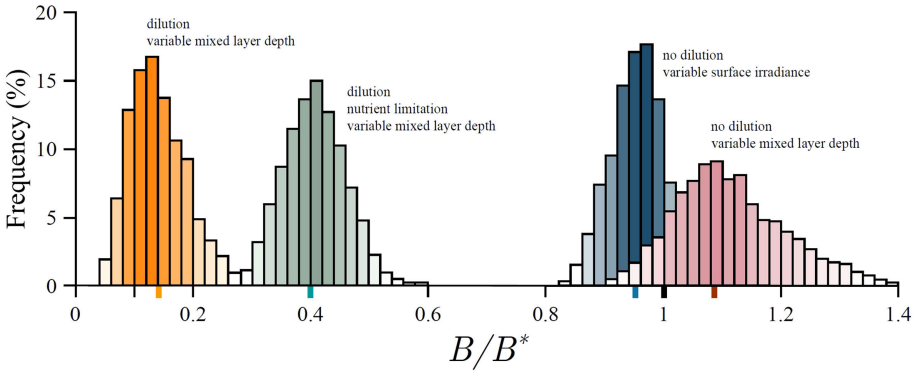


FIGURE 6
Distribution of the ratio of realized biomass B to the steady state biomass B^* for an example model run. Because of fragility biomass under variable surface irradiance (blue histogram) is on average lower (blue marker) than the steady state biomass under constant surface irradiance (black marker). In case of no dilution, and due to antifragility, biomass under variable mixed-layer depth (red histogram) is on average higher (red marker) than under constant mixed-layer depth (black marker). Taking dilution into account suppresses the biomass (orange histogram). However, taking dilution and nutrient limitation into account simultaneously raises the biomass from this suppressed state (green histogram). Average biomass for each scenario is given by the coloured marker on the abscissa. See Supplementary material for more information.

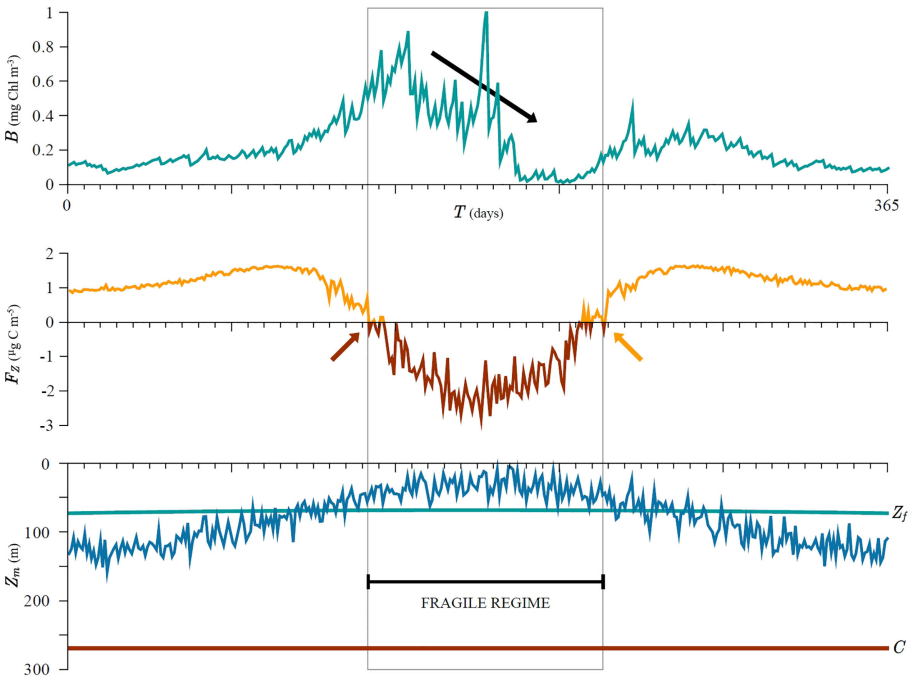


FIGURE 7
Simulated seasonal cycle of biomass, mixed layer depth and the resulting fragility. The seasonal cycle in biomass becomes distorted as soon as the mixed-layer depth (blue curve) crosses the fragility depth (green line). The distortion is noticed as a sharp drop in biomass over time (black arrow) which lasts until the system remains in the fragile state (grey area). Although the variability in mixed layer depth is constant over time it is amplified during the fragility regime and losses from dilution are harder to compensate by increased production from subsequent shallowing. The start and end of the fragility regime are correctly predicted as F_Z becomes negative and vice versa (orange and red curves/arrows). The critical depth C (red line) is deeper than the mixed-layer depth Z_m (blue curve) during the entire simulation, therefore the critical depth criterion is satisfied. See Supplementary material for more information.

Another more important distinction is the usage of theoretical terms in model structure. Economic theory as thus far used in fisheries literature augmented the biological theory by providing additional constraints and information on the optimal control of fisheries (Munro, 1992). In our work we have used economic insight to study a fundamental property of primary production in the pelagic ecosystem, namely fragility. The fragility property was hidden in the fundamental equations of primary production models, which rest on the photosynthesis light relation, represented by the photosyntehsis irradiance function (Platt and Jassby, 1976). It is at the level of the photosynthesis irradiance function that bio-physical coupling arises and consequently permeates to the ecosystem level by making watercolumn production either fragile or antifragile. Mathematically, the basic equations are non-autonomous and non-linear with respect to light which in turn makes these fragility effects possible.

Prior to this work fragility was an unrecognised property of marine primary production. Historically, stability of phytoplankton was viewed mostly through the lens of the Critical Depth Hypothesis (Lindeman and St. John, 2014; Sathyendranath et al., 2015; Behrenfeld and Boss, 2018). At its heart the Critical Depth Hypothesis, as mathematically formulated by Sverdrup (1953), asserts that mixed-layer phytoplankton biomass is sustainable if the critical depth surpasses the mixed-layer depth and vice versa (Figure 8). In their work Platt et al. (2003a) and Edwards et al. (2004) recognized the convergence of the critical depth to the mixed-layer depth and consequential suppression of biomass under stochastic forcing, which was stated as a potential explanation of the high nutrient low chlorophyll regions of the ocean. However, they only used two mixed-layer depths which consequently produced two steady states in biomass, a shallow and a deep state, and the system alternated between the two. Due to the bio-optical feedback the critical depth converged onto each mixed-layer depth and by doing so the biomass converged onto a steady state biomass. The deeper the mixed-layer the lower the biomass.

Recently, Kovač et al. (2021) extended the Critical Depth Theory by redefining the critical depth as either: optically uncoupled critical depth C (phytoplankton shading not taken into account) and optically coupled critical depth S (phytoplankton shading taken into account). Kovač et al. (2021) demonstrated that the condition $C>Z_m$ is necessary for the mixed-layer biomass to be sustained (Figure 8). In a sense, the optically uncoupled critical depth defines the carrying capacity for the biomass in the mixed-layer. Having met $C>Z_m$ the sign of the growth rate is then determined by the difference between S and Z_m , with the biomass converging onto a steady state $B^{\star}$. However, upon adding perturbations in the form of δZ_m the picture changes, as now the steady state biomass is either increased or suppressed, depending on the difference between Z_m and Z_f , where we recognize Z_f as a new depth horizon defined in (31). For mixed layers deeper than Z_f fragility acts favourably, whereas for mixed layers shallower than Z_f variability acts unfavourably. Below the fragility depth and above the optically uncoupled critical depth primary production can be sustained and is antifragile to perturbations in the mixed-layer depth (Figure 8).

Therefore, we conclude there is an optimal zone for the phytoplankton to thrive. If the mixed-layer depth is greater than the tipping depth and shallower than the optically uncoupled critical depth, variability acts favourably on primary production and consequently biomass. If the mixed-layer depth is shallower than the tipping depth, variability acts unfavourably on primary production and consequently biomass, regardless of the fact that it is shallower than the optically uncoupled critical depth. Even though the critical depth criterion is met, biomass can be suppressed due to variability in mixed-layer depth. Sverdrup's critical depth criterion remains a necessary condition for initiation of phytoplankton blooms. However, it may not be a sufficient condition, as noted by Platt et al. (1991). Fragility arising from fluctuations in the light or nutrient field would add an additional argument in support of that statement.

We should stress that this behaviour would not have been observed if we had not used a non-linear production light relationship, such as (9). If a linear production light relationship of the form $p^B(I)=\alpha^B I$ was used, the model would display neither fragile nor antifragile behaviour with respect to surface irradiance, since it would respond linearly to surface irradiance. It would however display only antifragility with respect to mixed-layer depth, the reason being that the average mixed-layer production is a positively curved strictly declining function of depth for a linear photosynthesis irradiance function and therefore does not exhibit fragility, but only antifragility. In this case the fragility depth Z_f equals zero. This implies mixed-layer production fragility is a consequence of production saturation. Therefore, when modelling photosynthesis it is important to use a proper description of the photosynthesis-light relationship, as the effect of fragility will only manifest in the case of a saturating photosynthesis irradiance function.

Other important aspects that were not taken into account are photoinhibition and photoadaptation. In case of photoinhibiton the condition of marginal production being positive (5) would cease to hold after certain light intensities. This would split the photosynthesis irradiance function into two regimes: fragile and antifragile. However, in the ocean photoinhibition takes place close to the surface and in most waters does not have a strong effect on total watercolumn production. Similarly, photoadaptation should also have an effect on marginal production and fragility, as due to photoadaptation phytoplankton may alter its photosynthesis parameters to adapt to the ambient light, and therefore directly change the magnitude of marginal production and fragility. Exploring the

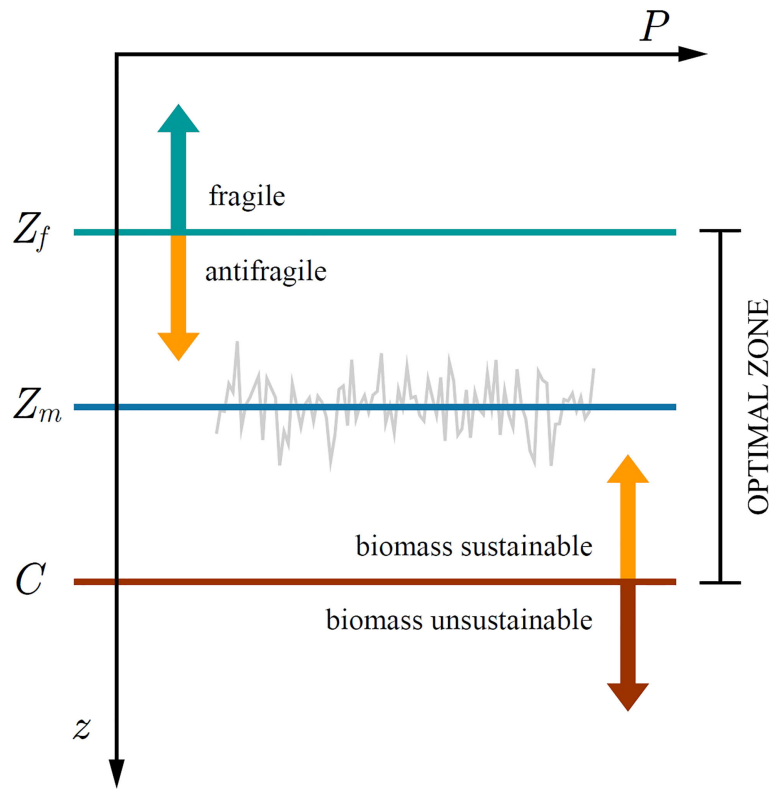


FIGURE 8
Illustration of the optimal zone for phytoplankton growth. At steady state the critical depth S converges onto the mixed layer depth Z_m. Below the optically uncoupled critical depth C biomass is unsustainable, whereas above C it is sustainable. Above the fragility depth Z_f phytoplankton biomass is suppressed from mixed-layer variability, whereas below Z_f it is increased. In the depth range from Z_f up to C phytoplankton can both be sustained and is antifragile to variability in mixed-layer depth.

effect of photoinhibition and photoadaptation on fragility is straightforward mathematically in the framework presented in this work. Both are plausible courses for future research.

6 Conclusions

The theory of ocean primary production has to a large extent survived untouched by the economic theory of production. As demonstrated in this paper, economic consideration of fragility has landed on fertile grounds in case of primary production. An economic concept of antifragility (Taleb, 2012) provided new insight into the biophysical system dynamics and revealed nuanced stability properties of phytoplankton photosynthesis. Going further, the economic theory of production and the biophysical theory of ocean primary production could benefit from stronger exchange of ideas, primarily with the goal of ocean conservation. Great care must be directed towards not flipping ocean primary production into a fragile regime and we must be careful that in our pursuit of a sustainable economy we do not make oceanic production, the base of oceanic economy, unsustainable due to our lack of knowledge about the system. The response of primary production to environmental perturbations needs to be explored in more detail and placed on firmer theoretical grounds if we are to understand the threats faced by the pelagic ecosystem in the near future. With this respect, investigating the differences between fragile and antifragile states at HOT and BATS would be a potential course for future research.

Data availability statement

Publicly available datasets were analyzed in this study. This data can be found here: https://hahana.soest.hawaii.edu/hot/hot-dogs/interface.html http://www.oceancolor.ucsb.edu/bbop

Author contributions

ŽK had the original idea. ŽK and SS formulated the mathematical model. ŽK derived the analytical expressions and implemented the model on the data sets. ŽK and SS wrote the original draft, both provided critical reviews and commentary on the draft, and wrote the final manuscript. All authors contributed to the article and approved the submitted version.

Funding

This work was supported by the Simons Collaboration on Computational Biogeochemical Modeling of Marine Ecosystems/CBIOMES (549947). This work is also a contribution to the Ocean-Colour Climate Change Initiative (OC-CCI) and the Biological Pump and Carbon Export Processes (BICEP) project of the European Space Agency. This work is a part of the activities of the National Centre for Earth Observations of the Natural Environmental Research council of the UK. This work has been supported in part by Croatian Science Foundation under the project MAUD (9849).

Conflict of interest

The authors declare that the research was conducted in the absence of any commercial or financial relationships that could be construed as a potential conflict of interest.

Publisher's note

All claims expressed in this article are solely those of the authors and do not necessarily represent those of their affiliated organizations, or those of the publisher, the editors and the reviewers. Any product that may be evaluated in this article, or claim that may be made by its manufacturer, is not guaranteed or endorsed by the publisher.

Supplementary material

The Supplementary Material for this article can be found online at: https://www.frontiersin.org/articles/10.3389/fmars.2022.963395/full#supplementary-material

References

Acemoglu, D. (2009). *Introduction to modern economic growth. 1st ed* (New Jersey, USA:University Press).

Behrenfeld, M. J., and Boss, E. S. (2014). Resurrecting the ecological underpinnings of ocean plankton blooms. *Annu. Rev. Mar. Sci.* 6, 167–194. doi: 10.1146/annurev-marine-052913-021325

Behrenfeld, M. J., and Boss, E. S. (2018). Student's tutorial on bloom hypotheses in the context of phytoplankton annual cycles. *Global Change Biol.* 24, 55–77. doi: 10.1111/gcb.13858

Boyce, D. G., Lewis, M. R., and Worm, B. (2010). Global phytoplankton decline over the past century. *Nature* 466, 591–596. doi: 10.1038/nature09268

Clark, C. W. (1976). *Mathematical bioeconomics* (New Jersey, USA:Wiley-Interscience).

Clark, C. W., Clarke, F. H., and Munro, G. R. (1979). The optimal exploitation of renewable resource stocks: Problems of irreversible investment. *Econometrica* 47 (1), 25–47. doi: 10.2307/1912344

Clark, C. W., and Munro, G. R. (1975). The economics of fishing and modern capital theory: A simplified approach. *J. Environ. Economics Manage.* 2, 92–106. doi: 10.1016/0095-0696(75)90002-9

Da, N., Foltz, G. R., and Balaguru, K. (2021). Observed global increases in tropical cyclone-induced ocean cooling and primary production. *Geophys. Res. Lett.* 48, e2021GL092574. doi: 10.1029/2021GL092574

Edwards, A. E., Platt, T., and Sathyendranath, S. (2004). The high-nutrient, low-chlorophyll regime of the ocean: limits on biomass and nitrate before and after iron enrichment. *Ecol. Model.* 171, 103–125. doi: 10.1016/j.ecolmodel.2003.06.001

Falkowski, P. G., and Oliver, M. J. (2007). The power of plankton. *Nat. Rev. Microbiol.* 5, 813–819. doi: 10.1038/nrmicro1751

Franks, P. J. S. (2015). Has sverdrup's critical depth hypothesis been tested? mixed layers vs. turbulent layers. *ICES J. Mar. Sci.* 72, 1897–1907. doi: 10.1093/icesjms/fsu175

Frölicher, T., Rodgers, K. B., Stock, C. A., and Ceung, W. W. L. (2016). Sources of uncertainties in 21st century projections of potential ocean ecosystem stressors. *Global Biogeochem. Cycles* 30, 1224–1243. doi: 10.1002/2015GB005338

Hays, G., Richardson, A. J., and Robinson, C. (2005). Climate change and marine plankton. *Trends Ecol. Evol.* 20 (6), 337–344. doi: 10.1016/j.tree.2005.03.004

Henson, S. A., Cael, B. B., Allen, S. R., and Dutkiewicz, S. (2021). Future phytoplankton diversity in a changing climate. *Nat. Commun.* 12, 5372. doi: 10.1038/s41467-021-25699-w

Jackson, T., Sathyendranath, S., and Platt, T. (2017). An exact solution for modeling photoacclimation of the carbon-to-chlorophyll ratio in phytoplankton. *Front. Mar. Sci.* 4, 283. doi: 10.3389/fmars.2017.00283

Jassby, A. D., and Platt, T. (1976). Mathematical formulation of the relationship between photosynthesis and light for phytoplankton. *Limnol. Oceanogr.* 21, 540–547. doi: 10.4319/lo.1976.21.4.0540

Jones, C. T., Craig, S. E., Barnett, A. B., MacIntyre, H. L., and Cullen, J. J. (2014). Curvature in models of the photosynthesis-irradiance response. *J. Phycol.* 50, 341–355. doi: 10.1111/jpy.12164

Kirk, J. T. O. (2011). *Light and photosynthesis in quatic ecosystems. 3rd ed* (Cambridge, UK:Cambridge University Press).

Kovač, Ž., Platt, T., S., S., and Antunović, S. (2017). Models for estimating photosynthesis parameters from *in situ* production profiles. *Prog. Oceanogr.* 159, 255-266. doi: 10.1016/j.pocean.2017.10.013

Kovač, Ž., Platt, T., and Sathyendranath, S. (2020). Stability and resilience in a nutrient-phytoplankton marine ecosystem model. *ICES J. Mar. Sci.* 77 (4), 1556–1572. doi: 10.1093/icesjms/fsaa067

Kovač, Ž., Platt, T., and Sathyendranath, S. (2021). Sverdrup meets lambert: analytical solution for sverdrup's critical depth. *ICES J. Mar. Sci. fsab013*, 78(4), 1398-1408. doi: 10.1093/icesjms/fsab013

Kovač, Ž., Platt, T., Sathyendranath, S., Morović, M., and Jackson, T. (2016b). Recovery of photosynthesis parameters from *in situ* profiles of phytoplankton production. *ICES J. Mar. Sci.* 73 (2), 275–285. doi: 10.1093/icesjms/fsv204

Kovač, Ž., Platt, T., Sathyendranath, S., Morović, M., and Lomas, M. W. (2018). Extraction of photosynthesis parameters from time series measurements of *in situ* production: Bermuda atlantic time-series study. *Remote Sens.* 10, 1–23. doi: 10.3390/rs10060915

Kovač, Ž., Platt, T., S., S., and Morović, M. (2016a). Analytical solution for the vertical profile of daily production in the ocean. *J. Geophys. Res.: Oceans* 121. doi: 10.1002/2015JC011293

Kulk, G., Platt, T., Dingle, J., Jackson, T., Johnsson, B., Bouman, H. A., et al. (2020). Primary production, an index of climate change in the ocean: Satellite-based estimates over two decades. *Remote Sens.* 12 (5), 826. doi: 10.3390/rs12050826

Kulk, G., Platt, T., Dingle, J., Jackson, T., Johnsson, B., Bouman, H. A., et al. (2021). Correction: Primary production, an index of climate change in the ocean: Satellite-based estimates over two decades. *Remote Sens.* 13 (17), 3462.

Kwiatkowski, L., Torres, O., Bopp, L., Aumont, O., Chamberlain, M., Christian, J. R., et al. (2020). Twenty-first century ocean warming, acidification, deoxygenation, and upper-ocean nutrient and primary production decline from cmip6 model projections. *Biogeosciences* 17, 3439–3470. doi: 10.5194/bg-17-3439-2020

Laufkötter, C., Vogt, M., Gruber, N., Aita-Noguchi, M., Aumont, O., Bopp, L., et al. (2015). Drivers and uncertainties of future global marine primary production in marine ecosystem models. *Biogeosciences* 12, 6955–6984. doi: 10.5194/bg-12-6955-2015

Lenton, T. M., Held, H., Kriegler, E., Hall, J. W., Lucht, W., Rahmstorf, S., et al. (2008). Tipping elements in the earth's climate system. *Proc. Natl. Acad. Sci.* 105, 1786–1793. doi: 10.1073/pnas.0705414105

Lenton, T., Rockstrom, J., Gaffney, O., Rahmstorf, S., Richardson, K., Steffen, W., et al. (2019). Climate tipping points - too risky to bet against. *Nature* 575, 592–595. doi: 10.1038/d41586-019-03595-0

Lindeman, C., and St. John, M. A. (2014). A seasonal diary of phytoplankton in the north atlantic. *Front. Mar. Sci.* 1 (37), 1–6. doi: 10.3389/fmars.2014.00037

Longhurst, A., Sathyendranath, S., and Platt, T. (1995). An estimate of global primary production in the ocean from satellite radiometer data. *J. Plankton Res.* 17, 1245–1271. doi: 10.1093/plankt/17.6.1245

Munro, G. R. (1992). Mathematical bioeconomics and the evolution of modern fisheries economics. *Bull. Math. Biol.* 54 (2/3), 163–184. doi: 10.1016/S0092-8240(05)80021-7

Pauly, D., Christensen, V., Guenette, S., Pitcher, T. J., Sumila, U. R., Walters, C. J., et al. (2002). Towards sustainability in world fisheries. *Nature* 418, 689–695. doi: 10.1038/nature01017

Perman, R., Ma, Y., Common, M., Maddison, D., and McGilvray, J. (2011). *Natural resource and environmental economics. 4th ed* (Gosport, UK:Pearson Education Limited).

Platt, T., Bird, D. F., and Sathyendranath, S. (1991). Critical depth and marine primary production. *Proc. R. Soc. B* 246, 205–217. doi: 10.1098/rspb.1991.0146

Platt, T., Broomhead, D. S., Sathyendranath, S., Edwards, A. M., and Murphy, E. J. (2003a). Phytoplankton biomass and residual nitrate in the pelagic ecosystem. *Proc. R. Soc. A* 459, 1063–1073. doi: 10.1098/rspa.2002.1079

Platt, T., Gallegos, C. L., and Harrison, W. G. (1980). Photoinhibition of photosynthesis in natural assemblages of marine phytoplankton. *J. Mar. Res.* 38, 687–701.

Platt, T., and Jassby, A. (1976). The relationship between photosynthesis and light for natural assemblages of coastal marine phytoplankton. *J. Phycol.* 12, 421–430. doi: 10.1111/j.1529-8817.1976.tb02866.x

Platt, T., and Sathyendranath, S. (1988). Oceanic primary production: Estimation by remote sensing at local and regional scales. *Science* 241, 1613–1620. doi: 10.1126/science.241.4873.1613

Platt, T., and Sathyendranath, S. (1991). Biological production models as elements of coupled, atmosphere-ocean models for climate research. *J. Geophys. Res.* 96, 2585–2592. doi: 10.1029/90JC02305

Platt, T., Sathyendranath, S., Edwards, A. M., Broomhead, D. S., and Ulloa, O. (2003b). Nitrate supply and demand in the mixed layer of the ocean. *Mar. Ecol. Prog. Ser.* 254, 3–9. doi: 10.3354/meps254003

Platt, T., Sathyendranath, S., and Ravindran, P. (1990). Primary production by phytoplankton: Analytic solutions for daily rates per unit area of water surface. *Proc. R. Soc. B* 241, 101–111. doi: 10.1098/rspb.1990.0072

Platt, T., Sythyendranath, S., White, G. N., Jackson, T., Saux Picart, S., and Bouman, H. (2017). Primary production: Sensitivity to surface irradiance and implications for archiving data. *Front. Mar. Sci.* 4, 387. doi: 10.3389/fmars.2017.00387

Regaudie-de Gioux, A., Lasternas, S., Agusti, S., and Duarte, C. M. (2014). Comparing marine primary production estimates through different methods and development of conversion equations. *Front. Mar. Sci.* 19), 1–14. doi: 10.3389/fmars.2014.00019

Richmond, P., Mimkes, J., and Hutzler, S. (2013). *Econophysics and physical economics. 1st ed* (Oxford University Press).

Sathyedranath, S., Longhurst, A., Caverhill, C. M., and Platt, T. (1995). Regionally and seasonally differentiated primary production in the north Atlantic. *Deep Sea Res. 1* 42, 1773–1802. doi: 10.1016/0967-0637(95)00059-F

Sathyendranath, S., Ji, R., and Browman, H. I. (2015). Revisiting sverdrup's critical depth hypothesis. *ICES J. Mar. Sci.* 72, 1892–1896. doi: 10.1093/icesjms/fsv110

Schaefer, M. B. (1957). Some considerations of populatiorr dynarnics and economics in relation to the managernent of the commercial fisheries. *J. Fish. Board Canada* 14 (5), 669–681. doi: 10.1139/f57-025

Stommel, H. (1961). Thermohahe convection with two stable regimes of flow. *Tellus* 13, 224–230. doi: 10.3402/tellusa.v13i2.9491

Sverdrup, H. U. (1953). On conditions for the vernal blooming of phytoplankton. *J. du Conseil Int. pour l'Exploration la Mer* 18, 287–295.

Taleb, N. N. (2012). *Antifragile: things that gain from disorder* (United States: The Random House Publishing).

Watson, W. G., and Rouusseaux, C. S. (2019). Global ocean primary production trends in the modern ocean color satellite record, (1998–2015). *Environ. Res. Lett.* 14, 124011. doi: 10.1088/1748-9326/ab4667

Weijer, W., Cheng, W., Drijfhout, S. S., Fedorov, A. V., Hu, A., Jackson, L. C., et al. (2019). Stability of the atlantic meridional overturning circulation: A review and synthesis. *J. Geophys. Res.: Oceans* 124 (8), 5336–5375. doi: 10.1029/2019JC015083

frontiers | Frontiers in Marine Science

TYPE Original Research
PUBLISHED 09 November 2022
DOI 10.3389/fmars.2022.1035399

Check for updates

OPEN ACCESS

EDITED BY
Griet Neukermans,
Ghent University, Belgium

REVIEWED BY
Márcio Silva de Souza,
Federal University of Rio Grande, Brazil
Yuqiu Wei,
Yellow Sea Fisheries Research Institute (CAFS), China

*CORRESPONDENCE
Robert J. W. Brewin
r.brewin@exeter.ac.uk

SPECIALTY SECTION
This article was submitted to Ocean Observation, a section of the journal Frontiers in Marine Science

RECEIVED 02 September 2022
ACCEPTED 10 October 2022
PUBLISHED 09 November 2022

CITATION
Maniaci G, Brewin RJW and Sathyendranath S (2022) Concentration and distribution of phytoplankton nitrogen and carbon in the Northwest Atlantic and Indian Ocean: A simple model with applications in satellite remote sensing. *Front. Mar. Sci.* 9:1035399. doi: 10.3389/fmars.2022.1035399

COPYRIGHT
© 2022 Maniaci, Brewin and Sathyendranath. This is an open-access article distributed under the terms of the Creative Commons Attribution License (CC BY). The use, distribution or reproduction in other forums is permitted, provided the original author(s) and the copyright owner(s) are credited and that the original publication in this journal is cited, in accordance with accepted academic practice. No use, distribution or reproduction is permitted which does not comply with these terms.

Concentration and distribution of phytoplankton nitrogen and carbon in the Northwest Atlantic and Indian Ocean: A simple model with applications in satellite remote sensing

Giuseppe Maniaci[1], Robert J. W. Brewin[1]* and Shubha Sathyendranath[2]

[1]College of Life and Environment Sciences, University of Exeter, Penryn, United Kingdom, [2]National Centre for Earth Observation, Plymouth Marine Laboratory, Plymouth, United Kingdom

Despite the critical role phytoplankton play in marine biogeochemical cycles, direct methods for determining the content of two key elements in natural phytoplankton samples, nitrogen (N) and carbon (C), remain difficult, and such observations are sparse. Here, we extend an existing approach to derive phytoplankton N and C indirectly from a large dataset of *in-situ* particulate N and C, and Turner fluorometric chlorophyll-a (Chl-a), gathered in the off-shore waters of the Northwest Atlantic and the Arabian Sea. This method uses quantile regression (QR) to partition particulate C and N into autotrophic and non-autotrophic fractions. Both the phytoplankton C and N estimates were combined to compute the C:N ratio. The algal contributions to total N and C increased with increasing Chl-a, whilst the C:N ratio decreased with increasing Chl-a. However, the C:N ratio remained close to the Redfield ratio over the entire Chl-a range. Five different phytoplankton taxa within the samples were identified using data from high-performance liquid chromatography pigment analysis. All algal groups had a C:N ratio higher than Redfield, but for diatoms, the ratio was closer to the Redfield ratio, whereas for *Prochlorococcus*, other cyanobacteria and green algae, the ratio was significantly higher. The model was applied to remotely-sensed estimates of Chl-a to map the geographical distribution of phytoplankton C, N, and C:N in the two regions from where the data were acquired. Estimates of phytoplankton C and N were found to be consistent with literature values, indirectly validating the approach. The work illustrates how a simple model can be used to derive information on the phytoplankton elemental composition, and be applied to remote sensing data, to map pools of elements like nitrogen, not currently provided by satellite services.

KEYWORDS

nitrogen, carbon, chlorophyll-a, Redfield, phytoplankton, satellite

Introduction

In recent years, growing attention has been drawn to unicellular phytoplankton owing to the significant role they play in global biogeochemical cycles and climate change (Falkowski, 1994; Falkowski et al., 2003; Litchman et al., 2015). By means of their photosynthetic activity, these photoautotrophic organisms produce new biomass at a faster rate than terrestrial plants. Global ocean carbon and oxygen production are largely influenced by phytoplankton metabolic processes. These efficient primary producers are not only responsible for the dynamics of food webs, but they also modulate the cycling of the most dominant biogenic elements, like carbon and nitrogen. Thus, the elemental composition of marine photoautotrophic phytoplankton has significant implications for ecosystems worldwide, as well as for the Earth's climate (Falkowski, 2012; Schoo et al., 2013; Kwiatkowski et al., 2018). Recent advances in our understanding of phytoplankton have suggested their stoichiometry is related to their spatiotemporal structure, diversity and composition, and is indicative of the quality of food availability and pathways of tropic energy transfer (Sardans et al., 2021).

The chlorophyll-a (Chl-a) concentration is widely used as a measure of the standing stock (biomass) of phytoplankton, since it is present (in one form or another) in all phytoplankton species. Chl-a can also be measured easily in the laboratory, the field, and through the remote sensing of ocean color, an efficient monitoring tool to observe synoptically surface phytoplankton distributions (Yentsch and Menzel, 1963; Phinney and Yentsch, 1985; Platt and Sathyendranath, 1988). However, there are limitations to using Chl-a as a measure of phytoplankton biomass. For example, the Chl-a concentration in phytoplankton can change independently of phytoplankton carbon biomass, through photo-acclimation (Behrenfeld et al., 2002; Jackson et al., 2017; Sathyendranath et al., 2020). Other metrics of phytoplankton biomass have been considered and used. The nitrogen (N) content in phytoplankton is often used by ecosystem modelers as a metric for phytoplankton biomass, owing to the limiting characteristic of nutrients for algal growth (Doney et al., 1996; Chai et al., 2002; Goebel et al., 2010). Alternatively, the algal content of carbon (C) is also considered a useful metric for measuring phytoplankton biomass, owing to its usually high concentration (relative to other elements) and direct links to the wider carbon cycle (Furuya, 1990; Li et al., 1993; Graff et al., 2012). However, unlike Chl-a, the phytoplankton C and N contents are notoriously challenging to measure directly in the field.

Considering that various metrics can be used for phytoplankton biomass, much effort has been invested on methods to convert among them, i.e., quantifying the C:Chl-a, N:Chl-a, and C:N ratios of phytoplankton. For field-based studies, quantifying these ratios and distinguishing between the contributions of autotrophic and non-autotrophic material (including heterotrophic and detrital contributions) to particulate organic carbon (POC) and nitrogen (PON) have been a major challenge (Eppley et al., 1992; Lü et al., 2009). As a result, available conversion factors between phytoplankton C, N and Chl-a are still imprecise and subject to significant uncertainty (Strickland, 1960; Lefèvre et al., 2003). Unavoidably, this also poses serious constraints to our understanding of the elemental stoichiometry of primary producers. The C and N cycles are, to a first order, coupled to each other at sea over large scales, as defined by the canonical Redfield ratio (Redfield, 1934). Constant ratios between phytoplankton carbon, nitrogen and Chl-a, are commonly employed in ecosystem modelling for simplicity (Karl et al., 2001; Geider and La Roche, 2002; Flynn, 2003). However, deviations in the Redfield ratio of up to 40% have been observed, with implications for model simulations of carbon and nutrient fluxes worldwide (Banse, 1977; Körtzinger et al., 2001; Moore et al., 2013). These variations highlight limits in using Redfieldian models, making it clear that better formulations are required to refine ecological models and Earth system studies (Sciandra, 1991; Dearman et al., 2003; Klausmeier et al., 2004a; Klausmeier et al., 2004b; Flynn, 2010).

Multiple methods have been proposed to distinguish and quantify the algal fractions of C and N from bulk properties in the ocean, including microscopic cell counting, flow cytometry, and x-ray microanalysis (Heldal et al., 2003; Olson et al., 2003; Llewellyn, 2004; Graff et al., 2015; Brewin et al., 2021). However, each method presents some disadvantages, and no standard approach has been established. Sathyendranath et al. (2009) developed a method of estimating the algal composition of C based on quantile regression analysis of C and Chl-a data. Building on this empirical approach, the present study infers the N:Chl-a and C:Chl-a ratios, and C:N stoichiometry of unicellular photoautotrophs in the ocean from total particulate carbon (PC), nitrogen (PN) and Chl-a field measurements, across a range of offshore environments. We use the approach to investigate the C:N ratio of multiple phytoplankton taxa and explore its applicability to satellite remote sensing, for mapping phytoplankton C, N and C:N over large spatial scales.

Material and methods

Data and study site

The dataset analyzed in this study builds on that used previously in Sathyendranath et al. (2009) to study the relationship between total PC and Chl-a. Here we extend the work to total PN and analyze its relationship with PC and Chl-a. *In-situ* total PC, PN and photosynthetic pigment data were collected on 17 cruises over a 13-year period across a variety of offshore environments in the NW Atlantic and the Arabian Sea, as shown in Figure 1. This dataset spanned a range of environmental condition, from oligotrophic to eutrophic waters

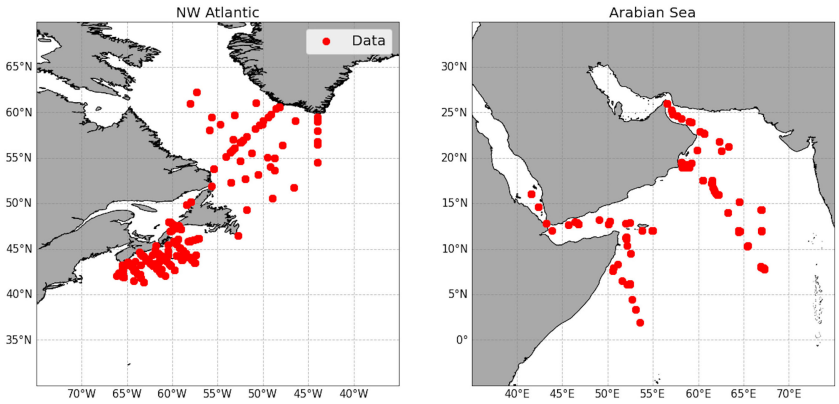


FIGURE 1
Maps of the sample collection sites for both the northwest Atlantic and the Arabian sea. Red dots indicate where the carbon and nitrogen data were located.

(Chl-a ranged from 0.07 - 14.8 mg m $^{-3}$). For further details on the different locations and times of the cruises, the reader is referred to Table 1 of Sathyendranath et al. (2009).

Water samples were collected with Niskin bottles from the euphotic zones (depth at which 99% of the surface light is absorbed) of the study sites. Over 90% of the samples were collected from <40 m below the water surface, whilst the remaining samples were from 40-80 m depth. Seawater (0.5-1.5 L) was filtered through a 25 mm GF/F filter prior to storage in liquid nitrogen at − 80 ° C (Stuart and Head, 2005). A Carbon, Hydrogen and Nitrogen (CHN) analyser was employed to derive the total PC and PN contents within the samples (Collos, 2002). These samples are expected to be composed predominantly of the particulate organic forms of C and N (i.e., POC and PON). Concentrations of Chl-a were measured using a Turner Designs fluorometer (Holm-Hansen et al., 1965) and high-performance liquid chromatography (HPLC) was adopted to derive accessory pigment compositions in addition to Chl-a. The total PC and PN compositions and Turner fluorometric Chl-a concentrations were used to compute the relationships between particulate carbon and Chl-a and particulate nitrogen and Chl-a. The elemental stoichiometry of bulk properties (e.g., PC:PN) was also estimated. The HPLC dataset was utilized as an independent set of measurements to distinguish phytoplankton functional groups dominating the samples. A fixed set of HPLC pigment criteria (as defined in Table 2 of Sathyendranath) allowed to discriminate the phytoplankton taxa present in each sample.

Statistical analysis

As evidenced above, measurements of total PC and PN can be straightforward to quantify. However, it is less practical to

TABLE 1 Parameters of the power law relationship of carbon (C) and nitrogen (N) fitted against chlorophyll-a.

Location	Y_{phy}	m	p	N	Source
Offshore	N	11.6	0.60	771	This Study
Offshore	C	83.7	0.57	773	This study
Offshore	C	64.6	0.63	831	Sathyendranath et al. (2009)*,$
North Atlantic	C	83.2	0.69	12	Buck et al. (1996)
Various locations	C	61.7	0.89	72	Marañón et al. (2014)
Global	C	72.4	0.91	451	Loisel et al. (2018)*
Southern Ocean	C	120	0.55	521	Thomalla et al. (2017)
Southern Ocean	C	42.7	0.86	521	Thomalla et al. (2017)*,$

*Values from other studies based on the QR method.
$Studies based on the QR method with samples > 500, and follow the q > 5/N criterion.
Phytoplankton estimates were produced by 1% quantile regression (QR) analyses based on *in-situ* bulk measurements (PC, PN and Chl-a). Parameters from Buck et al. (1996); Sathyendranath et al. (2009); Marañón et al. (2014); Loisel et al. (2018) and Thomalla et al. (2017) are also displayed, along with the number of data points used (N). $Y_i = m_i B^{p_i}$ is the fitted relationship. Y_{phy} is the phytoplankton N or C, m, and p are the parameters of the model.

TABLE 2 Mean with standard deviation (St. Dev.) and range of POC:PON, phytoplankton N:Chl-a, C:Chl-a, and C:N, for concurrent data on POC, PON and Chl-a.

Ratio	Mean ± St. Dev.	Range
POC:PON	7.5 ± 1.9	4.6 - 16.9
N:Chl-a	12.7 ± 4.8	4.0 - 33.3
C:Chl-a	92.9 ± 38.1	26.2 - 263.0
C:N	7.2 ± 0.3	6.6 - 7.9

derive corresponding estimates of algal and non-algal fractions from bulk measures. The approach utilized in this study, first developed by Sathyendranath et al. (2009) for use in quantifying phytoplankton C, overcomes this challenge by attempting to derive information on the elemental composition of autotrophic plankton from total particulate C and N pools over a range of Chl-a concentrations. This method builds on the notion that changes in the non-autotrophic component of suspended materials alter the elemental content of a given observation without affecting its chlorophyll levels; hence, the lowest estimate of total PC or PN of any given Chl-a observation corresponds to the phytoplanktonic contribution to that element. Specifically, the phytoplankton C and N so obtained are the upper bound, in the sense that there would always be some non-autotrophic component present in the samples, which would bias the phytoplankton C and N upwards.

Prior to analysis, the PC, PN and Turner Chl-a sets of measurements were log-transformed to linearize the relationships observed and decrease the influence of samples with high values of different C, N and Chl-a in the regressions (see also Legendre and Michaud, 1999). PC and PN were treated as dependent variables and were first analyzed by a simple least-squares regression against Turner Chl-a, following standard practice (see Buck et al., 1996; Sathyendranath et al., 2009; Marañón et al., 2014; Thomalla et al., 2017). The fitted equations for total C and N are expressed as

$$Y_i = m_i B^{p_i}, \quad (1)$$

where, Y is the predicted variable, B is Chl-a, and m and p are parameters of the power law model, and the subscript i denotes that the predicted variable (and parameters values for m and p) are either with reference to total PC or PN. The equation can be expressed in linear format in $\log_{10}$ space, as $\log_{10}(Y_i) = \log_{10}(m_i) + p_i \log10(B)$, with $\log_{10}(m_i)$ and p_i representing the intercept and slope of the linear regression, respectively.

Equation 1 was fitted using a quantile regression (QR) between the total Y_i and Chl-a (B), for both i = PC and PN. This allows the computation of a lower bound predominantly associated with the phytoplankton contribution to the element (either C or N), for a given Chl-a concentration. A 1% QR (q=0.01) was identified as the most appropriate quantile to define the lowest possible range of observations for phytoplanktonic contribution, following the $q > 5/N$ criterion (N being the number of total observations), as suggested by Rogers (1993), and considering N = 773 for C and 771 for N. This method provides an upper limit of the phytoplankton contribution to the total particulate C and N pools. The results from QR analyses for both C and N were then combined to compute changes in the C:N ratio of phytoplankton as a function of Chl-a. Uncertainties in C:N were computed by running an ensemble of simulations over the Chl-a range, varying the four parameters (slope and intercept of the C and of N equations) between their confidence intervals in every permutation, and taking the minimum and maximum values. As described above, HPLC pigment composition data were used to examine the phytoplankton types present in the samples. Thus, taxonomic groups were further exploited to compute the stoichiometry of different algal groups using the parameterized model and HPLC Chl-a as inputs.

Following an initial inspection of $\log_{10}$ scatter plots of PN and Chl-a, and PC and Chl-a, we observed that some unusual outliers in the data with surprisingly low PC and PN values for a given Chl-a concentration, relative to the entire dataset. The outliers were traced to three cruises. To avoid the influence of these discrepancies between the detected data points and the parent distribution on the subsequent investigations, samples from these three cruises were excluded from further analyses. All analyses for this study were carried out in Python and the quantile regressions were performed using the *QuantReg* package. This package estimates a QR model as a standard regression using iterative reweighted least squares. The uncertainties in the regression are also provided by default as an output from the analyses. An example Jupyter Notebook Python Script, processing the *in-situ* data and tuning the models is provided on this GitHub page (https://github.com/rjbrewin/POC-PON-Tchl-analysis).

Remote sensing data

The European Space Agency's Ocean Colour Climate Change Initiative (ESA OC-CCI, Version 5.0) data were used in this study (Sathyendranath et al., 2019). This consists of a time-series of processed (bias-corrected and merged) ocean-colour data (for more information see https://climate.esa.int). Datasets from satellite observations of ocean colour are publicly accessible from https://www.oceancolour.org. Two 8-day composite maps of Chl-a with a 4 km by 4 km spatial resolution were generated for the Northwest Atlantic and the Arabian Sea study sites, corresponding to the 10-17 June 2006 and the 22-29 March 2005, respectively. These periods were selected as relatively cloud-free (<20% cover). Satellite outputs and results from this study were combined to produce a map of Chl-a, phytoplankton C, N and C:N ratio, for the two sampling sites within the selected periods. This further application illustrates how *in-situ* data can be exploited to derive simple methods for estimations of the distribution of

phytoplankton elemental content and stoichiometry using remote sensing technology.

Results

Quantile regression

Upon regressing PC against Chl-a and PN against Chl-a from all data (see Figures 2A, D, 50% black lines), the overall correlations appeared highly significant (68% of the variation in PC was explained by Chl-a, with a P-value<0.001; 76% of the variation in PN was explained by Chl-a (P-value<0.001), and resulted in a mean conversion ratio of 211 for PC:Chl-a and 27.6 for PN:Chl-a. Slopes and intercepts between the 1% and 50% regressions were significantly different for PC (Figure 2A), with the 1% slope being steeper than the 50% slope (Figure 2C). The intercepts of the lower bound, 1%, and the upper bound, 50%, were significantly different for both PC and PN (Figures 2B, E), while a small overlap exists between the slopes of the PN regression (Figure 2F), related to larger uncertainties in the slope of the 1% quantile. The change in the slopes is such that the blue lines (1%) for both PC and PN converge towards the 50% percentile as the pigments reach higher concentrations. The slope of the 1% quantile regression for PN (0.60) was greater than that of C (0.57). The interpretation of the 1% quantile regression as being determined largely by phytoplankton C and N is consistent with the contributions of autotrophic C and N to total PC and PN increasing with Chl-a concentration, with highest contributions potentially during algal blooms conditions.

Our premise is that the 1% quantile regressions can be used to estimate phytoplankton C and N from Chl-a, using Eq. 1 and the parameters m and p (Table 1, top two entries). For phytoplankton C, the parameters (Cphyto = $83.7B^{0.57}$, where B is Chl-a, Table 1) sit within the range of values reported in the literature. Notably, the intercept (m) matches the value presented in Buck et al. (1996). For the parameters produced in the phytoplankton N analysis (Nphyto = $11.6B^{0.6}$) there are no prior results in the literature to compare with. However, estimates obtained here for the N:Chl-a ratio (Table 2) are consistent with the range of values in the literature (Yentsch and Vaccaro, 1958; Manny, 1969; Verity, 1981; Staehr et al., 2002). Therefore, confidence that this model yields reasonable estimates of phytoplankton C and N from Chl-a can be gained, considering the good agreement between model

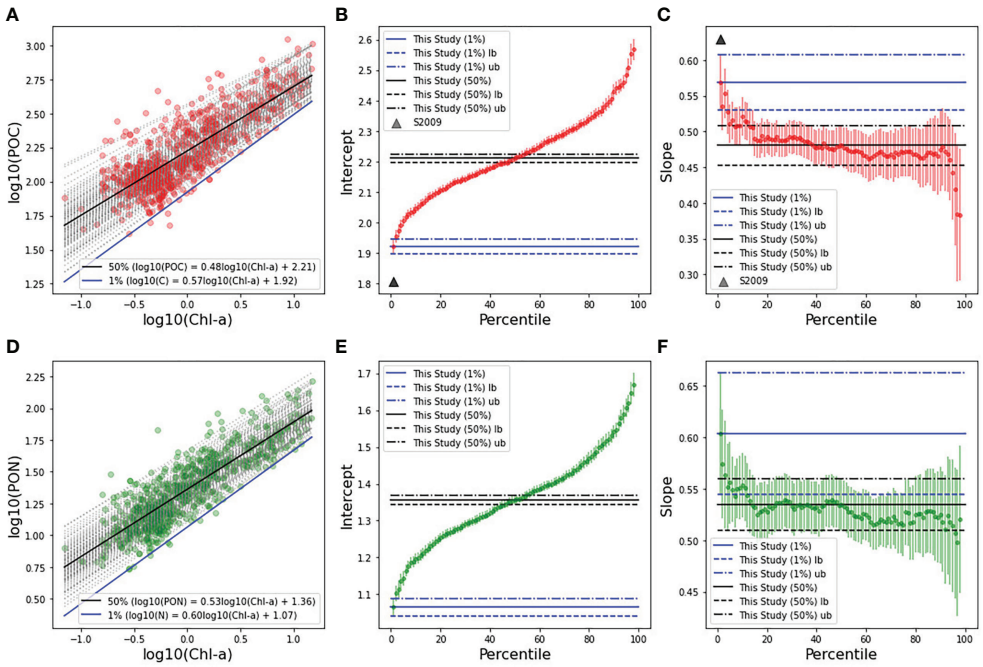


FIGURE 2
In-situ particulate carbon (top row) and nitrogen (bottom row), each plotted as a function of Turner chlorophyll-a from *in-situ* measurements. Least-squares fits to log 10 -transformed data, along with minimum carbon (Cphyto) and nitrogen (Nphyto) estimates by quantile regression (QR, q = 0.01) **(A, D)**. Quantile regression lines (from 1 to 99%) are plotted in grey dotted lines. The 1% percentile is highlighted in blue and the 50th percentile in black. Intercepts **(B, E)** and slopes **(C, F)** for the different quantile fits, including error margins for each regression line. 1% QRs and uncertainties (upper bounds, ub and lower bounds, lb) are shown by the continuous, dashed and dash-dotted lines in blue, (middle and right panels), while Sathyendranath et al. (2009) carbon parameter values are also displayed (triangle, panels **B, C**).

parameters (*m* and *p*) for C derived here and those from other studies, and the broad agreement of N:Chl-a ratio values between this and earlier observations.

Stoichiometry and phytoplankton groups

The 1% quantile regression models of phytoplankton C and N were used to estimate the C:N ratio as a function of Chl-a (Figure 3). Results suggest that the elemental stoichiometry of phytoplankton varies across the Chl-a range with the C:N ratio decreasing with increasing phytoplankton biomass, from around 8 at very low chlorophyll to 6 at high chlorophyll, intersecting the Redfield ratio towards higher phytoplankton biomass concentrations. This progression in the C:N ratio is consistent with the phytoplankton under oligotrophic conditions (low chlorophyll) being nitrogen limited, and those in eutrophic (high chlorophyll) conditions being nitrogen replete. However, the lower and upper bounds on the parameter estimates lead to considerable uncertainty margins (Figure 3), and suggest that results are not significantly different from Redfield over the Chl-a range studied. The C:N values are more robust over the intermediate concentrations along the chlorophyll range (where the majority of the Chl-a data is distributed), and the uncertainties are higher at the extremes where there is a smaller number of observations (Figure 3). Averages and ranges from the analysis, for all ratios, are provided in Table 2.

Amongst the six distinct phytoplankton types examined, the diagnostic pigment analysis revealed some samples were dominated by diatoms, prymnesiophytes, *Prochlorococcus*, other picocyanobacteria (e.g. *Synechococcus*) or green algae. Dinoflagellates did not emerge as dominating any of the samples, according to the criteria applied. Differences were observed in the stoichiometry of the five phytoplankton groups that were identified (Figure 4; Table 3). The C:N ratios estimated were higher than the Redfield ratio. Diatoms were the closest group to the standard 6.6 Redfield ratio. Green algae and smaller phytoplankton types, on the other hand, displayed the highest stoichiometric values among all groups observed.

Distribution of phytoplankton properties

Using remotely-sensed Chl-a as input to our models (Eq. 1), the distributions of phytoplankton C, N, and C:N were computed for the NW Atlantic and the Arabian Sea study sites (Figure 5). The maps generated highlight the different biogeochemical areas within the NW Atlantic and the Arabian Sea during early summer 2006 and early spring 2005, respectively for the two sites. Observations for the Atlantic area coincided with the spring bloom season characterized by considerable variability in phytoplankton biomass, ranging from oligotrophic to eutrophic conditions. In contrast, the Arabian Sea biome has more stable and lower levels of Chl-a during the early spring. High concentrations of phytoplankton C and N only covered a small proportion of the areas shown, with the majority of the regions being low in phytoplankton biomass. Applying the model to satellite data allows the production of maps at a variety of scales, in time and space, to study the phytoplanktonic biomass and stoichiometry. However, one needs to be cautious interpreting

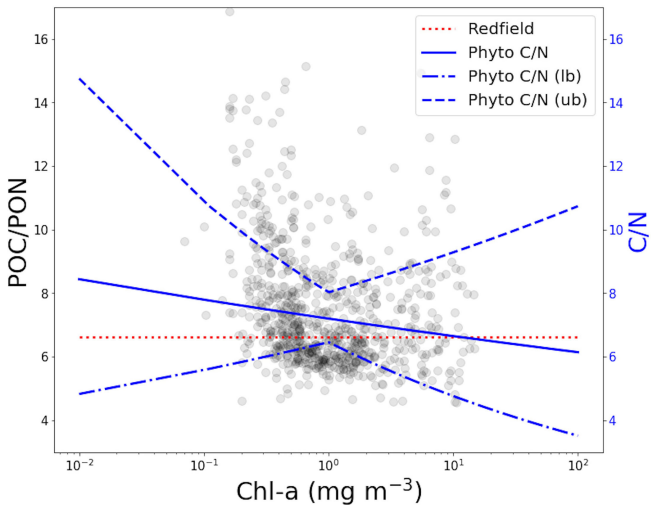


FIGURE 3
POC:PON against Chl-a showing the Redfield ratio (6.625, dotted red line), the phytoplankton C:N established by 1% QR regression analysis (blue line), and the relative uncertainties (upper bound, ub, dashedline line, and lower bound, lb, dot-dashedline).

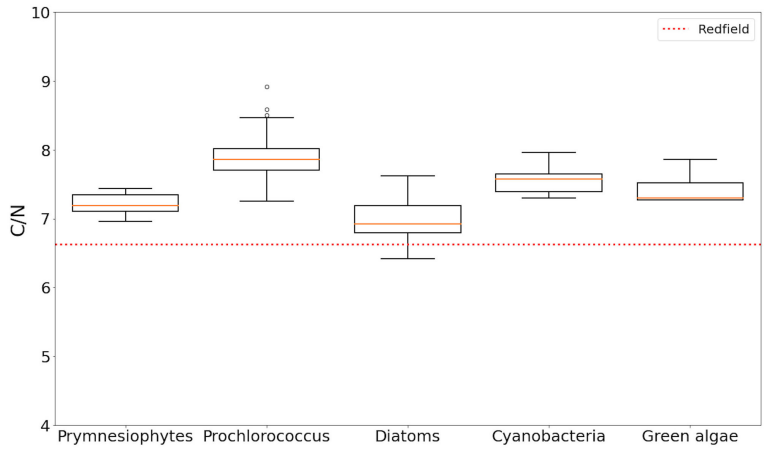


FIGURE 4
Boxplot of C:N ratios specific to the five phytoplankton taxa identified through HPLC analysis. Redfield ratio is highlighted by the dotted red line. See Table 3 for the mean and range of taxon-specific ratio.

TABLE 3 Taxon-specific mean and range of phytoplankton C:N.

Phytoplankton Group	Mean C:N (g/g)	Range C:N (g/g)
Prymnesiophytes	7.21	6.96 - 7.44
Prochlorococcus	7.88	7.26 - 8.92
Diatoms	6.99	6.42 - 7.62
Cyanobacteria	7.55	7.30 - 7.96
Green Algae	7.45	7.27 - 7.86

the maps in conditions outside the range of data for which the model was parameterized, for example, in oligotrophic waters <0.07 mg m $^{-3}$ Chl-a.

Discussion

Bulk properties and correlations

Good linear correlations were found between the observed $\log_{10}$-transformed PON and Chl-a, and POC and Chl-a concentrations (Figures 2A, D). Expectedly, the parameters of the fit in the relationship between POC and Chl-a are in good agreement with those presented in Sathyendranath et al. (2009) considering similar data were used. Estimates of the POC:Chl-a ratio in this study (mean 211, range 33-1286) are broadly consistent with the literature (e.g., 100-1000; Legendre and Michaud, 1999; Stramski et al., 2008; Rasse et al., 2017). However, published analyses of particulate nitrogen, and how this varies with Chl-a, are generally less abundant and, thus, harder to compare against. Stoichiometric observations with a mean POC:PON ratio of 7.5 (Table 2) are also in agreement with Redfield's findings (Tanoue and Handa, 1979; Sharp et al., 1980;

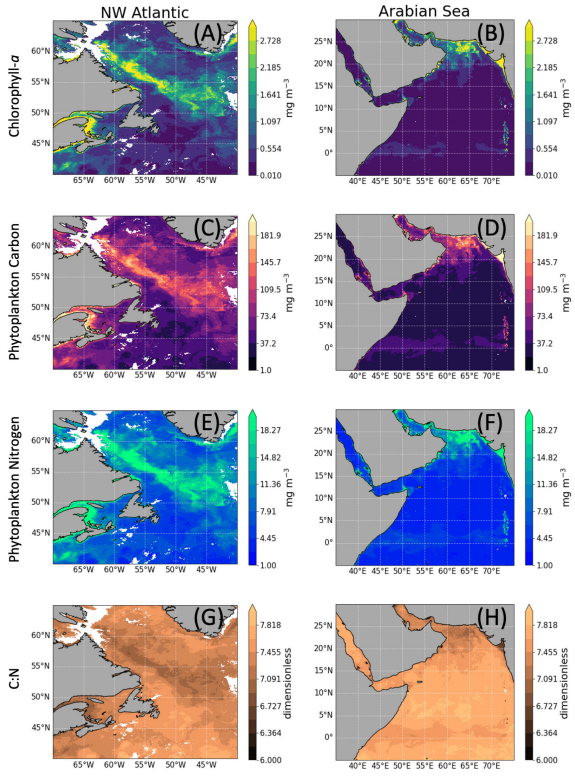


FIGURE 5
Satellite estimates of chlorophyll-a **(A, B)**, quantile regression-derived autotrophic carbon **(C, D)** and nitrogen **(E, F)**, and phytoplankton C:N ratio **(G, H)**. Maps were generated based on remotely sensed OC-CCI chlorophyll data for an 8 day relatively clear sky composite of the Northwest Atlantic [10-17/06/2006, left-hand side panels **(A, C, E, G)**] and the Arabian Sea [22-29/03/2005, right-hand side panels **(B, D, F, H)**] with a 4 km spatial resolution.

Sterner et al., 2008; Frigstad et al., 2011; Frigstad et al., 2014). This value may appear high compared to previous observations, but differences can be attributed to the different statistical approaches used and lack of sampling replications that results in varying levels of total POC.

The overall values produced fit within traditional ranges and indirectly validate the model used; hence, this approach represents a simple and efficient solution for quantifying estimates of phytoplankton C and N at sea, as well as the ratio between the two, using remotely sensed Chl-a. The satellite data represent an opportunity to extrapolate these relationships over large spatial and temporal scales. Such relationships can also be useful for testing complex marine ecosystem models. Nonetheless, regional differences in model parameters are likely present, and one should be cautious about applying these models to satellite data in different regions and ranges of Chl-a outside those used to tune the models (Redfield et al., 1963; Körtzinger et al., 2001; Sterner et al., 2008; Martiny et al., 2013).

Dynamic relationships of phytoplankton and non-autotrophic particles

Autotrophic standing stock, primary production, export production and sequestration can be quantified by studying various metrics, such as phytoplankton carbon content, nitrogen content and chlorophyll concentration. Conversion factors are often adopted to evoke the measures desired and can be derived using controlled phytoplankton cultures. However, these experiments are unlikely to represent natural conditions (Flynn, 2003; Franks, 2009; Anderson et al., 2010). In field studies, bulk measures of C and N are generally easy to measure but distinguishing between the algal and non-algal contributions to these bulk elements is challenging due to operational constraints. Whereas phytoplankton C and N are often used as measures of phytoplankton biomass, standardized protocols of their direct measurement at sea have not been established yet; for this reason, indirect means are often invoked. Several studies have explored the use of a linear regression models of the POC and Chl-a relationship, to discriminate algal composition from that of non-autotrophic and detrital particles (Steele and Baird, 1961; Tett et al., 1975; Eppley et al., 1992; Behrenfeld et al., 2005; Frigstad et al., 2011), though they do not account for the nonlinearity of the Chl-a and POC relationship.

Other methods have been employed with various degrees of success, but none are reported to perform without limitations. The detection of phytoplankton C fractions from satellite imagery has been proposed as another approach for making indirect estimations. Behrenfeld et al. (2005) used a linear approach to derive the algal contribution to backscattering, by first subtracting a fixed value related to non-algal particles. Later studies refined this method to account for the variability of non-algal particles, but these either rely on several assumptions or cannot efficiently remove the impact of non-algal particles at higher algal concentrations, including bacteria, bubbles, and other particles (e.g. plastics). These models are difficult to cross-validate due to the paucity of *in-situ* phytoplankton C data (Dall'Olmo et al., 2009; Bellacicco et al., 2019). Poorly known distribution and physical characteristics of smaller particles further constrain the reliability of any modelling and contribute to the natural limitations inherent to the use of backscattering (Stramski et al., 2004; Organelli et al., 2018). Martínez-Vicente et al. (2013) and Graff et al. (2015) derived phytoplankton C directly from flow cytometry, the former using phytoplankton abundances, cellular carbon per unit volume and mean cell volume. However, these models either rely on estimations from lab-based studies or are time-consuming and limited to samples analyzed by flow cytometry. A cell volume model has also served for conversions to retrieve phytoplankton N (Montagnes et al., 1994; Sun and Liu, 2003). An earlier investigation used the chlorosis levels in phytoplankton cells to obtain indirect estimates on their organic N concentration at sea based on the inverse relationship between the nitrogen: chlorophyll and the carotenoid:chlorophyll ratios (Yentsch and Vaccaro, 1958) using estimates from controlled experiments. Alternatively, the quantile regression approach used here and adopted from Sathyendranath et al. (2009) applies a nonlinear regression to the particulate N or C compositions fitted against Chl-a concentrations to account for the varying relationships between variables. Fixed ratios are frequently invoked in many global-scale studies (Aumont and Bopp, 2006; Follows et al., 2007; Dutkiewicz et al., 2009) even though deviations are well documented in the elemental composition of phytoplankton (Droop, 1983). The extent to which these ratios diverge from standard proportions have significant implications for the parametrization of these models and, consequently, for simulations of the N and C cycles, C-transfer efficiency up the food web, and air-sea gas exchange (Sterner and Elser, 2002; Ayata et al., 2013). The approach presented here, represents a simple avenue to estimating elemental ratios and stoichiometry in phytoplankton.

The variability in the phytoplankton C:Chl-a and N:Chl-a ratios can be explained as a direct result of changes in the physiological status of autotrophs. Algal organisms are not strictly homeostatic, and ambient conditions (e.g., availability of nutrients, light, and depth levels) can stimulate the regulation of their metabolism (i.e., respiration, exudation and storage), resulting in the acclimation of the photosynthetic apparatus – alteration of nutrient use efficiency and adjustment of Chl-a content. The net difference between acquisition and losses can lead to the consequent decoupling of cellular C, N and pigment contents in seemingly adaptive ways (Berman-Frank and Dubinsky, 1999). Environmental conditions also impact the phytoplankton community composition, representing an

additional factor determining stoichiometry (Clark et al., 2013; Talmy et al., 2014). Alternatively, the rationale of the QR approach develops on the notion that variability in total PC and PN within any given concentration of Chl-a is primarily associated with the variability of non-autotrophic particles. Ultimately, the relationship between phytoplankton C and N fitted against the Chl-a concentration range can be used to explore the stoichiometry of natural autotrophic composition in the sea utilizing a simple method that exploits straightforward concepts. Furthermore, the empirical models developed here (Table 1) can be of use to verify results from more complex marine ecosystem models where the phytoplankton C:chl-a and N:chl-a ratios are emergent properties of the simulations (de Mora et al., 2016). Data used were derived from up to 40 m below the water surface and spanned a range of trophic conditions across different biomes. Outputs should therefore be interpreted as representative of the surface mixed layer.

Elemental ratios of phytoplankton and their variability

The mean C:Chl-a and N:Chl-a ratios derived using the QR model are consistent with previous observations, for C (Verity, 2002; Lefèvre et al., 2003; Lü et al., 2009; Xiu and Chai, 2012; Jakobsen and Markager, 2016; Martínez-Vicente et al., 2017) and for N (Yentsch and Vaccaro, 1958; Manny, 1969; Verity, 1981; Staehr et al., 2002). Both the phytoplankton C and N to Chl-a fits display steeper slopes than their corresponding particulate regression (50% QR), suggesting an increasing contribution to PC and PN can be associated with phytoplankton at higher Chl-a concentrations. Thomalla et al. (2017) attempted to retrieve phytoplankton C adopting different methods including the QR, using the same dataset in some instances. They find that the range and distributions from the QR approach compare remarkably well with those generated using backscattering techniques based on both Stramski (1999) and Behrenfeld et al. (2005) approaches, reconciling the two techniques and supporting the use of the QR approach.

The phytoplankton C:N trend decreases from low to high chlorophyll waters, a direct result of the steeper slope in the relationship between phytoplankton N and Chl-a than phytoplankton C and Chl-a (0.60 > 0.57). Considerable uncertainties were observed over the extreme ends of the chlorophyll axis in this fit, challenging the accuracy of estimates and their applicability to real world scenarios (Figure 3). Nonetheless, the mean and range values are in broad agreement with earlier investigations (Körtzinger et al., 2001; Geider and La Roche, 2002; Staehr et al., 2002; Frigstad et al., 2011; Frigstad et al., 2014; Wagner et al., 2019). Stoichiometry estimates yielded are above the canonical 6.625 for most of the chlorophyll range, before approaching Redfield ratio and dropping below it at higher Chl-a. This inclination further emphasizes the argument that adopting a constant ratio to estimate elemental compositions of autotrophic cells are likely to lead to erroneous outcomes. Thus, we can speculate that the C:N ratio of phytoplankton in the surface mixed layer is highest when the algal biomass is lowest and it decreases as bloom conditions are approached, while its range remains close to Redfield across most of the chlorophyll axis.

The results from this study also show variations in C:N amongst phytoplankton groups. The taxon-specific ratios that emerge from these analyses were predominantly above or close to the Redfield ratio. This variance in the elemental composition between phytoplankton types may be associated with a difference in cell size (Morel and Bricaud, 1981; Grover, 1991; Tozzi et al., 2004; Griffiths and Harrison, 2009; Talmy et al., 2014), their nutritional status and cell activity (Klausmeier et al., 2004b; Halsey and Jones, 2015). The nutrient storage capacity of autotrophic cells is known to be size dependent. For example, diatoms can store large nutrient concentrations contributing to lower C:N ratio than small celled autotrophs in a nutrient replete environment as supported by wider phytoplankton culture studies (Lomas and Gilbert, 2000; Bertilsson et al., 2003; Heldal et al., 2003; Martiny et al., 2013). Thus, variations in stoichiometry with phytoplankton community composition can also play an important role in determining the bulk stoichiometry of phytoplankton. It could be speculated that a higher mean ratio could be induced by a possible dominance of small-celled autotrophs over diatoms. It is reasonable to assume that our results are subject to variation based on the dominant phytoplankton species within each community. However, for the same species, links between the cellular C and N content can be further modulated by metabolic functions (e.g., diverging rates of carbon fixation and nutrient acquisition), as previously mentioned.

This uncoupling can manifest in a response to factors not accounted for in this method, including alterations of nutrient and light availability and temperature (vertically and horizontally) (Verity, 1981; Behrenfeld et al., 2002; Staehr et al., 2002; Frigstad et al., 2011; Jackson et al., 2017). Environment conditions can influence metabolic functions in algal organisms encouraging adaptive mechanisms (acclimation), which may lead to bias in estimations if not accounted for. A change in the ratio can also be expected below the euphotic region (Schneider et al., 2003; Martiny et al., 2013). Phytoplankton estimates from remotely sensed chlorophyll will also benefit from incorporating per-pixel uncertainties, included in the satellite data, by propagating errors and producing supplementary maps reporting the quality of satellite products (Brewin et al., 2017; Martínez-Vicente et al., 2017; Sathyendranath et al., 2017). The QR method could also be applied to other limiting nutrients and elements, such as phosphorus and iron. Finally, considering the influence of stoichiometric variations on the dynamics of food webs, global nutrient and carbon cycling, and the Earth's climate, it is critical that we improve our understanding of phytoplankton C and N, and how these metrics vary in the ocean.

Conclusions

Despite the progress made and the new technologies developed in recent years, our understanding of the phytoplankton elemental composition at sea is still unsatisfactory. The ability to produce accurate measures of algal contribution to particulate N and C in the sea from bulk properties measured directly in the field is challenging, for both traditional and modern methods. Considering the global oceans and the atmosphere are expected to be increasingly affected by anthropogenic influences, better understanding of the elemental composition of phytoplankton is needed.

In this study, we analyzed a large dataset of the total particulate C and N and Chl-a in the NW Atlantic and the Indian Ocean to compute the phytoplankton N:Chl-a, C:Chl-a and C:N ratios, and their variations over the observed Chl-a range through the use of a simple and straightforward method. Results suggest that phytoplankton contribution to PC and PN increases with an increase in its biomass. Conversely, the phytoplankton C:N ratio decreases with increases in biomass. Stoichiometry of phytoplankton was further observed to follow taxon-specific variations, as demonstrated in the wider literature. Estimates generated here agree with the range of values from previous laboratory and field studies, and earlier applications of this method on different datasets have generated comparable results. Therefore, it can be deduced that the simple approach adopted here can be used to achieve reasonable results, and the estimates it produces could serve to test complex ecosystem models. The established ratios, combined with satellite-derived Chl-a can be used to estimate the phytoplankton C, N, C:N and their spatial distributions, demonstrating an immediate application of the model. Future replications of this method will benefit from the inclusion of additional elements, such as the particulate organic phosphorous or iron. Observations over a wider geographical scale could further assess the broad applicability of this method.

Data availability statement

The *in-situ* datasets and code used for data processing can be found in the following GitHub repository https://github.com/rjbrewin/POC-PON-TChl-analysis. This includes an Jupyter Notebook Python Script, that can be run through binder (https://mybinder.org) without having to install Python software. Datasets from satellite observations of ocean colour are publicly accessible from https://www.oceancolour.org.

Author contributions

SS provided the data and came up with the concept, with input from RB. GM and RB synthesized the data, ran the analysis and prepared the figures. GM wrote the first version of the manuscript, with input from RB, and prepared all tables. All authors contributed to the subsequent versions of the manuscript.

Funding

This work was supported through a European Space Agency (ESA) project "Biological Pump and Carbon Exchange Processes (BICEP)" and by the Simons Foundation Project "Collaboration on Computational Biogeochemical Modeling of Marine Ecosystems (CBIOMES)" (549947, SS). It was also supported by the UK National Centre for Earth Observation (NCEO). Additional support from the Ocean Colour Component of the Climate Change Initiative of the European Space Agency (ESA) is gratefully acknowledged. RB is funded by a UKRI Future Leader Fellowship (MR/V022792/1).

Acknowledgments

We acknowledge all those involved in the collection of data used in this study. This work was supported by a MSc project in Conservation and Biodiversity in the College of Life and Environmental Sciences, University of Exeter.

Conflict of interest

The authors declare that the research was conducted in the absence of any commercial or financial relationships that could be construed as a potential conflict of interest.

Publisher's note

All claims expressed in this article are solely those of the authors and do not necessarily represent those of their affiliated organizations, or those of the publisher, the editors and the reviewers. Any product that may be evaluated in this article, or claim that may be made by its manufacturer, is not guaranteed or endorsed by the publisher.

References

Anderson, L. G., Tanhua, T., Björk, G., Hjalmarsson, S., Jones, E. P., Jutterstr öm, S., et al. (2010). Arctic Ocean shelf-basin interaction : An active continent shelf CO_2 pump and its impact on the degree of calcium carbonate solubility. *Deep Sea Res. Part I: Oceanographic Res. Papers* 57, 869–879. doi: 10.1016/J.DSR.2010.03.012

Aumont, O., and Bopp, L. (2006). Globalizing results from ocean *in situ* iron fertilization studies. *Global Biogeochemical Cycles* 20, 1–15. doi: 10.1029/2005GB002591

Ayata, S. D., Lévy, M., Aumont, O., Sciandra, A., Sainte-Marie, J., Tagliabue, A., et al. (2013). Phytoplankton growth formulation in marine ecosystem models: Should we take into account photo-acclimation and variable stoichiometry in oligotrophic areas? *J. Mar. Syst.* 125, 29–40. doi: 10.1016/J.JMARSYS.2012.12.010

Banse, K. (1977). Determining the carbon-to-chlorophyll ratio of natural phytoplankton. *Mar. Biol.* 41, 199–212. doi: 10.1007/BF00394907

Behrenfeld, M., Boss, E., Siegel, D. A., and Shea, D. M. (2005). Carbon-based ocean productivity and phytoplankton physiology from space. *Global Biogeochemical Cycles* 19, 1–14. doi: 10.1029/2004GB002299

Behrenfeld, M. J., Marañón, E., Siegel, D. A., and Hooker, S. B. (2002). Photoacclimation and nutrient-based model of light-saturated photosynthesis for quantifying oceanic primary production. *Mar. Ecol. Prog. Ser.* 228, 103–117. doi: 10.3354/MEPS228103

Bellacicco, M., Vellucci, V., Scardi, M., Barbieux, M., Marullo, S., and D'ortenzio, F. (2019). Quantifying the impact of linear regression model in deriving bio-optical relationships: The implications on ocean carbon estimations. *Sensors* 19, 3032. doi: 10.3390/S19133032

Berman-Frank, I., and Dubinsky, Z. (1999). Balanced growth in aquatic plants: Myth or reality? Phytoplankton use the imbalance between carbon assimilation and biomass production to their strategic advantage. *BioScience* 49, 29–37. doi: 10.1525/BISI.1999.49.1.29

Bertilsson, S., Berglund, O., Karl, D. M., and Chisholm, S. (2003). Elemental composition of marine *Prochlorococcus* and *Synechococcus*: Implications for the ecological stoichiometry of the sea. *W. Limnology Oceanography* 48, 1721–1731. doi: 10.4319/LO.2003.48.5.1721

Brewin, R. J. W., Ciavatta, S., Sathyendranath, S., Jackson, T., Tilstone, G., Curran, K., et al. (2017). Uncertainty in ocean-color estimates of chlorophyll for phytoplankton groups. *Front. Mar. Sci.* 4. doi: 10.3389/FMARS.2017.00104

Brewin, R. J. W., Sathyendranath, S., Platt, T., Bouman, H., Ciavatta, S., Dall'Olmo, G., et al. (2021). Sensing the ocean biological carbon pump from space: A review of capabilities, concepts, research gaps and future developments. *Earth-Science Rev.* 217, 103604. doi: 10.1016/J.EARSCIREV.2021.103604

Buck, K. R., Chavez, F. P., and Campbell, L. (1996). Basin-wide distributions of living carbon components and the inverted trophic pyramid of the central gyre of the north Atlantic ocean, summer 1993. *Aquat. Microbial Ecol.* 10, 283–298. doi: 10.3354/AME010283

Chai, F., Dugdale, R. C., Peng, T. H., Wilkerson, F. P., and Barber, R. T. (2002). One-dimensional ecosystem model of the equatorial pacific upwelling system. Part I: model development and silicon and nitrogen cycle. *Deep Sea Res. Part II: Topical Stud. Oceanography* 49, 2713–2745. doi: 10.1016/S0967-0645(02)00055-3

Clark, J. R., Lenton, T. M., Williams, H. T. P., and Daines, S. J. (2013). Environmental selection and resource allocation determine spatial patterns in picophytoplankton cell size. *Limnology Oceanography* 58, 1008–1022. doi: 10.4319/LO.2013.58.3.1008

Collos, Y. (2002). "*Determination of particulate carbon and nitrogen in coastal waters*," In Pelagic ecology methodology. DV Subba Rao (A.A. Balkema Publishers, Tokyo), 333–341.

Dall'Olmo, G., Westberry, T. K., Behrenfeld, M. J., Boss, E., and Slade, W. H. (2009). Significant contribution of large particles to optical backscattering in the open ocean. *Biogeosciences* 6, 947–967. doi: 10.5194/BG-6-947-2009

Dearman, J. R., Taylor, A. H., and Davidson, K. (2003). Influence of autotroph model complexity on simulations of microbial communities in marine mesocosms. *Mar. Ecol. Prog. Ser.* 250, 13–28. doi: 10.3354/MEPS250013

de Mora, L., Butensch ön, M., and Allen, J. I. (2016). The assessment of a global marine ecosystem model on the basis of emergent properties and ecosystem function: a case study with ERSEM. *Geoscientific Model. Dev.* 9, 59–76. doi: 10.5194/GMD-9-59-2016

Doney, S. C., Glover, D. M., and Najjar, R. G. (1996). A new coupled, one-dimensional biological-physical model for the upper ocean: Applications to the JGOFS Bermuda Atlantic time-series study (BATS) site. *Deep-Sea Res. Part II: Topical Stud. Oceanography* 43, 591–624. doi: 10.1016/0967-0645(95)00104-2

Droop, M. R. (1983). 25 years of algal growth kinetics: A personal view. *Botanica Marina* 26, 99–112. doi: 10.1515/BOTM.1983.26.3.99

Dutkiewicz, S., Follows, M. J., and Bragg, J. G. (2009). Modeling the coupling of ocean ecology and biogeochemistry. *Global Biogeochemical Cycles* 23, 1–15. doi: 10.1029/2008GB003405

Eppley, R. W., Chavez, F. P., and Barber, R. T. (1992). Standing stocks of particulate carbon and nitrogen in the equatorial Pacific at 150° W. *J. Geophysical Res.* 97, 655–661. doi: 10.1029/91JC01386

Falkowski, P. G. (1994). The role of phytoplankton photosynthesis in global biogeochemical cycles. *Photosynthesis Res.* 39, 235–258. doi: 10.1007/BF00014586

Falkowski, P. G. (2012). Ocean science: The power of plankton. *Nature* 483, S17–S20. doi: 10.1038/483s17a

Falkowski, P. G., Laws, E. A., Barber, R. T., and Murray, J. W. (2003). *Phytoplankton and their role in primary, new, and export production*. In Ocean Biogeochemistry. Global Change — The IGBP Series. Ed. M.J.R. Fasham. (Springer, Berlin, Heidelberg), 99–121. doi: 10.1007/978-3-642-55844-3

Flynn, K. J. (2003). Do we need complex mechanistic photoacclimation models for phytoplankton? *Limnology Oceanography* 48, 2243–2249. doi: 10.4319/LO.2003.48.6.2243

Flynn, K. J. (2010). Ecological modelling in a sea of variable stoichiometry: Dysfunctionality and the legacy of redfield and monod. *Prog. Oceanography* 84, 52–65. doi: 10.1016/J.POCEAN.2009.09.006

Follows, M. J., Dutkiewicz, S., Grant, S., and Chisholm, S. W. (2007). Emergent biogeography of microbial communities in a model ocean. *Science* 315, 1843–1846. doi: 10.1126/SCIENCE.1138544/SUPPL_FILE/FOLLOWS-SOM.PDF

Franks, P. J. S. (2009). Planktonic ecosystem models: perplexing parameterizations and a failure to fail. *J. Plankton Res.* 31, 1299–1306. doi: 10.1093/PLANKT/FBP069

Frigstad, H., Andersen, T., Bellerby, R. G. J., Silyakova, A., and Hessen, D. O. (2014). Variation in the seston C:N ratio of the Arctic ocean and pan-Arctic shelves. *J. Mar. Syst.* 129, 214–223. doi: 10.1016/J.JMARSYS.2013.06.004

Frigstad, H., Andersen, T., Hessen, D. O., Naustvoll, L. J., Johnsen, T. M., and Bellerby, R. G. J. (2011). Seasonal variation in marine C:N:P stoichiometry: Can the composition of seston explain stable redfield ratios? *Biogeosciences* 8, 2917–2933. doi: 10.5194/BG-8-2917-2011

Furuya, K. (1990). Subsurface chlorophyll maximum in the tropical and subtropical western pacific ocean: Vertical profiles of phytoplankton biomass and its relationship with chlorophyll-a and particulate organic carbon. *Mar. Biol.* 107, 529–539. doi: 10.1007/BF01313438

Geider, R. J., and La Roche, J. (2002). Redfield revisited: Variability of C:N:P in marine microalgae and its biochemical basis. *Eur. J. Phycology* 37, 1–17. doi: 10.1017/S0967026201003456

Goebel, N. L., Edwards, C. A., Zehr, J. P., and Follows, M. J. (2010). An emergent community ecosystem model applied to the California current system. *J. Mar. Syst.* 83, 221–241. doi: 10.1016/J.JMARSYS.2010.05.002

Graff, J. R., Milligan, A. J., and Behrenfeld, M. J. (2012). The measurement of phytoplankton biomass using flow-cytometric sorting and elemental analysis of carbon. *Limnology Oceanography: Methods* 10, 910–920. doi: 10.4319/LOM.2012.10.910

Graff, J. R., Westberry, T. K., Milligan, A. J., Brown, M. B., Dall'Olmo, G., van Dongen-Vogels, V., et al. (2015). Analytical phytoplankton carbon measurements spanning diverse ecosystems. *Deep Sea Res. Part I: Oceanographic Res. Papers* 102, 16–25. doi: 10.1016/J.DSR.2015.04.006

Griffiths, M. J., and Harrison, S. T. L. (2009). Lipid productivity as a key characteristic for choosing algal species for biodiesel production. *J. Appl. Phycology* 21, 493–507. doi: 10.1007/S10811-008-9392-7

Grover, J. P. (1991). Resource competition in a variable environment: Phytoplankton growing according to the variable-internal-stores model. *Am. Nat.* 138, 811–835. doi: 10.1086/285254

Halsey, K. H., and Jones, B. M. (2015). Phytoplankton strategies for photosynthetic energy allocation. *Annu. Rev. Mar. Sci.* 7, 265–297. doi: 10.1146/annurev-marine-010814-015813

Heldal, M., Scanlan, D. J., Norland, S., Thingstad, F., and Mann, N. H. (2003). Elemental composition of single cells of various strains of marine *Prochlorococcus* and *Synechococcus* using x-ray microanalysis. *Limnology Oceanography* 48, 1732–1743. doi: 10.4319/lo.2003.48.5.1732

Holm-Hansen, O., Lorenzen, C. J., Holmes, R. W., and Strickland, J. D. H. (1965). Fluorometric determination of chlorophyll. *ICES J. Mar. Sci.* 30, 3–15. doi: 10.1093/ICESJMS/30.1.3

Jackson, T., Sathyendranath, S., and Platt, T. (2017). An exact solution for modeling photoacclimation of the carbon-to-chlorophyll ratio in phytoplankton. *Front. Mar. Sci.* 4. doi: 10.3389/FMARS.2017.00283

Jakobsen, H. H., and Markager, S. (2016). Carbon-to-chlorophyll ratio for phytoplankton in temperate coastal waters: Seasonal patterns and relationship to nutrients. *Limnology Oceanography* 61, 1853–1868. doi: 10.1002/LNO.10338

Karl, D. M., Björkman, K. M., Dore, J. E., Fujieki, L., Hebel, D. V., Houlihan, T., et al. (2001). Ecological nitrogen-to-phosphorus stoichiometry at station ALOHA. *Deep Sea Res. Part II: Topical Stud. Oceanography* 48, 1529–1566. doi: 10.1016/S0967-0645(00)00152-1

Klausmeier, C. A., Litchman, E., Daufreshna, T., and Levin, S. A. (2004a). Optimal nitrogen-to-phosphorus stoichiometry of phytoplankton. *Nature* 429, 171–174. doi: 10.1038/nature02454

Klausmeier, C. A., Litchman, E., and Levin, S. A. (2004b). Phytoplankton growth and stoichiometry under multiple nutrient limitation. *Limnology Oceanography* 49, 1463–1470. doi: 10.4319/LO.2004.49.4_PART_2.1463

Körtzinger, A., Koeve, W., Kähler, P., and Mintrop, L. (2001). C:N ratios in the mixed layer during the productive season in the northeast Atlantic ocean. *Deep Sea Res. Part I: Oceanographic Res. Papers* 48, 661–688. doi: 10.1016/S0967-0637(00)00051-0

Kwiatkowski, L., Aumont, O., Bopp, L., and Ciais, P. (2018). The impact of variable phytoplankton stoichiometry on projections of primary production, food quality, and carbon uptake in the global ocean. *Global Biogeochemical Cycles* 32, 516–528. doi: 10.1002/2017GB005799

Lefèvre, N., Taylor, A. H., Gilbert, F. J., and Geider, R. J. (2003). Modeling carbon to nitrogen and carbon to chlorophyll a ratios in the ocean at low latitudes: Evaluation of the role of physiological plasticity. *Limnology Oceanography* 48, 1796–1807. doi: 10.4319/LO.2003.48.5.1796

Legendre, L., and Michaud, J. (1999). Chlorophyll a to estimate the particulate organic carbon available as food to large zooplankton in the euphotic zone of oceans. *J. Plankton Res.* 21, 2067–2083. doi: 10.1093/PLANKT/21.11.2067

Litchman, E., de Tezanos Pinto, P., Edwards, K. F., Klausmeier, C. A., Kremer, C. T., and Thomas, M. K. (2015). Global biogeochemical impacts of phytoplankton: A trait-based perspective. *J. Ecol.* 103, 1384–1396. doi: 10.1111/1365-2745.12438

Li, W. K. W., Zohary, T., Yacobi, Y. Z., and Wood, A. M. (1993). Ultraphytoplankton in the eastern Mediterranean Sea: towards deriving phytoplankton biomass from flow cytometric measurements of abundance, fluorescence and light scatter. *Mar. Ecol. Prog. Ser.* 102, 79–87. doi: 10.3354/MEPS102079

Llewellyn, C. A. (2004). Phytoplankton community assemblage in the English channel: a comparison using chlorophyll a derived from HPLC-CHEMTAX and carbon derived from microscopy cell counts. *J. Plankton Res.* 27, 103–119. doi: 10.1093/plankt/fbh158

Loisel, H., Duforêt-Gaurier, L., Dessailly, S., Sathyendranath, S., Evers-King, H., Vantrepotte, V., et al. (2018). A satellite view of the particulate organic carbon and its algal and non-algal carbon pools. In *Proceedings of the Ocean Optics XXIV*, Dubrovnik, Croatia, 7–12.

Lomas, M. W., and Gilbert, P. M. (2000). Comparisons of nitrate uptake, storage, and reduction in marine diatoms and flagellates. *J. Phycology* 36, 903–913. doi: 10.1046/J.1529-8817.2000.99029.X

Lü, S., Wang, X., and Han, B. (2009). A field study on the conversion ratio of phytoplankton biomass carbon to chlorophyll- a in jiaozhou bay, china. *Chin. J. Oceanology Limnology* 27, 793–805. doi: 10.1007/S00343-009-9221-0

Manny, B. A. (1969). The relationship between organic nitrogen and the carotenoid to chlorophyll a ratio in five freshwater phytoplankton species. *Limnology Oceanography* 14, 69–79. doi: 10.4319/LO.1969.14.1.0069

Marañón, E., Cermeño, P., Huete-Ortega, M., López-Sandoval, D. C., Mouriño Carballido, B., and Rodríguez-Ramos, T. (2014). Resource supply overrides temperature as a controlling factor of marine phytoplankton growth. *PloS One* 9, e99312. doi: 10.1371/JOURNAL.PONE.0099312

Martínez-Vicente, V., Dall'Olmo, G., Tarran, G., Boss, E., and Sathyendranath, S. (2013). Optical backscattering is correlated with phytoplankton carbon across the Atlantic Ocean. *Geophysical Res. Lett.* 40, 1154–1158. doi: 10.1002/grl.50252

Martínez-Vicente, V., Evers-King, H., Roy, S., Kostadinov, T. S., Tarran, G. A., Graff, J. R., et al. (2017). Intercomparison of ocean color algorithms for picophytoplankton carbon in the ocean. *Front. Mar. Sci.* 4. doi: 10.3389/fmars.2017.00378

Martiny, A. C., Vrugt, J. A., Primeau, F. W., and Lomas, M. W. (2013). Regional variation in the particulate organic carbon to nitrogen ratio in the surface ocean. *Global Biogeochemical Cycles* 27, 723–731. doi: 10.1002/GBC.20061

Montagnes, D. J., Berges, J. A., Harrison, P. J., and Taylor, F. J. (1994). Estimating carbon, nitrogen, protein, and chlorophyll a from volume in marine phytoplankton. *Limnology Oceanography* 39, 1044–1060. doi: 10.4319/lo.1994.39.5.1044

Moore, C. M., Mills, M. M., Arrigo, K. R., Berman-Frank, I., Bopp, L., Boyd, P. W., et al. (2013). Processes and patterns of oceanic nutrient limitation. *Nat. Geosci.* 6, 701–710. doi: 10.1038/ngeo1765

Morel, A., and Bricaud, A. (1981). Theoretical results concerning light absorption in a discrete medium, and application to specific absorption of phytoplankton. *Deep Sea Res. Part A. Oceanographic Res. Papers* 28, 1375–1393. doi: 10.1016/0198-0149(81)90039-X

Olson, R. J., Shalapyonok, A., and Sosik, H. M. (2003). An automated submersible flow cytometer for analyzing pico- and nanophytoplankton: FlowCytobot. *Deep-Sea Res. Part I: Oceanographic Res. Papers* 50, 301–315. doi: 10.1016/S0967-0637(03)00003-7

Organelli, E., Dall'Olmo, G., Brewin, R. J. W., Tarran, G. A., Boss, E., and Bricaud, A. (2018). The open-ocean missing backscattering is in the structural complexity of particles. *Nat. Commun.* 9, 1–11. doi: 10.1038/s41467-018-07814-6

Phinney, D. A., and Yentsch, C. S. (1985). A novel phytoplankton chlorophyll technique: toward automated analysis. *J. Plankton Res.* 7, 633–642. doi: 10.1093/PLANKT/7.5.633

Platt, T., and Sathyendranath, S. (1988). Oceanic primary production: Estimation by remote sensing at local and regional scales. *Science* 241, 1613–1620. doi: 10.1126/SCIENCE.241.4873.1613

Rasse, R., Dall'Olmo, G., Graff, J., Westberry, T. K., van Dongen-Vogels, V., and Behrenfeld, M. J. (2017). Evaluating optical proxies of particulate organic carbon across the surface Atlantic Ocean. *Front. Mar. Sci.* 4, 367. doi: 10.3389/fmars.2017.00367

Redfield, A. C. (1934). On the proportions of organic derivatives in sea water and their relation to the composition of plankton. *James Johnstone Memorial Volume (University Press Liverpool)*, 1, 176–192.

Redfield, A. C., Ketchum, B. H., and Richards, F. (1963). The influence of organisms on the composition of sea water. *sea* 2, 26–77.

Rogers, W. (1993). Quantile regression standard errors. *Stata Tech. Bull.* 2, 133–137.

Sardans, J., Janssen, I. A., Ciais, P., Obersteiner, M., and Peñuelas, J. (2021). Recent advances and future research in ecological stoichiometry. *Perspect. Plant Ecology Evol. Systematics* 50, 125611. doi: 10.1016/j.ppees.2021.125611

Sathyendranath, S., Brewin, R. J. W., Brockmann, C., Brotas, V., Calton, B., Chuprin, A., et al. (2019). An ocean-colour time series for use in climate studies: The experience of the ocean-colour climate change initiative (OC-CCI). *Sensors* 19, 4285. doi: 10.3390/S19194285

Sathyendranath, S., Brewin, R. J. W., Jackson, T., Mélin, F., and Platt, T. (2017). Ocean-colour products for climate-change studies: What are their ideal characteristics? *Remote Sens. Environ.* 203, 125–138. doi: 10.1016/J.RSE.2017.04.017

Sathyendranath, S., Platt, T., Kovač, Ž., Dingle, J., Jackson, T., Brewin, R. J. W., et al. (2020). Reconciling models of primary production and photoacclimation. *Appl. Optics* 59, C100–C114. doi: 10.1364/AO.386252

Sathyendranath, S., Stuart, V., Nair, A., Oka, K., Nakane, T., Bouman, H., et al. (2009). Carbon-to-chlorophyll ratio and growth rate of phytoplankton in the sea. *Mar. Ecol. Prog. Ser.* 383, 73–84. doi: 10.3354/meps07998

Schneider, B., Schlitzer, R., Fischer, G., and N othig, E.-M. (2003). Depth-dependent elemental compositions of particulate organic matter (POM) in the ocean. *Global Biogeochemical Cycles* 17, 1–16. doi: 10.1029/2002GB001871

Schoo, K. L., Malzahn, A. M., Krause, E., and Boersma, M. (2013). Increased carbon dioxide availability alters phytoplankton stoichiometry and affects carbon cycling and growth of a marine planktonic herbivore. *Mar. Biol.* 160, 2145–2155. doi: 10.1007/S00227-012-2121-4

Sciandra, A. (1991). Coupling and uncoupling between nitrate uptake and growth rate in prorocentrum minimum (Dinophyceae) under different frequencies of pulsed nitrate supply. *Mar. Ecol. Prog. Ser.* 72, 261–269. doi: 10.3354/MEPS072261

Sharp, J. H., Perry, M. J., Renger, E. H., and Eppley, R. W. (1980). Phytoplankton rate processes in the oligotrophic waters of the central north Pacific Ocean. *J. Plankton Res.* 2, 335–353. doi: 10.1093/PLANKT/2.4.335

Staehr, P. A., Henriksen, P., and Markager, S. (2002). Photoacclimation of four marine phytoplankton species to irradiance and nutrient availability. *Mar. Ecol. Prog. Ser.* 238, 47–59. doi: 10.3354/meps238047

Steele, J. H., and Baird, I. E. (1961). Relations between primary production, chlorophyll and particulate carbon. *Limnology Oceanography* 6, 68–78. doi: 10.4319/lo.1961.6.1.0068

Sterner, R. W., Andersen, T., Elser, J. J., Hessen, D. O., Hood, J. M., McCauley, E., et al. (2008). Scale-dependent carbon:nitrogen:phosphorus seston stoichiometry in marine and freshwaters. *Limnology Oceanography* 53, 1169–1180. doi: 10.4319/LO.2008.53.3.1169

Sterner, R. W., and Elser, J. J. (2002). *Ecological stoichiometry: the biology of elements from molecules to the biosphere* (Princeton University Press, Princeton, New Jersey).

Stramski, D. (1999). Refractive index of planktonic cells as a measure of cellular carbon and chlorophyll a content. *Deep Sea Res. Part I: Oceanographic Res. Papers* 46, 335–351. doi: 10.1016/S0967-0637(98)00065-X

Stramski, D., Boss, E., Bogucki, D., and Voss, K. J. (2004). The role of seawater constituents in light backscattering in the ocean. *Prog. Oceanography* 61, 27–56. doi: 10.1016/J.POCEAN.2004.07.001

Stramski, D., Reynolds, R. A., Babin, M., Kaczmarek, S., Lewis, M. R., Röttgers, R., et al. (2008). Relationships between the surface concentration of particulate organic carbon and optical properties in the eastern south Pacific and eastern Atlantic oceans. *Biogeosciences* 5, 171–201. doi: 10.5194/bg-5-171-2008

Strickland, J. D. H. (1960). Measuring the production of marine phytoplankton. *Bull. Fisheries Res. Board Canada* 122, 1–172.

Stuart, V., and Head, E. (2005). *The BIO method*. In The 2nd SeaWiFS HPLC analysis round-robin experiment (SeaHARRE-2). Ed. SB Hooker. NASA/TM 2005-212785, Greenbelt, MD, 112.

Sun, J., and Liu, D. (2003). Geometric models for calculating cell biovolume and surface area for phytoplankton. *J. Plankton Res.* 25, 1331–1346. doi: 10.1093/plankt/fbg096

Talmy, D., Blackford, J., Hardman-Mountford, N. J., Polimene, L., Follows, M. J., and Geider, R. J. (2014). Flexible C:N ratio enhances metabolism of large phytoplankton when resource supply is intermittent. *Biogeosciences* 11, 4881–4895. doi: 10.5194/BG-11-4881-2014

Tanoue, E., and Handa, N. (1979). Distribution of particulate organic carbon and nitrogen in the Bering Sea and northern north pacific ocean. *Journal of the oceanographical society of Japan* 35, 47–62. doi: 10.1007/BF02108282

Tett, P., Cottrell, J. C., Trew, D. O., and Wood, B. J. B. (1975). Phosphorus quota and the chlorophyll: carbon ratio in marine phytoplankton1. *Limnology Oceanography* 20, 587–603. doi: 10.4319/LO.1975.20.4.0587

Thomalla, S. J., Ogunkoya, A. G., Vichi, M., and Swart, S. (2017). Using optical sensors on gliders to estimate phytoplankton carbon concentrations and chlorophyll-to-carbon ratios in the Southern Ocean. *Front. Mar. Sci.* 4. doi: 10.3389/FMARS.2017.00034

Tozzi, S., Schofield, O., and Falkowski, P. (2004). Historical climate change and ocean turbulence as selective agents for two key phytoplankton functional groups. *Mar. Ecol. Prog. Ser.* 274, 123–132. doi: 10.3354/MEPS274123

Verity, P. G. (1981). Effects of temperature, irradiance, and daylength on the marine diatom *Leptocylindrus danicus cleve*. Photosynthesis and cellular composition. *J. Exp. Mar. Biol. Ecol.* 55, 79–91. doi: 10.1016/0022-0981(81)90094-0

Verity, P. G. (2002). A decade of change in the skidaway river estuary II. particulate organic carbon, nitrogen, and chlorophyll a. *Estuaries* 25, 961–9750. doi: 10.1007/BF02691344

Wagner, H., Jebsen, C., and Wilhelm, C. (2019). Monitoring cellular C:N ratio in phytoplankton by means of FTIR-spectroscopy. *J. Phycology* 55, 543–551. doi: 10.1111/JPY.12858

Xiu, P., and Chai, F. (2012). Spatial and temporal variability in phytoplankton carbon, chlorophyll, and nitrogen in the North Pacific. *J. Geophysical Research: Oceans* 117, 11023. doi: 10.1029/2012JC008067

Yentsch, C. S., and Menzel, D. W. (1963). A method for the determination of phytoplankton chlorophyll and phaeophytin by fluorescence. *Deep Sea Res. Oceanographic Abstracts* 10, 221–231. doi: 10.1016/0011-7471(63)90358-9

Yentsch, C. S., and Vaccaro, R. F. (1958). Phytoplankton nitrogen in the oceans. *Limnology Oceanography* 3, 443–448. doi: 10.4319/LO.1958.3.4.0443

frontiers | Frontiers in Marine Science

TYPE Original Research
PUBLISHED 11 November 2022
DOI 10.3389/fmars.2022.1001098

Check for updates

OPEN ACCESS

EDITED BY
Astrid Bracher,
Alfred Wegener Institute Helmholtz Centre for Polar and Marine Research (AWI), Germany

REVIEWED BY
Eurico D'Sa,
Louisiana State University, United States
Nariane Bernardo,
São Paulo State University, Brazil

*CORRESPONDENCE
Carlos A. S. Araújo
araujocas81@gmail.com

SPECIALTY SECTION
This article was submitted to Ocean Observation, a section of the journal Frontiers in Marine Science

RECEIVED 22 July 2022
ACCEPTED 12 October 2022
PUBLISHED 11 November 2022

CITATION
Araújo CAS, Belzile C, Tremblay J-É and Bélanger S (2022) Environmental niches and seasonal succession of phytoplankton assemblages in a subarctic coastal bay: Applications to remote sensing estimates. *Front. Mar. Sci.* 9:1001098. doi: 10.3389/fmars.2022.1001098

COPYRIGHT
© 2022 Araújo, Belzile, Tremblay and Bélanger. This is an open-access article distributed under the terms of the Creative Commons Attribution License (CC BY). The use, distribution or reproduction in other forums is permitted, provided the original author(s) and the copyright owner(s) are credited and that the original publication in this journal is cited, in accordance with accepted academic practice. No use, distribution or reproduction is permitted which does not comply with these terms.

Environmental niches and seasonal succession of phytoplankton assemblages in a subarctic coastal bay: Applications to remote sensing estimates

Carlos A. S. Araújo[1,2]*, Claude Belzile[3], Jean-Éric Tremblay[2,4] and Simon Bélanger[1,2]

[1]Département de biologie, chimie et géographie et groupe BORÉAS, Université du Québec à Rimouski, Rimouski, QC, Canada, [2]Québec-Océan, groupe interinstitutionel de recherches océanographiques du Québec, Québec, QC, Canada, [3]Institut des sciences de la mer de Rimouski, Université du Québec à Rimouski, Rimouski, QC, Canada, [4]Département de biologie, Université Laval, Québec, QC, Canada

The seasonal and spatial variability of surface phytoplankton assemblages and associated environmental niches regarding major nutrients, physical (temperature and salinity), and optical characteristics (inherent and apparent optical properties) were investigated in an anthropized subarctic coastal bay, in the Gulf of St. Lawrence: the Bay of Sept-Îles (BSI), Québec, Canada. Seven major phytoplankton assemblages were identified by applying a combined Principal Component Analysis and Hierarchical Cluster Analysis procedures, using pigment concentrations and <20 μm autotrophic cell abundances as inputs. The resulting phytoplankton groups from BSI (n = 7) were more diverse than at a station monitored in a central portion of the St. Lawrence Estuary (n = 2). The temporal distribution of the phytoplankton assemblages of BSI reflected the major seasonal (spring to fall) signal of a nearshore subarctic environment. Before the freshet, spring bloom was dominated by large (microphytoplankton) cells (diatoms), and the succession followed a shift towards nanophytoplankton and picophytoplankton cells throughout summer and fall. Most of the phytoplankton assemblages occupied significantly different environmental niches. Taking temperature and the bio-optical properties (ultimately, the remote sensing reflectance) as inputs, a framework to classify five major groups of phytoplankton in the BSI area is validated. The demonstrated possibility to retrieve major phytoplankton assemblages has implications for applying remote sensing imagery to monitoring programs.

KEYWORDS

bio-optics, phytoplankton assemblages, phytoplankton phenology, remote sensing, nutrients, CDOM, HPLC, flow cytometry

1 Introduction

Coastal and nearshore transitional zones host diverse productive ecosystems and are commonly associated with high biodiversity. While energy sources and trophic linkages are complex (Lindeman, 1942; McMahon et al., 2021), primary production by phytoplankton is an important component of such ecosystems (Cloern et al., 2014; Winder et al., 2017). The variability of composition, biomass and production of phytoplankton communities will have a wide range of spatial and temporal scales, with temperate and polar coastal regions presenting a markedly complex seasonal pattern (Cloern and Jassby, 2008; Carstensen et al., 2015).

Phytoplankton assemblages are of particular interest for biogeochemical models, as they are intrinsically related to ecological processes (Le Quéré et al., 2005). Ocean color products derived from Earth Observation platforms can provide information about phytoplankton assemblages composition or their ecological roles (IOCCG, 2014). However, from the remote sensing perspective, the optical complexity of coastal and nearshore waters, and the general greater contribution of the chromophoric dissolved organic matter (CDOM) and particles other than phytoplankton to the bulk optical variability often hinders the ability to extract quantitative (and qualitative) information about phytoplankton in these environments (Sathyendranath et al., 1989).

Notwithstanding, trait-based concepts can be successfully used to explain the distribution of major phytoplankton assemblages along environmental gradients (Litchman et al., 2010; Roselli and Litchman, 2017). This approach may include diverse strategies of nutrient utilization (Litchman et al., 2007) that are modulated by temperature and light constraints (Edwards et al., 2016). Specifically, because various phytoplankton assemblages have different light requirements, the spectral quality of the light environment (or optical niches) will have consequences on shaping their composition (Stomp et al., 2007; Hintz et al., 2021).

In this study, we hypothesize that the composition of major phytoplankton assemblages in a nearshore coastal area will covary with temperature and the bulk optical properties of the environment. To test this hypothesis, the seasonal and spatial variability of the phytoplankton assemblages were investigated in a subarctic coastal bay (the Bay of Sept-Îles, Québec, Canada). The main objective was to identify the major assemblages and their respective environmental niches, in respect to nutrient concentrations, physical parameters (temperature and salinity), and bio-optical properties. We evaluated and demonstrated the potential of using sea surface temperature (SST, °C) and the remote sensing reflectance ($R_{rs}(\lambda)$, sr^{-1}, where λ indicates light wavelength), at selected wavelengths, to discriminate the major classes of phytoplankton assemblages found in the study area. SST and $R_{rs}(\lambda)$ are quantities that can be estimated by operational satellite sensors (see reviews of Minnett et al., 2019; and Werdell et al., 2018; respectively).

Understanding and predicting the effects of environmental change on natural communities and its consequences for ecosystem functioning is a major goal in ecology (Roselli and Litchman, 2017). In the context of climate change affecting coastal ecosystems (Harley et al., 2006), and particularly in Arctic and subarctic regions (Wassmann et al., 2011), the development of efficient tools to study and monitor phytoplankton assemblages is urgent. Furthermore, being subject of alteration of anthropogenic origin, problems related to phytoplankton such as eutrophication and harmful algal blooms in coastal zones are of major concern (Cloern, 2001; Glibert et al., 2005).

2 Methods

2.1 Study area and sampling design

The study area comprises the region around and within the Bay of Sept-Îles (BSI), in the north shore of the Gulf of St. Lawrence (GSL), Canada (Figure 1). The BSI is a semi-enclosed bay with a relatively narrow (~5 km) connection to the gulf and sheltered by the Sept-Îles archipelago. The bay has approximately 100 km^2 and a great proportion of it (~40%) is occupied by intertidal zones and depths shallower than 2 m. BSI has a mesotidal regime (with an average amplitude of 2 m), which varies in semidiurnal cycles, while its circulation patterns is also influenced by the inflow of four small rivers (Shaw, 2019). The Moisie River outlet (annual average discharge of ~490 m^3 s^{-1}), located ~20 km east of the bay, can also influence the nearshore waters of the region (Normandeau et al., 2013; Araújo and Bélanger, 2022). Besides, the BSI is considered as one of the coastal areas of the GSL likely to be most influenced by human activities, with the presence of harbors, major industrial ports and fisheries (Dreujou et al., 2021). Moreover, the BSI is a known region of occurrence of the toxic dinoflagellate *Alexandrium tamarense* in summer months, which was found to be linked to the Moisie River runoff (Weise et al., 2002).

The dataset used in this study consist of *in situ* profiles and discrete surface water samples collected on an array of stations, within the scope of the interdisciplinary project Canadian Healthy Oceans Network (CHONe2; see Ferrario et al., 2022, for further details about the project). More details about the sampling strategy and methods are found in Araújo and Bélanger (2022). The dataset provided a unique opportunity to investigate the spatial – order of 10^0 to 10^1 km – and seasonal variability of phytoplankton and bio-optical conditions of the nearshore environment of BSI (Figure 1; Table 1). The stations (Figure 1C) were sampled during seven field campaigns from

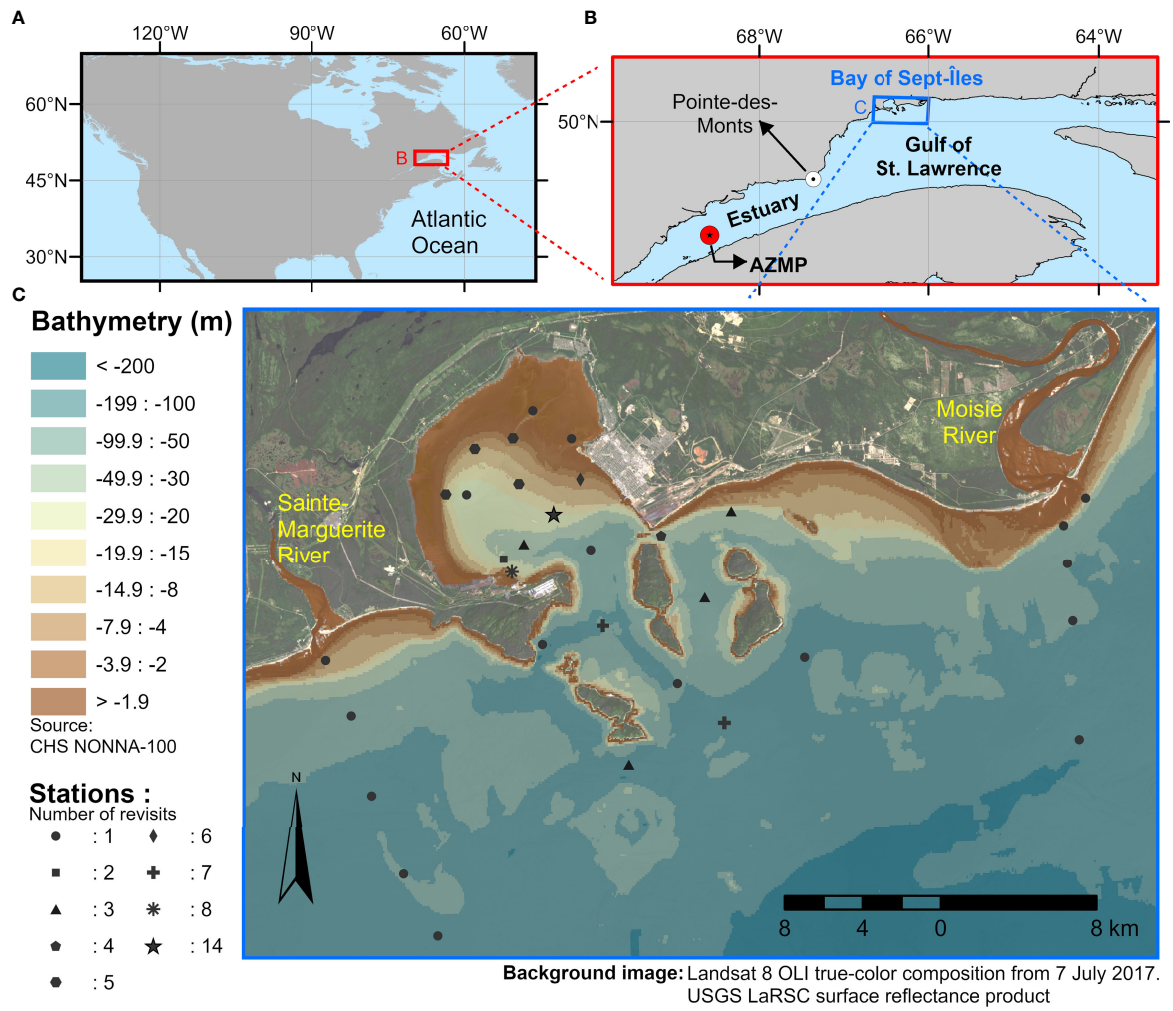


FIGURE 1
(A) The Estuary and Gulf of St. Lawrence in the North America context, and **(B)** study area sampling locations: the Bay of Sept-Îles and the AZMP buoy. **(C)** Spatial distribution and number of revisits of the sampling stations in the Bay of Sept-Îles.

late spring to early fall 2017 (BSI-1 to BSI-7, from early May to October), and one time in 2019 (BSI-8, early June). For comparison purposes, we also included a station in the middle of the St. Lawrence Estuary (the AZMP – Atlantic Zone Monitoring Program – buoy location, at Rimouski (RIKI) station, Figure 1B), visited on eleven occasions from July to October 2015 (described in Bélanger et al., 2017).

The discrete surface water samples were collected with a Niskin bottle (or bucket) and were kept cool in dark conditions until further laboratory procedures, which were made each day immediately after the cruise and consisted mainly of filtration operations. Optical and biogeochemical parameters obtained using *in situ* vertical profiles were matched to the closest measure of the depth of the discrete water sampling. A total of 108 samples was considered in this study (Table 1).

2.2 Phytoplankton assemblages

Phytoplankton assemblages were identified using a combined Principal Component Analysis (PCA) and Hierarchical Cluster Analysis (HCA) procedures, using pigment concentrations and cell abundances grouped in size classes as primary inputs.

Phytoplankton pigments were determined using High Performance Liquid Chromatography (HPLC), following the procedure described by Zapata et al. (2000). Briefly, water samples were filtered through 25 mm (or 47 mm) GF/F glass fiber filters, flash frozen in liquid nitrogen, and stored in cryogenic vials at -80°C until further analysis. The pigment extraction was made using methanol, followed by sonication and centrifugation procedures, before placing the samples in the

TABLE 1 Summary of the sampling strategy: Dates and number of water samples.

Key to field campaign location and survey: Period of sampling	Number of samples (*n*)
AZMP: from 23 July to 24 October 2015	11
BSI-1: early May (4 and 5) 2017	13
BSI-2: mid-May (21 and 22) 2017	13
BSI-3: early June (6 and 7) 2017	14
BSI-4: mid-June (22 and 23) 2017	10
BSI-5: July (18) 2017	5
BSI-6: September (6) 2017	6
BSI-7: October (7) 2017	6
BSI-8: June (1, 2, 4 and 5) 2019	30
Total	**108**

AZMP is the acronym for the Atlantic Zone Monitoring Program buoy location, and BSI is for the Bay of Sept-Îles.

HPLC analyzer (Agilent Technologies 1200 series). Detection and quantification of the pigments were estimated as described in Bidigare et al. (2005).

A total of twenty accessory pigments were considered in the analysis: chlorophylls *b* (Chlb), c_1, c_2 and c_3, Mg 2,4 divinyl pheoporphyrin a_5 monomethyl ester (MgDVP), peridinin (Peri), 19'-butanoyloxyfucoxanthin (But), fucoxanthin (Fuco), neoxanthin, prasinoxanthin, violaxanthin, 19'-hexanoyloxyfucoxanthin (Hex), diadinoxanthin, alloxanthin (Allo), diatoxanthin, zeaxanthin (Zea), lutein, crocoxanthin, α and β-carotene. Total chlorophyll-*a* (Chla) was considered as the sum of monovinyl chlorophyll-a, chlorophyllids and the allomeric and epimeric forms of chlorophyll-*a*.

Autotrophic cells (i.e., phycoerythrin- and phycocyanin-containing cyanobacteria and autotrophic eukaryotes) abundances (in cells mL^{-1}) were measured by flow cytometry. Duplicate 4 mL samples were placed in cryovials and fixed with glutaraldehyde Grade I (Sigma; 0.1% final concentration) in the dark at room temperature for 15 min, flash-frozen in liquid nitrogen, and then stored at -80°C until analysis. The analysis was made using a CytoFLEX flow cytometer (Beckman Coulter) fitted with a blue (488 nm) and a red laser (638 nm). The forward scatter, side scatter, orange fluorescence from phycoerythrin (582/42 nm BP) and red fluorescence from chlorophyll (690/50 nm BP) were measured using the blue laser. The red laser was used to excite the red fluorescence of phycocyanin (660/20 nm BP). Polystyrene microspheres of 2 µm diameter (Fluoresbrite YG, Polysciences) were added to each sample as an internal standard. Pico- (<2 µm) and nano-autotrophs (2-20 µm) were discriminated based on a forward scatter calibration using algal cultures. Since the abundance of phycocyanin-containing cyanobacteria was generally low (i.e., <100 cells mL^{-1}), they were not included in the analysis.

Prior to applying the PCA/HCA algorithms, each pigment was normalized by Chla and, together with cell abundances (pico- and nano-autotrophs), were standardized (z-scores), given the different nature (units) of inputs. The normalized and standardized data were then submitted to the PCA and the number of Principal Components (PCs) that explained most of the variability (> 80%) were selected to proceed to the HCA.

The HCA method classifies objects (i.e., phytoplankton pigments and size-class abundances) into groups (or clusters) that are similar. In this study, the clustering approach using Ward's minimum variance method (Ward, 1963) and paired Euclidean linkage distances was applied (as in Neukermans et al., 2016; and Reynolds and Stramski, 2019). The output of the HCA is a dendrogram in which the user defines a linkage distance cutoff value, which, in turn, will determine the number of clusters. For the optimal linkage distance value retrieval, we used the iterative L method procedure (Salvador and Chan, 2004; Neukermans et al., 2016). We also report the cophenetic correlation (Sokal and Rohlf, 1962), as a measure of how accurately a dendrogram maintains the pairwise distance between data objects.

2.2.1 Size-classes contribution to biomass

The fractional contribution of different size classes of phytoplankton to Chla – f_{pico} (picophytoplankton, mean diameter [D] < 2 µm); f_{nano} (nanophytoplankton, D = 2 to 20 µm); and f_{micro} (microphytoplankton, D > 20 µm) – was examined using two different approaches. The first approach (as in Uitz et al., 2006) uses the weighted contributions of seven diagnostic pigments concentrations (Fuco, Peri, Allo, But, Hex, Zea, and Chlb) to determine f_{pico}^{HPLC}, f_{nano}^{HPLC}, and f_{micro}^{HPLC}. For comparison, a second approach used picophytoplankton cell abundances (cells mL^{-1}) obtained from flow cytometry analysis. It includes eukaryotes and cyanobacteria cell abundances (A_{euk} and A_{cy}, respectively), with Chla cell quotas taken for the prasinophyte *Micromonas pusilla* (Q_{Mic}, equal to 2×10^{-8} µg Chl $cell^{-1}$; Montagnes et al., 1994) and the cyanobacteria *Synechococcus* sp. (Q_{syn}, equal to 1×10^{-9} µg Chl $cell^{-1}$; Morel et al., 1993), respectively. Thus, the fractional contribution of picophytoplankton, f_{pico}^{FC}, was determined by $f_{pico}^{FC} = 10^3[(A_{euk} \times Q_{Mic}) + (A_{cy} \times Q_{Syn})]/Chla$.

2.2.2 Taxonomic analysis by light microscopy

Phytoplankton cell identification was performed on selected samples (n = 16) to the lower rank possible (groups, genus, and species). Samples were preserved in acidic Lugol's solution and kept in the dark at 4°C until analysis. The counting of cells >2 µm was performed using an inverted microscope (Zeiss Axiovert 10) following the Utermöhl method with settling columns of 25 mL (Lund et al., 1958). A minimum of 400 cells were counted over at least three transects of 20 mm. Autotrophic phytoplankton were distributed in 10 taxonomic groups plus a group of unidentified flagellates. Unidentified cells accounted for an average of 20% of total cells abundance and, of those, ~60% were smaller than 5 µm.

2.3 Major nutrients and physical parameters

Concentrations of nitrite (NO_2^-), nitrate (NO_3^-) + NO_2^-, phosphate (PO_4^{3-}), and silicate ($Si(OH)_4^{4-}$) were determined using a colorimetric method with an Autoanalyzer 3 (Bran + Luebbe), as described in Bluteau et al. (2021). Prior to analytical procedures, water samples were filtered through 25 mm GF/F filters in acid-washed syringes and Swinnex. Concentrations of NO_3^- were determined by difference.

High-precision salinity (± 0.0003, in practical salinity units, PSU) was measured on discrete water samples using a calibrated Portasal salinometer (model 8410A, Guildline Instruments, Smiths Falls, ON). *In situ* vertical profiles of temperature and conductivity were taken using a calibrated CTD probe (SBE19, Sea-Bird Scientific, Bellevue, WA).

2.4 Inherent and apparent optical properties

The spectral backscattering and absorption coefficients ($b_b(\lambda)$ and $a(\lambda)$, respectively, in m^{-1}) are inherent optical properties (IOPs) that are related to the remote-sensing reflectance ($R_{rs}(\lambda)$), an apparent optical property, by the means of $R_{rs}(\lambda) \propto b_b(\lambda)/a(\lambda)$ (Morel and Prieur, 1977). Hence, the characterization of the IOPs is a primary requirement for discriminating phytoplankton assemblages when considering optical approaches (Reynolds and Stramski, 2019).

The total absorption coefficient, $a(\lambda)$, is decomposed by the additive contributions of pure water itself ($a_w(\lambda)$), chromophoric dissolved organic matter ($a_{cdom}(\lambda)$), non-algal particles ($a_{nap}(\lambda)$), and phytoplankton ($a_{phy}(\lambda)$) (Eq. 1). Similarly, $b_b(\lambda)$ is decomposed in backscattering of pure water ($b_{bw}(\lambda)$) and particulate matter $b_{bp}(\lambda)$) (Eq. 2).

$$a(\lambda) = a_w(\lambda) + a_{\mathbf{cdom}}(\lambda) + a_{\mathbf{nap}}(\lambda) + a_{\mathbf{phy}}(\lambda) \quad (1)$$

$$b_{\mathbf{b}}(\lambda) = b_{\mathbf{bw}}(\lambda) + b_{\mathbf{bp}}(\lambda) \quad (2)$$

The determination of the above IOPs for the present dataset is described in Araújo and Bélanger (2022). Briefly, $a_{cdom}(\lambda)$, $a_{nap}(\lambda)$, and $a_{phy}(\lambda)$ were determined using a benchtop PerkinElmer Lambda-850 spectrophotometer, equipped with an integrating sphere (used for particles only). The *in situ* b_{bp} was determined at six wavelengths using a HydroScat-6P (HS6) backscattering meter (HOBI Labs Inc., Bellevue, WA), and was corrected for salinity variations and loss due to attenuation along the pathlength. The spectral dependency of b_{bp} was modelled (non-least-squares algorithm) using a power-law function, as $b_{bp}(\lambda) = b_{bp}(\lambda_0)[\lambda/\lambda_0]^{\gamma}$, where γ is a dimensionless parameter describing the spectral dependency of b_{bp} relative to a reference wavelength (λ_0; defined as equal to 550 nm in this study). Low residual differences (means < 5%) between measured and modelled values of b_{bp} assured the validity of this equation on describing its spectral shape in the study area (Araújo and Bélanger, 2022). Seawater absorption and backscattering coefficients were retrieved from tabulated values available in the literature (Morel, 1974; Zhang et al., 2009; IOCCG, 2018).

The $R_{rs}(\lambda)$ was derived from *in situ* radiometric measurements using a Compact Optical Profiling System (C-OPS; Biospherical Instruments Inc., San Diego, CA), and followed the procedures described in Bélanger et al. (2017) and Mabit et al. (2022). Briefly, the system was equipped with sensors that measured the above-water downwelling irradiance, $E_d(\lambda, 0^+)$, and the upwelling radiance from vertical profiles in the water column, $L_u(\lambda, z)$. The processing schema included the extrapolation of $L_u(\lambda, z)$ to assess the water-leaving radiance, $L_w(\lambda, 0^+)$. The $R_{rs}(\lambda)$ is then calculated using $R_{rs}(\lambda) = L_w(\lambda, 0^+)/E_d(\lambda, 0^+)$. C-OPS radiometry data are collected at 19 wavelengths, thus, $R_{rs}(\lambda)$ was interpolated using a piecewise cubic polynomial function to obtain 1-nm resolution, while preserving its spectral shape (Reynolds and Stramski, 2019).

2.5 Statistical analysis

Descriptive statistics (mean and standard deviation) and one-way Analysis of Variance (ANOVA) were used to quantitatively compare the populations identified by the clusters obtained by the PCA/HCA procedures. Data were confirmed to exhibit normal distributions using the Lilliefors (or Kolmogorov-Smirnov) test prior to all ANOVAs, and differences between pairs of means (pairwise comparisons) were assessed using the Tukey Honest Significant Difference (Tukey's HSD) criterion *post-hoc* test. In the following, when a population of data presents *significant difference*, it means that ANOVA presented a *p-value* less than 5% of significance level ($p < 0.05$). Additionally, when individual groups (clusters) are compared to others (pairwise comparisons), the Tukey's HSD criterion is used. All data manipulations and statistics were done using MATLAB (MathWorks) software.

3 Results

3.1 Clusters of phytoplankton assemblages

The normalized and standardized phytoplankton pigments concentrations (n = 20) and pico- and nano-autotrophic cell abundances (eukaryotic and cyanobacteria; n = 4) were submitted to the Principal Component Analysis (PCA), and the seven first principal components explained 80.3% of the variance in the data set. In sequence, the projections of the

original data on the principal component vector space (scores) were computed and the seven first columns were used as input in the Hierarchical Cluster Analysis (HCA). Figure 2 shows the dendrogram as obtained by HCA, as well as the procedure used to determine the linkage distance and subsequent number of clusters (L method; Salvador and Chan, 2004).

The inset of Figure 2A shows the reductional approach necessary to obtain a lower number of groups, consisting of applying the L method to a limited range of possible clusters (Salvador and Chan, 2004; Neukermans et al., 2016). This approach revealed to be more adequate to our analysis, since the obtained linkage distance cutoff (Figure 2B) divided the dataset in seven groups, containing between 8 and 26 samples, in each individual cluster. The cophenetic correlation value for the HCA was 0.62, comparable to other reported values in the literature (e.g., Neukermans et al., 2016).

The variability of selected inputs is shown in Figure 3, whereas the mean and standard deviation of all 24 inputs are presented in Table S1 (Supplementary Material). Only the pigment 19' butanoyloxyfucoxanthin (But) did not present significant difference considering the seven classes of phytoplankton assemblages (one-way ANOVA, $p > 0.05$). The analysis of cell abundances and pigments to Chla ratios within the groups revealed a complex co-occurrence of diverse phytoplankton groups, as the assignment of taxonomic classes from pigment signatures is not always a straight-forward task (Roy et al., 1996). Despite these inherent limitations, we assessed characteristics of each group that could be used to distinguish them from the others. For such analysis, we used available information compiled in the literature that links phytoplankton pigments to taxonomic classes (e.g., Roy et al., 1996; Gibb et al., 2000; Kramer and Siegel, 2019).

The relative distribution of phytoplankton groups identified by light microscopy (LM) are presented in Figure S1 (Supplementary Material). The correspondence between the seven clusters and the taxonomic analysis by LM was not straight-forward. First, LM resolution limits the identification of cells smaller than 3 µm. Second, the strong coloration of the acidic Lugol's solution used the preserve the samples make it difficult to distinguish autotrophic from heterotrophic cells using LM (see Tremblay et al. 2009). On the contrary, HPLC pigment concentrations and flow cytometry measurements both account for autotrophic cells smaller than 3 µm. Moreover, a high number of unidentified cells (average 20%) and, specifically, unidentified flagellates (between 25 and 50%, Figure S1) were assigned by the LM technique. Nevertheless, LM analysis revealed the presence of important species that helped in the interpretation of the composition of the phytoplankton assemblages.

The first cluster (purple) presented the highest means (and significantly higher than almost all other groups) picoeukaryotes cell counts and Chla-normalized pigment concentrations of neoxanthin, prasinoxanthin, violaxanthin, and Chl *b*. Moreover, there were significantly higher means (although not the highest) concentrations of nanoeukaryotes, Chl c_1, β-carotene and Perid. From these characteristics, we related this group to the presence of prasinophytes (possibly *Micromonas* sp.) and dinoflagellates (hereafter referred to as PraD). From the LM analysis, the prasinophyte *Pyramimonas* sp. was representative for the group PraD.

The second cluster (red) presented the highest means of nanoeukaryotes, Perid, Hex, and diadinoxanthin, while picoeukaryotes, Chl c_1 and c_2, prasinoxanthin and β-carotene were also significantly higher than other groups (but not the

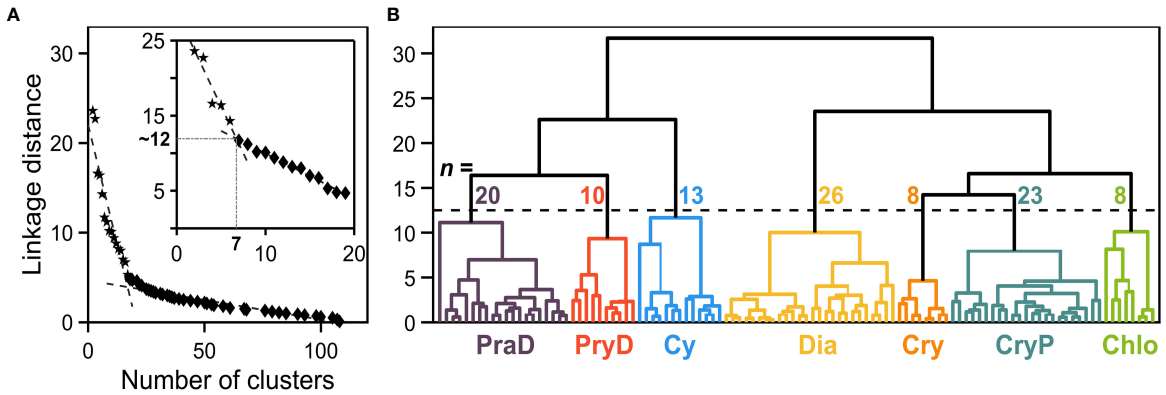


FIGURE 2
(A) Linkage distance as a function of the number of clusters obtained from the dendrogram (shown in **(B)**). The L-method (Salvador and Chan, 2004) is first applied considering all dataset (n =108), and then to a restricted range for the number of clusters (inset). The resulting "knee" corresponds to a linkage distance cutoff of 11.9, which divides the input dataset in seven clusters. **(B)** Dendrogram obtained from the Hierarchical Cluster Analysis. The dashed line corresponds to the linkage distance cutoff, and the number above each cluster shows the corresponding number of samples. The clusters are denoted by PraD (purple), PryD (red), Cy (blue), Dia (yellow), Cry (orange), CryP (teal) and Chlo (green).

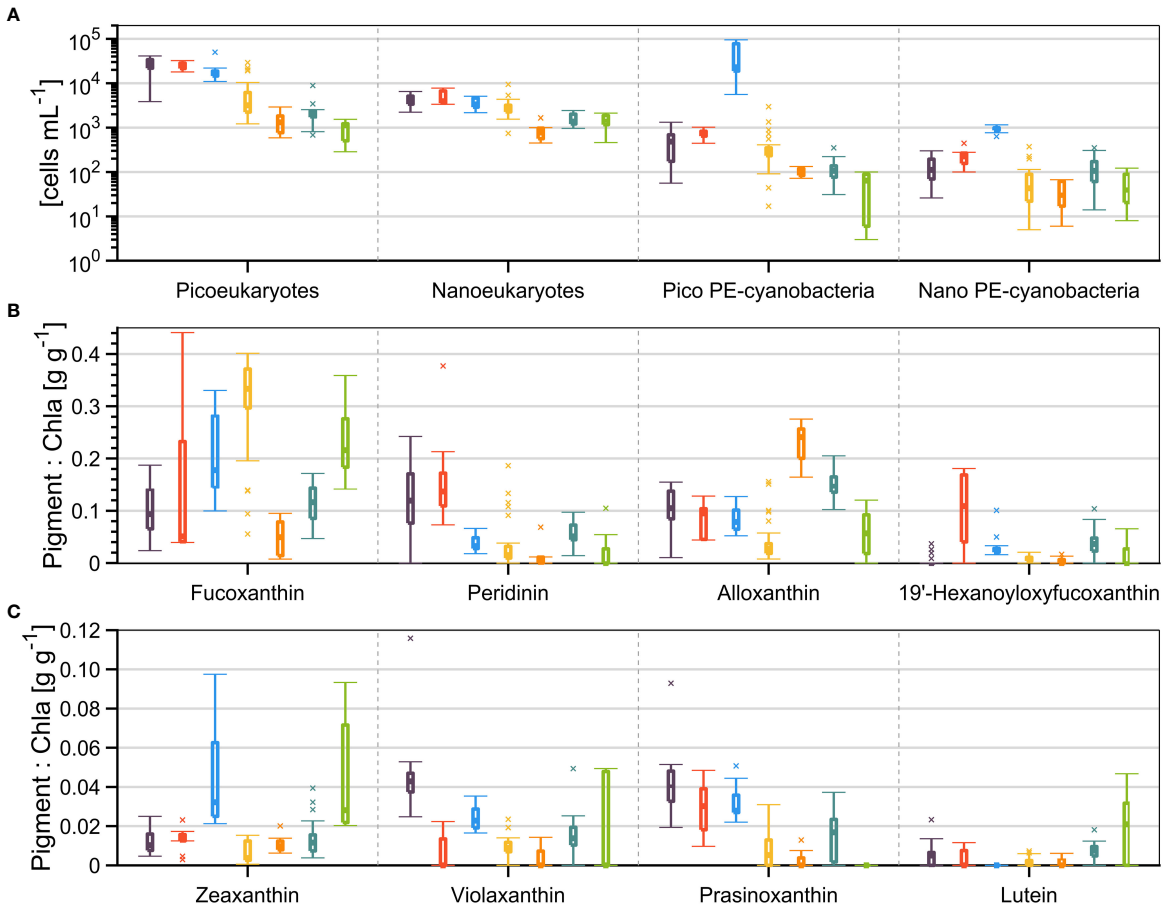


FIGURE 3
Variability (median, 25th and 75th percentiles, minimum, maximum and outliers) of **(A)** four classes of phytoplankton cell abundances **(B, C)** and eight accessory pigments to Chla ratios concentrations. The autotrophic cells concentration is separated by eukaryotes and phycoerythrin-containing (PE-) cyanobacteria, and by pico- (<2 µm) and nano-size (>2 and <20 µm) classes. The color code, associated to each cluster group, is the same as in Figure 2.

highest). We related this group to a relative dominance of prymnesiophytes and dinoflagellates (PryD). The LM analysis confirmed the presence and a relatively high abundance of the prymnesiophyte *Chrysocromulina* spp. in this group. The dinoflagellates *Gymnodinum* spp. and *Heterocapsa rotundata* were always representative in samples of groups PraD and PryD, while the toxic *A. tamarense* was also identified in these groups. Interestingly, the maximum concentration of *A. tamarense* (2920 cells L^{-1}) was observed in an anomalous sample (PryD-B, Figure S1) with a very high concentration of the diatom *Skeletonema costatum*.

The third cluster (blue) presented the highest means of pico- and nano-phycoerythrin-containing cyanobacteria, Zea, Chl c_3, and β-carotene, but also higher picoeukaryotes, neoxanthin, prasinoxanthin and Chl *b*. Thus, this group was related to a marked characteristic of occurrence of cyanobacteria (Cy), possibly *Synechococcus* sp. While presenting relatively high Fucoxanthin to Chla, the LM revealed in this group high abundances of the diatoms *Lennoxia faveolata*, *Leptocylindrus minimus*, *Skeletonema costatum*, *Thalassiosira conferta*, and *Chaetoceros* spp., but also the dinoflagellate *H. rotundata*.

The fourth (yellow) and most numerous cluster (n = 26) presented the highest means of Fuco, Chl c_1 and c_2, and was attributed to a dominance of diatoms (Dia). Cells enumerated by LM analysis revealed high abundances of the genus *Chaetoceros* (*C. debilis*, *C. convolutes*, *C. gelidus*, and *Chaetoceros* spp.) and the species *Thalassiosira nordenskioeldii*. Furthermore, the taxonomic groups identification of samples from group Dia revealed higher dominance of diatoms in relation to others (>50%, Figure S1), as expected.

The fifth (orange) and sixth (teal) clusters both presented the highest means of Allo and crocoxanthin, but the former had the highest means of α-carotene, while the latter had the highest means of MgDVP. We attributed these groups to be related to a marked presence of cryptophytes, but the sixth group had some important contribution from prasinophytes. Therefore, these groups were

10.3389/fmars.2022.1001098

denoted as Cry and CryP, respectively, with *Hemiselmis virescens* and *Plagioselmis prolonga* var. nordica being representative species. Moreover, these two groups were the most similar based on the dendrogram (Figure 2B). Finally, the seventh (green) cluster presented the highest mean of lutein, but also significantly higher concentrations of Zea than other groups (except Cy). We attributed this group to a relatively greater contribution of chlorophytes (Chlo) to the phytoplankton assemblages.

The numerical abundance of micro-, nano-, and pico-phytoplankton size-classes were examined in Figure S2. First, nanophytoplankton abundances obtained from flow cytometric measurements were compared to those obtained by light microscopy (LM), including unidentified cells (Figure S2A). Both measurements are comparable in terms of absolute values, but LM systematically underestimates the number of cells, comparatively, indicating a limitation of the former method to adequately account for this size class. Furthermore, a comparison of distribution of the three size-classes abundances (Figure S2B, with microphytoplankton abundances retrieved from the LM analysis) revealed a strong numerical dominance of picophytoplankton in all samples, except five samples where picophytoplankton represented ~50% of total cell abundance.

The fractional contribution of phytoplankton size classes to Chla (f_{pico},f_{nano}, and f_{micro}) are shown in Figure 4. The two methods used to estimate f_{pico} (f_{pico}^{FC} and f_{pico}^{HPLC}) were compared (Figure 4A) and presented a coefficient of determination (R^2) of 0.35. In general, the correspondences between the two methods presented different patterns when considering the different groups, with f_{pico}^{FC} underestimating f_{pico} in comparison to f_{pico}^{HPLC}, especially for the groups Dia, Cry, CryP, and Chlo, which were restricted to the lower range of variability (<25%). Nevertheless, the groups with higher values of f_{pico}, PraD and Cy, were noticeable in both methods.

Although the Uitz et al. (2006) method (used to determine f^{HPLC}) was developed using global relationships and may have constraints on applying to a coastal/nearshore dataset, as the one presented in this study, we investigated the size fractioned contributions of phytoplankton in the ternary diagram presented in Figure 4B. The different clustering groups presented distinguishable patterns of distribution. Most samples presented f_{micro}^{HPLC} higher than 50%, with the most noticeable contribution of this fraction for Dia. Specifically, the groups PraD and Cy presented a dispersion from f_{micro}^{HPLC} towards f_{pico}^{HPLC}, while this dispersion for the groups CryP, PryD, and, particularly for Cry, were towards f_{nano}^{HPLC}.Overall, the phytoplankton communities were well discriminated by the PCA/HCA procedures. Despite the picophytoplankton numerical dominance, the total biomass was dominated by microphytoplankton, with some variations within clusters.

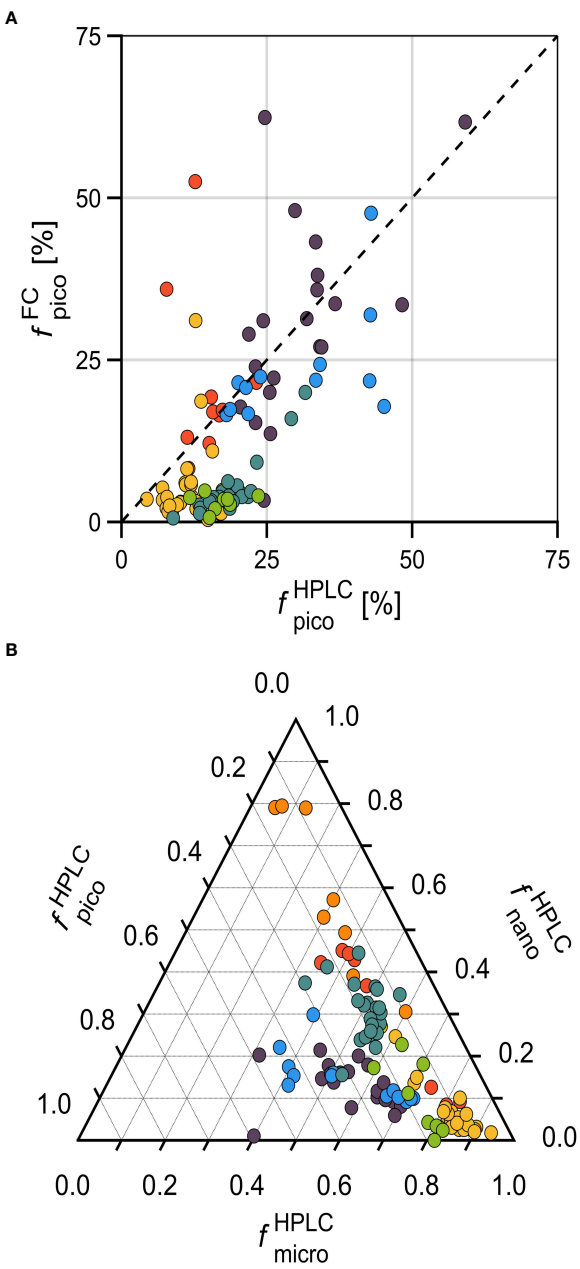


FIGURE 4
Relative (or fractional, *f*) contributions of phytoplankton size classes to Chla, for each phytoplankton cluster. **(A)** Two methods to obtain the picophytoplankton fractional contribution to Chla (f_{pico}): f_{pico}^{FC} and f_{pico}^{HPLC} (see text for details). **(B)** Ternary plot of f_{pico}^{HPLC}, f_{nano}^{HPLC}, and f_{micro}^{HPLC}. This approach (pigment-based) considers a global relationship using seven diagnostic pigments as inputs (Uitz et al., 2006). The color code is the same as in Figure 2.

3.2 Seasonal and spatial variability

The Chla biomass, the seasonal succession, and spatial variabilities within phytoplankton clusters are shown in Figure 5. In Bay of Sept-Îles (BSI), Chla medians were always between 1 and 3 mg m^{-3} for all groups, except for Chlo whose median is 0.66 mg m^{-3} (Figure 5A). No group is significantly different from the others, but PryD and Dia presented higher

means of Chla. In comparison, only two groups were present at AZMP (Dia and PraD) in the middle of the Lower St. Lawrence Estuary, during the period from July to October 2015, and Chla values were generally higher than in BSI, with values ranging from 1.02 to 11.43 mg m^{-3} (Figure 5B).

The seasonal evolution of the phytoplankton clusters of BSI are shown in Figure 5C, where the bars represent the relative contribution of each group during each campaign. Firstly, in early May 2017 (BSI-1) only the group Dia was found in BSI surface waters. About two weeks later (BSI-2), the group Dia was

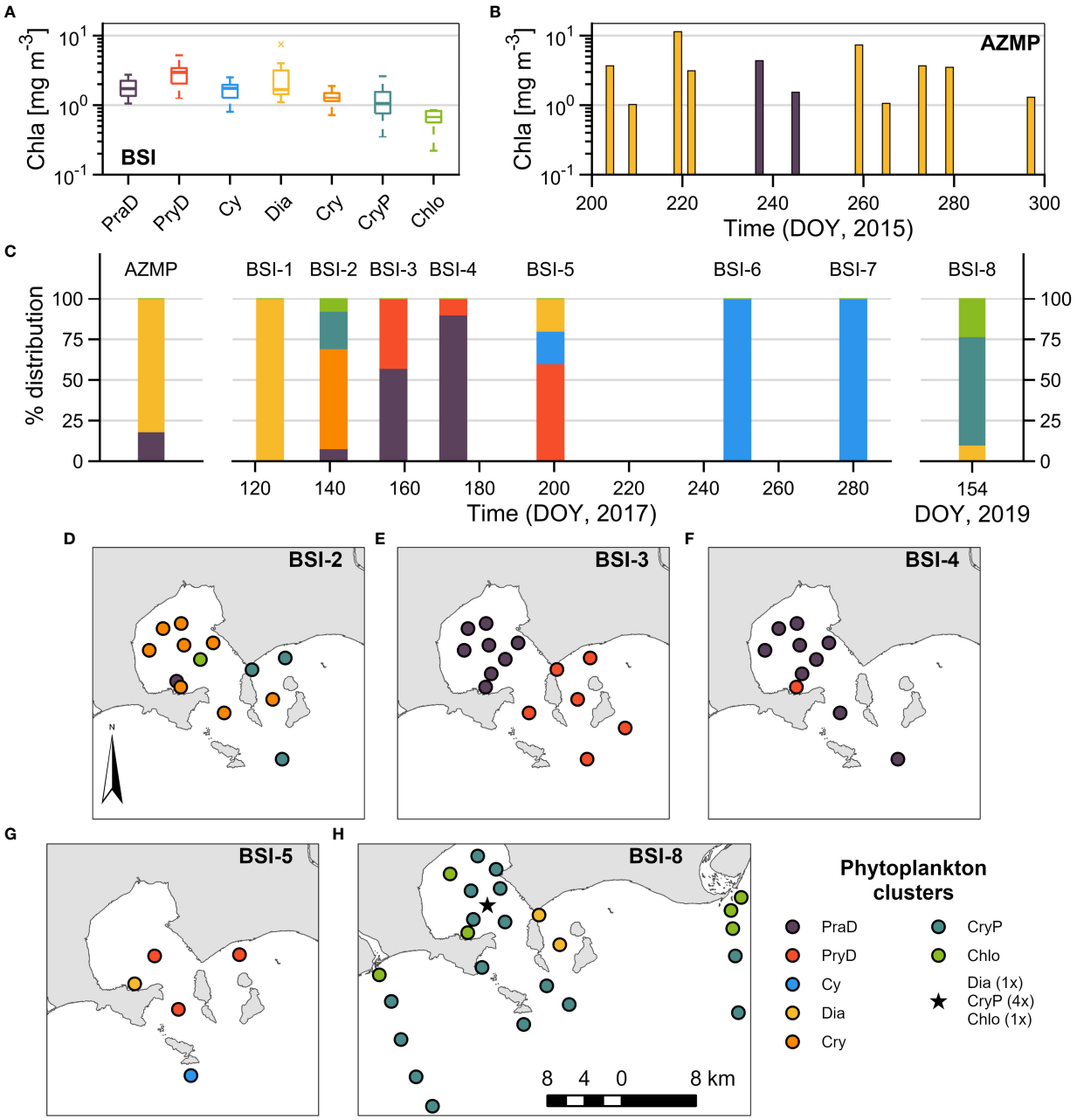


FIGURE 5
Temporal and spatial variability of the phytoplankton clusters. **(A)** Boxplots showing the variability of Chla for each cluster, for the Bay of Sept-Îles (BSI). **(B)** Bars showing the temporal variability of Chla in the AZMP buoy station (DOY = Day of Year). The color of the bars corresponds to the class of phytoplankton clusters. **(C)** Relative distribution of phytoplankton clusters for AZMP and for the temporal series in BSI (BSI-1 to 8; Table 1). **(D–H)** Spatial distribution for each campaign that presented noticeable variability of phytoplankton clusters.

replaced mainly by the groups Cry, CryP, and Chlo. Interestingly, the dominance of groups CryP and Chlo (but also some samples from Dia) was also observed in the field campaign of early June 2019 (BSI-8). In June 2017 (BSI-3 and 4) only groups PraD and PryD were found in BSI, followed in July (BSI-5) by the occurrence of PryD, Dia, and Cy. Finally, only group Cy was found in fall (BSI-6 and 7).

Although BSI-1, 6, and 7 were characterized by a single group, the other field campaigns presented heterogeneity regarding the phytoplankton assemblages, and their spatial distribution is shown in Figures 5D–H. The dominant groups in BSI-2, Cry and CryP, were generally found inside and outside the bay, respectively (Figure 5D). This spatial separation was even clearer in BSI-3 for the groups PraD (inside) and PryD (outside the bay). In BSI-5, the sample correspondent to Cy is in a station outside the bay. In the 2019 campaign (BSI-8), beside the dominance of CryP, the group Chlo was distributed in the riverine (freshwater) plumes, while two Dia samples were distributed in-between the islands east of the bay. These results evidence the seasonal succession of phytoplankton assemblages, but reveal that the spatial variability, at this scale, is also important.

3.3 Major nutrients and physical environment

The relationships between major nutrient concentrations, associated to each phytoplankton assemblage, are shown in Figures 6A, B, and the physical environment, as determined by temperature and salinity, are shown in Figure 6C. The mean and standard deviation of each variable for the Bay of Sept-Îles (BSI) of Figure 6 (plus nitrite and nutrient concentrations ratios) are summarized in Table 2. Samples from the Lower St. Lawrence Estuary (AZMP, squares in Figure 6) were differentiated from those of BSI. In addition, other samples from BSI were considered as outliers. First, two samples from the group Dia, in the campaign BSI-8 (Figure 5H), had environmental (and optical) characteristics typical of those from the group Chlo. This might be related to lateral advection of phytoplankton cells. Secondly, few samples from groups Chlo (2) and CryP (1) were found to have anomalous values of physical and optical (not shown) variables. These samples were obtained in turbulent hydrodynamic conditions close to riverine discharges. Water sampling might not reflect the same conditions as the data acquired by the *in situ* instrumentation (CTD, HS6, C-OPS). In the following, these outliers are not considered.

The nutrients and physical environment at the Lower St. Lawrence Estuary station (AZMP) are markedly different from those of BSI, when considering the same phytoplankton groups of these two locations. Nitrate and phosphate concentrations values were higher for AZMP (Figure 6B), while silicate concentrations were similar (Figure 6A). However, if only the group Dia is considered, silicate concentrations were also higher at AZMP (except for one sample). Interestingly, the Dia samples from AZMP were also associated with higher temperatures (mean of 8.2°C) than the ones from BSI (mean of 2.7°C), but with slightly lower salinities (means of 27.6 and 29.1, for AZMP and BSI, respectively) (Figure 6C).

All nutrient concentrations, nutrient ratios, and physical parameters were significantly different for the seven phytoplankton clusters (one-way ANOVA, $p < 0.05$). Samples from BSI-4, BSI-5, and BSI-6 (stars in Figure 6) field campaigns (Figure 5C, from mid-June to early September 2017) presented undetectable nitrate concentration (~0 μM). Thus, depleted nitrate conditions were noticeable for samples of groups PraD, PryD and Cy (right side of Figures 6A, B). Although we do not differentiate these samples from others of the same group in Table 2, silicate concentrations values for these population of samples were generally lower for PraD and PryD (comparing to the same groups in BSI-3), and higher for Cy (comparing to the same group in BSI-7). Notwithstanding, phosphate concentrations values (in the nitrate-depleted conditions) were comparable with others for PraD and PryD, and slightly lower for Cy. A single sample from group Cy (BSI-6) presented a nitrate concentration much higher than the detection limit (~0.36 μM), and it corresponded to the station farthest from the shore.

The nitrate concentrations associated to the different groups in BSI, as analyzed by pairwise comparisons (Tukey's HSD criterion), revealed that Chlo has higher concentration than all other groups, while CryP was higher than PraD, PryD, Cy, and Dia. Nitrite concentrations was higher in Cy than all other groups (except Chlo), while Dia has significantly lower concentrations than all other groups.

In non-depleted [NO_3^-] conditions, silicate concentrations (Figure 6A; Table 2) in groups PraD, PryD, and Cy presented very low variability. In Dia, silicate concentrations were significantly lower than all other groups (except Cy). Two groups, PraD and PryD, presented significantly lower values of phosphate concentrations (Figure 6B; Table 2) than others (Cy, Cry, CryP, and Chlo). Moreover, [PO_4^{3-}] in Chlo was significantly higher than Dia (besides Prad and PryD).

Nutrient ratios are commonly used to assess elemental limitation for phytoplankton production. The nitrate (plus nitrite) to silicate and the nitrate (plus nitrite) to phosphate ratios (dimensionless) are presented in Table 2. The [NO_3^-] + [NO_2^-] : [$Si(OH)_4^{4-}$] means were lower for groups PraD and PryD and highest for group Chlo. Nevertheless, Chlo also presented higher [NO_3^-] + [NO_2^-] : [PO_4^{3-}] means than all other groups (minus PryD), while Dia was significantly lower than Chlo and PryD.

The groups PraD, PryD, and Cy were found in warmer waters than the other groups (Figure 6C; Table 2). Conversely, the group Dia presented significantly lower temperatures when compared to all other groups. Dia and Cy (specifically the blue circles in Figure 6) were found in saltier waters (>28), while group Chlo presented significantly lower salinities than all other groups but PraD. Also

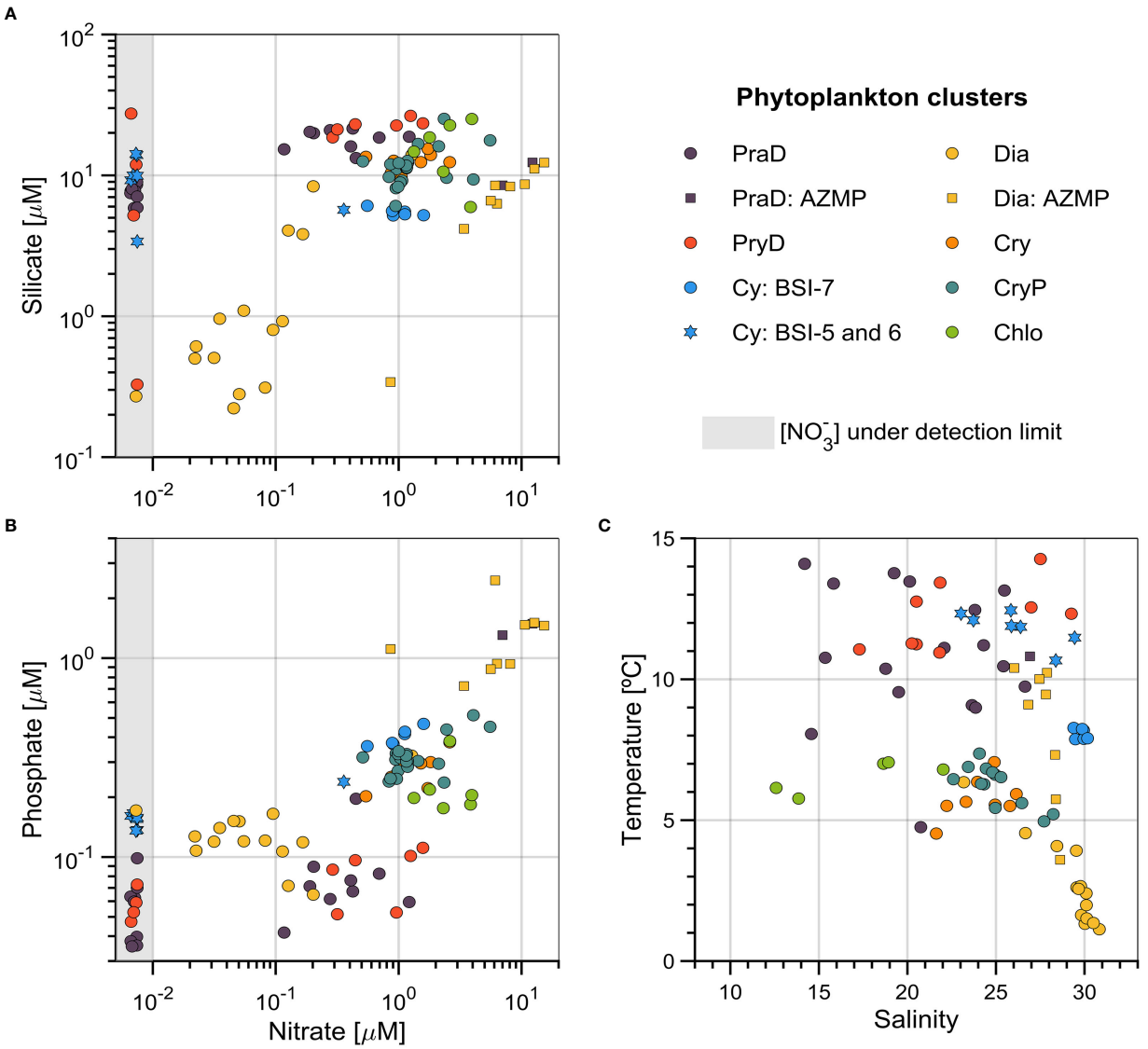


FIGURE 6
Nutrient concentrations and physical parameters relationships associated with each phytoplankton cluster. **(A)** Silicate ($[Si(OH)_4^{4-}]$) versus nitrate ($[NO_3^-]$); **(B)** phosphate ($[PO_4^{3-}]$) versus nitrate concentrations; and **(C)** temperature versus salinity. Samples from the Lower St. Lawrence Estuary station (AZMP) are presented by squares, and outliers from the Bay of Sept-Îles (BSI) are presented by diamonds. The gray-shaded area corresponds to undetectable nitrate levels (~0 μM).

noticeable is the narrow range of temperature (~8 °C) and salinity (~30) of some samples of group Cy, which were collected on BSI-7 (October 2017, Figure 5C). The groups associated with the presence of cryptophytes, Cry and CryP, and Chlo, presented low variability of temperatures (small standard deviation, Table 2).

The separation of group Cy between campaigns BSI-5 and 6 (stars in Figure 6) and BSI-7 were done because of the different environmental conditions in which the two sets of samples were found (e.g., nitrate depletion, temperature, salinity). The set of samples of group Cy in BSI-5 and 6 presented more similar environmental conditions to those of groups PraD and PryD. Optical conditions of group Cy from BSI-5 and 6 were also closely related to these groups (not shown). Therefore, in the following presentation of results only the set of BSI-7 are considered for the group Cy.

3.4 Optical characterization

The total and component-specific spectral absorption and backscattering coefficients are presented in Figure 7. For each

10.3389/fmars.2022.1001098

TABLE 2 Mean and (plus or minus) standard deviation of nutrient concentrations and physical parameters for each of the seven clusters of phytoplankton (PraD, PryD, Cy, Dia, Cry, CryP, and Chlo), for the Bay of Sept-Îles (BSI) region.

Environmental variable	PraD	PryD	Cy	Dia	Cry	CryP	Chlo
Nitrate, $[NO_3^-]$ (μM)	0.22 ± 0.32	0.49 ± 0.58	0.51 ± 0.56	0.16 ± 0.32	1.38 ± 0.67	**1.54 ± 0.18**	**2.64 ± 1.07**
Nitrite, $[NO_2^-]$ (μM)	0.10 ± 0.04	0.09 ± 0.03	**0.17 ± 0.05**	0.03 ± 0.04*	0.09 ± 0.02	0.08 ± 0.04	0.12 ± 0.04
Silicate†, $[Si(OH)_4^{4-}]$ (μM)	12.89 ± 5.93	18.01 ± 9.18	7.63 ± 3.49	2.44 ± 3.88*	12.57 ± 1.84	11.97 ± 4.07	16.28 ± 7.28
Phosphate, $[PO_4^{3-}]$ (μM)	0.07 ± 0.04*	0.07 ± 0.02*	0.27 ± 0.13	0.14 ± 0.06	0.28 ± 0.05	0.32 ± 0.07	0.23 ± 0.08
$[NO_3^-] + [NO_2^-] : [Si(OH)_4^{4-}]$ (dim.)	0.02 ± 0.02	0.04 ± 0.04	0.12 ± 0.12	0.15 ± 0.16	0.12 ± 0.05	0.14 ± 0.09	0.23 ± 0.22
$[NO_3^-] + [NO_2^-] : [PO_4^{3-}]$ (dim.)	4.87 ± 5.02	7.27 ± 6.50	2.00 ± 1.13	1.21 ± 1.30	5.21 ± 1.89	4.84 ± 2.57	**13.07 ± 6.60**
Salinity† (PSU)	21.11 ± 4.14	22.43 ± 4.08	**27.81 ± 2.53**	**29.11 ± 1.94**	24.11 ± 1.63	24.13 ± 3.82	16.82 ± 3.62*
Temperature† (°C)	**10.85 ± 2.44**	**12.20 ± 1.17**	**10.09 ± 2.00**	2.72 ± 1.50*	5.76 ± 0.74	6.24 ± 0.72	6.55 ± 0.57

All variables presented significantly difference (one-way ANOVA, $p < 0.05$). Bold values indicate groups that were significantly higher (Tukey's HSD criterion) than at least four or more other groups. Conversely, the asterisk (*) indicate when a group of samples were significantly lower than at least four or more other groups.
†Smirnov-Kolmogorov test rejects the null hypothesis at the 5% significance level, but Lilliefors test does not.

graph (A-F), each phytoplankton group curve is represented by the sample having the highest counts of median values, calculated for unitary wavelength within the visible spectral range (400 to 700 nm). Descriptive statistics and tests for some optical properties shown in Figures 7, 8 are presented in Table 3, for selected wavelengths, in the perspective of satellite remote sensing applications.

For most phytoplankton assemblages, CDOM absorption coefficient (a_{cdom}, Figure 7A) was approximately one order of magnitude higher than the other absorption components at wavelengths shorter than 500 nm. As expected, the group Chlo, found in fresher waters (Table 2) presented significantly higher $a_{cdom}(465)$ than other groups, minus PraD and CryP (Table 3). In contrast, groups more related to marine end-member waters (with saltier characteristics), such as Dia and Cy, presented lower values of $a_{cdom}(\lambda)$.

The non-algal particles absorption spectra (a_{nap}, Figure 7B) were much lower than a_{cdom}, but had similar relative magnitudes

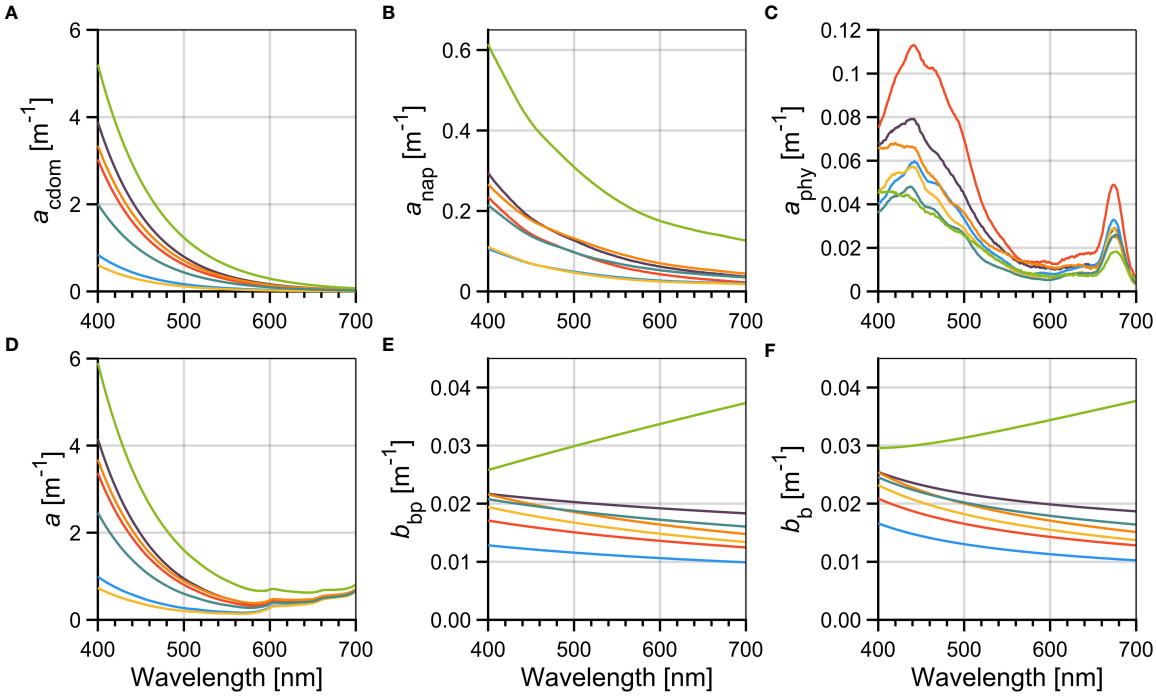


FIGURE 7
Inherent optical properties spectra: absorption coefficients of **(A)** chromophoric dissolved organic matter (a_{cdom}); **(B)** non-algal particles (a_{nap}); and **(C)** phytoplankton (a_{phy}); **(D)** total absorption coefficient (a); **(E)** particulate backscattering (b_{bp}); and **(F)** total backscattering coefficient (b_b). For each graph, the different lines represent the median spectra for each cluster of phytoplankton groups, and the color code is the same as in Figure 2.

when considering individual groups of phytoplankton, suggesting a co-variation between these two optical components. For example, $a_{nap}(465)$ in group Chlo was significantly higher than all others, while Dia and Cy values were significantly lower than for PraD and Cry.

The phytoplankton absorption coefficient spectra (a_{phy}, Figure 7C) was also much lower than a_{cdom} or a_{nap} and, thus, its influence in the total absorption coefficient (a , Figure 7D) is minimal (see also Araújo and Bélanger, 2022). For example, the fractional contribution of a_{phy} to the non-water absorption coefficient (= a_{cdom} + a_{nap} + a_{phy}) was maximal in the blue peak of a_{phy}(~465 nm), but higher mean values reached only 6.2 and 5.4% for groups Dia and Cy. Nevertheless, significantly higher values of $a_{phy}(465)$ and $a_{phy}(665)$ were found for group PryD, which also presented higher Chla values (Figure 5A).

As expected, the $a(\lambda)$ reflects the additive effects of a_{cdom} and a_{nap}, especially in the blue and green regions of the spectrum, while in the red the pure water absorption (a_w) dominates the absorption budget.

The particulate (b_{bp}) and total (b_b) backscattering coefficients are shown in Figures 7E, F. Most phytoplankton groups presented similar spectral characteristics of b_{bp} (and b_b), but group Chlo was higher than others at all wavelength ranges. Interestingly, the spectral variability of b_{bp} from group Chlo presented an odd behavior compared to the others, with increasing values with increasing wavelength. This group has significantly higher values of the spectral slope (γ) of b_{bp}, resulting in significantly higher $b_{bp}(655)$ (Table 3).

The spectra of backscattering to total absorption coefficient ratio (b_b/a) and the remote sensing reflectance (R_{rs}) are shown in Figure 8, for each phytoplankton assemblage. As for individual IOPs (Figure 7) the b_b/a and R_{rs} shown for each group corresponds to the mode (spectral domain) of median values for individual wavelengths. Although similarities are expected when comparing these two variables, it is important to note that inelastic scattering by water molecules (Raman) and by CDOM and phytoplankton pigments (fluorescence) are not considered in b_b/a. Furthermore, the approach we used does not consider changes in IOPs along the water column, that could result in changes in the light field in highly stratified waters (particularly in L_w, and consequently in R_{rs}). Notwithstanding, this latter situation is likely to happen under some circumstances in our study area (Araújo and Bélanger, 2022).

Most phytoplankton groups presented similar shape and magnitudes of the b_b/a spectra, observed in all wavelength ranges. The two exceptions were for groups Dia and Chlo that peaked in green (~560 nm) and red (~640 nm) regions, respectively. The combination of lower a and at-average b_b values give significant higher values of b_b/a in the blue (465) and green (566) regions for group Dia (Table 3). Similarly, the significantly higher values of b_b/a (665) for the group Chlo is explained by the high b_{bp} in the red region associated with this group, which is found in waters heavily influenced by terrigenous inputs.

Dissimilarities between b_b/a and R_{rs} were observable mainly in the red spectral range (>620 nm) and are mostly due to

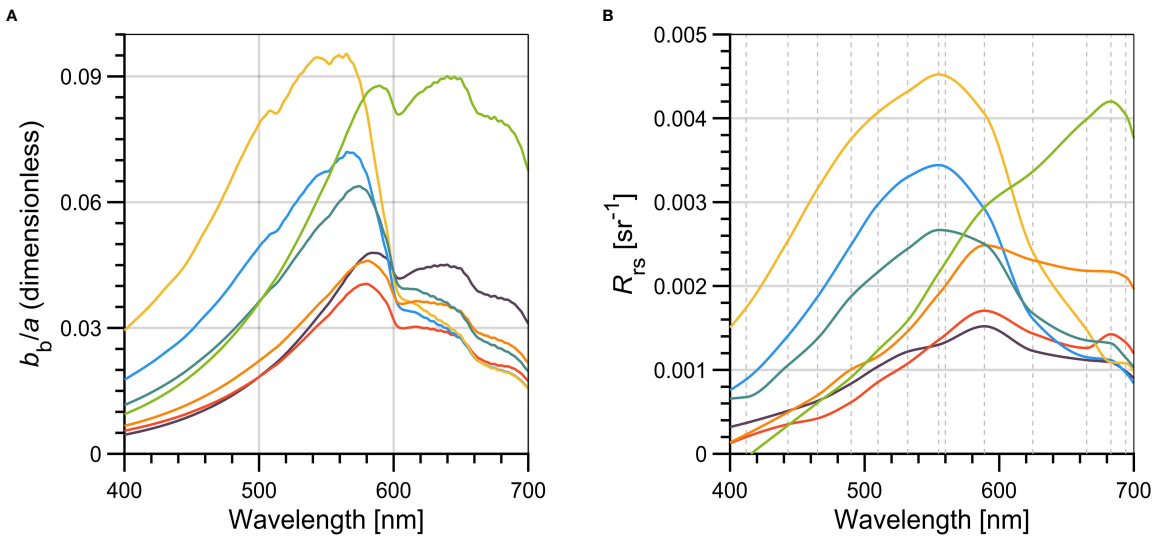


FIGURE 8
Spectra of **(A)** the ratio of total backscattering to total absorption coefficients (b_b/a), and **(B)** the measured remote sensing reflectance (R_{rs}). The vertical gray dashed lines on **(B)** indicates the original spectral bands of the C-OPS instrument used to derive R_{rs}. For each graph, the different lines represent the median spectra for each cluster of phytoplankton groups, and the color code is the same as in Figure 2.

10.3389/fmars.2022.1001098

TABLE 3 Mean and (plus or minus) standard deviation of temperature, inherent optical properties (including ratios), and remote sensing reflectance, at selected wavelengths, for each of the seven clusters of phytoplankton (PraD, PryD, Cy, Dia, Cry, CryP, and Chlo).

Optical parameters	PraD	PryD	Cy (BSI-7)	Dia	Cry	CryP	Chlo
$a_{cdom}(465)$ (m^{-1})	1.45 ± 0.76	1.05 ± 0.49	0.29 ± 0.04	0.34 ± 0.27*	1.29 ± 0.43	0.88 ± 0.52	**2.18 ± 0.71**
$b_{bp}(665)$ (m^{-1})	1.80 ± 0.64	1.28 ± 0.16	1.10 ± 0.43	1.67 ± 1.13	1.81 ± 0.54	1.73 ± 0.95	**3.64 ± 1.64**
b_b/a (465) ($\cdot 10^2$, dim.)	1.48 ± 0.76	1.13 ± 0.16	3.46 ± 0.77	**5.34 ± 1.71**	1.61 ± 0.54	2.34 ± 0.78	1.61 ± 0.97
b_b/a (566) ($\cdot 10^2$, dim.)	4.68 ± 2.09	3.63 ± 0.49	7.14 ± 1.98	**10.41 ± 3.16**	4.81 ± 1.64	6.03 ± 2.24	5.86 ± 2.60
b_b/a (665) ($\cdot 10^2$, dim.)	3.22 ± 1.10	2.35 ± 0.21	2.31 ± 0.83	3.37 ± 2.00	3.30 ± 0.91	3.23 ± 1.59	**6.81 ± 1.81**
$R_{rs}(465)$ ($\cdot 10^3$, sr^{-1})	0.67 ± 0.34	0.46 ± 0.18	**2.04 ± 0.36**	**2.60 ± 0.93**	0.74 ± 0.19	0.98 ± 0.31	0.57 ± 0.47
$R_{rs}(566)$ ($\cdot 10^3$, sr^{-1})	1.81 ± 0.72	1.54 ± 0.38	3.58 ± 0.61	**4.67 ± 1.47**	2.03 ± 0.37	2.41 ± 0.78	2.60 ± 1.07
$R_{rs}(665)$ ($\cdot 10^3$, sr^{-1})	1.34 ± 0.40	1.25 ± 0.22	1.17 ± 0.26	1.75 ± 1.01	1.48 ± 0.39	1.61 ± 0.85	**3.12 ± 0.96**

All variables presented significantly difference (one-way ANOVA, $p < 0.05$). Bold values indicate groups that were significantly higher (Tukey's HSD criterion) than at least four or more other groups. Conversely, the asterisk (*) indicate when a group of samples were significantly lower than at least four or more other groups.

inelastic scattering processes affecting R_{rs}. However, the characteristics of b_b/a spectra that are distinguishable for the phytoplankton groups Dia and Chlo are also observed in R_{rs} (Figure 8B; Table 3).

3.5 Seasonal succession and framework for remote sensing estimations

The variability of phytoplankton assemblages and nutrient concentrations, physical parameters, and optical properties revealed a clear seasonal signal, as summarized in Figure 9. Since riverine discharges are a major controlling factor in the optical environment in the BSI region (Araújo and Bélanger, 2022), the Moisie River discharge for years 2017, 2019, and the climatological median (1965-2021) is depicted in Figure 9A. It is expected to reflect the seasonality of the smaller rivers discharging directly into the bay (i.e., rivières Hall, des Rapides, aux-foins, du Poste). The values of the discharge peaks of 2017 and 2019 (~2,500 m^3 s^{-1}) were 60% higher than the historical median (from 1965 to 2021).

The group Dia occurred in BSI in April - early May (Figure 9B), before the spring freshet, and is related to the spring bloom, a common feature at high latitude estuaries (Carstensen et al., 2015). Lower water temperatures and the lowest light absorption characteristics (due to lower a_{cdom} and a_{nap}) are found.

Our interpretation of the spring bloom starting in the BSI region earlier than BSI-1 campaign (early May) is supported by samples collected in mid-April 2017 (Table S2, not used in this study due to incomplete dataset), where biomass (Chla) and Fucoxantin to Chla ratio were among the highest. The Dia samples observed in campaign BSI-1 were likely related to the end of the spring bloom, as indicated by the low nitrate and silicate concentrations. The presence of a subsurface chlorophyll maximum (SCM), a common feature in the Gulf of St. Lawrence (Vandevelde et al., 1987), was observed during field campaign BSI-1 (see Figure S3; Supplementary Material), with similar phytoplankton composition despite much higher Chla values (Table S2). Silicate and phosphate concentrations were comparable at the surface and within SCM, although SCM nitrate levels were one order of magnitude higher than surface samples.

The groups associated with cryptophytes, Cry and CryP, occurred approximately in phase with the peaks of the spring freshet (Figure 9B), and were characterized by an increase in temperature and decreasing salinities. As expected, the freshet increased the amount of CDOM and non-algal particles in the water column, increasing its absorbing and backscattering characteristics. Samples collected in the 2019 field campaign (BSI-8), in early June, had similar characteristics to those collected in BSI-2 (mid-May 2017), reflecting the timing of freshet peaks in each year.

The group Chlo was also dominant during the spring freshet and was found in the vicinity of river plumes (Figure 5H), characterized by lower salinities. This group was characterized by lower Chla values than others and was associated with very turbulent conditions (field observation). The significantly higher nitrate to phosphate ratio in this group (Table 2) reflects the generally higher values of $[NO_3^-]$ in the riverine endmembers (data not shown), in comparison to marine samples. Moreover, the suspended sediment- and CDOM-laden waters of river plumes waters generate the highest absorption and backscattering coefficient values of BSI. The highest b_b (and b_{bp}) values in the red portion of the spectrum characteristic of Chlo are explained by higher values of the spectral slope of b_{bp} (γ), which likely reflects higher concentrations of particulate organic matter (Araújo and Bélanger, 2022).

After the spring freshet, as water temperature continue to increase, the groups PraD and PryD occupied the BSI region, and this lasted throughout the summer. Significant lower phosphate concentrations were found to be associated with these two groups (Table 2), while nitrate depletion occurred a few days after their appearance (in-between BSI-3 and BSI-4 campaigns, Figure 9B). The nitrate-depleted conditions then continued in summer up to early fall.

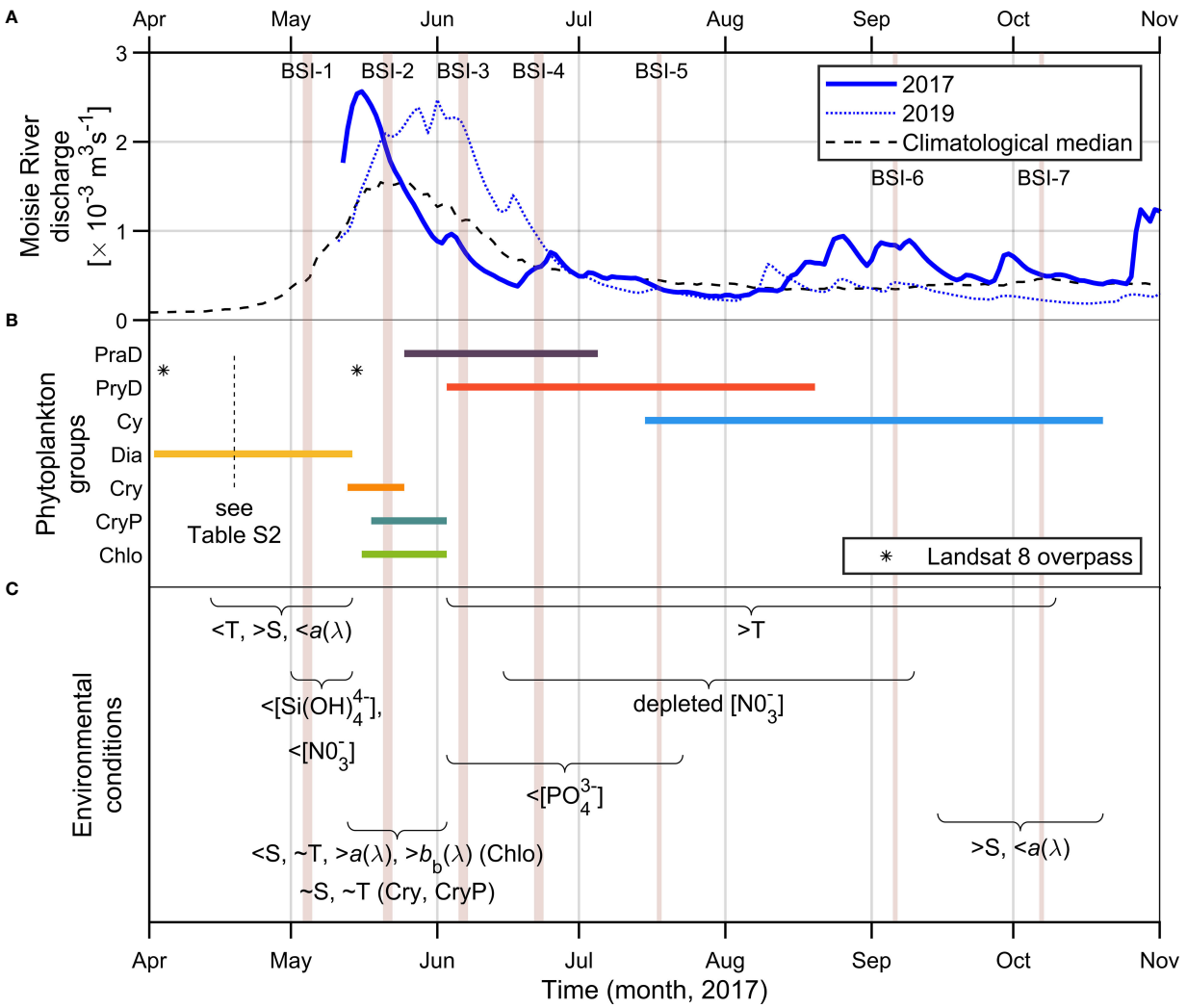


FIGURE 9
Seasonal succession of phytoplankton assemblages in the Bay of Sept-Îles (BSI). **(A)** Moisie River discharge for years 2017, 2019, and climatological median (1965-2021). Source: Ministère de l'Environnement et de la Lutte contre les changements climatiques (https://www.cehq.gouv.qc.ca/). **(B)** Phytoplankton assemblages distribution (see Table S2 in Supplementary Material for details of samples collected in April 19) and dates of Landsat 8 overpass in BSI (shown in Figure 11); and **(C)** environmental conditions as showed by nutrient concentrations and physical parameters (Temperature and Salinity, T and S) along the year 2017. The durations of the events of both occurrence of phytoplankton assemblages and environmental conditions are extrapolated from punctual field campaigns (BSI-1 to BSI-7, refer to Table 1), represented by vertical light gray lines.

The group dominated by PE-containing cyanobacteria, Cy, began dominating BSI waters in early fall, although its presence was already noted in mid-summer at the station farthest from the shore (BSI-5, Figure 5G). In mid-fall (BSI-7) nitrate concentrations were restored (Figure 6A and Table 2).

The shape and relative magnitudes of remote sensing reflectance ($R_{rs}(\lambda)$) reflected the importance of the bio-optical environment for the determination of phytoplankton assemblages in nearshore waters of BSI. Strong differences in R_{rs} (Figure 8B; Table 3), in the blue, green, and red bands (465, 566, and 665 nm, respectively), and in SST (Figure 6C; Table 2) between assemblages of phytoplankton suggested the potential of using multispectral and thermal infrared radiometer sensors onboard Earth Observation platforms to infer about them. An inverse framework where SST, $R_{rs}(645)$, $R_{rs}(566)$, and $R_{rs}(665)$ are used as inputs in the classification of BSI waters is therefore proposed (Figure 10).

Firstly, the group Chlo presented the highest values of a_{cdom} (465) and b_{bp} (665), resulting in low values of R_{rs} (465) and very high values of R_{rs} (665) and, consequently, were found in reddish waters. Considering this, using a simple threshold of the ratio R_{rs} (665)/R_{rs} (465), the group Chlo can be separated from others.

Secondly, the lowest values of a_{cdom} and a_{nap} for group Dia resulted in the highest values of R_{rs} (465) and R_{rs} (566), comparatively to other groups. Thus, the sum of R_{rs} in these two wavelengths is used to target group Dia, and SST is also included to better distinguish it from group Cy.

In a third step, taking advantage of different temperature niches occupied by the phytoplankton assemblages, another threshold is used to separate groups Cry and CryP from groups Cy, PraD, and PryD. Finally, the lower a_{cdom} of Cy, and its influence on R_{rs} (465), is used to separate this group from PraD and PryD (Figure 10).

In a simple validation exercise, the presented framework was applied to the *in situ* R_{rs} and SST measurements to verify its coherence. When compared to the original discrimination of the seven phytoplankton assemblages (re-grouped in five, as in Figure 10; n = 72) determined by the PCA/HCA method, the result of this empirical inversion succeeded for 92% of the samples. The samples where this procedure failed refer mainly to some isolated groups in the context of other dominant groups in the same field campaign, as for example a single PraD (Figure 5D) and a Dia sample (Figure 5H).

To test the applicability of this framework in real imagery, we processed two Landsat 8 images from 2017 (April 4 and May 15, stars in Figure 9B), downloaded as Level-1 Collection 2 data and distributed by the United States Geological Survey (USGS). The $R_{rs}(\lambda)$ thresholds presented in Figure 10 were tested and adjusted while contemplating the Spectral Response Function of the Operational Land Imager (OLI) of bands 2 (blue), 3 (green), and 4 (red). The two images were atmospherically-corrected using the dark spectrum fitting algorithm implemented in ACOLITE software (Vanhellemont, 2019; Vanhellemont, 2020c). For SST retrieval, the images of the Thermal Infrared Sensor (TIRS) were processed using the Thermal Atmospheric Correction Tool (TACT), also implemented in ACOLITE (Vanhellemont, 2020a; Vanhellemont, 2020b).

The application of the proposed framework in the two images (Figure 11) successfully targeted the dominance of group Dia in early April, as both R_{rs} values in the blue and green were higher than 0.005 sr^{-1} and SST values were the lowest when compared to other periods. Following the freshet, the classification of the image from mid-May also could detect the presence of the group Cry/CryP in nearshore waters of BSI, while the group Dia was more restricted to offshore waters. The occurrence of group Cy at this period of the year is probably a misclassification due to the overestimation of R_{rs} in the blue region from the atmospheric correction procedure (see Mabit et al., 2022). In this case, the classified group Cy would actually represent a dominance of phytoplankton assemblages from groups PraD and/or PryD. Overall, the application of the framework in remote sensing imagery showed to be suitable.

4 Discussion

The potential for identification of major phytoplankton assemblages from pigment concentrations and <20 µm autotrophic cell abundances, in a dynamic nearshore subarctic environment, was evaluated. The combined PCA and HCA techniques applied to these proxies demonstrated to be a good indicator of distinctive communities of phytoplankton in the studied area, and it was confirmed, to some extent, by the LM taxonomy analysis. This dataset was comprehensive in terms of temporal (seasonal, from mid-spring to early fall) and spatial (order of 10^0 to 10^1 km) scales. However, winter conditions, early phytoplankton spring bloom and pre-bloom (March-April), and mid-summer (August) conditions were missing.

The seven clusters revealed relevant characteristics associated to the following groups (Figure 3; Table S1): prasinophytes and dinoflagellates (PraD); prymnesiophytes and dinoflagellates (PryD); cyanobacteria (Cy); diatoms (Dia); cryptophytes (Cry); cryptophytes and prasinophytes (CryP); and chlorophytes (Chlo). These phytoplankton assemblages have been reported elsewhere in subarctic and temperate estuaries and coastal areas (Roy et al., 1996; Vallières et al., 2008; Vaulot et al., 2008; Blais et al., 2022). However, the nomenclature adopted in this study reflects pigment ratios characteristics used to distinguish the major phytoplankton assemblages but are not necessarily related to higher biomass or numerical dominance of one or another taxonomic class.

Flow cytometry and HPLC pigment analysis revealed complementary to each other on assigning the major classes of phytoplankton assemblages. For example, the presence of certain pigments (e.g., prasinoxanthin, 19'-hexanoyloxyfucoxanthin) allowed the determination of groups PraD and PryD, and they also presented a high number of picoeukaryotes (Figure 3). *Micromonas pusilla* and *Chrysocromulina* sp. are candidate species to be representative of these clusters, respectively, as they are ubiquitous in cold marine environments (see review of Vaulot et al., 2008). In addition, the ability to count the phycoerythrin-containing cyanobacteria using flow cytometry, while phycoerythrin is a pigment not detected by standard HPLC method, was an asset to identify assemblages dominated by cyanobacteria (group Cy), which is probably related to *Synechococcus* sp.

The biomass distribution along the size spectrum of phytoplankton communities brings with them relevant ecological information (Cloern, 2018; and references therein). The approach of Uitz et al. (2006) partitioned the relative contribution to Chla of three different size classes, and it showed coherency with our interpretation of community structure of the seven identified groups. The fractional contribution of picophytoplankton to Chla (f_{pico}) estimated from HPLC pigments (f_{pico}^{HPLC}) and from flow cytometry (f_{pico}^{FC}) were coherent, especially for groups PraD and Cy (Figure 4A).

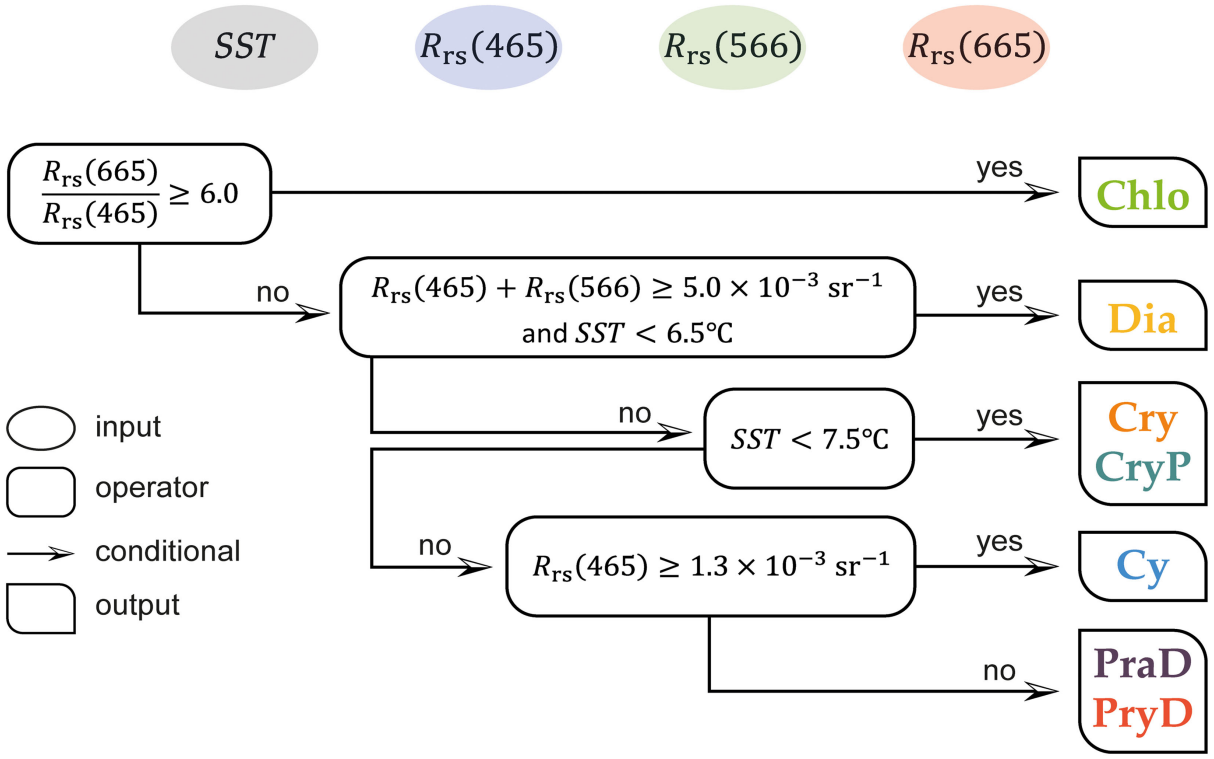


FIGURE 10
Idealized framework to separate the different phytoplankton assemblages using satellite-derived sea surface temperature (SST) and remote sensing reflectance in the blue (R_{rs} (465)), green (R_{rs} (566)), and red (R_{rs} (665)) regions of the spectrum.

The overall dominance of f_{micro}^{HPLC} over other fractions was noticeable for most of the phytoplankton assemblages, and comparable to other boreal coastal regions, such as in the Western English Channel and North Sea (Barnes et al., 2014). The general higher contribution of f_{micro} is expected in areas with relatively high biomass (Chla) and replenished nutrient conditions (Cloern, 2018; Brewin et al., 2019). The dispersion from f_{micro} (right corner of the ternary diagram shown in Figure 4B) towards f_{nano} (upper corner), for Cry, Cryp, and PryD, and towards f_{pico} (left corner), for PraD and Cy, agreed with the inferred characteristics of each group.

The samples from the middle of the Lower St. Lawrence Estuary (at PMZA station), collected from mid-summer to fall season (Table 1), presented only two phytoplankton assemblages (Dia and PraD), but relatively higher biomass compared to BSI. The nearshore BSI region has more variability in terms of physical and optical conditions than the PMZA location and, consequently, a more diverse microbial community, including phytoplankton, is expected. Although Dia and PraD assemblages were found in both PMZA and BSI, their nutrient and physical environments were very distinctive (Figure 6 and Table 2). The higher concentrations of all nutrients and salinity at PMZA are due to upwelled waters in the Lower St. Lawrence Estuary (Therriault et al., 1990) while BSI is influenced by the Gulf of St. Lawrence waters (see Koutitonsky and Bugden, 1991).

The seasonal variability of the phytoplankton assemblages is a common feature in temperate and polar coastal waters and estuaries (e.g., Ansotegui et al., 2003; Trefault et al., 2021). In addition, local river discharge in these environments is a major driver of phytoplankton composition (Domingues et al., 2005), biomass and production, particularly during the spring freshet (Malone et al., 1988). Overall, we found that the seasonal succession of phytoplankton assemblages in surface waters of BSI is intrinsically related to changes in the environmental niches that are largely driven by bio-optical conditions and sea surface temperature (SST).

Before the spring freshet, the group Dia fully occupied BSI surface waters, as expected for high-latitude spring blooms dominated by large cells (diatoms) (Tremblay et al., 2006; Carstensen et al., 2015). The low nutrient concentrations found during BSI-1 campaign suggest that phytoplankton growth was nutrient-limited at the time. While silicate depletion has been found to be responsible for the termination of an Arctic diatom bloom (Krause et al., 2019), the fact that silicate concentrations of ~0.2 – 1.1 μM persisted after nitrate had reached extremely low values of <0.1 μM indicates that the

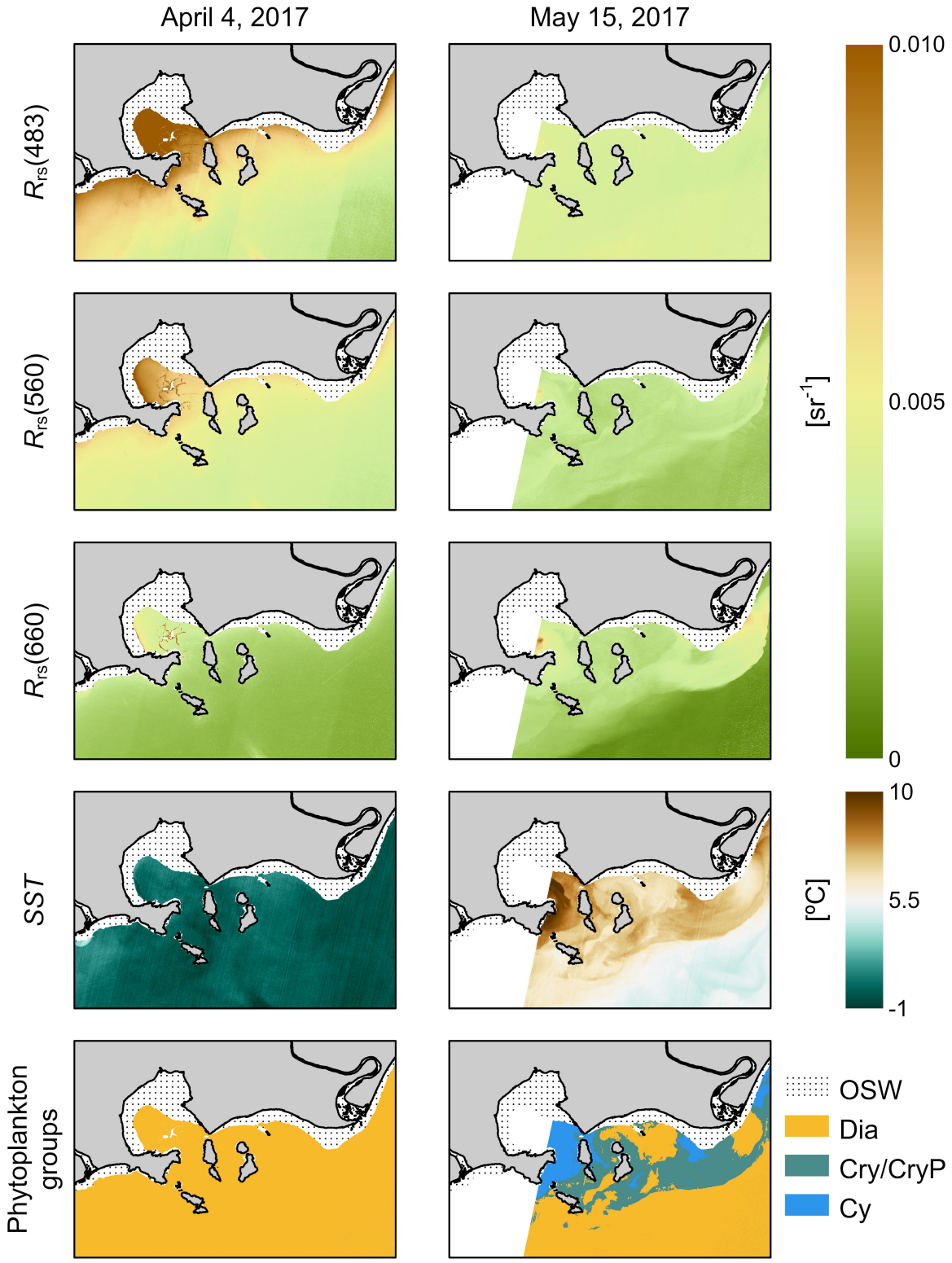


FIGURE 11
Application of the exposed framework shown in Figure 10 in satellite images of the Operational Land Imager (OLI) and the Thermal Infrared Sensor (TIRS) of Landsat 8. The atmospherically-corrected images of the blue, green, and red bands, the sea surface temperature, and the resulting classification of the groups of phytoplankton assemblages are shown for two dates: April 4 and May 15, 2017. OSW, optically-shallow waters.

latter presumably drives bloom termination in the surface waters of BSI (Figure 6). A major shift in the coastal light environment occurs when freshet brings massive concentration of terrigenous optical constituents.

During higher riverine discharges, the assemblages associated with cryptophytes (Cry and CryP) occupy the waters of BSI. The assemblages associated with chlorophytes (Chlo) were also found during the spring freshet and, due to the proximity of the riverine discharges, the highest light absorption and the most turbid conditions conferred to them less biomass compared to other assemblages.

After freshet and with warmer SST, the assemblages composed by dinoflagellates co-occurring with smaller phytoplankton cells (PraD and PryD) replace groups Cry and CryP in BSI. These assemblages were characterized by nitrate-depleted conditions just after their first appearance in BSI-3 (Figure 9), and by lower concentration of phosphate. Nitrate-depleted conditions were also found to be associated with phytoplankton communities related to small prymnesiophytes and prasinophytes in the North Atlantic and Chukchi Sea (Sieracki et al., 1993; Hill et al., 2005). Notably, the occurrence, or even blooms, of the toxic dinoflagellate *A. tamarense* are likely associated to these two groups, as previously reported in summer for BSI (Weise et al., 2002) and the Lower St. Lawrence Estuary (Fauchot et al., 2008; Roy et al., 2021).

At the end of summer and throughout fall, the assemblage associated with a high abundance of PE-containing cyanobacteria (Cy) dominates BSI waters. However, the environmental niche they occupy is distinguishable from those of PraD and PryD only by fall (BSI-7), when nitrate concentration levels are replenished, and saltier (and less absorbing) waters from the Gulf of St. Lawrence are found.

The seasonal variability of surface nutrients followed the general pattern of the Gulf of St. Lawrence, especially regarding the establishment of nitrate-depleted conditions in summer (Tremblay et al., 2000; Blais et al., 2019). Nutrient concentrations in the nearshore and coastal areas of the Bay of Sept-Îles were consistently lower than those of upwelled waters in the Lower St. Lawrence Estuary (AZMP buoy, Blais et al., 2019).

The ratio $[NO_3^-]$: $[PO_4^{3-}]$ was consistently lower than the Redfield value (16:1) but showed large differences between phytoplankton assemblages (Table 2). The lowest values observed for this ratio here are typical of coastal areas, including estuaries, indicating that N is generally the limiting factor for phytoplankton growth (Howarth et al., 2021; and references therein). Moreover, Howarth et al. (2021) also demonstrated that, in addition to the contribution of continental runoff to nutrient loads in coastal areas, the adjacent ocean also strongly affects nutrient availability in these areas. This is consistent with the observed nitrate concentrations in BSI during late fall.

The seasonal (spring to fall) succession of phytoplankton assemblages in BSI region exhibit a shift from large cells, in the spring bloom (Group Dia), to smaller ones (nano- and pico-phytoplankton size classes) from summer to fall. This shift started after the spring freshet, towards nanophytoplankton (cryptophytes, groups Cry and CryP), followed by pico- and nano-eukaryotes such as those of groups PraD and PryD, coexisting with dinoflagellates, and finally cyanobacteria (group Cy).

The CDOM-laden waters of BSI makes the a_{cdom} a determining IOP in shaping the R_{rs} , especially at shorter wavelengths (~ <600 nm). Another characteristic of BSI waters (and other nearshore zones of the St. Lawrence Estuary; see Araújo and Bélanger, 2022) is the generally flatter spectral shape of the particulate backscattering coefficient (approximately $-1 < \gamma < 0.5$) comparatively to other coastal waters (e.g., Antoine et al., 2011). Furthermore, the mass-specific $b_{bp}(\lambda)$ is very low compared to other regions, a characteristic of the particulate and dissolved organic-rich waters of BSI (Araújo and Bélanger, 2022). This is also reflected in the relatively lower $R_{rs}(\lambda)$ particularly in the red region of the spectrum, expected for a determined concentration of particles, when compared to other regions (Mabit et al., 2022).

Phytoplankton absorption (a_{phy}) represents a small fraction of the total absorption budget in BSI and, consequently, $R_{rs}(\lambda)$ signals are more sensitive to other optically active constituents than phytoplankton itself. This result implies that algorithms used to discriminate major phytoplankton assemblages that rely only on phytoplankton optical properties may have limited applications in BSI, as it is the case for other optically complex waters (e.g., Arctic ocean; Reynolds and Stramski, 2019). Nevertheless, significant differences in a_{phy} spectra between some groups were found. Moreover, analysis of the spectral shape of a_{phy} and the Chla-specific a_{phy} also revealed significant differences in the seasonal domain (Araújo and Bélanger, 2022). Taking these results into consideration, the phytoplankton absorption can be an asset to assess the major phytoplankton assemblages in BSI, as demonstrated for diverse locations by other studies (e.g., Hoepffner and Sathyendranath, 1991; Hoepffner and Sathyendranath, 1993; Devred et al., 2006; Oliveira et al., 2021; Sun et al., 2022).

Recent satellite missions and respective sensors covers the blue (~465 nm), green (~566 nm), and red (~665 nm) region of the spectrum, and with a relevant spatial resolution (order of $\sim 10^1$ m) for the scale of this study (see review of Werdell et al., 2018), allowing the retrieval of the remote sensing reflectance (R_{rs}) in these spectral bands. Another common satellite-derived parameter is the sea surface temperature (Minnett et al., 2019). Temperature is a major controlling factor of phytoplankton

phenology (e.g., Trombetta et al., 2019) and it was found to explain well the phytoplankton primary production in the estuary and Gulf of St. Lawrence, under low nutrient concentration circumstances (Babin et al., 1991). The results of the framework shown in Figure 10 and its application in remote sensing imagery (Figure 11) demonstrated that current Earth Observation satellites can be used to infer the general seasonal pattern of the major phytoplankton assemblages in the BSI region.

Although the proposed approach is empirical in nature, its foundations remits to the general bio-optical background and physical environment in which each assemblage is contextualized. Operational satellite missions such as the Landsat 8-9, carrying the Operational Land Imager (OLI) and the Thermal Infrared Sensor (TIRS), Sentinel-2, carrying the MultiSpectral Instrument (MSI), and Sentinel-3, carrying the Ocean and Land Color Instrument (OLCI), are examples of sensors that could be used to investigate the phytoplankton assemblages in coastal zones. The suitability of this approach was shown in two scenes collected by Landsat 8 OLI/TIRS in spring 2017 (Figure 11). However, inherent constraints to optical remote sensing such as persistent cloud cover over target regions and difficulties in atmospheric correction (a necessary step to obtain R_{rs} from top-of-atmosphere radiances) in highly absorbing waters, as it is the case of nearshore regions of the estuary and Gulf of St. Lawrence (Mabit et al., 2022), will limit their application. Another important constrain to consider is the potential difference between temperatures used in this study, collected by *in situ* thermometers, and those collected by satellite radiometers, which are related to the sea surface skin temperature (see Donlon et al., 2002; Minnett et al., 2011).

Our general hypothesis that the composition of major assemblages in a coastal area will covary with temperature and the bulk optical environment (IOPs) is confirmed. Furthermore, the premise that the IOPs characterization is a necessary step to investigate the phytoplankton assemblages using optical approaches (as in Reynolds and Stramski, 2019) in a coastal area was also confirmed. The composition of phytoplankton assemblages likely reflected major traits that were shaped by different environmental niches.

5 Conclusions

Given the intrinsic dynamic of coastal and estuarine areas, phytoplankton ecology monitoring is a major challenge for scientists and, consequently, is often overlooked by stakeholders, managers, and policy makers. The application of the proposed framework to retrieve major phytoplankton assemblages using satellite imagery would favor the monitoring of essential biodiversity variables in coastal ecosystems (Muller-Karger et al., 2018), deriving information about their distribution and with potential to extend it to functional traits. Although developed in the context of the subarctic Bay of Sept-Îles, similar approaches could be successfully implemented in other coastal regions, especially those that experience strong seasonal variability.

In view of ecological modelling (coupled with hydrodynamical modelling, as for an aquatic system), the information about major phytoplankton assemblages derived by satellite could be integrated into a monitoring program including automated buoys to collect high frequency meteorological and oceanographic data (Eulerian perspective), and regular (space and time) field campaigns to collect target biogeochemical and optical parameters.

Global warming has an important role in restructuring major phytoplankton assemblages (Benedetti et al., 2021) and developing new tools to systematically monitor these microorganisms that are key to coastal ecosystems are urgent. Moreover, bringing the scientific knowledge developed in this study into a broader context, such as its mapping onto a Social-Ecological-Environmental System, as presented by Ferrario et al. (2022), would bring benefits to society.

Data availability statement

The datasets generated and analyzed for this study can be found in the St. Lawrence Global Observatory repository (https://ogsl.ca/en/home-slgo/), under the CHONe II project dataset.

Author contributions

CA and SB designed the study. CB was responsible for the flow cytometry analysis. J-ÉT was responsible for the nutrient analysis. SB contributed to fundraising, fieldwork, and software development for optical data processing. CA conducted fieldwork, laboratory analysis, curated the data, and wrote the first draft of the manuscript. All authors contributed to manuscript revision, read and approved the submitted version.

Funding

The data used in this study was mainly supported by the interdisciplinary project “Canadian Healthy Oceans Network” (CHONe-2), funded by the Natural Sciences and Engineering Research Council of Canada (NSERC) and its partners: Department of Fisheries and Ocean Canada and INREST (representing the Port of Sept-Îles and the city of Sept-Îles).

CA was supported by PhD scholarships from CHONe-2 and the Fond de Recherche du Québec – Nature et technologies (FRQNT), through a grant of the Merit Scholarship Program for Foreign Students (PBEEE, grant number 263427). This study was also supported by a NSERC Discovery Grant of SB (RGPIN-2019-0670).

Acknowledgments

We acknowledge all people involved in the field work campaigns and laboratory analysis, with special thanks to Alexandre Théberge, Zélie Schuhmacher, and Dr. François-Pierre Danhiez. Thanks to Mélanie Simard and Julie Major for pigment analysis, to Sylvie Lessard for the phytoplankton identification and enumeration by light microscopy, to Gabrièle Deslongchamps and Jonathan Gagnon for nutrient analysis, to Raphäel Mabit for the C-OPS data processing, and to ARCTUS Inc. for kindly providing SST images processed using the TACT algorithm implemented in ACOLITE. CA also acknowledge Drs. Rick Reynolds and Michel Gosselin for insightful discussions in early versions of this manuscript.

Conflict of interest

The authors declare that the research was conducted in the absence of any commercial or financial relationships that could be construed as a potential conflict of interest.

Publisher's note

All claims expressed in this article are solely those of the authors and do not necessarily represent those of their affiliated organizations, or those of the publisher, the editors and the reviewers. Any product that may be evaluated in this article, or claim that may be made by its manufacturer, is not guaranteed or endorsed by the publisher.

Supplementary material

The Supplementary Material for this article can be found online at: https://www.frontiersin.org/articles/10.3389/fmars.2022.1001098/full#supplementary-material

References

Ansotegui, A., Sarobe, A., Trigueros, J. M., Urrutxurtu, I., and Orive, E. (2003). Size distribution of algal pigments and phytoplankton assemblages in a coastal–estuarine environment: Contribution of small eukaryotic algae. *J. Plankton Res.* 25, 341–355. doi: 10.1093/plankt/25.4.341

Antoine, D., Siegel, D. A., Kostadinov, T., Maritorena, S., Nelson, N. B., Gentili, B., et al. (2011). Variability in optical particle backscattering in contrasting bio-optical oceanic regimes. *Limnol. Oceanogr.* 56, 955–973. doi: 10.4319/lo.2011.56.3.0955

Araújo, C. A. S., and Bélanger, S. (2022). Variability of bio-optical properties in nearshore waters of the estuary and Gulf of St. Lawrence: Absorption and backscattering coefficients. *Estuar. Coast. Shelf Sci.* 264, 107688. doi: 10.1016/j.ecss.2021.107688

Babin, M., Therriault, J.-C., and Legendre, L. (1991). Potential utilization of temperature in estimating primary production from remote sensing data in coastal and estuarine waters. *Estuar. Coast. Shelf Sci.* 33, 559–579. doi: 10.1016/0272-7714(91)90041-9

Barnes, M., Tilstone, G., Smyth, T., Suggett, D., Astoreca, R., Lancelot, C., et al. (2014). Absorption-based algorithm of primary production for total and size-fractionated phytoplankton in coastal waters. *Mar. Ecol. Prog. Ser.* 504, 73–89. doi: 10.3354/meps10751

Bélanger, S., Carrascal-Leal, C., Jaegler, T., Larouche, P., and Galbraith, P. (2017). Assessment of radiometric data from a buoy in the St. Lawrence estuary. *J. Atmos. Ocean. Technol.* 34, 877–896. doi: 10.1175/JTECH-D-16-0176.1

Benedetti, F., Vogt, M., Elizondo, U. H., Righetti, D., Zimmermann, N. E. , and Gruber, N. (2021). Major restructuring of marine plankton assemblages under global warming. *Nat. Commun.* 12, 5226. doi: 10.1038/s41467-021-25385-x

Bidigare, R. R., Van Heukelem, L., and Trees, C. C. (2005). "Analysis of algal pigments by high-performance liquid chromatography," in *Algal culturing techniques*. Ed. R. A. Andersen (Burlington, MA: Elsevier Academic Press), 327–345. doi: 10.1016/b978-012088426-1/50021-4

Blais, M., Galbraith, P. S., Plourde, S., Scarratt, M., Devine, L., and Lehoux, C. (2019). Chemical and biological oceanographic conditions in the estuary and gulf of st. Lawrence during 2018. *DFO Can. Sci. Advis. Sec. Res. Doc.* 059, 64p.

Blais, M.-A., Matveev, A., Lovejoy, C., and Vincent, W. F. (2022). Size-fractionated microbiome structure in subarctic rivers and a coastal plume across DOC and salinity gradients. *Front. Microbiol.* 12. doi: 10.3389/fmicb.2021.760282

Bluteau, C. E., Galbraith, P. S., Bourgault, D., Villeneuve, V., and Tremblay, J.-É. (2021). Winter observations alter the seasonal perspectives of the nutrient transport pathways into the lower St. Lawrence estuary. *Ocean Sci.* 17, 1509–1525. doi: 10.5194/os-17-1509-2021

Brewin, R. J. W., Morán, X. A. G., Raitsos, D. E., Gittings, J. A., Calleja, M. L., Viegas, M., et al. (2019). Factors regulating the relationship between total and size-fractionated chlorophyll-a in coastal waters of the red Sea. *Front. Microbiol.* 10. doi: 10.3389/fmicb.2019.01964

Carstensen, J., Klais, R., and Cloern, J. E. (2015). Phytoplankton blooms in estuarine and coastal waters: Seasonal patterns and key species. *Estuar. Coast. Shelf Sci.* 162, 98–109. doi: 10.1016/j.ecss.2015.05.005

Cloern, J. E. (2001). Our evolving conceptual model of the coastal eutrophication problem. *Mar. Ecol. Prog. Ser.* 210, 223–253. doi: 10.3354/meps210223

Cloern, J. E. (2018). Why large cells dominate estuarine phytoplankton. *Limnol. Oceanogr.* 63, S392–S409. doi: 10.1002/lno.10749

Cloern, J. E., Foster, S. Q., and Kleckner, A. E. (2014). Phytoplankton primary production in the world's estuarine-coastal ecosystems. *Biogeosciences* 11, 2477–2501. doi: 10.5194/bg-11-2477-2014

Cloern, J. E., and Jassby, A. D. (2008). Complex seasonal patterns of primary producers at the land-sea interface. *Ecol. Lett.* 11, 1294–1303. doi: 10.1111/j.1461-0248.2008.01244.x

Devred, E., Sathyendranath, S., Stuart, V., Maass, H., Ulloa, O., and Platt, T. (2006). A two-component model of phytoplankton absorption in the open ocean: Theory and applications. *J. Geophys. Res.* 111, C03011. doi: 10.1029/2005JC002880

Domingues, R. B., Barbosa, A., and Galvão, H. (2005). Nutrients, light and phytoplankton succession in a temperate estuary (the guadiana, south-western Iberia). *Estuar. Coast. Shelf Sci.* 64, 249–260. doi: 10.1016/j.ecss.2005.02.017

Donlon, C. J., Minnett, P. J., Gentemann, C., Nightingale, T. J., Barton, I. J., Ward, B., et al. (2002). Toward improved validation of satellite sea surface skin temperature measurements for climate research. *J. Clim.* 15, 353–369. doi: 10.1175/1520-0442(2002)015<0353:TIVOSS>2.0.CO;2

Dreujou, E., Desroy, N., Carrière, J., Tréau de Coeli, L., McKindsey, C. W., and Archambault, P. (2021). Determining the ecological status of benthic coastal communities: A case in an anthropized sub-arctic area. *Front. Mar. Sci.* 8. doi: 10.3389/fmars.2021.637546

Edwards, K. F., Thomas, M. K., Klausmeier, C. A., and Litchman, E. (2016). Phytoplankton growth and the interaction of light and temperature: A synthesis at the species and community level. *Limnol. Oceanogr.* 61, 1232–1244. doi: 10.1002/lno.10282

Fauchot, J., Saucier, F. J., Levasseur, M., Roy, S., and Zakardjian, B. (2008). Wind-driven river plume dynamics and toxic alexandrium tamarense blooms in the st. Lawrence estuary (Canada): A modeling study. *Harmful Algae* 7, 214–227. doi: 10.1016/j.hal.2007.08.002

Ferrario, F., Araújo, C. A. S., Bélanger, S., Bourgault, D., Carrière, J., Carrier-Belleau, C., et al. (2022). Holistic environmental monitoring in ports as an opportunity to advance sustainable development, marine science, and social inclusiveness. *Elem. Sci. Anthr.* 10, 1–21. doi: 10.1525/elementa.2021.00061

Gibb, S., Barlow, R., Cummings, D., Rees, N., Trees, C., Holligan, P., et al. (2000). Surface phytoplankton pigment distributions in the Atlantic ocean: An assessment of basin scale variability between 50°N and 50°S. *Prog. Oceanogr.* 45, 339–368. doi: 10.1016/S0079-6611(00)00007-0

Glibert, P., Anderson, D., Gentien, P., Granéli, E., and Sellner, K. (2005). The global, complex phenomena of harmful algal blooms. *Oceanography* 18, 136–147. doi: 10.5670/oceanog.2005.49

Harley, C. D. G., Randall Hughes, A., Hultgren, K. M., Miner, B. G., Sorte, C. J. B., Thornber, C. S., et al. (2006). The impacts of climate change in coastal marine systems. *Ecol. Lett.* 9, 228–241. doi: 10.1111/j.1461-0248.2005.00871.x

Hill, V., Cota, G., and Stockwell, D. (2005). Spring and summer phytoplankton communities in the chukchi and Eastern Beaufort seas. *Deep. Res. Part II Top. Stud. Oceanogr.* 52, 3369–3385. doi: 10.1016/j.dsr2.2005.10.010

Hintz, N. H., Zeising, M., and Striebel, M. (2021). Changes in spectral quality of underwater light alter phytoplankton community composition. *Limnol. Oceanogr.* 66, 3327–3337. doi: 10.1002/lno.11882

Hoepffner, N., and Sathyendranath, S. (1991). Effect of pigment composition on absorption properties of phytoplankton. *Mar. Ecol. Prog. Ser.* 73, 11–23. doi: 10.3354/meps073011

Hoepffner, N., and Sathyendranath, S. (1993). Determination of the major groups of phytoplankton pigments from the absorption spectra of total particulate matter. *J. Geophys. Res.* 98, 22789. doi: 10.1029/93JC01273

Howarth, R. W., Chan, F., Swaney, D. P., Marino, R. M., and Hayn, M. (2021). Role of external inputs of nutrients to aquatic ecosystems in determining prevalence of nitrogen vs. phosphorus limitation of net primary productivity. *Biogeochemistry* 154, 293–306. doi: 10.1007/s10533-021-00765-z

IOCCG (2014). *Phytoplankton functional types from space*. Ed. S. Sathyendranath (Dartmouth, Canada: IOCCG).

IOCCG (2018). *Ocean optics and biogeochemistry protocols for satellite ocean colour sensor validation. volume 1: Inherent optical property measurements and protocols: absorption coefficient*. Eds. A. R. Neeley and A. Mannino (Dartmouth, Canada: IOCCG). doi: 10.25607/OBP-119

Koutitonsky, V. G., and Bugden, G. L. (1991). The physical oceanography of the gulf of st. Lawrence: A review wilh emphasis on the synoptic variability of the motion. *Can. Spec. Publ. Fish. Aquat. Sci.* 113, 57–90.

Kramer, S. J., and Siegel, D. A. (2019). How can phytoplankton pigments be best used to characterize surface ocean phytoplankton groups for ocean color remote sensing algorithms? *J. Geophys. Res. Ocean.* 124, 7557–7574. doi: 10.1029/2019JC015604

Krause, J. W., Schulz, I. K., Rowe, K. A., Dobbins, W., Winding, M. H. S., Sejr, M. K., et al. (2019). Silicic acid limitation drives bloom termination and potential carbon sequestration in an Arctic bloom. *Sci. Rep.* 9, 1–11. doi: 10.1038/s41598-019-44587-4

Le Quéré, C., Harrison, S. P., Colin Prentice, I., Buitenhuis, E. T., Aumont, O., Bopp, L., et al. (2005). Ecosystem dynamics based on plankton functional types for global ocean biogeochemistry models. *Glob. Change Biol.* 11, 2016–2040. doi: 10.1111/j.1365-2486.2005.1004.x

Lindeman, R. L. (1942). The trophic-dynamic aspect of ecology. *Ecology* 23, 399–417. doi: 10.2307/1930126

Litchman, E., de Tezanos Pinto, P., Klausmeier, C. A., Thomas, M. K., and Yoshiyama, K. (2010). Linking traits to species diversity and community structure in phytoplankton. *Hydrobiologia* 653, 15–28. doi: 10.1007/s10750-010-0341-5

Litchman, E., Klausmeier, C. A., Schofield, O. M., and Falkowski, P. G. (2007). The role of functional traits and trade-offs in structuring phytoplankton communities: Scaling from cellular to ecosystem level. *Ecol. Lett.* 10, 1170–1181. doi: 10.1111/j.1461-0248.2007.01117.x

Lund, J. W. G., Kipling, C., and Le Cren, E. D. (1958). The inverted microscope method of estimating algal numbers and the statistical basis of estimations by counting. *Hydrobiologia* 11, 143–170. doi: 10.1007/BF00007865

Mabit, R., Araújo, C. A. S., Singh, R. K., and Bélanger, S. (2022). Empirical remote sensing algorithms to retrieve SPM and CDOM in québec coastal waters. *Front. Remote Sens.* 3. doi: 10.3389/frsen.2022.834908

Malone, T. C., Crocker, L. H., Pike, S. E., and Wendler, B. W. (1988). Influences of river flow on the dynamics of phytoplankton production in a partially stratified estuary. *Mar. Ecol. Prog. Ser.* 48, 235–249. doi: 10.3354/meps048235

McMahon, K. W., Ambrose, W. G., Reynolds, M. J., Johnson, B. J., Whiting, A., and Clough, L. M. (2021). Arctic Lagoon and nearshore food webs: Relative contributions of terrestrial organic matter, phytoplankton, and phytobenthos vary with consumer foraging dynamics. *Estuar. Coast. Shelf Sci.* 257, 107388. doi: 10.1016/j.ecss.2021.107388

Minnett, P. J., Alvera-Azcárate, A., Chin, T. M., Corlett, G. K., Gentemann, C. L., Karagali, I., et al. (2019). Half a century of satellite remote sensing of sea-surface temperature. *Remote Sens. Environ.* 233, 111366. doi: 10.1016/j.rse.2019.111366

Minnett, P. J., Smith, M., and Ward, B. (2011). Measurements of the oceanic thermal skin effect. *Deep Sea Res. Part II Top. Stud. Oceanogr.* 58, 861–868. doi: 10.1016/j.dsr2.2010.10.024

Montagnes, D. J. S., Berges, J. A., Harrison, P. J., and Taylor, F. J. R. (1994). Estimating carbon, nitrogen, protein, and chlorophyll a from volume in marine phytoplankton. *Limnol. Oceanogr.* 39, 1044–1060. doi: 10.4319/lo.1994.39.5.1044

Morel, A. (1974). "Optical properties of pure water and pure seawater," in *Optical aspects of oceanography*. Eds. N. G. Jerlov and E. Steeman-Nielsen (New York, NY, USA: Academic Press), 1–24.

Morel, A., Ahn, Y.-H., Partensky, F., Vaulot, D., and Claustre, H. (1993). *Prochlorococcus* and *Synechococcus*: A comparative study of their optical properties in relation to their size and pigmentation. *J. Mar. Res.* 51, 617–649. doi: 10.1357/0022240933223963

Morel, A., and Prieur, L. (1977). Analysis of variations in ocean color. *Limnol. Oceanogr.* 22, 709–722. doi: 10.4319/lo.1977.22.4.0709

Muller-Karger, F. E., Hestir, E., Ade, C., Turpie, K., Roberts, D. A., Siegel, D., et al. (2018). Satellite sensor requirements for monitoring essential biodiversity variables of coastal ecosystems. *Ecol. Appl.* 28, 749–760. doi: 10.1002/eap.1682

Neukermans, G., Reynolds, R. A., and Stramski, D. (2016). Optical classification and characterization of marine particle assemblages within the western Arctic ocean. *Limnol. Oceanogr.* 61, 1472–1494. doi: 10.1002/lno.10316

Normandeau, A., Lajeunesse, P., and St-Onge, G. (2013). Shallow-water longshore drift-fed submarine fan deposition (Moisie river delta, Eastern Canada). *Geo-Marine Lett.* 33, 391–403. doi: 10.1007/s00367-013-0336-0

Oliveira, A. L., Rudorff, N., Kampel, M., Sathyendranath, S., Pompeu, M., Detoni, A. M. S., et al. (2021). Phytoplankton assemblages and optical properties in a coastal region of the south Brazil bight. *Cont. Shelf Res.* 227, 104509. doi: 10.1016/j.csr.2021.104509

Reynolds, R. A., and Stramski, D. (2019). Optical characterization of marine phytoplankton assemblages within surface waters of the western Arctic ocean. *Limnol. Oceanogr.* 64, 2478–2496. doi: 10.1002/lno.11199

Roselli, L., and Litchman, E. (2017). Phytoplankton traits, functional groups and community organization. *J. Plankton Res.* 39, 491–493. doi: 10.1093/plankt/fbx019

Roy, S., Chanut, J., Gosselin, M., and Sime-Ngando, T. (1996). Characterization of phytoplankton communities in the lower St. Lawrence estuary using HPLC-detected pigments and cell microscopy. *Mar. Ecol. Prog. Ser.* 142, 55–73. doi: 10.3354/meps142055

Roy, S., Pitcher, G. C., Kudela, R. M., Smith, M. E., Bernard, S., and Mazeran, C. (2021). "Ocean colour remote sensing of dinoflagellate blooms associated with paralytic shellfish poisoning," in *Observation of harmful algal blooms with ocean colour radiometry*. Eds. S. Bernard, R. M. Kudela, L.R. Lain and G. C. Pitcher (Dartmouth, Canada: International Ocean Colour Coordinating Group), 39–50. doi: 10.25607/OBP-1042

Salvador, S., and Chan, P. (2004). "Determining the number of clusters/segments in hierarchical clustering/segmentation algorithms," in *16th IEEE international conference on tools with artificial intelligence*, (Boca Raton, FL, USA: IEEE comput. soc). 576–584. doi: 10.1109/ICTAI.2004.50

Sathyendranath, S., Prieur, L., and Morel, A. (1989). A three-component model of ocean colour and its application to remote sensing of phytoplankton pigments in coastal waters. *Int. J. Remote Sens.* 10, 1373–1394. doi: 10.1080/01431168908903974

Shaw, J.-L. (2019). *Hydrodynamique de la Baie de Sept-Îles*, M.Sc. Thesis. (Rimouski, QC, Canada: Université du Québec à Rimouski).

Sieracki, M. E., Verity, P. G., and Stoecker, D. K. (1993). Plankton community response to sequential silicate and nitrate depletion during the 1989 north Atlantic spring bloom. *Deep. Res. Part II* 40, 213–225. doi: 10.1016/0967-0645(93)90014-E

Sokal, R. R., and Rohlf, F. J. (1962). The comparison of dendrograms by objective methods. *Taxon* 11, 33–40. doi: 10.2307/1217208

Stomp, M., Huisman, J., Stal, L. J., and Matthijs, H. C. P. (2007). Colorful niches of phototrophic microorganisms shaped by vibrations of the water molecule. *ISME J.* 1, 271–282. doi: 10.1038/ismej.2007.59

Sun, X., Shen, F., Brewin, R. J. W., Li, M., and Zhu, Q. (2022). Light absorption spectra of naturally mixed phytoplankton assemblages for retrieval of

phytoplankton group composition in coastal oceans. *Limnol. Oceanogr.* 67, 946–961. doi: 10.1002/lno.12047

Therriault, J.-C., Legendre, L., and Demers, S. (1990). "Oceanography and ecology of phytoplankton in the St.Lawrence estuary," in *Oceanography of a Large-scale estuarine system*. Eds. M. El-Sabh and N. Silverberg, (New York, NY, USA: Springer-Verlag) 269–295. doi: 10.1007/978-1-4615-7534-4_12

Trefault, N., de la Iglesia, R., Moreno-Pino, M., Lopes dos Santos, A., Gérikas Ribeiro, C., Parada-Pozo, G., et al. (2021). Annual phytoplankton dynamics in coastal waters from fildes bay, Western Antarctic peninsula. *Sci. Rep.* 11, 1368. doi: 10.1038/s41598-020-80568-8

Tremblay, G., Belzile, C., Gosselin, M., Poulin, M., Roy, S., and Tremblay, J. (2009). Late summer phytoplankton distribution along a 3500 km transect in Canadian Arctic waters: Strong numerical dominance by picoeukaryotes. *Aquat. Microb. Ecol.* 54, 55–70. doi: 10.3354/ame01257

Tremblay, J.É., Legendre, L., Klein, B., and Therriault, J.-C. (2000). Size-differential uptake of nitrogen and carbon in a marginal sea (Gulf of st. Lawrence, canada): Significance of diel periodicity and urea uptake. *Deep. Res. Part II Top. Stud. Oceanogr.* 47, 489–518. doi: 10.1016/S0967-0645(99)00116-2

Tremblay, J.É., Michel, C., Hobson, K. A., Gosselin, M., and Price, N. M. (2006). Bloom dynamics in early opening waters of the Arctic ocean. *Limnol. Oceanogr.* 51, 900–912. doi: 10.4319/lo.2006.51.2.0900

Trombetta, T., Vidussi, F., Mas, S., Parin, D., Simier, M., and Mostajir, B. (2019). Water temperature drives phytoplankton blooms in coastal waters. *PloS One* 14, 1–28. doi: 10.1371/journal.pone.0214933

Uitz, J., Claustre, H., Morel, A., and Hooker, S. B. (2006). Vertical distribution of phytoplankton communities in open ocean: An assessment based on surface chlorophyll. *J. Geophys. Res.* 111, C08005. doi: 10.1029/2005JC003207

Vallières, C., Retamal, L., Ramlal, P., Osburn, C. L., and Vincent, W. F. (2008). Bacterial production and microbial food web structure in a large arctic river and the coastal Arctic ocean. *J. Mar. Syst.* 74, 756–773. doi: 10.1016/j.jmarsys.2007.12.002

Vandevelde, T., Legendre, L., Therriault, J.-C., Demers, S., and Bah, A. (1987). Subsurface chlorophyll maximum and hydrodynamics of the water column. *J. Mar. Res.* 45, 377–396. doi: 10.1357/002224087788401151

Vanhellemont, Q. (2019). Adaptation of the dark spectrum fitting atmospheric correction for aquatic applications of the landsat and sentinel-2 archives. *Remote Sens. Environ.* 225, 175–192. doi: 10.1016/j.rse.2019.03.010

Vanhellemont, Q. (2020a). Automated water surface temperature retrieval from landsat 8/TIRS. *Remote Sens. Environ.* 237, 111518. doi: 10.1016/j.rse.2019.111518

Vanhellemont, Q. (2020b). Combined land surface emissivity and temperature estimation from landsat 8 OLI and TIRS. *ISPRS J. Photogramm. Remote Sens.* 166, 390–402. doi: 10.1016/j.isprsjprs.2020.06.007

Vanhellemont, Q. (2020c). Sensitivity analysis of the dark spectrum fitting atmospheric correction for metre- and decametre-scale satellite imagery using autonomous hyperspectral radiometry. *Opt. Express* 28, 29948. doi: 10.1364/OE.397456

Vaulot, D., Eikrem, W., Viprey, M., and Moreau, H. (2008). The diversity of small eukaryotic phytoplankton (≤3 μm) in marine ecosystems. *FEMS Microbiol. Rev.* 32, 795–820. doi: 10.1111/j.1574-6976.2008.00121.x

Ward, J. H. (1963). Hierarchical grouping to optimize an objective function. *J. Am. Stat. Assoc.* 58, 236–244. doi: 10.1080/01621459.1963.10500845

Wassmann, P., Duarte, C. M., Agustí, S., and Sejr, M. K. (2011). Footprints of climate change in the Arctic marine ecosystem. *Glob. Change Biol.* 17, 1235–1249. doi: 10.1111/j.1365-2486.2010.02311.x

Weise, A. M., Levasseur, M., Saucier, F. J., Senneville, S., Bonneau, E., Roy, S., et al. (2002). The link between precipitation, river runoff, and blooms of the toxic dinoflagellate *Alexandrium tamarense* in the St. Lawrence. *Can. J. Fish. Aquat. Sci.* 59, 464–473. doi: 10.1139/f02-024

Werdell, P. J., McKinna, L. I. W., Boss, E., Ackleson, S. G., Craig, S. E., Gregg, W. W., et al. (2018). An overview of approaches and challenges for retrieving marine inherent optical properties from ocean color remote sensing. *Prog. Oceanogr.* 160, 186–212. doi: 10.1016/j.pocean.2018.01.001

Winder, M., Carstensen, J., Galloway, A. W. E., Jakobsen, H. H., and Cloern, J. E. (2017). The land-sea interface: A source of high-quality phytoplankton to support secondary production. *Limnol. Oceanogr.* 62, S258–S271. doi: 10.1002/lno.10650

Zapata, M., Rodríguez, F., and Garrido, J. (2000). Separation of chlorophylls and carotenoids from marine phytoplankton: A new HPLC method using a reversed phase C8 column and pyridine-containing mobile phases. *Mar. Ecol. Prog. Ser.* 195, 29–45. doi: 10.3354/meps195029

Zhang, X., Hu, L., and He, M.-X. (2009). Scattering by pure seawater at high salinity. *Opt. Express* 17, 5698–5710. doi: 10.1364/OE.17.012685

frontiers | Frontiers in Marine Science

TYPE Original Research
PUBLISHED 20 January 2023
DOI 10.3389/fmars.2022.1048893

Check for updates

OPEN ACCESS

EDITED BY
Shubha Sathyendranath,
Plymouth Marine Laboratory,
United Kingdom

REVIEWED BY
Yuanli Zhu,
Ministry of Natural Resources, China
Cecile Dupouy,
UMR7294 Institut Méditerranéen d'océanographie (MIO), France

*CORRESPONDENCE
Lingling Jiang
jiangll@dlmu.edu.cn

SPECIALTY SECTION
This article was submitted to Ocean Observation, a section of the journal Frontiers in Marine Science

RECEIVED 20 September 2022
ACCEPTED 21 December 2022
PUBLISHED 20 January 2023

CITATION
Li Q, Jiang L, Chen Y, Tang J and Gao S (2023) Absorption-based algorithm for satellite estimating the particulate organic carbon concentration in the global surface ocean. *Front. Mar. Sci.* 9:1048893. doi: 10.3389/fmars.2022.1048893

COPYRIGHT
© 2023 Li, Jiang, Chen, Tang and Gao. This is an open-access article distributed under the terms of the Creative Commons Attribution License (CC BY). The use, distribution or reproduction in other forums is permitted, provided the original author(s) and the copyright owner(s) are credited and that the original publication in this journal is cited, in accordance with accepted academic practice. No use, distribution or reproduction is permitted which does not comply with these terms.

Absorption-based algorithm for satellite estimating the particulate organic carbon concentration in the global surface ocean

Qiang Li[1], Lingling Jiang[1*], Yanlong Chen[2], Junwu Tang[3] and Siwen Gao[2]

[1]College of Environmental Science and Engineering, Dalian Maritime University, Dalian, China, [2]National Marine Environmental Monitoring Center, Ministry of Ecology Environment, Dalian, China, [3]Laboratory for Regional Oceanography and Numerical Modelling, Qingdao National Laboratory for Marine Science and Technology, Qingdao, China

Particulate organic carbon (POC) in the surface ocean contributes to understanding the global ocean carbon cycle system. The surface POC concentration can be effectively detected using satellites. In open oceans, the blue-to-green band ratio (BG) algorithm is often used to obtain global surface ocean POC concentrations. However, POC concentrations are underestimated in waters with complex optical environments. To generate a more accurate global POC mapping in the surface ocean, we developed a new ocean color algorithm using a mixed global-scale *in situ* POC dataset with the concentration ranging from 11.10 to 4389.28 mg/m^3. The new algorithm (a-POC) was established to retrieve the POC concentration using the strong relationship between the absorption coefficient at 490 nm (a(490)) and POC, in which a(490) was from the Ocean Color Climate Change Initiative (OC-CCI) v5.0 suite. Afterward, the a-POC algorithm was applied to OC-CCI v5.0 data for special regions and the global ocean. The performances of the a-POC algorithm and the BG algorithm were compared by combining the match-ups of satellite data and *in situ* dataset. The results showed that the statistical parameters of the a-POC algorithm were similar to those of the BG algorithm in the Atlantic oligotrophic gyre regions, with a median absolute percentage deviation (MAPD) value of 22.04%. In the eastern coastal waters of the United States and the Chesapeake Bay, the POC concentration retrieved by the a-POC algorithm was highly consistent with the match-ups, and MAPD values were 33.06% and 26.11%. The a-POC algorithm was also applied to the Ocean and Land Color Instrument (OLCI) data pre-processed with different atmospheric correction algorithms to evaluate the universality. The result showed that the a-POC algorithm was robust and less sensitive to atmospheric correction than the BG algorithm.

KEYWORDS

satellite ocean color, absorption coefficient, global bio-optical algorithm, Ocean Color Climate Change Initiative, particulate organic carbon

1 Introduction

The ocean is a vast carbon reservoir, and the ocean carbon cycle is crucial in studying global climate change and environmental evolution (Hedges, 1992; Siegenthaler and Sarmiento, 1993). Particulate organic carbon (POC) and dissolved organic carbon (DOC) are two kinds of oceanic organic carbon (Amon and Benner, 1996; Jahnke, 1996; Chen et al., 2022). Although the stock of POC is small, its importance depends on its constituents (phytoplankton, bacteria, zooplankton, and organic detritus), which are responsible for relatively large carbon fluxes and short turnaround times (Stramska, 2009; Evers-King et al., 2017). In addition, POC is also an important indicator of ocean primary productivity (Behrenfeld et al., 2005). The flux from dissolved inorganic carbon (DIC) to POC through primary production is estimated to be about 50 Gt C/year, accounting for about 50% of global primary production (Liu et al., 2021). Due to POC transformation (e.g., remineralization), sedimentation, physical mixing, and horizontal ocean current transport, the concentration of POC (mg/m^3) in the surface ocean changes significantly on temporal and spatial scales (Field Christopher et al., 1998; Stramski et al., 1999; Gardner et al., 2006; Omand et al., 2015; Stramska and Cieszyńska, 2015). Therefore, the POC measured through traditional shipboard platforms or other *in situ* observation platforms cannot fully characterize POC changes on a global scale.

Ocean color remote sensing has the advantages of broad spatial coverage and long time series in obtaining bio-optical properties. It solves the drawback that the data obtained by traditional monitoring methods are dispersed in time and space. In the past few decades, ocean color remote sensing technology has been rapidly developed. For example, the Sea-viewing Wide-Field-of-view Sensor (SeaWiFS), Moderate Resolution Imaging Spectroradiometer (MODIS), Medium-Resolution Imaging Spectrometer (MERIS), Visible Infrared Imaging Radiometer Suite (VIIRS), and Ocean and Land Colour Instrument (OLCI) can send ocean color data to ground receiving stations almost every day. By applying specific retrieval algorithms to remote sensing data, ocean color remote sensing technology can obtain the distribution of oceanic POC concentrations on temporal and spatial scales (Loisel et al., 2002; Stramska and Stramski, 2005; Allison et al., 2010; Duforêt-Gaurier et al., 2010; Stramska, 2014; Stramska and Cieszyńska, 2015; Stramski et al., 2022).

Current POC concentration retrieval algorithms are mainly based on the inherent optical properties (IOPs), the apparent optical properties (AOPs), and water constituents (e.g., chlorophyll-a (Chla) and total suspended matter (TSM)). The first type is two-step algorithms based on IOPs. The relationship between AOPs and IOPs was first established, and then an empirical relationship between IOPs and POC concentration was formulated. These IOPs include the particulate backscattering coefficient (b_{bp}) and the particle beam attenuation coefficient (c_p). Stramski et al., 1999 used b_{bp} at 510 nm as a proxy to retrieve the POC concentration. Gardner et al., 2006 established a linear regression between c_p and the POC concentration to retrieve the POC concentration. However, the relationship between b_{bp}, c_p, and POC varied by sea area. At similar POC levels, the b_{bp} at 510 nm in the Antarctic Polar Front Zone was higher than that in the Ross Sea region, indicating a difference in the specific b_{bp} of carbon (Stramski et al., 1999; Stramski et al., 2001; Pabi and Arrigo, 2006; Stramski et al., 2008). Le et al., 2018 showed a relatively weak relationship between the POC concentration and the backscattering coefficient at 547 nm, and the coefficient of determination was 0.33. In addition, there is a significant change in the slope between c_p and POC concentrations (about twice as large) compared to the linear regression model for different sea areas worldwide (Gardner et al., 2006). Therefore, these algorithms may be limited in retrieving POC concentrations on a global scale.

The second type of algorithm obtains the POC concentration based on the empirical relationship between AOPs and the POC concentration. The typical empirical algorithm is the blue-to-green band ratio (BG) of remote sensing reflectance ($R_{rs}(\lambda)$, where λ is the light wavelength) (Stramski et al., 2008). The BG algorithm outperformed the b_{bp}-based two-step algorithm in the open ocean (Stramski et al., 2008; Allison et al., 2010). It was used by the National Aeronautics and Space Administration (NASA) Ocean Biology Processing Group to generate global POC products. Le et al., 2018 proposed an empirical POC concentration retrieval algorithm (CI_{POC}) based on a three-band $R_{rs}(\lambda)$ difference (i.e., Color Index) initially developed by Hu et al., 2012. However, the accuracy of empirical algorithms relies heavily on the variation of the *in situ* datasets used to establish the algorithms. The BG algorithm was established using *in situ* POC concentrations ranging from 12 to 270 mg/m^3, and the CI_{POC} algorithm was established using *in situ* POC concentrations less than 1000 mg/m^3. As a result, the BG and CI_{POC} algorithms had significant errors in coastal waters with complex optical environments (Duan et al., 2014; Evers-King et al., 2017; Le et al., 2017; Le et al., 2018; Lin et al., 2018; Jiang et al., 2019; Tran et al., 2019).

The third type of algorithm is based on the water constituents. Loisel et al., 2002 proposed a POC algorithm based on the combination of b_{bp} at 490 nm and Chla concentrations. However, this algorithm significantly underestimated the data in regions with high POC concentrations (Evers-King et al., 2017). In turbid regions such as coastal waters, the uncertain accuracy of Chla concentration retrieval can bring errors to further POC retrieval. Liu et al., 2019 established the relationship between TSM concentrations and POC concentrations using an *in situ* dataset collected in the Changjiang River Estuary. This relationship was verified through

the Geostationary Ocean Color Imager (GOCI) data. As the relationship between TSM and POC is not static, the ratio of POC to TSM in different water environments is greatly affected by the relative contribution of organic and inorganic particulate matter (Bishop, 1999). The lack of a recognized ocean color TSM retrieval model also increases the difficulty of algorithm generalization (Yu et al., 2019; Liu et al., 2021).

Since Stramski et al., 1999 proposed the backscattering of particulate matter as a proxy for POC, ocean color retrieval algorithms for POC concentration based on IOPs have been continuously investigated. Previous studies have suggested that the absorption coefficient (a(λ)) can serve as a proxy for organic particulate matter, particularly the wavelength λ at longer blue bands (Woźniak et al., 2010; Le et al., 2018). However, few POC algorithms based on a(λ) have been studied, especially on the direct establishment of the relationship between POC and a(λ) (Jiang et al., 2019). Often, a(λ) is subdivided into the following four components:

$$a(\lambda) = a_w(\lambda) + a_\Phi(\lambda) + a_{NAP}(\lambda) + a_{CDOM}(\lambda)$$

Subscripts w, Φ, NAP, and CDOM represent pure seawater, phytoplankton, nonalgal particles, and colored dissolved organic matter. Selecting a(λ) as a proxy for POC can describe the variability in phytoplankton and nonalgal particles, although doing so also mingled with the signal of CDOM, especially in coastal waters. Since the absorption coefficient of CDOM (a_{CDOM}) decays exponentially with increasing wavelength (Babin et al., 2003), this study focused on the relationship between a(490) and POC concentration. The OC-CCI data was combined with a global *in situ* POC dataset to establish an absorption-coefficient-based POC concentration retrieval algorithm (a-POC). Afterward, the performance of the a-POC algorithm was compared with that of the BG algorithm on a global and regional scale, and an uncertainty map was plotted. Finally, the a-POC algorithm was applied to other sensors, and its universality was evaluated.

2 Data and methods

2.1 *In situ* dataset

The *in situ* POC dataset used in this study was obtained from globally shared databases and an independently collected Bohai Sea dataset. The shared databases mainly consisted of datasets collected by Martiny et al., 2014 in the Dryad Digital Repository (https://datadryad.org/) and a large number of datasets provided by contributors in SeaBASS (https://seabass.gsfc.nasa.gov) (Werdell and Bailey, 2005). The Bohai Sea dataset was collected in the Bohai Sea of China. It included optical and biochemical parameters of the ocean surface (e.g., $R_{rs}(\lambda)$, the concentrations of Chla and POC). The water samples used to obtain biochemical parameters were collected at a depth of 0.5 m. $R_{rs}(\lambda)$ and Chla were measured in the same way as in the study of Jiang et al., 2020, where the optical measurement followed the NASA optics protocols (Mueller et al., 2003), and Chla was measured by the fluorometric method (Cui et al., 2010). The measurement method for POC concentration was according to the method provided by Sharp, 1974. Before analysis, samples were collected using GF/F filters with a pore size of 0.7 μm and pre-combusted (450 °C) and dried overnight at 65 °C. Filters were acidified by adding low-carbon HCl directly or by overnight exposure to concentrated HCl solution fumes in a desiccator to remove interference from particulate inorganic carbon (Hedges and Stern, 1984). The filter was then dried at 55°C, loaded into pre-combusted tin capsules, and converted to organic carbon in an elemental analyzer at 960 °C. Finally, the POC concentrations were calculated by subtracting the average organic carbon mass (measured on blank filters) from the organic carbon mass (measured on filters) and dividing it by the volume of the filtered sample. POC concentrations could be easily overestimated due to the inevitable errors in POC measurements, especially from dissolved organic carbon adsorbed on the filter (Gardner et al., 2003). Therefore, POC concentrations below 10 mg/m^3 were considered invalid in this study (Cetinić et al., 2012; Le et al., 2018). For shared databases that provide a sampling depth, the measurements from 10 m below the water surface were averaged to provide the "surface" value (Evers-King et al., 2017). The dataset was sampled from 1997 to 2020, with areas ranging from the open oceans to coastal waters, providing good representation on both temporal and spatial scales.

2.2 Satellite data

The European Space Agency (ESA) Ocean Color Climate Change Initiative (OC-CCI) project has produced a series of validated Essential Climate Variables (ECVs) with error characteristics by merging observational products from multiple satellite sensors. Since the first phase of OC-CCI was launched in 2010, several updates and improvements have been implemented, and the current OC-CCI project has progressed to version 5.0 (Sathyendranath et al., 2019; Sathyendranath et al., 2021). The OC-CCI v5.0 data is created by band-shifting (Mélin and Sclep, 2015) and bias-correcting SeaWiFS, MODIS-Aqua, VIIRS, and Sentinel3A-OLCI data to match MERIS data. The datasets are merged, and per-pixel uncertainty estimates are computed. In addition to $R_{rs}(\lambda)$ at MERIS wavelengths, Chla concentration, $k_d(490)$, and IOPs, the dataset also includes an optical water classification system, which divides water into 14 spectral classes based on fuzzy logic (Moore et al., 2001; Jackson et al., 2017). In this way, the dataset can focus on the spectral shape when differentiating classes.

In this study, the daily and monthly average composite OC-CCI v5.0 products with 4 km resolution (Sathyendranath et al., 2021), the OLCI Level-1B (L1B) Full-Resolution (FR, spatial resolution of 300 m) TOA remotely-sensed radiance products, and OLCI baseline products Level-2 (L2) FR were used. The OC-CCI v5.0 products were obtained from the ESA Climate Office Ocean Colour (https://climate.esa.int/en/projects/ocean-colour/), and the OLCI products were obtained from Copernicus Open Access Hub (https://scihub.copernicus.eu/). In OC-CCI v5.0 products, $R_{rs}(\lambda)$ were obtained using a mixed atmosphere correction algorithm (i.e., SeaDAS v7.5 for SeaWiFS; POLYMER v4.12 for MERIS, MODIS, VIIRS, and OLCI). On this basis, IOPs were obtained using a multiband quasi-analytical algorithm (QAA), in which the backscattering coefficients of pure seawater developed by Zhang et al., 2009 were used (Gordon and Wang, 1994a; Lee et al., 2002; Lee et al., 2009; Steinmetz et al., 2011).

The OLCI data were pre-processed with the Baseline Atmospheric Correction (BAC) and POLYMER atmospheric correction algorithms to obtain $R_{rs}(\lambda)$. BAC is based on the NIR black pixel assumption (Gordon and Wang, 1994b) and the bright pixel atmospheric correction algorithm (Moore et al., 1999). The switch between two modes for clear and turbid waters was determined with a turbid water flag. POLYMER is a spectral matching approach based on all available spectral bands from blue to NIR, and it is designed explicitly for atmospheric correction in the presence of sun glint (Steinmetz et al., 2011). The OLCI L1B products were pre-processed using POLYMER v4.13 processor to obtain $R_{rs}(\lambda)$, and $R_{rs}(\lambda)$ corrected by the BAC atmospheric correction algorithm were extracted from OLCI L2 products. Finally, the QAA_v5 algorithm was used to obtain IOPs products from $R_{rs}(\lambda)$ (Lee et al., 2002; Lee et al., 2009).

2.3 Match-up procedures

The match-ups between the satellite data and the *in situ* dataset were determined based on the satellite overpass time and sampling location. We selected a 1-day time window and extracted a surrounding 3-by-3 pixel box centered on the location of the *in situ* points. If the number of valid pixels in a pixel box was less than 6 or the center pixel was invalid, the pixel box was discarded. The water class memberships of the central pixels were extracted from the OC-CCI products, and the dominant OC-CCI water classes (i.e., the water classes corresponding to the highest membership value) were calculated. Furthermore, the mean and standard deviation were calculated for all satellite products with valid pixels in the pixel boxes. The *in situ* data were averaged if multiple *in situ* measurements were available in the same pixel.

Through the match-up procedure, 3580 valid match-ups were obtained. Their location distribution is shown in Figure 1, with POC concentrations ranging from 11.10 to 4389.28 mg/m^3. It can be seen that POC concentrations were lower in open oceans than in coastal waters. In some estuarine regions, such as the Chesapeake Bay and Norton Sound, the POC concentrations were high. Among 3580 match-ups, 2387 were selected for a-POC algorithm formulation, and the remaining 1193 match-ups were used to evaluate the performance of the a-POC algorithm. The frequency distribution of POC concentrations of match-ups is shown in Figure 2. The distribution of OC-CCI dominant water classes corresponding to the match-ups is illustrated in Figure 3. As the water class increases, the POC concentration shows an upward trend. Supplementary Table 1 shows the number of all match-ups, algorithm formulation match-ups, and algorithm validation match-ups in different OC-CCI dominant water classes. The distribution shows a bimodal

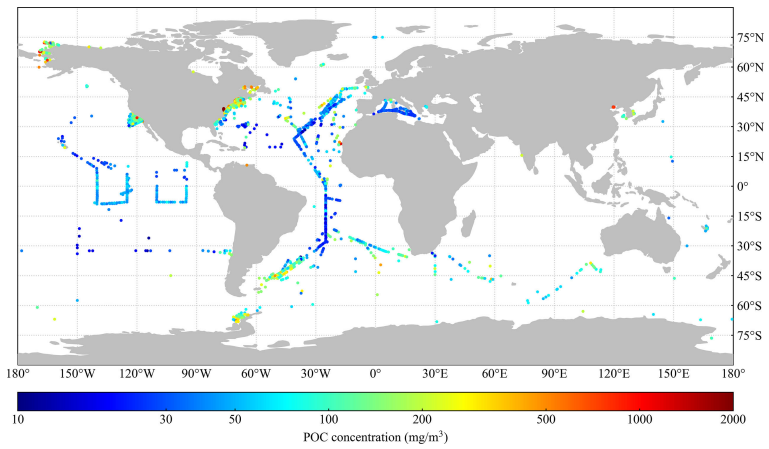


FIGURE 1
Geographical distribution of match-ups between the *in situ* dataset and satellite data. The color bar represents the average POC concentration (mg/m^3) 10 m below the water surface.

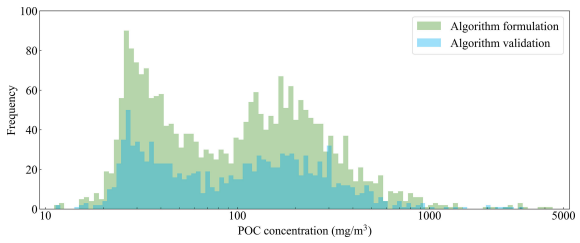


FIGURE 2
Histogram of POC concentration distribution for algorithm formulation match-ups and algorithm validation match-ups.

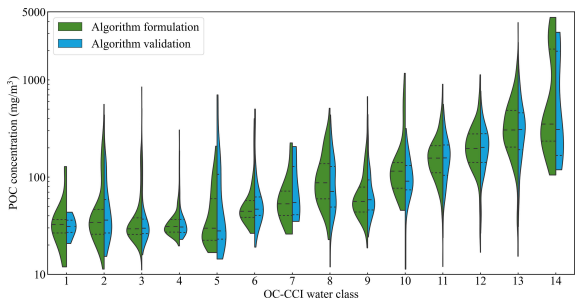


FIGURE 3
The distribution of OC-CCI dominant water classes corresponds to the match-ups. The height of the bulges on both sides indicates the density of the match-ups, and the black dashed lines represent the quartile lines.

trend, with more match-up distributions associated with water classes 2-4 and 11-13.

2.4 Statistical metrics

In addition to the visual measurement of the product images generated by the a-POC algorithm, the performance of the algorithm was also evaluated by six statistical metrics:

- Pearson correlation coefficient between the measured value (x_i) and the satellite-derived value (y_i), R;
- Slope (S) and intercept (I) between x_i and y_i from Model-II linear regression (Reduced Major Axis);
- The median absolute percentage deviation (MAPD, %) between x_i and y_i , calculated as the median of the respective absolute percentage deviation, $\mathrm{APD} = \frac{|y_i - x_i|}{x_i} \times 100$;
- Root-mean-square difference (RMSD, mg/m^3) between x_i and y_i , $\mathrm{RMSD} = \sqrt{\frac{1}{N}\sum(y_i - x_i)^2}$, where N is the number of match-ups used in the calculation;
- Bias between x_i and y_i , $\mathrm{Bias} = \frac{1}{N}\sum(y_i - x_i)$.

2.5 Formulation of a-POC algorithm

The relationship between the absorption coefficient and the POC concentration was established based on a(490). Figure 4 shows the cubic polynomial fit between the *in situ* POC concentration for algorithm formulation match-ups and the a(490) from the OC-CCI v5.0 product suite. The relationship between POC and a(490) in the a-POC algorithm is described as follows:

$$\mathrm{POC} = 10^{0.488x^3+0.947x^2+1.42x+3.41},$$

where $x=log_{10}a(490)$. The value for the squared correlation coefficient, R^2, between the POC concentration and a(490) obtained by cubic polynomial fitting was 0.77.

3 Results

3.1 Algorithm performance evaluation using algorithm validation match-ups

Figure 5 shows the frequency distribution of POC concentrations for algorithm validation match-ups and algorithm retrievals. The distribution of the algorithm validation match-ups showed a bimodal pattern, presenting at about 26 mg/m^3 and 200 mg/m^3. The a-POC algorithm underestimated the POC concentrations in the low-value interval, where the distribution clustered near 30 mg/m^3. When the POC concentration was higher than 100 mg/m^3, the a-POC algorithm roughly reproduced the histogram shape of the match-ups. For comparison, a similar evaluation was performed for the BG algorithm. The BG algorithm and a-POC algorithm had a similar histogram shape at the first peak, while the second peak significantly shifted to the left and was narrower than that of match-ups. In addition, the BG algorithm showed no frequency distribution when the POC concentration was higher than 800 mg/m^3, indicating that the POC concentration estimated by the BG algorithm reached saturation.

Statistical analysis was carried out, and the scatter plot and statistics metrics are shown in Figure 6 and Table 1, respectively.

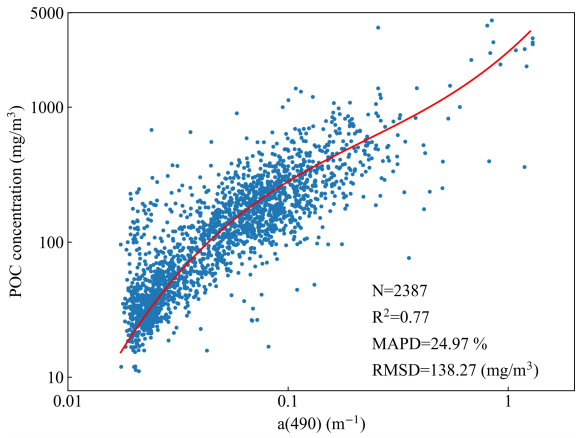


FIGURE 4
The relationship between the POC concentration and a(490) for algorithm formulation match-ups (N=2387) from the OC-CCI v5.0 product suite.

It can be seen that both a-POC and BG algorithms show significant correlations, with R^2 of 0.77 and 0.75 for a-POC and BG algorithms on the $\log_{10}$ scale, respectively. The a-POC algorithm had a smaller error than the BG algorithm, with a Bias value of -3.29 mg/m^3. The linear fitting line on the $\log_{10}$ scale was closer to the 1:1 line, with a slope value of 0.91. However, the BG algorithm significantly underestimated the POC concentrations in the high-value range, with a Bias value of -49.06 mg/m^3. The MAPD values of the two algorithms were similar, and the RMSD were 128.49 and 184.48 mg/m^3 for a-POC and BG algorithms, respectively. These results indicated that the a-POC algorithm was more suitable than the BG algorithm for retrieving POC concentrations, especially in regions with high POC concentrations (i.e., highly productive regions).

3.2 Algorithm applied to OC-CCI data

3.2.1 Algorithm performance per OC-CCI water class

The performance of the a-POC algorithm is further evaluated to respond to the regional optimization of user groups and the calculation of per-pixel uncertainty. Figure 7 summarizes the statistical metrics of a-POC and BG algorithms per OC-CCI water class. Water classes 1-6 represent cleaner open oceans, and 12-14 represent coastal waters with high scattering characteristics. The algorithms performed differently in different water classes. When water classes were less than 13, both algorithms showed lower error levels, indicating that the algorithms perform similarly in open oceans and slightly turbid waters. The a-POC algorithm performed better in classes 13 and 14 (i.e., high turbid waters), especially in class 14, which represents the most optically complex waters. In contrast, the BG algorithm heavily underestimated POC concentrations in these classes.

3.2.2 Algorithm applied in specific regions

In order to evaluate the applicability of the a-POC algorithm in waters with different turbidity degrees, *in situ* match-up

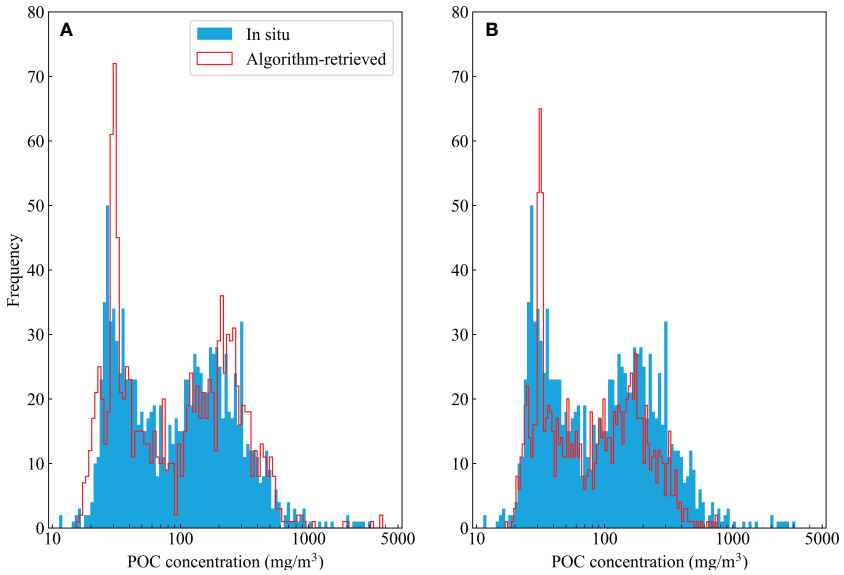


FIGURE 5
The frequency distribution of POC concentrations for algorithm validation match-ups and algorithm retrievals: **(A)** a-POC algorithm and **(B)** BG algorithm.

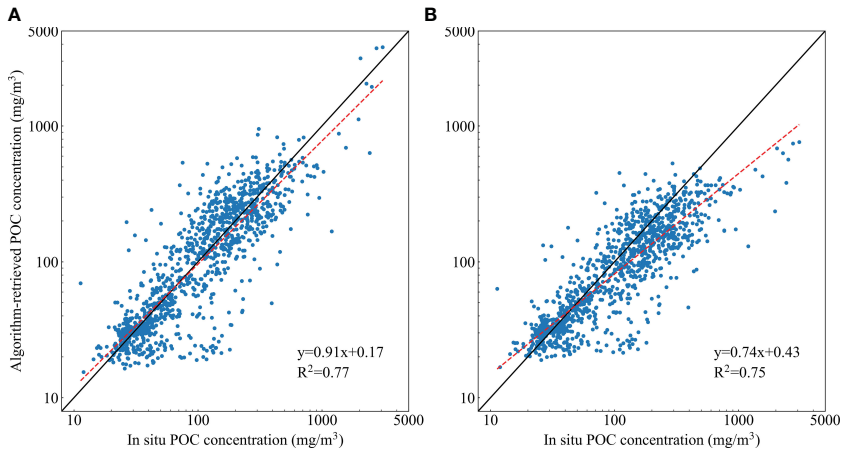


FIGURE 6
Correlation between *in situ* POC concentrations and the concentrations retrieved by **(A)** a-POC algorithm and **(B)** BG algorithm on the $\log_{10}$ scale. The solid black line represents the 1: 1 line, and the red dashed line represents the corresponding linear regression line for each algorithm. The optimal linear regression equation (y) and the square of the determining coefficient (R^2) on the $\log_{10}$ scale are also presented.

TABLE 1 Summary of statistical metrics characterizing the differences in POC concentration between the algorithm retrievals and values of algorithm validation match-ups.

Algorithm	R	S	I	MAPD (%)	RMSD (mg/m^3)	Bias (mg/m^3)
a-POC algorithm	0.85	0.85	20.74	25.11	128.49	-3.29
BG algorithm	0.73	0.31	62.64	24.99	184.48	-49.06

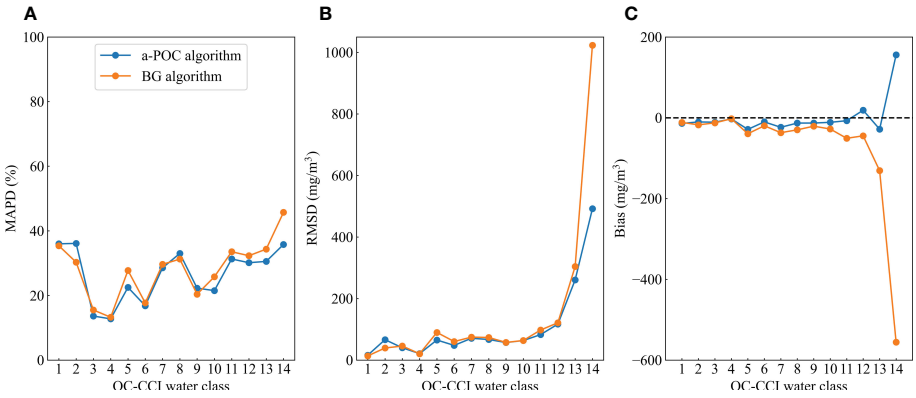


FIGURE 7
The statistical parameters of the algorithms per OC-CCI water class based on algorithm validation match-ups. **(A)** MAPD, **(B)** RMSD, and **(C)** Bias.

datasets of the Atlantic Meridional Transect 26 (AMT26), CLIVEC-CV6, and the Chesapeake Bay were selected for algorithm validation. The AMT26 dataset was collected in September-October 2016 from the Atlantic oligotrophic gyre regions, with several match-ups (N=38) and POC concentrations ranging from 15.79 to 43.88 mg/m^3 (Figures 8A, B). The CLIVEC-CV6 dataset was collected in June 2012 from the eastern coastal waters of the United States with typical coastal water characteristics (N=77), and the POC concentrations ranged from 109.83-635.25 mg/m^3 (Figures 8D, E). The Chesapeake Bay belongs to highly turbid waters, and the Chesapeake Bay dataset was from the discover_aq_2011 cruise in July 2011, N=19, and the POC concentrations range was 1442.13-4389.28 mg/m^3 (Figures 8G, H).

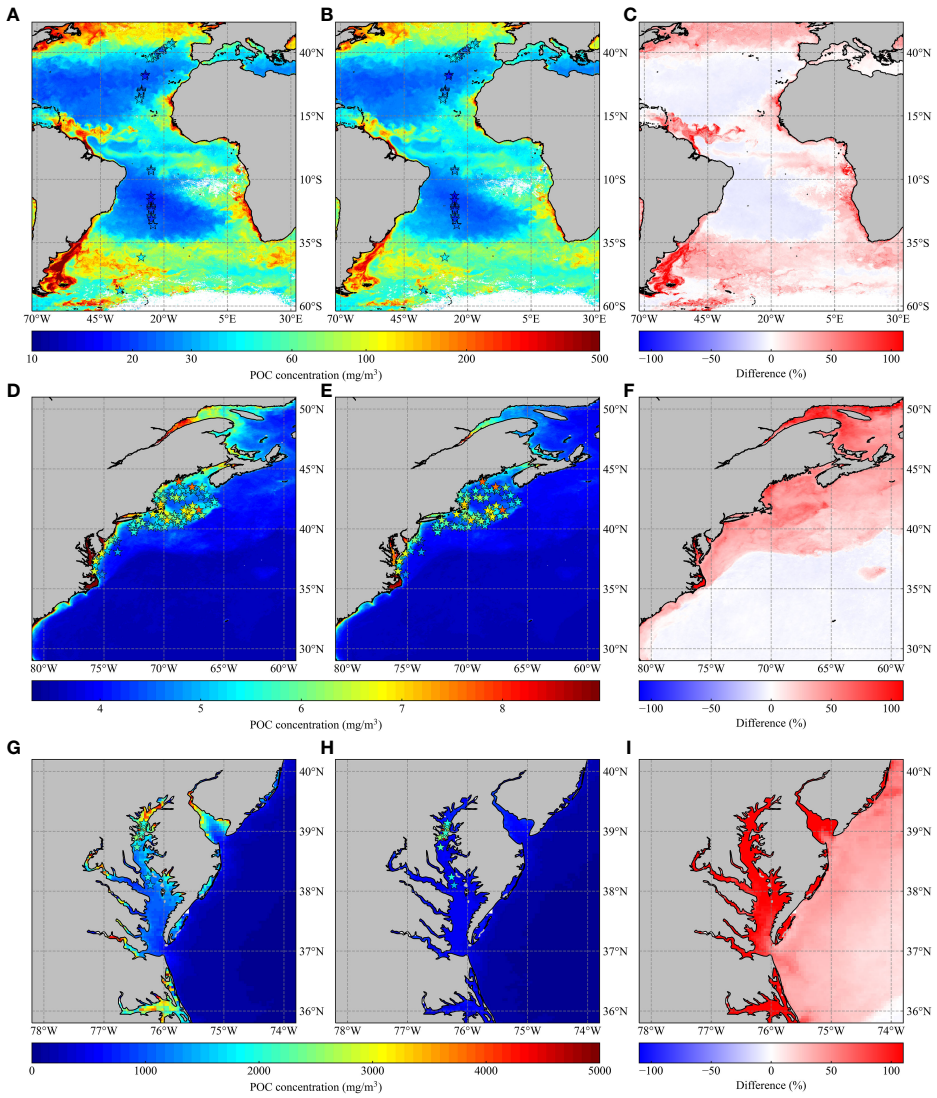


FIGURE 8
POC concentration distributions, including match-ups associated with **(A–C)** the Atlantic Meridional Transect 26 (AMT26), **(D–F)** the CLIVEC-CV6, and **(G–I)** the Chesapeake Bay datasets. The colors of scattered points correspond to the bottom color bar showing the POC concentrations of the match-ups. The background maps in **(A, B)** show the POC concentrations derived from a monthly average composite OC-CCI data in October 2016 using a-POC and BG algorithms, respectively. The patterns of panels **(D, E)** are similar to those of panels **(A, B)**; background maps were derived in June 2012. The patterns of panels **(G, H)** are similar to those of panels **(A, B)**; background maps were derived in July 2011. The percentage difference between the two algorithms is highlighted in **(C, F, I)**, and the color pattern corresponds to the bottom color bar displaying the difference values. The percentage difference is calculated as $100\times(POC_{a-POC}-POC_{BG})/POC_{BG}$.

The geographic and POC concentration distributions for match-ups of the AMT26, CLIVEC-CV6, and Chesapeake Bay datasets are shown in Figure 8. The background maps in panels (Figures 8A, D, G) and (Figures 8B, E, H) show POC concentrations derived from monthly average composite OC-CCI data associated with corresponding samples using a-POC and BG algorithms, respectively, and the percentage differences between the two algorithms are shown in panels (Figures 8C, F, I). Table 2 summarizes the statistical parameters between the POC concentrations retrieved by algorithms during the 1-day time window and the values of match-ups.

For the AMT26 dataset, both algorithms reproduced the POC concentrations of match-ups and achieved similar results. The a-POC algorithm had lower MAPD and Bias values, but RMSD values were slightly higher than those of the BG algorithm due to the overestimation of the POC concentrations of individual match-ups. It can be seen from the background maps of Figure 8 that the POC concentrations retrieved by the algorithms had high consistency in the oligotrophic gyre regions. For the CLIVEC-CV6 dataset, the statistical metrics of the a-POC algorithm outperformed those of the BG algorithm. In addition, both algorithms underestimated

TABLE 2 The summary of statistical metrics characterizing the differences in POC concentration between algorithm retrievals and match-ups in specific regions.

Dataset	Algorithm	MAPD (%)	RMSD (mg/m^3)	Bias (mg/m^3)
AMT26 (N=38)	a-POC algorithm	22.04	7.42	4.23
	BG algorithm	24.33	6.92	4.86
CLIVEC-CV6 (N=77)	a-POC algorithm	33.06	119.63	-67.76
	BG algorithm	51.01	155.49	-128.49
Chesapeake Bay (N=19)	a-POC algorithm	26.11	1016.92	-49.58
	BG algorithm	74.58	2135.84	-2029.41

POC concentrations, with Bias values of -67.76 and -128.49 mg/m^3, respectively. This result is also evidenced by the monthly average products in Figure 8, where the two algorithms had a significant percentage difference in the regions close to the shore.

Compared to AMT26 and CLIVEC-CV6, these two algorithms produced considerable differences between retrieved POC concentrations and the values of match-ups in the Chesapeake Bay. The a-POC algorithm showed significant advantages, with RMSD and Bias values of 1016.92 and -49.58 mg/m^3, respectively. However, the RMSD and Bias values for the BG algorithm were 2135.84 and -2029.41mg/m^3, respectively, and POC concentrations did not exceed 800mg/m^3, severely underestimated POC concentrations. Figure 8H shows that the BG algorithm saturated POC concentrations in the Chesapeake Bay, making the two algorithms produce a significant percentage difference of more than 100%.

Overall, the a-POC algorithm produced satisfactory results in open oceans, coastal waters, and highly turbid waters, with MAPD values of 22.04, 33.06, and 26.11%, respectively. It outperformed the BG algorithm, especially in coastal waters and highly turbid waters.

3.2.3 Algorithm applied in global surface ocean

We further assessed the performance of the a-POC algorithm at the macroscopic scale and compared it with the BG algorithm. Panels (A) and (B) in Figure 9 show the global POC concentration distribution generated by applying a-POC and BG algorithms to the OC-CCI monthly average composite data in March 2020, respectively. Both algorithms produced similar patterns of concentration change in most open oceans. In the equatorial Atlantic and Pacific Oceans, seawater is blown away on both sides of the equator due to the influence of easterly trade winds (Gill and Adrian, 1982). The divergence of surface ocean currents causes an upwelling of cold and nutrient-rich waters, producing productive phytoplankton bloom zones and leading to higher POC concentrations than in subtropical gyre regions (Liu and Wang, 2022). At high latitudes, ocean surface waters are cold with a slight vertical density gradient. The vertical mixing depth of the water is much greater than the depth of the euphotic layer (Siegel et al., 2002). Due to vertical mixing, there is an abundant supply of nutrients in the South Ocean, North Atlantic, and North Pacific, resulting in higher POC concentrations. The a-POC algorithm more precisely captured the spatial characteristics of high POC concentrations. In coastal waters, the a-POC algorithm produced higher POC concentrations than the BG algorithm.

As shown in Figure 9C, the POC concentrations retrieved by the two algorithms were extracted along a transect through the Atlantic Ocean at 20°W, and the POC concentration change was generated with latitude as the independent variable. The trend was consistent for both algorithms, with retrieved POC concentrations ranging from 10 to 1000 mg/m^3. The a-POC algorithm retrieved lower POC concentrations than the BG algorithm in the South Atlantic, consistent with the validation results of the AMT26 dataset. In the northwestern coastal region of Africa at 15-30°N, the a-POC algorithm showed reasonably higher POC concentrations, which can be demonstrated by the validation results in the coastal waters of the United States.

Precise POC concentration mapping in the global surface ocean can be used to estimate total pools of POC in the mixed layer, providing an insight into the global ocean carbon cycle. After considering seasonal and regional variations and assuming homogeneity of the mixed layer, the two algorithms were applied to all monthly average composite OC-CCI data in 2020. Afterward, the obtained POC concentrations were integrated over the mixed-layer depth. The mixed-layer depth data were derived from MIMOC (https://www.pmel.noaa.gov/mimoc/) (Schmidtko et al., 2013). The average total pools of POC estimated by a-POC and BG algorithms were 1.00 Pg C and 0.87 Pg C, respectively. The above evaluations indicated that the a-POC algorithm was robust in both open oceans and coastal waters compared with the BG algorithm. Thus, the total pool estimated by the a-POC algorithm was more credible.

3.3 Mapped uncertainties

Based on the performance of algorithms per OC-CCI water class in Section 3.2.1, the uncertainties of algorithms in the global surface ocean were mapped without *in situ* dataset

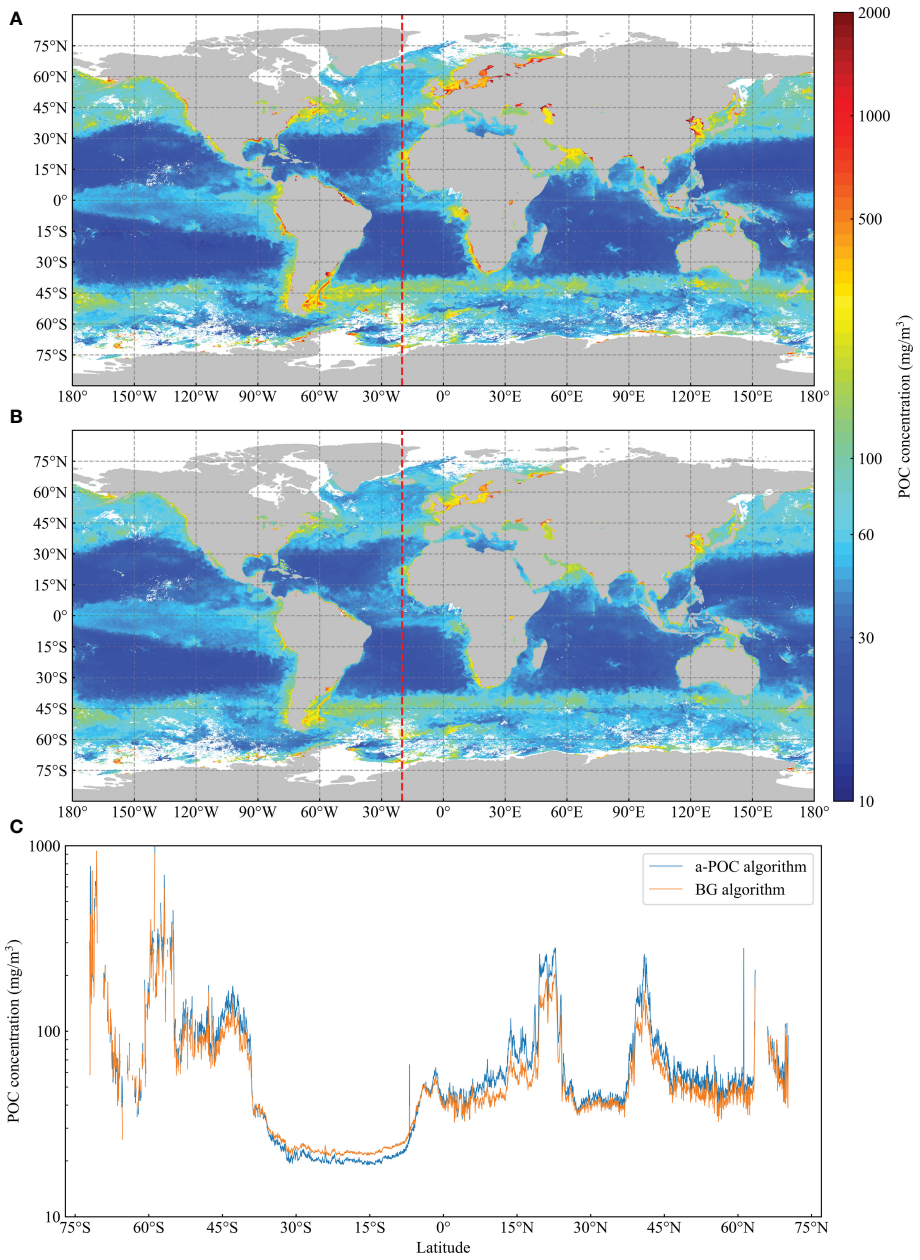


FIGURE 9
POC concentration distribution retrieved by **(A)** the a-POC algorithm and **(B)** the BG algorithm applied to monthly average composite OC-CCI data in March 2020, and **(C)** the POC concentration distribution along the 20°W transect through the Atlantic Ocean.

distribution. The uncertainty of each pixel is obtained by calculating a weighted average based on each water class percent membership and then multiplying it with the statistical parameters of the corresponding water class. Supplementary Figure 1 shows the distribution of the OC-CCI dominant water class in the global ocean in March 2020. From the open ocean to the mainland, there was an increasing trend of water classes, with classes 13 and 14 concentrated along the coasts of the northern hemisphere.

The calculation procedure for uncertainties was applied to the data in Figure 9 to obtain the statistical metric distribution of algorithms (Figure 10). In general, the trend of statistical metric distribution was consistent with the match-up validation results. Both algorithms performed similarly in open oceans (i.e., lower water classes), with lower MAPD, RMSD, and Bias values for the a-POC algorithm. As expected, the two algorithms showed significant differences in the southern Atlantic, the Baltic Sea, and the Yellow and Bohai Seas in China, where corresponding

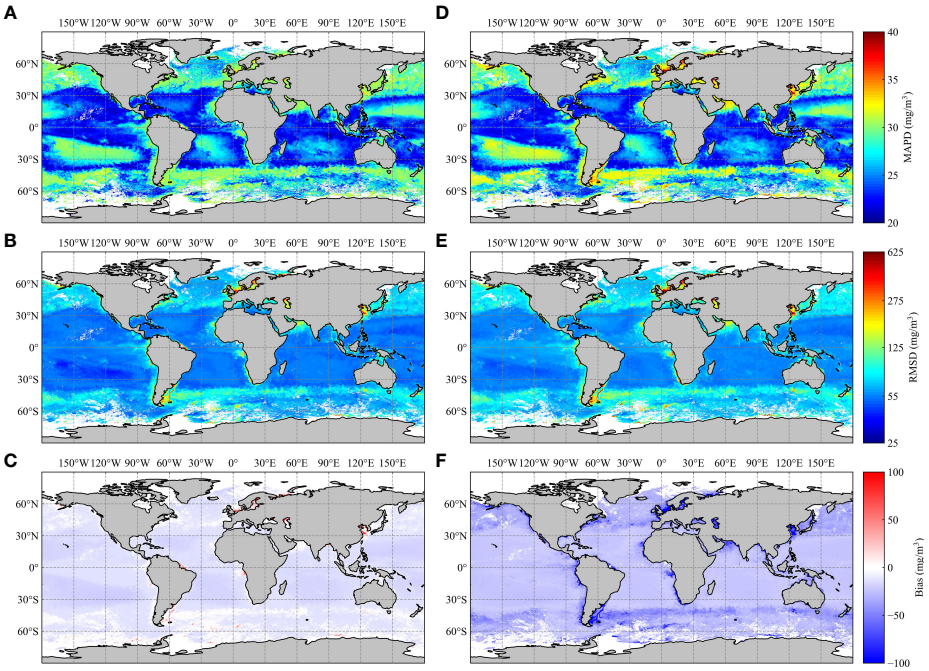


FIGURE 10
Distribution of statistical metrics MAPD, RMSD, and Bias associated with OC-CCI water class when **(A–C)** a-POC algorithm and **(D–F)** BG algorithm are applied to the monthly average OC-CCI data in March 2020.

OC-CCI water classes were high. In these regions, the a-POC algorithm slightly overestimated POC concentrations, while the BG algorithm underestimated POC concentrations with poor statistical metrics.

4 Discussion

4.1 Algorithm applied to OLCI data in Bohai Sea of China

The a-POC algorithm showed significant advantages over BG algorithms when applied to OC-CCI v5.0 data, and user groups may want to apply a-POC algorithms to specific ocean color sensors. To evaluate the universality of the a-POC algorithm to specific ocean color sensors and the sensitivity to different atmospheric correction algorithms, the a-POC and BG algorithms were applied OLCI data associated with the Bohai Sea dataset (Figure 11). The POC concentrations in the Bohai Sea dataset ranged from 338.0 to 1380.0 mg/m^3. The OLCI data were pre-processed by the BAC algorithm (Moore et al., 1999) and the POLYMER algorithm (Steinmetz et al., 2011). After the OLCI data pre-processing and match-up procedure, 23 match-ups were obtained for the BAC algorithm and 28 for the POLYMER algorithm, and the *in situ* sampling dates were June 14, September 19, and 23, 2017. As expected, the BAC algorithm has stricter quality flags than the POLYMER algorithm (Mograne et al., 2019; Renosh et al., 2020). The BAC algorithm reduced the match-ups by 5 due to the influence of the atmospheric correction failure flag. Figure 12 shows the scatter plots of *in situ* $R_{rs}(\lambda)$ versus OLCI-derived $R_{rs}(\lambda)$ at 443 nm, 490 nm, 560 nm, and 665 nm using the atmospheric correction algorithms. These bands were used by the QAA_V5 and BG algorithms to obtain the absorption coefficients and POC concentrations, respectively. The two atmospheric correction algorithms differed significantly at 443 nm. The $R_{rs}(443)$ obtained by the BAC algorithm were significantly underestimated and discrete, while those obtained by the POLYMER algorithm were more consistent with the *in situ* $R_{rs}(443)$. In other bands, both algorithms had similar performances at other bands.

Figure 11 found that the scatters were closer to the color of the background maps generated by the a-POC algorithm, i.e., the POC concentrations retrieved by the a-POC algorithm were closer to that of the match-ups. Furthermore, different atmospheric correction algorithms significantly impact the estimation of POC concentrations, which was especially true for the BG algorithm (Figures 11E–G). When the BG algorithm

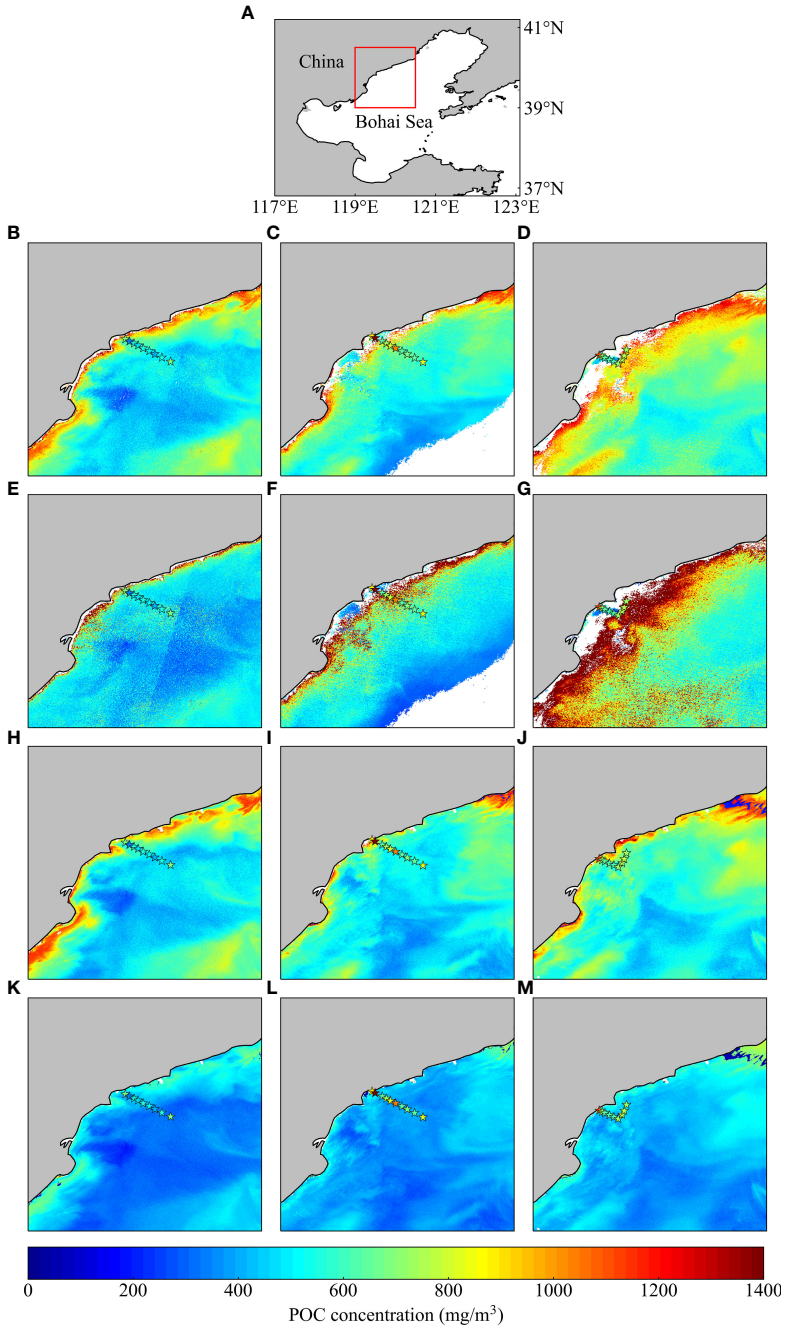


FIGURE 11
Distribution of POC associated with the Bohai Sea match-ups dataset. **(A)** The geographical location of the Bohai Sea. The red box corresponds to the range of the panels below. The color of scatters and background map in **(B–M)** corresponds to the bottom color bar representing the POC concentration. The background maps in **(B–G)** are POC concentrations retrieved by the **(B–D)** a-POC algorithm and **(E–G)** BG algorithm. These data are from OLCI data pre-processed by the BAC atmospheric correction algorithm on June 14, September 19, and 23, 2017. Panels **(H–M)** used the same date and color patterns as panels **(B–G)**, OLCI data were pre-processed by the POLYMER atmospheric correction algorithm, and POC concentrations were retrieved by the **(H–J)** a-POC algorithm and **(K–M)** BG algorithm.

was applied to OLCI data pre-processed by the BAC algorithm, a large amount of noise was generated, and the estimated POC concentrations were seriously inconsistent with the match-ups. Because the BG algorithm relies too much on the accuracy of R_{rs} (443), the strong absorption of CDOM and debris at 443 nm prevents the accurate identification of aerosol models from LUTs by the BAC algorithm, leading to a significant underestimation of R_{rs}(443) (Li et al., 2022). Therefore, an accurate atmospheric correction is essential for the BG algorithm. In contrast, the atmospheric correction has less

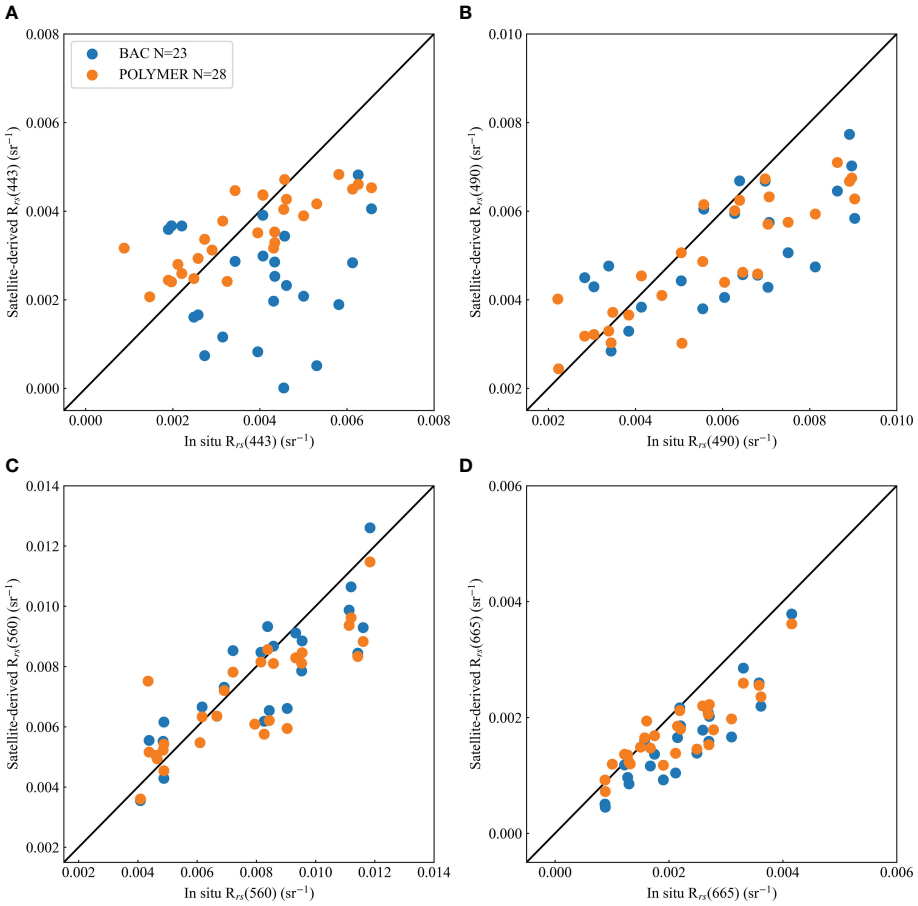


FIGURE 12
Scatter plots of OLCI remote sensing reflectance ($R_{rs}(\lambda)$) derived by the BAC algorithm and POLYMER algorithm with match-up $R_{rs}(\lambda)$ at **(A)** 443 nm, **(B)** 490 nm, **(C)** 560 nm, and **(D)** 665 nm. The solid black line represents the 1:1 line.

impact on the a-POC algorithm because the QAA algorithm weakens the dominance of $R_{rs}(443)$ in the calculation of absorption coefficients (Lee et al., 2002; Lee et al., 2009). For the OLCI data pre-processed by the POLYMER algorithm, the quality of the POC concentration distribution maps generated by both algorithms was significantly improved. Compared with the match-ups, the BG algorithm significantly underestimated POC concentrations (Figures 11H–M).

The statistical parameters between POC algorithms and match-ups are summarized in Table 3. Consistent with the image analysis, the POC concentrations were all overestimated to varying degrees when the POC algorithms were applied to the OLCI data pre-processed by the BAC algorithm. The Bias values for the a-POC and BG algorithms were 16.80 mg/m^3 and 741.83mg/m^3, respectively. In contrast, when the POC algorithms were applied to the OLCI data pre-processed by the POLYMER algorithm, both algorithms underestimated the POC concentrations, and Bias values were -89.04 mg/m^3 and -297.83mg/m^3, respectively. After applying the POC algorithms to the OLCI data pre-processed by the BAC and POLYMER algorithms, the RMSD value for the BG algorithm plummeted from 396.94 mg/m^3 to 66.26 mg/m^3. This result was contrary to the trend of MAPD because the noise generated by the BAC algorithm partially offsets the underestimation of POC concentrations retrieved by the BG algorithm. In comparison, the RMSD value of the a-POC algorithm decreased from 40.08 mg/m^3 to 35.97 mg/m^3, indicating that the a-POC algorithm was less sensitive to atmospheric correction than the BG algorithm. As expected, the BG algorithm was established solely based on *in situ* measurement data, making it a typical "in-water" algorithm. The accuracy of the BG algorithm is limited by the accuracy of the atmospheric correction algorithm (Hu et al., 2012; Le et al., 2018).

Because the Bohai Sea is surrounded by land on three sides, the water optical environment is more complex, and the water class is dominated by classes 13 and 14 (Supplementary Figure 1). It strongly demonstrates the results of Section 3.2 that the a-POC algorithm was more suitable for retrieving the POC concentrations in high turbid waters than the BG algorithm.

TABLE 3 Statistical metrics between POC concentrations in the Bohai Sea match-up dataset and algorithm retrievals applied to OLCI data pre-processed by different atmospheric correction algorithms.

Atmospheric correction	Count	Algorithm	MAPD (%)	RMSD (mg/m^3)	Bias (mg/m^3)
BAC	23	a-POC algorithm	29.92	40.08	16.80
		BG algorithm	33.85	396.94	741.83
POLYMER	28	a-POC algorithm	19.13	35.97	-89.04
		BG algorithm	40.77	66.26	-297.80

4.2 Influence of the IOPs on the POC concentration retrieval

The complexity of POC composition indicates that accurate retrieval of POC remains a great challenge. For example, changes in the species composition of the phytoplankton community or the contribution of phytoplankton and non-phytoplankton particles to the total POC can change the optical properties of the seawater (Grob et al., 2007; Ras et al., 2008). In addition, some non-POC components, such as air bubbles and mineral particles, can also cause changes in the optical environment of the water column, affecting the accurate acquisition of scattering of organic particulate matter (Tassan and Ferrari, 1995; Stramski and Tegowski, 2001). These variations cause changes in the relationship between b_{bp} and POC, introducing uncertainty in estimating the POC concentration of b_{bp}. Based on an *in situ* measurement dataset, Gardner et al., 2006 found a robust relationship between c_p and POC. However, satellite remote sensing retrieval of c_p is difficult because c_p is the sum of particulate absorption and total particulate scattering. Total particle scattering is dominated by forward scattering, to which R_{rs} is theoretically insensitive (Evers-King et al., 2017; Le et al., 2018). Although machine-learning methods are robust in retrieval studies of global ocean surface POC concentrations (Liu et al., 2021), a better understanding of the relationship between particle properties and IOPs can improve POC algorithms by providing insight into the composition of the total POC pool (Evers-King et al., 2017).

When b_{bp} and c_p in IOPs were verified and limited, scholars started focusing on absorption coefficients. Stramski et al., 2001 have demonstrated that organic particles contribute more to the absorption coefficient than the backscattering coefficient, especially for the phytoplankton community, which is the main contribution to the optical variability in open oceans. For high productivity waters, Woźniak et al. (2010) indicated that the variation range of POC-specific particulate absorption coefficients spans one order of magnitude, while the variation of particulate scattering spans two orders of magnitude, suggesting that the POC-specific absorption coefficients are more constrained.

The successful application of the BG algorithm in open oceans demonstrates that the absorption coefficient is a meaningful optical proxy for the POC. The variation of R_{rs} (443) and R_{rs}(560) used by the BG algorithm is mainly driven by the variation of the absorption coefficient (Stramski et al., 2008). Unlike in open oceans, the mineral particles and CDOM in coastal waters mainly contribute to optical properties. The absorption at the short blue bands (i.e., 412 nm and 443 nm) is strongly influenced by a_{CDOM}, which is one of the reasons for the poor performance of the BG algorithm in these waters (Le et al., 2018). In addition, the size and scope of *in situ* datasets used to build the empirical algorithm also impact the accuracy of the BG algorithm (Siegel et al., 2005; Evers-King et al., 2017).

In this study, a(490) was selected as a proxy for POC concentration. First, all types of particles (mineral-dominated, organic-dominated, and mixed) have stronger absorption in the longer blue and shorter green wavelengths range (Allison et al., 2010; Woźniak et al., 2010), especially around 500 nm (see Figure 4 in Woźniak et al., 2010). We tried to use both a(490) and a(510) as proxies for POC and establish the relationship. Compared with a(490), the variation of a(510) was more constrained, thus amplifying the error when retrieving the POC concentration despite the similar fitting performance. Second, selecting a(490) as a proxy can reduce the effects of absorption by CDOM, especially in coastal waters (Le et al., 2017; Le et al., 2018). The direct use of a (490) obtained from the QAA algorithm reduces the error introduced by using R_{rs} in a single band as a proxy for the absorption coefficient. Despite the extensive spatial and larger concentration distribution range of the *in situ* dataset used to develop the a-POC algorithm, the POC concentrations were slightly overestimated in open oceans while underestimated in highly productive waters. Errors may occur as all the empirical algorithms were established based on certain assumptions (Hu et al., 2012). The a-POC algorithm assumes that a_{CDOM} and absorption of nonalgal inorganic particles in seawater are covariant with the absorption of organic particulate matter. As a result, the a-POC algorithm misestimates the contribution of non-POC sources to the absorption coefficient. Due to the absence of optical property data in the *in situ* POC dataset, the a-POC algorithm is not an "in-water" algorithm. It cannot show the actual physical relationship between the absorption coefficient and the POC concentration. In addition, the *in situ* dataset used in this study

was derived from multiple cruises over a long period. The measurement method of POC concentration was difficult to standardize, creating uncertainty in the development of the a-POC algorithm. However, compared to "in-water" algorithms, the a-POC algorithm considers the partial errors introduced by atmospheric correction and the QAA algorithm, which helps the end-user to use the algorithm directly and to obtain higher accuracy.

5 Conclusions

In this study, a large *in situ* POC dataset was merged, which spans an extensive time and space and accurately captures the changing characteristics of seawater optical properties. The a-POC algorithm was formulated based on the *in situ* dataset. Compared with the BG algorithm, the application of the a-POC algorithm to the OC-CCI data improved the accuracy of POC concentration retrieval, especially in medium and high productivity waters. This improvement can be attributed to the robust relationship between the absorption coefficient at 490 nm from the OC-CCI v5.0 product suite and POC. As a result, the long-time series variation of POC concentrations in the global surface ocean was supported, and the estimation of total pools of POC in the mixed layer was promoted. Furthermore, the a-POC algorithm was also suitable for OLCI data, producing reliable results in the Bohai Sea of China. The a-POC algorithm was less sensitive to the influence of atmospheric correction algorithms, which was associated with low dependence on a single band when calculating the absorption coefficient using the QAA method. The a-POC algorithm was established based on the *in situ* POC dataset and the absorption coefficient of remote sensing data, which considered the uncertainty in the generation of remote sensing data. Therefore, when applying the a-POC algorithm to the original remote sensing data processed by different methods, the parameters of the algorithm need to be adjusted to reduce the error. In future field surveys, both the optical properties of seawater and biochemical parameters should be included in the measurement task, facilitating the verification of the genuine physical relationship between the absorption coefficient and the POC.

Data availability statement

Publicly available datasets were analyzed in this study. This data can be found here: https://seabass.gsfc.nasa.gov, https://datadryad.org/.

Author contributions

QL: All the calculations, preparation of figures, collation of the *in situ* database, and original draft preparation. LJ: Project administration, funding acquisition, review and editing, and investigation. YC: Project administration and collation of the *in situ* dataset in the Bohai Sea. JT: review and editing, methodology. SG: software and calculation code. All authors contributed to the article and approved the submitted version.

Funding

This work was supported by the<National Natural Science Foundation of China> under Grant (No. 42076186).

Acknowledgments

We would like to thank the Remote Sensing Group of the National Marine Environmental Monitoring Centre of China for providing partial *in situ* datasets. We would like to thank the scientists who contributed *in situ* data to the shared database for our use. We would like to thank the ESA climate office for providing the OC-CCI data. We would like to thank two reviewers for their thoughtful comments, which have helped us to improve this manuscript considerably.

Conflict of interest

The authors declare that the research was conducted in the absence of any commercial or financial relationships that could be construed as a potential conflict of interest.

Publisher's note

All claims expressed in this article are solely those of the authors and do not necessarily represent those of their affiliated organizations, or those of the publisher, the editors and the reviewers. Any product that may be evaluated in this article, or claim that may be made by its manufacturer, is not guaranteed or endorsed by the publisher.

Supplementary material

The Supplementary Material for this article can be found online at: https://www.frontiersin.org/articles/10.3389/fmars.2022.1048893/full#supplementary-material

References

Allison, D. B., Stramski, D., and Mitchell, B. G. (2010). Empirical ocean color algorithms for estimating particulate organic carbon in the southern ocean. *J. Geophysical Res: Oceans* 115 (C10). doi: 10.1029/2009JC006040

Amon, R. M. W., and Benner, R. (1996). Bacterial utilization of different size classes of dissolved organic matter. *Limnology Oceanography* 41 (1), 41–51. doi: 10.4319/lo.1996.41.1.0041

Babin, M., Stramski, D., Ferrari, G. M., Claustre, H., Bricaud, A., Obolensky, G., et al. (2003). Variations in the light absorption coefficients of phytoplankton, nonalgal particles, and dissolved organic matter in coastal waters around Europe. *J. Geophysical Res.: Oceans* 108, C7. doi: 10.1029/2001JC000882

Behrenfeld, M. J., Boss, E., Siegel, D. A., and Shea, D. M. (2005). Carbon-based ocean productivity and phytoplankton physiology from space. *Global Biogeochemical Cycles* 19 (1). doi: 10.1029/2004GB002299

Bishop, J. K. B. (1999). Transmissometer measurement of POC. *Deep Sea Res. Part I: Oceanographic Res. Papers* 46 (2), 353–369. doi: 10.1016/S0967-0637(98)00069-7

Cetinić, I., Perry, M. J., Briggs, N. T., Kallin, E., D'Asaro, E. A., and Lee, C. M. (2012). Particulate organic carbon and inherent optical properties during 2008 north Atlantic bloom experiment. *J. Geophysical Res: Oceans* 117 (C6). doi: 10.1029/2011JC007771

Chen, D., Zeng, L., Boot, K., and Liu, Q. (2022). Satellite observed spatial and temporal variabilities of particulate organic carbon in the East China Sea. *Remote Sens.* 14 (8), 1799. doi: 10.3390/rs14081799

Cui, T., Zhang, J., Groom, S., Sun, L., Smyth, T., and Sathyendranath, S. (2010). Validation of MERIS ocean-color products in the bohai Sea: A case study for turbid coastal waters. *Remote Sens. Environ.* 114 (10), 2326–2336. doi: 10.1016/j.rse.2010.05.009

Duan, H., Feng, L., Ma, R., Zhang, Y., and Arthur Loiselle, S. (2014). Variability of particulate organic carbon in inland waters observed from MODIS aqua imagery. *Environ. Res. Lett.* 9 (8), 84011. doi: 10.1088/1748-9326/9/8/084011

Duforêt-Gaurier, L., Loisel, H., Dessailly, D., Nordkvist, K., and Alvain, S. (2010). Estimates of particulate organic carbon over the euphotic depth from *in situ* measurements. application to satellite data over the global ocean. *Deep Sea Res. Part I: Oceanographic Res. Papers* 57 (3), 351–367. doi: 10.1016/j.dsr.2009.12.007

Evers-King, H., Martinez-Vicente, V., Brewin, R. J., Dall'Olmo, G., Hickman, A. E., Jackson, T., et al. (2017). Validation and intercomparison of ocean color algorithms for estimating particulate organic carbon in the oceans. *Front. Mar. Sci.* 4. doi: 10.3389/fmars.2017.00251

Field Christopher, B., Behrenfeld Michael, J., Randerson James, T., and Falkowski, P. (1998). Primary production of the biosphere: Integrating terrestrial and oceanic components. *Science* 281 (5374), 237–240. doi: 10.1126/science.281.5374.237

Gardner, W. D., Mishonov, A. V., and Richardson, M. J. (2006). Global POC concentrations from in-situ and satellite data. *Deep Sea Res. Part II: Topical Stud. Oceanography* 53 (5), 718–740. doi: 10.1016/j.dsr2.2006.01.029

Gardner, W. D., Richardson, M. J., Carlson, C. A., Hansell, D., and Mishonov, A. V. (2003). Determining true particulate organic carbon: bottles, pumps and methodologies. *Deep Sea Res. Part II: Topical Stud. Oceanography* 50 (3), 655–674. doi: 10.1016/S0967-0645(02)00589-1

Gill, A. E., and Adrian, E. (1982). *Atmosphere-ocean dynamics* (New York: Academic press).

Gordon, H. R., and Wang, M. (1994a). Influence of oceanic whitecaps on atmospheric correction of ocean-color sensors. *Appl. Optics* 33 (33), 7754–7763. doi: 10.1364/AO.33.007754

Gordon, H. R., and Wang, M. (1994b). Retrieval of water-leaving radiance and aerosol optical thickness over the oceans with SeaWiFS: a preliminary algorithm. *Appl. Optics* 33 (3), 443–452. doi: 10.1364/AO.33.000443

Grob, C., Ulloa, O., Claustre, H., Huot, Y., Alarcón, G., and Marie, D. (2007). Contribution of picoplankton to the total particulate organic carbon concentration in the eastern south pacific. *Biogeosciences* 4 (5), 837–852. doi: 10.5194/bg-4-837-2007

Hedges, J. I. (1992). Global biogeochemical cycles: progress and problems. *Mar. Chem.* 39 (1), 67–93. doi: 10.1016/0304-4203(92)90096-S

Hedges, J. I., and Stern, J. H. (1984). Carbon and nitrogen determinations of carbonate-containing solids1. *Limnology Oceanography* 29 (3), 657–663. doi: 10.4319/lo.1984.29.3.0657

Hu, C., Lee, Z., and Franz, B. (2012). Chlorophyll aalgorithms for oligotrophic oceans: A novel approach based on three-band reflectance difference. *J. Geophysical Research: Oceans* 117 (C1). doi: 10.1029/2011JC007395

Jackson, T., Sathyendranath, S., and Mélin, F. (2017). An improved optical classification scheme for the ocean colour essential climate variable and its applications. *Remote Sens. Environ.* 203, 152–161. doi: 10.1016/j.rse.2017.03.036

Jahnke, R. A. (1996). The global ocean flux of particulate organic carbon: Areal distribution and magnitude. *Global Biogeochemical Cycles* 10 (1), 71–88. doi: 10.1029/95GB03525

Jiang, L., Guo, X., Wang, L., Sathyendranath, S., Evers-King, H., Chen, Y., et al. (2020). Validation of MODIS ocean-colour products in the coastal waters of the yellow Sea and East China Sea. *Acta Oceanologica Sin.* 39 (1), 91–101. doi: 10.1007/s13131-019-1522-3

Jiang, G., Loiselle, S. A., Yang, D., Gao, C., Ma, R., Su, W., et al. (2019). An absorption-specific approach to examining dynamics of particulate organic carbon from VIIRS observations in inland and coastal waters. *Remote Sens. Environ.* 224, 29–43. doi: 10.1016/j.rse.2019.01.032

Lee, Z., Carder, K. L., and Arnone, R. A. (2002). Deriving inherent optical properties from water color: a multiband quasi-analytical algorithm for optically deep waters. *Appl. Optics* 41 (27), 5755–5772. doi: 10.1364/AO.41.005755

Lee, Z., Lubac, B., Werdell, J., and Arnone, R. (2009). "An update of the quasi-analytical algorithm (QAA_v5)," in *International ocean color group software report*.

Le, C., Lehrter, J. C., Hu, C., MacIntyre, H., and Beck, M. W. (2017). Satellite observation of particulate organic carbon dynamics on the Louisiana continental shelf. *J. Geophysical Research: Oceans* 122 (1), 555–569. doi: 10.1002/2016JC012275

Le, C., Zhou, X., Hu, C., Lee, Z., Li, L., and Stramski, D. (2018). A color-index-based empirical algorithm for determining particulate organic carbon concentration in the ocean from satellite observations. *J. Geophysical Research: Oceans* 123 (10), 7407–7419. doi: 10.1029/2018JC014014

Li, Q., Jiang, L., Chen, Y., Wang, L., and Wang, L. (2022). Evaluation of seven atmospheric correction algorithms for OLCI images over the coastal waters of qinhuangdao in bohai Sea. *Regional Stud. Mar. Sci.* 56, 102711. doi: 10.1016/j.rsma.2022.102711

Lin, J., Lyu, H., Miao, S., Pan, Y., Wu, Z., Li, Y., et al. (2018). A two-step approach to mapping particulate organic carbon (POC) in inland water using OLCI images. *Ecol. Indic.* 90, 502–512. doi: 10.1016/j.ecolind.2018.03.044

Liu, D., Bai, Y., He, X. Q., Tao, B. Y., Pan, D. L., Chen, C. T. A., et al. (2019). Satellite estimation of particulate organic carbon flux from changjiang river to the estuary. *Remote Sens. Environ.* 223, 307–319. doi: 10.1016/j.rse.2019.01.025

Liu, H., Li, Q., Bai, Y., Yang, C., Wang, J., Zhou, Q., et al. (2021). Improving satellite retrieval of oceanic particulate organic carbon concentrations using machine learning methods. *Remote Sens. Environ.* 256, 112316. doi: 10.1016/j.rse.2021.112316

Liu, X., and Wang, M. (2022). Global daily gap-free ocean color products from multi-satellite measurements. *Int. J. Appl. Earth Observation Geoinformation* 108, 102714. doi: 10.1016/j.jag.2022.102714

Loisel, H., Nicolas, J.-M., Deschamps, P.-Y., and Frouin, R. (2002). Seasonal and inter-annual variability of particulate organic matter in the global ocean. *Geophysical Res. Lett.* 29 (24), 49–41-49-44. doi: 10.1029/2002GL015948

Martiny, A. C., Vrugt, J. A., and Lomas, M. W. (2014). Concentrations and ratios of particulate organic carbon, nitrogen, and phosphorus in the global ocean. *Sci. Data* 1 (1), 140048. doi: 10.1038/sdata.2014.48

Mélin, F., and Sclep, G. (2015). Band shifting for ocean color multi-spectral reflectance data. *Optics Express* 23 (3), 2262–2279. doi: 10.1364/OE.23.002262

Mograne, M., Jamet, C., Loisel, H., Vantrepotte, V., Mériaux, X., Cauvin, A., et al (2019). Evaluation of five atmospheric correction algorithms over French optically-complex waters for the sentinel-3A OLCI ocean color sensor. *Remote Sens.* 11 (6), 668. doi: 10.3390/rs11060668

Moore, G. F., Aiken, J., and Lavender, S. J. (1999). The atmospheric correction of water colour and the quantitative retrieval of suspended particulate matter in case II waters: Application to MERIS. *Int. J. Remote Sens.* 20 (9), 1713–1733. doi: 10.1080/014311699212434

Moore, T. S., Campbell, J. W., and Hui, F. (2001). A fuzzy logic classification scheme for selecting and blending satellite ocean color algorithms. *IEEE Trans. Geosci. Remote Sens.* 39 (8), 1764–1776. doi: 10.1109/36.942555

Mueller, J. L., Morel, A., Frouin, R., Davis, C., Arnone, R., Carder, K., et al. (2003). "Ocean optics protocols for satellite ocean color sensor validation, revision 4. volume III," in *Radiometric measurements and data analysis protocols* (Greenbelt, MD: USA: Goddard Space Flight Space Center).

Omand, M. M., D'Asaro, E. A., Lee, C. M., Perry, M. J., Briggs, N., Cetinić, I., et al. (2015). Eddy-driven subduction exports particulate organic carbon from the spring bloom. *Science* 348 (6231), 222–225. doi: 10.1126/science.1260062

Pabi, S., and Arrigo, K. R. (2006). Satellite estimation of marine particulate organic carbon in waters dominated by different phytoplankton taxa. *J. Geophysical Research: Oceans* 111 (C9). doi: 10.1029/2005JC003137

Ras, J., Claustre, H., and Uitz, J. (2008). Spatial variability of phytoplankton pigment distributions in the subtropical south pacific ocean: comparison between *in situ* and predicted data. *Biogeosciences* 5 (2), 353–369. doi: 10.5194/bg-5-353-2008

Renosh, P. R., Doxaran, D., Keukelaere, L. D., and Gossn, J. I. (2020). Evaluation of atmospheric correction algorithms for sentinel-2-MSI and sentinel-3-OLCI in highly turbid estuarine waters. *Remote Sens.* 12 (8), 1285. doi: 10.3390/rs12081285

Sathyendranath, S., Brewin, R. J. W., Brockmann, C., Brotas, V., Calton, B., Chuprin, A., et al. (2019). An ocean-colour time series for use in climate studies: The experience of the ocean-colour climate change initiative (OC-CCI). *Sensors* 19 (19), 4285. doi: 10.3390/s19194285

Sathyendranath, S. J. T., Brockmann, C., Brotas, V., Calton, B., Chuprin, A., Clements, O., et al. (2021). ESA Ocean colour climate change initiative (Ocean_Colour_cci): Version 5.0 data. *NERC EDS Centre Environ. Data Analysis.* doi: 10.5285/1dbe7a109c0244aaad713e078fd3059a

Schmidtko, S., Johnson, G. C., and Lyman, J. M. (2013). MIMOC: A global monthly isopycnal upper-ocean climatology with mixed layers. *J. Geophysical Res: Oceans* 118 (4), 1658–1672. doi: 10.1002/jgrc.20122

Sharp, J. H. (1974). Improved analysis for "particulate" organic carbon and nitrogen from seawater1. *Limnology Oceanography* 19 (6), 984–989. doi: 10.4319/lo.1974.19.6.0984

Siegel, D. A., Doney, S. C., and Yoder, J. A. (2002). The north Atlantic spring phytoplankton bloom and sverdrup's critical depth hypothesis. *Science* 296 (5568), 730–733. doi: 10.1126/science.1069174

Siegel, D. A., Maritorena, S., Nelson, N. B., Behrenfeld, M. J., and McClain, C. R. (2005). Colored dissolved organic matter and its influence on the satellite-based characterization of the ocean biosphere. *Geophysical Res. Lett.* 32 (20). doi: 10.1029/2005GL024310

Siegenthaler, U., and Sarmiento, J. L. (1993). Atmospheric carbon dioxide and the ocean. *Nature* 365 (6442), 119–125. doi: 10.1038/365119a0

Steinmetz, F., Deschamps, P.-Y., and Ramon, D. (2011). Atmospheric correction in presence of sun glint: application to MERIS. *Optics Express* 19 (10), 9783–9800. doi: 10.1364/OE.19.009783

Stramska, M. (2009). Particulate organic carbon in the global ocean derived from SeaWiFS ocean color. *Deep Sea Res. Part I: Oceanographic Res. Papers* 56 (9), 1459–1470. doi: 10.1016/j.dsr.2009.04.009

Stramska, M. (2014). Particulate organic carbon in the surface waters of the north Atlantic: spatial and temporal variability based on satellite ocean colour. *Int. J. Remote Sens.* 35 (13), 4717–4738. doi: 10.1080/01431161.2014.919686

Stramska, M., and Cieszyńska, A. (2015). Ocean colour estimates of particulate organic carbon reservoirs in the global ocean – revisited. *Int. J. Remote Sens.* 36 (14), 3675–3700. doi: 10.1080/01431161.2015.1049380

Stramska, M., and Stramski, D. (2005). Variability of particulate organic carbon concentration in the north polar Atlantic based on ocean color observations with Sea-viewing wide field-of-view sensor (SeaWiFS). *J. Geophysical Research: Oceans* 110 (C10). doi: 10.1029/2004JC002762

Stramski, D., Bricaud, A., and Morel, A. (2001). Modeling the inherent optical properties of the ocean based on the detailed composition of the planktonic community. *Appl. Optics* 40 (18), 2929–2945. doi: 10.1364/AO.40.002929

Stramski, D., Joshi, I., and Reynolds, R. A. (2022). Ocean color algorithms to estimate the concentration of particulate organic carbon in surface waters of the global ocean in support of a long-term data record from multiple satellite missions. *Remote Sens. Environ.* 269, 112776. doi: 10.1016/j.rse.2021.112776

Stramski, D., Reynolds, R. A., Babin, M., Kaczmarek, S., Lewis, M. R., Röttgers, R., et al. (2008). Relationships between the surface concentration of particulate organic carbon and optical properties in the eastern south pacific and eastern Atlantic oceans. *Biogeosciences* 5 (1), 171–201. doi: 10.5194/bg-5-171-2008

Stramski, D., Reynolds, R. A., Kahru, M., and Mitchell, B. G. (1999). Estimation of particulate organic carbon in the ocean from satellite remote sensing. *Science* 285 (5425), 239–242. doi: 10.1126/science.285.5425.239

Stramski, D., and Tegowski, J. (2001). Effects of intermittent entrainment of air bubbles by breaking wind waves on ocean reflectance and underwater light field. *J. Geophysical Research: Oceans* 106 (C12), 31345–31360. doi: 10.1029/2000JC000461

Tassan, S., and Ferrari, G. M. (1995). Proposal for the measurement of backward and total scattering by mineral particles suspended in water. *Appl. Optics* 34 (36), 8345–8353. doi: 10.1364/AO.34.008345

Tran, T. K., Duforêt-Gaurier, L., Vantrepotte, V., Jorge, D. S. F., Mériaux, X., Cauvin, A., et al. (2019). Deriving particulate organic carbon in coastal waters from remote sensing: Inter-comparison exercise and development of a maximum band-ratio approach. *Remote Sens.* 11 (23), 2849. doi: 10.3390/rs11232849

Werdell, P. J., and Bailey, S. W. (2005). An improved in-situ bio-optical data set for ocean color algorithm development and satellite data product validation. *Remote Sens. Environ.* 98 (1), 122–140. doi: 10.1016/j.rse.2005.07.001

Woźniak, S. B., Stramski, D., Stramska, M., Reynolds, R. A., Wright, V. M., Miksic, E. Y., et al. (2010). Optical variability of seawater in relation to particle concentration, composition, and size distribution in the nearshore marine environment at imperial beach, California. *J. Geophysical Research: Oceans* 115 (C8). doi: 10.1029/2009JC005554

Yu, X., Lee, Z., Shen, F., Wang, M., Wei, J., Jiang, L., et al. (2019). An empirical algorithm to seamlessly retrieve the concentration of suspended particulate matter from water color across ocean to turbid river mouths. *Remote Sens. Environ.* 235, 111491. doi: 10.1016/j.rse.2019.111491

Zhang, X., Hu, L., and He, M.-X. (2009). Scattering by pure seawater: Effect of salinity. *Optics Express* 17 (7), 5698–5710. doi: 10.1364/OE.17.005698

frontiers | Frontiers in Marine Science

TYPE Original Research
PUBLISHED 23 January 2023
DOI 10.3389/fmars.2023.1051619

Check for updates

OPEN ACCESS

EDITED BY
Gemma Kulk,
Plymouth Marine Laboratory,
United Kingdom

REVIEWED BY
Thomas Jackson,
Plymouth Marine Laboratory,
United Kingdom
Maryam Alshehhi,
Khalifa University, United Arab Emirates

*CORRESPONDENCE
Yan Bai
baiyan@sio.org.cn

SPECIALTY SECTION
This article was submitted to Ocean Observation, a section of the journal Frontiers in Marine Science

RECEIVED 23 September 2022
ACCEPTED 06 January 2023
PUBLISHED 23 January 2023

CITATION
Yu S, Bai Y, He X, Gong F and Li T (2023) A new merged dataset of global ocean chlorophyll-a concentration for better trend detection.
Front. Mar. Sci. 10:1051619.
doi: 10.3389/fmars.2023.1051619

COPYRIGHT
© 2023 Yu, Bai, He, Gong and Li. This is an open-access article distributed under the terms of the Creative Commons Attribution License (CC BY). The use, distribution or reproduction in other forums is permitted, provided the original author(s) and the copyright owner(s) are credited and that the original publication in this journal is cited, in accordance with accepted academic practice. No use, distribution or reproduction is permitted which does not comply with these terms.

A new merged dataset of global ocean chlorophyll-a concentration for better trend detection

Shujie Yu[1,2], Yan Bai[2*], Xianqiang He[1,2], Fang Gong[2] and Teng Li[2]

[1]Ocean College, Zhejiang University, Zhoushan, China, [2]State Key Laboratory of Satellite Ocean Environment Dynamics, Second Institute of Oceanography, Ministry of Natural Resources, Hangzhou, China

Chlorophyll-a concentration (Chla) is recognized as an essential climate variable and is one of the primary parameters of ocean-color satellite products. Ocean-color missions have accumulated continuous Chla data for over two decades since the launch of SeaWiFS (Sea-viewing Wide Field-of-view Sensor) in 1997. However, the on-orbit life of a single mission is about five to ten years. To build a dataset with a time span long enough to serve climate change related studies, it is necessary to merge the Chla data from multiple sensors. The European Space Agency has developed two sets of merged Chla products, namely GlobColour and OC-CCI (Ocean Colour Climate Change Initiative), which have been widely used. Nonetheless, issues remain in the long-term trend analysis of these two datasets because the inter-mission differences in Chla have not been completely corrected. To obtain more accurate Chla trends in the global and various oceans, we produced a new dataset by merging Chla records from the SeaWiFS, MODIS (Medium-spectral Resolution Imaging Spectrometer), MERIS (Moderate Resolution Imaging Spectroradiometer), VIIRS (Visible Infrared Imaging Radiometer Suite), and OLCI (Ocean and Land Colour Instrument) with inter-mission differences corrected in this work. The fitness of the dataset on long-term Chla trend study was validated by using *in situ* Chla and comparing the trend estimates to the multi-annual variability of different satellite Chla records. The results suggest that our dataset can be used for long-term series analysis and trend detection. We also provide the global trend map in Chla over 23 years (1998–2020) and present a significant positive global trend with 0.67% ± 0.37%/yr.

KEYWORDS

chlorophyll-a concentration (Chla), ocean color (OC), merged data product, climate change, satellite data

1 Introduction

As an essential part of the global ecosystem, phytoplankton converts atmospheric carbon dioxide into organic carbon through photosynthesis; its primary productivity accounts for almost half of the global total (Field et al., 1998). Moreover, marine phytoplankton is very sensitive to climate change and is generally considered an excellent indicator of the impact of climate change on the marine ecosystem and environment. Understanding the time-series variation of phytoplankton is the basis for predicting how marine ecosystems respond to climate change (Muller-Karger et al., 2014).

The biomass of phytoplankton in the marine ecosystem can be characterized by chlorophyll-a (Chla) concentration in seawater, recognized as an essential climate variable (Bojinski et al., 2014) by the Global Climate Observing System (GCOS, 2011). To estimate the importance of phytoplankton to the global carbon cycle and its variation under the background of climate change, an expanded scope of observation in both time and space is needed (Johnson et al., 2009; Chavez et al., 2011). Long-time-scale climate change research also requires Chla data to have high accuracy and consistency to extract tiny climate-related signals from short-term dynamic changes and environmental disturbances (Henson et al., 2010). Ocean-color remote sensing is ideally suited for such studies because of its large-scale, relatively long-term, and high-frequency observations. At present, it is the only available means to understand and track near-surface Chla concentration and its variations in the global ocean comprehensively (Mélin, 2016).

Chla is one of the primary parameters of ocean-color satellite missions (O'Reilly et al., 1998; Morel et al., 2006; Maritorena et al., 2010). The ongoing series of satellite deployments have provided us with a continuous sequence of global Chla data for over two decades. Launched in 1997 by NASA, the Sea-viewing Wide Field-of-view Sensor (SeaWiFS) (McClain, 1998) has been recognized as the beginning of systematic global monitoring of the worldwide ocean (McClain et al., 2004). This mission ended in 2010 and was followed by the Moderate Resolution Imaging Spectroradiometer (MODIS) on the Aqua platforms and the European Space Agency's (ESA's) Medium-spectral Resolution Imaging Spectrometer (MERIS) on Envisat since 2002, NASA's Visible Infrared Imaging Radiometer Suite (VIIRS) on the SUOMI National Polar-Orbiting Partnership (SNPP) since 2012, and then ESA's Ocean and Land Colour Instrument (OLCI) on Sentinel-3A and Sentinel-3B since 2016 (McClain, 2009). As strong interannual signals such as the El Nino Southern Oscillation can affect the trend calculation over a decade (Ryan et al., 2006; Collins et al., 2010), Chla trend estimation on a long time scale requires a sequence beyond decades that exceeds the maximum life expectancy of a single satellite mission (Henson et al., 2010).

Merging datasets from different missions is an effective method for increasing the period of ocean-color satellites to meet the demand of detecting Chla changes on the climatic time scale (Gregg and Woodward, 1998; Maritorena and Siegel, 2005). The International Ocean-Colour Coordinating Group (IOCCG) released a report focusing on the issues associated with ocean-color data merging in 2007 (IOCCG, 2007). ESA launched the GlobColour project and the Climate Change Initiative (CCI) (Plummer et al., 2017) in 2005 and 2010, respectively, and produced continuous multi-sensor ocean-color datasets that have been widely used (Maritorena and Siegel, 2005; Pottier et al., 2006; IOCCG, 2007; Mélin et al., 2009; Maritorena et al., 2010; Kahru et al., 2012; Kahru et al., 2015; Ford and Barciela, 2017). The GlobColour project has provided two merged Chla products from September 1997 to date, namely AVW and Garver–Siegel–Maritorena (GSM), released in 2005 and kept updated. AVW is the weighted average of single-sensor Level 2 Chla products. GSM makes use of the normalized reflectances at the original sensor wavelengths, without intercalibration, to retrieve ocean-color data (Maritorena and Siegel, 2005). The OC-CCI project (ESA) provides merged ocean-color products, integrating remote sensing reflectance (Rrs) values from single sensors and retrieving various ocean-color parameters *via* selected algorithms (Sathyendranath et al., 2019).

However, inter-mission differences can be transmitted to these merged time series and thus interfere with the Chla trend detection (Hammond et al., 2018). In particular, trend detection based on multimission (merged or concatenated) data appears to be extremely sensitive to inter-mission biases (Mélin, 2016). Gregg and Rousseaux (2014) reported that, because of the difference between MODIS and SeaWiFS, a significant decreasing trend was detected when Chla records switched from SeaWiFS to MODIS in 2003 (or any year through 2007), whereas SeaWiFS (1998–2007) and MODIS-Aqua (2003–2012) global annual median Chla show no significant trend. Though these products have been strictly verified in terms of the accuracy of Chla concentration using *in situ* data or theoretical derivation, some caution is warranted when using them as a multidecadal climate data record (CDR). For OC-CCI products, bias correction has been applied to remote-sensing reflectance (Sathyendranath et al., 2017). Nevertheless, Mélin et al. (2017) stated that, in 1998–2007, the Chla trend derived from the OC-CCI product was significantly different from that derived from SeaWiFS in some areas of the Atlantic, and, in 2002–2012, it was also different from that derived from MODIS data in the Pacific. Moreover, the GlobColour data are not explicitly bias-corrected (Maritorena et al., 2010; Hammond et al., 2018).

Therefore, for Chla data that have been accumulated for more than 20 years, it is necessary to develop a better dataset specialized for trend analysis. In this study, a fast and straightforward method is adopted to combine the frequently used sensors SeaWiFS, MERIS, MODIS, VIIRS, and OLCI to eliminate the inter-mission differences between sensors, thus obtaining accurate long-term variations in Chla on a global scale. We have provided product validation using data from *in situ* and single sensors and confirm the improvements in Chla variation detection *via* comparison with existing merged products. The implications of the product are discussed under the background of climate change.

2 Materials and methods

2.1 Satellite and *in situ* data

This work employed data from five widely used sensors—SeaWiFS, MERIS, MODIS/Aqua, VIIRS/SNPP, and OLCI/Sentinel-3A (Figure 1)—to produce a monthly and 8-day-averaged merged

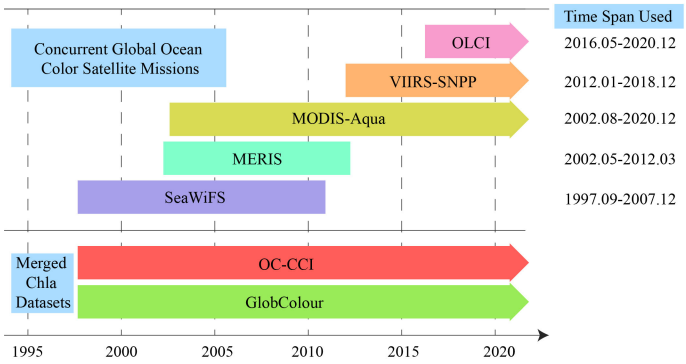


FIGURE 1
The time span of sensors and merged datasets.

Chla dataset from Sept. 1997 to Dec. 2020. The Chla data derived from SeaWiFS, MODIS/Aqua, and VIIRS/SNPP were obtained from the OceanColor website (National Aeronautics and Space Administration, NASA, https://oceancolor.gsfc.nasa.gov/l3/) archive of Level-3 gridded data associated with processing versions 2018.0 and the OCI (Ocean Color Index) algorithm. The Chla data derived from MERIS and OLCI/Sentinel-3A were obtained from the GlobColor website (ESA, https://hermes.acri.fr/) with processing versions 2016.0 for MERIS and 2017.2 for OLCI, respectively. The temporal resolutions of the satellite data are 8-day averages and monthly averages. The spatial resolution of SeaWiFS data is 9 km (resampled to 4 km before fusion), and that of other data is 4 km. We excluded the SeaWiFS record for 2008–2010 because of severe sensor issues that caused a significant loss of data (Gregg and Rousseaux, 2014). The first and last months of the MERIS record and the first month of OLCI were also eliminated for the same reason. VIIRS records after 2018 were also removed as they exhibited a massive Chla decrease on the global scale, which was not detected by MODIS nor OLCI.

An effective way to assess and validate the quality of our merged product is to compare it with other datasets. The merged Chla dataset we produced will be compared with two merged Chla products, the OC-CCI and GlobColour datasets. The ESA climate office provided the OC-CCI 8-day and monthly Chla products (version 5.2) with a 4-km resolution for 1997–2020 (https://climate.esa.int/en/projects/ocean-colour/). For GlobColour, as the weighted averages of single sensors have apparent disadvantages in ensuring the authenticity of the Chla trend detected, just like switching from one sensor to another at a particular point of time, we employed the GSM product rather than the AVW product. The GlobColour data (http://globcolour.info/) used in this study are the Level-3 gridded data, which are 8-day and monthly averages with a resolution of 4 km and developed, validated, and distributed by ACRI-ST, France.

To validate the accuracy of Chla data retrieved by the product, we adapted the global bio-optical *in situ* database constructed for ocean-color satellite remote sensing published by Valente et al. (2019). The database was composed of different sources, including MOBY (Marine Optical Buoy), BOUSSOLE (BOUée pour l'acquiSition de Séries Optiques à Long termE project), AERONET-OC (AErosol RObotic NETwork-Ocean Color), SeaBASS (SeaWiFS Bio-optical Archive and Storage System), NOMAD (NASA bio-Optical Marine Algorithm Dataset), MERMAID (MERIS Match-up *In situ* Database), AMT (Atlantic Meridional Transect), ICES (International Council for the Exploration of the Sea), HOT (Hawaii Ocean Time-series), and GeP&CO (Geochemistry, Phytoplankton, and Color of the Ocean), with an increased number of matchups with satellite records and spatiotemporal distribution. The compiled data span the period from 1997 to 2018 and have a total data volume of 79,924 samples. This dataset was initially built to develop and validate OC-CCI products (Sathyendranath et al., 2019).

Additionally, to illustrate the potential driving mechanism of climate change to the long-term trends of Chla, trends in sea surface temperature (SST) are presented in the discussion section. The monthly SST data were obtained from the AVHRR_OI (optimal interpolation) dataset (processing version 2.1) provided by the Group for High-Resolution Sea Surface Temperature, National Oceanic and Atmospheric Administration (https://www.ghrsst.org/), and have a 0.25° resolution.

2.2 Method of merging multiple sensors

The data-merging algorithm we built is for Level-3 Chla records. Space agencies have expended considerable effort on the calibration of instruments and assessing their stability over time, thus supporting a solid basis for using single-mission Chla products as reliable references for multi-annual time-variation analysis (Xiong et al., 2009; Eplee et al., 2012; Cao et al., 2013; IOCCG, 2013; Eplee et al., 2015; Mélin, 2016). Therefore, we adopted an efficient inter-mission bias-correction method that minimizes the trend signal modification from every single sensor. The principle of this method entails correcting inter-mission bias between two sensors using their overlapping observation period. This merging strategy was mentioned by Mélin et al. (2017) and used to build a standard sequence in which inter-mission biases between SeaWiFS and MODIS/Aqua were considered to be corrected to check the impact of inter-mission differences and drifts on Chla trend estimates. On this basis, we extended this method to the above five sensors and produced global monthly and 8-day-averaged Chla products from September 1997 to December 2020. The data production procedure is shown in Figure 2.

Because of the long on-orbit operation time of MODIS/Aqua(A) (i.e., from August 2002 to the present), the overlap with SeaWiFS(S),

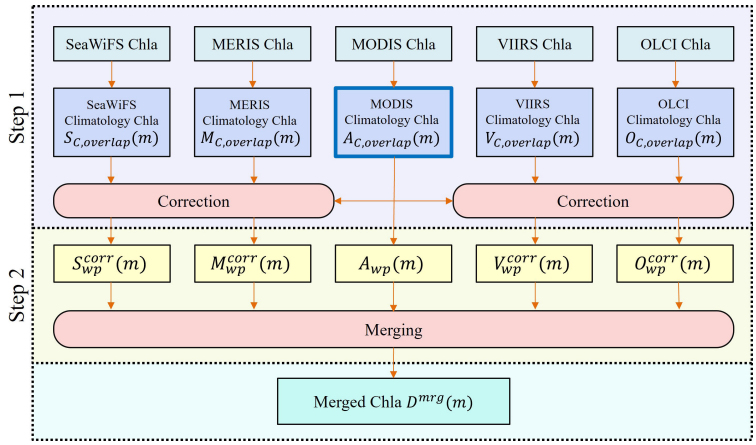


FIGURE 2
The procedure of multiple sensors Chla data merging.

MERIS(M), VIIRS(V), and OLCI(O) is more than five years, so MODIS/Aqua is regarded as the benchmark in this work. The first step is bias correction, which corrects the data derived by other sensors. For each pixel, the inter-mission bias between MODIS/Aqua (A) and the target sensor (X), $\Delta_{A,\,X}$, can be expressed as

$$\Delta_{A,\,X}(m) = A_{C,overlap}(m) - X_{C,overlap}(m)$$

where we use monthly data for example, m means the monthly data that were processed, and the '*C, overlap*' subscript indicates the climatological monthly Chla derived using the overlap period for the 8 days or month m. Taking SeaWiFS as an example, we see that the climatological January value is the average of the valid January values for the five years overlapping with MODIS, from 2003 to 2007, and so on for the other months and sensors. The corrected record of sensor X, $X_{wp}^{corr}(m)$, can be expressed as

$$X_{wp}^{corr}(m) = X_{wp}(m) + \Delta_{A,\,X}(m)$$

where the '*wp*' subscript means the whole on-orbit period of sensor X, and $X_{wp}(m)$ represents the entire original series of the target sensor X. The first step corrects the spatial and seasonal dependencies in inter-mission biases that have been noticed for ocean-color products in a simple manner and guarantees consistency for the merged Chla product (Mélin, 2016; Sathyendranath et al., 2019). Some negative values could result from considering the bias as an arithmetic difference, but the number of negative values is quite limited in practice, accounting for an average of 0.91% of the total valid pixels for SeaWiFS, 1.33% for MERIS, 0.18% for VIIRS, and 0.97% for OLCI. These negative values are regarded as invalid data and excluded from subsequent processing.

In the second step, merging is simply averaging the available data for a given pixel. Therefore, the merged series, $D^{mrg}(m)$, can be expressed as

$$D^{mrg}(m) = \frac{1}{N}\sum_{i=1}^{N} X(m)$$

where N represents the number of sensors in orbit for each month m and $X(m)$ indicates the corrected Chla of every single sensor and MODIS record.

2.3 Calculation of time-series trends

Trends showed in this work were based on linear regression analysis of monthly Chla anomaly data. Using anomaly data instead of monthly Chla data helps to avoid the interference of seasonal signals on interannual trend detection. The monthly anomaly sequence was obtained by subtracting the corresponding monthly climatological value from the monthly value. The anomaly sequence and corresponding date (e.g., months since the first month) were linearly fitted pixel by pixel, and the obtained slope is then regarded as the rate of change of Chla in units of μg/L/month, which is converted to μg/L/yr subsequently. For a certain region, we first calculate the regional average Chla value, and then obtain the anomaly sequence and calculate the trend at last. A statistically significant trend is one that exceeds the 95% confidence level (i.e., $p< 0.05$) under the t-test.

2.4 *In situ* data matchup

The *in situ* Chla data (Valente et al., 2019) were matched with corresponding satellite data to validate the merged products. First, the *in situ* data were gridded with a time window of 8 days and a spatial window of 4 km, the same as the satellite data resolution. The principle is that each sample can only belong to one grid. For the grid containing more than three samples, abnormal values were identified by the 3σ principle and eliminated. The averaged value of valid data in each grid was considered as the value of the grid. Then, matching-up processing basically followed the procedures adopted by the OC-CCI group (Sathyendranath et al., 2019): The nearest latitude and longitude identified the central pixel collocated with each *in situ* datum. The surrounding pixels (a 5 × 5 box with the *in situ* datum in the center) were selected for further analysis. Only those pixels with a valid central pixel and satisfying checks that Chla was within the 0.01–100 μg/L range and at a water depth of >50 m according to bathymetry were considered to be valid. Homogeneity criteria—that the coefficient of variation was<0.15 and at least 10 valid pixels were in the 5 × 5 box—were also used to exclude nonhomogeneous pixels to avoid the impact of the noise within satellite products on the

validation. In addition, high-latitude ocean regions (>66.5°) are excluded owing to the generally high Chla values in these regions that are not applicable for the CI-based Chla algorithm (Wang and Son, 2016). Finally, valid central pixels and corresponding gridded *in situ* data were matched to construct the database for product validation.

3 Results

3.1 Validation by *in situ* Chla data

Comparison with *in situ* measurements is one of the essential means of validating the quality of satellite products (Maritorena et al., 2010). After the procedures mentioned in section 2.4 were implemented, 19,836 groups of *in situ* data matched up with our product. As a reference, OC-CCI and GlobColour products were also involved. Finally, 15,599 groups of valid data were successfully matched with all OC-CCI, GlobColour, and our products. Their spatial and numerical distributions are shown in Figure 3.

Figure 4 shows how the three merged 8-day products compare with the corresponding gridded *in situ* observations. It indicates an acceptable agreement between the product generated in our study and the *in situ* data (Figure 4A), with a root mean squared error (RMSE) of 1.04 and R^2 = 0.75 based on $\log_{10}$ Chla. The statistics are similar to that of OC-CCI and GlobColour (Figures 4B, C), whose RMSE values are 0.98 and 0.91 and R^2 values are 0.78 and 0.79, respectively. The low degree of correlation may be because the sampling time of the *in situ* observations does not entirely match that of the satellite data (8 days) despite the gridding before matching up. Though no *in situ* observations were employed in the data processing, the accuracy of the Chla value of this work is not inferior to that of OC-CCI and GlobColour data. Validations with all the matched samples for three individual products were presented in Supplementary Material Figure S1, which also showed that the three products have similar accuracy, despite different matchup samples owing to different spatial coverage.

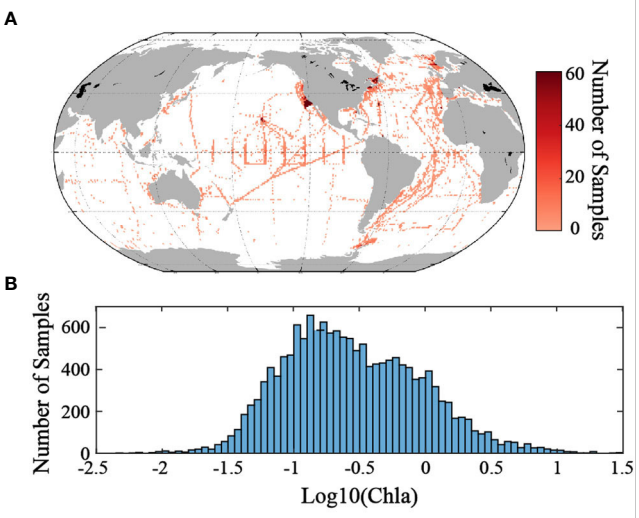


FIGURE 3
(A) Spatial and **(B)** numerical (bar plot) distribution of *in situ* Chla data matched up for the OC-CCI, GlobColour, and our merged products (15,599 in total); (Units of Chla: μg/L.).

3.2 Trend validation by using the original sensor sequence

This work is oriented toward producing a set of global satellite-derived Chla products with high reliability on the long-time-series trend analysis. Under the assumption that single sensors can be used as a benchmark time series as the trends they capture are the actual variability of Chla, the dataset we produce should be able to reproduce the trend patterns obtained by single-mission records over their respective periods. Mélin et al. (2017) proposed a protocol to assess the fitness of OC-CCI Chla data (version 3.0) using contingency matrices, Cohen's κ index, and the differences (and their distributions) between trend slopes. Contingency matrices were used to compare the trends (expressed in terms of significant increase, significant decrease, and not significant) associated with two satellite products. Cohen's κ index is used to quantify the magnitude of the agreement between two diagnostics (Cohen, 1960; Viera and Garrett, 2005; Warrens, 2011); the more κ value close to 1, the more consistent two diagnostics are. Here we apply the main principle of this protocol suggested by Mélin et al. (2017) to assess our dataset by comparing it with single sensor records.

3.2.1 Comparison with SeaWiFS for September 1997 to December 2007

The contingency matrix comparing trends derived by SeaWiFS and this study over the overlapping period (September 1997 to December 2007) is presented in Table 1. The diagnostics agree; that is, the slopes of linear regression *S* of both sequences are concurrently greater than 0 (Chla increase), less than 0 (Chla decrease), or not significant for >91.91% of the ocean over which the trend diagnostics apply (with 66.29% associated with nonsignificant trends and 25.62% associated with significant trends). Contradictory diagnostics characterize only 8.09% of the domain, and the worst case, in which significant trends for both products have opposite signs, almost never occurs (being found in only two pixels). The same comparisons were conducted on OC-CCI and GlobColour products (Table 1); 80.97% and 82.16% of the areas exhibit consistent diagnostics, respectively, both of which are ~10% lower than that in this study. The κ values of three products were 0.82, 0.59, and 0.63, respectively.

In addition to the consistency of diagnostics, the value of Chla trends was also validated. Figures 5A–C show the pixel-by-pixel comparison between the rate of change derived from SeaWiFS and that of the three merged products. It can be seen that the rate of change found in this study is most consistent with that of SeaWiFS at the pixel level (Figure 5A), with R^2 = 0.93 and RMSE = 0.008. The numerical distribution of the rate of change from OC-CCI is relatively discrete (Figure 5B), with R^2 = 0.20 and RMSE = 0.034, and the absolute value of which is underestimated compared with that of SeaWiFS. The rate of change of GlobColour is concentrated around 0, and the increasing trend is significantly underestimated (R^2 = 0.30 and RMSE = 0.024, Figure 5C).

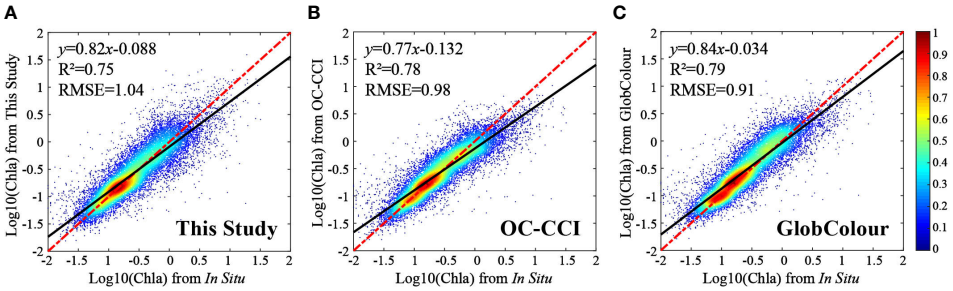


FIGURE 4
Comparison of *in situ* Chla data with the corresponding 8-day and merged satellite data from **(A)** this study, **(B)** OC-CCI, and **(C)** GlobColour. The color scale indicates the data density in pixels, the black lines are the linear fitting of *in situ* and satellite data, and the red dotted lines represent 1:1. Log10 (Chla) was used in the computation of the fitted equation and R^2. Chla was used in the computation of RMSE. (Units of Chla: μg/L.).

TABLE 1 Contingency matrices comparing trend analysis outcomes for SeaWiFS period.

(%)	This study			OC-CCI			GlobColour		
SeaWiFS	n.s.	$S^* \geq 0$	$S^* < 0$	n.s.	$S^* \geq 0$	$S^* < 0$	n.s.	$S^* \geq 0$	$S^* < 0$
n.s.	**66.29**	2.02	1.26	**60.31**	3.38	6.13	**59.47**	6.32	4.03
$S^* \geq 0$	3.76	**15.12**	0.00	8.20	**10.49**	0.01	5.01	**13.65**	0.04
$S^* < 0$	1.05	0.00	**10.50**	1.30	0.00	**10.17**	2.44	0.00	**9.04**

SeaWiFS and merged products are compared over September 1997 to December 2007. Percentage values quantify the number of pixels where the diagnostics on the trend slopes (S) apply. $S^* \geq 0$ denotes significant ($p < 0.05$) increasing trend; $S^* < 0$ indicates significant decreasing trend; n.s. stands for nonsignificant. The bold font emphasizes that the diagnostics from the two sequences agree.

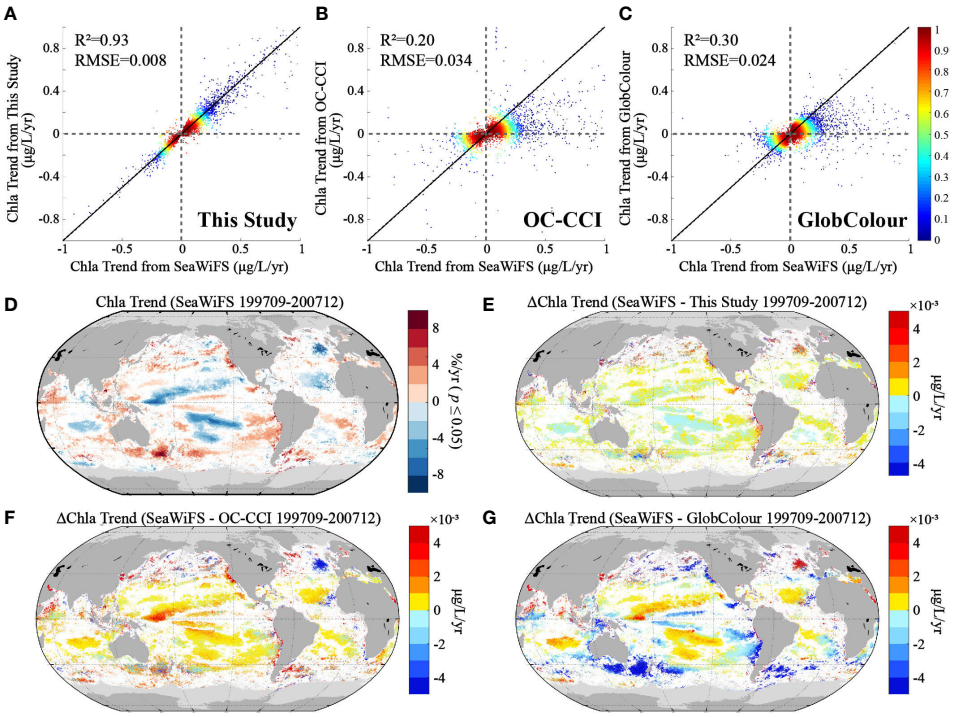


FIGURE 5
(A–C) Scatter plots of pixel-by-pixel Chla trends comparison between SeaWiFS and the three merged datasets from September 1997 to December 2007. **(D)** Chla trend maps in units of %/yr from SeaWiFS for September 1997 to December 2007. **(E–G)** Chla trends from SeaWiFS minus that from the three merged datasets in units of μg/L/yr. Black lines on the scatter plots represent the 1:1 line, and the color scale indicates the data density in pixels. The light gray on the maps represents insufficient data for making a trend calculation (i.e., the number of valid data collected in the statistical period (62 months) does not reach 50%), and the white color indicates that the SeaWiFS data show that the pixel has not changed significantly ($p < 0.05$).

The global distribution of ocean Chla variation from September 1997 to December 2007 derived from the SeaWiFS record is shown in Figure 5D. The regions with significant increases of Chla are mainly located in the Northwest Pacific, the edge of the South Pacific Basin, the South Atlantic, and the western North Indian Ocean, and the regions with decreases are concentrated in the North Atlantic, the center of the South Pacific Basin, the subtropical North Pacific, and the eastern Indian Ocean (Figure 5D). The spatial distributions of the differences between the rates of change from the SeaWiFS record and that of the merged products are shown in Figures 5E–G. The trends generated from this study are more consistent with that of the SeaWiFS record, with the differences ranging within $\pm 2 \times 10^{-3}$ μg/L/yr and slightly underestimating the growth rate in the mid and high latitudes of the northern hemisphere, the Arabian Sea, and the west coast of South America (Figure 5E). However, OC-CCI records in this period exhibit a noticeable disagreement, with the difference being generally positive. Specifically, the decreasing trends of Chla in the Pacific Ocean, Indian Ocean, and North Atlantic oligotrophic basin are overestimated, and the increasing trends in the South Pacific Basin, Arabian Sea, and coastal oceans are underestimated (Figure 5F). GlobColour underestimates the increasing trends of the Southern Ocean and along the margin of the Pacific and the decreasing trends of the oligotrophic basin to a great extent ($>4 \times 10^{-3}$ μg/L/yr, Figure 5G).

3.2.2 Comparison with MERIS for May 2002 to March 2012

Validations of the trend diagnosis, value, and distribution of trend differences were conducted by taking the MERIS record as a benchmark over the period of May 2002 to March 2012 similarly. As Table 2 indicates, the slopes of our product agree with the MERIS record for 85.94% of the ocean, representing the most incredible consistency among the three products. The portion is 11.05% and 5.68% higher than that of OC-CCI and GlobColour. The κ values of the three products were 0.70, 0.50, and 0.59, respectively, also indicating that our product has the highest agreement in trend diagnosis with MERIS.

As to the value of the trend, the trend from our product is the most consistent with the MERIS sequence, with the highest R^2 and lowest RMSE (Figure 6A). The slopes of the other two products have significant systematic bias and are concentrated near 0 (Figures 6B, C).

The trend map for the MERIS record (Figure 6D) shows that Chla increased dramatically at a rate of 5%–10%/yr in the low-latitude basin of the Pacific Ocean while decreasing in the western Indian Ocean and mid-latitude basins in the Pacific and Indian oceans by 5%–8%/yr throughout May 2002 to March 2012. Trends generated from this study have minor differences from that of the MERIS record, ranging mostly within $\pm 2 \times 10^{-3}$ μg/L/yr and underestimating the increasing trend in the mid- to low-latitude basin and the area near 60°S in the eastern Pacific (Figure 6E). Both OC-CCI and GlobColour dramatically overestimated the growing trend by $>3 \times 10^{-3}$ μg/L/yr in the low-latitude basin of the Pacific Ocean compared to the MERIS record (Figures 6F, G). Moreover, GlobColour also overestimated the decreasing trend in the western Indian Ocean.

3.2.3 Comparison with VIIRS for 2012 to 2018

In the case of VIIRS records throughout January 2012 to December 2018 (Table 3), our product and GlobColour have better diagnostic consistency with VIIRS, as the diagnostic trends are consistent in 82.74% and 85.73% of regions and with κ values 0.61 and 0.68 (versus only 74.8% and 0.46 for OC-CCI).

It can be seen that the consistency between our product and VIIRS is better than that for the other two products at the pixel level (Figure 7A). The numerical distribution of the Chla trends from OC-CCI is concentrated (Figure 7B), and, for GlobColour, it is relatively discrete but tends to be negative overall (Figure 7C).

The Chla records from VIIRS exhibit a significant negative trend overall from 2012 to 2018, especially in the Pacific low-latitude basin and the northeast Pacific marginal seas, with declining trends of >10%/yr (Figure 7D). Though our study generally underestimated the declining trend, the difference with VIIRS is slight, primarily within 2×10^{-3} μg/L/yr (Figure 7E). OC-CCI overestimates the decreasing rate in the mid and low latitudes of the Pacific to a large extent, but the rate is similar to that of our product in other regions (Figure 7F). GlobColour exhibits apparent bias, which leads to a significant overestimate of the declining trend worldwide by $>4 \times 10^{-3}$ μg/L/yr (Figure 7G).

Comparison with MODIS is shown in Supplementary Material (Table S1 and Figure S2). Since the MODIS record is used as a baseline in this study, the trends derived from our dataset are much more consistent with that from MODIS than OC-CCI and GlobColour.

4 Discussion

4.1 Global Chla trend

The trends obtained for SeaWiFS (September 1997 to December 2007), MERIS (May 2002 to March 2012), and VIIRS (January 2012 to December 2018) are presented in Figures 5D, 6D, 7D, respectively. It is noticeable that the oligotrophic subtropical gyres in the Pacific

TABLE 2 Contingency matrices comparing trend analysis outcomes for MERIS period.

(%)	This study			OC-CCI			GlobColour		
MERIS	n.s.	$S^* \geq 0$	$S^*<0$	n.s.	$S^* \geq 0$	$S^*< 0$	n.s.	$S^* \geq 0$	$S^*< 0$
n.s.	**62.65**	5.77	2.67	**54.73**	14.25	2.14	**58.71**	6.04	6.36
$S^* \geq 0$	1.15	**10.17**	0.00	0.87	**10.43**	0.00	2.32	**8.98**	0.02
$S^*< 0$	4.47	0.00	**13.12**	7.78	0.06	**9.73**	5.00	0.02	**12.57**

MERIS and merged products are compared over May 2002 to March 2012. Percentage values quantify the number of pixels where the diagnostics on the trend slopes (S) apply. $S^* \geq 0$ denotes significant ($p< 0.05$) increasing trend; $S^*< 0$ indicates significant decreasing trend; n.s. stands for nonsignificant. The bold font emphasizes that the diagnostics from the two sequences agree.

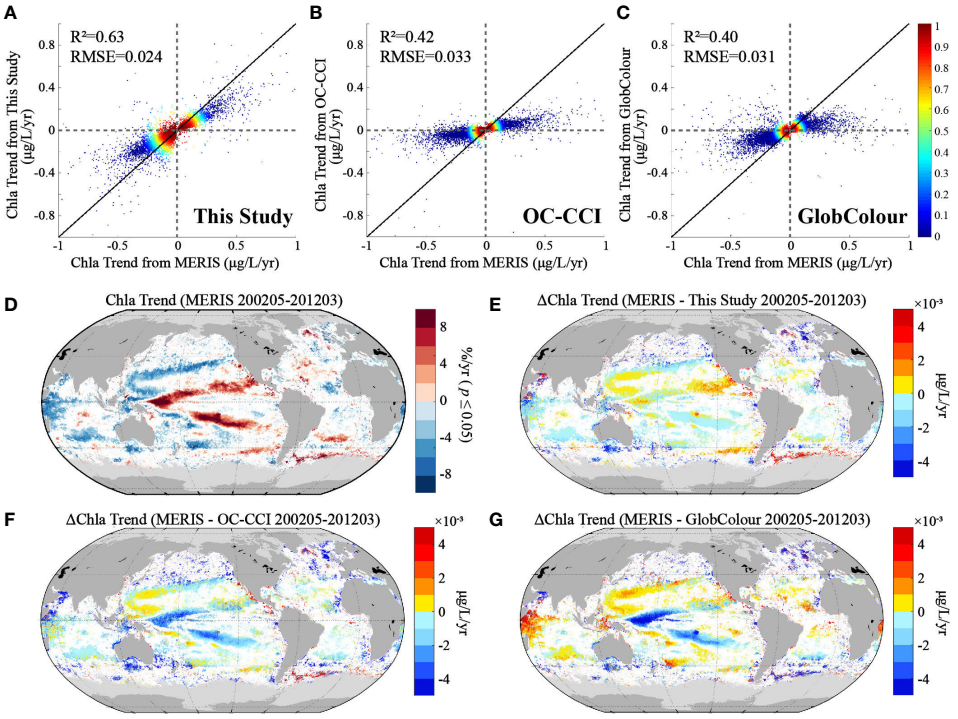


FIGURE 6
Pixel-by-pixel comparison of the Chla rate of change from MERIS and **(A)** this study, **(B)** OC-CCI, and **(C)** GlobColour. **(D)** Chla trend maps in units of %/yr from MERIS for May 2002 to March 2012. **(E–G)** Chla trends from MERIS minus that from the three merged datasets in units of μg/L/yr. Black lines on the scatter plots represent the 1:1 line, and the color scale indicates the data density in pixels. The bright gray on the maps represents insufficient data for estimating a trend (i.e., the number of valid data collected in the statistical period (60 months) does not reach 50%), and white indicates that the MERIS data show that the pixel has not changed significantly ($p < 0.05$).

witnessed significant negative trends from late 1997 to 2007, which was also mentioned in several previous studies (Vantrepotte and Mélin, 2009; Vantrepotte et al., 2011; Vantrepotte and Mélin, 2011). However, these trends were replaced by a positive signal in the following period, as Mélin et al. (2017) reported, and then reverted to a negative trend again. Transformations in trend also occurred in the north temperate Pacific and the western Indian Ocean, where Chla values exhibited an increasing trend before 2008 and then decreased afterward.

Time-series analysis for single sensors is limited to about ten years, while merged products enable trend detection over decades. Here we employed our product to calculate global Chla changes for 23 years (1998–2020, Figure 8A). Significant negative trends (which can reach −1% to −2% per year) are generally observed in the Pacific and Indian oligotrophic gyres. In contrast, significant positive trends are noticed in various regions, including the Southern Ocean, Southeast Pacific, South Atlantic gyres, and isolated patches in the north Arabian Sea and mid to high latitudes of the northern hemisphere.

Figure 8B shows the SST trend during this period. The SST in the Indian Ocean, the Northwest Atlantic, the mid- and low-latitude ocean basin and the northeastern part of the Pacific, including the Bering Sea, increased significantly. The sea area between 45°S–60°S of the Southern Ocean also became warmer. The negative trends in Chla in the subtropical oligotrophic gyres appeared to be consistent with the hypothesis of a more stratified and warming ocean (Doney, 2006). Increasing temperature strengthens the stratification of the upper ocean, which hinders the nutrient supply from the subsurface to the upper layer, thereby limiting phytoplankton growth and decreasing Chla (Behrenfeld et al., 2006; Irwin and Oliver, 2009; Behrenfeld et al., 2016). However, the increasing temperature in the middle to high latitudes could promote phytoplankton growth by becoming closer to the optimum growing temperature for some phytoplankton species

TABLE 3 Contingency matrices comparing trend analysis outcomes for VIIRS period.

(%)	This study			OC-CCI			GlobColour		
VIIRS	n.s.	$S^* \geq 0$	$S^* < 0$	n.s.	$S^* \geq 0$	$S^* < 0$	n.s.	$S^* \geq 0$	$S^* < 0$
n.s.	**63.64**	6.74	0.54	**57.95**	11.85	1.12	**63.43**	1.35	6.10
$S^* \geq 0$	0.46	**4.08**	0.00	0.46	**4.07**	0.00	2.21	**2.32**	0.00
$S^* < 0$	9.42	0.00	**15.12**	11.62	0.02	**12.91**	4.30	0.00	**20.29**

VIIRS and merged products are compared over January 2012 to December 2018. Percentage values quantify the number of pixels where the diagnostics on the trend slopes (S) apply. $S^* \geq 0$ denotes significant ($p < 0.05$) increasing trend; $S^* < 0$ indicates significant decreasing trend; n.s. stands for nonsignificant. The bold font emphasizes that the diagnostics from the two sequences agree.

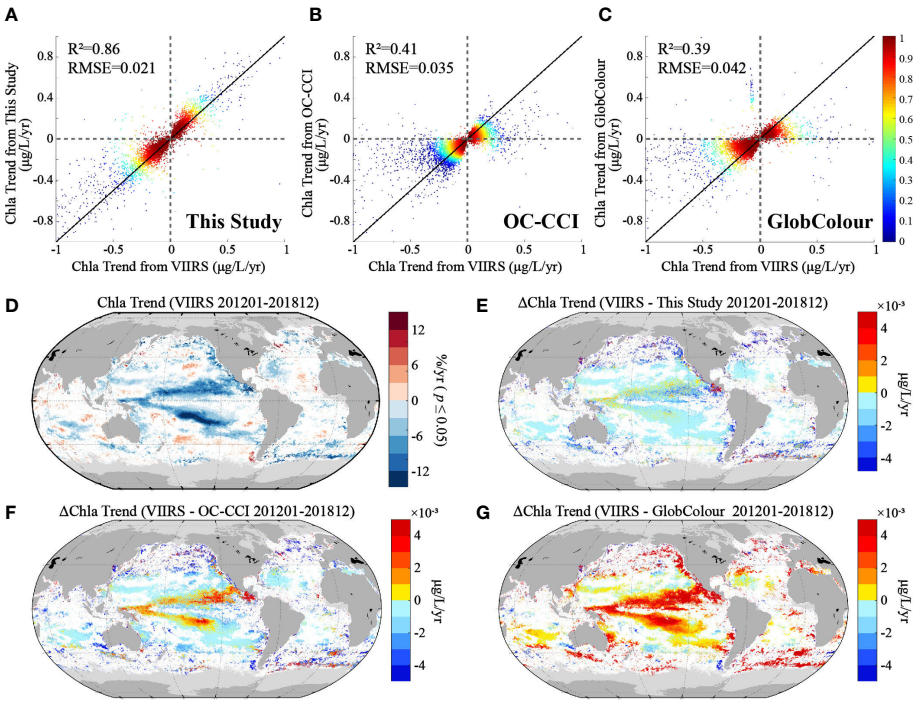


FIGURE 7
Pixel-by-pixel comparison of the Chla rate of change from VIIRS and **(A)** this study, **(B)** OC-CCI, and **(C)** GlobColour. **(D)** Chla trend maps in units of %/yr from VIIRS for January 2012 to December 2018. **(E–G)** Chla trends from VIIRS minus that from the three merged datasets in units of μg/L/yr. Black lines on the scatter plots represent the 1:1 line, and the color scale indicates the data density in pixels. The bright gray on the maps represents insufficient data for trend estimation (i.e., the number of valid data collected in the statistical period (41 months) does not reach 50%), and white indicates that the VIIRS data show that the pixel has not changed significantly ($p < 0.05$). .

(Thomas et al., 2012) and causing poleward shifts of phytoplankton communities at mid to low latitudes (Toggweiler and Russell, 2008; Gregory et al., 2009), thus leading to the increase in Chla here. Moreover, the generally positive trend of Chla in the Southern Ocean is also consistent with the widely reported conclusion that carbon sinks have increased significantly since 2000 (Lavender et al., 2015; DeVries et al., 2019; Gruber et al., 2019; Zhang et al., 2022).

Our product indicates that the global pelagic ocean Chla presented a significant increasing trend over 1998–2020 with a rate of 0.67% ± 0.37%/yr, which is a more positive value than found in a number of previous studies. Using the SeaWiFS record, Vantrepotte and Mélin (2011) found that, over the period 1997–2007, Chla decreased in most of the global ocean; our results from SeaWiFS original series are consistent with these findings (Figure 5D). Saulquin et al. (2013) reported a low-magnitude positive trend (2.83×10^{-4} μg/L/yr) in global Chla over September 1997 to April 2012 using combined data from SeaWiFS and MERIS. However, Hammond et al. (2017) calculated that the trend of marine Chla from September 1997 to December 2013 was −0.023% ± 0.12%/yr using the Bayesian hierarchical spatiotemporal model and the OC-CCI dataset. They further reported a global average weighted trend of 0.08 ± 0.35%/yr over the period 1997–2018 with prior information provided by the Coupled Model Intercomparison Project phase 5 output (Hammond et al., 2020). It is reasonable to get different trends when various periods and datasets are analyzed.

The global data were further divided into 12 regions (Figure 8E) according to Gregg and Rousseaux (2014) to quantify the Chla trend. Significant declines are observed in the North Central Atlantic and equatorial Atlantic, whereas, in the South Indian and South Atlantic oceans, Chla increases by 0.5%/yr. The downward trend in the North Atlantic was earlier mentioned by Gregg and Rousseaux (2014), who integrated SeaWiFS and MODIS records from 1998 to 2012 and reported that the rate of decline was 1.1%/yr. The rate of the decreasing trend we calculated for the North and Central Atlantic is much lower, being 0.46% ± 0.42%/yr. The differences could be attributed to the different datasets and the eight-year longer data span we used. The decline in the equatorial Atlantic (0.45% ± 0.17%/yr) is consistent with the result of Hammond et al. (2018), who, using the OC-CCI record, suggested that Chla in the Eastern Tropical Atlantic decreased by ~0.7%/yr from 1998 to 2016. The increased Chla in the South Indian and South Atlantic oceans may be associated with relatively stable temperature (Figure 8B) and stratification, as well as atmospheric soluble iron deposition enhancement (Hamilton et al., 2020).

In addition, it is worth noting that, from the trend map, many of the pixels in the North Pacific, North Atlantic, North Indian, and Antarctic oceans exhibit a significant increasing trend, but not from the perspective of the regional statistics. One possible reason for this difference is that, during data processing, we first calculate the regional average value of each month, and then we calculate its linear trend. The increasing signal may be interfered with or masked when the pixels that significantly declined and nonsignificantly changed (which also account for a considerable proportion) were also included in regional averaging. Another possible cause is the different data coverage before and after 2002 (Gregg and Casey, 2007). Before 2002, the spatial coverage of the merged data was relatively

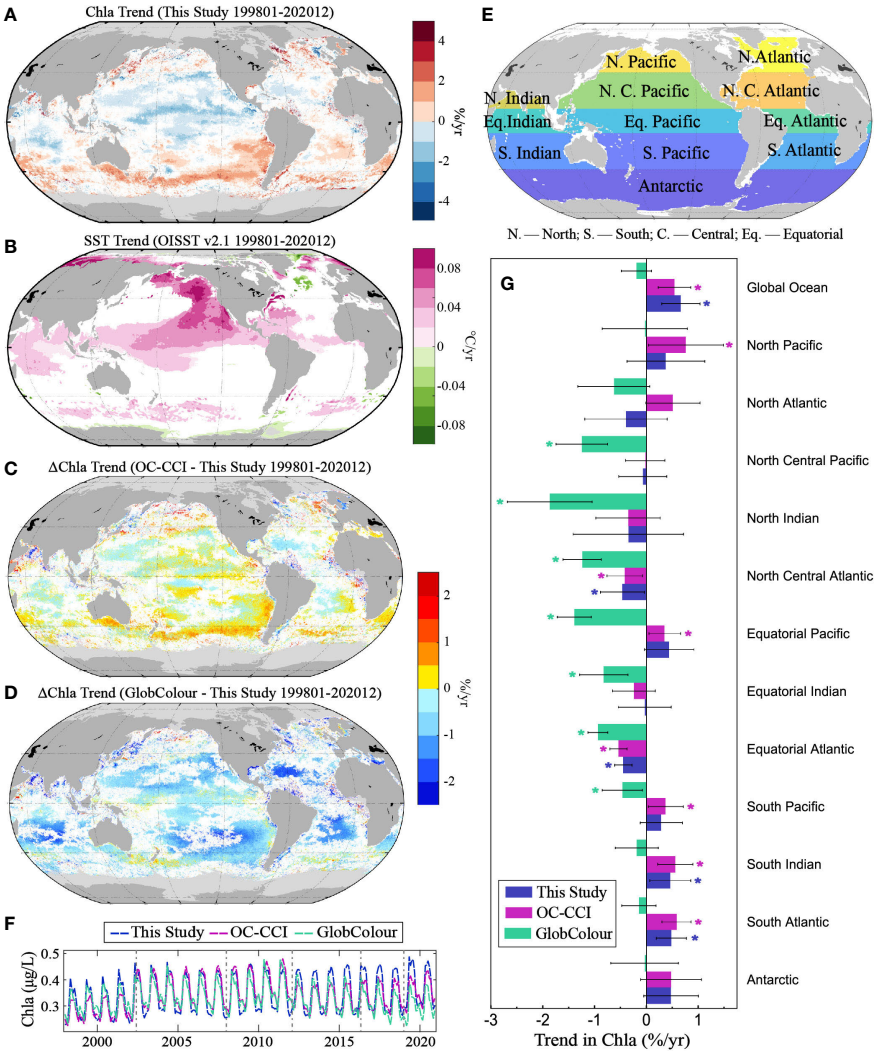


FIGURE 8
(A) Chla trend map derived from this study and **(B)** SST trend map from 1998 to 2020. **(C, D)** Trend differences between OC-CCI and GlobColour and that from this study in units of %/yr. **(E)** Basin definitions for the trend analysis (Gregg and Rousseaux, 2014), **(F)** time series curve of global Chla, and **(G)** Chla trends in global oceans and 14 basins from the three merged datasets. The light gray on the maps represents insufficient data from our dataset for making a trend calculation (i.e., the number of valid data collected in the statistical period (138 months) does not reach 50%), and white indicates that the pixel trend is insignificant ($p > 0.05$) according to our dataset. For **(G)**, the bar with an asterisk (*) marked indicates that the trend is significant ($p < 0.05$); error bars show 95% credible intervals of the rate of change.

insufficient as only SeaWiFS was in orbit, while at least two sets of satellite data were available at the same time after 2002, especially the introduction of MERIS and the processing of MERIS data with POLYMER (Steinmetz et al., 2011; van Oostende et al., 2022), improved the spatial coverage of the data considerably, especially in high latitudes, the intertropical convergence zone, and highly productive coastal regions. The data before 2002 may not represent the whole region with insufficient coverage, thus misleading the trend calculation. This problem exists in basically all multimission ocean-color datasets. However, (van Oostende et al., 2022) applied the temporal gap detection method (TGDM) to the OC-CCI record to homogenize the observations per pixel of the time series, which may be worth attempting to avoid artifacts trends in long-term analysis when significant coverage differences exist in the interested regions.

4.2 Trend difference between merged Chla datasets

Many studies on the trend of the Chla long-time series use the products from OC-CCI and GlobColour (Chen et al., 2014; Racault et al., 2015; Hammond et al., 2017; Sravanthi et al., 2017; Gbagir and Colpaert, 2020; Hammond et al., 2020; Moradi, 2021; Guo et al., 2022). Mélin et al. (2017) assessed the fitness for time-series analysis of OC-CCI Chla data (version 3, 1998–2015) and stated that the OC-CCI data had a remarkable agreement with single-mission products. However, it should not be taken for granted, as the results have evolved with the OC-CCI dataset versions (Mélin et al., 2017). Hammond et al. (2018) assessed the presence of discontinuities in both the OC-CCI dataset (version 3.1) and the GlobColour dataset

from September 1997 to December 2016 and found their effect in most regions worldwide, which leads to a corresponding difference in trend estimates, with a maximum difference of 2.9%/yr, and can even change the direction of trends.

In Section 3.2, we verified that our merged product has acceptable accuracy of the Chla value and fits to long-term Chla trend analysis and climate change related studies better than OC-CCI and GlobColour products as it is more consistent with the single-satellite sequence in the aspect of trend diagnosis. Figures 8C, D show the difference between the Chla variation rate calculated in this study and that of the two published merge products from 1998 to 2020. OC-CCI may overestimate the rising rate by 0.5%–1% per year in the Southern Ocean and Southeast Pacific, lose sight of the increase in the northwest Arabian Sea, and underrate the rising observed along the Northwest Pacific margin. GlobColour, however, shows an overall negative pattern, that is, an overstated downward trend over the Pacific and Indian oligotrophic gyres, an underestimated increasing rate at the North Atlantic high latitudes, Southern Ocean, and Southeast Pacific, and even a misdiagnosed growing trend in the north Arabian Sea and South Atlantic.

The global ocean Chla trend from OC-CCI is similar to that from our product, with a rising rate of 0.54% ± 0.31%/yr, while the trend from GlobColour indicates that it had not changed significantly (Figure 8G). The noticeable discontinuity can be captured from the global time-series Chla curve (Figure 8F) of OC-CCI and GlobColour with systematical high values over 2002–2012 resulting from the introduction of MERIS and the utilize of POLYMER to MERIS data (Steinmetz et al., 2011; van Oostende et al., 2022). In addition, GlobColour also has an obvious systematic low value after 2017. In terms of regional statistics, OC-CCI exhibits the same trends in regions where significant trends occurred according to our dataset, with slight differences in the rate of change (~0.1%/yr). It also indicates that Chla increased in the North, equatorial, and South Pacific oceans while there was no significant trend detected from our dataset. GlobColour exhibits overwhelming negative trends in most regions (7 out of 12) besides high latitudes, with no positive trend found. It should be noted that the decreasing trend revealed by GlobColour in the North Central, equatorial, and South Pacific oceans and the North and equatorial Indian oceans was not found in OC-CCI nor in our product. In general, the Chla trend generated from OC-CCI is closer to that from our products compared with GlobColor because the OC-CCI dataset has been corrected for Rrs bias (Lavender et al., 2015), while the GlobColour data are not explicitly bias-corrected but are instead merged by inversion with a bio-optical model (Maritorena et al., 2010).

5 Conclusions and implications

To better detect the long-term trend of sea surface Chla, we corrected and merged multi-sensor Chla data and produced a set of satellite-derived Chla products from September 1997 to 2020. Our product has similar accuracy to that of OC-CCI and GlobColour products in terms of Chla value, as has been validated by the *in situ* data. Moreover, the dataset has great potential to be used in climatology studies as it has excellent accuracy in Chla trends that is generally more consistent with single-mission records than OC-CCI and GlobColour products. Based on this dataset, we illustrated the linear trend of Chla and its distribution in various regions around the world over 23 years. The difference among trends estimated using the three merged products was also analyzed to provide a reliable Chla trend and stated that caution should be exercised when using existing merged products to calculate long-term trends.

Though the method we employed to correct bias between sensors is straightforward, we have performed a series of validations to prove the fitness of the dataset in long-term ecological research. Our method is an efficient operation and is easy to apply and extend. We used MODIS records as the benchmark, but, in the future, with the launch of new satellites and the continuous accumulation of Chla data, this method can be used to build new datasets quickly. It can also be extended to other missions and parameters such as SST, kd490, and Rrs from multiple missions. However, it should be stated that the method itself tends more toward mathematics and statistics and barely involves remote-sensing mechanisms. We have also assumed that the bias between sensors does not change with the aging of sensors during the overlap period. Although we have performed quality control for single-sensor data, in theory, though limited, the aging of sensors may impact the correction effect.

The key objective of this study is to create a new dataset for better trend detection and provide a reliable trend map of Chla in the past 23 years, and we have corrected the potential misunderstanding of global Chla changes generated by the OC-CCI and GlobColour datasets. Our data have been shared on Zenodo (https://doi.org/10.5281/zenodo.7092220). We hope our work can offer the community a reliable dataset to conduct Chla trends analysis globally and on different systems, provide a methodology reference for developing future ocean-color CDR and ECV products, and thus contribute to understanding the long-term trend of phytoplankton under climate change.

Data availability statement

The datasets presented in this study can be found in online repositories. The names of the repository/repositories and accession number(s) can be found below: https://doi.org/10.5281/zenodo.7092220.

Author contributions

SY: Methodology, Visualization, Writing – original draft. YB and XH: Resources; Writing - Review & Editing. FG: Writing - Review & Editing; English writing improving. TL: Methodology; Writing - Review & Editing. All authors contributed to the article and approved the submitted version.

Funding

This study was supported by the National Natural Science Foundation of China (Grants #41825014, #42176177, and# 42141001), the National Key Research and Development Program of China (Grant #2017YFA0603003) and Zhejiang Provincial Natural Science Foundation of China (2017R52001 and LR18D060001).

Acknowledgments

We thank NASA's Ocean Biology Processing Group (OBPG) and Ocean Color website (https://oceancolor.gsfc.nasa.gov/. Accessed on 17 December 2021) for providing the level-3 gridded chlorophyll concentration data derived from SeaWiFS, MODIS/Aqua, and VIIRS/SNPP. We thank ESA's GlobColor Project (https://hermes.acri.fr/. Accessed on 29 December 2021) for providing the level-3 gridded chlorophyll concentration data derived from MERIS and OLCI/Sentinel-3A and merged chlorophyll concentration dataset. We thank ESA's Ocean Colour Climate Change Initiative (OC-CCI) and the climate office (https://climate.esa.int/en/projects/ocean-colour/. Accessed on 23 December 2021) for providing the merged chlorophyll concentration dataset. We thank National Oceanic and Atmospheric Administration's Group for High-Resolution Sea Surface Temperature (https://www.ghrsst.org/. Accessed on 10 March 2022) for providing the AVHRR_OI (optimal interpolation) sea surface temperature dataset. We thank China's State Key Laboratory of Satellite Ocean Environment Dynamics(SOED), Second Institution of Oceanography(SIO), Ministry of Natural Resources (MNR) satellite ground station, satellite data processing and sharing center, and the marine satellite data online analysis platform (SatCO2) for their help with data collection and processing. Special thanks are given to the editor and the two reviewers for their useful comments and constructive suggestions.

Conflict of interest

The authors declare that the research was conducted in the absence of any commercial or financial relationships that could be construed as a potential conflict of interest.

Publisher's note

All claims expressed in this article are solely those of the authors and do not necessarily represent those of their affiliated organizations, or those of the publisher, the editors and the reviewers. Any product that may be evaluated in this article, or claim that may be made by its manufacturer, is not guaranteed or endorsed by the publisher.

Supplementary material

The Supplementary Material for this article can be found online at: https://www.frontiersin.org/articles/10.3389/fmars.2023.1051619/full#supplementary-material

References

Behrenfeld, M. J., O'Malley, R. T., Boss, E. S., Westberry, T. K., Graff, J. R., Halsey, K. H., et al. (2016). Revaluating ocean warming impacts on global phytoplankton. *Nat. Climate Change* 6 (3), 323–330. doi: 10.1038/nclimate2838

Behrenfeld, M. J., O'Malley, R. T., Siegel, D. A., McClain, C. R., Sarmiento, J. L., Feldman, G. C., et al. (2006). Climate-driven trends in contemporary ocean productivity. *Nature* 444 (7120), 752–755. doi: 10.1038/nature05317

Bojinski, S., Verstraete, M., Peterson, T. C., Richter, C., Simmons, A., and Zemp, M. (2014). The concept of essential climate variables in support of climate research, applications, and policy. *Bull. Am. Meteorological Soc.* 95 (9), 1431–1443. doi: 10.1175/BAMS-D-13-00047.1

Cao, C., Xiong, J., Blonski, S., Liu, Q., Uprety, S., Shao, X., et al. (2013). Suomi NPP VIIRS sensor data record verification, validation, and long-term performance monitoring. *J. Geophysical Research: Atmospheres* 118 (20), 11,664–611,678. doi: 10.1002/2013JD020418

Chavez, F. P., Messié, M., and Pennington, J. T. (2011). Marine primary production in relation to climate variability and change. *Annu. Rev. Mar. Sci.* 3, 227–260. doi: 10.1146/annurev.marine.010908.163917

Chen, X., Pan, D., Bai, Y., He, X., and Wang, T. (2014). Are the trends in the surface chlorophyll opposite between the south China Sea and the bay of Bengal? *Remote Sens. Ocean Sea Ice Coast. Waters Large Water Regions* 9240, 270–277. doi: 10.1117/12.2067584

Cohen, J.. (1960). A coefficient of agreement for nominal scales. *Educ. Psychol. Meas* 20 (1), 37–46. doi: 10.1177/001316446002000104

Collins, M., An, S.-I., Cai, W., Ganachaud, A., Guilyardi, E., Jin, F.-F., et al. (2010). The impact of global warming on the tropical pacific ocean and El niño. *Nat. Geosci.* 3 (6), 391–397. doi: 10.1038/ngeo868

DeVries, T., Le Quéré, C., Andrews, O., Berthet, S., Hauck, J., Ilyina, T., et al. (2019). Decadal trends in the ocean carbon sink. *Proc. Natl. Acad. Sci.* 116 (24), 11646–11651. doi: 10.1073/pnas.1900371116

Doney, S. C. (2006). Plankton in a warmer world. *Nature* 444 (7120), 695–696. doi: 10.1038/444695a

Eplee, R. E., Meister, G., Patt, F. S., Barnes, R. A., Bailey, S. W., Franz, B. A., et al. (2012). On-orbit calibration of SeaWiFS. *Appl. Optics* 51 (36), 8702–8730. doi: 10.1364/AO.51.008702

Eplee, R. E., Turpie, K. R., Meister, G., Patt, F. S., Franz, B. A., and Bailey, S. W. (2015). On-orbit calibration of the suomi national polar-orbiting partnership visible infrared imaging radiometer suite for ocean color applications. *Appl. Optics* 54 (8), 1984–2006. doi: 10.1364/AO.54.001984

Field, C. B., Behrenfeld, M. J., Randerson, J. T., and Falkowski, P. (1998). Primary production of the biosphere: Integrating terrestrial and oceanic components. *Science* 281 (5374), 237–240. doi: 10.1126/science.281.5374.237

Ford, D., and Barciela, R. (2017). Global marine biogeochemical reanalyses assimilating two different sets of merged ocean colour products. *Remote Sens. Environ.* 203, 40–54. doi: 10.1016/j.rse.2017.03.040

Gbagir, A.-M. G., and Colpaert, A. (2020). Assessing the trend of the trophic state of lake ladoga based on multi-year, (1997–2019) CMEMS GlobColour-merged CHL-OC5 satellite observations. *Sensors* 20 (23), 6881. doi: 10.3390/s20236881

GCOS, W. (2011). Systematic observation requirements for satellite-based data products for climate–2011 update. Geneva Switzerland: GCOS WMO. https://library.wmo.int/doc_num.php?explnum_id=3710

Gregg, W. W., and Casey, N. W. (2007). Sampling biases in MODIS and SeaWiFS ocean chlorophyll data. *Remote Sens. Environ.* 111 (1), 25–35. doi: 10.1016/j.rse.2007.03.008

Gregg, W. W., and Rousseaux, C. S. (2014). Decadal trends in global pelagic ocean chlorophyll: A new assessment integrating multiple satellites, *in situ* data, and models. *J. Geophys Res. Oceans* 119 (9), 5921–5933. doi: 10.1002/2014JC010158

Gregg, W. W., and Woodward, R. H. (1998). Improvements in coverage frequency of ocean color: Combining data from SeaWiFS and MODIS. *IEEE Trans. Geosci. Remote Sens.* 36 (4), 1350–1353. doi: 10.1109/36.701084

Gregory, B., Christophe, L., and Martin, E. (2009). Rapid biogeographical plankton shifts in the north Atlantic ocean. *Global Change Biol.* 15 (7), 1790–1803. doi: 10.1111/j.1365-2486.2009.01848.x

Gruber, N., Landschützer, P., and Lovenduski, N. S. (2019). The variable southern ocean carbon sink. *Annu. Rev. Mar. Sci.* 11, 159–186. doi: 10.1146/annurev-marine-121916-063407

Guo, J., Lu, J., Zhang, Y., Zhou, C., Zhang, S., Wang, D., et al. (2022). Variability of chlorophyll-a and secchi disk depth, (1997–2019) in the bohai Sea based on monthly cloud-free satellite data reconstructions. *Remote Sens.* 14 (3), 639. doi: 10.3390/rs14030639

Hamilton, D. S., Moore, J. K., Arneth, A., Bond, T. C., Carslaw, K. S., Hantson, S., et al. (2020). Impact of changes to the atmospheric soluble iron deposition flux on ocean biogeochemical cycles in the anthropocene. *Global Biogeochemical Cycles* 34 (3), e2019GB006448. doi: 10.1029/2019GB006448

Hammond, M. L., Beaulieu, C., Henson, S. A., and Sahu, S. K. (2018). Assessing the presence of discontinuities in the ocean color satellite record and their effects on

chlorophyll trends and their uncertainties. *Geophysical Res. Lett.* 45 (15), 7654–7662. doi: 10.1029/2017GL076928

Hammond, M. L., Beaulieu, C., Henson, S. A., and Sahu, S. K. (2020). Regional surface chlorophyll trends and uncertainties in the global ocean. *Sci. Rep.* 10 (1), 1–9. doi: 10.1038/s41598-020-72073-9

Hammond, M. L., Beaulieu, C., Sahu, S. K., and Henson, S. A. (2017). Assessing trends and uncertainties in satellite-era ocean chlorophyll using space-time modeling. *Global Biogeochemical Cycles* 31 (7), 1103–1117. doi: 10.1002/2016GB005600

Henson, S. A., Sarmiento, J. L., Dunne, J. P., Bopp, L., Lima, I., Doney, S. C., et al. (2010). Detection of anthropogenic climate change in satellite records of ocean chlorophyll and productivity. *Biogeosciences* 7 (2), 621–640. doi: 10.5194/bg-7-621-2010

IOCCG (2007). Ocean-Colour Data Merging W. Gregg (ed.) *Reports of the International Ocean-Colour Coordinating Group, No. 6*, Dartmouth, Canada: IOCCG. http://ioccg.org/wp-content/uploads/2015/10/ioccg-report-06.pdf

IOCCG (2013). In-flight Calibration of Satellite Ocean-Colour Sensors. Frouin, R. (ed.), Reports of the International Ocean-Colour Coordinating Group, No. 14. Dartmouth, Canada: IOCCG. Available at: https://ioccg.org/wp-content/uploads/2015/10/ioccg-report-14.pdf..

Irwin, A. J., and Oliver, M. J. (2009). Are ocean deserts getting larger? *Geophysical Res. Lett.* 36 (18), L18609. doi: 10.1029/2009GL039883

Johnson, K. S., Berelson, W. M., Boss, E. S., Chase, Z., Claustre, H., Emerson, S. R., et al. (2009). Observing biogeochemical cycles at global scales with profiling floats and gliders: prospects for a global array. *Oceanography* 22 (3), 216–225. doi: 10.5670/oceanog.2009.81

Kahru, M., Jacox, M. G., Lee, Z., Kudela, R. M., Manzano-Sarabia, M., and Mitchell, B. G. (2015). Optimized multi-satellite merger of primary production estimates in the California current using inherent optical properties. *J. Mar. Syst.* 147, 94–102. doi: 10.1016/j.jmarsys.2014.06.003

Kahru, M., Kudela, R. M., Manzano-Sarabia, M., and Mitchell, B. G. (2012). Trends in the surface chlorophyll of the California current: Merging data from multiple ocean color satellites. *Deep Sea Res. Part II: Topical Stud. Oceanography* 77, 89–98. doi: 10.1016/j.dsr2.2012.04.007

Lavender, S., Jackson, T., and Sathyendranath, S. (2015). The ocean colour climate change initiative. *Ocean Challenge* 21 (1), 3.

Maritorena, S., d'Andon, O. H. F., Mangin, A., and Siegel, D. A. (2010). Merged satellite ocean color data products using a bio-optical model: Characteristics, benefits and issues. *Remote Sens. Environ.* 114 (8), 1791–1804. doi: 10.1016/j.rse.2010.04.002

Maritorena, S., and Siegel, D. A. (2005). Consistent merging of satellite ocean color data sets using a bio-optical model. *Remote Sens. Environ.* 94 (4), 429–440. doi: 10.1016/j.rse.2004.08.014

McClain, C. R. (1998). Science quality SeaWiFS data for global biosphere research. *Sea Technol.* 39, 10–16.

McClain, C. R. (2009). A decade of satellite ocean color observations. *Annu. Rev. Mar. Sci.* 1, 19–42. doi: 10.1146/annurev.marine.010908.163650

McClain, C. R., Feldman, G. C., and Hooker, S. B. (2004). An overview of the SeaWiFS project and strategies for producing a climate research quality global ocean bio-optical time series. *Deep Sea Res. Part II: Topical Stud. Oceanography* 51 (1-3), 5–42. doi: 10.1016/j.dsr2.2003.11.001

Mélin, F. (2016). Impact of inter-mission differences and drifts on chlorophyll-a trend estimates. *Int. J. Remote Sens.* 37 (10), 2233–2251. doi: 10.1080/01431161.2016.1168949

Mélin, F., Vantrepotte, V., Chuprin, A., Grant, M., Jackson, T., and Sathyendranath, S. (2017). Assessing the fitness-for-purpose of satellite multi-mission ocean color climate data records: A protocol applied to OC-CCI chlorophyll-a data. *Remote Sens. Environ.* 203, 139–151. doi: 10.1016/j.rse.2017.03.039

Mélin, F., Zibordi, G., and Djavidnia, S. (2009). Merged series of normalized water leaving radiances obtained from multiple satellite missions for the Mediterranean Sea. *Adv. Space Res.* 43 (3), 423–437. doi: 10.1016/j.asr.2008.04.004

Moradi, M. (2021). Evaluation of merged multi-sensor ocean-color chlorophyll products in the northern Persian gulf. *Continental Shelf Res.* 221, 104415. doi: 10.1016/j.csr.2021.104415

Morel, A., Gentili, B., Chami, M., and Ras, J. (2006). Bio-optical properties of high chlorophyll case 1 waters and of yellow-substance-dominated case 2 waters. *Deep Sea Res. Part I: Oceanographic Res. Papers* 53 (9), 1439–1459. doi: 10.1016/j.dsr.2006.07.007

Muller-Karger, F. E., Kavanaugh, M. T., Montes, E., Balch, W. M., Breitbart, M., Chavez, F. P., et al. (2014). A framework for a marine biodiversity observing network within changing continental shelf seascapes. *Oceanography* 27 (2), 18–23. doi: 10.5670/oceanog.2014.56

O'Reilly, J. E., Maritorena, S., Mitchell, B. G., Siegel, D. A., Carder, K. L., Garver, S. A., et al. (1998). Ocean color chlorophyll algorithms for SeaWiFS. *J. Geophysical Research: Oceans* 103 (C11), 24937–24953. doi: 10.1029/98JC02160

Plummer, S., Lecomte, P., and Doherty, M. (2017). The ESA climate change initiative (CCI): A European contribution to the generation of the global climate observing system. *Remote Sens. Environ.* 203, 2–8. doi: 10.1016/j.rse.2017.07.014

Pottier, C., Garçon, V., Larnicol, G., Sudre, J., Schaeffer, P., and Le Traon, P.-Y. (2006). Merging SeaWiFS and MODIS/Aqua ocean color data in north and equatorial Atlantic using weighted averaging and objective analysis. *IEEE Trans. Geosci. Remote Sens.* 44 (11), 3436–3451. doi: 10.1109/TGRS.2006.878441

Racault, M.-F., Raitsos, D. E., Berumen, M. L., Brewin, R. J., Platt, T., Sathyendranath, S., et al. (2015). Phytoplankton phenology indices in coral reef ecosystems: Application to ocean-color observations in the red Sea. *Remote Sens. Environ.* 160, 222–234. doi: 10.1016/j.rse.2015.01.019

Ryan, J. P., Ueki, I., Chao, Y., Zhang, H., Polito, P. S., and Chavez, F. P. (2006). Western Pacific modulation of large phytoplankton blooms in the central and eastern equatorial pacific. *J. Geophysical Research: Biogeosciences* 111, G02013. doi: 10.1029/2005JG000084

Sathyendranath, S., Brewin, R. J., Brockmann, C., Brotas, V., Calton, B., Chuprin, A., et al. (2019). An ocean-colour time series for use in climate studies: the experience of the ocean-colour climate change initiative (OC-CCI). *Sensors* 19 (19), 4285. doi: 10.3390/s19194285

Sathyendranath, S., Brewin, R. J., Jackson, T., Mélin, F., and Platt, T. (2017). Ocean-colour products for climate-change studies: What are their ideal characteristics? *Remote Sens. Environ.* 203, 125–138. doi: 10.1016/j.rse.2017.04.017

Saulquin, B., Fablet, R., Mangin, A., Mercier, G., Antoine, D., and Fanton d'Andon, O. (2013). Detection of linear trends in multisensor time series in the presence of autocorrelated noise: Application to the chlorophyll-a SeaWiFS and MERIS data sets and extrapolation to the incoming sentinel 3-OLCI mission. *J. Geophysical Research: Oceans* 118 (8), 3752–3763. doi: 10.1002/jgrc.20264

Sravanthi, N., Ali, P. Y., and Narayana, A. (2017). Merging gauge data and models with satellite data from multiple sources to aid the understanding of long-term trends in chlorophyll-a concentrations. *Remote Sens. Lett.* 8 (5), 419–428. doi: 10.1080/2150704X.2016.1278308

Steinmetz, F., Deschamps, P.-Y., and Ramon, D. (2011). Atmospheric correction in presence of sun glint: application to MERIS. *Optics express* 19 (10), 9783–9800. doi: 10.1364/OE.19.009783

Thomas, M. K., Kremer, C. T., Klausmeier, C. A., and Litchman, E. (2012). A global pattern of thermal adaptation in marine phytoplankton. *Science* 338 (6110), 1085–1088. doi: 10.1126/science.1224836

Toggweiler, J. R., and Russell, J. (2008). Ocean circulation in a warming climate. *Nature* 451 (7176), 286–288. doi: 10.1038/nature06590

Valente, A., Sathyendranath, S., Brotas, V., Groom, S., Grant, M., Taberner, M., et al. (2019). A compilation of global bio-optical *in situ* data for ocean-colour satellite applications–version two. *Earth System Sci. Data* 11 (3), 1037–1068. doi: 10.5194/essd-11-1037-2019

van Oostende, M., Hieronymi, M., Krasemann, H., Baschek, B., and Röttgers, R. (2022). Correction of inter-mission inconsistencies in merged ocean colour satellite data. *Front. Remote Sens.* 74. doi: 10.3389/frsen.2022.882418

Vantrepotte, V., Loisel, H., Mériaux, X., Neukermans, G., Dessailly, D., Jamet, C., et al. (2011). Seasonal and inter-annual, (2002-2010) variability of the suspended particulate matter as retrieved from satellite ocean color sensor over the French Guiana coastal waters. *J. Coast. Res.*, Szczecin, Poland: ISSN 1750–1754.

Vantrepotte, V., and Mélin, F. (2009). Temporal variability of 10-year global SeaWiFS time-series of phytoplankton chlorophyll a concentration. *ICES J. Mar. Sci.* 66 (7), 1547–1556. doi: 10.1093/icesjms/fsp107

Vantrepotte, V., and Mélin, F. (2011). Inter-annual variations in the SeaWiFS global chlorophyll a concentration, (1997–2007). *Deep Sea Res. Part I: Oceanographic Res. Papers* 58 (4), 429–441. doi: 10.1016/j.dsr.2011.02.003

Viera, A. J., and Garrett, J. M.. (2005). Understanding interobserver agreement: the kappa statistic. *Family Medicine* 37 (5), 360–363.

Wang, M., and Son, S. (2016). VIIRS-derived chlorophyll-a using the ocean color index method. *Remote Sens. Environ.* 182, 141–149. doi: 10.1016/j.rse.2016.05.001

Warrens, M. J. (2011). Cohen's kappa is a weighted average. *Statistical Methodology* 8 (6), 473–484. doi: 10.1016/j.stamet.2011.06.002

Xiong, X., Sun, J., Xie, X., Barnes, W. L., and Salomonson, V. V. (2009). On-orbit calibration and performance of aqua MODIS reflective solar bands. *IEEE Trans. Geosci. Remote Sens.* 48 (1), 535–546. doi: 10.1109/TGRS.2009.2024307

Zhang, M., Cheng, Y., Bao, Y., Zhao, C., Wang, G., Zhang, Y., et al. (2022). Seasonal to decadal spatiotemporal variations of the global ocean carbon sink. *Global Change Biol.* 28 (5), 1786–1797. doi: 10.1111/gcb.16031

frontiers | Frontiers in Marine Science

TYPE Original Research
PUBLISHED 30 January 2023
DOI 10.3389/fmars.2023.1062413

Check for updates

OPEN ACCESS

EDITED BY
Astrid Bracher,
Alfred Wegener Institute Helmholtz Centre for Polar and Marine Research (AWI), Germany

REVIEWED BY
Heather Bouman,
University of Oxford, United Kingdom
Michael William Lomas,
Bigelow Laboratory for Ocean Sciences, United States

*CORRESPONDENCE
Jørgen Bendtsen
jorgen.bendtsen@sund.ku.dk

SPECIALTY SECTION
This article was submitted to Ocean Observation, a section of the journal Frontiers in Marine Science

RECEIVED 05 October 2022
ACCEPTED 13 January 2023
PUBLISHED 30 January 2023

CITATION
Bendtsen J, Vives CR and Richardson K (2023) Primary production in the North Atlantic estimated from *in situ* water column data observed by Argo floats and remote sensing.
Front. Mar. Sci. 10:1062413.
doi: 10.3389/fmars.2023.1062413

COPYRIGHT
© 2023 Bendtsen, Vives and Richardson. This is an open-access article distributed under the terms of the Creative Commons Attribution License (CC BY). The use, distribution or reproduction in other forums is permitted, provided the original author(s) and the copyright owner(s) are credited and that the original publication in this journal is cited, in accordance with accepted academic practice. No use, distribution or reproduction is permitted which does not comply with these terms.

Primary production in the North Atlantic estimated from *in situ* water column data observed by Argo floats and remote sensing

Jørgen Bendtsen[1]*, Clara R. Vives[2,3] and Katherine Richardson[4]

[1]Section for Geobiology, Globe Institute, University of Copenhagen, Copenhagen, Denmark, [2]Institute for Marine and Antarctic Studies, University of Tasmania, Hobart, TAS, Australia, [3]Australian Research Council Centre of Excellence for Climate Extremes, University of Tasmania, Hobart, TAS, Australia, [4]Center for Macroecology, Evolution and Climate, Globe Institute, University of Copenhagen, Copenhagen, Denmark

Combining information on the vertical distribution of nutrients and remote sensing can potentially improve estimates of ocean primary production (PP). Here, we employ *in situ* observations of chlorophyll *a* and nitrate from biogeochemical Argo floats deployed in the North Atlantic together with remote sensing to estimate PP and compare these results to estimates based on model approaches not including vertically resolved nutrient distributions. Analysis of the float data shows chlorophyll *a* distribution relates closely to both nutricline depth and latitude, and these relationships can be explained by nutrient and light availability. PP estimates based on satellite and Argo-observations also relate to both latitude and nutrient distributions. An analysis of these float-based PP estimates shows that large-scale patterns of total water column PP and associated variability are consistent with expected photosynthetic responses to different combinations of light and nutrient availability. When PP-estimates based solely on surface observations were plotted against light and nutrient fields, significant structural differences emerged compared with estimates that included subsurface observations, in particular in oligotrophic areas and areas with a shallow nutricline. The combination of *in situ* water column observations with remote sensing potentially opens a new phase in the estimation of ocean primary production.

KEYWORDS

primary production, nutrient availability, light availability, nutricline, BGC-Argo floats

1 Introduction

A weakness in estimating ocean primary production (PP) from remotely sensed surface data is that assumptions regarding the vertical distribution of PP are by necessity based on patterns derived from archived water column profiles, usually of chlorophyll distribution. Richardson and Bendtsen (2019) showed that the percentage of water column PP occurring below 10 m exhibits large geographic variability, i.e. ~10-90%, and that this variability can be

related to vertical nutrient distributions. In an ocean changing in response to climate change, the vertical structure of the water column and, as a result, vertical distributions of nutrients are also changing. Thus, the assumption that current vertical distributions of PP are similar to the historical ones becomes a potential source of error in PP estimates based only on the remote sensing of surface ocean characteristics. Here, we employ *in situ* nutrient distributions recorded using BGC-Argo floats in the North Atlantic to estimate PP and compare the results obtained to estimates based on more traditional methods using surface optical characteristics obtained through remote sensing. We find that the estimates based on float data are more consistent with expected photosynthetic response to varying light and nutrient combinations than estimates where *in situ* vertical nutrient distributions are not included.

Current estimates of global ocean primary production (PP) range between 36–67 Pg C yr^{-1} in data-driven models based on satellite observations (Sathyendranath et al., 2020) and between 23-56 Pg C yr^{-1} in mechanistic models implemented in ocean circulation models (Tagliabue et al., 2021). A global oceanic PP of 47 Pg C yr^{-1} was proposed as a representative global value in the latest IPCC report (Gulev et al., 2021), however, this estimate was associated with a low confidence. The relatively large spread between estimates derived using different PP-models reflects conceptual differences in model-architecture as well as different parameterizations of critical parameters for calculating PP (Kulk et al., 2020). Thus, improvement of the global PP-estimate requires both development of the conceptual model design and a better understanding of critical parameters of photosynthetic response to light and nutrients. Bottlenecks for further improvement of these models include the relative paucity of observational data used for estimating PP and a lack of knowledge concerning the distribution of the most important variables for determining PP, i.e., chlorophyll concentration, light/nutrient availability, and photosynthetic response characteristics. Satellite observation of surface optical characteristics cannot provide the information regarding subsurface distributions of chlorophyll and nutrients that is required for validating and improving existing models.

The distribution of chlorophyll is driven by the interplay between photosynthetic growth limited by light and nutrients, mortality due to grazing and microbial loss, and mixing and advection by ocean currents (e.g., Beckmann and Hense, 2007). Nevertheless, the subsurface chlorophyll distribution can, in many cases, be explained by phytoplankton growth and hydrography (Cullen, 1982). Nutrients in the open ocean are supplied to the productive surface waters through mixing with nutrient rich water from deeper in the water column. The degree of mixing varies with local dynamics due to actions from air-sea exchange and mixing by currents. This subsurface supply of nutrients often results in a nutrient depleted surface layer during the growth season and a steep nutricline towards nutrient-rich deeper water at the base of the productive layer. High concentrations of chlorophyll are therefore often associated with the depth of the nutricline where optimal conditions for phytoplankton growth in terms of nutrient availability and light are found (Herbland and Voituriez, 1979; Cullen, 2015).

The close relationship between chlorophyll and nutrient distributions led to the early suggestion that production might simply be estimated from vertical profiles of nutrients (Herbland and Voituriez, 1979). Vertical distributions of nutrients are, however, not routinely included in models estimating marine PP despite it being recognized that only about 25% of global ocean PP takes place in the upper 10 m and that the fraction of subsurface PP increases towards areas with a deep nutricline (Richardson and Bendtsen, 2019). Although general relationships between PP and subsurface nutrient distribution have been known for some time, the temporal and spatial variability in light and nutrient conditions between high and low latitudes, combined with limited *in situ* data for estimation of PP, have made it difficult to discern large-scale geographic patterns in PP based on local relationships between nutrients, light and PP.

The comprehensive data archive with measurements from Biogeochemical (BGC)-Argo floats constitutes a new and continuously updated data source that can supply information on parameters relevant for PP from below the immediate surface in that they collect measurements of biogeochemical variables, e.g., oxygen, chlorophyll *a* and nitrate, from the upper few kilometers of the global ocean (Argo, 2021). Combining these data with optical characteristics of the surface ocean determined by satellite mounted sensors provides a new opportunity for evaluating and optimizing large-scale PP-models against both satellite observations and *in situ* subsurface observations by floats.

In this study, we use subsurface nitrate and chlorophyll *a* fields obtained from the North Atlantic BGC-Argo archive to analyze the relationship between chlorophyll *a* and nutricline depth, and surface light observed from satellites. We apply a depth-resolved PP-model to quantify and analyze the distribution of PP in a diagram spanned by nutricline depth and surface light. We apply the PP-diagram to assess two simple PP-models driven only by surface fields. Finally, we discuss the potential of applying the same approach for evaluating other PP-models driven by observations or implemented in ocean circulation models, and the potential for estimating large-scale distributions of PP.

2 Methods

2.1 BGC-Argo data

For the study, we used data from biogeochemical Argo profiles for the period 2011-2022 in the North Atlantic, including the Mediterranean and subpolar areas, i.e., 0-80°N (Argo, 2000; Bittig et al., 2022). All profiles included nitrate observations were selected *via* the Argo data selection tool (Figure 1). The data set contained pressure, temperature, salinity, chlorophyll *a* (referred to as chlorophyll) and nitrate. A set of quality requirements was defined for each profile such that location and time of transmissions were well defined (i.e., a QC flag of 1 or 8) and the data coverage of pressure, temperature and salinity was at least 75% (i.e., a QC flag of either A or B) of all profile levels with good data (Argo, 2021). Individual quality checks were applied to all measurements (i.e., a QC flag of 1 or 2) and accepted chlorophyll measurements also included adjusted data due to non-photochemical quenching (i.e., a QC flag of 5). An additional set of criteria was applied for removing profiles with insufficient data coverage: the first pressure measurement should be in the upper 10 m and the upper 200 m of each profile should contain a minimum of 20 observations of all the variables applied in the analysis.

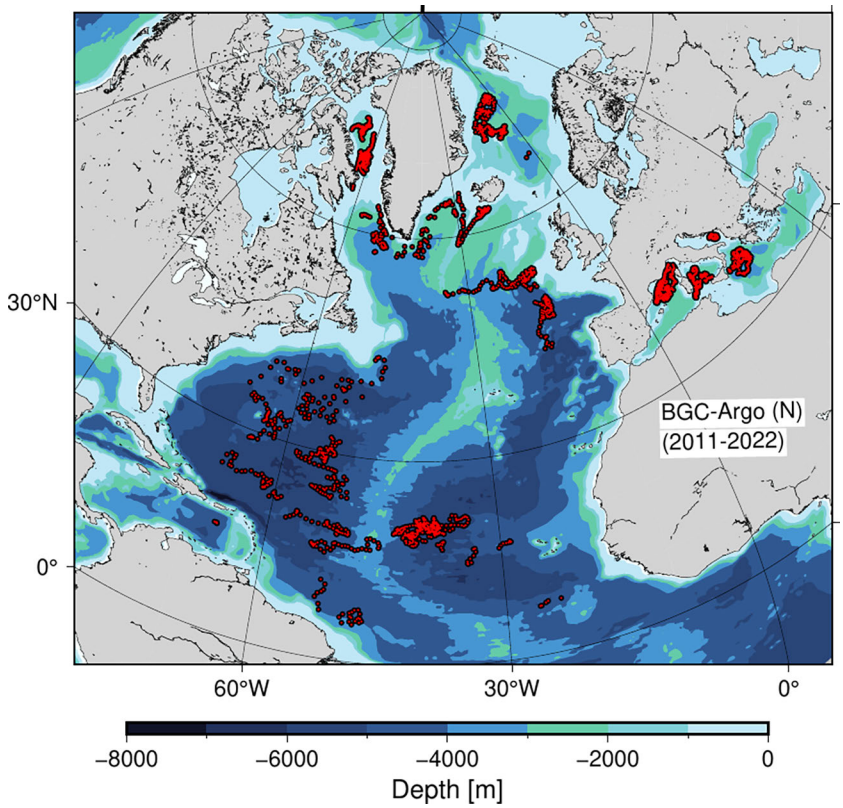


FIGURE 1
BGC-Argo profiles (red bullets) in the North Atlantic containing nitrate profiles (N) between 2011-2022.

In total, 4108 profiles were included in the data set of which 3680 were used for calculating PP and with a seasonal coverage between 707 - 1356 (Table 1). The data had a broad latitudinal distribution with more than 1000 profiles in each of the 20-degree latitude bands between 20-80°N and with a minimum coverage (n=190) in the tropical area between 0-20°N. Each three month period during the year included between 56 - 825 profiles in each 20-degree latitude band except for the tropical region (0-20°N), where the number of profiles ranged between 40-54. In total, 1395 profiles of the entire data set were obtained from the Mediterranean Sea between 35.2 - 43.8°N, and given the general oligotrophic nature of the area (e.g., Siokou-Frangou et al., 2010), these profiles were considered as representative for mid-latitude conditions and included in the analysis. Thus, all seasons and latitude bands were well represented by the data set.

TABLE 1 Temporal and spatial coverage of the BGC-Argo data set used for calculating PP including profiles with nitrate and chlorophyll measurements and associated satellite observations of surface PAR from the North Atlantic, Mediterranean and subpolar seas in the period 2011-2022.

Latitude (°N)	Jan-Mar	Apr-Jun	Jul-Sep	Oct-Dec	Sum
0-20	50	54	46	40	190
20-40	376	314	262	304	1256
40-60	225	330	223	267	1045
60-80	56	71	825	237	1189
Sum	707	769	1356	848	3680

The number of profiles are shown for each three month period and 20 degree latitude band.

2.2 Satellite data

Surface PAR (SPAR) was extracted from MODIS-satellite data binned in 8-day intervals and in 9x9 km resolution (Frouin et al., 1989; NASA Ocean Biology Processing Group, 2017). SPAR for each float was extracted from the corresponding 8-day period in the binned satellite data set that included the date of the profile transmission. Satellite values were extracted from the four center values in the geographical grid surrounding the location of the Argo float and their average value was assumed to represent the conditions at the location of the float. Missing values were disregarded and if all four nearest neighbors to the float were missing, then the SPAR value for the float was not defined. Similarly, sea surface temperature (SST) and surface chlorophyll *a* (Hu et al., 2012) were extracted from the MODIS data for calculating PP-parameters based on satellite derived surface values.

2.3 Analysis of BGC-Argo profiles

Four characteristic depth scales were applied in the analysis of the float profiles: the mixed layer depth (D_{MI}), the depth of the euphotic zone (D_{Eup}), the nutricline depth (D_{Nut}) and the depth of the deep chlorophyll maximum (DCM).

The D_{MI} was defined from a temperature difference of 0.2 °C between 10 m depth and the bottom of the mixed layer (de Boyer Montégut et al., 2004). The mixed layer depth characterizes the upper well mixed surface layer where properties of temperature and salinity are relatively constant.

A constant light attenuation (k_d) for photosynthetic available radiation (PAR) was parameterized from the average chlorophyll concentration in the mixed layer (Morel and Maritorena, 2001; Morel et al., 2007) and the PAR-profile was calculated according to Beer's law: PAR(z) = SPAR exp(k_d z), where *z* is the vertical coordinate (i.e., positive upwards, z ≤ 0). The euphotic depth (D_{Eup}), i.e., the depth range where photosynthesis is assumed to take place, was defined by the depth level where PAR was 0.1% of the surface value (Laws et al., 2014).

The depth of the nutricline (D_{Nut}) characterizes the vertical nutrient profile in relation to the euphotic zone. The nutricline depth was estimated from the nitrate distribution below the surface layer. When nitrate is the limiting nutrient for PP, the nitracline (D_{NO3}) will define D_{Nut}. However, conditions may exist where other nutrients, e.g., silicate (Hátún et al., 2017), iron (Nielsdóttir et al., 2009; Ryan-Keogh et al., 2013), etc., limit PP. Under these circumstances, the nutricline is not related to the nitrate concentration but nitrate will still be consumed in the nitrate-replete surface layer. Therefore, the nitracline below the nitrate-rich surface layer may indicate the depth extent of whatever nutrient(s) is limiting. This appeared possibly to be the case especially with respect to profiles collected at high latitudes, e.g., in the Baffin Bay, where profiles with high nitrate concentrations at the surface exhibited a DCM. In most of these profiles, the depth of the DCM was closely related to a gradient in the nitrate profile. Thus, D_{Nut} was calculated from two criteria: (1) if the surface concentration of nitrate was less than 1 µmole kg^{-1} the nutricline depth was found at the most shallow depth where the nitrate concentration was greater than 1 µmole kg^{-1}, or (2) the vertical gradient of D_{Nut} was a maximum. D_{Nut} was only calculated from profiles with nitrate data above 15 m. The concentration was determined by applying a linear interpolation and the vertical gradient was obtained from the slope of a linear regression of 10 m segments of nitrate.

The DCM was determined by the maximum value of the low-pass filtered (i.e., a 10 m running mean) chlorophyll fluorescence profile. In some areas, the DCM was centered around the depth interval with a significantly elevated chlorophyll concentration and, in those cases, the increased biomass was well-represented by the DCM. However, in some profiles, the DCM was found from a weakly stratified chlorophyll profile in relatively homogeneous mixed layers and, in these profiles, the DCM was not associated with a significant maximum of chlorophyll. This was particularly the case during the fall and winter seasons where chlorophyll variations in the deep mixed layers were relatively small. This was taken into account in the analysis. Here, the DCM is used for expressing the depth of the "deep" chlorophyll maximum. However, in many cases the maximum is located near or at the surface, in particular outside the growth season or in well mixed areas. Thus, we refer to the DCM also in such profiles, as a general term expressing the maximum chlorophyll concentration.

Profiles were also analyzed with respect to the vertically integrated chlorophyll (ΣChl, in units of mg chl m^{-2}) integrated from D_{Eup} to the surface. The Argo profiles were analyzed in four latitudinal bands, i.e., 0-20, 20-40, 40-60 and 60-80°N, which are referred to as the tropical, subtropical, mid-latitude and high-latitude areas, respectively. In general, R (R Core Team, 2021) was applied for the statistical analyses.

2.4 Primary production estimates from Argo floats

The total daily primary production in the water column (PP, in units of mg C m^{-2} d^{-1}) was estimated from the vertical distributions of satellite derived PAR and *in situ* observations of chlorophyll (chl) from the Argo-profiles, i.e., PP_{Prof} (Webb et al., 1974; Jassby and Platt, 1976):

$$PP_{Prof} = \int_0^{24h} \int_{-D_{Eup}}^{0} P^B_{max} chl(z) \left(1 - exp\left(-PAR(z)\frac{\alpha^B}{P^B_{max}}\right)\right) dz dt \quad (1)$$

where *t* is time and the time integral is integrated during a 24 hour period accounting for the daily solar insolation curve, and vertically from D_{Eup} to the surface.

The photosynthetic parameters describe the maximum photosynthetic rate (P^B_{max}) and the initial slope (α^B) of the chlorophyll-normalized PP versus PAR, respectively. The maximum photosynthetic rate was parameterized in terms of SST as originally formulated for the P^B_{opt} parameter in the VGPM-model (Behrenfeld and Falkowski, 1997). This parameterization has been shown to represent the general variation of P^B_{max} in different oceanic regions although they have been obtained by different incubation methods, i.e., *in situ* with natural insolation versus incubations in the laboratory (Bouman et al., 2005). Photosynthetic parameters obtained more recently from a global data set showed relatively large variation of P^B_{max} in comparison with the VGPM-parameterization (Richardson et al., 2016) and similarly, relatively large variation was found for values in the subpolar North Atlantic (Richardson and Bendtsen, 2021). Despite these concerns, the VGPM-parameterization is applied here as being representative of P^B_{max}.

The VGPM-parameterization of P^B_{max} implies that P^B_{max} increases from 1.3 to 6.6 mg C (mg chl)$^{-1}$ h^{-1} between 0 °C and 20 °C and gradually decreases towards higher temperatures (Behrenfeld and Falkowski, 1997). It should be noted that this temperature dependence implicitly covers a wide range of hydrographic regions and, therefore, also to some extent accounts for variability in other factors influencing P^B_{max}, e.g., phytoplankton community composition.

The parameterization of α^B applied is based on an analysis of surface and DCM values of α^B in different D_{NO3} intervals from the global ocean (Richardson and Bendtsen, 2019) and ranges between 1.6 and $4.6{\cdot}10^{-2}$ µg C (µg chl h µE m^{-2} s^{-1})$^{-1}$. The largest values are associated with the DCM, thus indicating a more efficient use of photons for photosynthesis under the dim light conditions below the surface than at higher light intensities. However, variations of photosynthetic parameters may depend on local nutrient and light conditions (Babin et al., 1996) and co-variation between α^B and P^B_{max} are to some extent already considered in the VGPM-parameterization of P^B_{opt} (Behrenfeld and Falkowski, 1997; Bouman et al., 2005). Therefore, we apply a constant value of α^B of $3.1{\cdot}10^{-2}$ µg C (µg chl h µE m^{-2} s^{-1})$^{-1}$, corresponding to the mid-point between the largest and smallest value in the study of Richardson and Bendtsen (2019), as

a representative value. In general, total PP estimates are about twice as sensitive to the value of P^B_{max} than the value of α^B (Morel et al., 1996). Thus, the applied parameterization of P^B_{max} is a critical component in the analysis of the large-scale distribution of PP.

2.5 Primary production estimates using surface fields

The general relationship between PP, light and nutrients estimated from Argo-profiles was compared with similar relationships obtained from two different PP-models based on surface observations, i.e. the VGPM-model (PP_{VGPM}; Behrenfeld and Falkowski, 1997), and the VPP-model ($PP_{VPP;}$ Richardson and Bendtsen, 2019).

PP in the VGPM-model is calculated as: $PP_{VGPM} = P^B_{opt}$ *chl*(surf) *f*(SPAR) D'_{eu}, and depends on P^B_{opt} derived from surface observations of SST, surface chlorophyll (*chl(surf)*), a light function depending on SPAR (*f(SPAR)*) and the euphotic depth (D'_{eu}). This model was analyzed in two cases where surface fields were extrapolated from Argo-measurements of SST and chlorophyll near the surface and the estimated D_{Eup} or from satellite observations of SST and chlorophyll and a parameterization of D'_{eu} that was representative for case 1 waters (Morel et al., 2007). The general distribution of the two cases was similar and only results of the PP_{VGPM} based on Argo-profiles are shown.

PP in the VPP-model is calculated as: $PP_{VPP} = PP_{10m}/\gamma$. This model estimates PP from primary production calculated from Eq. (1) but only in the upper 10 m, i.e. PP_{10m}. The ratio between total PP and PP_{10m} was calculated from a global data set of PP and analyzed in three nutricline depth intervals: D_{nut}< 20 m, 20-90 m and > 90 m, and the corresponding values of γ were 0.31, 0.19 and 0.11, respectively, e.g., 31% of total PP on average occurs in the upper 10 m in areas where the nutricline depth is less than 20 m. Here, we apply the same photosynthetic parameters of P^B_{max} and α as for calculating PP_{prof} and PP_{VGPM}.

PP_{VGPM} and PP_{VPP} are thus used here as two examples of a family of models estimating PP on the basis of surface optical characteristics observed by satellites against which PP-model estimates employing vertical distribution data for light, nutrients and chlorophyll could be compared.

3 Results

3.1 Nutricline depth and chlorophyll

The DCM was generally located below the D_{Nut} except in areas with a shallow nutricline (<30 m) or in profiles obtained during winter time (Figure 2). Relatively shallow DCMs associated with deep nutriclines (D_{Nut}>90m) were also mainly found during the winter period (Figure 2, triangles). The average depth of all DCMs in areas with a D_{Nut} less than 20 m was 32 m and it increased to 88 m in areas where D_{Nut} was larger than 90 m (Table 2). During the growth season from April-November the average DCM, binned in 20 m depth intervals, was generally located below D_{Nut}, except for areas with a shallow nutricline, i.e., less than 20 m (Figure 2, black circles). The latitudinal distribution of the DCM depth (colors, Figure 2) also showed a gradual increase from high latitudes (~35 m, Table 2) towards the tropics (~112 m). This increase in the depth of the DCM with latitude was associated with the deepening of the D_{Nut} towards subtropical and tropical areas.

Phytoplankton biomass was approximated by vertically integrating chlorophyll (ΣChl) in the water column. The greatest biomass was found at high latitudes (60-80 °N) where ΣChl typically varied between 20 - 100 mg chl *a* m^{-2} (Figure 2, blue circles) with an average of 38 mg chl *a* m^{-2} (Table 2). Values lower than 20 mg chl *a* m^{-2} were associated with profiles made during periods of low light intensities during the winter season (Figure 2, triangles) while the highest values (>50 mg chl *a* m^{-2}) were associated with phytoplankton blooms in the growth season at high- and midlatitudes. Mid-latitude areas exhibited a relatively large range of biomass (10-100 mg chl *a* m^{-2}) with an average value of 35 mg chl *a* m^{-2}, i.e., comparable to that found at high latitudes. Significantly lower phytoplankton biomass was found in

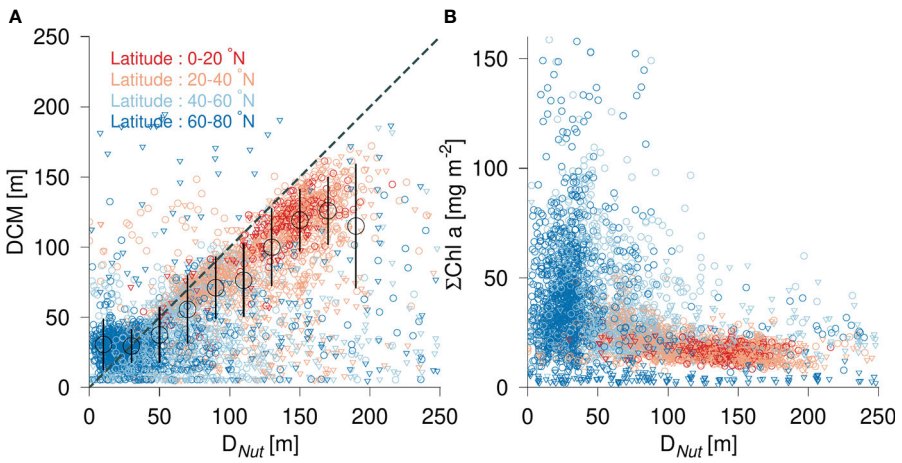


FIGURE 2
(A) Depth of the deep chlorophyll *a* maximum (DCM) versus nutricline depth (D_{Nut}) and binned average values during the growth season (April-October, black circles ± std. dev.). **(B)** Vertically integrated chlorophyll (ΣChl) versus D_{Nut}. Color shading shows the latitude of the corresponding profile. Observations are shown during the growth season (April-October, circles) and during winter time (November-March, triangles).

TABLE 2 Average values of all profiles (average ± std.dev, number of profiles in parenthesis) of the depth of the deep chlorophyll *a* maximum (DCM), vertically integrated chlorophyll *a* (ΣChl) and primary production calculated from Argo profiles (PP_{Prof}).

D_{Nut}	DCM	ΣChl	PP_{Prof}
m	*m*	*mg chl a* m^{-2}	*mg C* m^{-2} d^{-1}
0-20	32 ± 23 (413)	39 ± 31 (405)	736 ± 631 (380)
20-90	40 ± 24 (1994)	37 ± 24 (1990)	615 ± 526 (1843)
>90	88 ± 41 (1601)	19 ± 9 (1572)	306 ± 223 (1444)
Latitude (°N)			
0-20	112 ± 24 (224)	17 ± 4 (218)	296 ± 150 (190)
20-40	89 ± 36 (1302)	19 ± 6 (1291)	332 ± 192 (1256)
40-60	43 ± 27 (1082)	35 ± 22 (1057)	676 ± 550 (1045)
60-80	35 ± 25 (1466)	38 ± 28 (1466)	571 ± 569 (1189)

subtropical and tropical areas with an average ΣChl of 19 and 17 mg chl *a* m^{-2}, respectively.

The distribution of DCM and ΣChl in relation to nutricline depth and latitude motivated an analysis of the combined influence of light (represented by SPAR) and nutricline depth, i.e., representing the availability of nutrients. The distribution of DCM in a diagram spanned by D_{Nut} and SPAR showed a characteristic large-scale pattern, where a shallow DCM (<20 m) was associated with a relatively shallow D_{Nut}, whereas the deepest DCMs were found in oligotrophic areas with a deep D_{Nut} and a high SPAR (Figure 3). The vertically integrated chlorophyll distribution also showed a characteristic pattern with a well-defined maximum in areas of a relatively shallow D_{Nut} (<50 m) and modest insolation (SPAR ~ 40 E m^{-2} d^{-1}), and a gradual decrease of ΣChl with deeper D_{Nut} (Figure 3).

3.2 Nutricline depth and primary production

The distribution of PP_{Prof} in relation to D_{Nut} had some similarity to that found for ΣChl (Figure 4). The greatest PP_{Prof} was found at high latitudes and in subpolar areas with average values of 571 and 676 mg C m^{-2} d^{-1}, respectively (Table 2). The observed range (0 to >2 g C m^{-2} d^{-1}) at high and mid-latitudes (Figure 4, blue circles) was associated with low PP_{Prof} during the dark winter months and relatively high PP_{Prof} during the growth season. PP_{Prof} showed a gradual decrease towards subtropical and tropical areas where PP_{Prof} in general ranged between 50-500 mg C m^{-2} d^{-1} with average values of 332 and 296 mg C m^{-2} d^{-1}, respectively.

3.3 PP-diagram with light and nutrient

The entire PP_{prof} data set was analyzed in a manner similar to the approach used for chlorophyll in a diagram spanned by light and nutricline depth (Figure 5). PP_{Prof} had a maximum of ~1.4 g C m^{-2} d^{-1} for SPAR ~58 E m^{-2} d^{-1} and D_{Nut} ~10 m depth (Figure 5). Only a few profiles had a D_{Nut} less than ~10 m. Thus PP_{prof} generally decreased with increasing D_{Nut} for all light levels. PP_{Prof} at low light levels (<10 E m^{-2} d^{-1}) was less than 400 mg C m^{-2} d^{-1} and decreased below 200 mg C m^{-2} d^{-1} in areas with a D_{nut} deeper than ~90 m depth. In general,

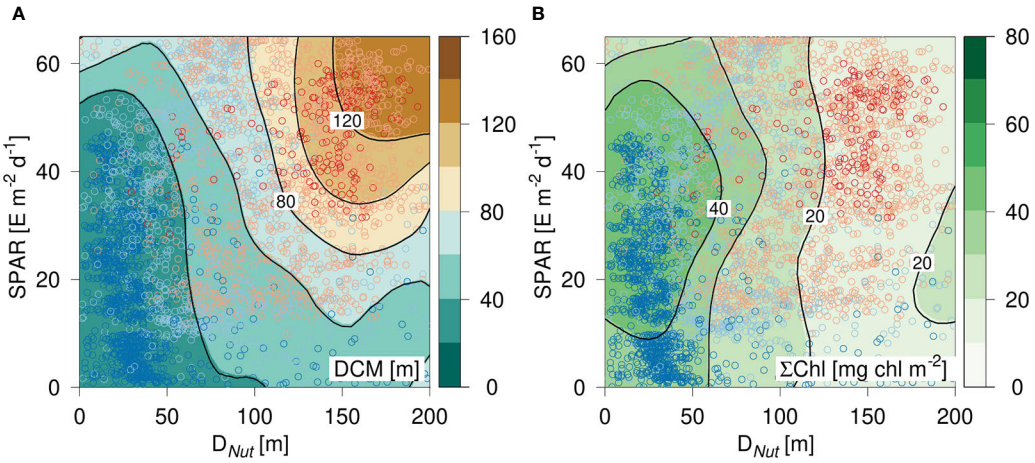


FIGURE 3
Diagram of **(A)** DCM and **(B)** vertically integrated chlorophyll (ΣChl) versus the corresponding nutricline depth (D_{Nut}) calculated from Argo-profiles and daily averaged Photosynthetic Available Radiation at the surface (SPAR) obtained from satellite observations. Color shading of the circles shows the latitude of the corresponding profile (see Figure 2).

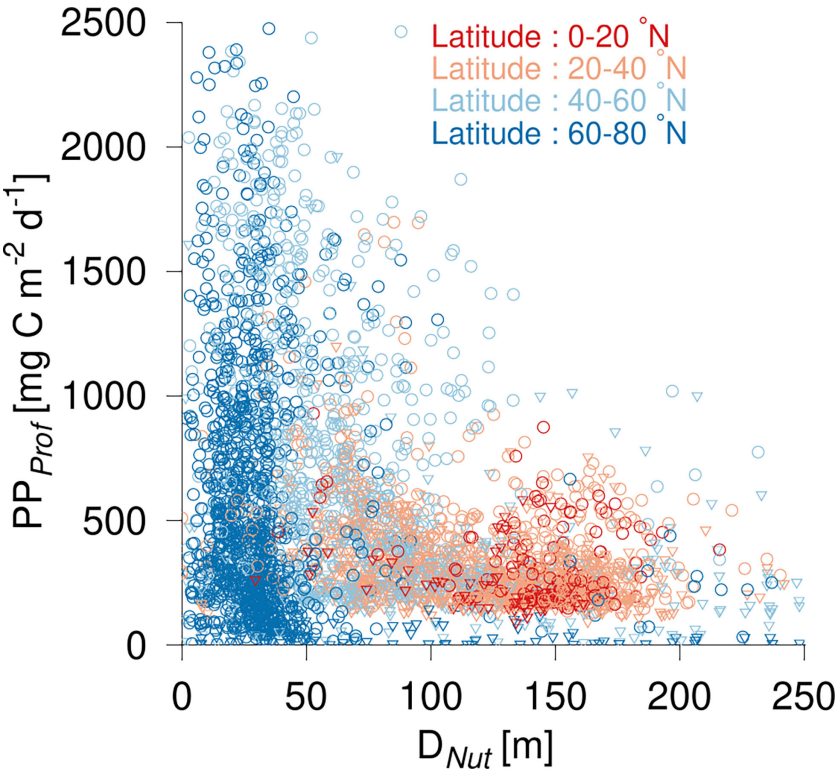


FIGURE 4
Primary production (PP_{Prof}) versus nutricline depth (D_{Nut}). Color shading shows the latitude of the corresponding profile. Observations are shown during the growth season (April-October, circles) and during winter time (November-March, triangles).

the lowest PP_{Prof}-values were seen in areas with a deep D_{nut} and low light levels, i.e., in areas with the deepest DCM (Figure 3). The majority of profiles with D_{nut}< 50 m were located at high- and mid-latitudes, whereas deep nutriclines and high light levels were mainly occupied with profiles from the subtropical and tropical areas. The lowest light levels (SPAR< 10 E m^{-2} d^{-1}) were recorded at high latitudes and represented conditions from the dark winter season. The tilted shape of the highest PP-values were shifted upward towards higher SPAR compared with the corresponding tilted distribution of ΣChl (Figure 3), showing the influence of light on the PP-estimate. Thus, the data suggest a general pattern that would be expected, i.e., water column PP_{Prof} decreasing gradually with increasing nutricline depth and increasing with increasing SPAR.

The general PP-distribution was analyzed further by considering the statistical variation of PP in the diagram spanned by SPAR and D_{nut} (Figure 6). The diagram was divided into equidistant intervals of SPAR of 5 E m^{-2} d^{-1} and D_{nut} of 20 m depth, and the corresponding values of the mean and standard deviation of PP were calculated. On average, there were 29 PP-values in each cell and cells with less than 5 PP-values were not considered. The PP-diagram based on the gridded average distribution of PP (Figure 6) was in accordance with the diagram based on all data (e.g., Figure 5). The diagram showed a similar peak value in areas with a shallow nutricline and high light levels, a general decrease towards deeper nutricline depths, and a general increase with increasing light levels. The relative error within each cell was defined from the ratio between the standard deviation of PP and the mean of the total PP (Figure 6) and was in general less than 60%. Areas with a shallow nutricline were in general associated with a relative error above 50%, whereas the relative error was less in areas with a deep nutricline. However, the largest variability of 50 - 80% was found in areas with nutricline depths between ~80 - 120 m depth and with relative high light levels between ~35 - 50 E m^{-2} d^{-1}.

3.4 Comparison of two surface-based PP-models

In the shallow nutricline interval (<50 m), the PP_{VGPM} and PP_{VPP} also showed a maximum at ~58 E m^{-2} d^{-1}. The minimum PP in the two models were seen in areas with a deep nutricline (>120 m) and relatively high light levels (>40 E m^{-2} d^{-1}). Thus, the two PP-models yielded significantly different estimates in regions characterized by a deep nutricline: PP_{Prof} showed an increase in PP with increasing light-levels while the two surface-based models showed a significant decrease. The structure of the two models was also different in areas with a shallow nutricline and low light levels, where a more gradual increase of PP with increasing light was seen in the PP_{Prof} than in the VGPM estimate.

4 Discussion

Analysis of the Argos data examined here shows a clear relationship between chlorophyll distribution and nutricline depth.

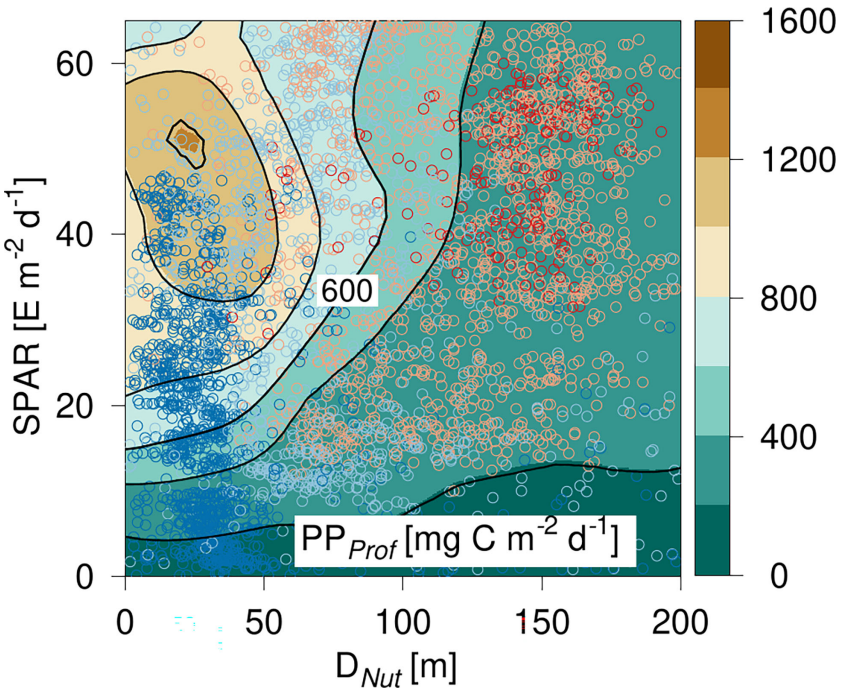


FIGURE 5
PP-diagram of primary production (PP) calculated from PP_{Prof} based on Argo-profiles. PP is shown versus the corresponding nutricline depth (D_{Nut}) calculated from Argo-profiles and daily averaged Photosynthetic Available Radiation at the surface (SPAR) obtained from satellite observations. Color shading of the circles shows the location of the corresponding profile (see Figure 2).

PP estimated using the Argos data also showed a clear relationship to nutricline depth.

4.1 Chlorophyll distributions and nutricline depth

The general relationship between the depth of the DCM and D_{Nut} showed that some DCMs tended to be located deeper than D_{Nut} at high latitudes. These profiles were generally made during winter (Figure 2, triangles). Otherwise, DCMs tended to be located deeper than D_{Nut}, where DCMs from the growth season were more closely related to D_{Nut} than during winter time. During the growth season, the depth levels of the DCM and D_{Nut} in the intermediate depth range between 20 - 90 m were in general accordance. Thus, this distribution from the entire North Atlantic of DCM and D_{nut} is in good accordance with previous findings (Herbland and Voituriez, 1979; Cullen, 1982; Cullen, 2015) and supports the hypothesis that the chlorophyll maximum is closely related to the nutrient distribution. In areas with a nutricline deeper than ~90 m, DCMs were generally

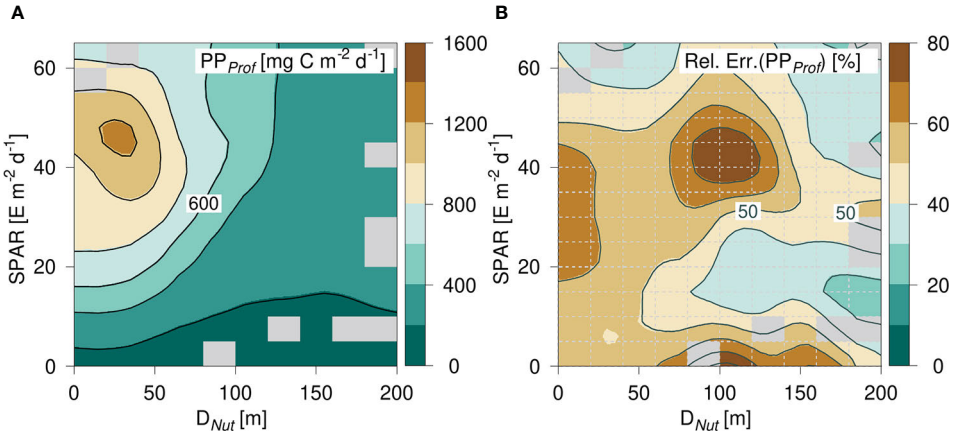


FIGURE 6
(A) PP-diagram of average primary production (PP) calculated from PP_{Prof} and **(B)** the relative error defined by σ(PP)/PP in each cell (cells are shown with gray dashed lines). Grid cells with less than 5 data points are filled (gray).

located above D_{Nut}. This general pattern is also in accordance with previous studies and can be explained by light limitation when D_{Nut} becomes too deep to support growth (Richardson and Bendtsen, 2019).

Some profiles at high and mid-latitudes showed that the DCM was deeper than D_{nut} in areas with D_{nut} less than 50 m also during the growth season (Figure 2). The binned average DCMs during the growth season was only deeper than D_{nut} in the depth range between 0 - 20 m. The relation between DCM and D_{nut} was thus weaker in these areas, suggesting that processes other than nutrient limitation could be important here. Fluorescence, and the ratios between fluorescence and chlorophyll, and carbon and chlorophyll can be affected by nutrient and light conditions (Westberry et al., 2016). The effects of light on phytoplankton are considered when estimating chlorophyll from fluorescence and chlorophyll concentrations are corrected in the adjusted BGC-Argo data (Roesler et al., 2017). Iron stress also causes increases in fluorescence (Behrenfeld and Milligan, 2013; Schallenberg et al., 2022) and decreases in the carbon to chlorophyll ratio (Westberry et al., 2016), which would ultimately appear as high chlorophyll from the floats. While iron limitation is not well-studied in the North Atlantic, it is possible that the reduction in chlorophyll at high latitudes during high SPAR (Figure 3) may be a result of growth limitation by micronutrients (e.g., Westberry et al., 2016) or due to photoinhibition (Yang et al., 2022). The photoprotective strategy in phytoplankton has been seen in Arctic phytoplankton species (Lacour et al., 2018) and is a prominent feature in polar waters (Kauko et al., 2017). A response from phytoplankton to iron limitation or excessive light could explain the relatively few profiles with a weak relation between DCM and D_{Nut} during the growth season at high latitudes. In summary, the location of the DCM, as well as the vertically integrated chlorophyll, generally showed a strong relationship to D_{Nut}.

4.2 Primary production versus light and nutricline depth

The relationships between PP_{Prof}, nutricline and latitude (Figure 4) suggested that D_{Nut} could be associated with nutrient availability in large areas of the ocean, and the latitudinal distribution indicated that part of the PP_{Prof} variation could be described by light conditions. This motivated the combined analysis in a diagram showing PP_{prof} versus D_{nut} calculated from Argo-profiles and PAR obtained from satellite observations (Figure 5). These two variables are only proxies for the *in situ* drivers of phytoplankton growth: PAR in the water column is modified by local attenuation and this is not accounted for by SPAR, and D_{Nut} only indirectly represents nutrient supply by mixing to the euphotic zone. However, both variables are closely related to light and nutrient supply for primary production and this is supported by the corresponding distributions of chlorophyll (Figure 3).

PP_{Prof} increases relatively quickly as SPAR increases in areas with a shallow nutricline, generally at high latitudes (Figure 6). In these areas, light is expected to be the primary limiting factor for PP, given availability of all other limiting micro-nutrients. Thus, light availability could explain the steady increase of PP_{Prof} with increasing light levels up to ~58 E m^{-2} d^{-1}. PP_{Prof} decreases at higher light levels (>60 E m^{-2} d^{-1}) in areas with a relatively shallow D_{nut} (<50 m). The reduced PP_{Prof} at the highest PAR may be explained by reduced photosynthesis due to photoinhibition (Falkowski and LaRoche, 1991; MacIntyre et al., 2002; van de Poll et al., 2011), or the limitation by another micro-nutrient such as iron (Behrenfeld and Milligan, 2013; Westberry et al., 2016). However, more profiles in high light and shallow nutricline conditions are required for analyzing this further. Areas characterized by low light levels and a deep D_{Nut} (i.e., SPAR<10 E m^{-2} d^{-1} and D_{Nut}>40 m) were only covered by few PP_{Prof}-data. indicating that D_{Nut} was in general less than ~40 m at high latitudes during winter.

The highest PP_{Prof} estimates (>1 g C m^{-2} d^{-1}) were seen in areas with a relatively shallow nutricline (<50 m) and were mainly located at mid- and high latitudes. This can be explained by the combination of high nutrient concentrations where D_{Nut} was shallow, and high light levels during the growth season. Low PP_{Prof} estimates in areas with a shallow D_{nut} can be explained by low light levels during the winter season. PP in the intermediate nutricline depth range (50-90 m) was generally below 1 g C m^{-2} d^{-1} and was mainly associated with profiles from mid-latitudes and the subtropical areas. Subtropical and tropical profiles were mainly available for areas where D_{Nut} was below 90 m.

The PP_{Prof} distribution was in good accordance with the expected variation with light and nutrient availability. In areas with a deep D_{Nut} (>100 m), PP_{Prof} increased steadily with light. Similarly, areas with a shallow D_{Nut}, i.e., mainly located at mid- and high-latitudes, showed an expected but also stronger increase of PP with increasing light at light levels below ~50 E m^{-2} d^{-1}. PP_{Prof} is proportional to the chlorophyll concentration (Eq. 1) and some similarity is also seen between PP_{Prof} and ΣChl (Figure 3). However, the consistent increase of PP with SPAR for any D_{Nut} depth level suggests a general relationship between PP_{Prof}, SPAR and nutrients in oligotrophic areas. PP_{Prof} was also found to gradually decrease with increasing D_{Nut} at all light levels.

The associated error-distributions showed that PP could be estimated with a relative error of less than 50% in large parts of the PP-diagram, in particular in areas with a deep nutricline depth. PP in these areas appears to be well constrained by light and nutricline depth. In areas with a shallow nutricline (<50 m), the relative error was between 50 - 60% and the largest variability was seen with modest to high light levels (20 - 40 E m^{-2} d^{-1}). These profiles were generally encountered at high latitudes (Figure 5), suggesting that the estimation of PP is more variable in the PP-diagram during spring and/or fall whereas the relative error decreases towards higher (summer) and lower (winter) light levels. The maximum variability is seen in the intermediate range of nutricline depths (~80 - 120 m) and light levels (~35 - 50 E m^{-2} d^{-1}), and this shows that PP estimated from this part of the PP-diagram is less well determined by light and nutricline depth. Profiles from this part of the diagram are mainly from the subtropical and tropical areas of the ocean, and the variability indicates that PP is also influenced by other processes.

Some of this variability could be explained by short-term variability in PP due to vertical mixing by mesoscale eddies (Johnson et al., 2010). Increased nutrient inputs from ocean eddies will tend to increase the PP-rate for a relatively long period, whereas nutricline depth levels tend to increase relatively quickly after a mixing event (e.g., Richardson and Bendtsen, 2017). Thus, profiles

obtained from these areas may include measurements made both before and after such mixing events. This might explain some of the variability in this part of the PP-diagram. In addition, while PP is calculated from float-based chlorophyll, it is important to take into account other factors that influence chlorophyll and fluorescence measures. Part of the variability in PP could be attributed to a sum of factors from iron limitation, to a change in community structure and species composition (Roesler et al., 2017). However, while the influence of these factors varies with area, the same chlorophyll measures were used to model PP, which would remove variability between profiles, leaving the relative variance the same.

There is only an indirect relationship between PP_{Prof} and D_{Nut}, however, the PP-diagram indicates that PP_{Prof} can be directly related to nutrient availability for a given level of SPAR. This is in line with earlier local studies showing relationships between PP and nutrient distributions (e.g., Herbland and Voituriez, 1979). The general distribution of PP_{Prof} shows a well-defined maximum in areas with a shallow nutricline (< 60 m) and SPAR-levels between ~40 - 50 E m^{-2} d^{-1} where PP_{Prof} reaches an average value of ~1 g C m^{-2} d^{-1}, and a general decrease of PP_{Prof} towards deeper nutriclines with typical PP values between 200 - 400 mg C m^{-2} d^{-1}. PP estimated from the averaged PP-diagram (Figure 6) has a relative error of about 50% compared with PP_{Prof}.

4.3 Comparing models in a PP-diagram

The PP-diagram provides a method for comparing estimates of the large-scale distributions of PP from different models in relation to light and nutricline depth. The VGPM-model (Behrenfeld and Falkowski, 1997) was parameterized from a large data set of *in situ* PP-measurements and has been applied in several studies and its strengths and shortcomings have been evaluated in previous studies (e.g., Carr et al., 2006). The VPP-model also depends on surface observations alone and was based on a simple relationship between PP and nutricline depths in a global data set (Richardson and Bendtsen, 2019). Therefore, we apply these two models as examples of a comparison in the PP-diagram of different surface-based PP-models with PP_{Prof}, i.e., PP estimated explicitly from *in situ* observations in the entire euphotic zone. The two models can be driven by observed satellite fields alone. However, in order to make a direct comparisons between PP_{Prof}, PP_{VGPM} and PP_{VPP}, all are here calculated from surface chlorophyll and surface temperature extrapolated from the uppermost measurement in the Argo-profile.

The PP_{VGPM} and PP_{VPP}-distributions showed a maximum at shallow nutricline depths and light levels between 30 - 60 E m^{-2} d^{-1}. The decrease in PP noted with increasing nutricline depth was in general accordance with PP_{Prof} (Figure 7). However, the maximum values in the PP_{Prof} distribution were ~1200 mg C m^{-2} d^{-1} whereas the corresponding maxima were ~1400 and 2000 mg C m^{-2} d^{-1} for the PP_{VGPM} and PP_{VPP}, respectively. Thus, both models resulted in a significantly higher peak value than PP_{Prof}. Both the PP_{VGPM}- and the PP_{VPP}-distributions decreased steadily with increasing SPAR-levels above ~20 E m^{-2} d^{-1} in areas with a deep nutricline (>130 m). This is not in accordance with the expected photosynthetic response for an increase in PAR and indicates that these models may underestimate PP in this part of the PP-diagram.

Previous analyses of PP estimated from the VGPM-model indicated that it underestimates PP in oligotrophic areas when compared to other PP-models (Westberry et al., 2008; Emerson, 2014) and the distributions in Figure 7 suggest that this could be an issue relevant for both surface-based PP-models due to a general underestimation of PP in tropical and subtropical areas with a deep nutricline. Oligotrophic areas with a deep nutricline are generally characterized by low surface concentrations of chlorophyll *a* (e.g., Richardson and Bendtsen, 2017), and these low chlorophyll values can explain the low estimates in this part of the PP-diagram.

Thus, we find a general structural difference between the two surface-based models and PP_{Prof}, where PP_{Prof} shows a more gradual increase with D_{nut}< 50 m and an expected increase with light in areas with a deep nutricline. It should be noted that both models show the same tilted structure as seen in the vertically integrated chlorophyll distributions for D_{Nut} less than ~90 m (Figure 3). This comparison demonstrates the applicability of the PP-diagram for identifying structural differences between PP-models in relation to observed fields of nutrients and light.

4.4 Applying nutrient observations in global PP-estimates

The comprehensive BGC-Argo data archive with high-resolution vertical nitrate profiles provides a new opportunity to include nitrate or, more generally, nutrients in the evaluation of PP-estimates from different models. Using this data archive, PP-estimates can be analyzed in relation to *in situ* observations of nutrient availability and satellite observations of SPAR, i.e., the two most critical factors for photosynthesis and biological production. The distribution of PP_{Prof} in relation to light and nutrient availability suggest that universal relations exist between large-scale PP, light and nutricline depth, and these relations may then be applied in the analysis of different PP-models and, more generally, for estimating large-scale patterns of PP from information about light and nutrients alone.

The general distribution of the PP-estimate versus light and nutrient availability showed that a PP-diagram can be applied for evaluating different PP-models. The differences between the two surface-based PP-models and PP_{Prof} examined in this study showed the potential of using nutrient information in the evaluation of global PP-patterns. At high latitudes characterized by shallow nutriclines, it is important to acknowledge the interchanging effects of light and nutrients between the seasons: where light is the dominant limiting factor in the winter and nutrients become limiting in the summer, when light is sufficient. Future work should include a distinction for high nutrient, low chlorophyll (HNLC) areas like the Southern Ocean, where iron and light primarily limit phytoplankton growth and primary production (Martin et al., 1990; Boyd et al., 2007).

Light and nutrient-based estimates of PP may also elucidate large-scale distributions of new production (NP), i.e., the fraction of PP based on newly available nitrate or nitrite (Dugdale and Goering, 1967). NP balances the export of organic matter on longer timescales (> month - years) and the fraction of PP exported out of the euphotic zone (i.e., the f-ratio; Eppley and Peterson, 1979) has been found to increase with PP and decrease with SST (Laws et al., 2011). Thus, the PP-diagram indicates that the corresponding NP-distribution would tend to have an even more steep gradient between areas with a shallow and a deep nutricline.

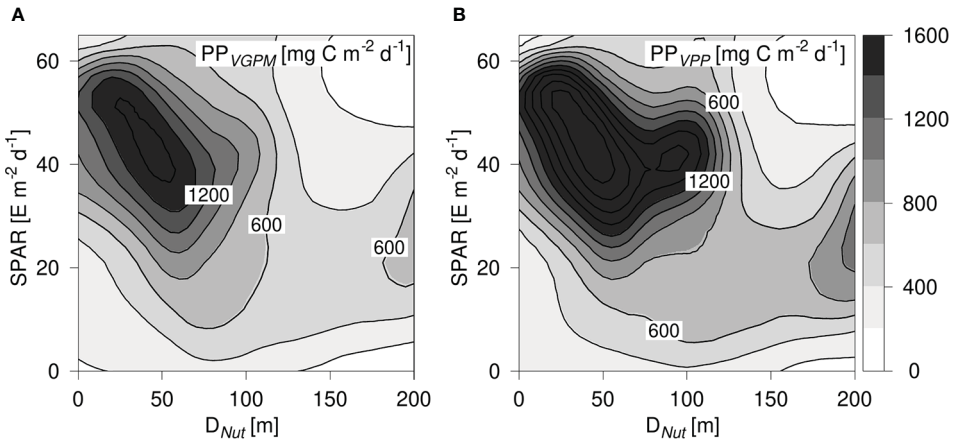


FIGURE 7
(A) PP-diagram of primary production calculated from PP_{VGPM} and, **(B)** PP_{VPP}. PP is shown versus the corresponding nutricline depth (D_{Nut}) calculated from Argo-profiles and daily averaged Photosynthetic Available Radiation at the surface (SPAR) obtained from satellite observations. Contours are shown in intervals of 200 mg C m^{-2} d^{-1}.

The models applied in this study represent examples among a suite of PP-models (e.g., Carr et al., 2006). PP-models may be solely driven by satellite observations (Westberry et al., 2008; Uitz et al., 2010; Silsbe et al., 2016), derived from ocean circulation models (Kwiatkowski et al., 2020) or by data-assimilation by combining observations and circulation models (Gregg and Rousseaux, 2019). However, the access to information about location, light and *in situ* nutrient conditions makes evaluations in a PP-diagram possible with these other model-products.

5 Conclusion

The influence of nutrient and light availability on primary production (PP) was analyzed from profiles of chlorophyll *a* and nitrate observed by BGC-Argo floats in the North Atlantic, including the Mediterranean and subpolar seas, during 2011-2022, and surface insolation of photosynthetically available radiation (SPAR) observed by satellite. The distributions of chlorophyll *a* and PP were analyzed in a diagram with respect to both surface light and nutricline depth. The large-scale distributions of chlorophyll *a* showed characteristic patterns with high concentrations of total chlorophyll *a* in areas with a relatively high daily insolation, i.e., a surface PAR of ~40 E m^{-2} d^{-1}, and nutricline depths of 40-50 m, and also a gradual increase of DCM with increasing nutricline depth and surface insolation. These patterns could be explained by nutrient and light availability and motivated a similar analysis of PP.

The PP-diagram obtained from the entire BGC-Argo data set showed a consistent decrease with increasing nutricline depth and, in general, an increase with increasing light. This general pattern of nutrient and light availability on PP reflects the strong influence from light in nutrient replete areas and the interaction with nutrients and light in areas with a deeper nutricline. These large-scale patterns suggest that a general relationship between PP, light, and nutrients may be applied for evaluating large-scale distributions of PP from various PP-models. This was demonstrated by comparing two different surface-based PP-models where structural differences between the Argos data based and surface data only approaches to estimating PP were identified in results generated at high latitudes during the summer season and for the oligotrophic North Atlantic. A PP-diagram can thus support the development of PP-models and reduce the current uncertainty regarding the magnitude of global ocean PP.

The PP-diagram indicates that the large-scale distribution of PP may follow a universal pattern determined from surface insolation and nutricline depth that potentially can be applied for estimating the total PP in the North Atlantic basin. Analysis of similar relationships for high-nutrient low-chlorophyll areas such as the Southern Ocean may thus provide basis for a new method for estimating PP at the global scale.

Data availability statement

The original contributions presented in the study are included in the article/supplementary material. Further inquiries can be directed to the corresponding author.

Author contributions

All authors listed have made a substantial, direct, and intellectual contribution to the work, and approved it for publication.

Funding

This study was supported by a grant from the Carlsberg Foundation (H.M. Queen Margrethe's and Vigdís Finnbogadóttir´s Interdisciplinary Research Centre on Ocean, Climate, and Society,

CF-20-0071). CV was funded by the Australian Research Council Centre of Excellence for Climate Extremes (CLEX; CE170100023).

Acknowledgments

The Argo data were collected and made freely available by the International Argo Program and the national programs that contribute to it (https://argo.ucsd.edu; https://www.ocean-ops.org). The Argo Program is part of the Global Ocean Observing System. This study has also been possible thanks to the publicly available satellite data from the Ocean Color website in the National Aeronautics and Space Administration (NASA; https://oceancolor.gsfc.nasa.gov/l3/). We acknowledge comments from a reviewer which improved the manuscript.

Conflict of interest

The authors declare that the research was conducted in the absence of any commercial or financial relationships that could be construed as a potential conflict of interest.

Publisher's note

All claims expressed in this article are solely those of the authors and do not necessarily represent those of their affiliated organizations, or those of the publisher, the editors and the reviewers. Any product that may be evaluated in this article, or claim that may be made by its manufacturer, is not guaranteed or endorsed by the publisher.

References

Argo (2000). *Argo float data and metadata from global data assembly centre (Argo GDAC)* (France: SEANOE, IFREMER). doi: 10.17882/42182

Argo (2021). *Argo user's manual*. doi: 10.13155/29825

Babin, M., Morel, A., Claustre, H., Bricaud, A., Kolber, Z., and Falkowski, P. G. (1996). Nitrogen- and irradiance-dependent variations of the maximum quantum yield of carbon fixation in eutrophic, mesotrophic and oligotrophic marine systems. *Deep-Sea Res.* 43, 1241–1272. doi: 10.1016/0967-0637(96)00058-1

Beckmann, A., and Hense, I. (2007). Beneath the surface: Characteristics of oceanic ecosystems under weak mixing conditions — a theoretical investigation. *Prog. Oceanogr.* 75, 771–796. doi: 10.1016/j.pocean.2007.09.002

Behrenfeld, M. J., and Falkowski, P. G. (1997). Photosynthetic rates derived from satellite-based chlorophyll concentration. *Limnol. Oceanogr.* 42, 1–20. doi: 10.4319/lo.1997.42.1.0001

Behrenfeld, M. J., and Milligan, A. J. (2013). Photophysiological expressions of iron stress in phytoplankton. *Ann. Rev. Mar. Sci.* 5, 217–246. doi: 10.1146/annurev-marine-121211-172356

Bittig, H., Wong, A., Plant, J.the Coriolis Argo data management team (2022). *BGC-argo synthetic profile file processing and format on Coriolis GDAC, v1.3*. (France: IFREMER) doi: 10.13155/55637

Bouman, H., Platt, T., Sathyendranath, S., and Stuart, V. (2005). Dependence of light-saturated photosynthesis on temperature and community structure. *Deep-Sea Res.* 52, 1284–1299. doi: 10.1016/j.dsr.2005.01.008

Boyd, P. W., Jickells, T., Law, C. S., Blain, S., Boyle, E. A., Buesseler, K. O., et al. (2007). Mesoscale iron enrichment experiments 1993-2005: synthesis and future directions. *Science* 315, 612–617. doi: 10.1126/science.1131669

Carr, M.-E., Friedrichs, M. A. M., Schmeltz, M., Aita, M. N., Antoine, D., Arrigo, K. R., et al. (2006). A comparison of global estimates of marine primary production from ocean color. *Deep-Sea Res. II* 53, 741–770. doi: 10.1016/j.dsr2.2006.01.028

Cullen, J. J. (1982). The deep chlorophyll maximum: Comparing vertical profiles of chlorophyll a. *Can. J. Fish. Aquat. Sci.* 39, 791–803. doi: 10.1139/f82-108

Cullen, J. J. (2015). Subsurface chlorophyll maximum layers: Enduring enigma or mystery solved? *Annu. Rev. Mar. Sci.* 7, 207–239. doi: 10.1146/annurev-marine-010213-135111

de Boyer Montégut, C., Madec, G., Fischer, A. S., Lazar, A., and Iudicone, D. (2004). Mixed layer depth over the global ocean: An examination of profile data and a profile-based climatology. *J. Geophys. Res.* 109, C12003. doi: 10.1029/2004JC002378

Dugdale, R. C., and Goering, J. J. (1967). Uptake of new and regenerated forms of nitrogen in primary productivity. *Limnol. Oceanogr.* 12, 196–206. doi: 10.4319/lo.1967.12.2.0196

Emerson, S. (2014). Annual net community production and the biological carbon flux in the ocean. *Global Biogeochem. Cycles* 28, 14–28. doi: 10.1002/2013GB004680

Eppley, R. W., and Peterson, B. J. (1979). Particulate organic matter flux and planktonic new production in the deep ocean. *Nature* 282, 677–680. doi: 10.1038/282677a0

Falkowski, P. G., and LaRoche, J. (1991). Acclimation to spectral irradiance in algae. *J. Phycology* 27, 8–14. doi: 10.1111/j.0022-3646.1991.00008.x

Frouin, R., Ligner, D. W., and Gautier, C. (1989). A simple analytical formula to compute clear sky total and photosynthetically available solar irradiance at the ocean surface. *J. Geophys. Res.* 94, 9731–9742. doi: 10.1029/JC094iC07p09731

Gregg, W., and Rousseaux, C. S. (2019). Global ocean primary production trends in the modern ocean color satellite record, (1998–2015). *Environ. Res. Lett.* 14, 124011. doi: 10.1088/1748-9326/ab4667

Gulev, S. K., Thorne, P. W., Ahn, J., Dentener, F. J., Domingues, C. M., Gerland, S., et al. (2021). "Changing state of the climate system," in *Climate change 2021: The physical science basis. contribution of working group I to the sixth assessment report of the intergovernmental panel on climate change*. Eds. V Masson-Delmotte, et al. 287–422. (Cambridge, United Kingdom and New York, NY, USA: Cambridge University Press).

Hátún, H., Azetsu-Scott, K., Somavilla, R., Rey, F., Johnson, C., Mathis, M., et al. (2017). The subpolar gyre regulates silicate concentrations in the north Atlantic. *Sci. Rep.* 7, 14576. doi: 10.1038/s41598-017-14837-4

Herbland, A., and Voituriez, B. (1979). Hydrological structure analysis for estimating the primary production in the tropical Atlantic ocean. *J. Mar. Res.* 37, 87–101.

Hu, C., Lee, Z., and Franz, B. A. (2012). Chlorophyll-a algorithms for oligotrophic oceans: A novel approach based on three-band reflectance difference. *J. Geophys. Res.* 117, C01011. doi: 10.1029/2011JC007395

Jassby, A. D., and Platt, T. (1976). Mathematical formulation of the relationship between photosynthesis and light for phytoplankton. *Limnol. Oceanogr.* 21540–547. doi: 10.4319/lo.1976.21.4.0540

Johnson, K. S., Riser, S. C., and Karl, D. M. (2010). Nitrate supply from deep to near-surface waters of the north pacific subtropical gyre. *Nature* 465, 1062–1065. doi: 10.1038/nature09170

Kauko, H. M., Taskjelle, T., Assmy, P., Pavlov, A. K., Mundy, C. J., Duarte, P., et al. (2017). Windows in Arctic sea ice: Light transmission and ice algae in a refrozen lead. *J. Geophys. Res. Biogeosci.* 122, 1486–1505. doi: 10.1002/2016JG003626

Kulk, G., Platt, T., Dingle, J., Jackson, T., Jönsson, B. F., Bouman, H. A., et al. (2020). Primary production, an index of climate change in the ocean: Satellite-based estimates over two decades. *Remote Sens.* 12, 826. doi: 10.3390/rs12050826

Kwiatkowski, L., Torres, O., Bopp, L., Aumont, O., Chamberlain, M., Christian, J. R., et al. (2020). Twenty-first century ocean warming, acidification, deoxygenation, and upper-ocean nutrient and primary production decline from CMIP6 model projections. *Biogeosciences* 17, 3439–3470. doi: 10.5194/bg-17-3439-2020

Lacour, T., Lariviere, J., Ferland, J., Bruyant, F., Lavaud, J., and Babin, M. (2018). The role of sustained photoprotective non-photochemical quenching in low temperature and high light acclimation in the bloom-forming arctic diatom thalassiosira gravida. *Front. Mar. Sci.* 5. doi: 10.3389/fmars.2018.00354

Laws, E. A., D'Sa, E., and Naik, P. (2011). Simple equations to estimate ratios of new or export production to total production from satellite-derived estimates of sea surface temperature and primary production. *Limnol. Oceanogr. Methods* 9, 593–601. doi: 10.4319/lom.2011.9.593

Laws, E. A., Letelier, R. M., and Karl, D. M. (2014). Estimating the compensation irradiance in the ocean: The importance of accounting for non-photosynthetic uptake of inorganic carbon. *Deep Sea Res.* 93, 35–40. doi: 10.1016/j.dsr.2014.07.011

MacIntyre, H. L., Kana, T. M., Anning, T., and Geider, R. J. (2002). Photoacclimation of photosynthesis irradiance response curves and photosynthetic pigments in microalgae and cyanobacteria. *J. phycol.* 38, 17–38. doi: 10.1046/j.1529-8817.2002.00094.x

Martin, J. H., Fitzwater, S. E., and Gordon, R. M. (1990). Iron deficiency limits phytoplankton growth in Antarctic waters. *Glob. Biogeochem. Cycles* 4, 5–12. doi: 10.1029/GB004i001p00005

Morel, A., Antoine, D., Babin, M., and Dandonneau, Y. (1996). Measured and modeled primary production in the northeast Atlantic (EUMELI JGOFS program): the impact of natural variations in photosynthetic parameters on model predictive skill. *Deep-Sea Res. I* 43, 1273–1304. doi: 10.1016/0967-0637(96)00059-3

Morel, A., Huot, Y., Gentili, B., Werdell, P. J., Hooker, S. B., and Franz, B. A. (2007). Examining the consistency of products derived from various ocean color sensors in open ocean (Case 1) waters in the perspective of a multi-sensor approach. *Remote Sens. Env.* 111, 69–88. doi: 10.1016/j.rse.2007.03.012

Morel, A., and Maritorena, S. (2001). Bio-optical properties of oceanic waters: A reappraisal. *J. Geophys. Res.* 106C4, 7163–7180. doi: 10.1029/2000JC000319

NASA Ocean Biology Processing Group (2017). *MODIS-Aqua Level 3 Mapped Photosynthetically Available Radiation Data Version R2018.0* (NASA Ocean Biology DAAC). doi: 10.5067/AQUA/MODIS/L3M/PAR/2018

Nielsdóttir, M. C., Moore, C. M., Sanders, R., Hinz, D. J., and Achterberg, E. P. (2009). Iron limitation of the postbloom phytoplankton communities in the Iceland basin. *Glob. Biogeochem Cycles* 23, GB3001. doi: 10.1029/2008gb003410

R Core Team (2021). *R: A language and environment for statistical computing* (Vienna, Austria: R Foundation for Statistical Computing). Available at: https://www.R-project.org/.

Richardson, K., and Bendtsen, J. (2017). Photosynthetic oxygen production in a warmer ocean: the Sargasso Sea as a case study. *Phil. Trans. R. Soc A*, 375, 20160329. doi: 10.1098/rsta.2016.0329

Richardson, K., and Bendtsen, J. (2019). Vertical distribution of phytoplankton and primary production in relation to nutricline depth in the open ocean. *Mar. Ecol. Prog. Ser.* 620, 33–46. doi: 10.3354/meps12960

Richardson, K., and Bendtsen, J. (2021). Distinct seasonal primary production patterns in the Sub-polar gyre and surrounding seas. *Front. Mar. Sci.* 8. doi: 10.3389/fmars.2021.785685

Richardson, K., Bendtsen, J., Kragh, T., and Mousing, E. A. (2016). Constraining the distribution of photosynthetic parameters in the global ocean. *Front. Mar. Sci.* 3. doi: 10.3389/fmars.2016.00269

Roesler, C., Uitz, J., Claustre, H., Boss, E., Xing, X., Organelli, E., et al. (2017). Recommendations for obtaining unbiased chlorophyll estimates from *in situ* chlorophyll fluorometers: A global analysis of WET labs ECO sensors. *Limnol. Oceanogr.: Methods* 15, 572–585. doi: 10.1002/lom3.10185

Ryan-Keogh, T. J., Macey, A. I., Nielsdóttir, M. C., Lucas, M. I., Steigenberger, S. S., Stinchcombe, M. C., et al. (2013). Spatial and temporal development of phytoplankton iron stress in relation to bloom dynamics in the high-latitude north Atlantic ocean. *Limnol. Oceanogr.* 58, 533–545. doi: 10.4319/LO.2013.58.2.0533

Sathyendranath, S., Platt, T., Žarko, K., Dingle, J., Jackson, T., Brewin, R. J. W., et al. (2020). Reconciling models of primary production and photoacclimation. *Appl. Opt.* 59, c100–c114. doi: 10.1364/AO.386252

Schallenberg, C., Strzepek, R. F., Bestley, S., Wojtasiewicz, B., and Trull, T. W. (2022). Iron limitation drives the globally extreme fluorescence/chlorophyll ratios of the southern ocean. *Geophys. Res. Lett.* 49, e2021GL097616. doi: 10.1029/2021GL097616

Silsbe, G. M., Behrenfeld, M. J., Halsey, K. H., Milligan, A. J., and Westberry, T. K. (2016). The CAFE model: A net production model for global ocean phytoplankton. *Global Biogeochem. Cycles* 30, 1756–1777. doi: 10.1002/2016GB005521

Siokou-Frangou, I., Christaki, U., Mazzocchi, M. G., Montresor, M., Ribera d'Alcalá, M., Vaqué, D., et al. (2010). Plankton in the open Mediterranean Sea: A review. *Biogeosci.* 7, 1543–1586. doi: 10.5194/bg-7-1543-2010

Tagliabue, A., Kwiatkowski, L., Bopp, L., Butenschön, M., Cheung, W., Lengaigne, M., et al. (2021). Persistent uncertainties in ocean net primary production climate change projections at regional scales raise challenges for assessing impacts on ecosystem services. *Front. Clim.* 3. doi: 10.3389/fclim.2021.738224

Uitz, J., Claustre, H., Gentili, B., and Stramski, D. (2010). Phytoplankton class-specific primary production in the world's oceans: Seasonal and interannual variability from satellite observations. *Global Biogeochem. Cycles* 24, GB3016. doi: 10.1029/2009GB003680

van de Poll, W. H., Lagunas, M., de Vries, T., Visser, R. J., and Buma, A. G. (2011). Non-photochemical quenching of chlorophyll fluorescence and xanthophyll cycle responses after excess PAR and UVR in chaetoceros brevis, phaeocystis antarctica and coastal Antarctic phytoplankton. *Mar. Ecol. Progr. Ser.* 426, 119–131. doi: 10.3354/meps09000

Webb, W. L., Newton, M., and Starr, D. (1974). Carbon dioxide exchange of alnus rubra. a mathematical model. *Oecologia* 17, 281–291. doi: 10.1007/BF00345747

Westberry, T. K., Behrenfeld, M. J., Siegel, D. A., and Boss, E. (2008). Carbon-based primary production modeling with vertically resolved photoaccumulation. *Glob. Biogeochem. Cycles* 22, GB2024. doi: 10.1029/2007GB003078

Westberry, T. K., Schultz, P., Behrenfeld, M. J., Dunne, J. P., Hiscock, M. R., and Maritorena, S. (2016). Annual cycles of phytoplankton biomass in the subarctic Atlantic and pacific ocean. *Global Biogeochem. Cycles* 30, 175–190. doi: 10.1002/2015GB005276

Yang, B., Gomez, F., Schmid, C., and Baringer, M. (2022). *In situ* estimates of net primary production in the open-ocean gulf of Mexico. *Limnol. Oceanogr. Lett.* 7, 427–434. doi: 10.1029/2020JG006116

frontiers | Frontiers in Marine Science

TYPE Original Research
PUBLISHED 03 February 2023
DOI 10.3389/fmars.2023.1050087

Check for updates

OPEN ACCESS

EDITED BY
Javier A. Concha,
European Space Research Institute (ESRIN), Italy

REVIEWED BY
Shengqiang Wang,
Nanjing University of Information Science and Technology, China
Yongxiang Hu,
Langley Research Center (NASA), United States

*CORRESPONDENCE
Peng Chen
chenp@sio.org.cn

SPECIALTY SECTION
This article was submitted to Ocean Observation, a section of the journal Frontiers in Marine Science

RECEIVED 21 September 2022
ACCEPTED 23 January 2023
PUBLISHED 03 February 2023

CITATION
Zhang Z, Chen P, Zhong C, Xie C, Sun M, Zhang S, Chen S and Wu D (2023) Chlorophyll and POC in polar regions derived from spaceborne lidar. *Front. Mar. Sci.* 10:1050087. doi: 10.3389/fmars.2023.1050087

COPYRIGHT
© 2023 Zhang, Chen, Zhong, Xie, Sun, Zhang, Chen and Wu. This is an open-access article distributed under the terms of the Creative Commons Attribution License (CC BY). The use, distribution or reproduction in other forums is permitted, provided the original author(s) and the copyright owner(s) are credited and that the original publication in this journal is cited, in accordance with accepted academic practice. No use, distribution or reproduction is permitted which does not comply with these terms.

Chlorophyll and POC in polar regions derived from spaceborne lidar

Zhenhua Zhang[1,2], Peng Chen[1,2]*, Chunyi Zhong[2], Congshuang Xie[2], Miao Sun[2], Siqi Zhang[2], Su Chen[2] and Danchen Wu[2]

[1]Southern Marine Science and Engineering Guangdong Laboratory (Guangzhou), Guangzhou, China, [2]State Key Laboratory of Satellite Ocean Environment Dynamics, Second Institute of Oceanography, Ministry of Natural Resources, Hangzhou, China

Polar regions have the most productive ecosystems in the global ocean but are vulnerable to global climate changes. Traditionally, the long-term changes occurred in an ecosystem are studied by using satellite-derived estimates of passive ocean color remote sensing measurements. However, this technology is severely limited by the inability to observe high-latitude ocean areas during lengthy polar nights. The spaceborne lidar can address the limitations and provide a decade of uninterrupted polar observations. This paper presents an innovative feed-forward neural network (FFNN) model for the inversion of subsurface particulate backscatter coefficients (bbp), chlorophyll concentration (Chl), and total particulate organic carbon (POC) from the spaceborne lidar. Non-linear relationship between lidar signal and bio-optical parameters was estimated through FFNN. The inversion results are in good agreement with biogeochemical Argo data, indicating the accuracy of the method. The annual cycles of Chl and POC were then analyzed based on the inversion results. We find that Chl, bbp, and POC have similar interannual variability but there are some subtle differences between them. Light limitation appears to be a dominant factor controlling phytoplankton growth in polar regions according to the results. Overall, the combined analysis of bbp, Chl, and POC contributes to a comprehensive understanding of interannual variability in the ecosystem in polar regions.

KEYWORDS

chlorophyll, bbp, POC, CALIOP, polar oceans, phytoplankton

Highlights

- New FFNN algorithm was proposed to retrieve bbp, Chl, and POC from spaceborne lidar
- CALIPSO measurements in the polar regions fill the gap of passive measurements

- Comparison with *in situ* data indicates that FFNN-based lidar products perform well
- Combined description of annual cycles of bbp, Chl, and POC in polar regions
- Analysis of key factors governing phytoplankton growth in polar regions

1 Introduction

Marine phytoplankton plays a key role in the marine food web and biogeochemical cycles (Xu et al., 2020) and its photosynthetic production of organic carbon is vital for regulating atmospheric carbon dioxide (Parekh et al., 2006). Changes in phytoplankton primary production have a critical impact on higher trophic levels like zooplankton and ichthyoplankton (Capuzzo et al., 2018). As a commonly used proxy of phytoplankton abundance (Gordon et al., 1980; Li et al., 2022), the chlorophyll concentration (Chl) is traditionally estimated by passive ocean color remote sensing measurements for long-term studies (Alvera-Azcárate et al., 2021). In fact, ocean color remote sensing has reshaped our understanding of upper-ocean biogeochemistry for the global oceans as well as in regional basins (Dickey et al., 2006; McClain, 2009; Blondeau-Patissier et al., 2014; Brewin et al., 2017; Jackson et al., 2017). However, passive remote sensing can only work during the daytime because of the need for sunlight (Jamet et al., 2019), which leaves vast high-latitude ocean areas unobserved during lengthy polar nights. As a result, only a limited amount of data is available for polar regions.

Recently, an active remote sensing technique, light detection and ranging (lidar) has drawn great attention because of its independence from sunlight, which could address the limitations of passive remote sensing. In practice, spaceborne lidar CALIOP has shown remarkable potential in research of ocean carbon stocks (Behrenfeld et al., 2013) and phytoplankton biomass (Behrenfeld et al., 2017). However, previous studies heavily relied on the CALIOP particulate backscatter coefficient (bbp) to derive total particulate organic carbon (POC) and phytoplankton biomass. Besides, CALIOP bbp inversion method needs to assume the conversion factor used to derive bbp from the backscatter coefficient at 180° (b_π) (Behrenfeld et al., 2019; Bisson et al., 2021). However, variabilities and inconsistencies of the conversion coefficient affect uncertainties to the retrieval of CALIOP bbp substantially (Berthon et al., 2007; Sullivan and Twardowski, 2009; Zhang et al., 2012; Chami et al., 2014; Hu et al., 2020).

This study intends to propose an innovative feed-forward neural network (FFNN) method to retrieve bbp, Chl, and POC from CALIOP measurements and study the interannual variability of phytoplankton based on the CALIOP-derived estimates of ocean variables. The remainder of the manuscript is organized as follows: data and methods are described in Section 2; after validation of the accuracy of the proposed method, the interannual variability is studied in Section 3; a discussion about the key factors governing phytoplankton growth in polar regions is presented in Section 4; conclusions and perspectives are provided in Section 5.

2 Materials and methods

2.1 Data

The data including CALIOP Level-1B V4.1 data products, Level-2 Merged Layer V4.20 products, and MODIS Level-3 9 km monthly averaged data are mainly used here. Launched in April 2006, CALIPSO flew in the "A-Train" constellation and followed Aqua within 2 minutes (Kim et al., 2013), which provided for near-simultaneous observations between them. As the main payload onboard CALIPSO, CALIOP is a nadir-pointing two-wavelength polarization-sensitive elastic backscatter lidar. CALIOP provides attenuated backscatter at 532 nm perpendicular component, 532 nm parallel component, and 1064 nm. The receiver footprint diameter is 90 m and the horizontal resolution is 333 m (Winker et al., 2009). The vertical resolution in water is 22.5 m (Lu et al., 2014). CALIOP Level-1B V4.1 product, which has significantly improved calibration accuracy compared with previous versions (Getzewich et al., 2018), is used for the ocean optic property inversion. Level-2 Merged Layer V4.20 product provides integrated attenuated backscatter (IAB) and aerosol optical depth (AOD) parameters.

MODIS is a key instrument aboard the Terra and Aqua satellite. As Aqua flies in the "A-Train" constellation as well, only MODIS products onboard Aqua are used for the simultaneity between different observations. The algorithms developed for the inversion bbp include Garver-Siegel-Maritorena algorithm (GSM) (Maritorena et al., 2002), Quasi Analytical Algorithm (QAA) (Lee et al., 2002), and Generalized Inherent Optical Property algorithm (GIOP) (Werdell et al., 2013). Since GIOP outperformed other inversion methods (Bisson et al., 2019), MODIS GIOP $b_{bp}443$ L3 9 km product is used here. MODIS POC is produced using blue-to-green band ratios (Stramski et al., 2008). MODIS Chl is derived based on the standard Ocean Color Chlorophyll (OC2) (O'Reilly et al., 1998) band ratio algorithm merged with the color index (CI) (Hu et al., 2012). *In situ* Chl were obtained from biogeochemical Argo data (Claustre et al., 2019) available from the Argo Data Assembly Center (ftp://ftp.ifremer.fr/ifremer/argo/dac/, last access: 20 May 2022) and used to validate the lidar-derived results. The spatial distribution of *in situ* data is shown in Supplementary Figure 1A, where blue dots represent all *in situ* data and red asterisks represent the matched data. Histograms of all data and matched data are shown in Supplementary Figures 1B, C. The mean values of all data and matched data are 0.50 mg/m^3 and 0.81 mg/^{3}, respectively. Sea ice extend is obtained from the Copernicus Climate Change Service (https://climate.copernicus.eu/sea-ice, last access: 5 June 2022) which is derived based on EAR5 (Hersbach et al., 2020; Bell et al., 2021). Estimates of photosynthetically available radiation (PAR) are from NASA Ocean Color website (https://oceancolor.gsfc.nasa.gov/, last access: 7 June 2022) that are derived from MODIS (Frouin et al., 2012). Monthly global reprocessed products of physical variables from ARMOR3D L4 distributed through the Copernicus Marine Environment Monitoring Service (https://resources.marine.copernicus.eu/product-detail/MULTIOBS_GLO_PHY_TSUV_3D_MYNRT_015_012, last access: 7 June 2022) are used for sea surface temperature (SST) and mixed layer depth (MLD).

2.2 Methods

2.2.1 CALIOP data preprocessing

For CALIOP data, the backscatter signal separated by the polarization beam splitter (PBS) at 532 nm is detected by photomultiplier tubes (PMTs). Due to the transient response of the detector, the subsequently measured signal intensity following the signal peak is greater than the true backscatter signal. The measured signal should be corrected by using deconvolution as follows (Lu et al., 2014):

$$\beta'(z) = [F]^{-1}\beta(z) \tag{1}$$

where $\beta'(z)$ is the corrected backscattered signal, $\beta(z)$ is the measured signal and $[F]$ is the matrix form of the transient function.

Due to the polarization crosstalk caused by the nonideal characteristics of PBS, a portion of the parallel polarization component is transformed into the perpendicular component. The effects of crosstalk can be removed as follows:

$$\beta_{\parallel,c} = \frac{\beta_{\parallel,m}}{1 - CT} \tag{2}$$

$$\beta_{\perp,c} = \beta_{\perp,m} - CT \times \beta_{\parallel,c} \tag{3}$$

where $\beta_{\parallel,c}$ and $\beta_{\perp,c}$ are corrected parallel and perpendicular signals, respectively. $\beta_{\parallel,m}$ and $\beta_{\perp,m}$ are measured parallel and perpendicular signals, respectively.

Then, the subsurface column-integrated backscatter of the perpendicular components, βw_+ can be calculated as follows (Behrenfeld et al., 2013):

$$\beta_{W+} = \delta_T \frac{\beta_S}{1 - 10\delta_T} \tag{4}$$

where, βs is the lidar surface backscatter that can be evaluated using co-located surface wind speed (Hu et al., 2008). δ_T is the total column-integrated depolarization ratio that can be calculated as follows (Dionisi et al., 2020):

$$\delta_T = \frac{\sum_{i=p}^{i=p+2} \beta_{\perp,c}}{\sum_{i=p}^{i=p+2} \beta_{\parallel,c}} \tag{5}$$

where p is the range bin of the peak surface return.

Generally, CALIOP bbp estimates were based on $\beta;w_+$, which has $b_{bp}^{CALIOP} \approx \frac{\beta_{w+}}{0.32 * 0.98^2}$ (Bisson et al., 2021). However, the conversion coefficient of 0.32 has its uncertainty and inconsistency. This value was reported as 1.43 in some studies (Sullivan and Twardowski, 2009; Zhang et al., 2014), or 1.06 in some other studies (Lee et al., 2013; Churnside et al., 2014; Churnside and Marchbanks, 2015). While others reported a value of 0.5 (Boss and Pegau, 2001; Chami et al., 2006; Whitmire et al., 2010). The variability of the conversion coefficient may introduce uncertainties to the retrieval of CALIOP bbp. Compared with previous studies, the nonlinear deep neural network algorithm does not require predetermined knowledge, which could be an effective alternative method.

2.2.2 Network configuration and evaluation protocol

In previous studies, CALIOP bbp was calculated based on $\beta;w_+$ (Lu et al., 2014; Bisson et al., 2021). Then, POC and phytoplankton biomass were estimated based on CALIOP bbp (Behrenfeld et al., 2013; Behrenfeld et al., 2017). The FFNN algorithm is used here to derive bbp, POC, and Chl from $\beta;w_+$ directly. Previous studies showed that δ_T parameters can provide valuable information about bbp and Chl (Dionisi et al., 2020). Overall, $\beta;w_+$, δ_T and latitude are used as input variables (or predictors). The FFNN algorithm could adjust the relationship between the output and CALIOP variables in terms of latitude (Murphy and Hu, 2021). As shown in Figure 1, a multilayer perceptron using a backpropagation network (MLP BPN) is used for the FFNN model. The model comprises an input layer, 10 hidden layers, and an output layer. The hidden layers have 100 nodes each. The configuration of the model is based on a series of tests and their statistical results. A sigmoid function was chosen as an activation function for neurons in hidden layers (Sharma et al., 2020), and a linear function was used for the output layer to generate the final results. The model was trained by using the optimization algorithm of root mean square prop (RMSprop) which divides the gradient by a running average of its recent magnitude (Hinton et al., 2012). In this study, CALIPSO lidar backscatter measurements at daytime in 2008 and collocated b_{bp}, POC, and Chl products from Aqua/MODIS are used for the training model. CALIOP variables are averaged 9 km along-track to match the MODIS data. There are 1,144,878 matched

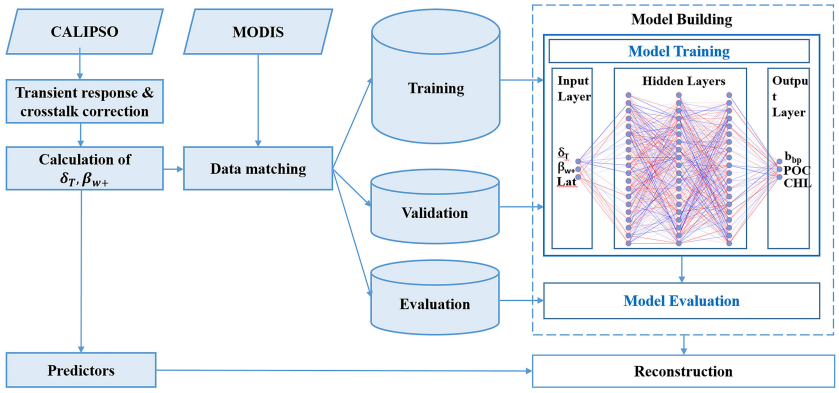


FIGURE 1
Flow chart of the FFNN including its architecture.

points and the dataset was randomly divided into 70% for FFNN training, 15% for model validation, and 15% for its evaluation. The evaluation data did not participate in the training. As shown in Supplementary Figure 2, the matched data cover almost all of the global oceans. Then, the FFNN algorithm is applied to b_{bp}, POC, and Chl inversion between 2008 and 2021.

2.2.3 Evaluation metrics

Coefficient of determination (R^2), root mean square error (RMSE), bias, mean absolute (MAE), and mean absolute percentage error (MAPE) are used to evaluate the results as follows:

$$R^2 = 1 - \frac{\sum (y_i - f_i)^2}{\sum (y_i - \bar{y})^2} \tag{6}$$

$$RMSE = \sqrt{\frac{\sum (y_i - f_i)^2}{N}} \tag{7}$$

$$\text{bias} = \frac{1}{N}\sum (y_i - x_i) \tag{8}$$

$$MAE = \frac{1}{N}\sum |y_i - x_i| \tag{9}$$

$$MAPE = \frac{1}{N}\sum \frac{|y_i - x_i|}{x_i} \tag{10}$$

where x_i is the true value, y_i is the prediction, f_i is the linear regression of y_i, and $\bar{y}$ is mean of y_i.

Linear correlation coefficient (r) is calculated to measure the strength of the linear relationship between phytoplankton parameters (Y) and marine environmental factors (X) as follows:

$$r = \frac{cov(XY)}{\sigma(X)\sigma(Y)} \tag{11}$$

where σ is the standard deviation of variables and $cov(*)$is their covariance.

3 Results

3.1 FFNN training results and model evaluation

The training process including the decreases in losses and increases in R^2 is shown in Figure 2. An early stopping callback was used when the losses of the model used for validation data are no longer reduced. The early stopping callback could avoid overfitting effectively. Generally, the R^2 of the validation data for bbp, POC, and Chl could be around 0.8. The evaluation of the model is shown in Figure 3. The subset of data used for evaluation did not participate in the training. Therefore, the evaluation data represented independent observations. The RMSE and R^2 of bbp are 0.0011 m^{-1} and 0.75, respectively. The RMSE and R^2 of POC are 36.74 mg/m^3 and 0.82, respectively. The RMSE and R^2 of Chl are 1.3 mg/m^3 and 0.84, respectively. Overall, the FFNN results have a good agreement with MODIS products.

Figure 4 shows the spatial distribution of climatologically averaged CALIOP bbp and MODIS bbp in polar regions in summer (the Arctic in June, July, and August; the Antarctic in December, January, and February) from 2009 and 2021, which did not participate in the development of the model. The results of CALIOP have similar spatial distribution compared with MODIS products. The percent difference shown in Figures 4C, F is around

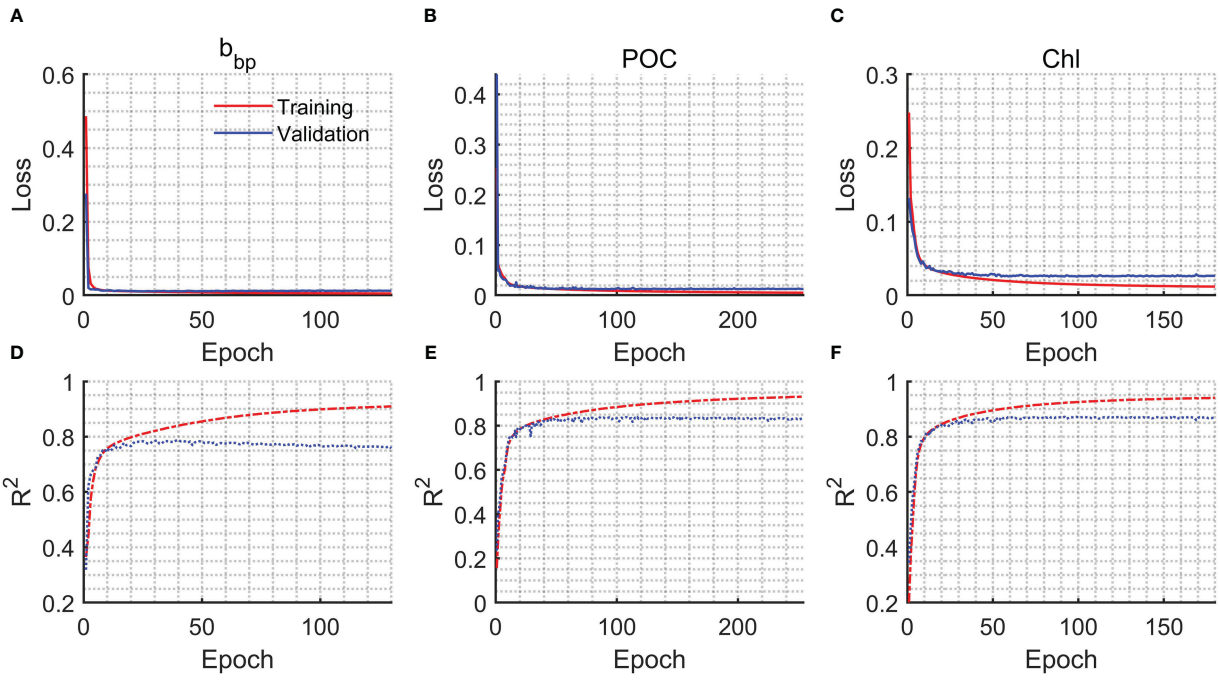


FIGURE 2
Loss and R2 versus epoch during the model training. **(A)** Loss of bbp, **(B)** loss of POC, **(C)** loss of Chl, **(D)** R2 of bbp, **(E)** R2 of POC, and **(F)** R2 of Chl.

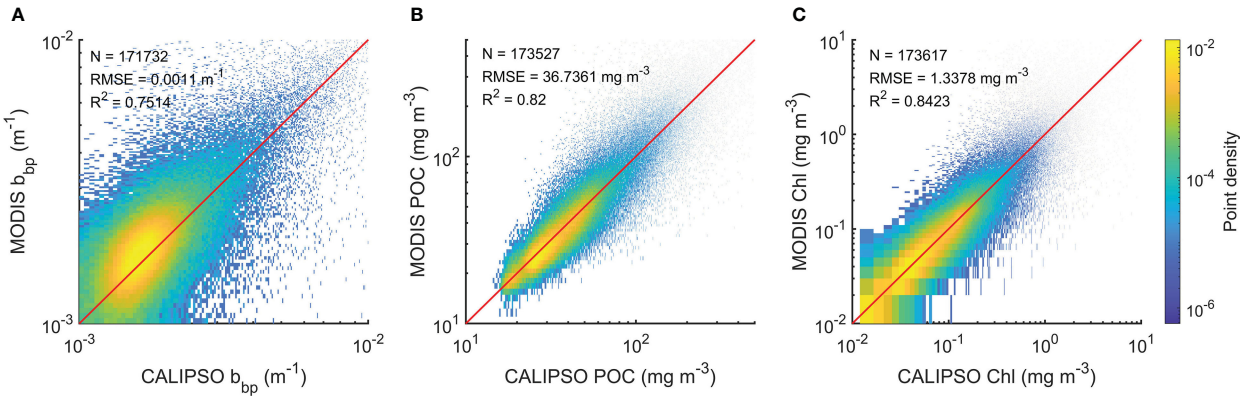


FIGURE 3
Evaluation of FFNN model. **(A)** Evaluation of bbp, **(B)** evaluation of POC, and **(C)** evaluation of Chl.

10%. Besides, the comparison with the Oregon State University (OSU) bbp data produced in previous studies (Behrenfeld et al., 2019), which can be downloaded from http://orca.science.oregonstate.edu/lidar_public_v2.php (accessed on 20 August 2022), is shown in Supplementary Figure 3. DNN-based CALIOP bbp have similar results and spatial distribution compared with previous studies in a global scale, but more details have been retained. The comparison of Chl between CALIOP and MODIS is shown in Figure 5. The difference in the Antarctic is slightly greater than that in the Arctic. But the percent difference is less than 25% shown in Figure 5F. The similar spatial distribution of POC between CALIOP and POC can be found in Figure 6. The results indicate that the FFNN method is effective for bbp, Chl, and POC inversion.

Figure 7 shows the data distribution in winter (the Arctic in December; the Antarctic in June). The deep blue represents the sea ice and the green color represents the distribution of Chl. It is clear that MODIS has poor coverage in polar regions in winter. Oppositely, CALIOP can observe high-latitude ocean areas even during lengthy polar nights. Therefore, CALIOP measurements can be a useful technique to study the phytoplankton and POC in polar areas.

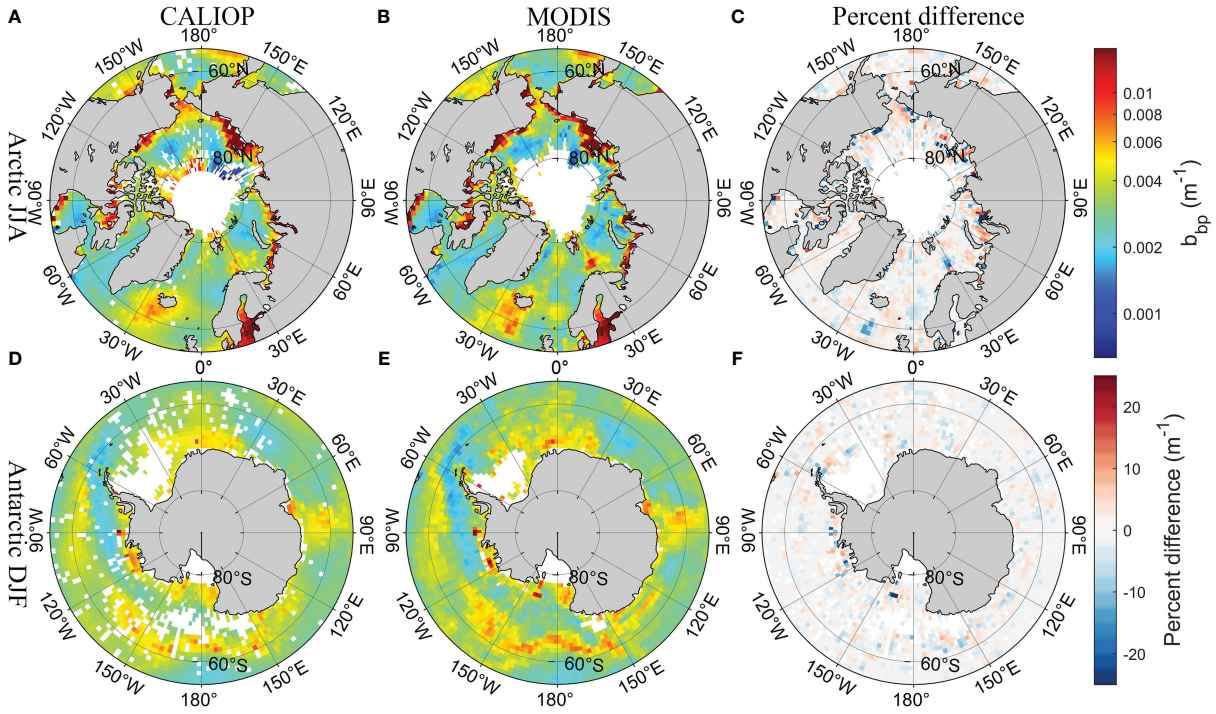


FIGURE 4
Comparisons of seasonal CALIOP bbp with MODIS bbp in polar regions in summer. **(A)** CALIOP bbp in the Arctic, **(B)** MODIS bbp in the Arctic, **(C)** percent difference between CALIOP bbp and MODIS bbp in the Arctic, **(D)** CALIOP bbp in the Antarctic, **(E)** MODIS bbp in the Antarctic, and **(F)** percent difference between CALIOP bbp and MODIS bbp in the Antarctic.

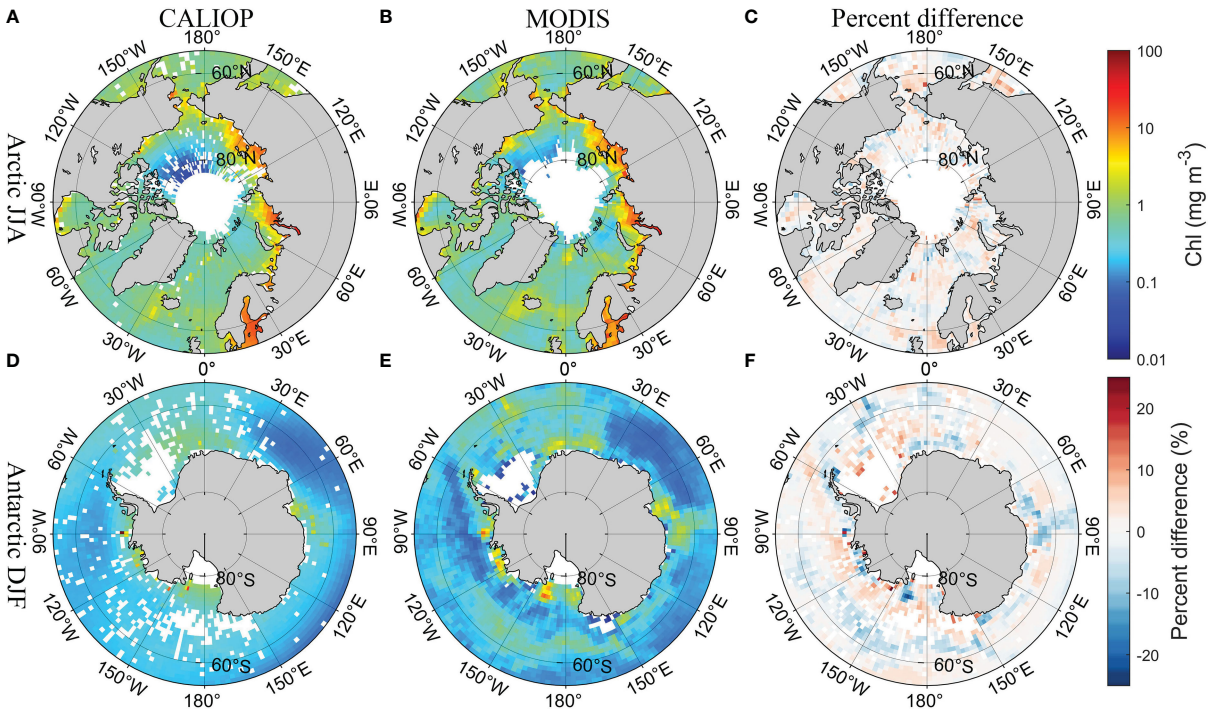


FIGURE 5
Comparisons of seasonal CALIOP Chl with MODIS Chl in polar regions in summer. **(A)** CALIOP Chl in the Arctic, **(B)** MODIS Chl in the Arctic, **(C)** percent difference between CALIOP Chl and MODIS Chl in the Arctic, **(D)** CALIOP Chl in the Antarctic, **(E)** MODIS Chl in the Antarctic, and **(F)** percent difference between CALIOP Chl and MODIS Chl in the Antarctic.

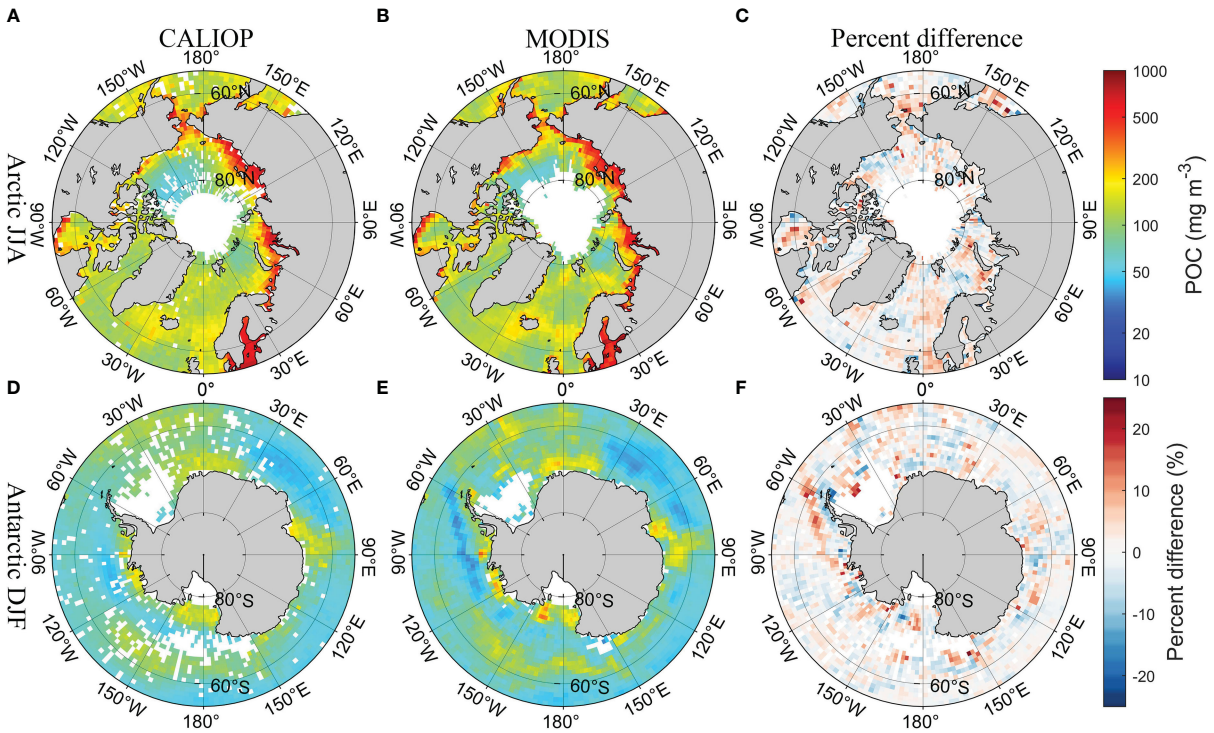


FIGURE 6
Comparisons of seasonal CALIOP POC with MODIS POC in polar regions in summer. **(A)** CALIOP POC in the Arctic, **(B)** MODIS POC in the Arctic, **(C)** percent difference between CALIOP POC and MODIS POC in the Arctic, **(D)** CALIOP POC in the Antarctic, **(E)** MODIS POC in the Antarctic, and **(F)** percent difference between CALIOP POC and MODIS POC in the Antarctic.

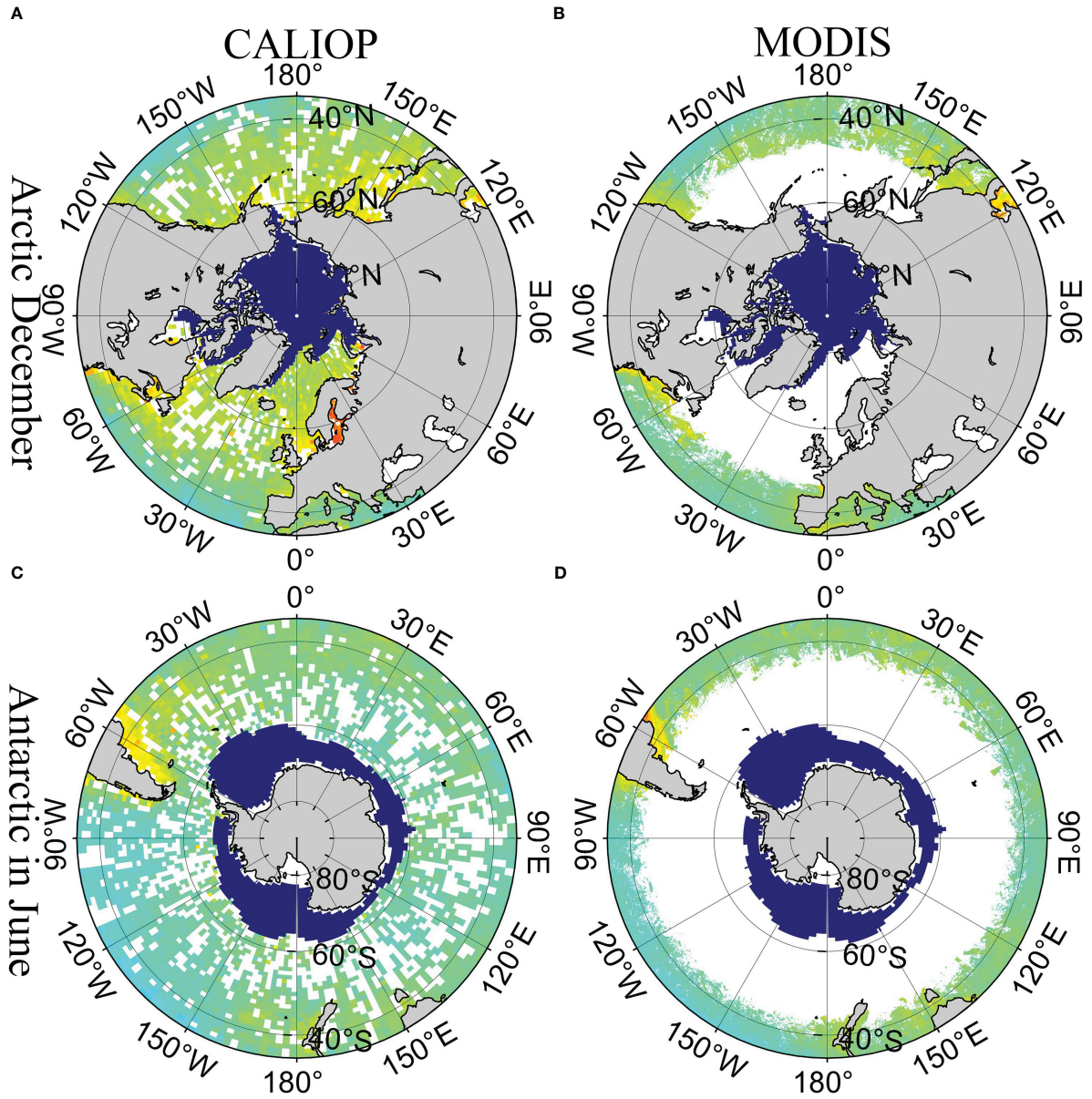


FIGURE 7
Distribution of CALIOP and MODIS in polar region in winter. **(A)** CALIOP data in the Arctic in December, **(B)** MODIS data in the Arctic in December, **(C)** CALIOP data in the Antarctic in June, and **(D)** MODIS data in the Antarctic in June. The deep blue represents the sea ice. The green color represents the Chl.

3.2 *In situ* validation

Figure 8 shows the matched data between Argo Chl and Chl derived from CALIOP and MODIS from 2010 to 2021. The data are matched if they fall within 9 km and occur within 12 hours of each other. The blue and red circles in Figure 8 represent the matched data point of CALIOP and MODIS, respectively. Dashed lines represent the best-fit functions and a green solid line represents the 1:1 line. There are 134 matched points in total and they are distributed around the green line. As shown in Table 1, R^2, RMSE, MAE, and MAPE between CALIOP and Argo are 0.5153, 0.6740, 0.5342, and 42.17%. The corresponding values of MODIS is 0.5902, 0.6379, 0.5150 and 38.82%. The biases of MODIS and CALIOP are 0.0972 and 0.0549, respectively. The Chl derived from CALIOP and MODIS agrees with the *in situ* measurements. The similar metrics with previous studies (Marrari et al., 2006; Moore et al., 2009; Hu et al., 2012; Moutier et al., 2019) indicate the FFNN algorithm can be used for retrieval of Chl from CALIOP.

3.3 Interannual variability

A spatial average of month Chl, bbp, and POC in polar regions has been performed to assess interannual variability. A large interannual variability and an apparent seasonal cycle in the average values can be found in Figure 9. In Arctic areas, Chl, bbp, and POC usually begin to increase in January and reach the maximum in summer. After that, the values begin to decrease. In Antarctic areas, Chl, bbp, and POC usually reach the peak in winter (in the northern hemisphere) and then begin to decrease. For Chl and POC, the values in the Antarctic are generally

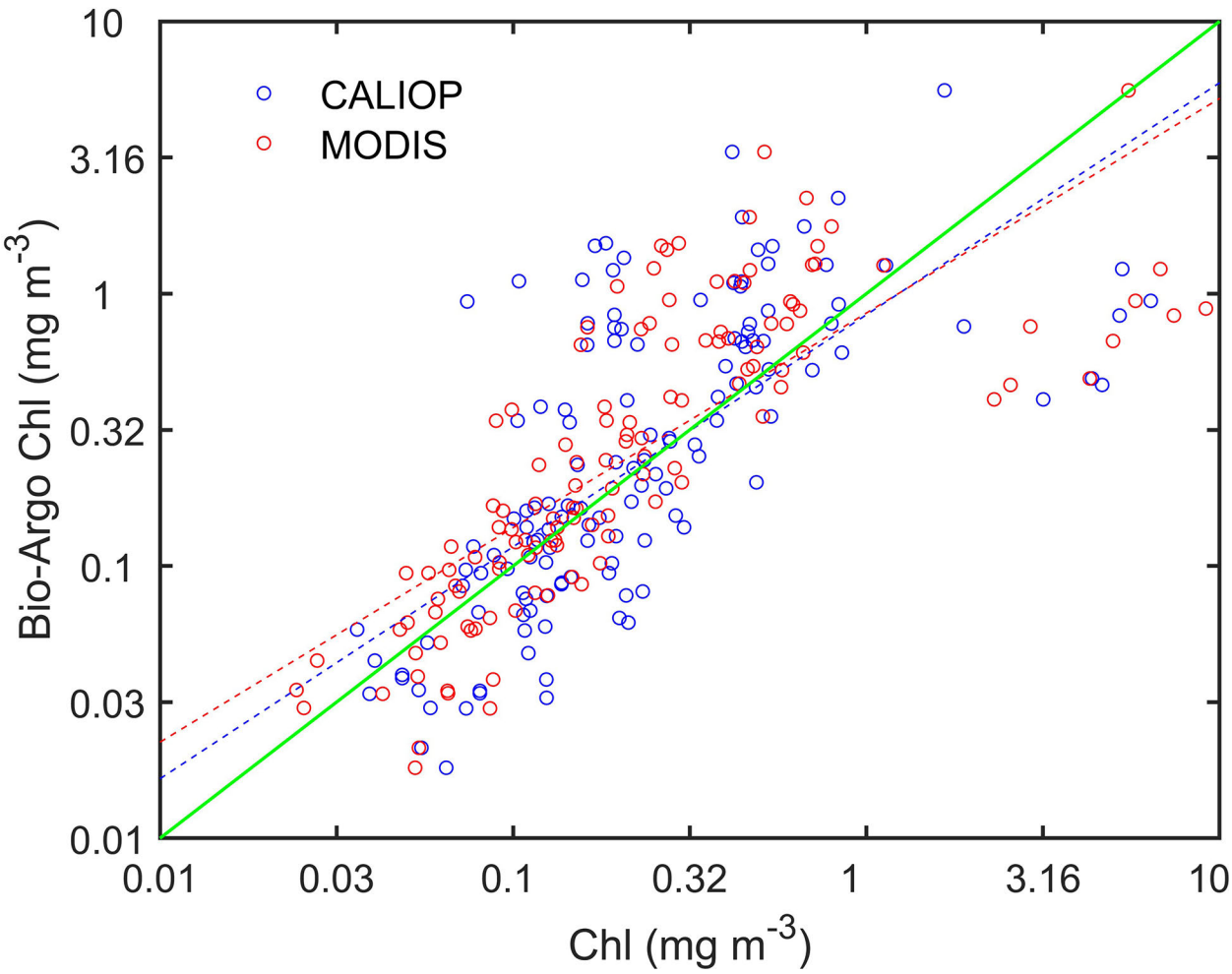


FIGURE 8
Matched data between Argo Chl and Chl produced by CALIOP and MODIS. The blue and red circles represent the matched data point of CALIOP and MODIS, respectively. Dashed lines represent the best-fit functions and a green solid line represents the 1:1 line.

smaller than the values in the Arctic. Even the maximum values in the Antarctic are still smaller than the minimum values in the Arctic. The results show that the Arctic region may have a more productive ecosystem, which is consistent with previous studies in which phytoplankton biomass in north polar zone is much greater than that in south polar zone (Behrenfeld et al., 2017) Besides, some previous studies show that Chl in Arctic ocean is greater than that in Southern Ocean (Lewis et al., 2016; Behera et al., 2020).as well. For bbp, there are usually two peaks in Arctic areas as shown in Figure 9B. The first peak is usually the maximum and occurs in July. The second peak is smaller and occurs in October. The specific month in which the Chl concentration, bbp, and POC reach the maximum values each year is shown in Figure 10. The maximum in the Antarctic occurs at a more concentrated time, usually in winter (north hemisphere), more specifically, in January. The time may shift to December or February in some years. The month in which the maximum of Chl concentration, bbp, and POC occurs is more consistent. However, the results in the Arctic are more complicated. The maximum can occur in any month from May to October, not just in summer. In some years such as 2007, 2019, and 2020, Chl, bbp, and POC can reach their maximum simultaneously. But in some years, the months in which maximum values occur are different. For example, the bbp reached its peak in June 2014. Then, the Chl reached its maximum in July subsequently and the maximum of POC occurred in August at last. The results show that there is a certain connection between Chl, bbp, and POC, but there are some subtle differences between them.

TABLE 1 Statistical analysis results of *in situ* Chl and remote sensing measurements.

	R^2	RMSE (mg m^{-3})	bias (mg m^{-3})	MAE (mg m^{-3})	MAPE
Argo vs MODIS	0.5912	0.6379	0.0972	0.5150	42.17%
Argo vs CALIOP	0.5153	0.6740	0.0549	0.5342	38.82%

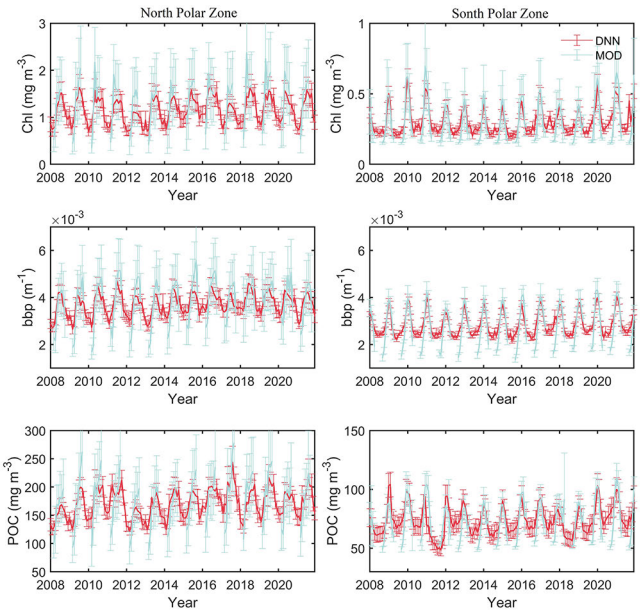


FIGURE 9
(Top) CALIOP-derived Chl spatial average in polar regions during 2007-2021. (Middle) bbp average in polar regions. (Bottom) POC average in polar regions.

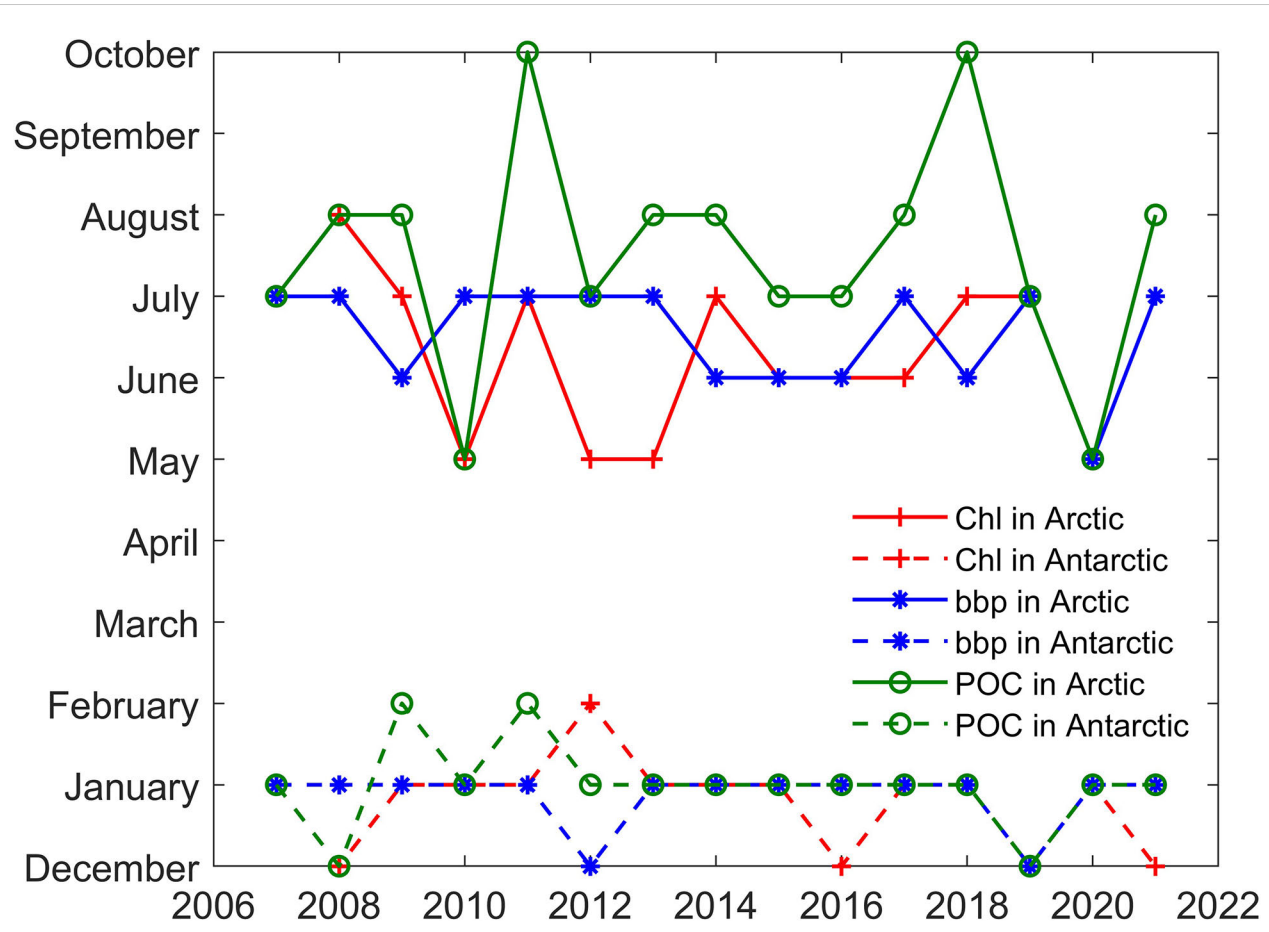


FIGURE 10
Month in which the Chl concentration, bbp, and POC reach the maximum values each year.

4 Discussion

The monthly change rate defined as $dx_m = x_m - x_{m-1}$ is calculated for Chl, bbp, and POC as shown in Figure 11, where m represents month. In the north polar region, the change rates of Chl and bbp usually become greater than zero from early spring when phytoplankton begin to grow. This may be caused by the combination of several factors. As shown in Figure 12, at this time the ice begins to melt, SST and PAR begin to rise, and MLD shoals. In May, the change rates of Chl and bbp reach the maximum, which indicates that phytoplankton reproduces rapidly. This may be caused by the proper PAR and SST as shown in Figure 12. The change rates of Chl and bbp usually start below zero in August, indicating the decline of phytoplankton. This is likely caused by the grazing of predators (Behrenfeld et al., 2017). The change rate of POC is much more complicated. There is no fixed month in which the change rate of POC reaches its peaks and it varies dramatically from year to year. This is related to the fluctuation of POC in the summer as shown in Figure 9. The change rate of Chl in the south polar region is much smaller than those in the north. This is largely because the prevalence of iron-limiting conditions constrains phytoplankton growth (de Baar, 2005; Boyd et al., 2007). As a result, the Chl and POC in the south are far lower than the values in the north. Table 2 shows the linear regression coefficient between bbp, Chl, POC, and environmental parameters. Note that all of the p values are less than 0.001, meaning that Chl, bbp, and POC are correlated with the SIE, PAR, SST, and MLD. But the impacts are different. It can be found that SIE and MLD have a negative impact on bbp, Chl, and POC. In terms of Chl, since the PAR has the highest correlation coefficient, it seems that phytoplankton is more affected by the light in polar areas. In fact, phytoplankton is often light-limited at higher latitudes (Riebesell et al., 2009). MLD likely has a great influence on bbp and the influence on POC of SIE in the Arctic is much greater than that in the Antarctic. The results indicate that environmentally driven factors of phytoplankton vary interannually at each pole (Behrenfeld et al., 2017).

The monthly climatological averages of Chl, bbp, POC, SIE, PAR, SST, and MLD and their corresponding change rate are shown in Figure 13. In the north polar zone, Chl, bbp, and POC begin to increase in March, after they have reached their minimum in February. In March, SIE is still increasing and reaches its maximum. The result shows that the phytoplankton blooms before the sea ice starts melting in Arctic areas. SST barely changes at this time. But PAR increases a lot in Match. Therefore, the growth of phytoplankton in spring may be largely triggered by the increase of PAR. The change rates of Chl, bbp, and POC have the maximum in May, which indicates phytoplankton blooms. Meanwhile, PAR has the largest change rate in May as well. MLD has the smallest change rate meaning that MLD shoals rapidly at this time. Then, Chl and bbp reach the peak in July and begin to decline in August subsequently. POC is still increasing in August and reaches its peak at this time. In the south polar zone, Chl, bbp, and POC begin to increase in August

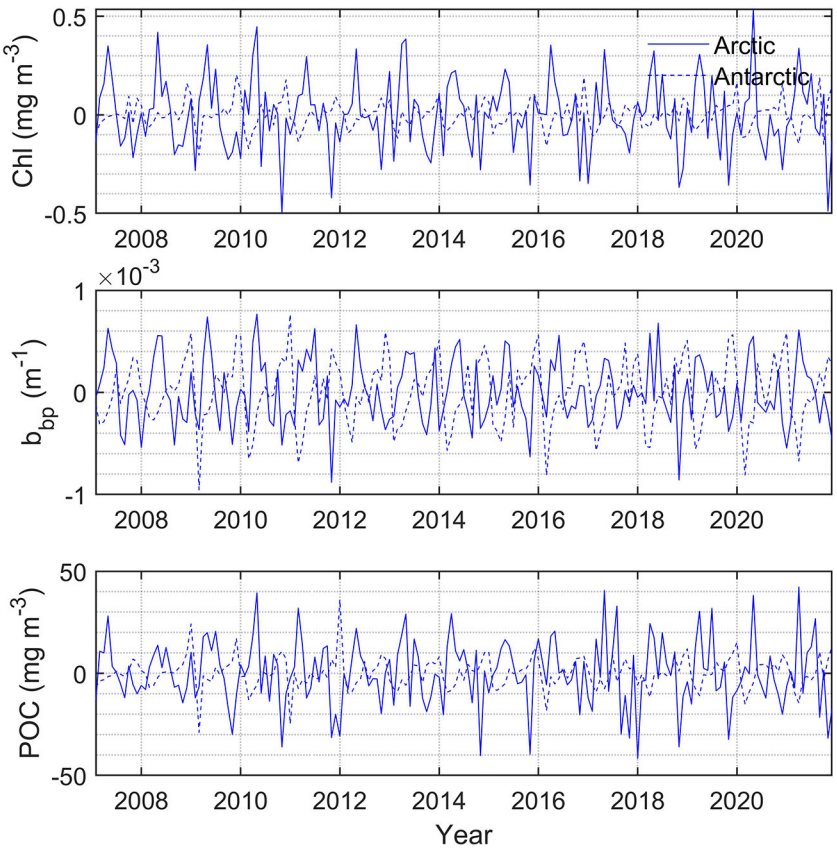


FIGURE 11
(Top) Chl change rate in polar regions during 2007-2021. (Middle) bbp change rate in polar regions. (Bottom) POC change rate in polar regions.

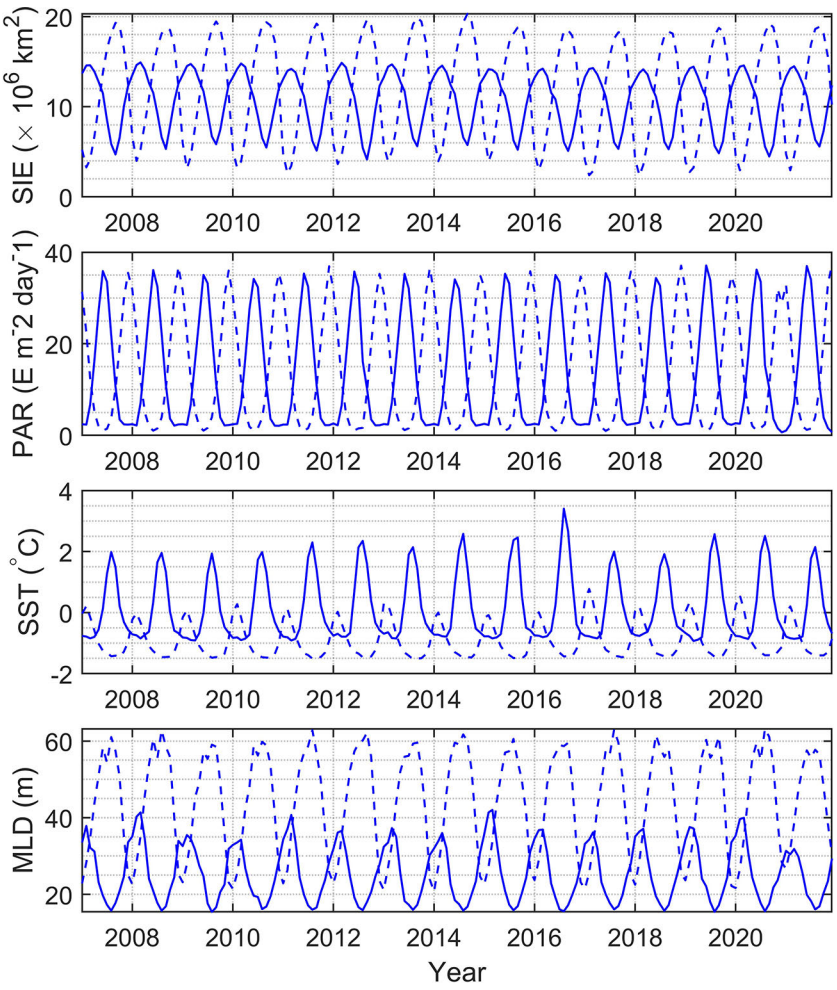


FIGURE 12
Spatial average of SIE, PAR, SST, and MLD in polar regions during 2007-2021. Solid and dashed lines represent the north and south polar zones, respectively.

when SIE is still increasing and SST is still decreasing. PAR begins to increase. Then Chl, bbp, and POC reach their maximums in January simultaneously. It can be found that Chl, bbp, and POC have a stronger correlation in Antarctic areas compared with Arctic areas. The results indicate that Chl, bbp, and POC have similar interannual variability but there are some subtle differences between them.

The total uncertainty (E) of DNN products can be expressed as the root of the squared sum of uncertainties stemming from measurement (M), representation (R), and prediction (P) errors: $E = \sqrt{M^2 + R^2 + P^2}$ (Gregor and Gruber, 2021). The measurement error includes the potential biases from the measurement MODIS and CALIOP data. The uncertainties of CALIOP δ_T and $\beta; w_+$ are about 1% and 10%, respectively(Lu et al., 2014). The uncertainty of MODIS bbp is approximately 30% (Bisson et al., 2019). The uncertainty of MODIS Chl is approximately 35% (Moore et al., 2009). The uncertainty of MODIS POC is approximately 25% (Evers-King et al., 2017). Therefore, the measurement errors of CALIOP-based bbp, Chl and POC are 32%, 36% and 27%, respectively. As the result of the fact that we developed the DNN model on a grid that is in many places coarser in time and space than the typical scales of variabilities of MODIS, the representation error is commonly assumed to be normally distributed with a bias of 0 on a global average (Gregor and Gruber, 2021). The prediction error is approximately 18% according to the validation data. Overall, the total uncertainties of CALIOP-based bbp, Chl and POC are 37%, 40% and 32%, respectively.

5 Conclusions

We proposed a new FFNN model for the retrieval of bbp, Chl, and POC from CALIOP. This data-based approach does not require additional assumptions regarding the relationship between b_{bp} and b(π). The FFNN is trained using the CALIPSO total ocean column-integrated depolarization ratio and subsurface column-integrated perpendicular backscatter together with collocated MODIS products. Non-linear relationship between lidar signal and bio-optical parameters was estimated through FFNN. Validation with independent data between CALIOP and MODIS with RMSE and R^2 of bbp are 0.0011 m^{-1} and 0.75, those of POC are 36.7 mg/m^3 and 0.82, and those of Chl are 1.3 mg/m^3 and 0.84, indicates that the retrieval results agree well with MODIS products and *in-situ* BGC-Argo data. In order to assess the model further, it was compared to *in situ* Argo Chl with R^2, RMSE, MAE, and MAPE between CALIOP and Argo are 0.5153, 0.6740,

10.3389/fmars.2023.1050087

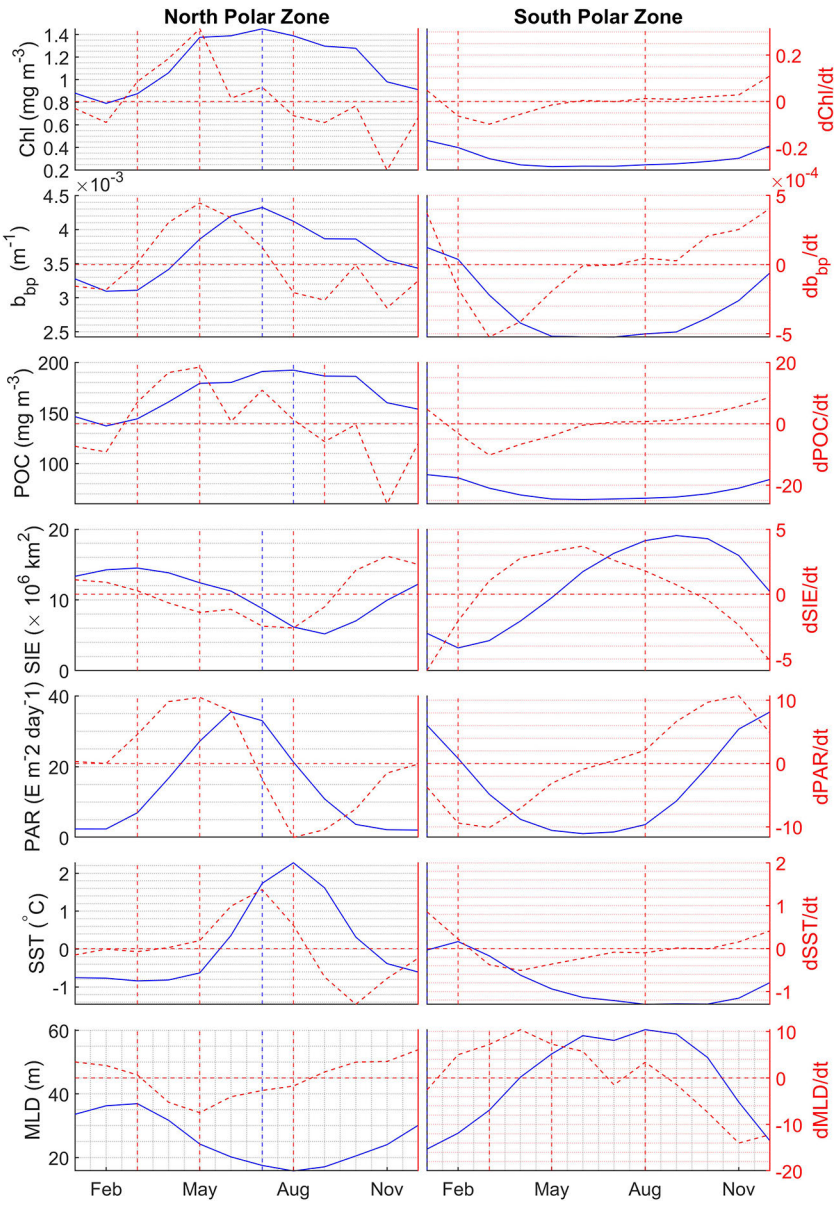


FIGURE 13
Monthly climatological average of Chl, bbp, POC, SIE, PAR, SST, and MLD represented by the blue solid lines, and their corresponding change rate represented by red dashed lines in the north polar zone (left panel) and south polar zone (right panel). Vertical lines represent the maximum values and the turning point when values begin to reduce or increase.

TABLE 2 Linear correlation coefficient between monthly average Chl, bbp, POC, and SIE, PAR, SST, MLD (N=178).

		SIE	PAR	SST	MLD
North polar region	Chl	-0.59	0.70	0.63	-0.75
	bbp	-0.62	0.66	0.68	-0.78
	POC	-0.63	0.49	0.61	-0.71
South polar region	Chl	-0.48	0.72	0.60	-0.76
	bbp	-0.63	0.79	0.76	-0.90
	POC	-0.46	0.64	0.58	-0.71

0.5342, and 42.17%, which demonstrates the effectiveness of the model. The performance of CALIOP product is close to MODIS after comparing it with Argo data. A merge product derived by combined active and passive remote sensing data could have a greater coverage and the algorithm used for the merge product will be further studied in the future to improve and produce the merge product.

Apparent seasonal cycles of phytoplankton can be observed. It was found that Chl, bbp, and POC have similar interannual variability but there are some subtle differences between them. Chl, bbp, and POC have a stronger correlation in Antarctic areas compared with Arctic areas. The combined analysis of bbp, Chl, and POC contributes to a comprehensive understanding of interannual variability in the ecosystem in polar regions. The coincidence of phytoplankton changes with PAR and the high linear regression coefficient indicates that sunlight is one key factor governing phytoplankton growth in polar regions. Future work should address the spatial variation of phytoplankton in polar regions.

Data availability statement

The original contributions presented in the study are included in the article/Supplementary Material. Further inquiries can be directed to the corresponding author.

Author contributions

ZZ: Conceptualization, Realization, and Writing-Original draft. PC: Supervision, Methodology, Reviewing. CX: Validation, Editing. CZ: Reviewing and Editing. MS: Validation and Editing. SZ: Editing. SC: Editing. DW: Editing. All authors contributed to the article and approved the submitted version.

Funding

National Key Research and Development Program of China (2022YFB3901703). This research was funded by the Key Special Project for Introduced Talents Team of Southern Marine Science and Engineering Guangdong Laboratory (GML2021GD0809), the National Natural Science Foundation (42276180; 41901305; 61991453), and the Key Research and Development Program of Zhejiang Province (2020C03100).

Acknowledgments

The authors gratefully acknowledge the NASA Langley Research Center for providing CALIOP data through the Atmospheric Science Data Center (https://asdc.larc.nasa.gov/data/CALIPSO/). We are grateful to the NASA Ocean Biology Processing Group for providing MODIS products (https://oceandata.sci.gsfc.nasa.gov/) and biogeochemical-Argo data from the Argo Data Assembly Center (ftp://ftp.ifremer.fr/ifremer/argo/dac/). We thank the reviewers for their suggestions, which significantly improved the presentation of the paper.

Conflict of interest

The authors declare that the research was conducted in the absence of any commercial or financial relationships that could be construed as a potential conflict of interest.

Publisher's note

All claims expressed in this article are solely those of the authors and do not necessarily represent those of their affiliated organizations, or those of the publisher, the editors and the reviewers. Any product that may be evaluated in this article, or claim that may be made by its manufacturer, is not guaranteed or endorsed by the publisher.

Supplementary material

The Supplementary Material for this article can be found online at: https://www.frontiersin.org/articles/10.3389/fmars.2023.1050087/full#supplementary-material

SUPPLEMENTARY FIGURE 1
The spatial distribution of in situ data **(A)** and histograms of all data **(B)** and matched data **(C)**.

SUPPLEMENTARY FIGURE 2
Point density of the matched data. **(A)** training data; **(B)** validation data; **(C)** evaluation data.

SUPPLEMENTARY FIGURE 3
Comparison between DNN-based CALIOP products with Oregon State University (OSU) CALIOP products in 2009. **(A)** DNN products **(B)** OSU products.

References

Alvera-Azcárate, A., van der Zande, D., Barth, A., Troupin, C., Martin, S., and Beckers, J.-M. (2021). Analysis of 23 years of daily cloud-free chlorophyll and suspended particulate matter in the greater north Sea. *Front. Mar. Sci.* 8. doi: 10.3389/fmars.2021.707632

Behera, N., Swain, D., and Sil, S. (2020). Effect of Antarctic sea ice on chlorophyll concentration in the southern ocean. *Deep Sea Res. Part II: Topical Stud. Oceanogr.* 178, 104853. doi: 10.1016/j.dsr2.2020.104853

Behrenfeld, M. J., Gaube, P., Della Penna, A., O'Malley, R. T., Burt, W. J., Hu, Y., et al. (2019). Global satellite-observed daily vertical migrations of ocean animals. *Nature* 576 (7786), 257–261. doi: 10.1038/s41586-019-1796-9

Behrenfeld, M. J., Hu, Y., Hostetler, C. A., Dall'Olmo, G., Rodier, S. D., Hair, J. W., et al. (2013). Space-based lidar measurements of global ocean carbon stocks. *Geophys. Res. Lett.* 40 (16), 4355–4360. doi: 10.1002/grl.50816

Behrenfeld, M. J., Hu, Y., O'Malley, R. T., Boss, E. S., Hostetler, C. A., Siegel, D. A., et al. (2017). Annual boom–bust cycles of polar phytoplankton biomass revealed by space-based lidar. *Nat. Geosci.* 10 (2), 118–122. doi: 10.1038/ngeo2861

Bell, B., Hersbach, H., Simmons, A., Berrisford, P., Dahlgren, P., Horányi, A., et al. (2021). The ERA5 global reanalysis: Preliminary extension to 1950. *Q. J. R. Meteorological Soc.* 147 (741), 4186–4227. doi: 10.1002/qj.4174

Berthon, J. F., Shybanov, E., Lee, E. G., and Zibordi, G. (2007). Measurements and modeling of the volume scattering function in the coastal northern Adriatic Sea. *Appl. Optics* 46 (22), 5189–5203. doi: 10.1364/AO.46.005189

Bisson, K. M., Boss, E., Werdell, P. J., Ibrahim, A., and Behrenfeld, M. J. (2021). Particulate backscattering in the global ocean: A comparison of independent assessments. *Geophys. Res. Lett.* 48 (2), e2020GL090909. doi: 10.1029/2020gl090909

Bisson, K. M., Boss, E., Westberry, T. K., and Behrenfeld, M. J. (2019). Evaluating satellite estimates of particulate backscatter in the global open ocean using autonomous profiling floats. *Opt Express* 27 (21), 30191–30203. doi: 10.1364/OE.27.030191

Blondeau-Patissier, D., Gower, J. F. R., Dekker, A. G., Phinn, S. R., and Brando, V. E. (2014). A review of ocean color remote sensing methods and statistical techniques for the detection, mapping and analysis of phytoplankton blooms in coastal and open oceans. *Prog. Oceanogr.* 123, 123–144. doi: 10.1016/j.pocean.2013.12.008

Boss, E., and Pegau, W.S.J.A.O. (2001). Relationship of light scattering at an angle in the backward direction to the backscattering coefficient. *Applied Optics* 40 (30), 5503–5507. doi: 10.1364/AO.40.005503

Boyd, P. W., Jickells, T., Law, C. S., Blain, S., Boyle, E. A., Buesseler, K. O., et al. (2007). Mesoscale iron enrichment experiments 1993-2005: synthesis and future directions. *Science* 315 (5812), 612–617. doi: 10.1126/science.1131669

Brewin, R. J. W., Ciavatta, S., Sathyendranath, S., Jackson, T., Tilstone, G., Curran, K., et al. (2017). Uncertainty in ocean-color estimates of chlorophyll for phytoplankton groups. *Front. Mar. Sci.* 4. doi: 10.3389/fmars.2017.0010

Capuzzo, E., Lynam, C. P., Barry, J., Stephens, D., Forster, R. M., Greenwood, N., et al. (2018). A decline in primary production in the north Sea over 25 years, associated with reductions in zooplankton abundance and fish stock recruitment. *Glob Chang Biol.* 24 (1), e352–e364. doi: 10.1111/gcb.13916

Chami, M., Marken, E., Stamnes, J., Khomenko, G., and Korotaev, G. (2006). Variability of the relationship between the particulate backscattering coefficient and the volume scattering function measured at fixed angles 111 (C5). doi: 10.1029/2005JC003230

Chami, M., Thirouard, A., and Harmel, T. (2014). POLVSM (Polarized volume scattering meter) instrument: an innovative device to measure the directional and polarized scattering properties of hydrosols. *Optics Express* 22 (21), 26403–26428. doi: 10.1364/OE.22.026403

Churnside, J. H., and Marchbanks, R. D. (2015). Subsurface plankton layers in the Arctic ocean. *Geophys. Res. Lett.* 42 (12), 4896–4902. doi: 10.1002/2015gl064503

Churnside, J. H., Sullivan, J. M., and Twardowski, M. S. (2014). Lidar extinction-to-backscatter ratio of the ocean. *Optics express* 22 (15), 18698–18706. doi: 10.1364/OE.22.018698

Claustre, H., Johnson, K. S., and Takeshita, Y. (2019). Observing the global ocean with biogeochemical-argo. *Annu. Rev. Mar. Sci.* 12 (1), 23–48. doi: 10.1146/annurev-marine-010419-010956

de Baar, H. J. W. (2005). Synthesis of iron fertilization experiments: From the iron age in the age of enlightenment. *J. Geophys. Res.* 110 (C9). doi: 10.1029/2004jc002601

Dickey, T., Lewis, M., and Chang, G. (2006). Optical oceanography: Recent advances and future directions using global remote sensing and *in situ* observations. *Rev. Geophys.* 44 (1). doi: 10.1029/2003RG000148

Dionisi, D., Brando, V. E., Volpe, G., Colella, S., and Santoleri, R. (2020). Seasonal distributions of ocean particulate optical properties from spaceborne lidar measurements in Mediterranean and black sea. *Remote Sens. Environ.* 247, 111889. doi: 10.1016/j.rse.2020.111889

Evers-King, H., Martinez-Vicente, V., Brewin, R. J. W., Dall'Olmo, G., Hickman, A. E., Jackson, T., et al. (2017). Validation and intercomparison of ocean color algorithms for estimating particulate organic carbon in the oceans. *Front. Mar. Sci.* 4. doi: 10.3389/fmars.2017.00251

Frouin, R. J., Frouin, R., McPherson, J., Ueyoshi, K., Franz, B. A., Ebuchi, N., et al. (2012). "A time series of photosynthetically available radiation at the ocean surface from SeaWiFS and MODIS data," in *Remote sensing of the marine environment II* (Kyoto, Japan: Proc.SPIE).

Getzewich, B. J., Vaughan, M. A., Hunt, W. H., Avery, M. A., Powell, K. A., Tackett, J. L., et al. (2018). CALIPSO lidar calibration at 532 nm: version 4 daytime algorithm. *Atmospheric Measurement Techniques* 11 (11), 6309–6326. doi: 10.5194/amt-11-6309-2018

Gordon, H. R., Clark, D. K., Mueller, J. L., and Hovis, W. A. (1980). Phytoplankton pigments from the nimbus-7 coastal zone color scanner: comparisons with surface measurements. *Science* 210 (4465), 63–66. doi: 10.1126/science.210.4465.63

Gregor, L., and Gruber, N. (2021). OceanSODA-ETHZ: A global gridded data set of the surface ocean carbonate system for seasonal to decadal studies of ocean acidification. *Earth System Sci. Data* 13 (2), 777–808. doi: 10.5194/essd-13-777-2021

Hersbach, H., Bell, B., Berrisford, P., Hirahara, S., Horányi, A., Muñoz-Sabater, J., et al. (2020). The ERA5 global reanalysis. *Q. J. R. Meteorological Soc.* 146 (730), 1999–2049. doi: 10.1002/qj.3803

Hinton, G., Srivastava, N., and Swersky, K. (2012) *Lecture 6a: Overview of mini-batch gradient descent, neural networks for machine learning, slides*. Available at: http://www.cs.toronto.edu/~tijmen/csc321/slides/lecture_slides_lec6.pdf.

Hu, C., Lee, Z., and Franz, B. (2012). Chlorophyll a algorithms for oligotrophic oceans: A novel approach based on three-band reflectance difference. *J. Geophys. Research: Oceans* 117 (C1). doi: 10.1029/2011jc007395

Hu, Y., Stamnes, K., Vaughan, M., Pelon, J., Weimer, C., Wu, D., et al. (2008). Sea Surface wind speed estimation from space-based lidar measurements. *Atmospheric Chem. Phys. Discussions* 8 (1), 2771–2793. doi: 10.5194/acpd-8-2771-2008

Hu, L., Zhang, X., Xiong, Y., Gray, D. J., and He, M. X. (2020). Variability of relationship between the volume scattering function at 180° and the backscattering coefficient for aquatic particles. *Appl. Optics* 59 (10), C31–C41. doi: 10.1364/ao.383229

Jackson, T., Sathyendranath, S., and Mélin, F. (2017). An improved optical classification scheme for the ocean colour essential climate variable and its applications. *Remote Sens. Environ.* 203, 152–161. doi: 10.1016/j.rse.2017.03.036

Jamet, C., Ibrahim, A., Ahmad, Z., Angelini, F., Babin, M., Behrenfeld, M. J., et al. (2019). Going beyond standard ocean color observations: Lidar and polarimetry. *Front. Mar. Sci.* 6. doi: 10.3389/fmars.2019.00251

Kim, M.-H., Kim, S.-W., Yoon, S.-C., and Omar, A. H. (2013). Comparison of aerosol optical depth between CALIOP and MODIS-aqua for CALIOP aerosol subtypes over the ocean. *J. Geophys. Research: Atmospheres* 118 (23), 13,241–213,252. doi: 10.1002/2013jd019527

Lee, Z., Carder, K. L., and Arnone, R. A. (2002). Deriving inherent optical properties from water color: a multiband quasi-analytical algorithm for optically deep waters. *Appl. Optics* 41 (27), 5755–5772. doi: 10.1364/AO.41.005755

Lee, J. H., Churnside, J. H., Marchbanks, R. D., Donaghay, P. L., and Sullivan, J. M. (2013). Oceanographic lidar profiles compared with estimates from *in situ* optical measurements. *Appl. Optics* 52 (4), 786–794. doi: 10.1364/AO.52.000786

Lewis, K. M., Mitchell, B. G., van Dijken, G. L., and Arrigo, K. R. (2016). Regional chlorophyll a algorithms in the Arctic ocean and their effect on satellite-derived primary production estimates. *Deep Sea Res. Part II: Topical Stud. Oceanogr.* 130, 14–27. doi: 10.1016/j.dsr2.2016.04.020

Li, X., Mao, Z., Zheng, H., Zhang, W., Yuan, D., Li, Y., et al. (2022). Process-oriented estimation of chlorophyll-a vertical profile in the Mediterranean Sea using MODIS and oceanographic float products. *Front. Mar. Sci.* 9. doi: 10.3389/fmars.2022.933680

Lu, X., Hu, Y., Trepte, C., Zeng, S., and Churnside, J. H. (2014). Ocean subsurface studies with the CALIPSO spaceborne lidar. *J. Geophys. Research: Oceans* 119 (7), 4305–4317. doi: 10.1002/2014jc009970

Maritorena, S., Siegel, D. A., and Peterson, A. R. (2002). Optimization of a semianalytical ocean color model for global-scale applications. *Appl. Optics* 41 (15), 2705–2714. doi: 10.1364/AO.41.002705

Marrari, M., Hu, C., and Daly, K. (2006). Validation of SeaWiFS chlorophyll a concentrations in the southern ocean: A revisit. *Remote Sens. Environ.* 105 (4), 367–375. doi: 10.1016/j.rse.2006.07.008

McClain, C. R. (2009). A decade of satellite ocean color observations. *Annu. Rev. Mar. Sci.* 1 (1), 19–42. doi: 10.1146/annurev.marine.010908.163650

Moore, T. S., Campbell, J. W., and Dowell, M. D. (2009). A class-based approach to characterizing and mapping the uncertainty of the MODIS ocean chlorophyll product. *Remote Sens. Environ.* 113 (11), 2424–2430. doi: 10.1016/j.rse.2009.07.016

Moutier, W., Thomalla, S., Bernard, S., Wind, G., Ryan-Keogh, T., and Smith, M. (2019). Evaluation of chlorophyll-a and POC MODIS aqua products in the southern ocean. *Remote Sens.* 11 (15), 1793. doi: 10.3390/rs11151793

Murphy, A., and Hu, Y. (2021). Retrieving aerosol optical depth and high spatial resolution ocean surface wind speed from CALIPSO: A neural network approach. *Front. Remote Sens.* 1. doi: 10.3389/frsen.2020.614029

O'Reilly, J. E., Maritorena, S., Mitchell, B. G., Siegel, D. A., Carder, K. L., Garver, S. A., et al. (1998). Ocean color chlorophyll algorithms for SeaWiFS. *J. Geophys. Research: Oceans* 103 (C11), 24937–24953. doi: 10.1029/98jc02160

Parekh, P., Dutkiewicz, S., Follows, M. J., and Ito, T. (2006). Atmospheric carbon dioxide in a less dusty world. *Geophys. Res. Lett.* 33 (3). doi: 10.1029/2005gl025098

Riebesell, U., Kortzinger, A., and Oschlies, A. (2009). Sensitivities of marine carbon fluxes to ocean change. *Proc. Natl. Acad. Sci. U.S.A.* 106 (49), 20602–20609. doi: 10.1073/pnas.0813291106

Sharma, S., Sharma, S., and Athaiya, A. (2020). Activation functions in neural networks. *Int. J. Eng. Appl. Sci. Technol.* 4 (12), 310–316.

Stramski, D., Reynolds, R. A., Babin, M., Kaczmarek, S., Lewis, M. R., Röttgers, R., et al. (2008). Relationships between the surface concentration of particulate organic carbon and optical properties in the eastern south pacific and eastern Atlantic oceans. *Biogeosciences* 5 (1), 171–201. doi: 10.5194/bg-5-171-2008

Sullivan, J. M., and Twardowski, M. S. (2009). Angular shape of the oceanic particulate volume scattering function in the backward direction. *Appl. Optics* 48 (35), 6811–6819. doi: 10.1364/AO.48.006811

Werdell, P. J., Franz, B. A., Bailey, S. W., Feldman, G. C., Boss, E., Brando, V. E., et al. (2013). Generalized ocean color inversion model for retrieving marine inherent optical properties. *Appl. Optics* 52 (10), 2019–2037. doi: 10.1364/AO.52.002019

Whitmire, A. L., Pegau, W. S., Karp-Boss, L., Boss, E., and Cowles, T. J. (2010). Spectral backscattering properties of marine phytoplankton cultures 18 (14), 15073–15093. doi: 10.1364/OE.18.015073

Winker, D. M., Vaughan, M. A., Omar, A., Hu, Y., Powell, K. A., Liu, Z., et al. (2009). Overview of the CALIPSO mission and CALIOP data processing algorithms. *J. Atmospheric Oceanic Technol.* 26 (11), 2310–2323. doi: 10.1175/2009jtecha1281.1

Xu, X., Lemmen, C., and Wirtz, K. W. (2020). Less nutrients but more phytoplankton: Long-term ecosystem dynamics of the southern north Sea. *Front. Mar. Sci.* 7. doi: 10.3389/fmars.2020.00662

Zhang, X., Boss, E., and Gray, D. J. (2014). Significance of scattering by oceanic particles at angles around 120 degree 22 (25) 31329–31336. doi: 10.1364/OE.22.031329

Zhang, X., Gray, D. J., Huot, Y., You, Y., and Bi, L. (2012). Comparison of optically derived particle size distributions: scattering over the full angular range versus diffraction at near forward angles. *Appl. Optics* 51 (21), 5085. doi: 10.1364/AO.51.005085

frontiers | Frontiers in Marine Science

TYPE Original Research
PUBLISHED 06 February 2023
DOI 10.3389/fmars.2023.1058460

Check for updates

OPEN ACCESS

EDITED BY
Astrid Bracher,
Alfred Wegener Institute Helmholtz Centre for Polar and Marine Research (AWI), Germany

REVIEWED BY
Jenny R. Hillman,
The University of Auckland, New Zealand
Maria Adelaide Ferreira,
Center for Marine and Environmental Sciences (MARE), Portugal

*CORRESPONDENCE
Alina Blume
alina@blume1.de
Dimosthenis Traganos
dimosthenis.traganos@dlr.de

SPECIALTY SECTION
This article was submitted to Ocean Observation, a section of the journal Frontiers in Marine Science

RECEIVED 30 September 2022
ACCEPTED 16 January 2023
PUBLISHED 06 February 2023

CITATION
Blume A, Pertiwi AP, Lee CB and Traganos D (2023) Bahamian seagrass extent and blue carbon accounting using Earth Observation.
Front. Mar. Sci. 10:1058460.
doi: 10.3389/fmars.2023.1058460

COPYRIGHT
© 2023 Blume, Pertiwi, Lee and Traganos. This is an open-access article distributed under the terms of the Creative Commons Attribution License (CC BY). The use, distribution or reproduction in other forums is permitted, provided the original author(s) and the copyright owner(s) are credited and that the original publication in this journal is cited, in accordance with accepted academic practice. No use, distribution or reproduction is permitted which does not comply with these terms.

Bahamian seagrass extent and blue carbon accounting using Earth Observation

Alina Blume*, Avi Putri Pertiwi, Chengfa Benjamin Lee and Dimosthenis Traganos*

German Aerospace Center (DLR), Remote Sensing Technology Institute, Photogrammetry and Image Analysis Department, Berlin, Germany

Seagrasses are among the world's most productive ecosystems due to their vast 'blue' carbon sequestration rates and stocks, yet have a largely untapped potential for climate change mitigation and national climate agendas like the Nationally Determined Contributions of the Paris Agreement. To account for the value of seagrasses for these agendas, spatially explicit high-confidence seagrass ecosystem assessments guided by nationally aggregated data are necessary. Modern Earth Observation advances could provide a scalable technological solution to assess the national extent and blue carbon service of seagrass ecosystems. Here, we developed and applied a scalable Earth Observation framework within the Google Earth Engine cloud computing platform to account the national extent, blue carbon stock and sequestration rate of seagrass ecosystems across the shallow waters of The Bahamas—113,037 km^2. Our geospatial ecosystem extent accounting was based on big multi-temporal data analytics of over 18,000 10-m Sentinel-2 images acquired between 2017-2021, and deep feature engineering of multi-temporal spectral, color, object-based and textural metrics with Random Forests machine learning classification. The extent accounting was trained and validated using a nationwide reference data synthesis based on human-guided image annotation, recent space-borne benthic habitat maps, and field data collections. Bahamian seagrass carbon stocks and sequestration rates were quantified using region-specific *in-situ* seagrass blue carbon data. The mapped Bahamian seagrass extent covers an area up to 46,792 km^2, translating into a carbon storage of 723 Mg C, and a sequestration rate of 123 Mt CO_2 annually. This equals up to 68 times the amount of CO_2 emitted by The Bahamas in 2018, potentially rendering the country carbon-neutral. The developed accounts fill a vast mapping blank in the global seagrass map —29% of the global seagrass extent—highlighting the necessity of including their blue carbon fluxes into national climate agendas and showcasing the need for more cost-effective conservation and restoration efforts for their meadows. We envisage that the synergy between our scalable Earth Observation technology and near-future nation-specific *in-situ* observations can and will support spatially-explicit seagrass and ocean ecosystem accounting, accelerating effective policy-making, blue carbon crediting, and relevant financial investments in and beyond The Bahamas.

KEYWORDS

blue carbon, seagrass, ecosystem accounting, Sentinel-2, Google Earth Engine (GEE), Earth Observation (EO), The Bahamas

1 Introduction

One of the most widespread coastal ecosystems is seagrass, a functional group of intertidal and subtidal flowering plants, which can be found in at least 159 countries across all continents except Antarctica (Short et al., 2011; UNEP, 2020). It contributes to animal and human well-being through a variety of ecosystem services, including carbon sequestration, coastal protection, and biodiversity preservation (UNEP, 2020). These services are estimated to have an economic value of US $3,400,000 per km^2 per year (Short et al., 2011). Analogous to terrestrial plants, seagrasses photosynthesize to store carbon in their biomass and soil, and therefore act as 'blue carbon' sinks and natural climate solutions (Macreadie et al., 2014). They can sequester carbon 35 times faster than tropical rain forests and account for up to 10% of the annual oceanic carbon burial, while only covering 0.2% of the ocean floor (Mcleod et al., 2011; Fourqurean et al., 2012; Duarte et al., 2013; Macreadie et al., 2015). More than 90% of the sequestered carbon is stored within the underlying soil, where it can be sustained for millennia due to anoxic conditions, vertical sediment accretion, and slow composition rates (Mcleod et al., 2011; Fourqurean et al., 2012; Macreadie et al., 2012; Duarte et al., 2013). Globally, the soil of seagrasses alone is estimated to store up to 8.4 Pg carbon (Fourqurean et al., 2012).

Seagrasses' ability to reduce atmospheric carbon dioxide concentrations supports the Paris Agreements' goal of limiting the global average temperature rise to below 1.5°C above pre-industrial levels (UNFCCC, 2016). However, the importance of integrating seagrass blue carbon into national climate agendas like the Nationally Determined Contributions (NDCs) remains largely overlooked (Dencer-Brown et al., 2022). Out of the 159 countries in which seagrasses grow, only 13 countries explicitly recognise seagrasses in their mitigation and/or adaptation strategies (UNEP, 2020; Cabo Verde, 2021; Republic of Seychelles, 2021; The Government of Mozambique, 2021). Moreover, this ecosystem has been declining globally at a rate of 1-2% per year since 1880, yet only 26% of its area lies within Marine Protected Areas (MPAs) (Waycott et al., 2009; UNEP, 2020; Dunic et al., 2021). Habitat loss is driven by a number of human and climate change induced factors like coastal development, boating, increased urban/agricultural run-off, sea level rise, and increased ocean temperatures (Waycott et al., 2011; Grech et al., 2012; Saunders et al., 2013).

The lack of recognition and protection arises from insufficient knowledge of spatially explicit seagrass distribution and related carbon accounts, especially in remote and/or data-poor areas (McKenzie et al., 2020; Macreadie et al., 2021). Recent advances in Earth Observation utilize high temporal and spatial resolution satellite data archives, cloud computing, and machine learning to minimize mapping uncertainties (Lyons et al., 2020; Traganos et al., 2022a; Traganos et al., 2022b). This provides an alternative to traditionally expensive and time-consuming surveying methods (Hossain et al., 2015; Veettil et al., 2020). The incorporation of country-scale seagrass carbon data with high-quality mapping products supports the assessment of the seagrass ecosystems' importance and its implementation into national climate agendas, and benefits relevant seascape management and conservation efforts (Roelfsema et al., 2014; McKenzie et al., 2020; Traganos et al., 2022b).

In this study, we aim to minimize the aforementioned data gaps by producing physical accounts of spatially explicit seagrass extent, carbon stock and sequestration rate for The Bahamas. For this, we developed a cloud-native Earth Observation framework using the cloud computing platform Google Earth Engine (GEE), multi-temporal high-resolution Sentinel-2 archives, and the machine learning classifier Random Forest (Breiman, 2001). The generated maps were combined with country- and region-specific *in-situ* carbon data to evaluate the importance of the seagrass ecosystem for the NDCs of The Bahamas.

2 Methods

2.1 Study site

The Bahamas is one of 13 countries which recognize seagrass in their NDCs, and the first one which set a measurable target—protecting 20% of their nearshore marine environment by 2020 (The Government of the Bahamas, 2015). The Bahamian archipelago consists of about 700 carbonate islands and is located in the tropical Western Atlantic (Buchan, 2000; The Commonwealth, 2022). Its coastline stretches along 3,542 km and its Exclusive Economic Zone covers an area of approximately 619,785 km^2 (Dataset ChartsBin statistics collector team, 2010; Flanders Marine Institute, 2019). Almost 20% of the Bahamian seascape is shallow with water depths under 25m (Landfall, 2021). It features coastal habitats like coral reefs, mangrove forests and seagrass beds (Mandoske, 2017). According to the best available information seagrasses cover an area between 26,400 and 56,930 km^2 (Schill et al., 2021; Dataset Allen Coral Atlas, 2022). The three main Bahamian seagrass species are *Thalassia testudinum*, *Syringodium filiforme*, and *Halodule wrightii* (Buchan, 2000; Green and Short, 2003; Dierssen et al., 2010). Low energy sites on San Salvador Island have been found to be dominated by the dense seagrass species of *Thalassia testudinum*, while the sparse species (*Syringodium filiforme* and *Halodule wrightii*) dominate higher-energy sites (Smith et al., 1990; Dierssen et al., 2010). Higher density seagrass species feature higher biomass and productivity (Buchan, 2000; van Tussenbroek et al., 2014).

2.2 Data

2.2.1 Earth Observation data

For our country-scale seagrass mapping procedure, we processed four years' worth of Sentinel-2 (S2) Bottom Of Atmosphere (Level 2A) imagery at 10m spatial resolution, acquired between March 28th, 2017 and March 28th, 2021 and available in GEE. The employed archive consists of 18,881 single 100x100-km tiles, covering an area of 633,063 km^2 (the country's Exclusive Economic Zone + land area).

2.2.2 Reference data

Our mapping procedure utilizes reference data of four coastal habitat classes: Seagrass, Sand, Coral/Algae and Rock/Rubble. These classes were selected following the requirements for remotely sensed benthic habitat classification of Kennedy et al. (2021).

Training data were assembled through a combination of expert-guided photo interpretation using the pre-processed S2 composite (Section 2.3.1 and Figure 4A) and modified seagrass mapping results of the Allen Coral Atlas (Dataset Allen Coral Atlas, 2022). Validation data were based on multiple data sources leveraging field data acquisitions with remotely sensed covariates, aggregated throughout the entire Bahamas (Roelfsema et al., 2021). Section 2.3.2 describes the pre-processing and modification of the reference data before sample points were taken.

2.2.3 Carbon data

We conducted a systematic literature review of seagrass blue carbon data before calculating areal carbon stock ranges and sequestration rates. A combination of keywords (locations, 'seagrass', species, '(blue) carbon', 'soil carbon' 'biomass', 'sequestration') was used to identify relevant articles. These were then screened for region- or species-specific data ranges and discarded when only averaged numbers for biomass and carbon stocks were stated.

The collected data were harmonized to calculate areal carbon stock ranges, which equal the sum of above-ground biomass (AGB) carbon, below-ground biomass (BGB) carbon, and soil carbon. Harmonization efforts were based on an AGB : BGB ratio of 1:2 and a biomass carbon to dry weight biomass ratio of 1:2.86 (Fourqurean et al., 2012). Final ranges were calculated after creating species-specific ranges, and the prevalence of species was taken into account to prevent incorrect weighting. Due to the lack of country-specific soil carbon data, a bioregional average was used (Fourqurean et al., 2012). Areal sequestration potentials of Bahamian seagrasses were based on averaged *in-situ* data.

2.3 Cloud-based Earth Observation framework

Our developed cloud-based Earth Observation framework features a plethora of successive big satellite and reference data analytics which transform pixels into nationwide seagrass ecosystem accounts (Figure 1). These big data analytics are split into three main technological pillars within our framework: (a) Multi-temporal Sentinel-2 Composition (2.3.1), (b) Training and Validation Data Harmonisation (2.3.2), and (c) Supervised Machine Learning Classification (2.3.3).

2.3.1 Multi-temporal Sentinel-2 composition

To create a high-quality S2 composite of the entire optically shallow water area of The Bahamas, the archive described in Section 2.2.1 was filtered for images with minimum cloud coverage and sun glint effects. To reduce the possibility of sun glint, images with a mean solar zenith angle of more than 70% were discarded. The collection was further filtered for cloud coverage, retaining images with a cloudy pixel percentage under 25%. This reduced the size of the S2 archive to

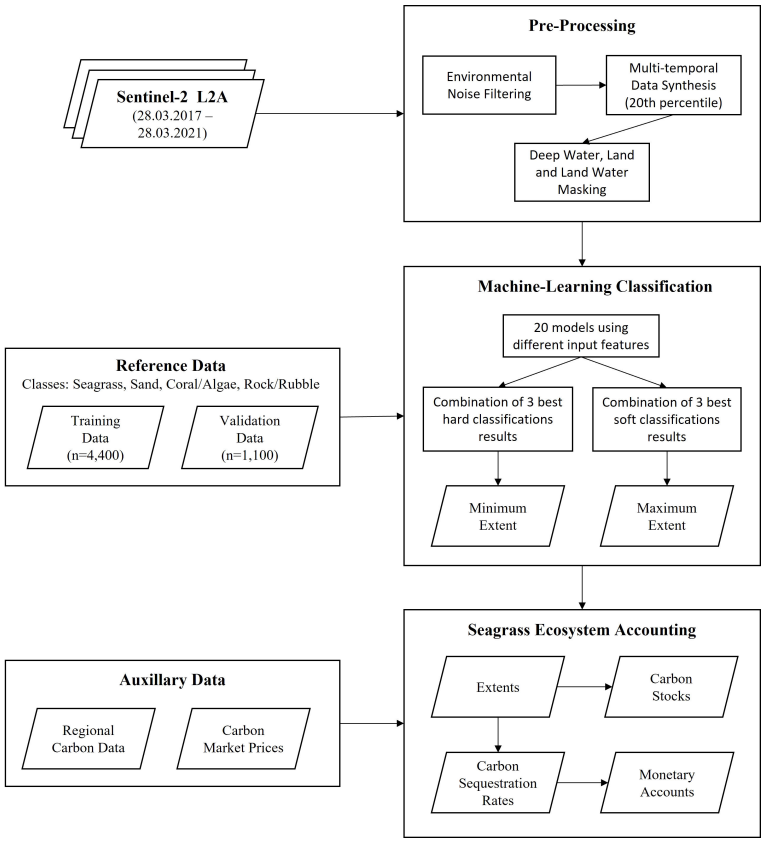


FIGURE 1
Schematic workflow of the cloud-native Earth Observation seagrass ecosystem accounting framework.

9,909 single tiles (52% of the original amount). After joining the archive with the corresponding S2 Cloud Probability dataset[1], pixels with a cloud probability over 30% were masked. Moreover, the QA60 and Scene Classification Map bands were utilized to discard pixels featuring cloud shadows, and opaque and cirrus clouds (Louisand L2A Team, 2019). The filtered archive was then statistically reduced to a single multi-temporal composite using the 20th percentile of each pixel's spectral value. This approach further reduces high-reflectance obstacles like remaining clouds and sun glint effects, waves, turbidity, and haze (Thomas et al., 2021; Traganos et al., 2022b). To further minimize misclassification, optically deep water, land and land water pixels were masked. The combined Otsu-thresholding and Canny edge filter method of Donchyts et al. (2016) was applied to the Modified Normalised Difference Water Index (MNDWI) to differentiate land from coastal waters (Xu, 2006). Optically deep waters were masked using Otsu-thresholding of the MNDWI and Shallow Water Index (Otsu, 1979; Traganos and Reinartz, 2018; Alkhatlan et al., 2019). All thresholding methods were based on suitable image subsets which allowed for a strong bi-modal histogram distribution and therefore better masking results. Input parameters like the Canny edge sensitivity threshold and the number of buckets for the Otsu-histograms were chosen based on an iterative approach (Traganos et al., 2022b). Land water bodies were masked using an edited version of the Global Administrative Unit Layers 2015 (Dataset FAO UN, 2014). The resulting optically shallow S2 composite was transformed to the below-surface remote sensing reflectance (r_{rs}) following Lee et al. (1998) and Traganos and Reinartz (2018).

We improved the model accuracy by incorporating a variety of features as the raster input for the classification: Simple Non-Iterative Clustering (SNIC)-based statistical properties, selected Gray-Level Co-occurrence Matrix (GLCM) layers of the first five bands, Hue, Saturation, and Value (HSV) of bands 2 to 4, and the first three eigenvalues of a Principal Component Analysis (PCA)[2] (Hassanein et al., 2018; Tassi and Vizzari, 2020; Google Earth Engine, 2022). We ran a Random Forest variable importance measure (VIM) of the GLCM layers to select the ten most important properties and eliminate the least relevant layers for the classification. These properties were then used as a base for the PCA. All additional layers were stacked together with the derived r_{rs} band layers.

2.3.2 Training and validation data harmonisation

We converted the validation and training data vectors into rasters of 10-m resolution and concatenated them with the corresponding S2 pixel values. To minimize the creation of mixed pixels through this approach, we used the minimum and the 80th percentile of the seagrass validation data to filter both validation and training data. This reduces the number of high-reflectance mixed pixels which are likely to represent a combination of the sand and seagrass habitat. Moreover, it harmonizes training and validation data by discarding training data pixels that do not fall into the spectral properties of the validation data. To prevent spatial auto-correlation between training and validation data, a 2,000m buffer was applied around the validation data and used as a mask for the training data. Figure 2 shows the spectral ranges of all four classes of the training and validation data.

2.3.3 Supervised machine learning classification

We designed 20 different supervised classification frameworks which were based on different input features (Supplement Table S1, S2) and the ensemble machine learning classifier RF. This classifier incorporates multiple self-learning decision trees and is robust against noise and outliers (Breiman, 2001). Following Lyons et al. (2020), the number of seeds was set to 42 and the number of trees to 15.

Each framework was based on training and validation points aggregated across the same locations (Figure 3). The RF classifier was trained using 2,000 seagrass data points and 800 points per non-seagrass class (sand, coral/algae, and rock/rubble). The validation data were based on 500 seagrass data points and 200 points per non-seagrass class. Due to the main focus of this work being the detection of seagrass, non-seagrass classes were later merged into one class to create a binary accuracy assessment.

The final results for the seagrass ecosystem extent were created by combining multiple classification frameworks. First, a hard classification of each framework was used to identify the three models with the highest F1-scores (the harmonized mean of producer's and user's accuracy) for seagrass. The corresponding maps of seagrass versus non-seagrass were then composed using the most common class per stacked pixel (ee.ImageCollection.mode) (Google Earth Engine, 2022). The resulting map equals the maximum seagrass ecosystem extent. Next, classification frameworks with F1-score for seagrass over 70% were used to generate per-pixel probabilities for each class—the so-called soft classification. Pixels which featured seagrass as the most probable class and which reached probabilities over 50% were assigned to seagrass. Akin to the maximum seagrass extent creation, the three frameworks with the highest F1-scores for seagrass were composed and the resulting map equals the minimum seagrass ecosystem extent. In the post-processing stage, we visually assessed the classification results and manually masked out optically deeper waters which were misclassified as seagrass.

2.3.4 Accuracy assessment

The accuracy of the Bahamian seagrass ecosystem extent was assessed using the metrics of overall accuracy (OA), producer's accuracy (PA), user's accuracy (UA), and the F1-score through error matrices based on 1,100 validation points for both the seagrass and non-seagrass class (Story and Congalton, 1986).

2.4 Blue carbon accounting

2.4.1 Physical accounting

Bahamian seagrass carbon stock ranges were calculated by multiplying our estimated minimum and maximum seagrass ecosystem extent with the corresponding areal carbon stock range (Supplement Table S3). We ran both Tier 1 and Tier 2 assessments

1 https://developers.google.com/earth-engine/datasets/catalog/COPERNICUS_S2_CLOUD_PROBABILITY

2 https://developers.google.com/earth-engine/guides/arrays_eigen_analysis

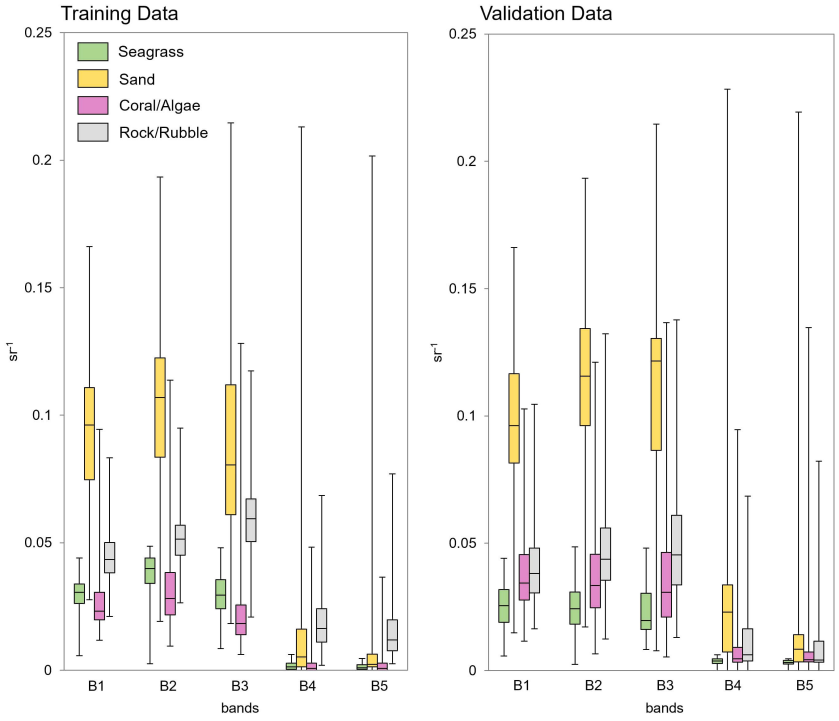


FIGURE 2
Spectral ranges of the training and validation data for the first five multi-temporal Sentinel-2 below-surface reflectance (r_{rs}) bands. [sr^{-1}] denotes the unit of the below-surface remote sensing reflectance.

following Howard et al. (2014). These assessments represent different levels of certainty, with Tier 1 featuring the highest uncertainty based on the use of published IPCC globally averaged carbon estimates. Tier 2 incorporates regional and/or county-specific carbon data (Section 2.2.3), therefore featuring reduced uncertainties (Howard et al., 2014). Seagrass carbon sequestration rates were calculated based on our calculated minimum and maximum seagrass ecosystem extent, and country-specific average sequestration rates.

2.4.2 Monetary accounting

We estimated the yearly monetary value of Bahamian seagrass blue carbon sequestration based on the European (European Commission, 2022) and California (C2ES, 2022) carbon credit market). Prices were acquired from Carbon Credits (Carbon Credits, 2022) on the 13th September, 2022 at 3.10pm and converted to EUR (Oanda, 2022). The European carbon credit market price for one ton of CO_2 was 67.71 EUR, while the California market price was 26.93 EUR.

3 Results

3.1 Ecosystem extent accounting

Figure 4 displays the mapped minimum and maximum extent of the seagrass ecosystem for Bahamian shallow waters at 10m resolution. Seagrasses cover an area between 39,210 and 46,792 km^2, which equals 6 to 8% of the country's Exclusive Economic Zone, and 35 to 41% of its optically shallow area. About 9 to 11% of the ecosystem lies within Marine Protected Areas (Dataset UNEP-WCMC, S.F, 2021).

Our mapping frameworks for minimum and maximum extent reach OAs of 71.00 and 76.55%, respectively. F1-scores for seagrass extent are at 61.71 and 74.76%, PAs at 51.40 and 76.40%, and UAs at 77.18 and 73.18%, respectively. Accuracies for the non-seagrass class can be found in the Supplementary Tables S4 and S5.

3.2 Blue carbon accounting

3.2.1 Physical accounting

Based on our classified ecosystem extent and the globally averaged aerial carbon estimates of the Tier 1 assessment, Bahamian seagrass can store between 35.7 million and 3.9 billion Mg C. Using the region-specific carbon data of the Tier 2 assessment, we estimate a Bahamian seagrass carbon storage of 594 to 723 million Mg. Moreover, we estimate that the classified ecosystem extent can sequester between 103 and 123 Mt CO_2, annually. Therefore, in 2018, Bahamian seagrasses had the potential to remove 57 to 68 times their annual CO_2 emissions (Friedlingstein et al., 2020).

3.2.2 Monetary accounting

At a European carbon market price of 67.71 EUR per ton of CO_2, Bahamian seagrass carbon sequestration is valued at 178,296 EUR per km^2 per year. This, combined with our classified ecosystem extents, translates to a total sequestration potential value of 6.99 billion to 8.34 billion EUR per year. The California carbon market price of 26.93 EUR per t CO_2 results in a yearly sequestration potential value of 70,913 EUR per km^2 and a total sequestration potential value of 2.78 billion to 3.32 billion EUR per year.

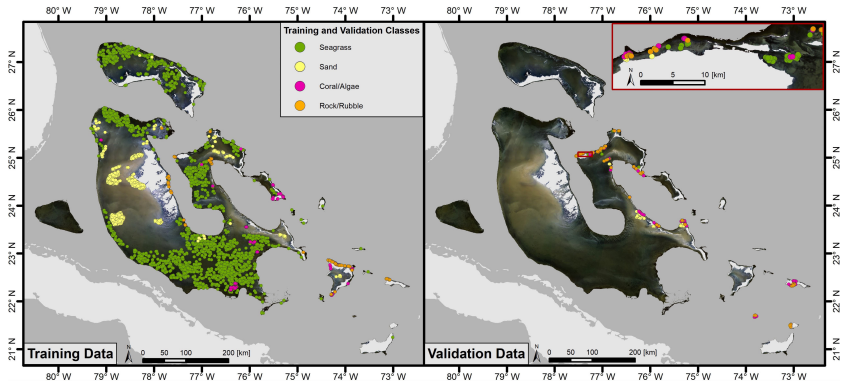


FIGURE 3
Distribution of the 4,400 training data and 1,100 validation data points of the four classes used in the supervised machine learning classification.

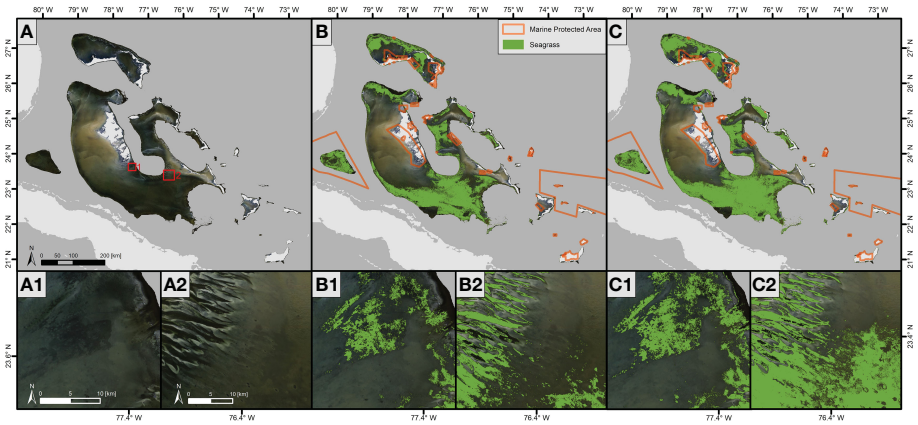


FIGURE 4
False-color Sentinel-2 composite (Bands 3-2-1) **(A)** overlaid with the mapped minimum **(B)** and maximum **(C)** seagrass extent, and Marine Protected Areas across The Bahamas. The location of the zoomed-in insets (A1) - (C2) is shown in panel **(A)**.

4 Discussion

4.1 National seagrass ecosystem accounts in The Bahamas

Leveraging our cloud-based, multi-temporal Earth Observation ecosystem accounting framework with country and region-specific reference data inventories, we produced the first national high-resolution (10m), spatially-explicit, ecosystem accounts of seagrass extent, carbon stock, and sequestration rate for The Bahamas, across more than 113,000 km^2 of shallow seafloor (Figure 3). Featuring a multitude of cutting-edge technological novelties—big satellite and reference data analytics, machine learning, cloud computing and dense feature engineering—we mapped up to 46,792 km^2 of nationwide seagrass meadows with an observed F1-score of 74.76% (Figure 4). Utilizing region-specific seagrass carbon data, this spatially-explicit extent translates to a Tier 2 blue carbon assessment up to 771.4 million Mg C and an annual blue carbon sequestration rate of 123 Mt CO_2 (Table 1). The second most important finding is that our seagrass ecosystem accounting efforts enrich our previously published research in 27 different tropical and temperate countries across the Mediterranean, East Africa and the Western Indian Ocean (Lee et al., 2022; Traganos et al., 2022a; Traganos et al., 2022b). The common denominator of all 28 national seagrass ecosystem accounting endeavors is the utilization of a standardized technological Earth Observation framework which supports an effective qualitative and quantitative comparison of its yielded physical accounts by minimizing both technological and environmental differences.

4.2 Mapping comparisons

In a global context, our maximum mapped seagrass extent shows that The Bahamas features the second largest seagrass meadow area after Australia (74,555 km^2). It is nearly three times larger than the

TABLE 1 Tier 1 and 2 carbon stocks for the classified minimum and maximum seagrass ecosystem extent.

Assessment	Carbon stock min (Mg)	Carbon stock max (Mg)
Tier 1	35,681,275.86	3,879,068,732.63
Tier 2	594,010,001.01	723,000,389.50

Mg denotes Megagrams.

Cuban seagrass meadow area, which represents the third largest seagrass habitat in the world (16,073 km^2). Moreover, our mapped maximum extent represents ~29% of the global seagrass extent (McKenzie et al., 2020).

Zooming in on the Bahamian EEZ, our remotely sensed seagrass extents can be quantitatively compared to five existing nationwide seagrass areal estimates—three of which have been calculated using moderate to high-resolution satellite image archives resulting in equally spatially-explicit Bahamian seagrass extents.

In the first-ever national-scale seagrass mapping effort, Wabnitz et al. (2008) employed the 30-m satellite image archives of Landsat 5 TM and 7 ETM+ to map 65,436 km^2 of nationwide dense and sparse seagrass meadows in The Bahamas; 33.2% more than our maximum seagrass extent. Based on their reported PAs and UAs, and the consensus that tropical seagrass beds are generally stable in their extent, we infer that the areal deviation might have been induced by technology: the 30-m spatial resolution of Landsat sensors results in a nine-times greater mapping unit (900 m^2) than the 10-m Sentinel-2 data (100 m^2). This means that one potentially misclassified seagrass pixel at 30 m would equal nine misclassified pixels at 10 m, amplifying the overestimation of the former mapping endeavor and reflecting the shortcoming of national seagrass extent mapping in Greece (Traganos et al., 2018). The two most recent spatially coincident mapping efforts utilized the 5-m PlanetScope image archive and a similar state-of-the-art Earth Observation framework to map between 26,354[3] and 53,930 km^2 of Bahamian seagrass meadows (Schill et al., 2021). Our minimum and maximum seagrass extents fall within the estimated range of the two aforementioned efforts. We, however, infer that the narrower quantitative differences between our nationwide extent and these two estimates are induced more by environmental factors (e.g., challenging discrimination between seagrasses and hard bottom algae of variable densities and, thus, spectral properties)—and less by technological factors like the difference in the mapping units of Sentinel-2 (100 m^2) and PlanetScope (25 m^2).

On the other hand, both remaining non-spatially-explicit estimates by UNEP-WCMC and Short (2018) and McKenzie et al. (2020) feature wide underestimating trends—2,227 and 2,250 km^2, respectively—approximately one order of magnitude less than our mapped minimum seagrass extent of 39,210 km^2. This observation corroborates our recent findings in the Mediterranean and East Africa (Traganos et al., 2018; Traganos et al., 2022a; Traganos et al., 2022b) reflecting the potential biases introduced by the utilization of non-data-driven and non-nation-specific mapping designs in blue carbon and, more broadly, coastal ecosystem accounting at both the physical and monetary level in and beyond The Bahamas (Bertram et al., 2021). We expand more into this latter issue in Section 4.4, namely the downstream implication regarding the uptake of such accounts in policy and financial crediting frameworks. It is important to note that all of the mapping comparisons were regionally-aggregated mapping efforts, at a minimum, which might have introduced biases due to the differences in spatial scales with the national scale of The Bahamas—in contrast to our nationally-aggregated seagrass extent account.

4.3 Current uncertainties

As every novel remote sensing assessment based on research and development, our presented and utilized ecosystem accounting framework is characterized by certain biases and uncertainties, induced by environmental and technological factors, including the reference data in use.

Despite our testing of an intensive feature engineering of pixel, object, colour and texture features (Section 2.3.1) and reference data normalization (Section 2.3.2) in our RF supervised machine learning models (Section 2.3.3), our seagrass ecosystem extent accounting was impacted by misclassifications mainly due to mixed pixels, spectral confusion between certain classes, and larger water depths. As shown in Supplementary Tables S1 and S4, which indicate PAs and UAs of both maximum seagrass and non-seagrass distribution, our tested models feature a somewhat solid balance between PAs and UAs for the seagrass class, with PAs consistently being 3-5% greater than UAs. Even the use of Bands 1-5 as the only input features in our RF machine learning experiments explain the variability in both classes, as demonstrated by their larger PA than UA (77.6 vs 73.1%). This shows that our machine learning feature engineering was already complex enough, as was the mode of the best models (Supplementary Table S1). Yet a greater PA means that our maximum seagrass extent is slightly overestimated while we observe an underestimation of ~1.4% of the merged class of coral/algae, sand, rocks and rubble. Additional biases might have been introduced due to the issue of mixed pixels owing to the spectral similarity between seagrasses and the mixed coral/algae class across the first Sentinel-2 bands (Figure 2), as well as the coarse mapping unit of 100 m^2 which is potentially unable to capture sparser seagrass meadows. Such spectral confusion and mixed pixels' impedance situation have been also observed across 5 to 30-m resolution optical remote sensing endeavors in The Bahamas (Wabnitz et al., 2008; Schill et al., 2021).

To test whether an improved training data design would benefit our seagrass extent ecosystem accounting, we ran a metadata analysis applying more accurate training data annotation for the seagrass and coral class following the suggestions of C. Roelfsema (personal communication, 10 August 2019). This analysis yielded qualitatively more accurate minimum and maximum Bahamas-wide seagrass extents of 55,388 and 64,481 km^2, respectively, and are closer to the national estimates of Wabnitz et al. (2008) and Schill et al. (2021). While the PA of the new maximum seagrass extent is identical to the original maximum one, the UA of the new maximum estimate dropped by 5.7% (Supplementary Table S6). This means that we introduced greater spectral variability in the seagrass training data points compared to the ones contained in the respective validation data points, which resulted in a greater overestimation of the Bahamian seagrass meadows. This indicates the need for more fit-for-purpose, i.e., spatially and temporally richer, *in situ* validation data points to improve coastal ecosystem accounting efforts using Earth Observation, like ours, highlighting the logistical importance of allocating more funding towards such high-quality field data collections.

The articulation of the various biases in our seagrass extent accounting is important because it justifies cascading biases in our blue carbon accounting. Utilizing the Tier 1 seagrass carbon assessment, and, thus, globally-averaged carbon values, results in a 100-fold difference between the minimum and maximum blue carbon stocks for Bahamian seagrasses. Utilizing the Tier 2 assessment, region-specific total seagrass carbon stocks

3 https://allencoralatlas.org/atlas/#6.92/24.0443/-77.0209

and bioregional averages, the range is narrowed to just a percentage difference of around 24.2% (Table 2). Despite the lack of country-specific seagrass soil carbon data in our blue carbon accounting, the Tier 2 maximum estimate (771.4 million Mg C) is only 3.8% lower than the only other existing nationwide seagrass blue carbon stock estimate (801.4 million Mg C; Mandoske, 2017) which relied on a Landsat 7-derived seagrass extent (57,481 km^2) and biophysical modeling. Yet, seagrass blue carbon features wide-ranging variability (due to e.g., soil carbon depth, density, patchiness, edge effects, proximity to the coastline, mangroves and tidal flats, seagrass bathymetry, species, sediment, inter-annual productivity). Added to the considerable contribution of Bahamian seagrass meadows to mitigate carbon emissions within the country, according to our accounting, new intensive field data collections of blue carbon stocks and fluxes, and respective blue carbon accounting should be established to improve our current estimates and support their effective uptake into current policy-making and carbon crediting frameworks for The Bahamas.

4.4 Applications of blue carbon accounting using Earth Observation

The synergy of Earth Observation technology and Ecosystem Accounting has more recently showcased promising results towards quantifying the nationwide natural climate solutions of blue carbon ecosystems[4] (Traganos et al., 2022a; Traganos et al., 2022b).

Our targeted case study area, The Bahamas, is the first country to include an explicit reference to seagrasses in its NDC *and* set a measurable target for the protection of its nearshore marine ecosystems—20% by 2020 (The Government of the Bahamas, 2015). Our spatially explicit seagrass ecosystem accounting for The Bahamas fills a significant mapping blank in the global estimates of seagrass extent, blue carbon stocks and sequestration rates. According to our accounts and the best available global estimates, Bahamian seagrass meadows potentially comprise up to 29% of the global seagrass area (McKenzie et al., 2020) and store up to 18.3% of the global seagrass blue carbon stocks (Fourqurean et al., 2012). These data turn the spotlight on The Bahamas as a global hot spot of seagrass distribution and blue carbon pool. More importantly, they provide a comprehensive and transparent basis for the uptake of seagrass meadows into Multilateral Environmental Agreements (e.g., NDC, MPAs, etc.) and blue carbon crediting mechanisms[5] (Macreadie et al., 2022). Here, we estimated that in 2018 Bahamas-wide seagrasses could sequester at least 57 times the annual carbon dioxide emissions of the country (Friedlingstein et al., 2020) with a potential annual value of at least 70,913 EUR/km^2. Yet, only up to 11% of these highly-productive seagrass meadows lie within the current MPAs of The Bahamas (Figure 4; UNEP-WCMC, 2021). The Bahamas and countries with equally extensive blue carbon ecosystems should establish long-term monitoring systems and policy-making strategies using the recent blueprint seagrass extent and blue carbon mapping project of Seychelles—the first to leverage dense Earth Observations and nationally aggregated field data to account and incorporate nationwide seagrasses into the NDC and climate change mitigation efforts (Lee et al., 2022).

4.5 Next steps

Our Bahamian seagrass ecosystem accounting increases the total mapped seagrass extent of DLR's Global Seagrass Watch project to around 76,000 km^2 across more than 306,000 km^2 of mapped seabed, 74,000 km of coastline in 28 temperate and tropical countries, and three seagrass bioregions (Lee et al., 2022; Traganos et al., 2022a; Traganos et al., 2022b). All of these high-resolution spatially explicit seagrass ecosystem extent accounts are produced through an ever-advancing standardized Earth Observation framework. Here, the two main advances are the synthesis of a harmonized nationally-aggregated reference dataset and deep feature engineering for the machine learning classification component. These resulted in qualitative and quantitative improvements in our nationwide seagrass mapping in contrast to our initial mapping endeavors in the Mediterranean and East Africa.

There are still considerable yet well-mapped showstoppers and uncertainties towards mainstreaming the natural climate solutions of blue carbon ecosystems to the biodiversity, societies and economies (Section 4.3; Macreadie et al., 2019; Macreadie et al., 2022; Williamson and Gattuso, 2022). While we showcase here that the state-of-the-art of Earth Observation technology can now provide scalability, confidence, and repeatability in blue carbon accounting, there is a notable lack of high-quality nation-specific *in situ* data on seagrass distribution, blue carbon stocks, and fluxes. Such data gaps impede the transparency, standardization and funding of long-term blue carbon accounting systems and their much-needed high-quality scalable insights. We envisage that these holistic monitoring systems could benefit from the amalgamation of Earth Observation technology, Ecosystem Accounting, biophysical and socio-economic modeling, and targeted nationally aggregated field data collections. This conceptual systems-level approach would ultimately evolve into a long-term decision support system for transparent and sustainable strategies for resilient blue carbon ecosystems, societies and economies. This interconnected resilience can and will be realized only through the effective collaboration and communication of all the pertinent stakeholders—scientists, NGOs, private technological entities, governments, policymakers, investors, and philanthropic foundations.

Data availability statement

The datasets generated during the current study—including the Sentinel-2 mosaic, and the minimum and maximum Bahamian seagrassextent, but excluding the validation data due to copyright, are available inthe following link: https://ablume.users.earthengine.app/view/bahamian-seagrass-extent-and-blue-carbon-accounting-using-eo.

Author contributions

AB co-designed the work; annotated training data; developed the reference data harmonization; designed and executed the cloud-based

4 https://www.abs.gov.au/methodologies/national-ocean-account-experimental-estimates-methodology/aug-2022

5 http://www.tribune242.com/news/2022/apr/29/pm-were-first-sell-blue-carbon-credits/

Earth Observation framework; ran the Tier 1 and Tier 2 blue carbon accounting; designed all figures and tables; and wrote the manuscript with the input of all co-authors. AP created the Simple Non-Iterative Clustering (SNIC)-based statistical properties and annotated training data. CL conceived and developed the HSV features. DT conceived the idea and supervised the entire research, from concept to writing. All authors contributed to the article and approved the submitted version.

Funding

AB, AP and DT acknowledge support from the DLR-funded Global Seagrass Watch Project. CL acknowledges support from a DLR-DAAD Research Fellowship (No. 57478193).

Acknowledgments

The authors acknowledge Chris Roelfsemma for sharing information regarding benthic habitats in the Bahamas.

Conflict of interest

The authors declare that the research was conducted in the absence of any commercial or financial relationships that could be construed as a potential conflict of interest.

Publisher's note

All claims expressed in this article are solely those of the authors and do not necessarily represent those of their affiliated organizations, or those of the publisher, the editors and the reviewers. Any product that may be evaluated in this article, or claim that may be made by its manufacturer, is not guaranteed or endorsed by the publisher.

Supplementary material

The Supplementary Material for this article can be found online at: https://www.frontiersin.org/articles/10.3389/fmars.2023.1058460/full#supplementary-material

References

Alkhatlan, A., Bannari, A., Ali, T. S., Abahussain, A., and Hameid, N. (2019). "Mapping submerged aquatic vegetation in shallow water of Arabian gulf using water spectral indices, field observations and landsat-OLI data," in *IGARSS 2019 - 2019 IEEE International Geoscience and Remote Sensing Symposium*. 302–305.

Bertram, C., Quaas, M., Reusch, T. B. H., Vafeidis, A. T., Wolff, C., and Rickels, W. (2021). The blue carbon wealth of nations. *Nat. Climate Change* 11 (8), 704–709. doi: 10.1038/s41558-021-01089-4

Breiman, L. (2001). Random forests. *Mach. Learn.* 45 (1), 5–32. doi: 10.1023/A:1010933404324

Buchan, K. C. (2000). The Bahamas. *Mar. pollut. Bull.* 41 (1), 94–111. doi: 10.1016/S0025-326X(00)00104-1

Cabo Verde (2021) *2020 update to the first nationally determined contribution (NDC)*. Available at: https://unfccc.int/sites/default/files/NDC/2022-06/Cabo%20Verde_NDC%20Update%202021.pdf.

Carbon Credits (2022) *Live carbon prices today*. Available at: https://carboncredits.com/carbon-prices-today/ (Accessed 29 September 2022).

C2ES (2022) *California Cap and Trade*. Available at: https://www.c2es.org/content/california-cap-and-trade/ (Accessed 29 September 2022).

Dataset Allen Coral Atlas (2022) *Imagery, maps and monitoring of the world's tropical coral reefs*. Available at: https://www.allencoralatlas.org/.

Dataset ChartsBin statistics collector team (2010). *Length of coastline by country* (ChartsBin). Available at: http://chartsbin.com/view/ofv.

Dataset FAO UN (2014). *Global administrative unit layers 2015, country boundaries*. Available at: https://developers.google.com/earth-engine/datasets/catalog/FAO_GAUL_2015_level1.

Dataset UNEP-WCMC, S.F (2021). *Global distribution of seagrasses (version 7.1). seventh update to the data layer used in green and short, (2003)* (Cambridge, UK: UN Environment World Conservation Monitoring Centre). doi: 10.34892/x6r3-d211

Dencer-Brown, A. M., Shilland, R., Friess, D., Herr, D., Benson, L., Berry, N. J., et al. (2022). Integrating blue: How do we make nationally determined contributions work for both blue carbon and local coastal communities? *Ambio* 51 (9), 1978–1993. doi: 10.1007/s13280-022-01723-1

Dierssen, H. M., Zimmerman, R. C., and La Drake and Burdige, D. (2010). Benthic ecology from space: optics and net primary production in seagrass and benthic algae across the great bahama bank. *Mar. Ecol. Prog. Ser.* 411, 1–15. doi: 10.3354/meps08665

Donchyts, G., Schellekens, J., Winsemius, H., Eisemann, E., and Van de Giesen, N. (2016). A 30 m resolution surface water mask including estimation of positional and thematic differences using landsat 8, SRTM and OpenStreetMap: A case study in the Murray-darling basin, Australia. *Remote Sens.* 8 (5), 386. doi: 10.3390/rs8050386

Duarte, C. M., Kennedy, H., Marbà, N., and Hendriks, I. (2013). Assessing the capacity of seagrass meadows for carbon burial: Current limitations and future strategies. *Ocean Coast. Manage.* 83, 32–38. doi: 10.1016/j.ocecoaman.2011.09.001

Dunic, J. C., Brown, C. J., Connolly, R. M., Turschwell, M. P., and Côté, I. M. (2021). Long-term declines and recovery of meadow area across the world's seagrass bioregions. *Global Change Biol.* 27, 4096–4109. doi: 10.1111/gcb.15684

European Commission (2022) *EU Emissions trading system (EU ETS)* (Accessed 29 September 2022).

Flanders Marine Institute (2019) *Maritime boundaries geodatabase: Maritime boundaries and exclusive economic zones (200NM)*. Available at: https://www.marineregions.org/.

Fourqurean, J. W., Duarte, C. M., Kennedy, H., Marbà, N., Holmer, M., Mateo, M. A., et al. (2012). Seagrass ecosystems as a globally significant carbon stock. *Nat. Geosci.* 5 (7), 505–509. doi: 10.1038/ngeo1477

Friedlingstein, P., Jones, M. W., O'Sullivan, M., Andrew, R. M., Bakker, D. C. E., Hauck, J., et al. (2020). Global carbon budget 2020. *Earth Syst. Sci. Data* 12 (4), 3269–3340. doi: 10.5194/essd-12-3269-2020

Google Earth Engine (2022) *ee.ImageCollection.mode [Online]*. Available at: https://developers.google.com/earth-engine/apidocs/ee-imagecollection-mode (Accessed 29 September 2022).

Grech, A., Chartrand-Miller, K., Erftemeijer, P., Fonseca, M., McKenzie, L., Rasheed, M., et al. (2012). A comparison of threats, vulnerabilities and management approaches in global seagrass bioregions. *Environ. Res. Lett.* 7. doi: 10.1088/1748-9326/7/2/024006

Green, E., and Short, F. (2003). *World atlas of seagrasses* (Berkeley, USA: University of California Press).

Hassanein, M., Lari, Z., and El-Sheimy, N. (2018). A new vegetation segmentation approach for cropped fields based on threshold detection from hue histograms. *Sensors* 18 (4), 1253. doi: 10.3390/s18041253

Hossain, M. S., Bujang, J. S., Zakaria, M. H., and Hashim, M. (2015). The application of remote sensing to seagrass ecosystems: an overview and future research prospects. *Int. J. Remote Sens.* 36 (1), 61–114. doi: 10.1080/01431161.2014.990649

Howard, J., Hoyt, S., Isensee, K., Telszewski, M., and Pidgeon, E. (2014). *Coastal blue carbon: Methods for assessing carbon stocks and emissions factors in mangroves, tidal salt marshes, and seagrasses* (Arlington, Virginia, USA: Conservation International, Intergovernmental Oceanographic Commission of UNESCO, International Union for Conservation of Nature).

Kennedy, E. V., Roelfsema, C. M., Lyons, M. B., Kovacs, E. M., Borrego-Acevedo, R., Roe, M., et al. (2021). Reef cover, a coral reef classification for global habitat mapping from remote sensing. *Sci. Data* 8 (1), 196. doi: 10.1038/s41597-021-00958-z

Landfall (2021) *Explorer chart: Bahamas*. Available at: https://www.landfallnavigation.com/explorer-charts-bahamas-turks-caicos.html (Accessed 6 August 2022).

Lee, Z., Carder, K. L., Mobley, C. D., Steward, R. G., and Patch, J. S. (1998). Hyperspectral remote sensing for shallow waters. i. a semianalytical model. *Appl. Optics* 37 (27), 6329–6338. doi: 10.1364/AO.37.006329

Lee, C. B., Traganos, D., Martin, L., Rowlands, G., and Reinartz, P. (2022). *Nationwide seagrass mapping using analysis-ready sentinel-2 and PlanetScope data to support the nationally determined contributions of Seychelles* (Annapolis, Maryland, USA: International Seagrass Biology Workshop 14).

Louis, J.L2A Team (2021). *S2 MPC level-2A algorithm theoretical basis document, 2.10 ed.*

Lyons, M. B., Roelfsema, C. M., Kennedy, E. V., Kovacs, E. M., Borrego-Acevedo, R., Markey, K., et al. (2020). Mapping the world's coral reefs using a global multiscale earth observation framework. *Remote Sens. Ecol. Conserv.* 6 (4), 557–568. doi: 10.1002/rse2.157

Macreadie, P. I., Allen, K., Kelaher, B. P., Ralph, P. J., and Skilbeck, C. G. (2012). Paleoreconstruction of estuarine sediments reveal human–induced weakening of coastal carbon sinks. *Global Change Biol.* 18 (3), 891–901. doi: 10.1111/j.1365-2486.2011.02582.x

Macreadie, P. I., Anton, A., Raven, J. A., Beaumont, N., Connolly, R. M., Friess, D. A., et al. (2019). The future of blue carbon science. *Nat. Commun.* 10 (1), 3998. doi: 10.1038/s41467-019-11693-w

Macreadie, P. I., Baird, M. E., Trevathan-Tackett, S. M., Larkum, A. W. D., and Ralph, P. J. (2014). Quantifying and modelling the carbon sequestration capacity of seagrass meadows – a critical assessment. *Mar. pollut. Bull.* 83 (2), 430–439. doi: 10.1016/j.marpolbul.2013.07.038

Macreadie, P. I., Costa, M. D. P., Atwood, T. B., Friess, D. A., Kelleway, J. J., Kennedy, H., et al. (2021). Blue carbon as a natural climate solution. *Nat. Rev. Earth Environ.* 2 (12), 826–839. doi: 10.1038/s43017-021-00224-1

Macreadie, P. I., Robertson, A. I., Spinks, B., Adams, M. P., Atchison, J. M., Bell-James, J., et al. (2022). Operationalizing marketable blue carbon. *One Earth* 5 (5), 485–492. doi: 10.1016/j.oneear.2022.04.005

Macreadie, P. I., Trevathan-Tackett, S. M., Skilbeck, C. G., Sanderman, J., Curlevski, N., Jacobsen, G., et al. (2015). Losses and recovery of organic carbon from a seagrass ecosystem following disturbance. *Proc. R. Soc. B: Biol. Sci.* 282 (1817), 20151537. doi: 10.1098/rspb.2015.1537

Mandoske, J. (2017). *Can blue carbon further conservation? approaches to conservation through a portfolio of blue carbon options: A case study in the Bahamas* (San Diego, USA: Capstone Projects).

McKenzie, L. J., Nordlund, L. M., Jones, B. L., Cullen-Unsworth, L. C., Roelfsema, C., and Unsworth, R. K. F. (2020). The global distribution of seagrass meadows. *Environ. Res. Lett.* 15 (7), 074041. doi: 10.1088/1748-9326/ab7d06

Mcleod, E., Chmura, G. L., Bouillon, S., Salm, R., Björk, M., Duarte, C. M., et al. (2011). A blueprint for blue carbon: toward an improved understanding of the role of vegetated coastal habitats in sequestering CO2. *Front. Ecol. Environ.* 9 (10), 552–560. doi: 10.1890/110004

Oanda (2022) *Währungsumrechner*. Available at: https://www.oanda.com/currency-converter/de/?from=EUR&to=USD&amount=1 (Accessed 13 September 2022).

Otsu, N. (1979). A threshold selection method from Gray-level histograms. *IEEE Trans. Systems Man Cybernetics* 9 (1), 62–66. doi: 10.1109/TSMC.1979.4310076

Republic of Seychelles (2021). *Seychelles' updated nationally determined contribution* (Seychelles: NDC Registry). Available at: https://unfccc.int/sites/default/files/NDC/2022-06/Seychelles%20-%20NDC_Jul30th%202021%20_Final.pdf.

Roelfsema, C. M., Lyons, M., Kovacs, E. M., Maxwell, P., Saunders, M. I., Samper-Villarreal, J., et al. (2014). Multi-temporal mapping of seagrass cover, species and biomass: A semi-automated object based image analysis approach. *Remote Sens. Environ.* 150, 172–187. doi: 10.1016/j.rse.2014.05.001

Roelfsema, C. M., Lyons, M., Murray, N., Kovacs, E. M., Kennedy, E., Markey, K., et al. (2021). Workflow for the generation of expert-derived training and validation data: A view to global scale habitat mapping. *Front. Mar. Sci.* 8. doi: 10.3389/fmars.2021.643381

Saunders, M. I., Leon, J., Phinn, S. R., Callaghan, D. P., O'Brien, K. R., Roelfsema, C. M., et al. (2013). Coastal retreat and improved water quality mitigate losses of seagrass from sea level rise. *Global Change Biol.* 19 (8), 2569–2583. doi: 10.1111/gcb.12218

Schill, S. R., McNulty, V. P., Pollock, F. J., Lüthje, F., Li, J., Knapp, D. E., et al. (2021). Regional high-resolution benthic habitat data from planet dove imagery for conservation decision-making and marine planning. *Remote Sens.* 13 (21), 4215. doi: 10.3390/rs13214215

Short, F. T., Polidoro, B., Livingstone, S. R., Carpenter, K. E., Bandeira, S., Bujang, J. S., et al. (2011). Extinction risk assessment of the world's seagrass species. *Biol. Conserv.* 144 (7), 1961–1971. doi: 10.1016/j.biocon.2011.04.010

Smith, G. W., Short, F. T., and Kaplan, D. I. (1990). "Distribution and biomass of seagrasses in San Salvador, Bahamas," in *Proceedings of the third symposium on the botany of the Bahamas*. Ed. R. Smith(Bahamian Field Station, San Salvador, Bahamas), 83.

Story, M., and Congalton, R. G. (1986). Accuracy assessment: A user's perspective. *Photogrammetric Eng. Remote Sens.* 52 (3), 397–399.

Tassi, A., and Vizzari, M. (2020). Object-oriented LULC classification in Google earth engine combining SNIC, GLCM, and machine learning algorithms. *Remote Sens.* 12 (22), 3776. doi: 10.3390/rs12223776

The Commonwealth (2022) *The Bahamas*. Available at: https://thecommonwealth.org/our-member-countries/bahamas (Accessed 29 August 2022).

The Government of Mozambique (2021) *Update of the first nationally determined contribution to the united nations framework convention on climate change*. Available at: https://unfccc.int/sites/default/files/NDC/2022-06/NDC_EN_Final.pdf.

The Government of The Bahamas (2015). *Intended nationally determined contribution (INDC) under the united nations framework convention on climate change (UNFCCC)* (NDC Registry).

Thomas, N., Pertiwi, A. P., Traganos, D., Lagomasino, D., Poursanidis, D., Moreno, S., et al. (2021). Space-borne cloud-native satellite-derived bathymetry (SDB) models using ICESat-2 and sentinel-2. *Geophysical Res. Lett.* 48 (6), e2020GL092170. doi: 10.1029/2020GL092170

Traganos, D., Aggarwal, B., Poursanidis, D., Topouzelis, K., Chrysoulakis, N., and Reinartz, P. (2018). Towards global-scale seagrass mapping and monitoring using sentinel-2 on Google earth engine: The case study of the Aegean and Ionian seas. *Remote Sens.* 10 (8), 1227. doi: 10.3390/rs10081227

Traganos, D., Lee, C. B., Blume, A., Poursanidis, D., Čižmek, H., Deter, J., et al. (2022a). Spatially explicit seagrass extent mapping across the entire Mediterranean. *Front. Mar. Sci.* 9. doi: 10.3389/fmars.2022.871799

Traganos, D., Pertiwi, A. P., Lee, C. B., Blume, A., Poursanidis, D., and Shapiro, A. (2022b). Earth observation for ecosystem accounting: spatially explicit national seagrass extent and carbon stock in Kenya, Tanzania, Mozambique and Madagascar. *Remote Sens. Ecol. Conserv.* doi: 10.1002/rse2.287

Traganos, D., and Reinartz, P. (2018). Mapping Mediterranean seagrasses with sentinel-2 imagery. *Mar. pollut. Bull.* 134, 197–209. doi: 10.1016/j.marpolbul.2017.06.075

UNEP (2020). "Seagrasses, the forgotten ecosystems," in *Foresight brief*, vol. 16. . Available at: https://wedocs.unep.org/20.500.11822/32643.

UNEP-WCMC and IUCN (2022) *Protected planet: Protected area profile for Bahamas from the world database of protected areas, July 2022* (Cambridge, UK: UNEP-WCMC and IUCN). Available at: www.protectedplanet.net (Accessed 29 September 2022).

UNFCCC (2016). "Report of the conference of the parties on its twenty-first session, held in Paris from 30 November to 13 December 2015. part one: Proceedings," in *Paris Climate Change Conference - November 2015* (Paris, France).

van Tussenbroek, B. I., Cortés, J., Collin, R., Fonseca, A. C., Gayle, P. M. H., Guzmán, H. M., et al. (2014). Caribbean-Wide, long-term study of seagrass beds reveals local variations, shifts in community structure and occasional collapse. *PloS One* 9 (3), e90600. doi: 10.1371/journal.pone.0090600

Veettil, B. K., Ward, R. D., Lima, M. D. A. C., Stankovic, M., Hoai, P. N., and Quang, N. X. (2020). Opportunities for seagrass research derived from remote sensing: A review of current methods. *Ecol. Indic.* 117, 106560. doi: 10.1016/j.ecolind.2020.106560

Wabnitz, C. C., Andréfouët, S., Torres-Pulliza, D., Müller-Karger, F. E., and Kramer, P. A. (2008). Regional-scale seagrass habitat mapping in the wider Caribbean region using landsat sensors: Applications to conservation and ecology. *Remote Sens. Environ.* 112 (8), 3455–3467. doi: 10.1016/j.rse.2008.01.020

Waycott, M., Duarte, C. M., Carruthers, T. J. B., Orth, R. J., Dennison, W. C., Olyarnik, S., et al. (2009). Accelerating loss of seagrasses across the globe threatens coastal ecosystems. *Proc. Natl. Acad. Sci.* 106 (30), 12377–12381. doi: 10.1073/pnas.0905620106

Waycott, M., McKenzie, L. J., Mellors, J., EllisonJoanna C, J. C., Sheaves, M. T., Collier, C., et al. (2011). "Vulnerability of mangroves, seagrasses and intertidal flats in the tropical pacific to climate change," in *Vulnerability of tropical pacific fisheries and aquaculture to climate change*. Eds. J. D. Bell, J. E. Johnson and A. J. Hobday, 297–368*.

Williamson, P., and Gattuso, J.-P. (2022). Carbon removal using coastal blue carbon ecosystems is uncertain and unreliable, with questionable climatic cost-effectiveness. *Front. Climate* 4. doi: 10.3389/fclim.2022.853666

Xu, H. (2006). Modification of normalised difference water index (NDWI) to enhance open water features in remotely sensed imagery. *Int. J. Remote Sens.* (Noumea, New Caledonia: Secretariat of the Pacific Community) 27 (14), 3025–3033. doi: 10.1080/01431160600589179

frontiers | Frontiers in Marine Science

TYPE Original Research
PUBLISHED 06 February 2023
DOI 10.3389/fmars.2023.1087604

Check for updates

OPEN ACCESS

EDITED BY
Astrid Bracher,
Alfred Wegener Institute Helmholtz Centre for Polar and Marine Research (AWI), Germany

REVIEWED BY
Martin Hieronymi,
Institute of Carbon Cycles, Helmholtz-Zentrum Hereon, Germany
Yuyuan Xie,
University of South Florida, United States

*CORRESPONDENCE
Guifen Wang
guifenwang@hhu.edu.cn

SPECIALTY SECTION
This article was submitted to Ocean Observation, a section of the journal Frontiers in Marine Science

RECEIVED 02 November 2022
ACCEPTED 16 January 2023
PUBLISHED 06 February 2023

CITATION
Lv H, Wang G, Xu W, Zhang Y and Jiang L (2023) Seasonal variability of satellite-derived primary production in the South China Sea from an absorption-based model. *Front. Mar. Sci.* 10:1087604. doi: 10.3389/fmars.2023.1087604

COPYRIGHT
© 2023 Lv, Wang, Xu, Zhang and Jiang. This is an open-access article distributed under the terms of the Creative Commons Attribution License (CC BY). The use, distribution or reproduction in other forums is permitted, provided the original author(s) and the copyright owner(s) are credited and that the original publication in this journal is cited, in accordance with accepted academic practice. No use, distribution or reproduction is permitted which does not comply with these terms.

Seasonal variability of satellite-derived primary production in the South China Sea from an absorption-based model

Hang Lv[1,2], Guifen Wang[1,2]*, Wenlong Xu[1,2], Yinxue Zhang[2,3] and Long Jiang[1,2]

[1]Jiangsu Province Engineering Research Center for Marine Bio-resources Sustainable Utilization, Hohai University, Nanjing, China, [2]College of Oceanography, Hohai University, Nanjing, China, [3]State Key Laboratory of Satellite Ocean Environment Dynamics, Second Institute of Oceanography, Ministry of Natural Resources, Hangzhou, China

Seasonal patterns of marine net primary production (NPP) are crucial for understanding the marine ecosystem and biogeochemical cycles. Uncoupling of seasonal variations between NPP and phytoplankton chlorophyll-a over different areas has attracted much attention. In this study, following a review of previous studies, monthly climatological NPP data from 2003 to 2020, estimated using the Size-fractioned Phytoplankton Pigment Absorption (a_{ph})-based NPP Model (SABPM), were selected to study the seasonal variability of NPP in the South China Sea (SCS). Results showed the spatial differences of NPP seasonality and its departures from climatology in extreme El Niño-Southern Oscillation (ENSO) and Indian Ocean Dipole (IOD) years. Cluster analysis for climatological monthly data identified significant differences of NPP seasonality in five typical regions. In coastal regions along the northern SCS and off eastern Vietnam, NPP exhibited the most obvious seasonal cycle with maximum (minimum) values in summer (winter), attributable mainly to river discharge and summer upwelling. In regions off northwestern Luzon and coast of southern SCS, NPP showed peaks in winter, which were related to strong mixing and upwelling. In northwestern SCS, NPP was high during May–September in phase with sea surface temperature and the primary controlling factors were found to be shallow nutricline depth and wind-driven mixing. Owing to the deep nutricline depth in the central basin, NPP exhibited little seasonal variability; only a weak signal was observed in spring in phase with photosynthetically active radiation. Local dynamics on regulating the nutrient supply and light availability contribute to these regional differences in NPP seasonality, which could also be affected by extreme climate events. The largest anomalies of the NPP seasonal cycle coincide with 2015/2016 ENSO and super IOD in 2020. During these events, enhanced (weakened) westerly winds caused fall (rise) of SLA and increase (decrease) of NPP in coastal regions along the northern SCS and that off eastern Vietnam. Overall, the a_{ph}-based model shows a new perspective to study the spatiotemporal variations of NPP in the SCS.

KEYWORDS

primary production, absorption-based model, seasonal variation, South China Sea, remote sensing

Introduction

Net primary production (NPP), which plays a key role in the functioning of marine ecosystems, is influenced by complex physicochemical conditions in the water column that include temperature, biomass, light, and the concentrations of nutrients (Montes-Hugo et al., 2009; Oziel et al., 2019). Given the importance of NPP in air-sea CO_2 exchange and global carbon cycle (Platt and Sathyendranath, 1988; Brewin et al., 2021), in evaluating future fisheries yields (Sarmiento and Gruber, 2002) as well as in regulating the climate (Reid et al., 2009), its apparent seasonal signal has received considerable attention from the scientific community.

Methods such as ^{14}C incubation and oxygen evolution have provided compelling NPP datasets for nearly 70 years (Nielsen, 1952; Williams et al., 2004). The seasonality of NPP has gradually been explained at numerous typical stations in various areas. In the North Pacific Subtropical Gyre region, represented by the Hawaii Ocean Time Series station (Karl and Lukas, 1996), NPP is high in summer and low in winter. In the North Atlantic Subtropical Gyre region, represented by the Bermuda Atlantic Time Series Study (Lohrenz et al., 1992), NPP is higher in winter and early spring than in other seasons. At a subarctic station in the western Pacific, algal blooms can result in high NPP in spring and summer, while at subtropical stations, NPP generally shows higher values in winter owing to the influence of subtropical mode water (Matsumoto et al., 2016). *In situ* observations of NPP are often limited temporally and spatially, and thus often only reflect local dynamic effects. Fortunately, the development of remote sensing techniques has enabled monitoring of NPP and exploration of its influencing factors on large spatiotemporal scales. Seasonal variation in NPP vary substantially among different regions owing to the strong relationship between environmental variables and photosynthetic parameters (Kulk et al., 2020; Kulk et al., 2021). The seasonal pattern of NPP in the Mediterranean Sea is considered to be generally high in winter and low in summer, consistent with the algal biomass in the west and the influence of photosynthetically active radiation (PAR) in the east (Bosc et al., 2004). In the Red Sea, NPP is regionally distinct and regulated by environmental factors such as sea surface temperature (SST), mixed layer depth (MLD), and PAR (Li W et al., 2020). Nutrient supply has been shown to be the main regulator of NPP in eastern boundary upwelling regions (Messié and Chavez, 2015). NPP could also change in response to upwelling and nutrient availability during the transition of climate events (Behrenfeld et al., 2001).

Over the last 30 years, researchers have proposed a number of NPP remote sensing models, which can be summarized in three main strategies (Lee Z et al., 2015), including CHL-based approach (e.g., Behrenfeld and Falkowski, 1997b), carbon-based approach (e.g., Behrenfeld et al., 2005; Westberry et al., 2008) and phytoplankton absorption-based approach (e.g., Ma et al., 2014; Silsbe et al., 2016; Tao et al., 2017a). Currently, an inversion strategy for NPP that could be used in all seas has yet to be established. A series of model comparison exercises demonstrated that the same model has different accuracy in different regions (Campbell et al., 2002; Carr et al., 2006), and that some results could not simulate the variability of NPP accurately (Lee YJ et al., 2015; Lee and Marra, 2022). In particular, the ocean color chlorophyll-a (CHL) algorithm is challenged by optically complex Case-2 waters, which could affect the performance of NPP models (Saba et al., 2011). Therefore, testing and applying more reliable models could help to explore seasonal variations of NPP in local areas.

The South China Sea (SCS) is the largest tropical marginal sea in the northwest Pacific Ocean, covering an area of 3.5 million km^2. The SCS is identified as a typical oligotrophic region where primary productivity is limited by nutrient availability (Tang et al., 1999). High values of CHL (> 2 mg m^{-3}) generally occur near the coast, while offshore concentrations are lower (< 0.3 mg m^{-3}) (Yu et al., 2019). Ecological processes in the SCS are strongly affected by atmospheric depositions driven by season monsoons (e.g., Lin et al., 2007), in addition to alterations driven by river discharge (Zhang et al., 2012; Zeng et al., 2022), coastal upwelling (Shaw et al., 1996; Jing et al., 2009; Yan et al., 2015), and Kuroshio invasion (Li L et al., 2020). During certain specific periods, NPP in the SCS responds to environmental events such as forest fires (Xiao et al., 2020) and climatic events such as ENSO (Liao et al., 2012).

Study on the seasonal variation in NPP in the SCS has attracted much attention in recent years. *In situ* NPP was found to be higher in winter than in summer and higher on the shelf than in the basin in the northern SCS (Chen and Chen, 2006). In areas near northwestern Luzon, the central coast of Vietnam, to the southeast of Hainan Island, and in northern parts of the Sunda Shelf, monsoon-driven upwelling might produce high CHL concentrations, which could further affect primary productivity (Liu et al., 2002; Ning et al., 2004). The limitations of *in situ* observations are now being broken by satellite remote sensing data, which can describe the patterns of NPP in SCS at high spatial and temporal resolution. As an established standard NPP model, the CHL-based Vertically Generalized Production Model (VGPM) has been widely used in studies on the SCS to determine the seasonal variation in NPP (Wang et al., 2008; Tan and Shi, 2009). On the basis of the VGPM, mean primary productivity in the entire SCS was shown to be highest in winter, decrease gradually in spring, start to rise in early summer, reach a smaller peak in August, and gradually increase back to winter conditions after autumn. Further subdivision of the SCS into typical regions reveals varying patterns in seasonal NPP (Wang et al., 2008; Tan and Shi, 2009). For example, NPP peaks in winter in the northwestern area of Luzon, while peaks occur in both winter and summer in the eastern area of Vietnam and in the Mekong River estuary. In the basin area, the magnitude of NPP variation is relatively weak. Overall, the seasonality of VGPM NPP in the SCS exhibits a favourable match with CHL, while being influenced by environmental factors such as SST (Shih et al., 2021).

However, the results of the VGPM might include large errors or even show contrasting variability in some areas of the SCS (Xie et al., 2020; Lee and Marra, 2022). For example, Xie et al. (2020) reversed the seasonal pattern in NPP in northern shelf waters of the SCS by replacing the CHL-based euphotic depth with that based on the inherent optical properties and by optimizing the model parameters using the nearest neighbor method. This result agreed with a series of field observations (Chen and Chen, 2006; Pan et al., 2015; Ye et al., 2015). Moreover, the influence of the selection of the remote sensing algorithm on the seasonal pattern of NPP cannot be ignored (Xu et al., 2016). There studies remind us to re-investigate the spatial variability of NPP seasonality and their influencing mechanisms in the SCS.

Consequently, it is a critical step to choose a more suitable NPP estimation model in advance to reveal the seasonal variations in the various typical regions of the SCS.

In this study, four typical remote sensing models were evaluated in terms of their suitability for application to the SCS, and NPP calculated by the Size-fractioned Phytoplankton Pigment Absorption (a_{ph})-based NPP Model (SABPM) was found to be most reliable for describing the seasonal cycle of NPP in the SCS. We performed cluster analysis on the reconstructed NPP by a data interpolating method (see Section 2.3 for details) and divided the SCS into five typical regions. For each region, we analyzed the seasonality of NPP, investigated the influence of environmental and dynamics factors, and examined how regional differences in NPP are driven by multiple processes. Moreover, the NPP seasonality exhibits departures from climatology in extreme ENSO and IOD years as mainly influenced by physical forcing in local area.

Data and methods

Data

To obtain a more accurate continuous spatiotemporal distribution of NPP in the SCS, we considered four typical NPP products estimated from Moderate Resolution Imaging Spectroradiometer (MODIS) data with their separate algorithms: the VGPM (Behrenfeld and Falkowski, 1997b), carbon-based productivity model (CbPM, Behrenfeld et al., 2005; Westberry et al., 2008), SABPM (Tao et al., 2017a) and carbon, absorption, and fluorescence euphotic-resolving NPP model (CAFE; Silsbe et al., 2016). SABPM is an a_{ph}-based model developed by considering how the size of phytoplankton affects the quantitative production of phytoplankton photosynthesis (Tao et al., 2017a). The above-mentioned NPP products can be downloaded from the Oregon State Ocean Productivity website (http://sites.science.oregonstate.edu/) and the Global Change Research Data Publishing & Repository (http://www.geodoi.ac.cn/). The main equations and key input parameters for each of the four NPP models are shown in Table 1. The main parameters in each model are also shown in Table 2. This study mainly used monthly MODIS products obtained from the NASA ocean-color website (http://oceancolor.gsfc.nasa.gov/), including SST (Kilpatrick et al., 2015), CHL concentration (Hu et al., 2012), PAR (Frouin et al., 2012), and euphotic zone depth (Z_{eu}, Lee et al., 2007). All of those products covered the period from January 2003 to December 2020 with the spatial resolution being 9 km.

To discuss the primary factors influencing NPP, a range of environmental dynamics parameters were also obtained: monthly sea level anomaly (SLA) calculated from sea surface height (the Copernicus Marine Environment Monitoring Service, https://resources.marine.copernicus.eu/, Ducet et al., 2000), MLD obtained from the Hybrid Coordinate Ocean Model (http://orca.science.oregonstate.edu/, Chassignet et al., 2007), and wind speed extracted from the 0.25° ERA-Interim reanalysis product (Dee et al., 2011), which is the latest global atmospheric reanalysis dataset developed by the European Centre for Medium-Range Weather Forecasts.

Wind stress (WS) and wind stress curl (WSC) were calculated as follows:

$$\vec{\tau} = \rho C \vec{u} \cdot |\vec{u}| \tag{1}$$

$$\nabla \times \vec{\tau} = \frac{\partial \tau_y}{\partial x} - \frac{\partial \tau_x}{\partial y} \tag{2}$$

where u is the wind speed vector, τ is the WS (direction is the same as the direction of the wind speed vector), τ_x and τ_y are the eastward and northward components of WS, respectively, ρ is air density above the sea surface, and C is the drag coefficient for neutral stability conditions (Hellerman, 1965).

In those products, monthly averaged data were collated uniformly to 9 km using the optimal interpolation solution provided by MATLAB routines.

Reconstructed data and validation

Data Interpolating Empirical Orthogonal Function (DINEOF) for filling data gaps is based on the Empirical Orthogonal Function (EOF), and it uses the dominant spatial patterns (EOF modes) extracted from a time series data to reconstruct missing data (Beckers and Rixen, 2003; Alvera-Azcárate et al., 2005). We implemented the DINEOF approach to fill the missing data in the SCS. Quantitative evaluation has shown that errors in DINEOF reconstructed data are usually within 2% (Liu and Wang, 2018; Liu and Wang, 2019). A cross-validation technique was applied in the DINEOF for the final reconstruction. The raw input data of SABPM included some areas of null values before the reconstruction (14% missing data), especially in spring. We use the DINEOF software in Fortran downloaded from the official website of DINEOF (http://modb.oce.ulg.ac.be/mediawiki/index.php/DINEOF).

Cluster analysis

The K-means algorithm is an iterative solution-based clustering analysis algorithm that can eliminate uncertainty generated by empirical choices in areas with large variations. This approach regroups pixels with seasonal cycle shapes, and then a single characteristic seasonal cycle is determined by calculating the center (average cycle) within each cluster that statistically represents the entire cluster. Drawing on previous approaches to analysis of surface CHL (Foukal and Thomas, 2014; Ardyna et al., 2017; Huang et al., 2022), we delineated ocean regions by performing a clustered k-means analysis on the DINEOF-reconstructed NPP products. The linkage algorithm was based on initial calculation of the cosine distance between the objects, which has the advantage of emphasizing mainly differences in the seasonal shape. Specifically, similar to Xu et al. (2020), a monthly climatological time series of the NPP was first created for each pixel of the SCS. The resulting climatological time series were normalized to a maximum value for each specific pixel. The normalized data were then subjected to k-means clustering, which considers statistics of the time series dataset and produces clusters that represent regions of similarity. One of the key challenges for the k-means algorithm is to determine the number of clusters in a dataset. Here, the optimal number of clusters was four, which was determined through use of a series of evaluation indicators in our dataset.

TABLE 1 The main equations of NPP models.

Model Name	Main Equations	References
VGPM	$NPP = CHL \times P_{opt}^{B} \times Z_{eu} \times 0.66125 \times \frac{PAR}{PAR+4.1} \times DL$ $P_{opt}^{B} = \sum_{i=o}^{7} h_i \times SST^i$	Behrenfeld and Falkowski, 1997a
CbPM	$NPP=C\times\mu\times Z_{eu}\times f(PAR)$ $C=(b_{bp}(443)-b_{bp}(443)_{NAP})\times SF$	Behrenfeld et al., 2005; Westberry et al., 2008
CAFE	$NPP = \int_{400}^{700} E_d(\lambda,0) \times a_{ph}(\lambda)/a(\lambda)d\lambda \times \phi_{max} \times tanh(E_K/E)$ $E(t,z,\lambda)=2\pi\times E(0^-,\lambda)\times sin(\pi\times t)\times exp^{(-K_d(\lambda)\times z)}\times E_u$ $K_d(\lambda)=m_0\times a(\lambda)+m_1\times[1-m_2\times\exp^{(-m_3\times a(\lambda))}]\times b_b(\lambda)$	Silsbe et al., 2016
SABPM	$NPP(z) = \frac{K_m}{K_m+PAR(z)}\phi_{max} \times \bar{a}_{ph}(z) \times PAR(z) \times exp(-\nu \times PAR(z))$ $PAR(z) = \int_{400}^{700} E_d(\lambda,0) \times exp(-K_d(\lambda) \times z)d\lambda$ $\bar{a}_{ph}(z) = \frac{\int_{400}^{700} a_{ph}(\lambda,z) \times E_d(\lambda,z)d\lambda}{\int_{400}^{700} E_d(\lambda,z)d\lambda}$ $K_d(\lambda)=M(\lambda)(K_d(490)-K_w(490))+K_w(\lambda)$	Ma et al., 2014; Tao et al., 2017a

Similarity index and correlation coefficient

To describe the interannual stability of seasonal patterns of NPP in different regions, we calculated a similarity index (SI, Kirkpatrick et al., 2000) as follows:

$$SI = 1 - \left(\frac{2 \times arccos\left[\frac{A \cdot B_i}{|A| \times |B_i|}\right]}{\pi}\right) \quad (3)$$

where A is the monthly climatological mean of NPP, and B_i is the monthly mean NPP in year i. The similarity index is also consistent with the linkage algorithm to calculate the cosine distance for K-cluster analysis (Torrecilla et al., 2011).

With equation (4), the correlation coefficient r is calculated for the influencing factor of NPP, which exhibit enough dynamic range in each of regions. A 95% confidence test was performed in the calculation.

$$r(X,Y) = \frac{\mathrm{Cov}(X,Y)}{\sqrt{\mathrm{Var}\ (X)\ \mathrm{Var}(Y)}} \quad (4)$$

where X and Y are the two parameters for correlation, Cov (X, Y) is the covariance of X and Y, Var (X) is the variance of X and Var (Y) is the variance of Y.

Results

Comparison of SABPM with other NPP models in the SCS

Spatial distributions of climatological NPP calculated by the four models exhibit substantially different seasonality in the SCS (Figure 1). In summer, VGPM NPP is higher (~1100 mg C m^{-2} d^{-1}) at shallow depths of 50 m with extensive low values (~260 mgC m^{-2} d^{-1}) in other regions (Figure 1A). In winter, the area with high values becomes larger (<200 m) in comparison with that in summer, and an area with a medium value (~600 mgC m^{-2} d^{-1}) appears between northwestern Luzon and the northern nearshore regions of the SCS (Figure 1B). In summer, CbPM NPP, CAFE NPP, and SABPM NPP exhibit similar spatial patterns (Figures 1C, E, G). The SCS could be divided into a high-value area shallower than approximately 200 m and a low-value area in deeper water, where the high-value area of CAFE NPP is smaller. In the high-value area, the regional averages of CbPM NPP, CAFE NPP, and SABPM NPP are 1029.3, 795.1, and 1109.9 mgC m^{-2} d^{-1}, respectively; in the low-value area, the regional averages are 622.4, 591.2, and 640.4 mgC m^{-2} d^{-1}, respectively. In winter, a low-value stripe (~200 mgC m^{-2} d^{-1}) is evident near 200-m isobath in the northern SCS in CbPM NPP (Figure 1D), whereas this phenomenon is not found in SABPM NPP (Figure 1H). CAFE NPP is lower (376.6 mgC m^{-2} d^{-1}) across the northern SCS in areas shallower than 200 m in winter (Figure 1F), which does not conform to the general rule that inshore NPP is higher than offshore NPP (Chavez et al., 2011). In northern and western parts of the SCS, the NPP estimated by CbPM, CAFE and SABPM is high in summer and low in winter, whereas the NPP estimated by VGPM shows the opposite pattern. To the northwest of Luzon, the results of each model reveal a seasonal cycle of high NPP in winter and low NPP in summer.

For comparison with *in situ* measurements obtained in the SCS (Xie et al., 2015; Bouman et al., 2018; Xie et al., 2020), we analyzed the averaged seasonal variation in NPP over two shelf areas in the SCS: water depth shallower than 50 m (Figure 2A) and water depth shallower than 200 m (Figure 2B). Estimates of NPP by VGPM show obviously larger values in winter than in summer, while the other models show the opposite variability. The peaks of seasonal climatological NPP (<50 m) estimated by VGPM, CbPM, SABPM, and CAFE are 1945.1, 1499.7, 1444.6, and 831.5 mgC m^{-2} d^{-1}, respectively, and the troughs are 1214.6, 737.4, 614.2, and 346.9 mgC m^{-2} d^{-1}, respectively. For shelf waters shallower than 200 m, the peaks of NPP values estimated by VGPM, CbPM, SABPM, and CAFE are 1213.2, 1094.0, 1146.8, and 987.9 mgC m^{-2} d^{-1}, respectively, and the troughs are 698.2, 613.1, 564.2, and 354.0 mgC m^{-2} d^{-1}, respectively. The magnitude and seasonal pattern of variations of

TABLE 2 List of Symbols.

Data source symbol	Description	Unit
PAR	Daily integrated photosynthetic active radiation	Ein m^{-2} d^{-1}
CHL	Chlorophyll-a concentration	mg m^{-3}
DL	Day length	hour
Z_{eu}	Euphotic zone depth	m
SST	Sea surface temperature	°C
P_{opt}^{B}	Maximum biomass-normalized photosynthesis parameter (Empirical parameters, a seventh-order polynomial function of SST)	mgC (mgCHL)$^{-1}$ h^{-1}
C	Phytoplankton carbon biomass	mg
μ	Phytoplankton community growth rate	d^{-1}
f	Empirical formulae relating to PAR	/
$b_{bp}(443)$	Particle backscattering coefficient at 443 nm	m^{-1}
$b_{bp}(443)_{NAP}$	Backscattering coefficient of non-algal particles (= 0.00035)	m^{-1}
SF	Scale factor (= 13000)	/
E_d	Quantum scalar irradiance	Ein m^{-2} nm^{-1}
$PAR(z)$	Integration of Ed (λ, z) over the wavelength range 400~700 nm	Ein m^{-2} d^{-1}
α_{ph}	Phytoplankton pigment absorption	m^{-1}
α	Absorption coefficient	m^{-1}
ϕ_{max}	Maximum value of the quantum yield	mol C Ein^{-1}
E_K	Light saturation parameter	Ein m^{-2} d^{-1}
$E(t, z, \lambda)$	Irradiance at time t, depth z, and wavelength λ	Ein m^{-2} nm^{-1}
E_u	A conversion factor (about 1.4)	/
b_b	Backscattering coefficient	m^{-1}
K_d	Diffuse attenuation coefficient	Ein m^{-2} d^{-1}
K_m	Irradiance where the quantum yield reaches half of its maximum value	μW cm^{-2} nm^{-1}
$\bar{a}_{ph}$	Spectrally averaged absorption coefficient over 400~700 nm	m^{-1}
v	Photoinhibition parameter (=0.01)	(Ein m^{-1} d^{-1})$^{-1}$
K_w	Diffuse attenuation coefficient of pure water	m^{-1}

SABPM NPP are most similar with those observed by Xie et al. (2020), which supports us choosing SABPM as the most suitable model, and these results could also be confirmed with observations obtained in the Taiwan Strait (Liu et al., 2007; Tseng et al., 2020).

The researchers conducted model sensitivity experiments by Monte Carlo methods, and the results revealed that VGPM and CbPM were strongly influenced by the accuracy of chlorophyll (Lee Z et al., 2015; Ma et al., 2014). Meanwhile the a_{ph}-based model which avoids the use of chlorophyll was found to be more accurate than other kinds of models (Tao et al., 2017b). This result is supported by previous studies comparing the application of NPP models in global ocean and regional areas, and the a_{ph}-based models always maintain good performances (Hirawake et al., 2012; Barnes et al., 2014; Ma et al., 2014; Silsbe et al., 2016; Tao et al., 2017b; Robinson et al., 2017; Wu et al., 2022). Given this strong generalization capability, extending an a_{ph}-based model such as SABPM to more unproven regions represent the most reliable approach at present.

Seasonality of NPP and its relations with environmental factors

Four regions were divided according to the cosine similarity of seasonal variation (Figure 3A). Owing to the geographical distance and potential for different influencing factors, we split yellow area into two parts, and further divided the SCS into five regions: the coastal ocean along the northern SCS (NC), coastal waters to the east of Vietnam (VE), area off northwestern Luzon and the southern SCS (LS), northwestern parts of the SCS (NW), and the central basin area (CB). Area NC & VE includes the shallow area (water depth of<200 m) in the north of the SCS, most of the Beibu Gulf, and the southern coast of Vietnam (10.2% of the SCS area). Area LS is the region near Luzon Island and the southern coast (5.3%). Areas NW (23.5%) and CB (61.0%) separate the remainder of the SCS from the southwest to the northeast. Area NW includes the western part of the SCS and the area around the 200-m isobath in the north, while area CB covers the remaining area including the basin. Figures 3B–E

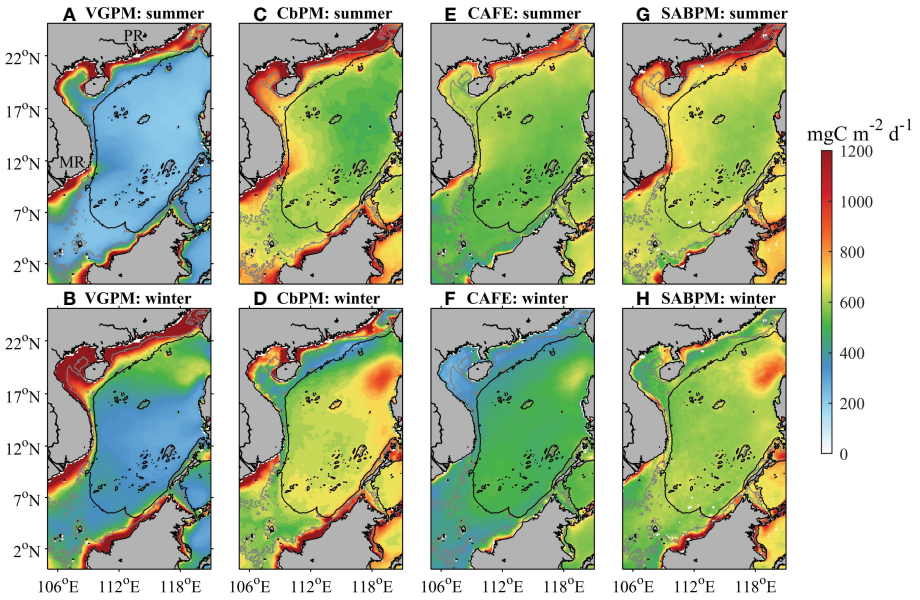


FIGURE 1
Climatological ocean NPP in summer and winter during 2002–2020 in the study area produced using four algorithms: **(A, B)** VGPM, **(C, D)** CbPM, **(E, F)** CAFE, and **(G, H)** SABPM. The grey lines are the 50 m isobaths and the black lines are the 200 m isobaths. The location of the Pearl River (PR) and the Mekong River (MR) is indicated in **(A)**.

shows the seasonal variations of NPP in these regions (discussed further in section 3.3), and the data are normalized by the maximum value.

$$Simpson's\ \ diversity\ \ index = 1 - \sum_{i=1}^{S}\left(\frac{n_i}{N}\right)^2 \quad (5)$$

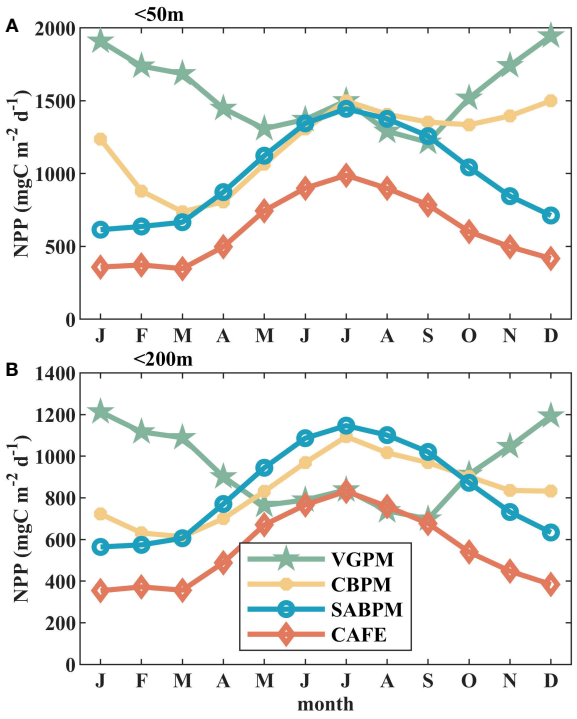


FIGURE 2
Monthly average variations of mean NPP calculated by the four algorithms in nearshore water: **(A)** less than 50 m and **(B)** less than 200 m.

A simplified form of Simpson's diversity index was used to indicate the stability of seasonal variation (Simpson, 1949; Huang et al., 2022). In equation 5, S is the number of climatological clustering partitions (S = 4), N is the number of years in this study (N = 18), n_i s the number of times that pixel has been clustered into region i by a single year. At this point a larger Simpson's diversity index indicates that the pixel is divided into different partitions more often. As shown in Figure 3F, lower values of Simpson's diversity index indicate less variable seasonality. The boundaries of the regions are plotted as green lines. The accuracy in relation to the Beibu Gulf is questionable owing to the serious amount of missing original NPP data (over 60% in winter), and this region is not considered in further discussion. Overall, the partition stability is high (average: 0.16, standard deviation: 0.16). A relatively less stable band exists from the southwest to the northeast as the boundary between regions NW and CB, and the widest part is in the central part of the SCS (Simpson index = 0.29 ± 0.16 in the blue box as shown in Figure 3F).

To quantify the difference between the SABPM NPP seasonality and the traditional results, the VGPM NPP is given simultaneously as a comparison. Figure 4 shows that the results of VGPM NPP correlate well with CHL and always have a seasonal cycle of high values in winter and low values in summer, except for region VE. However, uncoupling of seasonality variations between CHL and NPP in region NC has been investigated by Xie et al. (2020). They considered that the noncorresponding seasonal cycle is determined by river input. The seasonality of SABPM NPP is described as independent of CHL in regions NC and CB, and even negatively correlated in region NW. In region VE, the presence or absence of a winter peak is the main difference between CHL and SABPM NPP. On average, SABPM NPP is 170.9 and 312.9 mgC m^{-2} d^{-1} higher than VGPM NPP in regions NW and CB, respectively. This finding corresponds to the VGPM NPP being substantially lower than the field value measurements in the basin of the SCS (Tan and Shi, 2009; Huang et al., 2018);

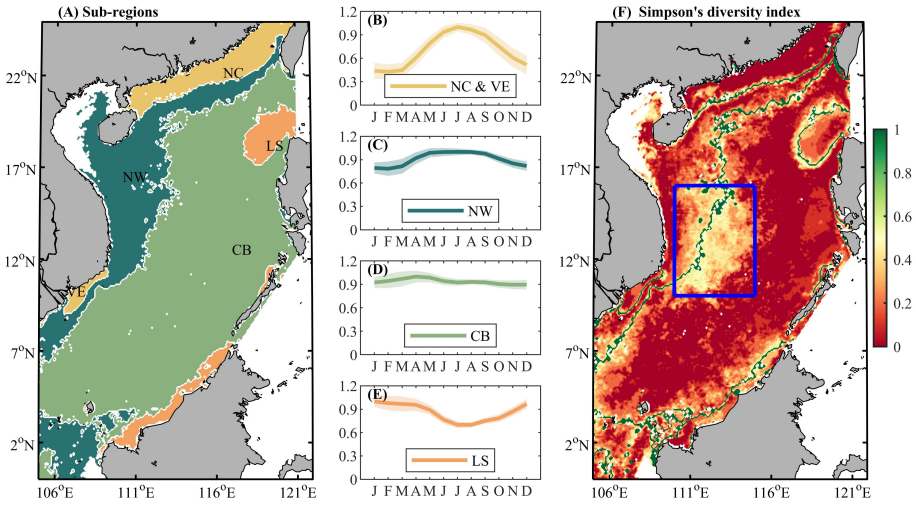


FIGURE 3
(A) Cluster-derived regions based on the climatological NPP seasonality during 2003–2021. **(B–E)** Temporal evolution of the centroid of four clusters obtained from k-means analysis. The colors of the curves correspond to those in **(A)**. Light color shading in **(B–E)** indicates ± one standard deviation. **(F)** The Simpson diversity index for measuring the stability of NPP seasonality (the closer to 0 the more stable). Larger values indicate less variable seasonality. Borders of these regions are shown in green for reference. A low-value area is framed by the blue box.

moreover, it suggests that, at least in parts of the SCS, NPP seasonality cannot be characterized simply by CHL.

In comparison with VGPM NPP and CHL, SABPM NPP exhibits more seasonal variability in the SCS (Figure 4). In region NC, NPP is high in summer and low in winter, with a peak value in July (1367.5 mgC m^{-2} d^{-1}). In region NW, NPP is higher during May–September with values in the range of 738.3–739.4 mgC m^{-2} d^{-1}. In region CB, NPP does not exhibit evident seasonal variability (range: 611.0–682.3 mgC m^{-2} d^{-1}), and there is only a weak signal in spring. In region LS, NPP is high in winter and low in summer with a peak value in January (933.7 mgC m^{-2} d^{-1}). Region VE is similar to region NC with peak NPP in August (1379.3 mgC m^{-2} d^{-1}).

In comparison with the seasonal clustering results for the surface CHL (Xu et al., 2020), there are relatively few typical subdivisions of the NPP in the deeper than 200 m region. Under the same clustering conditions, only northwestern Luzon was the common characteristic area, and the seasonality of surface CHL was far more complex (three more feature areas) in deeper water than the seasonality of NPP. This suggests that phytoplankton surface biomass and phytoplankton photosynthetic production capacity do not respond to the environment in exactly the same way. The role of environmental factors on NPP and the main driving processes of NPP in the SCS will be further discussed in this study.

Correlation coefficients between monthly climatological NPP values and the monthly climatological values of multiple parameters are shown in Figure 5, and the regional average correlation coefficients are listed in Table 3. Regions where the linear trend is not significant at the 95% confidence level are masked in Figure 5.

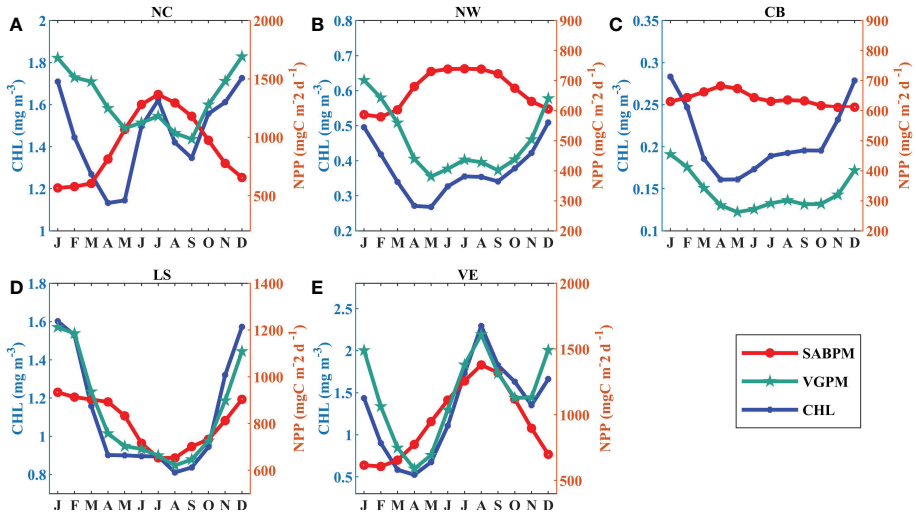


FIGURE 4
(A–E) Monthly average variations of mean NPP based on SABPM (red line), NPP based on VGPM (green line), and CHL (blue line) in the five regions shown in Figure 3A.

PAR exhibits positive correlation with NPP in most of the SCS, except for region LS, region VE, and a small area in the central part. CHL does not directly characterize NPP in the SCS. The correlation coefficients are positive in the coastal waters adjacent to Pearl River estuary, region LS, and region VE and negative in region NW. The relationship between MLD and NPP shows negative correlation, which is most significant in central and northern parts of the SCS. The relationship between SST and NPP is significantly positive in northern and western nearshore areas of the SCS, but negative in region LS. In region LS, southwestern and southeastern areas of the SCS, and western nearshore parts, SLA is correlated negatively with NPP, while a small area with positive correlation exists in the central part of the SCS. Z_{eu} is defined as 1% of the PAR depth, which has almost the opposite effect on NPP to that of CHL. Wind speed and its mixing effect are described by the 10-m zonal wind speed (U_{10}). In regions NC, VE, and NW, U_{10} is correlated positively with NPP, indicating increase in NPP when the southwesterly wind strengthens. Conversely, in region LS, U_{10} is correlated negatively with NPP, indicating increase in NPP when the northeasterly wind strengthens. Positive correlation between WSC and NPP is found at various nearshore locations in the SCS, corresponding to the location of upwelling occurrence. In order to describe the main influences of NPP in each region, we ranked them by the averaged correlation coefficient and took the top three: SST, PAR, and U_{10} in region NC; U_{10}, SST, and CHL in region LS; U_{10}, WSC, and MLD in region VE; SST, U_{10}, and MLD in region NW; PAR, MLD, and SLA in region CB.

Interannual variations of seasonal patterns of NPP in different regions

Section 3.2 revealed the regional seasonality of NPP in the SCS; however, concerns over whether this division strategy has stability and whether there will be specific years that do not satisfy this division need further study. Figure 6 reveals the interannual differences in NPP seasonal clustering, where the years have similar seasonal cycle shapes and the separation of each partition is also relatively stable interannually. On average, the similarity index values for the regions ranged from 0.92 to 0.97. Some relatively obvious outliers are evident in 2016 and 2020. In 2016 (2020), NPP exhibits relatively strong intraregional seasonal variability in each of regions, with similarity index values of 0.90 (0.91), 0.92 (0.88), 0.89 (0.88), 0.94 (0.93), and 0.97 (0.95) in regions NC, LS, VE, NW, and CB, respectively. All regions except NC exhibit the lowest similarity index values in 2020, indicating that the seasonal variations in this year are significantly different from the climatic average. In these years, NPP is considered to be influenced by the local and remote forcing of large-scale climatic modes such as the El Niño–Southern Oscillation (ENSO)/Indian Ocean Dipole (IOD) (Kong et al., 2019; Kuo and Tseng, 2020).

Discussion

Factors influencing regional differences in NPP seasonality

Except for the region LS, the spatial distribution of NPP seasonality differs from both the surface CHL (Yu et al., 2019) and surface carbon-to-CHL ratio (Xu et al., 2020) at least in waters deeper than 200 m in the SCS. This study suggests that there are two main reasons for this discordance: on the one hand, unlike NPP, surface CHL and surface carbon-to-CHL ratio do not contain vertical information, while there are still some errors in these two parameters obtained by satellite remote sensing. On the other hand, light conditions and nutrient availability are equally decisive factors for NPP. Therefore, the aim of this section is to discuss the direct and

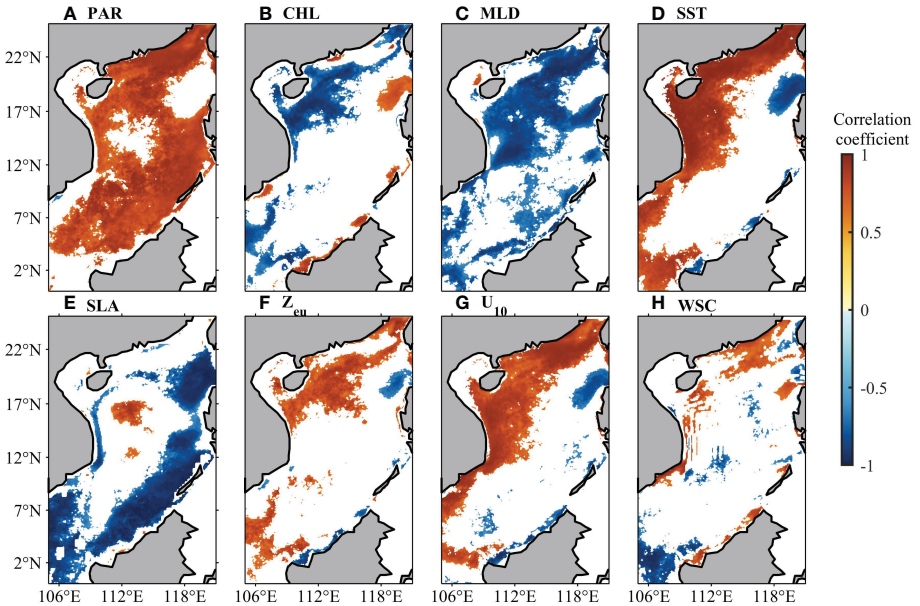


FIGURE 5
Correlation coefficients between monthly climatological NPP and **(A)** PAR, **(B)** CHL, **(C)** MLD, **(D)** SST, **(E)** SLA, **(F)** Z_{eu}, **(G)** 10-m zonal wind speed (U_{10}), and **(H)** WSC. Locations with nonsignificant correlations are plotted in white.

TABLE 3 Regional means of correlation coefficients with standard deviation shown in Figure 5.

Region	NC	LS	VE	NW	CB
PAR	0.87 (0.08)	-0.04 (0.36)	-0.06 (0.22)	0.60 (0.35)	0.70 (0.24)
CHL	-0.26 (0.51)	0.61 (0.20)	0.52 (0.22)	-0.50 (0.41)	-0.21 (0.37)
MLD	-0.43 (0.39)	0.29 (0.34)	-0.74 (0.23)	-0.68 (0.35)	-0.57 (0.22)
SST	0.96 (0.03)	-0.64 (0.20)	0.70 (0.08)	0.87 (0.12)	0.18 (0.38)
SLA	-0.32 (0.20)	-0.29 (0.57)	-0.64 (0.10)	-0.26 (0.48)	-0.53 (0.47)
Z_{eu}	0.50 (0.27)	-0.58 (0.20)	-0.31 (0.30)	0.51 (0.37)	0.28 (0.36)
U_{10}	0.84 (0.10)	-0.68 (0.19)	0.91 (0.06)	0.79 (0.29)	-0.00 (0.43)
WSC	0.45 (0.40)	0.40 (0.47)	0.75 (0.26)	0.12 (0.59)	-0.14 (0.36)

indirect influence of environmental parameters and dynamical processes on light conditions and nutrient supply.

In region NC, two areas of wind-driven summer upwelling are enhanced remarkably to the east of Guangdong and Qiongdong (Jing et al., 2009), while the peak of the Pearl River discharge occurs in July–August (Zhang et al., 2012; Xie et al., 2020). Together, they deliver nutrient-rich water to this region and PAR at this time is also higher than in winter, in accordance with the summer peak of NPP. The seasonal cycle of NPP in the VE region is the same as in the NC region, resulting in a higher NPP in summer than in winter. In addition to the upwelling driven by the alongshore wind stress (Wyrtki, 1961), nutrients transported by the Mekong River were also found to have a crucial impact on the summer peak of NPP (Zeng et al., 2022).

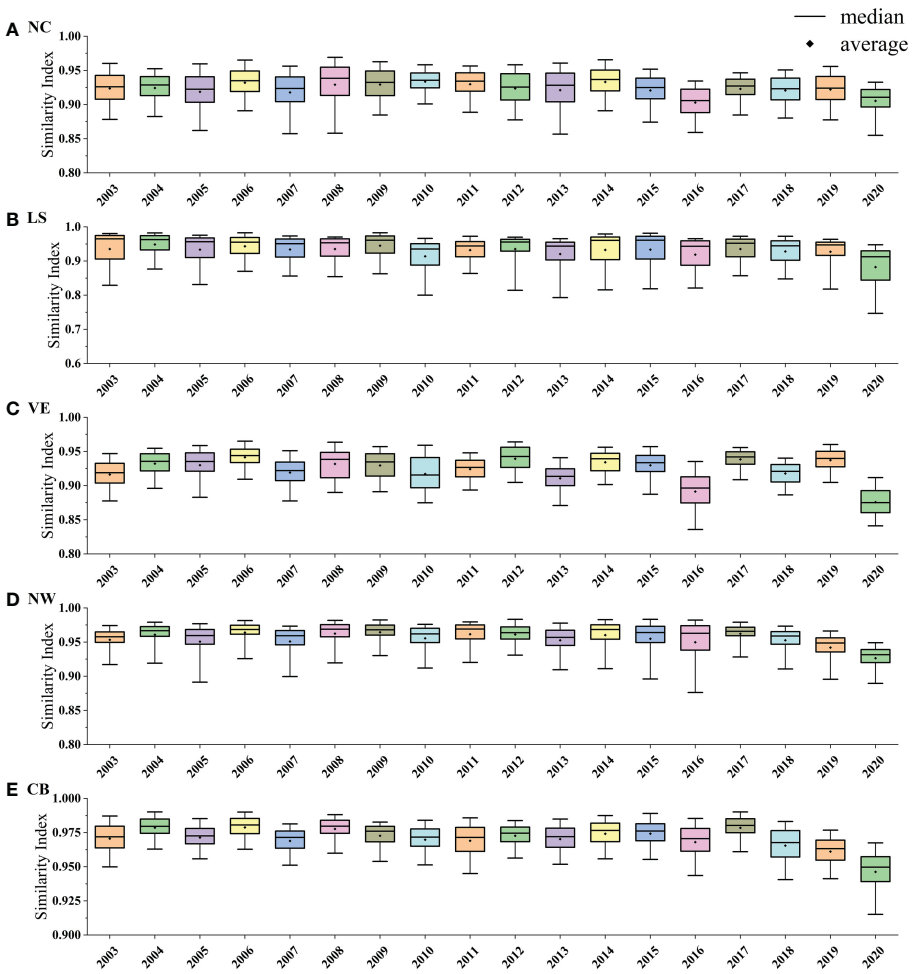


FIGURE 6
Quartile diagrams of similarity index between the seasonal variation of NPP for each year (2003–2020) and monthly climatology mean in typical regions: **(A)** NC, **(B)** LS, **(C)** VE, **(D)** NW and **(E)** CB. The rectangles, black lines, and black dots indicate the interquartile range, average, and median, respectively.

The local dynamical processes are more complex in region LS. During winter and spring, a zone of weak wind stress is formed in the direction downwind (west) of Luzon owing to the barrier effect of island against the northeasterly winds, resulting in generation of positive wind stress vorticity (He et al., 2015). Strong winter upwelling during November–January is observed in this region (Hu and Wang, 2016), driven by a combination of local wind and basin-scale circulation. Similarly, the seasonal cycle of NPP in the southern SCS is synchronized with that resulting from the influence of winter coastal upwelling off northwestern Borneo (Yan et al., 2015). Large amounts of nutrients are transported upward by the winter upwelling, when more phytoplankton could participate in photosynthetic reactions (surface CHL ~ 1.58 mg m^{-3}, above annual average of 42.0%), positively correlating with NPP. Meanwhile, both low SST (~ 27.9°C, below 5.7% of annual average) and strong northeasterly winds in winter further enhance nutrient mixing. In summary, NPP in region LS is higher in winter than in summer.

No obvious dynamical processes are evident in region NW except for southwesterly wind mixing, and the seasonality of light and nutrients is the decisive factor affecting the seasonality of NPP. Recent results (Du et al., 2021) show that nutrients exhibit a gradational distribution from the northwest to the southeast in summer, with a maximum value (up to 7.0 µmol L^{-1} at 0 to 50 m) in the northwestern SCS and a nutricline depth of approximately 20 m. Meanwhile, higher SST and a shallower MLD in summer contribute to reduction in CHL concentration in this region. In region NW, owing to oligotrophic environmental conditions, the effect of lower CHL concentration on NPP is not directly positively correlated, but it is affected by light penetration (Lee et al., 2005). Compared with the annual mean data, the lower CHL (~ 0.34 mg m^{-3}, below 7.4%) in summer leads to a higher diffuse attenuation coefficient (~ 0.05 m^{-1}, above 7.9%), which in turn produces stronger light penetration and deeper Z_{eu} (~ 87.3 m). Overall, the greatest PAR in summer is accompanied by the strongest light penetration, which allows more energy to penetrate into the nutrient layer, leading to a level of NPP that is consistently higher than in other seasons.

The obvious difference between region CB and region NW is the vertical distribution of nutrients (Du et al., 2021). In region CB, the annual nutricline depth is >60 m, where available light is almost dissipated. Therefore, in this region, NPP variation is minimal and the effects of all the environmental factors are almost insignificant. A weak signal of high NPP is evident in spring, corresponding to the highest PAR values. There is an area of low PAR correlation near the border between the northwest of region CB and region NW (the central SCS basin). An area of high nutrient concentration at approximately 50 m in autumn could help explain this discordant seasonality between NPP and PAR. Moreover, negative correlation between SLA and NPP occurs in an area extending southwestward from the Luzon Chanel to region CB, which might be related to mesoscale processes (Chelton et al., 2011).

SABPM is based on the radiative transfer theory of ocean optics, where the NPP is first calculated in layers and then integrated (Tao et al., 2017a; Tao et al., 2017b). This approach is strictly a physical process rather than an empirical relationship, except for the acquisition of light quantum yields (Lee Z et al., 2015). The CHL obtained by satellite remote sensing may cause two-step errors in the VGPM, but the uncertainty of input ocean color data in the a_{ph}-based model mainly originate from the remote-sensing reflectance (Lee Z et al., 2015). Based on the model comparison and the above analysis, we believe that the SABPM results are distinctive and provide a new perspective for NPP studies in the SCS. However, the seasonality of SABPM in the region NW and CB are still not validated by a large amount of field data and uncertainties exist. It is important to emphasize that the NPP seasonality is weak due to the lack of significant dynamics driving the CB region and may be subject to uncertainty caused by the model's own inputs.

In summary, the seasonality of NPP is influenced by a variety of environmental dynamics, but it fundamentally depends on the combined regulation of light conditions, nutrient concentration, and CHL concentration. In the future, as studies of the physiological state and vertical structures of phytoplankton deepens, estimation of NPP with more accurate size-fractionated models were expected to improve this understanding (Sathyendranath et al., 2020; Liu et al., 2022; Deng et al., 2022).

Factors influencing interannual variations in NPP seasonality

Interannual variation of NPP in the SCS is jointly regulated by ENSO and IOD (Kong et al., 2019). ENSO events produce thermocline/nutricline anomalies that alter the nutrient supply to the true euphotic zone, which in turn affect primary productivity (Hu et al., 2021; Li et al., 2022). Moreover, the fractions of micro- and nano-phytoplankton in the SCS tend to rise during La Nina events (Li et al., 2017). Section 3.4 revealed those years in which the seasonal patterns exhibited large differences from the climatological monthly mean. We suppose that such interannual variations is also related to the large-scale climate events and we discuss the following two special cases.

A maximum positive (negative) seasonal variability occurred along the coastal area of NC and VE in October 2016 (2020), resulting in the highest NPP of 1323.1 mgC m^{-2} d^{-1} (lowest NPP of 885.7 mgC m^{-2} d^{-1}). In October 2016 (2020), NPP above 32.2% (below 11.5%) of the climatology in these regions (Figures 7A, B, E) corresponded to a value of SLA that was 25.2% below (91.9% above) that of climatology (Figures 7C, D, F). In October 2016, the enhanced westerly winds (Figure 7G) in these regions (0.83 m s-1 higher than normal) favored the occurrence of upwelling, characterized by strong offshore Ekman transport and positive SLA (4 cm). Conversely, in October 2020, the westerly winds (Figure 7G) dropped by 1.38 m s-1, depressing the upwelling along the shelf. As a result, the offshore Ekman transport was weakened and the SLA decreased (14 cm). During these extreme events, anomalous NPP was associated with the negative SLA, indicating the important role of ENSO-related or IOD-related upwelling (Shu et al., 2018; Kong et al., 2019).

Also, this study found that 2020 was a special year with the most exceptional seasonal variation in NPP in the SCS. After a series of analyses similar to the process described above, NPP in each region was found to be low in March–April and November. We speculate that this is related to the low MLD in the SCS from 2019 onwards

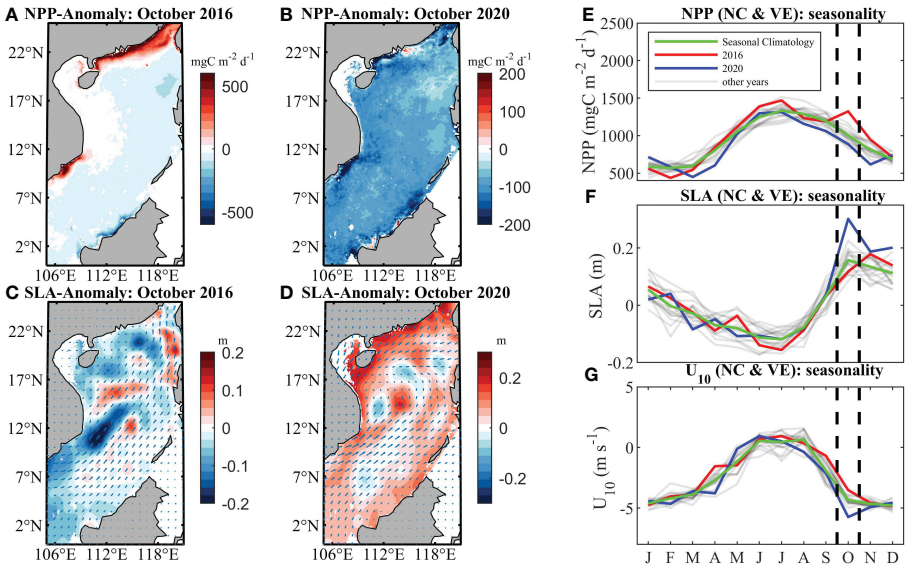


FIGURE 7
Spatial distribution of NPP in the SCS in October from **(A)** 2016 subtracted from the climatology and **(B)** 2020 subtracted from the climatology. Spatial distribution of SLA in the SCS in October from **(C)** 2016 subtracted from the climatology and **(D)** 2020 subtracted from the climatology. Vectors in **(C)** and **(D)** are the anomalous winds in 2016 and 2020. Seasonality of mean **(E)** NPP, **(F)** SLA and **(G)** U_{10} in the SCS for the climatology (green), 2016 (red), 2020 (blue) and other years (gray).

(super IOD from 2019 onwards may be the cause of the MLD and SLA anomalies, Utari et al., 2022), as the shallower MLD may have led to a compression of the nutrient-rich season. However, further analysis and more data are needed in the future to support this speculation.

Conclusion

Among the various NPP models available, including VGPM, CbPM, CAFE, and SABPM, the latter was found most reliable in describing the seasonal variation of NPP in the SCS. On the basis of a MODIS data product estimated using SABPM, this study investigated the seasonality of NPP by considering the spatial differences and the interannual variations. The main findings include the following. 1) NPP estimated with SABPM exhibits more spatial features of seasonality in the SCS. NPP is higher in summer than in winter in regions NC and VE, whereas it is higher in winter than in summer in region LS. The magnitude of NPP variability is relatively small in regions NW and CB, with relatively high values throughout summer in region NW and a weak signal of high NPP in spring in region CB. 2) Because nutrient limitation is one of the determinants of NPP in the SCS, high values in coastal areas are well matched with the occurrence of upwelling or river-derived input, while the main difference between regions NW and CB might be related to the depth of the nutricline. Other environmental factors including PAR, SST, MLD, and wind speed could also regulate the seasonal patterns in NPP by affecting the available light and nutrient distribution within the euphotic zone in different regions. 3) The interannual departures of NPP seasonality from climatology were observed with the largest anomalous changes coincides with the 2015–2016 ENSO and 2020 IOD events. Specific case analyses indicate that anomalous latitudinal wind speeds and SLA during these climate events could promote or hinder nutrient availability and then cause NPP anomalies. As SABPM shows potential for identifying annual signals, further applications for interannual NPP variability analysis are expected in the future.

Data availability statement

The raw data supporting the conclusions of this article will be made available by the authors, without undue reservation.

Author contributions

HL performed the data analysis and drafted the manuscript. GW initiated the idea of this study, contributed to the data analysis and helped improve the manuscript. WX, YZ and LJ participated in the discussions and helped improve the manuscript. All authors contributed to the article and approved the submitted version.

Funding

This work was supported by the National Natural Science Foundation of China (grant no. 42276189), and National Natural Science Foundation of China (grant no. 41776045).

Acknowledgments

We thank the NASA EARTHDATA (https://www.earthdata.nasa.gov/), the Oregon State Ocean Productivity website (http://sites.science.oregonstate.edu/ocean.productivity/), the Copernicus Marine Environment Monitoring Service (http://marine.copernicus.eu/) and the Global Change Research Data Publishing & Repository (https://doi.org/10.3974/geodb.2019.05.01.V1) for processing and distributing the primary datasets. We are grateful to Dr. Zui Tao for his help. We thank two reviewers for their precious comments on this manuscript. We thank James Buxton MSc, from Liwen Bianji (Edanz) (www.liwenbianji.cn/), for editing the English text of a draft of this manuscript.

Conflict of interest

The authors declare that the research was conducted in the absence of any commercial or financial relationships that could be construed as a potential conflict of interest.

Publisher's note

All claims expressed in this article are solely those of the authors and do not necessarily represent those of their affiliated organizations, or those of the publisher, the editors and the reviewers. Any product that may be evaluated in this article, or claim that may be made by its manufacturer, is not guaranteed or endorsed by the publisher.

References

Alvera-Azcárate, A., Barth, A., Rixen, M., and Beckers, J. M. (2005). Reconstruction of incomplete oceanographic data sets using empirical orthogonal functions: Application to the Adriatic Sea surface temperature. *Ocean Model.* 9 (4), 325–346. doi: 10.1016/j.ocemod.2004.08.001

Ardyna, M., Claustre, H., Sallée, J. B., d'Ovidio, F., Gentili, B., van Dijken, G., et al. (2017). Delineating environmental control of phytoplankton biomass and phenology in the southern ocean. *Geophys. Res. Lett.* 44 (10), 5016–5024. doi: 10.1002/2016GL072428

Barnes, M. K., Tilstone, G. H., Smyth, T. J., Suggett, D. J., Astoreca, R., Lancelot, C., et al. (2014). Absorption-based algorithm of primary production for total and size-fractionated phytoplankton in coastal waters. *Mar. Ecol. Prog. Ser.* 504, 73–89. doi: 10.3354/meps10751

Beckers, J. M., and Rixen, M. (2003). EOF calculations and data filling from incomplete oceanographic datasets. *J. Atmos. Oceanic Technol.* 20 (12), 1839–1856. doi: 10.1175/1520-0426(2003)020<1839:ECADFF>2.0.CO;2

Behrenfeld, M. J., Boss, E., Siegel, D. A., and Shea, D. M. (2005). Carbon-based ocean productivity and phytoplankton physiology from space. *Global Biogeochem. Cycles* 19 (1). doi: 10.1029/2004GB002299

Behrenfeld, M. J., and Falkowski, P. G. (1997a). A consumer's guide to phytoplankton primary productivity models. *Limnol. Oceanogr.* 42 (7), 1479–1491. doi: 10.4319/lo.1997.42.7.1479

Behrenfeld, M. J., and Falkowski, P. G. (1997b). Photosynthetic rates derived from satellite-based chlorophyll concentration. *Limnol. Oceanogr.* 42 (1), 1–20. doi: 10.4319/lo.1997.42.1.0001

Behrenfeld, M. J., Randerson, J. T., McClain, C. R., Feldman, G. C., Los, S. O., Tucker, C. J., et al. (2001). Biospheric primary production during an ENSO transition. *Science* 291 (5513), 2594–2597.

Bosc, E., Bricaud, A., and Antoine, D. (2004). Seasonal and interannual variability in algal biomass and primary production in the Mediterranean Sea, as derived from 4 years of SeaWiFS observations. *Global Biogeochem. Cycles* 18 (1). doi: 10.1029/2003GB002034

Bouman, H. A., Platt, T., Doblin, M., Figueiras, F. G., Gudmundsson, K., Gudfinnsson, H. G., et al. (2018). Photosynthesis–irradiance parameters of marine phytoplankton: synthesis of a global data set. *Earth Syst. Sci. Data* 10 (1), 251–266. doi: 10.5194/essd-10-251-2018

Brewin, R. J. W., Sathyendranath, S., Platt, T., Bouman, H., Ciavatta, S., Dall'Olmo, G., et al. (2021). Sensing the ocean biological carbon pump from space: A review of capabilities, concepts, research gaps and future developments. *Earth-Sci. Rev.* 217, 103604. doi: 10.1016/j.earscirev.2021.103604

Campbell, J., Antoine, D., Armstrong, R., Arrigo, K., Balch, W., Barber, R., et al. (2002). Comparison of algorithms for estimating ocean primary production from surface chlorophyll, temperature, and irradiance. *Global Biogeochem. Cycles* 16 (3), 9–1-9-15. doi: 10.1029/2001GB001444

Carr, M. E., Friedrichs, M. A. M., Schmeltz, M., Aita, M. N., Antoine, D., Arrigo, K. R., et al. (2006). A comparison of global estimates of marine primary production from ocean color. *Deep Sea Res. Part II: Topic. Stud. Oceanogr.* 53 (5-7), 741–770. doi: 10.1016/j.dsr2.2006.01.028

Chassignet, E. P., Hurlburt, H. E., Smedstad, O. M., Halliwell, G. R., Hogan, P. J., Wallcraft, A. J., et al. (2007). The HYCOM (hybrid coordinate ocean model) data assimilative system. *J. Mar. Syst.* 65 (1-4), 60–83. doi: 10.1016/j.jmarsys.2005.09.016

Chavez, F. P., Messié, M., and Pennington, J. T. (2011). Marine primary production in relation to climate variability and change. *Annu. Rev. Mar. Sci.* 3, 227–260. doi: 10.1146/annurev.marine.010908.163917

Chelton, D. B., Schlax, M. G., and Samelson, R. M. (2011). Global observations of nonlinear mesoscale eddies. *Prog. Oceanogr.* 91 (2), 167–216. doi: 10.1016/j.pocean.2011.01.002

Chen, Y. L. L., and Chen, H. Y. (2006). Seasonal dynamics of primary and new production in the northern south China Sea: The significance of river discharge and nutrient advection. *Deep Sea Res. Part I: Oceanogr. Res. Papers* 53 (6), 971–986. doi: 10.1016/j.dsr.2006.02.005

Dee, D. P., Uppala, S. M., Simmons, A. J., Berrisford, P., Poli, P., Kobayashi, S., et al. (2011). The ERA-interim reanalysis: Configuration and performance of the data assimilation system. *Q. J. R. Meteorol. Soc.* 137 (656), 553–597. doi: 10.1002/qj.828

Deng, L., Zhou, W., Xu, J., Cao, W., Liao, J., Zhao, J., et al. (2022). Estimation of vertical size-fractionated phytoplankton primary production in the northern south China Sea. *Ecol. Indic.* 135, 108546. doi: 10.1016/j.ecolind.2022.108546

Ducet, N., Le Traon, P. Y., and Reverdin, G. (2000). Global high-resolution mapping of ocean circulation from TOPEX/Poseidon and ERS-1 and-2. *J. Geophys. Res.: Oceans* 105 (C8), 19477–19498. doi: 10.1029/2000JC900063

Du, C., He, R., Liu, Z., Huang, T., Wang, L., Yuan, Z., et al. (2021). Climatology of nutrient distributions in the south China Sea based on a large data set derived from a new algorithm. *Prog. Oceanogr.* 195, 102586. doi: 10.1016/j.pocean.2021.102586

Foukal, N. P., and Thomas, A. C. (2014). Biogeography and phenology of satellite-measured phytoplankton seasonality in the California current. *Deep Sea Res. Part I: Oceanogr. Res. Papers* 92, 11–25.

Frouin, R., McPherson, J., Ueyoshi, K., and Franz, B. A. (2012). A time series of photosynthetically available radiation at the ocean surface from SeaWiFS and MODIS data. *Remote Sens. Mar. Environ. II. SPIE* 8525, 234–245. doi: 10.1117/12.981264

He, Y., Cai, S., Wang, D., and He, J. (2015). A model study of Luzon cold eddies in the northern south China Sea. *Deep Sea Res. Part I: Oceanogr. Res. Papers* 97, 107–123.

Hellerman, S. (1965). Computations of wind stress fields over the Atlantic ocean. *Monthly Weather Rev.* 93 (4), 239–244. doi: 10.1175/1520-0493(1965)093<0239:COWSFO>2.3.CO;2

Hirawake, T., Shinmyo, K., Fujiwara, A., and Saitoh, S. I. (2012). Satellite remote sensing of primary productivity in the Bering and chukchi seas using an absorption-based approach. *ICES J. Mar. Sci.* 69 (7), 1194–1204. doi: 10.1093/icesjms/fss111

Huang, K., Xue, H., Chai, F., Wang, D., Xiu, P., Xie, Q., et al. (2022). Inter-annual variability of biogeography-based phytoplankton seasonality in the Arabian Sea during 1998–2017. *Deep Sea Res. Part II: Topic. Stud. Oceanogr.* 105096.

Huang, Y., Yang, B., Chen, B., Qiu, G., Wang, H., Huang, B., et al. (2018). Net community production in the south China Sea basin estimated from *in situ* O2 measurements on an argo profiling float. *Deep Sea Res. Part I: Oceanogr. Res. Papers* 131, 54–61. doi: 10.1016/j.dsr.2017.11.002

Hu, Q., Chen, X., He, X., Bai, Y., Gong, F., Zhu, Q., et al. (2021). Effect of El niño-related warming on phytoplankton's vertical distribution in the Arabian Sea. *J. Geophys. Res.: Oceans* 126 (11), e2021JC017882.

Hu, C., Lee, Z., and Franz, B. (2012). Chlorophyll aalgorithms for oligotrophic oceans: A novel approach based on three-band reflectance difference. *J. Geophys. Res.: Oceans* 117 (C1).

Hu, J., and Wang, X. H. (2016). Progress on upwelling studies in the China seas. *Rev. Geophys.* 54 (3), 653–673. doi: 10.1002/2015RG000505

Jing, Z., Qi, Y., Hua, Z., Hua, Z. L., and Zhang, H. (2009). Numerical study on the summer upwelling system in the northern continental shelf of the south China Sea. *Continent. Shelf Res.* 29 (2), 467–478. doi: 10.1016/j.csr.2008.11.008

Karl, D. M., and Lukas, R. (1996). The Hawaii ocean time-series (HOT) program: Background, rationale and field implementation. *Deep Sea Res. Part II: Topic. Stud. Oceanogr.* 43 (2-3), 129–156. doi: 10.1016/0967-0645(96)00005-7

Kilpatrick, K. A., Podestá, G., Walsh, S., Williams, E., Halliwell, V., Szczodrak, M., et al. (2015). A decade of sea surface temperature from MODIS. *Remote Sens. Environ.* 165, 27–41. doi: 10.1016/j.rse.2015.04.023

Kirkpatrick, G. J., Millie, D. F., Moline, M. A., and Schofield, O. (2000). Optical discrimination of a phytoplankton species in natural mixed populations. *Limnol. Oceanogr.* 45 (2), 467–471. doi: 10.4319/lo.2000.45.2.0467

Kong, F., Dong, Q., Xiang, K., Yin, Z., Li, Y., and Liu, J. (2019). Spatiotemporal variability of remote sensing ocean net primary production and major forcing factors in the tropical Eastern Indian and Western pacific ocean. *Remote Sens.* 11 (4), 391. doi: 10.3390/rs11040391

Kulk, G., Platt, T., Dingle, J., Jackson, T., Jönsson, B. F., Bouman, H. A., et al. (2020). Primary production, an index of climate change in the ocean: Satellite-based estimates over two decades. *Remote Sens.* 12 (5), 826. doi: 10.3390/rs12050826

Kulk, G., Platt, T., Dingle, J., Jackson, T., Jönsson, B. F., Bouman, H. A., et al. (2021). Correction: Kulk et al. Primary production, an index of climate change in the ocean: Satellite-based estimates over two decades. *Remote Sens.* 12, 826. doi: 10.3390/rs13173462

Kuo, Y. C., and Tseng, Y. H. (2020). Impact of ENSO on the south China Sea during ENSO decaying winter–spring modeled by a regional coupled model (a new mesoscale perspective). *Ocean Model.* 152, 101655. doi: 10.1016/j.ocemod.2020.101655

Lee, Z., Du, K., Arnone, R., Liew, S., and Penta, B. (2005). Penetration of solar radiation in the upper ocean: A numerical model for oceanic and coastal waters. *J. Geophysical Research: Oceans* 110 (C9). doi: 10.1029/2004JC002780

Lee, Z., and Marra, J. F. (2022). The use of VGPM to estimate oceanic primary production: A "Tango" difficult to dance. *J. Remote Sens.* 2022. doi: 10.34133/2022/9851013

Lee, Z., Marra, J., Perry, M. J., and Kahru, M. (2015). Estimating oceanic primary productivity from ocean color remote sensing: A strategic assessment. *J. Mar. Syst.* 149, 50–59. doi: 10.1016/j.jmarsys.2014.11.015

Lee, Y. J., Matrai, P. A., Friedrichs, M. A., Saba, V. S., Antoine, D., Ardyna, M., et al. (2015). An assessment of phytoplankton primary productivity in the Arctic ocean from satellite ocean color/*in situ* chlorophyll-a based models. *J. Geophys. Res.: Oceans* 120 (9), 6508–6541. doi: 10.1002/2015JC011018

Lee, Z. P., Weidemann, A., Kindle, J., Arnone, R., Carder, K. L., Davis, C., et al. (2007). Euphotic zone depth: Its derivation and implication to ocean-color remote sensing. *J. Geophys. Res.: Oceans* 112 (C3).

Liao, X., Ma, J., and Zhan, H. (2012). Effect of different types of El niño on primary productivity in the south China Sea. *Aquat. Ecosyst. Health Manage.* 15 (2), 135–143. doi: 10.1080/14634988.2012.687655

Li, T., Bai, Y., Chen, X., Zhu, Q., Gong, F., Wang, D., et al. (2017). "Longtime variation of phytoplankton in the south China Sea from the perspective of carbon fixation," in *Remote sensing of the ocean, Sea ice, coastal waters, and Large water regions 2017*, vol. 10422. (SPIE), 94–104.

Lin, I. I., Chen, J. P., Wong, G. T. F., Wong, G. T., Huang, C. W., Lien, C. C., et al. (2007). Aerosol input to the south China Sea: Results from the moderate resolution imaging spectroradiometer, the quick scatterometer, and the measurements of pollution in the troposphere sensor. *Deep Sea Res. Part II: Topic. Stud. Oceanogr.* 54 (14-15), 1589–1601.

Li, W., Tiwari, S. P., El-Askary, H. M., Qurban, M. A., Amiridis, V., Manikandan, K. P., et al. (2020). Synergistic use of remote sensing and modeling for estimating net primary productivity in the red Sea with VGPM, eppley-VGPM, and CbPM models intercomparison. *IEEE Trans. Geosci. Remote Sens.* 58 (12), 8717–8734. doi: 10.1109/TGRS.2020.2990373

Liu, K. K., Chao, S. Y., Shaw, P. T., Gong, G. C., Chen, C. C., Tang, T. Y., et al. (2002). Monsoon-forced chlorophyll distribution and primary production in the south China Sea: observations and a numerical study. *Deep Sea Res. Part I: Oceanogr. Res. Papers* 49 (8), 1387–1412.

Liu, K. K., Chen, Y. J., Tseng, C. M., Lin, I. I., Liu, H. B., Snidvongs, A., et al. (2007). The significance of phytoplankton photo-adaptation and benthic–pelagic coupling to primary production in the south China Sea: Observations and numerical investigations. *Deep Sea Res. Part II: Topic. Stud. Oceanogr.* 54 (14-15), 1546–1574.

Liu, X., and Wang, M. (2018). Gap filling of missing data for VIIRS global ocean color products using the DINEOF method. *IEEE Trans. Geosci. Remote Sens.* 56 (8), 4464–4476. doi: 10.1109/TGRS.2018.2820423

Liu, X., and Wang, M. (2019). Filling the gaps of missing data in the merged VIIRS SNPP/NOAA-20 ocean color product using the DINEOF method. *Remote Sens.* 11 (2), 178. doi: 10.3390/rs11020178

Liu, H., Xie, Y., Browning, T. J., Xu, F., and Huang, B.. (2022). Phytoplankton photophysiology across tropical eddies: Deconvolving nutrient, light, and community signals. *Front. Mar. Sci.* 9, Art.Nr.934391. doi: 10.3389/fmars.2022.934391

Li, L., Wu, C., Sun, J., Song, S., Ding, C., Huang, D., et al. (2020). Nitrogen fixation driven by mesoscale eddies and the kuroshio current in the northern south China Sea and the East China Sea. *Acta Oceanol. Sin.* 39 (12), 30–41. doi: 10.1007/s13131-020-1691-0

Li, H., Zhang, J., Xuan, J., Wu, Z., Ran, L., Wiesner, M. G., et al. (2022). Asymmetric response of the biological carbon pump to the ENSO in the south China Sea. *Geophys. Res. Lett.* 49 (2), e2021GL095254. doi: 10.1029/2021GL095254

Lohrenz, S. E., Knauer, G. A., Asper, V. L., Tuel, M., Michaels, A. F., Knap, A. H., et al. (1992). Seasonal variability in primary production and particle flux in the northwestern Sargasso Sea: US JGOFS Bermuda Atlantic time-series study. *Deep Sea Res. Part A. Oceanogr. Res. Papers* 39 (7-8), 1373–1391. doi: 10.1016/0198-0149(92)90074-4

Ma, S., Tao, Z., Yang, X., Yu, Y., Zhou, X., Ma, W., et al. (2014). Estimation of marine primary productivity from satellite-derived phytoplankton absorption data. *IEEE J. Select. Top. Appl. Earth Observ. Remote Sens.* 7 (7), 3084–3092. doi: 10.1109/JSTARS.2014.2298863

Matsumoto, K., Abe, O., Fujiki, T., Sukigara, C., and Mino, Y. (2016). Primary productivity at the time-series stations in the northwestern pacific ocean: is the subtropical station unproductive? *J. Oceanogr.* 72 (3), 359–371. doi: 10.1007/s10872-016-0354-4

Messié, M., and Chavez, F. P. (2015). Seasonal regulation of primary production in eastern boundary upwelling systems. *Prog. Oceanogr.* 134, 1–18. doi: 10.1016/j.pocean.2014.10.011

Montes-Hugo, M., Doney, S. C., Ducklow, H. W., Fraser, W., Martinson, D., Stammerjohn, S. E., et al. (2009). Recent changes in phytoplankton communities associated with rapid regional climate change along the western Antarctic peninsula. *Science* 323 (5920), 1470–1473.

Nielsen, E. S. (1952). The use of radio-active carbon (C14) for measuring organic production in the sea. *ICES J. Mar. Sci.* 18 (2), 117–140. doi: 10.1093/icesjms/18.2.117

Ning, X. R., Chai, F., Xue, H., Cai, Y., Liu, C., Shi, J., et al. (2004). Physical-biological oceanographic coupling influencing phytoplankton and primary production in the south China Sea. *J. Geophys. Res.: Oceans* 109 (C10).

Oziel, L., Massicotte, P., Randelhoff, A., Ferland, J., Vladoiu, A., Lacour, L., et al. (2019). Environmental factors influencing the seasonal dynamics of spring algal blooms in and beneath sea ice in western Baffin bay. *Elementa: Sci. Anthropocene* 7.

Pan, X., Wong, G. T. F., Tai, J. H., and Ho, T. Y. (2015). Climatology of physical hydrographic and biological characteristics of the northern south China Sea shelf-sea (NoSoCS) and adjacent waters: Observations from satellite remote sensing. *Deep Sea Res. Part II: Topic. Stud. Oceanogr.* 117, 10–22. doi: 10.1016/j.dsr2.2015.02.022

Platt, T., and Sathyendranath, S. (1988). Oceanic primary production: estimation by remote sensing at local and regional scales. *Science* 241 (4873), 1613–1620.

Reid, P. C., Fischer, A. C., Lewis-Brown, E., Meredith, M. P., Sparrow, M., Andersson, A. J., et al. (2009). Impacts of the oceans on climate change. *Adv. Mar. Biol.* 56, 1–150. doi: 10.1016/S0065-2881(09)56001-4

Robinson, C. M., Cherukuru, N., Hardman-Mountford, N. J., Everett, J. D., McLaughlin, M. J., Davies, K. P., et al. (2017). Phytoplankton absorption predicts patterns in primary productivity in Australian coastal shelf waters. *Estuar. Coast. Shelf Sci.* 192, 1–16. doi: 10.1016/j.ecss.2017.04.012

Saba, V. S., Friedrichs, M. A. M., Antoine, D., Armstrong, R. A., Asanuma, I., Behrenfeld, M. J., et al. (2011). An evaluation of ocean color model estimates of marine primary productivity in coastal and pelagic regions across the globe. *Biogeosciences* 8 (2), 489–503. doi: 10.5194/bg-8-489-2011

Sarmiento, J. L., and Gruber, N. (2002). Sinks for anthropogenic carbon. *Phys. Today* 55 (8), 30–36. doi: 10.1063/1.1510279

Sathyendranath, S., Platt, T., Kovač, Ž, Dingle, J., Jackson, T., Brewin, R., et al. (2020). Reconciling models of primary production and photoacclimation. *Appl. opt.* 59 (10), C100–C114. doi: 10.1364/AO.386252

Shaw, P. T., Chao, S. Y., Liu, K. K., Pai, S. C., and Liu, C. T. (1996). Winter upwelling off Luzon in the northeastern south China Sea. *J. Geophys. Res.: Oceans* 101 (C7), 16435–16448. doi: 10.1029/96JC01064

Shih, Y. Y., Shiah, F. K., Lai, C. C., Chou, W. C., Tai, J. H., Wu, Y. S., et al. (2021). Comparison of primary production using *in situ* and satellite-derived values at the SEATS station in the south China Sea. *Front. Mar. Sci.* 8, 747763. doi: 10.3389/fmars.2021.747763

Silsbe, G. M., Behrenfeld, M. J., Halsey, K. H., Milligan, A. J., and Westberry, T. K. (2016). The CAFE model: A net production model for global ocean phytoplankton. *Global Biogeochem. Cycles* 30 (12), 1756–1777. doi: 10.1002/2016GB005521

Simpson, E. H. (1949). Measurement of diversity. *nature* 163 (4148), 688–688.

Shu, Y, Wang, D., Feng, M., Geng, B., Chen, J., Yao, J., et al. (2018). The contribution of local wind and ocean circulation to the interannual variability in coastal upwelling intensity in the Northern South China Sea. *J. Geophys. Research: Oceans* 123 (9), 6766–6778. doi: 10.1029/2018JC014223

Tang, D. L., Ni, I. H., Kester, D. R., and Müller-Karger, F. E. (1999). Remote sensing observations of winter phytoplankton blooms southwest of the Luzon strait in the south China Sea. *Mar. Ecol. Prog. Ser.* 191, 43–51. doi: 10.3354/meps191043

Tan, S. C., and Shi, G. Y. (2009). Spatiotemporal variability of satellite-derived primary production in the south China Sea 1998–2006. *J. Geophys. Res.: Biogeosci.* 114 (G3).

Tao, Z., Ma, S., Yang, X., and Wang, Y. (2017b). Assessing the uncertainties of phytoplankton absorption-based model estimates of marine net primary productivity. *Acta Oceanol. Sin.* 36 (6), 112–121. doi: 10.1007/s13131-017-1047-8

Tao, Z., Wang, Y., Ma, S., Lv, T., and Zhou, X. (2017a). A phytoplankton class-specific marine primary productivity model using MODIS data. *IEEE J. Select. Top. Appl. Earth Observ. Remote Sens.* 10 (12), 5519–5528. doi: 10.1109/JSTARS.2017.2747770

Torrecilla, E., Stramski, D., Reynolds, R. A., Millán-Núñez, E., and Piera, J. (2011). Cluster analysis of hyperspectral optical data for discriminating phytoplankton pigment assemblages in the open ocean. *Remote Sens. Environ.* 115 (10), 2578–2593. doi: 10.1016/j.rse.2011.05.014

Tseng, H. C., You, W. L., Huang, W., Chung, C. C., Tsai, A. Y., Chen, T. Y., et al. (2020). Seasonal variations of marine environment and primary production in the Taiwan strait. *Front. Mar. Sci.* 7, 38. doi: 10.3389/fmars.2020.00038

Utari, P. A., Saputra, O. F., and Lestiana, H. (2022). "The spatial and temporal impacts of mixed layer depth (MLD) variations in West sumatera coastal area," in *IOP Conference Series: Earth and Environmental Science*, Vol. 1047. 012022 (IOP Publishing).

Wang, H., Jin, Q. H., and Gao, S. (2008). A preliminary study on the response of marine primary production to monsoon variations in the south China Sea. *Acta Oceanol. Sin.* 27 (5), 21–35.

Westberry, T., Behrenfeld, M. J., Siegel, D. A., and Boss, E. (2008). Carbon-based primary productivity modeling with vertically resolved photoacclimation. *Global Biogeochem. Cycles* 22 (2). doi: 10.1029/2007GB003078

Williams, P. J. B., Morris, P. J., and Karl, D. M. (2004). Net community production and metabolic balance at the oligotrophic ocean site, station ALOHA. *Deep Sea Res. Part I: Oceanogr. Res. Papers* 51 (11), 1563–1578. doi: 10.1016/j.dsr.2004.07.001

Wu, J., Goes, J. I., do Rosario Gomes, H., Lee, Z., Noh, J. H., Wei, J., et al. (2022). Estimates of diurnal and daily net primary productivity using the geostationary ocean color imager (GOCI) data. *Remote Sens. Environ.* 280, 113183. doi: 10.1016/j.rse.2022.113183

Wyrtki, K. (1961). Physical oceanography of the southeast Asian waters (University of California, Scripps Institution of Oceanography).

Xiao, H. W., Luo, L., Zhu, R. G., Guo, W., Long, A. M., Wu, J. F., et al. (2020). Enhanced primary production in the oligotrophic south China Sea related to southeast Asian forest fires. *J. Geophys. Res.: Oceans* 125 (2), e2019JC015663.

Xie, Y., Huang, B., Lin, L., Laws, E. A., Wang, L., Shang, S., et al. (2015). Photosynthetic parameters in the northern south China Sea in relation to phytoplankton community structure. *J. Geophys. Res.: Oceans* 120 (6), 4187–4204. doi: 10.1002/2014JC010415

Xie, Y., Lin, L., Xiao, W., Yu, X., Lan, W., Huang, B., et al. (2020). Striking seasonal pattern of primary production in the river-dominated ocean margin of the northern south China Sea (NSCS-RiOMar) revealed by new field and remotely sensed data. *Prog. Oceanogr.* 189, 102470. doi: 10.1016/j.pocean.2020.102470

Xu, W., Wang, G., Jiang, L., Cheng, X., Zhou, W., Cao, W., et al. (2020). Spatiotemporal variability of surface phytoplankton carbon and carbon-to-Chlorophyll a ratio in the south China Sea based on satellite data. *Remote Sens.* 13 (1), 30. doi: 10.3390/rs13010030

Xu, H., Zhou, W., Li, A., and Ji, S. (2016). "Similarities and differences of oceanic primary productivity product estimated by three models based on modis for the open south China Sea," in International Conference on Geo-Informatics in Resource Management and Sustainable Ecosystem (Singapore: Springer), 328–336.

Yan, Y., Ling, Z., and Chen, C. (2015). Winter coastal upwelling off northwest Borneo in the south China Sea. *Acta Oceanol. Sin.* 34 (1), 3–10. doi: 10.1007/s13131-015-0590-2

Ye, H., Chen, C., Sun, Z., Tang, S., Song, X., Yang, C., et al. (2015). Estimation of the primary productivity in pearl river estuary using MODIS data. *Estuar. Coasts* 38 (2), 506–518. doi: 10.1007/s12237-014-9830-5

Yu, Y., Xing, X., Liu, H., Yuan, Y., Wang, Y., Chai, F., et al. (2019). The variability of chlorophyll-a and its relationship with dynamic factors in the basin of the south China Sea. *J. Mar. Syst.* 200, 103230. doi: 10.1016/j.jmarsys.2019.103230

Zeng, X., Bracco, A., and Tagklis, F. (2022). Dynamical impact of the Mekong river plume in the south China Sea. *J. Geophys. Res.: Oceans* 127 (5), e2021JC017572.

Zhang, W., Mu, S., Zhang, Y., and Chen, K. M. (2012). Seasonal and interannual variations of flow discharge from pearl river into sea. *Water Sci. Eng.* 5 (4), 399–409.

frontiers | Frontiers in Marine Science

TYPE Original Research
PUBLISHED 27 February 2023
DOI 10.3389/fmars.2023.1031901

Check for updates

OPEN ACCESS

EDITED BY
Javier A. Concha,
European Space Research Institute (ESRIN), Italy

REVIEWED BY
Xuerong Sun,
University of Exeter, Exeter, United Kingdom
Sanjiba Kumar Baliarsingh,
Indian National Centre for Ocean Information Services, India

*CORRESPONDENCE
Jutarak Luang-on
jtlair7997@gmail.com

SPECIALTY SECTION
This article was submitted to Ocean Observation, a section of the journal Frontiers in Marine Science

RECEIVED 30 August 2022
ACCEPTED 08 February 2023
PUBLISHED 27 February 2023

CITATION
Luang-on J, Ishizaka J, Buranapratheprat A, Phaksopa J, Goes JI, Maúre ER, Siswanto E, Zhu Y, Xu Q, Nakornsantiphap P, Kobayashi H and Matsumura S (2023) MODIS-derived green *Noctiluca* blooms in the upper Gulf of Thailand: Algorithm development and seasonal variation mapping.
Front. Mar. Sci. 10:1031901.
doi: 10.3389/fmars.2023.1031901

COPYRIGHT
© 2023 Luang-on, Ishizaka, Buranapratheprat, Phaksopa, Goes, Maúre, Siswanto, Zhu, Xu, Nakornsantiphap, Kobayashi and Matsumura. This is an open-access article distributed under the terms of the Creative Commons Attribution License (CC BY). The use, distribution or reproduction in other forums is permitted, provided the original author(s) and the copyright owner(s) are credited and that the original publication in this journal is cited, in accordance with accepted academic practice. No use, distribution or reproduction is permitted which does not comply with these terms.

MODIS-derived green *Noctiluca* blooms in the upper Gulf of Thailand: Algorithm development and seasonal variation mapping

Jutarak Luang-on[1,2*], Joji Ishizaka[3], Anukul Buranapratheprat[4], Jitraporn Phaksopa[5], Joaquim I. Goes[6], Elígio de Raús Maúre[7], Eko Siswanto[2], Yuanli Zhu[8], Qian Xu[1], Phattaranakorn Nakornsantiphap[9], Hiroshi Kobayashi[10] and Satsuki Matsumura[11]

[1]Graduate School of Environmental Studies, Nagoya University, Nagoya, Japan, [2]Earth Surface System Research Center, Research Institute for Global Change, Japan Agency for Marine-Earth Science and Technology, Yokohama, Japan, [3]Institute for Space-Earth Environmental Research, Nagoya University, Nagoya, Japan, [4]Department of Aquatic Science, Faculty of Science, Burapha University, Chonburi, Thailand, [5]Department of Marine Science, Faculty of Fisheries, Kasetsart University, Bangkok, Thailand, [6]Lamont-Doherty Earth Observatory, Columbia University, Palisades, NY, United States, [7]Department of Research and Study, Northwest Pacific Region Environmental Cooperation Center, Toyama, Japan, [8]Key Laboratory of Marine Ecosystem Dynamics, Second Institute of Oceanography, Ministry of Nature Resources, Hangzhou, China, [9]Department of Renewable Power Plant, Electricity Generating Authority of Thailand, Bangkok, Thailand, [10]University of Yamanashi, Kofu, Japan, [11]Japan Fisheries Research and Education Agency, Kanagawa, Japan

In recent decades, red tides of non-toxic harmful algal blooms have frequently occurred in monsoon-influenced tropical areas, particularly the green form of *Noctiluca scintillans* (hereafter green *Noctiluca*). However, our understanding of the mechanism of red tide formation is hindered by spatial and temporal constraints of field data. In this study, we used moderate resolution imaging spectroradiometer (MODIS) ocean color data along with a locally developed algal-bloom classification algorithm to investigate the seasonal variability of dominant red tides across the upper Gulf of Thailand (uGoT). During our July 2018 observation, a super green *Noctiluca* bloom with extraordinarily high chl-a (>1,469 mg m^{-3}) displayed a distinct spectral reflectance characteristic among red tides in blue-to-green and red-to-near infrared wavelengths. According to the distinctive *in situ* hyperspectral characteristics of uGoT algal blooms, we developed a classification algorithm for MODIS normalized at 488, 531, and 667 nm, which successfully discriminated green *Noctiluca* in three levels of blooms, namely, super (100%), strong (>80%), and weak (>40%), from other algal blooms (i.e., dinoflagellates, diatoms, cyanobacteria, and mixed red tide species) as well as non-bloom oceanic and coastal waters using MODIS data, as confirmed by uGoT red tide reports. Monthly MODIS-based discrimination composites from 2003 to 2021 revealed seasonal variability in the surface distribution and bloom frequency of green *Noctiluca* and other red tides according to the Asian monsoon seasons: the southwest monsoon (May–September) and the northeast monsoon (October–January of the following year). Green *Noctiluca*

blooms occurred farther from the shore and estuaries than other red tides (dinoflagellates and cyanobacteria), and were much more frequent than other red tides between the Tha Chin and Chao Phraya River mouths during the non-monsoon period (February to April). The frequency and distribution of green *Noctiluca* blooms, as well as other algal blooms, varied with the monsoon season. By comparing MODIS-derived algal blooms to monsoon-induced factors (i.e., sea surface winds, precipitation, and river discharge), we present an unprecedented overview of the spatial and temporal dynamics of red tides throughout the uGoT under Asian monsoon conditions. This research contributes to our understanding of the impact of climate change on phytoplankton dynamics.

KEYWORDS

algal bloom, Noctiluca scintillans, seasonal variability, monsoon, MODIS ocean color data, classification algorithm, phytoplankton, red tide

1 Introduction

The large dinoflagellate *Noctiluca scintillans* Macartney 1810 (syn. *miliaris* Suriray 1836) Kofoid and Swezy, 1921, hereafter referred to as *Noctiluca*, causes red tides of non-toxic harmful algal blooms worldwide (Harrison et al., 2011). As active *Noctiluca* blooms typically discolor seawater to an orange-red color owing to the presence of carotenoids, this phytoplankton is referred to as red *Noctiluca*. In the marine food web, *Noctiluca* plays an important role as a primary grazer of phytoplankton, and also consumes bacteria, small zooplankton, and fish eggs. As it requires external food, the blooming of this species has been commonly documented in areas of upwelling and other productive locations, particularly where diatoms are abundant, and may be connected to eutrophication (Fonda Umani et al., 2004; Harrison et al., 2011; Turkoglu, 2013). Although *Noctiluca* does not produce toxins like other dinoflagellates, massive *Noctiluca* blooms have the potential to reduce fish yield in aquaculture areas by consuming large amounts of fish eggs (Enomoto, 1956), and may act as a vector of phycotoxins to higher trophic levels or translocation to natural shellfish beds (Escalera et al., 2007).

Green *Noctiluca* (Figure 1) is an extraordinary form of *Noctiluca* that includes the individual photosynthetic endosymbiont *Protoeuglena noctilucae* (Wang et al., 2016). Endosymbiont photosynthetic pigments (i.e., chlorophyll *a* and *b*) contribute to the green color of *Noctiluca*, and the photosynthetic product provides energy to the host (Sweeney, 1971; Hansen et al., 2004; Saito et al., 2006). Because of these features, green *Noctiluca* is referred to as a mixotroph in the marine food web. According to Hansen et al. (2004), photosynthesis in green *Noctiluca* cells grown without prey increases with irradiance to approximately 200 ng C $cell^{-1}$ d^{-1} at an irradiance level of ~250–300 µmol photons m^{-2} s^{-1}. Photosynthesis was also more significant in green *Noctiluca* than phagotrophy, which only contributed 30% to the direct growth of green *Noctiluca* at an irradiance of 150 µmol photons m^{-2} s^{-1}. Conversely, green *Noctiluca* turned colorless when the endosymbiont vanished after approximately two weeks in a control culture without any feeding organisms, with all host cells dying after approximately one month (Lirdwitayaprasit, 2001).

Unlike red *Noctiluca*, which is more widely distributed, green *Noctiluca* is exclusively present in the western tropical Pacific and Indian Ocean, including the Bay of Bengal, Arabian Seas, Gulf of Oman, Gulf of Thailand, and Manila Bay (Harrison et al., 2011).



FIGURE 1
A cell of green *Noctiluca scintillans*. Photo by Dr. Vichaya Gunbua.

During an active bloom, the high cell density of green *Noctiluca* can continuously turn clear seawater into sticky dark green water for more than a week and potentially deplete the dissolved oxygen content, generating hypoxic conditions in the water column and resulting in massive fish mortality (Wattayakorn, 2006). In the last two decades, the increasing number and intensity of green *Noctiluca* blooms have had serious impacts on fisheries and tourism (Gomes et al., 2009; do Rosário Gomes et al., 2014; Goes et al., 2018). The dynamics of green *Noctiluca* are believed to be related to anthropogenic nutrient inputs and monsoons (Sriwoon et al., 2008; Goes et al., 2018), although the detailed mechanisms remain unclear.

The upper Gulf of Thailand (uGoT, Figure 2A), a shallow tropical semi-enclosed bay, is highly susceptible to hypertrophic and eutrophic conditions related to major river discharge along the northern coast, as well as water circulation patterns influenced by Asian monsoons (Buranapratheprat et al., 2021). As a result, non-toxic algal blooms generate red tides of various phytoplankton species in different locations multiple times per year, the most common of which are green *Noctiluca* and dinoflagellate *Ceratium furca* blooms (Lirdwitayaprasit, 2003). Green *Noctiluca* is commonly found in waters more than 10 m deep, with higher salinity (22–33 psu) than those inhabited by dinoflagellates (12–27 psu) (Lirdwitayaprasit et al., 2006). The vertical distribution of green *Noctiluca* can tolerate a wide range of salinity (10–31 psu), requiring an acclimation period to adapt to low salinity conditions (Lirdwitayaprasit et al., 2012). Sriwoon et al. (2008) reported that the seasonal cell abundance of green *Noctiluca* off the coast of Chonburi Province (i.e., off the northeastern coast of Thailand) is high (low) during the rainy (dry) season of the southwest (northeast) monsoon from May to September (November to February). Seasonal variability may result from the interaction between increased river discharge into the northern uGoT and the transfer of riverine nutrient inputs by eastward circulation generated by the monsoon along the northern coast (Buranapratheprat et al., 2002; Buranapratheprat et al., 2006; Yu et al., 2018). Chuenniyom et al. (2012) examined the green *Noctiluca* population in the Tha Chin estuary (off the north coast of Thailand) and observed a dense population in the outer part of the estuary with relatively high salinity, as well as a red tide during the high loading period of river discharge from November to December 2009. Moreover, ammonium nitrogen and dissolved inorganic nitrogen concentrations influence the total green *Noctiluca* population density, whereas orthophosphate phosphorus regulates the development of green *Noctiluca* red tides (Chuenniyom et al., 2012). Although the seasonal dynamics of green *Noctiluca* in northern coastal waters are related to an increase in riverine inputs and circulation induced by monsoons (Sriwoon et al., 2008; Chuenniyom et al., 2012), the overall dynamics of green *Noctiluca* and other red tides in the uGoT remain

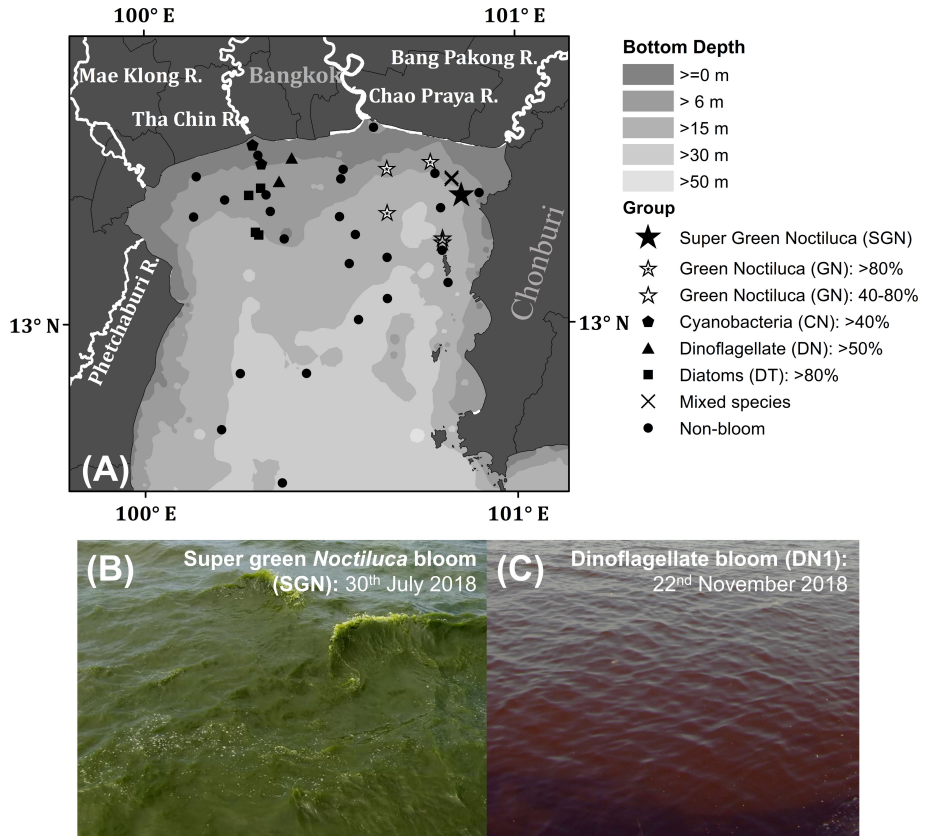


FIGURE 2
Map of sampling stations in the uGoT **(A)** and photos of the sea surface during super green *Noctiluca* **(B)** and dinoflagellate *Ceratium furca* **(C)** blooms. The symbols in **(A)** indicate water types during ship observations.

unknown. This is attributed to a lack of continuous tracking of the spatial and temporal variations in phytoplankton populations.

In previous research, satellite ocean color radiometry in the blue and green wavelength ranges has been applied to determine chlorophyll *a* (chl-a) concentrations, a key photosynthetic pigment prevalent in all phytoplankton groups, and clarify how total phytoplankton biomass varies under the influence of Asian monsoons in the uGoT (Buranapratheprat et al., 2009; Intacharoen et al., 2018; Luang-on et al., 2021). Furthermore, Suwanlertcharoen and Prukpitikul (2018) employed a satellite remote sensing technique to detect algal blooms in the uGoT using the maximum chlorophyll index, which is based on the red to near-infrared bands of Sentinel-3A, in conjunction with RGB false-color composite images. Although this method was successful at detecting intense green *Noctiluca* blooms in offshore regions with high maximum chlorophyll index values, it was unable to distinguish between specific groups of red tides. Therefore, better approaches for discriminating algal blooms with satellite ocean color data should be developed to improve our understanding of red tide dynamics in the uGoT.

Unlike the green color of *Noctiluca* caused by photosynthetic pigments of the endosymbiont, red tides of other phytoplankton species typically turn the seawater into red, brown, or reddish-brown colors (Chumnantana et al., 2006) depending on the major pigments of the phytoplankton. Using a reverse-phase high-performance liquid chromatography (HPLC) method, Furuya and Lirdwitayaprasit (2000) identified pigment markers of the green *Noctiluca* endosymbiont, including neoxanthin, violaxanthin, zeaxanthin, lutein, and chl-b in relation to chl-a. For other uGoT red tides, pigment markers include peridinin for dinoflagellates, fucoxanthin for diatoms, and zeaxanthin for cyanobacteria (Higgins et al., 2011), which can be used to quantify phytoplankton communities using CHEMical TAXonomy software (CHEMTAX), a program that estimates phytoplankton class abundance based on pigment marker concentrations (Mackey et al., 1996). Because the major light absorption peaks differ among the red tide marker pigments (Clementson and Wojtasiewicz, 2019), the different water colors during red tides are expected to have distinct spectral reflectance characteristics that can be measured and discriminated by satellite ocean color observations.

Recently, a unique reflectance signature of green *Noctiluca* was detected using a hyperspectral optical instrument with a fine spectral resolution employed in the oceanic waters of the northern Arabian seas (Dwivedi et al., 2015). The reflectance of green *Noctiluca* increases at wavelengths of 440–550 nm when compared with the spectra of diatom blooms and non-bloom waters. Dwivedi et al. (2015) and Baliarsingh et al. (2017) employed this unique feature to discriminate green *Noctiluca* (and red *Noctiluca*) from diatoms in moderate resolution imaging spectroradiometer (MODIS) data. Furthermore, Shang et al. (2014) reported that dinoflagellates exhibit lower reflectance values than diatoms and a less pronounced reflectance slope in the blue wavelengths (443–488 nm) in East China Sea coastal waters. This difference in spectral characteristics was utilized to create a bloom index, which was used to differentiate blooms from MODIS data by considering the fluorescence line height and total absorption coefficient. Tao et al. (2015) subsequently observed spectral absorption and reflectance characteristics of the two algal groups in the East China Sea. Distinct spectral differences were discovered in the green and red wavelengths and were applied to develop two indices for discriminating dinoflagellate *Prorocentrum donghaiense* from diatoms based on MODIS reflectance wavelengths. Shen et al. (2019) also proposed a method for distinguishing between dinoflagellates and diatoms based on a green-red spectral slope for medium resolution imaging spectrometer data. However, although the reflectance spectral characteristics of phytoplankton blooms can be used to classify red tides using satellite data, such an approach has never been attempted in turbid coastal waters containing more than two bloom groups, such as the uGoT.

Therefore, to improve our understanding of seasonal red tide dynamics, we employ ship observation data to develop a technique for remotely detecting and classifying green *Noctiluca* spp. and other phytoplankton blooms in the uGoT using MODIS data. First, we clarify the *in situ* spectral reflectance characteristics of green *Noctiluca* and other algal bloom waters using HPLC-CHEMTAX-derived phytoplankton compositions and chl-a concentrations. Second, we develop an algorithm for discriminating green *Noctiluca* blooms from other phytoplankton blooms according to the specific spectral features of each phytoplankton group. Then, we apply the algorithm to MODIS data and validate its performance with field reports of uGoT algal blooms. Seasonal variations in the surface distribution and frequency of green *Noctiluca* blooms and associated red tides are also investigated and discussed in relation to several environmental variables linked to Asian monsoons.

2 Data and methods

2.1 *In situ* data

Field observations were undertaken in the uGoT between 2017 and 2019 during favorable conditions for frequent red tides. We collected bio-optical data of phytoplankton bloom and non-bloom waters during wet (July to August) and dry (November to January) seasons characterized by the southwest and northeast monsoons, respectively. These observations resulted in 45 co-located measurements of chl-a concentration, phytoplankton pigments, and remote sensing reflectance collected around the uGoT (Figure 2A).

Chl-a and phytoplankton pigments in sea surface water samples were filtered through 25-mm Whatman GF/F glass-fiber filters under vacuum pressure of <0.01 MPa and immediately preserved prior to analysis in the laboratory. Chl-a was extracted in N, N-dimethyl formamide (Suzuki and Ishimaru, 1990) at ~4°C and measured using a pre-calibrated Turner Designs 10-AU Fluorometer (Welschmeyer, 1994). Phytoplankton pigment samples were immediately frozen and kept at approximately −80° C then measured in methanol extracts using the reverse-phase HPLC method (Van Heukelem and Thomas, 2001) and a Zorbax Eclipse XDB-C8 column (150 mm × 4.6 mm, 3.5 µm; Agilent Technologies).

The HPLC-measured pigment compositions were then inputted into CHEMTAX software to estimate the major phytoplankton groups within each sample. Eleven marker pigments that were dominant in the HPLC data (peridinin, 19'-butanoyloxyfucoxanthin, fucoxanthin, 19'-hexoyloxyfucoxanthin, alloxanthin, neoxanthin, violaxanthin, zeaxanthin, lutein, chl-b, and chl-a) were selected to classify eight different phytoplankton groups (dinoflagellates, cryptophytes, prymnesiophytes, haptophytes, cyanobacteria, diatoms, and chlorophytes in exponential and stationary phases). In this study, green *Noctiluca* was referred to as a chlorophyte because of the pigment composition of its endosymbiont (Furuya and Lirdwitayaprasit, 2000). The pigment-to-chl-a ratios used in the initial run in the CHEMTAX analysis were derived from previous studies in the East China Sea (Xu et al., 2019) and central Bohai Sea (Lu et al., 2018), as well as an experimental study on pigment changes during the evolution of green *Noctiluca* in the Gulf of Thailand (Furuya and Lirdwitayaprasit, 2000). The output ratio matrix from the previous run was used as the input for the next ratio matrix for fifteen runs of CHEMTAX, and the final ratio selected from the most stable ratio among the fifteen outputs were used to determine phytoplankton group compositions (Latasa, 2007). The initial and final pigment-to-chl-a ratios are presented in the Supplementary Appendix 1.

In situ remote sensing reflectance (R_{rs}) values between wavelengths of 320 nm and 950 nm were measured from shipboard by RAMSES hyperspectral radiometers (TriOS, Germany): one onboard sky-facing sensor was used to measure the sky irradiance (ACC-VIS) and two radiance sensors (ARC-VIS) with dome coverings were used to measure the water-leaving radiance immediately above the sea surface (see in Supplementary Appendix 2; Yang et al., 2018). The measured water-leaving radiance (L_w) and downwelling irradiance (E_d) were then calculated using the *in situ* R_{rs} as follows: $R_{rs}(\lambda)=L_w(\lambda)/E_d(\lambda)$, where λ is the wavelength. The R_{rs} values at all wavelengths were further normalized using R_{rs} at 547 nm to reveal the distinctive spectral characteristics of each dominant phytoplankton group.

2.2 Development of the algal-bloom classification algorithm

An algal-bloom classification algorithm was developed to discriminate water containing green *Noctiluca* blooms from that containing other algal blooms and non-bloom waters. The algorithm was based on 45 corresponding datasets of *in situ* and normalized R_{rs} spectra, CHEMTAX-derived phytoplankton composition, and chl-a (Figure 2A). *In situ* chl-a was initially considered to distinguish between algal blooms (≥10 mg m^{-3}) and non-blooms in coastal and oceanic waters (<10 and ≤1.5 g m^{-3}, respectively). Then, we investigated the distinctive R_{rs} spectral characteristics of algal bloom waters by comparing them with *in situ* chl-a and percentages of the CHEMTAX-derived phytoplankton group composition. To clarify the spectral characteristics of each algal bloom water sample, the R_{rs} spectra of each group were normalized. Owing to the distinct spectral characteristics of algal bloom waters and their high compatibility with MODIS data (see Supplementary Appendix 3), the normalized R_{rs} values in MODIS band-compliant wavelengths of 488, 531, and 667 nm were chosen to discriminate among water types for MODIS data. A simple grouping method was then performed using normalized R_{rs} values to develop the algal-bloom classification algorithm.

2.3 Satellite data processing

Level-2 (L2) MODIS ocean color products (1-km spatial resolution) from the Aqua satellite on cloudless days that coincided with reports of algal blooms (Table 2) during 2003–2021 were retrieved from the NASA Ocean Color website (https://oceancolor.gsfc.nasa.gov/). Data quality was controlled using the masks of LAND, HIGLINT, HILT, CLDICE, HISOLZEN, LOWLW, and NAVFAIL (https://www.oceancolor.gsfc.nasa.gov/atbd/ocl2flags/) after being reprojected to the geographical WGS84 coordinate system. Before applying the algal-bloom classification algorithm, the single MODIS R_{rs} values at 488 nm (R_{rs} 488), 531 nm (R_{rs} 531), 547 nm (R_{rs} 547), and 667 nm (667), as well as the normalized values at 488 nm (R_{rs} 488/R_{rs} 547), 531 nm (R_{rs} 531/R_{rs} 547), and 667 nm (R_{rs} 667/R_{rs} 547), were verified and improved based on *in situ* data (see Supplementary Appendix 3). The corrected MODIS data were then processed using the algal-bloom classification algorithm to classify seven groups of bloom waters and non-bloom oceanic and coastal waters, as shown in Figure 5. For algorithm validation, MODIS-derived algal-bloom classified images on cloudless days were compared with uGoT red tide reports (Table 2), and MODIS chl-a images were estimated using a local chl-a algorithm (Luang-on et al., 2021).

The percentage of the relative bloom frequency was calculated to investigate the seasonal dynamics of individual red tides. Monthly composite data for each water type were obtained by dividing the pixel number of each water type during 2003–2021 by the total number of monthly satellite images then multiplying by 100 at each location. It should be noted that, on the percentage frequency images, the green *Noctiluca* bloom is a composite of three bloom levels (>50%, >80%, and 100%). The results were then compared to monthly climatological data on river discharge, precipitation rate, and sea surface winds (Luang-on et al., 2021).

3 Results

3.1 *In situ* hyperspectral reflectance characteristics of algal blooms

During our observations in July and August 2018 and 2019, green *Noctiluca* blooms occurred in the northeastern uGoT. When incorporating November and December 2017 and 2018, other blooms of dinoflagellates, diatoms, and cyanobacteria occurred in the west of the uGoT near the Tha Chin River (Figure 2A). *In situ* chl-a, HPLC-CHEMTAX-derived phytoplankton group composition, and R_{rs} data indicate 16 stations of algal blooms, as shown in Figure 3. According to the chl-a concentration and phytoplankton composition, seven groups of algal bloom waters (Table 1) were classified according to the distinct R_{rs} characteristics

TABLE 1 A summary of the. R_{rs} categorization criteria for algal bloom waters based on *in situ* data obtained during 2017–2019.

Group no.	Chl-a concentration (mg m^{-3})	Chl-a level	Dominant phytoplankton group	% of the dominant group	Data number	Water type of phytoplankton blooms	
1	1,469	Very high	Chlorophyte	100	4	Green *Noctiluca* – super bloom	(SGN)
2	32–37	High	Chlorophyte	88–93	3	Green *Noctiluca* - strong bloom	(GN>80%)
3	29–30	Medium	Chlorophyte	43–61	2	Green *Noctiluca* – weak bloom	(GN>40%)
4	41–163	High	Dinoflagellate	60–96	2	Dinoflagellate bloom	(DN>60%)
5	11–13	Medium	Diatom	80–91	4	Diatom bloom	(DT>80%)
6	33–50	High	Cyanobacteria	52–57	2	Cyanobacteria bloom	(CN>50%)
7	18–26	Medium	Cryptophyte	48–54	2	Mixed species bloom	(MX)

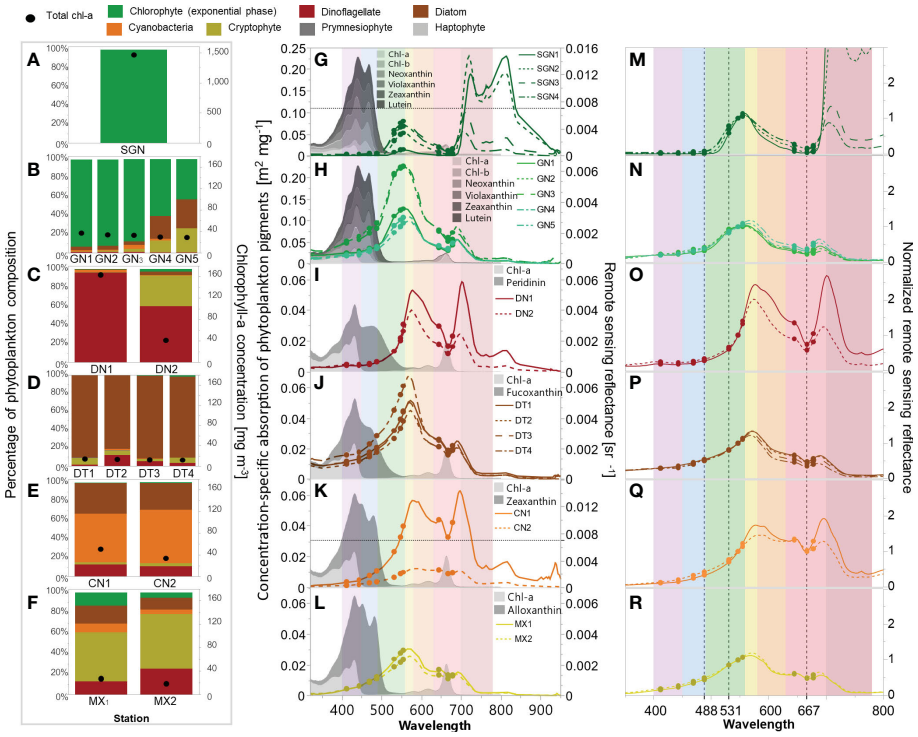


FIGURE 3
In situ chl-a and CHEMTAX-derived phytoplankton group composition (left), R_{rs} spectra and concentration-specific absorption of pigment markers of the dominant phytoplankton groups retrieved from Clementson and Wojtasiewicz (2019) employed in the CHEMTAX analysis (middle), and R_{rs} spectra normalized to R_{rs} 547 (right) of super green *Noctiluca* **(A, G, M)**, strong-to-weak green *Noctiluca* **(B, H, N)**, dinoflagellate **(C, I, O)**, diatom **(D, J, P)**, cyanobacteria **(E, K, Q)**, and mixed species **(F, L, R)** blooms. Dots **(G–R)** indicate *in situ* R_{rs} at MODIS wavelengths. Black dotted lines **(M–R)** indicate the normalized R_{rs} wavelengths used to discriminate among algal blooms. Color stripes **(G–R)** indicate purple (400–450), blue (451–490), green (491–560), yellow (561–580), orange (581–630), red (631–700), and near-infrared (701–780) wavelengths.

in blue, green, and red wavelengths of green *Noctiluca* and other algal bloom waters. These groups are described below.

Group 1. On July 30, 2018, we encountered a super bloom of green *Noctiluca* (SGN) with recorded cell densities greater than 1,500,000 cells L^{-1} at the sea surface, which turned the seawater dark green (Figure 2B). The recorded chl-a concentration was extremely high (>1,469 mg m^{-3}). The pigment composition measured by HPLC during the super bloom was similar to the findings of Furuya and Lirdwitayaprasit (2000). Neoxanthin, violaxanthin, lutein, and chl-b were detected in this study, but not zeaxanthin. Nonetheless, HPLC-CHEMTAX analysis revealed that the bloom was entirely green *Noctiluca* (100%) (Figure 3A). Owing to the instability of the surface water mass and bloom patch, four R_{rs} spectra were measured during the bloom (Figure 3G). The *in situ* R_{rs}

TABLE 2 Reports of red tides in the uGoT.

ID	Year	Month	Date	Location, Province	Algal groups	Dominant species	Density (cell L^{-1})
1	2009	Mar	n.d.	Tha Chin River mouth, Samut Sakhon	GN	*Noctiluca scintillans*	684–8,700
2	2016	Jan	n.d.	Cha-am Coast, Phetchaburi	GN	*Noctiluca scintillans*	535,000–3,642,000
3	2019	Aug	19–29	Wonnapha Beach to Laem Thaen, Chonburi	GN	*Noctiluca scintillans*	3,000–429,000
4	2019	Aug	27	Koh Loy, Chonburi	GN	*Noctiluca scintillans*	1,381–4,643
5	2019	Aug	27	Tham Phang Beach, Koh Sri Change, Chonburi	GN	*Noctiluca scintillans*	775
6	2010	Jul	n.d.	Tha Chin River mouth, Samut Sakhon	DN	*Ceratium furca*	127,841–2,752,872
7	2020	Feb	11–20	Phli Pier Bridge, Chonburi	DN	*Karenia* sp.	288,706–893,088
8	2020	Feb	11–20	Ang Sila, Chonburi	DN	*Karenia* sp.	92,196–682,500
9	2017	Jun	20	Koh Ran Dokmai, Chonburi	DT	*Leptocylindrus* sp.	1,384,574

Source: Marine and Coastal Resources Research & Development Institute, Department of Marine and Coastal Resources, Thailand. [Unpublished data].

spectra were relatively low in the violet to blue (400–490 nm; <0.00034 sr^{-1}) and red (min. between 664 and 668 nm;<0.00064 sr^{-1}) wavelengths. These relatively low R_{rs} characteristics have never been documented in the measured spectrum of green *Noctiluca* in the northern Arabian Sea (Dwivedi et al., 2015), although a peak in green (max. between 557 and 558 nm; 0.0008–0.0051 sr^{-1}) wavelengths corresponded to the noticeable green color of the bloom. Furthermore, extraordinarily high R_{rs} (>0.01 sr^{-1}) was observed in the red to near-infrared (NIR) wavelengths (~706 to ~825 nm), with decreasing R_{rs} in the visible wavelengths.

Groups 2 and 3. Strong (GN>80%) and weak (GN>40%) green *Noctiluca* blooms exhibited much lower chl-a concentrations (Figure 3B) than SGN blooms. The high NIR observed in the SGN spectra disappeared in these blooms (Figure 3H) and remained as only a small peak in the red-to-NIR wavelengths associated with the chlorophyll fluorescence peak. The signature of increasing reflectance from blue to green wavelengths for the green *Noctiluca* bloom spectrum reported in the Arabian Sea (Dwivedi et al., 2015) was also observed in the R_{rs} spectra of these groups, but was considerably lower in the blue wavelength and higher in the peak of the green wavelength (max. between 554 and 564 nm; 0.0028 to 0.0063 sr^{-1}).

Group 4. Dinoflagellate *Ceratium furca* blooms (DN>60%) had high chl-a (Figure 3C) and discolored the seawater to red (Figure 2C). Green R_{rs} values decreased rapidly from long to short wavelengths and were lower than those of the GN>80% and GN>40% blooms. This characteristic may be related to the enhanced absorption of peridinin, a marker pigment of dinoflagellates (Clementson and Wojtasiewicz, 2019). R_{rs} spectra showed two peaks in yellow (max. between 574 and 577 nm; 0.004 to 0.0053 sr^{-1}) and red-to-NIR (max. between 696 and 701 nm; 0.0025 to 0.0058 sr^{-1}) wavelengths. These two peaks arose during intense blooms, particularly the red-to-NIR peak.

Group 5. Diatom blooms (DT>80%) were observed in medium chl-a (Figure 3D), which had the lowest chl-a among all blooms. The R_{rs} spectra peaked in the yellow band (max. between 568 and 572 nm; 0.0045–0.0068 sr^{-1}), similar to dinoflagellate blooms; however, violet to green values were higher in diatom blooms. The higher reflectance in green wavelengths compared to dinoflagellate blooms was also observed in the bloom spectra in the East China Sea (Shang et al., 2014; Tao et al., 2015).

Group 6. Cyanobacteria blooms (CN>50%) were found in high chl-a waters with lower abundances of diatoms and dinoflagellates (Figure 3E). R_{rs} spectra with values gradually increasing from blue to green wavelengths were generally similar to those of DN>60% and DT>80% (Figure 3K). Otherwise, the increase in R_{rs} of cyanobacteria in the orange to red range was greater than that for dinoflagellates, particularly from 645 to 678 nm.

Group 7. Cryptophytes dominated a mixed red tide population observed in samples with medium chl-a concentration (Figure 3F). Because cryptophytes have never been proven to cause red tides in the uGoT, we refer to this group as mixed (MX) bloom water. The R_{rs} spectra gradually increased from blue to green, peaking in the yellow band (max. between 568 and 571 nm; 0.0026 to 0.0031 sr^{-1}, Figure 3L). This characteristic was similar to that of DT>80% blooms, but the R_{rs} values were much lower.

Normalizing the R_{rs} spectra by R_{rs} 547 (Figure 3M–R) helped highlight the differences in spectral characteristics for each algal bloom type. Normalized R_{rs} spectra, particularly in the blue (451–490 nm), green (491–560 nm), and red (581–700 nm) bands, showed the unique spectral characteristics of green *Noctiluca* in comparison to the other groups. Green *Noctiluca* had low normalized R_{rs} values in the blue and red wavelengths and a peak in the green band. These characteristics became clearer as the bloom intensity increased. Normalized R_{rs} spectra of DN>60% and CN>50% blooms, as well as DT>80% and MX blooms, were higher in red and blue-to-green wavelengths than those recorded for strong and weak GN blooms. These distinct spectral characteristics in the blue, green, and red wavelengths, which are expressed by the water color, provide an opportunity to distinguish green *Noctiluca* blooms from other blooms using satellite ocean color data.

3.2 Algal-bloom classification algorithm

Differences in the spectral signatures of *in situ* normalized R_{rs} values in blue, green, and red bands (Figure 3M–R) were utilized to

discriminate green *Noctiluca* blooms and classify water types based on MODIS wavelengths. Unlike former green *Noctiluca* discriminating approaches that used a cluster of differences in MODIS-retrieved R_{rs} 488 to R_{rs} 443 and R_{rs} 531 (Dwivedi et al., 2015; Baliarsingh et al., 2017), we used observed normalized R_{rs} values at 488, 531, and 667 nm for a straightforward approach to grouping water types based on chl-a levels and dominant phytoplankton composition in waters with more diverse algal bloom species. The seven types of bloom waters (i.e., SGN, GN>80%, GN>40%, DN>60%, DT>80%, CN>50%, and MX) and two types of non-bloom waters (i.e., coastal and oceanic waters) were thus classified as shown in Figure 4.

The normalized R_{rs} 488 results demonstrated an inverse relationship with chl-a levels, which were used to differentiate blooms from non-bloom waters. In this step, SGN blooms (very high chl-a), which had very low normalized R_{rs} 488 values, were independently separated from non-bloom coastal (low chl-a) and non-bloom oceanic (very low chl-a) waters. The low values (≤0.2) of SGN blooms corresponded to low R_{rs} spectral characteristics at blue wavelengths (Figure 3G, M). Meanwhile, high chl-a bloom waters with normalized R_{rs} 488 values ranging from 0.2 to 0.55 (i.e., GN>80%, DN>60%, and CN>50%) were distinguished using normalized R_{rs} 667 values. This cluster criterion was related to a shift in the R_{rs} values at red wavelengths (Figure 3H, I, K). For blooms with medium chl-a concentration (i.e., GN>40%, DT>80%, and MX), the normalized R_{rs} values were moderate, at 488 nm (0.2 and 0.55) and 667 nm (0.3 and 0.55). Normalized R_{rs} 488 values less than 0.4 differentiated GN>40% blooms from the other blooms. Normalized R_{rs} 531 values lower and higher than 0.84 were used to differentiate DT>80% and MX blooms, respectively.

Algorithm application and validation using MODIS data. The classification algorithm based on normalized R_{rs} 488, R_{rs} 531, and R_{rs} 667 data processed with daily MODIS data is summarized in Figure 5. MODIS R_{rs} verification showed compatibility between *in situ* and MODIS normalized R_{rs} 488 data (see Supplementary Appendix 3), as demonstrated in Luang-on et al. (2021). However, overestimation of the normalized R_{rs} 531 and underestimation of the normalized R_{rs} 667 were observed in this study. Therefore, correction of MODIS was conducted before

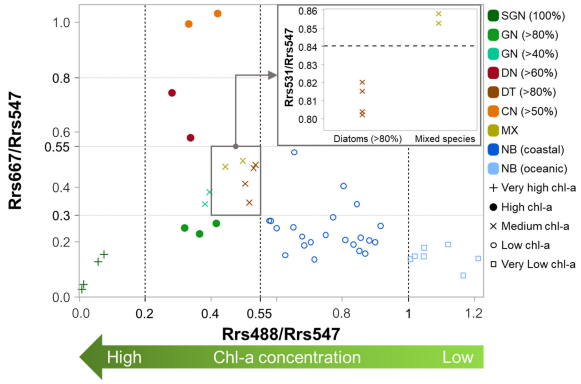


FIGURE 4
Discrimination of super green *Noctiluca* (SGB), green *Noctiluca* (GN), dinoflagellate (DN), diatom (DT), cyanobacteria (CN), and mixed species (MX) blooms, as well as non-bloom (NB) coastal and oceanic waters according to chl-a level and dominant phytoplankton composition using the normalized R_{rs} at 488, 531, and 667 nm in the uGoT.

applying the algal-bloom classification algorithm to the satellite data to improve its accuracy (Figures S3–S5).

MODIS-derived algal bloom images on cloudless days compared well with uGoT red tide reports in Table 2, demonstrating that the classification with MODIS data could detect red tide events (Figure 6), although the red tide reports do not always provide the exact incident date. Satellite images showed a bloom in the same area as recorded in the reports during the periods of GN blooms in March 2009, January 2016, and August 2019 (Figures 6A–1–C–1). The images also matched with the DN>60% blooms of *Ceratium furca* during July 2010 and *Karenia* sp. from February 11–20, 2020, as well as the following DT>80% bloom of *Leptocylindrus* sp. on June 20, 2017 (Figures 6D–1–F–1). These images further support our categorization findings, which fit our concept of an algal bloom in locations with high chl-a concentrations (≥10 mg m^{-3}, Figures 6A–2–F–2). Furthermore, our findings revealed that high chl-a levels around major river mouths may be caused by dinoflagellate and cyanobacterial blooms, as demonstrated by the image of the *C. furca* bloom (Figure 6D–1),

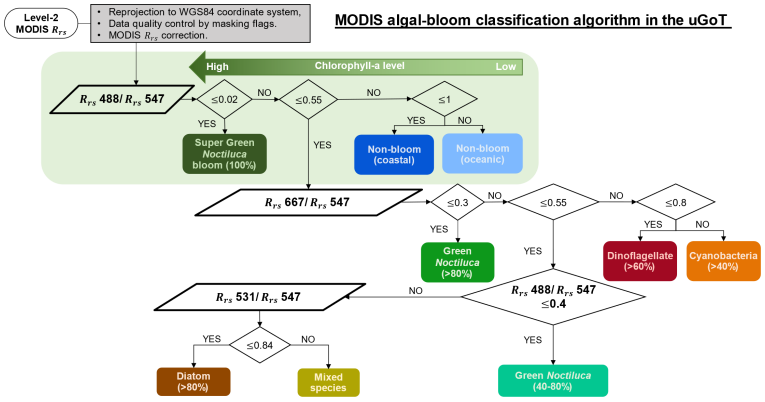


FIGURE 5
Flow diagram of MODIS data processing for discriminating algal blooms in the uGoT.

whereas GN blooms were located further from the shore. These findings reveal that our algorithm is capable of detecting red tides and studying their dynamics.

3.3 MODIS-derived seasonal distribution

Using the algal-bloom classification algorithm, the percentage of the relative bloom frequency of each phytoplankton group in each month was computed through the time series of corrected MODIS data (2003 – 2021) to investigate the seasonal spatial distribution and frequency patterns of algal blooms in different seasons: non-monsoon (NOM; February–April), southwest monsoon (SWM; May–September), and northeast monsoon (NEM; October–January of the following year) (Figure 7). To better understand the seasonal dynamics, the results were then compared to the seasonal variations in sea surface winds, precipitation, and river discharge in the uGoT, which we used to represent surface circulation and nutrient input, as shown in Figure 8.

In general, GN blooms occurred farther from the shore and estuaries than red tides of DN>60% and CN>50%, and were distributed seasonally in patterns similar to MX blooms. DT>80% blooms showed a distribution pattern similar to that of DN>60% blooms. The bloom frequency exceeded 50% or 15 days per month in all phytoplankton groups. However, the high bloom frequency of these blooms varied in areas with different monsoon seasons.

During the NOM period, southerly winds blow steadily, with an increase in precipitation and low river discharge. GN bloom area and frequency increased in the north between the Tha Chin and Chao Phraya Rivers, with averages of three to six days per month (9–19%) from the early to late season. The highest frequency was in April, at 68% or 21 days, which was similar to that of MX blooms. A few other blooms were also observed in more confined locations, particularly around estuaries and coasts.

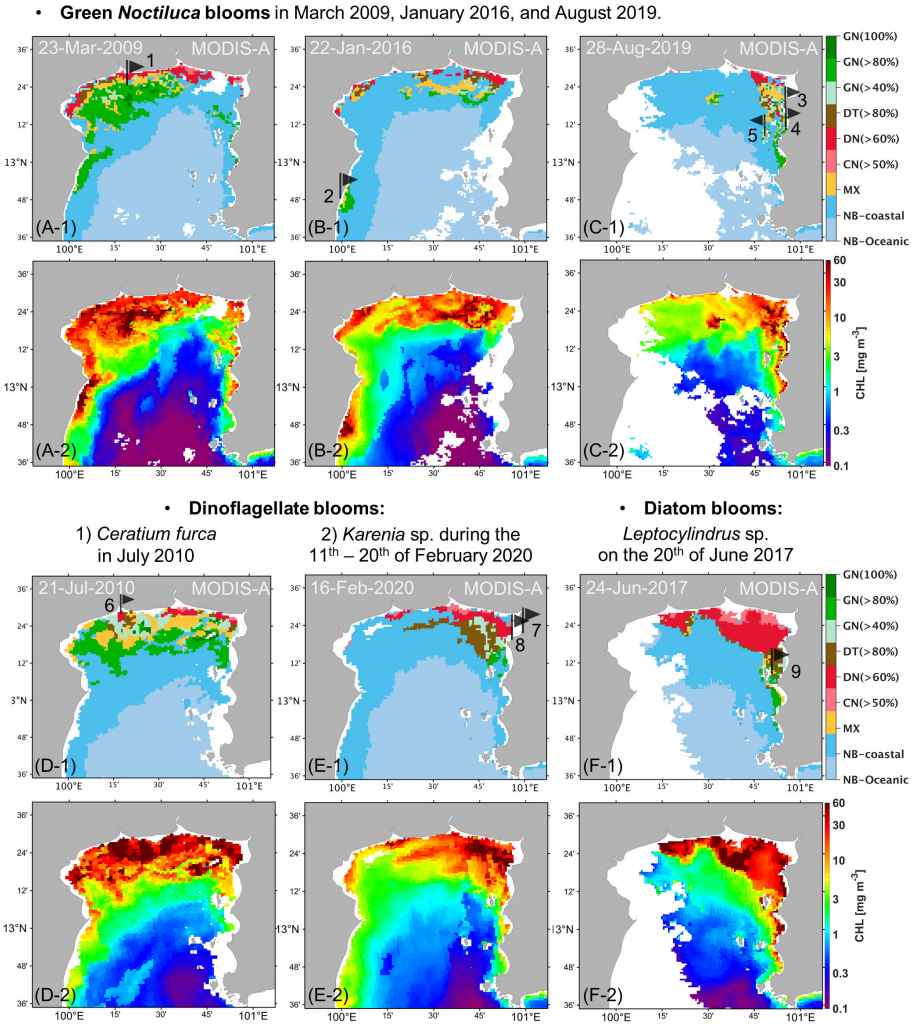


FIGURE 6
Daily MODIS data processed using the uGoT algal-bloom classification algorithm **(A, F-1)** and uGoT chl-a algorithm (Luang-on et al., 2021, **A, F-2)**. Red tide reports are indicated by black flags and numbers corresponding to Table 2.

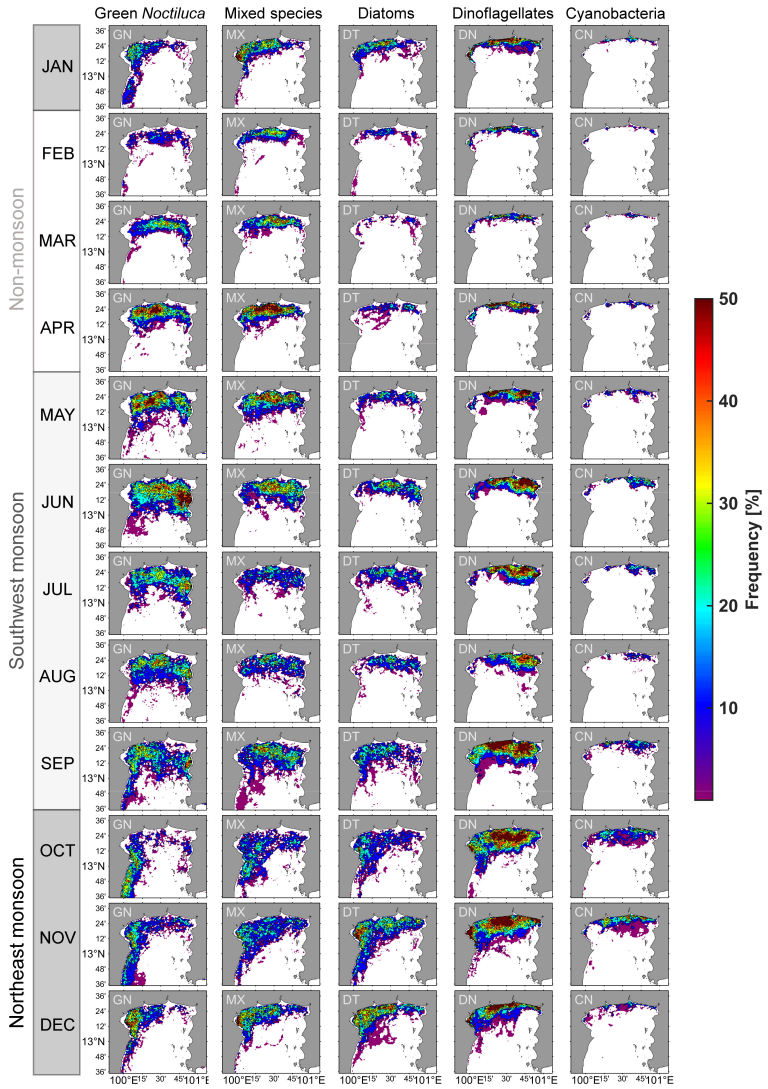


FIGURE 7
Monthly climatological distribution of the percentage bloom frequency of green *Noctiluca* (GN), mixed species (MX), diatom (DT), dinoflagellate (DN), and cyanobacteria (CN) blooms during 2003–2021. The percentage indicates the frequency of each phytoplankton bloom per data during this period. The white area had no blooms of any phytoplankton group. The minimum percentage was 5% (two times in 30 days).

During the SWM, the southwest monsoon wind peaked in June, resulting in heavy precipitation and an increase in river discharge throughout the season. All red tides experienced intense blooms in terms of area and frequency. GN blooms covered the largest area compared to other phytoplankton groups, and were observable in the upper part of the uGoT, particularly in the offshore and eastern regions between June and September. The blooms occurred on an average of four to five days per month (15–18%) and up to six days (20%) in June, with the most intense bloom in the east along the coast of Chonburi Province, lasting up to 22 days (74%), which coincided with the highest southwesterly wind magnitude. When river discharge was high in the late season, GN blooms decreased in frequency, and DN>60% blooms became more frequent, occurring on an average of five to seven days per month and up to 25 days (84%) in September, particularly between the rivers in the center and east of the uGoT. DT>80% and CN>50% blooms had a lower area coverage and frequency than GN and DN>60% blooms, predominately near western and eastern estuaries in the late season, respectively.

During the NEM, the northeast monsoonal wind dominated from November onward, resulting in less precipitation, whereas the highest river discharge occurred in October. All types of algal blooms frequently occurred from the Chao Phraya estuary to the west and south. GN blooms had a lower frequency in NEM than SWM, with an average frequency of four days (12–14%) every month throughout the season and up to 19 days (63%) in December. The main bloom area was along the western coast, beginning in the south in October and shifting north from November to December, similar to MX blooms. Others bloomed more frequently along the northern coast toward the west, whereas CN>50% bloom area was restricted to estuaries. DN>60% blooms were the most frequent, averaging up to eight days (25%) with a

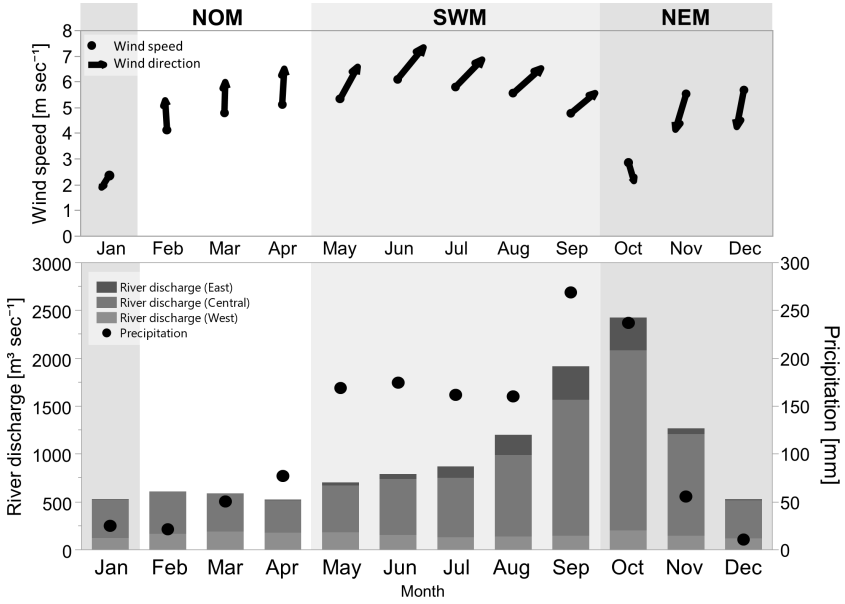


FIGURE 8
Monthly climatological data of sea surface wind speed and direction (upper), precipitation, and river discharge from the east, central, and west coasts of the uGoT (bottom) during 2003–2017; modified from Luang-on et al. (2021).

maximum frequency of 24 days (79%) in October at the highest river discharge in the outer Chao Phraya and Tha Chin estuaries, and shifting closer to the shore and estuaries when river discharge decreased in November. DT>80 blooms also increased in frequency, with an average frequency of up to five days (17%) from November to December. All blooms then faded in January upon weakening of the monsoon wind.

4 Discussion

4.1 Spectral characteristics of green *Noctiluca* blooms and other red tides

The hyperspectral reflectance of green *Noctiluca* blooms in uGoT coastal eutrophic waters showed unique spectral characteristics, with R_{rs} peaks in green (~554 to ~564 nm) and low R_{rs} values in the violet to blue (~400 to ~490 nm) and red (~630 to ~700 nm) wavelengths, especially when they evolved into SGN blooms (Figure 3G–H). The low R_{rs} values were attributed to high light absorption by photosynthetic pigments (i.e., chlorophylls, particularly chl-b) and by non-photosynthetic carotenoids (e.g., neoxanthin, violaxanthin, and lutein) in the violet to blue regions (Bricaud et al., 2004; Clementson and Wojtasiewicz, 2019). Carotenoid absorption is also responsible for the discoloration caused by red *Noctiluca* (Balch and Haxo, 1984; Shaju et al., 2018). Therefore, the relatively low reflectance in the violet and blue regions of SGN blooms was attributed to an increase in the photosynthetic pigments of the green endosymbiont.

An increase in the R_{rs} spectral slope between 440 nm and 550 nm reported by Dwivedi et al. (2015) for green *Noctiluca* in the open ocean Arabian Sea was also observed for the green *Noctiluca* blooms of the coastal uGoT. However, the steeper slope for green *Noctiluca* blooms of the uGoT was caused by the increase in the peak green wavelength and the lower R_{rs} values at short wavelengths compared to the spectra reported for Arabian Sea green *Noctiluca*. We suspect that these differences were caused by increased absorption by non-algal particles and colored dissolved organic matter, which are typical of coastal waters such as the uGoT.

Furthermore, our green *Noctiluca* spectra showed relatively high reflectance in the NIR wavelengths (~706 to ~825 nm) during SGN blooms (Figure 2B and 3A, G). This feature has never previously been reported in studies of green *Noctiluca* blooms, but has been observed in the reflectance spectra of red *Noctiluca* (Astoreca et al., 2005; Van Mol et al, 2007; Qi et al., 2019), floating macroalgae (Hu, 2022), and land vegetation (Govender et al., 2007). Reflectances higher than 700 nm are typically low because of high water absorption. However, this feature was not observed continuously, even during measurements at the same sampling point (Figure 3G). Green *Noctiluca* possesses an extraordinary ability to manage its buoyancy *via* regulation of intracellular ammonium and lipid concentrations (Lirdwitayaprasit et al., 2012; Goes et al., 2018). It can also accumulate at the sea surface when seawater conditions are stable. We presume that the high NIR reflectance was caused by the high density of green *Noctiluca* cells occupying the sea surface instead of water molecules, causing high backscattering of NIR (Van Mol et al., 2007). Because NIR wavelengths are commonly used in atmospheric correction algorithms, this elevated reflectance can lead to the saturation of reflectance and the elimination of some pixels of green *Noctiluca* blooms in satellite level-3 data, which include atmospheric failure masks, such as the maximum iterations reached for NIR iteration (Patt et al., 2003; Van Mol et al., 2007). We propose that this process

of pixel elimination be reconsidered so that NIR satellite ocean color level-3 data can be used for the detection of super blooms.

Differences in the spectral characteristics between green *Noctiluca* and other phytoplankton blooms were highlighted by the normalized R_{rs} spectra (Figure 3M–R). The absence of green *Noctiluca*-specific pigments increased (decreased) the normalized R_{rs} values in the blue (green) bands of other phytoplankton blooms. Moreover, the green peak of green *Noctiluca* was low in the spectra of DN>60% blooms; this could be attributed to the presence of peridinin, which uniquely generates high absorption between 500 nm and 550 nm (Bricaud et al., 2004). In the red region, all green *Noctiluca* spectra were lower than those of DN>60% and CN>50%, which was possibly attributed to the absorption of photosynthetic pigments and the scattering of cell structures. Therefore, the R_{rs} ratios between the blue, green, and red regions can be utilized to discriminate green *Noctiluca* blooms from other phytoplankton blooms.

4.2 Algorithm performance

Our algal-bloom classification algorithm (Figure 5) was developed to discriminate green *Noctiluca* from other algal bloom and non-bloom waters based on the distinctive *in situ* hyperspectral characteristics of uGoT algal blooms. This algorithm was then applied to satellite data by utilizing the unique normalized spectral characteristics of green *Noctiluca* in blue (R_{rs} 488/R_{rs} 547), green (.531/R_{rs} 547), and red (R_{rs} 667/R_{rs} 547) bands, as described in Section 4.1. The general concept of this classification algorithm was to use the normalized R_{rs} in blue (i.e., the ratio of blue to green wavelengths) to distinguish algal bloom and non-bloom waters because this value covaries with chl-a in the uGoT (Intacharoen et al., 2018; Luang-on et al., 2021). SGN blooms, which have relatively high chl-a and low R_{rs} in violet to blue wavelengths, were discriminated from other algal blooms and non-bloom waters by this blue-to-green ratio. Meanwhile, the normalized R_{rs} values in green and red bands were used to discriminate groups of algal blooms in medium and high chl-a waters, respectively.

Because GN>80% and GN>40% blooms have lower reflectance in the red band than in other groups, as well as in the blue band, low normalized R_{rs} in red was utilized to discriminate them from other dinoflagellates and cyanobacteria. Based on the specific features of low reflectance in blue and red bands, our algorithm was able to discriminate between the three levels of green *Noctiluca* blooms. The use of normalized R_{rs} allowed the classification of water types in relation to chl-a and green *Noctiluca* blooms, in contrast to other algorithms that do not specify the levels of blooms and utilize similar single R_{rs} in blue-to-green wavelengths without normalization (Dwivedi et al., 2015; Baliarsingh et al., 2017). However, in coastal waters with high concentrations of colored dissolved organic matter, which have high absorption in the blue light region, this algorithm should be used with caution for determining bloom and non-bloom waters according to the relationship between normalized R_{rs} in the blue band and chl-a concentration. In that case, using green and red wavelengths to determine bloom waters might be more effective, such as methods developed in East China Seas, in which the blooms are mainly caused by dinoflagellate and diatoms (Tao et al., 2015; Shen et al., 2019).

A comparison of MODIS-derived algal bloom images with uGoT red tide reports and chl-a images demonstrated that our algorithms could discriminate green *Noctiluca* from other algal blooms and non-bloom waters (Figure 6 and Table 2). Green *Noctiluca* blooms, which are often observed in coastal areas, were shown by our algorithm to be patchy in offshore areas, which is comparable to the results given by the maximum chlorophyll index described in Suwanlertcharoen and Prukpitikul (2018). Furthermore, the satellite images of our classification revealed that high chl-a in the nearshore and estuaries was likely caused by phytoplankton other than green *Noctiluca*. Thus, our classification algorithm described green *Noctiluca* blooms (weak to super blooms) and a variety of other red tides, that is, dinoflagellates, cyanobacteria, and mixed species blooms, in more detail than existing algorithms.

As demonstrated above, the application of our algal-bloom classification algorithms to MODIS data yielded useful information on water types. This allowed for the discrimination of green *Noctiluca* from other red tides in high chl-a coastal waters. This approach offers the potential to use multi-hyperspectral satellite data to monitor and study the dynamics of different red tides. To avoid errors caused by the difference in wavelengths in each satellite data, the correlation between R_{rs} values should be validated before applying the algorithm to identify the blooms.

4.3 Seasonal variability of green *Noctiluca* and other red tides

We used MODIS-derived bloom frequency images (Figure 7) to understand the seasonal dynamics of green *Noctiluca* and other red tides across the entire uGoT. The seasonal patterns of red tide distribution and areas with the highest bloom frequency in each red tide were distinct in each monsoon season. Monsoon-induced elements such as sea surface winds, precipitation, and river flow (Figure 8), which impact uGoT surface chl-a levels (Luang-on et al., 2021), are therefore expected to influence the seasonal variability of uGoT red tides. These elements are discussed in the following paragraphs.

River discharge. Strong precipitation increased river discharge from the SWM to early NEM, induced high nutrient loads (Thaipichitburapa et al., 2010; Yuenyong et al., 2019), decreased ocean salinity (Buranapratheprat et al., 2002; Yu et al., 2018), and enhanced surface stability (Buranapratheprat et al., 2008; Yu et al., 2018). The blooms of all phytoplankton groups, particularly GN in the SWM and DN>60% in the NEM (Figure 7), responded to the increase in anthropogenic nutrients. Enhanced surface stability owing to an increase in freshwater discharge may also facilitate the promotion of surface blooms of dinoflagellates, including green *Noctiluca*. Moreover, our findings showed that DN>60% blooms occurred mainly in estuaries and closer to the shore, which were more highly influenced by freshwater discharge than green *Noctiluca* blooms. This finding is consistent with the preferred

salinity range of dinoflagellates such as *Ceratium furca* (12–27 psu) and green *Noctiluca* (22–33 psu) (Lirdwitayaprasit et al., 2006), as well as the correlation between high salinity (25–29 psu) and green *Noctiluca* abundance reported by Chuenniyom et al. (2012). Thus, our results suggest that, in addition to contributing anthropogenic nutrients, river discharge may influence red tide distributions by regulating salinity levels.

Precipitation. In addition to causing high river discharge, precipitation can drain land-based nutrients from coastal aquaculture through runoff and tiny canals, stimulating high surface chl-a in the north of the uGoT (Luang-on et al., 2021). Our results demonstrated that high surface chl-a, even at low river discharge during the NOM, is related to green *Noctiluca* rather than other red tide species (Figure 7). The green *Noctiluca* succession can be explained by its mixotrophic ability, which allows it to consume external food, such as diatoms and other dinoflagellates, while still obtaining energy from the photosynthetic endosymbiont (Lirdwitayaprasit, 2015; Goes et al., 2018). Lirdwitayaprasit (2015) demonstrated that, without an external food supply, green endosymbionts disappeared after approximately two weeks of incubation, and *Noctiluca* host cells died about a month later. Therefore, a small increase in precipitation draining land-based nutrients should be sufficient to trigger green *Noctiluca* blooms.

Monsoon winds. The SWM and NEM generate eastward and westward transportation, respectively (Buranapratheprat et al., 2002; Buranapratheprat et al., 2006; Yu et al., 2018; Luang-on et al., 2021). This monsoon influence can be seen in the changes in hotspots of green *Noctiluca* and other algal blooms (Figure 7). During the SWM, green *Noctiluca* blooms occurred most frequently in the west, especially between June and September, which is consistent with red tide reports from both local notifications and documentation (Lirdwitayaprasit et al., 2006; Sriwoon et al., 2008). The eastward circulation that transports river discharge and phytoplankton cells may promote blooms. Furthermore, we discovered that green *Noctiluca* blooms were abundant throughout the season in nearly half of the uGoT, particularly offshore rather than in coastal areas. However, this pattern shifted to the western coast during the transition to the NEM from October to the end of the NEM, corresponding to westward transportation. In addition, only a high bloom frequency of green *Noctiluca* occurred in the southwest in October and November. The green *Noctiluca* distribution, which extends slightly further than that of other red tide groups, might be attributed to its large cell vacuole, which is filled with ammonium ions, causing high buoyancy (Elbrächter and Qi, 1998). This suggests that green *Noctiluca* cells could be transported into the southern gulf during the NEM. Meanwhile, strong southerly winds may cause aggregation of green *Noctiluca* cells and promote blooming in the north between the two rivers in the absence of a monsoon influence.

The seasonal dynamics of red tides based on seasonal variations in MODIS-derived blooms and monsoon-induced variables are presented in Figure 9. During the NOM, southerly winds may push high-salinity water masses to the north during low river discharge, resulting in the aggregation of green *Noctiluca* cells. Increasing nutrient levels owing to increasing precipitation may promote green *Noctiluca* blooms. Nonetheless, an increase in green *Noctiluca* cells, which feed on other phytoplankton, may have a controlling effect on the populations of other red tides. The SWM generates high precipitation and increases river discharge, resulting in a high nutrient load. All phytoplankton are then promoted, and red tides of green *Noctiluca* and dinoflagellates are likely to develop as the surface stability increases. Meanwhile, salinity levels can determine the bloom area of both red tides. Because of eastward circulation, green *Noctiluca* blooms accumulate and are promoted in the east rather than in other areas. During the NEM, all blooms shift to the west because of Westward transportation. This transportation might allow the discharge of freshwater from major rivers, promoting dinoflagellates and other algal blooms along the northern coast, whereas green *Noctiluca* might be transported to the south because of its passive buoyancy.

Therefore, our algal-bloom classification algorithm based on MODIS data can be used to better understand the seasonal variability of green *Noctiluca* and other red tides, which can be influenced by monsoon-induced factors that regulate nutrient input, salinity, surface stability, and surface circulation. Our findings also demonstrate that green *Noctiluca* is more extensive

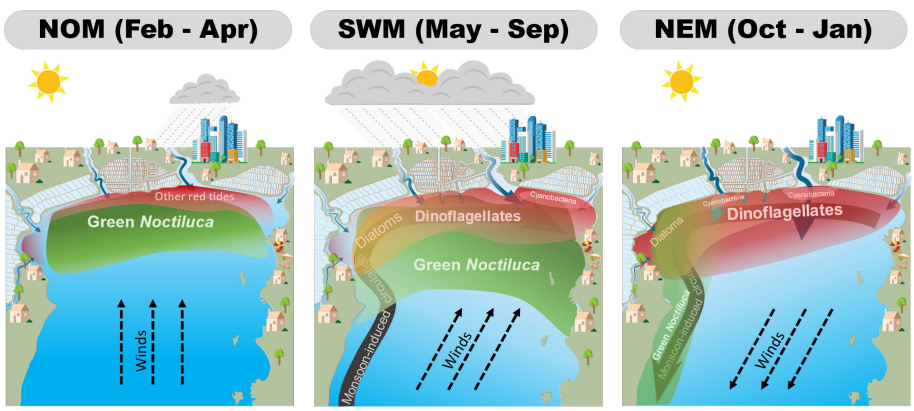


FIGURE 9
Synopsis of the seasonal dynamics of uGoT red tides under non-monsoon (left), southwest monsoon (middle), and northeast monsoon (right) conditions.

than other red tide groups because of its feeding behavior, in addition to these parameters. In addition to detecting and monitoring blooms, our approach can be used to examine the dynamics of red tides in the uGoT.

5 Conclusion

In this study, we clarified the unique hyperspectral reflectance characteristics of green *Noctiluca* and other algal blooms (i.e., dinoflagellates, diatoms, cyanobacteria, and mixed species) using new *in situ* bio-optical datasets collected in the uGoT between 2017 and 2019. A suite of algal-bloom classification algorithms was developed based on the normalized R_{rs} values at 488, 531, and 667 nm, which are compatible with the MODIS wavelengths. The satellite R_{rs} was verified and corrected before applying the algorithms to MODIS data. The algorithms performed well with MODIS data, effectively distinguishing green *Noctiluca* blooms from other phytoplankton blooms and non-bloom waters, as well as revealing bloom dynamics. The seasonal variability of green *Noctiluca* and other algal blooms was clarified by comparing MODIS-derived bloom frequency images to monsoon-induced parameters. We confirmed that these parameters can influence red tide variations, emphasizing the effects of Asian monsoons on phytoplankton variation in the uGoT. This study reveals the mechanisms of seasonal red tide dynamics in relation to monsoon-induced variables. Thus, our results build confidence in the application of satellite ocean color observations for monitoring the dynamics of red tides in regional coastal waters influenced by human pollution and the global climate.

Data availability statement

The original contributions presented in the study are included in the article/Supplementary Material. Further inquiries can be directed to the corresponding author.

Author contributions

JL-O collected the samples, analyzed the field and satellite data, developed the algal-bloom classification algorithm, and wrote this manuscript. JI contributed to project administration, supervision, and funding acquisition. AB and JP made the contribution of ship observations and sample analysis in Thailand, as well as manuscript revision. JG and ES also contributed to the writing revision and edition. EM assisted with satellite data analysis. YZ, QX, and PN helped with the sample collection and measurements. HK and SM contributed *in situ* bio-optical data to validate satellite R_{rs} data. All authors contributed to the article and approved the submitted version.

Funding

This work was supported by the Sasakawa Scientific Research Grant of the Japan Science Society (JSS-29-714); ISEE International Joint Research Program and Japan; Global Change Observation Mission-Climate (GCOM-C) project of the Japan Aerospace Exploration Agency (JAXA); and Grants-in-Aid for Scientific Research (KAKENHI JP21H05317) funded by the Ministry of Education, Culture, Sports, Science, and Technology-Japan (MEXT). JG is supported by NASA grants 80LARC21DA002-GLIMR AABO8078, NNX17AG66G-ECO4CAST and NOAA GST SA18-CUNY01.

Acknowledgments

We gratefully acknowledge the data support provided by the Royal Irrigation Department (Thailand) and the Department of Marine and Coastal Resources (Thailand). We also thank the following people for their facilitation of the ship observation and sample analysis in Thailand and Japan, without whose help this work would never have been possible: Prof. Dr. Shettapong Meksumpun and Assistant Prof. Suchai Worachananat of Kasetsart University, Dr. Vichaya Gunbua of Burapha University, and Assistant Prof. Yoshihisa Mino of Nagoya University.

Conflict of interest

The authors declare that the research was conducted in the absence of any commercial or financial relationships that could be construed as a potential conflict of interest.

Publisher's note

All claims expressed in this article are solely those of the authors and do not necessarily represent those of their affiliated organizations, or those of the publisher, the editors and the reviewers. Any product that may be evaluated in this article, or claim that may be made by its manufacturer, is not guaranteed or endorsed by the publisher.

Supplementary material

The Supplementary Material for this article can be found online at: https://www.frontiersin.org/articles/10.3389/fmars.2023.1031901/full#supplementary-material

References

Astoreca, R., Rousseau, V., Ruddick, K. G., van Mol, B., Parent, J.-Y., and Lancelot, C. (2005). "Optical properties of algal blooms in an eutrophicated coastal area and its relevance to remote sensing", *in Remote Sensing of the Coastal Oceanic Environment*. 58850V-58850V–11. doi: 10.1117/12.615160

Balch, W. M., and Haxo, F. T. (1984). Spectral properties of noctiluca miliaris suriray, a heterotrophic dinoflagellate. *J. Plankton Res.* 6, 515–525. doi: 10.1093/plankt/6.3.515

Baliarsingh, S. K., Dwivedi, R. M., Lotliker, A. A., Sahu, K. C., Kumar, T. S., and Shenoi, S. S. C. (2017). An optical remote sensing approach for ecological monitoring of red and green noctiluca scintillans. *Environ. Monit Assess.* 189, 330. doi: 10.1007/s10661-017-6037-9

Bricaud, A., Claustre, H., Ras, J., and Oubelkheir, K. (2004). Natural variability of phytoplanktonic absorption in oceanic waters: Influence of the size structure of algal populations. *J. Geophys Res. Oceans* 109, C11010. doi: 10.1029/2004JC002419

Buranapratheprat, A., Morimoto, A., Phromkot, P., Mino, Y., Gunbua, V., and Jintasaeranee, P. (2021). Eutrophication and hypoxia in the upper gulf of Thailand. *J. Oceanogr.* 77, 831–841. doi: 10.1007/s10872-021-00609-2

Buranapratheprat, A., Niemann, K. O., Matsumura, S., and Yanagi, T. (2009). MERIS imageries to investigate surface chlorophyll in the upper gulf of Thailand. *Coast. Mar. Sci.* 33, 22–28. doi: 10.15083/00040700

Buranapratheprat, A., Yanagi, T., and Matsumura, S. (2008). Seasonal variation in water column conditions in the upper gulf of Thailand. *Cont Shelf Res.* 28, 2509–2522. doi: 10.1016/j.csr.2008.07.006

Buranapratheprat, A., Yanagi, T., and Sawangwong, P. (2002). Seasonal variations in circulation and salinity distributions in the upper gulf of Thailand: Modeling approach. *Mer* 40, 147–155.

Buranapratheprat, A., Yanagi, T., Sojisuporn, P., and Chinorost, B. (2006). Influence of local wind field on seasonal circulations in the upper gulf of Thailand. *Coast. Mar. Sci.* 30, 19–26.

Chuenniyom, W., Meksumpun, C., and Meksumpun, S. (2012). Impacts of nutrients and related environmental factors on distribution and size structure of noctiluca scintillans populations of the eutrophic tha chin estuary, Thailand. *Water Sci. Technol.* 65, 1994–2002. doi: 10.2166/wst.2012.099

Chumnantana, R., Marine, P., and Resources, C. (2006). Causative phytoplankton of red tide phenomena in the upper Gulf of Thailand (Technical Paper no. 1/2006). Marine and Coastal Resources Research and Development Institute, Bangkok. Available at: https://www.dmcr.go.th/detailLib/2124.

Clementson, L. A., and Wojtasiewicz, B. (2019). Dataset on the absorption characteristics of extracted phytoplankton pigments. *Data Brief* 24, 103875. doi: 10.1016/j.dib.2019.103875

do Rosário Gomes, H., Goes, J. I., Matondkar, S. G. P., Buskey, E. J., Basu, S., Parab, S., et al. (2014). Massive outbreaks of noctiluca scintillans blooms in the Arabian Sea due to spread of hypoxia. *Nat. Commun.* 5, 4862. doi: 10.1038/ncomms5862

Dwivedi, R., Rafeeq, M., Smitha, B. R., Padmakumar, K. B., Thomas, L. C., Sanjeevan, V. N., et al. (2015). Species identification of mixed algal bloom in the northern Arabian Sea using remote sensing techniques. *Environ. Monit Assess.* 187, 51. doi: 10.1007/s10661-015-4291-2

Elbrächter, M., and Oi, Z. (1998) "Aspects of Noctiluca (Dinophyceae) population dynamics," in *Physiological ecology of harmful algal blooms*, eds. D M Anderson, A D Cambella, and G M Hallegraeff, 315–335.

Enomoto, Y. (1956) On the occurrence and the food of noctiluca scintillans (Macartney) in the waters adjacent to the west coast of Kyushu, with special reference to the possibility of the damage caused to the fish eggs by that plankton (Accessed July 26, 2022).

Escalera, L., Pazos, Y., Moroño, Á., and Reguera, B. (2007). Noctiluca scintillans may act as a vector of toxigenic microalgae. *Harmful Algae* 6, 317–320. doi: 10.1016/j.hal.2006.04.006

Fonda Umani, S., Beran, A., Parlato, S., Virgilio, D., Zollet, T., de Olazabal, A., et al. (2004). Noctiluca scintillans macartney in the northern Adriatic Sea: Long-term dynamics, relationships with temperature and eutrophication, and role in the food web. *J. Plankton Res.* 26, 545–561. doi: 10.1093/plankt/fbh045

Furuya, K., and Lirdwitayaprasit, T. (2000). Pigment composition of pedinomonas noctilucae (Pedinophyceae), an endosymbiont of green noctiluca (Dinophyceae). *La mer* 38, 95–97.

Goes, J. I., Gomes, H., do, R., Al-Hashimi, K., and Buranapratheprat, A. (2018). "Ecological drivers of green noctiluca blooms in two monsoonal-driven ecosystems," in *Global ecology and oceanography of harmful algal blooms. ecological studies (Analysis and synthesis)*, vol. 232 . Eds. P. M. Glibert, E. Berdalet, M. A. Burford, G. C. Pitcher and M. Zhou (Cham: Springer), 327–336. doi: 10.1007/978-3-319-70069-4_17

Gomes, H., do, R., Matondkar, S. G. P., Parab, S. G., Goes, J. I., Pednekar, S., et al. (2009). Unusual blooms of the green noctiluca miliaris (dinophyceae) in the Arabian Sea during the winter monsoon. *Geophysical Monograph Ser.* 185, 347–363. doi: 10.1029/2008GM000831

Govender, M., Chetty, K., and Bulcock, H. (2007). A review of hyperspectral remote sensing and its application in vegetation and water resource studies. *Water SA* 33, 145–151. doi: 10.4314/wsa.v33i2.49049

Hansen, P. J., Miranda, L., and Azanza, R. (2004). Green noctiluca scintillans: A dinoflagellate with its own greenhouse. *Mar. Ecol. Prog. Ser.* 275, 79–87. doi: 10.3354/meps275079

Harrison, P. J., Furuya, K., Glibert, P. M., Xu, J., Liu, H. B., Yin, K., et al. (2011). Geographical distribution of red and green noctiluca scintillans. *Chin. J. Oceanology Limnology* 29, 807–831. doi: 10.1007/s00343-011-0510-z

Higgins, H. W., Wright, S. W., and Schlüter, L. (2011). "Quantitative interpretation of chemtaxonomic pigment data," in *Phytoplankton pigments: Characterization, chemotaxonomy and applications in oceanography*. Eds. S. Roy, C. A. Llewellyn, E. S. Egeland and G. Johnsen (Cambridge: Cambridge University Press), 257–313.

Hu, C. (2022). Hyperspectral reflectance spectra of floating matters derived from hyperspectral imager for the coastal ocean (HICO) observations. *Earth Syst. Sci. Data* 14, 1183–1192. doi: 10.5194/essd-14-1183-2022

Intacharoen, P., Dasananda, S., and Buranapratheprat, A. (2018). MODIS-based observation of sea surface chlorophyll-a concentration over upper gulf of Thailand. *Suranaree J. Sci. Technol.* 25, 59–72.

Kofoid, C. A., and Swezy, O. (1921). The free-living unarmored dinoflagellata. *Memoirs Univ. California* 5, 1–562. doi: 10.5962/bhl.title.24995

Latasa, M. (2007). Improving estimations of phytoplankton class abundances using CHEMTAX. *Mar. Ecol. Prog. Ser.* 329, 13–21. doi: 10.3354/meps329013

Lirdwitayaprasit, T. (2003). "Red tide in the inner gulf of Thailand", in *Workshop on Red Tide Monitoring in Asian Coastal Waters*. (University of Tokyo), 53–56.

Lirdwitayaprasit, T. (2001). "Culture of green Noctiluca under laboratory conditions: I. Feeding behavior and sexual reproduction", in *Proceedings of the Fifth IOC/WESTPAC International Science Symposium* 27–31.

Lirdwitayaprasit, T., Chuabkarnrai, P., Nitithamyong, C., and Furuya, K. (2012). Effect of salinity on vertical migration of green noctiluca under laboratory conditions. *Coast. Mar. Sci.* 35, 70–72. doi: 10.15083/00040636

Lirdwitayaprasit, T., Meksumpun, S., Rungsura, S., and Furuya, K. (2006). Seasonal variations in cell abundance of noctiluca scintillans in the coastal waters off chonburi province, the upper gulf of Thailand. *Coast. Mar. Sci.* 30, 80–84. doi: 10.15083/00040753

Lu, L., Jiang, T., Xu, Y., Zheng, Y., Chen, B., Cui, Z., et al. (2018). Succession of phytoplankton functional groups from spring to early summer in the central bohai Sea using HPLC–CHEMTAX approaches. *J. Oceanogr* 74, 381–392. doi: 10.1007/s10872-018-0469-x

Luang-on, J., Ishizaka, J., Buranapratheprat, A., Phaksopa, J., Goes, J. I., Kobayashi, H., et al. (2021). Seasonal and interannual variations of MODIS aqua chlorophyll–2017) in the upper gulf of Thailand influenced by Asian monsoons. *J. Oceanogr.* 78, 209–228. doi: 10.1007/s10872-021-00625-2

Mackey, M. D., Mackey, D. J., Higgins, H. W., and Wright, S. W. (1996). CHEMTAX - a program for estimating class abundances from chemical markers: Application to HPLC measurements of phytoplankton. *Mar. Ecol. Prog. Ser.* 144, 265–283. doi: 10.3354/meps144265

Patt, F. S., Barnes, R. A., Eplee, R. E., Jr., Franz, B. A., Robinson, W. D., et al. (2003). SeaWiFS Post Launch Technical Report Series: Algorithm updates for the fourth SeaWiFS data reprocessing. eds. S. B. Hooker and E. R. Firestone Greenbelt, Maryland: National Aeronautics and Space Administration, Goddard Space Flight Center. Available at: https://oceancolor.gsfc.nasa.gov/docs/technical/seawifs_reports/postlaunch/post_vol22_abs/.

Qi, L., Tsai, S. F., Chen, Y., Le, C., and Hu, C. (2019). In Search of Red Noctiluca scintillans Blooms in the East China Sea. *Geophys. Res. Lett.* 46, 5997–6004. doi: 10.1029/2019GL082667

Saito, H., Furuya, K., and Lirdwitayaprasit, T. (2006). Photoautotrophic growth of noctiluca scintillans with the endosymbiont pedinomonas noctilucae. *Plankton Benthos Res.* 1, 97–101. doi: 10.3800/pbr.1.97

Shaju, S. S., Akula, R. R., and Jabir, T. (2018). Characterization of light absorption coefficient of red noctiluca scintillans bloom in the south Eastern Arabian Sea. *Oceanologia* 60, 419–425. doi: 10.1016/j.oceano.2017.12.002

Shang, S., Wu, J., Huang, B., Lin, G., Lee, Z., Liu, J., et al. (2014). A new approach to discriminate dinoflagellate from diatom blooms from space in the East China Sea. *J. Geophys Res. Oceans* 119, 4653–4668. doi: 10.1002/2014JC009876

Shen, F., Tang, R., Sun, X., and Liu, D. (2019). Simple methods for satellite identification of algal blooms and species using 10-year time series data from the East China Sea. *Remote Sens Environ.* 235, 111484. doi: 10.1016/j.rse.2019.111484

Sriwoon, R., Pholpunthin, P., Lirdwitayaprasit, T., Kishino, M., and Furuya, K. (2008). Population dynamics of green noctiluca scintillans (Dinophyceae) associated with the monsoon cycle in the upper gulf of Thailand. *J. Phycol* 44, 605–615. doi: 10.1111/j.1529-8817.2008.00516.x

Suwanlertcharoen, T., and Prukpitikul, S. (2018). Detection of phytoplankton blooms in the upper gulf of Thailand using sentinel-3A OLCI imagery. *Environ. Nat. Resour J.* 16, 9–20. doi: 10.14456/ennrj.2018.2

Suzuki, R., and Ishimaru, T. (1990). An improved method for the determination of phytoplankton chlorophyll using n, n-dimethylformamide. *J. Oceanographical Soc. Japan* 46, 190–194. doi: 10.1007/BF02125580

Sweeney, B. M. (1971). Laboratory studies of a green noctiluca from new Guinea. *J. Phycol.* 7 (1), 53–58. doi: 10.1111/j.1529-8817.1971.tb01478.x

Tao, B., Mao, Z., Lei, H., Pan, D., Shen, Y., Bai, Y., et al. (2015). A novel method for discriminating prorocentrum donghaiense from diatom blooms in the East China Sea using MODIS measurements. *Remote Sens Environ.* 158, 267–280. doi: 10.1016/j.rse.2014.11.004

Thaipichitburapa, P., Meksumpun, C., and Meksumpun, S. (2010). Province-based self-remediation efficiency of the tha chin river basin, Thailand. *Water Sci. Technol.* 62, 594–602. doi: 10.2166/wst.2010.293

Turkoglu, M. (2013). Red tides of the dinoflagellate noctiluca scintillans associated with eutrophication in the Sea of marmara (the dardanelles, Turkey). *Oceanologia* 55, 709–732. doi: 10.5697/oc.55-3.709

Van Heukelem, L., and Thomas, C. S. (2001). Computer-assisted high-performance liquid chromatography method development with applications to the isolation and analysis of phytoplankton pigments. *J. Chromatogr A* 910, 31–49. doi: 10.1016/S0378-4347(00)00603-4

Van Mol, B., Ruddick, K., Astoreca, R., Park, Y., and Nechad, B. (2007). Optical detection of a noctiluca scintillans bloom. *EARSeL eProceedings* 6, 130–137.

Wang, L., Lin, X., Goes, J. I., and Lin, S. (2016). Phylogenetic analyses of three genes of pedinomonas noctilucae, the green endosymbiont of the marine dinoflagellate noctiluca scintillans, reveal its affiliation to the order marsupiomonadales (Chlorophyta, pedinophyceae) under the reinstated name protoeu. *Protist* 167, 205–216. doi: 10.1016/j.protis.2016.02.005

Wattayakorn, G. (2006). "Environmental issues in the gulf of Thailand," in *The environment in Asia pacific harbours*. Ed. E. Wolanski (Dordrecht: Springer), 249–259. doi: 10.1007/1-4020-3655-8_16

Welschmeyer, N. A. (1994). Fluorometric analysis of chlorophyll a in the presence of chlorophyll b and pheopigments. *Limnol Oceanogr* 39, 1985–1992. doi: 10.4319/lo.1994.39.8.1985

Xu, Q., Sukigara, C., Goes, J. I., Gomes, R., Zhu, Y., and Wang, S. (2019). Interannual changes in summer phytoplankton community composition in relation to water mass variability in the East China Sea. *J. Oceanogr* 75, 61–79. doi: 10.1007/s10872-018-0484-y

Yang, M. M., Ishizaka, J., Goes, J. I., Gomes, H., do, R., de Raus Maúre, E., et al. (2018). Improved MODIS-aqua chlorophyll-a retrievals in the turbid semi-enclosed ariake bay, Japan. *Remote Sens (Basel)* 10, 1335. doi: 10.3390/rs10091335

Yu, X., Guo, X., Morimoto, A., and Buranapratheprat, A. (2018). Simulation of river plume behaviors in a tropical region: Case study of the upper gulf of Thailand. *Cont Shelf Res.* 153, 16–29. doi: 10.1016/j.csr.2017.12.007

Yuenyong, S., Nimsuwan, N., Buranapratheprat, A., Gunboa, V., Jintasaeranee, P., Thaipichitburapa, P., et al. (2019). Water quality of the bangpakong river during 2016–2018. *Burapha Sci. J.* 24, 138–155.

frontiers | Frontiers in Marine Science

TYPE Original Research
PUBLISHED 13 March 2023
DOI 10.3389/fmars.2023.1052286

Check for updates

OPEN ACCESS

EDITED BY
Arun Chakraborty,
Indian Institute of Technology
Kharagpur, India

REVIEWED BY
Yunhai Li,
Ministry of Natural Resources, China
D. Swain,
Indian Institute of Technology
Bhubaneswar, India

*CORRESPONDENCE
Eko Siswanto
ekosiswanto@jamstec.go.jp

SPECIALTY SECTION
This article was submitted to
Ocean Observation,
a section of the journal
Frontiers in Marine Science

RECEIVED 23 September 2022
ACCEPTED 24 February 2023
PUBLISHED 13 March 2023

CITATION
Siswanto E, Sarker MLR, Peter BN, Takemura T, Horii T, Matsumoto K, Taketani F and Honda MC (2023) Variations of phytoplankton chlorophyll in the Bay of Bengal: Impact of climate changes and nutrients from different sources.
Front. Mar. Sci. 10:1052286.
doi: 10.3389/fmars.2023.1052286

COPYRIGHT
© 2023 Siswanto, Sarker, Peter, Takemura, Horii, Matsumoto, Taketani and Honda. This is an open-access article distributed under the terms of the Creative Commons Attribution License (CC BY). The use, distribution or reproduction in other forums is permitted, provided the original author(s) and the copyright owner(s) are credited and that the original publication in this journal is cited, in accordance with accepted academic practice. No use, distribution or reproduction is permitted which does not comply with these terms.

Variations of phytoplankton chlorophyll in the Bay of Bengal: Impact of climate changes and nutrients from different sources

Eko Siswanto[1]*, Md. Latifur Rahman Sarker[2], Benny N. Peter[3], Toshihiko Takemura[4], Takanori Horii[5], Kazuhiko Matsumoto[1], Fumikazu Taketani[1] and Makio C. Honda[1]

[1]Earth Surface System Research Center, Research Institute for Global Change, Japan Agency for Marine-Earth Science and Technology, Yokohama, Japan, [2]Department of Geography and Environmental Studies, University of Rajshahi, Rajshahi, Bangladesh, [3]Department of Physical Oceanography, Kerala University of Fisheries and Ocean Studies, Kerala, India, [4]Research Institute for Applied Mechanics, Kyushu University, Fukuoka, Japan, [5]Center for Coupled Ocean-Atmosphere Research, Research Institute for Global Change, Japan Agency for Marine-Earth Science and Technology, Yokosuka, Japan

Phytoplankton biomass, quantified as the concentration of chlorophyll-a (CHL), is the base of the marine food web that supports fisheries production in the Bay of Bengal (BoB). Nutrients from river discharge, the ocean subsurface layer, and the atmosphere have been reported to determine CHL in the BoB. Which source of nutrients mainly determines CHL in different parts of the bay has not been determined. Furthermore, how climate variations influence nutrient inputs from different sources and their impacts on CHL have not been detailed. To address these questions, we used relationships between satellite-derived CHL and *in situ* river discharge data (a proxy for river-borne nutrients) from 1997 to 2016, physical variables, and modeled dust deposition (DD), a proxy for atmosphere-borne nutrients. Nutrients supplied from the ocean subsurface layer were assessed based on variations in physical parameters (i.e., wind stress curl, sea surface height anomaly, and sea surface temperature). We found that nutrients from the Ganges and Brahmaputra Rivers were important for CHL along the northern coast of the bay. By increasing rainfall and river discharge, La Niña extended high-CHL waters further southward. Nutrients from the ocean subsurface layer determine CHL variations mainly in the southwestern bay. We suggest that the variations in the supply of nutrients from the subsurface layer are related to the generation of mesoscale cyclonic eddies during La Niña, a negative Indian Ocean Dipole, or both. Climate-driven cyclonic eddies together with cyclones can intensify Ekman divergence and synergistically lead to a pronounced increase in CHL in the southwestern bay. Nutrients from the atmosphere mainly determine CHL in the central/eastern BoB. We further suggest that DD in the central/eastern BoB is influenced by ENSO with a 6–7-month time lag. CHL in the central/eastern bay responds to the ENSO 6–7 months after the ENSO peak because of the 6–7-month lag between ENSO and

DD. This report provides valuable information needed to plan necessary actions for climate adaptation in local fisheries activities by elucidating how climate variations influence phytoplankton.

KEYWORDS

phytoplankton chlorophyll-a, satellite ocean color, nutrient supply, atmospheric deposition, mesoscale eddy, river discharge, climate changes

1 Introduction

The Bay of Bengal (BoB), among the largest of the Large Marine Ecosystems (LMEs) in the world, is bounded by the Asian continent in the north, the eastern coast of India in the west, and the Andaman Sea in the east. In the south, the bay is open to the Indian Ocean. The surrounding countries of India, Bangladesh, Sri Lanka, Myanmar, the Maldives, Thailand, Malaysia, and Indonesia have reached a consensus on a strategic action program to solve existing socioeconomic issues (e.g., Elayaperumal et al., 2019) because of the social and economic importance of the bay.

One of the key determinants of the services the BoB provides to nearby societies and economies is phytoplankton primary production, a common metric of which is phytoplankton biomass or chlorophyll-a concentration (CHL, mg m^{-3}). Primary production is the production of organic matter at the base of the marine food web and supports the secondary production of biomass by marine organisms at higher trophic levels. Previous studies have reported a strong relationship between CHL, or primary production, and fisheries production in a wide variety of marine ecosystems in coastal waters and the open ocean (Nixon and Thomas, 2001; Nixon and Buckley, 2002). The production of the tropical Hilsa fishery, which contributes to the society and economy of India, Bangladesh, and Myanmar, is controlled by primary production in the BoB (Hossain et al., 2020).

Light, in addition to nutrients, is an important determinant of primary production in the BoB, especially in the northern part of the bay because of the high turbidity associated with high sediment inputs from the Ganges and Brahmaputra Rivers (GBR) (Kumar et al., 2010). Because of the large influx of freshwater from the GBR, the water column in the northern BoB is strongly stratified. This stratification inhibits the influx of inorganic nutrients from the ocean subsurface layer to the euphotic zone, especially in the central part of the bay and during boreal summer (Kumar et al., 2002). In the part of the bay where light is not a limiting factor, the input of inorganic nutrients is thought to be the major determinant of primary production in the BoB.

There are at least three major sources of inorganic nutrients that support primary production in the BoB. Previous studies have mentioned how inputs of inorganic nutrients from rivers and ocean subsurface waters cause seasonal variations in CHL in the BoB (e.g., Gomes et al., 2000; Levy et al., 2007; Vinayachandran, 2009; Siswanto et al., 2022). The GBR, which globally ranks fourth with respect to freshwater discharge into the sea (an average of 1,032 km^3 $year^{-1}$) (Dai and Trenberth, 2002), supplies nutrients that elevate CHL along the northern coast of the bay during the boreal summer (e.g., Vinayachandran, 2009; Kay et al., 2018). Inputs of nutrients associated with wind-driven upwelling and vertical mixing have been reported to elevate CHL and cause a strong seasonal cycle of CHL in mainly the western and/or southwestern bay (e.g., Shetye et al., 1991; Gomes et al., 2000; Vinayachandran and Mathew, 2003; Martin and Shaji, 2015; Xu et al., 2021). During the boreal summer, CHL variations along the western coast of the bay are influenced mainly by coastal upwelling due to local longshore wind stress (Shetye et al., 1991; Gomes et al., 2000). CHL enhancement during the fall is associated with the westward propagation of an upwelling Rossby wave (a reflection of an equatorial, upwelling Kelvin wave from the eastern boundary of the BoB) along the coast of the bay (e.g., Rao et al., 2010; Sreenivas et al., 2012; Gulakaram et al., 2018). During the winter, CHL concentrations are highest, and nutrients are entrained by strong, northeasterly, wind-driven Ekman pumping and/or vertical mixing (e.g., Xu et al., 2021).

In addition to nutrient inputs from rivers and ocean subsurface layers, atmospheric dust deposition (DD, μg m^{-2} s^{-1}) is also a potential source of inorganic nutrients that can fertilize the bay. Grand et al. (2015) have pointed out that the concentration of nutrients in the surface waters of the BoB is highly consistent with the distribution of mineral atmospheric DD, except in the northern BoB, where nutrients are largely supplied by the GBR. Yadav et al. (2016) have recently confirmed that atmospheric DD increases CHL even in coastal areas where the input of river-borne nutrients is high.

While the relationships between CHL and nutrients have been widely studied on seasonal timescales, the relative contributions of different sources of nutrients to determining CHL, especially on interannual timescales, have not been delineated spatially. Deducing the impacts of climate changes on primary production in the BoB and hence the BoB LME requires understanding the major sources of nutrients that determine interannual variations in CHL in the bay. Climate variations such as the El Niño/Southern Oscillation (ENSO) and the Indian Ocean Dipole (IOD) do not directly drive primary production in the ocean but instead alter nutrient inputs by modifying river discharges, upwelling/downwelling, and atmospheric circulation.

Furthermore, because there is a strong relationship between phytoplankton primary production and fisheries production, understanding the impacts of climate changes on primary

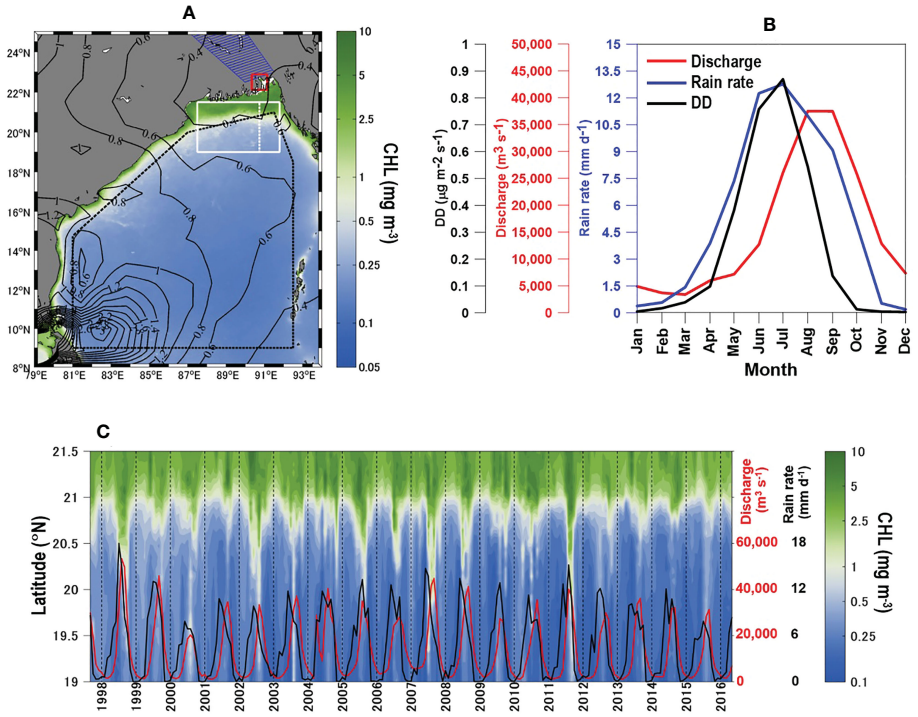


FIGURE 1
(A) Annual means of satellite-derived CHL (shaded map) overlaid by the SPRINTARS-modeled DD (contour map). The red square indicates the approximate position of the mouth of the GBR. The white rectangle adjacent to the north coast of the bay is the area where CHL was averaged zonally (east-west direction, log scale), and its meridional time series is presented in **(C)**. The red and black solid lines in **(C)** are time series of GBR discharge and rainfall, respectively. The north-south dashed white line (inside the white box **(A)** in front of the river mouth) is a transect line where CHL, CHL anomaly, and normalized water-leaving radiance at a wavelength of 555 nm (nLw_{555}) were extracted and are presented in Figures 2A–C. **(B)** Monthly climatological means of DD (black line), rain rate (blue line), and GBR discharge (red line). The DD data were extracted from the region of the BoB bounded by a dashed black polygon in **(A)**. Rainfall data were extracted from the blue hatched polygon in **(A)**, which was part of the catchment area of the GBR.

production in the BoB is important for fisheries management, i.e., for planning the actions of fishery activities/industries that are needed to adapt to climate change. In this study, we employed multi-year satellite-derived CHL observations (a proxy of phytoplankton primary production), *in situ* GBR discharge, and models of DD to assess the region-wise influence of nutrients from different sources (i.e., rivers, ocean subsurface layer, and the atmosphere) on interannual variations of CHL in the BoB, to identify the mechanisms that may introduce nutrients from different sources into the bay, and to link those mechanisms with climate variations.

2 Methodology

2.1 Study area

Figure 1A shows the area selected for this study. The satellite-derived CHL in the offshore area is low (<0.5 mg m^{-3}), but the CHL in the coastal area is high (>2 mg m^{-3}) because of the input of terrigenous inorganic nutrients from the adjacent river systems. The wide area of high CHL in the northern coastal area is attributable to discharges from large rivers such as the GBR (e.g., Gomes et al., 2000). On average, GBR discharge peaks in late summer (August/September, Figure 1B). Note that the summer season used in this manuscript refers to boreal summer (June–September). This high river discharge is associated with a large amount of rainfall that peaks 1–2 months earlier (June or July) than the peak of river discharge. CHL in the coastal region increases because of the summer peaks in rainfall and river discharge (hence in river-borne nutrient supply) and is then dispersed southward during the summer (Figure 1C).

Because of the upwelled/entrained nutrients from the ocean subsurface layer, CHL is enhanced in the northern summer and peaks in the northern winter, especially over the western/southwestern BoB. Increases in nutrient concentrations that enhance CHL are associated with local longshore wind stress (Shetye et al., 1991; Gomes et al., 2000), westward propagation of upwelling Rossby waves (Rao et al., 2010; Sreenivas et al., 2012; Gulakaram et al., 2018), and strong northeasterly winds (e.g., Xu et al., 2021) during the summer, fall, and winter, respectively.

In addition, the BoB receives large amounts of dust from fallout that also peaks around summer (July) (Figure 1B). Aerosol dust over the BoB is transported from southwest Asia, northeast Asia, and the Middle East (Banerjee and PrasannaKumar, 2016; Banerjee et al., 2019). During summer, a high plume of DD intrudes into the BoB from the southwest (Figure 1A). This plume is attributable to high emissions from dust sources, high rainfall over the BoB, and a

slight deflection (southeastward to northeastward) of winds around the southern Indian Peninsula (Banerjee et al., 2019).

2.2 Data sources and analysis

We used satellite-derived monthly CHL blended from multiple ocean color sensors with 4-km resolution downloaded from the ESA OC-CCI (https://esa-oceancolour-cci.org/), monthly sea surface height anomaly (SSHA, cm) with 25-km resolution downloaded from the AVISO+ Satellite Altimetry Data (https://www.aviso.altimetry.fr/), monthly rainfall with 25-km resolution downloaded from the Asia-Pacific Data Research Center (http://apdrc.soest.hawaii.edu/), and daily sea surface temperature (SST, °C) with 4-km resolution retrieved by the Advanced Very High-Resolution Radiometer and downloaded from NOAA (https://www.nodc.noaa.gov/). The daily SST data were then averaged to produce monthly mean SSTs. Variations in SST and SSHA are used widely to assess nutrient inputs from ocean subsurface layers associated with physical processes (e.g., Siswanto, 2015). We also calculated the wind stress curl (curl, N m^{-3}) following Large and Pond (1981) from monthly wind fields acquired from the Cross-Calibrated Multi-Platform (CCMP) project (http://podaac.jpl.nasa.gov) as an indicator of upwelling.

We used *in situ* GBR discharge data acquired from the Bangladesh Water Development Board (https://www.bwdb.gov.bd/) as a proxy for river-borne nutrient input. We used atmospheric DD data as proxies of nutrient inputs from the atmosphere and modeled atmospheric DD using SPRINTARS (Takemura et al., 2003), a numerical model developed by the Research Institute for Applied Mechanics, Kyushu University (https://sprintars.riam.kyushu-u.ac.jp/). We used Nino3.4 as a metric of El Niño/Southern Oscillation (ENSO) variability (http://www.cpc.ncep.noaa.gov/data/indices/sstoi.indices) and the dipole mode index (DMI) as a metric of Indian Ocean Dipole (IOD) variability (http://www.jamstec.go.jp/aplinfo/sintexf/iod/dipole_mode_index.html).

One of the objectives of this study was to determine whether climate variations influence CHL by modulating supplies of nutrients from different sources. Because climate variations have an interannual timescale, the seasonal cycles and long-term trends of CHL and other geophysical variables must be removed from their time series before the effects of changes in sources of nutrients can be detected. To assess whether the ocean subsurface layer or atmospheric deposition was a more important source of inorganic nutrients in different parts of the offshore regions of the BoB, we conducted a multiple linear regression analysis (MLRA) that related CHL to other environmental variables following the approach used by Siswanto (2015) and Nathans et al. (2012). The approach included removing seasonal variations and trends from variables and standardizing them so that they all had means of zero and standard deviations of one. Standardization facilitates the comparison of the importance of one independent variable to that of other variables in determining the variance of CHL. The MLRA required that no data be missing. An empirical, orthogonal function-based data interpolation (e.g., Alvera-Azcarate et al., 2005) was used to fill in missing data in the CHL and SST satellite imageries. Figure S1 in the Supplementary Information shows the numbers and percentages of valid CHL and SST pixels used for interpolation.

3 Results

3.1 Spatial variability of the importance of nutrients from different sources

High CHL in the northern BoB was confined mainly to the area north of ~21°N or within ~200 km offshore of the mouth of the GBR (Figures 1A, C). The time series of meridional CHL variation derived from a meridional transect south of the GBR mouth showed southward dispersion of high CHL during summer, when rainfall intensity and river discharge peak (Figure 2A). Tan et al. (2006) and Siswanto et al. (2011) have reported that CHL in the coastal region is systematically overestimated by satellite-retrieved CHL because of the high concentration of total suspended matter, which is generally quantified by satellite-retrieved normalized water-leaving radiance at a wavelength of 555 nm (nLw_{555}). They have found that the variation of satellite-derived CHL in the coastal region can be considered to reflect real variations in phytoplankton biomass if nLw_{555} <2.0 mW cm^{-2} μm^{-1} sr^{-1}.

Figure 2C shows temporal variations of nLw_{555} along the meridional transect line off the mouth of the GBR shown in Figure 1A. During the peak discharge of the GBR in summer, the area where the nLw_{555} exceeded 2.0 mW cm^{-2} μm^{-1} sr^{-1} was confined mainly to the area north of 21°N. Variations of CHL south of 21°N, including the high CHL that is dispersed further southward, can be considered to reflect high phytoplankton biomass due to elevated primary productivity modulated by nutrients from rivers, especially from the GBR.

Along the northern coast of the BoB, nutrients from rivers are likely important for phytoplankton in coastal regions only as far as about 200 km from the river mouths. The distance from the river mouths would depend on the intensity of rainfall and interannual variations of river discharge; thus, CHL variation in the BoB offshore region is likely attributable to variations in other sources of nutrients.

To identify which source of nutrients was most important in determining the offshore variations of CHL in the BoB on an interannual basis, we used a MLRA with CHL as the dependent variable. The independent variables were DD and a physical variable (i.e., CHL = f[SST, DD], CHL = f[SSHA, DD], and CHL = f[curl, DD]). We ran the MLRA with SST, SSHA, and curl independently because variations in SST, SSHA, and curl are not independent but instead are highly dependent on oceanographic physical processes. Figures 3A–C show partial regression coefficients (β) for SST (β_{SST}), DD (β_{DD}), and the coefficients of determination (R^2) derived from the MLRA of CHL = f(SST, DD). Similarly, Figures 3D–F show the β_{SSHA}, β_{DD}, and R^2 produced by the MLRA of CHL = f(SSHA, DD), and Figures 3G–I show the β_{Curl}, β_{DD}, and R^2 produced by CHL = f(curl, DD). There is much seasonal variability in CHL as well as in the independent variables SST, SSHA, curl, and DD. Prior to running the MLRAs, we removed seasonal cycles and long-term trends from the variables (see *Section 2.2*) to focus the analysis on interannual variations. Our results therefore concern interannual variability unrelated to seasonal cycles.

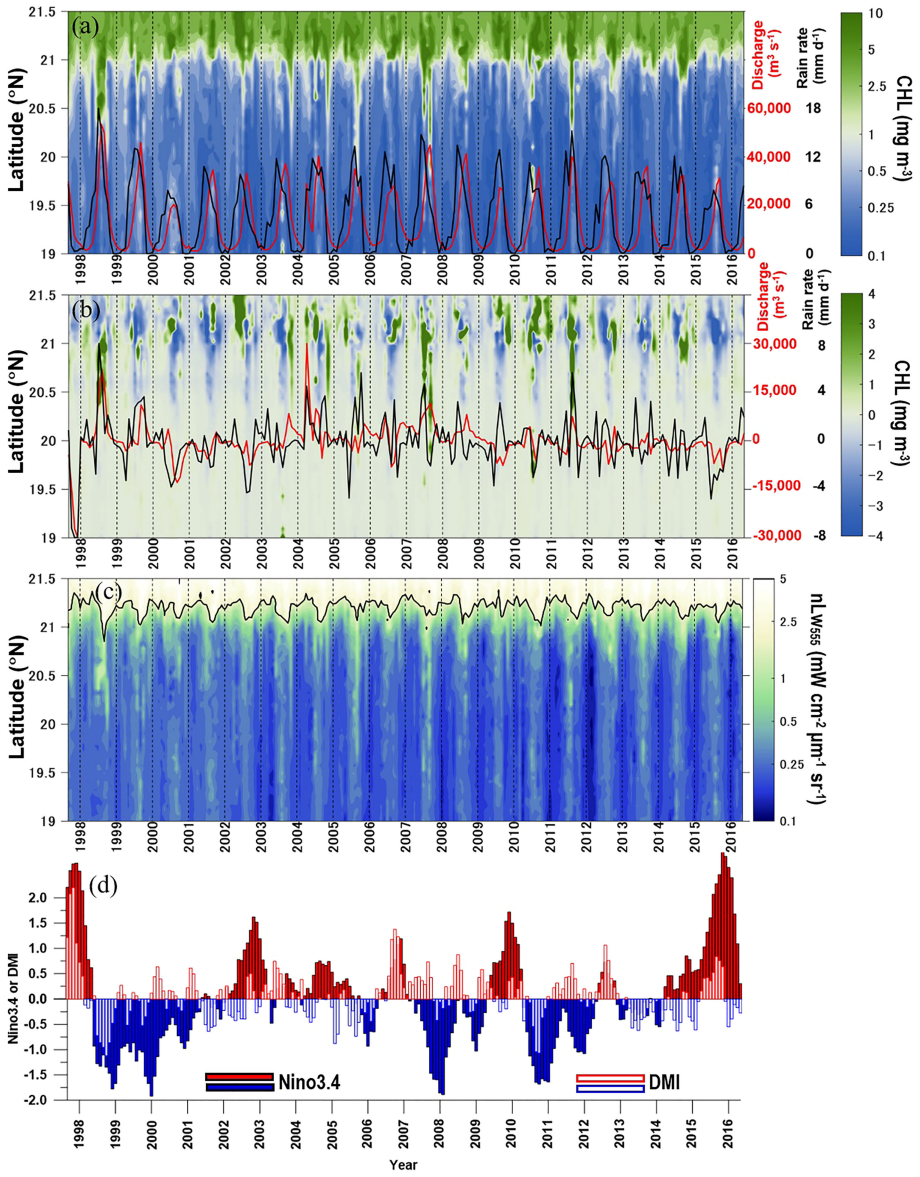


FIGURE 2
Time series of **(A)** CHL meridional variations along the white dashed transect line in Figure 1A. Panel **(B)** is the same as panel **(A)**, except that it shows a CHL anomaly. Panel **(C)** is the same as panel **(A)** except that it shows nLw_{555}. The red and black lines in **(A)** are time series of GBR discharge and rain rate, respectively. The red and black lines in **(B)** show the anomalies in GBR discharge and rain rate. The black contour line in **(C)** indicates the satellite-retrieved normalized water-leaving radiance at a wavelength of 555 nm (nLw_{555}) of 2.5 mW cm^{-2} μm^{-1} sr^{-1}. The time series of Nino3.4 and DMI are shown in **(D)** to indicate climate variations of the El Niño/Southern Oscillation and Indian Ocean Dipole.

Negative values of β_{SST}, which were especially common in the southwestern BoB indicated by box A in Figure 3A, indicated an increase in CHL associated with surface cooling (hence an increase in nutrient concentrations due to upwelling, vertical mixing, or both) (e.g., Shetye et al., 1991; Gomes et al., 2000; Vinayachandran and Mathew, 2003; Martin and Shaji, 2015; Xu et al., 2021). The hypothesis that nutrients introduced from the ocean subsurface layer by upwelling led to increases in CHL in the southwestern part of the bay was also supported by the negative β_{SSHA} (Figure 3D) and positive β_{Curl} (Figure 3G). A negative β_{SSHA} implies that an increase in CHL was associated with a negative SSHA due to upwelling. A positive β_{Curl} means that an increase in CHL was associated with a positive curl, which is also indicative of upwelling. As shown in Table 1, the values of the mean β_{SST} (−0.25), mean β_{SSHA} (−0.20), and mean β_{curl} (0.26) averaged over box A were larger in magnitude than the mean β_{DD} (0.14–0.15). The implication is that variations in the supply of nutrients from the ocean subsurface layer contributed more than variations in the supply of nutrients from atmospheric deposition to the interannual variations of CHL in the southwestern BoB. The mean R^2 (0.15–0.18) resulting from the three MLRAs (Figures 3C, F, I, Table 1) implies that variations in the supply of nutrients from the ocean subsurface layer explain 15%–18% of the interannual variations of CHL in the southwestern BoB.

In the central/eastern BoB, nutrients from upwelled/entrained water and atmospheric deposition could together explain about 15% (R^2 = 0.15–0.16, Table 1) of the interannual variance of CHL. In

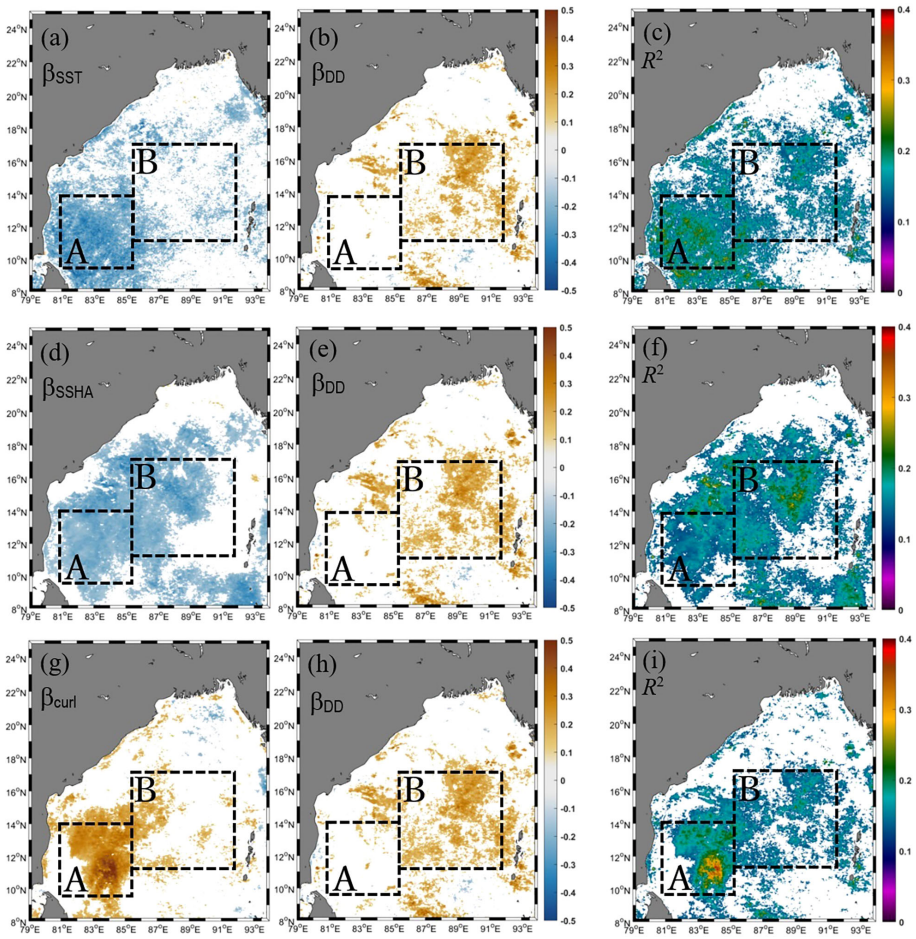


FIGURE 3
Spatial variations of **(A)** β_{SST}, **(B)** β_{DD}, and **(C)** R^2 obtained from a multiple linear regression analysis with CHL as the dependent variable and SST and dust deposition (DD) as independent variables (i.e., CHL = f[SST, DD]). Panels **(D, E)**, and **(F)** are the same as **(A–C)**, except that CHL = f(SSHA, DD). Panels **(G, H)**, and **(I)** are the same, except that CHL = f(curl, DD). Areas where β values were insignificant at the 95% confidence level (*p*-value >0.05) are masked out (white areas). Yellow (blue) areas in the panels indicate significant positive (negative) associations between CHL and the independent variables. Black dashed box A indicates the part of the southwestern bay where the time series of SST, curl, CHL, and SSHA were extracted from and are presented in Figures 4B, C. The dashed box B indicates the central/eastern bay where the time series of CHL, SST, DD, curl, and SSHA were extracted and are presented in Figures 4D, E.

general, the spatial averages of the mean β_{SST} (−0.17), mean β_{SSHA} (−0.20), and mean β_{curl} (0.17) over box B were comparable with the mean β_{DD} (0.18–0.19). However, the significant β_{DD} occurred in different areas (the eastern part of box B) than the significant β_{SST}, β_{SSHA}, and β_{curl} (the western part of box B) (Figures 3A, B, D, E, G, H). It is therefore likely that deposited nutrients are particularly important for phytoplankton in the western part of box B, or in general, in the western part of the bay. The fact that β_{SST}, β_{SSHA}, and β_{DD} were insignificant in the northern coastal region indicates that river-borne inorganic nutrients were likely more important in determining variations of phytoplankton CHL in the central/eastern bay.

TABLE 1 Mean values of partial regression coefficients β_{SST}, β_{SSHA}, β_{curl}, and β_{DD} averaged over the southwestern and central/eastern BoB and their coefficients (R^2) in multiple linear regression analyses.

Variables	Southwestern BoB		Central/eastern BoB	
	β	R^2	β	R^2
SST DD	−0.25 0.14	0.17	−0.17 0.17	0.15
SSHA DD	−0.20 0.14	0.15	−0.20 0.18	0.16
Curl DD	0.26 0.15	0.18	0.17 0.18	0.15

3.2 Possible linkages with climate variations

3.2.1 BoB northern coastal region

There is interannual variation over the seasonal cycle of high CHL during summer/fall along the northern coast of the BoB (Figures 1C, 2A). The CHL interannual variation can be seen more obviously in terms of the variation of the meridional CHL anomaly along the meridional transect line (19.0°N–21.5° N, Figure 2B).

Expansions of high-CHL waters further southward (up to about 300 km south of the GBR mouth) were obvious during the summer/fall of 1998, 2005, 2007, and 2011. Those years were characterized by anomalously high rainfall over the catchment area and high discharges from the GBR (Figure 2B). The years 1998, 2005, and 2011 were La Niña years and negative-IOD

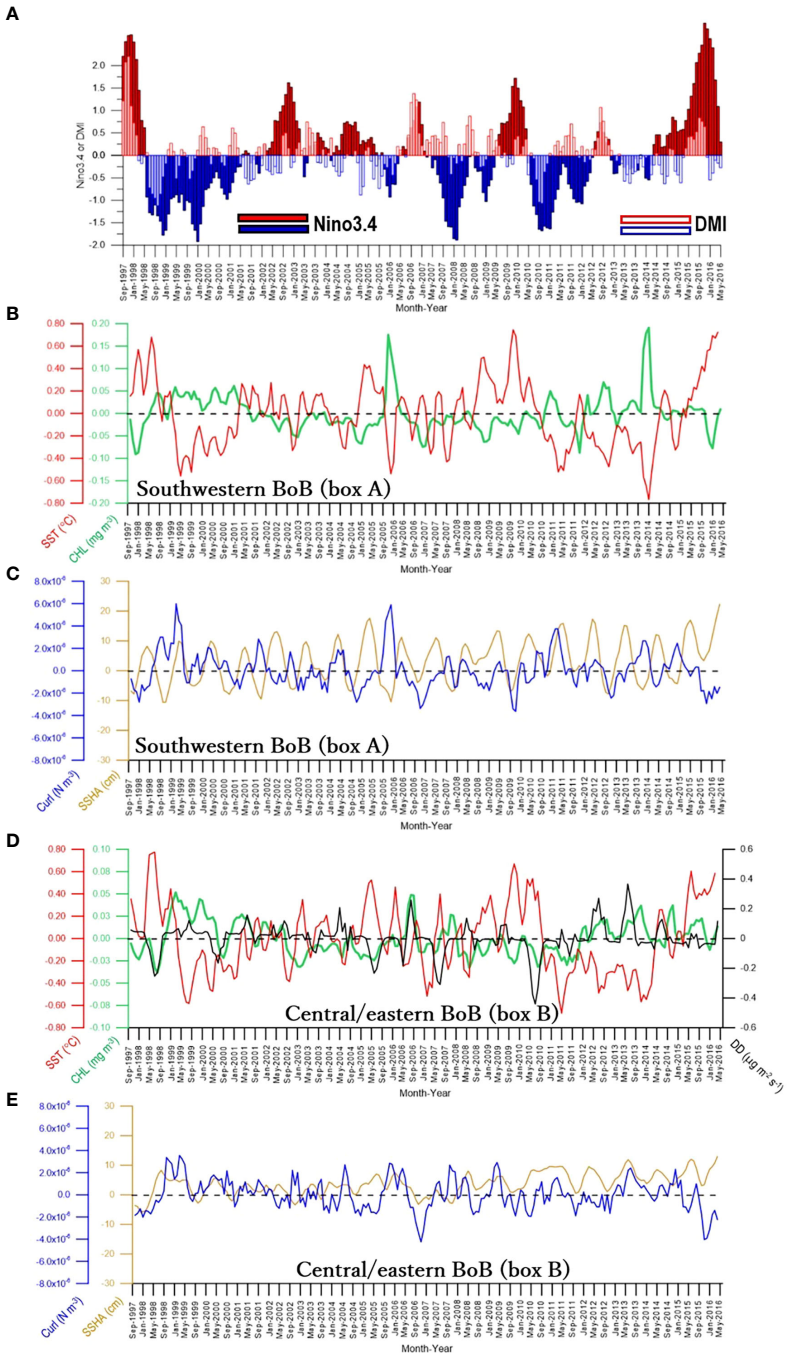


FIGURE 4
(A) Time series of Nino3.4 (closed bars) and DMI (open bars) to be compared with time series of **(B)** CHL and SST, and **(C)** curl and SSHA extracted from box A (see Figure 3) in the southwestern bay. Panels **(D, E)** are time series of SST, CHL, DD, curl, and SSHA extracted from box B (see Figure 3) in the central/eastern bay.

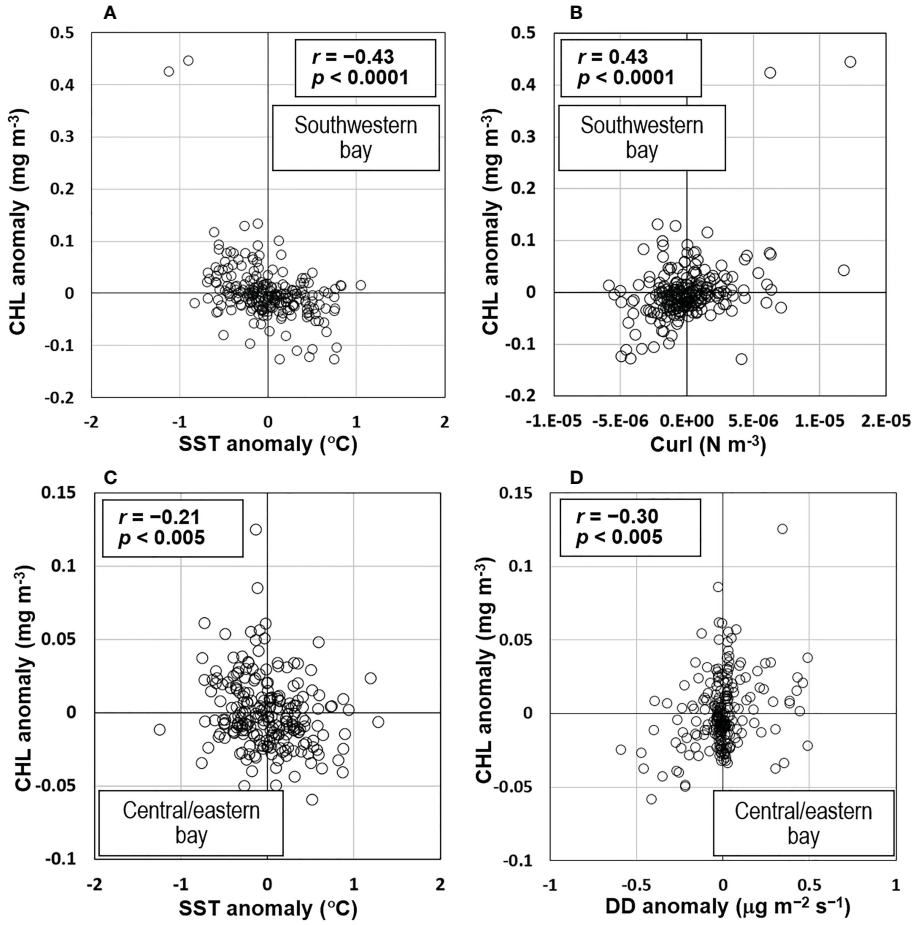


FIGURE 5
Scatter plots of CHL anomalies versus anomalies of **(A)** SST and **(B)** curl derived from the southwestern Bay of Bengal (BoB), and versus anomalies of **(C)** DD and **(D)** SST, derived from the central/eastern BoB.

(nIOD) years (hereafter La Niña/nIOD), whereas 2007 was a La Niña year (Figure 2D).

3.2.2 BoB southwestern region

To assess whether nutrient inputs from the ocean subsurface layer that determine interannual variations of CHL in the southwestern BoB were correlated with climate variations, we plotted time series of CHL, SST, curl, and SSHA along with the Nino3.4 and DMI (Figures 4A–C). In general, CHL varied inversely with SST but positively with curl. Such an inverse relationship between CHL and SST and a positive relationship between CHL and curl can also be seen in the corresponding scatter plots (Figures 5A, B). The correlation coefficients between CHL and SST (−0.43, DF = 224) and between CHL and curl (0.43, DF = 224) were statistically significant (two-tailed *t*-test, $p < 0.0001$) (Table 2). The negative correlation between CHL and SST indicated that entrained cold (hence nutrient-rich) water was associated with high CHL. The entrainment could have been driven by upwelling and/or vertical mixing. The positive curl would be associated with upwelling or Ekman divergence processes. The positive correlation between CHL and curl therefore indicated that upwelling was the major physical process that entrained nutrients from the ocean's subsurface layer to enhance CHL.

TABLE 2 Results of regression analysis performed by relating CHL to SST, curl, SSHA, and DD in the southwestern and central/eastern BoB.

Variables	Southwestern BoB		Central/eastern BoB	
	r	*p*-value	*r*	*p*-value
SST	−0.43	<0.0001	−0.21	<0.005
Curl	0.43	<0.0001	0.14	<0.05
SSHA	−0.21	<0.005	−0.001	NS
DD	0.07	NS	0.30	<0.0001

In the table, NS stands for "not significant" and r is the correlation coefficient. The statistics were computed with 224 degrees of freedom.

Interestingly, in general, the negative correlation between CHL and SST (Figures 4B, 5A) and the positive correlation between CHL and curl (Figures 4B, C, 5B) were likely linked with ENSO, IOD, or both. For instance, negative CHL, positive SST, and negative curl variations were obvious during the concurrent El Niño and positive IOD (hereafter El Niño/pIOD) in 1997, El Niño/pIOD in 2009, and the 2017 El Niño. In contrast, positive CHL, negative SST, and positive curl anomalies were evident during the La Niña/nIOD of 1998, the La Niña of 1999, the La Niña/nIOD of 2005, and the La Niña/nIOD of 2013. This pattern indicates that atmosphere–ocean interactions associated with interannual climate variations of ENSO and IOD drive the supply of inorganic nutrients from the ocean subsurface layer, and an increase in the supply of nutrients (indicated by low SST) to the surface layer leads to increases in CHL.

Compared to SST and curl, SSHA was more weakly correlated with CHL (0.21, DF = 224), but the correlation was still statistically significant (p <0.005) (Table 2). The strong seasonality of SSHA in the BoB is associated with westward-propagating Rossby waves (Sreenivas et al., 2012; Gulakaram et al., 2018) that likely weaken the relationship between CHL and SSHA on an interannual timeframe. Westward-propagating Rossby and coastal Kelvin waves (that traverse along the BoB coast) are generated at the eastern boundary of the BoB. They are feedback from eastward-propagating equatorial Kelvin waves.

3.2.3 BoB central/eastern region

In the central/eastern BoB, the time series of CHL, SST, and DD anomalies show that CHL generally varies inversely with SST but positively with DD. This pattern is apparent in the corresponding scatter plots (Figures 4D, 5C, D). The strongest interannual association was between CHL and DD, for which the correlation coefficient was 0.30 (p <0.0001, DF = 244, Table 2, Figure 5D). CHL and SST were also significantly correlated (r = −0.21, p <0.005, DF = 224, Table 2, Figure 5C). CHL was significantly correlated with curl (r = 0.14, DF = 224) (Figure 4E) but with a lower level of confidence (p <0.05). There was no significant correlation between CHL and SSHA (r = −0.001, p >0.05, DF = 224, Figures 4D, E, Table 2).

Despite the significant correlation between CHL and DD in the central/eastern BoB, neither CHL nor DD was clearly associated with either ENSO or IOD. Neither CHL nor DD were significantly correlated with those climate indices (Table 3). The lack of association between CHL, DD, and variations of climate is likely due to the time lag between the time when the climate event peaked and the time of DD entering the BoB (see *Discussion*). In contrast, as shown in Table 3, the significant correlations between SSHA and Nino3.4 (r = −0.18), between SSHA and DMI (r = −0.35), between curl and Nino3.4 (r = −0.32), and between curl and DMI (r = −0.20) indicate that curl and SSHA were influenced by both ENSO and IOD.

Climate variations had opposite effects on SSHA and curl (Table 3). The negative correlations between the SSHA and climate indices (Table 3) indicate that El Niño and pIOD led to upwelling, but the negative correlations between the curl and climate indices (Table 3) indicate that they led to downwelling. Regardless of these apparently contradictory relationships, one of the reasons for the lack of association between CHL and climate variations in the central BoB was probably the formation of a freshwater lens associated with the influx of freshwater from river discharge that restricted climate-related atmosphere–ocean interactions (e.g., Kumar et al., 2002; Vinayachandran et al., 2002; Felton et al., 2014; Kay et al., 2018).

4 Factors responsible for anomalously high CHL

Here we will elaborate on the atmosphere-land-ocean interactions that were probably responsible for the remarkably high CHL anomalies in the coastal region of the northern BoB (Figure 2), box A in the southwestern BoB, and box B in the central/eastern BoB (Figure 3). We first discuss the mechanisms responsible for the high CHL in the coastal region, followed by the mechanisms probably responsible for the high CHL in the southwestern and central/eastern BoB.

As reported by Perves and Henebry (2015), the amount of rainfall over the GBR basin increases by more than 100% (compared to the long-term mean rainfall) during years of La Niña alone or La Niña/nIOD. The anomalously high CHL and/or southward dispersion of high-CHL waters along the northern coast of the bay during the La Niña/nIOD or La Niña years of 1998, 2005, 2007, and 2011 can be attributed to high river discharges and hence large influxes of river-

TABLE 3 Results of regression analysis performed by relating climate indices (Nino3.4, DMI) to CHL, SST, curl, SSHA, and DD in the southwestern and central/eastern BoB.

	Southwestern BoB				Central/eastern BoB			
	Nino3.4		DMI		Nino3.4		DMI	
Variables	*r*	*p*-value	*r*	*p*-value	*r*	*p*-value	*r*	*p*-value
CHL	−0.27	<0.0001	−0.13	NS	−0.11	NS	0.06	NS
SST	0.36	<0.0001	−0.01	NS	0.25	<0.0001	−0.05	NS
SSHA	0.10	NS	−0.13	NS	−0.18	<0.01	−0.35	<0.0001
Curl	−0.30	<0.0001	−0.15	<0.05	−0.32	<0.0001	−0.20	<0.005
DD	0.01	NS	−0.02	NS	0.08	NS	0.01	-NS

In the table, NS stands for "not significant" and r is the correlation coefficient. The statistics were computed with 224 degrees of freedom. Regressions were performed on pairs of variables during the same months (the correlations were not time-lagged).

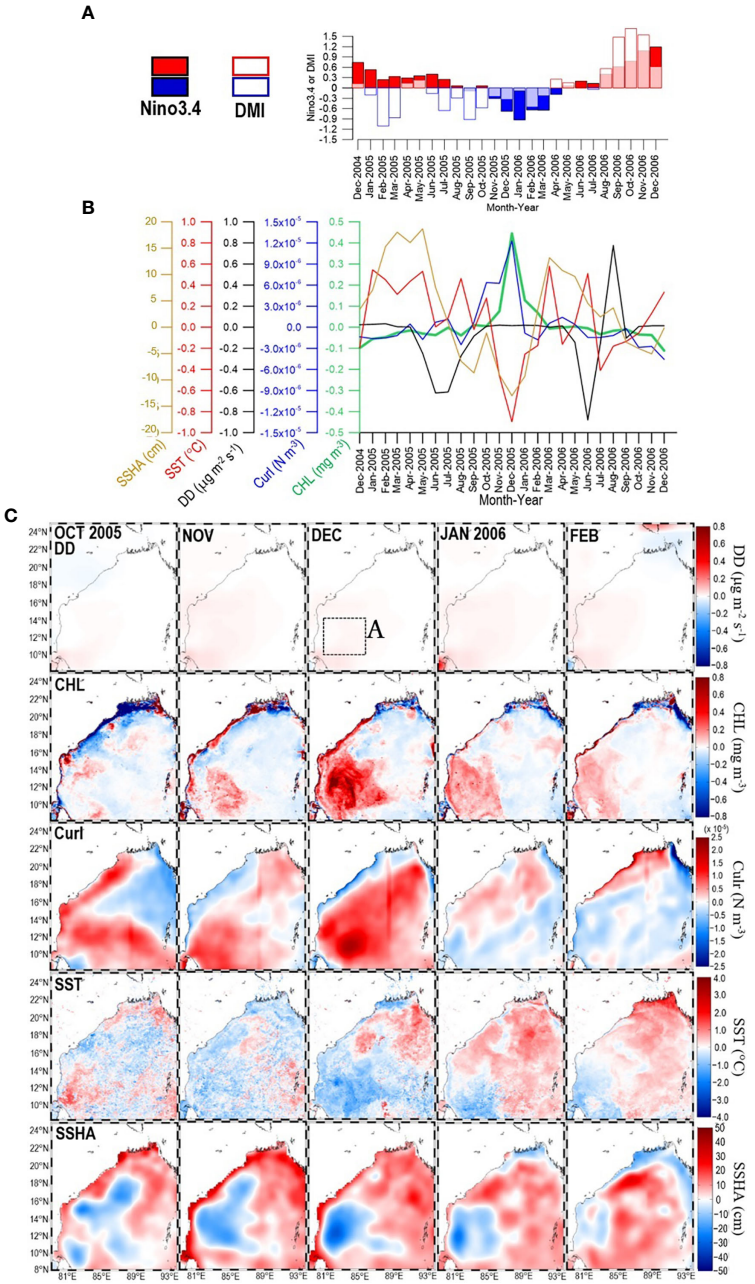


FIGURE 6
(A) Time series of Nino3.4 and DMI during the period from December 2004 to December 2006. Within that period, panel **(B)** shows time series of SSHA, SST, DD, curl, and CHL extracted from box A panel **(C)**-1st row) in the southwestern bay. Panel **(C)** shows maps of DD (1st row), CHL (2nd row), curl (3rd row), SST (4th row), and SSHA (5th row) for the period from October 2005 to February 2006.

borne nutrients associated with La Niña, nIOD, or both. In contrast, during the El Niño years of 1997, 2002, 2009, and 2015, there was no apparent southward dispersion of high-CHL waters (Figures 2A, B) because of the low amounts of rainfall and low river discharges during those El Niño years (Perves and Henebry, 2015). The implication is that there is a teleconnection between basin-scale climate variations of ENSO and/or IOD and land-ocean interaction, i.e., variations of river-borne inorganic nutrient supply and primary production in coastal waters.

Between September 1997 and May 2016, there were two obvious, anomalous peaks of CHL in the southwestern BoB that were accompanied by negative SST, negative SSHA, and positive curl anomalies (Figures 4B, C). The first CHL peak occurred during December 2005 (Figure 6B), a year influenced by La Niña/nIOD (Figure 6A) (see also Li et al., 2017; Chen and Li, 2018). That CHL peak resulted from a spatially large, positive CHL anomaly (Figure 6C-2nd row). That spatially large, positive CHL anomaly was enabled by nutrients supplied from the ocean subsurface layer, as indicated by the positive curl, negative SST, and negative SSHA anomalies (Figure 6C-3rd, 4th, and 5th rows). Previous work has suggested that the high CHL in December 2005 resulted from the passage of cyclones (Ali et al., 2007; Chen et al., 2013; Sridevi et al.,

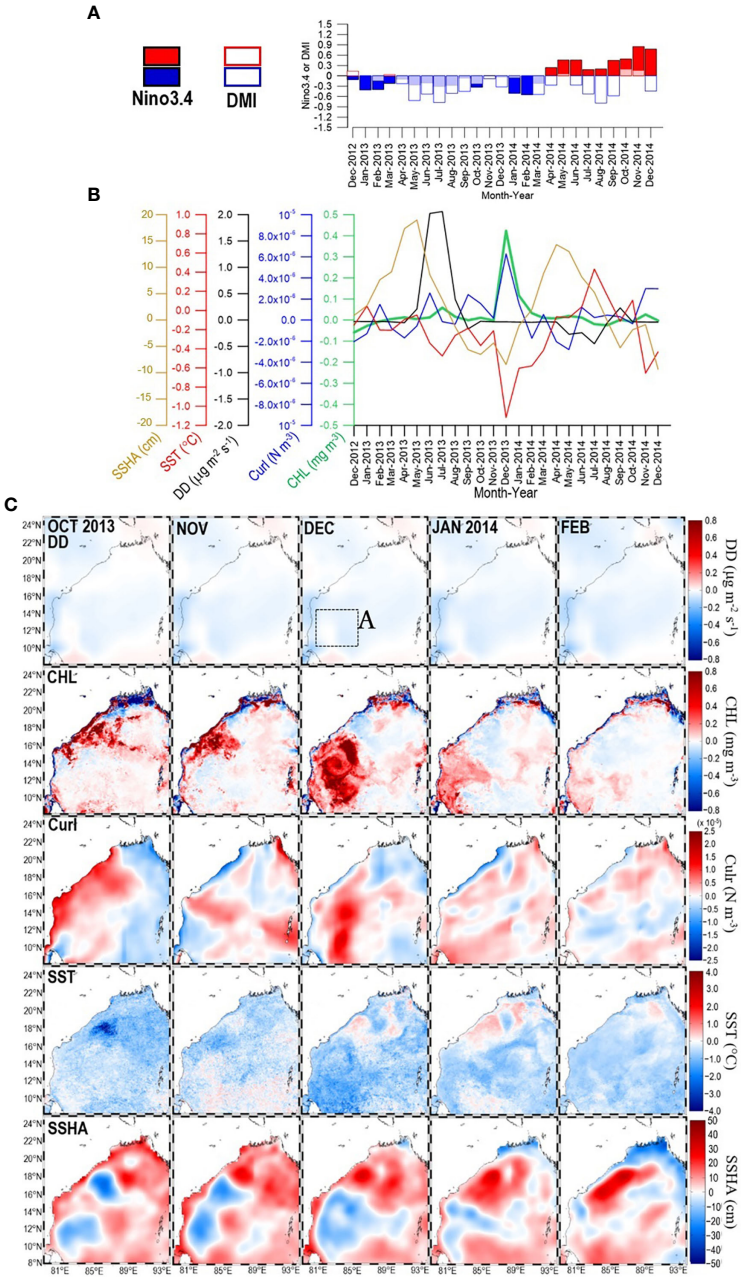


FIGURE 7
(A) Time series of Nino3.4 and DMI during the period from December 2012 to December 2014. Within that period, panel **(B)** shows time series of SSHA, SST, DD, curl, and CHL extracted from box A panel **(C)**-1st row) in the southwestern bay. Panel **(C)** shows maps of DD (1st row), CHL (2nd row), curl (3rd row), SST (4th row), and SSHA (5th row) for the period from October 2013 to February 2014.

2019). An input of nutrients from the atmosphere is unlikely the explanation for the high CHL because the DD from October 2005 to February 2006 was normal (Figure 6C-1st row), and DD is generally low in December (Figure 1B) (see also Solmon et al., 2015).

A similar combination of anomalously high CHL accompanied by positive curl, negative SST, and negative SSHA was also apparent in December 2013 (Figures 7B, C-2nd, 3rd, 4th, and 5th rows). These observations indicate that the upwelling of nutrients enhances CHL. Atmospheric inputs were not a cause of the enhancement of CHL because the DD anomalies were negative (Figure 7C-1st row), and December is in the season of low DD (Figure 1B) (Solmon et al., 2015). Oceanographic conditions during this period were also influenced by the 2013 La Niña/nIOD (Figure 7A). Jayaram et al. (2019) have suggested that two cyclones that passed over adjacent areas caused the highest CHL anomaly observed in December 2013.

Regardless of the inorganic nutrient composition of DD, the fact that previous studies have shown that increased phytoplankton growth in various ocean basins can be associated with the SPRINTARS-modeled DD (Kitajima et al., 2009; Calil et al., 2011; Fukushima, 2014) indicates that the deposition of inorganic nutrients from the atmosphere is an important source of

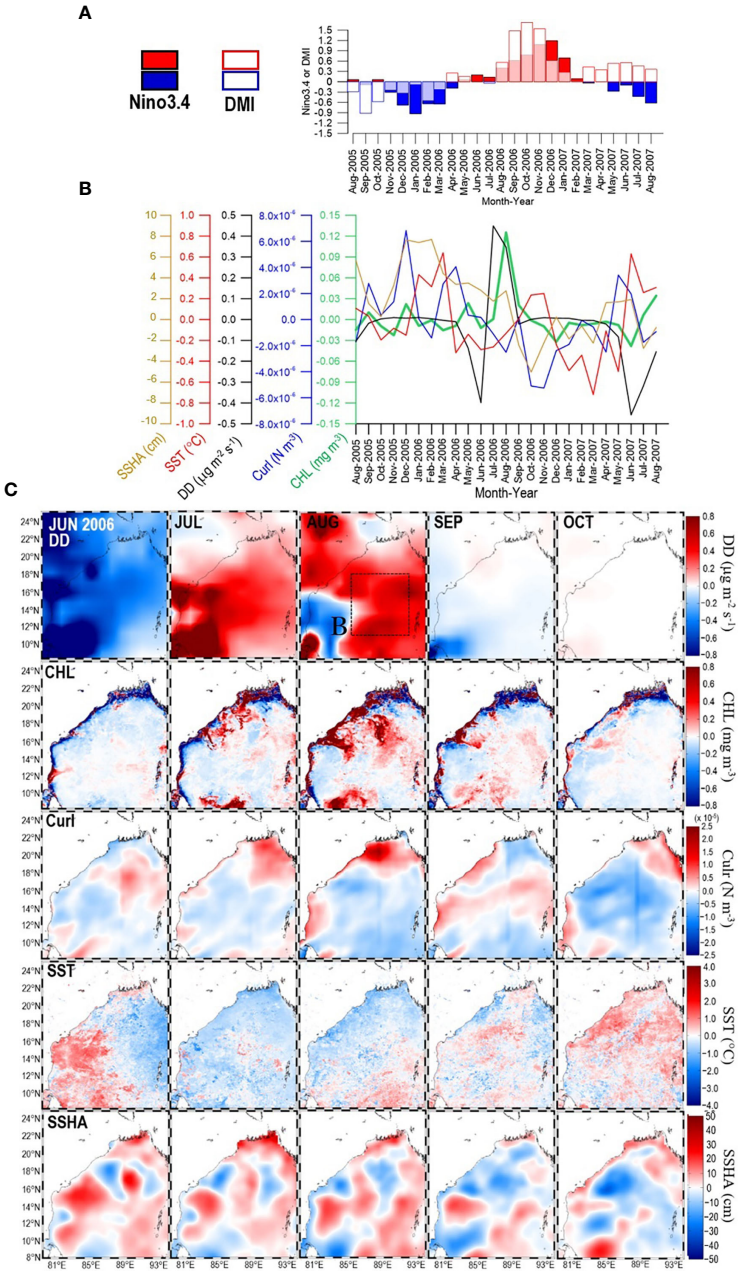


FIGURE 8
(A) Time series of Nino3.4 and DMI during the period from August 2005 to August 2007. Within that period, panel **(B)** shows time series of SSHA, SST, DD, curl, and CHL extracted from box B panel **(C)**-1st row) in the central/eastern bay. Panel **(C)** shows maps of DD (1st row), CHL (2nd row), curl (3rd row), SST (4th row), and SSHA (5th row) for the period from June 2006 to October 2006.

nutrients for phytoplankton growth. We therefore expected that the SPRINTARS-modeled DD would to some degree alter CHL in the BoB, particularly in the central/eastern bay, where nutrient supplies from river discharge are generally considered to be low. Indeed, we found a significant correlation between CHL and DD in the central/eastern BoB.

However, the role of atmospheric deposition, which is suggested by the significant, positive correlation between CHL and DD (r = 0.30, Table 2), must be interpreted with caution because there was a significant negative (positive) correlation between CHL and SST (CHL and curl) (Table 2); therefore, nutrient inputs from the ocean subsurface layer may also have played an important role. For instance, from May 2012 to May 2014, positive DDs were accompanied not only by positive CHL but also by negative SST (Figure 4D). During this study, only the DD in July–August 2006 likely indicated atmospheric deposition that enhanced CHL in August 2006 (Figures 8B, C-1st and 2nd rows). However, DD might contribute some nutrients because

patches of negative SSHA (an indication of upwelling) were observed approximately in the positive CHL areas, though negative curl data indicated downwelling conditions (Figures 8B, C-3rd, 4th, and 5th rows).

5 Discussion

In general, CHL in the southwestern BoB was negatively and significantly correlated with Nino3.4 ($r = -0.27$, $p < 0.0001$, Table 3). CHL therefore tended to be low (high) during El Niño (La Niña). Similarly, there was a negative (but insignificant) correlation between CHL and DMI, i.e., CHL was low (high) during pIOD (nIOD). A similar negative but insignificant CHL–DMI correlation in the southwestern part of the bay has also been reported by Xu et al. (2021). Our analysis indeed showed that ENSO rather than the DMI seemed to have a larger influence on the SST and curl (Table 3). We therefore hypothesize that elucidation of the impacts of climate variations on the biogeophysical variability of the BoB should include consideration of ENSO cycles.

Except for the southwestern BoB, much of the BoB during the La Niña/nIOD period from October 2005 to February 2006 was characterized by a positive SSHA (Figure 6C-5th row). This positive SSHA is known to be associated with a strengthened downwelling Kelvin wave in the equatorial Indian Ocean that is driven by a strong westward wind stress anomaly during La Niña/nIOD (Sreenivas et al., 2012; Roman-Stork et al., 2021). This downwelling equatorial Kelvin wave is reflected westward from the eastern coast of the bay as a downwelling Rossby wave and is characterized by positive SSHA (Rao et al., 2010). However, the SSHA tends to be negative over the southwestern BoB because during La Niña/nIOD, a strong westward wind stress anomaly creates cyclonic wind stress over the southwestern BoB (see Sreenivas et al., 2012).

The 2005 La Niña/nIOD-driven cyclonic wind stress led to the generation of a mesoscale cyclonic eddy over the same area of high CHL in the southwestern BoB (Figures 6C-2nd row, 9A). Previous studies have attributed this high CHL to cyclone Fanoos, which traversed the BoB from 15 to 22 December 2005 (Ali et al., 2007; Sridevi et al., 2019). However, during October–November 2005, before the arrival of cyclone Fanoos, the positive curl and negative SSHA indicated that a mesoscale cyclonic eddy already existed (Figure 6C-3rd and 5th rows; see also Sridevi et al., 2019). An enhancement of CHL was already apparent in October 2005 (Figure 6C-2nd row). An Ekman divergence associated with La Niña/nIOD was already occurring and was likely strengthened by cyclone Fanoos. The result was a pronounced positive CHL anomaly in December 2005. The increase in CHL could not be attributed to atmospheric input of nutrients because the DD was normal during the period from October 2005 to February 2006 (Figure 6C-1st row).

Analysis of the CHL enhancement during the December 2013 La Niña/nIOD requires consideration of the fact that two cyclones passed over the western/southwestern BoB from late November to early December 2013: Cyclone Leher (24–28 November) and Cyclone Madi (5–12 December) (Jayaram et al., 2019). The high CHL in December 2013 (Figures 7B, C-2nd row) was the result of a CHL bloom from 25 November to 2 December 2013 that preceded Cyclone Madi's arrival (Jayaram et al., 2019). The implication is that Cyclone Madi was not the only driver of the high CHL in December 2013. Although patches of increased CHL along the track of cyclone Leher are apparent in the study of Jayaram et al. (2019), the locations and spatial patterns that show Cyclone Leher-driven Ekman pumping and that show increased CHL are not in the same places. It is therefore unlikely that the CHL bloom in the southwestern BoB was associated with the passage of Cyclone Leher. The positive curl and negative SSHA (Figure 7C-3rd and 5th rows) suggest that a cyclonic eddy already existed in October–November 2013 (see also Sridevi et al., 2019). We therefore suggest that the cyclonic eddy that formed in association with the 2013 La Niña/nIOD and the cyclones may have synergistically enhanced Ekman divergence and produced a prominent, positive CHL anomaly in December 2013. The presence of a cyclonic eddy that preceded cyclone Madi has also

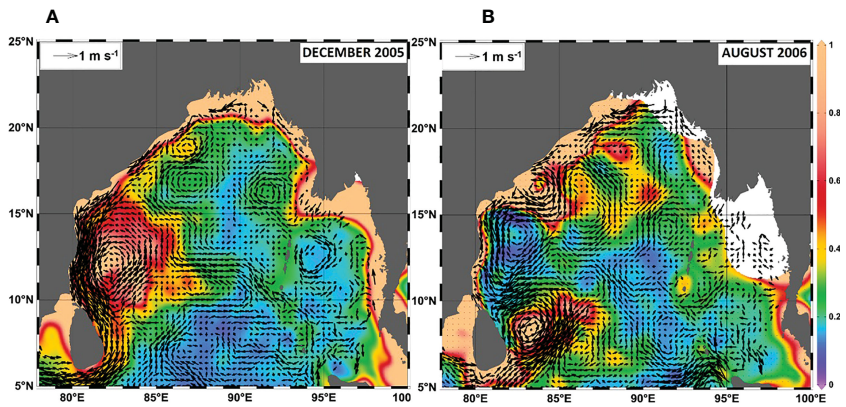


FIGURE 9
(A) Surface currents estimated by combining surface drifter and altimetry observations following the method of Uchida and Imawaki (2003) and plotted over the CHL in **(A)** December 2005 and **(B)** August 2006.

been mentioned by Chen et al. (2013) and Chowdhury et al. (2022), but those authors did not discuss the connection between the cyclonic eddy that preceded cyclone Madi and the 2013 La Niña/nIOD.

Mahala et al. (2015) and Roose et al. (2022) have recently mentioned that more cyclones are generated in the BoB during La Niña, nIOD, or both. This pattern is associated with anomalous equatorial westerly winds during La Niña, nIOD, or both that favor cyclone formation. Equatorial westerlies also favor cyclonic eddy formation in the southwestern BoB (see Sreenivas et al., 2012). The above-mentioned synergistic effect of mesoscale cyclonic eddies and tropical cyclones over the southwestern BoB is therefore likely to be more frequent during La Niña, nIOD, or both, and hence the CHL in the southwestern BoB will be greatly enhanced during those times.

The negative anomalies of DD from October 2013 to February 2014 (Figure 7C-1st row) and the seasonal minimum of DD during this period (Figure 1B) (see also Solmon et al., 2015) confirmed that nutrients upwelled from the ocean subsurface layer by climate-driven cyclonic eddies and cyclone passages were the only sources of nutrients that enhanced CHL in December 2013. The enhancements of CHL during the 1998 La Niña/nIOD, 1999 La Niña, and 2010 La Niña/nIOD were less remarkable than the enhancements during the 2005 and 2013 La Niña/nIOD. One reason was that the areas where phytoplankton bloomed during those climatic events were not entirely within the southwestern BoB (maps not shown). The entire CHL bloom was therefore not counted when the CHL within box A was averaged in the southwestern BoB.

Based on field experiments, Yadav et al. (2016) have also mentioned that inorganic nutrients from dust enhance CHL by factors of 1.5–4 in the coastal region of the western BoB. Patches of positive β_{DD} around western bay coastal areas in our study that were approximately the same as the study area of Yadav et al. (2016) confirmed that phytoplankton production in coastal waters also seemed to be sensitive to atmospheric DD.

We observed no correlations between DD in the central/eastern BoB and climate variations in the same months (no time lag) (Table 3). There may, however, be a time lag between climate variations and DDs (e.g., Banerjee and PrasannaKumar, 2016). To determine whether there was a time lag between climate variations and DDs in the BoB, we investigated the relationship between Nino3.4 and DD with different time lags. Figure 10A shows the correlations and reveals that DDs were highly correlated with Nino3.4 variations that occurred 6–8 months earlier (r <−0.20, p <0.01). The highest correlations were observed with a 7-month lag (Nino3.4 leading, r = −0.24, DF = 217, p <0.005). Interestingly, high correlations between Nino3.4 and CHL (r <−0.20, p <0.01) were also observed with time lags of 6–7 months (Figure 10B).

The probable explanation for the negative correlations between Nino3.4–DD and Nino3.4 versus CHL 6–7 months later is that La Niña causes anomalously low precipitation in the dust source regions (i.e., southwestern Asia, the Middle East, and Eastern Africa) that leads to more dust generation during the following summer (Banerjee and PrasannaKumar, 2016). High DD that partially enhanced CHL in August 2006 (Figures 8B, C-1st and 2nd rows) was apparent following the 2005 La Niña peak (January, Figure 8A). Similar La Niña–DD lagged co-variations were also apparent for other years: a La Niña peak in December 1998 preceded a DD peak in June 1999; a La Niña peak in January 2008 preceded high DD in May–June 2009; a La Niña peak in December 2011 preceded high DD in June–July 2012; and a La Niña in December 2012 preceded high DD in May–June 2013 (Figures 4A, D). In contrast and consistent with Banerjee and PrasannaKumar (2016), El Niño peaks were followed by low DD in the following summers: an El Niño peak in December 1997 preceded low DD in July 1998, and an El Niño peak in December 2009 preceded a very low DD in July 2010.

Because the deposition of dust generated from the same sources mentioned above is important in determining primary production in the Arabian Sea (Tandule et al., 2022) and because we found a significant correlation between DD and CHL in the central/eastern BoB (r = 0.30, Table 2), we suggest that DD plays an important role in determining primary production in the BoB, especially in the central/eastern bay. In addition, the Nino3.4–DD and Nino3.4–CHL (Figure 10) lagged correlations indicated that

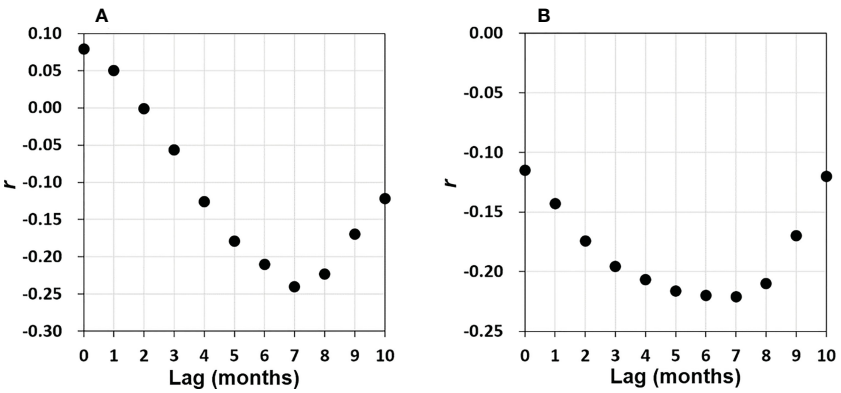


FIGURE 10
(A) A plot of r (DD anomaly versus Nino3.4) derived from linear regressions with various time lags (months, Nino3.4 leads DD). Panel **(B)** is the same as panel **(A)** but for CHL anomaly versus Nino3.4.

ENSO influences DD (and hence CHL) in the BoB 6–8 months after the peak of ENSO.

However, when assessing the impact of DD on CHL in the central/eastern bay, it is important to note that there may also have been a contribution of nutrients from other sources, even during the high DD in August 2006 (Figure 8B, C-1st row). During August, nutrient inputs from the ocean subsurface layer are likely to be limited by the formation of a barrier layer associated with the flux of freshwater from the GBR that restricts climate-related atmosphere–ocean interactions (e.g., Vinayachandran et al., 2002; Felton et al., 2014; Kay et al., 2018). Moderate increases in CHL in the central/eastern BoB (box B) may therefore be largely associated with DD. But episodic cyclonic eddies, such as the eddies that form off the western coast (Figure 9B), may also supply nutrients from the ocean subsurface layer and enhance CHL in the coastal region. Coastal waters with high CHL may be transported into the central/eastern bay by surface circulation. A more quantitative analysis would be required to assess the contributions of nutrients from the atmosphere and ocean subsurface layer separately (e.g., Siswanto, 2015).

Understanding how climate impacts phytoplankton CHL in the BoB by altering nutrient inputs from different sources would be valuable for local fisheries management because fisheries production in the BoB is largely controlled by phytoplankton primary production, and a common metric of phytoplankton production is CHL (Hossain et al., 2020). Climate change may reduce or increase local fisheries production by similarly changing CHL. This report may therefore be used as a reference by fisheries-related stakeholders in planning necessary adaptations to fisheries activities in response to climate change.

6 Conclusions

This study revealed that variations of nutrient inputs (inferred from variations of physical parameters) from different sources (river discharge, ocean subsurface layer, and atmosphere) cause variations of phytoplankton CHL in different parts of the BoB from year to year. Nutrients from the GBR are important for CHL mainly in the coastal region at distances up to ~200 km from the northern coast of the BoB. By increasing the amount of rainfall (hence the supply of river-borne nutrients from the GBR), La Niña can extend high-CHL waters further southward (~300 km from the coast). Variations in the supply of nutrients from the ocean subsurface layer determine interannual variations of phytoplankton CHL, mainly in the southwestern BoB. This variation in nutrient supply is linked with ENSO, IOD, or both through the generation of mesoscale cyclonic eddies during La Niña/nIOD. Such La Niña/nIOD-related mesoscale cyclonic eddies, together with the passage of cyclones, may synergistically intensify Ekman divergence, which results in a pronounced CHL enhancement in the southwestern bay. Nutrients deposited from the atmosphere make a nontrivial contribution to the interannual variations in CHL in the central/eastern BoB. This study also suggests that there is a lag of 6–7 months between the peaks of ENSO and the variations of DD and associated enhancements of CHL in the central/eastern BoB. Because phytoplankton are the base of the marine food web, local fishery production is also expected to be affected by climate variations that modulate CHL.

Data availability statement

Publicly available datasets were analyzed in this study. This data can be found here: https://esa-oceancolour-cci.org/; http://marine.copernicus.eu/; https://www.aviso.altimetry.fr/; https://www.nodc.noaa.gov/; http://apdrc.soest.hawaii.edu/; and http://podaac.jpl.nasa.gov/.

Author contributions

ES conceptualized and led the study. MS assisted with river discharge data acquisition and analysis. BP assisted with ocean surface circulation computation from global drifter and altimetry data. TT modeled and provided atmospheric dust deposition data. TH assisted with discussion concerning climate changes and teleconnection of physical oceanographic process. KM, FT, and MH assisted with discussion on the impacts of atmospheric deposition on ocean primary production. MH assisted with financial support and led the research project. All authors contributed to the article and approved the submitted version.

Funding

This research was financially supported by a Grants-in-Aid for Scientific Research (KAKENHI JP18H04144) from the Ministry of Education, Culture, Sports, Science, and Technology-Japan and by the Climate Adaptation Framework Project (CAF2017-RR02-CMY-Siswanto) funded by the Asia-Pacific Network for Global Change Research.

Acknowledgments

We thank the Ocean Color Climate Change Initiative Project (CHL; https://esa-oceancolour-cci.org/), the Copernicus Marine Environment Monitoring Service (SSHA; http://marine.copernicus.eu/, https://www.aviso.altimetry.fr/), the NASA National Oceanographic Data Center (SST, https://www.nodc.noaa.gov/), the Asia-Pacific Data Research Center (rain rate, http://apdrc.soest.hawaii.edu/), the Cross-Calibrated Multi-Platform project (wind fields, http://podaac.jpl.nasa.gov/), and the Bangladesh Water Development Board (river discharge, https://www.bwdb.gov.bd/) for processing and distributing the primary datasets.

Conflict of interest

The authors declare that the research was conducted in the absence of any commercial or financial relationships that could be construed as a potential conflict of interest.

Publisher's note

All claims expressed in this article are solely those of the authors and do not necessarily represent those of their affiliated organizations, or those of the publisher, the editors and the reviewers. Any product that may be evaluated in this article, or claim that may be made by its manufacturer, is not guaranteed or endorsed by the publisher.

Supplementary material

The Supplementary Material for this article can be found online at: https://www.frontiersin.org/articles/10.3389/fmars.2023.1052286/full#supplementary-material

SUPPLEMENTARY FIGURE 1
(A) Spatial distribution of the total number of CHL valid pixels used for CHL interpolation to fill missing data due to cloud coverage. Note that there were a total of 225 CHL imageries from September 1997 to May 2016. Panel **(B)** is the same as panel **(A)**, but for valid SST pixels.

References

Ali, M. M., Jagadeesh, P. S. V., and Jain, S. (2007). Effects of eddies on bay of Bengal cyclone intensity. *EOS* 88 (8), 93–95. doi: 10.1029/2007EO080001

Alvera-Azcarate, A., Barth, A., Rixen, M., and Beckers, J. M. (2005). Reconstruction of incomplete oceanographic data sets using empirical orthogonal functions: Application to the Adriatic Sea. *Ocean Modell.* 9, 325–346. doi: 10.1016/j.ocemod.2004.08.001

Banerjee, P., and PrasannaKumar, S. (2016). ENSO modulation of interannual variability of dust aerosols over the Northwest Indian ocean. *J. Clim.* 29 (4), 1287–1303. doi: 10.1175/JCLI-D-15-0039.1

Banerjee, P., Satheesh, S. K., Moorthy, K. K., Nanjundiah, R. S., and Nair, V. S. (2019). Long-range transport of mineral dust to the northeast Indian ocean: Regional versus remote sources and the implications. *J. Clim.* 32 (5), 1525–1549. doi: 10.1175/JCLI-D-18-0403.1

Calil, P. H. R., Doney, S. C., Yumimoto, K., Eguchi, K., and Takemura, T. (2011). Episodic upwelling and dust deposition as bloom triggers in low-nutrient, low-chlorophyll regions. *J. Geophys. Res.* 116, C6. doi: 10.1029/2010JC006704

Chen, M., and Li, T. (2018). Why 1986 El nino and 2005 la Nina evolved different from a typical El nino and la Nina. *Clim. Dyn.* 51, 4309–4327. doi: 10.1007/s00382-017-3852-1

Chen, X., Pan, D., Bai, Y., He, X., Chen, C. T. A., and Hao, Z. (2013). Episodic phytoplankton bloom events in the bay of Bengal triggered by multiple forcings. *Deep. Res. Part I Oceanogr. Res. Pap.* 73, 17–30. doi: 10.1016/j.dsr.2012.11.011

Chowdhury, R. R., Kumar, S. P., and Chakraborty, A. (2022). A study on the physical and biogeochemical responses of the bay of Bengal due to cyclone madi. *J. Oper. Oceanogr.* 15 (2), 104–125. doi: 10.1080/1755876X.2020.1817659

Dai, Y., and Trenberth, K. E. (2002). Estimates of freshwater discharge from continents: Latitudinal and seasonal variations. *J. Hydromet.* 3 (6), 660–687. doi: 10.1175/1525-7541(2002)003<0660:eofdfc>2.0.co;2

Elayaperumal, V., Hermes, R., and Brown, D. (2019). An ecosystem based approach to the assessment and governance of the bay of Bengal Large marine ecosystem. *Deep-Sea Res. II* 163, 87–95. doi: 10.1016/j.dsr2.2019.01.001

Felton, C. S., Subrahmanyam, B., Murty, V. S. N., and Shriver, J. F. (2014). Estimation of the barrier layer thickness in the Indian ocean using aquarius salinity. *J. Geophys. Res.* 119 (7), 4200–4213. doi: 10.1002/2013jc009759

Fukushima, H. (2014). "Variability in mineral dust deposition over the north pacific and its potential impact on the ocean productivity," in *Western Pacific air-Sea interaction study*. Eds. M. Uematsu, Y. Yokouchi, Y. W. Watanabe, S. Takeda and Y. Yamanaka (Terrapub, Tokyo) 51–60. doi: 10.5047/w-pass.a01.006

Gomes, H. R., Goes, J. I., and Saino, T. (2000). Influence of physical processes and freshwater discharge on the seasonality of phytoplankton regime in the bay of Bengal. *Cont. Shelf Res.* 20, 313–330. doi: 10.1016/S0278-4343(99)00072-2

Grand, M. M., Measures, C. I., Hatta, M., Hiscock, W. T., Buck, C. S., and Landing, W. M. (2015). Dust deposition in the eastern Indian ocean: The ocean perspective from Antarctica to the bay of Bengal. *Global Biogeochem. Cycles* 29, 357–374. doi: 10.1002/2014GB004898

Gulakaram, V. S., Vissa, N. K., and Bhaskaran, P. K. (2018). Role of mesoscale eddies on atmospheric convection during summer monsoon season over the bay of Bengal: A case study. *J. Ocean Eng. Sci.* 3, 343–354. doi: 10.1016/j.joes.2018.11.002

Hossain, M. S., Sarker, S., Sharifuzzaman, S. M., and Chowdhury, S. R. (2020). Primary productivity connects hilsa fishery in the bay of Bengal. *Sci. Rep.* 10, 5659. doi: 10.1038/s41598-020-62616-5

Jayaram, C., Bhaskar, T. V. S. U., Kumar, J. P., and Swain, D. (2019). Cyclone enhanced chlorophyll in the bay of Bengal as evidenced from satellite and BGC-argo float observations. *J. Indian Soc Rem. Sen.* 47 (11), 1875–1882. doi: 10.1007/s12524-019-01034-1

Kay, S., Caesar, J., and Janes, T. (2018). "Marine dynamics and productivity in the bay of Bengal," in *Ecosystem services for well-being in deltas*. Eds. R. Nicholls, C. Hutton, W. Adger, S. Hanson, M. Rahman and M. Salehin (Cham: Palgrave Macmillan). doi: 10.1007/978-3-319-71093-8_14

Kitajima, S., Furuya, K., Hashihama, F., Takeda, S., and Kanda, J. (2009). Latitudinal distribution of diazotrophs and their nitrogen fixation in the tropical and subtropical western north pacific. *J. Geophys. Res.* 54 (2), 537–547. doi: 10.4319/lo.2009.54.2.0537

Kumar, S. P., Muraleedharan, P. M., Prasad, T. G., Gauns, M., Ramaiah, N., De Souza, S. N., et al. (2002). Why is the bay of Bengal less productive during summer monsoon compared to the Arabian Sea? *Geophys. Res. Lett.* 29 (24). doi: 10.1029/2002GL016013

Kumar, S. P., Narvekar, J., Nuncio, M., Kumar, A., Ramaiah, N., Sardesai, S., et al. (2010). Is the biological productivity in the bay of Bengal light limited? *Curr. Sci.* 98 (10), 1331–1339.

Large, W. G., and Pond, S. (1981). Open ocean momentum flux measurements in moderate and strong winds. *J. Phys. Oceanogr.* 11, 324–336. doi: 10.1175/1520-0485(1981)011<0324:OOMFMI>2.0.CO:2

Levy, M., Shankar, D., Andre, J.-M., Shenoi, S. S. C., Durand, F., and de Boyer Montegut, C. (2007). Basin-wide seasonal evolution of the Indian ocean's phytoplankton blooms. *J. Geophys. Res.* 112, C12014. doi: 10.1029/2007JC004090

Li, J., Liang, C., Tang, Y., Liu, X., Lian, T., Shen, Z., et al. (2017). Impacts of the IOD-associated temperature and salinity anomalies on the intermittent equatorial undercurrent anomalies. *Clim. Dyn.* 51, 1391–1409. doi: 10.1007/s00382-017-3961-x

Mahala, B. K., Nayak, B. K., and Mohanty, P. K. (2015). Impacts of ENSO and IOD on tropical cyclone activity in the bay of Bengal. *Nat. Hazard* 75, 1105–1125. doi: 10.1007/s11069-014-1360-8

Martin, M. V., and Shaji, C. (2015). On the eastward shift of winter surface chlorophyll-a bloom peak in the bay of Bengal. *J. Geophys. Res.* 120, 2193–2211. doi: 10.1002/2014JC010162

Nathans, L. L., Oswald, F. L., and Nimon, K. (2012). Interpreting multiple linear regression: a guidebook of variable importance. *Pract. Assessment Res. Eval.* 17 (9). doi: 10.7275/5fex-b874

Nixon, S. W., and Buckley, B. A. (2002). 'A strikingly rich zone'–nutrient enrichment and secondary production in coastal marine ecosystems. *Estuaries* 25, 782–796. doi: 10.1007/BF02804905

Nixon, S., and Thomas, A. (2001). On the size of the Peru upwelling ecosystem. *Deep-Sea Res. I* 48, 2521–2528. doi: 10.1016/S0967-0637(01)00023-1

Perves, M. S., and Henebry, G. M. (2015). Spatial and seasonal response of precipitation in the Ganges and Brahmaputra river basins to ENSO and Indian ocean dipole modes: implications for flooding and drought. *Nat. Hazards Earth Syst. Sci.* 15, 147–162. doi: 10.5194/nhess-15-147-2015

Rao, R. R., Girish Kumar, M. S., Ravichandran, M., Rao, A. R., Gopalakrishna, V. V., and Thadathil, P. (2010). Interannual variability of kelvin wave propagation in the wave guides of the equatorial Indian ocean, the coastal bay of Bengal and the southeastern Arabian Sea during 1993-2006. *Deep. Res. Part I Oceanogr. Res. Pap.* 57, 1–13. doi: 10.1016/j.dsr.2009.10.008

Roman-Stork, H. L., Subrahmanyam, B., and Trott, C. B. (2021). Mesoscale eddy variability and its linkage to deep convection over the bay of Bengal using satellite altimetric observations. *Adv. Space Res.* 68 (2), 378–400. doi: 10.1016/j.asr.2019.09.054

Roose, S., Ajayamohan, R. S., Ray, P., Mohan, P. R., and Mohanakumar, K. (2022). ENSO influence on bay of Bengal cyclogenesis confined to low latitudes. *NPJ Clim. Atmos. Sci.* 5 (31). doi: 10.1038/s41612-022-00252-8

Shetye, S. R., Shenoi, S. S. C., Gouveia, A. D., Michael, G. S., Sundar, D., and Nampoothiri, G. (1991). Wind-driven coastal upwelling along the western boundary of the bay of Bengal during the southwest monsoon. *Cont. Shelf Res.* 11 (11), 1397–1408. doi: 10.1016/0278-4343(91)90042-5

Siswanto, E. (2015). Atmospheric deposition – another source of nutrients enhancing primary productivity in the eastern tropical Indian ocean during positive Indian ocean dipole phases. *Geophys. Res. Lett.* 42 (13), 5378–5386. doi: 10.1002/2015GL064188

Siswanto, E., Tang, J., Yamaguchi, H., Ahn, Y.-H., Ishizaka, J., Yoo, S., et al. (2011). Empirical ocean-color algorithms to retrieve chlorophyll-a, total suspended matter, and colored dissolved organic matter absorption coefficient in the yellow and East China seas. *J. Oceanogr.* 67 (5), 627–650. doi: 10.1007/s10872-011-0062-z

Siswanto, E., Sarker, M. D. L., and Peter, B. N. (2022). Spatial variability of nutrient sources determining phytoplankton Chlorophyll-a concentrations in the Bay of Bengal. *APN Sci. Bull.* 12 (1), 66–74. doi: 10.30852/sb.2022.1834

Solmon, F., Nair, V. S., and Mallet, M. (2015). Increasing Arabian dust activity and the Indian summer monsoon. *Atmos. Chem. Phys.* 15, 8051–8064. doi: 10.5194/acp-15-8051-2015

Sreenivas, P., Gnanaseelan, C., and Prasad, K. V. S. R. (2012). Influence of El niño and Indian ocean dipole on sea level variability in the bay of Bengal. *Glob. Planet. Change* 80–81, 215–225. doi: 10.1016/j.gloplacha.2011.11.001

Sridevi, B., Srinivasu, K., Bhavani, T. S. D., and Prasad, K. V. S. R. (2019). Extreme events enhance phytoplankton bloom in the south-western bay of Bengal. *Indian J. Geo Mar. Sci.* 48 (02), 253–258.

Takemura, T., Nakajima, T., Higurashi, A., Ohta, S., and Sugimoto, N. (2003). Aerosol distributions and radiative forcing over the Asia pacific region simulated by spectral radiation-transport model for aerosol species (SPRINTARS). *J. Geophys. Res.: Atmos.* 108 (D23). doi: 10.1029/2002JD003210

Tan, C. K., Ishizaka, J., Matsumura, S., Yusoff, F., and Mohamed, M. (2006). Seasonal variability of SeaWiFS chlorophyll a in the malacca straits in relation to Asian monsoon. *Cont. Shelf Res.* 26 (2), 168–178. doi: 10.1016/j.csr.2005.09.008

Tandule, C. R., Gogoi, M. M., Kotalo, R. G., and Babu, S. S. (2022). On the net primary productivity over the Arabian Sea due to the reduction in mineral dust deposition. *Sci. Rep.* 12, 7761. doi: 10.1038/s41598-022-11231-7

Uchida, H., and Imawaki, S. (2003). Eulerian mean surface velocity field derived by combining drifter and satellite altimeter data. *Geophys. Res. Lett.* 30 (5), 1229. doi: 10.1029/2002GL016445

Vinayachandran, P. N. (2009). "Impact of physical processes on chlorophyll distribution in the bay of Bengal" in *Indian Ocean biogeochemical processes and ecological variability*. Eds. J. D. Wiggert, R. R. Hood, S. W. A. Naqvi, K. H. Brink and S. L. Smith. (AGU, Washington, D.C.) 185. doi: 10.1029/2008GM000705

Vinayachandran, P. N., and Mathew, S. (2003). Phytoplankton bloom in the bay of Bengal during the northeast monsoon and its intensification by cyclones. *Geophys. Res. Lett.* 33 (11), 1572. doi: 10.1029/2002GL016717

Vinayachandran, P. N., Murty, V. S. N., and Ramesh Babu, V. (2002). Observations of barrier layer formation in the bay of Bengal during summer monsoon. *J. Geophys. Res.: Oceans* 107 (C12). doi: 10.1029/2001JC000831

Xu, Y., Wu, Y., Wang, H., Zhang, Z., Li, J., and Zhang, J. (2021). Seasonal and interannual variabilities of chlorophyll across the eastern equatorial Indian ocean and bay of Bengal. *Prog. Oceanogr.* 198, 102661. doi: 10.1016/j.pocean.2021.102661

Yadav, K., Sarma, V. V. S. S., Rao, D. B., and Kumar, M. D. (2016). Influence of atmospheric dry deposition of inorganic nutrients on phytoplankton biomass in the coastal bay of Bengal. *Mar. Chem.* 187, 25–34. doi: 10.1016/j.marchem.2016.10.004

frontiers | Frontiers in Marine Science

TYPE Original Research
PUBLISHED 17 March 2023
DOI 10.3389/fmars.2023.1082109

Check for updates

OPEN ACCESS

EDITED BY
Javier A. Concha,
European Space Research Institute (ESRIN), Italy

REVIEWED BY
Yan Bai,
Ministry of Natural Resources, China
Zhidan Wen,
Northeast Institute of Geography and Agroecology (CAS), China

*CORRESPONDENCE
Jan El Kassar
jan.elkassar@met.fu-berlin.de

†These authors have contributed equally to this work and share first authorship

SPECIALTY SECTION
This article was submitted to Ocean Observation, a section of the journal Frontiers in Marine Science

RECEIVED 27 October 2022
ACCEPTED 03 March 2023
PUBLISHED 17 March 2023

CITATION
El Kassar J, Juhls B, Hieronymi M, Preusker R, Morgenstern A, Fischer J and Overduin PP (2023) Optical remote sensing (Sentinel-3 OLCI) used to monitor dissolved organic carbon in the Lena River, Russia.
Front. Mar. Sci. 10:1082109.
doi: 10.3389/fmars.2023.1082109

COPYRIGHT
© 2023 El Kassar, Juhls, Hieronymi, Preusker, Morgenstern, Fischer and Overduin. This is an open-access article distributed under the terms of the Creative Commons Attribution License (CC BY). The use, distribution or reproduction in other forums is permitted, provided the original author(s) and the copyright owner(s) are credited and that the original publication in this journal is cited, in accordance with accepted academic practice. No use, distribution or reproduction is permitted which does not comply with these terms.

Optical remote sensing (Sentinel-3 OLCI) used to monitor dissolved organic carbon in the Lena River, Russia

Jan El Kassar[1*†], Bennet Juhls[2†], Martin Hieronymi[3], Rene Preusker[1], Anne Morgenstern[2], Jürgen Fischer[1] and Pier Paul Overduin[2]

[1]Department of Geosciences, Institute of Meteorology, Working Group (WG) Radiation and Remote Sensing, Freie Universität Berlin (FUB), Berlin, Germany, [2]Geosciences, Permafrost Research, Alfred Wegener Institute Helmholtz Centre for Polar and Marine Research (AWI), Potsdam, Germany, [3]Institute of Carbon Cycles, Helmholtz-Zentrum Hereon, Geesthacht, Germany

In the past decades the Arctic has experienced stronger temperature increases than any other region globally. Shifts in hydrological regimes and accelerated permafrost thawing have been observed and are likely to increase mobilization of organic carbon and its transport through rivers into the Arctic Ocean. In order to better quantify changes to the carbon cycle, Arctic rivers such as the Lena River in Siberia need to be monitored closely. Since 2018, a sampling program provides frequent *in situ* observations of dissolved organic carbon (DOC) and colored dissolved organic matter (CDOM) of the Lena River. Here, we utilize this ground truth dataset and aim to test the potential of frequent satellite observations to spatially and temporally complement and expand these observations. We explored all available overpasses (~3250) of the Ocean and Land Colour Instrument (OLCI) on Sentinel-3 within the ice-free periods (May – October) for four years (2018 to 2021) to develop a new retrieval scheme to derive concentrations of DOC. OLCI observations with a spatial resolution of ~300 m were corrected for atmospheric effects using the Polymer algorithm. The results of this study show that using this new retrieval, remotely sensed DOC concentrations agree well with *in situ* DOC concentrations (MAPD=10.89%, RMSE=1.55 mg L^{-1}, r^2=0.92, n=489). The high revisit frequency and wide swath of OLCI allow it to capture the entire range of DOC concentrations and their seasonal variability. Estimated satellite-derived DOC export fluxes integrated over the ice-free periods of 2018 to 2021 show a high interannual variability and agree well with flux estimates from *in situ* data (RMSD=0.186 Tg C, MAPD=4.05%). In addition, 10-day OLCI composites covering the entire Lena River catchment revealed increasing DOC concentration and local sources of DOC along the Lena from south to north. We conclude that moderate resolution satellite imagers such as OLCI are very capable of observing DOC concentrations in large/wide rivers such as the Lena River despite the relatively coarse spatial resolution. The global coverage of remote sensing offers the expansion to more rivers in order to improve our understanding of the land-ocean carbon fluxes in a changing climate.

KEYWORDS

Sentinel-3, Ocean and Land Colour Instrument (OLCI), CDOM, DOC, Lena River, fluxes, monitoring, Arctic

1 Introduction

Arctic temperatures increase four times faster than global temperatures (Rantanen et al., 2022). At the same time, high latitude rivers and their catchments are strongly affected by climate change. The discharge and biogeochemistry at the mouth of a river is a direct response to processes in the terrestrial and aquatic environment within a defined upstream area (Holmes et al., 2013). Measuring the suspended and dissolved load in Arctic rivers can therefore be a tool for observing the impact of climate change to their catchments. Warming and consequently degrading permafrost is expected to mobilize large amounts of organic carbon that was previously stored in frozen soil and sediment, which is then susceptible to decomposition, sedimentation and/or transport *via* rivers into the Arctic Ocean (Guo et al., 2007; Frey & McClelland, 2009; Wild et al., 2019). Major changes in riverine land-to-sea fluxes of organic matter, especially dissolved organic matter and its colored dissolved fraction (colored dissolved organic matter, CDOM), can affect the Arctic Ocean in multiple ways, such as decreasing transparency of the water, increasing radiative heating of the surface waters (Soppa et al., 2019; Pefanis et al., 2020), and acidification of the shelf waters (Semiletov et al., 2016). These processes will change the marine ecosystem and primary production in the Arctic shelf seas (Terhaar et al., 2021).

Organic carbon in aquatic systems is classified as dissolved organic carbon (DOC), the carbon fraction of dissolved organic matter (DOM), and particulate organic carbon (POC), the carbon contained within living (e.g., phytoplankton, zooplankton) and non-living (detritus) material. Once offshore, most POC is deposited in shelf sea sediments (Charkin et al., 2011; Wegner et al., 2013) whereas DOM is subject to slow microbial decomposition, (photo)mineralization, and further transport into the central Arctic Ocean (Carlson & Hansell, 2015; Brüchert et al., 2018; Juhls et al., 2019).

The Arctic Ocean contains only 1% of the global ocean volume (Menard & Smith, 1966; Opsahl et al., 1999) but receives 10% of global river discharge (Aagaard & Carmack, 1989) and an annual total riverine DOC flux of 25–36 Tg (Raymond et al., 2007). Of all Arctic rivers, the Lena River has the highest annual DOC flux (5.7 to 7.3 Tg C yr^{-1}) (Stedmon et al., 2011; Holmes et al., 2012; McClelland et al., 2016; Juhls et al., 2020), which varies strongly between the seasons (Juhls et al., 2020). During winter, when the river is covered with ice, only about 10% of the annual DOC flux is exported (Holmes et al., 2012; Juhls et al., 2020), while the bulk of the DOC is associated with the spring freshet. Warming air temperatures, permafrost thaw and changing precipitation are lengthening the ice-free period (Prowse et al., 2011), shifting the timing and magnitude of the hydrograph and catchment DOC sources (Ye et al., 2003).

Estimates of DOC fluxes for Arctic rivers have high uncertainties due to insufficient observations. *In situ* monitoring of Arctic rivers in their mouth regions is challenging due to their remoteness. While the daily discharge of the big Arctic rivers has been monitored at gauging stations for many decades (Peterson et al., 2002; McClelland et al., 2006; Shiklomanov et al., 2021), sampling is a logistical challenge, especially during ice break-up and the critical freshet period. Despite these challenges, Arctic rivers have been monitored within the PARTNERS and ArcticGRO programs (e.g., Stedmon et al., 2011; Holmes et al., 2012; McClelland et al., 2016), providing year-round and interannual estimates of changing water composition for a set of circumpolar rivers that drain into the Arctic Ocean. However, the number of samples for each river has been limited to about 3-7 samples per year. In ArcticGRO the Lena River is sampled in Zhigansk (66.766° N, 123.374°E), approximately 800 km upstream from the river mouth and 500 km upstream of the gauge station at Kyusyur (Figure 1). Changes to the load of organic carbon in these final 800 km of the river are not reflected in estimates of land-to-sea fluxes based on these samples. To further improve DOC export flux estimates and to better capture the seasonal variability, a new sampling program of the Lena River began in April 2018 with a sampling frequency of every few days over the whole year. This sampling program is located in the central Lena River delta, at the Samoylov Island Research Station about 80 km upstream of the river mouth (Figure 1). The sampling program and initial data are described by Juhls et al. (2020). Analyses include DOC concentrations and CDOM absorption.

Optical remote sensing offers an alternative way to monitor the organic carbon load of surface waters and provides the chance to monitor the river along its entire course, although only during the ice-free season with sufficient sunlight. DOC itself does not have distinct spectral features which makes direct retrievals from remote sensing unfeasible. Thus, we aim at deriving the colored fraction of the dissolved organic matter (CDOM) that we can then translate to DOC using a stable relationship for the Lena River. CDOM strongly absorbs light in the short wavelength range and is a known proxy for concentrations of DOC in inland and coastal waters (Matsuoka et al., 2013; Juhls et al., 2019). Thanks to the robust relationship between CDOM absorption ($a_{CDOM}(\lambda)$) and DOC concentration (e.g., Matsuoka et al., 2017; Juhls et al., 2019), satellite-derived $a_{CDOM}(\lambda)$ can be used to derive DOC concentrations. While there are a number of studies using remote sensing to estimate surface water DOC concentrations in Arctic coastal and shelf waters (Fichot et al., 2016; Matsuoka et al., 2017; Juhls et al., 2019; Soppa et al., 2019; Lewis & Arrigo, 2020; Juhls et al., 2022), only a few studies show the potential of using satellite data for the retrieval of $a_{CDOM}(\lambda)$ and DOC in Arctic rivers (Griffin et al., 2011; Herrault et al., 2016; Griffin et al., 2018; Huang et al., 2019). These studies make use of high resolution satellite sensors such as SPOT5, Landsat TM, ETM+ and OLI or Sentinel-2 MSI. While these satellite sensors have a suitable spatial resolution (10 to 30 m) to monitor narrow river channels, their revisit frequency and swath width are relatively low (several days and 185 - 290 km, respectively). Strong seasonal variations in DOC concentrations can thus not be captured. Additionally, the sparse availability of *in situ* data limits the number of matchups with satellite data and can impede a thorough validation of the retrieval. While individual scenes are large enough to capture specific segments of a river's reach (Griffin et al., 2011), they are not large enough to estimate watershed-scale variability in DOC concentration. Other polar-orbiting sensors such as the Ocean and Land Colour Imager (OLCI) on the Sentinel-3 satellites have a much higher revisit frequency

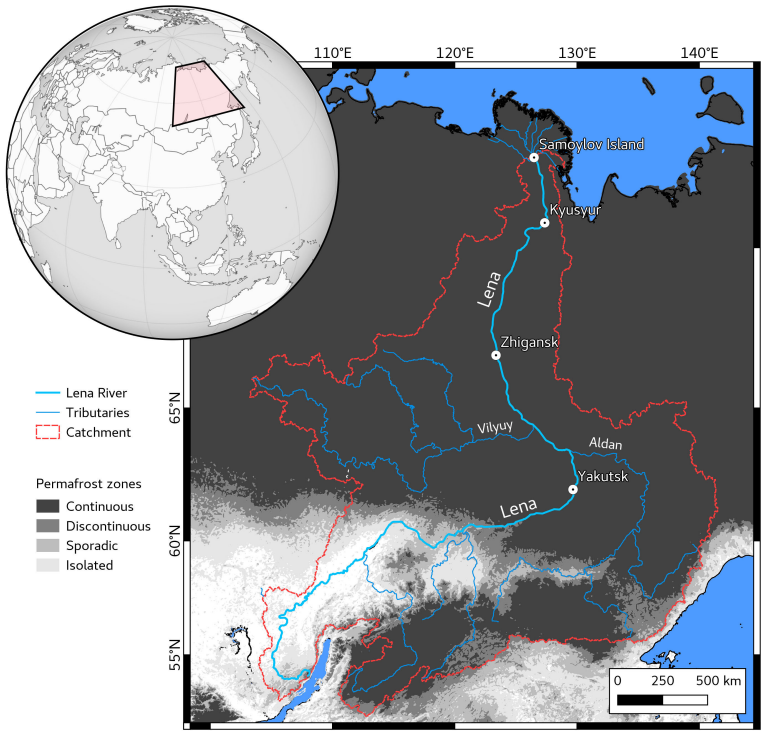


FIGURE 1
Map of the Lena River, its catchment and underlying permafrost zones (from Obu et al., 2019).

(multiple times per day in polar regions), better spatial coverage (1270 km swath), and better spectral characteristics (more bands and narrower spectral response functions (SRF)). However, OLCI's spatial resolution is much coarser (300 m at full resolution), which is sufficient only for wide rivers.

Aquatic color remote sensing and the retrieval of constituents such as $a_{CDOM}(\lambda)$ is challenging in inland and coastal waters (IOCCG, 2000) and even more so if used in high latitudes (IOCCG, 2015). The major challenges are 1) the atmospheric correction (AC) of the signal the satellite received; and 2) the retrieval of the water constituents from the atmospherically corrected reflectance. AC is one of the most critical parts in any study on water bodies utilizing remote sensing since it attempts to remove the influence of the atmosphere (e.g., molecular scattering, aerosol scattering, and gaseous absorption) and adjacency effects (e.g., contributions from adjacent snow, ice or land pixels) on the signal of interest, which is used to derive information about water constituents. The signal of interest – the water-leaving reflectance (ρ_W) – is only a fraction of the total signal a satellite instrument receives. In combination with the ambiguity of the signal from the water body, this can decrease the overall quality of ACs.

One of the major difficulties for the retrieval of water constituents is the strong variability of type and concentration of constituents with varying optical properties that create ambiguity and can produce similar reflectance spectra. Disentangling the contributions to the optical properties of the water and deducing the concentration of each constituent over a wide selection of water types remains difficult. For OLCI there are multiple retrieval schemes that derive a diverse catalog of optical parameters such as $a_{CDOM}(\lambda)$, some of which show reasonable performance in optically complex Arctic coastal waters despite the described challenges (Matsuoka et al., 2013; Hieronymi et al., 2017; Juhls et al., 2019). However, these retrieval algorithms show large uncertainties in $a_{CDOM}(\lambda)$ or do not capture the full range of $a_{CDOM}(\lambda)$ in Arctic rivers such as the Lena. This is likely related to the difficulty in separating the fraction of absorption from non-algal particles (NAP) and CDOM (IOCCG, 2000; Babin et al., 2003). Griffin et al. (2011); Griffin et al. (2018) and Huang et al. (2019) showed that regional empirical band ratios developed solely for the retrieval of $a_{CDOM}(\lambda)$ and consequently estimated DOC concentration perform well in Arctic rivers.

We hypothesize that moderate resolution imagers such as OLCI offer both a higher revisit frequency and finer spectral resolution while still resolving inland waters such as lakes and rivers. In this study, we present a new regional retrieval to derive DOC concentration in the Lena River using optical remote sensing.

With the help of the retrieval, we test the potential of high revisit frequency Sentinel-3 OLCI satellite data to monitor organic carbon load, estimate DOC fluxes and identify the geographical and temporal heterogeneity of river organic carbon concentration along the entire Lena River throughout the ice-free period.

2 Data and methods

2.1 Study area

In this study, we focus on the Lena River, which is one of the largest Arctic rivers, exporting about 588 km^3 yr^{-1} to the Arctic Ocean (Holmes et al., 2012). About 70% of the catchment lies in the zone of continuous permafrost, 24% in the zones of discontinuous, sporadic, and isolated permafrost, and 6% is free of permafrost. 72% of the catchment is covered by mostly evergreen forest, 12% is covered by shrubland and 3% is covered by wetland (Amon et al., 2012). The two main tributaries are the Vilyuy River and the Aldan River (Figure 1). The Lena River has a total length of about 4300 km and its width ranges from 2 to 10 km in most parts of its stretch, depending both on latitude and season. During boreal winter (November to April) the majority of the Lena is frozen over and discharge is at its lowest. Ice break-up usually occurs in the end of May, simultaneously with the annual peak in discharge. Strong precipitation events in the catchment can create smaller peaks in discharge later in the year. The warming climate of the Arctic leads to a shift towards earlier break-ups, later freeze-ups and an increase in winter-discharge (Juhls et al., 2020).

2.2 *In situ* data

Samples for *in situ* CDOM absorption ($a_{CDOM}(\lambda)$) and concentrations of dissolved organic carbon (DOC) were taken at the Research Station Samoylov Island in the central Lena River Delta (Figure 1). 199 samples for paired $a_{CDOM}(\lambda)$ and DOC measurements were used in this study. They covered the ice-free periods of four years. Details on sample processing and analysis of the samples are described in Juhls et al. (2020). Samples were collected at daily to weekly intervals. In order to obtain daily data for $a_{CDOM}(\lambda)$ and DOC from the samples, we linearly interpolated between sampling dates. The temporal distance between two real samples exceeded two days in only 3% of interpolated daily data. A daily sampling rhythm was maintained during the ice break-up period, which is the period of most significant and rapid changes. This makes linear interpolation sufficient, since the significant variations in DOC along the hydrograph happen on a weekly scale (except during the spring freshet, Juhls et al., 2020).

To estimate DOC fluxes, we used the discharge of the Lena River published by ArcticGRO (Shiklomanov et al., 2021). The discharge data were corrected for the distance difference between the gauge station at Kyusyur and water sampling station at Samoylov Island (more details in Juhls et al., 2020).

2.3 Satellite data

2.3.1 Download and subsetting

We downloaded all available Sentinel-3 A/B OLCI L1 full resolution scenes from https://finder.creodias.eu/for the period from May to October for the years 2018 to 2021, which covered the sampling site (126.47°N, 72.371°E). In total, we found and used 3257 scenes. See Figure 2 for a detailed depiction of all available scenes per day.

2.3.2 Atmospheric correction

Atmospheric correction of satellite imagery is one of the most critical steps towards reliable estimates of water constituents such as DOC. The atmospheric contribution to the satellite signal can be >90% above dark rivers like the Lena River with high CDOM content (IOCCG, 2010). In this work, we used the AC method Polymer (v4.13) for retrieving normalized water-leaving reflectances ($\rho_W(\lambda)$) (Steinmetz et al., 2011; Steinmetz & Ramon, 2018). Polymer was originally developed for oceanic and coastal waters, but shows good results for inland waters and marginal seas, too (Qin et al., 2017; Warren et al., 2019). Moreover, Polymer is relatively robust to land or snow/ice adjacency effects, which is essential for river remote sensing. Since, to our best knowledge, no radiometric data from the Lena River water are available, a direct radiometric validation is not possible. However, in previous studies on satellite-retrieved DOC, Polymer showed a good performance and demonstrated a high robustness for Arctic waters impacted by riverine fluxes (Juhls et al., 2022). This is in line with findings by König et al. (2019) that even in very high latitudes with sun zenith angles of >60°, surrounded by ice potentially causing adjacency effects, Polymer performs best and produces reasonable results even in the high contrast Arctic sea ice.

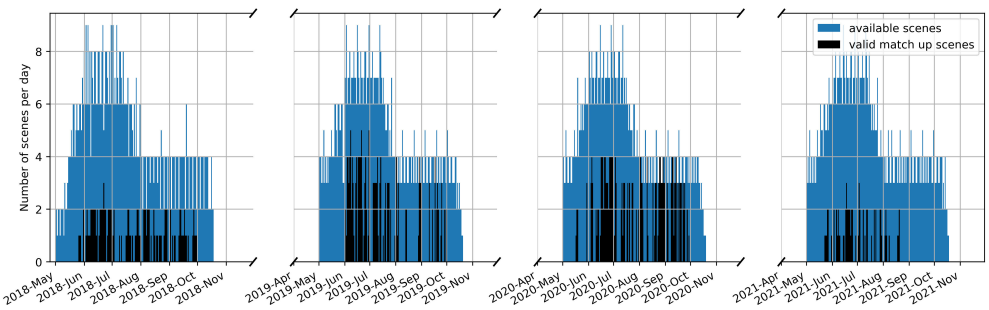


FIGURE 2
Number of available Sentinel-3 OLCI scenes (blue) and used Sentinel-3 OLCI scenes (black) per day.

2.3.3 Extraction and temporal and spatial collocation with *in situ* data

Pixels from all processed satellite swaths were collocated with the data collected at Samoylov Island. Reflectances were then filtered according to the flags CLOUD_BASE, L1_INVALID, NEGATIVE_BB, OUT_OF_BOUNDS, EXCEPTION, THICK_AEROSOL, HIGH_AIR_MASS, INCONSISTENCY provided by the Polymer AC and the duplicate flag provided by the OLCI Level 1 data. Furthermore, all pixels that contained any negative ρ_W in any of the bands in the visible range were excluded. The water level and subsequently the width of the channels of the Lena River is very variable. Thus, since we wanted to obtain as many matchups spanning as wide a range of conditions as possible, we decided against a rigid river-land-mask. Instead, we applied a simple land mask using an empirically determined threshold value of 0.03 for the atmospherically corrected reflectance at 865 nm (ρ_{NIR}, NIR: near infrared). This threshold was set very restrictively in order to exclude any mischaracterisation of a land pixel as water. As a result, most satellite observations were extracted within the deep part of the wide main channel of the Lena River (Figure 3).

The filtered data were then regridded on a 300 by 300 m grid (0.0089° by 0.0027°, geographic projection). All valid pixels within a 10 km radius around Samoylov Island were treated as individual measurements per collocated *in situ* observation and used for the development and evaluation of the algorithm described in the following section. We chose this approach because in the branched river landscape the water-leaving reflectances in a 10 km radius can be very heterogeneous and the homogeneity criterion usually used for matchups (i.e., 3x3 or 5x5 macro-pixel with a coefficient of variation <15%, (e.g., EUMETSAT, 2019)) cannot be applied. Instead, all pixels that were not masked by Polymer are used for algorithm development, not just the median values. This also allows for a better quantification of uncertainties for the regression coefficients. Furthermore, *in situ* measurements from an expedition in August 2019 (Fuchs et al., 2022) show a very small variability (range of 0.6 mg L^{-1} between minimum and maximum) in DOC concentration for >20 measurements for different depths at >10 locations across ~100 km in the Lena River Delta. Given that the Lena River is well mixed (Gonçalves-Araujo et al., 2015; Laukert et al., 2017) and channels are directly connected throughout the year (Juhls et al., 2021), we assume a strong homogeneity of dissolved constituents (i.e., DOC) on small regional scales.

All available swaths within 24 hours of an *in situ* observation were taken into consideration. We were able to find 489 scenes (~15% of all scenes) with valid pixels that fit the matchup-criteria. The scenes were distributed over 249 days (i.e., multiple scenes per day, see Figure 2) and contained a sum of about 120000 pixels. These matchup-pixels were used for the evaluation and algorithm development. The number of available days per year with matchups varied between 37 to 79. *In situ* data were available from 20 April 2018 until 23 August 2021 and satellite data were limited to the time span of available *in situ* data.

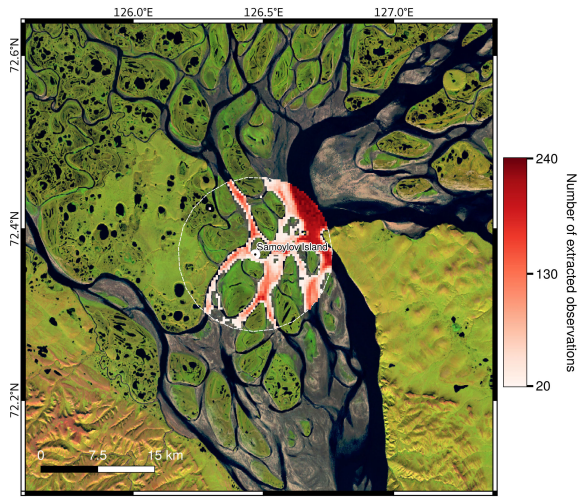


FIGURE 3
Central Lena River Delta and the 10 km radius around Samoylov Island (white dashed line) where satellite observations were extracted. Red colors show the number of extracted satellite observations for each pixel within the radius. Background image is a multi-year mosaic of Landsat 8 OLI created with google earth engine.

2.4 Bootstrapping and evaluation metrics

In our study, the main tool for finding a suitable relationship and retrieval algorithm for $a_{CDOM}(\lambda)$ is the bootstrapping approach. Bootstrapping describes the repeated creation of random subsamples of a dataset and their analysis in order to find statistical measures and their associated accuracy (Efron & Tibshirani, 1994). We use this approach to find the optimal retrieval of $a_{CDOM}(\lambda)$ from satellite observations of the Lena River. We used a repetition of 1000 times and a random sample size of 80 matchups per repetition. Before random sampling, data were separated into equal bins along the target variable (i.e. *in situ* $a_{CDOM}(\lambda)$) and the predictor (i.e. ρ_W ratio). Bins which contained less than one point were discarded, in order to dispose of any extreme outliers. Ideally, this approach results in a linear relationship between the predictor and the target variable, indicated by a high Pearson Correlation Coefficient. The parameters of this relationship were estimated using the orthogonal distance regression (ODR). By minimizing the orthogonal distance function for each data-pair to a polynomial function the relationship between two datasets can be found (Boggs & Rogers, 1990). We are looking for the relationship between the predictor (satellite observation) and the target variable (*in situ* observation). This gives us the fit parameters offset (α) and slope (β). In the end, the median of all estimated fit parameters yields the optimal model to retrieve $a_{CDOM}(\lambda)$ from ρ_W. In order to ensure an independent evaluation of the retrieval, pixels that were used in the bootstrapping were discarded from the statistical assessment. Both in algorithm development and in algorithm evaluation, we used the Pearson Correlation Coefficient (R^2), Bias, Mean Absolute Percentage Deviation (MAPD) and Root Mean Square Deviation (RMSD) defined as follows:

10.3389/fmars.2023.1082109

$$R^2(insitu, sat) = \frac{COV(insitu, sat)}{\sigma(insitu) \cdot \sigma(sat)} \quad \text{(Eq. 1)}$$

where COV is the covariance and σ denotes the standard deviation.

$$Bias(insitu, sat) = \frac{1}{N}\sum_{i=1}^{N}(insitu_i - sat_i) \quad \text{(Eq. 2)}$$

$$MAPD(insitu, sat) = \frac{100\,\%}{N}\sum_{i=1}^{N}\left|\frac{insitu_i - sat_i}{insitu_i}\right| \quad \text{(Eq. 3)}$$

$$RMSD(insitu, sat) = \sqrt{\frac{1}{N}\sum_{i=1}^{N}(insitu_i - sat_i)^2} \quad \text{(Eq. 4)}$$

where N is the number of data pairs.

2.5 DOC satellite retrieval development

While many studies that retrieve $a_{CDOM}(\lambda)$ from optical remote sensing focus on λ=443 nm, we focus on $a_{CDOM}(\lambda)$ at λ=254 nm ($a_{CDOM}(254)$) because this wavelength represents the lignin absorption peak, which is a tracer for terrestrial organic matter (Fichot et al., 2016). Since most DOC in rivers originates from land, at 254 nm the relationship between $a_{CDOM}(\lambda)$ and DOC is strongest.

In the first step, we tested the exponential of the ratios of all available ρ_W bands (e^{ratio}) against *in situ* measured $a_{CDOM}(254)$ to find the optimal bands for the ratio describing the level of $a_{CDOM}(254)$ in the Lena River. After that, a fit was calculated for the ratio of the chosen bands using the bootstrapping method described above.

Overall, there were several reflectance ratios (red over green) that exhibited strong correlations with *in situ* measured $a_{CDOM}(254)$. The $\rho_W(674)/\rho_W(560)$ and $\rho_W(681)/\rho_W(620)$ bands performed best (R^2= 0.95-0.96). The performance using $\rho_W(665)/\rho_W(560)$ showed only a slightly lower R^2 (0.94). We chose the bands $\rho_W(665)$ and $\rho_W(560)$ for several reasons: 1) the red and green bands from Polymer AC show much lower uncertainties than the blue spectral range, 2) increased CDOM absorption considerably reduce the water-leaving signal in all but the green-red range, 3) the band at $\rho_W(681)$ may be influenced by chlorophyll-a fluorescence and introduce a further source of uncertainty and, lastly, 4) these bands were also available on OLCI's predecessor, the Medium Resolution Imaging Spectrometer (MERIS), to allow the application of this retrieval to MERIS full-resolution images in the future.

The initial fit for $a_{CDOM}(254)_{SAT}$ follows:

$$a_{CDOM\ SAT\ ini}(254) = \alpha + \beta \cdot e^{\rho_W(665)/\rho_W(560)} \quad \text{(Eq.5)}$$

where α= −33.675 and β = 34.434

Due to the co-variation of shape and height of ρ_W spectra (Supplementary Figure 1), we assume that sediment load co-varies with $a_{CDOM}(\lambda)$ most of the time. Despite increasing absorption by CDOM the water-leaving reflectances at 620 nm increased. This increase in overall signal is caused by corresponding increases in backscattering by sediments in the Lena River. We attributed the high residuals of the initial fit (initial $a_{CDOM}(254)_{SAT}$ - $a_{CDOM}(254)_{\text{in situ}}$) to the influence of sediment and found a strong negative correlation to $\log_e(\rho_W(620))$ at R^2= -0.72. In order to reduce the influence of sediment concentration variation on our $a_{CDOM}(254)$ retrieval, we fitted (using the bootstrap method described above) the residuals with $\log_e(\rho_W(620))$.

$$Residuals_{SAT\ ini-in\ situ} = \alpha + \beta \cdot log_e(\rho_W(620)) \quad \text{(Eq.6)}$$

where α= −130.857 and β =−31.267

The final retrieval for $a_{CDOM}(254)$ can be described as (Supplementary Figure 2):

$$a_{CDOM\ SAT}(254) = 34.434 \cdot e^{\frac{\rho_W(665)}{\rho_W(560)}} - 33.675\ -31.267\ \cdot log_e(\rho_W(620)) - 130.857 \quad \text{(Eq.7)}$$

In order to compare with other $a_{CDOM}(\lambda)$ retrieval algorithms, we also report the equation for 443 nm (Supplementary Information).

The good relationship we determined between the red-green ratio and *in situ* measured aCDOM was confirmed by forward simulations using a simple bio-optical IOP model and aligns well with findings of other studies which relied on red-green ratios to retrieve CDOM (e.g., Mabit et al., 2022).

Satellite-retrieved $a_{CDOM}(254)$ was then converted to DOC concentration using an ODR linear regression fit (Equation 8) for *in situ* $a_{CDOM}(254)$ and DOC in the ice-free periods. (Supplementary Figure 3). From this follows:

$$DOC_{SAT} = \frac{a_{CDOM}(254)_{SAT} - 9.28}{8.55} \quad \text{(Eq.8)}$$

For the matchup comparison with the *in situ* data, we calculated the median of the satellite-retrieved $a_{CDOM}(254)_{SAT}$ and DOC_{SAT}.

2.6 DOC fluxes

Daily *in situ* and satellite DOC fluxes are calculated using the daily DOC concentrations and the *in situ* measured discharge is corrected for the distance between Kyusyur (location of gauge station) and Samoylov Island (see Juhls et al. (2020) for details). For the DOC_{SAT} concentrations, a daily average was taken over DOC_{SAT} that was retrieved within a 20 km radius around Samoylov Island and interpolated linearly between available observations. The DOC fluxes (both from *in situ* and satellite) were then integrated over the longest time period available for each of the four years with the exception of 2021, where *in situ* observations are not yet available after the end of August. The investigated periods were between the beginning of June and end of September for the years 2018 to 2020 and between the beginning of June to the end of August for 2021.

10.3389/fmars.2023.1082109

2.7 DOC_{SAT}-transects along the Lena River

By mosaicking multiple satellite overpasses, we created 10-day composite maps of the DOC_{SAT} concentrations of the Lena River on the regular 0.0089° by 0.0027° grid. Note that this leads to slightly coarser (~500 m) and finer (~250 m) resolutions in lower and higher latitudes, respectively. From these composites we extracted the DOC concentrations along a transect following the main Lena River stem (light blue in Figure 1) from 111.49°N, 59.00°E to 126.70°N, 72.29°E. We applied the same data filtering criteria as described above. A gaussian filter was applied to reduce the noise in the DOC_{SAT} fields and transects. Where no satellite data could be extracted along the centerline, the transect was filled with linear interpolation.

3 Results

3.1 Retrieval of CDOM absorption at 254 nm

In total, about 35% of all available matchup pixels were used in the bootstrap. The remaining matchups are shown in Figure 4. The high correlation (R^2=0.89), a slope of 1.0, and the low negative bias of 1.18 m^{-1} indicate the good performance of the retrieval algorithm. At higher $a_{CDOM}(254)$ levels, higher deviation from the linear fit results in the elevated RMSD of 16.16 m^{-1} and MAPD of 12.83%. However, only in a very few cases (<2%) relative $a_{CDOM}(254)_{SAT}$ errors exceed 3 standard deviations (62%, 44.5 m^{-1}) when compared to $a_{CDOM}(254)_{in\ situ}$(Supplementary Figure 4). In the very first satellite observations of each year as well as in the mid to late September 2019 higher relative differences appear more frequently.

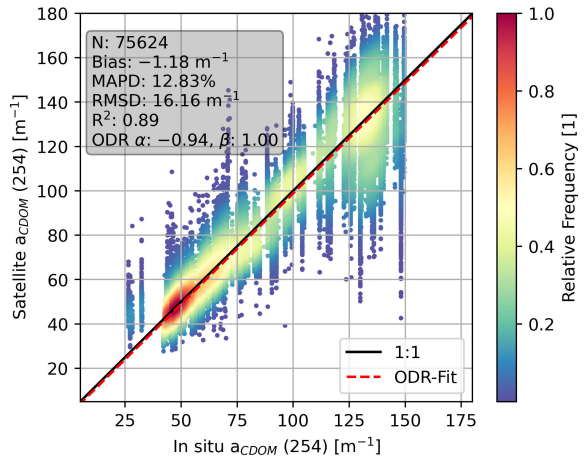


FIGURE 4
Evaluation of the $a_{CDOM}(254)$ algorithm by comparing *in situ* measured and satellite-derived $a_{CDOM}(254)$. Only data that were not used in the bootstrapping are shown here. The color of points indicates the relative frequency of occurrence.

3.2 Monitoring DOC concentrations with Sentinel-3 OLCI

The DOC_{SAT} concentrations were retrieved with data from the twin satellites Sentinel-3 A and B for the period between end of May and end of September for the years 2018 to 2021. A high number of valid satellite observations – often multiple per day – could be retrieved within this period (Figure 2). The DOC_{SAT} retrieval scheme model reported in this study, shows a good agreement with the *in situ* DOC concentrations (R^2: 0.92, BIAS: 0.12 mg L^{-1}, MAPD: 10.89%, RMSD: 1.55 mg L^{-1}) (Figure 5). For all four years, satellite observations for DOC are available before the concentration peak during spring freshet when ice is still present in some parts of the Lena River. The complete range of seasonal variability can be retrieved from satellite with the highest concentration in spring after the ice break-up and lowest in dry summer months (Figure 6). The timing and height of the DOC_{SAT} concentration peaks in spring are captured with only small deviations when compared to *in situ* observations (<10 days,< 14%). In 2021, the satellite observation density is lower compared to the other year. In consequence, both the spring freshet and a peak in late summer cannot be captured with high certainty by satellite data. Overall, the performance of the satellite retrieval shows no systematic dependence on the year or season. In contrast to the overestimation of $a_{CDOM}(254)_{in\ situ}$in September 2019, there is no significant deviation in DOC_{SAT} when compared to *in situ* DOC (Supplementary Figure 5).

3.3 Daily and integrated DOC fluxes

We calculated the DOC fluxes for the ice-free period (early June to end of September) for each year using *in situ* data and satellite data (Figure 7). The flux estimates (mean of *in situ* and satellite-derived) show high interannual variations from 3.48 Tg C (in 2019) to 5.3 Tg C (in 2018). The flux within the ice-free period accounts for up to 75% of the annual flux (based on year-round *in situ* data).

A comparison of DOC fluxes estimated with *in situ* measured DOC and remotely sensed DOC_{SAT} (both linearly interpolated to daily resolution) shows that range and timing of peaks and lows in daily DOC fluxes are captured without substantial differences (R^2=0.97, MAPD=19.92%, RMSD=9.68 Mg C d^{-1}, Supplementary Figure 6). Interannual variations of the concentration peak height during the spring freshet in early June are captured almost identically by both observation methods. In 2018 and 2020, satellite observations slightly overestimate the spring concentration peak compared to the *in situ* data.

The lower observation density in 2021 compared to the other years, likely leads to the higher difference between *in situ* and satellite-based estimations of DOC-fluxes. Overall DOC_{SAT} fluxes are within +/-6.02% of the *in situ* derived fluxes (Table 1).

3.4 DOC_{SAT} concentrations along the main course of the Lena River

Using all available satellite observations within a 10-day period, we are able to show a synoptic picture of DOC_{SAT} concentrations

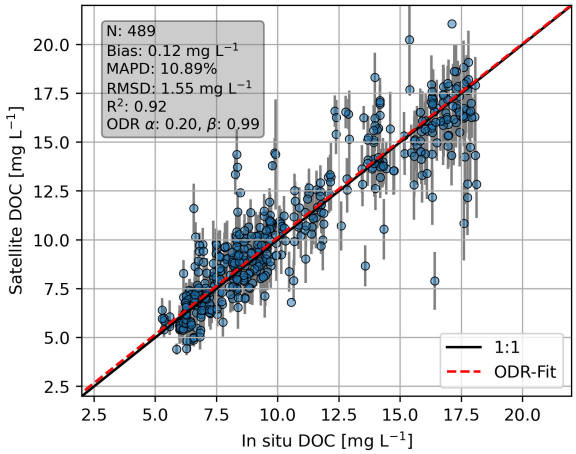


FIGURE 5
Matchup comparison between *in situ* measured DOC concentrations and DOC_{SAT} concentrations using the new exp-band ratio. The grey vertical bars indicate the standard deviation associated with the median DOC_{SAT} values.

along the entire main Lena River (Figure 1) over a total length of more than 3000 km. Figure 8 shows the DOC_{SAT} concentration maps for two periods: **a)** first 10 days of June during the peak annual discharge, and **b**) 10 days at the end of August/beginning of September during the low flow period.

In June (Figure 8A), DOC_{SAT} concentrations range between 10.1 and 18.6 mg L^{-1}, whereas during the summer period (Figure 8B), concentrations range between 3.4 and 8.5 mg L^{-1}. The satellite-extracted DOC concentrations in both periods show a downstream increase along most of the Lena River. In the June composite, the DOC_{SAT} concentrations are sharply decreasing before reaching the delta. In the summer composite, DOC_{SAT} concentrations are at a considerably lower level (<4 mg L^{-1}) upstream. After the confluence of the two biggest tributaries – the Aldan and Vilyuy River – DOC_{SAT} concentration increases until the Lena River reaches the delta.

4 Discussion

4.1 Potential for monitoring DOC concentration, their fluxes and catchment variability with Sentinel-3 OLCI

Our results demonstrate the potential of monitoring DOC concentrations with remote sensing (Sentinel-3 OLCI) to complement and extend *in situ* DOC monitoring (Figures 6, 7). Despite the challenge of persistent cloud cover, the entire ice-free period can be monitored with OLCI due to the frequent revisit time of Sentinel-3 and the resulting high frequency of valid observations. In many cases, multiple valid observations per day could be obtained (Figure 2). Thus, the full seasonal variability of DOC concentration as well as most short-term events can be captured. The high observational density allows more direct estimates of DOC_{SAT} fluxes (simple linear interpolation between observations) without the need to employ load estimator models (e.g., LOADEST, Runkel et al., 2004) as was done in many previous studies that reported flux estimates (e.g., Raymond et al., 2007; Holmes et al., 2012; Wild et al., 2019). These models rely on the relationship of discharge to DOC concentrations, which is not always stable and can thus lead to substantial errors.

Figure 7 and Table 1 show that flux estimates from *in situ* and satellite observations agree well for the years 2018 to 2020 (1.13 to 4.86%). Only in 2021, the difference between both flux estimates is higher (6%). The slightly higher DOC_{SAT} fluxes in 2018 and 2020 are a result of the overestimation during the spring freshet. This higher difference in flux estimates is likely the result of extensive and very persistent cloud-cover in August 2021 in combination with exceptionally wide-spreading smoke plumes originating from wildfires over the extraction region. Due to the lower satellite observation density in that period, not all of the short-term DOC concentration increase (visible in the *in situ* observation) could be captured by satellite monitoring. However, in two cases in August 2021 the distance between samples exceeded eight days. This is also visible in a "jump" in DOC concentrations between two non-interpolated samples while before and after these two samples extended gaps can be seen (Figure 5). The absence of data might veil local extreme points similar to a feature seen in August 2018 while DOC_{SAT} indicates such tendencies. This further underlines the merit of high frequency satellite observations to complement gaps in *in situ* records.

This study presents, to our knowledge, the first ever satellite-derived quasi-daily summer DOC concentration monitoring and flux estimates of DOC of the Lena River. Previous studies, which reported flux estimates, were based entirely on *in situ* samples (Raymond et al., 2007; Stedmon et al., 2011; Holmes et al., 2012; Wild et al., 2019). Other studies that employed remote sensing to monitor DOC_{SAT} concentrations in Arctic rivers (Griffin et al., 2011; Herrault et al., 2016; Griffin et al., 2018; Huang et al., 2019) used single scenes from a variety of optical satellite sensors, however, not including Sentinel-3 OLCI to show the potential of remote sensing regarding its quality compared to *in situ* data.

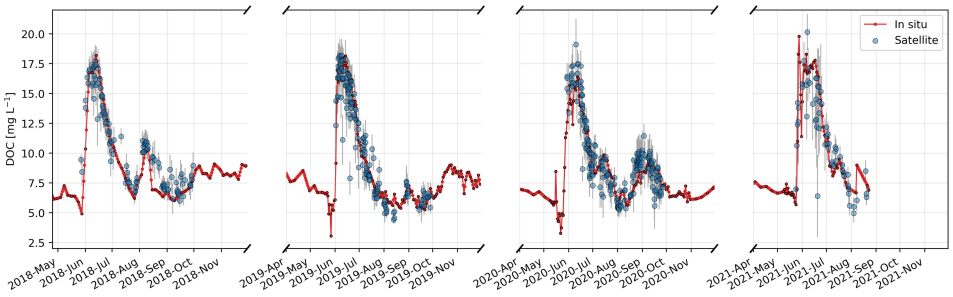


FIGURE 6
Time series (2018 to 2021) for the summer months with *in situ* measured DOC concentration (red line) and DOC_{SAT} concentration (blue circles). The grey vertical bars show the standard deviation associated with the median DOC_{SAT} values. Black outlines around the *in situ* data mark an actual sample. Only satellite observations with a corresponding *in situ* sample are shown.

Nevertheless, they did not provide daily or even weekly time series or flux estimates for longer periods. In a study focusing on the Chesapeake Bay estuary in lower latitudes, Cao & Tzortziou (2021) showed that a combined use of Landsat-8 OLI and Sentinel-2 MSI data can result in up to weekly observations.

The main reason for the usage of sensors with higher spatial resolution (SPOT5, Landsat TM, ETM+ and OLI or Sentinel-2 MSI) is that they offer the application of remote sensing on smaller rivers, but at the same time they are very limited in their capacity for monitoring due to their substantially lower revisit frequency (resulting in only a few to dozen valid observations per year) when compared to Sentinel-3 OLCI. For big rivers such as the Lena River, however, the coarser spatial resolution of Sentinel-3 OLCI compared to, e.g., Sentinel-2 MSI does not affect the capability to find sufficient valid pixels in the river channel and even still allows observing cross channel variability at wide parts of the Lena River (Supplementary Figure 7). In addition, OLCI's higher spectral resolution and narrower spectral response functions compared to Sentinel-2 MSI (Supplementary Figure 8) allows better spectral characterization of optically active constituents such as CDOM. In order to enable a flexible use of the presented retrieval, only bands that can be found both in Sentinel-3 OLCI and on its predecessor Envisat MERIS (2002 to 2012) were used. The inclusion of MERIS data in future studies will substantially extend the time series to almost two decades (MERIS: 2002 to 2012, OLCI: 2016 to present).

Since optical remote sensing observations are limited to the ice-free period, combinations of using satellite data, *in situ* data and models can help to obtain year-round fluxes. Bertin et al. (2022) used satellite-derived observations from the Moderate Imaging Spectrometer (MODIS) in the coastal bays surrounding the Mackenzie Delta in combination with a load estimation model to obtain export DOC fluxes of the Mackenzie River. However, the authors point out that the 1 km spatial resolution of MODIS is not sufficient to extract the signal within the river channels.

Influences of oceanic waters and processes such as flocculation within the coastal zones might alter the original river DOC concentration and affect export flux estimates. Even without the use of models to complement the ice-covered period, for the Lena River, most of the annual DOC export can be observed solely by satellite remote sensing since up to 75% of the annual DOC flux is transported in summer during the ice-free season. Permafrost thaw related changes in organic carbon fluxes from Arctic rivers are expected to affect mostly the warm periods in summer, when active permafrost degradation and mobilization of organic carbon can be observed. Therefore, despite the limitation of optical remote sensing for DOC monitoring a limited period in the year due to light and ice conditions, it is still a valuable tool for identifying potential future trends. In addition, as the ice cover duration shortens with ongoing warming, the period amenable to remote sensing lengthens.

The use of Sentinel-3 OLCI at full resolution not only allows monitoring the river at a single location, due to the large overlapping swaths and resulting frequent coverage it also offers the opportunity to map the DOC_{SAT} concentration along large parts of the river and its catchment to identify up/downstream trends or local sinks and sources of DOC. Two examples of large-scale 10-day composites (Figure 7) show the potential of remote sensing to capture the geographical variability of DOC concentration within the main Lena River. In both composites, the increase of DOC concentrations from south to north indicates a downstream accumulation of DOC in the Lena River across its catchment. This downstream loading of DOC_{SAT} agrees with findings by Griffin et al. (2011) for the Kolyma River despite the substantially smaller scales that were investigated in that study (300 km compared to >3000 km in this study). The very high DOC_{SAT} concentrations within the southern parts of the Lena River and the sharp decrease at the very downstream end in the spring period (early June, Figure 7A) likely reflects the spring ice break-up and the pulse of associated short-term annual maximum peak of DOC concentrations (Figure 6) draining through the Lena River into the Arctic Ocean. In the late-summer composite (Figure 7B), we could identify substantial inflows of high DOC concentrations from tributaries (Aldan and Vilyuy River) resulting in the increase of Lena River DOC_{SAT} concentrations downstream of the confluences. The large-scale 10-day composites contain DOC_{SAT} observations for almost the entire length of the Lena River and parts of its tributaries and further demonstrates the advantage of Sentinel-3 OLCI compared to other satellites with higher spatial resolution but substantial lower revisit frequency and swath width. Since the DOC_{SAT} shown in the composites is based on $a_{CDOM}(254)_{SAT}$

10.3389/fmars.2023.1082109

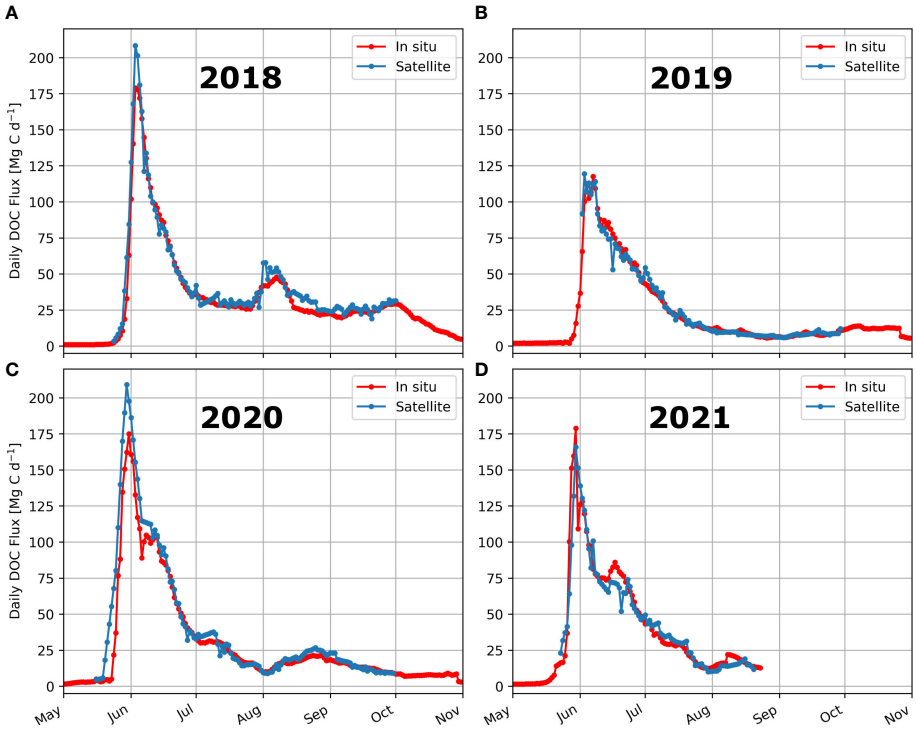


FIGURE 7
Daily DOC fluxes estimated from *in situ* samples (red) and satellite observations (blue) for **(A)** 2018, **(B)** 2019, **(C)** 2020, and **(D)** 2021.

from a locally tuned retrieval, degrading accuracy for other locations of the river is to be expected. While the exact quantities of $a_{CDOM}(254)_{SAT}$ and DOC_{SAT} might be off by a certain factor, we are confident that general trends and gradients will be retained.

4.2 Advances and challenges of optical remote sensing to monitor rivers

The $a_{CDOM}(254)_{SAT}$ retrieval algorithm developed and applied in this study shows a reasonably good performance (R^2=0.89, Bias=-1.18 m^{-1}, RMSD=16.16 m^{-1}, MAPD=12.83%). The striping along the y-axis is caused by the allocation of a high number of pixels from single scenes per *in situ* measurement within the 10 km radius around Samoylov Island. Including all pixels results in a significant variability of retrieved $a_{CDOM}(254)_{SAT}$, however, the vast majority of pixels (see colour in Figure 4 indicating the relative frequency) align with the 1:1 line, indicated by the yellow to red colour. The overestimation of $a_{CDOM}(254)$ and subsequently DOC during the extremely chaotic period within the ice break-up in late May to early June (Supplementary Figure 5) could be related to remnants of submerged ice or floating debris influencing the satellite retrieval. There are several further possible factors throughout the ice-free period that might influence the performance of DOC_{SAT} concentration retrieval such as the residual influence of phytoplankton (e.g., phycocyanin absorption peak at 620 nm), which is not yet accounted for in the retrieval algorithm. CDOM and DOC are assumed to be distributed homogeneously in the Lena River within a few kilometers and within the water column. However, in some cases there are slight gradients in satellite-retrieved concentrations, e.g., between the edge and center of the river stem, which are likely related to retrieval errors due to the

TABLE 1 Discharge, *in situ* measured DOC flux and satellite DOC flux and corresponding deviation for the four years. .

Period	2018-06-02 to 2018-09-30	2019-06-02 to 2019-09-30	2020-06-02 to 2020-09-30	2021-06-02 to 2021-08-23*
Discharge flux; 10^9 m^3	516.72	313.25	381.23	282.3
***in situ* DOC flux; Tg C**	5.241	3.483 (annual: 4.674)	4.020 (annual: 5.77))	3.448
satellite DOC flux; Tg C	5.496	3.523	4.188	3.24
absolute difference (relative; %)	-0.255 (+4.86%)	-0.039 (+1.13%)	-0.168 (+4.19%)	0.219 (-6.02%)

*In 2021, in situ data is available only until 23 August, reducing the period for flux estimate comparisons.

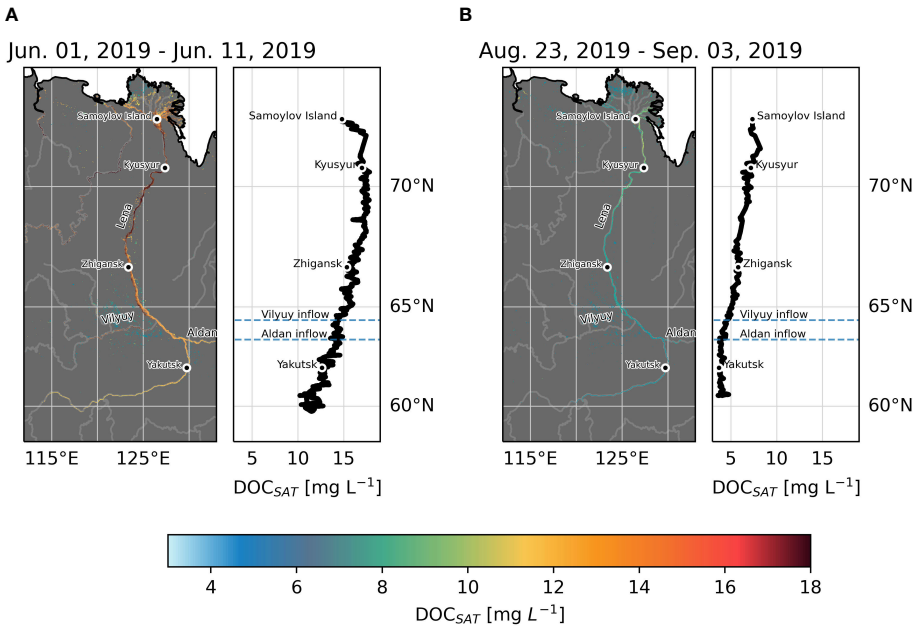


FIGURE 8
10-day Sentinel-3 OLCI DOC$_{SAT}$ concentration composites for the Lena River catchment and extracted transect along the main Lena River stem for **(A)** early June 2019 and **(B)** late August/beginning of September 2019.

impact of particles. Applying the median over all available satellite pixels within a 10 km radius we get a value that represents the current state fairly well. Missing pixels (i.e., ice, clouds, non-converged AC) in a given scene reduce the number of available pixels and can constrain available pixels to a certain area. This might introduce biases and explain some of the larger deviations. None of the following factors had a significant effect on the performance parameters: the number of pixel observations, the standard deviation of the pixels ($\rho_W(665)/\rho_W(560)$) corresponding to a matchup, the spatial distance of the pixels to the *in situ* measurement (up to 10 km), or the temporal offset to an *in situ* observation within a 24-hour time frame.

Nevertheless, the retrieval presented in this study substantially outperforms other state-of-the-art $a_{CDOM}(\lambda)$ retrieval for optically complex and/or coastal Arctic waters. Using the same atmospheric correction (Polymer), the $a_{CDOM}(443,440)$ retrieval algorithms Garver–Siegel–Maritorena model for the Arctic (gsmA) (Matsuoka et al., 2013) and the OLCI Neural Network Swarm (ONNS) (Hieronymi et al., 2017) deliver significantly poorer performances when compared to *in situ* data (Supplementary Figure 9). Of the two algorithms, ONNS shows better results at a R^2 of 0.43 and RMSD of 2.6 m^{-1}, however, it fails to resolve the higher $a_{CDOM}(440)$. This shows that for waters that are optically dominated by one constituent (in this case CDOM), a locally tuned custom algorithm is superior to algorithms that retrieve a set of constituents over a wide array of optical water types. However, band-ratio algorithms such as the one presented in this study need to be adapted if they are planned to be used in other regions or rivers with the same accuracy and precision. This applies both to the satellite retrieval of $a_{CDOM}(\lambda)$ and especially its conversion to DOC_{SAT}, for which sufficient *in situ* data and matchups are necessary that cover the entire range of occurring concentration. Furthermore, the choice of atmospheric correction algorithm and resulting spectra can influence the performance of $a_{CDOM}(\lambda)$ retrievals. The algorithm presented in this study was developed with spectra that were corrected using Polymer. The other retrieval schemes (i.e., ONNS, gsmA) might perform better with spectra from different atmospheric corrections. In the case of the ONNS algorithm, neural networks and a blending of their results are chosen through an optical water type classification. Reflectances from the atmospheric correction Case 2 Regional CoastColour (C2RCC, Brockmann et al., 2016) are better exploitable than reflectances from Polymer using the water type classification scheme of ONNS and Juhls et al. (2022) showed that $a_{CDOM}(440)_{SAT}$ from ONNS performed worked better with C2RCC spectra, rather than Polymer spectra. A new atmospheric correction is currently under development specially designed for ONNS (Hieronymi et al., 2023). Optical remote sensing at high latitudes suffers from a number of challenges. The polar night, low sun elevation in shoulder seasons, and ice and cloud cover substantially reduce the period in which river water can be monitored by remote sensing. The Arctic is prone to a frequent and persistent cloud cover and, in addition, wildfires emit smoke, which can impede optical remote sensing or at least make atmospheric correction even more challenging. Wildfire induced smoke has heavily influenced the observation density in 2021, when large parts of northern Siberia were covered in dense smoke plumes. Another challenge for using remote sensing for river monitoring is the sufficient widths of the river channel relative to the satellite sensor resolution to ensure uncontaminated pixels far enough from the shoreline. Due to the strong seasonality of the hydrograph, the width of the Lena River decreases with lower water level in late summer, reducing the

potential number of valid river pixels that are not influenced by the land. Smaller channels that can be observed at high water levels disappear at low water levels.

Despite these challenges, depending on the number of available clear-sky pixels, a composite spanning the whole catchment of the Lena River can be created using just one to two days of OLCI data. Such composites allow insights into the large-scale distribution of DOC_{SAT} in the Lena River and its short-term dynamics.

5 Conclusion

Satellite sensors such as Sentinel-3 OLCI are traditionally not thought of as capable of monitoring inland waters such as rivers. This study shows that despite being limited to large rivers there is a big potential in the use of moderate resolution imagers for inland river monitoring. We present a new DOC_{SAT} retrieval scheme for Sentinel-3 OLCI for the Lena River that shows a good agreement with *in situ* data collected in the Lena River Delta. The high revisit frequency of the polar orbiting Sentinel-3 satellites can overcome the persistent cloud or wildfire smoke coverage and provides a striking density of remotely sensed observations for surface river water DOC concentrations. Using these high density observations, we were able to calculate DOC_{SAT} fluxes for the spring to fall period for four consecutive years which agree highly with DOC fluxes calculated with *in situ* data. The limitation of optical remote sensing to the ice-free season is compensated by the low DOC fluxes within the ice-covered period. Thus, we can still capture up to 70-75% of the annual DOC flux. Remotely sensed observations are and will become an even more important tool to capture intra-annual and interannual differences and potential trends in DOC fluxes that might be associated with climate change and permafrost thaw induced mobilization of organic carbon. In addition to monitoring DOC fluxes at a single location of the Lena River, we used 10-day Sentinel-3 OLCI composites to derive the DOC concentration along the Lena River. This enabled us to identify increases in DOC concentration from north to south on large scales and helped to pinpoint the tributaries Aldan and Vilyuy as important sources for DOC in the Lena River. The synoptical capacities of satellite-derived observations can provide crucial information to improve our understanding of sources, dynamics and fate of organic carbon in Arctic rivers.

Continuous *in situ* monitoring of Arctic rivers means high logistical and financial costs and is often limited to single locations and/or short time periods. This study shows that satellite-borne DOC monitoring can spatially and temporally complement and expand *in situ* observations to provide a better spatio-temporal coverage. In future studies, the global coverage of satellites can be exploited to expand this work on other (Arctic) rivers if sufficient *in situ* data availability allows an evaluation of the quality of remotely sensed observations. Further, data from other satellite sensors such as MERIS can be used with the presented DOC_{SAT} retrieval scheme in order to expand time series and detect potential trends during the past 20 years that can reveal the impact of climate change and expected consequent carbon mobilization from thawing permafrost in the Arctic. One of the challenges for spatially and temporally expanding the satellite monitoring of rivers is the high amount of data and computation power that is needed. Cloud storage and processing could play an important role in making these feasible.

Data availability statement

The datasets presented in this study can be found in online repositories. The names of the repository/repositories and accession number(s) can be found below: The *in situ* data sets used here are partly already and will further be made available online: https://doi.org/10.1594/PANGAEA.913197.

Author contributions

The initial idea and concept and methodology was developed by JE and BJ. Data acquisition and processing was done by JE, BJ, RP and MH. The writing of the original draft was led by JE and BJ and PO, MH, AM, RP, and JF contributed. Review and editing were done by JE, BJ, PO, MH, AM, RP, JF. All authors contributed to the article and approved the submitted version.

Funding

BJ has been funded by the European Space Agency (ESA) as part of the Climate Change Initiative (CCI) fellowship (ESA ESRIN/Contract No. 4000133761/21/I-NB). This research has been supported by the EU Horizon 2020 programme (Nunataryuk, grant no. 773421). MH has been funded by the Helmholtz research programme "Changing Earth – Sustaining our Future" Subtopic 4.1.

Acknowledgments

The Lena River Water Monitoring was conducted in the frame of the Russian-German LENA Expeditions and based at Research Station Samoylov Island. We thank all colleagues and station staff involved in the organizational and logistical support of the monitoring program. We especially thank Sergey Volkov, Andrei Astapov, and Ekaterina Abramova for the water sampling on Samoylov Island. Further we thank Antje Eulenburg, Martha Lütjen, Pia Esterl, Birgit Heim and Henrike Walther for their expertise and dedication to the analysis. For logistical support related to the Samoylov Lena River monitoring and Lena expeditions we thank Dr. Sofia Antonova, Jan Kahl, and Volkmar Aßmann. We acknowledge support by the Open Access Publication Initiative of Freie Universität Berlin.

Conflict of interest

The authors declare that the research was conducted in the absence of any commercial or financial relationships that could be construed as a potential conflict of interest.

Publisher's note

All claims expressed in this article are solely those of the authors and do not necessarily represent those of their affiliated organizations, or those of the publisher, the editors and the reviewers. Any product that may be evaluated in this article, or claim that may be made by its manufacturer, is not guaranteed or endorsed by the publisher.

Supplementary material

The Supplementary Material for this article can be found online at: https://www.frontiersin.org/articles/10.3389/fmars.2023.1082109/full#supplementary-material

References

Aagaard, K., and Carmack, E. C. (1989). The role of sea ice and other fresh water in the Arctic circulation. *J. Geophysical Res.* 94 (C10), 14485. doi: 10.1029/jc094ic10p14485

Amon, R. M. W., Rinehart, A. J., Duan, S., Louchouarn, P., Prokushkin, A., Guggenberger, G., et al. (2012). Dissolved organic matter sources in large Arctic rivers. *Geochimica Cosmochimica Acta* 94, 217–237. doi: 10.1016/j.gca.2012.07.015

Babin, M., Stramski, D., Ferrari, G. M., Claustre, H., Bricaud, A., Obolensky, G., et al. (2003). Variations in the light absorption coefficients of phytoplankton, nonalgal particles, and dissolved organic matter in coastal waters around Europe. *J. Geophysical Research: Oceans* 108 (7), 3211–3231. doi: 10.1029/2001jc000882

Bertin, C., Matsuoka, A., Mangin, A., Babin, M., and le Fouest, V. (2022). Merging satellite and *in situ* data to assess the flux of terrestrial dissolved organic carbon from the Mackenzie river to the coastal Beaufort Sea. *Front. Earth Sci.* 10 (January). doi: 10.3389/feart.2022.694062

Boggs, P. T., and Rogers, J. E. (1990). Orthogonal distance regression. *Center for Computing and Applied Mathematics, US Department of Commerce* 1989, 183–194. doi: 10.1090/conm/112/1087109

Brockmann, C., Doerffer, R., Peters, M., Stelzer, K., Embacher, S., Ruescas, A., et al. (2016). "Evolution of the C2RCC neural network for Sentinel 2 and 3 for the retrieval of ocean colour products in normal and extreme optically complex waters," in *Proceeding of Living Planet Symposium*, Prague: ESA SP, Volume 740. Available at: https://www.brockmann-consult.de/wp-content/uploads/2017/11/sco1_12brockmann.pdf.

Brüchert, V., Bröder, L., Sawicka, J. E., Tesi, T., Joye, S. P., Sun, X., et al. (2018). Carbon mineralization in laptev and East Siberian sea shelf and slope sediment. *Biogeosciences* 15 (2), 471–490. doi: 10.5194/bg-15-471-2018

Cao, F., and Tzortziou, M. (2021). Capturing dissolved organic carbon dynamics with landsat-8 and sentinel-2 in tidally influenced wetland–estuarine systems. *Sci. Total Environ.* 777, 145910. doi: 10.1016/j.scitotenv.2021.145910

Carlson, C. A., and Hansell, D. A. (2015). "DOM sources, sinks, reactivity, and budgets," in *Biogeochemistry of marine dissolved organic matter: Second edition*. doi: 10.1016/B978-0-12-405940-5.00003-0

Charkin, A. N., Dudarev, O. V., Semiletov, I. P., Kruhmalev, A. V., Vonk, J. E., Sánchez-García, L., et al. (2011). Seasonal and interannual variability of sedimentation and organic matter distribution in the buor-khaya gulf: The primary recipient of input from Lena river and coastal erosion in the southeast laptev Sea. *Biogeosciences* 8 (9), 2581–2594. doi: 10.5194/bg-8-2581-2011

Efron, B., and Tibshirani, R. J. (1994). *An introduction to the bootstrap* (New York, USA: Chapman and Hall/CRC). doi: 10.1201/9780429246593

EUMETSAT (2019) *Recommendations for sentinel-3 OLCI ocean colour product validations in comparison with in situ measurements-matchup protocols*. Available at: http://www.eumetsat.int.

Fichot, C. G., Benner, R., Kaiser, K., Shen, Y., Amon, R. M. W., Ogawa, H., et al. (2016). Predicting dissolved lignin phenol concentrations in the coastal ocean from chromophoric dissolved organic matter (CDOM) absorption coefficients. *Front. Mar. Sci.* 3 (FEB). doi: 10.3389/fmars.2016.00007

Frey, K. E., and McClelland, J. W. (2009). Impacts of permafrost degradation on arctic river biogeochemistry. *Hydrological Processes* 23 (1), 169–182. doi: 10.1002/hyp.7196

Fuchs, M., Palmtag, J., Juhls, B., Overduin, P. P., Grosse, G., Abdelwahab, A., et al. (2022). High-resolution bathymetry models for the Lena delta and kolyma gulf coastal zones. *Earth System Sci. Data* 14 (5), 2279–2301. doi: 10.5194/essd-14-2279-2022

Gonçalves-Araujo, R., Stedmon, C. A., Heim, B., Dubinenkov, I., Kraberg, A., Moiseev, D., et al. (2015). From fresh to marine waters: Characterization and fate of dissolved organic matter in the Lena river delta region, Siberia. *Front. Mar. Sci.* 2. doi: 10.3389/fmars.2015.00108

Griffin, C. G., Frey, K. E., Rogan, J., and Holmes, R. M. (2011). Spatial and interannual variability of dissolved organic matter in the kolyma river, East Siberia, observed using satellite imagery. *J. Geophysical Research: Biogeosciences* 116 (3), 1–12. doi: 10.1029/2010JG001634

Griffin, C. G., McClelland, J. W., Frey, K. E., Fiske, G., and Holmes, R. M. (2018). Quantifying CDOM and DOC in major Arctic rivers during ice-free conditions using landsat TM and ETM+ data. *Remote Sens. Environ.* 209 (October 2017), 395–409. doi: 10.1016/j.rse.2018.02.060

Guo, L., Ping, C. L., and Macdonald, R. W. (2007). Mobilization pathways of organic carbon from permafrost to arctic rivers in a changing climate. *Geophysical Res. Lett.* 34 (13), 1–5. doi: 10.1029/2007GL030689

Herrault, P. A., Gandois, L., Gascoin, S., Tananaev, N., le Dantec, T., and Teisserenc, R. (2016). Using high spatio-temporal optical remote sensing to monitor dissolved organic carbon in the Arctic river yenisei. *Remote Sens.* 8 (10), 803–820. doi: 10.3390/rs8100803

Hieronymi, M., Bi, S., Müller, D., Schütt, E. M., Behr, D., and Brockmann, C. (2023). Ocean color atmospheric correction methods in view of usability for different optical water types. *Front. Mar. Sci* 10.

Hieronymi, M., Müller, D., and Doerffer, R. (2017). The OLCI neural network swarm (ONNS): A bio-geo-optical algorithm for open ocean and coastal waters. *Front. Mar. Sci.* 4 (MAY). doi: 10.3389/fmars.2017.00140

Holmes, R. M., Coe, M. T., Fiske, G. J., Gurtovaya, T., Mcclelland, J. W., Shiklomanov, A. I., et al. (2013). "Climate change impacts on the hydrology and biogeochemistry of Arctic rivers," in *Climatic change and global warming of inland waters: Impacts and mitigation for ecosystems and societies*, 3–26.

Holmes, R. M., McClelland, J. W., Peterson, B. J., Tank, S. E., Bulygina, E., Eglinton, T. I., et al. (2012). Seasonal and annual fluxes of nutrients and organic matter from Large rivers to the Arctic ocean and surrounding seas. *Estuaries Coasts* 35 (2), 369–382. doi: 10.1007/s12237-011-9386-6

Huang, J., Wu, M., Cui, T., and Yang, F. (2019). Quantifying DOC and its controlling factors in major arctic rivers during ice-free conditions using sentinel-2 data. *Remote Sens.* 11 (24), 2904–2924. doi: 10.3390/rs11242904

IOCCG (2000) *IOCCG report number 03: Remote sensing of ocean colour in coastal, and other optically-complex, waters*. Available at: http://www.vliz.be/imis/imis.php?module=ref&refid=134621&request=147862.

IOCCG (2010) *IOCCG report number 10: Atmospheric correction for remotely-sensed ocean-colour products*. Available at: http://www.ioccg.org/reports/report10.pdf.

IOCCG (2015) *IOCCG report number 16: Ocean colour remote sensing in polar seas general introduction*. Available at: www.ioccg.org/reports/IOCCG_Report_16_2015.pdf.

Juhls, B., Antonova, S., Angelopoulos, M., Bobrov, N., Grigoriev, M., Langer, M., et al. (2021). Serpentine (Floating) ice channels and their interaction with riverbed permafrost in the Lena river delta, Russia. *Front. Earth Sci.* 9 (July). doi: 10.3389/feart.2021.689941

Juhls, B., Matsuoka, A., Lizotte, M., Bécu, G., Overduin, P. P., el Kassar, J., et al (2022). Seasonal dynamics of dissolved organic matter in the Mackenzie delta, Canadian Arctic waters: Implications for ocean colour remote sensing. *Remote Sens. Environment* 283, 113327–113346. doi: 10.1016/j.rse.2022.113327

Juhls, B., Paul Overduin, P., Hölemann, J., Hieronymi, M., Matsuoka, A., Heim, B., et al. (2019). Dissolved organic matter at the fluvial-marine transition in the laptev Sea using *in situ* data and ocean colour remote sensing. *Biogeosciences* 16 (13), 2693–2713. doi: 10.5194/bg-16-2693-2019

Juhls, B., Stedmon, C. A., Morgenstern, A., Meyer, H., Hölemann, J., Heim, B., et al. (2020). Identifying drivers of seasonality in Lena river biogeochemistry and dissolved organic matter fluxes. *Front. Environ. Sci.* 8 (May). doi: 10.3389/fenvs.2020.00053

König, M., Hieronymi, M., and Oppelt, N. (2019). Application of sentinel-2 msi in arctic research: Evaluating the performance of atmospheric correction approaches over arctic sea ice. *Front. Earth Sci.* 7 (February). doi: 10.3389/feart.2019.00022

Laukert, G., Frank, M., Bauch, D., Hathorne, E. C., Rabe, B., von Appen, W. J., et al. (2017). Ocean circulation and freshwater pathways in the Arctic Mediterranean based on a combined Nd isotope, REE and oxygen isotope section across fram strait. *Geochimica Cosmochimica Acta* 202, 285–309. doi: 10.1016/j.gca.2016.12.028

Lewis, K. M., and Arrigo, K. R. (2020). Ocean color algorithms for estimating chlorophyll a, CDOM absorption, and particle backscattering in the Arctic ocean. *J. Geophysical Research: Oceans* 125 (6), 1–23. doi: 10.1029/2019JC015706

Mabit, R., Araújo, C. A. S., Singh, R. K., and Bélanger, S. (2022). Empirical remote sensing algorithms to retrieve SPM and CDOM in québec coastal waters. *Front. Remote Sens.* 3 (April). doi: 10.3389/frsen.2022.834908

Matsuoka, A., Boss, E., Babin, M., Karp-Boss, L., Hafez, M., Chekalyuk, A., et al. (2017). Pan-Arctic optical characteristics of colored dissolved organic matter: Tracing dissolved organic carbon in changing Arctic waters using satellite ocean color data. *Remote Sens. Environ.* 200 (December 2016), 89–101. doi: 10.1016/j.rse.2017.08.009

Matsuoka, A., Hooker, S. B., Bricaud, A., Gentili, B., and Babin, M. (2013). Estimating absorption coefficients of colored dissolved organic matter (CDOM) using a semi-analytical algorithm for southern Beaufort Sea waters: Application to deriving concentrations of dissolved organic carbon from space. *Biogeosciences* 10 (2), 917–927. doi: 10.5194/bg-10-917-2013

McClelland, J. W., Déry, S. J., Peterson, B. J., Holmes, R. M., and Wood, E. F. (2006). A pan-arctic evaluation of changes in river discharge during the latter half of the 20th century. *Geophysical Res. Lett.* 33 (6), 1–4. doi: 10.1029/2006GL025753

McClelland, J. W., Holmes, R. M., Peterson, B. J., Raymond, P. A., Striegl, R. G., Zhulidov, A. V., et al. (2016). Particulate organic carbon and nitrogen export from major Arctic rivers. *Global Biogeochemical Cycles* 30 (5), 629–643. doi: 10.1002/2015GB005351

Menard, H. W., and Smith, S. M. (1966). Hypsometry of ocean basin provinces. *J. Geophysical Res.* 71 (18), 4305–4325. doi: 10.1029/JZ071i018p04305

Obu, J., Westermann, S., Bartsch, A., Berdnikov, N., Christiansen, H. H., Dashtseren, A., et al. (2019). Northern hemisphere permafrost map based on TTOP modelling for 2000–2016 at 1 km2 scale. *Earth-Science Rev.* 193 (April), 299–316. doi: 10.1016/j.earscirev.2019.04.023

Opsahl, S., Benner, R., and Amon, R. M. W. (1999). Major flux of terrigenous dissolved organic matter through the Arctic ocean. *Limnology Oceanography* 44 (8), 2017–2023. doi: 10.4319/lo.1999.44.8.2017

Pefanis, V., Losa, S. N., Losch, M., Janout, M. A., and Bracher, A. (2020). Amplified Arctic surface warming and Sea ice loss due to phytoplankton and colored dissolved material. *Geophysical Res. Lett.* 47 (21). doi: 10.1029/2020GL088795

Peterson, B. J., Holmes, R. M., McClelland, J. W., Vörösmarty, C. J., Lammers, R. B., Shiklomanov, A. I., et al. (2002). Increasing river discharge to the Arctic ocean. *Science* 298 (5601), 2171–2173. doi: 10.1126/science.1077445

Prowse, T., Alfredsen, K., Beltaos, S., Bonsal, B., Duguay, C., Korhola, A., et al. (2011). Past and future changes in arctic lake and river ice. *Ambio* 40 (SUPPL. 1), 53–62. doi: 10.1007/s13280-011-0216-7

Qin, P., Simis, S. G. H., and Tilstone, G. H. (2017). Radiometric validation of atmospheric correction for MERIS in the Baltic Sea based on continuous observations from ships and AERONET-OC. *Remote Sens. Environ.* 200 (August), 263–280. doi: 10.1016/j.rse.2017.08.024

Rantanen, M., Karpechko, A. Y., Lipponen, A., Nordling, K., Hyvärinen, O., Ruosteenoja, K., et al. (2022). The Arctic has warmed nearly four times faster than the globe since 1979. *Commun. Earth Environ.* 3 (1), 1–10. doi: 10.1038/s43247-022-00498-3

Raymond, P. A., McClelland, J. W., Holmes, R. M., Zhulidov, A. V., Mull, K., Peterson, B. J., et al. (2007). Flux and age of dissolved organic carbon exported to the Arctic ocean: A carbon isotopic study of the five largest arctic rivers. *Global Biogeochemical Cycles* 21 (4), 1–9. doi: 10.1029/2007GB002934

Runkel, R. L., Crawford, C. G., and Cohn, T. A. (2004). Load estimator (LOADEST): A FORTRAN program for estimating constituent loads in streams and rivers. *Techniques Methods U.S. Geological Survey. U.S. Department Interior* 4, 69. doi: 10.3133/tm4A5

Semiletov, I., Pipko, I., Gustafsson, Ö., Anderson, L. G., Sergienko, V., Pugach, S., et al. (2016). Erratum: Acidification of East Siberian Arctic shelf waters through addition of freshwater and terrestrial carbon (Nature geoscience, (2016) 9 (361-365)). *Nat. Geosci.* 9 (6), 368. doi: 10.1038/ngeo2726

Shiklomanov, A. I., Holmes, R. M., McClelland, J. W., Tank, S. E., and Spencer, R. G. M. (2021). *ArcticGRO discharge dataset* (Arctic Great Rivers Observatory). Available at: https://www.arcticrivers.org/data.

Soppa, M. A., Pefanis, V., Hellmann, S., Losa, S. N., Hölemann, J., Janout, M. A., et al. (2019). Assessing the influence of water constituents on the radiative heating of laptev Sea shelf waters. *Front. Mar. Sci.* 6 (APR). doi: 10.3389/fmars.2019.00221

Stedmon, C. A., Amon, R. M. W., Rinehart, A. J., and Walker, S. A. (2011). The supply and characteristics of colored dissolved organic matter (CDOM) in the Arctic ocean: Pan Arctic trends and differences. *Mar. Chem.* 124 (1–4), 108–118. doi: 10.1016/j.marchem.2010.12.007

Steinmetz, F., Deschamps, P.-Y., and Ramon, D. (2011). Atmospheric correction in presence of sun glint: Application to MERIS. *Optics Express* 19 (10), 9783. doi: 10.1364/oe.19.009783

Steinmetz, F., and Ramon, D. (2018). "Sentinel-2 MSI and sentinel-3 OLCI consistent ocean colour products using POLYMER," in *Remote sensing of the open and coastal ocean and inland waters*. Eds. R. J. Frouin and H. Murakami (Honolulu, USA: SPIE), 13. doi: 10.1117/12.2500232

Terhaar, J., Lauerwald, R., Regnier, P., Gruber, N., and Bopp, L. (2021). Around one third of current Arctic ocean primary production sustained by rivers and coastal erosion. *Nat. Commun.* 12 (1), 1–10. doi: 10.1038/s41467-020-20470-z

Warren, M. A., Simis, S. G. H., Martinez-Vicente, V., Poser, K., Bresciani, M., Alikas, K., et al. (2019). Assessment of atmospheric correction algorithms for the sentinel-2A MultiSpectral imager over coastal and inland waters. *Remote Sens. Environ.* 225 (March), 267–289. doi: 10.1016/j.rse.2019.03.018

Wegner, C., Bauch, D., Hölemann, J. A., Janout, M. A., Heim, B., Novikhin, A., et al. (2013). Interannual variability of surface and bottom sediment transport on the laptev Sea shelf during summer. *Biogeosciences* 10 (2), 1117–1129. doi: 10.5194/bg-10-1117-2013

Wild, B., Andersson, A., Bröder, L., Vonk, J., Hugelius, G., McClelland, J. W., et al. (2019). Rivers across the Siberian Arctic unearth the patterns of carbon release from thawing permafrost. *Proc. Natl. Acad. Sci. United States America* 116 (21), 10280–10285. doi: 10.1073/pnas.1811797116

Ye, B., Yang, D., and Kane, D. L. (2003). Changes in Lena river streamflow hydrology: Human impacts versus natural variations. *Water Resour. Res.* 39 (7), 1–14. doi: 10.1029/2003WR001991

frontiers | Frontiers in Marine Science

TYPE Original Research
PUBLISHED 03 April 2023
DOI 10.3389/fmars.2023.1052307

Check for updates

OPEN ACCESS

EDITED BY
Victor Martinez-Vicente,
Plymouth Marine Laboratory,
United Kingdom

REVIEWED BY
Stella Psarra,
Hellenic Centre for Marine Research (HCMR), Greece
Zcaronarko Kovaccaron,
University of Split, Croatia

*CORRESPONDENCE
John F. Marra
jfm7780@brooklyn.cuny.edu

SPECIALTY SECTION
This article was submitted to Ocean Observation, a section of the journal Frontiers in Marine Science

RECEIVED 23 September 2022
ACCEPTED 13 March 2023
PUBLISHED 03 April 2023

CITATION
Marra JF, Chamberlin WS, Knudson CA, Rhea WJ and Ho C (2023) Parameters for the depth of the ocean's productive layer *Front. Mar. Sci.* 10:1052307. doi: 10.3389/fmars.2023.1052307

COPYRIGHT
© 2023 Marra, Chamberlin, Knudson, Rhea and Ho. This is an open-access article distributed under the terms of the Creative Commons Attribution License (CC BY). The use, distribution or reproduction in other forums is permitted, provided the original author(s) and the copyright owner(s) are credited and that the original publication in this journal is cited, in accordance with accepted academic practice. No use, distribution or reproduction is permitted which does not comply with these terms.

Parameters for the depth of the ocean's productive layer

John F. Marra[1,2*], W. Sean Chamberlin[3], Carol A. Knudson[4], W. Joseph Rhea[5] and Cheng Ho[4]

[1]Earth and Environmental Sciences, Brooklyn College of the City University of New York, Brooklyn, NY, United States, [2]Earth and Environmental Sciences, Graduate Center of the City University of New York, New York, NY, United States, [3]Earth Sciences, Fullerton College, Fullerton, CA, United States, [4]Lamont-Doherty Earth Observatory of Columbia University, Palisades, NY, United States, [5]Naval Research Laboratory, Washington, DC, United States

Here we compare various parameters that are used to define the depth of the ocean's productive layer, the euphotic zone, during the initiation of the spring phytoplankton bloom in the North Atlantic (47°N/20°W). These are (1) the compensation depth (*Zc*, where gross photosynthesis balances autotrophic respiration), (2) the depth horizon of 1% of surface photosynthetic active irradiance (Ed(0$^-$,PAR), (3) depth horizon of 1% of surface Ed(488), and (4) the depth of the bottom of the fluorescence maximum. We also use two related parameters, the depth of the mixed layer and the ratio of integral gross production to integral respiration as a scaling factor for a proxy for the critical depth. Over the course of the observational period (25 April - 7 May, 1989), the mixed layer decreased from 162 to 20 m, and *Zc* decreased from 64 to 35 m. The depth of 1%Ed(0$^-$,PAR) followed the trajectory of *Zc*, while Ed(488) and the depth of the bottom of the fluorescence maximum were about 10 m deeper, on average. These data support the criterion of the depth of "1%PAR" to describe the productive layer for more productive areas of the ocean. However, 1% of Ed(488) or the bottom of the fluorescence maximum could be used over a broader range of trophic conditions.

KEYWORDS

radiometer, productivity, respiration, euphotic depth, PAR, fluorescence

Introduction

For decades, oceanographers have defined the depth limit of ocean productivity operationally, that is, by mutual agreement. Following Ryther (1956), the productive layer, or euphotic zone, extends to the depth at which irradiance declines to 1% of its surface value. Below that depth, according to Ryther (1956), "no appreciable photosynthesis" occurs. It is a definition that has endured. However, the actual depth of the ocean's productive layer is complicated by the ability of phytoplankton to adapt to low levels of irradiance, including a lowered respiratory demand at depth. Further, the productive layer may be defined by species differences. Observations of significant chlorophyll-a concentrations below the 1% light level have been widely reported (e.g.,

Laws et al., 2014), and many species (e.g., *Planktoniella* sp. and *Navicula* sp. in Goldman, 1993) appear able to thrive at very low irradiance levels. Thus, the so-called "euphotic zone" may be considered an optical parameter with limited biological relevance, as noted by Ryther (1956), and recently by Wu et al. (2021). As Banse (2004) pointed out, "The 1% depth for moonlight is about as deep as that for sunlight."

Oceanographers often approximate the irradiance decline with depth using an attenuation coefficient averaged over depth. The corresponding compensation irradiance—a light intensity where gross photosynthesis is balanced by respiration—may be applied at physiological time scales (e.g., Falkowski et al., 1985; Geider et al., 1986), over the growth of a population (Langdon, 1987), or even at the community level (Regaudie-de-Gioux and Duarte, 2010). Knowledge of the compensation irradiance permits calculation of an analogous compensation *depth*, the distance below the sea surface at which the compensation irradiance is reached. Thus, if we know the compensation irradiance, we can also know the compensation depth and the depth of the ocean's productive layer. As Patten (1961) puts it, "All the complexity of trophodynamic action devolves to this single variable…."

Gran and Braarud (1935) and later, Riley (1942), introduced mixing into the dynamics of the productive layer, noting that if respiration was a small fraction of production, that phytoplankton could be mixed below the compensation depth and still have positive primary production. Sverdrup (1953) extended these ideas such that they could be applied more broadly (Behrenfeld and Boss, 2017). His "critical depth" theory also addressed the balance between respiration and photosynthesis integrated over depth, and including surface irradiance and light attenuation. When the mixing depth (from the surface) of the phytoplankton is less than the depth where integral photosynthesis equals integral respiration, then the phytoplankton can accumulate. In Sverdrup (1953) model, shoaling of the mixed layer shallower than the critical depth initiates the spring bloom in the North Atlantic.

Outside of laboratory studies, the compensation irradiance for phytoplankton is poorly known (e.g., Geider et al., 1992; Langdon, 1998). Marra (2004) calculated a compensation irradiance that corresponded with the 1% light depth for PAR using the time courses of chlorophyll-a at different depths over the course of the boreal North Atlantic spring bloom, assuming a critical depth criterion, and arguing for an autotrophic compensation irradiance. Even so, the 1% irradiance horizon for the euphotic zone depth has been widely criticized. In middle and high latitudes, the compensation irradiance changes seasonally (Lorenzen, 1976; Banse, 2004; Kirk, 2011). Using satellite-derived ocean color to mark the initiation of the North Atlantic spring bloom, Siegel et al. (2002) found compensation irradiances higher than those observed in laboratory culture. But since ocean color measures only biomass changes, it includes losses from grazing as well as autotrophic respiration.

Determining the compensation irradiance, the compensation depth, or the critical depth, in natural populations remains challenging largely because autotrophic respiration is not directly measurable by the methods used to measure primary production. Fluxes of oxygen will estimate respiration, but the autotrophic component to community respiration cannot be discriminated. Dissolved oxygen fluxes will estimate community respiration in incubations kept in the dark. Autotrophic respiration may only be estimated assuming the dark consumption of oxygen is the same as that occurring in the light. Marra and Barber (2004) showed how autotrophic respiration could be estimated from dawn-to-dusk and 24-hr incubations with ^{14}C. Based on a larger data set, Marra (2009) confirmed Marra and Barber (2004) and showed agreement between gross production estimated from both ^{14}C and from ^{18}O incubations.

Marra et al. (2014) estimated the depth of the productive layer in the NW Atlantic using measured rates of net primary production and calculations of respiration and gross primary production. Although the data are limited, the depth of the productive layer exceeded the 1% light depth and corresponded most closely with the 1% depth for blue light, i.e., 490 nm, the most penetrating wavelength. Laws et al. (2014) reported similar findings at station ALOHA with a compensation irradiance equal to 0.1% of surface light (400–700 nm) and 1% of blue light at 475 nm. Using optical and biological measurements to estimate the euphotic zone depth at the Hawaii Ocean Time-series and Bermuda Atlantic Time-series, Wu et al. (2021) found compensation irradiances generally aligned with the 0.5% depth of surface intensity or 1.5% depth for blue light (490 nm).

Compensation irradiance from various studies (compiled in Table 1) vary by an order of magnitude and seem not to depend on whether the community or autotrophic compensation depth is estimated. Thus, considerable disagreement remains over the appropriate definition of compensation depth based on surface light intensity. Here, we re-analyze data from the first (pilot) experiment of the Joint Global Ocean Flux Study (JGOFS), the North Atlantic Bloom Experiment (NABE) in April-May 1989. Data from the first process leg of that experiment (24 April–8 May) still retain features that speak to current ideas surrounding the specification of the ocean's productive layer.

Methods

The North Atlantic Bloom Experiment (NABE) was the initial process study of the Joint Global Ocean Flux Study (JGOFS), an international program. NABE included ships from the United Kingdom, Germany, Netherlands, and Canada. The U. S. component of NABE consisted of three cruises aboard the RV Atlantis II in April and May of 1989. The first cruise deployed sediment traps, and the succeeding two cruises observed the initiation and progression of the North Atlantic spring bloom from 34°N to 60°N along the longitude of 20°W. The data reported here came from the second of the three cruises, Atlantis II cruise 119-4.

The relevant core data are listed on the JGOFS website (http://usjgofs.whoi.edu/jg/dir/jgofs/nabe/atlantisII/), although not all the data collected was submitted to the website. For example, only 24-hr incubations for primary production measurements were an identified JGOFS data contribution. We also did 14-hr (dawn-to-dusk) incubations for ^{14}C assimilation (e.g., Knudson et al., 1989), and together with the 24-hr incubation data, were used to calculate gross primary production, autotrophic respiration and the compensation depth, as described below. The JGOFS website

TABLE 1 Literature values of the compensation depth estimated in nature.

Study	Ec, mol photons/m^2/d	Type
Jenkin (1937), incubation of diatom cultures at various depths in the water column	0.5	Autotrophic
Najjar & Keeling (1997), estimated from a depth shift in the oxygen anomaly	0.3	Community
Siegel et al. (2002) from initial increases in satellite ocean color in the North Atlantic	1.0–1.8	Community
Wiggert et al. (2002), based on a model of production v. consumption	0.2	Community
Marra (2004) from chlorophyll-a changes during the spring bloom in the North Atlantic	0.1–0.3	Autotrophic
Laws et al. (2014) estimated by linear regressions of difference between light and dark-bottle ^{14}C uptake	0.054	Autotrophic ()?
Wu et al. (2021) estimated from *in situ* data sets	0.17–0.36	Autotrophic ()?

includes a summary of the methods for each of the parameters reported here. Details of the methods for *in situ* primary productivity can also be found in Knudson et al. (1989); Chipman et al. (1993), and Marra and Ho (1993), and Kiddon et al. (1995). Importantly, depths for the productivity measurements were collected at 5-10 m intervals over 3-50 m, and not in accordance with light depths. A typical set of sampling depths would be 3, 10, 20, 30, 40, and 50 m. The complete set of values is reported on the JGOFS website noted above.

Surface daily PAR data are provided on the JGOFS website by W. Broenkow (Moss Landing Marine Laboratories). PAR as a function of depth was measured with a Biospherical 4-pi PAR sensor lowered through the water column at local noon each day (Knudson et al., 1989). These data are also reported by Kiddon et al. (1995). Attenuation coefficients were calculated from linear regressions of the natural logarithm of PAR as a function of depth. We also calculated attenuation coefficients from (less frequent) casts using a Biospherical Marine Environmental Recorder (MER-2040) for PAR (quanta cm^{-2} s^{-1}), Ed(488) (mW cm^{-2} nm^{-1}), and chlorophyll-a fluorescence. These data are also available through the JGOFS data website with the methods specified.

Mixed layer depths were determined from the early-morning CTD casts near the time of the collection of water for the biological measurements (see Marra and Ho, 1993; Marra, 1995).

Calculations for the parameters

We calculate five separate parameters. First is the depth where 1% of surface irradiance (PAR) remains, the traditional and consensus definition for the depth of the euphotic zone. Thus,

$$E1\,\% = -4.506/Kd(PAR) \quad (1)$$

where PAR refers to photosynthetically active radiation, 4.506 is the natural log of 1%, i.e., ln(0.01). Kd(PAR) was determined from the slope of the linear regression of ln(Ed(PAR,z), where z is depth.

$$Kd(PAR) = ln[Ed(PAR, 0^-)/Ed(PAR, Z)] \quad (2)$$

Similarly, for downwelling blue light,

$$Kd(Ed488) = ln[Ed(488, 0^-]/Ed(488, Z) \quad (3)$$

Inspection of the profiles reveals that ln(PAR) and ln(Ed488) as a function of depth are very close to linear, resulting in a depth-independent value for each day of the cruise.

The second parameter is the depth of the mixed layer, which regulates much of surface ocean dynamics. Here we define the depth of the mixed layer as the depth at which the difference from the surface temperature is 0.2°C.

The remaining three parameters result from biological processes. These are the compensation depth, the depth of the base of the fluorescence maximum, and a proxy for the critical depth.

The compensation depth occurs where gross primary productivity equals autotrophic respiration. Autotrophic respiration, R_p (mmols C m^{-3} d^{-1}) was calculated as in Marra and Barber (2004) and Marra et al. (2014). Thus,

$$R_p = (A_L - A_{L+D})/f \quad (4)$$

where A_L is the assimilation after a dawn-dusk incubation, and A_{L+D} is the carbon assimilation after 24 h, dawn to dawn. Using this method, R_p can only be calculated at the daily time scale. The factor f is the fraction of darkness each day, which for the late April–early May timeframe at 47°N is 10/24 = 0.42. Daily gross production, G (mmols C m^{-3} d^{-1}), can be calculated similarly as,

$$G = A_{L+D} + (A_L - A_{L+D})/f \quad (5)$$

and we define net production, P (mmols C m^{-3} d^{-1}), as

$$P = A_{L+D} \quad (6)$$

The compensation depth, Zc, is the depth where

$$G = R_p \quad (7)$$

To estimate *Zc*, we determined the intersection of the regression lines from values at the bottom three depths for both *G* and R_p.

There have been questions about the importance of "dark uptake" of ^{14}C during the incubations, which has potential importance deeper in the euphotic zone. It can be shown, however, that if dark uptake during the day is the same as at night, then in relating daytime and nighttime assimilation, dark uptake cancels out in both estimates.

The fourth parameter is the depth of the base of the fluorescence maximum. Estimating this depth objectively is a difficult problem. As for estimating *Zc*, we used the intersection of two regression

lines, one from the bottom of the profile and the other from the depth of the fluorescence maximum itself to the depth where fluorescence is at background. An example profile is presented in the Appendix.

Finally, we use a related parameter, a proxy for the critical depth (Sverdrup, 1953). Since we have daily measurements of the depth of the mixed layer, it is useful to see if our approximation of the critical depth can be interpreted with those changes. Our simplified proxy derives from Gran and Braarud (1935) and Riley (1942), where the ratio of photosynthesis to respiration in phytoplankton subject to vertical mixing indicates how deep the productive layer can extend. For example, if respiration is 20% of photosynthesis, phytoplankton can be mixed to five times (1/0.2) the compensation depth and maintain their population. We use the ratio of the integrated gross production (G) to integrated autotrophic respiration (R_p) to thus extend the compensation depth (with the integrals approximated according to the trapezoidal rule), and use the 1% light depth as a more direct estimate of the compensation depth, as shown below (see Results). Accordingly,

$$Dc \quad (\int_0^z G / \int_0^z Rp) \cdot E1\% \qquad (8)$$

where here, Dc is the proxy critical depth, $E1\%$ refers to the 1% light depth, as defined above, and z = 50 m. We chose this simplified proxy for the critical depth to be more independent of the other parameters. Following Gran and Braarud (1935), we recognize that this parameter is approximate and, in relation to the mixed layer depth, describes only a potential for increasing phytoplankton biomass (provided no other loss processes apply).

Results

The results are summarized in Figure 1 and Table 2. Mixed layer depths decrease throughout the observational period, with the exception of 4 May (YD124). On that day, the Atlantis II re-positioned for other projects and passed through a hydrographic boundary (see McGillicuddy et al., 1995). Nevertheless, after 1 May, the mixed layer depth remained shallower than 60 m and most often, 30 m or less (see also Marra, 1995). Plots of the vertical distributions of ^{14}C assimilation can be found in Kiddon et al. (1995) and the depth-time changes to chlorophyll-a can be found in Marra and Ho (1993).

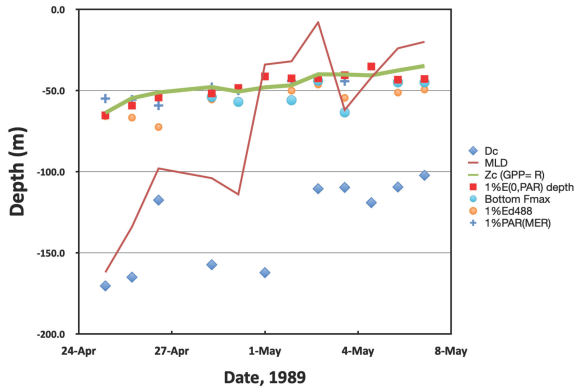


FIGURE 1
Time course of the various parameters over the observational period. There are no appropriate ^{14}C assimilation data for 28 April. Also, there was no fluorescence maximum for the first three days of observations. Dc is a proxy for the critical depth (Eq. 8). Dc for 29 April and 2 May exceed -200 m (see Table 2) and are not plotted. MLD = mixed layer depth, Zc is the compensation depth. 1% Ed(488) and 1%PAR(MER) are data from the Biospherical Marine Environmental Recorder (MER-2040).

The compensation depth (Zc), where $G = R_p$, also decreased more or less steadily over the observational period, from about 60 m to about 35 m. For the first three days of observation (25, 26, 27 April), our proxy for the critical depth (Dc in Figure 1) approximates the mixed layer depth, but slightly deeper. After that, Dc is always deeper than the mixed layer depth.

TABLE 2 Values (in meters) of the five parameters associated with euphotic zone depth (see Figure 1) plus areal chlorophyll-a (intChla; mg m^{-3}).

YD	day-month	Dc	MLD	intChla	Zc	1% Ed (0¯,PAR)	1% Ed (0¯,488)	Base of Fluorescence maximum
115	25-Apr	-170.4	-162.0	32.22	-63.76	-65.30	-65.88	ND
116	26-Apr	-165.0	-134.0	47.14	-54.72	-59.29	-66.71	ND
117	27-Apr	-117.5	-98.0	39.53	-51.18	-54.29	-72.52	ND
118	29-Apr	-157.3	-104.0	45.39	-47.85	-51.79	-55.56	-54
119	30-Apr	-246.6	-114.0	41.25	-50.69	-48.45	-57.42	-57
120	1-May	-162.2	-34.0	34.53	-48.05	-41.34	ND	ND
121	2-May	-241.3	-32.0	48.38	-46.77	-42.51	-50.11	-56
122	3-May	-110.5	-8.0	32.92	-40.00	-42.51	-46.31	-44
123	4-May	-109.7	-62.0	49.16	-40.14	-40.59	-54.55	-63.5
124	5-May	-119.1	-42.0	51.43	-40.67	-35.20	ND	ND
125	6-May	-109.5	-24.0	33.05	-37.64	-43.33	-51.27	-45
126	7-May	-102.3	-20.0	59.15	-34.86	-42.91	-49.40	-45

ND, no data.

The results for the optical properties conflict at times with previous work. First, regardless of whether the measurements come from the submersible radiometers (Knudson et al., 1989) or the MER-2040, the depth of 1% of E(PAR,0$^-$) closely approximates the compensation depth, *Zc*. In addition, the depth of 1% of Ed(488) was uniformly greater than *Zc* (see Figure 1 and Table 2).

No defined sub-surface fluorescence maximum was observed for the first three days of observations (25, 26, 27 April). Subsequently, a sub-surface fluorescence maximum developed on 28 April. However, we have no day-long experiments on that day. The first defined sub-surface fluorescence maximum during productivity measurements occurred on 29 April (YD118). On this date, the depth of the bottom of the fluorescence maximum is slightly deeper than *Zc*, and more so on 4 May when the ship re-positioned. On balance, however, there is good agreement between the depth of the base of the fluorescence maximum and *Zc*.

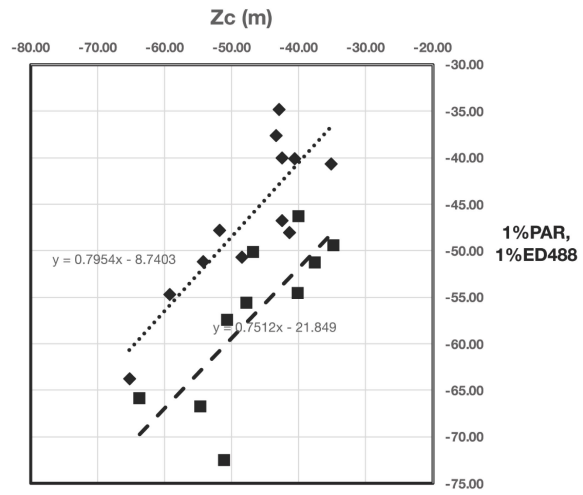


FIGURE 2
Linear regressions of the depth of 1%Ed(0$^-$,PAR) (diamonds) and 1% Ed(488) (squares) with Zc (x-axis). The slope of the regression of 1% Ed(0$^-$,PAR) on Zc is not significantly different from 1.

Discussion

Overall, we find good agreement among the four parameters estimating the compensation depth, and therefore the depth of the productive layer during the initiation of the spring bloom at the NABE site. Based on our proxy for the critical depth, we conclude that the phytoplankton community always had the physiological capability to bloom, mostly as a result of the shoaling of the mixed layer, with the possible exception of the initial three days of observations.

As suggested by Marra et al. (2014), the best indicators of the depth of the productive layer are the depth of penetration to 1% of near-surface Ed(488) and the depth at the base of the fluorescence maximum. The justification for these parameters is that 488 nm is the wavelength of light with maximum penetration in the open ocean (e.g., Liu et al., 2020). The base of the fluorescence maximum would be the depth that encompasses the entire autotrophic community. The samples analyzed in that work were locations in the Sargasso Sea, Gulf Stream, and Slope Water, obtained in summer, and generally oligotrophic. The exception was a continental shelf station where the most penetrating wavelength shifted from the blue to the green [Ed(532)].

For the North Atlantic Bloom Experiment (NABE) in the northeast Atlantic, the closest agreement with optical properties and the compensation depth is the 1% light depth for Ed(PAR) (Figure 1). While Ed(488) remained the most penetrating wavelength of light, the 1% light depth for Ed(488) was, on average, 13 m deeper than the 1% light depth for Ed(PAR) (Figure 2). Similarly, the bottom of the fluorescence maximum was about 7 m deeper on average than the compensation depth.

These results are at odds with those of Marra et al. (2014) and Wu et al. (2021). They do agree, however, with the assessment given in Marra (2004), for 60°N/20°W in the North Atlantic at a similar time of year. The reason may be the differing communities on either side of the Atlantic, which span the phytoplankton species inhabiting oligotrophic waters in the Sargasso Sea and Gulf Stream, and the mesotrophic waters in the eastern North Atlantic during the spring bloom period. In an analysis of pigments, Vaillancourt et al. (2018) found that *Prochlorococcus* and haptophytes dominated the phytoplankton communities in the Sargasso Sea and Gulf Stream, where deeper compensation depths were found. On the other hand, diatoms were abundant during the NABE, until about 5 May (YD 124) when silicate became undetectable, giving way to prasinophytes (Sieracki et al., 1993).

The differing communities of phytoplankton brings up the question of whether irradiance percentages (as used here) or absolute values should be reported for the compensation irradiance and corresponding depth. Many have criticized the use of percentages, such as the "1% light depth" (e.g., Lorenzen, 1976; Banse, 2004) because over seasons and latitudes, the actual values will change appreciably. However, if we accept that different phytoplankton will have differing compensation points (Falkowski and Owens, 1978; Hobson and Guest, 1983; Langdon, 1993), then a compensation depth based on irradiance percentages would seem to capture the variability that absolute values of irradiance would not. Also, 1% of Ed(488) or the bottom of the fluorescence maximum are also found to be good indicators of the depth of the productive layer, and could be used over a broader range of trophic conditions. In any case, these observations warrant further measurements of the compensation depths for phytoplankton photosynthesis across seasons and geographic areas.

Data availability statement

The raw data supporting the conclusions of this article will be made available by the authors, without undue reservation.

Author contributions

JM is the primary author with contributions from WC. WC and CK supplied critical assistance with data collection at sea and data

organization. WR supplied the spectral radiometer data. AK organized the data and prepared the data report, with assistance from CH. All authors contributed to the article and approved the submitted version.

Conflict of interest

The authors declare that the research was conducted in the absence of any commercial or financial relationships that could be construed as a potential conflict of interest.

Publisher's note

All claims expressed in this article are solely those of the authors and do not necessarily represent those of their affiliated organizations, or those of the publisher, the editors and the reviewers. Any product that may be evaluated in this article, or claim that may be made by its manufacturer, is not guaranteed or endorsed by the publisher.

Supplementary material

The Supplementary Material for this article can be found online at: https://www.frontiersin.org/articles/10.3389/fmars.2023.1052307/full#supplementary-material

SUPPLEMENTARY FIGURE 1
Example relative fluorescence profile from 30 April. The base of the fluorescence maximum was estimated to be the intersection of two regression lines, one from the fluorescence maximum to an inflection point, and the other from the bottom of the profile to the inflection point.

References

Banse, K. (2004). Should we continue to use the 1% light depth convention for estimating the compensation depth of phytoplankton for another 70 years? *Limnol. Oceanogr. Bull.* 13, 49–51. doi: 10.1002/lob.200413349

Behrenfeld, M. J., and Boss, E. S. (2017). Student's tutorial on bloom hypotheses in the context of phytoplankton annual cycles. *Global Change Biol.* 24, 55–77. doi: 10.1111/gcb.13858

Chipman, D. W., Marra, J., and Takahashi, T. (1993). Primary production at 47N and 20W in the north Atlantic ocean: A comparison between ^{14}C incubation method and the mixed layer carbon budget. *Deep-Sea Res. II* 40, 151–169. doi: 10.1016/0967-0645(93)90011-B

Falkowski, P. G., and Owens, T. G. (1978). Effects of light intensity on photosynthesis and dark respiration in six species of marine phytoplankton. *Mar. Biol.* 45, 289–295. doi: 10.1007/BF00391815

Falkowski, P. G., Dubinsky, Z., and Wyman, K. (1985). Growth-irradiance relationships in phytoplankton. *Limnol. Oceanogr.* 30, 311–321. doi: 10.4319/lo.1985.30.2.0311

Geider, R. J. (1992). "Respiration: Taxation without representation?," in *Primary productivity and biogeochemical cycles in the sea*. Eds. P. G. Falkowski and A. D. Woodhead (New York: Plenum Press), 333–360.

Geider, R. J., Osborne, B. A., and Raven, J. A. (1986). Growth photosynthesis and maintenance metabolic cost in the diatom *Phaeodactylum tricornutum* at very low light levels. *J. Phycol.* 22, 39–48. doi: 10.1111/j.1529-8817.1986.tb02513.x

Goldman, J. C. (1993). Potential role of large oceanic diatoms in new primary production. *Deep Sea Res. I* 40, 159168. doi: 10.1016/0967-0637(93)90059-C

Gran, H. H., and Braarud, T. (1935). A quantitative study on the phytoplankton of the bay of fundy and the gulf of Maine (including observations on hydrography, chemistry, and morbidity). *J. Biol. Board Canada* 1, 219–467. doi: 10.1139/f35-012

Hobson, L. A., and Guest, K. P. (1983). Values of net compensation irradiation and their dependencies on photosynthetic efficiency and respiration in marine unicellular algae. *Mar. Biol.* 74, 1–7. doi: 10.1007/BF00394268

Jenkin, P. M. (1937). Oxygen production by the diatom *Cosinodiscus exentricus* (Ehr.) in relation to submarine illumination in the English channel. *J. Mar. Biol. Assoc. United Kingdom* 22, 301–342. doi: 10.1017/S0025315400012030

Kiddon, J., Bender, M. L., and Marra, J. (1995). Production and respiration in the 1989 north Atlantic spring bloom: An analysis of irradiance-dependent changes. *Deep-Sea Res. I* 42, 553–576. doi: 10.1016/0967-0637(95)00008-T

Kirk, J. T. O. (2011). *Light and photosynthesis in aquatic ecosystems. 3rd ed* (Cambridge: Cambridge University Press), 649.

Knudson, C., Chamberlin, W. S., and Marra, J. (1989). *Primary production and irradiance data for U.S. JGOFS (Leg 2) ATLANTIS II (Cruise 119-4)* (Palisades, NY: Lamont-Doherty Earth Observatory), 11.

Langdon, C. (1987). On the causes of interspecific differences in the growth-irradiance relationship for phytoplankton. part 1. a comparative study of the growth-irradiance relationship of three marine phytoplankton species: *Skeletonema costatum, olisthodiscus luteus* and *Gonyaulax tamarensis*. *J. Plankton Res.* 9 (3), 459–482. doi: 10.1093/plankt/9.3.459

Langdon, C. (1988). On the causes of interspecific differences in the growth-irradiance relationship for phytoplankton. II. a general review. *J. Plankton Res.* 10 (6), 1291–1312. doi: 10.1093/plankt/10.6.1291

Langdon, C. (1993). The significance of respiration in production measurements based on oxygen. *ICES Mar. Sci. Symposium* 197, 69–78.

Laws, E. A., Letelier, R. M., and Karl, D. M. (2014). Estimating the compensation irradiance in the ocean: The importance of accounting for non-photosynthetic uptake of inorganic carbon. *Deep-Sea Res.* 193, 35–40. doi: 10.1016/j.dsr.2014.07.011

Liu, Q., Liu, D., Zhu, X., Zhou, Y., Le, C., Mao, Z., et al. (2020). Optimum wavelength of spaceborne oceanic lidar in penetration depth. *J. Quantitative Spectrosc. Radiative Transfer* 256, 1–7. doi: 10.1016/j.jqsrt.2020.107310

Lorenzen, C. J. (1976). "Primary production in the sea," in *Ecology of the seas*. Eds. D. Cushing and J. J. Walsh (Hoboken: Blackwell Scientific Publications), 173–185.

Marra, J. (1995). Primary production in the north Atlantic ocean: Scaling, measurements, and optical determinants. *Phil. Trans. R. Soc. Lond. B* 348, 153–160. doi: 10.1098/rstb.1995.0057

Marra, J. (2004). The compensation irradiance for phytoplankton in nature. *Geophysical Res. Lett.* 31, L06305. doi: 10.1029/2003GL018881

Marra, J. (2009). Net and gross productivity: Weighing in with ^{14}C. *Aquat. Microbial Ecol.* 56. doi: 10.3354/ame01306

Marra, J., and Barber, R. T. (2004). Phytoplankton and heterotrophic respiration in the surface layer of the ocean. *Geophys. Res. Lett.* 31, L09314. doi: 10.1029/2004GL019664

Marra, J., and Ho, C. (1993). Initiation of the spring bloom in the northeast Atlantic (47°N, 20°W): a numerical simulation. *Deep Sea Res.* 40, 55–73. doi: 10.1016/0967-0645(93)90006-9

Marra, J., Lance, V. P., Vaillancourt, R. D., and Hargreaves, B. R. (2014). Resolving the ocean's euphotic zone. *Deep Sea Res. I* 83, 45–50. doi: 10.1016/j.dsr.2013.09.005

McGillicuddy, D., McCarthy, J., and Robinson, A. (1995). Coupled physical-biological modeling of the spring bloom in the north Atlantic (I): Three dimensional bloom and post-bloom processes. *Deep Sea Res. I* 42, 1313–1357. doi: 10.1016/0967-0637(95)00035-5

Najjar, R. G., and Keeling, R. F. (1997). Analysis of the mean annual cycle of the dissolved oxygen anomaly in the world ocean. *J. Mar. Res.* 55, 117–151. doi: 10.1357/0022240973224481

Patten, B. (1961). Plankton energetics in raritan bay. *Limnol. Oceanogr.* 6, 369–387. doi: 10.4319/lo.1961.6.4.0369

Regaudie-de-Gioux, A., and Duarte, C. M. (2010). Compensation irradiance for planktonic community metabolism in the ocean. *Global Biogeochem. Cycles* 24, GB4013. doi: 10.1029/2009GB003639

Riley, G. A. (1942). The relationship of vertical turbulence and spring diatom flowering. *J. Mar. Res.* 5, 67–87.

Ryther, J. H. (1956). Photosynthesis in the ocean as a function of light intensity. *Limnol. Oceanogr.* 1, 61–70. doi: 10.4319/lo.1956.1.1.0061

Siegel, D. A., Doney, S. C., and Yoder, J. A. (2002). The north Atlantic spring phytoplankton bloom and sverdrup's critical depth hypothesis. *Science* 296, 730–733. doi: 10.1126/science.1069174

Sieracki, M. E., Verity, P. G., and Stoecker, D. K. (1993). Plankton community response to sequential silicate and nitrate depletion during the 1989 north Atlantic spring bloom. *Deep-Sea Res. II* 40, 213–225. doi: 10.1016/0967-0645(93)90014-E

Sverdrup, H. U. (1953). On conditions for the vernal blooming of phytoplankton. *J. Conseil perm. Int. Explor. Mer* 18, 287–295. doi: 10.1093/icesjms/18.3.287

Vaillancourt, R. D., Lance, V. P., and Marra, J. F. (2018). Phytoplankton chemotaxonomy within contiguous optical layers across the western north Atlantic ocean and its relationship to environmental parameters. *Deep-Sea Res. I* 139, 14–26. doi: 10.1016/j.dsr.2018.05.007

Wiggert, J. D., Murtugudde, R. G., and McClain, C. R. (2002). Processes controlling interannual variations in wintertime (Northeast monsoon) primary productivity in the central Arabian Sea. *Deep-Sea Res. II* 49 (12), 2319–2343. doi: 10.1016/S0967-0645(02)00039-5

Wu, J., Lee, Z., Xie, Y., Goes, J., Shang, S., Marra, J. F., et al. (2021). Reconciling between optical and biological determinants of the euphotic zone depth. *J. Geophysical Research: Oceans* 126, e2020JC016874. doi: 10.1029/2020JC016874

frontiers | Frontiers in Marine Science

TYPE Original Research
PUBLISHED 05 May 2023
DOI 10.3389/fmars.2023.1052166

Check for updates

OPEN ACCESS

EDITED BY
Salvatore Marullo,
Energy and Sustainable Economic Development (ENEA), Italy

REVIEWED BY
Vittorio Ernesto Brando,
National Research Council (CNR), Italy
Jamie Shutler,
University of Exeter, United Kingdom

*CORRESPONDENCE
Marit van Oostende
marit.oostende@hereon.de

RECEIVED 23 September 2022
ACCEPTED 18 April 2023
PUBLISHED 05 May 2023

CITATION
van Oostende M, Hieronymi M, Krasemann H and Baschek B (2023) Global ocean colour trends in biogeochemical provinces.
Front. Mar. Sci. 10:1052166.
doi: 10.3389/fmars.2023.1052166

COPYRIGHT
© 2023 van Oostende, Hieronymi, Krasemann and Baschek. This is an open-access article distributed under the terms of the Creative Commons Attribution License (CC BY). The use, distribution or reproduction in other forums is permitted, provided the original author(s) and the copyright owner(s) are credited and that the original publication in this journal is cited, in accordance with accepted academic practice. No use, distribution or reproduction is permitted which does not comply with these terms.

Global ocean colour trends in biogeochemical provinces

Marit van Oostende[1]*, Martin Hieronymi[1], Hajo Krasemann[1] and Burkard Baschek[2]

[1]Department of Optical Oceanography, Institute of Carbon Cycles, Helmholtz-Zentrum Hereon, Geesthacht, Germany, [2]Deutsches Meeresmuseum, Stralsund, Germany

Satellite-derived ocean colour data provide continuous, daily measurements of global waters and are an essential tool for monitoring these waters in a changing climate. Merging observations from different satellite sensors is necessary for long-term and continuous climate research because the lifetime of these sensors is limited. A key issue in deriving long-term trends from merged ocean colour data is the inconsistency between the spatiotemporal coverage of the different sensor datasets that can lead to spurious multi-year fluctuations or trends in the time series. This study used the merged ocean colour satellite dataset produced by the Ocean Colour Climate Change Initiative (OC-CCI version 6.0) to infer global and local trends in optically active constituents. We applied a novel correction method to the OC-CCI dataset that results in a spatiotemporally consistent dataset, allowing the examination of long-term trends of optically active constituents with greater accuracy. We included sea surface temperature, salinity, and several climate oscillations in our analysis to gain insight into the underlying processes of derived trends. Our results indicate a significant increase in chlorophyll-*a* concentration in the polar waters, a decrease in chlorophyll-*a* concentration in some equatorial waters, and point to ocean darkening, predominantly in the polar waters, due to an increase in non-phytoplankton absorption. This study contributes to broader knowledge of global trends of optically active constituents and their relation to a changing environment.

KEYWORDS

ocean colour, essential climate variables, climate research, climate change initiative, satellite remote sensing, time series, temporal gap detection method

1 Introduction

Ocean colour remote sensing is a technique using satellite sensors for global observations of optically active constituents in the upper layer of the ocean. Such observations can be used to infer information about phytoplankton biomass, indicated by the concentration of the pigment chlorophyll-*a* in water (hereafter Chl-*a*), as well as other constituents, including organic- and inorganic carbon. These optically active constituents are important indicators of ocean ecosystem health and productivity, and

can be used to estimate the ocean's role in the global carbon cycle and to quantify feedbacks on climate variability and change. Consistent, stable, and accurate datasets are essential for climate research and ocean colour is considered one of the Essential Climate Variables (ECVs) by the Global Climate Observing System (GCOS, 2011; GCOS, 2016). The Coastal Zone Color Scanner (CZCS) was launched as a 'proof of concept' mission in 1978. Since the launch of the first operational ocean colour sensor with global coverage in 1997, various sensors have been developed and launched that measure ocean colour. These sensors measure radiance at the top of atmosphere from which the remote sensing reflectance (R_{rs}) can be derived. This reflectance is used to infer various optically active constituents in the water column. The most commonly used constituent is the Chl-*a*, which is a proxy for marine phytoplankton biomass (Cullen, 1982). Other estimated optical properties in water include the diffuse attenuation (K_d), absorption by phytoplankton (a_{ph}), absorption by detrital and dissolved organic matter (a_{dg}), and particulate backscattering (b_{bp}) coefficients. In open ocean waters, phytoplankton and its associated substances mainly determine the absorption and scattering coefficients, whereas in coastal waters the non-phytoplankton sources, e.g. organic matter from river discharge, have a greater influence (Morel and Prieur, 1977; Kirk, 2011).

Climate change has a significant impact on the global aquatic ecosystem, which in turn affect society, biodiversity, and the carbon cycle (Bindoff et al., 2019). The temperature of global surface water will continue to rise in the coming decades, in proportion to greenhouse gas emissions (Gattuso et al., 2015). The response of phytoplankton composition and dynamics to climate variability is complex and depends on light and nutrient availability (Behrenfeld et al., 2006). The direct and indirect effects of increasing water temperature can result in different responses of phytoplankton growth due to intricate interactions of physical and chemical variables. One widely accepted theory of phytoplankton response to warming surface waters is that the increased stratification of the water column results in reduced nutrient flux into the surface and consequently causes reduced productivity in nutrient-limited surface waters (e.g. Behrenfeld et al., 2006; Boyce et al., 2010; Racault et al., 2012; Lewandowska et al., 2014; Dunstan et al., 2018). Conversely, warming of surface waters can also lead to increased productivity because of higher metabolic rates of phytoplankton, longer bloom seasons due to reduced ice cover, or increased vertical migration (Brown et al., 2004; Pabi et al., 2008; Kahru et al., 2011; Lewandowska et al., 2014; Wirtz et al., 2022). Warming of surface waters may also shift the timing of blooms and cause species migration (Ardyna et al., 2014; Deppeler and Davidson, 2017; Friedland et al., 2018; Ardyna and Arrigo, 2020). Climate change can also result in more frequent extreme events, such as heatwaves (Bernhard et al., 2022) or intensified precipitation (O'Gorman, 2015), which can increase inflow of organic material, either detrital or dissolved, into the coastal aquatic ecosystems that affects light availability and in turn can limit phytoplankton growth (Bidigare et al., 1993; Mustaffa et al., 2020). Several studies (Juhls et al., 2019; Mustaffa et al., 2020; Konik et al., 2021) refer to this increasing absorption of the waters as "ocean darkening", and argue that the water transparency is decreasing due to climate-driven changes of the environment. Increased water absorption leads to a higher rate of melting of sea ice and alterations in the surface heat fluxes affecting the atmosphere (Soppa et al., 2019). Evaporation, terrestrial runoff, precipitation, and mixing processes all regulate surface salinity, which can change growing conditions for phytoplankton species (Wells et al., 2020). Global salinity changes are consistent with broad scale surface water warming patterns (Durack and Wijffels, 2010). Previous studies have produced conflicting results regarding trends of global Chl-*a* or phytoplankton productivity. Some studies identified an overall declining trend (Behrenfeld et al., 2006; Boyce et al., 2010; Boyce et al., 2014; Gregg et al., 2014; Hammond et al., 2017), while others indicated no trend (Gregg et al., 2017; Kulk et al., 2020) or even an increasing trend (Antoine et al., 2005; Hammond et al., 2020). Regardless of these varying conclusions, all these studies agree that the strength and direction of Chl-*a* varies depending on the region.

The Ocean Colour Climate Change Initiative (OC-CCI) is a project aims to produce a highly comprehensive and consistent time series of multi-sensor global satellite data products suitable for climate research (Sathyendranath et al., 2019). The dataset (version 6.0) consists of merged records measured by six different satellite sensors; OrbView-2-SeaWiFS, MODIS-A, and SNPP-VIIRS by NASA/NOAA (United States), and Envisat-MERIS, OLCI-A, and OLCI-B by ESA/EUMETSAT (Europe). The use of different ocean colour sensors, each with unique spectral-, spatial-, and temporal characteristics, complicate the consistency of the time series. The OC-CCI group applied a thorough bias correction to the dataset, but inter-mission inconsistencies in the time series remain due to the different coverage of the surface waters between the input sensor datasets (Van Oostende et al., 2022). This can lead to higher average Chl-*a* concentrations in the time series when, e.g. the MERIS sensor is active, which is more capable of observing highly productive coastal- and high latitude regions compared to most other sensors in the dataset. Previous trend analysis studies that use merged ocean colour data either omit coastal and polar waters due to the larger uncertainty or the presented time series likely exhibit artefacts related to the inter-mission coverage inconsistencies (e.g. in Kahru et al., 2012; Kahru et al., 2015; Navarro et al., 2017; Sankar et al., 2019; Kulk et al., 2020; Joseph et al., 2021). However, it is important to monitor phytoplankton dynamics in polar and coastal regions because they are under pressure from climate change and anthropogenic activities (e.g. Burke, 2001; Deppeler and Davidson, 2017; Bindoff et al., 2019; Ardyna and Arrigo, 2020).

Recently, Van Oostende et al. (2022) introduced a method to resolve the inter-mission coverage inconsistency issue: the Temporal Gap Detection Method (TGDM). This method corrects the different observation capabilities of the satellite sensors that introduce artefacts in long-term fluctuations and trends, independent from variable values. The TGDM homogenises the temporal observation distribution per geographic pixel, minimising the observation inconsistencies. The main advantage of this method is that the resulting time series allow more reliable use of merged ocean colour data for long-term statistical- and trend analysis. As previous long-term studies that use merged ocean colour data rely on uncorrected data, we aim to estimate global and regional trends

in ocean colour variables, that is now unaffected by inter-mission coverage inconsistencies. Climatic variables and indices, such as sea surface temperature, sea surface salinity, and climate oscillations were included to help explain the underlying processes of derived ocean colour trends. Additionally, we include a trend analysis of non-phytoplankton absorption (a_{dg}), to gain insight into the phenomenon of ocean darkening.

2 Materials and methods

Table 1 contains all the variables and associated units used in this study. Each variable is described in detail in the sections 2.1-2.3.

2.1 Optically active variables

The OC-CCI dataset, produced by the European Space Agency's (ESAs) Ocean Colour Climate Change Initiative project (OC-CCIv6.0, https://esa-oceancolour-cci.org/), is a dataset spanning nearly 25 years from September 1997 to June 2022. It is composed of merged satellite data from five ocean colour sensors: SeaWiFS, MERIS, MODIS, VIIRS, OLCI-A, and OLCI-B. The data were atmospherically corrected, band-shifted to match MERIS spectral bands (412, 443, 490, 510, 560, 665 nm), bias corrected, and binned to derive a multi-sensor daily remote-sensing reflectance (R_{rs}) product with a ~4 km spatial resolution. All dependent ocean colour variables were determined from the reflectance product: the Chl-*a* concentration, attenuation-, absorption-, and backscattering coefficients. The Chl-*a* was determined by a blended merge of several band ratio algorithms (OCI, OCI2, OC2, and OCx) weighted by the relative levels of optical water type classes (Moore et al., 2009). The diffuse attenuation coefficient at 490 nm for downwelling irradiance (K_d490) is an apparent optical property (AOP) related to light availability and penetration in water bodies and depends on the inherent optical properties (IOPs). IOPs depend only on the medium and are therefore independent of light availability (Kirk, 2011). The total absorption (a_{tot}) is the sum of absorption of the water column, particles and dissolved matter. The absorption of phytoplankton (a_{ph}), and absorption by detrital and dissolved organic matter (a_{dg}) were distinguished in the dataset. The IOPs were determined with the Quasi-Analytical Algorithm (QAA: Lee et al., 2009) and the K_d490 with the semi-analytical Lee et al. (2005) method. The optically active constituents that were used in this study include uncertainty estimates provided in the dataset that were determined with a large *in situ* match-up dataset (Valente et al., 2019), except for a_{tot} and b_{bp}. The a_{tot} is not included because it is the sum of absorption of water (a_w), a_{ph}, and a_{dg} for which uncertainties were estimated. The backscattering (b_{bp}) had insufficient *in situ* data for the matchup analysis (Jackson et al., 2022). The product validation report provided by the OC-CCI group describes the validation process of the dataset (Jackson et al., 2021) and additional details of this dataset can be found in e.g. Sathyendranath et al. (2019) and Jackson et al. (2022). All absorption coefficients in this study refer to a wavelength of 443 nm, except for b_{bp}, where a wavelength of 510 nm was used. The sinusoidal projection was used because of the equal area gridding, which is beneficial for trend analysis (Jackson et al., 2022).

2.2 Climate variables

In addition to ocean colour variables, other essential climate variables (ECVs: GCOS, 2011; GCOS, 2016) were used in this study, namely sea surface temperature (SST) and sea surface salinity (SSS). For these ECVs, the same time span was used as that of the OC-CCI dataset (1997-2022). The climatological SST data were produced by the ESA's Climate Change Initiative programme (SST-CCIv2.1, level 4). The data contain the daily temperature in units Kelvin (K) adjusted to a standard depth of 20 cm that were merged from multiple instruments with a spatial resolution of 0.05° x 0.05° (Good et al., 2019). The source of the monthly composite salinity dataset was the Ocean Reanalysis System 5 (ORAS5 v0.1), prepared by the

TABLE 1 An overview of the variables used in this study with their corresponding units.

Variable group	Parameter	Quantity	SI Units
Optical constituents and properties	**Chl-*a***	Pigment chlorophyll-*a* concentration	mg m^{-3}
	K_d490	Diffuse attenuation coefficient of downwelling irradiance at 490 nm	m^{-1}
	$a_{tot}443$	Total absorption coefficient at 443 nm	m^{-1}
	$a_{ph}443$	Phytoplankton absorption coefficient at 443 nm	m^{-1}
	$a_{dg}443$	Detrital and coloured dissolved organic matter absorption coefficient at 443 nm	m^{-1}
	$b_{bp}510$	Backscattering coefficient of particles at 510 nm	m^{-1}
Climate variables	**SST**	Sea surface temperature	C°
	SSS	Sea surface salinity	PSU
Climate indices	**SOI**	Southern Oscillation Index	–
	IOD	Indian Ocean Dipole	–
	NAO	North Atlantic Oscillation	–

European Centre for Medium-Range Weather Forecasts (ECMWF). The salt concentration close to the ocean surface is expressed in practical salinity units (PSU) with a spatial resolution of 0.25° x 0.25° (Zuo et al., 2018). Both the SST and salinity data were constructed by combining data into a global gap-free consistent dataset and were downloaded from the Copernicus' website in June 2022: https://cds.climate.copernicus.eu/.

2.3 Climate indices

Three climate oscillations were included in the analysis: the Southern Oscillation Index (SOI), the Indian Ocean Dipole (IOD), and the North Atlantic Oscillation (NAO). The SOI is defined as the normalised sea-level pressure difference index between Tahiti and Darwin and is used as an indication of the intensity of the El Niño/Southern Oscillation (ENSO). Negative values of the SOI coincide with El Niño episodes and positive values with La Niña episodes. The IOD is defined by the difference in sea surface temperature between areas located in the western and eastern Indian Ocean. Positive phases of the IOD are associated with reduced precipitation, warm land surface anomalies, reversed direction of wind in the central Indian Ocean, and lowered sea level in the east and raised sea level in the central and western Indian Ocean (Saji and Yamagata, 2003). The NAO describes the difference in atmospheric pressure between the Icelandic Low and Azores High. Its positive phase is linked to strong westerly winds and increased sea surface temperature in the North Atlantic (Hurrell et al., 2003; Wang et al., 2004). The indices are visualised in Figure 1 for the same time span as of the OC-CCI data (1997-2022) and were all downloaded from the National Oceanic and Atmospheric Administration's (NOAA) website in June 2022: https://psl.noaa.gov/data/climateindices/list/.

2.4 Longhurst provinces

The global waters were divided into the biogeochemical provinces proposed by Longhurst et al. (1995); Longhurst, 2007).

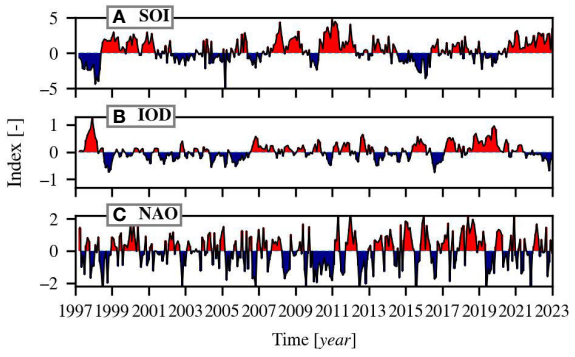


FIGURE 1
The climate indices of the **(A)** Southern Oscillation Index (SOI), **(B)** the Indian Ocean Dipole (IOD) and, **(C)** North Atlantic Oscillation (NAO). Red indicates positive phases and blue negative phases.

These provinces are defined by distinct physical and biological characteristics, such as mixed layer depth, solar irradiance, and phytoplankton patterns. Each province belongs to one of four different biomes: the polar-, coastal-, trade winds-, or westerly wind biomes.

The 54 Longhurst provinces, each with associated province codes, oceans, and biomes are illustrated in Figure 2 and listed in Table A1 in the Appendix. The shape files of the Longhurst provinces were obtained in April 2022 from the website: https://www.marineregions.org.

2.5 Methods

2.5.1 Temporal gap detection method

First, the global daily OC-CCI data were partitioned into the Longhurst provinces. The Temporal Gap Detection Method (TGDM: Van Oostende et al., 2022) was then applied to each Longhurst province separately. The aim of this method is to filter out unequally observed data over time per geographic pixel and as a result avoids biases in statistics and trends caused by the different spatio-temporal coverage between the sensor input data. Apparent jumps occur in time series of optical properties, when missions join or drop out of the dataset. The main reasons for the inconsistencies within the merged dataset are the different atmospheric corrections, the inconsistent flagging for invalidity between missions, and the overall capabilities of the sensors. Polar-, coastal-, and cloudy regions generally are more affected by these inter-mission inconsistencies. For example, the MERIS sensor has a significantly better coverage of the highly productive shelf waters compared to the SeaWiFS and MODIS sensors. Therefore, when MERIS joins the dataset, much higher values of Chl-*a* suddenly appear in the global time series. The higher Chl-*a* values are not incorrect, the only change in the time series is that these type of waters are now included in the dataset. The jumps in the time series should not be confused with natural change, and must be corrected before performing trend analysis.

The TGDM functions as follows: each day within the data of a geographic pixel was scanned for observation availability within a time window of ± *n* days. If there were no observations for that day or in the time window around it, this day of the year was masked out in every year of that specific geographical pixel. This scanning and filtering is performed on all geographic pixels in the dataset. A time window that is too long may not sufficiently reduce the biased multi-year fluctuations or trends, whereas a time window that is too short results in excessive removal of observations. An optimisation procedure has been applied to find the optimal time window length. This method is proposed and described thoroughly by Van Oostende et al. (2022).

The filtering method used in this manuscript is essentially the same as the TGDM offered by Van Oostende et al. (2022), with some minor adjustments. Firstly, the optimal time window length was determined for each Chl-*a* time series of the Longhurst provinces separately. Secondly, thresholds of maximum percentage data loss were applied for each biome to ensure that a reasonable number of data records remained available for further

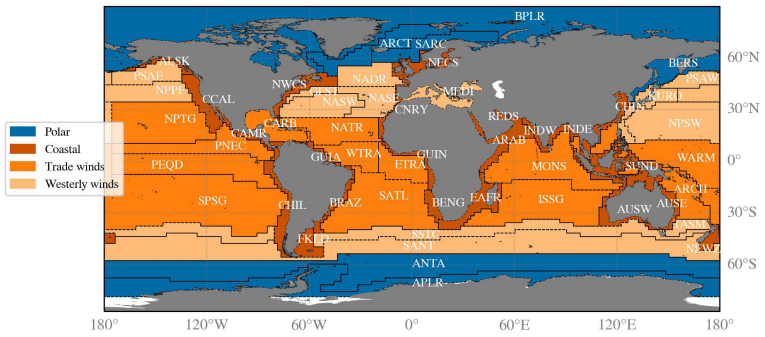


FIGURE 2
The Longhurst biogeochemical provinces with their four letter acronyms (in white) displayed within the province. The corresponding province descriptions are detailed in Table A1. The colours indicate the four biomes that consist of multiple combined provinces.

analysis. The thresholds used were: trades and westerlies 50%, polar 85%, and coastal 75%. Lastly, this manuscript used version 6 of the OC-CCI dataset, whereas Van Oostende et al. (2022) used version 5. The main differences of the new version, which are of interest for applying the TGDM, are that it has been extended to 2022, includes the OLCI-B sensor, and the active periods of the sensors have been changed. The MODIS and VIIRS sensors have been dropped after 2019 because of data quality concerns due to ageing sensors (Jackson et al., 2022). There are now five, slightly altered broad sub-periods that are used for the optimisation procedure:

1. 9/1997 - 4/2002 only SeaWiFS available
2. 5/2002 - 4/2012 MERIS and MODIS join
3. 5/2012 - 5/2016 VIIRS is launched and MERIS ends
4. 6/2016 - 12/2019 OLCI joins
5. 1/2020 - 6/2022 MODIS and VIIRS end of usage

The Appendix contains a table that shows all optimised time window lengths, and the percentage of data masked per province (Table A2).

Like for the OC-CCI data, the SST-CCI data are merged data from different satellite sensors (Merchant et al., 2019). We expected inconsistency between the missions to be only a secondary effect in the SST data. Both the OC and SST compiling CCI teams already eliminated pure instrumental inter-mission biases. Unlike the analysis of OC data, where the algorithms are affected by the different capabilities in Case-2 or coastal waters compared to the open ocean and thus unevenly flag and discard these pixels that have on the average higher loaded coastal waters, the SST analysis only loses data mainly due to cloud coverage. Nevertheless, we visually inspected the monthly mean time series of each Longhurst region, and since they show no apparent inter-mission bias, we had not applied the TGDM to the SST-CCI data.

2.5.2 Pre-processing of data

Monthly mean composites of Chl-*a*, K_d490, $a_{tot}443$, $a_{dg}443$, $a_{ph}443$, and $b_{bp}510$ were generated by combining all remaining daily records that passed through the TGDM filter. Pixel centres of the ocean colour variables within 4 km from the coastline were excluded due to the larger error associated with these areas, compared to pixels farther from the coastline (Lee et al., 2010). A monthly means composite of the daily sea surface temperature was prepared as well. The salinity data were already a monthly average composite. Monthly average composites of the bias were prepared of the SST, Chl-*a*, and $a_{dg}443$ datasets. These were used for uncertainty estimation and validation of derived trends, i.e. the trend should be larger than the inherent dataset bias. Unfortunately, there was no per-pixel bias available for the salinity data.

All the following statistical- and trend analyses were performed on de-seasonalised, monthly-averaged time series of each ocean colour and climate variable because otherwise the annual cycle would dominate the analyses. De-seasonalisation in this paper always refers to the process of removing the signal caused by seasonality from the time series. These de-seasonalised time series were prepared by decomposing the monthly composites of each variable into a trend-, seasonal- and residual component with *Seasonal-Trend decomposition using Loess* (STL: Cleveland et al., 1990). The resulting de-seasonalised, monthly-averaged time series consist of the combined trend- and residual components of the decomposed time series.

2.5.3 Statistical- and trend analyses

The statistical relationship between the time series of Chl-*a* and each optically active constituent was derived globally and for each biome and ocean. The purpose of this correlation analysis was to infer statistical relationships between these optically active constituents and reduce data processing. All ocean colour variables were produced from the same reflectance data, and with high and significant correlation between variables, it is redundant to perform analyses on each product. The ocean colour time series were tested for normality using the Shapiro-Wilk test (Shapiro and Wilk, 1965) to determine the appropriate correlation method. The Spearman correlation method can be applied to non-normally distributed data, whereas the Pearson correlation method is not appropriate in this case. Since approximately one third of the optically active- and climate variables were not normally distributed, all statistical relationships in this study were performed using the Spearman's rank correlation for the sake of consistency. A significance of at least 95% was used for all

correlations. Statistical relationships were also determined between Chl-*a* and the climate indices and variables to help explain underlying processes.

The non-parametric Mann-Kendall test was used to identify statistically significant trends over time (Mann, 1945; Kendall, 1948). When the resulting τ is not zero and the p-value is greater than 0.95, then the slope of the linear trend was estimated with the non-parametric Sen's slope (Sen, 1968). This method is insensitive to outliers and has been used in numerous studies that derived trends from ocean colour variables (e.g. Kahru et al., 2011; Frey et al., 2021; Pitarch et al., 2021; Wang et al., 2021). The trend analysis included seasonal and annual Chl-*a*-, temperature-, salinity trends for each Longhurst province, and Chl-*a* trends of the different biomes, oceans, and globally.

3 Results

3.1 Statistical relationships between variables

The correlation coefficient between Chl-*a* and the other investigated optically active constituents is positive globally and in each biome and ocean (Figure 3). The $a_{dg}443$ is generally well correlated to Chl-*a* because Chl-*a* degradation products are usually the main source of $a_{dg}443$ in open waters. The slightly lower correlation between these two variables in the Pacific Ocean, which largely consists of oligotrophic waters, may be due to the delay between the bloom and its breakdown products. These types of waters generally have lower estimation errors for absorption and Chl-*a* compared to high productive waters (Moore et al., 2009; Lee et al., 2010). The lower correlation between Chl-*a* and $a_{dg}443$ in the coastal biome indicates terrestrial carbon influx. The weaker correlation between $a_{ph}443$ and Chl-*a* may seem counterintuitive as they both are phytoplankton related quantities. However, the relationship between a_{ph} and Chl-*a* is variable due to the package effect and pigment composition (Bricaud et al., 1995). The a_{ph} is associated with larger inaccuracy compared to the other optical variables (Moore et al., 2009; Lee et al., 2010).

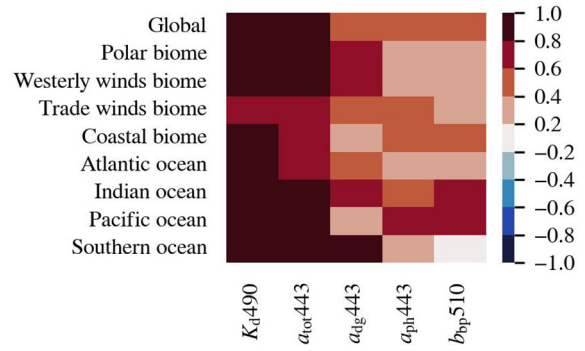


FIGURE 3
Spearman correlation between de-seasonalised, monthly-averaged time series of Chl-*a*, and the optically active constituents in the biomes, oceans, and globally ($p < 0.005$).

Figure 4 demonstrates the correlation between Chl-*a* and the climate variables and indices. The Chl-*a* in low latitude-, nutrient-poor provinces are generally negatively correlated to temperature, which implies that increased temperature causes ocean stratification that limits vertical mixing and thus nutrient availability for phytoplankton. The Chl-*a* in provinces located at higher latitudes that receive limited sunlight, are generally positively correlated with temperature. This could be explained by (a combination of): increased light conditions because of melting ice, increased metabolic rate, and poleward migration of phytoplankton species. Many statistical relationship patterns between Chl-*a* and salinity are similar to patterns between Chl-*a* and temperature, but reversed. The positive relationship between Chl-*a* and salinity in the open ocean provinces can be indirectly attributed to vertical mixing processes related to temperature. Chl-*a* is generally indirectly related to salinity in coastal provinces, as they are both influenced by interactions between terrestrial runoff, precipitation, and mixing processes. The Chl-*a* and SOI show the strongest correlation in provinces that are near Tahiti and Darwin (e.g. PEQD and SUND). El Niño phases may restrict phytoplankton growth in or near the pacific equatorial upwelling zones and enhance phytoplankton growth in Southeast Asian- and Australian waters. Thereby, phytoplankton growth enhances in upwelling regions because of enhanced sea level pressure that increases the upwelling nutrient rich waters (Racault et al., 2017). La Niña phases can have the opposite effect. During the time span of this study there have been seven El Niño and seven La Niña phases (Figure 1). The correlation patterns of Chl-*a* with IOD are quite similar to the correlation patterns between Chl-*a* and temperature because the IOD is calculated by the difference in sea surface temperature. The NAO phases are linked to westerly wind strength that could either enhance or limit phytoplankton growth through vertical mixing or strat0ification.

3.2 Trends in the global aquatic ecosystems

Both Figures 5, 6 demonstrate the linear trend direction and magnitude of Chl-*a* over time. Figure 5 illustrates the time series of Chl-*a* globally, and in the biomes and oceans, while Figure 6 shows annual and seasonal relative trends of Chl-*a*, salinity, and temperature in each Longhurst province. The absolute values of trends shown in Figure 6 are available in Table A2 in the Appendix, which also contains information on the averages, standard deviations, and other details for each Longhurst region. The global Chl-*a* is slightly increasing with 0.002 ± 0.001 mg m^{-3} per decade. However, the underlying global uncertainty of the dataset (0.021 mg m^{-3}) is larger than the global trend. The Chl-*a* trend direction and magnitude depend heavily on the latitude, as Chl-*a* increases in most high latitude provinces and decreases in provinces located nearer to the equator. The polar waters experience the greatest increasing Chl-*a* trends, ranging between 0.027–0.132 ±

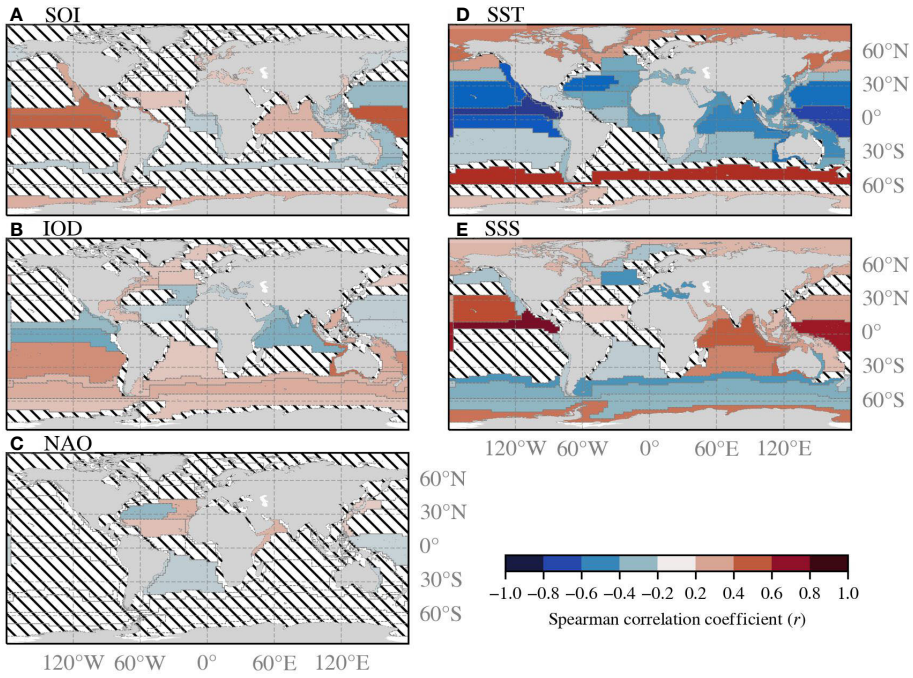


FIGURE 4
(A–E) Represent the correlation coefficient between the climate variables and the de-seasonalised, monthly-averaged Chl-*a* time series of each Longhurst province. The correlation coefficient is shown only when the significance is greater than 95%. Slanted lines indicate that the correlation is not significant.

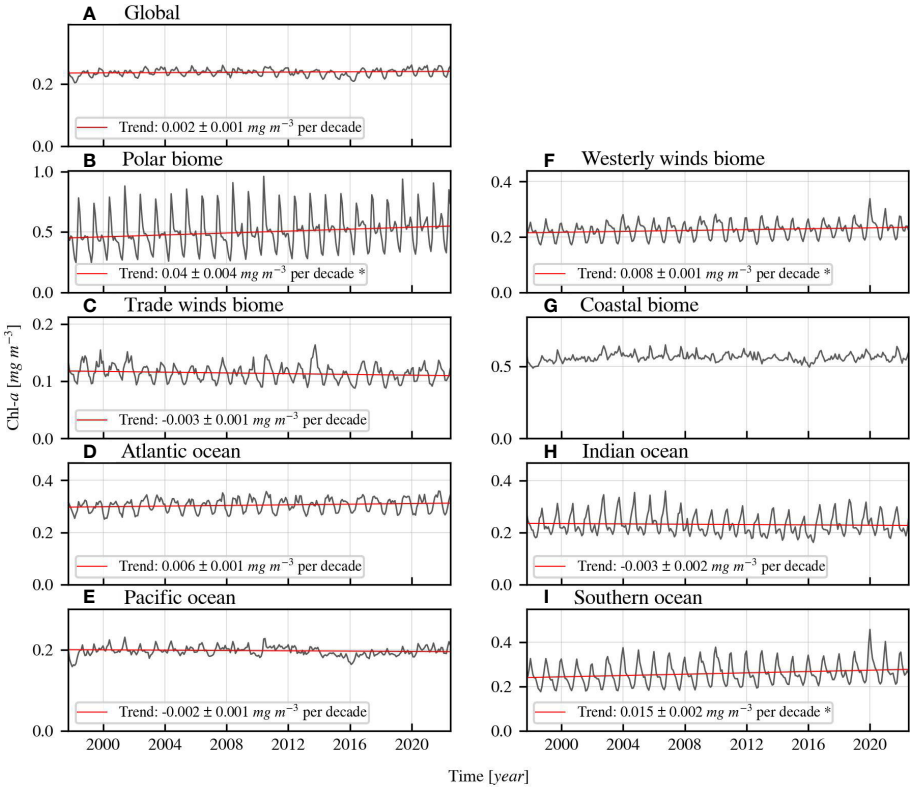


FIGURE 5
(A–I) Monthly-averaged Chl-*a* time series of biomes, oceans, and globally with regression lines. The linear regression lines are based on the de-seasonalised (using STL) time series and derived Sen slopes. They are only displayed when the Kendall's τ indicates significant (>95%) trend. The star (*) behind the formula indicates that the derived trend is larger than the uncertainty of the dataset in the region.

10.3389/fmars.2023.1052166

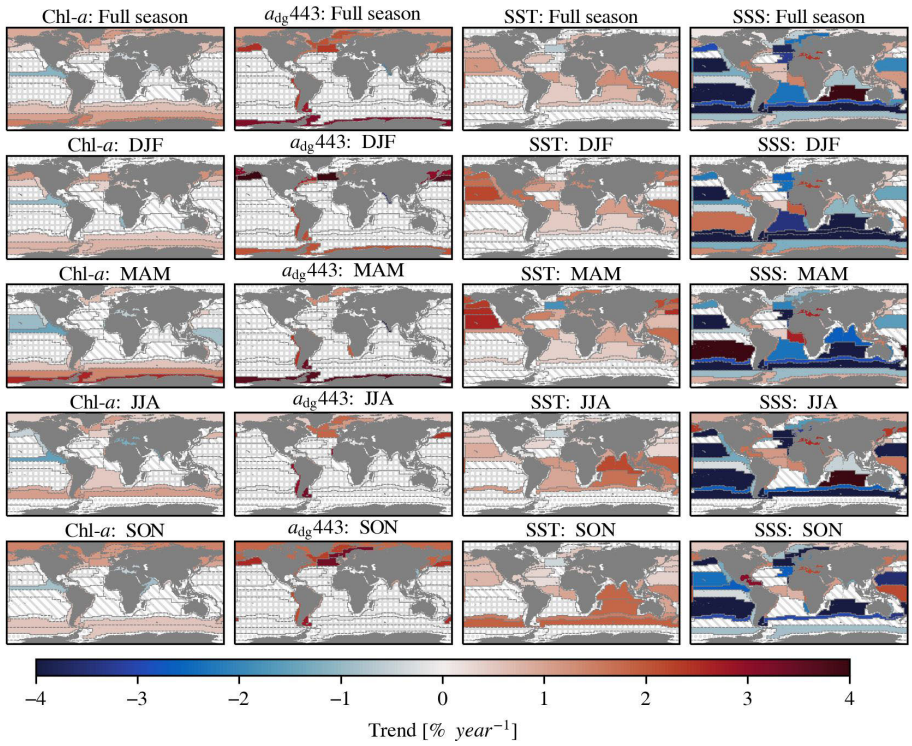


FIGURE 6
The Sen's slope of Chl-*a*, non-phytoplankton absorption at 443 nm (a_{dg}443), sea surface temperature (SST) and sea surface salinity (SSS) in percent per year. The upper row figures show the trends over a full year and the other rows the trends of specific seasons. Seasons are indicated with a combination of the first letter of the respective month (e.g. December, January, and February = DJF). The trend is only displayed when the Kendall's τ is significant (>95%). The slanted lines indicate an insignificant τ. The dots indicate provinces where the spatial coverage of the ocean colour variables in the specified season is less than 20% compared to the annual spatial coverage. The trend is not shown when it is smaller than the uncertainty of the underlying province dataset, and is indicated with squares (Appendix: Figure A1). The salinity data did not have any inherent uncertainty information available.

0.004–0.03 mg m^{-3} per decade. These observations indicate a change in the growth conditions for phytoplankton.

Global warming is evident when looking at the sea surface temperature trends that are increasing in 28 of 54 regions in the range of 0.128–0.477 ± 0.021–0.104 C° per decade. These increasing temperatures affect phytoplankton growth globally. The surface waters of the open ocean are generally freshening, except in the central Atlantic Ocean. The direction of the trend is variable in the coastal provinces. The salinity increased in 20 of 54 provinces with 0.015–0.266 ± 0.006–0.038 PSU per decade and decreased in 25 of 54 provinces with 0.015–0.118 ± 0.003–0.035 PSU per decade. These trends indicate changes in the hydrological cycle, e.g. precipitation and glacier melting, that affect nutrient availability. Additionally, our results suggest that the ocean is darkening, but predominantly in the polar regions, since the non-phytoplankton absorption increased in 13 of 54 provinces, with trends ranging between 0.307–1.164 ± 0.053–0.356 x10^{2} m^{-1} per decade. Darkening of waters affect phytoplankton growth by changing the light conditions and is caused by increased decomposition products from marine organisms and increased terrestrial runoff inputs. Coastal waters are usually influenced by terrestrial runoff, whereas open waters are not. The polar waters are typically mentioned with regards to darkening due to increased terrestrial input over time due to climate change (e.g. Konik et al., 2021).

4 Discussion

4.1 Changes in global aquatic ecosystems

We detected trends in optically active constituents over a period of almost 25 years, both globally and in different biogeochemical provinces. This study used time series with improved consistency that is necessary for climate research. All trends discussed here are significant ($p<0.05$) and are larger than the inherent dataset bias (Appendix: Figure A1), unless otherwise indicated. Our results indicate that global Chl-*a* is mostly increasing in the polar waters and decreasing in some equatorial waters. The overall global trend is much smaller than the inherent uncertainty of the dataset (0.002 ± 0.001 mg m^{-3} per decade < 0.021 mg m^{-3}), therefore we conclude that there no clear global trend direction of Chl-*a*. This is in line with findings by Gregg et al. (2017) and Kulk et al. (2020), but contradicts other studies that found a global decreasing trend (Behrenfeld et al., 2006; Boyce et al., 2010; Boyce et al., 2014; Gregg et al., 2014; Hammond et al., 2017), or global increasing trend (Antoine et al., 2005; Hammond et al., 2020). A direct numerical comparison between our results and these studies is impossible because differences can be explained by the use of different time scales, regions, methods, and data sources. Our findings support the conclusions of previous studies that demonstrated that the

magnitude and direction of the Chl-*a* trends vary substantially locally. We observed that Chl-*a* increased in 22 of 54 regions with 0.011–0.123 ± 0.002–0.026 mg m^{-3} per decade and decreased in 6 of 54 regions with 0.012–0.062 ± 0.004–0.019 mg m^{-3}per decade. Besides changes in phytoplankton dynamics, we indicate that mainly polar waters and some coastal waters are darkening, as the non-phytoplankton absorption increases significantly in these provinces.

Admittedly, the current length of the time series is not long enough yet for definitive conclusions regarding the effect of climate change on phytoplankton dynamics (Henson et al., 2010). It is still important to monitor the state of global waters and response of phytoplankton to a changing environment. The necessary time scale for deriving Chl-*a* trends is approximately 20–40 years and depends on the region (Henson et al., 2010). With the current time scale, it is possible that we detect trends that are caused by climate indices, e.g. the North Atlantic Oscillation because it has been overwhelmingly positive over the last decade (Figure 1) and may affect Chl-*a* trends (e.g. Henson et al., 2009; Ferreira et al., 2019; Barbedo et al., 2020).

4.1.1 Polar biome

This study demonstrates a strong increase in Chl-*a* in all polar provinces coinciding with warming trend of the surface waters. The northernmost province has the highest increase of Chl-*a* of 0.123 ± 0.026 mg m^{-3} per decade. The diminishing ice cover, increased growth rate, and possibly species migration are the likely reason for the positive correlation that we found between Chl-*a* and temperature (r: 0.2-0.4). The productivity in the polar waters is typically light and temperature dependent (Sakshaug and Slagstad, 1991). Rising temperatures due to global warming lead to decreasing ice cover, which extends the growing season and intensity of phytoplankton blooms as more light is available (Pabi et al., 2008; Ardyna et al., 2014; Arrigo and Van Dijken, 2015; Kahru et al., 2016; Lewis et al., 2020; Frey et al., 2021). Thereby, increasing surface temperatures in polar waters enhances the phytoplankton growth rate and causes northward phytoplankton migration that changes the species composition (Henson et al., 2021).

We observed significant increase of Chl-*a* in the polar water of the Southern Ocean provinces (0.027–0.093 ± 0.004–0.03 mg m^{-3} per decade), consistent with findings of studies by Hammond et al. (2020) and Sathyendranath et al. (2022). The water is freshening in the open waters of the Southern Ocean, likely due to the ice melting. We found a negative relationship between Chl-*a* and salinity in the open water province of the Southern Ocean (ANTA: r 0.3). In contrast, we found that the surface salinity is increasing near the Antarctic coast, which was also reported by Chaigneau and Morrow (2002) and Kolbe et al. (2021). In the coastal Southern Ocean province the salinity is positively related to Chl-*a* (APLR: r 0.4), which may be caused by the stronger vertical mixing in these shallower coastal waters and larger brine rejection in the local autumn and winter because of ice cover thinning (Chaigneau and Morrow, 2002; Holland et al., 2006).

In addition to the increase of Chl-*a*, we also found significant increase of non-phytoplankton absorption in 5 out of 6 polar provinces (not in ANTA). The sources of this increased absorption are increased terrestrial input and/or marine decomposition products. Several studies have found that the dissolved organic carbon in the Arctic Ocean is increasing because of permafrost thawing (Juhls et al., 2019; Mustaffa et al., 2020; Konik et al., 2021; Bernhard et al., 2022). Whereas, Chl-*a* in the Southern Ocean is highly correlated (r>0.8) with non-phytoplankton absorption, which suggests that the absorption originates from marine decomposition products. This increasing non-phytoplankton absorption leads to darker waters that absorb more light and result in stronger warming of the surface water (Soppa et al., 2019).

4.1.2 Westerly winds biome

In this study, we present evidence that the Chl-*a* is generally increasing in the westerly wind provinces (6 out of 13), but the increase is not as strong as in the polar provinces (0.011–0.033 mg m^{-3} ± 0.002–0.01 mg m^{-3} per decade). Interestingly, Chl-*a* is strongly increasing in the autumn in northern subarctic waters of the Pacific Ocean (PSAE and PSAW: 0.04–0.07 mg m^{-3} per decade), which indicates that secondary blooms could be occurring more frequently or have a larger biomass. The Antarctic Circumpolar Current is experiencing strengthening westerly winds (Wang et al., 2011) that possibly increases phytoplankton growth by enhancing vertical mixing in the nutrient-limited Southern Ocean waters (SSTC and SANT: 0.011–0.017 ± 0.002–0.006 mg m^{-3} per decade). Climate change can affect the strength of winds in these provinces and thus the mixed layer depth that affects the phytoplankton dynamics, but definitive trends are difficult to derive (for now) because of productivity correlation with natural oscillations, e.g. the El Niño oscillation (Henson et al., 2009). Further research is needed to fully understand the impacts of climate change on phytoplankton dynamics in these dynamic regions.

4.1.3 Trade winds biome

We found decreasing Chl-*a* trends in the trade wind provinces of the equatorial Pacific and Indian Ocean, in agreement with several studies (Behrenfeld et al., 2006; Hammond et al., 2020; Sathyendranath et al., 2022). However, almost all of these trends are currently smaller than the inherent bias of the dataset. Except for the North Pacific equatorial province (PNEC), which is decreasing with 0.019 ± 0.006 mg m^{-3} per decade. This province has a high negative correlation with SST (r: -0.8) and a high positive correlation with salinity (r: 0.8). The negative correlation between Chl-*a* and surface temperature in these nutrient-limited regions are likely caused by global warming that enhances stratification of the water column and as a result reduces phytoplankton growth rates waters (e.g. Behrenfeld et al., 2006; Boyce et al., 2010; Racault et al., 2012; Lewandowska et al., 2014; Dunstan et al., 2018).

4.1.4 Coastal biome

The coastal provinces are extremely diverse environments that are influenced by land-water exchange processes. Climate change and anthropogenic activities affect numerous regions of this ecosystem (Bindoff et al., 2019). We demonstrated that the Chl-*a* is changing in many provinces and highlight some of them here.

We observe increasing Chl-*a* trends in the China Sea (CHIN: 0.019 ± 0.018 mg m^{-3} per decade). This is supported by previous

research that linked eutrophication of coastal waters to human activities that increase nutrients in the river discharge (Zhou et al., 2020; Wang et al., 2021).

The eastern boundary upwelling systems (BENG, CCAL, CHIL, and CNRY) are highly productive waters defined by continuous cold wind-driven upwelling nutrient-rich water (Kämpf and Chapman, 2016). The upwelling in the Benguela current is forced by global sea-level pressure that is a response to climate change, whereas the upwelling in the other eastern boundary upwelling systems are largely forced by climate oscillations (Bonino et al., 2019). The Chl-*a* decreases in the Benguela province (BENG: -0.027 ± 0.013 mg m^{-3} per decade), which could be explained by decreased upwelling of nutrient-rich water. However, the trend of upwelling is highly dependent on the time period chosen for trend analysis (Bonino et al., 2019).

We show that the Chl-*a* in the southern coastal provinces of the New Zealand and Eastern Australian shelves is significantly increasing (AUSE and NEWZ: 0.012–0.025 ± 0.003–0.007 mg m^{-3} per decade). Our findings are supported by the increasing Chl-*a* trends found by Kelly et al. (2015), who also reported rapidly increasing salinity and temperature. They argue that the water is more nutrient rich because of increased southerly extension of the East Australian Current and its eddy field. Thompson et al. (2009) reported opposing trends, but used different areas, time scales, and data sources. Additionally, we found relatively high values of Chl-*a* (and $a_{dg}443$) between 2019 and 2021 in the time series of these waters, similar to Tang et al. (2021). They attributed this to the increased forest fires that were caused by enhanced droughts and climate change driven warming.

Many coastal waters in the Indian Ocean are associated with climatic fluctuations of the IOD and SOI (INDW, ARAB, and AUSW: r -0.4-0.4). The strongly seasonal productivity of the western Indian coastal province (INDW) coincides with the monsoon (June-September), whereas productivity in the eastern Indian coastal province (INDE) is less dependent on the monsoon, and is more affected by major river discharges (Longhurst, 2007). Climate change induced glacier melt and increased precipitation in the Ganges and Brahmaputra basins increase peak flow and discharge into the eastern Indian coastal basin during the monsoon (Nepal and Shrestha, 2015). We found that water is freshening in the SON months, which supports their findings. We found an increasing Chl-*a* trend in the eastern Indian waters (0.014 ± 0.009 mg m^{-3} per decade), as opposed to e.g. Behrenfeld et al. (2006) and Gregg et al. (2017). They found that Chl-*a* declines in both the eastern and western Indian coastal waters. We do indicate a negative Chl-*a* trend in the western Indian province (-0.054 ± 0.019 mg m^{-3} per decade).

4.2 Limitations

The limitation of using TGDM is that daily data records are lost and that seasonality could change since records are filtered depending on the recurrence of observations in every year. An optimised filtering strength (time window) was used to minimise initial data loss and find the optimal reduction of inter-mission inconsistencies per Longhurst province. The strictness, i.e. the length of the time window, and consequently the number of records masked to achieve temporal consistency, differs greatly per province (Appendix: **A2**A2). This resulted in a slightly larger number of total retained data records of the original dataset, 74%, compared to 70%, when using a universal time window of 27 days for the full OC-CCI v5 dataset (Van Oostende et al., 2022). Data gaps are effectively removed because the use of monthly composites. Another limitation of this study is that some biogeochemical provinces vary significantly optically and biologically and it would be beneficial to separate some of them into smaller provinces. For example, the Mediterranean- and Black Sea should be separated and the Baltic Sea should be separated from the rest of the greater North Sea.

It is important to note that the input SeaWiFS dataset (1997–2010) was atmospherically corrected with *l2gen* (SeaDAS 7.5; Franz et al., 2007), and the other sensors with POLYMER (v4.1: Steinmetz et al., 2011; Steinmetz et al., 2016). The *l2gen* processor flags more pixels for invalidity than POLYMER, e.g., observations that consist of high-sensor zenith angels or high values of brightness (Müller et al., 2015). The TGDM circumvents this issue by removing pixels that have not been observed consistently over time (Van Oostende et al., 2022).

There is larger uncertainty associated with optically active constituents retrieved from coastal and polar waters and typically have larger errors compared to other regions (Zheng et al., 2014; IOCCG, 2019; Werdell et al., 2019). Since the Chl-*a* and $a_{dg}443$ are produced by almost the same method (apart from atmospheric correction) and validated extensively with *in situ* match-ups, we believe it is justified to derive trends in these areas. Thereby, we only show trends that are larger than the inherent uncertainty of the dataset. Unfortunately, uncertainty estimates were not available for the salinity dataset (in our timespan and regions). Due to the limited timescale of the OC-CCI dataset, the bias is currently larger than the trends in most provinces with lower constituent concentrations (e.g. in the trade wind provinces). With future temporal extensions of the dataset, we will likely able to derive trends in these areas.

5 Conclusions

A key challenge in deriving long-term trends from merged ocean colour data is the inconsistency between the spatiotemporal coverage of the input sensor datasets, which can lead to both spurious multi-year fluctuations and trends in the time series. We corrected this inconsistency in the dataset and analysed the derived global and local trends. Our main results demonstrate that global phytoplankton dynamics change in response to different climate feedbacks and indicate a darkening of predominantly polar waters, associated with increasing organic carbon in water. We recommend that future studies that intend to use time series based on merged satellite datasets consider whether their data are affected by inter-mission coverage inconsistencies and, if necessary, apply a method

to minimise these. Additionally, previous studies that used time series based on merged ocean colour datasets may benefit from re-evaluating their findings. Future research should further investigate global and local trends in optically active constituents, especially when these time series become long enough to draw definitive conclusions on the effects of climate change on global waters and phytoplankton dynamics.

Data availability statement

Publicly available datasets were analyzed in this study. This data can be found here: https://www.oceancolour.org/ https://climate.esa.int/en/projects/sea-surface-temperature/ https://cds.climate.copernicus.eu/cdsapp#!/dataset/reanalysis-oras5?tab=form.

Author contributions

All authors jointly developed the concept and work plan. MO performed the calculations, preparated the figures, had lead on writing the manuscript. All authors contributed to the article and approved the submitted version.

Acknowledgments

This work is a contribution to the Ocean Colour Climate Change Initiative of the European Space Agency and was supported by the Helmholtz Association within the Earth and Environment research program. We thank Rüdiger Röttgers, Michael Novak, Sjoerd Koopman, and the reviewers for their valuable commentary.

Conflict of interest

The authors declare that the research was conducted in the absence of any commercial or financial relationships that could be construed as a potential conflict of interest.

Publisher's note

All claims expressed in this article are solely those of the authors and do not necessarily represent those of their affiliated organizations, or those of the publisher, the editors and the reviewers. Any product that may be evaluated in this article, or claim that may be made by its manufacturer, is not guaranteed or endorsed by the publisher.

Supplementary material

The Supplementary Material for this article can be found online at: https://www.frontiersin.org/articles/10.3389/fmars.2023.1052166/full#supplementary-material

References

Antoine, D., Morel, A., Gordon, H. R., Banzon, V. F., and Evans, R. H. (2005). Bridging ocean color observations of the 1980s and 2000s in search of long-term trends. *J. Geophys. Res. Ocean.* 110, 1–22. doi: 10.1029/2004JC002620

Ardyna, M., and Arrigo, K. R. (2020). Phytoplankton dynamics in a changing Arctic ocean. *Nat. Clim. Change* 10, 892–903. doi: 10.1038/s41558-020-0905-y

Ardyna, M., Babin, M., Gosselin, M., Devred, E., Rainville, L., and Tremblay, J. E. (2014). Fall phytoplankton blooms. *Geophys. Res. Lett.* 41, 6207–6212. doi: 10.1002/2014GL061047

Arrigo, K. R., and Van Dijken, G. L. (2015). Continued increases in Arctic ocean primary production. *Prog. Oceanogr.* 136, 60–70. doi: 10.1016/J.POCEAN.2015.05.002

Barbedo, L., Bélanger, S., and Tremblay, J.É. (2020). Climate control of sea-ice edge phytoplankton blooms in the Hudson bay system. *Elementa* 8, 1–25. doi: 10.1525/elementa.039

Behrenfeld, M. J., O'Malley, R. T., Siegel, D. A., McClain, C. R., Sarmiento, J. L., Feldman, G. C., et al. (2006). Climate-driven trends in contemporary ocean productivity. *Nature* 444, 752–755. doi: 10.1038/nature05317

Bernhard, P., Zwieback, S., and Hajnsek, I. (2022). Accelerated mobilization of organic carbon from retrogressive thaw slumps on the northern taymyr peninsula. *Cryosphere* 16, 2819–2835. doi: 10.5194/TC-16-2819-2022

Bidigare, R. R., Ondrusek, M. E., and Brooks, J. M. (1993). Influence of the Orinoco river outflow on distributions of algal pigments in the Caribbean Sea. *J. Geophys. Res.* 98, 2259–2269. doi: 10.1029/92JC02762

Bindoff, N. L., Cheung, W. W. L., Kairo, J. G., Arístegui, J., Guinder, V. A., Hallberg, R., et al. (2019). "Changing ocean, marine ecosystems, and dependent communities," in *IPCC special report on the ocean and cryosphere in a changing climate*. Eds. H.-O. Pörtner, D. C. Roberts, V. Masson-Delmotte, P. Zhai, M. Tignor, E. Poloczanska, et al (Cambridge, UK and New York, NY, USA: Cambridge University Press), 447–587. doi: 10.1017/9781009157964.007

Bonino, G., Di Lorenzo, E., Masina, S., and Iovino, D. (2019). Interannual to decadal variability within and across the major Eastern boundary upwelling systems. *Sci. Rep.* 9, 1–14. doi: 10.1038/s41598-019-56514-8

Boyce, D. G., Dowd, M., Lewis, M. R., and Worm, B. (2014). Estimating global chlorophyll changes over the past century. *Prog. Oceanogr.* 122, 163–173. doi: 10.1016/j.pocean.2014.01.004

Boyce, D. G., Lewis, M. R., and Worm, B. (2010). Global phytoplankton decline over the past century. *Nature* 466, 591–596. doi: 10.1038/nature09268

Bricaud, A., Babin, M., Morel, A., and Claustre, H. (1995). Variability in the chlorophyll-specific absorption coefficients of natural phytoplankton: analysis and parameterization. *JGR Oceans* 100(C7), 13321–13332. doi: 10.1029/95JC00463

Brown, J. H., Gillooly, J. F., Allen, A. P., Savage, V. M., and West, G. B. (2004). Toward a metabolic theory of ecology. *Ecology* 85, 1771–1789. doi: 10.1890/03-9000

Burke, L. A., Kura, Y., Kassem, K., Revenga, C., Spalding, M., and McAllister, D. (2001). *Pilot Analysis of Global Ecosystems: Coastal Ecosystems*. Washington, DC: World Resources Institute, p. 77

Chaigneau, A., and Morrow, R. (2002). Surface temperature and salinity variations between Tasmania and Antarctica 1993-1999. *J. Geophys. Res.* 107 (C12), SRF 22-1–SRF 22-8. doi: 10.1029/2001JC000808

Cleveland, R. B., Cleveland, W. S., McRae, J. E., and Terpenning, I. (1990). STL: a seasonal-trend decomposition procedure based on loess. *J. Off. Stat.* 6, 3–73. doi: 10.1007/978-1-4613-4499-5_24

Cullen, J. J. (1982). The deep chlorophyll maximum: comparing vertial profiles of chlorophyll a. *Can. J. Fish. Aquat. Sci.* 39, 791–803. doi: 10.1139/f82-108

Deppeler, S. L., and Davidson, A. T. (2017). Southern ocean phytoplankton in a changing climate. *Front. Mar. Sci.* 4. doi: 10.3389/fmars.2017.00040

Dunstan, P. K., Foster, S. D., King, E., Risbey, J., Kane, T. J. O., Monselesan, D., et al. (2018). Global patterns of change and variation in sea surface temperature and chlorophyll a. *Scientific Reports* 8, 14624. doi: 10.1038/s41598-018-33057-y

Durack, P. J., and Wijffels, S. E. (2010). Fifty-year trends in global ocean salinities and their relationship to broad-scale warming. *J. Clim.* 23, 4342–4362. doi: 10.1175/2010JCLI3377.1

Ferreira, A., Garrido-Amador, P., and Brito, A. C. (2019). Disentangling environmental drivers of phytoplankton biomass off Western Iberia. *Front. Mar. Sci.* 6. doi: 10.3389/FMARS.2019.00044/FULL

Franz, B. A., Bailey, S. W., Werdell, P. J., and Mcclain, C. R. (2007). Sensor-independent approach to the vicarious calibration of satellite ocean color radiometry. *Appl. Opt.* 46, 5068–5082. doi: 10.1364/AO.46.005068

Frey, K. E., Comiso, J. C., Cooper, L. W., Grebmeier, J. M., and Stock, L. V. (2021). "Arctic Ocean primary productivity: the response of marine algae to climate warming and Sea ice decline" in. *Arctic Report Card*. Eds., T. A. Moon, M. L. Druckenmiller and R. L. Thoman, doi: 10.25923/kxhb-dw16

Friedland, K. D., Mouw, C. B., Asch, R. G., Ferreira, A. S. A., Henson, S., Hyde, K. J. W., et al. (2018). Phenology and time series trends of the dominant seasonal phytoplankton bloom across global scales. *Glob. Ecol. Biogeogr.* 27, 551–569. doi: 10.1111/geb.12717

Gattuso, J. P., Magnan, A., Billé, R., Cheung, W. W. L., Howes, E. L., Joos, F., et al. (2015). Contrasting futures for ocean and society from different anthropogenic CO2 emissions scenarios. *Science* 349 (6243), aac4722. doi: 10.1126/science.aac4722

GCOS. (2011). *Systematic observation requirements for satellite-based products for climate*. Available at: www.wmo.int/pages/prog/gcos/Publications/gcos-154.pdf.

GCOS. (2016). *The global observing system for climate: implementation needs*. Available at: https://library.wmo.int/doc_num.php?explnum_id=3417.

Good, S. A., Embury, O., Bulgin, C. E., and Mittaz, J. (2019). ESA Sea Surface temperature climate change initiative (SST_cci): level 4 analysis climate data record, version 2.1. doi: 10.5285/aced40d7cb964f23a0fd3e85772f2d48

Gregg, W. W., Ecile, C., and Rousseaux, S. (2014). Decadal trends in global pelagic ocean chlorophyll: a new assessment integrating multiple satellites, *in situ* data, and models. *J. Geophys. Res. Ocean.* 119, 5921–5933. doi: 10.1002/2014JC010158

Gregg, W. W., Rousseaux, C. S., and Franz, B. A. (2017). Global trends in ocean phytoplankton: a new assessment using revised ocean colour data. *Remote Sens Lett.* 8 (8), 1102–1111. doi: 10.1080/2150704X.2017.1354263

Hammond, M. L., Beaulieu, C., Henson, S. A., and Sahu, S. K. (2020). Regional surface chlorophyll trends and uncertainties in the global ocean. *Sci. Rep.* 10 (1), 15273. doi: 10.1038/s41598-020-72073-9

Hammond, M. L., Beaulieu, C., Sahu, S. K., and Henson, S. A. (2017). Assessing trends and uncertainties in satellite-era ocean chlorophyll using space-time modeling. *Global Biogeochem. Cycles* 31, 1103–1117. doi: 10.1002/2016GB005600

Henson, S. A., Cael, B. B., Allen, S. R., and Dutkiewicz, S. (2021). Future phytoplankton diversity in a changing climate. *Nat. Commun.*. 12, 5372. doi: 10.1038/s41467-021-25699-w

Henson, S. A., Dunne, J. P., and Sarmiento, J. L. (2009). Decadal variability in north Atlantic phytoplankton blooms. *J. Geophys. Res. Ocean.* 114, C04013. doi: 10.1029/2008JC005139

Henson, S. A., Sarmiento, J. L., Dunne, J. P., Bopp, L., Lima, I., Doney, S. C., et al. (2010). Detection of anthropogenic climate change in satellite records of ocean chlorophyll and productivity. *Biogeosciences* 7, 621–640. doi: 10.5194/bg-7-621-2010

Holland, M. M., Bitz, C. M., and Tremblay, B. (2006). Future abrupt reductions in the summer Arctic sea ice future abrupt reductions in the summer Arctic sea ice. *Geophys. Res. Lett.* 33, L23503. doi: 10.1029/2006GL028024

Hurrell, J. W., Kushnir, Y., Ottersen, G., and Visbeck, M. (2003). An overview of the north atlantic oscillation. *Geophys. Monogr. Ser.* 134, 1–35. doi: 10.1029/134GM01

IOCCG. (2019). *Uncertainties in ocean colour remote sensing. no. 18*. Ed. F. Mélin Dartmouth (Canada: International Ocean-Colour Coordinating Group). doi: 10.25607/OBP-696

Jackson, T., Sathyendranath, S., Groom, S., and Calton, B. (2022) *Product user guide for v6.0 dataset. D4.2. ocean colour climate change initiative (OC_CCI) – phase 3*. Available at: https://docs.pml.space/share/s/fzNSPb4aQaSDvO7xBNOCIw.

Jackson, T., Volpe, G., Sathyendranath, S., and Groom, S. (2021). *Product validation and intercomparison report (Plymouth)*. (Plymouth Marine Laboratory (PML) and ESA Climate Office) (https://climate.esa.int). Available at: https://docs.pml.space/share/s/xztLpMNRka9rqoeSQFw5A

Joseph, D., Rojith, G., Zacharia, P. U., Sajna, V. H., Akash, S., and George, G. (2021). Spatio-temporal variations of chlorophyll from satellite derived data and CMIP5 models along Indian coastal regions. *J. Earth Syst. Sci.* 130, 1–12. doi: 10.1007/s12040-021-01663-6

Juhls, B., Overduin, P. P., Hölemann, J., Hieronymi, M., Matsuoka, A., Heim, B., et al. (2019). Dissolved organic matter at the fluvial-marine transition in the laptev Sea using *in situ* data and ocean colour remote sensing. *Biogeosciences* 16, 2693–2713. doi: 10.5194/BG-16-2693-2019

Kahru, M., Brotas, V., Manzano-Sarabia, M., and Mitchell, B. G. (2011). Are phytoplankton blooms occurring earlier in the Arctic? *Glob. Change Biol.* 17, 1733–1739. doi: 10.1111/j.1365-2486.2010.02312.x

Kahru, M., Kudela, R. M., Manzano-Sarabia, M., and Greg Mitchell, B. (2012). Trends in the surface chlorophyll of the California current: merging data from multiple ocean color satellites. *Deep. Res. Part II Top. Stud. Oceanogr.* 77–80, 89–98. doi: 10.1016/j.dsr2.2012.04.007

Kahru, M., Lee, Z. P., Kudela, R. M., Manzano-Sarabia, M., and Greg Mitchell, B. (2015). Multi-satellite time series of inherent optical properties in the California current. *Deep. Res. Part II Top. Stud. Oceanogr.* 112, 91–106. doi: 10.1016/j.dsr2.2013.07.023

Kahru, M., Lee, Z., Mitchell, B. G., and Nevison, C. D. (2016). Effects of sea ice cover on satellite- detected primary production in the Arctic ocean. *Arct. Ocean. Biol. Lett.* 12. doi: 10.1098/rsbl.2016.0223

Kämpf, J., and Chapman, P. (2016). "The functioning of coastal upwelling systems". In: *Upwelling Systems of the World*., (Springer, Cham) p. 31–65. doi: 10.1007/978-3-319-42524-5_2

Kelly, P., Clementson, L., and Lyne, V. (2015). Decadal and seasonal changes in temperature, salinity, nitrate, and chlorophyll in inshore and offshore waters along southeast Australia. *J. Geophys. Res. Ocean.* 120, 4226–4244. doi: 10.1002/2014JC010485

Kendall, M. G. (1948). Rank Correlation Methods. [Pp. vii 160. London: Charles Griffin and Co. Ltd., 42 Drury Lane, 18s.]. *Journal of the Institute of Actuaries*. 75 (1), 140–141. doi: 10.1017/S0020268100013019

Kirk, J. T. O. (2011). *Light and photosynthesis in aquatic ecosystems. 3rd ed* (Cambridge, UK: Cambridge University Press). doi: 10.1017/CBO9781139168212

Kolbe, M., Roquet, F., Pauthenet, E., and Nerini, D. (2021). Impact of thermohaline variability on Sea level changes in the southern ocean. *J. Geophys. Res. Ocean.* 126 (9), e2021JC017381. doi: 10.1029/2021JC017381

Konik, M., Darecki, M., Pavlov, A. K., Sagan, S., and Kowalczuk, P. (2021). Darkening of the Svalbard fjords waters observed with satellite ocean color imagery in 1997–2019. *Front. Mar. Sci.* 8. doi: 10.3389/fmars.2021.699318

Kulk, G., Platt, T., Dingle, J., Jackson, T., Jönsson, B. F., Bouman, H. A., et al. (2020). Primary production, an index of climate change in the ocean: satellite-based estimates over two decades. *Remote Sens.* 12, 1–27. doi: 10.3390/rs12050826

Lee, Z. P., Arnone, R., Hu, C., Werdell, P. J., and Lubac, B. (2010). Uncertainties of optical parameters and their propagations in an analytical ocean color inversion algorithm. *Appl. Opt.* 49, 369–381. doi: 10.1364/AO.49.000369

Lee, Z. P., Darecki, M., Carder, K. L., Davis, C. O., Stramski, D., and Rhea, W. J. (2005). Diffuse attenuation coefficient of downwelling irradiance: an evaluation of remote sensing methods. *J. Geophys. Res. C Ocean.* 110, 1–9. doi: 10.1029/2004JC002573

Lee, Z. P., Lubac, B., Werdell, J., and Arnone, R. (2009) *An update of the quasi-analytical algorithm (QAA_v5). tech. report, int. ocean colour coord. gr*. Available at: http://www.ioccg.org/groups/software.html.

Lewandowska, A. M., Boyce, D. G., Hofmann, M., Matthiessen, B., Sommer, U., and Worm, B. (2014). Effects of sea surface warming on marine plankton. *Ecol. Lett.* 17, 614–623. doi: 10.1111/ele.12265

Lewis, K. M., Van Dijken, G. L., and Arrigo, K. R. (2020). Changes in phytoplankton concentration now drive increased Arctic ocean primary production. *Sci. (80-.).* 369, 198–202. doi: 10.1126/science.aay8380

Longhurst, A. R. (2007). *Ecological geography of the Sea. 2nd ed* (London: Academic Press). doi: 10.1016/B978-0-12-455521-1.X5000-1

Longhurst, A., Sathyendranath, S., Platt, T., and Caverhill, C. (1995). An estimate of global primary production in the ocean from satellite radiometer data. *J. Plankton Res.* 17, 1245–1271. doi: 10.1093/PLANKT/17.6.1245

Mann, H. B. (1945). Nonparametric tests against trend. *Econometrica* 13, 245. doi: 10.2307/1907187

Merchant, C. J., Embury, O., Bulgin, C. E., Block, T., Corlett, G. K., Fiedler, E., et al. (2019). Satellite-based time-series of sea- surface temperature since 1981 for climate applications. *Sci. Data* 6, 223. doi: 10.1038/s41597-019-0236-x

Moore, T. S., Campbell, J. W., and Dowell, M. D. (2009). A class-based approach to characterizing and mapping the uncertainty of the MODIS ocean chlorophyll product. *Remote Sens. Environ.* 113, 2424–2430. doi: 10.1016/j.rse.2009.07.016

Morel, A. A., and Prieur, L. (1977). Analysis of variations in ocean color. *Limnol. Oceanogr.* 22, 709–722. doi: 10.4319/LO.1977.22.4.0709

Müller, D., Krasemann, H., Brewin, R. J. W., Brockmann, C., Deschamps, P. Y., Doerffer, R., et al. (2015). The ocean colour climate change initiative: i. a methodology for assessing atmospheric correction processors based on in-situ measurements. *Remote Sens. Environ.* 162, 242–256. doi: 10.1016/j.rse.2013.11.026

Mustaffa, N. I. H., Kallajoki, L., Biederbick, J., Binder, F. I., Schlenker, A., and Striebel, M. (2020). Coastal ocean darkening effects *via* terrigenous DOM addition on plankton: an indoor mesocosm experiment. *Front. Mar. Sci.* 7. doi: 10.3389/fmars.2020.547829

Navarro, G., Almaraz, P., Caballero, I., Vázquez, Á., and Huertas, I. E. (2017). Reproduction of spatio-temporal patterns of major mediterranean phytoplankton groups from remote sensing OC-CCI data. *Front. Mar. Sci.* 4. doi: 10.3389/fmars.2017.00246

Nepal, S., and Shrestha, A. B. (2015). Impact of climate change on the hydrological regime of the indus, Ganges and Brahmaputra river basins: a review of the literature. *Int. J. Water Resour. Dev.* 31, 201–218. doi: 10.1080/07900627.2015.1030494

O'Gorman, P. A. (2015). Precipitation extremes under climate change. *Curr. Clim. Change Rep.* 1, 49–59. doi: 10.1007/s40641-015-0009-3

Pabi, S., Van Dijken, G. L., and Arrigo, K. R. (2008). Primary production in the Arctic ocean 1998-2006. *J. Geophys. Res. Ocean.* 113, 1998–2006. doi: 10.1029/2007JC004578

Pitarch, J., Bellacicco, M., Marullo, S., and van der Woerd, H. J. (2021). Global maps of forel-ule index, hue angle and secchi disk depth derived from twenty-one years of monthly ESA-OC-CCI data. *Earth Syst. Sci. Data* 13, 481–490. doi: 10.5194/essd-13-481-2021

Racault, M. F., Le Quéré, C., Buitenhuis, E., Sathyendranath, S., and Platt, T. (2012). Phytoplankton phenology in the global ocean. *Ecol. Indic.* 14, 152–163. doi: 10.1016/j.ecolind.2011.07.010

Racault, M., Sathyendranath, S., and Brewin, R. J. W. (2017). Impact of El niño variability on oceanic phytoplankton. *Front. Mar. Sci.* 4, 133. doi: 10.3389/fmars.2017.00133

Saji, N. H., and Yamagata, T. (2003). Possible impacts of Indian ocean dipole mode events on global climate. *Clim. Res.* 25, 151–169. doi: 10.3354/cr025151

Sakshaug, E., and Slagstad, D. (1991). Light and productivity of phytoplankton in polar marine ecosystems: a physiological view. *Polar Res.* 10, 69–86. doi: 10.3402/POLAR.V10I1.6729

Sankar, S., Thondithala Ramachandran, A., Franck Eitel, K. G., Kondrik, D., Sen, R., Madipally, R., et al. (2019). The influence of tropical Indian ocean warming and Indian ocean dipole on the surface chlorophyll concentration in the eastern Arabian Sea. *Biogeosciences Discuss.*, 1–23. doi: 10.5194/bg-2019-169

Sathyendranath, S., Brewin, R. J. W. W., Brockmann, C., Brotas, V., Calton, B., Chuprin, A., et al. (2019). An ocean-colour time series for use in climate Studies : the experience of the ocean-colour climate (OC-CCI). *Sensors* 19, 2–31. doi: 10.3390/s19194285

Sathyendranath, S., Groom, S. B., Jackson, T., Volpe, G., and Calton, B. (2022) *ESA Ocean colour climate change initiative-phase 3 climate assessment report*. Available at: https://docs.pml.space/share/s/vS7lSM2DRBqrM9APK-PJkw.

Sen, P. K. (1968). Estimates of the regression coefficient based on kendall's tau. *J. Am. Stat. Assoc.* 63, 1379–1389. doi: 10.1080/01621459.1968.10480934

Shapiro, S. S., and Wilk, M. B. (1965). Biometrika trust an analysis of variance test for normality (Complete samples). *Source: Biometrika* 52, 591–611. doi: 10.2307/2333709

Soppa, M. A., Pefanis, V., Hellmann, S., Losa, S. N., Hölemann, J., Martynov, F., et al. (2019). Assessing the influence of water constituents on the radiative heating of laptev Sea shelf waters. *Front. Mar. Sci.* 6, 221. doi: 10.3389/fmars.2019.00221

Steinmetz, F., Deschamps, P.-Y., and Ramon, D. (2011). Atmospheric correction in presence of sun glint: application to MERIS. *Opt. Express* 19, 9783. doi: 10.1364/oe.19.009783

Steinmetz, F., Ramon, D., and Deschamps, P.-Y. (2016) *ATBD v1 - polymer atmospheric correction algorithm*. Available at: https://docs.pml.space/share/s/M05k8Lw3QLeXSIiA3X87UQ.

Tang, W., Llort, J., Weis, J., G Perron, M. M., Basart, S., Li, Z., et al. (2021). Widespread phytoplankton blooms triggered by 2019-2020 Australian wildfires. *Nature* 597, 370–375. doi: 10.1038/s41586-021-03805-8

Thompson, P. A., Baird, M. E., Ingleton, T., and Doblin, M. A. (2009). Long-term changes in temperate Australian coastal waters: implications for phytoplankton. *Mar. Ecol. Prog. Ser.* 394, 1–19. doi: 10.3354/meps08297

Valente, A., Sathyendranath, S., Brotas, V., Groom, S., Grant, M., Taberner, M., et al. (2019). A compilation of global bio-optical in situ data for ocean-colour satellite applications - version two. *Copernicus Publications: Earth System Science Data* 11 (3), 1037–1068. doi: 10.5194/essd-11-1037-2019

Van Oostende, M., Hieronymi, M., Krasemann, H., Baschek, B., and Röttgers, R. (2022). Correction of inter-mission inconsistencies in merged ocean colour satellite data. *Front. Remote Sens.* 3, 1–17. doi: 10.3389/frsen.2022.882418

Wang, W., Anderson, B. T., Kaufmann, R. K., and Myneni, R. B. (2004). The relation between the north Atlantic oscillation and SSTs in the north Atlantic basin. *J. Clim.* 17, 4752–4759. doi: 10.1175/JCLI-3186.1

Wang, Z., Kuhlbrodt, T., and Meredith, M. P. (2011). On the response of the Antarctic circumpolar current transport to climate change in coupled climate models. *J. Geophys. Res. Ocean.* 116, 1–17. doi: 10.1029/2010JC006757

Wang, Y., Tian, X., and Gao, Z. (2021). Evolution of satellite derived chlorophyll-a trends in the bohai and yellow seas during 2002–2018: comparison between linear and nonlinear trends. *Estuar. Coast. Shelf Sci.* 259, 107449. doi: 10.1016/J.ECSS.2021.107449

Wells, M. L., Karlson, B., Wulff, A., Kudela, R., Trick, C., Asnaghi, V., et al. (2020). Future HAB science: directions and challenges in a changing climate. *Harmful Algae* 91, 101632. doi: 10.1016/j.hal.2019.101632

Werdell, P. J., Mckinna, L. I. W., Boss, E., Ackleson, S. G., Craig, S. E., Gregg, W. W., et al. (2019). An overview of approaches and challenges for retrieving marine inherent optical properties from ocean color remote sensing. *Prog. Oceanogr.* 160, 186–212. doi: 10.1016/j.pocean.2018.01.001

Wirtz, K., Smith, S. L., Mathis, M., and Taucher, J. (2022). Vertically migrating phytoplankton fuel high oceanic primary production. *Nat. Clim. Change* 12, 750–756. doi: 10.1038/s41558-022-01430-5

Zheng, G., Stramski, D., and Reynolds, R. A. (2014). Evaluation of the quasi-analytical algorithm for estimating the inherent optical properties of seawater from ocean color: comparison of Arctic and lower-latitude waters. *Remote Sens. Environ.* 155, 194–209. doi: 10.1016/j.rse.2014.08.020

Zhou, Y., Wang, L., Zhou, Y., and Mao, X.z. (2020). Eutrophication control strategies for highly anthropogenic influenced coastal waters. *Sci. Total Environ.* 705, 135760. doi: 10.1016/J.SCITOTENV.2019.135760

Zuo, H., Balmaseda, M. A., Mogensen, K., and Tietsche, S. (2018). OCEAN5: the ECMWF ocean reanalysis system and its real-time analysis component. *ECMWF Technical Memoranda*, No. 823. doi: 10.21957/la2v0442

frontiers | Frontiers in Marine Science

TYPE Original Research
PUBLISHED 15 June 2023
DOI 10.3389/fmars.2023.1196352

Check for updates

OPEN ACCESS

EDITED BY
Astrid Bracher,
Alfred Wegener Institute Helmholtz Centre for Polar and Marine Research (AWI), Germany

REVIEWED BY
Shengqiang Wang,
Nanjing University of Information Science and Technology, China
Piotr Kowalczuk,
Polish Academy of Sciences, Poland

*CORRESPONDENCE
Shun Bi
Shun.Bi@hereon.de

RECEIVED 29 March 2023
ACCEPTED 19 May 2023
PUBLISHED 15 June 2023

CITATION
Bi S, Hieronymi M and Röttgers R (2023) Bio-geo-optical modelling of natural waters.
Front. Mar. Sci. 10:1196352.
doi: 10.3389/fmars.2023.1196352

COPYRIGHT
© 2023 Bi, Hieronymi and Röttgers. This is an open-access article distributed under the terms of the Creative Commons Attribution License (CC BY). The use, distribution or reproduction in other forums is permitted, provided the original author(s) and the copyright owner(s) are credited and that the original publication in this journal is cited, in accordance with accepted academic practice. No use, distribution or reproduction is permitted which does not comply with these terms.

Bio-geo-optical modelling of natural waters

Shun Bi*, Martin Hieronymi and Rüdiger Röttgers

Department of Optical Oceanography, Institute of Carbon Cycles, Helmholtz-Zentrum Hereon, Geesthacht, Germany

The color of natural waters – oceanic, coastal, and inland – is determined by the spectral absorption and scattering properties of dissolved and particulate water constituents. Remote sensing of aquatic ecosystems requires a comprehensive understanding of these inherent optical properties (IOPs), their interdependencies, and their impact on ocean (water) color, i.e., remote-sensing reflectance. We introduce a bio-geo-optical model for natural waters that includes revised spectral absorption and scattering parameterizations, based on a comprehensive analysis of precisely measured IOPs and water constituents. In addition, specific IOPs of the most significant phytoplankton groups are modeled and a system is proposed to represent the optical variability of phytoplankton diversity and community structures. The model provides a more accurate representation of the relationship between bio-geo-optical properties and can better capture optical variability across different water types. Based on the evaluation both using the training and independent testing data, our model demonstrates an accuracy of within ±5% for most component IOPs throughout the visible spectrum. We also discuss the potential of this model for radiative transfer simulations and building a comprehensive synthetic dataset especially for optically complex waters. Such datasets are the crucial basis for the development of satellite-based ocean (water) color algorithms and atmospheric correction methods. Our model reduces uncertainties in ocean color remote sensing by enhancing the distinction of optically active water constituents and provides a valuable tool for predicting the optical properties of natural waters across different water types.

KEYWORDS

inherent optical properties, ocean color, remote sensing, phytoplankton types, optically complex waters, essential climate variable

1 Introduction

During the transfer of solar radiation through the atmosphere and water, light is absorbed and scattered, i.e., its energy is converted into another form such as heat and its direction of propagation is changed. In aquatic science, light absorption and scattering properties of a water body are also called inherent optical properties (IOPs) because they do not depend on the ambient light field in the medium. Interactions of sunlight in the upper water layer create the ocean (water) color, an apparent optical property (AOP), from which information about IOPs can be derived. Therefore, IOP modeling is used in the context

with ocean color algorithm development. Spectral IOPs are fed into radiative transfer models, such as HydroLight (Mobley, 1994), to simulate remote-sensing reflectance, R_{rs}, and other interactions with (sun) light.

The color of natural waters contains a wealth of information about important constituents present in them, e.g., on primary production and pools of organic and inorganic carbon (Brewin et al., 2023). Therefore, ocean color is considered as an *Essential Climate Variable* (GCOS, 2011). The optically active components include phytoplankton, biogenic and minerogenic detritus, and chromophoric dissolved organic matter (CDOM). Interpreting the color information in terms of the concentrations and type of the different components requires the knowledge of the bio-geo-optical properties of the water body (Bricaud et al., 1998; Boss et al., 2001; Morel and Maritorena, 2001; Stavn and Richter, 2008). Optical remote sensing of aquatic ecosystems necessitates understanding the relationship between component concentrations and their IOPs, namely an "IOP model", and how IOPs relate to relevant signals, such as the remote-sensing reflectance. However, the challenge of bio-geo-optical modeling of natural waters is that values of IOPs in optically complex waters, e.g., coastal waters, can vary by orders of magnitude (Twardowski et al., 2001; Mobley et al., 2004; Zheng et al., 2015; Hieronymi et al., 2017).

Water reflectance and other apparent optical properties can be calculated numerically and analytically under all light conditions (so-called forward modeling). To simplify this modeling, Morel and Prieur (1977) divided water bodies in nature into *Case-1* and *Case-2* types according to their optical properties. It is important to note that this binary classification does not imply high or low values of optical properties but instead represents a difference in the model assumptions (Mobley et al., 2004). For *Case-1* waters, all optical properties (except pure water) are related to the phytoplankton biomass, which is parameterized by its total concentration of the pigment Chlorophyll *a*, [Chl], because it reflects the concentrations of most of the components due to the biological processes of phytoplankton (Morel and Maritorena, 2001). For *Case-2* waters, omitting sea bottom effects, the IOPs are not only related to [Chl] but also to other components from terrigenous or benthic inputs (Prieur and Sathyendranath, 1981; Sathyendranath et al., 1989; Werdell et al., 2018). This leads to the fact that, assuming the IOPs of pure water are known, for *Case-1* the bio-optical model requires only one variable, [Chl], which greatly simplifies the complexity of the model, while for *Case-2* waters, the IOP model requires more inputs, which are not covariant. However, the global ocean does not always conform to the ideal *Case-1* type, and Lee and Hu (2006) found that only about 60% of the ocean can be classified as such (depending on the used criterion), underscoring the complexity of a major part of natural waters. Another reason for the subdivision is the optimization of ocean color products from satellite remote sensing. As the boundaries of *Case-1* and *Case-2* are not always clear, the use of fuzzy-logic optical water type (OWT) classifications based on R_{rs} has been established in recent years, allowing suitable algorithms to be selected and seamless results to be produced (Moore et al., 2001; Moore et al., 2014; Mélin and Vantrepotte, 2015; Hieronymi et al., 2017; Jackson et al., 2017; Bi et al., 2019).

Component IOPs of *Case-2* waters are usually treated separately, which is commonly referred to as a "Four-term" model (IOCCG, 2006 and references therein), including the four components pure water, CDOM, detritus, and phytoplankton as the four important components. However, one should note that, as per *Case-2* definition, there are certainly other sources of IOPs, e.g., air bubbles (Stramski and Tegowski, 2001) or zooplankton (Basedow et al., 2019), which, however, are out of scope in this study (but any other components can be added easily to our model). The number "Four" here should be regarded as a "manageable number" as discussed in Stramski et al. (2001), which is a general concept of IOP assembly, and each component can be further separated into subcomponents based on how modelers understand the bio-geo-optical progress (Stramski et al., 2001, 2004). IOPs of pure water are typically parameterized as a function of wavelength, temperature, and salinity (Röttgers et al., 2016). The magnitude and spectral slope of CDOM vary significantly with molecular weight, source, and status of photobleaching of the relevant absorbing molecules (Röttgers and Doerffer, 2007; Helms et al., 2008), with the slope values usually present a lower variability in *Case-2* waters (Babin et al., 2003b). Detritus refers to the non-living organic and inorganic matter in the water column. It can be challenging to differentiate between biogenic (from living organisms) and non-biogenic (minerogenic, from rocks and minerals) detritus due to their similar spectral shapes and non-additive properties (Stramski et al., 2001; Roesler and Boss, 2008; Röttgers et al., 2014a). However, by incorporating their individual concentrations in a forward bio-optical model, it is possible to understand their respective impacts on particulate IOPs across various water environments (Ramírez-Pérez et al., 2018; Lo Prejato et al., 2020). In *Case-1* waters, it is reasonable to assume that detritus IOPs are more related to phytoplankton biomass due to its degradation, whereas in hydro-dynamically mixed shallow waters, they are more related to inorganic suspended matter concentrations. Phytoplankton IOPs show significant variability, with different phytoplankton groups exhibiting different spectral attributes (Bricaud et al., 1983; Sathyendranath et al., 1987; Hoepffner and Sathyendranath, 1991; Bracher et al., 2017). This variability can be attributed to the diversity of phytoplankton groups and species and their varying pigmentation, structural and morphological characteristics, which affect their light-interacting properties. This highlights the importance of considering the phytoplankton community composition when modeling IOPs and interpreting the results.

The main focus of building an IOP model is on the absolute values and spectral shapes (mostly from the ultra-violet to the near-infrared range) of the IOPs of individual components. The absolute values of the IOP components are related to their concentrations, and are typically described using mass-specific IOP coefficients. The spectral shape of mass-specific IOP is not dependent on the component concentrations in the water, and is instead a property of the component itself, determined by its biological, physical, and chemical properties. Some component IOP spectra are relatively simple, such as the absorption coefficient of CDOM, a_g (where the subscript *g* stands for the methodologically more appropriate term *gelbstoff*), which exhibits a monotonically decreasing trend with

wavelength, and can be well approximated by an exponential function in a certain wavelength range. Some are more complex, such as the absorption coefficient of phytoplankton, a_{ph}, which has a large peak in the blue-green spectral range and a narrower peak in the red spectral range. In larger absorbing phytoplankton particles, spectral scattering measurements (Bricaud et al., 1983; Roesler and Boss, 2003; Zhou et al., 2012) or simulations (Bernard et al., 2009; Organelli et al., 2018; Robertson Lain and Bernard, 2018) tend to show more peak-valley features. The feature is primarily due to the suppressions within absorption bands, which probably causes the inapplicability of assuming the scattering spectrum as a smooth power-law function (Babin et al., 2003a).

In satellite remote sensing of waters, there are many influencing factors, which produce partly similar features in the top-of-atmosphere radiance signal; these include the solar and observational angles, from the atmosphere especially the Rayleigh scattering from air molecules and aerosol influences, reflection effects at the water surface, and in the water column the IOPs of the different components. This can lead to ambiguities in the signal. Thus, accurate IOP modeling is important for the development of water algorithms, but also as a basis for atmospheric correction models. It allows the construction of large synthetic data sets without *in situ* measurements with unpredictable errors and possible data gaps (IOCCG, 2006). This is particularly important for the training of neural networks, which are used for about two decades for the inversion of remote sensing reflectance into IOPs, especially to solve the ambiguities for optically complex waters (Schiller and Doerffer, 1999; Doerffer and Schiller, 2000). However, due to simplification of bio-geo-optical properties, the simulations were based on several limiting assumptions and oversimplifications (Schiller and Doerffer, 1999; Doerffer and Schiller, 2007). To address these limitations, Hieronymi et al. (2017) developed an optical water type (OWT) classification and used a set of OWT-specific neural networks for a much wider range of applications including extremely absorbing or scattering waters; in addition, different phytoplankton groups were considered, but still with lacked confidence in the phytoplankton scattering coefficient due to the lack of observations. Note that it is important to consider phytoplankton community distribution in the forward modeling, since the phytoplankton diversity can result in varying cell sizes and pigment compositions, making the standard ocean color algorithm inapplicable across different water environments (Szeto et al., 2011; Bracher et al., 2017; IOCCG, 2019). For instance, *coccolithophores* exhibit IOPs and [Chl] that significantly differ from other types of algae, leading to distortion in the spectral band ratio (IOCCG, 2014). Detection of *coccolithophores* is often challenging, as they are usually only flagged when their brightness exceeds a certain threshold (Balch and Mitchell, 2023). To extend the dilemma further: in *Case-2* waters, the relationships between water components are more intricate and often random (Woźniak and Dera, 2007). Thus, despite numerous *in situ* measurements since decades, a universal approach for all natural waters remains elusive (IOCCG, 2019). Hence, a radiative transfer modeling framework specific to algorithm development, such as the ONNS in-water algorithm (Hieronymi et al., 2017), is necessary. Given that, previous forward models based on deterministic functions, e.g., fixed parameters, may not capture all the variability, and utilizing reasonable random values can improve flexibility in simulations (IOCCG, 2006; Zheng et al., 2015; Loisel et al., 2023).

The aim of this study is to develop a bio-geo-optical IOP model that accurately reproduces IOPs from given component concentrations, and can effectively capture variations in optical properties across different water types. By conducting a detailed and comprehensive analysis of *in situ* data with high accuracy and a wide range, this model will provide guidance for feeding radiative transfer simulations such as HydroLight, which allows the creation of a new synthetic database. The findings of this study will enhance our understanding of the composition of the planktonic community and its impact on optical variability. Also, we will review the specific IOP assumptions, the spectral scattering in particular, on remote sensing reflectance. This will have important implications for ocean color remote sensing including boundary conditions for the atmospheric correction.

2 Fundamental concept of the IOP model

All symbols, abbreviations, and units used are presented in Table 1. IOPs are represented as the sum of light absorption or scattering by water molecules and by various dissolved and particulate constituents. Previous laboratory studies (Twardowski et al., 2001; Vaillancourt et al., 2004) have already demonstrated the separation of absorption and scattering based on observations. By adopting the widely accepted conceptual separation of IOPs (Mobley, 1994), the total absorption and total scattering coefficients can be formulated as:

$$a_t(\lambda) = a_w(\lambda) + a_d(\lambda) + a_g(\lambda) + a_{ph}(\lambda) \quad (1)$$

and

$$b_t(\lambda) = b_w(\lambda) + b_d(\lambda) + b_{ph}(\lambda), \quad (2)$$

where λ is the wavelength of light and the subscripts w, d, g, and ph stand for the four components: pure water, detritus, *gelbstoff*, and phytoplankton, respectively (no particulate scattering is usually attributed to the dissolved *gelbstoff*). However, if other components are important in a specific context, they can be added (Stramski et al., 2001). The attenuation coefficient is the sum of absorption and scattering, expressed as. The total particulate IOPs are represented as the sum of that of detritus and phytoplankton: $a_p(\lambda) = a_d(\lambda) + a_{ph}(\lambda)$ and $b_p(\lambda) = b_d(\lambda) + b_{ph}(\lambda)$. The subscript gp is used to represent the IOPs calculated as the sum of CDOM (*gelbstoff*) and total particulates.

The light backscattering coefficients of water components are determined by

$$b_{bx}(\lambda) = \tilde{b}_{bx} b_x(\lambda), \quad (3)$$

where the subscript x represents different components (w, d, or ph), and $\tilde{b}_{bx}$ is the backscattering probability (or backscattering ratio). This ratio is the fraction of backward scattered light to total scattered light and is assumed to be constant, as no significant

TABLE 1 List of symbols, abbreviations, definitions, and units.

Symbol or abbreviation	Description	Unit
Abbreviations		
AOP	Apparent optical property	
IOP	Inherent optical property	
CV	Coefficient of variance, CV = standard deviation/mean	–
NIR	Near infrared spectral range	
UV	Ultraviolet spectral range	
VIS	Visible spectral range	
WOPP	Water Optical Properties Processor	
Short for concentrations		
CDOM	Colored dissolved organic matter, expressed as $a_g(440)$	m^{-1}
[Chl]	Concentration of chlorophyll *a*, Chl	mg/m^3
[ISM]	Concentration of inorganic suspended matter, ISM	g/m^3
[OSM]	Concentration of organic suspended matter, OSM	g/m^3
[TSM]	Concentration of total suspended matter, TSM	g/m^3
Short for phytoplankton groups		
Brown	Brown-colored phytoplankton group	
Cocco	*Coccolithophores* phytoplankton group	
Crypt	*Cryptophytes* phytoplankton group	
CyanB	Blue-green-colored *Cyanobacteria* phytoplankton group	
CyanR	Red-colored *Cyanobacteria* phytoplankton group	
Green	Green-colored phytoplankton group	
Symbols		
A_{xd}, S_{xd}*, C_{xd}	Coefficients of the exponential function with a constant for $a^*_{bd}(\lambda)$ and $a^*_{md}(\lambda)$ where *x* stands for *b* and *d*, respectively.	m^{-1}, nm^{-1}, m^{-1}
$a^*_{bd}(\lambda)$	Chl-specific biogenic detritus absorption coefficient	m^2/mg
$a_d(\lambda)$	Absorption coefficient of detritus	m^{-1}
$a_g(\lambda)$	Absorption coefficient of *gelbstoff* or colored dissolved organic matter (CDOM)	m^{-1}
$a^+_g(\lambda)$	Normalized $a_g(\lambda)$ at the reference wavelength, $a^+_g(\lambda) = a_g(\lambda)/a_g(\lambda_0)$	–
$a_{gp}(\lambda)$	Total absorption coefficient without pure water, $a_{gp}(\lambda) = a_t(\lambda) - a_w(\lambda)$	m^{-1}
$a^*_{md}(\lambda)$	Mass-specific minerogenic detritus absorption coefficient	m^2/g
$a_p(\lambda)$	Absorption coefficient of total particulate matter, $a_p(\lambda) = a_{ph}(\lambda) + a_d(\lambda)$	m^{-1}
$a_{ph}(\lambda)$	Absorption coefficient of phytoplankton	m^{-1}
$a^*_{ph}(\lambda)$	Chl-specific absorption coefficient of detritus	m^2/mg
$a^+_{ph}(\lambda)$	Normalized $a_{ph}(\lambda)$ at the reference wavelength, $a^+_{ph}(\lambda) = a_{ph}(\lambda)/a_{ph}(\lambda_0)$	–
$a^*_{ph,i}(\lambda)$	Chl-specific absorption coefficient of the *i*-th phytoplankton group	m^2/mg
$a_t(\lambda)$	Total absorption coefficient	m^{-1}
$a_w(\lambda)$	Absorption coefficient of pure water	m^{-1}
b_0, *n*, *m*	Coefficients of the model for $b^{GM83}_{ph}(\lambda)$	m^2/mg, -, -

(Continued)

10.3389/fmars.2023.1196352

TABLE 1 Continued

Symbol or abbreviation	Description	Unit
$b_{bd}(\lambda)$	Backscattering coefficient of detritus	m^{-1}
$b_{bph}(\lambda)$	Backscattering coefficient of phytoplankton	m^{-1}
$b_{bp}(\lambda)$	Backscattering coefficient of total particulate matter	m^{-1}
$b_{bt}(\lambda)$	Total backscattering coefficient	m^{-1}
$b_{bw}(\lambda)$	Backscattering coefficient of pure water	m^{-1}
$b_d(\lambda)$	Scattering coefficient of detritus	m^{-1}
$b_p(\lambda)$	Scattering coefficient of total particulate matter	m^{-1}
$b_{ph}(\lambda)$	Scattering coefficient of phytoplankton derived by the IOP model in this study	m^{-1}
$b^*_{ph}(\lambda)$	Chl-specific scattering coefficient	m^2/mg
$b^{\mathrm{Adj}}_{ph}(\lambda)$	Adjusted $b^{\mathrm{GM83}}_{ph}(\lambda)$ to the magnitude of $b_{ph}(\lambda)$	m^{-1}
$b^{\mathrm{GM83}}_{ph}(\lambda)$	Scattering coefficient of phytoplankton derived by the Gordon and Morel (1983) model	m^{-1}
$b_t(\lambda)$	Total scattering coefficient	m^{-1}
$b_w(\lambda)$	Scattering coefficient of pure water	m^{-1}
$\tilde{b}_{bd}$	Backscattering probability of detritus	–
$\tilde{b}_{bph}$	Backscattering probability of phytoplankton	–
$\tilde{b}_{bph,i}$	Backscattering probability of the i-th phytoplankton group	–
$c_d(\lambda)$	Attenuation coefficient of detritus	m^{-1}
$c_{gp}(\lambda)$	Total attenuation coefficient without pure water, $c_{gp}(\lambda) = c_t(\lambda) - c_w(\lambda)$	m^{-1}
$c_p(\lambda)$	Attenuation coefficient of total particulate matter	m^{-1}
$c_{ph}(\lambda)$	Attenuation coefficient of phytoplankton	m^{-1}
$c^*_{ph}(\lambda)$	Chl-specific attenuation coefficient of phytoplankton	m^2/mg
$c^+_{ph}(\lambda)$	Normalized $c_{ph}(\lambda)$ at the reference wavelength, $c^+_{ph}(\lambda) = c_{ph}(\lambda)/c_{ph}(\lambda_0)$	–
$c^*_{ph,i}(\lambda)$	Chl-specific attenuation coefficient of the i-th phytoplankton group	m^2/mg
$c_t(\lambda)$	Total attenuation coefficient	m^{-1}
$c_w(\lambda)$	Attenuation coefficient of pure water	m^{-1}
$F_{ph,i}$	Fraction of the i-th phytoplankton group with the value between 0 and 1	–
G^w_0, G^w_1, G^p_0, G^p_1	G coefficients in the Lee et al. (2011) model to calculate $R_{rs}(\lambda)$	–
γ_d	Power law exponent of $c_d(\lambda)$	–
γ_{ph}	Power law exponent of $c^+_{ph}(\lambda)$	–
$k(\lambda)$	Sum of total absorption coefficient and backscattering coefficient, $a_t(\lambda) + b_{bt}(\lambda)$	m^{-1}
λ	Light wavelength	nm
λ_0	Light reference wavelength	nm
N_{ph}	Number of phytoplankton groups	–
$p_1, p_2, \ldots, p_n$	Intermediate parameters in the "Two-term" IOP model (Table 3)	
$R_{rs}(\lambda)$	Remote-sensing reflectance	sr^{-1}
R	A random value between 0 and 1	–
S	Water salinity	PSU

(Continued)

TABLE 1 Continued

Symbol or abbreviation	Description	Unit
S_d	Exponential slope value of $a_d(\lambda)$	nm^{-1}
S_g	Exponential slope value of $a_d(\lambda)$	nm^{-1}
T	Water temperature	°C
$\omega_d(\lambda)$	Single-scattering albedo of detritus	–
$\omega_{ph}(\lambda)$	Single-scattering albedo of phytoplankton	–
$\omega_p(\lambda)$	Single-scattering albedo of total particulate matter	–

spectral changes have been observed (Twardowski et al., 2001; Vaillancourt et al., 2004). While $\tilde{b}_{bx}$ is normally calculated using volume scattering functions that describe the angular distribution of scattered light (Mobley, 1994; Harmel et al., 2021), in this study, fully radiative transfer simulations are not required as the focus is on forward modeling. Therefore, $\tilde{b}_{bx}$ is used as a simplification in the modeling work instead of the entire volume scattering function.

The single-scattering albedo, $\omega(\lambda)$, is the ratio of scattering to attenuation:

$$\omega_x(\lambda) = b_x(\lambda)/c_x(\lambda), \tag{4}$$

where the subscript x denotes total particle or individual components. $\omega(\lambda)$ is a dimensionless optical parameter combining $a(\lambda)$ and $b(\lambda)$ and is useful in optical modeling (Stramski et al., 2007). The total scattering coefficient $b(\lambda)$ can be easily determined if the shape of $c(\lambda)$ and $\omega(\lambda)$ are given.

2.1 The Four-term IOP model for complex waters

As mentioned in the introduction, the "Four-term" IOP model manages all components in Eqs. (1) and (2), separately. The IOPs of pure water are known and are not the subject of further modeling. The fundamental concepts of constructing IOPs of *gelbstoff*, detritus, and phytoplankton – so that it fits to our observational data – are illustrated in the following. The corresponding parameterizations, which we determined based on analyses of measured data, are given in section 3.2.

The absorption of *gelbstoff* in surface water, as a proxy of CDOM, can be expressed as:

$$a_g(\lambda) = a_g(\lambda_0)a_g^+(\lambda), \tag{5}$$

where the reference wavelength, λ_0, is usually at 440 nm, and $a_g^+(\lambda)$ is the normalized $a_g(\lambda)$ at λ_0, which has typically a nearly exponential shape in the visible spectral range, which is most relevant in the ocean color context. To substitute the exponential function into Eq. (5), $a_g(\lambda)$ can be written as

$$a_g(\lambda) = a_g(\lambda_0)\exp(-S_g(\lambda-\lambda_0)), \tag{6}$$

where S_g is the spectral slope estimated by nonlinear regression for a specific wavelength range, such as 350 to 500 nm (Babin et al., 2003b). The form of Eq. (6) has been widely accepted to compare the CDOM absorption coefficients across different systems but may have a risk when extrapolate to longer wavelengths, e.g., > 500 nm.

The absorption coefficient of detritus, $a_d(\lambda)$, is assumed to be controlled by both phytoplankton [Chl] and inorganic suspended matter, [ISM]. Following the concept of Ramírez-Pérez et al. (2018) and Lo Prejato et al. (2020), the absorption coefficient is constructed as:

$$a_d(\lambda) = [\mathrm{Chl}]a_{bd}^*(\lambda) + [\mathrm{ISM}]a_{md}^*(\lambda), \tag{7}$$

where $a_{bd}^*(\lambda)$ is the Chl-specific biogenic detritus absorption coefficient in the unit (m^2/mg) and $a_{md}^*(\lambda)$ is the mass-specific minerogenic detritus in (m^2/g). Note that the units of [Chl] and [ISM] are (mg/m^3) and (g/m^3), respectively.

The scattering of detritus is determined by the subtraction of its absorption from its attenuation:

$$b_d(\lambda) = c_d(\lambda) - a_d(\lambda)\,. \tag{8}$$

The attenuation coefficient of detritus, $c_d(\lambda)$, is described as a power law function to avoid any negative values:

$$c_d(\lambda) = c_d(\lambda_0)\left(\frac{\lambda_0}{\lambda}\right)^{\gamma_d}, \tag{9}$$

where the reference wavelength, λ_0, is often at 550 nm for its lower susceptibility to phytoplankton absorption, and γ_d is the power law exponent. Using Eq. (9), we can determine the spectral shape of c_d. To ensure a positive scattering value obtained from Eq. (8), we calculate the magnitude of its attenuation based on the single-scattering albedo at λ_0, $\omega_d(\lambda_0)$, which is a relative IOP parameter and can be empirically obtained. The magnitude of the spectrum, represented by $c_d(\lambda_0)$, can be then calculated by:

$$c_d(\lambda_0) = \frac{a_d(\lambda_0)}{1-\omega_d(\lambda_0)}\,. \tag{10}$$

The absorption coefficient of phytoplankton is expressed as

$$a_{ph}(\lambda) = [\mathrm{Chl}]a_{ph}^*(\lambda), \tag{11}$$

where a_{ph}^* in (m^2/mg) is the Chl-specific absorption coefficient, and [Chl] is commonly regarded as a proxy of the total phytoplankton concentration.

To capture the natural variability in phytoplankton IOPs due to the occurrence of different taxonomic groups, several phytoplankton groups with different optical properties and pigment compositions are considered. The Chl-specific absorption coefficient for

phytoplankton is then expressed as:

$$a^*_{ph}(\lambda) = \sum_{i=1}^{N_{ph}} f_{ph,i} a^*_{ph,i}(\lambda), \quad (12)$$

where $f_{ph,i}$ is the fraction from 0 to 1 of each group in sum equal to 1, and N_{ph} is the number of different groups used. $f_{ph,i}$ represents the proportionate contribution of each group to the total chlorophyll *a* concentration.

We define $a^+_{ph}(\lambda)$ as the normalized spectrum of phytoplankton absorption coefficient spectrum with respect to its value at the reference wavelength, which can be expressed as:

$$a^+_{ph}(\lambda) = \frac{a^*_{ph}(\lambda)}{a^*_{ph}(\lambda_0)} = \frac{a_{ph}(\lambda)}{a_{ph}(\lambda_0)}, \quad (13)$$

where λ_0 is the reference wavelength. Eq. (13) means one can obtain the spectral shape by any given phytoplankton absorption or specific absorption spectrum. Because we will afterwards obtain $a_{ph}(\lambda)$ once $a_{ph}(\lambda_0)$ is provided. This value is deemed as the spectral magnitude and can be obtained based on its relationship with [Chl]. The relationship is often described using a power law function:

$$a_{ph}(\lambda_0) = A[\mathrm{Chl}]^E, \quad (14)$$

where A is the scale factor, and the power exponent, E, is often observed to be slightly below one in global data sets (Bricaud et al., 1998; Woźniak and Dera, 2007). E represents the effects of pigment packaging and its interaction with phytoplankton cell size. Combining Eqs. (13) and (14), $a_{ph}(\lambda)$ of specific phytoplankton groups can be spectrally determined.

The reference wavelength λ_0 is often set at 443 nm (Bricaud et al., 2004). However, in this study, it was set at 676 nm, a wavelength where chlorophyll *a* is the dominating pigment absorption, and where a^*_{ph} is assumed to be very similar between different taxonomic groups, while variations at 443 nm would be larger due to a different pigment composition in each group.

Having $c_{ph}(\lambda) = [\mathrm{Chl}]c^*_{ph}(\lambda)$, the Chl-specific attenuation coefficient of phytoplankton, $c^*_{ph}(\lambda)$, is expressed as the sum of those of the different groups:

$$c^*_{ph}(\lambda) = \sum_{i=1}^{N_{ph}} f_{ph,i} c^*_{ph,i}(\lambda). \quad (15)$$

The phytoplankton Chl-specific scattering spectrum, $b^*_{ph}(\lambda)$, is then taken from the difference between those for attenuation and absorption:

$$b^*_{ph}(\lambda) = c^*_{ph}(\lambda) - a^*_{ph}(\lambda). \quad (16)$$

The backscattering of phytoplankton, b_{bph}, is calculated by multiplying $b_{ph}(\lambda)$ with the weighted sum of the backscattering probabilities of each phytoplankton group, $\tilde{b}_{bph}$, which is expressed as:

$$\tilde{b}_{bph} = \sum f_{ph,i} \tilde{b}_{bph,i}. \quad (17)$$

For phytoplankton groups for which $c^*_{ph}(\lambda)$ in Eq. (16) is unavailable, we will use $\omega_{ph}(\lambda_0)$ and re-normalized $c_{ph}(\lambda)$ at the reference wavelength, i.e., $c^+_{ph}(\lambda)/c^+_{ph}(\lambda_0)$, to determine $c^*_{ph}(\lambda)$:

$$c^*_{ph}(\lambda) = \frac{c^+_{ph}(\lambda)}{c^+_{ph}(\lambda_0)} \times \frac{a^*_{ph}(\lambda_0)}{1 - \omega_{ph}(\lambda_0)}, \quad (18)$$

where λ_0 is set at 676 nm likewise and $\omega_{ph}(\lambda_0)$ can be empirically obtained from the measurements or literature for specific phytoplankton groups, which controls the magnitude of $c^*_{ph}(\lambda)$, and $c^+_{ph}(\lambda)$ only serves the spectral shape and can be assumed safely as a power law function $(\lambda_0/\lambda)^{\gamma_{ph}}$ where the exponent γ_{ph} determines the spectral slope. The power law function was also used to extrapolate $c^*_{ph}(\lambda)$ beyond the measured wavelength range.

2.2 The Two-term IOP model for phytoplankton dependence only

While the "Four-term" IOP model is highly adaptable, it may not be the most efficient option for simulating *Case-1* waters, which make up the majority of the Earth's oceans and are influenced by only two principal components: pure water and phytoplankton. Although the "Four-term" model can simulate these waters, it often requires more computational time and the gain in accuracy is small. To improve efficiency, we added a "Two-term" IOP model, as a supplement, by following the data synthesis process outlined in the IOCCG (2006), but using the setups for pure water and phytoplankton from the "Four-term" model (section 2.1) to mimic different phytoplankton groups. In the "Two-term" model, the fraction of phytoplankton groups from pico-phytoplankton to micro-phytoplankton is constrained by varying limits based on [Chl] levels. At low [Chl] levels, oceanic groups dominate, while other groups become mixed in as [Chl] increases (Brewin et al., 2010; Losa et al., 2017). However, in the "Four-term" model, there are no bounded limits as phytoplankton communities may be not correlated with [Chl] in optically complex water such as coastal and inland waters. The fraction setting is a preliminary biological limit that prevents unrealistic scenarios, but can be further refined with additional knowledge inputs.

3 Model development

3.1 Data sets

3.1.1 Fundamental data set for the model developing

The IOP model was developed using the "Hereon" data set collected by scientists of the Helmholtz-Zentrum Hereon in Germany (Röttgers et al., 2023). The comprehensive data set includes various water systems, including coast (the southern North Sea), river (the Elbe River), and ocean (the Atlantic Ocean), representing both *Case-1* and *Case-2* waters, which makes it suitable for building the IOP model. The data collection and processing methods of the coast and river parts (N=794) are detailed in Röttgers et al. (2023). However, the ocean part (N=40), which follows the same protocols, is not yet published. This part of data is primarily used for identifying and characterizing an oceanic

phytoplankton group. Except that the [ISM] measurements are not available in the ocean part, the *Hereon* data set contains parameters of water constituents including [Chl], concentration of total suspended matter, [TSM], and concentration of organic suspended matter, [OSM]. [ISM] is calculated by subtracting [OSM] from [TSM]. The uncertainties of [TSM] and [OSM] measurements are given as the standard deviation using the method proposed in Röttgers et al. (2014b). Measurements of spectral IOPs, namely $c_{gp}(\lambda)$, $c_p(\lambda)$, $a_{gp}(\lambda)$, $a_p(\lambda)$, $a_g(\lambda)$, $a_d(\lambda)$, $a_{ph}(\lambda)$, $b_p(\lambda)$, and $b_{bp}(\lambda)$, are provided in the *Hereon* data.

3.1.2 External data sets for the model evaluation

Several external *in situ* data sets were considered to evaluate the IOP model. The "C22" data set, collected by Castagna et al. (2022), was obtained from turbid and eutrophicated Belgian inland and coastal waters, and it provides co-measured component concentrations, IOPs, and R_{rs}. The "HYPERMAQ", gathered by Lavigne et al. (2022), consists of water samples from coastal and inland waters with co-measured component concentrations and IOPs. The "M17", compiled by Mouw et al. (2017), contains samples from a four-year period in Lake Superior, a large freshwater lake that is dominated by CDOM. These data sets are utilized to test the "Four-term" IOP model with [Chl], [ISM], and $a_g(440)$ as inputs. Additionally, the "OC-CCI v3" data set by Valente et al. (2022), which is the third version of the collection for the ESA Ocean Colour-Climate Change Initiative (OC-CCI), was also utilized. This data set mainly comprises oceanic samples, including [Chl], a_{ph}, a_{dg}, b_{bp}, and R_{rs}, and was aggregated within ±2 nm of satellite bands. It was used to test the "Two-term" IOP model with [Chl] as input.

Furthermore, three simulated data sets were included to assess the coverage of optical properties. The "L23" database by Loisel et al. (2023), with a special focus on *Case-1* waters, was synthesized following the process in IOCCG (2006), but its data distribution was constrained to fit the global distribution based on satellite products. The "CCRR" by Nechad et al. (2015), with a focus on *Case-2* waters, was simulated based on *in situ* measurements collected in the ESA Coast Colour Round Robin project (see specifications in their Table 11). The "C2X" database by Hieronymi et al. (2016, 2017). addresses all natural waters, including *Case-1* and extremely absorbing or scattering waters, though with some different IOP assumptions (see later discussion). Table 2 presents the sample number and the ranges of component concentrations.

3.2 Analysis of *in situ* data and parameterization of the IOP model

3.2.1 Pure water

The real part of the spectral refractive index of water, as well as water absorption and water scattering, are used as a function of wavelength, water temperature, and salinity. The calculation of pure water IOPs is based on the Water Optical Properties Processor (WOPP) (Röttgers et al., 2016 and references therein). The pure water light absorption coefficient in the UV/VIS part (< 510 nm) is taken from Mason et al. (2016).

3.2.2 CDOM

Figure 1 shows CDOM absorption spectra from the coastal, river, and oceanic waters from *Hereon*, *C22*, and *M17*. The spectral slope of most *Case-2* waters exhibits relatively limited variation, with even more consistency observed in the turbid river data. However, variability in spectral slope is observed in *Hereon – Ocean* due to different sources of organic matters, photodegradation, precipitation, and microbial alteration of CDOM (Kieber et al., 2006; Helms et al., 2008). The distribution of S_g in the data set is consistent with previous reports in European coastal waters (Babin et al., 2003b) of 0.0176 ± 0.002 nm^{-1}, and the shape is comparable to the determination in the Ligurian Sea (Ramírez-Pérez et al., 2018).

Initially, we used the exponential function, Eq. (6), to fit $a_g(\lambda)$ measurements from the *Hereon* data within the 350~500 nm range. This yielded a mean S_g value of 0.0174 ± 0.0014 nm^{-1}, with fitted slope values varying in a narrow range. However, using this mean slope caused a discrepancy between modeled $a_g(\lambda)$ values and measured values at longer wavelengths, with the modeled $a_g(560)$ by Eq. (6) being approximately 20% lower than the real measurements on average. To address this issue, we identified a normalized spectrum from measurements with the nearest S_g values

TABLE 2 The summary of IOP data sets used in this study.

Name	Reference	N	[Chl]	[ISM]	$a_g(440)$
Hereon	Röttgers et al. (2023)	834	0~54	0~240	0~1.1
C22	Castagna et al. (2022)	77	0~400	1~800	0.3~2.8
HYPERMAQ	Lavigne et al. (2022)	179	1~180	0~450	1.8~3.5
M17	Mouw et al. (2017)	37	0~6	0~2	0~2.1
OC-CCI v3	Valente et al. (2022)	6,766	0~78	N/A	N/A
C2X	Hieronymi et al. (2016, 2017)	100,000	0~200	0~1,500	0~20
CCRR	Nechad et al. (2015)	5,000	0~214	0~500	0~15
L23	Loisel et al. (2023)	29,880	N/A	N/A	0~0.4

Unit: [Chl] (mg/m^3), [ISM] (g/m^3), $a_g(440)$, (m^{-1}).
The Hereon data set was used for model training, while the remaining data sets were used for evaluation.
N/A means data are not available.

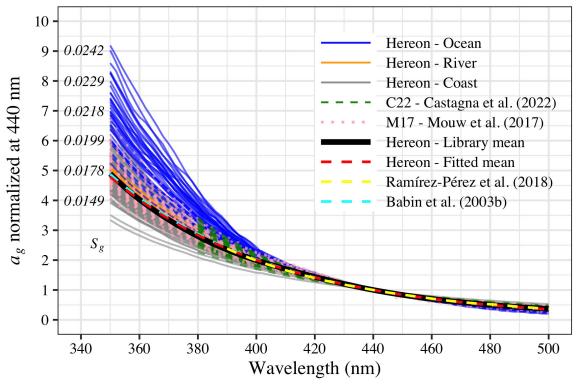


FIGURE 1
Normalized CDOM absorption spectra, $a_g^+(\lambda)$, from data sets *Hereon* (grouped into ocean, river, and coast), *C22* (Castagna et al., 2022), and *M17* (Mouw et al., 2017), as well as from modeled spectra by Ramírez-Pérez et al. (2018) and Babin et al. (2003b). The red dashed line represents the fitted $a_g^+(\lambda)$ spectrum based on the exponential function, Eq. (6), with a mean S_g value of 0.0174 nm^{-1}. The black solid line indicates the mean spectrum of the $a_g^+(\lambda)$ library in the IOP model (*see text*). Spectral slopes for a_g on the left.

(see black solid line in Figure 1). To account for the variability of the $a_g(\lambda)$ shape in the UV, we constrained the percentage difference of S_g between the fitted mean value to be less than 0.1%, resulting in a library of twelve $a_g^+(\lambda)$ spectra (not shown). Such random selection of $a_g^+(\lambda)$ exhibits deviations of 0.7685 and 0.0543 at 300 and 350 nm, respectively. Finally, in the "Four-term" IOP model, Eq. (5) will be used to model $a_g(\lambda)$ by providing $a_g(440)$ and randomly selecting an $a_g^+(\lambda)$ spectrum from the library.

3.2.3 Detritus

To determine $a_{bd}^*(\lambda)$ and $a_{md}^*(\lambda)$ in Eq. (7), we formulated a linear matrix equation at each wavelength:

$$\begin{bmatrix} [\mathrm{ISM}]_1 & [\mathrm{Chl}]_1 \\ [\mathrm{ISM}]_2 & [\mathrm{Chl}]_2 \\ \cdots & \cdots \\ [\mathrm{ISM}]_n & [\mathrm{Chl}]_n \end{bmatrix} \times [a_{md}^*(\lambda_i),\ a_{bd}^*(\lambda_i)]^{\mathrm{T}} = \begin{bmatrix} a_d(\lambda_i)_1 \\ a_d(\lambda_i)_2 \\ \cdots \\ a_d(\lambda_i)_n \end{bmatrix}, \quad (19)$$

where n denotes the number of samples used to solve the equation matrix, i denotes the wavelength number, and here T denotes the transpose sign. This equation satisfies the condition $a_{md}^*(\lambda_i) > 0$ and $a_{bd}^*(\lambda_i) > 0$.

To reduce noise effects in the solution of Eq. (19), we applied constraints to the *Hereon* data for [Chl], [ISM], and $a_d(\lambda)$ measurements. Any detritus absorption spectra that showed remnants of pigment absorption were discarded. The coefficients of variation (CV) of each component concentration were calculated as the ratio of its standard deviation to the mean value (Röttgers et al., 2014b). To select for accurate, detritus dominated measurements, we applied the following constraints: CV(TSM) ≤ 0.3, CV(OSM) ≤ 0.3, and the proportion of detritus of total particle absorption, $a_d(550)/a_p(550) \geq 0.5$. Note that the values used here for constraints are arbitrary to ensure sufficient samples to solve Eq. (19). As a result, there were $n = 80$ data combinations in Eq. (19). To avoid biased results, we used a "Markov-chain" Monte Carlo algorithm by Meersche et al. (2009) to solve Eq. (19). 3,000 iterations were used as suggested by this algorithm. The results are presented as points in Figures 2A, B. The variability of $a_{bd}^*(\lambda)$ is higher than that of $a_{md}^*(\lambda)$, and the separation of biogenic and minerogenic components has a significant impact on the shape of $a_d(\lambda)$, depending on the ratio of [Chl] and [ISM]. Even though we conducted quality control on $a_d(\lambda)$, a slight peak around 676 nm still appeared in the determined $a_{bd}^*(\lambda)$, as observed in a similar study by Ramírez-Pérez et al. (2018). This peak may be due to imperfect bleaching of pigments, so we excluded the region around 676 nm for the non-linear regression of $a_{bd}^*(\lambda)$.

We employed an exponential function with a constant to fit $a_{bd}^*(\lambda)$ and $a_{md}^*(\lambda)$ as there were non-zero signals in the near infrared (Röttgers et al., 2014a). This function is given by:

$$a_{xd}^*(\lambda) = A_{xd} \exp\left(-S_{xd}^*(\lambda - \lambda_0)\right) + C_{xd}, \quad (20)$$

where the subscript x denotes biogenic and minerogenic detritus as b and m, respectively, and λ_0 represents the reference wavelength at 550 nm. We tested the function with and without a constant C_{xd} and found that including the constant yielded better results, which is consistent with the findings in Woźniak and Dera (2007). The Meersche et al. (2009) method resulted in $a_{xd}^*(\lambda_i)$ as a normal distribution per wavelength, so we performed an exponential fit at different quantiles, ranging from 0 to 1, of $a_{bd}^*(\lambda)$ and $a_{md}^*(\lambda)$. The quantile of 0.5 indicates the maximum of the distribution, representing the average condition for the selected data. For this average condition, the coefficients are $A_{bd} = 0.0004\ m^{-1}$, $S_{bd}^* = 0.0158\ nm^{-1}$, $C_{bd} = 0.001\ m^{-1}$, $A_{md} = 0.0135\ m^{-1}$, $S_{md}^* = 0.0104\ nm^{-1}$, and $C_{md} = 0.0122\ m^{-1}$. The coefficients of Eq. (20) for other quantiles in the *Hereon* data set are listed in the Supplementary Material (Table A3). Although higher quantiles may suggest a higher organic composition of particles, we found no significant correlation and therefore this requires further investigation before being used.

Measurement of attenuation and scattering of detritus alone are technically not feasible. Therefore, we began by analyzing total particles and selecting again detritus-dominated samples to represent the IOPs of detritus. Subsequently, we used these IOPs to parameterize the spectral slope of attenuation, γ_d, and the single-scattering albedo of detritus at the reference wavelength, $\omega_d(\lambda_0)$, in Eqs. (9) and (10), respectively. We applied two constraints to the training data: 1) $a_d(550)/a_p(550) \geq 0.85$ and 2) only surface samples (water depth ≤ 12 m). Based on these criteria, we obtained 24 samples where we assumed that the $c_p(\lambda)$ spectra represented $c_d(\lambda)$. The distribution of γ_d and $\omega_d(550)$ for these samples are shown in Figures 2C, D, respectively. The mean value of γ_d is 0.3835 ± 0.1277 nm^{-1}, which follows a normal distribution function. As γ_d decreases, the spectrum gradually flattens, indicating that detritus increasingly dominates, which has been reported by other studies too (Voss, 1992; Boss et al., 2001; Twardowski et al., 2001; Neukermans et al., 2012). To satisfy a normal distribution, we re-transformed the single-scattering albedo of detritus, $\omega_d(550)$, using $\log_{10}(1 - \omega_d(550))$. The resulting mean value of transformed $\omega_d(550)$ is −1.3390 ± 0.0618 (mean of 0.9542 on its original scale). The determined $\omega_d(\lambda)$ spectrum (not shown) is comparable to laboratory measurements of most terrigenous

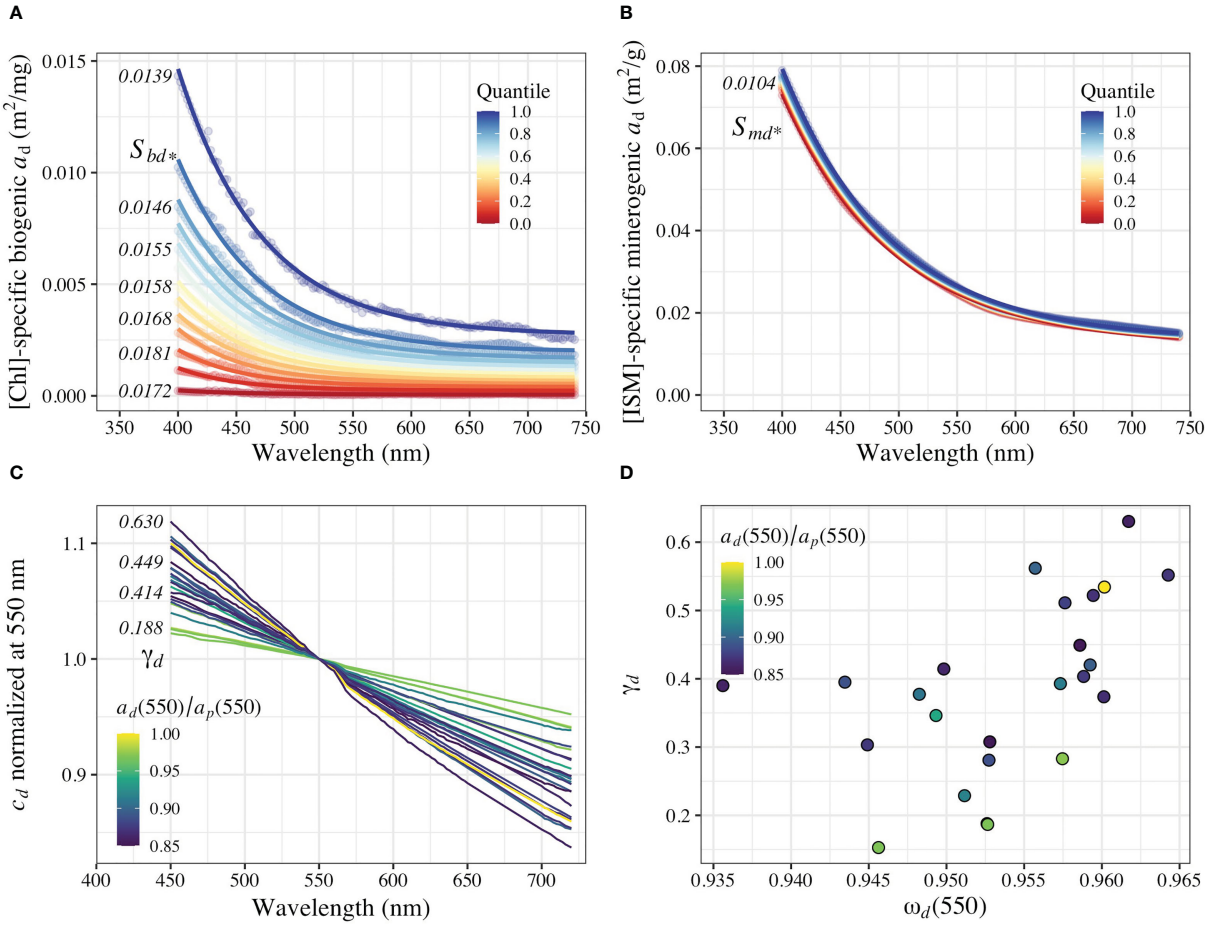


FIGURE 2
Spectral coefficients of detritus. **(A)** Chl-specific biogenic detritus absorption, m^2/mg. **(B)** ISM-specific minerogenic detritus absorption, m^2/g. **(C)** Normalized particle attenuation spectra at 550 nm. Note that the Y-axis does not start from the origin. **(D)** Scatter plot of ω_d (550) and γ_d (550). Determined on varying quantiles, points fitted in exponential functions with constant. Normalized attenuation spectra fitted based on power law function. Spectral slopes for a^*_{bd}, a^*_{md}, and c_d on the left of panels **(A–C)**.

particles (Stramski et al., 2007). Finally, we set the backscattering probability of detritus, $\tilde{b}_{bd}$, as 0.0216 based on these measurements.

To summarize, the "Four-term" IOP model follows a process where a quantile value between 0 and 1 is randomly chosen from the fitting results to determine $a^*_{bd}(\lambda)$ and $a^*_{md}(\lambda)$ using Eq. (20). Next, $a_d(\lambda)$ is calculated based on [Chl] and [ISM] using Eq. (7). γ_d and $\omega_d(550)$ are randomly generated from normal distributions based on their statistical parameters to determine $c_d(\lambda)$. Finally, $b_d(\lambda)$ is obtained using Eq. (8), and $b_{bd}(\lambda)$ is calculated by multiplying $b_d(\lambda)$ with $\tilde{b}_{bd}$. One should note that the random terms used for detritus IOPs are derived from the *Hereon* statistics and are already representative. However, they can be adjusted to other specific environments, which is relatively more convenient compared to other models that require the replacement of entirely new specific-IOPs.

3.2.4 Phytoplankton

The relationships between [Chl] and $a_{ph}(676)$ from the *Hereon* data is shown in Figure 3A, after excluding outliers (i.e., water depth > 12 m and ten samples with obvious a_{ph} noise). A power law function, Eq. (14), was initially used to fit the data. However, for lower [Chl] values (≤ 1 mg/m^3), we found that a linear relationship ($E = 1$) was more appropriate. Therefore, $a_{ph}(676)$ can be expressed using a hybrid function:

$$a_{ph}(676) = \begin{cases} 0.0237[\mathrm{Chl}]^{1.0000}, & [\mathrm{Chl}] \le 1 \ \ \mathrm{mg/m^3} \\ 0.0237[\mathrm{Chl}]^{0.8987}, & [\mathrm{Chl}] > 1 \ \ \mathrm{mg/m^3} \end{cases}. \quad (21)$$

To account for natural variation, the equation allows a deviation within ±20% of the A coefficient (i.e., 0.0112~0.0501) (Bricaud et al., 1995). Figure 3B demonstrates that this range agrees well with other data sets and other fitting models (Bricaud et al., 1995; Bricaud et al., 1998; Churilova et al., 2017; Castagna et al., 2022).

To capture the optical features of phytoplankton diversity, we selected spectral properties of seven different phytoplankton groups. Five of these groups represent the essence of distinguishable phytoplankton absorption spectra of algal cultures determined in preliminary work by the authors (Xi et al., 2015; Hieronymi et al., 2017; Xi et al., 2017) and include: (1) a brown group (*Heterokontophyta* [including diatoms], *Dinophyta*, and *Haptophyta*), (2) a green group (*Chlorophyta*), (3) the

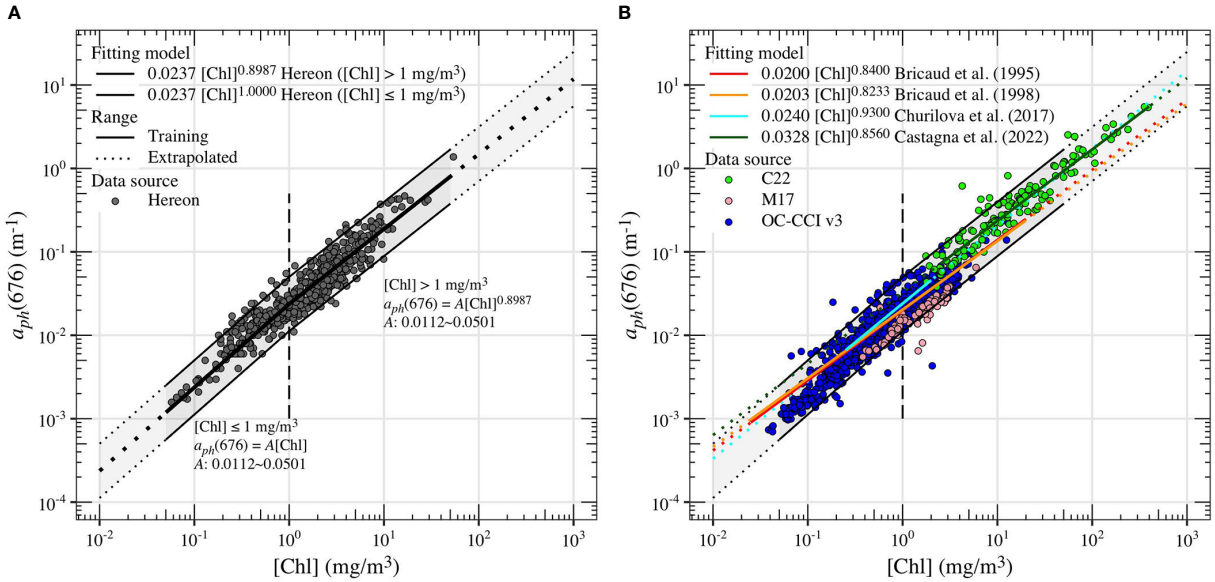


FIGURE 3
Relationship between [Chl] and a_{ph} (676) on the $\log_{10}$ scale with different regression curves from previous studies and the *Hereon* data. The solid lines denote the training data range and the dashed lines are extrapolated. Points in panel **(A)** are for the Hereon data and panel **(B)** for the external data sets.

Cryptophyceae; (4) a blue-green-colored *Cyanobacteria* and (5) a red-colored *Cyanobacteria*. In addition, two other groups were considered: (6) "Phytoplankton Case-1" for oligotrophic *Case-1* waters and (7) a group representing *Coccolithophores*. The "Phytoplankton Case-1" group shall represent a small-sized group of widely distributed oceanic phytoplankton (*Synechococcus* and *Prochlorococcus*), that play an important role in global primary production. The corresponding IOP data for this group were collected in the tropical-subtropical North Atlantic Ocean (*RV Sonne*, SO287, 12/2021-01/2022) following the same protocol as in Röttgers et al. (2023). *Coccolithophores* are marine group that are abundant in temperate zones and exhibit strong particulate scattering, which can dominate ocean color properties. Without blooms, their b_{bph} typically accounts for approximately 10~20% of total b_{bp}, whereas during intense blooms, b_{bph} can account for over 90% of total b_{bp} (Balch et al., 1991; Balch and Mitchell, 2023). The specific IOP data for the *Coccolithophore* group were taken from measurements of the unialgal culture *Coccolithus huxleyi* by Bricaud et al. (1983).

In our previous studies (Xi et al., 2015, 2017), we measured the absorption coefficients of two *Cyanobacteria* groups, the "Green" group and the *Cryptophytes* from cultures, but their attenuation and scattering coefficients were not available for this study. To estimate these coefficients, we made a first guess. We determined the Chl-specific IOPs of the "Brown" group from a subset of the *Hereon* data that was dominated by this phytoplankton group. We excluded samples collected in the Atlantic Ocean and samples with $a_d(560)/a_p(560) \geq 0.3$ and [Chl]< 1 mg/m^3, which is additionally based on the constrain settings for calculating $a^*_{ph}(676)$. Since it is impossible to measure the true $c_{ph}(\lambda)$ in a natural sample, we used $b_p(\lambda)$ and $c_p(\lambda)$ to represent $b_{ph}(\lambda)$ and $c_{ph}(\lambda)$ for the constrained samples. The single-scattering albedo of phytoplankton at 676 nm, ω_{ph} (676), for the "Brown" group has a mean value of 0.8952 ± 0.0107. The corresponding spectra of $a_{ph}(\lambda)$, $b_p(\lambda)$, and $c_p(\lambda)$ are shown in Figure 4, which do not exhibit any obvious spectral features in the attenuation coefficients, likely due to the rather large cell size of this phytoplankton group. Therefore, we assumed that, for groups without measured attenuation coefficients, they are spectrally constant over the wavelength, which is not true in reality but should be considered as a reasonable way to mimic the shape of scattering spectra by subtraction. Once we determined $\omega_{ph}(676)$ for each group, we calculated the magnitude of phytoplankton attenuation using Eq. (18). The values of $\omega_{ph}(676)$ for the *Coccolithophores* and the "Phytoplankton Case-1" group were 0.9562 and 0.8485 according to their respective measurements. Considering the size difference between phytoplankton groups, we adjusted $\omega_{ph}(676)$ to 0.88 for the *Cryptophytes* (usually smaller than the "Brown" group), 0.9 for the two *Cyanobacteria* groups, and retained 0.8592 for the "Green" group. Mixing all phytoplankton groups resulted in a varying $\omega_{ph}(676)$ between 0.8525 and 0.9541, which is consistent with previous studies (Stramski et al., 2001; Babin et al., 2003a; Oubelkheir et al., 2006). Figure 5 presents spectra of IOPs (absorption, scattering, attenuation, and single-scattering of albedo coefficients) for phytoplankton groups, pure water, detritus, and CDOM. The corresponding spectra data are provided in Data Sheet 1 of the Supplementary Material.

The backscattering probabilities of phytoplankton, $\tilde{b}_{bph}$, is assumed to be spectrally independent (Twardowski et al., 2001; Harmel et al., 2021). Based on the data reported by previous studies (Bricaud et al., 1983; Ahn et al., 1992; Gregg and Rousseaux, 2017), $\tilde{b}_{bph}$ of each group are assigned as 0.002 for the "Brown" group and the *Cryptophytes*, 0.003 for the two *Cyanobacteria* groups, 0.007 for the "Green" group, the *Coccolithophores*, and the "Phytoplankton Case-1" group. $\tilde{b}_{bph}$ is then calculated as the sum of all group fractions.

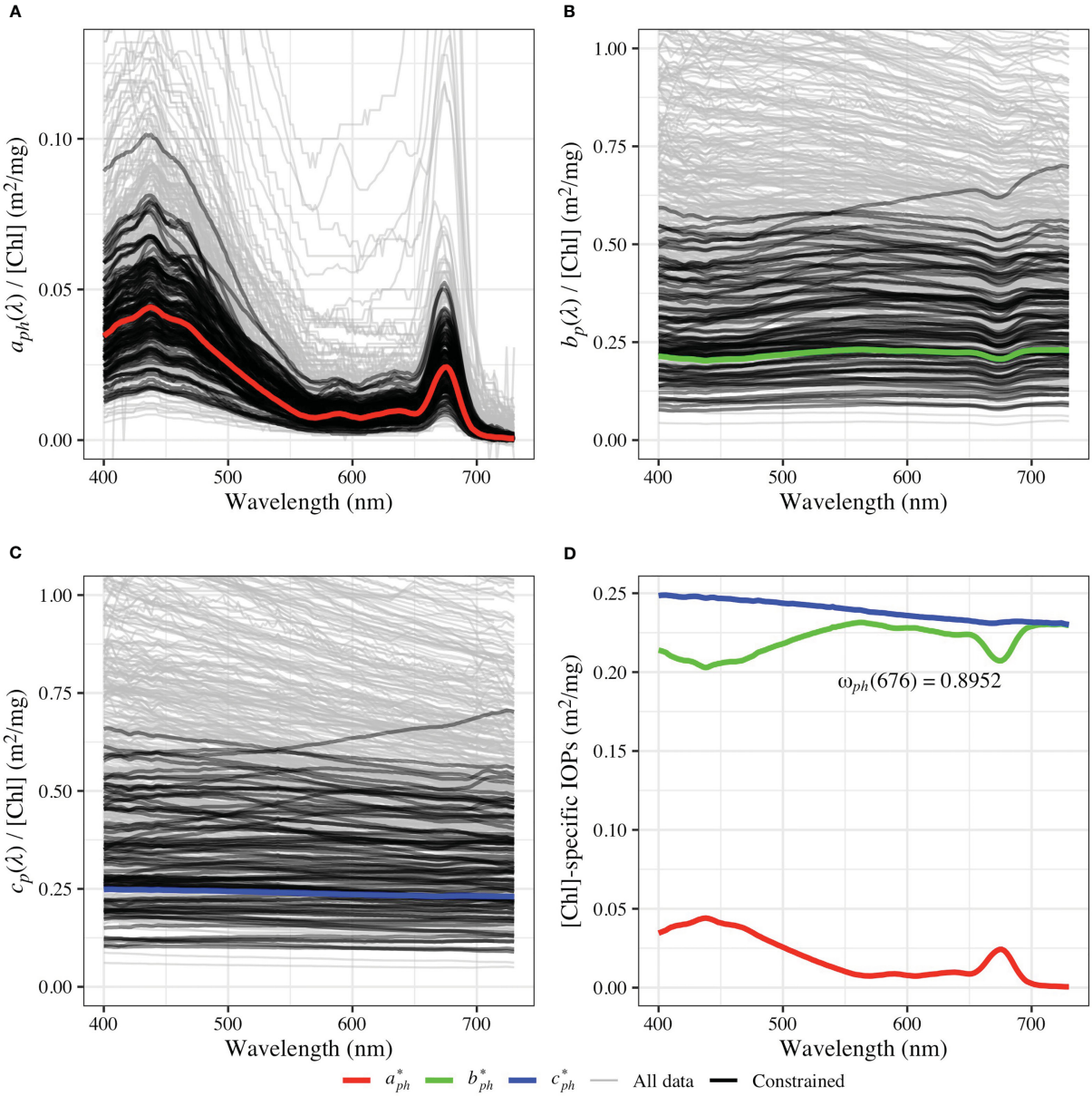


FIGURE 4
The spectra of Chl-specific IOPs of the "Brown" group, derived from a subset of the *Hereon* data. Panels **(A–C)** present the phytoplankton IOP spectra, normalized by [Chl], for absorption, scattering, and attenuation, respectively. The thick black spectra correspond to constrained samples used to determine IOPs. Panel **(D)** shows the calculated Chl-specific IOPs.

To simplify the phytoplankton IOP for oligotrophic *Case-1* water, which is typically dominated by *Synechococcus* sp. and *Prochlorococcus* sp., we applied constraints to the occurrence of the different groups in the "Two-term" model but not in the "Four-term" model. The distribution of phytoplankton groups was estimated based on open access High Performance Liquid Chromatography (HPLC) data (Kramer and Siegel, 2021) and the CHEMTAX method (Mackey et al., 1996), using the results as a reference. The initial and final pigment ratio matrices can be found in Tables A1, A2 of the Supplementary Material. To account for natural variability in phytoplankton absorption and scattering, we performed random sampling and shuffling to obtain the fractions of the phytoplankton groups, f_{ph}, within the upper and lower limits. The fraction library for sampling is presented in Figure A1 of the Supplementary Material. Details of the calculation steps for the "Four-term" and "Two-term" IOP models can be found in Table 3; and a flow chart summarizing the process is provided in Supplemental Figure A2. The relevant data and codes for the IOP model are provided in the section Data Availability Statement.

3.3 Benchmark tests

3.3.1 Other IOP models

In this study, we compared our proposed IOP model with two other models, R18 (Ramírez-Pérez et al., 2018) and L23M (Loisel et al.,

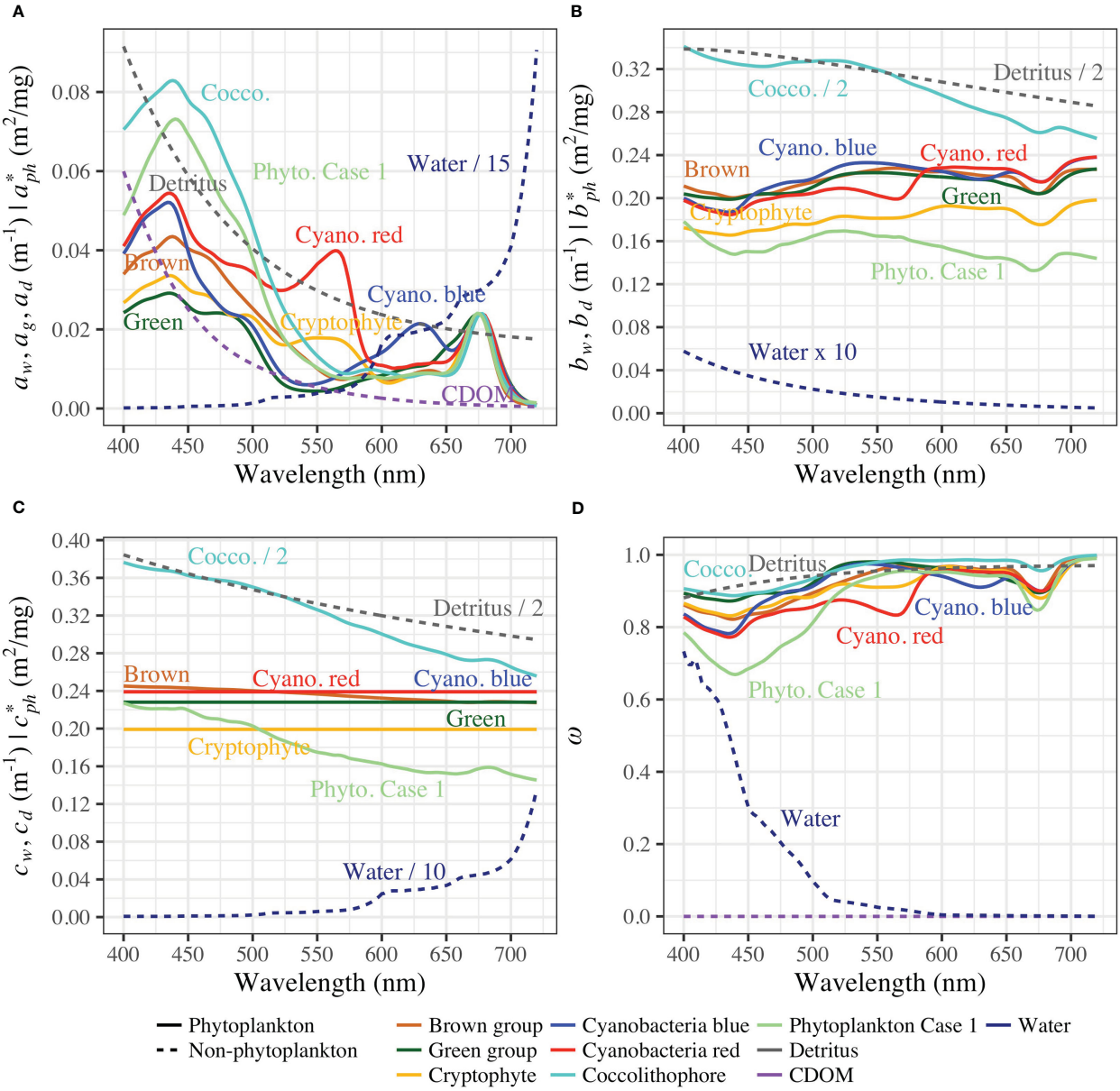


FIGURE 5
Specific IOPs of phytoplankton groups compared with IOPs of other components. Spectral absorption **(A)**, scattering **(B)**, attenuation **(C)**, and single-scattering albedo coefficients **(D)** of phytoplankton groups (solid lines) and exemplary non-phytoplankton components (dashed lines): water (with temperature = 20°C and salinity = 15 PSU), detritus (with [ISM] = 1 g/m^3 and [Chl] = 3 mg/m^3), and CDOM (with a_g (440) = 0.03 m^{-1}). Some spectra are re-scaled for better visualization.

2023). We didn't consider models designed for retrieving IOPs from AOPs, as our focus is on forward modeling. It should be noted that the performance of a model depends on its inputs and the type of water it is applied to. A superior model should be able to capture the majority of IOPs across various optical water types and accurately reproduce IOPs when component concentrations are provided.

The R18 model estimates specific IOP coefficients of water components using a deconvolution method, based on data from optically complex waters in the Ligurian Sea. Its outputs are deterministic and depend solely on the input variables [Chl], [TSM], and a_g(440).

The L23M model (the "M" indicating it's a model, as opposed to the name of their data set) was developed as part of the study by Loisel et al. (2023) to create the *L23* data set (refer to Table 2). The L23M model is not deterministic, meaning that it does not always produce the same result given the same inputs. This is because the model incorporates random values, which are used to account for natural variability. Its non-deterministic result may fluctuate with changes in random values. To address this, we repeated model runs 30 times for a given input, and calculated the mean and standard deviation for comparison purposes. The same procedure was also implemented for our model.

TABLE 3 Calculation steps of the "Four-term" and "Two-term" IOP models.

Component	Calculation of the "Four-term" model	Calculation of the "Two-term" model
Pure water	$a_w(\lambda)$, $b_w(\lambda)$, $b_{bw}(\lambda)$ from WOPP(λ, $\boldsymbol{T}$, $\boldsymbol{S}$)	
CDOM	$a_g(\lambda) = a_g(440) \times a_g^*(\lambda)$	$a_g(\lambda) = a_g(440)\exp(-S_g(\lambda - 440))$ S_g randomly between 0.0100 ~ 0.0200 nm^{-1} $a_g(440) = p_1 a_{ph}(440)$ $p_1 = 0.3 + (5.7Ra_{ph}(440))/(0.02 + a_{ph}(440))$
Detritus	$a_d(\lambda) = [\mathbf{Chl}]a_{bd}^*(\lambda) + [\mathbf{ISM}]a_{md}^*(\lambda)c_d(\lambda) = c_d(550)(\lambda/550)^{\gamma_d}$ $c_d(550) = a_d(550)/(1 - \omega_d(550))$ $\omega_d(550) = 1 - 10^{R_\omega}$ where $R_\omega$follows N(-1.3390, 0.0618) $\gamma_d$follows N(0.3835, 0.1277) $b_d(\lambda) = c_d(\lambda) - a_d(\lambda)$ $b_{bd}(\lambda) = \tilde{b}_{bd}b_d(\lambda)$ and $\tilde{b}_{bd} = 0.0216$	$a_d(\lambda) = a_d(440)\exp(-S_d(\lambda - 440))$ S_d randomly between 0.007 and 0.015 $a_d(440) = p_2 a_{ph}(440)$ $p_2 = 0.1 + (0.5Ra_{ph}(440))/(0.05 + a_{ph}(440))$ $b_d(\lambda) = b_d(550)(550/\lambda)^{p_3}$ $b_d(550) = p_4[\mathbf{Chl}]^{0.766}$ $p_3 = -0.5 + (2.0 + 1.2R)/(1 + [\mathbf{Chl}]^{0.5})$ p_4 randomly between 0.06 and 0.60 $b_{bd}(\lambda) = \tilde{b}_{bd}b_d(\lambda)$ and $\tilde{b}_{bd} = 0.0183$
Phytoplankton	IOPs determined from seven groups without limited bounds, i.e., $f_{ph,i}$ from 0 to 1. $a_{ph}(\lambda) = [\mathbf{Chl}]a_{ph}^*(\lambda)$ $a_{ph}(676) = A[\mathrm{Chl}]^E$ A: 0.0237 and between 0.0112 ~ 0.0501 E: 1.0000 for [Chl] ≤ 1mg/m^3; 0.8938 for [Chl] > 1 mg/m^3 $c_{ph}^*(\lambda) = \frac{c_{ph}^+(\lambda)}{c_{ph}^+(676)} \times \frac{a_{ph}^*(676)}{1 - \omega_{ph}(676)}$ $b_{ph}^*(\lambda) = c_{ph}^*(\lambda) - a_{ph}^*(\lambda)$ $b_{bph}(\lambda) = \tilde{b}_{bph}b_{ph}(\lambda)$ and $\tilde{b}_{bph} = \sum f_{ph,i}\tilde{b}_{bph,i}$	Same as the "Four-term" model (the left cell) but with limited bounds of phytoplankton fraction, $f_{ph,i}$, of [Brown, Green, Crypt, CyanB, CyanR, Cocco, PhyC1]. The upper limit is: [0.5, 0.5, 0.3, 0.5, 0.5, 0.1, 1.0]. The lower limit varies with [Chl], mg/m^3: [0.0, 0.0, 0.0, 0.0, 0.0, 0.0, 1.0] if [Chl]< 0.05; [0.0, 0.0, 0.0, 0.0, 0.0, 0.0, 0.5] if [Chl] ≥ 0.05 and ≤ 0.2; [0.0, 0.0, 0.0, 0.0, 0.0, 0.0, 0.2] if [Chl] ≥ 0.2 and ≤ 1; [0.2, 0.0, 0.0, 0.0, 0.0, 0.0, 0.2] if [Chl] > 1.

The normal distribution is represented by N(mean, standard deviation). The bold-faced variables are the primary inputs. R is a random generator producing values from 0 to 1. The calculation steps of the "Two-term" model for CDOM and detritus are based on the process in IOCCG (2006).

3.3.2 Remote-sensing reflectance model and simulations

In this study, we adopted the formula proposed by Lee et al. (2011) to simulate $R_{rs}(\lambda)$ based on the absorption and backscattering coefficients obtained from IOP models. The formula is given as:

$$R_{rs}(\lambda) = \left(G_0^w + G_1^w \frac{b_{bw}(\lambda)}{k(\lambda)}\right)\frac{b_{bw}(\lambda)}{k(\lambda)} + \left(G_0^p + G_1^p \frac{b_{bp}(\lambda)}{k(\lambda)}\right)\frac{b_{bp}(\lambda)}{k(\lambda)}, \quad (22)$$

where $k(\lambda) = a_t(\lambda) + b_{bt}(\lambda)$. The coefficients G are dependent on solar zenith angle and viewing direction, with values for solar zenith angle = 30° and nadir viewing direction being $G_0^w = 0.05881474$, $G_1^w = 0.05062697$, $G_0^p = 0.03997009$, and $G_1^p = 0.1398902$.

To demonstrate the potential of our IOP models in building a synthetic database, we generated a wide range of component concentrations and fed them into Eq. (22). Note that these simulations are a simplified showcase and a full radiative transfer model, such as HydroLight, will be utilized in the future. The range of concentrations was collected from the data sets listed in Table 2. We calculated their mean and standard deviation values and assumed a $\log_{10}$-normal distribution with twice the standard deviation to obtain more samples at extremely low and high values (Campbell, 1995). The concentration specifications are presented in Table 4. We generated 1,000 random combinations and to capture more variability in *Case-2* waters, we used these combinations eight and four times in "Four-term" and "Two-term" models, respectively, resulting in 12,000 simulations.

3.3.3 Alternative phytoplankton scattering assumption

Many contemporary inversion models, used for deriving IOPs from AOPs, commonly employ power law functions to represent particle scattering or backscattering (Lee et al., 2002; Maritorena et al., 2002; Morel et al., 2002; Werdell et al., 2013; Liu et al., 2020).

TABLE 4 The specifications of component concentrations in the IOP simulation.

Parameter	Unit	Random generator	Bound limits
[Chl]	mg/m^3	N(0.121, 0.858)	[0.02, 1,000]
[ISM]	g/m^3	N(0.386, 1.637)	[0.001, 2,000]
$a_g(440)$	m^{-1}	N(-0.671, 0.969)	[0.0001, 50]

Concentrations are obtained using an exponential function with base 10. The power value is determined by a random generator, N(mean, standard deviation) which satisfies a normal distribution. Bound limits are defined for each parameter as the lower and upper boundaries.

Although this parameterization has been successful in retrieving IOPs for decades, there is less confidence in the accuracy of scattering coefficients (Roesler and Boss, 2003) due to the non-smooth nature of the scattering spectra, as observed from *in situ* measurements and theoretical models (Babin et al., 2003a; Stavn and Richter, 2008; Bernard et al., 2009). In contrast, particulate attenuation spectra, such as those in the *Hereon* data set shown in Figure 4, exhibit more smoothness, whereas scattering spectra tend to be more irregular in the wavelength range where absorption spectra display peaks. This is believed to result from the compensation of strong absorption peaks by phytoplankton (Twardowski et al., 2001). This raises the question of how the use of a smoothed power law function for scattering spectra in the presence of spectral features affects the accuracy of the ocean color algorithm.

In this study, we used the Gordon and Morel (1983) model, which is a common option in HydroLight, to examine the impact of the b_{ph} assumption on R_{rs} simulation. The power law model is expressed as:

$$b_{ph}^{\mathrm{GM83}}(\lambda) = b_0[\mathrm{Chl}]^n \left(\frac{\lambda_0}{\lambda}\right)^m, \tag{23}$$

where $b_{ph}^{\mathrm{GM83}}(\lambda)$ represents the $b_{ph}(\lambda)$ by the above model, λ_0 = 550 nm, $b_0 = 0.3$, $n = 0.62$, and $m = 1$. The term $b_0[\mathrm{Chl}]^n$ denotes that $b_{ph}(550)$ is dependent on [Chl], and the spectral shape is controlled by the exponent m. The observed difference in magnitude may be due to the varying relationship between $b_{ph}(550)$ and [Chl] across different aquatic systems. To account for this magnitude effect, we adjusted $b_{ph}^{\mathrm{GM83}}(\lambda)$ by normalizing its $b_{ph}^{\mathrm{GM83}}(550)$ to the value obtained from our IOP model. This leads to $b_{ph}^{\mathrm{Adj}}(\lambda)$, which is calculated as:

$$b_{ph}^{\mathrm{Adj}}(\lambda) = b_{ph}^{\mathrm{GM83}}(\lambda)\frac{b_{ph}(550)}{b_{ph}^{\mathrm{GM83}}(550)}, \tag{24}$$

where $b_{ph}(\lambda)$, for the sake of simplification, is the phytoplankton scattering coefficients by our IOP model. We conducted a sensitivity analysis to compare the simulated R_{rs} using b_{ph}, which is assumed as the reference, and the two modified scattering assumptions b_{ph}^{GM83} and b_{ph}^{Adj}.

3.4 Statistical metrics for evaluating model performance

This study evaluated the performance of an IOP model by comparing its ability to reproduce co-measured concentrations and IOP results using component concentrations as input. The aim was to demonstrate the capability to accurately describe the bio-optical process. To evaluate the performance, several statistical metrics including linear regression were utilized. The squared correlation coefficient, R^2, measures how well a model fits the observed data. The slope, S, represents the change in the measured value for each unit increase in the estimated values, while the intercept, I, represents the systematic offset when comparing measurements and estimations. Better fits are indicated by R^2 and S values closer to one and I value closer to zero. Additionally, the unbiased median percentage difference, D, was used to evaluate the accuracy of IOP models, with lower values indicating better accuracy. D was calculated as the median of $(X - Y)/(X + Y) \times 200\,\%$, where X and Y are measurement and estimation values. The measurement and estimation values are scaled using a logarithmic base 10 transformation prior to the calculation of these statistical metrics.

4 Results and discussion

4.1 Reproducibility of IOP models

Recall that the two-term model takes only [Chl] as input, while the four-term model takes [Chl], [ISM], and $a_g(440)$ as inputs. The R18 model uses [Chl], [TSM], and $a_g(440)$, while the L23M model takes only $a_{ph}(\lambda)$. All of these models output spectral IOPs of the components. In this section, we compared these benchmark models in terms of a_{ph}, a_d, a_g, a_{gp}, b_p, and b_{bp}, focusing specifically on the results at 440 nm. Scatter plots for the *Hereon* data set and the external data sets are in Figures 6, 7, respectively. Additional scatter plots at other wavelengths are provided in the Supplementary Material (Figures A3, A4: 560 and 670 nm). Figure 8 shows spectral analysis to evaluate model performance from 400 to 700 nm. Multispectral samples were excluded in the spectral analysis to avoid outliers, primarily from *OC-CCI v3*, resulting in different valid estimation numbers (N) in scatter plots and spectra plots, but this does not significantly affect the spectral trend.

Figure 6 shows the reproduced IOPs for the *Hereon* data from our model in comparison with two other models, whereby for our model, the "Two-term" setup was applied to the oceanic data in *Hereon* and the "Four-term" setup to coastal and river data. The comparison between the two- and four-term results of the "oceanic" samples indicates no significant deviation, which is crucial for the seamless modeling of IOPs during the transition from *Case-1* to *Case-2* waters. Figure 6A demonstrated accurate $a_{ph}(440)$ estimates with a slope close to one, which verifies the reliability of the $a_{ph}^{*}(\lambda)$ determination and the phytoplankton group spectral shapes, as the result at 440 nm can be regarded as being extrapolated from 676 nm. The percentage difference in a_{ph} from 400 to 700 nm, shown in Figure 8 (A7), was within approximately ±5%, with some results within ±10%. The evaluation of $a_d(440)$ in Figure 6D revealed good performance across a range of four orders of magnitude, especially when $a_d(440)$ was greater than 0.1 m^{-1}, where the particulate matter was dominated by the inorganic component. However, the $a_d(440)$ estimation was more scattered for lower values, possibly due to increased variability in the $a_{bd}^{*}(\lambda)$ shape due to increased organic components and uncertainties in concentration inputs caused by general measurement errors for organically dominated [TSM], hence [ISM]. The spectral statistical results of a_d in Figure 8 (A8) exhibited relatively consistent values across the wavelength range, with percentage differences between ±5%. The $a_g(440)$ results, shown in Figure 6G, were in line with the "Four-term" input, while the "Two-term" results were dependent on the random parameter values. Despite the wide variation range, the error lines covered the measured values. The statistical results of a_g in Figure 8 (A9) showed percentage differences within ±5% up to 600 nm, but

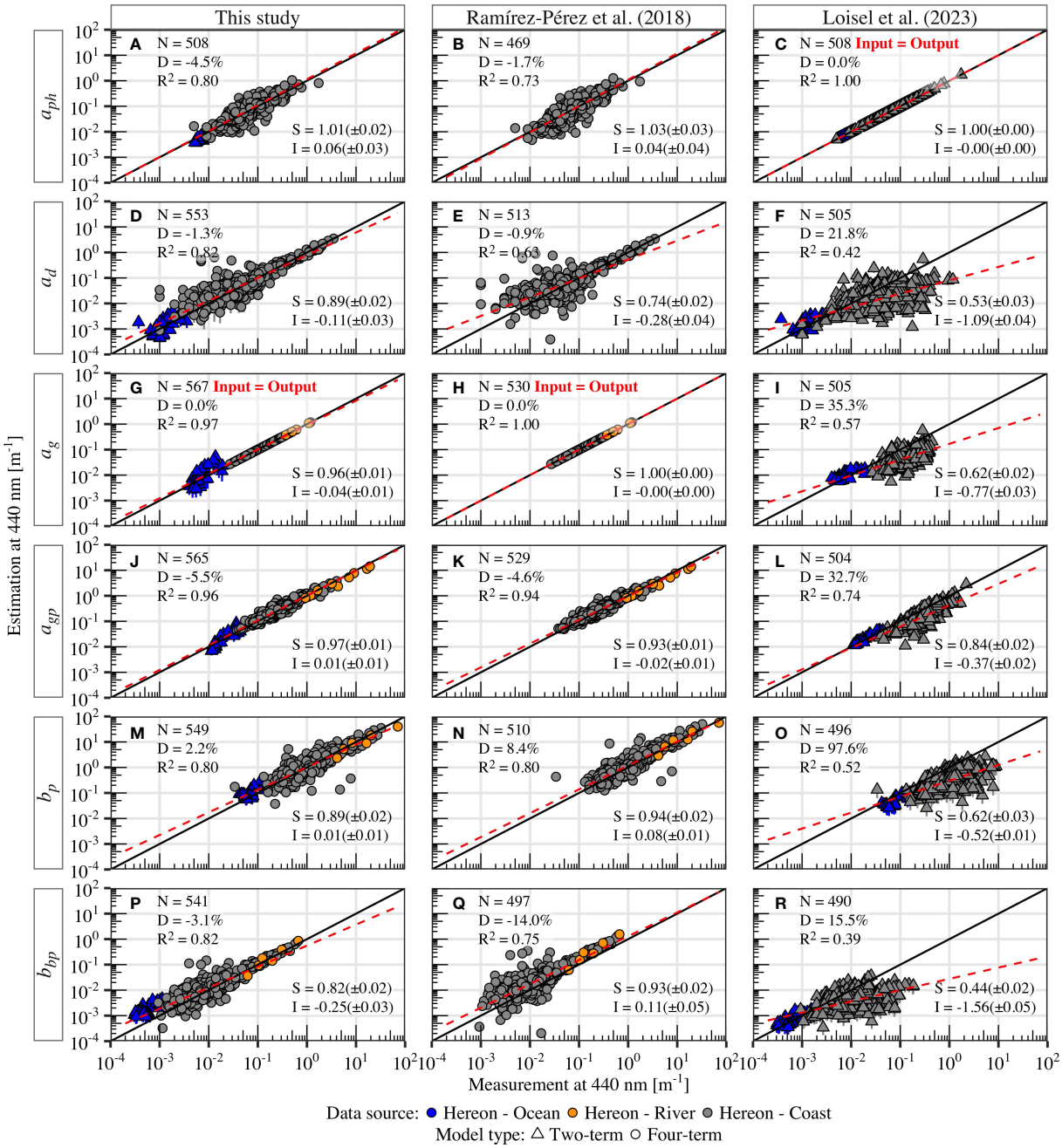


FIGURE 6
Evaluation of IOP estimates at 440 nm from our proposed model, from Ramírez-Pérez et al. (2018), and Loisel et al. (2023). Color shows the different parts in the *Hereon* data, shape indicates the model type, black line is 1:1, red line is linear regression. Point denotes the mean value of repeated runs and error bar shows the variation using random parameters (defined in Table 3). Statistics: the number of points (*N*), the unbiased median percentage difference (*D*), the coefficient of determination (R^2), and linear regression slope and intercept (*S* and *I*), with standard deviation in brackets. Panels with notes in red text mean input equals to output. The reason for the absence of results for *Hereon – Ocean* in R18 is the unavailability of the input parameter [TSM] in that specific part of the data. The panels are labeled from **(A–R)** corresponding to the different models across the variables.

degradation was observed beyond 600 nm as the values approached zero. Our IOP model performed well in the evaluation of $a_{gp}(440)$, the sum of $a_{ph}(440)$, $a_d(440)$, and $a_g(440)$, across different water types and over wavelengths, with no outliers observed. The $b_p(440)$ estimates, shown in Figure 6M, were accurate across three orders of magnitude, but with a few outliers due to higher measurement variation of [TSM]. The $b_{bp}(440)$ results were close to the 1-to-1 line for values greater than 0.01 m^{-1}, but with some deviations in the low-value region, especially for the "Two-term" model in the oceanic data. The spectral distribution of statistical values for b_p and b_{bp} in Figure 8A remained consistent, with percentage differences within ±5%.

The R18 model generally yielded comparable results at 440 nm to our model, albeit with some differences for certain parameters.

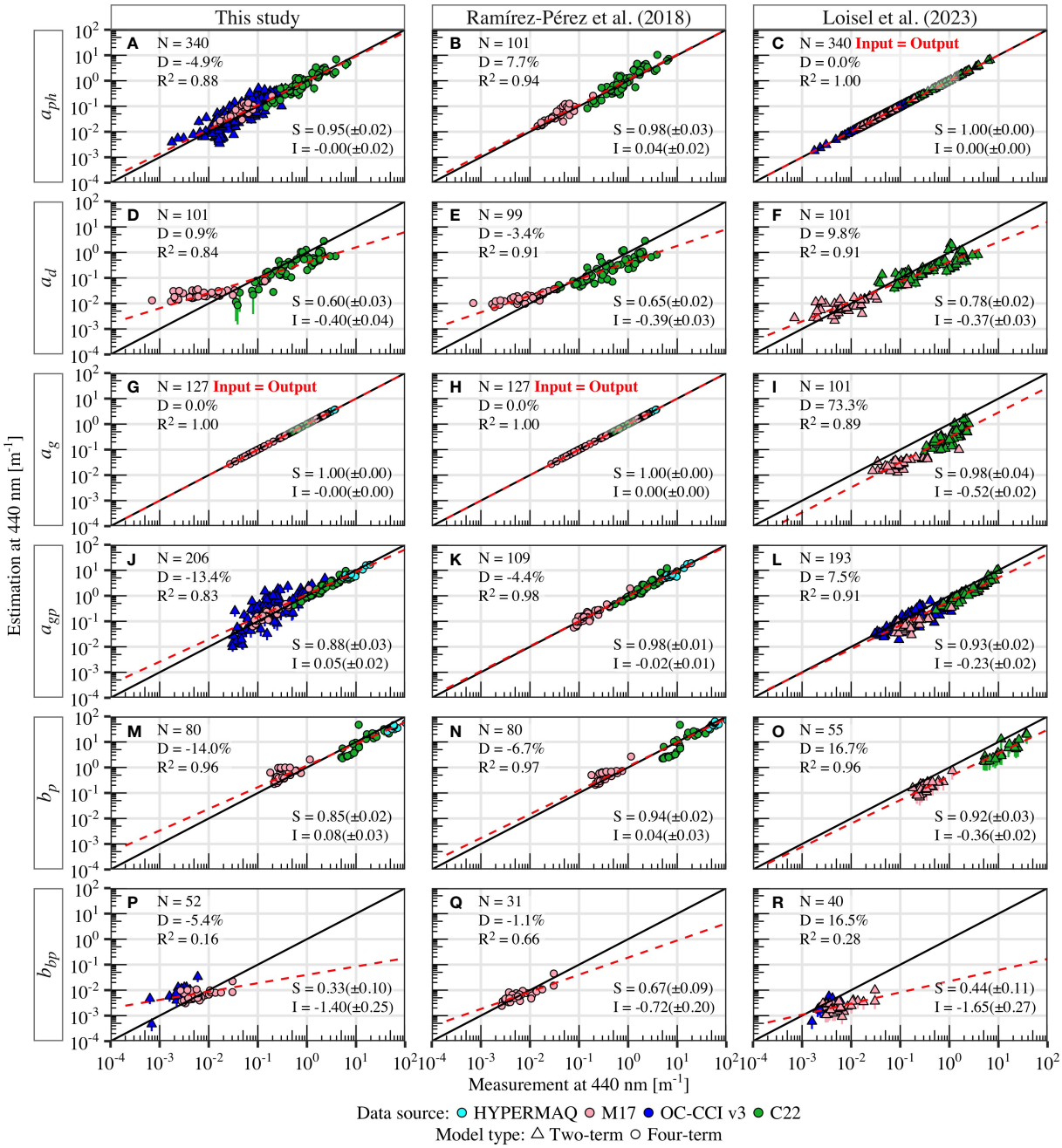


FIGURE 7
Same as Figure 6 but for external data sets: *HYPERMAQ*, *M17*, *OC-CCI v3*, and *C22*, shown in different colors.

Specifically, R18 model underestimated a_d at longer wavelengths, as shown in Figure 8 (A8), with a slope of 0.78 lower than that of our model (0.93) at 560 nm, and with 0.71 lower than 0.99 at 670 nm. This difference could be due to the imperfect separation of biogenic and minerogenic parts of detritus in R18, as the pigment residuals in longer wavelengths, e.g., ≥ 560 nm, were still evident in their $a^*_{bd}(\lambda)$, leading to the underestimation of $a^*_{md}(\lambda)$ in these wavelengths. Additionally, consistent discrepancies between measurements and estimations of $b_p(\lambda)$ and $b_{bp}(\lambda)$ were observed across wavelengths, which were also found in other data sets, as shown in Figure 8B. Based on the points of *Hereon – Ocean* and some points of *Hereon – Coast* resembling oceanic waters, as shown in Figure 6, the L23M model demonstrates favorable results for *Case-1* waters when $a_{ph}(\lambda)$ spectra are provided. Conversely, the model generally underestimates all IOPs for *Case-2* waters across the wavelength range concerned, as demonstrated in Figure 8B. This outcome is anticipated since the model is primarily designed for global oceanic waters. The superior performance of the L23M model for *Hereon – Ocean* is primarily due to the fact that $a_{ph}(\lambda)$ is its primary input, which mainly governs the total IOPs.

Figure 7 displays an independent evaluation of IOP models based on *in situ* data from external sources. Our model performs

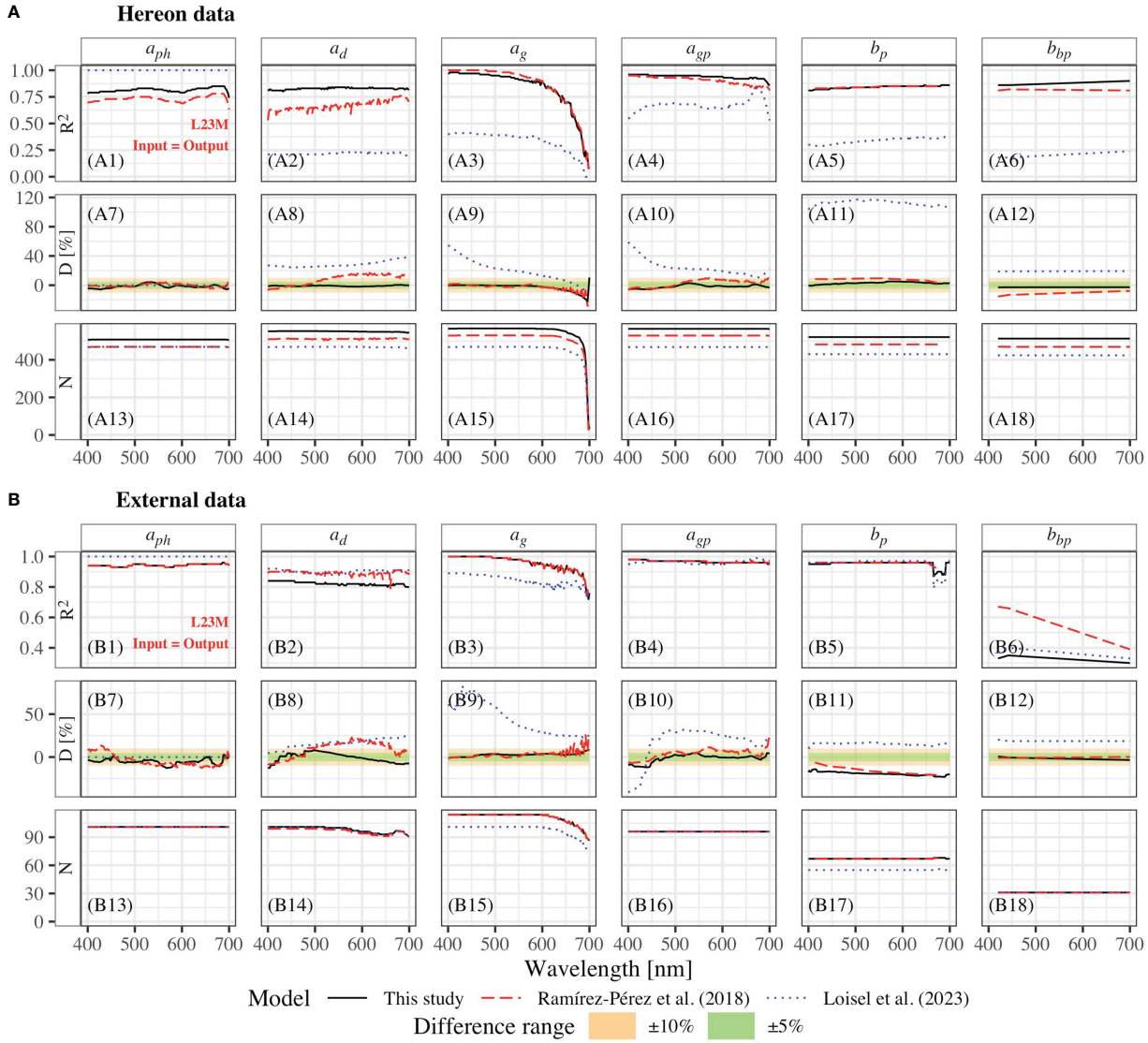


FIGURE 8
Statistical metric spectral distribution for component IOPs: R^2, percentage difference (D), and number of valid estimations (N). The lines represent our proposed model, Ramírez-Pérez et al. (2018), and Loisel et al. (2023). Panel **(A)** uses the *Hereon* data, while panel **(B)** uses external data sets listed in Table 2. The wavelength range is from 400 to 700 nm. The two colored shadows represent the percentage differences of ±5% and ±10%, respectively. The model inputs equal to the model outputs for a_{ph} in the Loisel et al. (2023) model. Some spectra overlap due to the closely similar values.

better in estimating $a_{ph}(440)$ for various water types, including CDOM-dominated lakes from *M17*, eutrophic lakes from *C22*, and oceanic waters from *OC-CCI v3*, as evidenced by the lower percentage difference. In addition, our model produces a larger number of estimated $a_{ph}(440)$ values, which may interfere with the reliability of other statistical metrics if other models are unable to estimate these points. However, the $a_d(440)$ results are slightly underestimated in *C22* and overestimated *M17* in both our model and R18. The higher [ISM] values observed in M17 compared to similar samples in the *Hereon* data may explain the overestimation of $a_d(440)$, which can also be observed from the overestimation of $b_p(\lambda)$ in Figures 7M, N. The overestimation of $a_d(\lambda)$ was slightly reduced by L23M in Figure 7F, when only [Chl] was used to model $a_d(\lambda)$. One should consider the uncertainty associated with component concentration when using IOP models (IOCCG, 2019). Despite this, the overall performance of $a_{gp}(440)$ remains strong by our model, with an R^2 of 0.83, even in the presence of more variability in *OC-CCI v3*. The spectral percentage difference of a_{gp} mostly fell within ±10%, as shown in Figure 8 (B10). The $b_p(440)$ estimates by our model are slightly underestimated for extremely turbid water (mainly from *HYPERMAQ*). For such highly turbid waters, the uncertainty of *in situ* measurements should be considered (IOCCG, 2019). Only a few of points of $b_{bp}(\lambda)$ are observed due to the limited data from these external data sets. The different performance between our model and R18 in estimating $b_{bp}(440)$ may result from the use of similar measurement devices in the studies of R18 and M17. The reason for the absence of results for *Hereon – Ocean* and *OC-CCI v3* in R18 is the unavailability of the input parameter [TSM] in that specific part of the data. Note that the smaller data size and larger measurement uncertainties in the

external data sets compared to the *Hereon* data can impact statistical results in Figure 8B. Nonetheless, our model still demonstrates consistent and robust performance across the spectrum, with most components falling within a ±10% difference range.

To summarize, our IOP model shows comparable performance as other the two models in terms of reproducing IOPs from concentrations in specific water environments and in terms of absolute values and spectral shapes. However, our model provides a higher amount of reproducibility across diverse optical water types, encompassing oceanic, coastal, and inland waters. Our spectral statistical metrics demonstrate that the estimations of model have a percentage difference of within ±5% for most component IOPs throughout the visible spectrum, with some falling within ±10%, which is essential for meeting the accuracy requirements outline in GCOS (2011) for developing ocean color algorithms. Another advantage of our IOP model is its flexibility, allowing for replacement of specific model parameters with more optimal values in special scenarios. Although these parameters defined so far have proven to be representative, this enables continuous improvement and refinement of the model over time.

4.2 Do we capture most optical variability?

In the previous section, we established that our IOP model can accurately reproduces water optical properties based on component concentrations. However, we also need to determine whether the model can capture most of the optical variability, which depends on the concentration range and the dynamic range of model parameters like γ and ω. We admit that our current ranges may not encompass some extreme scenarios. For instance, to address the underestimation depicted in Figure 7M, we increased the original value of $\omega_d(550)$ and reduced γ_d to simulate a highly turbid water type. By adjusting model parameters such as γ and ω, the resulting ranges offer valuable insights into the appropriate direction for fine-tuning the model. Although these modifications improved that particular case, they lay outside 96% of the training data distribution. Despite this, we used the original model parameters established in section 3.2 and the concentration range provided in Table 4 to do the simulation as a showcase, which is used to test the data coverage with other data sets.

The data distribution presented in Figure 9 compares *in situ* measurements and simulated data sets. Panels (A) and (C) show our simulated data and *in situ* measurements, while panels (B) and (D) compare other simulated data sets. Our selection of 560 nm was intended to showcase the data distribution, but it is worth noting that the results for other wavelengths are also comparable. The $a_p(560)$ and $\omega_p(560)$ relationships demonstrate the ratio of b_p to c_p as particle absorption increases. The $a_p(560)$ values of *Hereon* vary up to four orders of magnitude, with *C22* and *HYPERMAQ* having higher values, and *M17* varying over a smaller range with lower values. Despite the variation in $a_p(560)$, Figure 9A demonstrates that the variation in $\omega_p(560)$ is relatively stable, with measured values as low as about 0.9 and simulated values as low as 0.8. As anticipated, the "Four-term" model contributes to most of the value variation. Figure 9B indicates that other simulated data sets have similarities, with the *L23* data set having a comparable distribution to our simulations, albeit with fewer points where $a_p(560)$ is greater than 0.1. The simulated *CCRR* data set shows a wider distribution in $a_p(560)$ but stable $\omega_p(560)$, primarily due to a constant γ_d and a [Chl]-related γ_{ph}. However, the simulated *C2X* data set displays more pronounced differences, with some points having significantly lower $\omega_p(560)$ values for high $a_p(560)$ and phytoplankton-dominated water, suggesting that only 20% of the light is scattered for a given high particle concentration, resulting in low reflectance, which is inconsistent with real-world observations. The primary reason for such low $\omega_p(560)$ values is the inappropriate parameterization of $b_{ph}(\lambda)$ in *C2X*. These points have lower $b_{ph}(\lambda)$ values with relatively higher $a_{ph}(\lambda)$ (not shown). Figures 9C, D show the relationship between $a_{gp}(560)$ and $b_{bp}(560)$, with $b_{bp}(560)$ increasing as $a_{gp}(560)$ increases in the measured data, suggesting a stable proportion of $a_g(560)$ in $a_{gp}(560)$ that co-varies with [Chl], as reflected in *CCRR* and *L23*. *C2X* contains simulations of extremely absorbing waters, resulting in simulated points below the distribution of other data due to high CDOM absorption. Our simulated data, using a similar concentration limit from *C2X*, has a wider coverage compared to the *C2X* distribution, with most points originating from the "Four-term" model (CDOM is independent of [Chl]), while *C2X* has some data gaps.

For practical reasons, the study limited the number of IOP components to a manageable amount instead of including all particle species in water (Stramski et al., 2004). In the "Four-term" model, a_g was modeled using a few spectra (N=12) with similar shapes (S_g = 0.0174 nm^{-1} ± 0.1%). The resulting model was able to accurately reproduce the CDOM spectrum with precise a_g(440) values. In the "Two-term" model, a_g was correlated to [Chl] with a random value, resulting in relatively greater variability, but still covering the range of values observed in oceanic waters. The shape of specific detritus absorption, a_d^*, varies across different aquatic environments but is generally limited on a local scale (Woźniak and Dera, 2007). The slope of minerogenic detritus absorption, S_{md}^*, in our study, 0.0104 nm^{-1} in Figure 2B, was consistent with values observed in other natural water basins (Woźniak and Dera, 2007). The combination of biogenic and minerogenic detritus in our model enhances its applicability across different regions, which is important for simulating IOPs of complex waters on a global scale. The use of different quantiles (quasi-organic proportion of the total particle) to define a_{bd}^* aligns with the observed increase in biogenic detritus absorption when organic matter dominates. The slopes of our simulated a_d values range from 0.0068 to 0.015 (as per the definition in Stramski et al. (2019), based on the natural logarithmic transformation at 440 and 550 nm), which are generally consistent with previous studies, e.g., 0.0095~0.0148 in Zheng et al. (2015) and 0.0031~0.0169 in Stramski et al. (2019), but lack the "flat" shapes (lower values) found in Stramski et al. (2019) due to limited data in the training set, which can be expanded in the future to incorporate such extreme scenarios. The IOP model proposed in this study includes seven phytoplankton groups that are used as general "color" groups, rather than specific phytoplankton species or functional types that have different absorption and scattering properties. By using these general groups, the model can capture the increased variability in

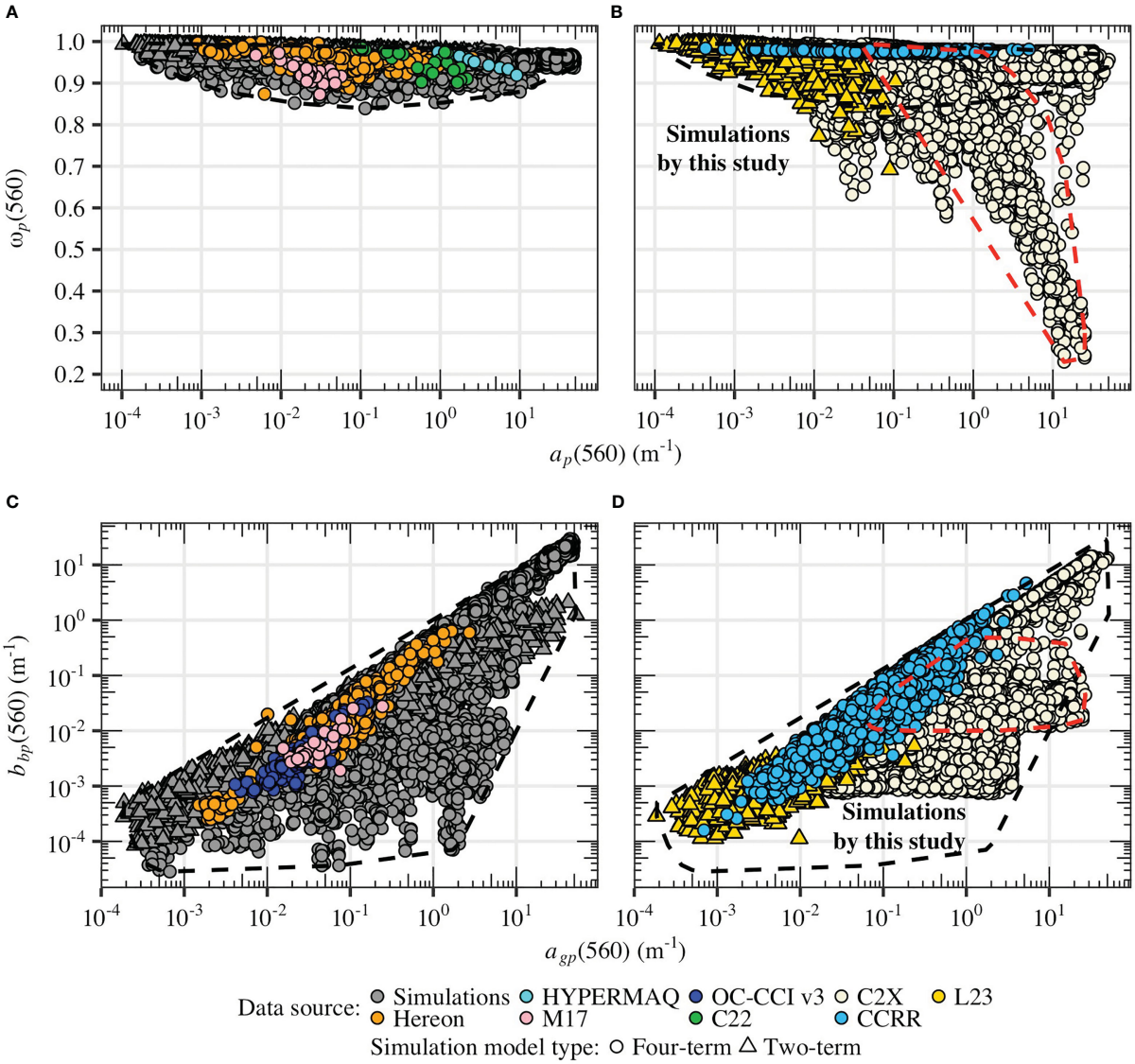


FIGURE 9
Data coverage comparison for IOPs at 560 nm of our simulated data with measured (left) and other simulated (right) data. **(A, B)** show scatter plots of particulate absorption versus the single-scattering albedo. **(C, D)** show the total non-water absorption versus total particulate backscattering. The black dashed outline is the convex hull of our simulations and the red one is highlighted part in the C2X data set that [Chl] ≥ 50 mg/m^3 and [ISM] ≤ 50 g/m^3.

phytoplankton IOPs that is visually seen in natural systems. In other words, the phytoplankton groups in our model are not based on specific biological characteristics, but rather on their broad spectral characteristics, allowing for more flexibility and accuracy in predicting phytoplankton IOPs. Variables $a_{ph}(412)/a_{ph}(443)$ and $a_{ph}(555)/a_{ph}(490)$, used to describe the shape of a_{ph} in Zheng et al. (2015), were found to be in good agreement with other *in situ* and simulated data sets, within the ranges of 0.8~1.0 and 0.2~1.0, respectively. Although some ranges may not be covered, it is not necessary to add more phytoplankton groups if no color differences are added. Our IOP model is also able to simulate *coccolithophore* blooms with a 490 nm reflectance peak by multiplying its absorption coefficient by 0.02, which is biologically based on the vanishing of the absorbing algae cells but remaining high scattering from detached coccoliths (Neukermans and Fournier, 2018; Cazzaniga et al., 2021).

Complete coverage of the optical diversity of as many natural waters as possible is also important for the exploitation of optical water type classification methods. Existing methods (e.g., Moore et al., 2014; Hieronymi et al., 2017; Jackson et al., 2017; Bi et al., 2021) can only partially cover the optical variability; many complex waters are out-of-scope for these methods, which is reflected in too low class memberships (not shown in detail here). This also applies to the classifiability of R_{rs} from various ocean color atmospheric corrections (Hieronymi et al., 2023). Both aspects identify potential weaknesses of the OWT methods, which should be revised in the future, e.g., by means of our IOP model. It is noteworthy that the analysis here did not account for variability when modeling IOP to

R_{rs}, and we simplified backscattering as a spectral constant rather than a sophisticated phase function or a volume scattering function. This could impact the R_{rs} angular distribution in many complex waters (Harmel et al., 2016). When analyzing OWT frameworks, environmental factors, and sun-viewing geometries should also be considered and varied (Bi et al., 2023).

4.3 Sensitivity analysis of phytoplankton scattering assumption

Figure 10 demonstrates that the disparity in R_{rs} between modeled $b_{ph}(\lambda)$ and $b_{ph}^{GM83}(\lambda)$ was more noticeable at high [Chl] (>100 mg/m^3), with $b_{ph}^{GM83}(\lambda)$ showing lower values (up to 0.02 sr^{-1} difference) due to the modeled $b_{ph}(550)$ discrepancy. At low [Chl] (< 1 mg/m^3), $b_{ph}^{GM83}(\lambda)$ displayed slightly higher R_{rs} values (up to 0.003 sr^{-1} or 40% difference). The most significant differences were observed in the green and NIR (540~590 nm and 700~730 nm), with differences of up to 90%, while the blue region (400~450 nm) was the least affected as non-phytoplankton signals prevail. Renormalizing $b_{ph}^{GM83}(\lambda)$ to $b_{ph}^{Adj}(\lambda)$, which makes $b_{ph}^{Adj}(560)$ equal to $b_{ph}(560)$, significantly reduced differences in R_{rs} except for higher [Chl] (>100 mg/m^3). However, the values in NIR were still lower than those with $b_{ph}(\lambda)$ by up to 0.004 sr^{-1} (or 35%). Figure 11 presents six intuitive samples of IOPs and R_{rs} ordering by increasing [Chl] values. The use of $b_{ph}^{GM83}(\lambda)$ underestimated $b_p(\lambda)$ from concentrations evaluated in the training

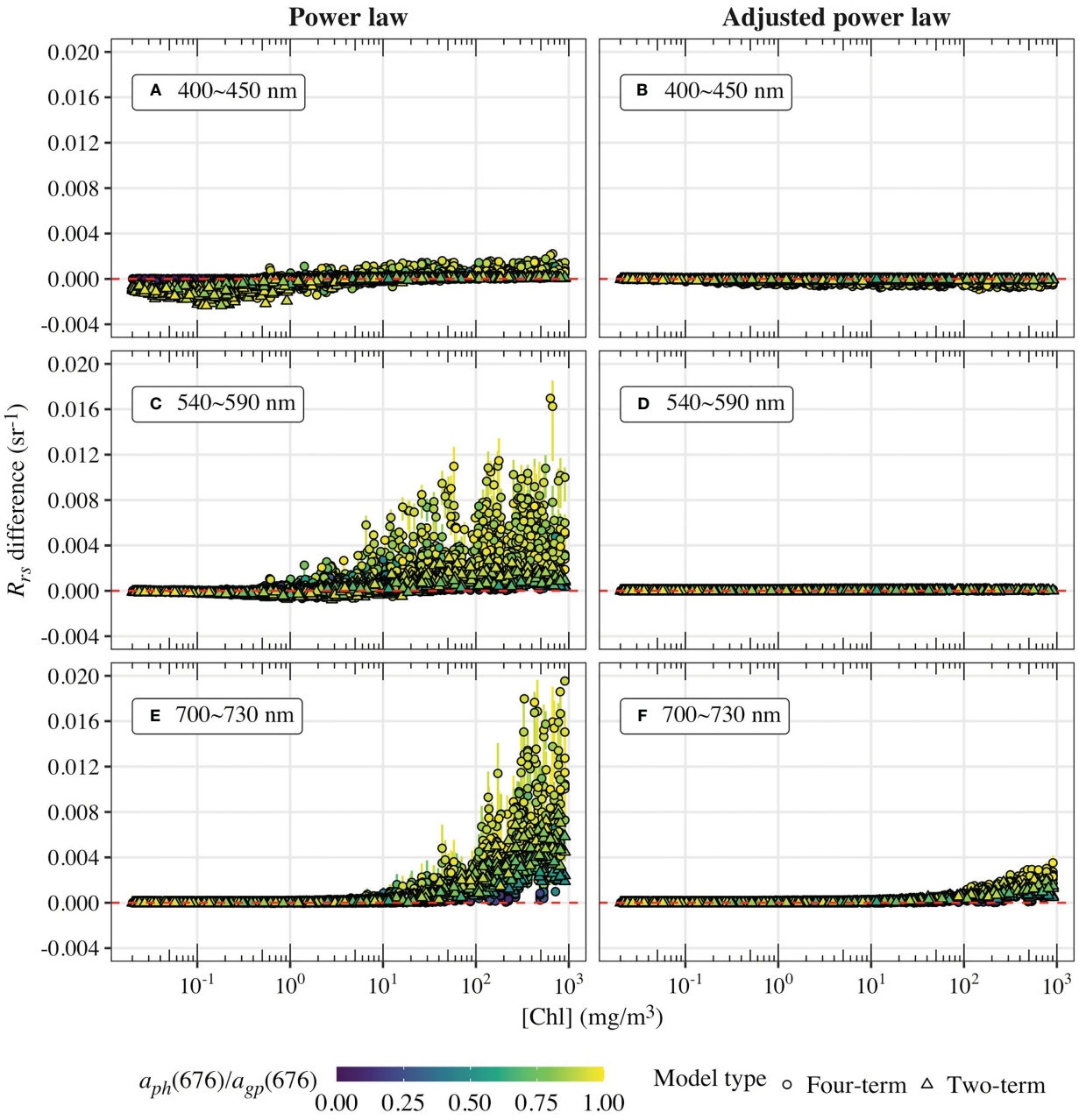


FIGURE 10
The difference in R_{rs} due to the scattering assumption of phytoplankton. Points and error bars indicate the mean and range of differences at selected wavelengths. The first column (Power law) represents the results using $b_{ph}^{GM83}(\lambda)$, while the second column (Adjusted power law) $b_{ph}^{Adj}(\lambda)$ (*see text*). Panels **(A, B)** for 400~450 nm; **(C, D)** for 540~590 nm; **(E, F)** for 700~730 nm.

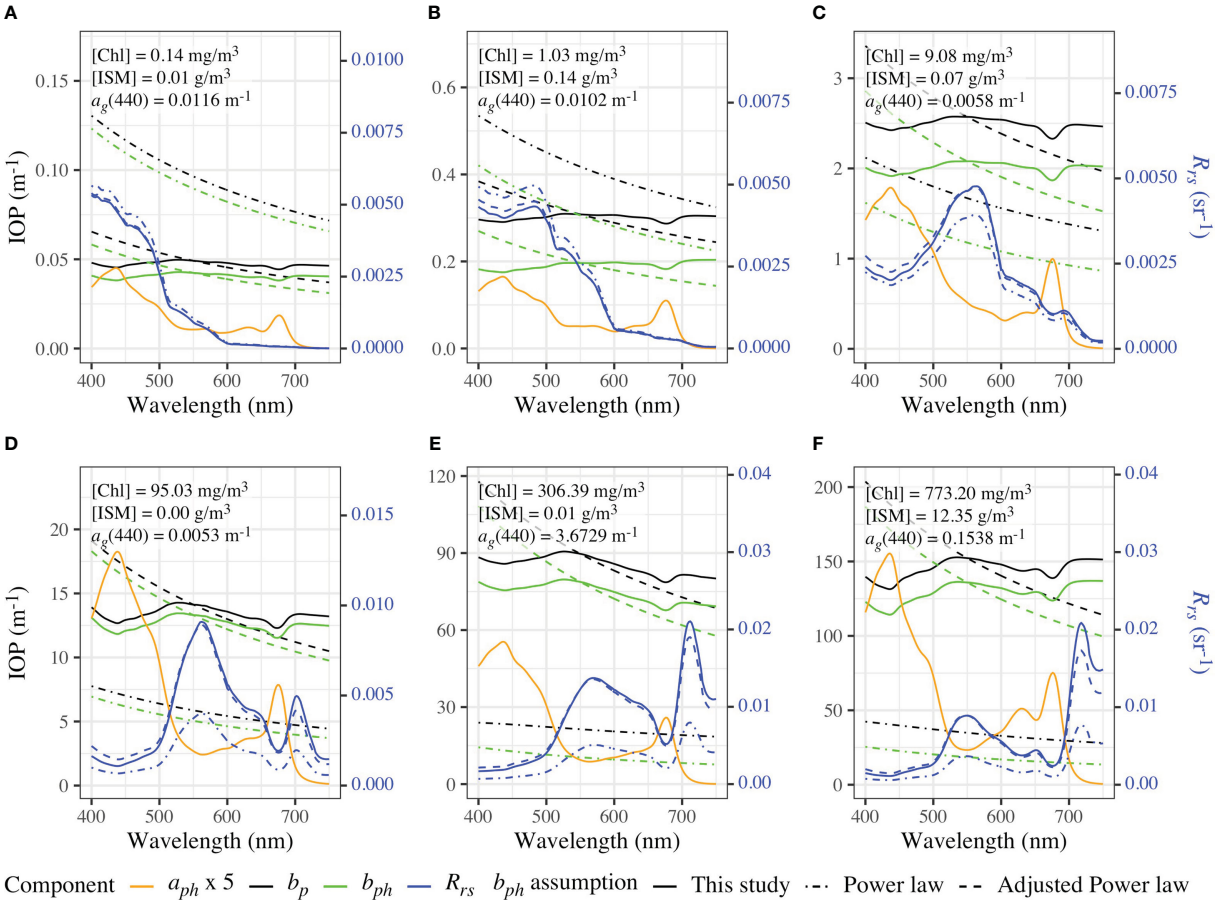


FIGURE 11
Comparison of the impact of phytoplankton scattering assumptions on IOPs and R_{rs} in six simulated samples varying from low to high [Chl]. The component concentrations are displayed in the corner of each panel. Panels **(A–F)** sorted by increasing [Chl].

and testing data sets (not shown) and did not fit the spectral features of phytoplankton observed in the measured b_p data (Castagna et al., 2022; Röttgers et al., 2023), resulting in suppressed R_{rs} values in the green and longer wavelengths for high [Chl]. This contradicts the high NIR reflectance commonly seen during algal blooms (Hieronymi et al., 2017; Bi et al., 2019; Castagna et al., 2022). The differences were significantly mitigated by using $b_{ph}^{\mathrm{Adj}}(\lambda)$, although the shape difference still remains.

The sensitivity analysis results, on the forward modeling aspect, revealed that the assumption of b_{ph} shape has a limited impact on R_{rs} modeling, provided that the b_{ph} magnitude is reasonable. This finding may explain why some inversion models perform well, despite using a simplified power law function for scattering shape. However, it is worth noting that the simplified scattering shape may not accurately represent the scattering spectra and may lead to variance transference between scattering and absorption in the non-linear optimizing approach, as discussed in Roesler and Boss (2003) from the perspective of inversion modeling. Furthermore, a power law function may not be sufficient for modeling optically complex water, particularly at high biomass, where scattering dominates over absorption in water color (McLeroy-Etheridge and Roesler, 1998).

It is important to note that adjusting b_{ph} to b_{ph}^{Adj}, as presented in this section, is an ideal scenario that may not always be feasible due to limited knowledge of b_{ph} magnitude in many practical cases. As discussed about the *C2X* in Figure 9B, modeling absorption and scattering of phytoplankton (detritus as well) separately can lead to significant uncertainties when the input concentrations are outside their training ranges. To address this issue, a relative IOP parameter, the single-scattering albedo, is used in our new model, which has been proven to improve accuracy. Additionally, attenuation, unlike scattering, is relatively simpler to mathematically describe (Twardowski et al., 2001; Roesler and Boss, 2003). Therefore, we suggest an improved parameterization of phytoplankton IOPs in terms of both their spectral shape and magnitude, which has been shown to be applicable for various natural water types.

5 Conclusion

In this study, we introduce a new bio-geo-optical model that can compute spectral inherent optical properties (IOPs) of water constitutes, providing a valuable tool for predicting and

understanding the optical properties of natural water. The model presents several advantages including the consideration of the absorption of detritus from biogenic and minerogenic sources, distinctive optical signatures of the phytoplankton communities, and a novel strategy for modeling scattering coefficients that avoids unrealistic simulations observed in previous studies. To parameterize the model, we perform a detailed and comprehensive analysis of high-quality *in situ* data from optically complex water, and evaluate the model performance using both training and independent data sets. Our model demonstrates promising capabilities in reproducing consistent spectral IOPs from concentrations across different natural water types, including oceanic, coastal, and inland waters. Based on the evaluation both using the training and independent data sets, our model demonstrates an accuracy of within ±5% for most component IOPs throughout the visible spectrum, with some falling within ±10%.

Our new model offers a high degree of freedom, allowing for extensive customization and adaptability when applied to new aquatic systems that extend beyond the training data set. This flexibility enables researchers to fine-tune the framework according to specific requirements, enhancing its practicality and convenience. To fill the gap in previous studies, we generate a showcase data set based on our new model and a simple R_{rs} model, which demonstrates better coverage of the majority of optical variability when compared to several published synthetic data sets. This provides valuable guidance for radiative transfer simulations and building a comprehensive synthetic database for the ocean color community, which should help better distinguish optically active water constituents and thereby reduce uncertainties in ocean color remote sensing. The relevant data and code of the model are available in the section Data Availability Statement.

Data availability statement

The major part of training data set used this study, Hereon, is available on PANGAEA (doi.pangaea.de/10.1594/PANGAEA.950774). The R code for running the model in this study is available in a compiled package, which can be accessed at https://github.com/bishun945/IOPmodel. A web application is also provided to test and run the model at https://bishun945.shinyapps.io/IOPmodel/. Further inquiries can be directed to the corresponding author/s.

Author contributions

The original draft was written by SB under the guidance of RR and MH, who also contributed to the initial paper plan. RR performed the synthesis of the *Hereon* data set, while MH and RR contributed to the model parameterization. SB synthesized external data sets and implement models included in the manuscript. SB was involved in the development of the model, data processing, and figure production, with input from RR and MH. All authors contributed to the article and approved the submitted version.

Funding

The Helmholtz Association with the research program Earth and Environment (PoF IV) funded this study. Additional support was provided by the Hereon-I^{2}B project PhytoDive. This work builds on fundamental results from the EnMAP scientific preparation program of the DLR Space Administration with funds from the German Federal Ministry for Economic Affairs and Energy, specifically the grants 50EE1718 and 50EE1257.

Acknowledgments

We would like to express our gratitude to the Master and Crew of FS Sonne during SO287 for their valuable assistance and support during the research cruise. We are particularly grateful to Kerstin Heymann and Henning Burmester for their help during the cruise, and to Kerstin Heymann for conducting the chlorophyll measurements. We also extend our appreciation to Dariusz Stramski for generously providing their model data, Simon Wright for providing the CHEMTAX software, Zhongping Lee for providing their model lookup table, and David McKee for providing the model coefficients for the R18 model. We thank Hongyan Xi and Xuerong Sun for the discussion on CHEMTAX. We are also grateful to Daniel Jorge, Bouchra Nechad, André Valente, Colleen Mouw, Héloïse Lavigne, Alexandre Castagna, and their colleagues for providing their data sets, which were vital for our research. We thank the R core team and authors of the R packages for their work in developing and maintaining the free software utilized in this study. We would like to thank the editor Astrid Bracher, and two reviewers for their helpful comments.

Conflict of interest

The authors declare that the research was conducted in the absence of any commercial or financial relationships that could be construed as a potential conflict of interest.

Publisher's note

All claims expressed in this article are solely those of the authors and do not necessarily represent those of their affiliated organizations, or those of the publisher, the editors and the reviewers. Any product that may be evaluated in this article, or claim that may be made by its manufacturer, is not guaranteed or endorsed by the publisher.

Supplementary material

The Supplementary Material for this article can be found online at: https://www.frontiersin.org/articles/10.3389/fmars.2023.1196352/full#supplementary-material

References

Ahn, Y. H., Bricaud, A., and Morel, A. (1992). Light backscattering efficiency and related properties of some phytoplankters. *Deep Sea Res. Part Oceanogr. Res. Pap.* 39, 1835–1855. doi: 10.1016/0198-0149(92)90002-B

Babin, M., Morel, A., Fournier-Sicre, V., Fell, F., and Stramski, D. (2003a). Light scattering properties of marine particles in coastal and open ocean waters asrelated to the particle mass concentration. *Limnol. Oceanogr.* 48, 843–859. doi: 10.4319/lo.2003.48.2.0843

Babin, M., Stramski, D., Ferrari, G. M., Claustre, H., Bricaud, A., Obolensky, G., et al. (2003b). Variations in the light absorption coefficients of phytoplankton, nonalgal particles, and dissolved organic matter in coastal waters around Europe. *J. Geophys. Res.* 108, 3211. doi: 10.1029/2001JC000882

Balch, W. M., Holligan, P. M., Ackleson, S. G., and Voss, K. J. (1991). Biological and optical properties of mesoscale coccolithophore blooms in the gulf of Maine. *Limnol. Oceanogr.* 36, 629–643. doi: 10.4319/lo.1991.36.4.0629

Balch, W. M., and Mitchell, C. (2023). Remote sensing algorithms for particulate inorganic carbon (PIC) and the global cycle of PIC. *Earth-Sci. Rev.* 239, 104363. doi: 10.1016/j.earscirev.2023.104363

Basedow, S. L., McKee, D., Lefering, I., Gislason, A., Daase, M., Trudnowska, E., et al. (2019). Remote sensing of zooplankton swarms. *Sci. Rep.* 9, 686. doi: 10.1038/s41598-018-37129-x

Bernard, S., Probyn, T. A., and Quirantes, A. (2009). Simulating the optical properties of phytoplankton cells using a two-layered spherical geometry. *Biogeosci. Discuss* 6, 1497–1563. doi: 10.5194/bgd-6-1497-2009

Bi, S., Li, Y., Liu, G., Song, K., Xu, J., Dong, X., et al. (2021). Assessment of algorithms for estimating chlorophyll-a concentration in inland waters: a round-robin scoring method based on the optically fuzzy clustering. *IEEE Trans. Geosci. Remote Sens.* 60, 1–17. doi: 10.1109/TGRS.2021.3058556

Bi, S., Li, Y., Xu, J., Liu, G., Song, K., Mu, M., et al. (2019). Optical classification of inland waters based on an improved fuzzy c-means method. *Opt. Express* 27, 34838–34856. doi: 10.1364/OE.27.034838

Bi, S., Röttgers, R., and Hieronymi, M. (2023). A transfer model to determine the above-water remote-sensing reflectance from the underwater remote-sensing ratio. *Opt. Express.* 31, 10512–10524. doi: 10.1364/OE.482395

Boss, E., Twardowski, M. S., and Herring, S. (2001). Shape of the particulate beam attenuation spectrum and its inversion to obtain the shape of the particulate size distribution. *Appl. Opt.* 40, 4885. doi: 10.1364/AO.40.004885

Bracher, A., Bouman, H. A., Brewin, R. J. W., Bricaud, A., Brotas, V., Ciotti, A. M., et al. (2017). Obtaining phytoplankton diversity from ocean color: a scientific roadmap for future development. *Front. Mar. Sci.* 4. doi: 10.3389/fmars.2017.00055

Brewin, R. J. W., Sathyendranath, S., Hirata, T., Lavender, S. J., Barciela, R. M., and Hardman-Mountford, N. J. (2010). A three-component model of phytoplankton size class for the Atlantic ocean. *Ecol. Model.* 221, 1472–1483. doi: 10.1016/j.ecolmodel.2010.02.014

Brewin, R. J. W., Sathyendranath, S., Kulk, G., Rio, M.-H., Concha, J. A., Bell, T. G., et al. (2023). Ocean carbon from space: current status and priorities for the next decade. *Earth-Sci. Rev.* 240, 104386. doi: 10.1016/j.earscirev.2023.104386

Bricaud, A., Babin, M., Morel, A., and Claustre, H. (1995). Variability in the chlorophyll-specific absorption coefficients of natural phytoplankton: analysis and parameterization. *J. Geophys. Res.* 100, 13321. doi: 10.1029/95JC00463

Bricaud, A., Claustre, H., Ras, J., and Oubelkheir, K. (2004). Natural variability of phytoplanktonic absorption in oceanic waters: influence of the size structure of algal populations. *J. Geophys. Res.* 109, C11010. doi: 10.1029/2004JC002419

Bricaud, A., Morel, A., Babin, M., Allali, K., and Claustre, H. (1998). Variations of light absorption by suspended particles with chlorophyll *a* concentration in oceanic (case 1) waters: analysis and implications for bio-optical models. *J. Geophys. Res. Oceans* 103, 31033–31044. doi: 10.1029/98JC02712

Bricaud, A., Morel, A., and Prieur, L. (1983). Optical efficiency factors of some phytoplankters1: phytoplankton optical properties. *Limnol. Oceanogr.* 28, 816–832. doi: 10.4319/lo.1983.28.5.0816

Campbell, J. W. (1995). The lognormal distribution as a model for bio-optical variability in the sea. *J. Geophys. Res.* 100, 13237. doi: 10.1029/95JC00458

Castagna, A., Amadei Martínez, L., Bogorad, M., Daveloose, I., Dassevile, R., Dierssen, H. M., et al. (2022). Optical and biogeochemical properties of Belgian inland and coastal waters. *Earth Syst. Sci. Data.* 14, 2697–2719. doi: 10.5194/essd-14-2697-2022

Cazzaniga, I., Zibordi, G., and Mélin, F. (2021). Spectral variations of the remote sensing reflectance during coccolithophore blooms in the Western black Sea. *Remote Sens. Environ.* 264, 112607. doi: 10.1016/j.rse.2021.112607

Churilova, T., Suslin, V., Krivenko, O., Efimova, T., Moiseeva, N., Mukhanov, V., et al. (2017). Light absorption by phytoplankton in the upper mixed layer of the black Sea: seasonality and parametrization. *Front. Mar. Sci.* 4. doi: 10.3389/fmars.2017.00090

Doerffer, R., and Schiller, H. (2000). "Neural network for retrieval of concentrations of water constituents with the possibility of detecting exceptional out of scope spectra," in *IGARSS 2000. IEEE 2000 International Geoscience and Remote Sensing Symposium. Taking the Pulse of the Planet: The Role of Remote Sensing in Managing the Environment. Proceedings (Cat. No.00CH37120)*, Honolulu, HI, USA 2,714–717 (IEEE). doi: 10.1109/IGARSS.2000.861680

Doerffer, R., and Schiller, H. (2007). The MERIS case 2 water algorithm. *Int. J. Remote Sens* 28, 517–535. doi: 10.1080/01431160600821127

GCOS (2011) *Systematic observation requirements for satellite-based products for climate.* Available at: https://library.wmo.int/doc_num.php?explnum_id=3710.

Gordon, H. R., and Morel, A. Y. (1983) *Remote assessment of ocean color for interpretation of satellite visible imagery: a review* (Accessed January 26, 2022).

Gregg, W. W., and Rousseaux, C. S. (2017). Simulating PACE global ocean radiances. *Front. Mar. Sci.* 4. doi: 10.3389/fmars.2017.00060

Harmel, T., Agagliate, J., Hieronymi, M., and Gernez, P. (2021). Two-term reynolds–McCormick phase function parameterization better describes light scattering by microalgae and mineral hydrosols. *Opt. Lett.* 46, 1860. doi: 10.1364/OL.420344

Harmel, T., Hieronymi, M., Slade, W., Röttgers, R., Roullier, F., and Chami, M. (2016). Laboratory experiments for inter-comparison of three volume scattering meters to measure angular scattering properties of hydrosols. *Opt. Express* 24, A234. doi: 10.1364/OE.24.00A234

Helms, J. R., Stubbins, A., Ritchie, J. D., Minor, E. C., Kieber, D. J., and Mopper, K. (2008). Absorption spectral slopes and slope ratios as indicators of molecular weight, source, and photobleaching of chromophoric dissolved organic matter. *Limnol. Oceanogr.* 53, 955–969. doi: 10.4319/lo.2008.53.3.0955

Hieronymi, M., Bi, S., Müller, D., Schütt, D., Behr, D., Brockmann, C., et al (2023). Ocean color atmospheric correction methods in view of usability for different optical water types. *Front. Mar. Sci.* 10.

Hieronymi, M., Krasemann, H., Müller, D., Brockmann, C., Ruescas, A. B., Stelzer, K., et al. (2016). "Ocean colour remote sensing of extreme case-2 waters," in *Proc. Living Planet Symposium*, Prague, Czech Republic. 1–5, ESA SP-740.

Hieronymi, M., Müller, D., and Doerffer, R. (2017). The OLCI neural network swarm (ONNS): a bio-Geo-Optical algorithm for open ocean and coastal waters. *Front. Mar. Sci.* 4. doi: 10.3389/fmars.2017.00140

Hoepffner, N., and Sathyendranath, S. (1991). Effect of pigment composition on absorption properties of phytoplankton. *Mar. Ecol. Prog. Ser.* 73, 11–23. doi: 10.3354/meps073011

IOCCG (2006). *Remote sensing of inherent optical properties: fundamentals, tests of algorithms, and applications*. Ed. Z.-P. Lee (Dartmouth, Canada: IOCCG).

IOCCG (2014). *Phytoplankton functional types from space*. Ed. S. Sathyendranath (Dartmouth, Canada: IOCCG).

IOCCG (2019). *Uncertainties in ocean colour remote sensing*. Ed. F. Mélin (Dartmouth, Canada: International Ocean Colour Coordinating Group). doi: 10.25607/OBP-696

Jackson, T., Sathyendranath, S., and Mélin, F. (2017). An improved optical classification scheme for the ocean colour essential climate variable and its applications. *Remote Sens. Environ.* 203, 152–161. doi: 10.1016/j.rse.2017.03.036

Kieber, R. J., Whitehead, R. F., Reid, S. N., Willey, J. D., and Seaton, P. J. (2006). Chromophoric dissolved organic matter (CDOM) in rainwater, southeastern north Carolina, USA. *J. Atmospheric Chem.* 54, 21–41. doi: 10.1007/s10874-005-9008-4

Kramer, S. J., and Siegel, D. A. (2021). *Global HPLC phytoplankton pigment data compilation, version 2*. PANGAEA. doi: 10.1594/PANGAEA.938703

Lavigne, H., Dogliotti, A., Doxaran, D., Shen, F., Castagna, A., Beck, M., et al. (2022). The HYPERMAQ dataset: bio-optical properties of moderately to extremely turbid waters. *Earth Syst. Sci. Data* 14, 4935–4947. doi: 10.5194/essd-14-4935-2022

Lee, Z., Carder, K. L., and Arnone, R. A. (2002). Deriving inherent optical properties from water color: a multiband quasi-analytical algorithm for optically deep waters. *Appl. Opt.* 41, 5755. doi: 10.1364/AO.41.005755

Lee, Z., Du, K., Voss, K. J., Zibordi, G., Lubac, B., Arnone, R., et al. (2011). An inherent-optical-property-centered approach to correct the angular effects in water-leaving radiance. *Appl. Opt.* 50, 3155. doi: 10.1364/AO.50.003155

Lee, Z., and Hu, C. (2006). Global distribution of case-1 waters: an analysis from SeaWiFS measurements. *Remote Sens. Environ.* 101, 270–276. doi: 10.1016/j.rse.2005.11.008

Liu, G., Li, L., Song, K., Li, Y., Lyu, H., Wen, Z., et al. (2020). An OLCI-based algorithm for semi-empirically partitioning absorption coefficient and estimating chlorophyll a concentration in various turbid case-2 waters. *Remote Sens. Environ.* 239, 111648. doi: 10.1016/j.rse.2020.111648

Loisel, H., Jorge, D. S. F., Reynolds, R. A., and Stramski, D. (2023). A synthetic database generated by radiative transfer simulations in support of studies in ocean optics and optical remote sensing of the global ocean. *Earth Syst. Sci. Data Discuss.* doi: 10.5194/essd-2023-80

Lo Prejato, M., McKee, D., and Mitchell, C. (2020). Inherent optical properties-reflectance relationships revisited. *J. Geophys. Res. Oceans* 125, e2020JC016661. doi: 10.1029/2020JC016661

Losa, S. N., Soppa, M. A., Dinter, T., Wolanin, A., Brewin, R. J. W., Bricaud, A., et al. (2017). Synergistic exploitation of hyper- and multi-spectral precursor sentinel measurements to determine phytoplankton functional types (SynSenPFT). *Front. Mar. Sci.* 4. doi: 10.3389/fmars.2017.00203

Mackey, M., Mackey, D., Higgins, H., and Wright, S. (1996). CHEMTAX - a program for estimating class abundances from chemical markers:application to HPLC measurements of phytoplankton. *Mar. Ecol. Prog. Ser.* 144, 265–283. doi: 10.3354/meps144265

Maritorena, S., Siegel, D. A., and Peterson, A. R. (2002). Optimization of a semianalytical ocean color model for global-scale applications. *Appl. Opt.* 41, 2705. doi: 10.1364/AO.41.002705

Mason, J. D., Cone, M. T., and Fry, E. S. (2016). Ultraviolet (250–550 nm) absorption spectrum of pure water. *Appl. Opt.* 55, 7163. doi: 10.1364/AO.55.007163

McLeroy-Etheridge, S. L., and Roesler, C. S. (1998). Are the inherent optical properties of phytoplankton responsible for the distinct ocean colors observed during harmful algal blooms. *Ocean Opt. XIV*. 1, 109–116.

Meersche, K. V., Soetaert, K., and Oevelen, D. V. (2009). xsample(): an *R* function for sampling linear inverse problems. *J. Stat. Software* 30, 1–15. doi: 10.18637/jss.v030.c01

Mélin, F., and Vantrepotte, V. (2015). How optically diverse is the coastal ocean? *Remote Sens. Environ.* 160, 235–251. doi: 10.1016/j.rse.2015.01.023

Mobley, C. D. (1994). *Light and water: radiative transfer in natural waters* (Academic press).

Mobley, C., Stramski, D., Bissett, P., and Boss, E. (2004). Optical modeling of ocean waters: is the case 1 - case 2 classification still useful? (San Diego). *Oceanography* 17, 60–67. doi: 10.5670/oceanog.2004.48

Moore, T. S., Campbell, J. W., and Feng, H. (2001). A fuzzy logic classification scheme for selecting and blending satellite ocean color algorithms. *IEEE Trans. Geosci. Remote Sens.* 39, 1764–1776. doi: 10.1109/36.942555

Moore, T. S., Dowell, M. D., Bradt, S., and Verdu, A. R. (2014). An optical water type framework for selecting and blending retrievals from bio-optical algorithms in lakes and coastal waters. *Remote Sens. Environ.* 143, 97–111. doi: 10.1016/j.rse.2013.11.021

Morel, A., Antoine, D., and Gentili, B. (2002). Bidirectional reflectance of oceanic waters: accounting for raman emission and varying particle scattering phase function. *Appl. Opt.* 41, 6289. doi: 10.1364/AO.41.006289

Morel, A., and Maritorena, S. (2001). Bio-optical properties of oceanic waters: a reappraisal. *J. Geophys. Res. Oceans* 106, 7163–7180. doi: 10.1029/2000JC000319

Morel, A., and Prieur, L. (1977). Analysis of variations in ocean color: ocean color analysis. *Limnol. Oceanogr.* 22, 709–722. doi: 10.4319/lo.1977.22.4.0709

Mouw, C. B., Ciochetto, A. B., Grunert, B., and Yu, A. (2017). Expanding understanding of optical variability in lake superior with a 4-year dataset. *Earth Syst. Sci. Data* 9, 497–509. doi: 10.5194/essd-9-497-2017

Nechad, B., Ruddick, K. G., Schroeder, T. A., Oubelkheir, K., Blondeau-Patissier, D., Cherukuru, N. R., et al. (2015). CoastColour round robin data sets: a database to evaluate the performance of algorithms for the retrieval of water quality parameters in coastal waters. *Earth Syst. Sci. Data* 7, 319–348. doi: 10.5194/essdd-8-173-2015

Neukermans, G., and Fournier, G. (2018). Optical modeling of spectral backscattering and remote sensing reflectance from emiliania huxleyi blooms. *Front. Mar. Sci.* 5. doi: 10.3389/fmars.2018.00146

Neukermans, G., Loisel, H., Mériaux, X., Astoreca, R., and McKee, D. (2012). *In situ* variability of mass-specific beam attenuation and backscattering of marine particles with respect to particle size, density, and composition. *Limnol. Oceanogr.* 57, 124–144. doi: 10.4319/lo.2012.57.1.0124

Organelli, E., Dall'Olmo, G., Brewin, R. J. W., Tarran, G. A., Boss, E., and Bricaud, A. (2018). The open-ocean missing backscattering is in the structural complexity of particles. *Nat. Commun.* 9, 5439. doi: 10.1038/s41467-018-07814-6

Oubelkheir, K., Clementson, L. A., Webster, I. T., Ford, P. W., Dekker, A. G., Radke, L. C., et al. (2006). Using inherent optical properties to investigate biogeochemical dynamics in a tropical macrotidal coastal system. *J. Geophys. Res.* 111, C07021. doi: 10.1029/2005JC003113

Prieur, L., and Sathyendranath, S. (1981). An optical classification of coastal and oceanic waters based on the specific spectral absorption curves of phytoplankton pigments, dissolved organic matter, and other particulate materials1: optical classification. *Limnol. Oceanogr.* 26, 671–689. doi: 10.4319/lo.1981.26.4.0671

Ramírez-Pérez, M., Twardowski, M., Trees, C., Piera, J., and McKee, D. (2018). Inversion of *In situ* light absorption and attenuation measurements to estimate constituent concentrations in optically complex shelf seas. *J. Geophys. Res. Oceans* 123, 720–737. doi: 10.1002/2017JC013453

Robertson Lain, L., and Bernard, S. (2018). The fundamental contribution of phytoplankton spectral scattering to ocean colour: implications for satellite detection of phytoplankton community structure. *Appl. Sci.* 8, 2681. doi: 10.3390/app8122681

Roesler, C. S., and Boss, E. (2003). Spectral beam attenuation coefficient retrieved from ocean color inversion. *Geophys. Res. Lett.* 30, 1468. doi: 10.1029/2002GL016185

Roesler, C. S., and Boss, E. (2008). *In situ* measurement of the inherent optical properties (IOPs) and potential for harmful algal bloom detection and coastal ecosystem observations 68. Chapter 5, 153-206 in M. Babin, C. S. Roesler and J. Cullen [eds.] *Real-Time Coastal Observing Systems for Ecosystem Dynamics and Harmful Algal Bloom*. UNESCO.

Röttgers, R., Bi, S., Burmester, H., Heymann, K., Hieronymi, M., Krasemann, H., et al. (2023). Water inherent optical properties and concentrations of water constituents from the German bight and adjacent regions. *PANGAEA*. doi: 10.1594/PANGAEA.950774

Röttgers, R., and Doerffer, R. (2007). Measurements of optical absorption by chromophoric dissolved organic matter using a point-source integrating-cavity absorption meter: CDOM absorption. *Limnol. Oceanogr. Methods* 5, 126–135. doi: 10.4319/lom.2007.5.126

Röttgers, R., Doerffer, R., McKee, D., and Schönfeld, W. (2016) *The water optical properties processor (WOPP): pure water spectral absorption, scattering and real part of refractive index model. technical report no WOPP-ATBD/WRD6*. Available at: https://calvalportal.ceos.org/tools.

Röttgers, R., Dupouy, C., Taylor, B. B., Bracher, A., and Woźniak, S. B. (2014a). Mass-specific light absorption coefficients of natural aquatic particles in the near-infrared spectral region. *Limnol. Oceanogr.* 59, 1449–1460. doi: 10.4319/lo.2014.59.5.1449

Röttgers, R., Heymann, K., and Krasemann, H. (2014b). Suspended matter concentrations in coastal waters: methodological improvements to quantify individual measurement uncertainty. *Estuar. Coast. Shelf Sci.* 151, 148–155. doi: 10.1016/j.ecss.2014.10.010

Sathyendranath, S., Lazzara, L., and Prieur, L. (1987). Variations in the spectral values of specific absorption of phytoplankton: phytoplankton specific absorption. *Limnol. Oceanogr.* 32, 403–415. doi: 10.4319/lo.1987.32.2.0403

Sathyendranath, S., Prieur, L., and Morel, A. (1989). A three-component model of ocean colour and its application to remote sensing of phytoplankton pigments in coastal waters. *Int. J. Remote Sens.* 10, 1373–1394. doi: 10.1080/01431168908903974

Schiller, H., and Doerffer, R. (1999). Neural network for emulation of an inverse model operational derivation of case II water properties from MERIS data. *Int. J. Remote Sens.* 20, 1735–1746. doi: 10.1080/014311699212443

Stavn, R. H., and Richter, S. J. (2008). Biogeo-optics: particle optical properties and the partitioning of the spectral scattering coefficient of ocean waters. *Appl. Opt.* 47, 2660. doi: 10.1364/AO.47.002660

Stramski, D., Babin, M., and Woźniak, S. B. (2007). Variations in the optical properties of terrigenous mineral-rich particulate matter suspended in seawater. *Limnol. Oceanogr.* 52, 2418–2433. doi: 10.4319/lo.2007.52.6.2418

Stramski, D., Boss, E., Bogucki, D., and Voss, K. J. (2004). The role of seawater constituents in light backscattering in the ocean. *Prog. Oceanogr.* 61, 27–56. doi: 10.1016/j.pocean.2004.07.001

Stramski, D., Bricaud, A., and Morel, A. (2001). Modeling the inherent optical properties of the ocean based on the detailed composition of the planktonic community. *Appl. Opt.* 40, 2929. doi: 10.1364/AO.40.002929

Stramski, D., Li, L., and Reynolds, R. A. (2019). Model for separating the contributions of non-algal particles and colored dissolved organic matter to light absorption by seawater. *Appl. Opt.* 58, 3790. doi: 10.1364/AO.58.003790

Stramski, D., and Tegowski, J. (2001). Effects of intermittent entrainment of air bubbles by breaking wind waves on ocean reflectance and underwater light field. *J. Geophys. Res. Oceans* 106, 31345–31360. doi: 10.1029/2000JC000461

Szeto, M., Werdell, P. J., Moore, T. S., and Campbell, J. W. (2011). Are the world's oceans optically different? *J. Geophys. Res. Oceans* 116, 2011JC007230. doi: 10.1029/2011JC007230

Twardowski, M. S., Boss, E., Macdonald, J. B., Pegau, W. S., Barnard, A. H., and Zaneveld, J. R. V. (2001). A model for estimating bulk refractive index from the optical backscattering ratio and the implications for understanding particle composition in case I and case II waters. *J. Geophys. Res. Oceans* 106, 14129–14142. doi: 10.1029/2000JC000404

Vaillancourt, R. D., Brown, C. W., Guillard, R. R. L., and Balch, W. M. (2004). Light backscattering properties of marine phytoplankton: relationships to cell size, chemical composition and taxonomy. *J. Plankton Res.* 26, 191–212. doi: 10.1093/plankt/fbh012

Valente, A., Sathyendranath, S., Brotas, V., Groom, S., Grant, M., Jackson, T., et al. (2022). A compilation of global bio-optical *in situ* data for ocean-colour satellite applications – version three. *Earth Syst. Sci. Data* 14, 5737–5770. doi: 10.5194/essd-14-5737-2022

Voss, K. J. (1992). A spectral model of the beam attenuation coefficient in the ocean and coastal areas. *Limnol. Oceanogr.* 37, 501–509. doi: 10.4319/lo.1992.37.3.0501

Werdell, P. J., Franz, B. A., Bailey, S. W., Feldman, G. C., Boss, E., Brando, V. E., et al. (2013). Generalized ocean color inversion model for retrieving marine inherent optical properties. *Appl. Opt.* 52, 2019. doi: 10.1364/AO.52.002019

Werdell, P. J., McKinna, L. I. W., Boss, E., Ackleson, S. G., Craig, S. E., Gregg, W. W., et al. (2018). An overview of approaches and challenges for retrieving marine inherent optical properties from ocean color remote sensing. *Prog. Oceanogr.* 160, 186–212. doi: 10.1016/j.pocean.2018.01.001

Woźniak, B., and Dera, J. (2007). *Light absorption in sea water* (New York, NY: Springer).

Xi, H., Hieronymi, M., Krasemann, H., and Röttgers, R. (2017). Phytoplankton group identification using simulated and *In situ* hyperspectral remote sensing reflectance. *Front. Mar. Sci.* 4. doi: 10.3389/fmars.2017.00272

Xi, H., Hieronymi, M., Röttgers, R., Krasemann, H., and Qiu, Z. (2015). Hyperspectral differentiation of phytoplankton taxonomic groups: a comparison between using remote sensing reflectance and absorption spectra. *Remote Sens.* 7, 14781–14805. doi: 10.3390/rs71114781

Zheng, G., Stramski, D., and DiGiacomo, P. M. (2015). A model for partitioning the light absorption coefficient of natural waters into phytoplankton, nonalgal particulate, and colored dissolved organic components: a case study for the Chesapeake bay. *J. Geophys. Res. Oceans* 120, 2601–2621. doi: 10.1002/2014JC010604

Zhou, W., Wang, G., Sun, Z., Cao, W., Xu, Z., Hu, S., et al. (2012). Variations in the optical scattering properties of phytoplankton cultures. *Opt. Express* 20, 11189. doi: 10.1364/OE.20.011189

frontiers | Frontiers in Marine Science

TYPE Original Research
PUBLISHED 19 June 2023
DOI 10.3389/fmars.2023.1197311

Check for updates

OPEN ACCESS

EDITED BY
Gemma Kulk,
Plymouth Marine Laboratory,
United Kingdom

REVIEWED BY
Ravidas Krishna Naik,
National Centre for Polar and Ocean Research (NCPOR), India
Joanna Stoń-Egiert,
Polish Academy of Sciences, Poland

*CORRESPONDENCE
Elisabetta Canuti
elisabetta.canuti@ec.europa.eu

RECEIVED 30 March 2023
ACCEPTED 24 May 2023
PUBLISHED 19 June 2023

CITATION
Canuti E (2023) Phytoplankton pigment *in situ* measurements uncertainty evaluation: an HPLC interlaboratory comparison with a European-scale dataset.
Front. Mar. Sci. 10:1197311.
doi: 10.3389/fmars.2023.1197311

COPYRIGHT
© 2023 Canuti. This is an open-access article distributed under the terms of the Creative Commons Attribution License (CC BY). The use, distribution or reproduction in other forums is permitted, provided the original author(s) and the copyright owner(s) are credited and that the original publication in this journal is cited, in accordance with accepted academic practice. No use, distribution or reproduction is permitted which does not comply with these terms.

Phytoplankton pigment *in situ* measurements uncertainty evaluation: an HPLC interlaboratory comparison with a European-scale dataset

Elisabetta Canuti*

Joint Research Centre, European Commission, Ispra, Italy

Phytoplankton pigment data play a crucial role in ecological studies, enabling the identification of algal groups and estimation of primary production rates. Accurate measurements of chlorophyll *a* (TChl *a*) and other marine pigments are essential for the development of bio-optical algorithms and the validation of satellite data products. High-performance liquid chromatography (HPLC) is the gold standard method for quantifying multiple pigments in a single water sample. This study aims to investigate the uncertainties associated with phytoplankton pigment quantification by comparing duplicate sample analyses conducted by two laboratories, the Joint Research Centre of the European Commission (*J*) and the DHI Group, Denmark (*D*). The analyses were performed using the same HPLC method. The dataset comprised 957 natural samples collected between 2012 and 2017 from various European seas, representing different trophic conditions with TChl a concentrations ranging from 0.083 to 27.35 mg/m^3. The study compared the results of the two independent analyses for TChl a and primary phytoplankton pigments, including chlorophyll b, chlorophyll c, carotens, fucoxanthin, 19′-butanoyloxyfucoxanthin, diadinoxanthin, diatoxanthin, 19′-hexanoyloxyfucoxanthin, peridin, and zeaxanthin. The percent difference between the two analyses was calculated to assess the uncertainties associated with pigment quantification. The mean percent difference observed between the two independent analyses of TChl a was 10.8%. For the primary phytoplankton pigments, the associated mean percent difference was 16.9%. These results meet the requirements of 15% and 25% uncertainties, respectively, which are applicable for the validation of satellite data products. The comparative analysis between the two laboratories demonstrates that the uncertainties associated with phytoplankton pigment quantification are within acceptable ranges for the validation of satellite data products. Moreover, the study investigates the propagation of uncertainties in diagnostic pigment values to phytoplankton indexes, which are derived using pigment-based algorithms to characterize phytoplankton populations according to functional types.

KEYWORDS

chlorophyll *a*, phytoplankton pigments, HPLC, inter-laboratory comparison, uncertanties

1 Introduction

The identification of phytoplankton pigments has a wide range of applications as chemotaxonomic markers to identify community composition (Jeffrey et al., 1997; Mackey, et al., 1996; Wright and Jeffrey, 2005; Roy et al., 2011), species and their biomass in seawater (Vidussi et al., 2001; Uitz et al., 2006; Hirata et al., 2011) and plays a role in the development, refinement, and validation of satellite algorithms for mapping phytoplankton biomass, functional types, and size classes (e.g., Brewin et al., 2010; Mouw et al., 2017).

Ocean color data validation, satellite bio-optical algorithm development, and ocean productivity models within the framework of marine ecosystem studies, also require high-quality *in situ* measurements of chlorophyll *a* (TChl *a*) and primary pigment concentrations. Validation of satellite products of TChl *a* is particularly relevant as it is listed as an essential climate variable (GCOS, 2011). The phytoplankton pigments of algae can be routinely quantified through liquid chromatographic screening methods to separate known pigments quantitatively. More than 30 high-performance liquid chromatography (HPLC) methods are reported in the literature (Roy et al., 2011) as commonly implemented for phytoplankton pigment determination. The HPLC methods primarily utilized for remote sensing validation activities are based on C8 and C18 chromatographic columns. In the JGOFS Protocols for the Joint Global Ocean Flux Study Core Measurements (1994), the Wright et al. (1991) method was recommended as the HPLC method for determining TChl *a*. In the oceanographic community, the Zapata et al. (2000) and Van Heukelem and Thomas (2001) methods have gained widespread adoption over the past decade. These two methods offer the advantage of enabling the simultaneous analysis of multiple pigments and unknowns in a single run (Wright and Jeffrey, 2005), while also exhibiting superior resolution for chlorophylls *c* compared to Wright's approach (1991).

Moreover, to ensure a continuous high standard in sample analysis, regular participation in comparison exercises involving international laboratories or comparison with a certified reference laboratory are required. The so-called round-robin exercises have been conducted in the past decades to assess the performance of HPLC methods applied for pigment determination, and uncertainties of 15% have been documented for TChl *a* and other pigments (Latasa et al., 1996; Claustre et al., 2004). It is worth highlighting that the majority of studies tend to focus on TChl *a* analysis, while comparatively fewer investigations are dedicated to other pigments. This disparity is noteworthy as it limits our understanding of the broader spectrum of pigments present in various samples. Natural samples, such as those obtained from different marine environments, exhibit a diverse range of pigments with unique functional roles. Understanding the full pigment profile of natural samples requires comprehensive HPLC comparisons that encompass not only TChl *a* but also other pigments such as chlorophyll *b*, carotenoids, and phycobilins. The SeaWiFS HPLC Analysis Round-Robin Experiment (SH) and the HPLC/DAD Intercomparison on Phytoplankton Pigments (HIP) exercises have compared laboratories on several pigments, relying on both pigment standard and natural samples in their statistics. Such exercises have the great merit of allowing the comparison of methods and performance among the participating institutes, typically 4 to 11 (Table 1) on different water types. In SH and HIP exercises (with the exception of HIP-3), a quality assurance (QA) subset of laboratories was defined that represented the state-of-the-art results based on agreed parameters of performance metrics (Hooker et al., 2005). The TChl *a* average uncertainties for the QA subset were invariant to water type and lower than 8%, while a result lower than 25% for primary pigments was reached in all the exercise with the exception of SH-4, which was focused on eutrophic waters (Hooker et al., 2010). Although the level of agreement requested for remote sensing applications is demonstrated to be achievable, some participants not part of the QA have shown differences much higher than 15% for the TChl *a*, and than 25% on average on primary pigments (Hooker et al., 2005; Hooker et al., 2009; Hooker et al., 2010; Hooker et al., 2012; Canuti et al., 2016; Canuti et al., 2022). A known limit of the comparison of marine pigments is the lack of certified reference materials (CRMs);

TABLE 1 Overview of the outcomes from the initial five HIP comparison exercises and the five SeaHARRE (SH) trials.

Exercise	Year	Lab	Meth	TChl *a*	TChl *b*	TChl *c*	Caro	But	Hex	Allox	Diad	Diat	Fuco	Per	Zea	PPig
SH-1	1999	4	4	7	14	26.5	17.6	23.6	24.8	38.9	16	55.8	8.8	13	11.4	21.5
SH-2	2002	8	5	5.9	16.5	21.8	16.8	30.6	9.5	20.3	8.7	20.6	4.7	15.4	21.4	16.0
SH-3	2004	8	3	6.3	13.9	14.9	13.2	14.6	6	4.2	5	17.8	10.6	30.5	9.6	12.2
SH-4	2006	10	3	6.4	12.4	20.4	9.6	87.2	57.5	13	9.3	49.8	6.6	66.6	19	29.8
SH-5	2008	12	4	5.4	8.3	14.4	17.9	21.3	22.9	8.5	12.1	35.3	5.9	15.8	9.9	14.8
HIP-1	2010	3	2	7.8	12.4	12.7	16.5	10	8.6	9.5	12.3	17.2	9.3	13.7	13.9	12.0
HIP-2	2011	6	4	4.5	9.7	8	24.1	7.2	6.9	13.7	4.9	13.3	6.2	16.8	21.3	11.4
HIP-3	2012	6	5	18.3	9.7	30.8	32.7	17.8	26.5	25.5	28.9	23.2	29.6	15.1	39.9	24.8
HIP-4	2014	5	3	6.2	15	11.3	3.7	8.4	6.9	5.1	6.5	19.4	4.9	24.8	5.8	9.8
HIP-5	2019	8	5	6.3	12.7	13.9	16.7	15.6	11.6	14	11	22.8	11.8	37.3	30.1	17

The table presents the exercise year, participant count (Lab), the number of compared methods (Meth), and the absolute percent difference (%APD) for field samples encompassing all primary pigments and their average (PPig). Table 2 provides a reference for the acronyms used.

instead, pigment standards certified by analysis from a select few producers (e.g., DHI, DK, and carotenature, CH) were commonly used.

The current study first aims to investigate the uncertainties associated with phytoplankton pigment quantification by comparing the analyses performed on duplicate samples by a certified laboratory and an accredited laboratory applying the same method (Van Heukelem and Thomas, 2001): the Joint Research Centre of the European Commission (*J*) and the DHI Group, Denmark (*D*). The comparison with one accredited laboratory allows for a focused examination of the same method applied to various water types and is significant as both laboratories have shown good performance in previous intercomparison exercises (e.g., Canuti et al., 2016). The chromatographic method selected here has been successfully applied to a wide range of pigment concentrations, including oligotrophic (Hooker et al., 2009) and eutrophic coastal waters (Hooker et al., 2005). However, the most relevant aspect of the study is the data set available for analysis, made up of batches of natural samples collected at 957 measurement stations during ship-based oceanographic campaigns and analyzed by both laboratories. These data are representative of different trophic conditions and water types of the European Seas, with TChl *a* concentration in the range of 0.083–27.35 mg/m^3, allowing an extensive comparison to be conducted. The phytoplankton pigments considered for the present exercise are the chlorophylls and the carotenoids most commonly used in marine chemotaxonomic and photo-physiological studies, including the major marker pigments used for classification of phytoplankton groups in ecological studies (Roy et al., 2011). Phytoplankton pigment datasets are commonly used to characterize algal species in terms of phytoplankton functional types (PFTs) or phytoplankton size classes (PSCs). Related investigations have been pursued in the context of ocean color remote sensing, as this would allow a synoptic description of PFTs or PSCs (e.g., IOCCG, 2014; Mouw et al., 2017; Xi et al., 2020). The two most widely used PFT methods are CHEMTAX (Mackey et al., 1996) and diagnostic pigment (DP) analyses. The *a priori* assumption underlying the chemotaxonomy methods is the covariance of pigments. The inherent uncertainties of chemotaxonomy methods are due to the widespread occurrence of most pigments across many different taxa (IOCCG, 2014). Another known limit is the association of a single pigment with a taxon even though it could be, in some case, not representative of the entire group, e.g., some *Dinoflagellates* spp. have types of "non-canonical" plastids instead of the Peridinin (Matsumoto et al., 2011), and there are known cases (Naik et al., 2011) where the chemotaxonomy alone leads to incomplete interpretation of the taxa distribution. Despite these considerations, most of the validation of remote sensing methods for assessing phytoplankton community composition is based on chemotaxonomy derived from HPLC pigments. Tracing uncertainties and building uncertainty budgets for descriptors of phytoplankton populations are tasks in progress (Bracher et al., 2017), where uncertainties associated with field data of diagnostic pigments are needed (Xi et al., 2021). The present study obviously contributes to that effort. A second contribution is to explore how uncertainties in diagnostic pigment values propagate to phytoplankton indexes that are at the basis of pigment-based algorithms deriving descriptors of phytoplankton populations such as PFTs (Hirata et al., 2011), therefore providing a benchmark value for that step.

2 Materials and methods

2.1 Nomenclature and use of diagnostic pigments

The nomenclature adopted for total chlorophylls and the other pigments is the one established by the Scientific Committee on Oceanographic Research (SCOR) Working Group 78 (Jeffrey et al., 1997). The individual pigments could be used to obtain the pigment associations and to derive macrovariables such as sums, ratios, and indices (Table 2).

Vidussi et al. (2001) introduced a method that established a connection between diagnostic accessory pigments (peridinin, 19′-butanoyloxyfucoxanthin, fucoxanthin, 19′-hexanoyloxyfucoxanthin, alloxanthin, chlorophyll *b*, and zeaxanthin) and various taxonomic groups of phytoplankton, enabling the derivation of PFTs across three distinct size classes. These size classes encompassed micro- (> 20 μm), nano- (2–20 μm), and picoplankton (0.2–2 μm), representing a comprehensive range of trophic conditions and taxonomic classes, including diatoms, dinophytes, cryptophytes, haptophytes, green algae, and prokaryotes (Tables 2, 3). Building upon this foundation, Uitz et al. (2006) further refined the methodology by incorporating weighting coefficients for the same set of seven diagnostic pigments. This algorithm required the quantification of DPs using HPLC. These DPs formed a minimal set of marker pigments capable of detecting the primary phytoplankton types (as outlined in Table 3). The determination of PFTs relied on estimating the abundance of each phytoplankton group based on the established relationship between TChl *a* and their respective quantities (Uitz et al., 2006; Brewin et al., 2010; Hirata et al., 2011). In this work, we apply the known relationships between pigment abundances without any additional adjustments to the coefficients, adhering to the methodology outlined by previous studies.

X_n indicates a portion of nanoplankton contributing to Hex, and Y_p indicates a portion of picoplankton in Hex (Brewin et al., 2010)

2.2 Sampling

The duplicate natural samples used to support the investigation were collected by the Joint Research Centre (JRC) between 2012 and 2017 across the European Seas during 11 different oceanographic cruises in the framework of the Bio-Optical Mapping of Marine Properties (BiOMaP, Zibordi et al., 2011) program and 26 measuring campaigns at the Acqua Alta Oceanographic Tower (AAOT) located in the Gulf of Venice, Italy, northern Adriatic Sea (45.31° N, 12.51° E). To minimize the intraseries variability due to different operators and filtering procedures, a common standard operative procedure was adopted. The water batch for replicate production was collected using Niskin or Plexiglas sampling bottles. In the case of a surface batch, the water was collected 1 m below the surface. Samples were

TABLE 2 Individual pigments and pigment associations to derive macrovariables as sums, ratios, and indices and their acronyms.

	Compound name		Compound name
	Primary pigments (PPig)		Secondary and tertiary pigments
TChl *a*	Total chlorophyll *a* (chlorophyllide-*a* + monovinyl chlorophyll *a* + divinyl chlorophyll *a*)	MVChl *a*	Monovinyl chlorophyll *a*
TChl *b*	Total chlorophyll *b* (monovinyl chlorophyll *b* + divinyl chlorophyll *b*)	DVChl *a*	Divinyl chlorophyll *a*
TChl *c*	Total chlorophyll *c* (chlorophyll *c1*+ chlorophyll *c2* + chlorophyll *c3*)	Chlide *a*	Chlorophyllide *a*
Car	Carotenes (bb-carotene +be-carotene)	Pheo *a*	Pheophorbide *a*
Allox	Alloxanthin	Phy *a*	Pheophytin *a*
But	19′-Butanoyloxyfucoxanthin	Pras	Prasinoxanthin
Diad	Diadinoxanthin	Viol	Violaxanthin
Diat	Diatoxanthin	Neo	Neoxanthin
Fuco	Fucoxanthin	Lut	Lutein
Hex	19′-Hexanoyloxyfucoxanthin		
Peri	Peridinin		
Zea	Zeaxanthin		
	Pigment sum (PSum)		**Pigment index (PIndex)**
TChl	Total chlorophyll (TChl *a* + TChl *b* + TChl *c*)	mPF	Microplankton proportion factor $(\frac{\text{Fuco + Peri}}{\text{DP}})$
PPC	Photoprotective carotenoids (Allo + Diad + Diato + Zea + Caro)	nPF	Nanoplankton proportion factor $(\frac{\text{Hex + But + Allo}}{\text{DP}})$
PSC	Photosynthetic carotenoids (ButFuco + Fuco + Hex + Peri)	pPF	Picoplankton proportion factor $(\frac{\text{Zea + TChl b}}{\text{DP}})$
PSP	Photosynthetic pigments (PSC + TChl)		
TAcc	Total accessory pigment (PPC + PSC +TChl *b* + TChl *c*)		
TPig	Total pigment (TAcc + TChl *a*)		
DP	Total diagnostic pigment (PSC +Allo +Zea + TChl *b*)		

TABLE 3 Phytoplankton size classes (PSCs), phytoplankton functional types (PFTs), diagnostic pigments, and their taxonomic meaning.

PSCs/PFTs	Diagnostic pigments	Estimation formula
Microplankton (> 20 µm)	Fuco, Peri	1.41 (Fuco+Peri)/DP
Nanoplankton (2–20 µm)	Hex	(X_n 1.27 Hex + 1.01 TChl *b* +0.35 But +0.60 Allo)/DP
Picoplankton (0.2–2 µm)	Zea, Hex, TChl *b*	(0.86 Zea+Y*p* 1.27 Hex)/DP
Diatoms	Fuco	1.41 Fuco/DP
Dinoflagellates	Peri	1.41 Peri/DP
Haptophytes	But, Hex	(Nano-green algae)
Green algae	TChl *b*	1.01 TChl *b*/DP
Prokaryotes	Zea	0.86 Zea/DP
Pico-eukaryotes	Hex, TChl *b*	(Pico-prokaryotes)
Prochlorococcus sp.	DVChl *a*	0.74 DVChl *a*/TChl *a*

*X_n = 0.5 and Y_p = 0.5 for TChl a 0.04 mg/m^3; Y_p increasing at 1 at TChl a = 001 mg/m^3; X_n increasing at 1 at TChl a = 0.08 mg/m^3.

collected at the surface for all the ship-based campaigns and at the additional depths of 8 and 14 m during the AAOT measurement campaigns. The water batch was filtered through a polyethylene (PE) mesh size of 300 µm (Kartell, Milan, Italy) and collected in a 10-L polypropylene (PP) bottle. The water was kept well mixed. The filtration volumes were evenly distributed among two cylinders previously rinsed. The filters used for the comparison were 25 mm GF/F (nominal pore size, 0.7 µm). The two filtrations were conducted in parallel under a mild vacuum (not exceeding 0.5 atm). At the end of the water passage, a few extra seconds of vacuum were applied to dry the filter before storage. The filters were then folded in two parts with the filtrate inside, wrapped in aluminum foil, flash frozen in liquid nitrogen, and stored until their arrival at the JRC Marine Optical Laboratory. The samples were successively moved to a −80°C freezer (ThermoFisher, USA) until shipped in dry ice (−40°C) to the *D*, where the laboratory analysis was performed. The water volume filtered varied from 60 ml (N02 cruise) to 2,000 ml (I02 cruise) and was established according to the water absorption coefficient measured *in situ* by an ac-9 meter (WET Labs Inc., USA) at 412 nm. The complete list of natural samples and their locations are summarized in Table 4 and displayed in Figure 1.

The datasets considered in the following analysis refer to 957 samples: 614 belonging to oceanographic cruises and approximately one third (343 samples) collected at AAOT.

The table provides information on surface TChl *a* range (min and max), average concentration (mean), and standard deviation (SD) for all campaigns, except for the AAOT campaign, where the TChl *a* data pertain to all depth samples collected at the specific site.

2.3 Analytical method

The quantitative HPLC method applied by the two laboratories for the determination of phytoplankton pigments is the Van Heukelem and Thomas (2001) method. However, the single laboratory implementation could differ from the method originally published.

The *D* method is described in detail in Schlüter et al. (2016). The main information reported here is that described by *D* in the test reports delivered together with the results of accredited pigment analysis and have to be considered the conditions of analysis for the accredited method (DHI Internal Method SOP No. 30/852:05). The filters are transferred to vials with 3 ml of 95% acetone with an internal standard (vitamin E). The samples are mixed on a vortex mixer, sonicated in an ice-cold sonication bath for 10 min, extracted at 4°C for 20 h, and mixed again. The samples are then filtered through a 0.2-µm Teflon syringe filter into HPLC vials and placed in the cooling rack of the HPLC system together with the vials with mixed pigments. The samples were analyzed by a Shimadzu LC-10ADVP HPLC composed of one pump (LC-10ADVP), a photodiode array detector (SPD-M10AVP), an SCL-10ADVP system controller with LC Solution software, a temperature-controlled auto sampler (set at 4°C), a column oven (CTO-10ASVP), and a degasser. A buffer consisting of 28 mM aqueous tetrabutylammoniumacetate (TBAA) and the sample are injected in the HPLC in the ratio 5:2 using a pretreatment program and mixing in the loop before injection, for a total of 500 µl. The solvents used are methanol and 28 mM aqueous TBAA. The solvent gradient, with a constant flow of 1.1 ml/min consists of solvent A ((70:30) methanol:28 mM aqueous TBAA, pH 6.4) and solvent B (100% methanol). The time gradient program was at 0 min: 95% A, 5% B; 22 min: 5% A, 95% B; 30 min: 95% A, 5% B; 31 min: 100% A, 0% B; 34 min: 100% A, 0% B; 35 min 5% A, 95% B; and 41 min: stop. The column was an Eclipse XDB-C8, 3.5 µm particle size, 150 × 4.6 Φ mm (Agilent Technologies, Santa Clara, California, USA). The temperature of the column oven was set to 60°C. The HPLC was calibrated with pigment standards from DHI Lab Products, Denmark. The internal standard was detected at 222 nm, while

TABLE 4 Overview of the HPLC pigment database categorized by cruise, date, geographical area, and number of stations (*N*).

Cruises	Dates	Geographical area	N	TChl *a* (mg/m^3)			
				Mean	SD	Min	Max
WM	23 March–9 April 2012	Western Mediterranean Sea	73	0.3407	0.485	0.083	3.402
BL07	31 August–13 September 2012	Black Sea	90	0.8316	1.239	0.234	6.920
BL08	13–15 September 2012	Black Sea	14	0.4127	0.115	0.191	0.557
L04	21–25 March 2013	Ligurian Sea	25	1.0967	0.612	0.245	3.343
O01	11–27 April 2014	Western Mediterranean Sea	53	0.3762	0.338	0.098	1.797
A02	29 March–14 April 2015	Adriatic Sea	64	0.6111	1.184	0.183	8.943
N02	9–16 July 2015	North Sea	52	5.7720	2.633	2.068	13.764
K09	4–11 June 2016	Black Sea	53	0.6783	0.581	0.212	2.820
K10	12–24 June 2016	Black Sea	82	2.6181	4.759	0.172	27.535
E03	26 May–11 June 2017	Eastern Mediterranean Sea	49	0.0938	0.277	0.045	1.899
I02	28 April–14 September 2017	Iberian Sea	59	0.9604	0.867	0.085	3.766
AAOT		45.31° N, 12.51° E	343	1.3680	1.214	0.097	10.264

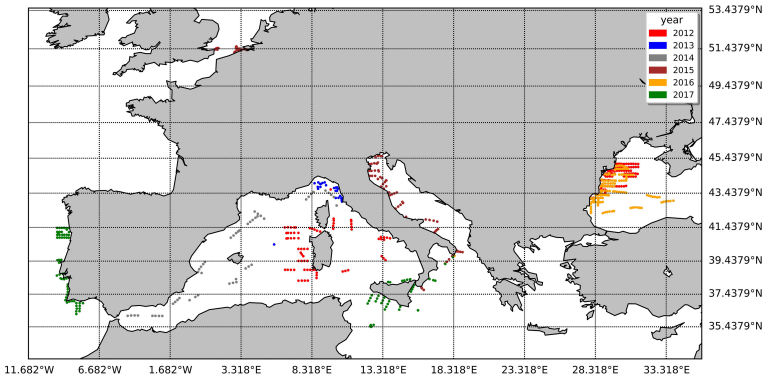


FIGURE 1
The spatial arrangement of the natural samples utilized in this study, with distinct colors representing various years.

the rest of the pigments were detected and identified by online PDA analysis at 450 nm. The derived pigment concentrations of each sample are provided through Excel sheets. As declared in the *D* Test Reports, "the precision of the HPLC method is approximately 1%." Chl *c*1 is partly co-eluted with Chl *c*2. Still, their peaks are separated by the HPLC software, and Chl *c*1 is calculated by the response factor (RF) of Chl *c*2.

The *J* method is described in detail in Hooker et al. (2010). The samples are cut in pieces into a 10-ml polypropylene plastic tube (Corning Inc., Arizona, USA) with 2.5 ml of 0.025 g/L of internal standard (α-tocopherol, Honeywell, North Carolina, USA) dissolved in acetone (HPLC gradient, Merck, Darmstadt, Germany) and 150 µl of MilliQ water, and soaked for 1 h at −20° C. They are successively sonicated for 90 s in ice with a sonication probe (BANDELIN electronic, Berlin, Germany). The samples are then soaked for 3.5–4 h at −20°C, extracted through a 0.2-µm Teflon syringe filter into an amber vial, mixed by vortex, and transferred into a HPLC vial. Samples are preserved at 4°C in the thermostated auto sampler until the analysis is performed. The samples were analyzed by a 1200 Agilent Tech HPLC composed of a degasser (G1379A), a quaternary pump (G1311A), a photodiode array detector (G1315D), a temperature-controlled auto sampler (G1329A) set at 4°C, a column oven (G1316A) set at 60°C, and a system controller with Open LAB CDS control software. The column was an Eclipse Zorbax Eclipse XDB-C8, 3.5 µm particle size, 150 × 4.6 Φ mm (Agilent Technologies, Santa Clara, California, USA). The sample is mixed in a 900-µl preinjection loop with a buffer consisting of 28 mM aqueous TBAA (150 µl sample +375 µl buffer) before the injection into the HPLC. With respect to the original method, the solvent gradient consisted of three solvents: solvent A ((70:30) methanol:28 mM aqueous TBAA, pH 6.5), solvent B (100% methanol), and solvent C (100% acetone). All the solvents are suitable for chromatographic analysis. The acetone was flowed for 1 min at the end of each sample to avoid a carry-over to the next analysis The flow rate was 1.1 ml/min except when the solvent C was added (flow rate = 1.3 ml/min). The time program was at 0 min: 95% A, 5% B; 22 min: 5% A, 95% B; 24.5 min: 5% A, 95% B; 24.75 min: 5% A, 65% B, 30% C; 25.75 min: 5% A, 65% B; 30% C (flow 1.3 ml/min); 25.85 min: 5% A, 65% B, 30% C 100%; 26.10 min 95% A, 5% B; and 32 min: stop. The HPLC was calibrated with pigment standards (DHI Lab Products, Denmark). The calibration curve consisted of nine points covering from a dilution close to three times the signal-to-noise ratio (SNR) concentration to the standard concentration (Hooker et al., 2005). The calibration curves were checked for linearity in the full analysis range. The low-limit of detection (LOD) is assumed to be three times the instrumental SNR at each quantification wavelength. Peaks below the LOD are considered not identified. The internal standard was detected at 222 nm; MV Chl *a*, DVChl *a*, Chlide *a*, Pheo *a*, Phy *a* were detected at 665 nm; all other pigments were detected at 450 nm. Chl *c*1 is quantified using the RF of Chl *c*2, and the DVChl *b* is quantified using the RF of MVChl *b*.

The extraction procedure constitutes the main difference between the two methods (see Table 5 for details): *D* soaks the samples for 20–24 h and uses a sonication bath for sample disruption. Conversely, *J* soaks the sample for 3.5–4 h and uses a sonication probe for sample disruption. It is expected that the different extraction time does not affect the quantification of pigments (Wasmund et al., 2006). In addition, the chromatographic methods (Table 5) differ by minor adjustments of the mobile phase gradient (i.e., the acetone rinse for *J* and a total analysis time of 32 min for *J* and 41 min for *D*).

The pigment concentrations (P_p) are calculated by each laboratory as:

$$P_p = \frac{V_x}{V_f} \frac{\widetilde{P_p^i}}{V_c} \quad [1]$$

where $\widetilde{P_p}$ is the pigment concentration as obtained from HPLC, V_x is the extraction volume, V_f is the volume of the water filtered for each sample, and V_c is the amount of sample injected into the column.

2.4 Quality assurance and laboratory performance

The *J* is Quality Standard ISO 9001 certified, while the *D* is DANAK quality accredited (ISO/IEC 17025:2005) for

TABLE 5 A summary of sample extraction for Φ 25 mm GF/F (0.7 µm pore size) and HPLC conditions for *J* and *D*: injection, mobile and stationary phases and detector acquisition settings.

Extraction conditions							
Lab.	Extraction solvent	Extraction volume (ml)	Soaking time	Disruption method	Disruption time	Clarification	Extraction time and temperature
J	AC 100% containing 0.0025 µg/ml of α-tocopherol	2.5 + 0.150 of distilled water	1 h + 3.5 to 4 h after sonication	Sonication	90 s in cold ice	0.2 µm PTFE syringe filter	4.5–5 h (−20°C)
D	AC 95% containing 0.0025 µg/ml of vitamin E acetate	3	20–24 h	Sonication bath	10 min in ice cold	0.2 µm Teflon syringe filter	20–24 h
HPLC conditions							
Lab.	Sample injected (µl)	Buffer/ sample injection (µl)	Stationary phase and temp.	Mobile phase, flowrate (ml/min) and analysis total time	Detection: PDA wavelength (nm) acquired		
J	135	375 + 150	C8, 3.5 µm, 4.6 × 150 mm, 60°C	**A:** 70:30 methanol: 0.028 M TBAA; **B:** MeOH; **C:** AC; **flow:** 1.1 ml/min; 32 min	450 nm carotenoids, chlorophylls *c* and *b*; 665 nm chlorophyll *a* and derived		
D	143	Ratio 5:2	C8, 3.5 µm, 4.6 × 150 mm, 60°C	**A:** 70:30 methanol: 0.028 M TBAA; **B:** MeOH; **flow:** 1.1 ml/min; 41 min	450 nm carotenoids, chlorophylls		

TBA, Tetra butyl Ammonium hydroxyl acetate; AC, Acetone; MeOH, Methanol.

phytoplankton analysis. *D* and *J* both participated in the SeaWiFS HPLC Analysis Round-Robin Experiment (SeaHARRE-4, Hooker et al., 2010) and the HPLC Intercomparisons on Phytoplankton Pigments (HIP-1 and HIP-4, Canuti et al., 2016). During these comparison exercises, the laboratory uncertainties on standard and on natural samples were assessed following a chemo-metrics criteria approach that has already been adopted in several HPLC intercomparison exercises on phytoplankton pigments (Claustre et al., 2004; Hooker et al., 2005; Hooker et al., 2009; Hooker et al., 2010 and Hooker et al., 2012; Canuti et al., 2016). Summary results for *J* and *D* in such exercises are provided here to give background on the expected performance of these laboratories.

The parameters considered are percent differences or variation coefficients of the quantities identified as being the most relevant to describe the quality of the chromatography analysis. In the present work, only an overview of the performance metrics calculation is given. In such intercomparison exercises, N_S batches of samples are distributed to the participants, with each sample having typically two or three replicates. The true value of the concentration of each batch of samples is assumed to be the mean concentration of samples among participating laboratories or methods. For pigment p, the mean pigment concentration ($\overline{P_p}$) for each sample series S_k is calculated as:

$$\bar{P}_p(S_k) = \frac{1}{N}\sum_{i=1}^{n} P_p^i(S_k) \quad [2]$$

where i refers to the laboratory, $P_p^i(S_k)$ is the average pigment concentration for pigment p over the replicates for sample S_k, and N is the number of participants.

The variation coefficient (CV), ξ, expressed as the percent ratio of the standard deviation, σ, in the replicates with respect to the average concentration of the replicates is a measure of the precision achieved for a sample:

$$\xi_p^i(S_k) = 100\ \frac{\sigma_j^i(S_k)}{\bar{P}_p^i(S_k)} \quad [3]$$

ξ values are calculated for each pigment, sample, and participant, and the mean precision for a specific laboratory i and pigment p is obtained by averaging over the N_S samples S_k:

$$\overline{\xi_p^i} = \frac{1}{N_S}\sum_{k=1}^{N_S} \xi_p^i(S_k) \quad [4]$$

An unbiased percent difference ψ_p^i, or its modulus $|\psi_p^i|$, is selected as an indicator of a method accuracy, with reference to the laboratory average $\overline{P_p}$:

$$\psi_p^i(S_k) = 100\ \frac{P_p^i(S_k) - \bar{P}_p(S_k)}{\bar{P}_p(S_k)} \quad [5]$$

Similarly to Eq. [4], the accuracy $|\overline{\psi_p^i}|$for laboratory i and pigment p is computed by taking the average of $|\psi_p^i(S_k)|$ over the N_S samples.

Using the results of the HIP-4 exercise conducted in 2011 (Canuti et al., 2016), the accuracy and precision on natural samples of primary pigments primary pigments (PPig) were, respectively, 4.7% and 6.4% for *D* and 5.5% and 7.4% for *J*, which ranks the methods used in the two laboratories as "quantitative methods" according to the SeaHARRE-2 quality scheme. Considering the low concentration range of most of the samples included in HIP-4 (< 1 mg/m^3), an additional parameter of interest to assess the quality of the methods is the accuracy of the HPLC

calibration curve, which was found to have an average value of 4.3% for *J* (corresponding to "quantitative" performance) and 0.9% for *D* ("state-of-art" performance).

The criteria established in Aiken et al. (2009) and used for assessing the quality of data sets used for bio-optical algorithm development (Hirata et al., 2011) were also applied to evaluate the internal consistency of the single database. The co-variation of log-transformed TChl *a* and sum of accessory pigments TAcc (Table 2) (Trees et al., 2000) was verified independently for each of the 11 oceanographic cruises and for the 26 AAOT sampling campaigns.

Overall, the results described in this section suggest that the two laboratories are associated with a fairly high range of performance and that the comparison of their results can serve as a benchmark to evaluate the level of uncertainties that can be expected for HPLC measurements.

2.5 Statistical analysis

The statistical approach used for comparing the results is suggested in the EURACHEM/CITAC Guideline (2000) for analytical method comparison and validation. The ordinary least squares (OLS) was calculated between the two laboratories for the log-transformed primary pigments and TChl *a*. As in the present study, we do not need to give outliers greater weight than other observations; the least absolute deviations (LAD) approach, which has the advantage of giving equal emphasis to all observations, was also applied. The root square mean logarithmic difference was also used for evaluating the method differences, defined as (for pigment *p*):

$$\mathrm{RMSLD} = \sqrt[2]{\frac{1}{N_S}\sum_{k=1}^{N_S}(\log_{10} P_p^J(S_k) - \log_{10} P_p^D(S_k))^2} \qquad [6]$$

The unbiased percent difference (%PD) and the absolute percent difference (%APD) were selected to evaluate the differences between the data sets from *D* and *J* and determine if any trend could be associated with a specific range of pigment concentrations, the geographic area, or changes in the operator responsible for the sample preconditioning. The %PD distribution was also used to assess the normality of the uncertainties among the samples in the study. %PD is defined by taking the average concentration as the reference value (denominator), and %APD is the %PD absolute value:

$$\%\,\mathrm{PD}_p(S_k) = 200\,\frac{P_p^J(S_k) - P_p^D(S_k)}{P_p^J(S_k) + P_p^D(S_k)} \qquad [7]$$

$$\%\,\mathrm{APD}_p(S_k) = 200\left|\frac{P_p^J(S_k) - P_p^D(S_k)}{P_p^J(S_k) + P_p^D(S_k)}\right| \qquad [8]$$

Bland and Altman (1995); Bland and Altman (1999) underlined that any two methods designed to measure the same quantity should have a good correlation if compared on samples chosen in such a way that the quantity to be determined varies considerably. As a consequence, high correlation does not necessarily imply that there is good agreement between the two methods. In the present work, along with a regression approach, the magnitude of disagreement between the two sets of laboratory analyses was assessed, for each pigment *p*, by considering the logarithmic difference of results from the two methods against their logarithmic average (Bland and Altman, 1986). The mean value is considered by the two statisticians as the most appropriate reference to look at the ratio of the pairs of measurements, while a log transformation (base 2) of the measurements before the analysis enables standardization of the approach. The results are represented through the Bland–Altman, B&A, plots (*x*-axis: mean ($\log_2 P_p^D(S_k)$; $\log_2 P_p^J(S_k)$) ; *y*-axis: ($\log_2 P_p^J(S_k) - \log_2 P_p^D(S_k)$) that allow identification of any systematic bias between the measurements or possible outliers.

3 Results

The determination coefficients between TAcc and TChl *a* for the two laboratories were calculated for each of the ship-based campaigns and for all the AAOT natural samples, including those at different depths (Figure 2). The co-variations were overall good ($r^2 > 0.95$). The *J* and *D* laboratories were then compared through scatter plots with a specific focus on the PPig. The determination coefficient, r^2, the slope of linear regression (OLS), and the slope for the LAD regression were calculated for all log-transformed PPig (Table 6; Figure 3). In their studies, Bland and Altman (1999) established that the limit of agreement could be determined when the differences between the data from the two laboratories are normally distributed and the standard deviation and the mean are the same across the entire range of measurements. The normal distribution of the difference in our case was verified by observing the histogram plot and by using D'Agostino–Pearson test. If differences are not normally distributed, as in our case, Altman and Bland suggest that a logarithmic transformation of the original data can be tried. The comparison through logarithmic Bland and Altman plots (B&A plots) was considered for each primary pigment of the data set (Figure 4). The LAD slope is between 0.97 and 1.08 for all the PPig (Table 6), indicating a remarkable match. This is confirmed by the determination coefficient, whose value varies from 0.76 for Zea to 0.95 for Fuco (0.91 for TChl *a*). All pigments exhibited an RSMLD lower than 0.32, with TChl *a* having a value of 0.16. Based on the assessment of B&A plots, there appears to be a bias between the two laboratories, resulting in an overestimation of *J*, particularly for xanthophylls and carotenoids (Zeax, Diato, Peri, Allo), with the exception of Caro, where the trend suggests an underestimation of *J*. The B&A plots evidence that the number of outliers is highest for the pigments with the lowest ranges of concentration, while for TChl *a*, TChl *b*, TChl *c*, Fuco, and Caro, approximately 95% of the natural samples are within the limit of agreement (within 1.96 standard deviation) (Figure 4).

Coherently with the B&A plots, %PD tends to be higher for lower values of the pigment concentration: the %PD highest values (> 50%) are seen for all pigments at concentrations lower than 0.5 mg/m^3 (Figure 5). With measurement stations located mostly in clear or only moderately turbid waters (Figure 1), most of the samples analyzed in support to this comparison had concentrations

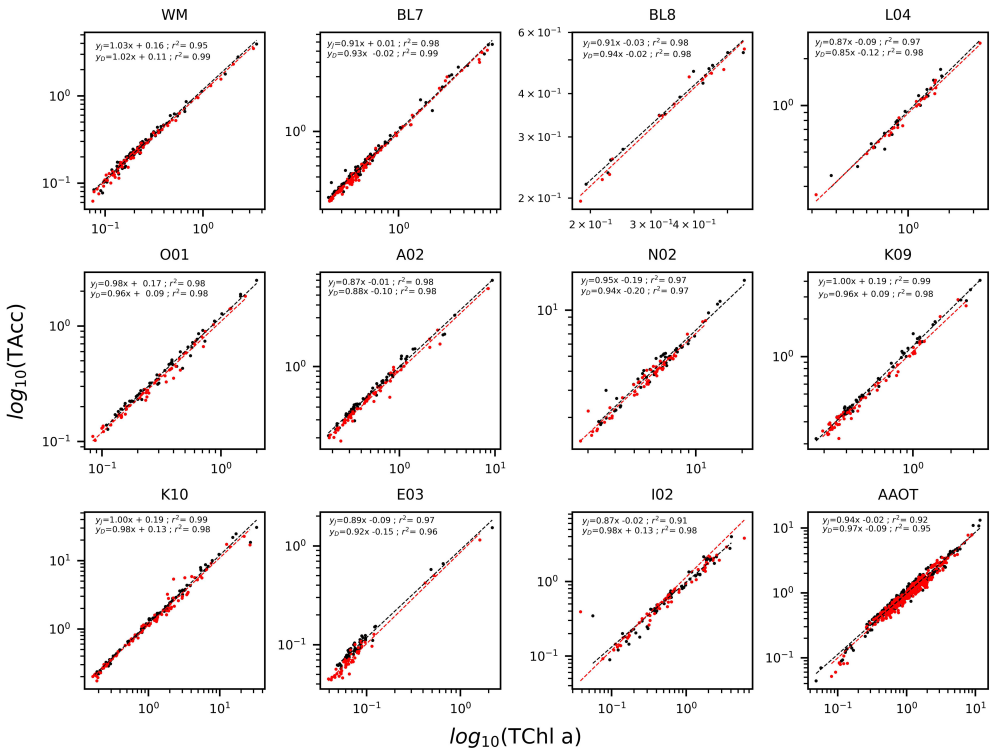


FIGURE 2
Log-linear regression of accessory pigments (TAcc) versus TChl *a* for the Oceanographic Campaigns and the AAOT for *J* (black) and *D* (red). Data are presented in $\log_{10}$ scale.

in the range of 0.05–0.5 mg/m^3 for PPig and lower than 0.05 mg/m^3 for the secondary pigments (Figure 5; Table 7). Lower correlations between laboratories occurred when pigments were quantified close to the instrumental LOD. This behavior has already been observed in previous intercomparisons and confirmed that the false-positive/negative quantifications performed near LOD thresholds may cause an increase in the bias (Hooker et al., 2005; Canuti et al., 2016). Considering the whole data set, *J* overestimates TChl *a* by 10.6% and PPig by 16.9% (Table 8), confirming the presence of a systematic bias as suggested by the B&A plot analysis. The analytical method had an impact on the distribution of differences among pigments. In this regard, we could observe that for all the campaigns, %PD were lower (−5.8%) for Caro and close to 0 for Zea and TChl *b* (−0.3% and 0.9%, respectively), despite the fact that the concentration of Zea was lower than 1 mg/m^3 for all the samples. In the absence of specific tests on extraction on replicates

TABLE 6 Summary of the results of linear regression analysis applied to log-transformed data (OLS and LAD), root mean squared logarithmic difference (RMSLD), and of the Bland–Altman (B&A) plots.

Pigment	r^2	OLS: slope	LAD: slope	RMSLD	B&A plots (% within 1.96 SD)
TChl *a*	0.91	0.95	0.99	0.16	95.8
TChl *b*	0.89	1.03	1.05	0.18	94.5
TChl *c*	0.89	0.95	0.99	0.19	94.6
Caro	0.90	0.95	0.97	0.14	94.7
Peri	0.90	1.05	1.08	0.23	85.8
But	0.78	0.93	1.01	0.20	91.6
Fuco	0.95	0.97	0.99	0.18	95.6
Hex	0.84	0.92	0.99	0.18	90
Allo	0.87	1.06	1.07	0.27	90.9
Diato	0.83	0.94	0.98	0.32	82.9
Zea	0.76	0.95	0.98	0.21	92.5

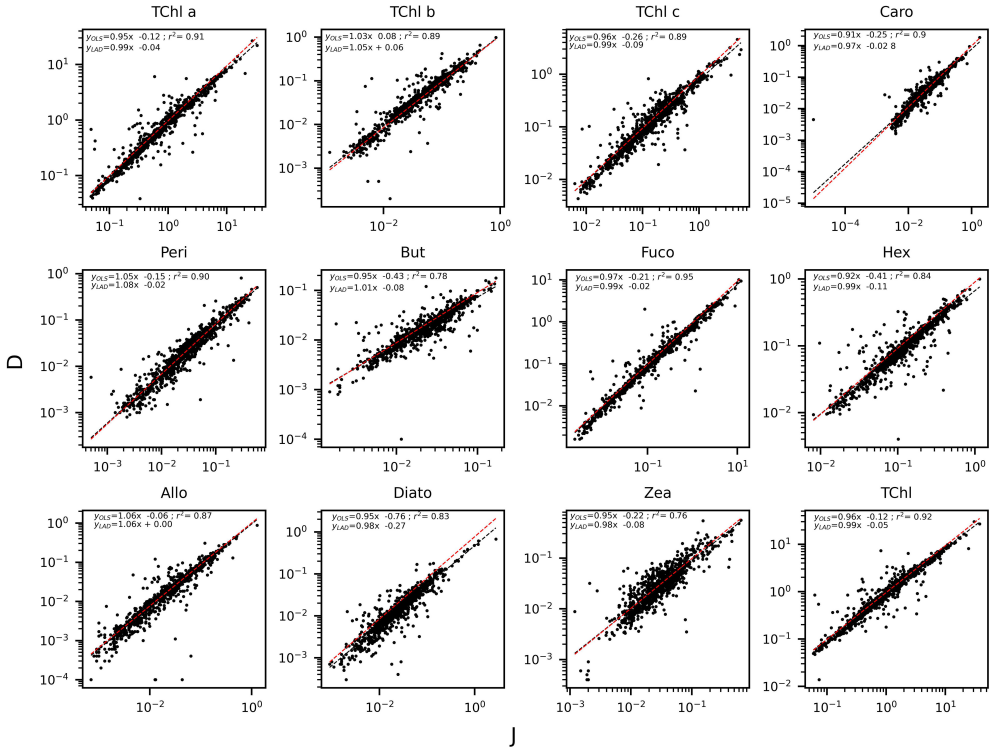


FIGURE 3
Regression applied to the log transformed value of the PPig: curve and equation for OLS (in black) and LAD (in red).

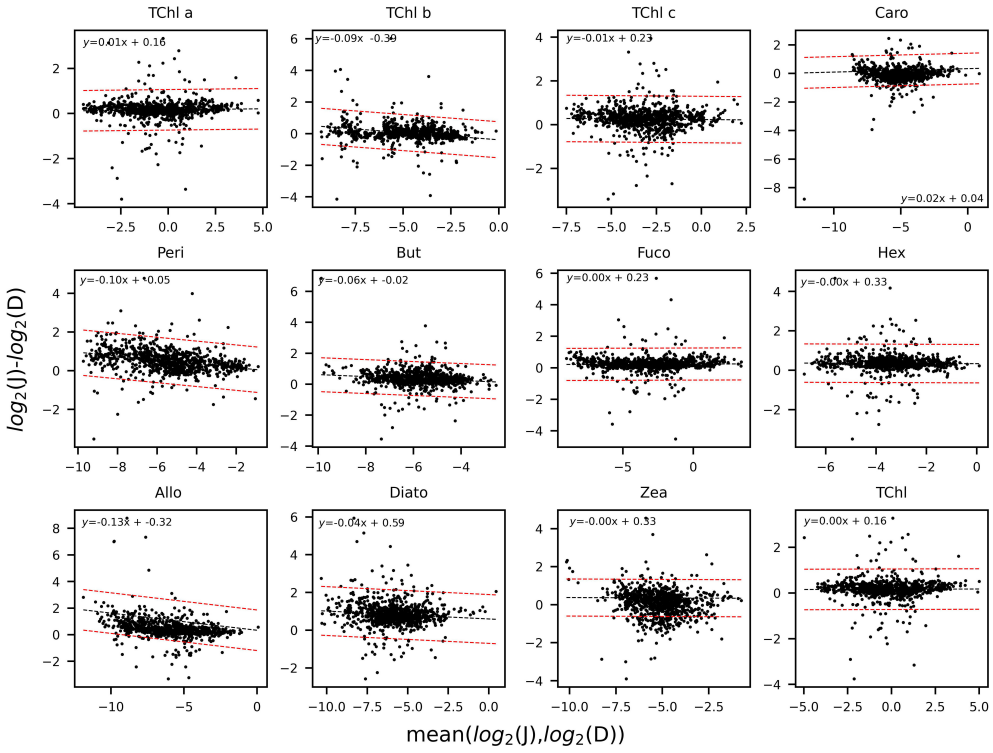


FIGURE 4
Bland and Altman plots for the PPig: TChl *a*, TChl *b*, TChl *c*, Caro, Peri, But, Fuco, Hex, Allo, Diato, Zea, and the TChl. The limit of agreement, in red, encompasses the data points within 1.96 standard deviations. The trend-line between the two laboratories is in black.

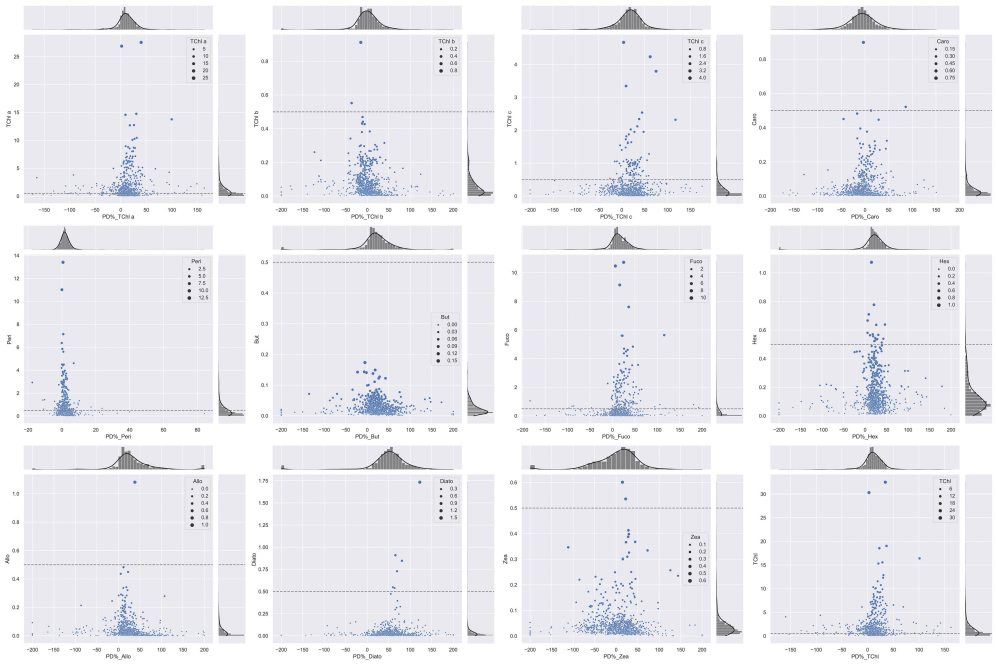


FIGURE 5
Scatter plot displaying invariant histograms of the marginal distribution for PD% and pigment concentrations (mg/m^3). The horizontal and vertical axes represent TChl *a*, TChl *b*, TChl *c*, Caro, Peri, But, Fuco, Hex, Allo, Diato, Zea, and TChl. The dashed lines indicate the 0.5-mg/m^3 threshold for each primary pigment, and the legend corresponds to each pigment concentration.

of natural samples and of the analysis of common standards, it is not possible to attribute observed differences to the extraction procedure, to the chromatographic separation, or to a combination of the two.

The closest results between the laboratories were observed for the samples collected on AAOT: for TChl *a*, the average %PD is 8.2% versus 11.9% for the ship-based oceanographic campaigns and 15.3% versus 17.4% for what concerns the PPig. This could be explained by the large number of campaigns and major confidence in the filtration procedure (i.e., the volume of water to use for preconditioning the filter) and by the fact that, proportionally, the most oligotrophic conditions (associated with high %PD) were mostly found during oceanographic campaigns. The comparison of the surface data (one third of the total AAOT samples) with samples collected at 8 and 14 m depth exhibits comparable %PD for TChl *a*. Differences in results between AAOT and oceanographic campaigns also suggest that the inhomogeneity of preconditioned samples may affect the assumed equivalence of duplicates and

TABLE 7 Summary of the distribution of PPig concentration throughout the entire dataset (in mg/m^3).

	Mean	SD	Min	25%	50%	75%	Max
TChl *a*	1.334	2.144	0.045	0.310	0.658	1.402	27.535
TChl *b*	0.064	0.075	0.001	0.018	0.038	0.082	0.912
TChl *c*	0.244	0.399	0.006	0.055	0.124	0.264	4.669
Caro	0.047	0.070	0.001	0.012	0.024	0.051	0.899
Peri	0.644	0.983	0.021	0.156	0.327	0.709	13.408
But	0.025	0.021	0.000	0.011	0.018	0.033	0.174
Fuco	0.427	0.950	0.002	0.038	0.112	0.370	10.727
Hex	0.133	0.121	0.000	0.058	0.097	0.163	1.074
Allo	0.040	0.066	0.000	0.005	0.019	0.045	1.081
Diato	0.035	0.085	0.001	0.009	0.018	0.035	1.734
Zea	0.044	0.056	0.001	0.016	0.029	0.047	0.601

It includes details such as the minimum and maximum values, the average concentration (mean), the concentration distribution at the 25th, 50th, and 75th percentiles, and the standard deviation (std).

consequently the agreement between independent analyses, regardless of the pigment concentration.

The %PD was further considered in relation to the sampling campaign (all results detailed in Table 8) to evaluate if the water type and a change in the operator, generating an inhomogeneity in the duplicate samples, may also impact the difference distribution. It can be noticed that when the TChl *a* average concentration is close to 1 mg/m^3 (campaigns L04, BL7, I02 and AAOT), the %PD values (in modulus) are lower (from −1% to 8%), independently from the marine basin considered. This suggests that the methods are optimized for analysis of samples with a TChl *a* pigment content around 1 mg/m^3. Other considerations, considering the differences between campaigns, indicate that an increase in %PD for low concentrations is by no means a general rule. The E03 (Eastern Mediterranean Sea) and K09 (Black Sea) campaigns had a comparable number of samples (49 and 53 respectively), were

TABLE 8 Overview of the unbiased percentage difference (%PD) across various parameters (PPig, PSum, PRatios, and PIndices) comparing two laboratories.

Code	TChl *a*	TChl *b*	TChl *c*	Caro	Peri	But	Fuco	Hex	Allo	Diato	Zea	PPig
WM	12.8	20.2	13.8	−12.8	−13.8	18	9.9	20	25.1	53	19.9	15.1
BL7	7.9	−3.3	16.3	−18.6	2.2	12.9	9.9	20.1	26.8	43.5	4.5	11.1
BL8	2.6	−12.2	5.1	−25.6	−6.1	16.1	5	11.2	53.4	29.2	11	8.2
L04	−1.1	−14.6	3.9	−18	0.6	4.9	4.1	7.9	3.7	9.8	2.4	0.3
O02	18.3	8.5	20.3	−2.4	18.4	24.4	17.5	25.6	28	50	37	22.3
A02	9.1	3.6	24.4	0.7	39.6	1.1	9.7	17.6	16.6	35	8.9	15.1
N02	12.6	2.3	24.6	2.7	16.7	11.6	13.3	−7.7	5.5	58.9	−17.5	11.2
K09	24.1	12	42.8	6.6	44.8	52.2	32.7	39.3	63.2	75	−36.9	32.4
K10	12.2	0.3	25.3	−6.3	22	37.8	11.9	19.7	47.4	54.6	−64.7	14.6
E03	15.6	12.1	28.6	16.2	58.1	26	38.4	23.3	**>100**	64.6	14.2	37.7
I02	7.3	−12.9	12.1	−11.9	15.4	13.2	21.5	9.6	35.3	66	−17	12.6
AAOT	8.2	−3	7.3	−6.3	35.8	19.5	14.3	22.3	17.6	41.7	10.5	15.3
ALL	10.6	0.9	16.2	−5.8	25	20.3	15.5	20.2	30.1	48.2	−0.3	16.9
OC	11.9	3.1	21.2	−5.6	18.9	20.7	16.1	19	37.1	51.9	−6.4	17.4

	TChl	PPC	PSC	PSP	TAcc	TPig	DP	TAcc/ TChl *a*	PPC/ TPig	PSC/ TPig	PSP/ TPig	mPF	nPF	pPF
WM	13.2	18.7	18.0	14.5	17.5	15.2	18.4	4.8	−2.6	3.9	−0.8	−6.8	1.2	0.7
BL7	8.4	11.5	12.5	9.7	11.8	10.0	11.1	4.0	−2.1	1.9	−0.3	−3.4	8.3	−6.6
BL8	1.7	6.2	5.7	2.8	4.1	3.4	4.6	1.4	−0.9	3.5	−0.8	−3.4	7.4	−3.6
L04	−1.3	2.2	6.2	0.5	2.6	0.7	2.5	3.7	−1.6	2.0	−0.2	3.0	4.6	−13.7
O02	18.6	25.6	24.1	20.3	23.9	21.3	25.0	5.6	−3.3	4.0	−1.0	−2.4	0.2	2.5
A02	11.2	13.3	16.1	12.6	16.0	12.7	13.6	7.5	−4.0	0.9	−0.1	0.8	3.3	−9.7
N02	13.9	13.5	13.9	13.9	15.5	13.8	12.3	2.9	−1.1	−1.1	0.1	1.2	−0.8	−12.7
K09	25.3	24.3	38.8	29.0	31.0	27.8	26.0	6.9	−3.7	−4.2	1.4	12.5	15.3	−35.2
K10	13.5	15.9	18.7	15.0	17.5	14.9	14.0	5.3	−2.7	1.5	0.0	0.9	10.4	−33.7
E03	16.8	27.0	27.6	19.3	26.3	20.8	23.7	10.4	−4.2	6.6	−1.4	20.6	1.4	−10.4
I02	6.0	6.4	16.5	8.7	8.0	7.6	3.8	0.8	−0.3	−0.6	1.0	16.7	9.7	−20.7
AAOT	7.5	17.6	18.5	10.5	14.8	11.4	15.6	6.8	−3.3	6.7	−0.9	1.3	5.5	−14.8
ALL	10.8	16.5	18.8	13.0	16.2	13.4	15.2	5.7	−2.8	3.4	−0.4	2.5	5.7	−14.2
OC	12.6	15.9	18.9	14.4	16.9	14.5	15.0	5.1	−2.6	1.6	−0.1	3.2	5.8	−13.8

The analysis includes data from a specific oceanographic campaign, samples collected at the AAOT (AAOT), the complete dataset (ALL), and exclusively the ship-based Oceanographic Campaigns (OC).
Values exceeding 100 % PD are in bold.

performed within a year, and finally, the time delay between collection and analysis was comparable. E03 TChl *a* concentration was on average noticeably lower than during K09 (0.098 and 0.678 mg/m^3, respectively), but the associated PD% is 15.6%, while it is 24.1% for K09 (Table 8). Similar differences could be appreciated considering the %APD, where the TChl *a* associated with E03 is 16.9% while itis 26.3% during K09 (Table 9). On the other hand, the BL8 campaign (Black Sea, TChl *a* of 0.413 mg/m^3 on average) shows lower differences (2.6% for TChl *a* and 8.2% for PPig) than K09. We could conclude that the marine basin and the water type are not influencing the performance of the two laboratories.

Sample storage was considered as well. In a few cases, the samples were analyzed at different times by the two laboratories. *J* analyzed the WM campaign's samples 5 years after their collection. It was expected that for these samples the MVChl *a* could be partially degraded in DVChl *a* and Chlide *a*. Jeffrey et al. (1997) recovered 98% and 83% of the original TChl *a* concentration in microalgae after storage at −196°C for 60 and 328 days, respectively. WM was compared with E03 and I02 campaigns, where E03 and

TABLE 9 Overview of the absolute percentage difference (%APD) across various parameters (PPig, PSum, PRatios, and PIndices) comparing two laboratories.

Code	TChl *a*	TChl *b*	TChl *c*	Caro	Peri	But	Fuco	Hex	Allo	Diato	Zea	PPig
WM	24.9	40.9	30.6	27.8	81.6	30.4	28.5	32.7	49.1	33.5	30.6	63.5
BL7	16.1	19.9	23.5	28.3	16.7	23.8	18.4	26.3	42.6	22.5	40.9	47.9
BL8	3	12.8	11.3	25.6	8.6	17	5	11.2	54.3	7.8	17.6	29.2
L04	12.9	14.7	17.8	19.3	39.2	18.9	16.7	19.8	16.4	19.3	26.8	26.5
O02	23.5	37	29.5	14.3	95.1	28.9	22.2	30.3	35.2	32.6	39.5	53.3
A02	25.2	29.8	36.2	25.1	74.7	37.2	25.7	38.3	31.3	27.4	32.2	50.3
N02	20.5	17.7	32	14.9	25.6	57.4	21	49.8	21.5	25.9	53	65.9
K09	26.3	15.3	44.4	12.5	46.8	59.8	35.2	40.4	64.4	37.9	39.5	75
K10	12.9	20.6	25.6	14.2	21.8	53	12.1	24.1	52.9	21.9	70.6	54.6
E03	16.9	14.8	29.8	19.4	58.1	27.2	38.4	23.8	113.6	31.7	18.5	64.8
I02	28.1	28.9	30.3	32.2	44.5	37.3	32	44.7	47.1	34.7	31.6	89.7
AAOT	17.6	20.7	26.7	19.4	47.3	28.5	22.3	29	29.8	30.4	37.4	67
ALL	19	22.8	28.1	21.1	46.7	34.9	23.1	30.9	46.5	27.1	36.5	57.3
OC	19.1	22.9	28.3	21.3	46.6	35.5	23.2	31	48	26.8	36.4	56.4

	TChl	PPC	PSC	PSP	TAcc	TPig	DP	TAcc/ TChl *a*	PPC/ TPig	PSC/ TPig	PSP/ TPig	mPF	nPF	pPF
WM	25.8	29.8	30.5	26.8	28.4	26.6	28.9	7.6	4.0	13.4	3.0	18.7	5.5	16.0
BL7	16.4	20.6	20.5	17.6	19.3	17.8	19.2	4.3	2.3	6.2	1.2	5.8	8.5	12.0
BL8	3.3	8.2	5.7	3.4	4.9	3.9	5.6	2.2	1.5	4.4	1.0	5.2	7.9	6.2
L04	12.8	15.1	18.1	14.0	15.5	14.1	15.3	4.2	1.9	2.7	0.3	3.7	5.4	13.7
O02	24.4	30.5	28.7	25.7	28.9	26.5	29.3	6.5	3.8	6.3	1.5	7.8	3.2	8.8
A02	26.3	27.8	31.7	27.1	29.6	27.1	28.2	9.1	4.8	4.3	0.8	8.6	6.8	13.0
N02	21.6	21.3	21.7	21.6	23.1	21.6	20.1	3.3	1.3	4.5	0.4	2.0	16.0	14.7
K09	27.3	26.5	40.5	31.0	32.8	29.8	28.5	9.0	4.9	10.1	2.5	15.6	19.4	37.9
K10	13.6	17.2	18.7	15.0	17.5	14.9	14.3	10.7	5.9	6.4	1.1	4.7	10.9	35.3
E03	17.6	27.7	28.0	20.0	26.4	21.3	23.9	17.4	10.5	11.1	2.9	21.1	4.2	10.8
I02	26.0	22.7	33.3	24.7	21.9	23.3	22.0	16.1	9.6	15.9	3.5	22.5	30.6	25.3
AAOT	17.4	26.0	24.9	18.8	22.0	19.5	22.5	8.7	4.2	11.0	1.4	4.5	8.7	20.0
ALL	19.4	22.8	25.2	20.5	22.5	20.5	21.5	8.3	4.6	8.0	1.6	10.0	10.6	17.8
OC	19.5	22.5	25.2	20.6	22.6	20.6	21.4	8.2	4.6	7.8	1.6	10.5	10.8	17.6

The analysis includes data from a specific oceanographic campaign, samples collected at the AAOT (AAOT), the complete dataset (ALL), and exclusively the ship-based Oceanographic Campaigns (OC).

I02 samples were analyzed within a year from collection and no degradation of MVChl *a* is expected (Jeffrey et al., 1997). The TChl *a* results for the three campaigns are comparable to what is observed over all the stations: *J* overestimated *D* by 12.8% for WM, 15.6% and 7.3%, respectively, for E03 and I02 (Table 8). The MVChl *a* is on average 9.9% higher for *J* with respect to *D*. We should thus expect a lower overestimation of MVChl *a* for WM with respect to E03 and I02 due to an increasing contribution of Chlide *a* and DVChl *a* to TChl *a*. In the WM campaign, MVChl *a* quantified by *J* was 13.8% higher than *D*'s value, while this overestimation is 17.8% in the case of E03, and is not observed for I02, with *J and D* values of MVChl *a* very close (*J*< *D* by 0.9%). In the good analysis practice, 1 year is considered the maximum interval between sample collection and analysis (Jeffrey et al., 1997) The case described here indicates that time longer than 1 year between collection and analyses (5 years for WM) did not appear to affect the final quantification of TChl *a*.

It was expected that for higher-level variables (i.e., pigment sum, see Table 2) the differences between *J* and *D* should decrease as the concentration increases (Tables 8, 9). The TChl and DP generally follow the expected trend (differences between laboratories over all samples of 10.8% and 15.2%, respectively). TPig and other sums show differences around 15%, similar to or lower than those encountered for the single PPig. As for the pigment indexes PIndex used to evaluate the proportion for micro- (mPF), nano- (nPF), and picoplankton (pPF), the difference is low for the mPF and nPF fractions (2.5% and 5.7%, respectively, and of 10.0% and 10.6% APD), and higher for pPF (−14.2% PD and 17.8%APD). Looking at results across campaigns, it can be observed that pPF was high (unbiased % PD of −35.2% and −33.7% and %APD of 37.9% and 35.3%, respectively) for the K09 and K10 campaigns (Black Sea, late summer) but not so for BL7 and BL8 (Black Sea, early summer), where the values are −6.6% and −3.6% for pPF, respectively (12.0% and 6.2%, if we considered the %APD), thus suggesting that the basin itself is not a source of differences. The %PD values of mPF and nPF are usually found below 10% (in modulus).

The average %PD can be interpreted in terms of accuracy for the concentration of the various pigments. Accuracy estimates can be fed into error propagation techniques applied to algorithms dedicated to the calculation of PFT's abundance or PSCs (e.g., Mouw et al., 2017). Additional information required for error propagation is the possible error correlation existing among pairs of pigments. This point has been explored here by using the 611 stations of the oceanographic campaigns and correlating the difference *J*–*D* for pairs of diagnostic pigments (Table 10). In general, the correlation (i.e., Pearson correlation coefficient) between differences is fairly low, but there are cases where the correlation is close to or exceeds 0.5. The highest being between TChl *a* and Fuco (> 0.9), other remarkable correlations were found between TChl *a* and Caro and TChl *c* (> 0. 7), and similarly between Fuco and TCl *c* and Caro (> 0.7).

To quantify the impact that uncertainties on pigment concentrations might have on PFTs and PSCs, the pigment distributions from the two laboratories were independently used as input to the model of Hirata et al. (2011) (summarized in Table 3), with results elaborated with the Data-Interpolating Variational Analysis (DIVA) software tool of the Ocean Data View software (https://odv.awi.de) to visualize the observations spatially interpolated (Figure 6). These maps should not be interpreted as actual PFT or PSC distributions, as oceanographic campaigns in a given basin took place in different periods, but they offer an efficient overview of the agreement between the distributions obtained from the two data sets. In general, the *J* and *D* distributions appear fairly coherent, with some exceptions. PSCs show a good agreement, confirming the results obtained for the pigment index (Tables 8, 9), which is not surprising as the formula are comparable. The picoplankton fraction observed in the Black Sea shows some differences between *J* and *D* in line with those observed for pPF in this specific basin (particularly for K09 and K10). For PFTs, the largest differences are seen for diatoms (higher values for *J*) and, to a much lesser extent, for dinoflagellates.

TABLE 10 Pearson correlation coefficient, *r*, between the differences (*J* minus *D*) for the diagnostic pigments.

r	TChl a	TChl b	TChl c	Caro	Peri	But	Fuco	Hex	Allo	Diato	Zea
TChl *a*		0.500	**0.682**	**0.759**	0.423	0.300	**0.929**	0.167	0.578	0.619	0.128
TChl *b*	0.500		0.322	0.590	0.480	0.345	0.396	0.291	0.259	0.166	0.345
TChl *c*	**0.682**	0.322		0.678	0.346	0.271	**0.787**	0.101	0.346	0.290	0.074
Caro	**0.759**	0.590	0.678		0.466	0.436	**0.778**	0.210	0.223	0.131	0.359
Peri	0.423	0.480	0.346	0.466		0.280	0.346	0.368	0.505	0.140	0.345
But	0.300	0.345	0.271	0.436	0.280		0.291	**0.667**	0.117	0.016	0.298
Fuco	**0.929**	0.396	**0.787**	**0.778**	0.346	0.291		0.085	0.396	0.493	0.035
Hex	0.167	0.291	0.101	0.210	0.368	**0.667**	0.085		0.166	0.093	0.365
Allo	0.578	0.259	0.346	0.223	0.505	0.117	0.396	0.166		**0.661**	0.072
Diato	0.619	0.166	0.290	0.131	0.140	0.016	0.493	0.093	**0.661**		−0.072
Zea	0.128	0.345	0.074	0.359	0.345	0.298	0.035	0.365	0.072	−0.072	

In bold are highlighted correlation higher than 0.5

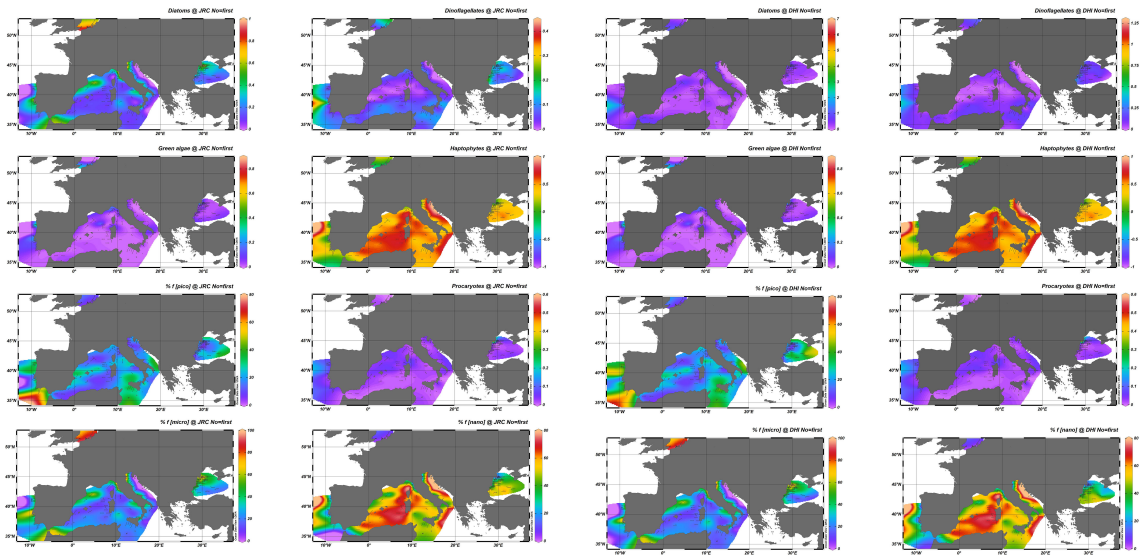


FIGURE 6
Synoptic distribution of surface PFTs (diatoms, dinoflagellates, green algae, haptophytes, procaryotes) expressed as fraction 0–1 of the TChl *a* and PSCs (pico-, nano-, microplankton expressed as) % fraction of the TChl *a* for *J* and *D* datasets. The DIVA software tool (Data-Interpolating Variational Analysis) of the Ocean Data View (ODV) software is used for spatial interpolation.

4 Discussion and conclusions

The present exercise relied on a unique data set of 957 measurement stations covering several European basins, for which samples could be analyzed for pigment concentration by two quality-certified laboratories. An average difference of 10.6% was observed for TChl *a* for concentrations across a wide range of values (0.083 to 27.35 mg/m^3). If interpreted in terms of accuracy, this result fully satisfies the requirement of a 15% accuracy threshold associated with TChl *a*, measurement recommended for the validation of satellite data products. The average differences for PPig is 16.9%, with systematic differences (biases) observed for the *J* values of PPig with respect to those from *D for* chlorophylls and several xanthophylls. However, for some pigments (i.e., Zea and Caro), the differences are close to 0 or very low, regardless of the pigment concentration or the basin considered. This indicates that the extraction methods employed by the laboratories may diversely influence the quantification results in relation to the pigment's chemical structure. Overall, differences between *J* and *D* were lowest for natural samples containing approximately 1 mg/m^3 of TChl *a*, suggesting that both methods are optimized for a target analysis around this concentration.

Other aspects observed concern the time of preservation and the homogeneity of the samples. In terms of preservation, for the Western Mediterranean Sea oceanographic campaign, the long time between collection and analyses (5 years) does not appear to affect the final quantification of TChl *a*. On the other hand, the analysis of the data set by single campaign suggested that in several cases, the difference between laboratories could result from the in-homogeneity of duplicate samples, regardless of the pigments concentration or the basin characteristics, but in the absence of series of replicates, it was not possible to support this correlation statistically. In the intercomparison exercises, where the participants are usually four laboratories or more, the distribution of triplicates of each natural sample together with the analysis of standards provided to all the participants, allows to clearly address if the statistical differences among participants are due to the methods or to the samples inhomogeneity.

As for the higher-level variables, the differences between laboratories are, of course, in line with the results given for the individual pigments. The average difference for TChl *a* and DP is 10.8% and 15.2%, respectively. Pigment indexes, which are simple indicators for PSCs, showed a good agreement, with larger differences for the picoplankton fraction pPF (average of 14%) that can be explained by larger differences observed for Zea. This result for pPF can also be traced to the impact of two Black Sea campaigns (K09 and K10) that usually show higher differences for all quantities. In view of developing error propagation models for PFT or PSC algorithms, the analysis correlating differences between the two laboratories indicates a modest degree of error correlation, but exceptions suggest the need for further investigation. It is nevertheless stressed that this result is valid for *in situ* pigment data and would not necessarily apply to pigment concentration obtained by dedicated algorithms.

In general, it was observed that, regardless of the pigment concentration, the inhomogeneity in the water sample preparation may affect the assumed equivalence of duplicates and consequently the agreement between independent analyses. In conclusion, the comparison with an accredited laboratory is a good option for developing a new method or continuously assessing an existing one. To take one step further and properly address the differences between laboratories, the comparison should include certified standards analyzed at regular time intervals and, in the case of natural sample collection, a series of replicates (minimum three to be analyzed by each laboratory) to build a

proper statistic on the natural samples collected. As illustrated by this study and previous intercomparison exercises, defining uncertainty values associated with single *in situ* pigment measurement is no easy task, but it is required to promote pigment data as fiducial reference measurements. It would also be a good practice before ingesting pigment data into global data bases of pigment data.

Data availability statement

The raw data supporting the conclusions of this article will be made available by the authors, without undue reservation.

Author contributions

EC has made contributions to this paper in the areas of conception, study design, analytic performance, and calculation.

Funding

The study has been supported by the European Commission Directorate-General for Defense, Industry and Space (DG DEFIS) and the Copernicus Programme.

Acknowledgments

The author would like to acknowledge all colleagues who alternated in the collection of the samples replicated in the different BiOMaP cruises and AAOT campaigns. Support provided by the European Commission Directorate-General for Defense, Industry and Space (DG DEFIS) and the Copernicus Programme is gratefully acknowledged.

Conflict of interest

The author declares that the research was conducted in the absence of any commercial or financial relationships that could be construed as a potential conflict of interest.

Publisher's note

All claims expressed in this article are solely those of the authors and do not necessarily represent those of their affiliated organizations, or those of the publisher, the editors and the reviewers. Any product that may be evaluated in this article, or claim that may be made by its manufacturer, is not guaranteed or endorsed by the publisher.

References

Aiken, J., Pradhan, Y., Barlow, R., Lavender, S., Poulton, A., Holligan, P., et al. (2009). Phytoplankton pigments and functional types in the Atlantic ocean: a decadal assessment 1995-2005. *Deep Sea Res. Part II: Topical Stud. Oceanography* 56 (15), 899–917. doi: 10.1016/j.dsr2.2008.09.017

Bland, J. M., and Altman, D. G. (1986). Statistical methods for assessing agreement between two methods of clinical measurement, the lancet 327, 8476, 307–310. doi: 10.1016/S0140-6736(86)90837-8

Bland, J. M., and Altman, D. G. (1995). Comparing methods of measurement: why plotting difference against standard method is misleading. *Lancet*. 346, 1085–1087. doi: 10.1016/S0140-6736(95)91748-9

Bland, J. M., and Altman, D. G. (1999). Measuring agreement in method comparison studies. *Stat. Methods Med. Res.* 8, 135–160. doi: 10.1177/096228029900800204

Bracher, A., Bouman, H. A., Brewin, R. J. W., Bricaud, A., Brotas, V., Ciotti, A. M., et al. (2017). Obtaining phytoplankton diversity from ocean color: a scientific roadmap for future development. *Front. Mar. Sci.* 4. doi: 10.3389/fmars.2017.00055

Brewin, R. J. W., Sathyendranath, S., Hirata, T., Lavender, S. J., Barciela, R. M., and Hardman-Mountford, N. J. (2010). A three-component model of phytoplankton size class for the Atlantic ocean ecological modelling. *Ecol. Model.* 221, 11, 1472–1483. doi: 10.1016/j.ecolmodel.2010.02.014

Canuti, E., Artuso, F., Bracher, A., Brotas, V., Devred, E., Dimier, C., et al. (2022). *The fifth HPLC intercomparison on phytoplankton pigments (HIP-5) technical report, EUR 31334 EN* (Luxembourg: Publications Office of the European Union). doi: 10.2760/563102

Canuti, E., Ras, J., Grung, M., Röttgers, R., Costa Goela, P., Artuso, F., et al. (2016). *HPLC/DAD intercomparison on phytoplankton pigments (HIP-1, HIP-2, HIP-3 and HIP-4), EUR 28382 EN* (Luxembourg: Publications Office of the European Union).

Claustre, H., Hooker, S. B., Van Heukelem, L., Berthon, J.-F., Barlow, R., Ras, J., et al. (2004). An intercomparison of HPLC phytoplankton methods using *in situ* samples: application to remote sensing and database activities. *Mar. Chem.* 85, 41–61. doi: 10.1016/j.marchem.2003.09.002

EURACHEM/CITAC Guideline (2000). *Quantify uncertainties in analytical measurements, 2nd edition*. Available at: https://eurachem.org/index.php/publications/pubarch/81-gdquam20002.

GCOS (2011). "Systematic observation requirements for satellite-based products for climate," in *GCOS-154, supplemental details to the satellite-based component of the "Implementation plan for the global observing system for climate in support of the UNFCC"*. Geneva: UNFCC.

Hirata, T., Hardman-Mountford, N. J., Brewin, R. J. W., Aiken, J., Barlow, R., Suzuki, K., et al. (2011). Synoptic relationships between surface chlorophyll- a and diagnostic pigments specific to phytoplankton functional types. *Biogeosciences* 8, 311–327. doi: 10.5194/bg-8-311-2011

Hooker, S. B., Clementson, L., Thomas, C. S., Schluter, L., Allerup, M., Ras, J., et al. (2012). *The fifth SeaWiFS HPLC analysis round-robin experiment (SeaHARRE-5) NASA tech* (Greenbelt, Maryland: NASA Goddard Space Flight Center), 95.

Hooker, S. B., Thomas, C. S., Van Heukelem, L., Schluter, L., Ras, J., Claustre, H., et al. (2010). *The forth SeaWiFS HPLC analysis round-robin experiment (SeaHARRE-4) NASA tech* (Greenbelt, Maryland: NASA Goddard Space Flight Center), 74.

Hooker, S. B., Van Heukelem, L., Thomas, C. S., Claustre, H., Ras, J., Barlow, R., et al. (2005). *The second SeaWIFS HPLC analysis round-robin experiemnt /SeaHARRE-2)*.

Hooker, S. B., Van Heukelem, L., Thomas, C. S., Claustre, H., Ras, J., Schluter, L., et al. (2009). *The third SeaWiFS HPLC analysis round-robin experiment (SeaHARRE-3) NASA tech* (Greenbelt, Maryland: NASA Goddard Space Flight Center), 106.

IOCCG (2014). *Phytoplankton functional types from space*. in Reports of the International Ocean-Colour Coordinating Group, No. 15. Ed. S. Sathyendranath (Dartmouth, Canada: IOCCG), 156.

Jeffrey, S. W., Mantoura, R. F. C., and Wright, S. W. (1997). "Monographs on oceanographic methodology," in *Phytoplankton pigments in oceanography* (Paris: UNESCO).

JGOFS Protocols for the Joint Global Ocean Flux Study Core Measurements (1994). "Intergovernmental oceanographic commission, scientific Committee on oceanic research," in *Manual and guides*, vol. 29. (Paris: UNESCO), 91–96.

Latasa, M., Bidigare, R. R., Ondrusek, M. E., and Kennicutt., M. C. (1996). HPLC analysis of algal pigments: a comparison exercise among laboratories and recommendations for improved analytical performance. *Mar. Chem.* 51, 315–324. doi: 10.1016/0304-4203(95)00056-9

Mackey, M., Mackey, D., Higgins, H. W., and Wright, S. W. (1996). CHEMTAX - a program for estimating class abundances from chemical markers: application to HPLC measurements of phytoplankton. *Mar. Ecol. Prog. Ser.* 144, 265–283. doi: 10.3354/meps144265

Matsumoto, T., Shinozaki, F., Chikuni, T., Yabuki, A., Takishita, K., Kawachi, M., et al. (2011). Green-colored plastids in the dinoflagellate genus *Lepidodinium* are of core chlorophyte origin. *Protist* 162 (2), 268–276. doi: 10.1016/j.protis.2010.07.001

Mouw, C. B., Hardman-Mountford, N. J., Alvain, S., Bracher, A., Brewin, R. J. W., Bricaud, A., et al. (2017). A consumer's guide to satellite remote sensing of multiple phytoplankton groups in the global ocean. *Front. Mar. Sci.* 4. doi: 10.3389/fmars.2017.00041

Naik, R. K., Anil, A. C., Narale, D. D., Chitari, R. R., and Kulkarni, V. V. (2011). Primary description of surface water phytoplankton pigment patterns in the bay of Bengal. *J. Sea Res.* 65 (4), 435–441. doi: 10.1016/j.seares.2011.03.007

Roy, S., Llewellyn, C., Egeland, E., and Johnsen, G. (2011). "Phytoplankton pigments: characterization, chemotaxonomy and applications in oceanography," in *Cambridge Environmental chemistry series* (Cambridge: Cambridge University Press), 314–342.

Schlüter, L., Behl, S., Striebel, M., and Stibor, H. (2016). Comparing microscopic counts and pigment analyses in 46 phytoplankton communities from lakes of different trophic state. *Freshw. Biol.* 61, 1627–1639. doi: 10.1111/fwb.12803

Trees, C. C., Clark, D. K., Bidigare, R. R., Ondrusek, M. E., and Mueller, J. L. (2000). Accessory pigments versus chlorophyll a concentrations within the euphotic zone: a ubiquitous relationship. *Limnol. Oceanogr.* 5, 1130–1143. doi: 10.4319/lo.2000.45.5.1130

Uitz, J., Claustre, H., Morel, A., and Hooker, S. B. (2006). Vertical distribution of phytoplankton communities in open ocean: an assessment based on surface chlorophyll. *J. Geophys. Res.* 111, C08005. doi: 10.1029/2005JC003207

Van Heukelem, L., and Thomas, C. S. (2001). Computer-assisted high performance liquid chromatography method development with applications to the isolation and analysis of phytoplankton pigments. *J. Chromatogr. A* 910 (1), 31–49. doi: 10.1016/S0378-4347(00)00603-4

Vidussi, F., Claustre, H., Manca, B., Lucchetta, A., and Marty, J. C. (2001). Phytoplankton pigment distribution in relation to upper thermocline circulation in the eastern Mediterranean Sea during winter. *J. Geophys. Res.* 136 (C9), 19,939–19,956. doi: 10.1029/1999JC000308

Wasmund, N., Topp, I., and Schories, D. (2006). Optimising the storage and extraction of chlorophyll samples. *Oceanologia* 48 (1), 177–186.

Wright, S. W., and Jeffrey, S. W. (2005). "Pigment markers for phytoplankton production," in *Marine organic matter: biomarkers, isotopes and DNA. the handbook of environmental chemistry*, vol. 2N . Ed. J. K. Volkman (Berlin, Heidelberg: Springer).

Wright, S. W., Jeffrey, S. W., Mantoura, R. F. C., Llewellyn, C. A., Bjornland, T., Repeta, D., et al. (1991). Improved HPLC method for the analysis of chlorophylls and carotenoids from marine phytoplankton. *Mar. Ecol. Prog. Ser.* 77, 183–196. doi: 10.3354/meps077183

Xi, H., Losa, S. N., Mangin, A., Garnesson, P., Bretagnon, M., and Demaria, J. (2021). Global chlorophyll a concentrations of phytoplankton functional types with detailed uncertainty assessment using multi-sensor ocean color and sea surface temperature satellite products. *J. Geophys. Res.: Oceans* 126, e2020JC017127. doi: 10.1029/2020JC017127

Xi, H., Losa, S. N., Mangin, A., Soppa, M. A., Garnesson, P., Demaria, J., et al. (2020). Global retrieval of phytoplankton functional types based on empirical orthogonal functions using CMEMS GlobColour merged products and further extension to OLCI data. *Remote Sens. Environ.* 240, 111740. doi: 10.1016/j.rse.2020.111704

Zapata, M., Rodriguez, F., and Garrido, J. L. (2000). Separation of chlorophylls and carotenoids from marine phytoplankton: a new HPLC method using reverse phase C8 column and pyridine-containing mobile phase. *Mar. Ecol. Prog. Ser.* 195, 29–45. doi: 10.3354/meps195029

Zibordi, G., Berthon, J.-F., Mélin, F., and D'Alimonte, D. (2011). Cross-site consistent in situ measurements for satellite ocean color applications: the BiOMaP radiometric dataset. *Remote Sens. Environ.* 115 (8), 2104–2115. doi: 10.1016/j.rse.2011.04.013

frontiers | Frontiers in Marine Science

TYPE Original Research
PUBLISHED 20 July 2023
DOI 10.3389/fmars.2023.1129876

Check for updates

OPEN ACCESS

EDITED BY
Javier A. Concha,
European Space Research Institute (ESRIN), Italy

REVIEWED BY
Jonathan J. Sherman,
National Oceanic and Atmospheric Administration (NOAA), United States
Ilaria Cazzaniga,
Joint Research Centre, Italy
Surya Prakash Tiwari,
King Fahd University of Petroleum and Minerals, Saudi Arabia

*CORRESPONDENCE
Martin Hieronymi
martin.hieronymi@hereon.de

RECEIVED 22 December 2022
ACCEPTED 22 June 2023
PUBLISHED 20 July 2023

CITATION
Hieronymi M, Bi S, Müller D, Schütt EM, Behr D, Brockmann C, Lebreton C, Steinmetz F, Stelzer K and Vanhellemont Q (2023) Ocean color atmospheric correction methods in view of usability for different optical water types.
Front. Mar. Sci. 10:1129876.
doi: 10.3389/fmars.2023.1129876

COPYRIGHT
© 2023 Hieronymi, Bi, Müller, Schütt, Behr, Brockmann, Lebreton, Steinmetz, Stelzer and Vanhellemont. This is an open-access article distributed under the terms of the Creative Commons Attribution License (CC BY). The use, distribution or reproduction in other forums is permitted, provided the original author(s) and the copyright owner(s) are credited and that the original publication in this journal is cited, in accordance with accepted academic practice. No use, distribution or reproduction is permitted which does not comply with these terms.

Ocean color atmospheric correction methods in view of usability for different optical water types

Martin Hieronymi[1]*, Shun Bi[1], Dagmar Müller[2], Eike M. Schütt[1,3], Daniel Behr[1], Carsten Brockmann[2], Carole Lebreton[2], François Steinmetz[4], Kerstin Stelzer[2] and Quinten Vanhellemont[5]

[1]Department of Optical Oceanography, Institute of Carbon Cycles, Helmholtz-Zentrum Hereon, Geesthacht, Germany, [2]Brockmann Consult GmbH, Hamburg, Germany, [3]Earth Observation and Modelling, Department of Geography, Kiel University, Kiel, Germany, [4]HYGEOS, Lille, France, [5]Royal Belgian Institute of Natural Sciences, Operational Directorate Natural Environments, Brussels, Belgium

Satellite remote sensing allows large-scale global observations of aquatic ecosystems and matter fluxes from the source through rivers and lakes to coasts, marginal seas into the open ocean. Fuzzy logic classification of optical water types (OWT) is increasingly used to optimally determine water properties and enable seamless transitions between water types. However, effective exploitation of this method requires a successful atmospheric correction (AC) over the entire spectral range, i.e., the upstream AC is suitable for each water type and always delivers classifiable remote-sensing reflectances. In this study, we compare five different AC methods for Sentinel-3/OLCI ocean color imagery, namely IPF, C2RCC, A4O, POLYMER, and ACOLITE-DSF (all in the 2022 current version). We evaluate their results, i.e., remote-sensing reflectance, in terms of spatial exploitability, individual flagging, spectral plausibility compared to *in situ* data, and OWT classifiability with four different classification schemes. Especially the results of A4O show that it is beneficial if the performance spectrum of the atmospheric correction is tailored to an OWT system and vice versa. The study gives hints on how to improve AC performance, e.g., with respect to homogeneity and flagging, but also how an OWT classification system should be designed for global deployment.

KEYWORDS

atmospheric correction, ocean color, optical water types, satellite remote sensing, essential climate variable, Sentinel-3/OLCI

1 Introduction

Ocean Color (OC) has been identified as an Essential Climate Variable (ECV), because of its capability to observe various aspects of the marine environment synoptically at global scales (GCOS, 2011; Hollmann et al., 2013). The color of the ocean is determined by absorption and scattering interactions of sunlight with water, free-floating particles and dissolved substances in the upper water layer (current state of research on this is summarized by Bi et al., 2023). Color, or more specifically the remote-sensing reflectance, R_{rs}, is defined as the spectral (back-scattered) water-leaving radiance, L_w, in proportion to the total down-welling plane irradiance, E_d. The reference point lies directly above the sea surface at the bottom-of-atmosphere (BOA). The spectral range of R_{rs} includes not only the visible (VIS) range, which is perceived as color often defined for wavelengths from 380 to 760 nm, but also parts of the ultraviolet (UV) and near-infrared (NIR) spectral range; it is primarily determined by the pure water absorption (e.g., Bi et al., 2023). Space-borne ocean color sensors, however, measure spectral radiances, L_{TOA}, at the top-of-atmosphere (TOA) from the given viewing direction. This signal is strongly influenced by light interactions in the atmosphere, like scattering by air molecules, and aerosols or absorption by atmospheric gases, but also by light reflections at the sea surface (e.g., IOCCG, 2010; Frouin et al., 2019). Moreover, whitecaps and air bubbles in water, not related to the actual ocean color, contribute to the water-leaving signal (e.g., Dierssen, 2019). The process of retrieving unobstructed remote-sensing reflectance at surface level from TOA radiance is typically referred to as atmospheric correction (AC).

Spectral remote-sensing reflectance is the fundamental parameter from which biogeo-optical properties and corresponding concentrations of optically active water constituents can be derived. The concentration of the pigment chlorophyll-a in water, *Chl*, is widely used as a proxy for the phytoplankton biomass in the upper water layer; *Chl* is also considered as an ECV as it is linked to the marine carbon-cycle. The Global Climate Observing System (GCOS, 2011) defines a target accuracy requirement for R_{rs} (strictly speaking for the water-leaving radiance) of 5% specifically for the blue and green wavelengths and 30% for *Chl*. This applies to so-called Case-1 (C1) waters whose inherent optical properties (IOPs) primarily depend on phytoplankton, its abundance and its degradation products; this is generally the case for open oceans. In contrast, all "optically complex" waters of marginal seas, coastal and inland water bodies are summarized as Case-2 (C2) where additional water constituents such as non-algal particles (*NAP*) and colored dissolved organic matter (*CDOM*) considerably influence the water color (Morel and Prieur, 1977; Bi et al., 2023). *CDOM* is primarily leached from decaying detritus and terrestrial organic matter, but it can also be yielded from precipitation with elevated *CDOM* levels in continentally influenced rainwater (Kieber et al., 2006). The accepted uncertainties of R_{rs} and subsequent ocean color products are considerably higher for Case-2 waters and GCOS recommends the implementation of specifically tailored algorithms. Based on this rationale, EUMETSAT for example offers two independent *Chl* products (based on different AC methods) from the operational Ocean and Land Color Instrument (OLCI) on board the Sentinel-3 satellites, namely *CHL_OC4ME* for Case-1 and *CHL_NN* for Case-2 waters. User consultations, however, reveal a clear priority for ocean color algorithms that work across C1-C2 waters, or at least that demarcate the boundary between the two; moreover, appropriate and steady ocean color products are required for climate change studies (Sathyendranath et al., 2017).

The usage of branching and blending of specialized algorithms for seamless transition and case-optimized phytoplankton estimates has increased over the course of the recent years. Smith et al. (2018) and Kajiyama et al. (2018) for example have developed OLCI-specific bipartite switching algorithms for regionally optimized *Chl* retrievals. More holistic approaches involve a pre-classification of R_{rs} spectra into several optical water types (OWT) in order to display the full spectral diversity of oceanic, coastal, and inland waters (e.g., Moore et al., 2001; Martin Traykovski and Sosik, 2003; Vantrepotte et al., 2012; Shi et al., 2013; Moore et al., 2014; Mélin and Vantrepotte, 2015; Minu et al., 2016; Eleveld et al., 2017; Hieronymi et al., 2017; Jackson et al., 2017; Spyrakos et al., 2018; Soomets et al., 2019; Uudeberg et al., 2020; Jia et al., 2021; Wei et al., 2022). However, effective exploitation of this method presumes a successful atmospheric correction over the entire spectral range. Residual errors from imperfect atmospheric correction, which are not reproducible by combination of mean OWT reflectance spectra, can result in very low total memberships and therefore, prove the unfitness of the processing constellation for this case. This leads to the need that the upstream AC method is within the scope for each water type and that it delivers always-sufficient total memberships.

There are various sensor-specific AC methods, which supply remote-sensing reflectance mostly optimized for either oceanic, coastal or inland waters, e.g., described in IOCCG (2010) or Frouin et al. (2019). The corresponding AC performance can differ significantly depending on the selected evaluation data, optical water types, applied flagging, sensor properties like camera boundaries, the presence of transparent clouds or sun glint (e.g., Goyens et al., 2013; Müller et al., 2015a; Müller et al., 2015b; Qin et al., 2017; Tilstone et al., 2017; Mograne et al., 2019). Frouin et al. (2019) listed a number of significant issues for atmospheric correction including clouds, adjacency effects, whitecaps, the Earth atmosphere's curvature, multiple scattering, and polarization. Moreover, atmospheric corrections have serious difficulties in cases with high *CDOM* or *NAP* concentrations in water, i.e., very dark or bright, so called extreme Case-2 waters (Hieronymi et al., 2016; Hieronymi et al., 2017). Absorption of dissolved organic matter causes an exponential reduction of the reflectance especially in the blue; this is from a TOA-reflectance point of view, a comparable spectral effect as Rayleigh scattering by air molecules and hence ambiguous. Absorbing or extremely absorbing Case-2 waters (C2A, C2AX) are characterized by low spectral R_{rs} with maximum in the green and in cases with very high *CDOM*-content (i.e., $a_{CDOM}(440) > 1\ m^{-1}$) in the yellow, red, or even NIR spectral range. Particles in water absorb, but above all also scatter light, which leads to increased reflectance at higher concentrations, partly also in the NIR. The spectral absorption

and much higher scattering of non-algae particles also have an approximately exponential course, as does the Rayleigh influence. At relatively high *NAP* concentrations of 1 g m^{-3}, one speaks of scattering Case-2 waters (C2S); at *NAP* > 100 g m^{-3} of extremely scattering waters (C2SX) respectively. Furthermore, AC problems arise in the presence of very high concentrations of phytoplankton and floating scum with non-negligible NIR reflectance (e.g., Reinart and Kutser, 2006). Clearly, a combination of different AC algorithms can potentially improve an all-water-type-embracing R_{rs}-retrieval; examples are given in Shi and Wang (2009); Aurin et al. (2013); Bi et al. (2018); Liu et al. (2019), and Schroeder et al. (2022). However, programmatic linking of fundamentally different AC algorithms can be challenging and switching may lead to spatial inconsistency or artefacts in the retrievals.

Several AC methods exist for ocean color imagery of Sentinel-3/OLCI. However, their range of validity is not always clear and they do not always fulfil all requirements for unlimited usability of OWT-based water algorithms like the ONNS algorithm by Hieronymi et al. (2017). In this study, we compare five conceptually different atmospheric correction methods for Sentinel-3/OLCI (specified in Table 1): 1) the standard (baseline) Level-2 AC – Instrument Processing Facility (IPF), 2) the alternative Level-2 AC C2RCC, 3) a novel atmospheric correction for diverse optical water types (A4O) by Hieronymi et al. (in prep.), 4) POLYMER by Steinmetz et al. (2011), and 5) the Dark Spectrum Fitting (DSF) implemented in ACOLITE by Vanhellemont and Ruddick (2021). There are also other methods available that can be applied to OLCI (e.g., Guanter et al., 2010; Gossn et al., 2019; Schroeder et al., 2022), but we focus on these five ACs as representative examples of diverse approaches. Based on optically diverse Sentinel-3/OLCI images, we compare the capacity for data exploitation, the spatial plausibility and homogeneity (noise), and analyze the AC output, namely R_{rs}, in view of different OWT classification schemes. Moreover, we show comparisons with *in situ* match-up data. We are thereby attempting to demarcate the scope of application for each AC method and identify potentials for future improvements.

2 Applied methods and evaluation data

2.1 Atmospheric correction methods under consideration

2.1.1 IPF

The European Space Agency (ESA), together with the European Organisation for the Exploitation of Meteorological Satellites (EUMETSAT), operates the Sentinel series of satellites from the European Union Copernicus Programme. EUMETSAT provides Level-2 (L2) standard water products for Sentinel-3/OLCI. Our work refers to data of the ocean color "baseline atmospheric correction" from the Instrument Processing Facility (IPF), which has been operational since 2021 (OLCI Collection-3). The reflectances provided are the basis for the estimation of the chlorophyll-a concentration in Case-1 water, *CHL_OC4ME*. The AC was developed for the open ocean and is based on work of Gordon and Wang (1994); further developments of this method were summarized by Gordon (2021). Significant further developments regarding MERIS and OLCI are based on Antoine and Morel (1998), and Antoine and Morel (1999); Moore et al. (1999), and Nobileau and Antoine (2005). Major updates of IPF have been introduced in the Sentinel-3/OLCI L2 report for baseline collection (EUMETSAT, 2021); the report includes several comparisons with *in situ* data and reference missions, and lists the recommended flags. Particularly noteworthy is the recently implemented revision of the so-called bright pixel correction within the AC, which is applied everywhere, but brings improvements especially in *NAP*-dominated coastal waters.

2.1.2 C2RCC

The OLCI L2 processing includes a second "alternative" AC whose results are not provided, but they form the basis for the L2 Case-2 water products like chlorophyll-a concentration, *CHL_NN*. The AC uses neural networks (NN) for the retrieval of R_{rs} and also

TABLE 1 Examined atmospheric correction methods for Sentinel-3/OLCI ocean color processing with AC-specific masking (plus INVALID and LAND for all).

AC	Full name and Version	Original scope	Flags for invalid pixel expression	Additional warning flags
IPF	IPF L2-WFR OLCI Collection-3 OL_L2M.003.00	C1	CLOUD, CLOUD_AMBIGUOUS, CLOUD_MARGIN, COSMETIC, SATURATED, SUSPECT, HISOLZEN, HIGHGLINT, SNOW_ICE, AC_FAIL, ADJAC, WHITECAPS, RWNEG_[O2-O8]	TURBID_ATM, TIDAL, MEGLINT, AC_FAIL, WHITE_SCATT, LOWRW, HIGHRW, ANNOT, RWNEG_[O1, O9-12, O16-18, O21]
C2R	C2RCC v1.7 including IPF gains	C2S, C2A	RHOW_OOR, IDEPIX_CLOUD, IDEPIX_CLOUD_BUFFER, IDEPIX_CLOUD_SHADOW, IDEPIX_SNOW_ICE, RTOSA_OOR	RTOSA_OOS, CLOUD_RISK
A4O	A4O v0.23 (2022-01-19)	C1, C2S/X, C2A/X	CLOUD_RISK, SEA_ICE	FLOATING, SUSPECT, GLINT_RISK, ADJACENCY, RTOA_EXCESS
POL	POLYMER v4.14 (2021-12-17)	C1, C2S, C2A	CLOUD_BASE, OUT_OF_BOUNDS, EXCEPTION, THICK_AEROSOL, HIGH_AIR_MASS	NEGATIVE_BB, EXTERNAL_MASK, CASE2, INCONSISTENCY
DSF	ACOLITE-DSF v2022-10-25.0	C2S/X	NIR_SWIR_THRES, CIRRUS, TOA_THRESH, NEGATIVE, EXTENT	

There are sometimes additional flags for subsequent water algorithms that are not shown here.

goes back to the MERIS heritage with works of Doerffer and Schiller (2007). The original Case-2 Regional (C2R) algorithm, which contains AC and water algorithms, was optimized for coastal waters of the North Sea. The algorithm was further developed in the CoastColour project (ESA) and is now known as C2RCC (Brockmann et al., 2016). C2RCC is available in the Sentinel Toolbox (SNAP). The neural networks used in the OLCI L2 processing and those of C2RCC are identical. However, there are small differences between OLCI operational NN products and outputs from the SNAP C2RCC processing due to some different pre-processing steps. In this study, the IPF-derived SVC gains (from Collection 3) are used for C2RCC processing directly on OLCI L1B data, which is done slightly different in the OLCI L2 ground segment NN processing (EUMETSAT, 2021). The application of sensor-specific and AC-specific system vicarious calibration (SVC) gains may have the biggest impact also in comparison with previous studies; in some studies, such as Cazzaniga et al. (2023), the same SVC gains are applied, in earlier studies than 2021, other SVC gains were used in some cases (e.g., Giannini et al., 2021). The pixel identification tool IdePix was used for cloud detection and corresponding additional flagging (Brockmann et al., 2013). Against usual recommendations to use equal processing levels for match-up analysis, the non-normalized R_{rs} product of C2RCC is used, which has a broader spectral range in the NIR necessary for some OWT models.

2.1.3 A4O

In the course of the last few years, Hieronymi et al. (in prep.) developed a novel atmospheric correction for diverse optical water types (A4O). The basis was C2RCC, but with fundamental conceptual revision to optimize classifiability with the OWT framework implemented in the OLCI Neural Network Swarm (ONNS) water algorithm (Hieronymi et al., 2017). The aim of A4O is to be applicable to all natural waters, from Case-1 to extremely scattering or absorbing Case-2 waters. Special attention was dedicated to phytoplankton diversity. A4O applies an ensemble of different neural networks and provides fully normalized R_{rs}. In addition, there are other differences to C2RCC; these include the specification of water temperature and salinity using global climatological data, the treatment of ocean whitecaps, the expansion of features in the NN training data, flagging, and an option for spectral and spatial smoothing of the signal. The IPF-SVC gains are also taken into account here primarily to compensate for sensor-specific differences, i.e., the instruments on Sentinel-3A and -3B. The invalid pixel expression refers primarily to an own cloud masking, all visible water areas are valid in principle (non-physical negative reflectance is never delivered). However, there are a number of warning flags, e.g., for pixels with possible land influence or strong sun glint signal, where results might be faulty. It is planned to publish A4O and ONNS in SNAP in the medium term.

2.1.4 POLYMER

POLYMER is an AC algorithm originally developed for oceanic and coastal waters (Steinmetz et al., 2011; Steinmetz and Ramon, 2018). It uses a spectral fitting scheme that relies on two models: a polynomial-like model of atmospheric reflectance and a model of water reflectance. It was developed primarily for correcting sun-glint contamination on images of the MERIS sensor, and has then been applied to several multispectral and hyperspectral sensors including OLCI. In addition to sun glint correction, it is also robust to aerosol contamination and other atmospheric and surface effects such as thin clouds and adjacency effects (Steinmetz and Ramon, 2018; Zhang et al., 2019). POLYMER is the only method in this study that does not use the IPF-SVC gains because all bands are used simultaneously for atmospheric correction. Thus, specific gains are used, generated by a dedicated spectrally coupled SVC scheme.

2.1.5 ACOLITE-DSF

The Dark Spectrum Fitting (DSF) algorithm as implemented in ACOLITE, was originally developed for aquatic applications of satellite data with high spatial resolution in the meter to decameter scale, e.g., the Landsat series, Sentinel-2/MSI, Pléiades, and PlanetScope (Vanhellemont and Ruddick, 2018; Vanhellemont, 2019a; Vanhellemont, 2019b; Vanhellemont, 2020). Vanhellemont and Ruddick (2021) adapted the AC for Sentinel-3/OLCI especially for mapping of suspended particulate matter and chlorophyll-a concentration in turbid coastal waters. Thus, the main scope of ACOLITE-DSF is for aquatic applications for inland and coastal waters, but it can also be used over clearer waters and even land. The gains from IPF-SVC are also being considered here.

2.2 Reference satellite and match-up data

2.2.1 Selected scenes for spatial analysis

Ten full-resolution OLCI (Level-1) scenes were selected for analysis of the spatial AC performance (pixel size 300 m at nadir, swath width approximately 1270 km). They cover a wide variety of optical water types, regions, sun elevations, and sensor-viewing angles relative to the sun (Table 2; Appendix Figure A1). Approximately 47% of the observed Earth surface in the images is covered by water. Of these water areas, 36% are flagged for cloud-risk and 9% for sun-glint according to the A4O designation. For a representative analysis of these scenes, common masks were used where all 5x5 pixels around a central pixel must be valid. This is to eliminate possible cloud artefacts, cloud shadows, sun glint, and land adjacency effects as much as possible. The freely visible and in principle unrestricted water areas were visually checked. However, many of these water pixels are masked by the individual AC methods; especially IPF masks large areas because it produces negative R_{rs} values here. The selected free water areas cover 31.5 million pixels. Inland waters account for 4%. About 0.6% of the pixels show a characteristic red edge increase of TOA reflectance caused by floating biomass at the sea surface and are labelled as FLOATING in A4O. Hieronymi et al. (2016) suggested a definition for extremely scattering waters with $R_{rs}(865) \geq 0.005$ sr^{-1}; thus, the coverage of bright pixels depends on the AC method and is up to 4%.

TABLE 2 Selected test scenes with large cloud-free areas that cover high optical diversity (shown in Appendix Figure A1).

Scene	Sensor-Date-UTC	Region	Special features
#1	S3A-20160720-092821	Barents Sea	High latitudes, bloom of coccolithophores
#2	S3A-20160720-093421	North Sea, Wadden Sea	Moderately to extremely scattering waters, tidal areas, *in situ* data
#3	S3A-20170114-130626	South Atlantic Ocean, Rio de la Plata estuary	Extremely scattering waters, clear oceanic waters, sun glint, South Atlantic Anomaly
#4	S3A-20170527-015236	Yellow Sea, East China Sea, Yangtze, Lake Taihu	Extremely scattering waters, tidal areas, large rivers, absorbing aerosols, sun glint
#5	S3A-20170529-092334	Mediterranean Sea	Large areas with clear waters, sun glint
#6	S3A-20170913-080730	Black Sea, Aegean Sea	Clear and absorbing waters
#7	S3A-20180715-093613	North Sea, Baltic Sea	Intense bloom of cyanobacteria partly with scum
#8, #9	S3A-20200601-092517, S3B-20200601-084546	North Sea, Baltic Sea	Inter-comparison of S3A and S3B with different observation angles, absorbing waters
#10	S3B-20200406-093801	North Sea, Baltic Sea	High OWT diversity

2.2.2 Match-up data from *in situ* measurements and satellite observations

2.2.2.1 AERONET-OC

Independent validation was carried out for match-ups between OLCI imagery and AERONET-OC *in situ* measurement data (Zibordi et al., 2009) from 2016 to 2020 distributed through the ESA OC-CCI *in situ* database (Valente et al., 2022). The data set was limited to OLCI bands (± 2 nm). All R_{rs} measurements are normalized following Park and Ruddick (2005). The stations are widely distributed geographically, but often near coasts or in inland waters (GLO – Gloria, Black Sea; GDT – Gustav Dalen Tower, Baltic Sea; HLH – Helsinki Lighthouse, Baltic Sea; LIS – LISCO, Long Island Sound; LUC – Lucinda, East Coast of Australia; MVC – MVCO, US East Coast; PAL – Palgrunden, Lake in Sweden; VEN – Venice, Adriatic Sea; WAV – Wavecis_site_csi_6, Gulf of Mexico). Therefore, the water types are very similar and the data are not representative of the full range of all natural waters. In the cases where the entire spectra are available, the maximum reflectance lies at 560 nm in 89% cases of the data, only 11% have the maximum at 490 or 510 nm; there is no *in situ* data included with the maximum in blue bands<490 nm or at bands >560 nm. The vast majority of the data counts as Case-2 water. For band-wise comparisons, however, data from Case-1 waters are also included. Some of the AERONET-OC data from the Baltic Sea and the Black Sea represent distinct blooms of cyanobacteria or coccolithophores (e.g., Cazzaniga et al., 2021; Zibordi et al., 2022; Cazzaniga et al., 2023). However, for a comparison of AC results at all 16 (out of 21) OLCI bands, *in situ* data are often missing, especially in red and NIR bands. In general, band-shifting methods can be used to derive OLCI spectra from different band configurations, and the mean percentage retrieval error in the spectral range between 400 and 600 nm is usually less than 5%, but for red and NIR bands the uncertainties are much larger (Hieronymi, 2019). For this reason, additional band shifting was not used in this work, since the main purpose of the match-up comparison is to show the spectral plausibility of the AC results.

2.2.2.2 Other *in situ* data

In order to be able to rudimentary quantify the spatial scenes in the transition from coastal water types and also to contextualize very turbid waters that are not covered in AERONET-OC, exemplary further *in situ* measurement data are considered. Firstly, reflectance measured by Hieronymi et al. in the North Sea/German Bight (OLCI match-up with scene #2) with a protocol described in Tilstone et al. (2020) and normalized with Park and Ruddick (2005). Secondly, OLCI match-ups with the PANTHYR system (Vansteenwegen et al., 2019) that is located in turbid coastal waters in Belgium. The data are provided by Vanhellemont and Ruddick (2021); ACOLITE-DSF was specially designed for these waters and a comparison with the AC candidates (albeit in different versions for ACOLITE-DSF, IPF, and C2RCC, but without A4O) was discussed in their original paper. Approximately half of the PANTHYR data are considered as extremely scattering waters using the above-mentioned definition, the other are C2S.

2.2.2.3 Match-up procedure

The Calvalus system (Fomferra et al., 2012) was used to identify OLCI image matches with *in situ* data within three hours of the satellite overpass. Altogether, there are 2545 match-ups between 2016 and 2020 for the nine AERONET-OC stations and 62 for PANTHYR (2019-2020) for OLCI-A & B. For some stations, there are only a few spectral bands for the comparison and the match-up number varies for each AC according to the filtering of valid data points. Duplicated-flagged values are not used. Mini-scenes of about 10x10 pixels in size were selected at IPF, C2RCC, and A4O, and 5x5 macro-pixels were extracted from them. In the case of POLYMER and ACOLITE-DSF, the complete scenes were processed first and the macro-pixels extracted from them. ACOLITE-DSF can be rather sensitive to size of the scene or sub-scene, and it is usually recommended to use a spatially limited study area with a single aerosol retrieval. For larger scenes, as used here, the aerosol retrieval is tiled and interpolated to the full extent. Individual tile contents may skew the results between tile centers.

The aggregation of the 5x5 macro-pixel follows mostly the procedure described in Müller et al. (2015a). The valid pixel expressions of each AC (Table 1) are applied; all valid pixels are screened for outliers per band using a threshold of 2.5 standard deviations. From the remaining valid pixels their mean value, μ, and standard deviation, σ, is calculated and the number of valid observations (excluding the outliers) is recorded. Based on the percentage coefficient of variation, *CV*, a match-up is considered in further analysis, if the spatial homogeneity is high for the particular band and therefore $CV = \sigma/\mu \times 100\% < 15\%$. Second, at least half of the pixels in the macro-pixel must be valid. These criteria are checked for each data point and band independently, so that AC solutions with some noise in a part of the spectral range may lose good match-ups here but retain part of the spectrum in other spectral regions. The number of match-ups will therefore vary per band, which allows some interpretation in terms of spatial noise.

To compare the performance of the AC methods, we use the match-up statistics recommended by EUMETSAT (2022). Besides the well-known linear regression statistics with the correlation coefficient (*r*), we use the root-mean-square-error (*RMSE*), median absolute deviation (*mdAD*), median absolute percentage deviation (*mdAPD*), the spectral angle mapper (*SAM*), and the Chi-squared test (χ^2).

2.3 Optical water type frameworks

The classification of natural waters into optical water types serves the purpose of comparability and, in the case of large-scale satellite image processing, the selection and blending of results of suitable algorithms. Basically, characteristic R_{rs}-spectra and their covariance are given to define a class. An OWT algorithm tries to combine class-specific spectra in such a way that the input R_{rs}-spectrum can be reproduced, whereby weights are assigned to the contributing classes. The number of defined classes, shape and amplitude of the mean spectra, as well as the mathematical determination of the class weights can vary greatly in the different approaches (see Figure 1).

In order to evaluate results of the five AC methods with regard to OWT, four OWT classification methods were selected with different emphases, e.g., focusing on marine or inland waters. For the selection of the OWT methods, it was necessary to consider the degree of affiliation to the cluster centers. Therefore, methods based on fuzzy logic clustering and using the Mahalanobis distance and χ^2-distribution to calculate the total membership values were chosen (Moore et al., 2001; Moore et al., 2014). Furthermore, only hyperspectral or at least OLCI band-based OWT methods were selected, but no methods using band ratios or concentration thresholds. For the selection, it was also important to represent a wide variety of spectral forms that are considered important in the different methods. Therefore, in general, other classification approaches could be considered that might provide more robust results for the AC methods under consideration or that are not too focused on either marine or inland waters. The used OWT classification methods are:

1. J17 (Jackson et al., 2017) is an OWT method that was developed in the frame of ESA's Ocean Colour Climate

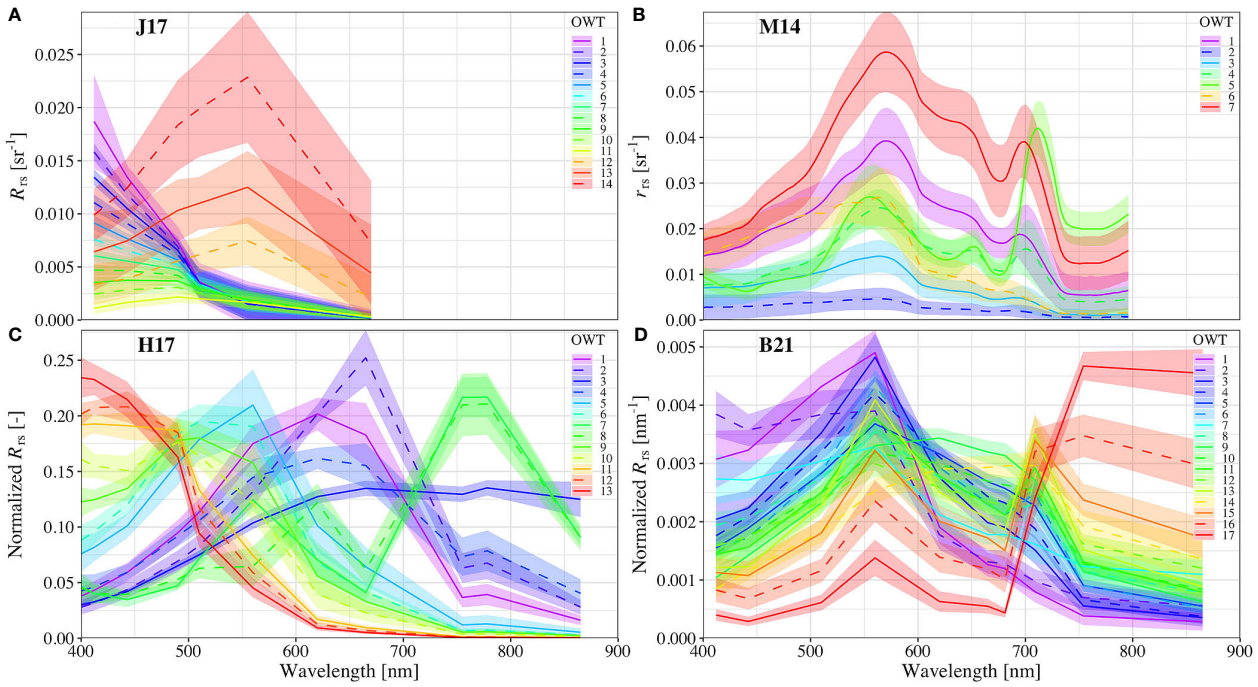


FIGURE 1
Spectral reflectance of optical water types from four frameworks by **(A)** Jackson et al. (2017), **(B)** Moore et al. (2014), **(C)** Hieronymi et al. (2017), and **(D)** Bi et al. (2019), and Bi et al. (2021). The line denotes the original spectral centroid of each water type and the shaded ribbon denotes the standard deviation from respective training datasets.

Change Initiative (OC-CCI). Millions of pixels from merged satellite data were selected for clustering. 11 spectral types for marine waters were identified, and three additional "highly-turbid" coastal spectra from Moore et al. (2014) were also adopted. The original publication referred to the OC-CCI dataset v2 with SeaWIFS bands; in 2020, new optical water class set were defined for the dataset v5 for MERIS-referenced data with POLYMER (v4.12) as the atmospheric correction (Sathyendranath et al., 2021). Thus, the adapted OWT method uses 14 classes and six OLCI bands between 412 and 665 nm.

2. M14 (Moore et al., 2014) uses hyperspectral R_{rs} between 400 and 800 nm that are primarily representative for coastal regions and lakes, where the centroids were trained based on *in situ* measurements. The approach distinguishes seven classes, but actually no blue (oceanic) waters. Their original OWT analysis actually refers to the underwater remote-sensing ratio, r_{rs}, which can be transferred above-water to R_{rs}.
3. H17 (Hieronymi et al., 2017) is a more holistic approach to OWT classification as it aims to cover "most natural waters", from the open ocean to extremely absorbing or scattering waters. The basis of H17 are radiative transfer simulations with Hydrolight (Mobley, 1994), which is a common approach with the AC methods C2RCC and A4O. The latter was even optimized in terms of OWT classifiability with H17. The OWT scheme uses 11 OLCI bands from 400 to 865 nm and distinguishes 13 classes. In order to avoid conflict with possible negative reflectances, the spectra are transformed by $\log_{10}(R_{rs} + 1)$ and brightness-normalized, so that the classification is based on the shape of the spectrum alone.
4. B21 is an extended OWT framework based on the works of Bi et al. (2019), and Bi et al. (2021), developed specifically for inland waters. The hyperspectral training data, which were resampled to 15 OLCI bands from 400 to 865 nm, were mostly measured at large lakes, reservoirs, and rivers across China. The approach differentiates 17 classes including eutrophic and hypertrophic cases with high biological productivity and even surface scum. The spectra are normalized by dividing them by their integrals because, according to their reasoning, the composition of inland waters varies greatly, which changes the shape of the reflectance spectrum rather than the magnitude.

The selected OWT frameworks have different approaches to classifying the spectra. In H17 and B21 the spectra are normalized (albeit in different ways) to highlight differences in spectral shapes between types, while in J17 and M14 differences in the magnitude of the spectra are taken into account. Therefore, it is expected that the interpretation of atmospherically corrected data will depend in part on the region observed by the satellite, as the different waters for which these methods were initially developed are very different. For example, B21 will not be able to represent oceanic water due to the lack of "blue types", while J17 will have difficulty distinguishing eutrophic inland waters, which are not foreseen in the marine model of POLYMER, on which J17 is based. In addition to the selected OWT frameworks, we also use the (OLCI) wavelength of the R_{rs} maximum as a direct and intuitive indication for water types; a similar approach using the spectrally-weighted Apparent Visible Wavelength has been shown to be effective for different optical conditions (Vandermeulen et al., 2020). In general, the maximum reflectance in clear seawater is at shorter wavelengths (more blue or green), whereas in turbid water the maximum is shifted towards longer wavelengths (more green, brown, and red).

2.4 Evaluation of the classifiability

In optical fuzzy logic classification, the class membership is calculated by the cumulative χ^2 distribution with n degrees of freedom (band number) and the Mahalanobis distance between the spectrum and the OWT centroid, normalized by the OWT standard deviation (see calculation details in Moore et al., 2001). To assess the classifiability of an AC-derived spectrum, we calculate the total membership for the OWT classification scheme, u_t. An ideal classification result should give u_t close to (or even slightly higher than) one. At lower u_t, the classification is performing poorly with a threshold on totally non-classifiable defined as $u_t \leq 10^{-8}$. Such cases can occur either because of insufficient type representation in the framework or because of errors of the spectral shape or intensity itself, i.e., underperformance of atmospheric correction, uncorrected influences from adjacency effects or bottom reflections, etc. (Moore et al., 2014). Jackson et al. (2017) also mentioned that u_t should not be much larger than one in the ideal classification result either, which indicates overlap and redundancy between types. However, in this study, we allow u_t to be greater than one, because using frameworks across different water areas will inevitably induce overlap between types. We define five levels of classifiability as shown in Table 3. A spectrum is not classifiable if no OWT can be assigned, whereas OWT memberships are distributed between the classes at the other four levels. Evaluation criteria have been discussed in various publications, e.g., Mélin et al. (2011); Vantrepotte et al. (2012), or Hieronymi et al. (2017); the chosen levels are arbitrary, but work reasonably well for the evaluation of the classification. After all, the percentages of classifiable values in the different water types as well as in the entire data set are calculated. The higher the percentage of high or medium values, the better the classifiability of R_{rs}.

TABLE 3 Classification levels related to the total membership from all classes.

Assignable levels	u_t ranges
Non-classifiable	$u_t \leq 10^{-8} \approx 0$
Below-threshold	$0 < u_t < 10^{-4}$
Low	$10^{-4} \leq u_t < 0.3$
Medium	$0.3 \leq u_t < 0.8$
High	$u_t \geq 0.8$

3 Results

3.1 Spatial homogeneity and plausibility of satellite data

The various atmospheric correction methods provide individual masks at different levels indicating performance limits and uncertainties (Table 1). Flagging is usually a trade-off between limited validity with suspect results at some spectral bands and still useful results in another spectral range. Many ocean color algorithms utilize only one or a few bands for which the AC results can be adequate. Other in-water algorithms use many bands across the spectrum, e.g., principle component analysis or some neural networks. For OWT applications, the whole spectrum is important. Overcorrection of an AC manifests often in negative R_{rs}, usually either in blue (especially IPF) or NIR bands; in any case, this is not a physically plausible result and may be an invalid input to the in-water algorithm. Looking at the whole spectrum, IPF and POLYMER produce very large areas with negative reflectances, both about half of the free water area (albeit the values are often very close to zero). The IPF expression for valid pixels requires positive reflectances at least in the central VIS range (412-665 nm), which cannot be satisfied over large parts and is the main reason for >50% invalid masking (Table 4). POLYMER does not have this restrictive flagging, so everything remains valid. Depending on the processing settings, ACOLITE-DSF does not output negative reflectances, but its flagging results as *NaN* in the output files, which is the main contributor to the 20% invalid flagging (these cases also occur in C2SX waters, for which ACOLITE-DSF was designed, e.g., visible in Figures 2-A5, C5). C2RCC and A4O apply neural networks to approximate log-transformed R_{rs} directly from R_{TOA} without subtracting individual contributions from Rayleigh scattering or glint. Resulting negative reflectances are ruled out, because of the log-transformation and the value range of the NN training. This is an important advantage with regard to continuous usability of the results with different types of water and allows R_{rs} estimation even for very small values close to zero with less noise. The slightly more sensitive cloud detection in C2RCC processing with IdePix results in an additional 1% masking of the water areas.

Figure 2 shows extracts of satellite images (#3, #7, #2, and #1; Table 2; Appendix Figure A1) of the AC results for $R_{rs}(560)$ with respective invalid flagging. Spatial noise usually transfers to the ocean color products and is thus an indicator for AC performance. In this context, the South Atlantic Anomaly (SAA) area (Figure 2A) is special; clear spectral outliers of individual bands occur here in isolated pixels and the peaks are usually noticeably higher at longer wavelengths. Some AC methods succeed in smoothing the pixel spectrum, thereby reducing spatial discontinuities. C2RCC produces the most visible noise in this area (Figure 2-A2), which is probably due to the use of neural networks that are very sensitive to small spectral changes. A4O also uses NNs, but has significantly lower spatial noise due to various processing steps, including a dedicated spectral smoothing for suspect outliers and averaging of the results of different NNs (Figure 2-A3). Moreover, an option is recommended for A4O that applies a Gaussian filter over 3x3 macro-pixels, which smooths results for water areas, attenuates cloud artefacts, and tears down camera boundaries. ACOLITE-DSF, as applied here, interpolates atmospheric parameters over a large spatial region, which effectively reduces the AC-induced noise level.

Looking at the spatial homogeneity criterion (*CV*) at different wavelengths for homogeneous areas of 100x100 pixels (Appendix Figure A1), we see a low and comparable noise levels of the AC-input radiance at TOA for Case-1 and -2 waters; in the SAA area, *CV* values are about twice as high (Table 4). In Case-1 water in the SAA (scene #3, Appendix Figure A1), we see the biggest differences of $CV(R_{rs})$ between A4O and C2RCC, with A4O having the least noise of all the methods. In another (presumably clearer) Case-1 water sea area in the Mediterranean Sea (east of the island Sardinia,

TABLE 4 Evaluation of selected spatial features for 31.5 million free water pixels in ten test scenes for the five atmospheric correction models.

Feature	L_{TOA}	IPF	C2R	A4O	POL	DSF
Invalid flagged water area		51.3	1.0	0	0	20.5
$R_{rs}(412)< 0$		18.5	0	0	0.5	0
$R_{rs}(865)< 0$		40.2	0	0	46.7	0
CV(412) in Case-1 waters	0.4	4.3	5.3	0.9	7.8	2.0
CV(560) in Case-1 waters	0.8	9.3	4.9	1.0	4.6	3.6
CV(665) in Case-1 waters	1.3	55.4	7.0	3.6	27.0	7.3
CV(412) in Case-1 waters (SAA)	0.9	9.3	16.0	5.3	17.8	9.7
CV(560) in Case-1 waters (SAA)	1.8	14.0	133.6	3.8	8.7	12.4
CV(665) in Case-1 waters (SAA)	4.0	129.1	>1000	9.5	63.0	36.1
CV(412) in Case-2 waters	0.4	>1000	15.5	2.6	33.0	2.9
CV(560) in Case-2 waters	0.6	7.6	18.9	1.5	6.2	3.6
CV(665) in Case-2 waters	1.0	24.7	16.5	1.8	11.1	10.2

The coefficients of variations of AC-derived R_{rs} refer to homogeneous subsets of 100x100 pixels; corresponding values of initial TOA radiance are included for comparison (see Appendix Figure A1). All values have the unit [%].

10.3389/fmars.2023.1129876

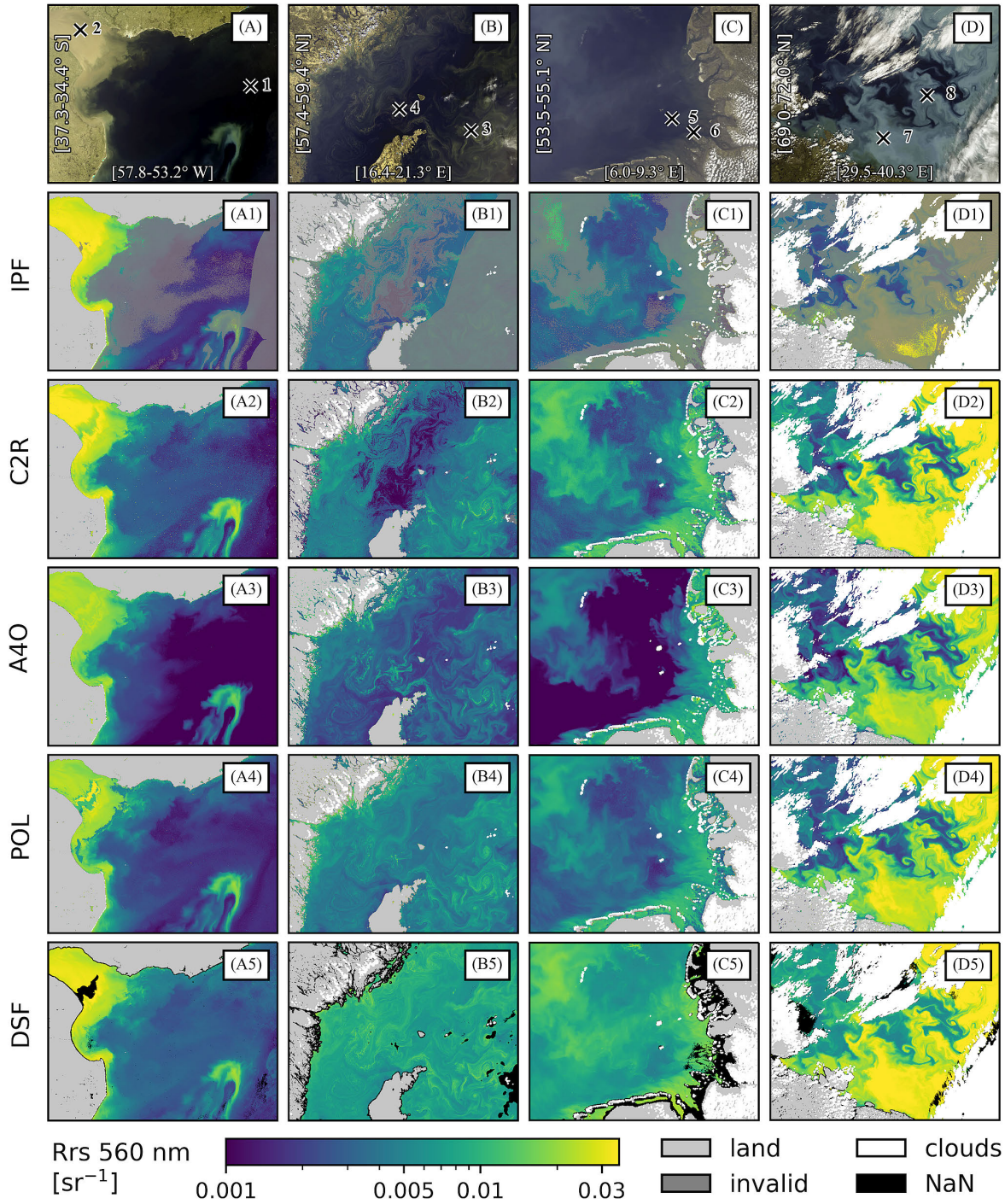


FIGURE 2
Subsets from OLCI images (see Appendix Figure A1). The top row shows RGB images of L1 radiance at top-of-atmosphere **(A–D)**; points for spectral comparisons are marked there (see Figure 3). The five rows below show the results for $R_{rs}(560)$ of the compared AC methods: IPF **(A1-D1)**, C2RCC **(A2-D2)**, A4O **(A3-D3)**, POLYMER **(A4-D4)**, and ACOLITE-DSF **(A5-D5)**. Areas of AC-specific invalid pixel expressions are highlighted transparently or with *NaN*.

scene #5, Appendix Figure A1), the noise of C2RCC is significantly lower and comparable to the other methods, IPF and POLYMER have the highest noise in the red band at 665 nm above the valid-match-up threshold of 15%. In this very clear blue water, $R_{rs}(665)$ becomes very small and approaches zero. In fact, the variability of $R_{rs}(665)$ in case of IPF and POLYMER is pure random noise, in A4O water mass structures are still clearly visible and determine *CV* (665), and in C2RCC one can see weak noisy structures as well. ACOLITE-DSF, which is not designed for such clear water, provides an $R_{rs}(665)$ image with much higher values compared to the other ACs (factor 10 higher). Because ACOLITE-DSF does not perform pixel-by-pixel atmospheric correction, it shows clear

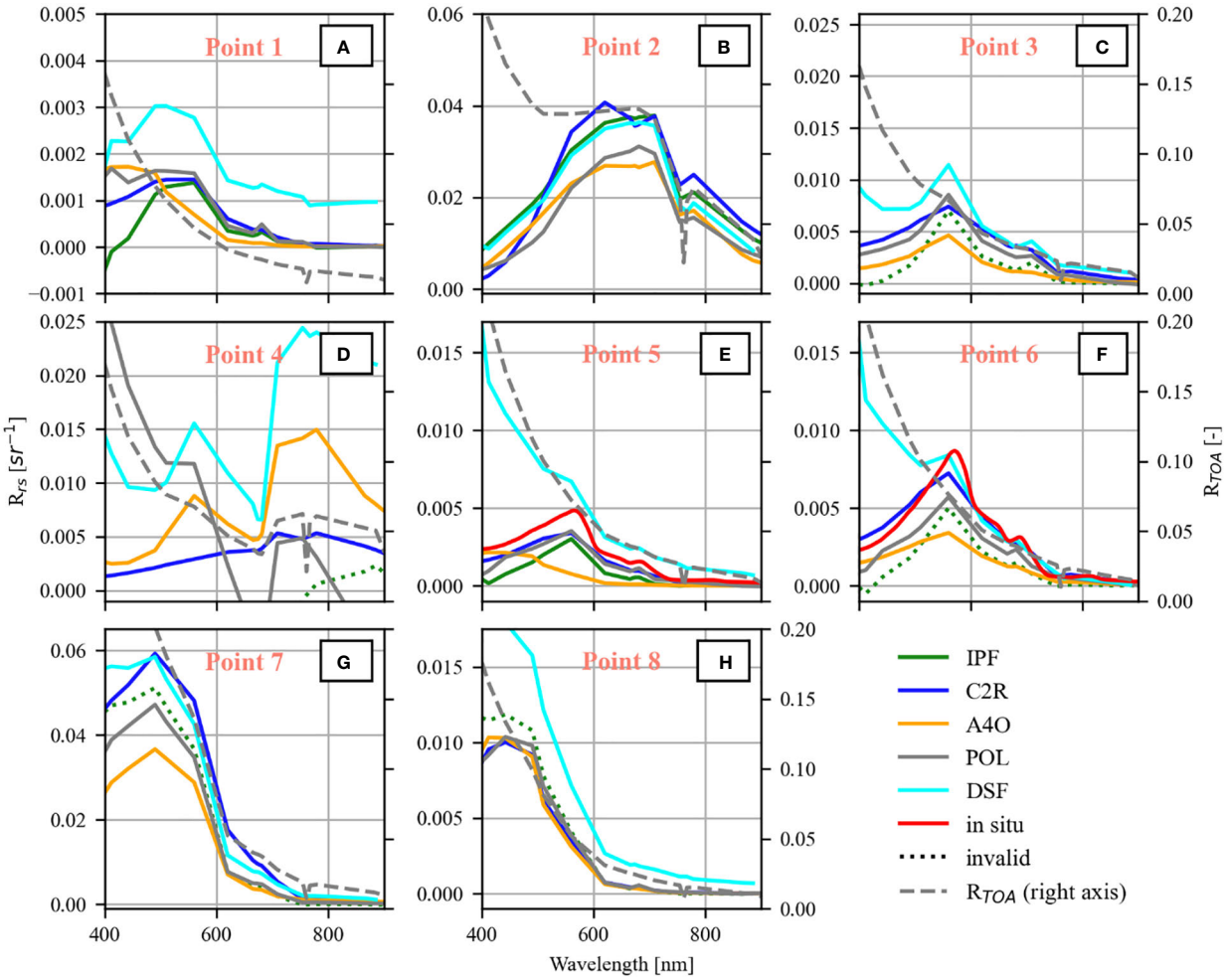


FIGURE 3
(A–H) Comparison of spectral remote-sensing reflectance derived from the different AC methods for eight points marked in Figure 2. The right axis and the corresponding grey dashed lines show the initial TOA reflectance. **(E, F)** include corresponding normalized *in-situ* measurements.

atmospheric structures such as cirrus clouds, which are completely decoupled from the water; in fact, the signal is not only "water-leaving" therefore $R_{rs}(665)$ is invalid by definition (but not adequately flagged). In another uniform area in Case-2 waters (in the southern Baltic Sea, scene #8, Appendix Figure A1), the noise for IPF and POLYMER in blue bands is very high. In the red band, POLYMER has higher R_{rs} and therefore less noise here than in comparison with Case-1 waters. Overall, the results from A4O are spatially the most homogeneous over the entire spectrum whereby the noise level is only moderately increased compared to the TOA input signal.

In the presence of undetected, partially sub-visible clouds such as contrails, C2RCC and A4O tend to overestimate the atmospheric contribution, i.e., R_{rs} is usually lower than ambient. This is less visible for IPF and POLYMER. ACOLITE-DSF does not correct for small-scale clouds by construction. Consequently, cloud artefacts are reflected as amplification of R_{rs}, increasingly at longer wavelengths (e.g., slightly visible in Figure 2-C5). For small-scale broken clouds, all AC methods have large uncertainties. Spatial inconsistencies related to high optical thicknesses, different aerosol conditions, and cloud shadows are further uncertainty factors (IOCCG, 2019).

A visual comparison of all satellite images shows that POLYMER best dissolves the individual camera borders. A4O and IPF reduce the borders significantly; ACOLITE-DSF and C2RCC often have strong gradients here. POLYMER and IPF deliver particularly good homogeneity across the image width (if R_{rs} is relatively high). Moreover, POLYMER is the only one that produces relatively homogeneous and consistent results even in areas with high sun glint influence, which means that significantly larger areas from a satellite image can be exploited, e.g., shown by Müller et al., 2015a; Müller et al., 2015b (retrieved spectra from sun glint areas were not further evaluated in this study). A4O and C2RCC also produce results in sun glint, but both with noticeable angular dependencies and uncertainties (corresponding warning flags are partly raised).

However, POLYMER has a specific flaw with occasional discontinuities due to algorithmic instability under some circumstances. Conditions typically affected are dark waters, thick aerosol plumes, low sun elevation, land proximity or strong ocean

color gradients. These situations tend to reduce the ratio of "water" signal over "atmospheric" signal. The minimization scheme used in POLYMER reveals those instabilities as vertical stripy artifacts, e.g., visible in Figure 2-A4 or in scene #7. Often these cases are characterized by high reflectance values in the blue. Looking at the entire cloud- and glint-free water surface of all scenes, there is an affected area of approx. 1%, which is, however, not flagged. Coasts, lakes, and rivers are particularly affected by the spatial discontinuities, as they often occur close to land.

In the top row of Figure 2, some points are marked whose R_{rs} spectra are shown in Figure 3. In the figure, the initial TOA reflectances are also shown dashed with reference to uniform right axes. AC results that are flagged invalid were displayed in dotted lines. The figure illustrates that the solutions of the different AC methods to the same input can be very different. Mostly A4O marks the lower and ACOLITE-DSF the upper result margin. The result of IPF is over large areas of the VIS in the mid-range of the delivered solutions, but often (unnecessarily) flagged. There are indeed some areas where the spectral shape is very similar, only the magnitude is different (points 2, 3, 7, and 8); in this case, the assignment to an OWT class is usually the same. Remarkably, these cases are considered difficult for atmospheric correction, such as in the Rio de la Plata estuary with its high sediment load or with relatively high cyanobacteria concentrations in the Baltic Sea. Nevertheless, both cases exhibit areas that show extreme spatial and spectral discontinuities and incorrect estimations. A good example of this is point 4, where due to very high concentrations of cyanobacteria and possibly floating scum, a significant increase in TOA reflectance occurs in the NIR. Only IPF is flagged invalid here. ACOLITE-DSF has *NaN* areas near the point, where the invalid-threshold at 1020 nm is reached (Figure 2B). Only A4O and ACOLITE-DSF follow the TOA signal in a plausible way and provide R_{rs} like those that would be expected in such situations (e.g., Reinart and Kutser, 2006; Qi et al., 2014; Hunter et al., 2016; Bi et al., 2023; Cazzaniga et al., 2023); the other ACs are completely wrong spectrally. C2RCC yields a R_{rs} spectrum that resembles *NAP*-rich water and, ironically, is well classifiable in some OWT methods such as H17, whereas, the A4O result is assigned in the correct class but with partly low total memberships. C2RCC provides a discontinuous $R_{rs}(560)$ image (Figure 2-B2) in the situation with significantly lower values than TOA requires. But on a side note, C2RCC estimates the phytoplankton absorption from the spectrum, from which the L2 product *CHL_NN* is derived, which in this case yields high concentration values, roughly reflecting the TOA image.

Figures 2D, 3G, H show another example of a phytoplankton bloom, namely coccolithophores, which particularly strongly scatter in relation to the absorption; a sharp gradient is visible from the bright turquoise bloom to the dark blue ocean. The R_{rs} spectra of the five ACs are similar in both cases and show the high dynamic range of possible values, which is thoroughly comparable with AERONET-OC data during coccolithophore blooms (Cazzaniga et al., 2021).

For many *NAP*-rich waters, such as rivers and estuaries, one can see similar spectral patterns as in Figure 3B. Often POLYMER and A4O are close together but slightly lower than the other ACs. However, pixels in inland waters that have some distance to land are widely invalid-flagged by the AC methods, only A4O claims to be mostly valid. The 300 m pixel size further limits the usability of OLCI for inland waters and especially rivers. Nevertheless, many lakes are eutrophic or hyper-eutrophic and have comparatively high algae concentrations, often with reflectance features like shown in Figure 3D; here only A4O provides largely plausible spectral shapes (e.g., scene #4, Lake Taihu).

There are *in situ* data for points 5 and 6 showing the transition from coast to open North Sea; in fact, there would be further match-ups in more turbid water closer to the coast, but ACOLITE-DSF does not provide results there (Figure 2C). It is worth noting that this is the area for which C2RCC was originally developed. It is therefore not surprising that C2RCC performs well here. At point 6, all ACs show a comparable spectral shape, although significantly lower in some cases, especially A4O (Figure 3F). ACOLITE-DSF fits the *in situ* spectrum very well between 510 nm and the NIR, but at shorter wavelengths there is a strong mismatch, possibly due to the slightly hazy and spatially variable atmosphere. Point 5 is further out in the open sea, where the terrestrial *CDOM* is largely diluted. At this point, C2RCC, POLYMER, and IPF provide spectra that agree quite well with the measurement (Figure 3E). ACOLITE-DSF fits well between 560 and 620, but otherwise retrieves an overestimated spectrum. A4O interprets the signal incorrectly as a blue ocean spectrum, showing that A4O can have difficulties in the transition zone. It is similar for point 1, but here with even greater variability in the results of the different ACs (Figure 3A). Figure 3 illustrates that in general there are not always consistent results from different atmospheric corrections, which would also be reflected in strongly deviating ocean color products.

3.2 Match-up analysis

Figure 4 shows the comparison of R_{rs} at selected bands (412, 490, 560, 665, and 865 nm) from match-ups between OLCI A+B data and *in situ* measurements at nine AERONET-OC stations (colors stand for the individual stations). The results of the five AC methods are shown per row. The contours illustrate the density of the measurements and indicate the 10-, 50-, and 90-percentile lines. Scatterplots do not show the interconnections between the bands, this becomes more visible when looking at the full spectra and evaluating the spectral angle mapper. Thus, Figure 5 shows a subset of data from Figure 4 (from the Black Sea, Baltic Sea, and a lake) from a spectral perspective. In addition, corresponding results of the PANTHYR system from turbid coastal waters are shown in the right column. Some AERONET-OC stations measure at fewer OLCI bands, resulting in different maximum numbers of match-ups per band; PANTHYR measures hyper-spectrally (but band averaged data are used for the comparison).

The already mentioned findings on AC flagging and especially the spatial homogeneity criterion (Table 4) are reflected in the number of valid match-ups. Due to the very low noise level, A4O yields significantly more accepted match-ups with AERONET-OC than all other methods, in blue bands at least twice as many points (at 412 nm $N = 2255$) and in the NIR, for example, 473 vs. 4 points from IPF. Additional warning flags can often identify clear outliers,

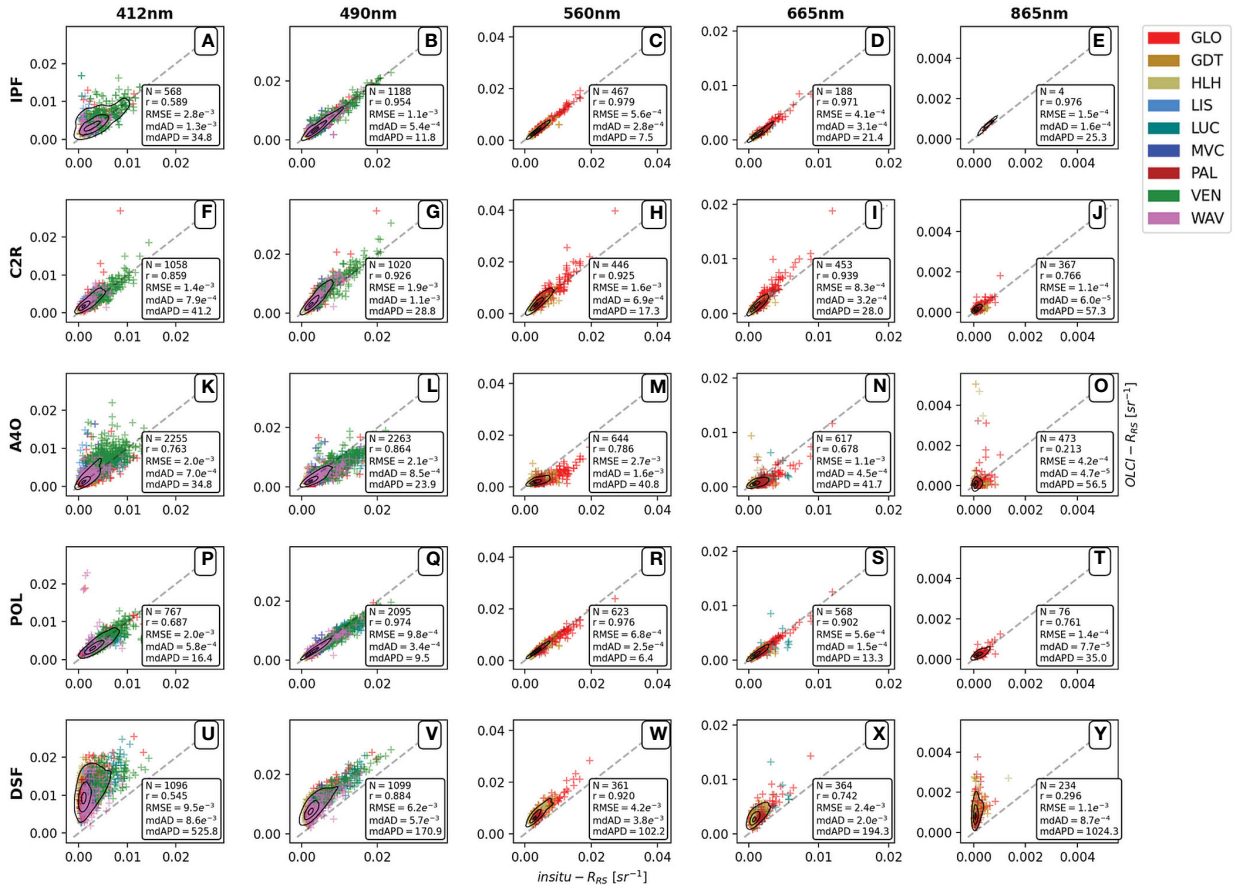


FIGURE 4
Comparison of satellite-derived R_{rs} with AERONET-OC *in situ* data for OLCI bands at 412, 490, 560, 665 and 865 nm for IPF **(A–E)**, C2RCC **(F–J)**, A4O **(K–O)**, POLYMER **(P–T)**, and ACOLITE-DSF **(U-Y)**. The colors represent different stations. The contours indicate the density distribution.

which are incorporated into the determination of statistical performance, as can be well seen in Figure 5. The obvious outliers in A4O (all associated with clouds) are few and far less than the match-ups sorted out else (Figures 4K–O, 5I–L). Due to the very large differences in individual match-ups, the following analysis does not include a Common Best Quality approach (Müller et al., 2015a).

With respect to the IPF, the retrieved R_{rs} agree quite well with the AERONET-OC data, with the exception of a number of data points with overestimation in blue bands (considering that many negative values are not taken into account due to masking, see Table 4). The slopes of the regression lines are very close to one. The correlation coefficients for the bands 490 nm to 865 nm range from 0.954 to 0.979; in the blue spectral region, it is significantly lower at 0.589. For PANTHYR data, the correlations are also high, namely >0.85 for all bands except at 412 nm, where r = 0.493. In fact, IPF's correlation coefficients for central VIS bands are among the highest and *RMSE*/deviations are among the lowest for both datasets. However, there are insufficient matches in the NIR to meaningfully evaluate the performance. Compared to the other ACs, the number of valid data is lowest for the blue, red, and NIR bands. Mainly the invalid flagging due to negative reflectances as well as the noise-related uncertainties are responsible for the big loss of match-ups. The spectral comparison reveals the partial difficulties of IPF in short wavelengths, but on the whole the good agreement with the measured reflectances, obviously in comparison with the C2S/X data too (Figures 5A–D). An occasional discontinuity of the first three bands is also visible in Figure 3; this could have an influence on OWT applications.

The C2RCC processing in this work includes SVC gains (sometimes not done), which are particularly effective in blue bands. Thereby C2RCC achieves the highest correlation (0.859 for AERONET-OC and 0.618 for PANTHYR) and smallest *RMSE* (0.0014 and 0.0046) in the blue band at 412 nm (but not smallest deviations *mdAD* or *mdAPD*). C2RCC tends to retrieve slightly overestimated R_{rs}; all biases are positive. With respect to our complex-water-dominated data set, Cazzaniga et al. (2022) conclude similar assessments for C2RCC, but for comparisons with clear waters, they show a general underestimate of reflectance from C2RCC. However, the correlation coefficients are high for the entire spectrum, even at 865 nm, in both cases $r > 0.76$, but the values are more scattered than, for example, for IPF or POLYMER. The spectral comparison shows good agreement in all orders of magnitude of the measured values; χ^2 and *SAM* are generally among the lowest (Figures 5E–H). This implies a potentially good classifiability for Case-2 waters, for which C2RCC was optimized.

10.3389/fmars.2023.1129876

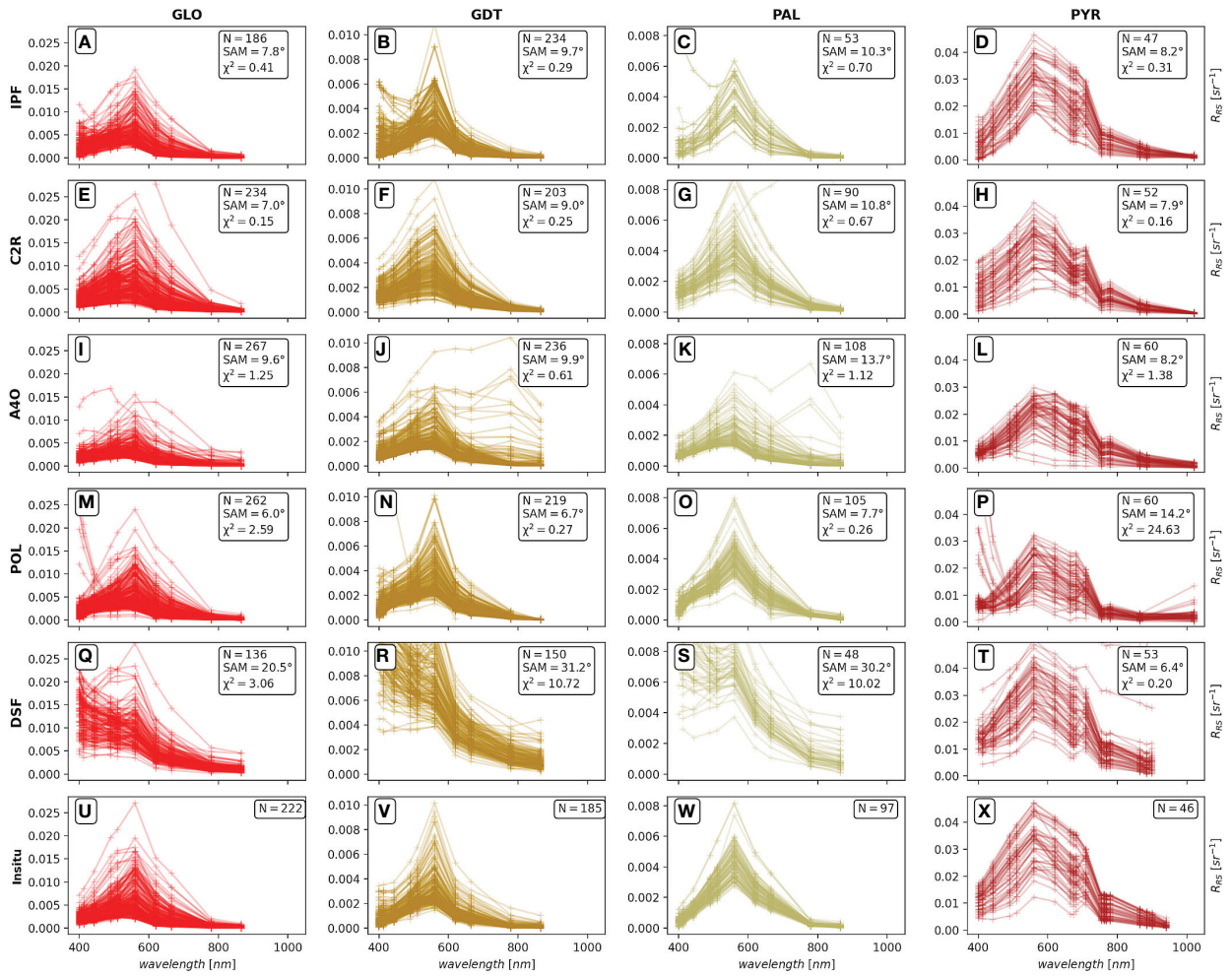


FIGURE 5
Satellite-derived R_{rs} spectra of IPF **(A-D)**, C2RCC **(E-H)**, A4O **(I-L)**, POLYMER **(M-P)**, and ACOLITE-DSF **(Q-T)** compared with *in situ* data **(U-X)** from selected AERONET-OC stations (Gloria, Gustav Dalen Tower, Palgrunden) and PANTHYR (right). The statistical parameters refer to complete spectra at ten OLCI bands.

For A4O, this is the very first comparison with AERONET-OC or PANTHYR *in situ* measurements. Despite the very high number of match-ups that were achieved by A4O, which suggests that potentially difficult cases are included in the assessment (but not in the other methods), clear statistical correlations can be demonstrated. All outliers visible in Figures 5J, K (both Baltic Sea) are exclusively related to cloud margins and often recognizable algal blooms in the vicinity. Nonetheless, a medium to strong positive linear correlation is achieved for all bands except the NIR, which is corrupted by some outliers (despite that, the lowest absolute deviation is obtained in the NIR). A4O reaches the second best correlation for blue bands with a value of 0.763; in contrast, in the important green band at 560 nm, A4O has the lowest correlation coefficient in comparison with the other ACs (0.786). There is a clear tendency that values are underestimated in the central VIS. This becomes visible in Figures 5I–L (and Figure 3) too and is echoed in χ^2. However, apart from few outliers and partly lower values, A4O shows a very similar spectral shape as the measured values. This holds also true for the turbid scattering waters (Figure 5L), but two "false blue" spectra appear as well, similar to the coastal-ocean transition zone in Figure 3E.

POLYMER applies not such rigorous flagging as IPF, so the main factor for relative loss of match-up points comes from spatial homogeneity of low reflectances (*CV*). The *in situ* data used here are more representative of Case-2 waters, where POLYMER's noise in blue bands is relatively high (Table 4), as shown by the relatively low *N* at 412 nm (Figure 4P), but this is also true for NIR bands (Figure 4T). However, POLYMER and A4O deliver the most match-ups in the central VIS, with more than 2000 at 490 nm, twice as many as at IPF, C2RCC, or ACOLITE-DSF. The statistical characteristics prove the very good performance of POLYMER; but in C2SX waters, the values are only in the average range with the worst evaluations of all ACs in the blue band. Nevertheless, some outliers significantly affect the metrics, well visible in the spectral plots; these are usually associated with the mentioned strip-like spatial inconsistencies (e.g., visible in Figure 2-A4 or scene #7 in the Gulf of Finland). Admittedly, POLYMER has corresponding warning flags that partly identify these cases, but also mark many productive waters. In principle, the spectral shape from POLYMER is well reproduced, although occasionally with recognizable residuals from the polynomial regression in the shorter

wavelength range. Usually, these features are not found in *in situ* measurement data (Figures 5M–P), so this can become problematic for correct OWT identification again.

This is also the first comparison of ACOLITE-DSF for OLCI products with AERONET-OC data. Apart from the blue bands, slightly better correlations can be obtained than with A4O, at 560 nm, r = 0.92. In general, an overestimation of reflectance is recognizable, with the highest values for *RMSE*, *mdAD*, *mdAPD*, *SAM*, and χ^2 everywhere. The overestimation is caused by use of the minimum aerosol optical thickness retrieval in an image sub-tile, leading to an underestimation of atmospheric reflectance and hence overestimation of water reflectance. This clearly becomes a significant uncertainty when the water signal is very low compared to the atmospheric signal, as it is here for the AERONET-OC match-ups. For waters with relatively low reflectance values in the blue (in principle, especially C2A/X), there are clear shape problems that are critical for OWT applications. The agreement with measured values is significantly better for the C2S/X waters for which ACOLITE-DSF was developed. *SAM* and χ^2 are among the smallest here, this also applies to the central visible range for *RMSE*, *mdAD*, *mdAPD*; however, the correlation coefficients are among the lowest. ACOLITE-DSF gives results close to the 1:1 line for PANTHYR data for all bands (not shown); all other AC methods underestimate the reflectance, sometimes significantly.

3.3 OWT classifiability

The OWT analysis of cloud- and sun-glint-free water surfaces refers only to the individual flags for invalid AC, spatial homogeneity is not taken into account. As already noted, invalid masking leads to 51% and 20% data loss for IPF and ACOLITE-DSF, respectively (Table 4). If one ignores the masks in IPF, one actually gets very similar OWT class distributions. In principle, the OWT methods can exploit slightly negative reflectances.

Figures 6, 7 show percentage distributions of the levels of OWT classifiability of AC-derived R_{rs} using four different OWT classification schemes. The numbers above the bars in Figure 6 (except for the last three columns) illustrate the percentage allocation of classes with maximum memberships in the OWT frameworks (see Figure 1 for the spectral shapes). The numbers in the color bars indicate the percentage of the assigned classification level (if >10%), all classifiable contributions sum to 100%. In the example of IPF and J17 in Figure 6A, 21% of cases with maximum membership in class 1 have medium ($0.3 \leq u_t < 0.8$) total membership and 78% have only low membership ($10^{-4} \leq u_t < 0.3$). The total fraction of spectra of class 1 is less than 0.1% of all IPF-J17-classifiable free water pixels (for such small fractions, the value is not written above). Figure 7 shows the corresponding distribution of classification results but sorted by the OLCI waveband with the maximum reflectance provided by the AC method. Each subplot in Figures 6, 7 includes three additional bars: "ALL" summarizes the total distribution over all pixels including non-classifiable and flag-invalid pixels; "BLOOM" considers cases that are flagged with the FLOATING mask of A4O with the characteristic red edge enhancement of R_{TOA}, this is typical for intense cyanobacteria blooms; and "C2SX" is for waters with $R_{rs}(865) \geq 0.005$ (depends on AC). C2SX and BLOOM are typical cases for coastal and inland waters. The distributions in C2SX (yellow numbers) and BLOOM (green numbers) refer to different numbers of total valid pixels per AC, e.g., only 5% of the BLOOM pixels are not flagged and therefore valid in IPF, but 100% are valid in A4O. When interpreting, one should keep in mind that the shape of the reflectance provided may be wrong for the given situation, but the spectrum may be well classified in a different class. Orange colors in Figures 6, 7 represent the level with too low contributions of the classes to be considered "classifiable"; this shows the potential of relaxing the threshold (10^{-4}) and indicates too narrow tolerance for class memberships of the OWT systems.

First, let us analyze the total distributions sorted by wavebands with satellite-derived R_{rs} maximum (Figure 7). There are some differences visible between the five AC methods, although the absolute numbers are not equally representative since some features occur rarely in the test scenes. However, the distributions of IPF, C2RCC, and POLYMER are quite comparable, with roughly 20% at 412 nm, 20-30% at 490 nm, and 40% at 560 nm. A4O has about 40, 20, and 30% of these bands, resulting in roughly twice as many "blue" spectra. ACOLITE-DSF has in more than 67% of cases an absolute R_{rs} maximum at the first band (400 nm), further 16% at 412 nm, 9% at 490 nm, and only 5% at 560 nm. Typical examples of this spectral behavior can be seen in Figures 3, 5Q–T. This blue maximum is characteristic of atmospheric path reflectance and indicates again the under-correction by ACOLITE-DSF for low reflectance targets.

J17 is the OWT framework that utilizes the least bands as input, which is favorable for obtaining higher membership values, and focuses on ocean and coastal waters. Moreover, J17 was developed based on satellite data that were atmospherically corrected with POLYMER. It is therefore not surprising that POLYMER has the greatest distribution of water types and overall good classifiability per class; the classifiability only degrades for the turbid water classes (Figure 6M). POLYMER, C2RCC, and A4O each achieve >70% high or medium total memberships, indicating good classifiability. Without invalid masking, IPF would come to a similar level; with masking, it achieves only 33%. ACOLITE-DSF only reaches about 20%. ACOLITE-DSF mainly produces four types of spectra, turbid (85% in OWTs 12-14) or very clear water (9% in OWT 1), but mostly with low memberships. In the used test scenes, the first three classes of J17, representing oligotrophic ocean water, are almost non-represented in the other ACs (still 1% in POLYMER). J17 lacks specific classes for C2SX and eutrophic waters (BLOOM); if the AC produces such spectra, they are assigned elsewhere or are not classifiable – the same holds true for the other OWT schemes. Of the (in IPF only 5%) valid BLOOM pixels, most are well-classifiable; however, in C2RCC, the spectra often look like scattering waters, which are less well classifiable (only 49% good). C2SX waters occur much more frequently in the scenes, whereby particularly high spectra (such as in Figure 5X) are not classifiable. This is one of the reasons why A4O, with its potential underestimation of reflectance, achieves better classification results. Given the diversity of spectral maxima, A4O consistently provides useful memberships, even in rare cases with R_{rs} maximum at bands >560 nm (Figure 7I); but also IPF and ACOLITE-DSF provide many well classifiable spectra for these cases.

M14 focuses on coastal and inland waters with the fewest classes. The class distributions and classifiability of valid results

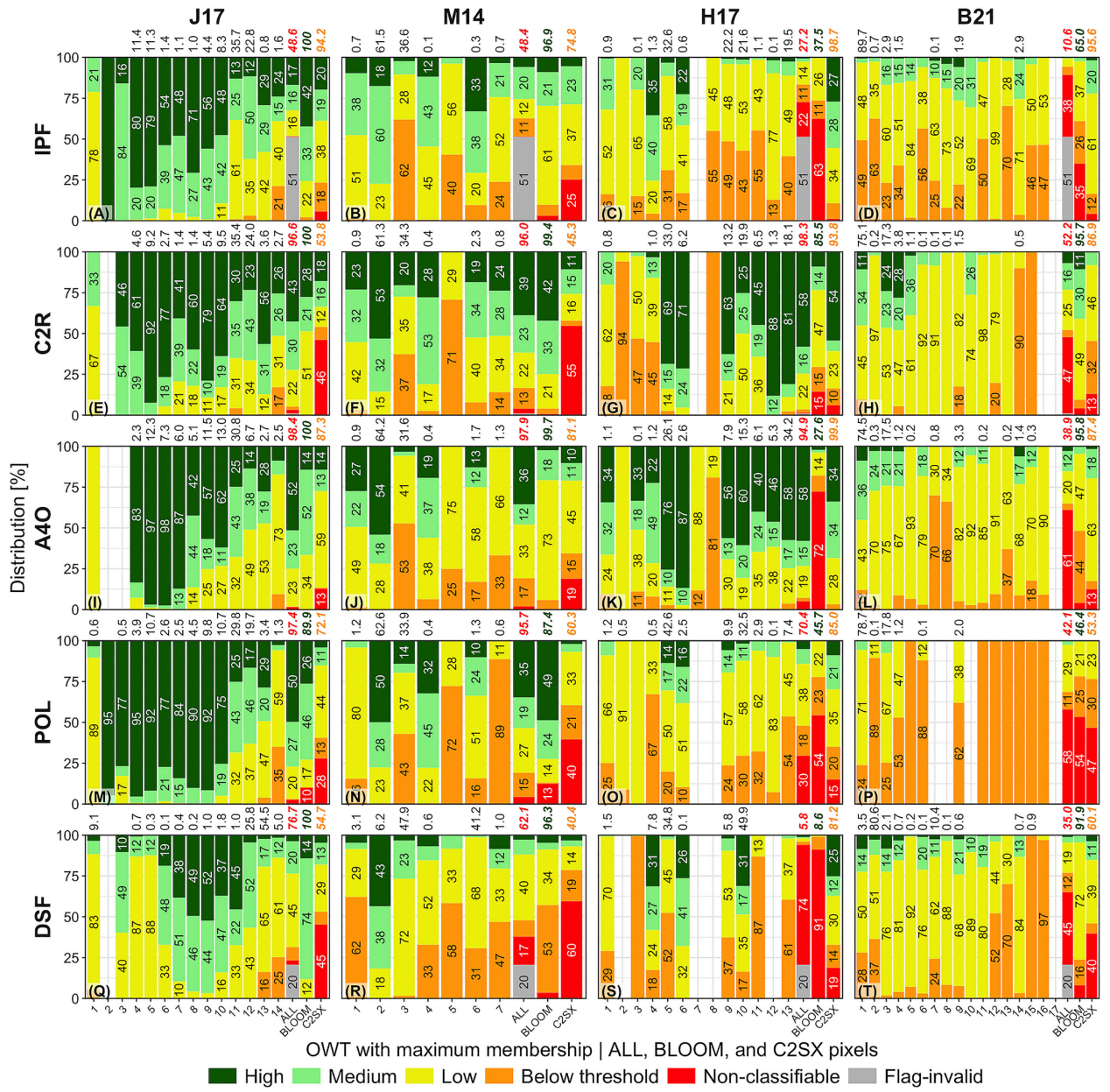


FIGURE 6
OWT classifiability of AC results of IPF **(A-D)**, C2RCC **(E-H)**, A4O **(I-L)**, POLYMER **(M-P)**, and ACOLITE-DSF **(Q-T)** for free-water pixels from ten OLCI scenes using four OWT methods with different numbers of classes. X-axis: OWT class allocation with maximum memberships, the last three columns each show total distribution for all pixels (31.5 million = 100%), only pixels with floating algae (BLOOM, <0.6% of all), and only extremely scattering waters (C2SX, 4%). The percentage of classifiable pixels is noted at the top (not shown if the share is smaller than 0.1%) and related to the total percentage share, which is indicated as a red number. Y-axis: distribution of total class membership for classifiable pixels (total memberships >0; see Table 3). Empty spaces show that the class is not present.

from IPF, C2RCC, A4O, and POLYMER are comparable. More than 95% fall into OWT 2 or 3 with 48 (A4O) to 62% (C2RCC) well-classifiable cases. ACOLITE-DSF produces a different class distribution with 48% in OWT 3 and 41% in 6, where overall the reflectances are less classifiable. Waters with high *NAP* concentration are often non-classifiable, only A4O achieves up to 81% classifiable results. In the case of red edge enhancement (BLOOM), A4O yields reasonably correct spectra, but achieves only lower memberships with M14 than the sometimes certainly incorrect results of C2RCC and POLYMER (as Figure 3D).

H17, just like A4O and C2RCC, was developed on the basis of Hydrolight radiative transfer simulations considering comparable inherent optical properties for the marine model, furthermore all three methods operate in a log-transformed form, therefore the two ACs have advantages here. Particular emphasis is placed on the spectral shape and the allowed variances are quite narrow in the H17 scheme, so that even relatively small deviations can lead to poor classification results. In fact, reflectances from IPF and ACOLITE-DSF are practically unclassifiable with H17, but almost all pixels with C2RCC and A4O with 74% medium or high

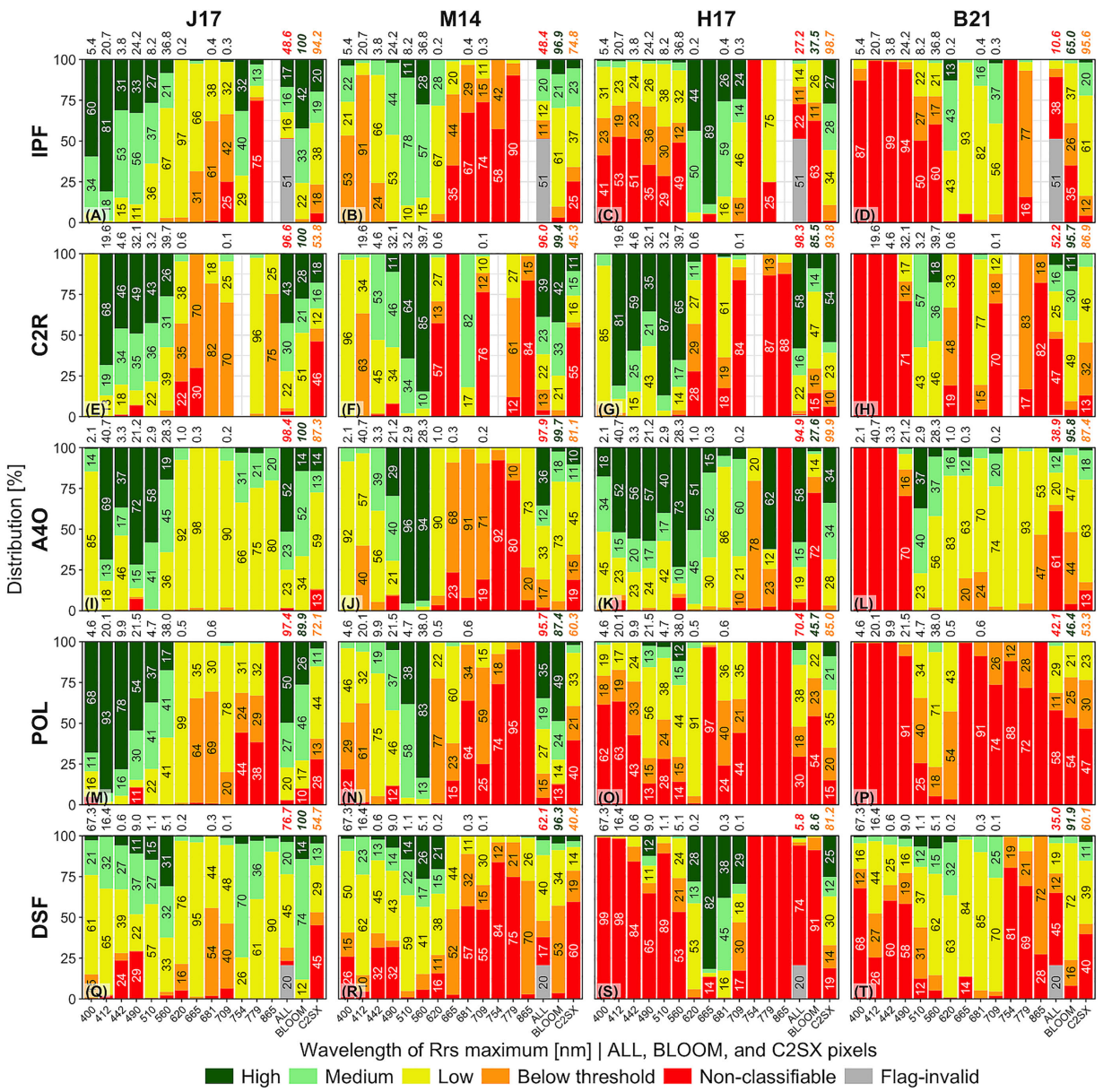


FIGURE 7
Same OWT classifiability of AC results as in Figure 6, but at X-axis with the OLCI wavelength of the R_{rs} maximum and corresponding percentage distribution noted at the top (this distribution is independent of the OWT method and therefore the same for all).

memberships are. Only half of the POLYMER reflectances can be classified as having weights above the threshold, but total membership remains mostly low. Insufficient memberships are usually found in highly scattering or productive waters, or when POLYMER provides negative reflectances in Case-1 waters. A4O matches all defined classes, but has low memberships for productive waters OWTs 7-8, that are masked with BLOOM. The reason for low memberships is likely the particularly high variance of natural R_{rs} at NIR bands, which is not well captured by the H17 χ^2-distribution. However, it is important that the class is identified correctly, which enables post-classification adaptation for optimal water algorithm selection. All other ACs do not deliver such spectral shapes; (wrong) C2RCC can be relatively well classified. The majority of spectra provided by IPF, POLYMER, or ACOLITE-DSF with the maximum in the short wavelengths (<560 nm) are not classifiable with H17, bright pixel spectra of IPF and ACOLITE-DSF, however, are often well classifiable. This shows that low reflectance values play a major role in the log-transformed classification and that the associated noise-level of some bands leads to shape variations not expected by H17.

Method B21 distinguishes most classes but has a focus on inland and coastal waters with little regard for the ocean. In addition, the shape is also given more consideration here, and the allowed variations are fairly limited. None of the AC methods succeeds in providing comprehensive spectra that can be classified with the method of B21. For C2RCC, nevertheless, half of the pixels are classifiable with u_t above the threshold (>10^{-4}). For all ACs, at least 85% of the classifiable cases are distributed among the first

three OWTs; the other 14 classes are sparsely used. C2RCC, A4O, and ACOLITE-DSF yield >90% usable spectra for BLOOM-labelled pixels. Again, C2RCC provides a higher percentage of well-classifiable results, but these are not in the intended classes (OWTs 14-17). A4O provides such spectra, the majority of which have useful memberships. Figure 7T shows slight advantages for the classifiability of ACOLITE-DSF spectra with the maximum in shorter wavelengths.

4 Discussions and outlook

4.1 Evaluation of AC methods

Inter-comparison results are often a snapshot in time, as both AC and water algorithms undergo continuous evolution. This paper refers to the most recent AC versions (as of October 2022) and is authored by some of their main developers. It is clear that the methods are at different maturity levels and that some have been optimized using observational data, which is also reflected in the effort for uncertainty products and flagging. A4O by Hieronymi et al. is a further development of C2RCC, but is not yet publicly available and there is no official reference for it as well. IPF is used in operational service, but one must also appreciate the continuous developments, where with the OLCI Collection-3 (since 2021) improvements have been achieved, e.g., for coastal waters (Zibordi et al., 2022). One cannot say that this is a Case-1 ocean color specific algorithm anymore, because the comparisons with Case-2 dominated match-up data document good agreement over most of the spectrum (with specific problems described here). Our comparisons with AERONET-OC and other data show better agreements for IPF than previously reported (especially also with regard to the previous IPF version Collection 2), e.g., Liu et al., 2021; Tilstone et al., 2021; Vanhellemont and Ruddick, 2021; Li et al., 2022; or Windle et al., 2022. One influencing factor is certainly the consideration of recommended flags and the use of the same IPF-SVC gains for all AC methods (except for POLYMER). Ideally, AC-specific SVC gains should be used, but these are not yet available for C2RCC, A4O, and ACOLITE-DSF; specially fitted SVC would have the potential to significantly improve their results. In the mentioned studies, likewise other versions of C2RCC, POLYMER, and ACOLITE-DSF are used; nevertheless, some similar observations can be confirmed, like the principal suitability of C2RCC and POLYMER for Case-2 waters especially for the central visible range. A4O and ACOLITE-DSF have partly less favorable ratings compared to AERONET-OC data, but both procedures are currently undergoing a greater dynamic in their development (they have undergone several updates in 2022). For all ACs, suitable methods must be found in the future to better identify obvious outliers in order to achieve better spatial and statistical evaluations. This also includes even better cloud identification. Considering the strict invalid flagging of IPF, however, one potentially loses considerable amounts of observational data, which should be reconsidered.

Spatial homogeneity, which has a strong impact on the number of match-ups, should be given more attention in future. For this purpose, measures to homogenize atmospheric properties at macro-pixel level (A4O & ACOLITE-DSF) as well as the log-transformation of the R_{rs} retrieval for very small values (A4O & C2RCC) have proven to be efficient. In combination with spectral smoothing (as in A4O), this is also advantageous for large areas affected by the South Atlantic Anomaly. One may argue that using a non-strict pixel-by-pixel atmospheric correction limits the high spatial resolution (of up to 300 m), however, relevant atmospheric and oceanographic features are usually larger in area and AC-induced noise is a significant source of uncertainty for ocean color products.

High accuracy over all magnitudes of retrieved R_{rs} is expected over the entire spectral range for various applications. Recent reviews summarize the requirements for ocean color remote sensing and especially atmospheric correction, e.g., in terms of deriving inherent optical properties of water (Werdell et al., 2018), phytoplankton diversity (Bracher et al., 2017), carbon content (Brewin et al., 2023), and essential biodiversity variables (Muller-Karger et al., 2018) – and this goes beyond the OLCI bands, also for future hyperspectral applications.

The selected AC method has often a significant influence on the derived ocean color products, e.g., the estimate of the concentration of carbon in water or the phytoplankton biomass with corresponding primary production. Juhls et al. (2022) for example compared *in situ* data with OLCI match-up results from IPF, C2RCC, and POLYMER and, moreover, different models for the estimation of *CDOM* absorption. This was done in order to investigate fluxes of related dissolved organic carbon from a large river across the turbid coastal zone into the clear Arctic Ocean, thus in high latitudes (here, POLYMER is identified as the most suitable). The strongest optical effect of *CDOM* is visible in the blue bands, where, according to our study, C2RCC and A4O have slight advantages also in terms of noise and spectral behavior; ACOLITE-DSF has noticeable problems. In this example, the actual performance may be inconsistent along the optical gradient, especially at short wavelengths; OWT-optimized water algorithms could potentially contribute to reducing the uncertainties (if the classification is successful).

Concentrations of phytoplankton in the order of $Chl > 1$ mg m^{-3} are usually necessary to hyper-spectrally distinguish special pigment absorption features and thereby phytoplankton diversity; moreover, the central visible range (450 to 650 nm) is particularly important for that (e.g., Xi et al., 2015; Xi et al., 2017; Bi et al., 2023). The intensity and spectral shape of the reflectance in the case of "moderate" algal blooms are generally well reproduced by all AC methods investigated (e.g., Figure 3C). Results from the current version of A4O, however, mostly show an underestimation (which may also have to do with influences of the angle normalization that still need to be clarified). At higher *Chl* (>10 mg m^{-3}), the red edge absorption feature becomes important in the *Chl* retrieval (e.g., Gons, 1999; Ruddick et al., 2001). High concentrations of cyanobacteria with possible scum at the water surface, which is a frequent phenomenon in inland waters and the Baltic Sea, are a particular challenge for AC. Spectra from IPF, C2RCC, and POLYMER are mostly untrustworthy here and the results are partly not sufficiently accompanied by warnings (Figure 3D). A4O, which has a specific warning flag for this, provides a plausible spectral

shape and indicates enhanced R_{rs} uncertainties in corresponding products (which is also reasoned by the usual small-scale heterogeneity of such blooms). The spectra from A4O can be assigned to the designated water classes in H17 and B21, but often with low memberships. In the shown example (Figure 3D), the shape of ACOLITE-DSF is also plausible except for the first two bands that are likely overestimated and may be impacted by smile correction artefacts (the spectra are usually not well-classifiable in H17 or B21). However, there is a possible advantage of the dark-spectrum-fitting approach in the range 500-700 nm, which can be helpful for phycocyanin feature detection (a marker for cyanobacteria).

The other example with a bloom of coccolithophores (Figure 3G) shows comparable spectral shapes delivered by all ACs, but also clear differences in the brightness of the retrieved reflectance (although all results are of a realistic order of magnitude, e.g., Cazzaniga et al., 2021). Methods to remotely sense particulate inorganic carbon focus on optical detection of coccolithophores, e.g., with a color index made from ratios of green, red, and NIR bands (Mitchell et al., 2017; Brewin et al., 2023); here significant differences would occur depending on the AC used. Regarding the exploitation of red and NIR bands in ocean-water algorithms (also important for the estimation of the fluorescence line height), the spatial homogeneity and negative reflectances are improvable for IPF and POLYMER, and the removal of artefacts from small-scale atmospheric variability for ACOLITE-DSF.

4.2 Discussion on OWT frameworks

The distinction of optical water types is important for many aspects of marine biology, physical oceanography, underwater visibility, etc., and the definition of specific properties has a long tradition (e.g., Jerlov, 1976). Current research aims to determine reliable water quality characteristics from satellite data for the entire aquatic continuum of land-coast-ocean. However, a balance between effort and benefit must be found here and care must be taken in satellite images to ensure no unwanted discontinuities arise. There may be specific challenges for oceanographic or limnological questions, e.g., with regard to water constituents, sun glint, whitecaps, shallow water, or adjacency effects, but from an optical remote sensing point of view, it does not make much sense to reduce oneself to one application. This common disconnection actually hinders reliable studies on matter transfer from land to the sea, which is important for the carbon cycle, for example.

The lack of classes with characteristic optical features is a problem for all OWT methods that were examined, e.g., classes representative of oligotrophic ocean, very high *NAP* concentrations, or hyper-eutrophic waters are often missing. On the other hand, there may be spectral classes that are difficult to explain from an IOP perspective. Especially inland water OWT frameworks are often based on clustering of large *in situ* data collections, which include potential measurement errors such as adjacency effects, bottom reflections or inadequate sky-glint correction. Consequently, classes with questionable mean reflectances can also be defined. Some OWT frameworks are primarily used to evaluate the quality of R_{rs} spectra (e.g., Wei et al., 2016). An independent control is the Quality Water Index Polynomial (QWIP) method of Dierssen et al. (2022). The QWIP score for hyperspectral data should not exceed 0.2, for multispectral data as for OLCI the nominal threshold can be relaxed to 0.3, values above the threshold should be subject to additional checks. In fact, the QWIP method does not include "green types" with R_{rs} maximum in the NIR, such as defined by B21. However, few classes of B21, e.g., their OWT 2, receive a QWIP score close to 0.2 (note that some OWT frameworks like Spyrakos et al. (2018) define classes with higher scores that possibly fail the QWIP quality control). The B21 OWT 2 class-mean spectrum has a local minimum at 440 nm (Figure 1D). Our OWT analysis shows that B21-classifiable spectra of IPF, C2RCC, A4O, and POLYMER are in this OWT 2 with less than 1%, whereas 80% of ACOLITE-DSF spectra fall into this class. The comparisons with AERONET-OC indicate an underestimation of the atmospheric signal of ACOLITE-DSF in blue bands; furthermore, there is reason to conclude that adjacency effects, e.g., from bright clouds, play a role (Bulgarelli and Zibordi, 2018). Indeed, QWIP can be used directly for quality control for satellite-derived R_{rs}, e.g., Turner et al. (2022) compared results from ACOLITE-DSF and POLYMER (in other versions) as well as the standard NASA SeaDAS algorithm for OLCI (L2gen) for an estuary at the US East Coast finding POLYMER to be the preferred approach. Applying the QWIP score to the AC results of our study for valid free water pixels in the scenes and assuming a threshold of ≤0.2 gives 100% reliable R_{rs} for A4O and C2RCC, 99% for POLYMER, 81% for IPF, and 45% for ACOLITE-DSF. With a less stringent threshold of ≤0.3, ACOLITE-DSF achieves about 88% quality-assured Rrs. With a very strict QWIP score of ≤0.1, A4O still reaches 99.4%. This means that virtually all results from A4O, C2RCC and POLYMER pass the QWIP quality control with slight advantages for A4O. But as mentioned, the retrieved R_{rs} can actually have the "wrong" shape.

The ability to fill all classes and generally good classifiability of reflectances from POLYMER in the J17 framework or from A4O in H17 shows the great advantages of matching AC and OWT frameworks. As described, however, there is a danger of over-valuing false spectra from the AC or measurements/simulations. Nevertheless, it has also proven ineffective not to allow large variances from the expected spectrum, i.e., potential errors of the AC. Obviously good spectra from IPF or POLYMER, but also from A4O, cannot be classified well with H17. This is especially true for B21, where in principle the results of all ACs do not fulfil the expectations.

A comprehensive evaluation of the OWT systems and of the performance of different atmospheric corrections is difficult because the actual areas of application and validity overlap sometimes only slightly, i.e., inland waters vs. ocean. Large areas of inland waters are invalid flagged or at least have warning flags raised, so it is not surprising that almost all data fall into one or only a few designated ocean classes for M14 or B21. However, some of the AC methods give plausible and usable results for inland waters, which is partly evident in the comparison with AERONET-OC. Leaving aside the fact that there are also erroneous estimates of the R_{rs} shape, C2RCC and A4O produce classifiable results of at least 95% of the cases in the OWT frameworks J17, M14, and H17, where A4O covers more

intended classes. POLYMER also achieves this classifiability rate for J17 and M14, but only 70% for H17. Considering the recommended flags, the suitability of IPF and ACOLITE-DSF in the investigated classifications is insufficient. The work by Liu et al. (2021) also compares IPF, C2RCC, POLYMER, and other OLCI AC methods in context with the optical water type and quality control framework of Wei et al. (2016), which differentiates 22 classes; they conclude that POLYMER has best performance followed by C2RCC and IPF.

Figure 3A illustrates a remaining problem, namely that fundamentally different spectral shapes of the derived R_{rs} can often occur in the transition from coast to sea, when the freshwater *CDOM* concentration is diluted. In some cases, there are features in the TOA signal that can be used to flag potential uncertainties, e.g., a red-edge enhancement (Figure 3D). The ambiguities of the optical effects of different components in the water, at the air-sea interface, and in the atmosphere are relatively large for spectrally smooth TOA reflectance with color nuances of blue. Without systematic comparisons with suitable *in situ* data, we have no means of determining which spectral shape is correct, i.e., which OWT is present. For this purpose, more hyperspectral fiducial reference measurements especially with maximum R_{rs} at wavelengths ≤510 nm are needed.

5 Conclusions

Five atmospheric correction methods for Sentinel-3/OLCI ocean color imagery were compared in terms of spatial and spectral results and individual flagging. The models under investigation are the most recent versions of OLCI L2 baseline atmospheric correction (IPF), C2RCC, a new method A4O, POLYMER, and ACOLITE-DSF. The extent to which AC methods provide useful and continuous results for a wide variety of natural waters was investigated. For this purpose, the satellite-derived remote-sensing reflectances were evaluated in four optical water type schemes.

Flagging leads in some cases to major limitations in data exploitation even for clearly visible water areas; IPF recommends very strict criteria, resulting in 50% less coverage in our satellite imagery. Output of R_{rs} with negative values is a major issue here. However, we have also shown that many cases are inadequately flagged by the AC methods; an example are high concentrations of cyanobacteria at the sea surface. Only A4O has a dedicated warning flag for floating algae, but A4O is valid here and delivers as the only one reasonable R_{rs} over the entire spectrum. Nevertheless, a revision of the individual flags with respect to spatial and spectral inconsistencies is recommended for all AC methods. Cloud and cloud shadow detection also need to be improved for all methods, as corresponding deficiencies are reflected in the derived water quality products.

Pixel-based approximation of atmospheric properties and reflectance leads to AC-induced spatial noise. High spatial heterogeneity, especially at low reflectance (and overcorrected negative values), leads to considerable losses of possible match-ups with *in situ* measurement data. The noise level can be effectively reduced by means of log-transformation in the R_{rs} retrieval process and appropriate smoothing, which is both applied in A4O. Mainly because of its high spatial homogeneity, A4O achieves significantly more match-ups with AERONET-OC data than all other methods, namely at least twice as many points in the blue and NIR bands. The number of match-ups achieved also affects the statistical evaluation of R_{rs} retrieval performance. Comparison with *in situ* data, which are more representative of coastal and inland waters, shows that the spectral shape and magnitude of R_{rs} is essentially well reproduced by IPF, C2RCC, and POLYMER, at least in the central visible range. The current version of A4O mostly gives a reasonable shape of R_{rs}, but often slightly lower values than observed. ACOLITE-DSF provides good matches for bright pixel, i.e., highly scattering waters, but has significant deficits for low water reflectance in particular in the short wavelengths. Hyperspectral *in situ* data in the 400 to 865 nm range are unfortunately not available for all water types, especially clear oceanic and hyper-eutrophic cases are missing; however, this would be important to have for future OWT-related validation of AC methods.

Optical water type classification is used for the selection of appropriate water quality algorithms and seamless blending of their results. This requires good classifiability of the AC-derived R_{rs} and it is advantageous if all spectral forms of R_{rs} can be reproduced. Comparison of the five AC methods shows that A4O provides the greatest optical flexibility. A4O provides more than 95% usable results for three OWT frameworks, namely by Jackson et al. (2017); Moore et al. (2014), and Hieronymi et al. (2017); furthermore, A4O populates most classes, including hyper-eutrophic cases. C2RCC also achieves >95% useful results for the three OWT frameworks, but has failing retrievals for intense cyanobacterial blooms. For the OWT method by Jackson et al. (2017), the reflectances of POLYMER are best classifiable; this OWT scheme was developed on the basis of such data. POLYMER also gives mostly well-classifiable results for M14, but falls off for H17. The general classifiability of R_{rs} from IPF is comparable to POLYMER, but considering the recommended valid-pixel-expression, the suitability of IPF for OWT classification is insufficient. ACOLITE-DSF is very focused on waters with high concentrations of non-algal particles; there are significant problems at low marine reflectances, limiting broad application in the OWT context. The results of all AC methods, for the most part, could not be well-classified using the OWT system of Bi et al. (2019), and Bi et al. (2021), which has its focus of application on inland waters; yet comparisons with *in situ* data suggest that the rough shape of R_{rs} is well reproduced by most ACs.

So far, OWT algorithms have focused too much either on marine or limnological applications; for a comprehensive usability, missing classes should be added. The classification schemes of Hieronymi et al. (2017) provides a good basis, as it includes representative classes for ocean, coastal and inland waters. However, this method in particular shows that error tolerances should be increased in order to achieve better classifiability of AC results, which is the basis for a fully comprehensive exploitation of an OWT system. The focusing of an OWT system on the spectral shape, through log-transformed normalization, increases the sensitivity to noise and small inaccuracies, and thus leads to reduced classification performance. It is generally advantageous if

the OWT classification system is aligned with the performance spectrum of the atmospheric correction and vice versa.

Data availability statement

The ten OLCI scenes used in this work were saved as NetCDF files along with all the results of the five atmospheric correction models and made available at the open repository Zenodo (Hieronymi et al., 2023). The data can be found online at: https://doi.org/10.5281/zenodo.7567534.

Author contributions

MH conceptualized the study, prepared, and wrote the original draft. MH, ES, DB, CL, and DM were in charge of the data curation and satellite data processing. SB performed independent OWT analysis. DM performed independent match-up analysis. MH and ES conducted the spatial-spectral studies. MH, KS, CB, FS, QV, and DM delivered background information on atmospheric correction methods. All authors contributed to the article and approved the submitted version.

Funding

The Helmholtz Association with the research program Earth and Environment (PoF IV) funded this study. Additional support was provided by the Hereon-I^{2}B project PhytoDive and the European Copernicus Marine Environment Monitoring Service (EU, 77-CMEMS-TAC-OC). Moreover, this work benefited from achievements of the following projects: CoastColour (ESA), OC-CCI (ESA), SEOM-C2X (ESA), OC-BPC (EUMETSAT), and WEnMAP (BMWi & DLR, 50EE1718).

Acknowledgments

This work is based on free and open satellite data from the European Union's Copernicus Programme provided by ESA and EUMETSAT. In addition, *in situ* data from AERONET-OC were used, for which we thank the PIs: G. Zibordi, S. Ahmed, A. Gilerson, S. Kratzer, T. Schroeder, H. Feng, H.M. Sosik, A. Weidemann, B. Gibson, and R. Arnone. Moreover, D. Vansteenwegen, the Flemish Marine Institute, and POM West-Vlaanderen are thanked for the installation, operation and provision of PANTHYR data. We also thank R. Röttgers, H. Krasemann, C. Mazeran, M. Peters, M. Böttcher, and V. Brando for inspiring discussions and support. Finally, we would like to thank the editor, J.A. Concha, and three experts for their thorough review of the paper and helpful comments.

Conflict of interest

Authors KS, DM, CL, and CB are employed by the company Brockmann Consult GmbH, Germany. Author FS is employed by the company HYGEOS, France.

The remaining authors declare that the research was conducted in the absence of any commercial or financial relationships that could be construed as a potential conflict of interest.

The handling editor JC declared a past co-authorship with the author QV and reviewer IC declared a past collaboration with the author DM to the handling editor.

Publisher's note

All claims expressed in this article are solely those of the authors and do not necessarily represent those of their affiliated organizations, or those of the publisher, the editors and the reviewers. Any product that may be evaluated in this article, or claim that may be made by its manufacturer, is not guaranteed or endorsed by the publisher.

References

Antoine, D., and Morel, A. (1998). Relative importance of multiple scattering by air molecules and aerosols in forming the atmospheric path radiance in the visible and near-infrared parts of the spectrum. *Appl. Opt.* 37 (12), 2245–2259. doi: 10.1364/AO.37.002245

Antoine, D., and Morel, A. (1999). A multiple scattering algorithm for atmospheric correction of remotely sensed ocean colour (MERIS instrument): principle and implementation for atmospheres carrying various aerosols including absorbing ones. *Int. J. Remote Sens.* 20 (9), 1875–1916. doi: 10.1080/014311699212533

Aurin, D., Mannino, A., and Franz, B. (2013). Spatially resolving ocean color and sediment dispersion in river plumes, coastal systems, and continental shelf waters. *Remote Sens. Environ.* 137, 212–225. doi: 10.1016/j.rse.2013.06.018

Bi, S., Hieronymi, M., and Röttgers, R. (2023). Bio-geo-optical modelling of natural waters. *Front. Mar. Sci.* 10. doi: 10.3389/fmars.2023.1196352

Bi, S., Li, Y., Liu, G., Song, K., Xu, J., Dong, X., et al. (2021). Assessment of algorithms for estimating chlorophyll-a concentration in inland waters: a round-robin scoring method based on the optically fuzzy clustering. *IEEE Trans. Geosci. Remote Sens.* 60, 1–17. doi: 10.1109/TGRS.2021.3058556

Bi, S., Li, Y., Wang, Q., Lyu, H., Liu, G., Zheng, Z., et al. (2018). Inland water atmospheric correction based on turbidity classification using OLCI and SLSTR synergistic observations. *Remote Sens.* 10 (7), 1002. doi: 10.3390/rs10071002

Bi, S., Li, Y., Xu, J., Liu, G., Song, K., Mu, M., et al. (2019). Optical classification of inland waters based on an improved fuzzy c-means method. *Opt. Express.* 27, 34838–34856. doi: 10.1364/OE.27.034838

Bracher, A., Bouman, H. A., Brewin, R. J., Bricaud, A., Brotas, V., Ciotti, A. M., et al. (2017). Obtaining phytoplankton diversity from ocean color: a scientific roadmap for future development. *Front. Mar. Sci.* 4. doi: 10.3389/fmars.2017.00055

Brewin, R. J. W., Sathyendranath, S., Kulk, G., Rio, M.-H., Concha, J. A., Bell, T. G., et al. (2023). Ocean carbon from space: current status and priorities for the next decade. *Earth-Science Rev.* 240, 104386. doi: 10.1016/j.earscirev.2023.104386

Brockmann, C., Doerffer, R., Peters, M., Kerstin, S., Embacher, S., and Ruescas, A. (2016). "Evolution of the C2RCC neural network for sentinel 2 and 3 for the retrieval of ocean colour products in normal and extreme optically complex waters," in *Proc. living planet symposium.*, vol. SP-740. (Prague, Czech Republic: ESA), 1–6.

Brockmann, C., Paperin, M., Danne, O., and Ruescas, A. (2013). "Multi-sensor cloud screening and validation: IdePix and PixBox," in *Proc. living planet symposium.*, vol. SP-722. (Edinburgh, UK ESA), 9–13.

Bulgarelli, B., and Zibordi, G. (2018). On the detectability of adjacency effects in ocean color remote sensing of mid-latitude coastal environments by SeaWiFS, MODIS-a, MERIS, OLCI, OLI and MSI. *Remote Sens. Environ.* 209, 423–438. doi: 10.1016/j.rse.2017.12.021

Cazzaniga, I., Zibordi, G., and Mélin, F. (2021). Spectral variations of the remote sensing reflectance during coccolithophore blooms in the Western black Sea. *Remote Sens. Environ.* 264, 112607. doi: 10.1016/j.rse.2021.112607

Cazzaniga, I., Zibordi, G., and Mélin, F. (2023). Spectral features of ocean colour radiometric products in the presence of cyanobacteria blooms in the Baltic Sea. *Remote Sens. Environ.* 287, 113464. doi: 10.1016/j.rse.2023.113464

Cazzaniga, I., Zibordi, G., Mélin, F., Kwiatkowska, E., Talone, M., Dessailly, D., et al. (2022). Evaluation of OLCI neural network radiometric water products. *IEEE Geosci. Remote Sens. Let.* 19, 1–5. doi: 10.1109/LGRS.2021.3136291

Dierssen, H. M. (2019). Hyperspectral measurements, parameterizations, and atmospheric correction of whitecaps and foam from visible to shortwave infrared for ocean color remote sensing 7, 14. doi: 10.3389/feart.2019.00014

Dierssen, H. M., Vandermeulen, R. A., Barnes, B. B., Castagna, A., Knaeps, E., and Vanhellemont, Q. (2022). QWIP: a quantitative metric for quality control of aquatic reflectance spectral shape using the apparent visible wavelength. *Front. Remote Sens.* 3. doi: 10.3389/frsen.2022.869611

Doerffer, R., and Schiller, H. (2007). The MERIS case 2 water algorithm. *Int. J. Remote Sens.* 28 (3-4), 517–535. doi: 10.1080/01431160600821127

Eleveld, M. A., Ruescas, A. B., Hommersom, A., Moore, T. S., Peters, S. W., and Brockmann, C. (2017). An optical classification tool for global lake waters. *Remote Sens.* 9 (5), 420. doi: 10.3390/rs9050420

EUMETSAT (2021). *Sentinel-3 OLCI L2 report for baseline collection OL_L2M_003.*.

EUMETSAT (2022). *Recommendations for sentinel-3 OLCI ocean colour product validations in comparison with in situ measurements – matchup protocols.*.

Fomferra, N., Böttcher, M., Zühlke, M., Brockmann, C., and Kwiatkowska, E. (2012). "Calvalus: full-mission EO cal/val, processing and exploitation services," in *Proc. IEEE international geoscience and remote sensing symposium (IGARSS'12).*(Munich, Germany), 5278–5281.

Frouin, R. J., Franz, B. A., Ibrahim, A., Knobelspiesse, K., Ahmad, Z., Cairns, B., et al. (2019). Atmospheric correction of satellite ocean-color imagery during the PACE era. *Front. Earth Sci.* 7. doi: 10.3389/feart.2019.00145

GCOS (2011). "Systematic observation requirements for satellite-based products for climate," in *2011 update.*, vol. 154. (WMO GCOS Rep.), 127.

Giannini, F., Hunt, B. P., Jacoby, D., and Costa, M. (2021). Performance of OLCI sentinel-3A satellite in the northeast pacific coastal waters. *Remote Sens. Environ.* 256, 112317. doi: 10.1016/j.rse.2021.112317

Gons, H. J. (1999). Optical teledetection of chlorophyll a in turbid inland waters. *Environ. Sci. Technol.* 33 (7), 1127–1132. doi: 10.1021/es9809657

Gordon, H. R. (2021). Evolution of ocean color atmospheric correction: 1970–2005. *Remote Sens.* 13 (24), 5051. doi: 10.3390/rs13245051

Gordon, H. R., and Wang, M. (1994). Retrieval of water-leaving radiance and aerosol optical thickness over the oceans with SeaWiFS: a preliminary algorithm. *Appl. Opt.* 33 (3), 443–452. doi: 10.1364/AO.33.000443

Gossn, J. I., Ruddick, K. G., and Dogliotti, A. I. (2019). Atmospheric correction of OLCI imagery over extremely turbid waters based on the red, NIR and 1016 nm bands and a new baseline residual technique. *Remote Sens.* 11 (3), 220. doi: 10.3390/rs11030220

Goyens, C., Jamet, C., and Schroeder, T. (2013). Evaluation of four atmospheric correction algorithms for MODIS-aqua images over contrasted coastal waters. *Remote Sens. Environ.* 131, 63–75. doi: 10.1016/j.rse.2012.12.006

Guanter, L., Ruiz-Verdú, A., Odermatt, D., Giardino, C., Simis, S., Estellés, V., et al. (2010). Atmospheric correction of ENVISAT/MERIS data over inland waters: validation for European lakes. *Remote Sens. Environ.* 114 (3), 467–480. doi: 10.1016/j.rse.2009.10.004

Hieronymi, M. (2019). Spectral band adaptation of ocean color sensors for applicability of the multi-water biogeo-optical algorithm ONNS. *Opt. Express.* 27 (12), A707–A724. doi: 10.1364/OE.27.00A707

Hieronymi, M., Bi, S., Müller, D., Schütt, E. M., Behr, D., Brockmann, C., et al. (2023). Supplementary dataset to the publication by Hieronymi et al.: "Ocean color atmospheric correction methods in view of usability for different optical water types". *Zenodo*. doi: 10.5281/zenodo.7567534

Hieronymi, M., Krasemann, H., Müller, D., Brockmann, C., Ruescas, A. B., Stelzer, K., et al. (2016). "Ocean colour remote sensing of extreme case-2 waters," in *Proc. Living planet symposium*, vol. SP-740. (Prague, Czech Republic: ESA), 1–5.

Hieronymi, M., Müller, D., and Doerffer, R. (2017). The OLCI neural network swarm (ONNS): a bio-Geo-Optical algorithm for open ocean and coastal waters. *Front. Mar. Sci.* 4. doi: 10.3389/fmars.2017.00140

Hollmann, R., Merchant, C. J., Saunders, R., Downy, C., Buchwitz, M., Cazenave, A., et al. (2013). The ESA climate change initiative: satellite data records for essential climate variables. *Bull. Am. Meteorological Soc.* 94 (10), 1541–1552. doi: 10.1175/BAMS-D-11-00254.1

Hunter, P. D., Matthews, M. W., Kutser, T., and Tyler, A. N. (2016). "Remote sensing of cyanobacterial blooms in inland, coastal, and ocean waters," in *Handbook of cyanobacterial monitoring and cyanotoxin analysis.*. Eds. J. Meriluoto, L. Spoof and G. A. Codd, 89–99. doi: 10.1002/9781119068761.ch9

IOCCG (2010). *Atmospheric correction for remotely-sensed ocean-colour products.* Vol. 10. Ed. M. Wang (Dartmouth, Canada: Reports of the International Ocean-Colour Coordinating Group), 84. doi: 10.25607/OBP-101

IOCCG (2019). *Uncertainties in ocean colour remote sensing.* Vol. 18. Ed. F. Mélin (Dartmouth, Canada: Reports of the International Ocean-Colour Coordinating Group), 164. doi: 10.25607/OBP-696

Jackson, T., Sathyendranath, S., and Mélin, F. (2017). An improved optical classification scheme for the ocean colour essential climate variable and its applications. *Remote Sens. Environ.* 203, 152–161. doi: 10.1016/j.rse.2017.03.036

Jerlov, N. G. (1976). *Marine optics.* (Elsevier). Available at: https://books.google.de/books?hl=de&lr=&id=tzwgrtnW_lYC&oi=fnd&pg=PP1&ots=23jJaYPV6i&sig=K7jZxQsizMxC_QOZ1rS2rQeL72o#v=onepage&q&f=false.

Jia, T., Zhang, Y., and Dong, R. (2021). A universal fuzzy logic optical water type scheme for the global oceans. *Remote Sens.* 13 (19), 4018. doi: 10.3390/rs13194018

Juhls, B., Matsuoka, A., Lizotte, M., Bécu, G., Overduin, P. P., El Kassar, J., et al. (2022). Seasonal dynamics of dissolved organic matter in the Mackenzie delta, Canadian Arctic waters: implications for ocean colour remote sensing. *Remote Sens. Environ.* 283, 113327. doi: 10.1016/j.rse.2022.113327

Kajiyama, T., D'Alimonte, D., and Zibordi, G. (2018). Algorithms merging for the determination of chlorophyll-a concentration in the black Sea. *IEEE Geosci. Remote Sens. Let.* 16 (5), 677–681. doi: 10.1109/LGRS.2018.2883539

Kieber, R. J., Whitehead, R. F., Reid, S. N., Willey, J. D., and Seaton, P. J. (2006). Chromophoric dissolved organic matter (CDOM) in rainwater, southeastern north Carolina, USA. *J. Atmo. Chem.* 54 (1), 21–41. doi: 10.1007/s10874-005-9008-4

Li, Q., Jiang, L., Chen, Y., Wang, L., and Wang, L. (2022). Evaluation of seven atmospheric correction algorithms for OLCI images over the coastal waters of qinhuangdao in bohai Sea. *Regional Stud. Mar. Sci.* 56, 102711. doi: 10.1016/j.rsma.2022.102711

Liu, H., He, X., Li, Q., Hu, X., Ishizaka, J., Kratzer, S., et al. (2021). Evaluation of ocean color atmospheric correction methods for sentinel-3 OLCI using global automatic *in situ* observations. *IEEE Trans. Geosci. Remote Sens.* 60, 1–19. doi: 10.1109/TGRS.2021.3136243

Liu, H., Hu, S., Zhou, Q., Li, Q., and Wu, G. (2019). Revisiting effectiveness of turbidity index for the switching scheme of NIR-SWIR combined ocean color atmospheric correction algorithm. *Int. J. Appl. Earth Obs. Geoinf.* 76, 1–9. doi: 10.1016/j.jag.2018.10.010

Martin Traykovski, L. V., and Sosik, H. M. (2003). Feature-based classification of optical water types in the Northwest Atlantic based on satellite ocean color data. *J. Geophys. Res. Oceans.* 108 (C5). doi: 10.1029/2001JC001172

Mélin, F., and Vantrepotte, V. (2015). How optically diverse is the coastal ocean? *Remote Sens. Environ.* 160, 235–251. doi: 10.1016/j.rse.2015.01.023

Mélin, F., Vantrepotte, V., Clerici, M., D'Alimonte, D., Zibordi, G., Berthon, J.-F., et al. (2011). Multi-sensor satellite time series of optical properties and chlorophyll-a concentration in the Adriatic Sea. *Prog. Oceanogr.* 91, 229–244. doi: 10.1016/j.pocean.2010.12.001

Minu, P., Lotliker, A. A., Shaju, S. S., Ashraf, P. M., Kumar, T. S., and Meenakumari, B. (2016). Performance of operational satellite bio-optical algorithms in different water types in the southeastern Arabian Sea. *Oceanologia.* 58 (4), 317–326. doi: 10.1016/j.oceano.2016.05.005

Mitchell, C., Hu, C., Bowler, B., Drapeau, D., and Balch, W. M. (2017). Estimating particulate inorganic carbon concentrations of the global ocean from ocean color measurements using a reflectance difference approach. *J. Geophys. Res. Oceans.* 122 (11), 8707–8720. doi: 10.1002/2017JC013146

Mobley, C. D. (1994). *Light and water: radiative transfer in natural waters.* (Academic press).

Mograne, M. A., Jamet, C., Loisel, H., Vantrepotte, V., Mériaux, X., and Cauvin, A. (2019). Evaluation of five atmospheric correction algorithms over French optically-complex waters for the sentinel-3A OLCI ocean color sensor. *Remote Sens.* 11 (6), 668. doi: 10.3390/rs11060668

Moore, G. F., Aiken, J., and Lavender, S. J. (1999). The atmospheric correction of water colour and the quantitative retrieval of suspended particulate matter in case II waters: application to MERIS. *Int. J. Remote Sens.* 20 (9), 1713–1733. doi: 10.1080/014311699212434

Moore, T. S., Campbell, J. W., and Feng, H. (2001). A fuzzy logic classification scheme for selecting and blending satellite ocean color algorithms. *IEEE Trans. Geosci. Remote Sens.* 39, 1764–1776. doi: 10.1109/36.942doi

Moore, T. S., Dowell, M. D., Bradt, S., and Verdu, A. R. (2014). An optical water type framework for selecting and blending retrievals from bio-optical algorithms in lakes and coastal waters. *Remote Sens. Environ.* 143, 97–111. doi: 10.1016/j.rse.2013.11.021

Morel, A., and Prieur, L. (1977). Analysis of variations in ocean color. *Limnology Oceanography.* 22 (4), 709–722. doi: 10.4319/lo.1977.22.4.0709

Müller, D., Krasemann, H., Brewin, R. J., Brockmann, C., Deschamps, P. Y., Doerffer, R., et al. (2015a). The ocean colour climate change initiative: i. a methodology for assessing atmospheric correction processors based on in-situ measurements. *Remote Sens. Environ.* 162, 242–256. doi: 10.1016/j.rse.2013.11.026

Müller, D., Krasemann, H., Brewin, R. J., Brockmann, C., Deschamps, P. Y., Doerffer, R., et al. (2015b). The ocean colour climate change initiative: II. spatial and temporal homogeneity of satellite data retrieval due to systematic effects in atmospheric correction processors. *Remote Sens. Environ.* 162, 257–270. doi: 10.1016/j.rse.2015.01.033

Muller-Karger, F. E., Hestir, E., Ade, C., Turpie, K., Roberts, D. A., Siegel, D., et al. (2018). Satellite sensor requirements for monitoring essential biodiversity variables of coastal ecosystems. *Ecol. Appl.* 28 (3), 749–760. doi: 10.1002/eap.1682

Nobileau, D., and Antoine, D. (2005). Detection of blue-absorbing aerosols using near infrared and visible (ocean color) remote sensing observations. *Remote Sens. Environ.* 95 (3), 368–387. doi: 10.1016/j.rse.2004.12.020

Park, Y.-J., and Ruddick, K. G. (2005). Model of remote-sensing reflectance including bidirectional effects for case 1 and case 2 waters. *Appl. Opt.* 44 (7), 1236–1249. doi: 10.1364/AO.44.001236

Qi, L., Hu, C., Duan, H., Cannizzaro, J., and Ma, R. (2014). A novel MERIS algorithm to derive cyanobacterial phycocyanin pigment concentrations in a eutrophic lake: theoretical basis and practical considerations. *Remote Sens. Environ.* 154, 298–317. doi: 10.1016/j.rse.2014.08.026

Qin, P., Simis, S. G., and Tilstone, G. H. (2017). Radiometric validation of atmospheric correction for MERIS in the Baltic Sea based on continuous observations from ships and AERONET-OC. *Remote Sens. Environ.* 200, 263–280. doi: 10.1016/j.rse.2017.08.024

Reinart, A., and Kutser, T. (2006). Comparison of different satellite sensors in detecting cyanobacterial bloom events in the Baltic Sea. *Remote Sens. Environ.* 102 (1-2), 74–85. doi: 10.1016/j.rse.2006.02.013

Ruddick, K. G., Gons, H. J., Rijkeboer, M., and Tilstone, G. (2001). Optical remote sensing of chlorophyll a in case 2 waters by use of an adaptive two-band algorithm with optimal error properties. *Appl. Opt.* 40 (21), 3575–3585. doi: 10.1364/AO.40.003575

Sathyendranath, S., Brewin, R. J., Jackson, T., Mélin, F., and Platt, T. (2017). Ocean-colour products for climate-change studies: what are their ideal characteristics? *Remote Sens. Environ.* 203, 125–138. doi: 10.1016/j.rse.2017.04.017

Sathyendranath, S., Jackson, T., Brockmann, C., Brotas, V., Calton, B., Chuprin, A., et al. (2021). *ESA Ocean colour climate change initiative (Ocean_Colour_cci): version 5.0 data*. (NERC EDS Centre for Environmental Data Analysis). doi: 10.5285/1dbe7a109c0244aaad713e078fd3059a

Schroeder, T., Schaale, M., Lovell, J., and Blondeau-Patissier, D. (2022). An ensemble neural network atmospheric correction for sentinel-3 OLCI over coastal waters providing inherent model uncertainty estimation and sensor noise propagation. *Remote Sens. Environ.* 270, 112848. doi: 10.1016/j.rse.2021.112848

Shi, K., Li, Y., Li, L., Lu, H., Song, K., Liu, Z., et al. (2013). Remote chlorophyll-a estimates for inland waters based on a cluster-based classification. *Sci. Tot. Environ.* 444, 1–15. doi: 10.1016/j.scitotenv.2012.11.058

Shi, W., and Wang, M. (2009). An assessment of the black ocean pixel assumption for MODIS SWIR bands. *Remote Sens. Environ.* 113 (8), 1587–1597. doi: 10.1016/j.rse.2009.03.011

Smith, M. E., Lain, L. R., and Bernard, S. (2018). An optimized chlorophyll a switching algorithm for MERIS and OLCI in phytoplankton-dominated waters. *Remote Sens. Environ.* 215, 217–227. doi: 10.1016/j.rse.2018.06.002

Soomets, T., Uudeberg, K., Jakovels, D., Zagars, M., Reinart, A., Brauns, A., et al. (2019). Comparison of lake optical water types derived from sentinel-2 and sentinel-3. *Remote Sens.* 11 (23), 2883. doi: 10.3390/rs11232883

Spyrakos, E., O'Donnell, R., Hunter, P. D., Miller, C., Scott, M., Simis, S. G. H., et al. (2018). Optical types of inland and coastal waters. *Limnology Oceanography.* 63 (2), 846–870. doi: 10.1002/lno.10674

Steinmetz, F., Deschamps, P. Y., and Ramon, D. (2011). Atmospheric correction in presence of sun glint: application to MERIS. *Opt. Express.* 19 (10), 9783–9800. doi: 10.1364/OE.19.009783

Steinmetz, F., and Ramon, D. (2018). "Sentinel-2 MSI and sentinel-3 OLCI consistent ocean colour products using POLYMER," in *Proc. SPIE remote sensing of the open and coastal ocean and inland waters.*, vol. Vol. 10778. (Honolulu, USA), 46–55. doi: 10.1117/12.2500232

Tilstone, G., Dall'Olmo, G., Hieronymi, M., Ruddick, K., Beck, M., Ligi, M., et al. (2020). Field intercomparison of radiometer measurements for ocean colour validation. *Remote Sens.* 12 (10), 1587. doi: 10.3390/rs12101587

Tilstone, G., Mallor-Hoya, S., Gohin, F., Couto, A. B., Sá, C., Goela, P., et al. (2017). Which ocean colour algorithm for MERIS in north West European waters? *Remote Sens. Environ.* 189, 132–151. doi: 10.1016/j.rse.2016.11.012

Tilstone, G. H., Pardo, S., Simis, S. G., Qin, P., Selmes, N., Dessailly, D., et al. (2021). Consistency between satellite ocean colour products under high coloured dissolved organic matter absorption in the Baltic Sea. *Remote Sens.* 14 (1), 89. doi: 10.3390/rs14010089

Turner, K. J., Tzortziou, M., Grunert, B. K., Goes, J., and Sherman, J. (2022). Optical classification of an urbanized estuary using hyperspectral remote sensing reflectance. *Opt. Express.* 30 (23), 41590–41612. doi: 10.1364/OE.472765

Uudeberg, K., Aavaste, A., Kõks, K. L., Ansper, A., Uusõue, M., Kangro, K., et al. (2020). Optical water type guided approach to estimate optical water quality parameters. *Remote Sens.* 12 (6), 931. doi: 10.3390/rs12060931

Valente, A., Sathyendranath, S., Brotas, V., Groom, S., Grant, M., Jackson, T., et al. (2022). A compilation of global bio-optical *in situ* data for ocean colour satellite applications–version three. *Earth System Sci. Data.* 14 (12), 5737–5770. doi: 10.5194/essd-14-5737-2022

Vandermeulen, R. A., Mannino, A., Craig, S. E., and Werdell, P. J. (2020). 150 shades of green: using the full spectrum of remote sensing reflectance to elucidate color shifts in the ocean. *Remote Sens. Environ.* 247, 111900. doi: 10.1016/j.rse.2020.111900

Vanhellemont, Q. (2019a). Adaptation of the dark spectrum fitting atmospheric correction for aquatic applications of the landsat and sentinel-2 archives. *Remote Sens. Environ.* 225, 175–192. doi: 10.1016/j.rse.2019.03.010

Vanhellemont, Q. (2019b). Daily metre-scale mapping of water turbidity using CubeSat imagery. *Opt. Express.* 27 (20), A1372–A1399. doi: 10.1364/OE.27.0A1372

Vanhellemont, Q. (2020). Sensitivity analysis of the dark spectrum fitting atmospheric correction for metre-and decametre-scale satellite imagery using autonomous hyperspectral radiometry. *Opt. Express.* 28 (20), 29948–29965. doi: 10.1364/OE.397456

Vanhellemont, Q., and Ruddick, K. (2018). Atmospheric correction of metre-scale optical satellite data for inland and coastal water applications. *Remote Sens. Environ.* 216, 586–597. doi: 10.1016/j.rse.2018.07.015

Vanhellemont, Q., and Ruddick, K. (2021). Atmospheric correction of sentinel-3/OLCI data for mapping of suspended particulate matter and chlorophyll-a concentration in Belgian turbid coastal waters. *Remote Sens. Environ.* 256, 112284. doi: 10.1016/j.rse.2021.112284

Vansteenwegen, D., Ruddick, K., Cattrijsse, A., Vanhellemont, Q., and Beck, M. (2019). The pan-and-tilt hyperspectral radiometer system (PANTHYR) for autonomous satellite validation measurements–prototype design and testing. *Remote Sens.* 11 (11), 1360. doi: 10.3390/rs11111360

Vantrepotte, V., Loisel, H., Dessailly, D., and Mériaux, X. (2012). Optical classification of contrasted coastal waters. *Remote Sens. Environ.* 123, 306–323. doi: 10.1016/j.rse.2012.03.004

Wei, J., Lee, Z., and Shang, S. (2016). A system to measure the data quality of spectral remote-sensing reflectance of aquatic environments. *J. Geophys. Res. Oceans.* 121 (11), 8189–8207. doi: 10.1002/2016JC012126

Wei, J., Wang, M., Mikelsons, K., Jiang, L., Kratzer, S., Lee, Z., et al. (2022). Global satellite water classification data products over oceanic, coastal, and inland waters. *Remote Sens. Environ.* 282, 113233. doi: 10.1016/j.rse.2022.113233

Werdell, P. J., McKinna, L. I., Boss, E., Ackleson, S. G., Craig, S. E., Gregg, W. W., et al. (2018). An overview of approaches and challenges for retrieving marine inherent optical properties from ocean color remote sensing. *Prog. Oceanography.* 160, 186–212. doi: 10.1016/j.pocean.2018.01.001

Windle, A. E., Evers-King, H., Loveday, B. R., Ondrusek, M., and Silsbe, G. M. (2022). Evaluating atmospheric correction algorithms applied to OLCI sentinel-3 data of Chesapeake bay waters. *Remote Sens.* 14 (8), 1881. doi: 10.3390/rs14081881

Xi, H., Hieronymi, M., Krasemann, H., and Röttgers, R. (2017). Phytoplankton group identification using simulated and *in situ* hyperspectral remote sensing reflectance. *Front. Mar. Sci.* 4. doi: 10.3389/fmars.2017.00272

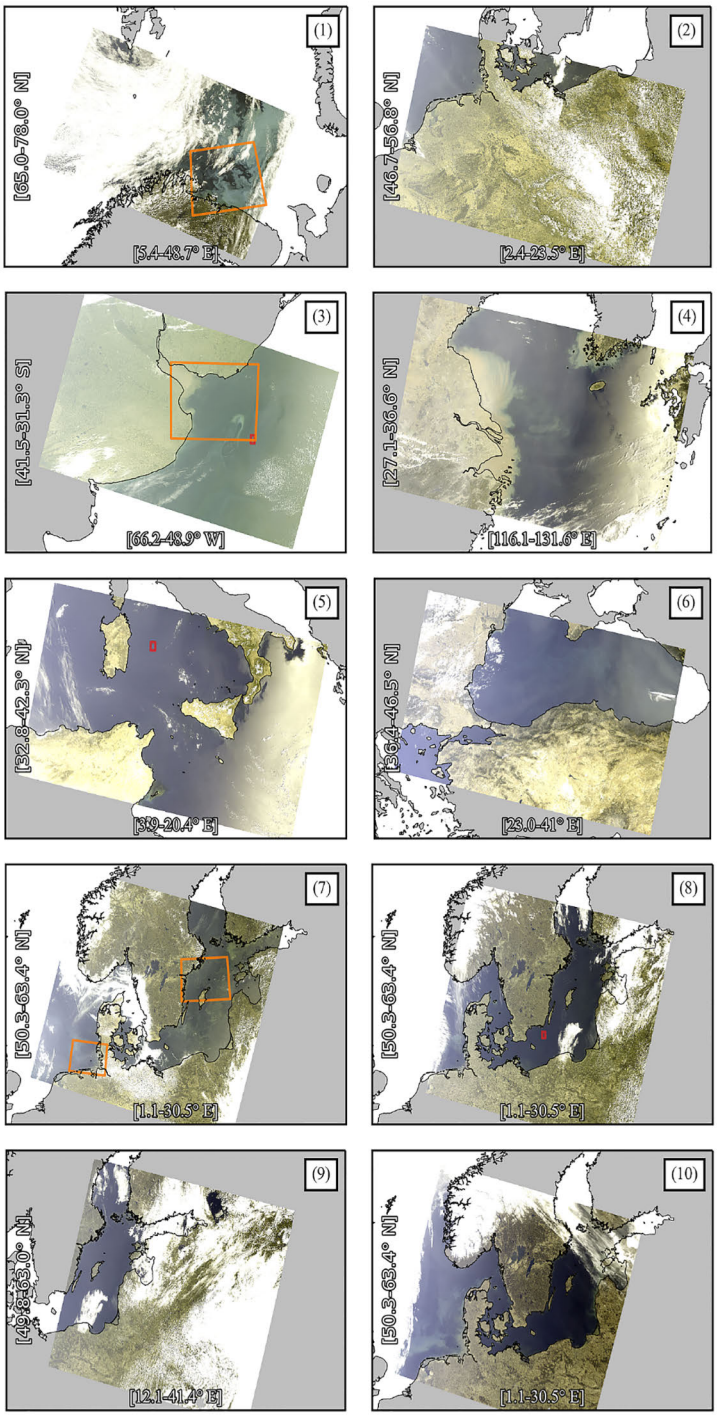
Xi, H., Hieronymi, M., Röttgers, R., Krasemann, H., and Qiu, Z. (2015). Hyperspectral differentiation of phytoplankton taxonomic groups: a comparison between using remote sensing reflectance and absorption spectra. *Remote Sens.* 7 (11), 14781–14805. doi: 10.3390/rs71114781

Zhang, M., Hu, C., and Barnes, B. B. (2019). Performance of POLYMER atmospheric correction of ocean color imagery in the presence of absorbing aerosols. *IEEE Trans. Geosci. Remote Sens.* 57 (9), 6666–6674. doi: 10.1109/TGRS.2019.2907884

Zibordi, G., Kwiatkowska, E., Mélin, F., Talone, M., Cazzaniga, I., Dessailly, D., et al. (2022). Assessment of OLCI-a and OLCI-b radiometric data products across European seas. *Remote Sens. Environ.* 272, 112911. doi: 10.1016/j.rse.2022.112911

Zibordi, G., Mélin, F., Berthon, J. F., Holben, B., Slutsker, I., Giles, D., et al. (2009). AERONET-OC: a network for the validation of ocean color primary products. *J. Atmospheric Oceanic Tech.* 26 (8), 1634–1651. doi: 10.1175/2009JTECHO654.1

Appendix 1



APPENDIX FIGURE A1
Overview of all ten OLCI scenes used (Table 2) in vertical near-side perspective. RGB images created from L_{TOA}. Marked in red are the 100x100 pixel areas for estimating spatial homogeneity (Table 4). The image sections in Figure 2 are shown in orange.

frontiers | Frontiers in Marine Science

TYPE Correction
PUBLISHED 26 October 2023
DOI 10.3389/fmars.2023.1307517

Check for updates

OPEN ACCESS

EDITED AND REVIEWED BY
Javier A. Concha,
European Space Research Institute (ESRIN), Italy

*CORRESPONDENCE
Martin Hieronymi
martin.hieronymi@hereon.de

RECEIVED 04 October 2023
ACCEPTED 13 October 2023
PUBLISHED 26 October 2023

CITATION
Hieronymi M, Bi S, Müller D, Schütt EM, Behr D, Brockmann C, Lebreton C, Steinmetz F, Stelzer K and Vanhellemont Q (2023) Corrigendum: Ocean color atmospheric correction methods in view of usability for different optical water types. *Front. Mar. Sci.* 10:1307517. doi: 10.3389/fmars.2023.1307517

COPYRIGHT
© 2023 Hieronymi, Bi, Müller, Schütt, Behr, Brockmann, Lebreton, Steinmetz, Stelzer and Vanhellemont. This is an open-access article distributed under the terms of the Creative Commons Attribution License (CC BY). The use, distribution or reproduction in other forums is permitted, provided the original author(s) and the copyright owner(s) are credited and that the original publication in this journal is cited, in accordance with accepted academic practice. No use, distribution or reproduction is permitted which does not comply with these terms.

Corrigendum: Ocean color atmospheric correction methods in view of usability for different optical water types

Martin Hieronymi[1]*, Shun Bi[1], Dagmar Müller[2], Eike M. Schütt[1,3], Daniel Behr[1], Carsten Brockmann[2], Carole Lebreton[2], François Steinmetz[4], Kerstin Stelzer[2] and Quinten Vanhellemont[5]

[1]Department of Optical Oceanography, Institute of Carbon Cycles, Helmholtz-Zentrum Hereon, Geesthacht, Germany, [2]Brockmann Consult GmbH, Hamburg, Germany, [3]Earth Observation and Modelling, Department of Geography, Kiel University, Kiel, Germany, [4]HYGEOS, Lille, France, [5]Royal Belgian Institute of Natural Sciences, Operational Directorate Natural Environments, Brussels, Belgium

KEYWORDS

atmospheric correction, ocean color, optical water types, satellite remote sensing, essential climate variable, Sentinel-3/OLCI

A corrigendum on

Ocean color atmospheric correction methods in view of usability for different optical water types

by Hieronymi M, Bi S, Müller D, Schütt EM, Behr D, Brockmann C, Lebreton C, Steinmetz F, Stelzer K and Vanhellemont Q (2023) *Front. Mar. Sci.* 10:1129876. doi: 10.3389/fmars.2023.1129876

Error in Figure

In the published article, there was an error in Figure 3 as published. Figure 3 shows a comparison of the reflectance results of all atmospheric correction methods for selected points marked in Figure 2. In the published version of Figures 3D, F, points 4 and 6 do not match the exact positions in Figure 2, instead the points were slightly shifted in waters where ACOLITE-DSF did not give results (NaN), the DSF spectra are accordingly not shown. In the corrected version, points 4 and 6 agree with the positions in Figure 2, DSF provides results here. The explaining text in the publication refers, among other things, to these two spectra, which are now displayed as well. All other results remain identical. The corrected Figure 3 and its caption appear below.

The authors apologize for this error and state that this does not change the scientific conclusions of the article in any way. The original article has been updated.

Publisher's note

All claims expressed in this article are solely those of the authors and do not necessarily represent those of their affiliated organizations, or those of the publisher, the editors and the reviewers. Any product that may be evaluated in this article, or claim that may be made by its manufacturer, is not guaranteed or endorsed by the publisher.

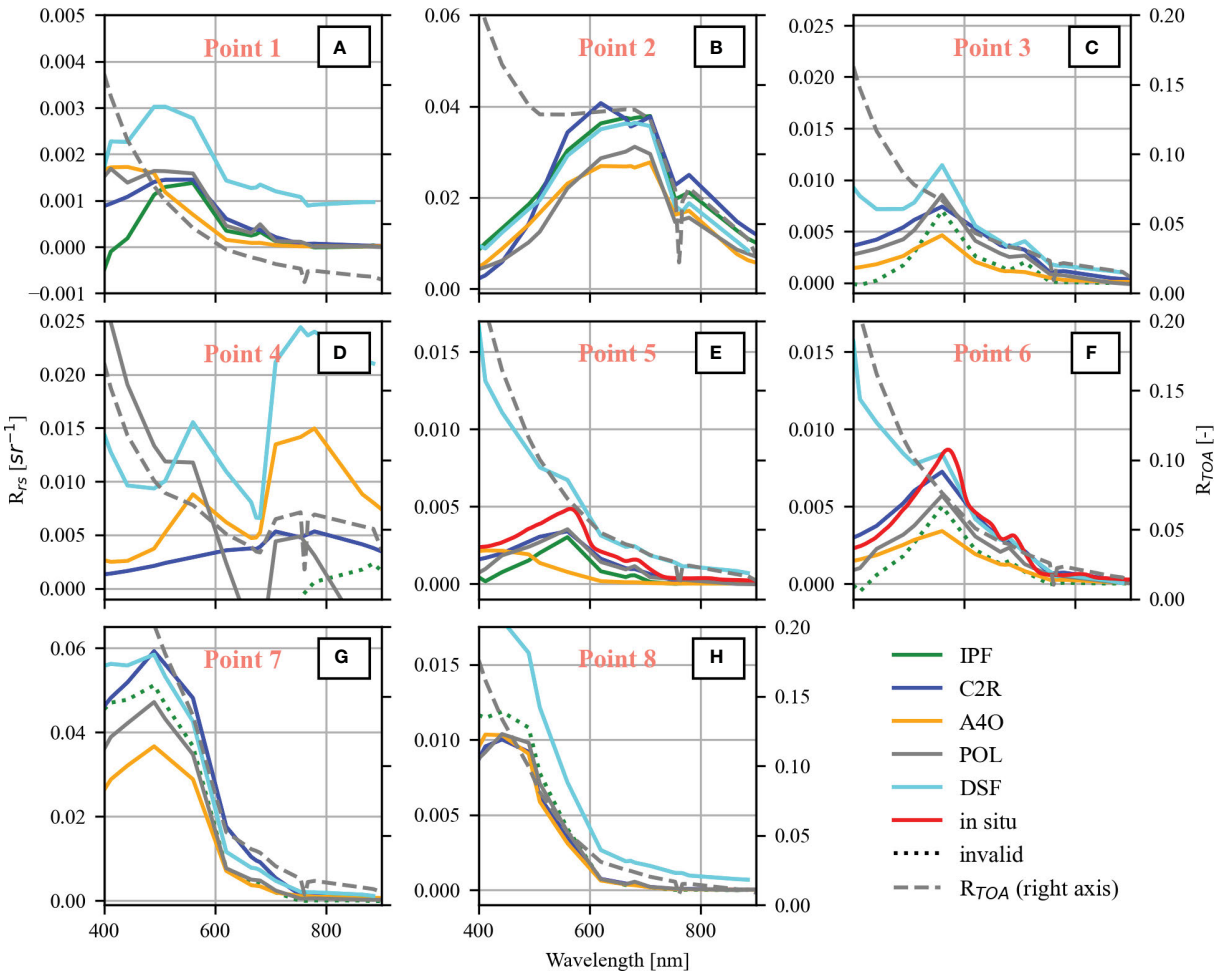


FIGURE 3
(A–H) Comparison of spectral remote-sensing reflectance derived from the different AC methods for eight points marked in Figure 2. The right axis and the corresponding grey dashed lines show the initial TOA reflectance. **(E, F)** include corresponding normalized *in-situ* measurements.

frontiers | Frontiers in Marine Science

TYPE Review
PUBLISHED 21 August 2023
DOI 10.3389/fmars.2023.1149938

Check for updates

OPEN ACCESS

EDITED BY
Jeremy Werdell,
National Aeronautics and Space Administration, United States

REVIEWED BY
Monique Messié,
Monterey Bay Aquarium Research Institute (MBARI), United States
Greg M. Silsbe,
University of Maryland, College Park, United States

*CORRESPONDENCE
Bror F. Jönsson
brj@pml.ac.uk

RECEIVED 23 January 2023
ACCEPTED 06 July 2023
PUBLISHED 21 August 2023

CITATION
Jönsson BF, Kulk G and Sathyendranath S (2023) Review of algorithms estimating export production from satellite derived properties.
Front. Mar. Sci. 10:1149938.
doi: 10.3389/fmars.2023.1149938

COPYRIGHT
© 2023 Jönsson, Kulk and Sathyendranath. This is an open-access article distributed under the terms of the Creative Commons Attribution License (CC BY). The use, distribution or reproduction in other forums is permitted, provided the original author(s) and the copyright owner(s) are credited and that the original publication in this journal is cited, in accordance with accepted academic practice. No use, distribution or reproduction is permitted which does not comply with these terms.

Review of algorithms estimating export production from satellite derived properties

Bror F. Jönsson[1]*, Gemma Kulk[1,2] and Shubha Sathyendranath[1,2]

[1]Earth Observation Science & Applications, Plymouth Marine Laboratory, Plymouth, United Kingdom, [2]National Centre for Earth Observation, Plymouth Marine Laboratory, Plymouth, United Kingdom

Whereas the vertical transport of biomass from productive surface waters to the deep ocean (the biological pump) is a critical component of the global carbon cycle, its magnitude and variability is poorly understood. Global-scale estimates of ocean carbon export vary widely, ranging from ~5 to ~20 Gt C y^{-1} due to uncertainties in methods and unclear definitions. Satellite-derived properties such as phytoplankton biomass, sea surface temperature, and light attenuation at depth provide information about the oceanic ecosystem with unprecedented coverage and resolution in time and space. These products have been the basis of an intense effort over several decades to constrain different biogeochemical production rates and fluxes in the ocean. One critical challenge in this effort has been to estimate the magnitude of the biological pump from satellite-derived properties by establishing how much of the primary production is exported out of the euphotic zone, a flux that is called export production. Here we present a review of existing algorithms for estimating export production from satellite-derived properties, available *in-situ* datasets that can be used for testing the algorithms, and earlier evaluations of the proposed algorithms. The satellite-derived products used in the algorithm evaluation are all based largely on the Ocean Colour Climate Change Initiative (OC-CCI) products, and carbon products derived from them. The different resources are combined in a meta-analysis.

KEYWORDS

carbon export, biological pump, satellite oceanography, ocean color, net community production, biogeochemistry, algorithms

1 Introduction

The recirculation of major nutrients and carbon in the ocean is strongly controlled by the vertical export of particulate organic matter from the surface ocean to the ocean's interior (Figure 1 and e.g. Falkowski et al., 1998; Sabine et al., 2004; Honjo et al., 2008; Siegel et al., 2022). Marine phytoplankton transform CO_2 to organic carbon via photosynthesis with light as the energy source (Eppley, 1972; Geider et al., 1998), a

critical biological process that is the foundation of most marine ecosystems (Sarmiento and Bender, 1994; Pauly and Christensen, 1995). The resulting chemical energy bound as organic carbon is used in marine food webs to build other types of biomass and as energy for autotrophic and heterotrophic organisms. While the carbon fixation by phytoplankton (or Primary Production, PP) in marine ecosystems is of vital significance (e.g. Platt et al., 1989; Pauly and Christensen, 1995; Fasham, 2003; Marinov et al., 2008; Chavez et al., 2011), there has been a longstanding debate about how to quantify its magnitude (Platt et al., 1989; Quay and Karl, 2010; Duarte et al., 2013; Williams et al., 2013). Methods to observe or infer different components of primary production have been developed (Bender et al., 1987; Cullen, 2001; Fasham, 2003) that are valid over varying spatial and temporal domains (Balch et al., 2022), and there are significant differences in how different researchers define biological production (Williams, 1993; Cullen, 2001). Most of the biomass generated by PP in the euphotic (sunlit) zone is consumed by heterotrophs and remineralized in the upper ocean. The remaining part is called Net Community Production (NCP) and if aggregated over sufficiently large temporal and spatial scales, they equate to Export Production (EP). Organic carbon resulting from EP is transported to deeper waters by, among other pathways, the downward vertical flux of Particulate or Dissolved Organic Carbon (POC, DOC), often referred to as the "biological pump" (BCP, Volk and Hoffert, 1985). See Siegel et al. (2022) for an exhaustive discussion about the Biological Carbon Pump (BCP) and other processes that sequester carbon from the surface ocean to deeper waters. As with PP, the understanding of the magnitude and spatiotemporal variability of the biological pump remains limited (Burd et al., 2010; Britten and Primeau, 2016).

Satellite-based ocean color products have provided an unprecedented resource to study ocean biogeochemistry and biological oceanography with high spatiotemporal resolution and coverage (Groom et al., 2019; McClain et al., 2022) and significant effort has been allocated to also assess the biological pump from space with limited success (Siegel et al., 2022). One critical challenge has been to quantify community respiration (Westberry et al., 2012) and to establish the ratio of PP that is exported out from the euphotic zone (Britten and Primeau, 2016; Siegel et al., 2016; Siegel et al., 2022). The large uncertainties associated with satellite-based EP products has led to global-scale estimates of ocean carbon export that vary from ~ 5 to 20 Gt C y^{-1} (Dunne et al., 2007; Henson et al., 2011; Laws et al., 2011; Siegel et al., 2016; Siegel et al., 2022).

1.1 Fluxes and relationships

The main approach to estimate EP from remotely sensed products is based on empirical correlations identified from regression analysis of *in-situ* observations of vertical POC fluxes in combination with properties that can be derived from satellite (e.g. Stukel et al., 2015). This method has so far generated algorithms with arguably limited ability to predict EP (e.g. Stukel et al., 2015; Palevsky et al., 2016). The many challenges to estimate export fluxes from satellite-derived properties are further complicated by differences and inconsistencies in how EP and export fluxes are defined and quantified. We will describe the most common definitions in the following sections and summarize them in Table 1.

1.1.1 Gross primary production

GPP is the total rate of carbon production by autotrophic organisms before correction for losses due to excretion or respiration, or in other words the gross conversion of inorganic carbon to its organic state (Cullen, 2001; Fasham, 2003) by autotrophs. GPP can in theory be derived from first principles (e.g. Lawrenz et al., 2013, and references).

1.1.2 Net primary production

NPP is the net rate at which autotrophic organisms assimilate carbon. This is normally defined as GPP minus the fraction used by primary producers for cellular respiration and maintenance. (Bender et al., 1987; Platt et al., 1989; Williams, 1993; Behrenfeld and Falkowski, 1997; Cullen, 2001; Fasham, 2003). NPP is also the portion of carbon fixation from photosynthesis that is available to heterotrophic organisms in the ecosystem (Chavez et al., 2011). NPP has primarily been measured *in-situ* using the ^{14}C method developed by Nielsen (1952), where collected samples are incubated with a known amount of radioactive ^{14}C-bicarbonate that labels the dissolved inorganic carbon pool (e.g. Platt and Jassby, 1976; Bender et al., 1987; Cullen, 2001; Fasham, 2003). Other approaches to estimate NPP are based on measuring changes of O_2 in light-dark incubations and different isotopic methods (e.g. ^{18}O ^{13}C, Bender et al., 1987; Cullen, 2001; Chavez et al., 2011). Typically, the shorter the duration of the incubation method (of order 1 hour), the more the measurement is considered to approach GPP. Longer incubations (order 10 hours) lead to estimates of NPP.

One major development has been the ability to estimate PP from satellite-derived properties (e.g. Eppley et al., 1985; Platt et al., 1988; Sathyendranath et al., 1991; Behrenfeld and Falkowski, 1997; Friedrichs et al., 2009), providing depth-integrated estimates with unprecedented spatial resolution and coverage. Note that, in principle, the method of Platt and Sathyendranath, based on short (1-2h) photosynthesis-irradiance experiment, may be considered to estimate GPP, whereas the method of Behrenfeld and colleagues, based on *in situ* incubation of one day, approaches NPP. A common approach to quantify PP in the surface ocean from satellite derived properties is based on a concept where stocks of carbon biomass or chlorophyll are combined with auxiliary properties to estimate rates of photosynthesis (e.g. Platt et al., 1988; Behrenfeld and Falkowski, 1997; Arrigo et al., 1998; Westberry et al., 2008). Another approach is to use Inherent Optical Properties (IOPs) to estimate NPP by combining satellite-based proxies for energy absorption in the water column with inferences of the efficiency when absorbed energy is converted into carbon biomass (Antoine et al., 1996; Lee et al., 1996; Smyth et al., 2005; Silsbe et al., 2016).

1.1.3 Net community production

NCP represents the net increase of biomass or carbon in the ecosystem of interest, or NPP minus community respiration of all

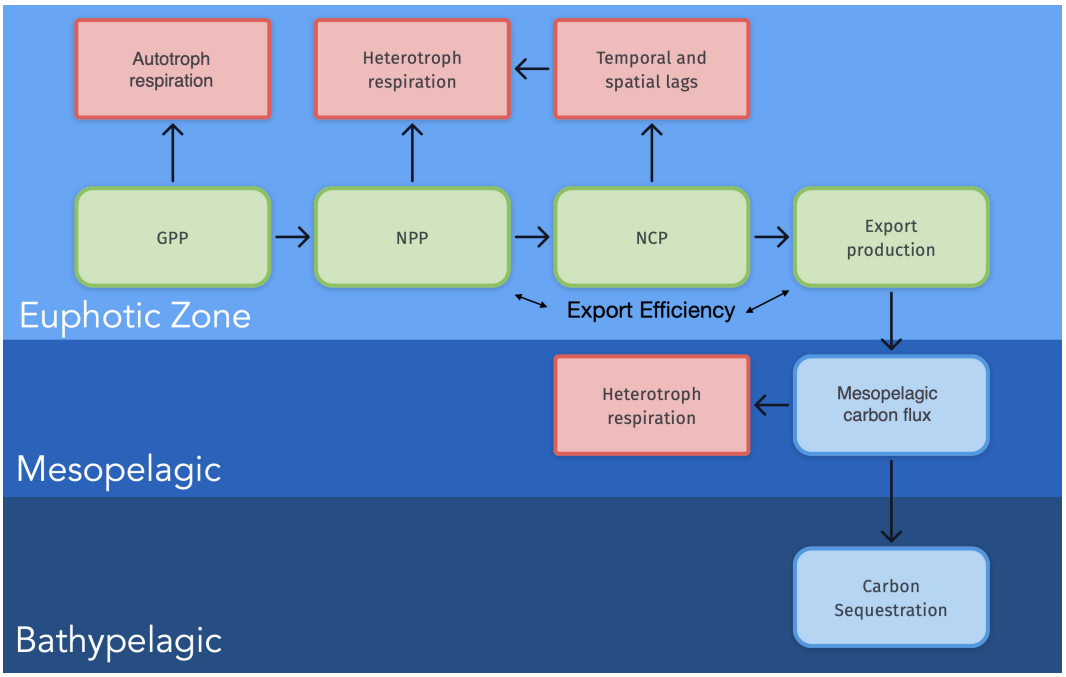


FIGURE 1
Conceptual model of the relationships between different terms describing carbon fluxes in the Ocean. Each term is defined in the text and Table 1.

heterotrophs (Williams, 1993; Cullen, 2001; Fasham, 2003). NCP estimates must be constrained to a defined domain in time and space to be of practical use. A method that aggregates results over the mixed layer can provide diametrically different results for a specific region compared with one that includes the part of the photic zone below the base of the mixed layer or parts of the mesopelagic. Likewise, NCP over short timescales should be interpreted very differently than annual averages (Fasham, 2003).

1.1.4 Export production

Export Production (EP, Laws, 1991) is the net production of organic carbon above a specified horizon and is assumed to be equivalent with NCP when the system is in steady-state and all temporal lags are accounted for. EP is an important property for the global carbon cycle by constraining the sequestration of organic carbon to deeper waters. EP is by definition only valid over significantly longer timescales than any processes directly controlling production and respiration. Hence, it is not possible to directly convert *In-situ* measurements of mixed layer NCP to EP since the newly-produced biomass might be consumed before it can be exported to the aphotic zone. It is also not yet possible to derive mechanistic relationships between EP satellite-based products. EP serves as the upper bound for transport of POC from the euphotic zone to the bathypelgic (e.g. Platt et al., 1989; Siegel et al., 2016; Siegel et al., 2022).

1.1.5 Export flux

If EP reflects the aggregated production of carbon above a depth horizon available for export to deeper waters, Eflux represents the direct or indirect measurement of this transport. Eflux is defined as

TABLE 1 Different terms associated with Biological Production that are relevant for algorithm development.

Gross Primary Production	GPP	Total production of organic carbon by autrotrophs
Net Primary Production	NPP	GPP less losses to respiration by autrotrophs
Net Community Production	NCP	GPP less all community respiration in the defined system
Export Production	EP	NCP integrated over sufficient time and space to satisfy dynamic steady state conditions. The part of biological production in the euphotic zone that is exported to deeper waters.
Export Flux	EFlux	Permanent flux of particulate carbon over a depth horizon below the euphotic zone
ef-ratio	ef-ratio	The ratio between new or export production and NPP in a steady state system.
Export Efficiency	Ef	The ratio of NPP that is exported across a vertical horizon.

the flux of material over a depth horizon and normally quantified via sediment traps (Dunne et al., 2005; Buesseler et al., 2007) or by measuring the reduction of particle-reactive ^{234}Th in comparison to its longer-lived parent ^{238}U in the water column (e.g. Bisson et al., 2018, and references therein). The ^{234}Th method determines the downward flux of POC by integrating the deficit of ^{234}Th in the upper water column and couples it to the POC/^{234}Th ratio in sinking particles. Samples can be collected with much higher vertical resolution than traps, allowing for the estimation of POC flux at or very near Z_{eu} without the need for a common reference depth. In contrast to EP, Eflux can be estimated across any temporal or spatial scale. Factors controlling the regional, temporal, and depth variations of POC/^{234}Th ratios are however poorly understood (Puigcorbe et al., 2020). Other sources of uncertainty arise from neglecting physical processes and the necessary assumption of steady state in the Th isotope system (Buesseler et al., 2006).

1.1.6 Export efficiency

The fraction of PP that is exported out of the euphotic zone (EP/NPP) can be described as the carbon export efficiency (Ef). This is a non-dimensional ratio that describes how inefficient the ecosystem is in retaining carbon in the upper layer of the ocean. The more efficient the pelagic ecosystem is, the more inefficient the carbon export is, to the point where all carbon is recycled, and no carbon will be exported (Buesseler, 1998).

1.1.7 e-ratio

A special case of Ef is the e-ratio, or the flux of particulate organic carbon at the base of the euphotic zone divided by NPP, (Murray et al., 1996).

1.1.8 f-ratio

Eppley and Peterson (1979) characterized export efficiency as the ratio of New to Total photosynthetic production, or the f-ratio. This idea is based on the concept of distinguishing NPP driven by nitrogen compounds originating from different processes in the ecosystem. New production is fueled by nutrients (usually NO_3^{-}) recently introduced to the euphotic zone (either from deeper waters or via lateral processes) (Dugdale and Goering, 1967) in contrast to production from rapidly recycled compounds such as ammonium. Export production would then be equal to New production if the system is in a steady state and all transformations between ammonium and NO_3^{-} occur outside the euphotic zone (Laws et al., 2011).

The f-ratio was originally believed to be significant by being directly related to Ef, but this interpretation relied on the assumption that nitrification mainly occur below the euphotic zone, something that more recent measurements have questioned (Dore and Karl, 1996; Yool et al., 2007). Platt et al. (1989) also suggested that elevated new production is directly driven by perturbations in the physical forcing which challenges a necessary assumption of steady state.

1.1.9 ef-ratio

Laws et al. (2000) combined the e- and f-ratios to an ef-ratio based on the assumption that new production should balance export production if a system is in steady-state. This ratio makes it possible to combine measurements of new and export production.

1.1.10 pe-ratio

A more precise definition of the e-ratio is the pe-ratio, or "the ratio between the export of rapidly sinking particulate matter (particle export) and the total production of organic matter by photosynthesis (primary production)" (Murray et al., 1996; Dunne et al., 2005). The pe-ratio shows similar spatial patterns as the f-ratio on global scales, especially when identifying eutrophic and oligotrophic regions.

1.2 Structure of the review

With this review we have aimed to assess how different published algorithms that use satellite-derived properties to calculate EP perform. Our approach has been to leverage already existing evaluation studies where different models have been compared with each other, and only directly compare algorithms or validation datasets when no existing information is available. Earlier studies evaluating EP algorithms each use slightly varying approaches and were often conducted to compare newly developed algorithms with already existing ones. We address these differences by performing a kind of meta-analysis where different evaluations and validation datasets are compared together with the respective algorithms. We have followed the guidelines for systematic reviews prescribed in Khan et al. (2003) when applicable.

The review begins with a brief description of existing EP algorithms, followed by a presentation of different datasets that can be useful for the evaluation satellite-based EP algorithms. Next, we discuss earlier studies that evaluates EP algorithms, including our own comparison where we use the Dunne et al. (2005); Bisson et al. (2018), and Mouw et al. (2016a) datasets to assess the different EP algorithms. Finally, we discuss the different evaluations and provide a recommendation about which algorithm to use.

2 Export production algorithms

A number of different approaches to constrain and scale EP using different satellite derived properties have been proposed over the years. Most algorithms are developed to provide some kind of export efficiency ratio that then can be scaled with PP estimates to generate properties that are comparable to observations of EP. It is not well defined if either satellite-derived PP products or EP algorithms are assuming that the biological production is defined as GPP, NPP, or something in between, while this is not always clear from *in-situ* measurements either (Balch et al., 2022). As a result, we use the term PP to designate primary production without specifying if it is GPP or NPP. All relationships except for those of Betzer et al. (1984); Pace et al. (1987), and the re-parametrization of Siegel et al. (2014) by Stukel et al. (2015) are designed to provide global estimates of EP. Terms used in the the algorithms are summarized in Table 2.

2.1 Eppley and Peterson, 1979

$$EP = 0.0025 \cdot PP^2 (PP \leq 200) \quad (1)$$

$$EP = 0.5 \cdot PP (PP > 200) \quad (2)$$

Eppley and Peterson (1979)'s seminal paper is to our knowledge the first study that suggested a quantitative relationship between PP and EP. They base their algorithm solely on PP, with two different scaling factors if the magnitude of PP is above or below 200 mg C m^{-2} d^{-1}.

2.2 Suess, 1980

$$EP = \frac{PP}{0.0238z + 0.212} \quad (3)$$

Suess (1980) uses one scaling factor for PP and adds a depth dependency as to predict organic carbon flux at any depth across a depth horizon below the base on the euphotic zone. The algorithm was derived from sediment trap data.

2.3 Betzer et al., 1984

$$EP = \frac{0.0409 PP^{1.41}}{z^{0.628}} \quad (4)$$

The Betzer et al. (1984) relationship was derived from on ^{14}C based PP and POC flux observations using a free-drifting sediment trap at 900 m. The trap was deployed at four locations between 12° N and 6°S at 153°W in the Pacific Ocean.

2.4 Pace et al., 1987

$$EP = 3.523 z^{-0.734} PP^{1.000} \quad (5)$$

Pace et al. (1987) expanded on Suess (1980) by including the vertical flux of both POC and particulate organic nitrogen (PON) based on *in-situ* observations from the Vertical Transport and Exchange (VERTEX) program in the north-east Pacific Ocean.

2.5 Baines et al., 1994

$$EP = PP \cdot 10^{-0.67 + 0.30 \log_{10} Chl + 0.27 (\log_{10} Chl)^2} \quad (6)$$

The algorithm of Baines et al. (1994) is derived from a relationship between the e-ratio, PP, Efluxes, and the depth of the euphotic zone. All three variables are independently predicted from Chl with an R^2 *of* 0.54 – 0.90.

2.6 Laws et al., 2000

$$EP = PP \cdot (0.62 - 0.02 SST) \quad (7)$$

This algorithm is based on a relationship between Ef, SST, and the f-ratio derived from data in Table 3 of Laws et al. (2000). We use the equation as described by Henson et al. (2011).

2.7 Dunne et al., 2005

$$Ef = -0.0101 SST + 0.0582 \cdot \ln PP/Z_{eu} + 0.419; 0.04 < Ef < 0.72 \quad (8)$$

$$Ef = -0.0081 SST + 0.0668 \cdot \ln Chl/Z_{eu} + 0.426 \quad (9)$$

$$EP = PP \cdot \begin{cases} 0.04 \text{ if } & Ef < 0.04 \\ 0.72 \text{ if } & Ef > 0.72 \\ Ef & \text{otherwise} \end{cases} \quad (10)$$

Dunne et al. (2005) is based on trap and ^{234}Th observations together with PP from $H^{14}CO_3^-$ incubations at different depths, SST, Zeu, and Chl. Ef is constrained to fall between 0.04 and 0.72 (Dunne et al., 2005; Stukel et al., 2015).

2.8 Henson et al., 2011

$$EP = PP \cdot 0.23 * e^{-0.08 \cdot SST} \quad (11)$$

The Henson et al. (2011) model is parameterized to estimate export at the 100 m depth horizon. (Henson et al., 2011; Stukel et al., 2015).

2.9 Laws et al., 2011

The algorithms in Laws et al. (2011) is a further development of Laws et al. 2000. They introduce two relationships: which is equation 2 in in Laws et al. (2011), and

TABLE 2 Input and output parameters for the different algorithms.

Input parameters		
chl	Chlorophyll	mg m^{-3}
SST	Sea Surface Temperature	°C
PP	Gross or Net Primary Production	mg C m^{-2} d^{-1}
Z	Depth level across which to calculate export	m
Z_{eu}	Depth of the euphotic zone	m
Output parameter		
EP	Export Production	mg C m^{-2} d^{-1}

$$EP = PP \cdot \frac{(0.5857 - 0.0165SST) \cdot PP}{51.7 + PP} \quad (12)$$

$$EP = PP \cdot 0.04756(0.78 - \frac{0.43 \cdot SST}{30}) \cdot PP^{0.307} \quad (13)$$

Equation 12 is based on contours in Figure 2 of Laws et al. (2000) and evaluated in Stukel et al. (2015), both equations 12 and 13 are evaluated in Li and Cassar (2016).

2.10 Westberry et al., 2012

$$\begin{aligned} EP &= PP - 1.01 \cdot PP^{0.82} \quad (all\ \ data) \\ EP &= PP - 0.93 \cdot PP^{0.78} \quad (open\ \ ocean) \end{aligned} \quad (14)$$

Westberry et al. (2012) uses a number of empirical relationships between PP and respiration (R) to assess NCP and EP. Part of their analysis is to generate regional PP-R relationships by dividing available observations into broad latitudinal zones with different nutrient dynamics.

2.11 Siegel et al., 2014

$$AlgEP = f_{Alg} \cdot PP_M \quad (15)$$

$$G_M = PP_M - \frac{\partial P_M}{\partial t} - m_{ph}P_m - AlgEZ \quad (16)$$

$$G_S = PP_S - \frac{\partial P_S}{\partial t} - m_{ph}P_s \quad (17)$$

$$FecEP = f_{FecM} \cdot G_M + f_{FecS} \cdot G_S \quad (18)$$

$$EP = AlgEP + FecEP \quad (19)$$

Siegel et al. (2014) algorithm divides EP is to different size classes based on the assumed ability to assess the community structure of phytoplankton assemblages via satellite-derived properties. The different terms are specified as follows: *AlgEP* is the total vertical flux of sinking algal cells and aggregates and *FecEP* is the total vertical flux of sinking fecal material released from zooplankton grazers. f_{Alg} is the fraction of microphytoplankton production that sinks out of the base of the euphotic zone (assumed by Siegel et al. (2014) to be 0.1) and PP_M is the PP of microphytoplankton. f_{FecM} and f_{FecS} are the fractions of grazing on microphytoplankton and smaller (<20 μ m) phytoplankton, respectively, that contribute to fecal matter export from the euphotic zone (assumed by Siegel et al. (2014) to be 0.3 and 0.1, respectively). G_M and G_S are the grazing rates on microphytoplankton and small phytoplankton and are derived from phytoplankton mass balance budgets.

2.12 Li & Cassar, 2016

$$EP = \frac{8.57PP}{17.9 + SST} \quad (20)$$

The Li and Cassar (2016) model was developed using a Genetic Programing approach to statistically optimize the Laws et al. (2000) and Henson et al. (2011) relationships using O_2/Ar-based NCP estimates.

3 *In situ* data for evaluation

The Dunne et al. (2005) compilation of *in-situ* pe-ratios is based on 122 field observations from approximately 40 oceanographic studies with global distribution. The dataset includes estimates of PP, Chl a, New Production, nutrients, oxygen or carbon based estimates of EP, particle export estimates based on sinking flux from sediment traps and/or ^{234}Th, and the carbon-to-chlorophyll ratio. Physical parameters include mixed layer temperature and the depth of the euphotic zone (minimum of the 1% light level or sampling zone), The data coverage is presented in Figure 3. They find that, In general, pe-ratios are high (>0.4) in the Polar regions, moderate (0.3–0.4) in coastal regions and open ocean regions supporting phytoplankton blooms, and low (0.05–0.2) elsewhere. The data can be accessed as supplementary information to the Dunne et al. (2005) publication.

The Stukel et al. (2015) datasets are based on 32 Lagrangian process studies where shallow-drifting sediment traps were combined with ^{238}U-^{234} Th measurements to quantify EP (Buesseler et al., 2007). These Lagrangian studies where conducted between 2 and 5 days either within in the California Current Ecosystem (CCE) Long Term Ecological Research (LTER) or the Costa Rica Dome (CRD) FLUx and Zinc Experiments (FLUZiE) programs. Drifters were drogued at 15 m depth and tracked by satellite with either experimental incubation bottles or VERTEX-style sediment traps attached below (Stukel et al., 2013). This experimental setup allowed for simultaneous measurement of carbon export, food web processes (PP, protozoan grazing, mesozooplankton grazing, size-spectra of phytoplankton community), and net changes of *in-situ* Chl. The datasets consist of observations from 7 cruises (Figure 2) and can be located via the acknowledgments section of Stukel et al. (2015) or as supplementary information to the publication.

The Li and Cassar (2016) algorithm development and evaluation used a global dataset of mixed layer O_2/Ar based NCP estimates either from discrete samples analyzed in the lab or continuous underway measurements (Reuer et al., 2007; Cassar et al., 2009; Jönsson et al., 2013). NCP can be derived from O_2/Ar measurements by assuming a mass balance of biological O_2 in the mixed layer. Oxygen saturation at the ocean surface is influenced by biological (i.e., PP) and physical processes (e.g., bubble injection and temperature changes). Ar and O_2 have similar temperature

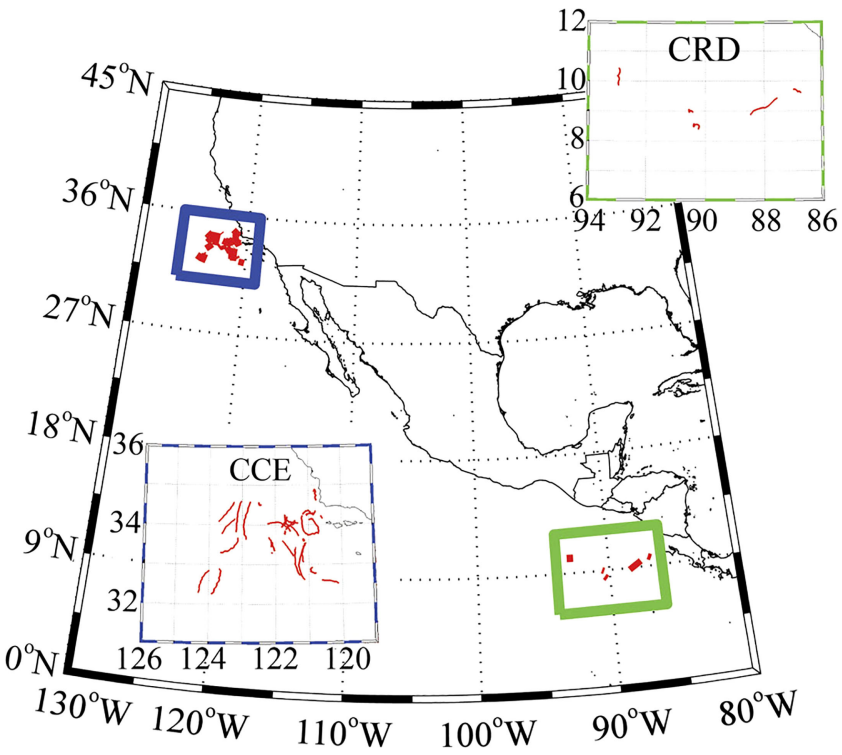


FIGURE 2
Lagrangian experiment locations in the Stukel et al. (2015) study. CCE drifter tracks (blue box, upper right). CRD drifter tracks (green box, lower left). Image from Stukel et al. (2015).

dependencies (Craig and Hayward, 1987). Combined with their similar solubilities, they have almost equivalent responses to processes such as temperature or air pressure change and bubble-mediated gas exchange. As such, oxygen concentration due to physical processes can be accounted for with measurements of the O_2/Ar saturation state.

The dataset contains observations from 1999 to 2009 (n = 689,566) averaged to a 0.083° × 0.083° grid, yielding n=14,795 samples with a mean coefficient of variation (CV) of 0.12 per gridcell (Figure 4). The O_2/Ar super saturation is converted to an NCP proxy using QSCAT/NCEP blended wind speeds (Reuer et al., 2007). Samples with negative NCP are removed due to potential biases associated with vertical mixing of O_2-undersaturated waters (Reuer et al., 2007; Jönsson et al., 2013). Note that positive NCP values may also be biased by vertical mixing where vertical mixing brings O_2-undersaturated water to the surface and the estimates should be regarded as lower bounds on the true NCP. Conversely, positive biases in NCP could occur in regions with high biological O_2 below the mixed layer (e.g., deep chlorophyll maximum). Because of these uncertainties, O_2/Ar NCP data below 1.0 mmol O_2 m^2 d^{-1} are removed from the dataset. Additional uncertainties and biases (e.g., gas exchange parameterization and lack of steady state in biological O_2 in the mixed layer) are further discussed in Jönsson et al. (2013). Data access is described in Li and Cassar (2016).

The Mouw et al. (2016a) dataset consists of Particulate Organic Carbon (POC) flux estimated from sediment traps and ^{234}Th compiled across the global ocean including six long-term time series locations. The data set contains 15,792 individual POC flux estimates at 674 unique locations collected between 1976 and 2012 (Figure 3). Where available, the flux of other minerals is also reported. Of the observations across the globe, 85% are concentrated in the Northern Hemisphere, time series sites accounts for 36% of the data, while 71% of the data are measured at ≥500 m with the most common deployment depths between 1000 and 1500 m. The dataset is archived in the PANGAEA data repository (Mouw et al., 2016b).

The Bisson et al. (2018) dataset is based on observations from sediment traps at depths less than 200 meters and ^{234}Th measurements converted to POC flux at Zeu. The data is selected to represent different sampling methodologies and spatiotemporal scales, and totals 1,719 observations from 1984 to 2014.

The Puigcorbe et al. (2020) dataset does not include POC flux observations but POC/^{234}Th ratios that can be indirectly used to constrain EP and evaluate EP models. The collection contains of 9,318 measurements with a global coverage collected between 1989 and 2018 from the surface to > 5500 m, and divided into three size fractions (∼< 0.7 μm, ∼ 1–50 μm, ∼> 50 μm). The data has an uneven distribution with some areas highly sampled (e.g., China Sea, Bermuda Atlantic Time Series station) while others regions are sparsely covered (the south-eastern Atlantic, the south Pacific, and the south Indian Oceans). The dataset is archived in the PANGAEA data repository (Puigcorbe, 2019).

Ceballos-Romero et al. (2022) provide a comprehensive dataset of^{234}Th measurements sampled across the global ocean between 1967 and 2018. The compilation includes a total of 56 631 data

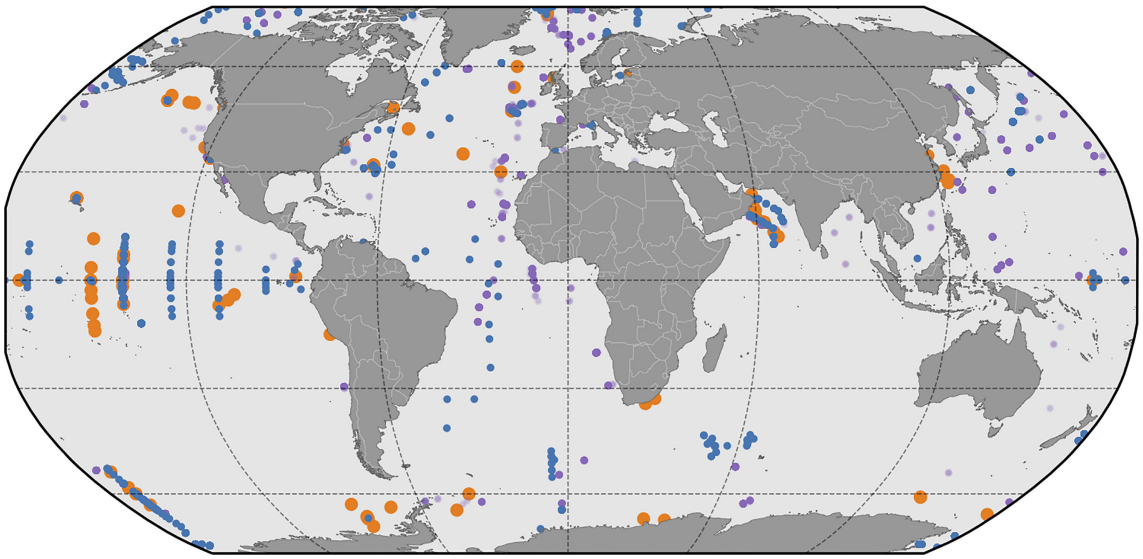


FIGURE 3
Locations of *in-situ* POC flux observations presented in Dunne et al. (2005), (orange markers), Bisson et al. (2018), (green markers) and Mouw et al. (2016a); Mouw et al. (2016b), blue markers for observations shallower than 200 meters, purple for observations deeper than 200 meters).

points together with appropriate metadata including geographic location, date, and sample depth. When available, water temperature, salinity, ^{238}U (over 18 200 data points), and particulate organic nitrogen is included. Data source and method information (including ^{238}U and ^{234}Th) is also detailed along with valuable information for future data analysis such as bloom stage and steady-/non-steady-state conditions at the sampling moment. While not directly applicable in this study, this dataset provides a valuable resource for future EP algorithm development and evaluation.

4 Algorithm evaluations

The instrumental Dunne et al. (2005) study provided not only relationships between PP or Chl and EP that are widely used in ecosystem modeling, but also comparisons of a variety of empirical parameterizations with the data synthesis described in section 3.1. The observed pe-ratios were combined with *in-situ* observations of mixed layer temperature, depth-integrated chlorophyll, depth-integrated PP, new production, particle export, depth of the euphotic zone (minimum of the 1% light level or sampling zone), and the carbon-to-chlorophyll ratio. They found that the Eppley and Peterson (1979), (Figure 5A) algorithm has the lowest coefficient of determination (9%), which they attributed to the parameterization relying on the integral of PP alone. The Baines et al. (1994), (Figure 5B) algorithm added euphotic zone depth in addition to the depth-integral of PP and was able to account for a higher fraction of the variance (38%), while not improving the relative uncertainty (64%). A different approach was used by Baines et al. (1994), (Figure 5C) where chlorophyll concentrations were utilized as the predictive variable. Their parameterization was able to account for a slightly higher variance (40%) while also decreasing the relative uncertainty (46%), but showed a strong bias to low values at higher pe-ratios. Dunne et al. (2005) found that the Laws et al. (2000), (Figure 5D) algorithm succeeded in reproducing large-scale structures in the data and accounted for nearly half of the variance (47%), while decreasing the relative error to 43%. The major shortcoming of this algorithm was in reproducing variability in pe-ratios at high temperatures. Dunne et al. (2005) suggested that "a weaker temperature dependence for phytoplankton and bacterial metabolism than for zooplankton metabolism" accounts for this misfit.

The algorithm developed by Dunne et al. (2005), (Figures 5E, F) provided a reasonable fit to the compiled dataset of observations, with an R^2 of 58% and a relative uncertainty of 33%. The algorithm had low skill in areas with the highest pe-ratios and sites with a combination of very high pe-ratios and low to moderate PP. This discrepancy if compensated for using biomass instead of PP improved R^2 to 61% with a relatively low relative error (35%). Dunne et al. (2005) explained this improvement with biomass integrating ecosystem processes better over time than PP.

Li and Cassar (2016) evaluated a number of algorithms described in section 2 by matching O_2/Ar- derived NCP observations (see section 3.3) with satellite derived 8-day 0.083° × 0.083° SeaWiFS Chl and PAR, VGPM NPP, and AVHRR SST. The standard SeaWiFS Chl algorithm was shown to underestimate [Chl] by a factor of 2 to 3 in the Southern Ocean at the time when Li and Cassar (2016) conducted the evaluation (Kahru and Mitchell, 2010) and were improved by using a blending scheme presented by Kahru and Mitchell (2010). VGPM NPP was based on the recalculated Chl data product. Phytoplankton size composition was derived using Li et al. (2013) and VGPM NPP for the algorithm developed by Siegel et al. (2014), together with the other parameters as presented in Siegel et al. (2014). See Li and Cassar (2016) for more detailed descriptions of the data sources.

Li and Cassar (2016) used the satellite-derived data to calculate export production for the Eppley and Peterson (1979); Betzer et al.

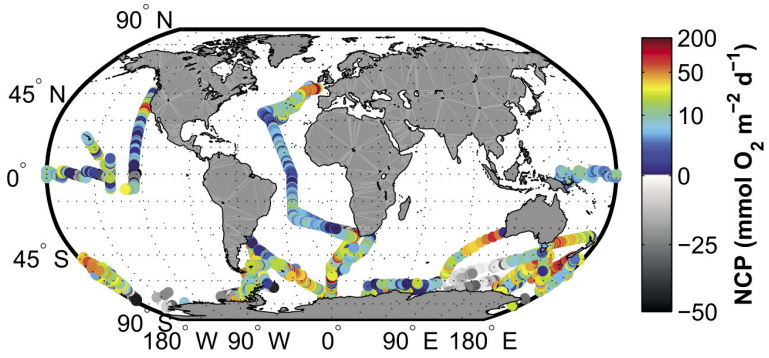


FIGURE 4
Global map of O2/Ar measurements from Li and Cassar (2016). Samples with positive values are color coded. Samples with negative values are shown using a gray scale. Image from Li and Cassar (2016).

(1984); Baines et al. (1994); Laws et al. (2000); Dunne et al. (2005); Laws et al. (2011); Westberry et al. (2012), and Siegel et al. (2014) algorithms. They also used the data together with observed O_2/Ar-NCP to develop the Li and Cassar (2016) algorithm. The main assumption here was that the O2/Ar-NCP is a valid proxy for EP. One could expect Li and Cassar (2016) to outperform the other algorithms since the observational dataset was used to train the algorithm, but this was not the case (Figure 6). Instead, all EP predicting algorithms showed surprisingly similar results. Eppley & Peterson (1979); Betzer et al. (1984), and Baines et al. (1994) showed almost identical distributions in the regressions against observations with R^2s between 0.58 and 0.65. The algorithms of Eppley & Peterson (1979) and Betzer et al. (1984) in particular tended to overestimate low NCP values. The different Laws et al. (2000); Laws et al. (2011) algorithms all provided a smaller spread around the 1:1 line and a slightly better R^2 (0.64-0.7). The algorithms of Laws et al. (2000) also overestimated low NCP, while the algorithm of Laws et al. (2011); (Equation 12 and 13) showed symmetrical distributions. The Dunne et al. (2005) algorithm, on the other hand, tended to underestimate NCP. This tendency was even greater for Westberry et al. (2012) and Siegel et al. (2014), which also showed among the lowest R^2s (0.62 and 0.55, respectively). This is particularly surprising for the algorithm of Westberry et al. (2012), which was developed using a framework that was based on the assumption of NCP being a good general proxy for EP. The two algorithms developed by Li and Cassar (2016) showed, as expected, a good skill in predicting O_2/Ar-NCP. Their Support Vector Regression (SVR) approach had the highest R^2, but seemed to have a floor where values below a certain threshold were not being predicted. This could be a consequence of how the SVR was configured. The fact that all approaches showed similar and relatively good skills in predicting O_2/Ar- NCP and EP is surprising, as the various algorithms model different components of the biological pump.

The Stukel et al. (2015) EP algorithm comparison is based on a Lagrangian approach where *in-situ* rates of NPP, EP and auxiliary parameters were observed concurrently in a water mass. They do this by compiling results from Lagrangian process studies in the North Eastern Pacific Ocean (see Stukel et al., 2015, and section 3.2 for details). One main advantage of this approach is the ability to disentangle errors associated with inaccuracies of remote sensing products (e.g., PP, Chl, and SST) and errors associated with the model used to estimate EP. Their intention was not to conduct a definitive comparison of competing satellite algorithms, but rather to begin a process that assess and hopefully improves the different assumptions and parameterizations in current satellite algorithms, especially Siegel et al. (2014).

Satellite algorithms for EP are generally designed to predict export at either Z_{eu} or 100 meters. While the observations used by Stukel et al. (2015) were within 30 m of Z_{eu}, they scaled all data to Z_{eu} using the ambient PAR at the depth of sampling. All EP algorithms were evaluated using *in-situ* input properties (e.g., SST, Chl, PP) as the goal was not to assess the corresponding satellite products. All water column rates and standing stock measurements were depth integrated, except when models made explicit reference to sea surface values, for methodological reasons. Stukel et al. (2015) noted that Dunne et al. (2005) and Laws et al. (2011) are parametrized to predict total EP including active transport by diel vertically migrating organisms and passive export of DOC, leading to a positive bias since sediment traps and ^{234}Th only measure POC fluxes. Stukel et al. (2013) estimated that the active transport by diel migration is about 19% of the total sinking flux in the CCE region, providing a lower constraint on this bias.

Figure 7 shows the resulting comparisons between satellite algorithms and *in-situ* measurements. At a first look, it seems that no algorithm performed significantly better or worse than any other. Dunne et al. (2005) and Siegel et al. (2014) had R^2 coefficients of determination of 0.37, whereas the R^2 for Henson et al. (2011) and Laws et al. (2011) were 0.27. Stukel et al. (2015) re-parameterized Siegel et al. (2014) using their *in-situ* observations and improved the R^2 to 0.38. It should be noted that all algorithms have been developed and parameterized to function in a global setting in all physical, chemical, and biological settings. This study

Stukel et al. (2015) performed a comparison in one specific region with a small subset of ecosystem dynamics and conditions.

Puigcorbe et al. (2017) compared Dunne et al. (2005); Laws et al. (2011), and Henson et al. (2011) using PP estimates from three different satellite-derived primary production models and a regional dataset of POC fluxes based on ^{234}Th from the North Western Atlantic Ocean. They found that Dunne et al. (2005) and Laws et al. (2011) were closest to the observations but showed a 3-fold difference and no clear trends. Henson et al. (2011) consistently provided lower export estimates than the observations. Their explanation is that a stronger dependency on temperature by Henson et al. (2011) leads to low export fluxes (¡ 2 mmol C m^{-2} d $^{-1}$) throughout the study area. They also observe a significant overestimation of EP by Dunne et al. (2005) in their equatorial

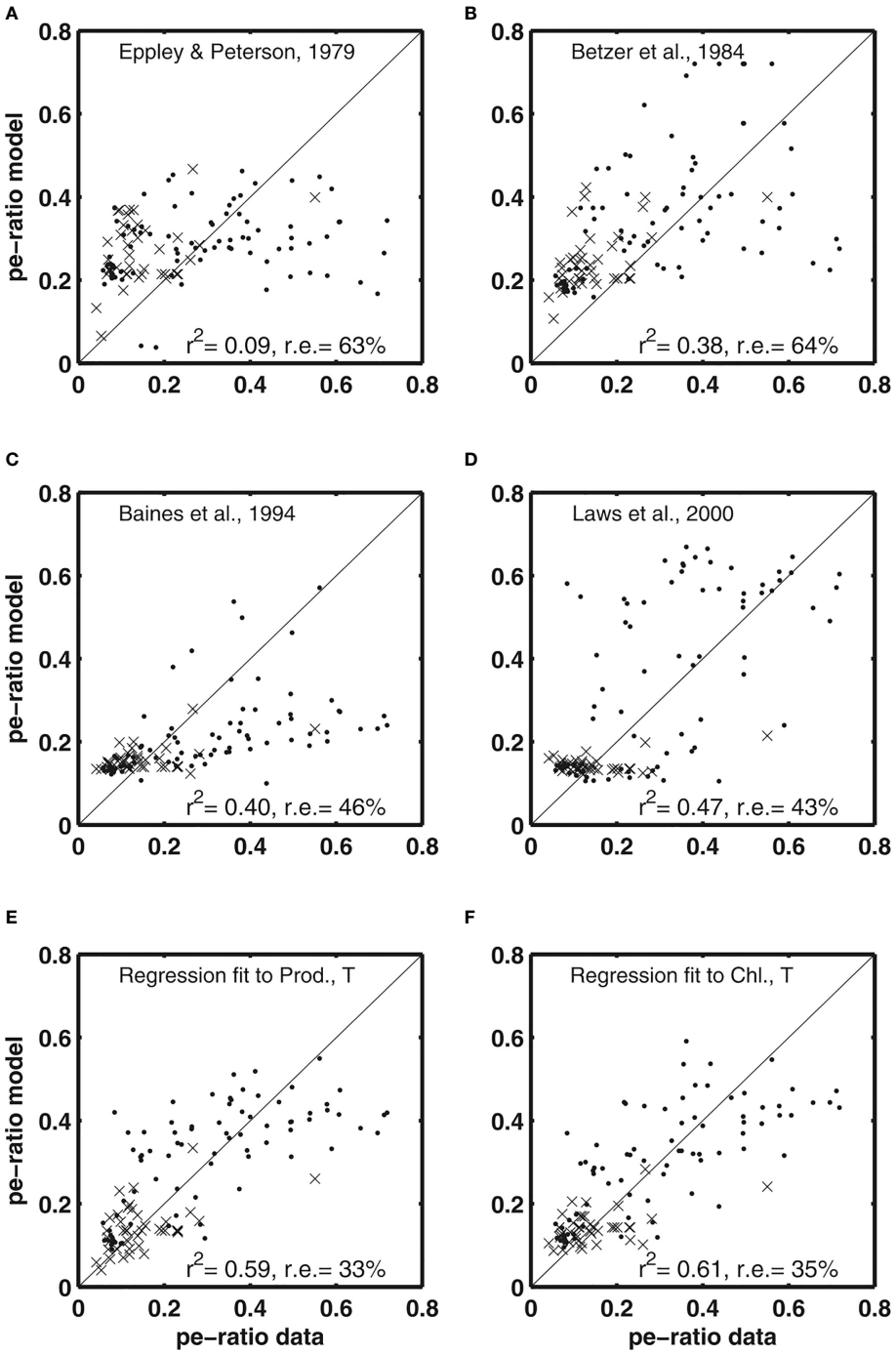


FIGURE 5
Comparison of particle export ratio estimates by Dunne et al. (2005) of various models described in section 2 using data described in section 3.1. Panels **(A-D)** show results based on algorithms described in sections 2.1, 2.3, 2.5, and 2.6, and panels **(E, F)** the two algorithms described in section 2.7. Symbols are grouped by temperature into less than 14°C (crosses) and greater than 14°C (dots). Image from Dunne et al. (2005).

domain and that Laws et al. (2011) seems to underestimate EP both in the northern half of their oligotrophic domain and at several riverine stations.

5 Evaluating the different EP models using three *in situ* databases

The evaluations described so far are all promoting a new algorithm (Dunne et al., 2005; Li and Cassar, 2016) or re-parameterizing an existing algorithm (Stukel et al., 2015). While the different approaches are thorough and the results consistent between the three studies, we believe it worthwhile to evaluate the different algorithms from a neutral starting point. For this, we use the published dataset of POC fluxes by Dunne et al. (2005); Mouw et al. (2016a); Mouw et al. (2016b), and Bisson et al. (2018). We matched the Mouw et al. (2016a); Mouw et al. (2016b) and Bisson et al. (2018) data with monthly satellite-derived SST from the Group for High Resolution Sea Surface Temperature/Operational Sea Surface Temperature and Ice Analysis (UKMO, 2005, GHRSST/OSTIA), Chl and Kd_{490} from Ocean Colour Climate Change Initiative (Sathyendranath, 2021, OC-CCI), and PP from the Biological Pump and Carbon Exchange Processes project (Kulk et al., 2021, BICEP). It should be noted that different satellite-based PP products vary considerably (Bisson et al., 2018; Siegel et al., 2022), which can affect the calculated EP estimates Bisson et al. (2018). We found, however, that different PP products had only a limited influence on the skill of the EP algorithms evaluated in this

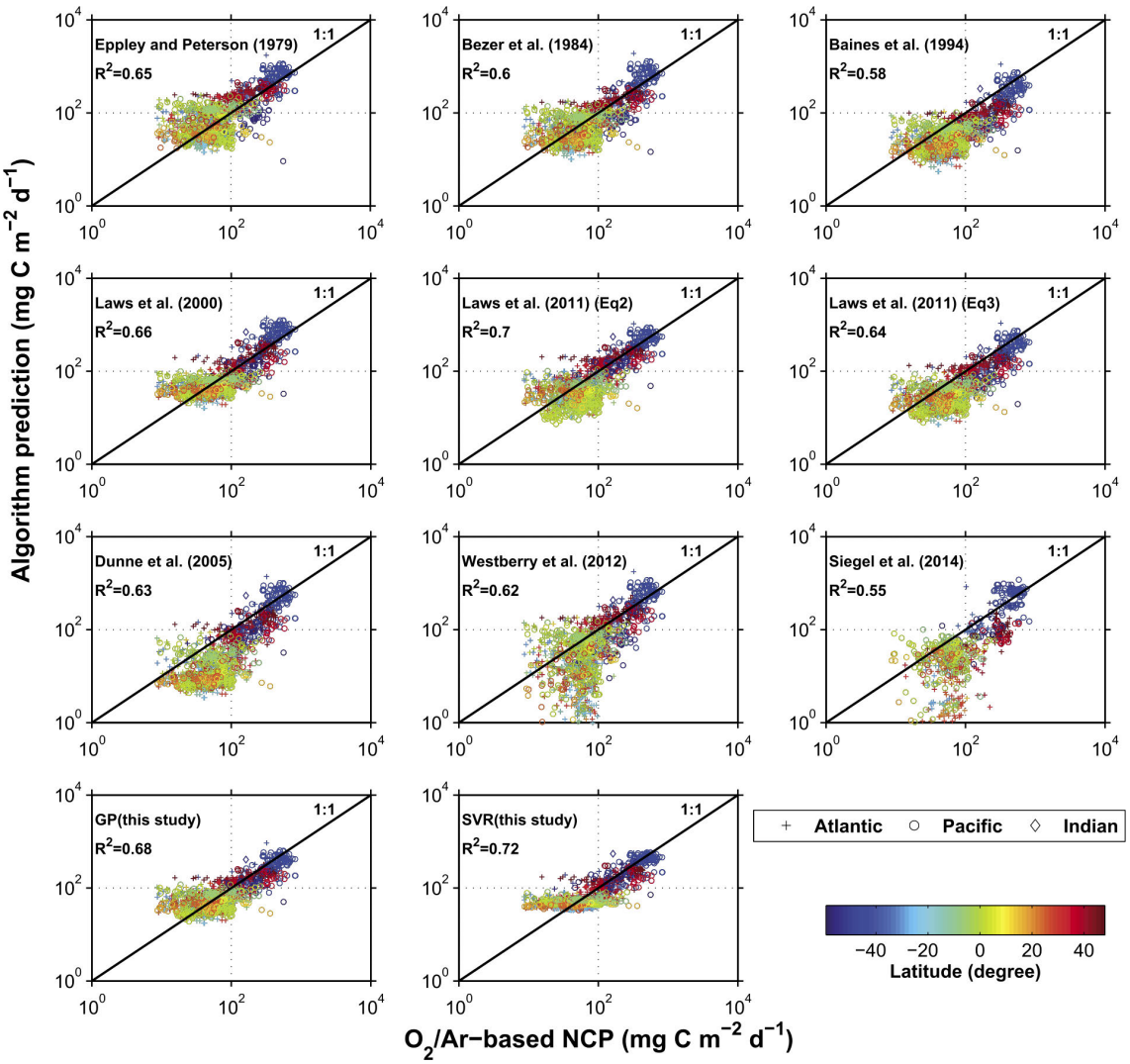


FIGURE 6
Comparison of satellite algorithms of carbon export production by Li and Cassar (2016). O_2/Ar-derived NCP was converted to C using a stoichiometry of O_2/C=1.4 (Laws, 1991). Samples with O_2/Ar-NCP estimates<1.0 mmol O_2 m^2 d^{-1} were excluded. Phytoplankton size composition was derived using Li et al. (2013) and VGPM NPP for the algorithm developed by Siegel et al. (2014), together with the other parameters as presented in Siegel et al. (2014). Image from Li and Cassar (2016).

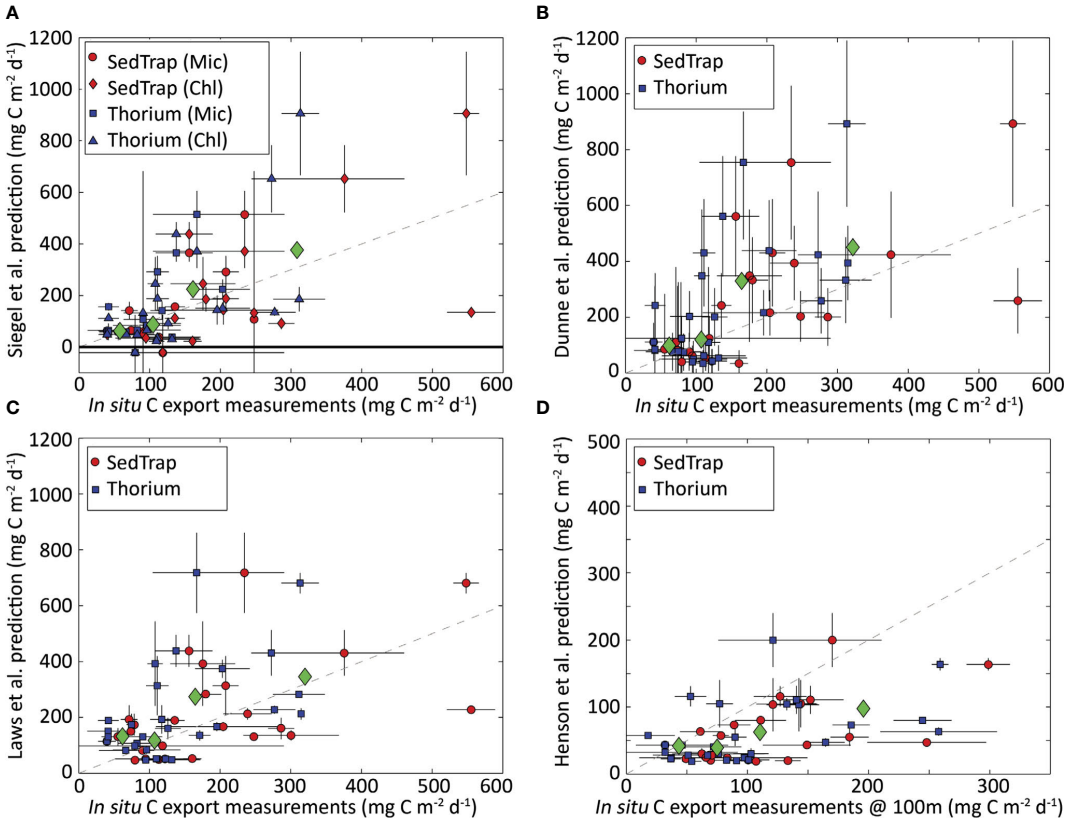


FIGURE 7
Comparison between satellite algorithms and *in-situ* measurements by Stukel et al. (2015). **(A)** Siegel et al. (2014) vs sediment-trap-(circles and diamonds) and ^{234}Th-derived (squares and triangles) measurements. Circles and squares are based on results using microscopy to determine the fraction of microphytoplankton. **(B–D)** Dunne et al. (2005); Laws et al. (2011), and Henson et al. (2011) algorithms, respectively, with circles showing sediment trap data and squares showing ^{234}Th data. All panels show export normalized to the base of the Z_{eu}, except panel D, which shows export at 100m. Green diamonds show arithmetic mean of predicted and measured export for each quartile of the measurements (35-85, 85-125, 125-205, and 205-560 mg C m^{-2} d^{-1} for base of Z_{eu}; 18-65, 65-89, 89-140, and 140-300 mg C m^{-2} d^{-1} for 100m). Dashed lines depict a 1:1 relationship. Error bars show one standard error (for *in-situ* measurements) and propagation of measurement standard error through satellite algorithms (for predictions). Image from Stukel et al. (2015).

study and we therefore chose to only present results based on one PP product.

We begin by calculating global EP flux estimates averaged over the years 1998–2020 for all algorithms using the earlier mentions satellite-derived products (all values presented in Table 3). The flux estimates are between 1 and 140 Gt C y^{-1}, a much larger range of uncertainty than normally presented for EP. If only algorithms with one of the top three skills scores in any of our evaluations (red colors in Tables 3, 4, 5) are included, the range is 1–9 Gt C y^{-1}, This result is more in line with earlier published estimates (Dunne et al., 2007; Henson et al., 2011; Laws et al., 2011; Siegel et al., 2016; Siegel et al., 2022).

Dunne et al. (2005) does not report any information about sampling dates, which means that we are not able to match satellite-derived properties to the dataset. Instead, we rely on properties included in the dataset (n=125), all which we believe to be based on *in-situ* observations. There is 487 satellite matchups for Mouw et al. (2016b) observations between 100 and 200 meter, and 1,058 matchups for Bisson et al. (2018). All observations used in the comparisons are shown in Figure 3. The three datasets covers similar regions, but do not necessarily include the same observations. This is to be expected since our use of the Mouw et al. (2016b) and Bisson et al. (2018) datasets are limited to the time of ocean color satellite coverage (1998 to present) whereas the Dunne et al. (2005) dataset has a cutoff some years before publication. Bisson et al. (2018) have several long transects included that are not part of Mouw et al. (2016b).

When visually comparing *in-situ* POC fluxes with predicted EP calculated using the Dunne et al. (2005); Laws et al. (2000), and Li and Cassar (2016) algorithms (Figures 8–10) we see similar patterns. Comparing the Dunne et al. (2005) algorithm in its corresponding *in-situ* dataset results, as expected, in the same correlation as reported by the paper. A more interesting finding is that the two other algorithms have similarly good skill in predicting EP. The main exception is a slight offset from the 1:1 line by Li and Cassar (2016). When using *in-situ* POC flux from Mouw et al. (2016b) dataset together with matched satellite properties, we see quite different results where neither observations from deep waters (purple markers) nor data from shallow water at less than 200 m depth (blue markers) are predicted particularly well. The main issue seems to be that low observed values are not predicted as low values by the algorithm, which results in EP being significantly overestimated compared to observations. Here, the relationship

TABLE 3 Performance metrics for different export production models evaluated using the Dunne et al. (2005) dataset.

Algorithm	R^2	MAE	RMSE	MAPE	sMAPE	Bias	Global flux (Gt C y^{-1})
Eppley and Peterson (1979)	0.09	0.99	1.20	0.74	0.45	0.99	20
Suess (1980)	0.36	0.82	1.01	0.62	0.40	0.82	15
Betzer et al. (1984)	-4.11	2.76	2.84	1.43	1.75	2.76	1.2
Pace et al. (1987)	0.52	0.71	0.87	0.32	0.34	0.71	4.9
Baines et al. (1994)	-12.57	4.59	4.63	2.65	1.03	4.59	140
Laws et al. (2000)	0.71	0.53	0.67	0.32	0.31	0.53	6
Dunne et al. (2005)	0.86	0.39	0.47	0.24	0.23	0.39	2.0
Henson et al. (2011)	-0.19	1.24	1.37	0.60	0.91	1.24	1.7
Laws et al. (2011)	0.69	0.55	0.70	0.30	0.30	0.55	7.1
Laws et al. (2011)	0.40	0.82	0.97	0.37	0.43	0.82	5.9
Westberry et al. (2012)	0.10	1.00	1.19	0.69	0.44	1.00	27
Li and Cassar (2016)	0.74	0.52	0.64	0.38	0.30	0.52	8.7

All EP values are log-transformed. Higher is better for R^2 while lower is better for the other metrics. Red colors denote the three algorithms with highest skill according to each metric. The final column contains global flux estimates averaged over the years 1998–2020 using each respective algorithm and satellite-derived data described in the text.

between POC flux and EP based on the Dunne et al. (2005) dataset could arguably act as an upper constraint when applying the algorithms to the Mouw et al. (2016b) dataset. We find a less coherent pattern when *in-situ* POC flux from Bisson et al. (2018) is plotted against EP from the three algorithms. The distribution of values in Bisson et al. (2018) is trending higher than Mouw et al. (2016b), but EP predicted by Dunne et al. (2005) falls within the same range for both *in-situ* datasets, leading to a notable underestimation by the algorithm. This pattern can be found for Li and Cassar (2016), but is less pronounced, whereas Laws et al. (2000) generates EP predictions that are quite symmetrically distributed around the 1:1 line. Figures for the other algorithms can be found in the Supplementary Materials.

Finally, we compare log transformed predictions of EP from the different satellite-based models to *in-situ* observations of POC flux using a number of metrics: coefficient of determination (R^2, Wright, 1921), Mean Absolute Error (MAE, Chicco et al., 2021), Root Mean Square Error (RMSE, Nevitt and Hancock, 2000), Mean Absolute Percent Error (MAPE, Myttenaere et al., 2016), symmetric Mean Absolute Percentage Error (sMAPE Makridakis, 1993), and Bias. Please see Chicco et al. (2021) and Seegers et al. (2018) for a more detailed discussion about each metric and their utility. All values are presented in Tables 3–5. We find that most models have limited to very limited skill when evaluated with R2 against the Mouw et al. (2016b) or Bisson et al. (2018) datasets, whereas several models perform better with Dunne et al. (2005); Li and Cassar (2016), and

TABLE 4 Performance metrics for different export production models evaluated using the Mouw et al. (2016a); Mouw et al. (2016b) dataset.

Algorithm	R^2	MAE	RMSE	MAPE	sMAPE	Bias
Eppley and Peterson (1979)	-2.79	2.01	2.30	0.74	0.49	2.01
Suess (1980)	-2.10	1.76	2.08	0.66	0.44	1.76
Betzer et al (1984)	-0.66	1.28	1.52	0.40	0.46	1.28
Pace et al (1987)	-0.18	0.79	1.29	0.33	0.24	0.79
Baines et al. (1994)	-11.29	3.94	4.10	1.37	0.76	3.94
Laws et al. (2000)	-1.44	1.23	1.98	0.56	0.34	1.23
Dunne et al. (2005)	-0.10	0.90	1.33	0.36	0.32	0.90
Henson et al. (2011)	-0.64	1.10	1.63	0.45	0.38	1.10
Laws et al. (2011)	-1.39	1.30	1.96	0.58	0.36	1.30
Laws et al. (2011)	-0.70	0.98	1.65	0.46	0.30	0.98
Westberry et al. (2012)	-3.60	2.27	2.54	0.83	0.53	2.27
Li and Cassar (2016)	-1.47	1.45	1.99	0.63	0.40	1.45

Only observations between 100 and 200 meters are included and all EP values are log-transformed. Higher is better for R^2 while lower is better for the other metrics. Red colors denote the three algorithms with highest skill according to each metric.

TABLE 5 Performance metrics for different Export Production models evaluated using the Bisson et al. (2018) dataset.

Algorithm	R^2	MAE	RMSE	MAPE	sMAPE	Bias
Eppley and Peterson (1979)	-1.47	1.63	1.94	0.60	0.39	1.63
Suess (1980)	-1.06	1.45	1.77	0.54	0.36	1.45
Betzer et al (1984)	-2.46	1.88	2.30	0.50	0.66	1.88
Pace et al (1987)	-0.30	0.98	1.41	0.34	0.28	0.98
Baines et al. (1994)	-7.48	3.24	3.49	1.11	0.63	3.24
Laws et al. (2000)	-0.32	0.92	1.40	0.37	0.25	0.92
Dunne et al. (2005)	-0.99	1.29	1.67	0.38	0.41	1.29
Henson et al. (2011)	-0.62	1.25	1.56	0.39	0.39	1.25
Laws et al. (2011)	-0.38	0.97	1.43	0.39	0.26	0.97
Laws et al. (2011)	-0.36	0.95	1.42	0.35	0.27	0.95
Westberry et al. (2012)	-2.00	1.83	2.14	0.67	0.43	1.83
Li and Cassar (2016)	-0.44	1.06	1.46	0.42	0.28	1.06

All EP values are log-transformed. Higher is better for R^2 while lower is better for the other metrics. Red colors denote the three algorithms with highest skill according to each metric.

Laws et al. (2000) at the top, when comparing predicted EP to *in-situ* POC fluxes in Dunne et al. (2005) dataset using *in-situ* properties only. These results are in accordance with the earlier presented visual comparisons. The other metrics show similar patterns.

6 Discussion and conclusions

The EP algorithms described here assume different definitions of export efficiency, are based on different products for deriving PP from satellite products (who themselves have different assumptions

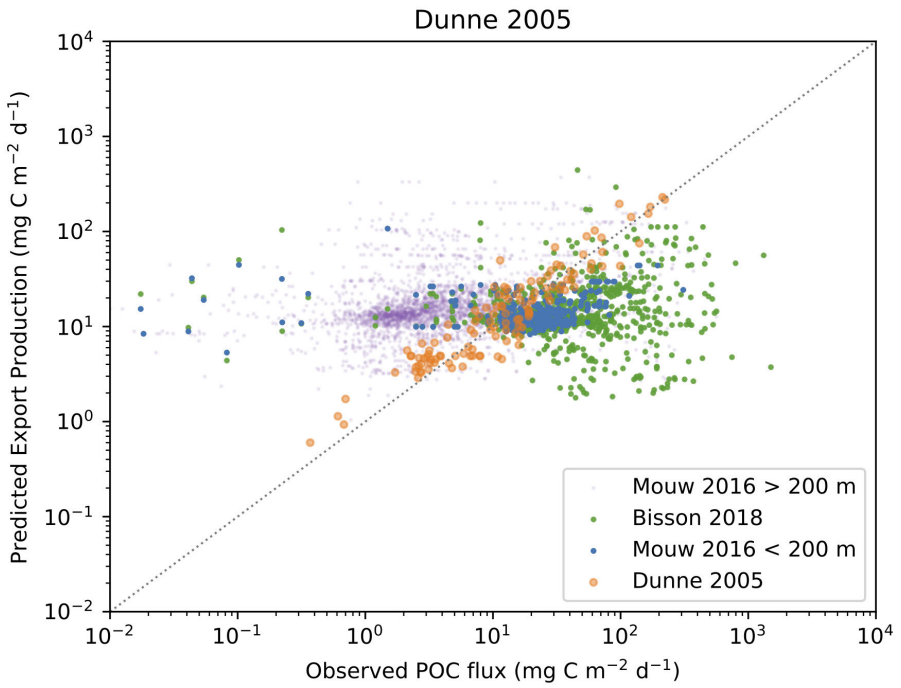


FIGURE 8
Observed POC flux and EP calculated using the Dunne et al. (2005) algorithm. *In-situ* observations are from Dunne et al. (2005), orange markers) Mouw et al. (2016a); Mouw et al. (2016b), (blue markers for observations shallower than 200 meters and purple for observations deeper than 200 meters), and Bisson et al. (2018), (green markers).

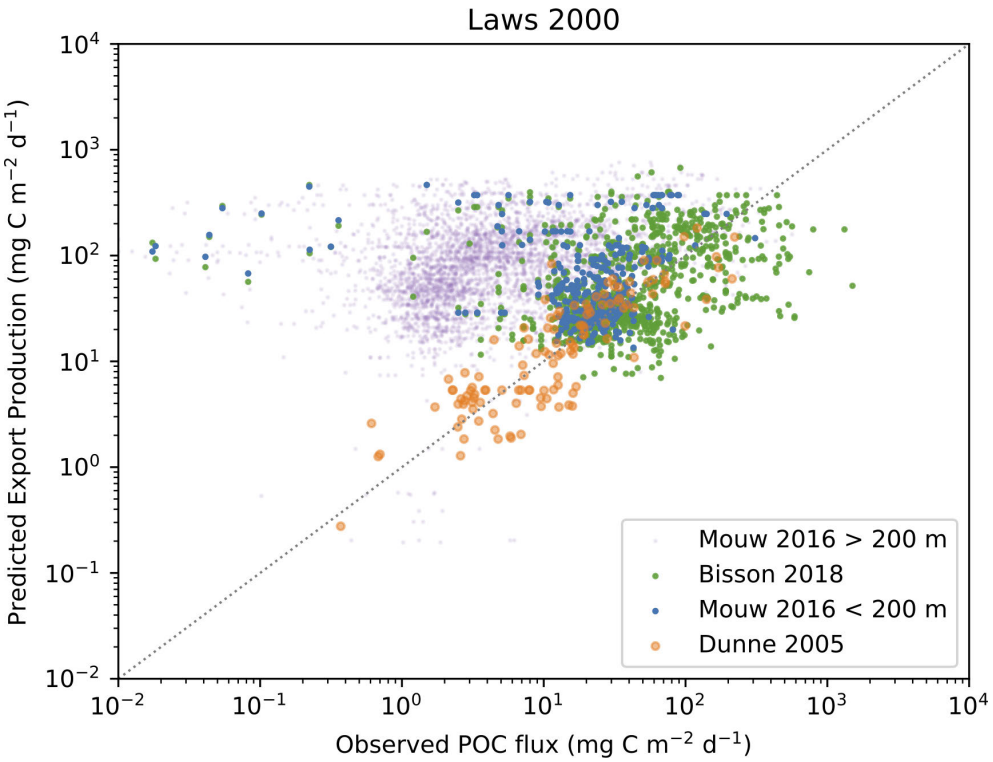


FIGURE 9
Observed POC flux and EP calculated using the Laws et al. (2000) algorithm. *In-situ* observations are from Dunne et al. (2005), (orange markers) Mouw et al. (2016a); Mouw et al. (2016b), (blue markers for observations shallower than 200 meters and purple for observations deeper than 200 meters), and Bisson et al. (2018), (green markers).

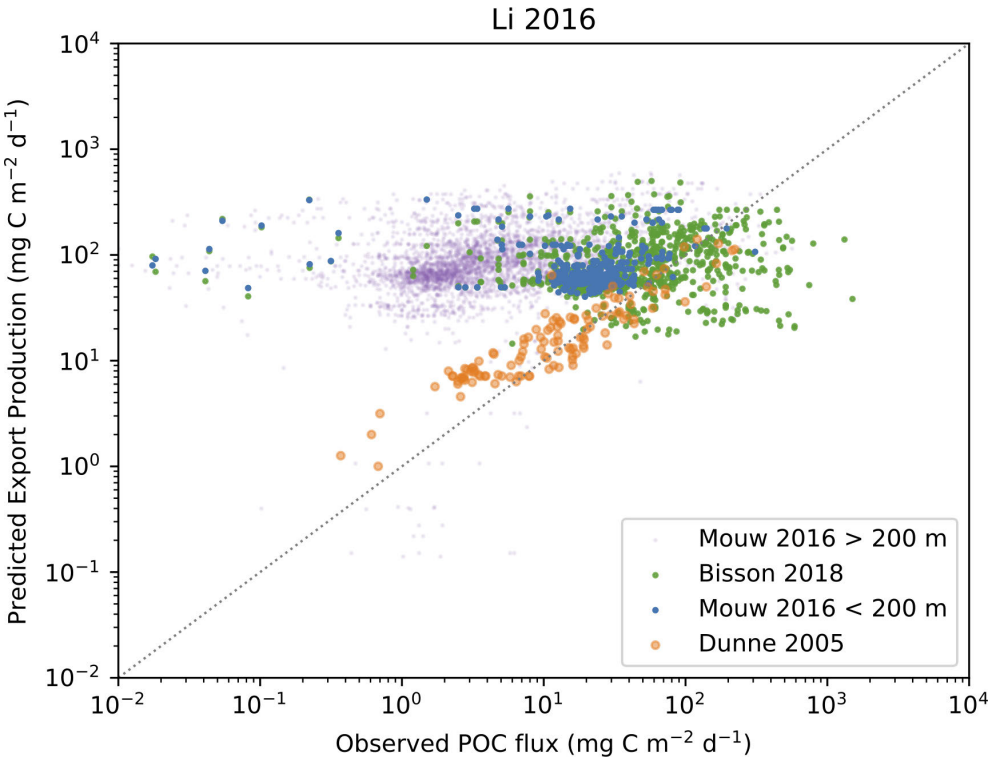


FIGURE 10
Observed POC flux and EP calculated using the Li and Cassar (2016) algorithm. *In-situ* observations are from Dunne et al. (2005), (orange markers) Mouw et al. (2016a); Mouw et al. (2016b), (blue markers for observations shallower than 200 meters and purple for observations deeper than 200 meters), and Bisson et al. (2018), (green markers).

about PP), and are developed using different *in-situ* datasets. Still, the skill of predicting export production is surprisingly similar among the different algorithms. Both the Dunne et al. (2005) and Li and Cassar (2016) algorithm evaluations showed that their own model provides the best results, which is not too surprising since they were developed using the evaluation data. The advantage is, however, modest for Dunne et al. (2005) and insignificant for Li and Cassar (2016). The Stukel et al. (2015) evaluation used a Lagrangian *in-situ* dataset collected with the Siegel et al. (2014) algorithm in mind and performed a re-parameterization of said algorithm, but only achieved a modest improvement in skill measured as R^2. The authors argued that other statistical methods are more useful to evaluate EP algorithms and Siegel et al. (2014) showed a larger improvement by those metrics.

There is only a slight correlation between how complex an algorithm is and how well it performs. Siegel et al. (2014) is arguably the most complex approach and showed good results in the Stukel et al. (2015) study, but was performing rather poorly in Li and Cassar (2016). The simplest approach is by Eppley and Peterson (1979), which is the only algorithm evaluated that uses PP as the sole independent input feature. It performed worse than other algorithms in Dunne et al. (2005) but reasonably well in Li and Cassar (2016). This might suggest that SST is a more important factor when estimating carbon fluxes at depth than EP from the euphotic zone.

We find that using the Mouw et al. (2016b) dataset together with satellite-derived properties provide a poor correlation between observed POC flux and predicted EP for the Dunne et al. (2005) algorithm, the reason for this is not entirely clear. Some possible explanations are problems with the satellite-derived products used or differences in how the Dunne et al. (2005) and Mouw et al. (2016b) datasets represent the global ocean. Another possible reason is (we assume) that all properties used in the Dunne et al. (2005) dataset are specifically sampled in connection to the POC flux observations. One could expect a better connection between surface processes and thermocline fluxes when observed over appropriate temporal and spatial scales. This suggestion would also explain the good correlations found by Stukel et al. (2015) and Li and Cassar (2016), the latter by not relying of thermocline fluxes in the evaluation.

A future step to better understand the contrasting results seen in this study is to re-evaluate all models with all available datasets. It is a reasonable assumption that empirical relationships between available satellite-derived products and EP differ significantly between different regions of the ocean (Sathyendranath et al., 1991; Stukel et al., 2015; Britten and Primeau, 2016; Li and Cassar, 2016). Recent syntheses of *in-situ* observations within the BICEP and EXPORTS projects have created the potential to re-parametrize existing algorithms and to perform new regression analyses on regional scales. An alternative promising approach to estimate EP from space is to use satellite-derived properties for data assimilation in biogeochemical models. Two recent examples are studies by DeVries and Weber (2017) and Nowicki et al. (2022) where they quantify the biological pump by using satellite and oceanographic tracer observations to constrain rates and patterns of organic matter production, export, and remineralization in an inverse model framework.

Author contributions

BJ: Conceptualization, design of the work, literature review, draft, and revision of the text. GK: Conceptualization and revision of the text. SS: Funding and conceptualization. All authors contributed to the article and approved the submitted version.

Funding

Funding for this work was provided by the European Space Agency project "Biological Pump and Carbon Exchange Processes (BICEP)" and by the Simons Collaboration on Computational Biogeochemical Modeling of Marine Ecosystems (CBIOMES) (549947 SS). Additional support from the National Centre for Earth Observations of the UK is acknowledged.

Conflict of interest

The authors declare that the research was conducted in the absence of any commercial or financial relationships that could be construed as a potential conflict of interest.

Publisher's note

All claims expressed in this article are solely those of the authors and do not necessarily represent those of their affiliated organizations, or those of the publisher, the editors and the reviewers. Any product that may be evaluated in this article, or claim that may be made by its manufacturer, is not guaranteed or endorsed by the publisher.

Supplementary material

The Supplementary Material for this article can be found online at: https://www.frontiersin.org/articles/10.3389/fmars.2023.1149938/full#supplementary-material

References

Antoine, D., Andre, J.-M., and Morel, A. (1996). Oceanic primary production: 2. estimation at global scale from satellite (coastal zone *color scanner) chlorophyll. Global Biogeochemical Cycles* 10, 57–69. doi: 10.1029/95GB02832

rrigo, K. R., Worthen, D., Schnell, A., and Lizotte, M. (1998). Primary production in southern ocean waters. *J. Of Geophysical Research-Oceans* 103, 15587–15600. doi: 10.1029/98JC00930

Baines, S. B., Pace, M. L., and Karl, D. M. (1994). Why does the relationship between sinking flux and planktonic primary production differ between lakes and oceans? *Limnology Oceanography* 39, 213–226. doi: 10.4319/lo.1994.39.2.0213

Balch, W. M., Carranza, M., Cetinic, I., Chaves, J., Duhamel, S., Fassbender, A., et al. (2022). *Ioccg ocean optics and biogeochemistry protocols for satellite ocean colour sensor validation volume 7.0. aquatic primary productivity field protocols for satellite validation and model synthesis*. Dartmouth, NS, Canada: International Ocean Colour Coordinating Group (IOCCG), Vol. volume 7.0. doi: 10.25607/OBP-1835

Behrenfeld, M. J., and Falkowski, P. G. (1997). A consumer's guide to phytoplankton primary productivity models. *Limnology And Oceanography* 42, 1479–1491. doi: 10.4319/lo.1997.42.7.1479

Bender, M. L., Grande, K., Johnson, K. S., Marra, J., Williams, P. J. L. B., Sieburth, J., et al. (1987). A comparison of 4 methods for determining planktonic community production. *Limnology And Oceanography* 32, 1085–1098. doi: 10.4319/lo.1987.32.5.1085

Betzer, P. R., Showers, W. J., Laws, E. A., Winn, C. D., DiTullio, G. R., and Kroopnick, P. M. (1984). Primary productivity and particle fluxes on a transect of the equator at 153 ° w in the pacific ocean. Deep Sea Research Part A. *Oceanographic Res. Papers* 31, 1–11. doi: 10.1016/0198-0149(84)90068-2

Bisson, K. M., Siegel, D. A., DeVries, T., Cael, B. B., and Buesseler, K. O. (2018). How data set characteristics influence ocean carbon export models. *Global Biogeochemical Cycles* 32, 1312–1328. doi: 10.1029/2018gb005934

Britten, G. L., and Primeau, F. W. (2016). Biome-specific scaling of ocean productivity, temperature, and carbon export efficiency. *Geophysical Res. Lett.* 43, 5210–5216. doi: 10.1002/2016gl068778

Buesseler, K. O. (1998). The decoupling of production and particulate export in the surface ocean. *Global Biogeochemical Cycles* 12, 297–310. doi: 10.1029/97GB03366

Buesseler, K. O., Antia, A. N., Chen, M., Fowler, S. W., Gardner, W. D., Gustafsson, O., et al. (2007). An assessment of the use of sediment traps for estimating upper ocean particle fluxes. *J. Mar. Res.* 65, 345–416. doi: 10.1357/002224007781567621

Buesseler, K., Benitez-Nelson, C., Moran, S., Burd, A., Charette, M., Cochran, J., et al. (2006). An assessment of particulate organic carbon to thorium-234 ratios in the ocean and their impact on the application of 234th as a poc flux proxy. *Mar. Chem.* 100, 213–233. doi: 10.1016/j.marchem.2005.10.013

Burd, A. B., Hansell, D. A., Steinberg, D. K., Anderson, T. R., Arístegui, J., Baltar, F., et al. (2010). Assessing the apparent imbalance between geochemical and biochemical indicators of meso- and bathypelagic biological activity: What the heck is wrong with present calculations of carbon budgets? *Deep Sea Res. Part II: Topical Stud. Oceanography* 57, 1557–1571. doi: 10.1016/j.dsr2.2010.02.022

Cassar, N., Barnett, B. A., Bender, M. L., Kaiser, J., Hamme, R. C., and Tilbrook, B. (2009). Continuous high-frequency dissolved o2/ar measurements by equilibrator inlet mass spectrometry. *Analytical Chem.* 81, 1855–1864. doi: 10.1021/ac802300u

Ceballos-Romero, E., Buesseler, K. O., and Villa-Alfageme, M. (2022). Revisiting five decades of 234th data: a comprehensive global oceanic compilation. *Earth System Sci. Data* 14, 2639–2679. doi: 10.5194/essd-14-2639-2022

Chavez, F. P., Messie, M., and Pennington, J. T. (2011). Marine primary production in relation to climate variability and change. *Annu. Rev. Mar. Sci.* 3, 227–260. doi: 10.1146/annurev.marine.010908.163917

Chicco, D., Warrens, M. J., and Jurman, G. (2021). The coefficient of determination r-squared is more informative than smape, mae, mape, mse and rmse in regression analysis evaluation. *PeerJ Comput. Sci.* 7, e623. doi: 10.7717/peerj-cs.623

Craig, H. C., and Hayward, T. (1987). Oxygen supersaturation in the ocean - biological versus physical contributions. *Science* 235, 199–202. doi: 10.1126/science.235.4785.199

Cullen, J. J. (2001). "Primary production methods," in *Encyclopedia of Ocean Sciences* (Cambridge, Massachusetts: Elsevier), 2277–2284. doi: 10.1006/rwos.2001.0203

DeVries, T., and Weber, T. (2017). The export and fate of organic matter in the ocean: New constraints from combining satellite and oceanographic tracer observations. *Global Biogeochemical Cycles* 31, 535–555. doi: 10.1002/2016gb005551

Dore, J. E., and Karl, D. M. (1996). Nitrification in the euphotic zone as a source for nitrite, nitrate, and nitrous oxide at station aloha. *Limnology Oceanography* 41, 1619–1628. doi: 10.4319/lo.1996.41.8.1619

Duarte, C. M., Regaudie-De-Gioux, A., Arrieta, J. M., Delgado-Huertas, A., and Agusti, S. (2013). The oligotrophic ocean is heterotrophic. *Ann Rev Mar Sci* 5, 551–569. doi: 10.1146/annurev-marine-121211-172337

Dugdale, R. C., and Goering, J. J. (1967). Uptake of new and regenerated forms of nitrogen in primary productivity. *Limnology Oceanography* 12, 196–206. doi: 10.4319/lo.1967.12.2.0196

Dunne, J. P., Armstrong, R. A., Gnanadesikan, A., and Sarmiento, J. L. (2005). Empirical and mechanistic models for the particle export ratio. *Global Biogeochemical Cycles* 19, n/a–n/a. doi: 10.1029/2004gb002390

Dunne, J. P., Sarmiento, J. L., and Gnanadesikan, A. (2007). A synthesis of global particle export from the surface ocean and cycling through the ocean interior and on the seafloor. *Global Biogeochemical Cycles* 21, GB4006. doi: 10.1029/2006GB002907

Eppley, R. W. (1972). Temperature and phytoplankton growth in sea. *Fishery Bull.* 70, 1063–1085.

Eppley, R. W., and Peterson, B. J. (1979). Particulate organic matter flux and planktonic new production in the deep ocean. *Nature* 282, 677–680. doi: 10.1038/282677a0

Eppley, R. W., Stewart, E., Abbott, M. R., and Heyman, U. (1985). Estimating ocean primary production from satellite chlorophyll. Introduction to regional differences and statistics for the Southern California Bight. *J. Of Plankton Res.* 7, 57–70. doi: 10.1093/plankt/7.1.57

Falkowski, P. G., Barber, R. T., and Smetacek, V. (1998). Biogeochemical controls and feedbacks on ocean primary production. *Science* 281, 200–206. doi: 10.1126/science.281.5374.200

M. J. R. Fasham (Ed.) (2003). "Ocean biogeochemistry," in *The Role of the Ocean Carbon Cycle in Global Change* (Berlin, Heidelberg: Springer Berlin Heidelberg). doi: 10.1007/978-3-642-55844-3

Friedrichs, M. A. M., Carr, M.-E., Barber, R. T., Scardi, M., Antoine, D., Armstrong, R. A., et al. (2009). Assessing the uncertainties of model estimates of primary productivity in the tropical Pacific Ocean. *J. Mar. Syst.* 76, 113–133. doi: 10.1016/j.jmarsys.2008.05.010

Geider, R. J., MacIntyre, H., and Kana, T. M. (1998). A dynamic regulatory model of phytoplanktonic acclimation to light, nutrients, and temperature. *Limnology And Oceanography* 43, 679–694. doi: 10.4319/lo.1998.43.4.0679

Groom, S., Sathyendranath, S., Ban, Y., Bernard, S., Brewin, R., Brotas, V., et al. (2019). Satellite ocean colour: Current status and future perspective. *Front. Mar. Sci.* 6. doi: 10.3389/fmars.2019.00485

Henson, S. A., Sanders, R., Madsen, E., Morris, P. J., Moigne, F. L., and Quartly, G. D. (2011). A reduced estimate of the strength of the ocean's biological carbon pump. *Geophysical Res. Lett.* 38, n/a–n/a. doi: 10.1029/2011gl046735

Honjo, S., Manganini, S. J., Krishfield, R. A., and Francois, R. (2008). Particulate organic carbon fluxes to the ocean interior and factors controlling the biological pump: A synthesis of global sediment trap programs since 1983. *Prog. Oceanography* 76, 217–285. doi: 10.1016/j.pocean.2007.11.003

Jonsson, B. F., Dunne, J. P., and Bender, M. L. (2013). Evaluation of the Southern Ocean O 2/Ar-based NCP estimates in a model framework. *J. Of Geophysical Research-Biogeosciences* 118, 385–399. doi: 10.1002/jgrg.20032

Kahru, M., and Mitchell, B. G. (2010). Blending of ocean colour algorithms applied to the Southern Ocean. *Remote Sens. Lett.* 1, 119–124. doi: 10.1080/01431160903547940

Khan, K. S., Kunz, R., Kleijnen, J., and Antes, G. (2003). Five steps to conducting a systematic review. *J. R. Soc. Med.* 96, 118–121. doi: 10.1177/014107680309600304

Kulk, G., Platt, T., Dingle, J., Jackson, T., Jonsson, B., Bouman, H., et al. (2021). Computation record.: Computation of marine phytoplankton primary production. Dataset.

Lawrenz, E., Silsbe, G., Capuzzo, E., Ylostalo, P., Forster, R. M., Simis, S. G. H., et al. (2013). Predicting the electron requirement for carbon fixation in seas and oceans. *PloS One* 8, e58137. doi: 10.1371/journal.pone.0058137

Laws, E. A. (1991). Photosynthetic quotients, new production and net community production in the open ocean. *Deep Sea Res. Part A. Oceanographic Res. Papers* 38, 143–167. doi: 10.1016/0198-0149(91)90059-o

Laws, E. A., D'Sa, E., and Naik, P. (2011). Simple equations to estimate ratios of new or export production to total production from satellite-derived estimates of sea surface temperature and primary production. *Limnology Oceanography: Methods* 9, 593–601. doi: 10.4319/lom.2011.9.593

Laws, E. A., Falkowski, P. G., Smith, W. O., Ducklow, H., and McCarthy, J. J. (2000). Temperature effects on export production in the open ocean. *Global Biogeochemical Cycles* 14, 1231–1246. doi: 10.1029/1999gb001229

Lee, Z. P., Carder, K. L., Marra, J., Steward, R. G., and Perry, M. J. (1996). Estimating primary production at depth from remote sensing. *Appl. Optics* 35, 463. doi: 10.1364/ao.35.000463

Li, Z., and Cassar, N. (2016). Satellite estimates of net community production based on o2/ar observations and comparison to other estimates. *Global Biogeochemical Cycles* 30, 735–752. doi: 10.1002/2015gb005314

Li, Z., Li, L., Song, K., and Cassar, N. (2013). Estimation of phytoplankton size fractions based on spectral features of remote sensing ocean color data. *J. Geophysical Research: Oceans* 118, 1445–1458. doi: 10.1002/jgrc.20137

Makridakis, S. (1993). Accuracy measures: theoretical and practical concerns. *Int. J. Forecasting* 9, 527–529. doi: 10.1016/0169-2070(93)90079-3

Marinov, I., Follows, M. J., Gnanadesikan, A., Sarmiento, J. L., and Slater, R. D. (2008). How does ocean biology affect atmospheric pCO(2)? Theory and models. *J. Geophyiscal Res.* 113, C07032. doi: 10.1029/2007JC004598

McClain, C. R., Franz, B. A., and Werdell, P. J. (2022). Genesis and evolution of nasa's satellite ocean color program. *Front. Remote Sens.* 3. doi: 10.3389/frsen.2022.938006

Mouw, C. B., Barnett, A., McKinley, G. A., Gloege, L., and Pilcher, D. (2016a). Global ocean particulate organic carbon flux merged with satellite parameters. *Earth System Sci. Data* 8, 531–541. doi: 10.5194/essd-8-531-2016

Mouw, C. B., Barnett, A., McKinley, G. A., Gloege, L., and Pilcher, D. (2016b). Global ocean particulate organic carbon flux merged with satellite parameters. *Earth system Sci. Data* 8 (2), 531–541. doi: 10.1594/PANGAEA.855600. Datasetsupplement to: Mouw, colleen b; 638 barnett, audrey; mckinley, galen a; gloege, lucas; pilcher, darren (2016).

Murray, J. W., Young, J., Newton, J., Dunne, J., Chapin, T., Paul, B., et al. (1996). Export flux of particulate organic carbon from the central equatorial Pacific determined using a combined drifting trap-234Th approach. *Deep Sea Res. Part II: Topical Stud. Oceanography* 43, 1095–1132. doi: 10.1016/0967-0645(96)00036-7

Myttenaere, A. d., Golden, B., Grand, B. L., and Rossi, F. (2016). Mean absolute percentage error for regression models. *Neurocomputing* 192, 38–48. doi: 10.1016/j.neucom.2015.12.114

Nevitt, J., and Hancock, G. R. (2000). Improving the root mean square error of approximation for nonnormal conditions in structural equation modeling. *J. Exp. Educ.* 68, 251–268. doi: 10.1080/00220970009600095

Nielsen, E. S. (1952). The use of radio-active carbon (C14) for measuring organic production in the sea. *ICES J. Mar. Science: J. du Conseil* 18, 117–140. doi: 10.1093/icesjms/18.2.117

Nowicki, M., DeVries, T., and Siegel, D. A. (2022). Quantifying the carbon export and sequestration pathways of the ocean's biological carbon pump. *Global Biogeochemical Cycles* 36, e2021GB007083. doi: 10.1029/2021gb007083

Pace, M. L., Knauer, G. A., Karl, D. M., and Martin, J. H. (1987). Primary production, new production and vertical flux in the eastern pacific ocean. *Nature* 325, 803–804. doi: 10.1038/325803a0

Palevsky, H. I., Quay, P. D., and Nicholson, D. P. (2016). Discrepant estimates of primary and export production from satellite algorithms, a biogeochemical model, and geochemical tracer measurements in the north pacific ocean. *Geophysical Res. Lett.* 43, 8645–8653. doi: 10.1002/2016gl070226

Pauly, D., and Christensen, V. (1995). Primary production required to sustain global fisheries. *Nat. (News Views)* 374, 255–257. doi: 10.1038/374255a0

Platt, T., Harrison, W., Lewis, M. R., Li, W., Sathyendranath, S., SMITH, R. E., et al. (1989). Biological production of the oceans: the case for a consensus. *Mar. Ecol. - Prog. Ser.* 52, 77–88. doi: 10.3354/meps052077

Platt, T., and Jassby, A. D. (1976). The relationship between photosynthesis and light for natural assemblages 666 of coastal marine phytoplankton1. *J. Phycology* 12, 421–430. doi: 10.1111/j.1529-8817.1976

Platt, T., Sathyendranath, S., Caverhill, C. M., and Lewis, M. R. (1988). Ocean primary production and available light: further algorithms for remote sensing. Deep Sea Research Part A. *Oceanographic Res. Papers* 35, 855–879. doi: 10.1016/0198-0149(88)90064-7

Puigcorbe, V. (2019). Global database of oceanic particulate organic carbon to particulate ^{234} th 672 ratios. doi: 10.1594/PANGAEA.911424. Dataset.

Puigcorbe, V., Masqu e, P., and Moigne, F. A. C. L. (2020). Global database of ratios of particulate organic carbon to thorium-234 in the ocean: improving estimates of the biological carbon pump. *Earth System Sci. Data* 12, 1267–1285. doi: 10.5194/essd-12-1267-2020

Puigcorbe, V., Roca-Martı, M., Masque, P., Benitez-Nelson, C., Loeff, M.R.v.d., Bracher, A., et al. (2017). Latitudinal distributions of particulate carbon export across the north western atlantic ocean. *Deep Sea Res. Part I: Oceanographic Res. Papers* 129, 116–130. doi: 10.1016/j.dsr.2017.08.016

Quay, P. D., and Karl, D. M. (2010). Measuring primary production rates in the ocean: Enigmatic results between incubation and non-incubation methods at Station ALOHA. Global. *Biogeochemical Cycles* 24, GB3014. doi: 10.1029/2009GB003665

Reuer, M. K., Barnett, B. A., Bender, M. L., Falkowski, P. G., and Hendricks, M. B. (2007). New estimates of southern ocean biological production rates from O2/ar ratios and the triple isotope composition of O2. *Deep Sea Res. Part I: Oceanographic Res. Papers* 54, 951–974. doi: 10.1016/j.dsr.2007.02.007

Sabine, C. L., Feely, R. A., Gruber, N., Key, R. M., Lee, K., Bullister, J. L., et al. (2004). The oceanic sink for anthropogenic co2. *Science* 305, 367–371. doi: 10.1126/science.1097403

Sarmiento, J. L., and Bender, M. L. (1994). Carbon biogeochemistry and climate change. *Photosynthesis Res.* 39, 209–234. doi: 10.1007/BF00014585

Sathyendranath, S. (2021). Esa ocean colour climate change initiative (ocean colour cci): Global chlorophyll-a data products gridded on a geographic projection, version 4.2. centre for environmental data analysis. *Dataset* 197.

Sathyendranath, S., Platt, T., Horne, E. P. W., Harrison, W. G., Ulloa, O., Outerbridge, R., et al. (1991). Estimation of new production in the ocean by compound remote sensing. *Nature* 353, 129–133. doi: 10.1038/353129a0

Seegers, B. N., Stumpf, R. P., Schaeffer, B. A., Loftin, K. A., and Werdell, P. J. (2018). Performance metrics for the assessment of satellite data products: an ocean color case study. *Optics Express* 26, 7404. doi: 10.1364/oe.26.007404

Siegel, D. A., Buesseler, K. O., Behrenfeld, M. J., Benitez-Nelson, C. R., Boss, E., Brzezinski, M. A., et al. (2016). Prediction of the export and fate of global ocean net primary production: The exports science plan. *Front. Mar. Sci.* 3, 18.1–18.28. doi: 10.3389/fmars.2016.00022

Siegel, D. A., Buesseler, K. O., Doney, S. C., Sailley, S. F., Behrenfeld, M. J., and Boyd, P. W. (2014). Global assessment of ocean carbon export by combining satellite observations and food-web models. *Global Biogeochemical Cycles* 28, 181–196. doi: 10.1002/2013gb004743

Siegel, D. A., DeVries, T., Cetinic, I., and Bisson, K. M. (2022). Quantifying the ocean's biological pump and its carbon cycle impacts on global scales. *Annu. Rev. Mar. Sci.* 15. doi: 10.1146/annurev-marine-040722-115226

Silsbe, G. M., Behrenfeld, M. J., Halsey, K. H., Milligan, A. J., and Westberry, T. K. (2016). The CAFE model: A net production model for global ocean phytoplankton. *Global Biogeochemical Cycles* 30, 1756–1777. doi: 10.1002/2016gb005521

Smyth, T. J., Tilstone, G. H., and Groom, S. B. (2005). Integration of radiative transfer into satellite models of ocean primary production. *J. Geophysical Res.* 110, C10014. doi: 10.1029/2004jc002784

Stukel, M. R., Kahru, M., Benitez-Nelson, C. R., Decima, M., Goericke, R., Landry, M. R., et al. (2015). Using lagrangian-based process studies to test satellite algorithms of vertical carbon flux in the eastern north pacific ocean. *J. Geophysical Research: Oceans* 120, 7208–7202. doi: 10.1002/7222015jc011264

Stukel, M., Ohman, M., Benitez-Nelson, C., and Landry, M. (2013). Contributions of mesozooplankton to vertical carbon export in a coastal upwelling system. *Mar. Ecol. Prog. Ser.* 491, 47–65. doi: 10.3354/meps10453

Suess, E. (1980). Particulate organic carbon flux in the oceans—surface productivity and oxygen utilization. *Nature* 288, 260–263. doi: 10.1038/288260a0

UKMO (2005). Ghrsst level 4 ostia global foundation sea surface temperature analysis. doi: 10.5067/GHOST-4FK01. Dataset.

Volk, T., and Hoffert, M. I. (1985). Ocean Carbon Pumps: Analysis of Relative Strengths and Efficiencies in Ocean-Driven Atmospheric CO2 Changes. In *The Carbon Cycle and Atmospheric CO2: Natural Variations Archean to Present* (eds. E. T. Sundquist and W. S. Broecker). doi: 10.1029/GM032p0099

Westberry, T. K., Behrenfeld, M. J., Siegel, D. A., and Boss, E. S. (2008). Carbon-based primary productivity modeling with vertically resolved photoacclimation. *Global Biogeochemical Cycles* 22, GB2024. doi: 10.1029/2007GB003078

Westberry, T. K., Williams, P. J., l., B., and Behrenfeld, M. J. (2012). Global net community production and the putative net heterotrophy of the oligotrophic oceans. *Global Biogeochemical Cycles* 26, n/a–n/a. doi: 10.1029/2011gb004094

Williams, P. J. L. B. (1993). On the definition of plankton produktion terms. *ICES Mar. Sci. Symp. (ICES)*, 9–19.

Williams, P. J. L. B., Quay, P. D., Westberry, T. K., and Behrenfeld, M. J. (2013). The olig otrophic ocean is autotrophic. *Annu. Rev. Mar. Sci.* 5, 535–549. doi: 10.1146/annurev-marine-121211-172335

Wright, S. (1921). Correlation and causation. *J. Agric. Res.* 20, 557–585.

Yool, A., Martin, A. P., Fernandez, C., and Clark, D. R. (2007). The significance of nitrification for oceanic new production. *Nature* 447, 999–1002. doi: 10.1038/nature05885

frontiers | Frontiers in Marine Science

TYPE Methods
PUBLISHED 05 September 2023
DOI 10.3389/fmars.2023.1118226

Check for updates

OPEN ACCESS

EDITED BY
Jamie Shutler,
University of Exeter, United Kingdom

REVIEWED BY
Žarko Kovač,
University of Split, Croatia
Heather Bouman,
University of Oxford, United Kingdom

*CORRESPONDENCE
Tebatso M. Moloto
Tebatso.Martin@gmail.com

†PRESENT ADDRESS
Deon C. Louw,
Debmarine Namibia (DBMN),
Windhoek, Namibia

RECEIVED 07 December 2022
ACCEPTED 01 August 2023
PUBLISHED 05 September 2023

CITATION
Moloto TM, Thomalla SJ, Smith ME, Martin B, Louw DC and Koppelmann R (2023) Remote sensing of phytoplankton community composition in the northern Benguela upwelling system.
Front. Mar. Sci. 10:1118226.
doi: 10.3389/fmars.2023.1118226

COPYRIGHT
© 2023 Moloto, Thomalla, Smith, Martin, Louw and Koppelmann. This is an open-access article distributed under the terms of the Creative Commons Attribution License (CC BY). The use, distribution or reproduction in other forums is permitted, provided the original author(s) and the copyright owner(s) are credited and that the original publication in this journal is cited, in accordance with accepted academic practice. No use, distribution or reproduction is permitted which does not comply with these terms.

Remote sensing of phytoplankton community composition in the northern Benguela upwelling system

Tebatso M. Moloto[1,2*], Sandy J. Thomalla[2,3], Marie E. Smith[4,5], Bettina Martin[6], Deon C. Louw[7†] and Rolf Koppelmann[6]

[1]Unit for Environmental Sciences and Management, North-West University, Potchefstroom, South Africa, [2]Southern Ocean Carbon-Climate Observatory (SOCCO), Council for Scientific and Industrial Research (CSIR), Cape Town, South Africa, [3]Marine and Antarctic Research for Innovation and Sustainability, University of Cape Town, Cape Town, South Africa, [4]Coastal Systems and Earth Observation Research Group, CSIR, Cape Town, South Africa, [5]Department of Oceanography, University of Cape Town, Cape Town, South Africa, [6]Institute of Marine Ecosystem and Fishery Science, University of Hamburg, Hamburg, Germany, [7]National Marine Information and Research Centre, Ministry of Fisheries and Marine Research, Swakopmund, Namibia

Marine phytoplankton in the northern Benguela upwelling system (nBUS) serve as a food and energy source fuelling marine food webs at higher trophic levels and thereby support a lucrative fisheries industry that sustain local economies in Namibia. Microscopic and chemotaxonomic analyses are among the most commonly used techniques for routine phytoplankton community analysis and monitoring. However, traditional *in situ* sampling methods have a limited spatiotemporal coverage. Satellite observations far surpass traditional discrete ocean sampling methods in their ability to provide data at broad spatial scales over a range of temporal resolution over decadal time periods. Recognition of phytoplankton ecological and functional differences has compelled advancements in satellite observations over the past decades to go beyond chlorophyll-*a* (Chl-*a*) as a proxy for phytoplankton biomass to distinguish phytoplankton taxa from space. In this study, a multispectral remote sensing approach is presented for detection of dominant phytoplankton groups frequently observed in the nBUS. Here, we use a large microscopic dataset of phytoplankton community structure and the Moderate Resolution Imaging Spectroradiometer of aqua satellite match-ups to relate spectral characteristics of in water constituents to dominance of specific phytoplankton groups. The normalised fluorescence line height, red-near infrared as well as the *green*/*green* spectral band-ratios were assigned to the dominant phytoplankton groups using statistical thresholds. The ocean colour remote sensing algorithm presented here is the first to identify phytoplankton functional types in the nBUS with far-reaching potential for mapping the phenology of phytoplankton groups on unprecedented spatial and temporal scales towards advanced ecosystem understanding and environmental monitoring.

KEYWORDS

satellite remote sensing, phytoplankton community structure, algorithm development, northern Benguela, Namibia, MODIS-Aqua

1 Introduction

The Benguela Upwelling System (BUS), situated on the south western coast of Africa in the South Eastern Atlantic ocean (Figure 1A), is estimated to be the most productive Eastern Boundary Upwelling System (Carr, 2002; Carr and Kearns, 2003; Chavez and Messié, 2009). It stretches from Cape Agulhas in South Africa along the Namibian coast to Cape Frio and northwards into Angolan waters (Hutchings et al., 2009; Kampf and Chapman, 2016). The central perennial Lüderitz upwelling cell positioned at 27.5° S in Namibia (Figure 1A) partitions the BUS into the southern and northern BUS (Duncombe Rae, 2005; Lett et al., 2007; Hutchings et al., 2009). The perennial upwelling in the nBUS is driven by strong equatorward south easterly alongshore winds with a strong seasonality, tending to peak in late winter to early spring (August-September) and in autumn (April-May) (Hutchings et al., 2009; Louw et al., 2016). These winds induce an Ekman transport of coastal surface waters offshore, forcing the deep, cold and nutrient-enriched waters to upwell into the euphotic zone where they fuel the high productivity characteristic of the region in the form of marine phytoplankton blooms (Shillington et al., 2006; Lass and Mohrholz, 2008; Lachkar and Gruber, 2012). This increase of productivity in the food web supports a diverse ecosystem and a very lucrative commercial fisheries industry contributing to both economic growth and food security (Allison et al., 2009; Stock et al., 2017).

Marine phytoplankton contribute nearly half of the global primary production and serve as a direct food and energy source fuelling marine food webs at higher trophic levels (Field et al., 1998; Kwak and Park, 2020). In addition, phytoplankton blooms play an important role in global climate regulation through their contribution to the net annual uptake of atmospheric CO_2 (Arrigo et al., 1999; Caldeira and Duffy, 2000; Tortell et al., 2008; Pollard et al., 2009) and the production and release of aerosol particle precursors (e.g. dimethyl sulfide (DMS) gas and volatile organic carbons (VOCs)) that modulate cloud formation (Charlson et al., 1987; Stefels, 2000; Lizotte et al., 2017). This is of particular relevance in the nBUS, which is characterised by the presence of one of the largest and most persistent stratiform marine cloud decks that contribute to the variability and long-term trends of global albedo with impacts on both regional and global climate.

Marine phytoplankton encompass a diverse community of organisms, whose dominance varies in response to physicochemical variability in environmental conditions, that subsequently determines their ecological and biogeochemical function. For instance, diatoms are typically large cells that grow fast reaching high concentrations and due to their silica ballast and increased density, tend to sink fast and are considered very effective exporters of organic carbon to the deep ocean and important role players in the biological carbon pump (Smetacek, 1999; Brownlee and Taylor, 2002). Coccolithophores on the other hand are calcifiers that reduce seawater alkalinity and the carbonate concentration of surface waters in the process that forms their coccoliths (external calcium carbonate platelets), which impacts the ocean-atmosphere exchange of CO_2 (Brownlee and Taylor, 2002; Riebesell and Rost, 2004; Mcclelland et al., 2016). Together with dinoflagellates (Keller, 1989), coccolithophores have the highest intracellular dimethylsulfoniopropionate (DMSP) content and are considered prominent climate-active DMS gas producers (Archer et al., 2001; Lizotte et al., 2017) that may impact cloud formation and the radiation budget. Cyanobacteria on the other hand fix atmospheric nitrogen (N_2) in a process that contributes to N_2 input into the ocean to compensate for N_2 loss from denitrification (Agawin et al., 2007). Moreover, there are some bloom-forming and toxin-producing

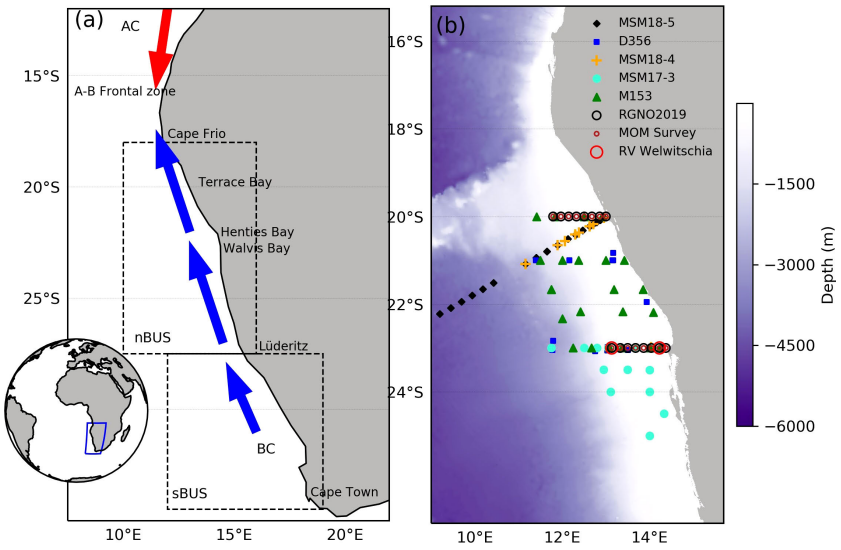


FIGURE 1
Map of western Africa showing the location of the Benguela Upwelling System (blue rectangle, inset). The BUS is partitioned into the northern (nBUS) and southern (sBUS) region separated by the Lüderitz upwelling cell at 27° S **(A)**. The nBUS is bound by the cold water from the Benguela current (BC) and the warm water from the Angola current (AC) that converge at the Angola-Benguela frontal zone (A-B frontal zone). The right panel **(B)** shows bathymetry and the geolocations of stations sampled in the nBUS for Chl-a and phytoplankton community structure on the RV Meteor (M153) (green triangles) and Mirabilis RGNO2019 (black open circles). The geolocations of all additional cruise data (Table 1) are similarly identified with unique symbols as per the figure legend.

phytoplankton species (e.g. diatoms of *Pseudo-nitzschia* spp.), commonly referred to as harmful algal blooms (HABs) that are detrimental to both humans and aquatic life and have devastating consequences for the fisheries industry with important economic ramifications (Hoagland et al., 2002; Dermastia et al., 2022). As such, phytoplankton community structure and diversity is considered a key component of marine ecosystems as they have a direct impact on food web energy supply, fisheries and food security, ecosystem health and climate (Otero et al., 2020; Bestion et al., 2021). It is therefore crucial to study and understand phytoplankton community composition and its variability, especially in the face of global warming and the changing climate. The knowledge of the phytoplankton community composition and its sensitivity to climate forcing can provide a valuable understanding of ecological balance in marine ecosystems (Kruk et al., 2011), which can aid in informed policy drafting decisions for improved implementation of sustainable fisheries and environmental management for the protection and conservation of ecosystems.

Phytoplankton communities are highly dynamic and susceptible to seasonal (and intra-seasonal), interannual and long term variability in environmental drivers such as wind driven mixing (Louw et al., 2016), upwelling (Hansen et al., 2014) and radiative forcing. The nBUS is reported to have been progressively impacted by longer-term variability associated with climate change and other human-induced activities that have resulted in drastic changes to the ecosystem over the last decades. For example, fish catches and populations (sardines and anchovy most notably) have dramatically declined over the past five decades as a result of overfishing and possible environmental events such as hypoxia and Benguela Niños, that negatively affect organisms at both lower and higher trophic levels (Cury and Shannon, 2004). Moreover, upwelling indices indicate a decline in the frequency of upwelling events in recent years (2009 and 2014) in the nBUS (Lamont et al., 2018; Polonsky and Serebrennikov, 2020), with major implications for ocean productivity in support of marine food webs and the biological carbon pump. Consequently, there is a necessity for routine monitoring of phytoplankton as key roleplayers in this unique marine ecosystem for effective management as a scientific priority towards a better understanding and predictive ability of their role in maintaining ecosystem balance and climate feedback. Efforts to acquire long-term datasets towards adequately monitoring the nBUS for assessment of ecosystem changes have been made by the National Marine Information and Research Centre (NatMIRC, Namibia). The monitoring programme involves discrete *in situ* field observations collected quasi-monthly along two longitudinal transects off the coast of Namibia. These data have been used to assess trends in phytoplankton biomass (Louw et al., 2016), bloom-forming and toxin-producing diatoms of the genus *Pseudo-nitzschia* (Louw et al., 2017) and other environmental variables for nearly two decades. Field observations, although very useful in studying and monitoring marine ecosystems, are nonetheless severely limited in their regional and temporal coverage. Furthermore, they are labour intensive, costly and unable to provide near real-time monitoring observations.

Satellite ocean colour remote sensing observations have the ability to surpass traditional ocean sampling methods, that involve discrete samples collected on-board research vessels, owed to their large spatial and temporal scale resolution and ability to provide near real time information. Early studies of ocean colour remote sensing by satellite focused on the computation of global phytoplankton biomass using chlorophyll-*a* concentration ([Chl-*a*]) as a proxy, which improved our understanding of synoptic scale ocean primary production and biogeochemistry (O'Reilly et al., 1998). However, recognition of the importance of different phytoplankton taxonomic groups and their varying biogeochemical functions has compelled the need for the development of satellite products with the ability to resolve complex phytoplankton dynamics from space. At the forefront of this endeavour is the ability to provide information on the composition of the phytoplankton community (phytoplankton functional types – PFTs) in which each PFT represents a group of species aggregated according to distinct functional characteristics (e.g. size structure or taxonomic composition). More recent advancements in ocean colour remote sensing have seen the development of indirect techniques to derive phytoplankton functional types and size distribution such as the abundance-based algorithms that are based on [Chl-*a*] (Vidussi et al., 2001; Uitz et al., 2006; Hirata et al., 2011; Brewin et al., 2015). Spectral-based approaches on the other hand are more direct and rely primarily on the unique characteristics of light absorption and backscattering of different phytoplankton taxa, which can be retrieved from water-leaving reflectance. Variations in photosynthetic pigment composition, morphology, size, shape, and inner structure of different phytoplankton species is what drives the characteristics of inherent optical properties of surface waters that can subsequently be used to differentiate phytoplankton groups or species from satellite ocean colour remote sensing (Aguirre-Gomez et al., 2001; Vaillancourt et al., 2004; Soja-Wozniak et al., 2018). One example of this type of approach is the dual ratio approach, which utilises the ratio between 2 spectral bands to identify specific phytoplankton functional types. For instance, Bernard et al. (2005) used the 665 nm and 709 nm *red*/*red* band-ratio of the Medium Resolution Imaging Spectrometer (MERIS) sensor to identify HABs in the southern Benguela upwelling system (sBUS). Another approach uses spectral band differences to derive phytoplankton optical fingerprints. Typically, these algorithms are used to identify algal blooms of a particular taxa using three adjacent spectral bands in the red and near infrared or blue-green spectral regions that quantify the amplitude of a specific peak of absorption. One particularly useful example of this approach utilises the [Chl-*a*] fluorescence peak signal between 678 and 683 nm. Quantification of this signal, known as the fluorescence line height (FLH) (Letelier and Abbott, 1996; Kritten et al., 2020), is based on the height of the reflectance peak above a baseline formed between the two adjacent wavebands (Letelier and Abbott, 1996; Kritten et al., 2020). This approach has previously been applied to identify HABs in the coastal waters of SW Florida (Hu et al., 2005) and the sBUS (Smith and Bernard, 2020). Past and current ocean colour satellite sensors with appropriate wavebands in the red and near infrared (NIR) spectral regions, that are able to

use these approaches, include the Moderate Resolution Imaging Spectroradiometer of aqua (MODIS-Aqua) [2002-present], the Ocean and Land Colour Imager (OLCI) [2016-present], and the MERIS sensors [2002-2012] (Letelier and Abbott, 1996).

Although there exist a limited number of satellite ocean colour remote sensing algorithms for aiding in the detection of multiple phytoplankton functional types (Aiken et al., 2007) and HABs in the sBUS (Bernard et al., 2005; Smith and Bernard, 2020), there is, to our knowledge, no satellite ocean colour remote sensing algorithm for detection of phytoplankton functional groups in the nBUS counterpart. While the regional abundance-based phytoplankton size class model of Lamont et al. (2019) for the BUS provides useful information on the variability of phytoplankton size functional types (picophytoplankton, nanophytoplankton and microphytoplankton), it is not able to approximate functional phytoplankton group composition (needed for the assessment of their various key ecological functions). The optical based algorithms derived by Aiken et al. (2007) and Smith and Bernard (2020) on the other hand are geared at providing information on the functional composition of phytoplankton for the sBUS (specifically diatoms, *Pseudo-nitzschia*, dinoflagellates, flagellates & mixed communities) and it cannot be assumed that they are applicable to the nBUS (or to different satellite products).

This study addresses the need for an ocean colour remote sensing algorithm for the detection of phytoplankton groups in the nBUS. It does so by first selecting the most suitable satellite sensor for the nBUS based on matchups between *in situ* and satellite (MODIS-Aqua, MERIS/OLCI) derived [Chl-*a*]. It subsequently follows a similar methodological approach to the algorithm developed for the sBUS by Smith and Bernard (2020) by identifying the spectral reflectance characteristics unique to stations dominated by particular phytoplankton functional groups. A combination of these unique optical characteristics is then used to derive an algorithm that can be applied to ocean colour data from the nBUS to elicit broad scale high resolution information on the likely distribution of the dominant functional types. Such an algorithm will allow observations of the spatio-temporal distribution and variability of key phytoplankton groups on an unprecedented scale in the nBUS, which is a scientific priority for understanding the marine food web and detecting its response to a changing climate in this globally important upwelling region.

2 Materials and methods

2.1 *In situ* data

2.1.1 Expeditions

This study focused on the nBUS off the coast of Namibia (Figure 1A) within the latitudes and longitudes of 20–26° S and 9–15° E, which included the Cape Frio, Central and the Lüderitz upwelling cells. Two expeditions were carried out on-board the RV Meteor (M153) and Mirabilis (RGNO2019) for data collection (Figure 1B). Cruise M153 took place from 15 February to 15 March 2019 covering both the northern and southern Benguela upwelling systems whereas cruise RGNO2019 took place from 9 to 10 of May 2019 covering 2 longitudinal transects (23 and 20° S). The stations sampled during the two expeditions (41 in total) are presented in Figure 1B. Seawater samples were collected in surface waters (0-5 m) using Niskin bottles attached to a conductivity-temperature-depth (CTD) carousel setup on-board the RV Meteor and Mirabilis. These data were supplemented with additional data from previous cruises in the region covering the period between 2001 and 2020 (Figure 1B; Table 1).

2.1.2 Chlorophyll-a

For the M153 and RGNO2019 cruises total [Chl-*a*], 200 ml of seawater was filtered through glass microfiber filters (Whatman GF/F, 25 mm diameter, 0.7 µm pore size) and stored immediately in the freezer (-20 °C) for later analysis. Total [Chl-*a*] was determined following the method of Welschmeyer (1994). Chl-a was extracted from the GF/F filters by addition of 9 mL of 90% acetone for 24 hr in the dark at -20 °C. These were then transferred into glass tubes and fluorescence was measured using a Turner (Model 10AU) fluorometer. The [Chl-*a*] was determined from a seven-point [Chl-*a*] calibration curve and represented as equivalents of chlorophyll-*a* (µg l^{-1}).

2.1.3 Phytoplankton cell counts

For the M153 and RGNO2019 cruises phytoplankton cell enumeration and taxonomic identification, water from the Niskin bottles was transferred to 200 mL glass amber bottles and immediately preserved with acidic Lugol iodine solution, shaken gently and stored in the dark at room temperature for later analysis in the land-based laboratory. The Lugol-preserved phytoplankton cells were settled in a 25 ml glass/plastic chamber for 24 hours prior to analysis. The phytoplankton cells were identified and counted using a Zeiss Axiovert 200 inverted light microscope following the Utermöhl (1958) method. Cells were counted and identified to genus and to species level where possible. Approximately 400 cells were counted to achieve an estimation of cell concentration with ±10% precision, whereas at least 50-200 cells were counted when cells occurred in smaller concentrations with a precision of approximately 15–30% (Anderson and Throndsen, 2004). Although microscopic taxonomic identification of phytoplankton provides a resolution to genus and species levels, counted cells in this study were only grouped into diatoms, flagellates, dinoflagellates, cyanobacteria, coccolithophores, and others/unknown.

2.1.4 Additional *in situ* data sources

The M153 and RGNO2019 cruise datasets (detailed above) were supplemented with additional [Chl-*a*] and phytoplankton cell count data from multiple expeditions from publicly available, published and unpublished sources that were conducted in the nBUS covering the period between 2001 and 2020 (Table 1), to make a total pool of 252 stations. Data from the additional sources were similarly obtained from samples collected in the top 5 m and were similarly assessed for [Chl-*a*] using a fluorometer according to

TABLE 1 Research expeditions in the northern Benguela upwelling system off Namibia where concurrent [Chl-*a*] and phytoplankton cell count samples were collected between 2001 and 2019.

Cruise expedition	Date	Source
RV Meteor 153 (M153)	15 February – 15 March 2019	This study [ab]
RV Mirabilis (RGNO2019)	9 – 10 May 2019	This study [ab]
Maria S. Merian (MSM18-5)	27 August – 15 September 2011	Wasmund et al., 2014 [ab]
Discovery 356 (D356)	11 September – 07 October 2010	Wasmund, 2011a; Wasmund, 2011b [ab]
Maria S. Merian (MSM18-4)	16 – 19 August 2011	Wasmund, 2015b; Wasmund, 2015c [ab]
Maria S. Merian (MSM17/3)	30 January – 02 February 2011	Wasmund, 2012, Wasmund, 2015a [ab]
RV Mirabilis (MOM survey)	January 2004 – February 2020	NatMIRC unpublished monitoring data [ab]
RV Mirabilis (MOM survey	February 2001 – December 2012	Louw et al., 2016 [a]
RV Welwitschia	February 2001 – December 2012	Matlakala, 2019 [ab]

[a] = [Chl a] data.
[b] = phytoplankton cell counts data.
Detailed spatial locations of the various studies appear in Figure 1B.

the principle of Welschmeyer (1994) and phytoplankton cell counts according to the method of Utermöhl (1958). The geolocations of the additional stations sampled are shown in Figure 1B with the respective sampling dates and data sources summarised in Table 1.

2.2 Satellite data

2.2.1 Data acquisition and processing

Daily Level-2 (L2) 1 km resolution ocean colour satellite data from the Moderate Resolution Imaging Spectroradiometer on board the Aqua satellite (MODIS-Aqua), the Medium Resolution Imaging Spectrometer (MERIS) on board Envisat, and the Ocean and Land Colour Instrument (OLCI) on board Sentinel-3 were obtained from the National Aeronautics and Space Administration (NASA) OceanColor Web (https://oceancolor.gsfc.nasa.gov/), MERIS catalogue and inventory (MERCI, http://meris-ds.eo.esa.int/oads/access/) and the Copernicus online data access website (CODA, https://coda.eumetsat.int/), respectively. The OLCI [Chl-*a*] data were derived from OLCI reflectance bands using the blended switching algorithm of Smith et al. (2018), which was developed specifically for the high biomass waters of the southern Benguela. The standard MODIS-Aqua [Chl-*a*] product is based on an empirical relationship derived from remote sensing reflectance (*Rrs*) between 440 and 670 nm and *in situ* [Chl-*a*]. This product is a combination of the standard OC3 algorithm (O'Reilly et al., 2000) and the colour index (CI) algorithm (Hu et al., 2012), where the OC3 algorithm is applied at [Chl-*a*] >0.2 mg m^{-3}, whereas the CI algorithm is applied at [Chl-*a*]<0.15 mg m^{-3}, and a weighted blending approach is applied between 0.15 and 0.2 mg m^{-3}.

Other products obtained from MODIS L2 include the L2 flags, the nFLH and the remote sensing reflectance (*Rrs*) at 412, 443, 469, 488, 531, 547, 555, 645, 667 and 678 nm wavebands of the visible spectrum. The normalised fluorescence line height (nFLH, W m^{-2} μm^{-1} sr^{-1}) (Letelier and Abbott, 1996) is a standard product provided with the MODIS L2 Ocean colour data derived as follows:

$$nFLH = L_w678 - L_w667 - \left[(L_w748 - L_w667) * \left(\frac{678-667}{748-667}\right)\right] \quad (1)$$

where L_w is the normalised water-leaving radiance.

2.2.2 Matchups with *in situ* data

The L2 data from MODIS-Aqua, MERIS and OLCI were matched to field observation stations and extracted using a 5 x 5 pixel box centred around the *in situ* measurements as satellite navigation may not be accurate to a single pixel. The multi-pixel box increases the number of pixels of satellite retrievals and the possibility of a valid *in situ* matchup. A time window of ≤12 hrs between the satellite overpass and *in situ* observations was given preference as a temporal threshold for coincidence. However, when coincident satellite and *in situ* observations weren't available within a 12 hr window, this criteria was relaxed to allow matchups to be considered within a ≤24 hr time window. The mean was then calculated for valid pixels within the 5 x 5 pixel box for [Chl-*a*], nFLH and *Rrs* at spectral bands in the visible range as outlined above, together with their respective statistical error metrics (e.g. standard deviations).

2.3 Data quality control

A set of quality control measures were adopted to minimise the inclusion and effect of bad/erroneous data from the L2 satellite data using a set of corrective measures as outlined in Figure S1. The *L2flags* product contains science and quality "flags", with set atmospheric correction thresholds that were used to eliminate invalid pixels. Briefly, pixels were masked and excluded when flagged as "land" (pixel is over land), "clouds" (cloud contamination), "chlfail" (satellite ocean colour [Chl-*a*] algorithm failure), "higlint" (sunglint detected via reflectance exceeds threshold), "hisatzen" (sensor view zenith angle exceeds 60 °), "lowlw" (very low water-leaving radiance), and "hilt" (observed radiance very high or saturated). In an effort to

remove invalid averaged matchup retrievals, further exclusion criteria were applied following Bailey and Werdell (2006), which removes matchups where fewer than 13 pixels were valid (i.e. where<50% of the 25 pixels within a 5 x 5 pixel box were valid). Furthermore, mean values whose standard deviations were >50% of the mean (indicative of large variability within the 5 x 5 pixel box) were removed to ensure spatial stability or homogeneity. Quality control measures applied to *in situ* [Chl-*a*] measurements included removal of measurements that were below the minimum detection threshold of the Turner fluorometer (<0.02 ug l^{-1}). Finally, *in situ* stations were excluded that were too close to one another and overlapped with a 5 x 5 pixel box (a flow diagram detailing the data quality control steps can be found in Figure S1 in the Supplementary Material).

2.4 Evaluation of MODIS-Aqua and MERIS/OLCI [Chl-*a*] algorithms

Statistical uncertainties between matchups of satellite ocean colour derived [Chl-*a*] and *in situ* fluorometric derived [Chl-*a*] were used to determine the most appropriate satellite sensor for algorithm development. The MERIS mission covered the period between 2002 and 2012, whereas OLCI and MODIS-Aqua were launched in 2016 and 2002, respectively, and both are still operational (at the time of writing). OLCI was developed on MERIS heritage with a similar spectral setup in order to provide continuity in algorithms and derived data; for this reason the match-ups from these two sensors were combined to create a single dataset. However, only the datasets covering the period between 2002-2012 and 2016-present were used for MODIS-Aqua so as to facilitate a fair comparison with MERIS/OLCI in this evaluation. Statistical metrics were used to quantify the agreement between *in situ* [Chl-*a*] and satellite-derived observations. Prior to the analysis, both the *in situ* and satellite retrievals were log-transformed. The statistics used for comparison were the mean relative error (MRE), mean absolute relative difference (MARD), median relative difference (MedRD), root mean squared error (RMSE) and relative bias, the exact equations of which can be found in the Supplementary Material indicated as equations S1 - S5.

In addition, a linear regression model was used to assess the degree of agreement between the *in situ* and satellite-derived [Chl-*a*]. The intercept, slope and coefficient of determination (R^2) were computed.

2.5 Algorithm development

2.5.1 Subdividing the data by phytoplankton group dominance

The quality-controlled *in situ* data were subdivided according to phytoplankton group dominance. Dominance, in the context of this study, was typically achieved when a phytoplankton group contributed more than 50% to the total phytoplankton community abundance. It should be noted however that the nBUS is, for the most part, diatom-dominated (See Figure S3 on the Supplementary Material) and therefore the majority of the datasets were considered diatom dominated. For diatoms only, dominance was instead defined as a ≥70% contribution to the total phytoplankton community with a cell concentration of ≥500,000 cells l^{-1}. For flagellates and dinoflagellates, dominance was considered when cells were >50% of the total cell abundance. No cell count minima was set for these subsets as these stations typically did not reach high cell concentrations (i.e. >10^6 cells L^{-1}).

Further analysis of the data showed dominance for dinoflagellates in both low [Chl-*a*] and high [Chl-*a*] (>4 µg l^{-1}) waters. Dinoflagellate dominance was thus subdivided into either low biomass or high biomass dominance (LB and HB, respectively). For HB dinoflagellate-dominated waters, dominance was considered when contributing >50% to the total cell abundance with cell counts of ≥10^6 cells L^{-1}. Unfortunately, there were no *in situ* stations where either coccolithophores or cyanobacteria met the criteria for dominance. As such, this study focused only on identifying unique spectral characteristics of diatoms, flagellates and dinoflagellates from the satellite spectral matchup data. In addition, unique spectral characteristics were determined for a phytoplankton community that was considered mixed, i.e. when all the identifiable groups (including coccolithophores and cyanobacteria) and unidentifiable groups (i.e. classified as "other" in the phytoplankton taxonomic datasets) each contributed<50% to the total phytoplankton abundance with no set cell count minima.

2.5.2 Determining unique optical characteristics

The remote sensing spectral characteristics associated with dominance of the aforementioned phytoplankton groups were assessed using 4 approaches, namely 1) *Rrs* at different spectral bands, 2) dual-band *Rrs* ratios, 3) spectral band difference approaches and 4) a [Chl-*a*] abundance-based approach. For these approaches, the magnitude and shape of *Rrs* at 10 spectral bands were compared between waters dominated by the different phytoplankton groups. For dual-band spectral ratios, a total of 87 different ratio combinations among the violet, blue, green and red spectral regions were investigated. The spectral band difference or line height (LH) was calculated at eight different adjacent spectral band-triplets between 410 and 678 nm. LH is a measure of the height of the *Rrs* at a "signal" band above a baseline formed by any two given spectral bands, and was calculated as follows:

$$LH = Rrs_signal - Rrs_left - (Rrs_right - Rrs_left) \times \left(\frac{\lambda_{signal} - \lambda_{left}}{\lambda_{right} - \lambda_{left}} \right) \quad (2)$$

Where λ is the wavelength value at a spectral band of interest, Rrs_signal is the Rrs value at the signal band centred between two spectral bands, Rrs_left is the Rrs to the left of Rrs_ signal, Rrs_right is the Rrs to the right of Rrs_ signal, λ_{signal} is the λ value of Rrs_signal whereas λ_{right} and λ_{left} are the λ values of Rrs to the right and left of the Rrs_signal respectively. The nFLH, a downloadable L2 MODIS-aqua product as described in the "*data acquisition*" section above, is a well-known example.

Spectral reflectance peaks may occur near 685 nm in low to moderate [Chl-a] waters as a consequence of [Chl-*a*] fluorescence

emission (Gordon, 1979). However, this [Chl-*a*] fluorescence peak may be masked in high phytoplankton biomass waters (e.g. [Chl-*a*] > 20 μg l^{-1}) as a result of increased absorption and backscattering by phytoplankton coupled with increased water absorption (Gordon, 1979; Schalles, 2006; Gilerson et al., 2007); this is often observed as a shift in the red reflectance peak towards the NIR region. In this study, we quantify this red shift as a ratio between a red (*Rrs*667) and NIR (*Rrs*748) spectral bands, the red-NIR ratio (*RNR*). The *Rrs*748 is not provided in the standard L2 MODIS files, and is instead calculated from the available nFLH, *Rrs*667 and *Rrs*678, and solar spectral irradiance values from Thuillier et al. (2003) as follows:

$$Rrs748 = \left(\left(\frac{81 \star Rrs678 \star 1481.93}{11}\right) - \left(\frac{81 \star nFLH}{11}\right) - \left(\frac{70 \star Rrs667 \star 1517.73}{11}\right)\right) \div 1288.25 \quad (3)$$

The *RNR* was then calculated as:

$$RNR = \frac{Rrs748}{Rrs667} \quad (4)$$

[Chl-*a*] was used as a proxy for phytoplankton abundance for the development of the abundance-based algorithm, based primarily on the understanding that at high biomass the phytoplankton community was dominated by either diatoms or dinoflagellates.

2.6 Statistical analysis

Box and whisker plots were used to graphically display the distribution and statistical parameters of the data which included the median (Q_2), lower (Q_1 or 25th percentile) and upper (Q_3 or 75th percentile) quartiles as well as the lower (Q_0 or minimum) and upper (Q_4 or maximum) extremes of the datasets. The box represents the interquartile interval where 50% of the data is distributed. The whiskers display the lower (minimum) and upper (maximum) extremes of the datasets. Outliers were defined as data points that are 1.5 times higher than the interquartile range (IQR) calculated from both the lower (Q_1) and upper (Q_3) quartiles and indicated as circles in the box and whisker plots. The 25th and 75th percentiles were used to define optical signature thresholds associated with dominance of the phytoplankton groups under investigation. The Matplotlib, Scipy.stats, Numpy and Sklearn.metrics Python (version 3.7.3) packages were used for statistical data analysis.

3 Results

3.1 Evaluation of MODIS-Aqua and MERIS/OLCI [Chl-*a*] algorithms in the nBUS in comparison with *in situ* data

For both MODIS-Aqua and MERIS/OLCI sensors, the quality-controlled [Chl-*a*] match-up datasets were used for comparison (Figure 2), which covered the *in situ* [Chl-*a*] range of 0.18 – 36.25

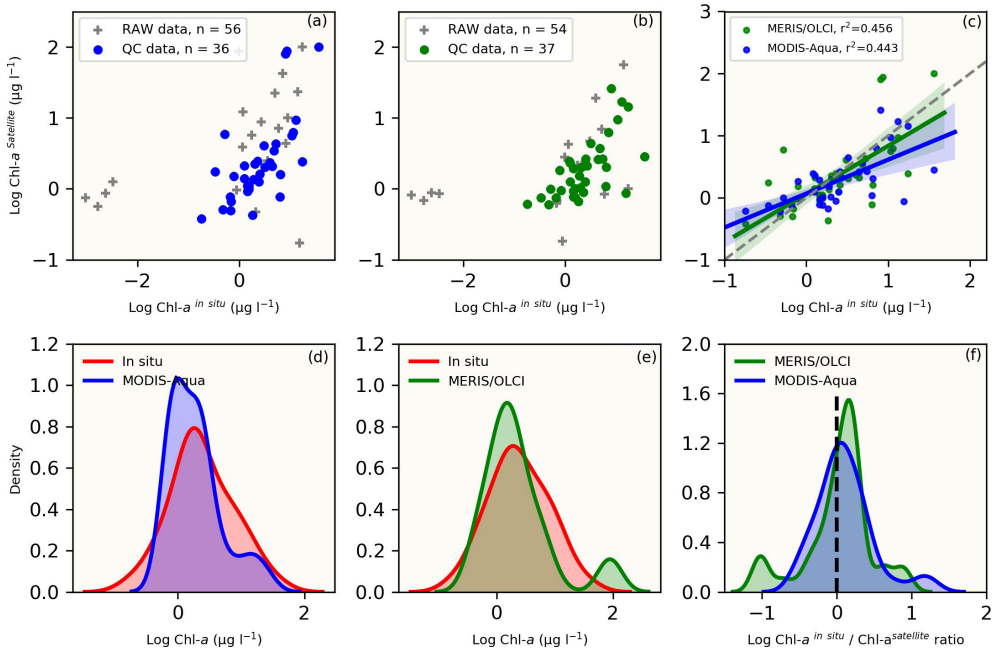


FIGURE 2
The top panel shows raw and quality-controlled (QC) *in situ* versus satellite [Chl-*a*] data for the **(A)** MODIS-Aqua (blue dots), **(B)** MERIS/OLCI (green dots) and raw data (grey crosses) **(C)** linear regression statistics with 95% confidence intervals (shaded areas) for the QC [Chl-*a*] comparisons between MODIS-Aqua (blue shaded line) and MERIS/OLCI (green shaded line). The number of QC datasets used for comparative analysis (n) are indicated. The bottom panel compares the data distribution between *in situ* (red) and satellite-derived [Chl-*a*] using the Kernel density estimation (KDE) plots for **(D)** MODIS-Aqua (blue) and **(E)** MERIS/OLCI (green). **(F)** is a direct comparison of the ratio of *in situ* to satellite [Chl-*a*] between the two sensors (blue: MODIS-Aqua; green: MERIS/OLCI). All datasets were log-transformed prior to plotting and statistical analysis.

µg l^{-1}. The matchup datasets were reduced from n=56 and 54 stations to n= 36 and 37 for MODIS-Aqua and MERIS/OLCI respectively, following the application of the stringent quality control measures outlined in Figure S1. Scatter plots of the comparisons between *in situ* and satellite [Chl-*a*] are shown in Figures 2A, B with the data that passed quality control being easily identified from the raw data that did not. Statistical parameters of the linear regressions between the quality-controlled data showed a positive correlation between *in situ* [Chl-*a*] and satellite retrievals. The Pearson correlation coefficient (r) was similar for both sensors, with MODIS-Aqua having a slightly lower correlation (r = 0.67) than that of MERIS/OLCI (r = 0.68) (Figure 2C).

Both sensors showed a similar [Chl-*a*] distribution when compared to co-located *in situ* [Chl-*a*] observations (Figures 2D, E), with MERIS/OLCI having a few data points outside the maximum range of the *in situ* [Chl-*a*] centred at ~2 ug l^{-1} (Figure 2E). In order to better understand the distribution between the datasets, the log-transformed $[\text{Chl-}a]^{in\ situ}/[\text{Chl-}a]^{satellite}$ ratio was determined (Figure 2F) and showed that the apex of distribution for MODIS-Aqua was closer to zero (i.e. the 1:1 line), while the majority of the data was distributed within a positive ratio for both satellites. This positive distribution is indicative of a general tendency for both sensors to underestimate *in situ* [Chl-*a*]. This was similarly evident for both sensors in the negative mean relative error (MRE) (-44.6% and -38.7% for MERIS/OLCI and MODIS-Aqua respectively) and the negative median relative errors (-32.5% and -13.9% for MERIS/OLCI and MODIS-Aqua respectively) (Table 2). Similar findings (i.e. overestimation at lower [Chl-*a*] and underestimation at higher [Chl-a]) were reported by Dogliotti et al. (2009) for MODIS-Aqua when compared with SeaWiFS for the Argentinean Patagonian continental shelf between 38° S and 55° S, which they attributed to differences in phytoplankton composition across a similar range of [Chl-*a*].

Comparison of MODIS-Aqua to *in situ* [Chl-*a*] for the full dataset (n=179) (i.e. not limited to the time period that coincided with MERIS/OLCI), showed similar statistical results (data distribution and error margins) (Figures 3A, B). An overall [Chl-*a*] underestimation tendency is similarly observed as shown in Figures 3C, C inset), the statistical metrics of which (MRE, MARE, RMSE, MedRE and Bias) are also summarised in Table 2, with a tendency to overestimate at very low [Chl-*a*] concentrations (Figure 3D). Overall, it can be observed from the log ratio distribution in Figure 3D that the MODIS-Aqua satellite algorithm compared well with *in situ* measurements and that the error margins improved when the expanded full data matchups were used.

3.2 Deriving phytoplankton optical fingerprints from ocean colour remote sensing

3.2.1 Remote sensing reflectance

Figure 4 shows the *Rrs* characteristics across 10 spectral wave bands in the visible range for oceanic waters dominated by different phytoplankton community groups, namely diatoms, HB and LB dinoflagellates, flagellates and mixed assemblage. These *Rrs* spectra showed considerable differences in magnitude and shape among the phytoplankton groups, which is subsequently exploited for deriving optical fingerprints that are characteristic for specific groups. For example, the *Rrs* minima observed in the longer wavelengths (i.e. red region: 645, 667 and 678 nm) is evident for all phytoplankton groups except HB dinoflagellates, whose *Rrs* minima is in the shorter violet/blue region (412/443 nm) (Figure 4). LB dinoflagellates had a characteristic maxima in the violet/blue region (412/443 nm) of the spectra, while for both HB dinoflagellates and flagellates, the *Rrs* magnitude increased with increasing wavelength from violet/blue-to-green with the *Rrs* maxima located in the green spectral region (555 nm) for HB dinoflagellates & (547 nm) for flagellates.

TABLE 2 Statistical metrics used for comparison of satellite-derived and *in situ* [Chl-*a*] match-ups between the MODIS-Aqua and MERSI/OLCI sensors in the northern Benguela.

Statistical metrics	Satellite sensor		
	MERIS/OLCI	MODIS-Aqua	Full MODIS-Aqua data
n	36	37	179
MRE (%)	-44.618	-38.739	-7.443
MARE	0.803	0.279	0.429
RMSE	0.445	0.393	0.320
Median	0.332 $^{in\ situ;}$ 0.224 ^{satellite}	0.305 $^{in\ situ;}$ 0.263 ^{satellite}	0.408 $^{in\ situ;}$ 0.227 ^{satellite}
MedRE (%)	-32.354	-13.902	-44
Ratio*	1.649	2.138	0.182
Bias	0.009	0.008	0.002
Slope	0.776	0.547	0.478

*: mean Chl-a $^{in\ situ/}$Chl-a ^{sat} ratio.
n: number of data matchups.

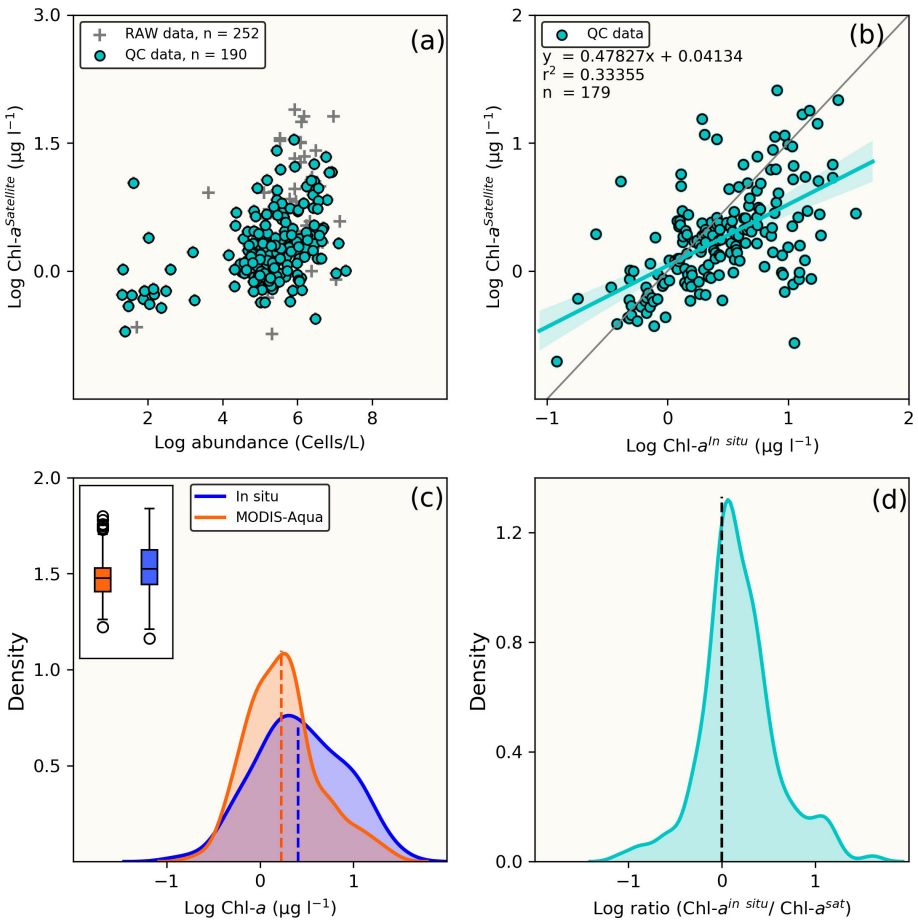


FIGURE 3
Comparison between full (n = 179) *in situ* [Chl-*a*] dataset and MODIS-Aqua satellite match-up retrievals. **(A)** Raw and quality controlled datasets, **(B)** Linear statistical regression of QC Chl-a between *in situ* and MODIS-Aqua match-ups, **(C)** Comparative overview of [Chl-*a*] distribution from *in situ* and MODIS-Aqua using the Kernel density estimate plots and boxplots (inset). The dotted vertical lines indicate the mean [Chl-*a*] and **(D)** distribution plot of log-transformed $[Chl\text{-}a]^{in\ situ}/[Chl\text{-}a]^{satellite}$ ratio.

3.2.2 Remote sensing reflectance spectral band-ratios

Multiple spectral band-ratios were investigated to identify optical signatures typical of waters dominated by the various phytoplankton groups under investigation. Boxplots of band-ratios were used to assign thresholds associated with the probability of dominance by each group based on the 25th and 75th percentiles of the datasets (Figures 5A–D). The *green/violet*, *blue/violet*, *violet/violet*, *blue/blue* and *red/violet* spectral band-ratios yielded no obvious unique spectral thresholds that may be assigned to dominance of any group as the data distribution (box plots) were within similar overlapping ranges (data not shown). However, characteristic dual spectral band-ratio thresholds were identified for *red/blue* (*Rrs*678/*Rrs*488), *green/green* (*Rrs*547/*Rrs*531), *red/red* (*Rrs*645/*Rrs*678) and *green/blue* (*Rrs*555/*Rrs*488) ratios that could describe a high probability for the presence of diatoms, LB dinoflagellates, HB dinoflagellates, flagellates and mixed communities. These differentiations are graphically represented in Figures 5A–D and the threshold values summarised in Table 3. The LB dinoflagellates had characteristically low *red/blue*, *green/green* and *green/blue* ratios, while diatoms occupied an intermediate *green/green* and *green/blue* band-ratios. The HB dinoflagellates had characteristically high *green/green*, *red/red* and *green/blue* band-ratios (Figures 5A–D blue shading). Although HB dinoflagellates typically had a higher *red/blue* ratio than diatoms, they expressed a large overlap (Figure 5A teal shading). Flagellates overlapped the mixed assemblage in the *green/green* ratio (Figure 5B magenta shading) but occupied a relatively unique, yet narrow distribution band in the *red/blue* ratio (Figure 5A purple shading), while the mixed community had a distinct *red/red* band-ratio (Figure 5C orange shading).

3.2.3 Spectral band difference, *RNR* and [Chl-*a*]

The characteristic spectral band difference, *RNR* and [Chl-*a*] for detection of conditions associated with dominance of diatoms, LB dinoflagellates, HB dinoflagellates, flagellates and mixed communities were investigated and are graphically represented in Figure 6, with thresholds indicated. The threshold values for spectral band difference are summarised in Table 3. Both diatom and HB dinoflagellate-dominated waters shared a characteristic of high nFLH (Figure 6A, teal shade), although diatoms displayed the highest nFLH by comparison. However, HB dinoflagellates had a higher *RNR* and [Chl-*a*] biomass and a lower line height at 531 nm (LH531) than diatoms (Figures 6B–D). Although generally having

10.3389/fmars.2023.1118226

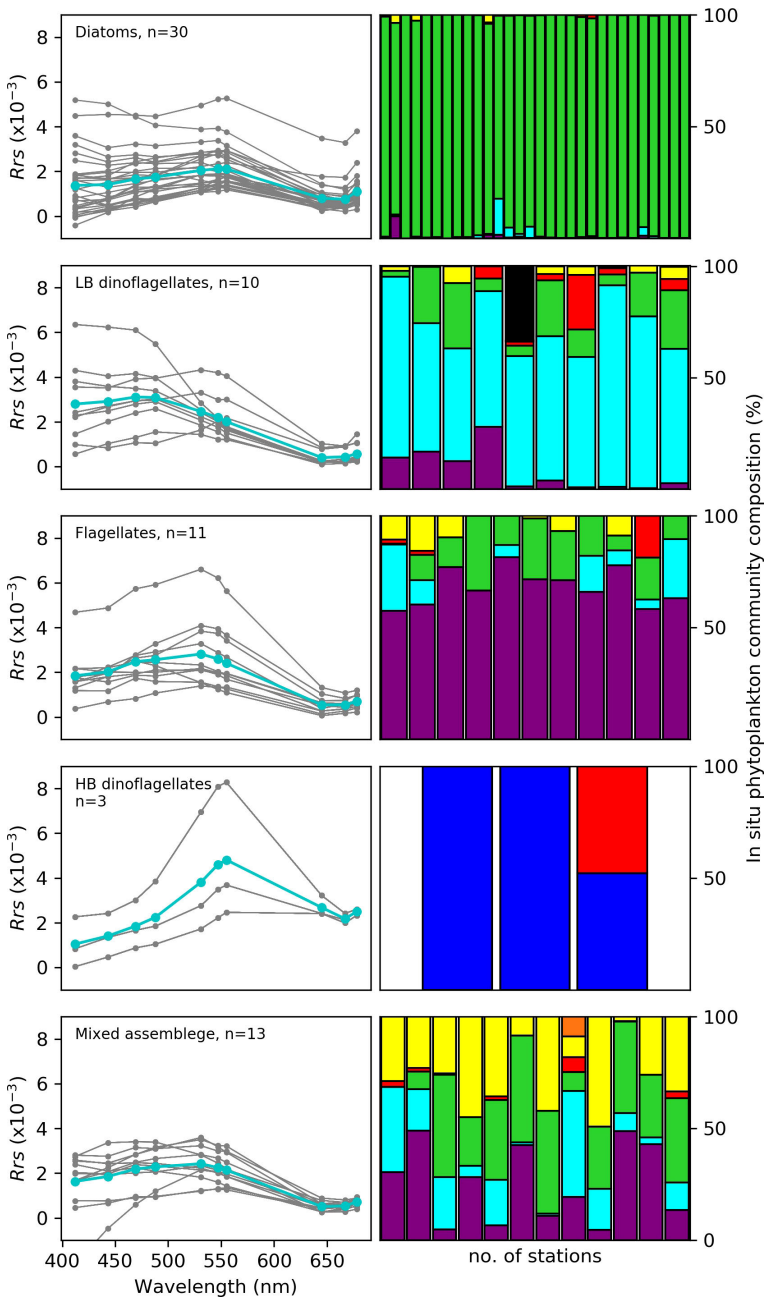


FIGURE 4
The remote sensing spectral reflectance (*Rrs*) in the visible range of the spectrum with wavebands at 412, 443, 469, 488, 531, 547, 555, 645, 667 and 678 for samples from the nBUS waters dominated by the phytoplankton groups (Diatoms, flagellates, low (LB) and high (HB) biomass dinoflagellates and Mixed assemblage from the MODIS-Aqua satellite sensor are shown in the left panel. The cyan line indicates the mean *Rrs* at each spectral band and the number of match-ups (n) are indicated. The coloured bars on the right panel represent the corresponding % phytoplankton community composition at each station per phytoplankton group. The colours refer to diatoms (green), LB dinoflagellates (turquoise), HB dinoflagellates (blue), flagellates (purple), coccolithophores (red), cryptophytes (orange), cyanobacteria (black) and other/unknown (yellow).

similar spectral features to other phytoplankton groups, the flagellate-dominated waters represent a discernible nFLH range between diatoms and dinoflagellates (Figure 6A, purple shade). Unlike their high biomass counterparts, the LB dinoflagellates had the lowest nFLH, *RNR* and were generally dominant in low [Chl-*a*] conditions (Figures 6A–C). The spectral band difference and [Chl-*a*] features of the mixed community showed no unique characteristics and were thus indistinguishable from other groups using these approaches. It should be noted that several line heights were calculated at various spectral wavelengths and were distributed similarly for all the groups (data not shown). Generally, variability in line height was observed in the green spectral regions (531, 547 and 555 nm) with a resolution between diatoms and HB dinoflagellates while the remaining groups showed no obvious line height thresholds unique to them. Important to note is that a final category was defined as "low *Rrs* signal", where the *Rrs* signal

10.3389/fmars.2023.1118226

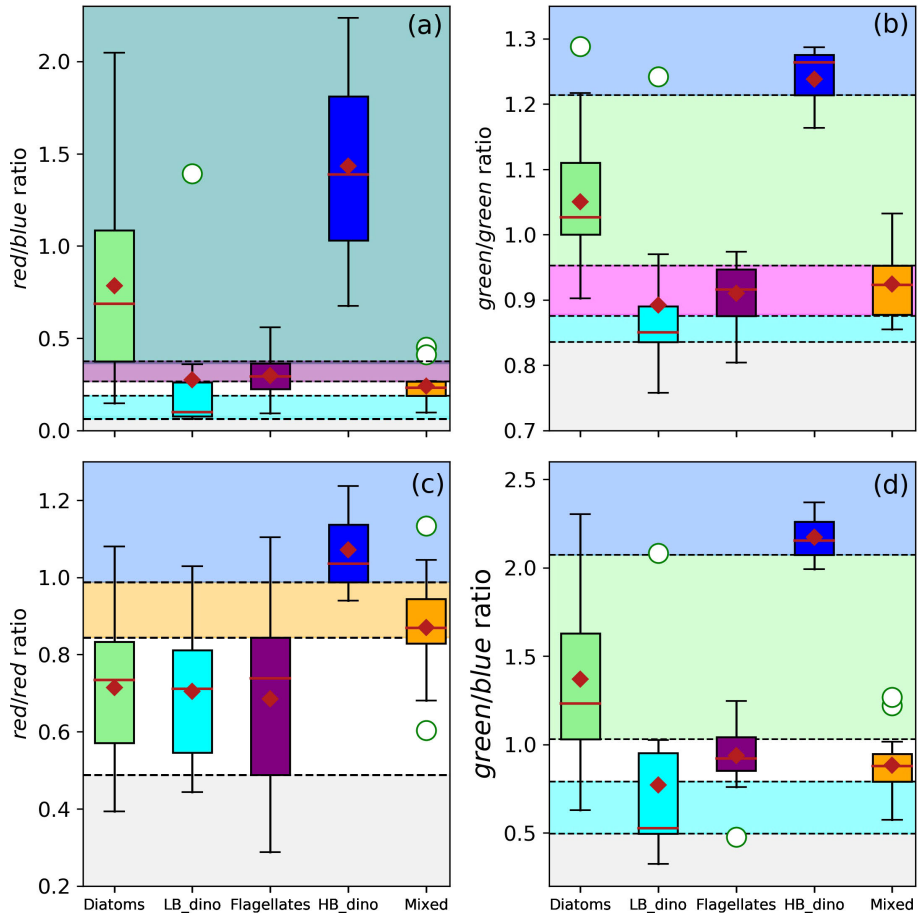


FIGURE 5
Boxplots of the dual-spectral band ratios for waters associated with dominance of diatoms, LB dinoflagellates (LB_dino), flagellates, mixed community and HB dinoflagellates (HB_dino). The thresholds of the *red/blue* (*Rrs*678/*Rrs*488) **(A)**, *green/green* (*Rrs*547/*Rrs*531) **(B)**, *red/red* (*Rrs*645/*Rrs*678) **(C, D)** *green/blue* (*Rrs*555/*Rrs*488) band-ratios are indicated by the dashed horizontal lines and colour shaded bands (light green = Diatoms; cyan = LB dinoflagellates, purple = Flagellates, blue = HB dinoflagellates, orange = Mixed, teal = Diatoms/HB dinoflagellates, magenta = Flagellates/Mixed). Statistical parameters such as the median, mean and outliers are indicated as the red line, red diamond and white circles respectively.

was considered too low to confidently retrieve any discernible signal due to a low signal-to-noise ratio, these low *Rrs* criteria were defined by the lowest 25th percentile of the distribution of each *Rrs* variable and are summarised in Table 3.

3.3 Algorithm development

Our approach to detecting phytoplankton community characteristics from space investigates statistical thresholds based on [Chl-*a*] biomass, dual band-ratios and spectral band differences to exploit small variations in the *Rrs* characteristics associated with dominance of specific phytoplankton groups. If the *Rrs* spectrum from a pixel is within a range defined by the threshold values for waters associated with the dominance of a particular phytoplankton group, then it is assigned to reflect the likelihood of that phytoplankton group being dominant. These thresholds are summarised in Table 3.

Given the identified thresholds for the various phytoplankton groups from the remote sensing variables indicated in Table 3, the next step was to determine the most suitable variables for algorithm development. To do this, we assess 1) the algorithms' ability to confidently classify/distinguish multiple phytoplankton groups, 2) the characteristics of the linear relationship between the variables in Table 3 and [Chl-*a*], with the understanding that biomass is likely to influence the spectral characteristics of *Rrs* and 3) the range in [Chl-*a*] that is typical for each of the defined thresholds for the various phytoplankton groups, favouring variables that allow for the classification of a number of phytoplankton groups within a similar range of [Chl-*a*]. While some algorithms are suitable for detection of specific phytoplankton groups during high biomass blooms, we embark on developing an algorithm that is suitable for the detection of dominant groups even in low [Chl-*a*] (non-bloom) conditions. To assist with the assessment of these criteria, we examined the linear relationship between the *Rrs* variables and [Chl-*a*] (Figures 7A–F). Each of the three criteria is presented in detail below:

1) Can the *Rrs* variable confidently distinguish multiple PFTs?

In Figure 7A, the *red/blue* ratio defining flagellates and LB dinos are tightly clustered together with a low range of variability in the

10.3389/fmars.2023.1118226

TABLE 3 Summary of MODIS-Aqua spectral threshold characteristics for waters dominated by various phytoplankton groups in the nBUS.

Phytoplankton group	MODIS-Aqua remote sensing variables							
	Band-ratios					Spectral band difference		
	Red: Blue (488/678)	Green: Green (547/531)	Red: Red (645/678)	RNR (748/667)	Green: Blue (555/488)	nFLH	LH531	Log Chla
Diatoms	>0.363	>0.952 <1.214	–	>0.221 <0.593	>1.031 <2.073	>0.392	>-0.189 < 0.231	>0.385 < 1.264
LB dinoflagellates	>0.064 <0.189	>0.758 <0.875	–	>0.029 <0.221	>0.496 <0.792	>0.124 <0.186	–	>-0.030 < 0.189
Flagellates	>0.266 <0.363	>0.875 <0.952	–	–	–	>0.294 <0.392	–	–
Mixed community	–	>0.875 <0.952	>0.844 <0.988	–	–	>0.186 <0.294	–	–
HB dinoflagellates	>0.363	> 1.214	>0.988	>0.593	>2.073	>0.392	>-0.365 <-0.189	>1.264
Low *Rrs* signal	<0.064	<0.758	–	<0.029	<0.496	<0.124	<-0.365	<-0.030

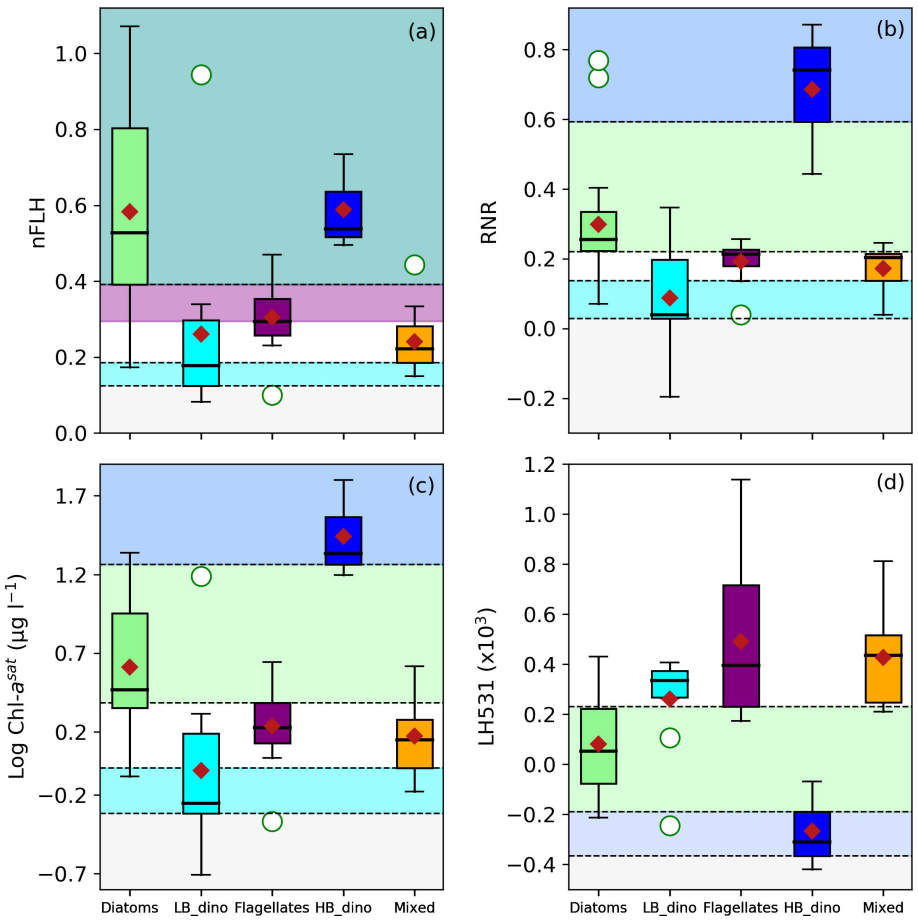


FIGURE 6
Boxplots of **(A)** nFLH, **(B)** RNR, **(C)** log-transformed [Chl-*a*] and **(D)** line height at 531 nm (LH531) for waters associated with dominance of Diatoms, LB dinoflagellates (LB_dino), Flagellates, HB dinoflagellates (HB_dino) and Mixed communities. The threshold ranges are indicated by the dotted horizontal lines and colour schemes (green = Diatoms; cyan = LB_dino; purple = Flagellates; blue = HB_dino; red = Mixed; teal scale = Diatoms/HB dinoflagellates). The median, mean and outliers are indicated as the bold black line, red diamond and white circles respectively.

10.3389/fmars.2023.1118226

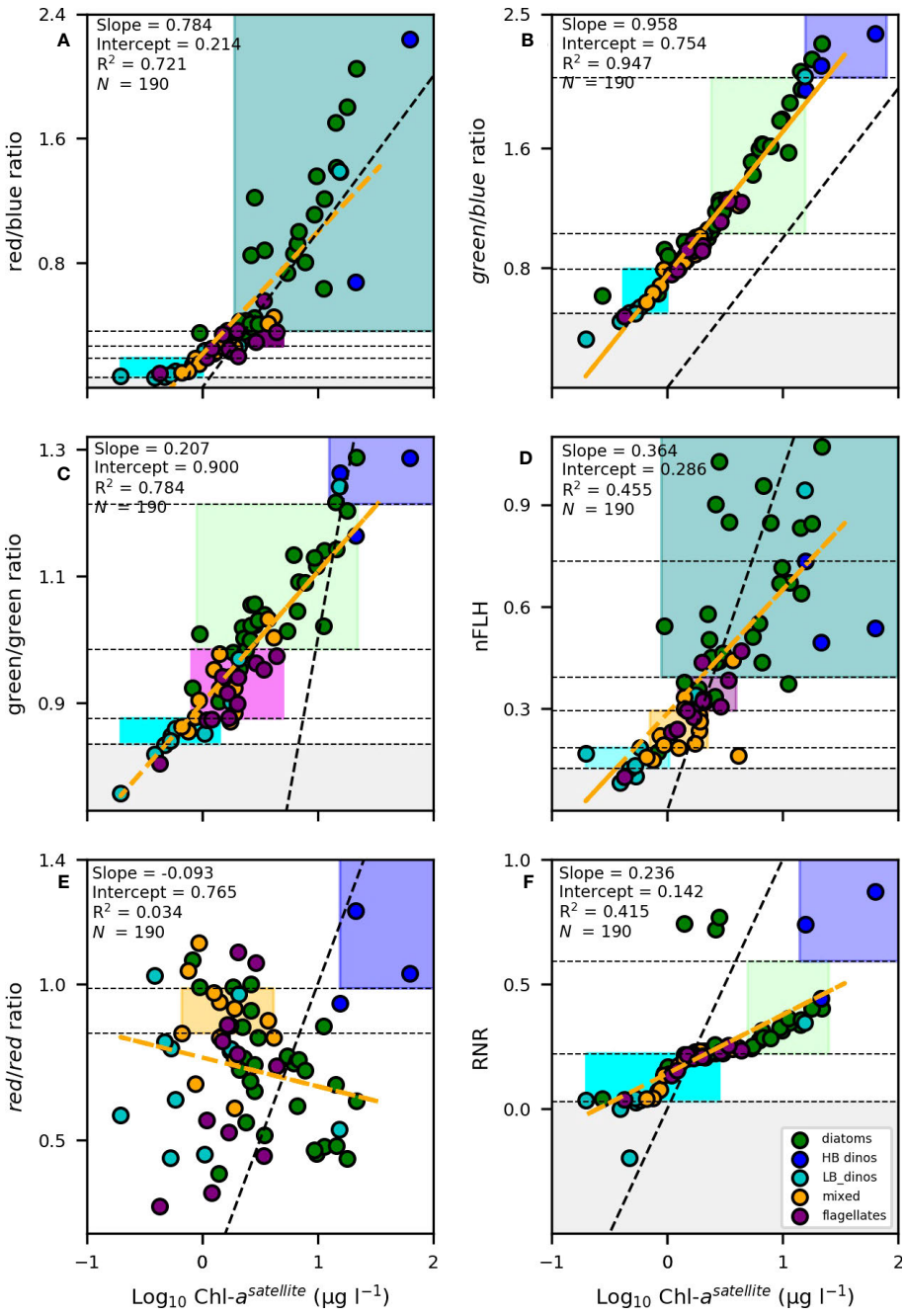


FIGURE 7
Linear regression analysis between [Chl-*a*] against the **(A)** *red/blue*, **(B)** green/*blue*, **(C)** *green/green*, **(D)** nFLH, **(E)** *red/red* and **(F)** RNR band-ratio, algorithms, [Chl-a] data was log-transformed prior to analysis. The linear regression is shown by the dashed orange line. The black dotted line represents the theoretical 1:1 relationship. The coefficient of determination (R^2), slope, intercepts and number of samples (*N*) are indicated. The samples representing dominance by diatoms, LB dinoflagellates (LB_dino), HB dinoflagellates (HB_dino), flagellates and mixed communities are indicated as green, cyan, blue, purple and orange dots respectively. The shaded areas denote the unique spectral characteristic thresholds for each group (green = diatoms, cyan = LB dinoflagellates, orange = mixed, purple = flagellates, blue = HB dinoflagellates, magenta = mixed/flagellates, teal = diatoms/HB dinoflagellates).

optical identifier making it difficult to distinguish them from each other. In addition, there was overlap in the range of diatoms and HB dinos. In Figure 7E, although more broad, it is clear that the majority of PFTs share a similar range of variability in the red/red ratio hampering an ability to identify the majority of PFTs.

2) Is variability in the *Rrs* signal biomass dependent?

A strong positive linear relationship and slope close to 1 was observed between [Chl-*a*] and the *red/blue* (r^2 = 0.721, slope = 0,784) and *green/blue* band-ratios (r^2 = 0.947, slope = 0.958) (Figures 7A, B, respectively), suggesting that these optical signals were, for the most part, biomass-driven. This is not surprising as the global ocean colour remote sensing algorithms for [Chl-*a*] retrieval

10.3389/fmars.2023.1118226

from the MODIS-Aqua are based on the ratio of the red, blue and green spectral bands. Using biomass as a criteria (or any other variable that is strongly dictated by biomass) constrains the algorithm's ability to detect a particular phytoplankton group outside of the assigned biomass range. This is highlighted by the absence of any overlap (i.e. vertical stacking) of the PFT boxes defined by the green/blue ratio in Figure 7B.

3) Is there overlap in the range of [Chl-*a*] for different PFTs?

Although the *green/green* band-ratio (Figure 7C) showed a similar positive linear relationship with [Chl-*a*] (r^2 = 0.784), it had a much lower slope (slope = 0.207), while nFLH and RNR both displayed weak linear relationships and lower slopes (r^2 = 0.455, slope = 0.364, Figure 7D and r^2 = 0.415, slope = 0.236, Figure 7F, respectively). When the slope is more gradual (i.e. Figure 7C, D, F), the range in [Chl-*a*] encompassed for each *Rrs* identifier is broader. Moreover, for these optical signatures, there is a larger range of variability evident in the *Rrs* identifiers for a similar range in [Chl-*a*] concentration. This is highlighted by the overlap in [Chl-a] among the groups but with varying *Rrs* signatures (i.e. the vertical stacking of PFT boxes across a similar range of [Chl-*a*]).

Given the above, the *red/blue* (Figure 7A), *green/blue* (Figure 7B), and *red/red* (Figure 7E) band-ratios were not considered further and eliminated as viable variables for further algorithm formulation. On the other hand, nFLH and the *green/green* band-ratio were considered the most suitable candidates for further development of the phytoplankton PFT algorithm. In addition, the *RNR* spectral band-ratio was also considered, in particular as a means of discriminating dinoflagellates from diatoms under high biomass conditions (i.e. when [Chl-*a*] > 8).

Unsurprisingly, there are overlaps in some optical signatures of different phytoplankton groups. For instance, both diatoms and HB dinoflagellates have an overlapping nFLH range (0.392) (Figure 7D, teal shading) and both flagellates and mixed communities share a similar range in the *green/green* ratio (Figure 7C, magenta shading). However, they have other unique signatures that allow a combination of criteria to be used to separate them out. For example, in the case of diatoms and HB dinoflagellates we use the *green/green* and *RNR* band-ratios to distinguish the two groups (Figure 8A). That is, if nFLH is > 0.392 then that pixel can be classified as either a diatom or a HB dinoflagellate. However, if the *RNR* is > 0.593 and the *green/green* ratio is >1.214 then that pixel is more likely to be dominated by HB dinoflagellates and as such is assigned that category. However, if the *green/green* ratio is<1.214 and the *RNR* is< 0.593 then it is more likely a diatom and is assigned as such within the given nFLH range. The use of combined algorithms of spectral characteristics increases the robustness and reliability of the algorithm, while at the same time allowing groups to be detected across a broad range of [Chl-*a*]. For example, diatoms can be detected across the full range of their green/green and nFLH criteria, so long as the *RNR* is not high, in which case it is assigned to HB dinos.

Similarly, in the case of flagellates and mixed communities, despite an overlap in their *green/green* ratio, they could be distinguished from each other based on the unique statistical signature within their nFLH distribution (Figure 6A). That is, a pixel with a *green/green* band-ratio between 0.875 and 0.952 could be classified as either flagellate-dominated or a mixed community. However, if the nFLH is between 0.294 and 0.392 then it would be assigned to reflect flagellate dominance, whereas if the nFLH is between 0.186 and 0.294 it would reflect a mixed community (Figure 8B). LB dinoflagellates on the other hand have a distinct *green/green* band-ratio and nFLH threshold, and unlike diatoms, HB dinoflagellates, flagellates and mixed community, were distinguished using individual thresholds of the *green/green* band-ratio and nFLH for their detection. Pixels are regarded as 'other/unknown' phytoplankton when no algorithm threshold criteria is met. A flowchart of the algorithm decision making tree (application) for discrimination and classification of the various phytoplankton groups in the nBUS is shown in Figure S2 of the Supplementary Material.

3.4 Algorithm validation

The algorithm was tested for accuracy and compared against randomly selected independent *in situ* datasets for diatoms.

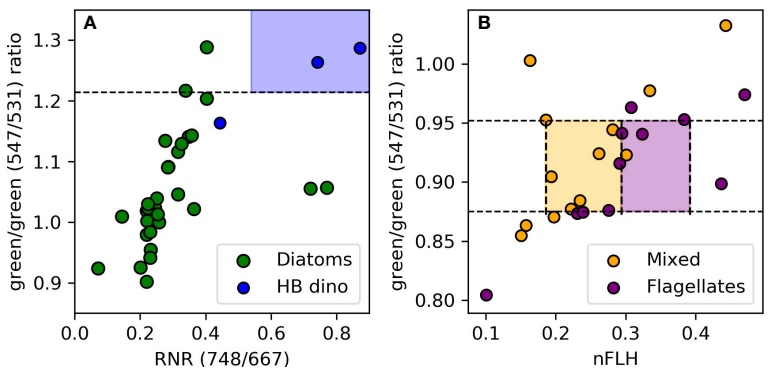


FIGURE 8
(A) Discrimination of diatom from dinoflagellate blooms based on differences in their RNR signals given their shared high *green/green* (>1.214) band-ratio and nFLH (>0.392) spectral characteristics. **(B)** Flagellates and the mixed communities are distinguished based on their nFLH spectral characteristics given their similarities in their green/green. and nFLH spectral characteristics. The blue, orange and purple colour shadings indicate the spectral characteristics unique to HB dinoflagellates, mixed community and flagellates respectively.

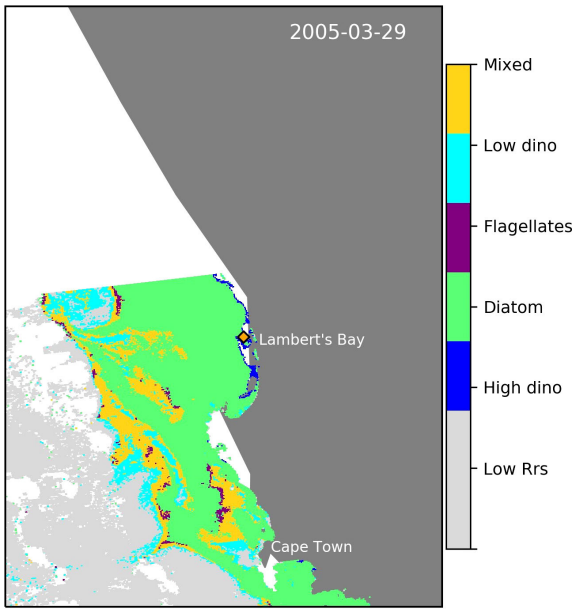


FIGURE 9
Evidence of the algorithm's ability to detect a known harmful dinoflagellate bloom in the sBUS (Fawcett et al., 2007). The sampled coastal station in Lamert's Bay is indicated by the orange diamond.

Unfortunately, this was only possible to do with diatoms, as this was the only phytoplankton group that dominated at enough stations to allow partitioning of the datasets into testing and validation groups. All other groups had so few stations in which they dominated that all had to be used to derive the most robust algorithm possible. The diatom validation was achieved by comparing observations with predictions (considered when *in situ* validation datasets' *Rrs* spectra fell within the algorithm detection thresholds). It should be noted that diatom dominance of validation datasets were similarly defined using the same criteria used to define diatom dominance for training datasets. A total of 7 datasets were used for validation of the diatom detection component of the algorithm for the nBUS. The quantitative validation results for diatoms, calculated as overall accuracy of the algorithm, was calculated as follows:

$$\textit{Algorithm accuracy} = \left(\frac{Cc}{Tc}\right) \times 100\% \quad (5)$$

where Cc is the correct classifications and Tc is the total classification from the independent diatom dominance datasets not used in the algorithm training datasets. We compared the optical characteristics of the validation data for stations dominated by diatoms against the algorithm thresholds and our algorithm compared well with the independent *in situ* observations of diatom dominance. Of the 7 stations, 5 matched with algorithm thresholds (i.e. were correctly classified by the algorithm). This translates to a percentage accuracy of 71.429%. The validation results demonstrate the algorithm's ability to translate MODIS-Aqua *Rrs* observations to distributions of phytoplankton communities in the nBUS. The diatom-dominated stations that were not correctly classified had lower *green/green* and nFLH values that were below our algorithm's minimum detection thresholds. In addition, they occurred in waters with low [Chl-*a*] that were between 1-2 µg l^{-1}. However, we were able to correctly classify 3 stations of diatoms within the same [Chl-*a*] range based on their *Rrs* characteristics.

Although we did not have sufficient *in situ* HB dinoflagellate dominated station data to validate the algorithm, we were able to demonstrate its ability to detect a known dinoflagellate bloom identified in the southern Namaqua Benguela upwelling system 3.5 km from Lambert's Bay (Cape Town, South Africa) in the sBUS (Fawcett et al., 2007) (Figure 9).

4 Discussion

Forming the base of marine food webs, phytoplankton are key ecological role players in upwelling systems and the global ocean. Knowledge of their composition and their regional, seasonal and interannual distribution and trends is key to understanding possible climate-linked ecosystem changes with implications on ecosystem health, economy, food security and climate response. Satellite remote sensing is one of the only tools that can provide the spatial, temporal and multi-decadal data information on phytoplankton needed to adequately investigate their important role in ecosystem function. Thus, there is a need for ocean colour remote sensing algorithms that can discriminate between phytoplankton functional types. Discrimination between diatoms and dinoflagellates is particularly relevant to ecology, local aquaculture and recreational activities as some of the bloom-forming and toxin-producing species belonging to these groups have been reported in the nBUS (Dijerenge, 2015; Louw et al., 2017; Gai et al., 2018), which may be harmful to both marine life and humans. Substantial work has been done using ocean colour algorithms and modelling techniques to detect phytoplankton community structure in the southern Benguela (Bernard et al.,

2005; Aiken et al., 2007; Evers-King, 2014; Smith and Bernard, 2020), but none as yet for the northern Benguela. This study is the first to derive an ocean colour remote sensing algorithm for the nBUS using a large compiled *in situ* microscopy dataset with satellite match-ups for detection and mapping of the most frequently encountered phytoplankton groups.

4.1 Determining the most appropriate satellite sensor for algorithm development

The first step in this endeavour was to determine which satellite product to use based on the availability of spectral bands in the red and near infrared regions. We approached this decision by comparing the two available ocean colour remote sensing algorithms of [Chl-*a*] to *in situ* measurements in order to test how well they performed in the high biomass coastal waters of the nBUS. MODIS-Aqua provided more data near the 1:1 ratio than MERIS/OLCI, suggesting a good approximation of *in situ* [Chl-*a*] (Figure 2F). Although MERIS/OLCI had a higher slope (0.766) than MODIS-Aqua (0.547), it contained more statistical errors (MRD, MAE, RMSE, MARD) against *in situ* [Chl-*a*] than MODIS-Aqua (as summarised in Table 2). We are however cognisant that fluorometry-derived Chl-a may be biased towards higher concentrations when compared to high-performance liquid chromatography (HPLC), particularly in the presence of Chl-c due to potential overlap in emission spectra (Moutier et al., 2019). It should however be noted that the Chl-a datasets used in the current study were measured using the non-acidification technique (Welschmeyer, 1994), which minimises the fluorescence effects of Chl-c, Chl-b and phaeopigments while optimizing the sensitivity of [Chl-*a*]. Although both products performed admirably, the MODIS-Aqua sensor observations cover a larger temporal scale when compared to the now discontinued MERIS and recent OLCI satellite sensors, which allows for a much longer analysis of trend detection in the northern Benguela, particularly for the period between 2012-2015 where there is a data gap during the transition from MERIS to OLCI sensors. The MODIS-Aqua product was thus selected for algorithm development and further investigations of optical fingerprints of the dominant phytoplankton taxonomic groups in the northern BUS. Although the MODIS-aqua ocean colour retrieval of [Chl-*a*] was determined to be statistically less erroneous than MERIS/OLCI for the nBUS, it should be noted that this step in our approach was not intended as a sensor validation study, which would instead involve the use of *in situ* radiometric reflectance measurements compared against concurrent satellite observations and is considered outside of the scope of this study.

The three most prominent drivers of variability between *in situ* and satellite derived [Chl-*a*] likely reflect the impact of atmospheric correction, different approaches to measuring *in situ* [Chl-*a*] and averaging across space and time. Atmospheric correction measures are necessary to overcome interference from atmospheric variables (e.g. aerosols, dust, clouds, scattered light etc.). The nBUS experiences dynamic annual, seasonal, and event scale atmospheric influences from terrestrial aerosol sources of dust plumes from the Namib desert (Shikwambana and Kganyago, 2022), intense fog (Spirig et al., 2017) as well as coastal sulphur eruptions (Ohde and Dadou, 2018), which may interfere with accurate atmospheric correction, and subsequent [Chl-*a*] retrievals from satellite-derived reflectance adding to regular ocean-atmosphere contributions from moisture and aerosols (e.g. sea spray) (Mayer et al., 2020). Additionally, discrepancies between [Chl-*a*] derived from fluorometry versus HPLC can impact the performance of the satellite algorithm. These discrepancies are likely to be region or season specific as they depend on the constituent pigments in the water that are in turn dictated by phytoplankton community dominance which varies both regionally and temporally. Another possible source of error is the scale difference between *in situ* sampling and match-up retrievals. The match-ups in the current study are derived from multi-pixel boxes which cover a spatial range of 13 – 25 km^2. Ship-board measurements on the other hand are based on sampling 0.1 – 2 L of seawater from a specific latitude-longitude location. Given the small-scale spatial heterogeneity or patchiness of phytoplankton abundance in the ocean (Pei et al., 2017; Scheinin and Asmala, 2020), averaging [Chl-*a*] over a multi-pixel box may produce discrepancies between measured and satellite derived [Chl-*a*]. Efforts are made to minimise the effects of this error by exclusion of multi-pixel boxes with mean values that have a coefficient of variation (CV) greater than 0.15 (Bailey and Werdell, 2006). Finally, it was challenging to obtain large numbers of match-ups in time and space in the relatively data-poor region of the nBUS. Although we initially prioritised matchups within 12 hours of sampling, to minimise temporal discrepancies, the subsequent small number of match up stations that passed quality control (n=73) meant that we had to relax the time window constraint to 24 hours, which increased our database to n=190. A comparison of the relationships generated by the two data sets against *in situ* [Chl-*a*] (i.e. n=73 and n = 190) showed no substantial differences in the statistical relationships (i.e. slopes remained comparable at 0.632 and 0.478 respectively, while the correlation coefficients remained similarly comparable at 0.744 and 0.578 respectively). We suspect that the above-mentioned variables, either in combination or on their own, as well as other factors not mentioned here, may have contributed to the observed discrepancies between satellite retrievals and *in situ* measurements of [Chl-*a*].

4.2 Phytoplankton optical fingerprints

Differences were observed in the *Rrs* spectral characteristics of waters dominated by different phytoplankton groups. These differences in optical characteristics can be attributed to differences in cellular pigment composition (and content), morphology, size and abundance (Vaillancourt et al., 2004; Mao et al., 2010). The size and pigment differences of various phytoplankton taxa in the nBUS have been shown previously (Hansen et al., 2014; Barlow et al., 2018). For example, Hansen et al. (2014) highlighted differences in water masses associated with different phytoplankton taxa and abundance at different upwelling stages from MODIS-aqua as testament to variability in *Rrs* (at 412

nm, 554 nm and 665 nm). Although differences in optical signatures can be exploited from space to distinguish different phytoplankton groups, there nonetheless remains the potential for overlap between different species that may occupy a similar size distribution and/or pigment content, and/or range of abundance. Optical indices from *Rrs* characteristics are complicated further by the complex interplay between the effects of cell size and abundance. For example, optical model simulations show that higher cell counts increase absorption and backscatter coefficients in smaller sized cells whereas these signals decrease with increasing cell size and lower cell abundance (Laiolo et al., 2021). Furthermore, the pigment packaging effect (a reduction in light absorption from high intracellular [Chl-*a*], particularly in the blue wavelengths) increases with increasing cell size being more pronounced in larger cells (> 10 μm) such as diatoms (Soja-Wozniak et al., 2020; Laiolo et al., 2021). The observed optical signatures that are assigned in this study to different phytoplankton groups are generated from a net effect of the optical impacts from the communities dominant size structure, pigment composition and biomass at which any one group commonly occurs. Regardless of the complexity of the inter-relationships between the multiple drivers of *Rrs* characteristics, our optical proxy accumulates these signals to statistically discern the band-ratio ranges typical of each group that may subsequently be used to identify them. In light of this, the band-ratios, RNR and nFLH fluorescence signals can still be recognised as effective signals for characterising the presence of different phytoplankton groups. A purely abundance-based approach on the other hand makes the assumption that different species dominate at different typical biomass thresholds, and as such, is not able to distinguish between phytoplankton blooms of two different species with a similar abundance (Uitz et al., 2006; Hirata et al., 2011). Although all four approaches to derive optical fingerprints for the different phytoplankton groups were investigated in this study, the final algorithm used a combination of only 2 approaches (i.e. the band-ratio and spectral band difference approach to the exclusion of individual *Rrs* at different spectral bands and [Chl-*a*] abundance-based approaches). This multi-layered ocean colour remote sensing algorithm for phytoplankton group detection in the nBUS increases the robustness of the algorithm in that a pixel typically has to meet at least two criteria between the *green*/*green*, *RNR* and nFLH before it is assigned as either a diatom, dinoflagellate, flagellate or mixed community.

Band-ratio algorithms, particularly in the blue-green spectral bands, are typically designed for global applications over optically deep ocean waters for [Chl-*a*] retrievals (O'Reilly et al., 2000). In coastal waters, optically active non-phytoplankton materials such as coloured dissolved organic matter (CDOM) are capable of light absorption in the blue and violet spectral regions in particular (Morel et al., 2010; Coble, 2013). Their absorption in the blue spectral region typically dominates that of phytoplankton in estuarine and coastal areas (D'Sa and Kim, 2017; Isada et al., 2021). As such, the blue-violet region of the *Rrs* spectra is likely to have a larger error associated with it that may undermine our ability to capture phytoplankton-driven characteristics. To overcome this limitation, we instead make use of spectral bands in the red-NIR (i.e. nFLH and *RNR*) and green (i.e. *green*/*green*) regions for phytoplankton group classification in the nBUS. Similarly, although the nFLH signal could also be influenced by CDOM, the absorption of CDOM in the red-NIR is very low and its influence on nFLH is considered negligible, making nFLH and other algorithms utilizing the red-NIR spectral bands ideal candidates for phytoplankton bloom detection and classification in optically complex coastal waters such as the dynamic nBUS. Such algorithms (i.e. those utilising the *Rrs*665/*Rrs*709 band-ratio) have previously been successfully developed, validated and applied in the sBUS for phytoplankton bloom detection (Bernard et al., 2005). Smith and Bernard (2020) later discriminated HABs of diatoms from dinoflagellates using the maximum line height approach (MLH), a spectral band difference algorithm analogous to nFLH which computes the MLH between two line heights calculated at *Rrs*681 and *Rrs*709 spectral bands, coupled with the line height ratio (ratio of line heights calculated at 681 and 709 nm). In the current study, we adopted a similar approach (use of products with spectral bands in the red and near infrared spectral regions) but for different satellite products (i.e. nFLH) and used in combination with a *green*/*green* spectral band-ratio and thresholds that best suited the unique waters in the nBUS.

It is recognised that the ability to distinguish different phytoplankton groups may be hampered by pixel averaging when their distribution is spatially heterogeneous e.g. at the transition between inshore and offshore communities (e.g. Barlow et al., 2018). The 5x5 pixel match-up box centred around the *in situ* station in the current study spans an area of between 16 - 25 km^2. It is thus possible that individual pixels may be dominated by different groups, which can introduce errors in community identification when averaging across a 5x5 pixel box. As a precaution to minimise this effect, we use the standard deviation to identify boxes that express high variability and exclude them from further analysis.

4.3 Algorithm application

Using the algorithm as depicted in Figure S2 in the Supplementary Material, we translate the *green*/*green*, RNR band-ratios as well as nFLH data from the MODIS-Aqua according to the thresholds listed in Table 3 to an example map of the distribution of the phytoplankton community in the nBUS for 28 April 2009 (Figures 10). From these maps (Figures 10B-D) it is clear how the spatial distribution of particular *Rrs* characteristics can be used to identify the phytoplankton groups. Diatoms were the most spatially abundant group, which is typical of high biomass inshore waters of the Benguella (Matlakala, 2019). Bloom conditions (Figure 10A; [Chl-*a*] >2 ug l^{-1}) were typically encountered inshore with a filament extending offshore at 22°S. These blooms were primarily dominated by diatoms, which are the most frequently observed blooms in the nBUS (Hansen et al., 2014; Louw et al., 2017; Matlakala, 2019). Diatoms were easily distinguished from their high nFLH and high *green*/*green* ratios (Figures 10B, C, respectively). Dinoflagellates typically dominated in low [Chl-*a*] conditions and were generally distributed further offshore (~140 km from shore), where the waters are typically warmer and nutrient-limited (Mohrholz et al., 2014). This is consistent with the literature

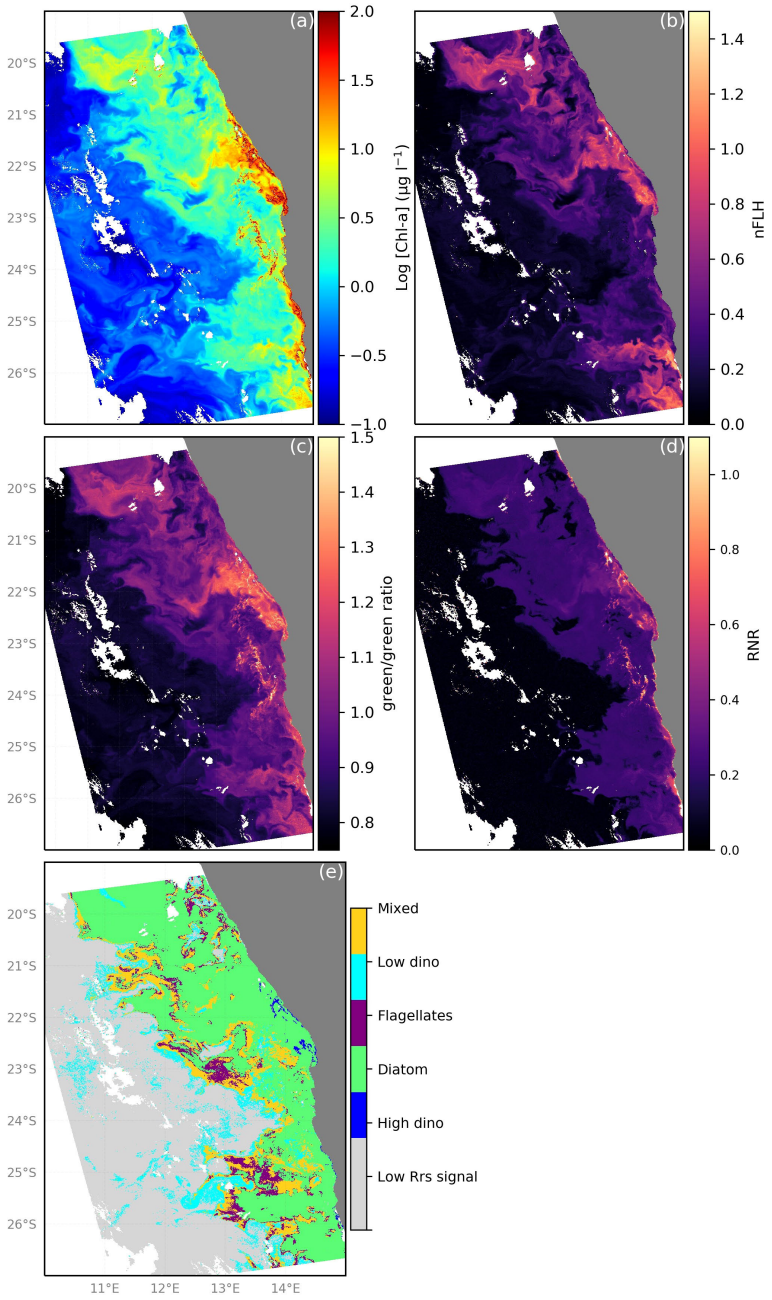


FIGURE 10
Demonstration of phytoplankton group dominance classification by the proposed ocean colour remote sensing algorithm for phytoplankton community from MODIS-Aqua observations for 11 March 2019 in the nBUS. **(A)** [Chl-*a*] distribution, **(B)** The observed nFLH, **(C)** green/green (*Rrs*547/*Rrs*531) band-ratio, **(D)** red/near-infrared (*Rrs*748/*Rrs*667) band-ratio and **(E)** application of the algorithm indicating the distribution of dominant phytoplankton groups in the nBUS.

(Hansen et al., 2014; Wasmund et al., 2014; Matlakala, 2019) and provides further confidence in the algorithm's abilities. Dinoflagellates were also evident in low [Chl-*a*] waters closer to shore (north of 22°S latitude) near the A-B front, where the shelf is narrower and there is typically evidence of a warm water intrusion from the Angola current (Hutchings et al., 2009; Rouault et al., 2018). There was however some evidence of HB dinoflagellates within the inshore high [Chl-*a*] bloom, which have been observed to occur inshore typically in winter (Dijerenge, 2015; Matlakala, 2019). These dinoflagellate blooms are readily distinguished from diatoms by their characteristically high *RNR* signature (Figure 10D). Large patches of spatially cohesive flagellates were evident typically offshore (notably at ~23°S and 25°S) and identified by their unique green/green and nFLH combination. The most common flagellates identified in the Benguela are nanoflagellates, most commonly observed in the mid-shelf region and further offshore in the Namibian upwelling system (Hansen et al., 2014; Barlow et al., 2018), which is in agreement with our algorithm's predictions of the spatial distribution of this group from the example maps. Very low [Chl-*a*] waters were coincident with

extremely low values of nFLH, green/green and *RNR* and characterised as waters with an *Rrs* signal too low to confidently identify as any phytoplankton group. Of note is that despite a clear [Chl-*a*] gradient (i.e. a typical decrease in biomass from inshore to offshore, Figure 10A), there is evidence of the algorithm being able to classify diatom, dinoflagellate and flagellate dominated communities as well as mixed community assemblages in both low and high [Chl-*a*] conditions (Figures 10A, E). From this example image it is clear how the high spatial and temporal coverage of satellite remote sensing can be harnessed to our advantage to better understand the dynamics, distribution, phenology and trends in phytoplankton community composition.

4.4 Recognising algorithm limitations

4.4.1 Use of microscopy data

In situ phytoplankton data is a prerequisite for ocean colour algorithm development and validation for satellite remote sensing of phytoplankton from space. Inaccurate or incomplete *in situ* data undermines our ability to correctly associate optical signatures to cells that aren't identified and may therefore lead to erroneous assignment of optical signatures to other phytoplankton groups, making accurate *in situ* measurements a scientific priority for increasing the accuracy and confidence of remote sensing and model development. Techniques such as microscopy are traditionally used in field observations for phytoplankton enumeration and taxonomic identification, providing valuable information for studying the diversity of phytoplankton taxa for assessing ecosystem health and balance, environmental monitoring and conservation, climatology and aiding aquaculture and fisheries industries with HABs detection among others (Anderson and Throndsen, 2004; Louw et al., 2017). Microscopic cell count techniques are particularly useful in that they provide identification of cells to species level. Although phytoplankton community information can be derived from these techniques, they have their limitations. For instance, analysis is dependent on highly trained and skilled people with thorough taxonomic expertise; these methods can be expensive, labour-intensive, time consuming, and may produce low precision unless a very large number of cells are counted (Anderson and Throndsen, 2004). Differential preservation of cells can lead to preferential cell loss and can thus introduce bias to sample classification (Williams et al., 2016). The use of preservatives greatly affects the observed community composition depending on which preservative is used [e.g. Lugol's solution (either acidic or neutral) or formalin)] and for how long the samples were stored prior to analysis (Williams et al., 2016). For instance, armoured dinoflagellates are well preserved in all types of Lugols for up to 8 months whereas unarmoured dinoflagellates are only well preserved in acid Lugols for the same period. Microflagellates and diatoms are well preserved in acid Lugols (3 months and ~4 months respectively), while diatoms can also be stored in neutral Lugols (up to 2 months). Coccolithophores on the other hand are poorly preserved in acid Lugols and instead require neutral Lugols (2 weeks) (Williams et al., 2016). Phytoplankton samples from cruise campaigns in the current study were preserved in acidified (Meteor M153) and neutral (RGNO2019) Lugol's solutions and analysed within 3 months of sampling. As such, coccolithophores may be misrepresented in both samples due to preferential preservation, this in addition to their small size which makes them harder to enumerate. Dinoflagellates (armoured and naked), diatoms and flagellates on the other hand are more likely to be well represented as they are generally well preserved in acidic Lugols even 225 days after sampling as opposed to the neutral Lugols with optimum preservation of samples for 28 days (Williams et al., 2016). In this regard, samples preserved in neutral lugol solution from the RGNO2019 cruise that were analysed after a month (but within 3 months) may be underrepresenting some of these groups (i.e. diatoms, flagellates, coccolithophores). Furthermore, smaller (picophytoplankton) and fragile cells are not easy to identify and quantify; as a result they may be under-represented. Indeed, the absence of an occurrence of coccolithophore dominance in this study may be due to their small size (making them harder to identify and enumerate) together with a poor ability to adequately preserve them in Lugols solution (Williams et al., 2016). Finally, interpersonal differences from data analysed in different laboratories may also undermine the precision of microscopic analyses. Identification of pigment markers of phytoplankton groups using high-performance liquid chromatography (HPLC) has been adopted as an alternative proxy for phytoplankton community analysis (Kheireddine et al., 2017; Kramer et al., 2020). This method has some advantages against microscopic analysis such as being highly reproducible and allowing the quantification and identification of smaller and more fragile cells, including cells that would normally be degraded by sample preservation with Lugols (Paul et al., 2021; Flander-Putrle et al., 2022). Advancements in the classification of phytoplankton groups has been made possible with the aid of specialised computer software such as CHEMTAX, which facilitates the classification of phytoplankton groups by means of pigment-to-Chl-*a* ratios (Mackey et al., 1996). However, pigment analysis is not able to provide the same level of detail as microscopy as they are not able to identify individual phytoplankton species. Also, similarities in photosynthetic pigments across multiple taxa make it difficult to distinguish different groups with confidence. Arguably, the future of phytoplankton enumeration lies within the realm of imaging with *in situ* cameras, holographic cameras and imaging flow cytometry. Although not without their own set of challenges (Giering et al., 2020), these approaches can generate images used to derive concentration and biodiversity information, as well as organism-specific size and shape (Boss et al., 2022). Given the strengths and weaknesses of all the various approaches, it is clear that no one technique can be considered the holy grail for phytoplankton community analysis and it is generally recommended that different techniques are integrated in order to provide a more comprehensive analysis of phytoplankton communities.

4.4.2 Limited datasets for development and validation

Although there was arguably an adequate sample size for stations with diatom dominance (n = 37) to allow this phytoplankton group to be more robustly characterised and

partitioned into two sets of independent training (n=30) and validation (n=7), the number of matchup stations observing dominance of HB dinoflagellates (n=3), LB dinoflagellates (n=10), flagellates (n=11) and mixed phytoplankton community (n=13) were small. The qualitative nature of our algorithm only allows an indication of the dominance of one group in the presence of others and does not estimate the relative composition of each group nor the abundance of each group. It is recognised that these small data sets (which are further constrained by the necessity for satellite matchups in a region that is characterised by a persistent stratocumulus cloud deck) severely limit the robustness of the algorithm being developed. The authors are nonetheless committed to working with currently available and accessible data to explore the expansion of this data set for the purposes of validation of the existing algorithm and for future refinement with improved statistics as more data becomes available over time. In spite of the recognised limitations, it is clear that there is a dire need for such an algorithm and that the one proposed here provides a good first approach that can be applied retrospectively to 20 years of ocean colour data for important investigations that characterise the distribution patterns, phenology and trends of key phytoplankton groups in the region.

5 Conclusions

In the majority of the studies of community structure dynamics in the nBUS to date, microscopy has been the most commonly used technique for identifying phytoplankton distribution (Hansen et al., 2014; Dijerenge, 2015; Barlow et al., 2018) and environmental monitoring (Louw et al., 2017; Matlakala, 2019), although some studies used a combination of microscopy and pigment analysis (Barlow et al., 2018), with the limitations of both being clear. Satellite-based remote sensing of ocean colour is the only observational capability that can provide synoptic views of upper ocean phytoplankton characteristics at high spatial and temporal resolution (~1 km, ~daily) and a high temporal extent (global scales, for years to decades). It is thus important that we maximise the value of remote sensing observations by developing ecosystem-appropriate, well characterised products. This study takes advantage of unique spectral features (reflectance, reflectance ratios and spectral band difference) of oceanic waters dominated by various phytoplankton groups to create an ocean colour remote sensing algorithm for phytoplankton classification. Our future work will focus on acquiring additional *in situ* data for improvement and validation of the algorithm while venturing into discrimination of bloom types (e.g. non-HABs from HABs of diatoms of *Pseudo-nitzschia* species and dinoflagellates) and the detection of other key species (e.g. coccolithophores). Despite its limitations, the algorithm has enormous potential for mapping the distribution and phenology of phytoplankton groups on an unprecedented spatial and temporal scale in the nBUS. The intention is for this algorithm to be used for environmental monitoring of these phytoplankton types to better understand their spatial and temporal dynamics and environmental controls. In addition, application to the 20-year MODIS-aqua observation time series will allow an investigation of possible trends in community structure adjustments with important ecosystem implications for ocean-atmosphere exchange and energy transfer in support of the fisheries and aquaculture industries of Namibia.

Data availability statement

Publicly available datasets were analysed in this study. This data can be found here: The MODIS-Aqua data can be found at NASA's ocean colour website https://oceancolor.gsfc.nasa.gov/. The MERIS data can be accessed through the MERIS catalogue and inventory (MERCI, http://meris-ds.eo.esa.int/oads/access/). The OLCI data can be found at the Copernicus online data access website (CODA, https://coda.eumetsat.int/). Phytoplankton counts and chlorophyll-a data can be accessed on the publicly available and accessible Pangaea database website at https://www.pangaea.de/.

Author contributions

The authors confirm their contribution to the manuscript as follows: Conceptualization: ST; MS. Methodology: MS; ST; TM. Data acquisition: TM; MS; ST; DL; BM; RK. Data curation: TM. Visualization (figures): TM. Formal analysis: TM; MS; ST. Manuscript 1st draft: TM. Supervision: ST; MS. Reviewing & editing: TM; MS; ST; BM; RK. Project administration: ST; MS. Funding acquisition: ST. All authors read, edited and approved the final version of the manuscript.

Funding

This research was supported as part of the Alliance for Collaboration on Climate and Earth Systems Science (ACCESS)-funded PLankton in a coupled oceAn-aTmOsphere system (PLATO) project by the National Research Foundation (NRF, South Africa, Grant No 114691) and the Council for Scientific and Industrial Research (CSIR, South Africa) through its Southern Ocean Carbon-Climate Observatory (SOCCO) programme funded by the Department of Science and Innovation (DSI, South Africa) and the parliamentary grant (SNA2011112600001). BM and RK as well as the use of the *RV Meteor* were funded by a grant from the Federal Ministry of Education and Research in Germany (FKZ 03F0797C).

Acknowledgments

We are grateful to Norbert Wasmund and Lebogang M. Matlakala for providing additional microscopy cell counts and [Chl-*a*] data. We would like to thank Kurt Hanselmann and colleagues at the National Marine Information and Research Centre (NatMIRC) for the RGNO2019 cruise organization and invaluable laboratory support. We thank Werner Ekau for organizing the Meteor M153 cruise that formed part of the Trophic TRAnsfer eFFICency in the Benguela Current (TRAFFIC) project.

Conflict of interest

The authors declare that the research was conducted in the absence of any commercial or financial relationships that could be construed as a potential conflict of interest.

Publisher's note

All claims expressed in this article are solely those of the authors and do not necessarily represent those of their affiliated organizations, or those of the publisher, the editors and the reviewers. Any product that may be evaluated in this article, or claim that may be made by its manufacturer, is not guaranteed or endorsed by the publisher.

Supplementary material

The Supplementary Material for this article can be found online at: https://www.frontiersin.org/articles/10.3389/fmars.2023.1118226/full#supplementary-material

References

Agawin, N. S. R., Rabouille, S., Veldhuis, M. J.W., Servatius, L., Hol, S., van Overzee, M. J., et al. (2007). Competition and facilitation between unicellular nitrogen-fixing cyanobacteria and non – nitrogen-fixing phytoplankton species. *Limnology Oceanography* 52 (5), 2233–2248. doi: 10.4319/lo.2007.52.5.2233

Aguirre-Gomez, R., Weeks, A. R., and Boxshall, S. R. (2001). The identification of phytoplankton pigments from absorption spectra. *Int. J. Remote Sens.* 22, 315–338. doi: 10.1080/014311601449952

Aiken, J., Fishwick, J. R., Lavender, S. J., Moore, G. F., Sessions, H., Bernard, S., et al. (2007). Validation of MERIS reflectance and chlorophyll during the BENCAL cruise October 2002: Preliminary validation of new demonstration products for phytoplankton functional types and photosynthetic parameters. *Int. J. Remote Sens.* 28 (3–4), 497–516. doi: 10.1080/01431160600821036

Allison, E. H., Perry, A. L., Badjeck, M., Adger, W. N., Brown, K., Halls, A. S., et al. (2009). Vulnerability of national economies to the impacts of climate change on fisheries. *Fish Fisheries* 10, 173–196. doi: 10.1111/j.1467-2979.2008.00310.x

Anderson, P., and Throndsen, J. (2004). 'Estimating Cell numbers', in *Manual on Harmful Marine Microalgae. 2nd edition*. Paris France: UNESCO p. 770. doi: 10.25607/OBP-1370

Archer, S. D., Widdicombe, C. E., Tarran, G. A., Rees, A. P., and Burkill, P. H.. (2001). Production and turnover of particulate dimethylsulphoniopropionate during a coccolithophore bloom in the northern North Sea. *Aquat. Microbial Ecol.* 24, 225–241. doi: 10.3354/ame024225

Arrigo, K. R., Robinson, D. H., Worthen, D. L., Dunbar, R. B., Ditullio, G. R., Vanwoert, M., et al. (1999). Phytoplankton community structure and the drawdown of nutrients and CO 2 in the Southern Ocean. *Science* 283, 365–368. doi: 10.1126/science.283.5400.365

Bailey, S. W., and Werdell, P. J. (2006). A multi-sensor approach for the on-orbit validation of ocean color satellite data products. *Remote Sens. Environ.* 102 (1–2), 12–23. doi: 10.1016/j.rse.2006.01.015

Barlow, R., Lamont, T., Louw, D., Gibberd, M. J., Airs, R., and van der Plas, A. (2018). Environmental influence on phytoplankton communities in the northern Benguela ecosystem. *Afr. J. Mar. Sci.* 40 (4), 355–370. doi: 10.2989/1814232X.2018.1531785

Bernard, S., Balt, C., Pitcher, G., Probyn, T., Fawcett, A., and Du Randt, A.. (2005). "The use of MERIS for harmful algal bloom monitoring in the Southern Benguela," in *Proceedings of the MERIS (A)A TSR workshop*. Ed. H. Sawaya-Lacoste (Fracati, Italy: ESA Publ. Division), 1–7.

Bestion, E., Haegeman, B., Codesal, A. S., Garreau, A., Huet, M., Barton, S., et al. (2021). Phytoplankton biodiversity is more important for ecosystem functioning in highly variable thermal environments. *PNAS* 118 (35), 1–10. doi: 10.1073/pnas.2019591118

Boss, E., Waite, A. M., Karstensen, J., Trull, T., Muller-karger, F., Sosik, H. M., et al. (2022). Recommendations for plankton measurements on oceanSITES moorings with relevance to other observing sites. *Front. Mar. Sci.* 9 (July). doi: 10.3389/fmars.2022.929436

Brewin, R. J. W., Sathyendranath, S., Jackson, T., Barlow, R., Brotas, V., Airs, R., et al. (2015). Influence of light in the mixed-layer on the parameters of a three-component model of phytoplankton size class. *Remote Sens. Environment. Elsevier Inc.* 168, 437–450. doi: 10.1016/j.rse.2015.07.004

Brownlee, C., and Taylor, A. R. (2002). "Algal calcification and silification," in *Encyclopedia of life sciences* (Macmillan Publishers Ltd, Nature Publishing Group).

Caldeira, K., and Duffy, P. B. (2000). The role of the Southern Ocean in uptake and storage of anthropogenic carbon dioxide. *Science* 287, 620–623. doi: 10.1126/science.287.5453.620

Carr, M. (2002). Estimation of potential productivity in Eastern Boundary Currents using remote sensing. *Deep-Sea Res. II* 49, 59–80. doi: 10.1016/S0967-0645(01)00094-7

Carr, M., and Kearns, E. J. (2003). Production regimes in four Eastern Boundary Current systems. *Deep-Sea Res. II* 50, 3199–3221. doi: 10.1016/j.dsr2.2003.07.015

Charlson, R. J., Lovelock, J. E., Andreae, M. O., and Warren, S. G.. (1987). Oceanic phytoplankton, atmospheric sulphur, cloud albedo and climate. *Nature* 326 (6114), 655–661. doi: 10.1038/326655a0

Chavez, F. P., and Messié, M. (2009). Progress in oceanography: A comparison of eastern boundary upwelling ecosystems. *Prog. Oceanography. Elsevier Ltd* 83 (1–4), 80–96. doi: 10.1016/j.pocean.2009.07.032

Coble, P. G. (2013). "Colored dissolved organic matter in seawater," in *Subsea optics and imaging*. (Florida: Woodhead Publishing Limited), 98–118. doi: 10.1533/9780857093523.2.98

Cury, P., and Shannon, L. (2004). Regime shifts in upwelling ecosystems: observed changes and possible mechanisms in the northern and Southern Benguela. *Prog. Oceanography* 60, 223–243. doi: 10.1016/j.pocean.2004.02.007

Dermastia, T. T., Ara, S. D., Dolenc, J., and Mozetič, P.. (2022). Toxicity of the diatom genus Pseudo-nitzschia (Bacillariophyceae): insights from toxicity tests and genetic screening in the Northern Adriatic Sea. *Toxins* 14 (60), 1–17. doi: 10.3390/toxins14010060

Dijerenge, K. J. (2015). *Analysis of marine biotoxins: Paralytic and Lipophilic Shellfish Toxins in Mussels (Mytilus galloprovincialis) along the Namibian Coastline, University of Namibia.* (Namibia: University of Namibia). https://repository.unam.edu.na/handle/11070/1466.

Dogliotti, A. I., Schloss, I. R., Almandoz, G. O., and Gagliardini, D. A. (2009). Evaluation of SeaWiFS and MODIS chlorophyll-a products in the Argentinean Patagonian Continental Shelf (38° S-55° S). *Int. J. Remote Sens.* 30 (1), 251–273. doi: 10.1080/01431160802311133

D'Sa, E. J., and Kim, H. (2017). Surface gradients in dissolved organic matter absorption and fluorescence properties along the New Zealand sector of the Southern Ocean. *Front. Mar. Sci.* 4 (21), 1–14. doi: 10.3389/fmars.2017.00021

Duncombe Rae, C. M. (2005). A demonstration of the hydrographic partition of the Benguela upwelling ecosystem at 26° 40 ' S. *Afr. J. Mar. Sci.* 27 (3), 617–628. doi: 10.2989/18142320509504122

Evers-King, H. (2014). Phytoplankton community structure determined through remote sensing and in situ optical measurements.. PhD thesis. (South Africa: University of Cape Town).

Fawcett, A., Pitcher, G. C., Bernard, S., Cembella, A. D., and Kudela, R. M. (2007). Contrasting wind patterns and toxigenic phytoplankton in the Southern Benguela upwelling system. *Mar. Ecol. Prog. Ser.* 348, 19–31. doi: 10.3354/meps07027

Field, C. B., Behrenfeld, M. J., Randerson, J. T., and Falkowski, P. (1998). Primary production of the biosphere : integrating terrestrial and oceanic components. *Science* 281, 237–241. doi: 10.1126/science.281.5374.237

Flander-Putrle, V., Francé, J., and Mozetič, P. (2022). Phytoplankton pigments reveal size structure and interannual variability of the coastal phytoplankton community (Adriatic sea). *Water* 14 (1), 23. doi: 10.3390/w14010023

Gai, F. F., Hedemand, C. K., Louw, D. C., Grobler, K., Krock, B., Moestrup, Ø., et al. (2018). 'Morphological, molecular and toxigenic characteristics of Namibian Pseudo-nitzschia species – including Pseudo-nitzschia bucculenta sp. nov. *Harmful Algae* 76 (May), 80–95. doi: 10.1016/j.hal.2018.05.003

Giering, S. L. C., Cavan, E. L., Basedow, S. L., Briggs, N., Burd, A. B., Darroch, L. J., et al. (2020). Sinking organic particles in the ocean–flux estimates from *in situ* optical devices. *Front. Mar. Sci.* 6. doi: 10.3389/fmars.2019.00834

Gilerson, A., Zhou, J., Hlaing, S., Ioannou, I., Schalles, J., Gross, B., et al. (2007). Fluorescence component in the reflectance spectra from coastal waters. Dependence on water composition. *Optics Express* 15 (24), 15702–15721. doi: 10.1029/2002GL016185

Gordon, H. R. (1979). Diffuse reflectance of the ocean: the theory of its augmentation by chlorophyll a fluorescence at 685 nm. *Appl. Optics* 18 (8), 1161. doi: 10.1364/ao.18.001161

Hansen, A., Ohde, T., and Wasmund, N. (2014). Succession of micro- and nanoplankton groups in ageing upwelled waters off Namibia. *J. Mar. Syst.* 140 (PB), 130–137. doi: 10.1016/j.jmarsys.2014.05.003

Hirata, T., Hardman-Mountford, N. J., Brewin, R. J. W., Aiken, J., Barlow, R., Suzuki, K., et al. (2011). Synoptic relationships between surface Chlorophyll- a and diagnostic pigments specific to phytoplankton functional types. *Biogeosciences* 8, 311–327. doi: 10.5194/bg-8-311-2011

Hoagland, P., Anderson, D. M., Kaoru, Y., and White, A. W. (2002). The economic effects of harmful algal blooms in the United States : estimates, assessment issues, and information needs. *Estuaries* 25 (4), 819–837. doi: 10.1007/BF02804908

Hu, C., Muller-karger, F. E., Taylor, J. C., Carder, K. L., Kelble, C., Johns, E, et al. (2005). Red tide detection and tracing using MODIS fluorescence data : A regional example in SW Florida coastal waters. *Remote Sens. Environ.* 97, 311–321. doi: 10.1016/j.rse.2005.05.013

Hu, C., Lee, Z., and Franz, B. (2012). Chlorophyll a algorithms for oligotrophic oceans: A novel approach based on three-band reflectance difference. *J. Geophysical Research: Oceans* 117 (1), 1–25. doi: 10.1029/2011JC007395

Hutchings, L., van der Lingen, C. D., Shannon, L. J., Crawford, R. J. M., Verheye, H. M. S., Bartholomae, C. H., et al. (2009). The Benguela Current: An ecosystem of four components. *Prog. Oceanography* 83 (1–4), 15–32. doi: 10.1016/j.pocean.2009.07.046

Isada, T., Abe, H., Kasai, H., and Nakaoka, M.. (2021). Dynamics of nutrients and colored dissolved organic matter absorption in a wetland-influenced subarctic coastal region of Northeastern Japan: contributions from mariculture and eelgrass meadows. *Front. Mar. Sci.* 8 (711832), 1–19. doi: 10.3389/fmars.2021.711832

Kampf, J., and Chapman, P. (2016). "The benguela current upwelling system," in *Upwelling systems of the world.* (Switzerland: Springer), 251–314. doi: 10.1007/978-3-319-42524-5

Keller, M. D. (1989). Dimethyl sulfide production and marine phytoplankton: the importance of species composition and cell size. *Biol. Oceanography* 6, 375–382. doi: 10.1080/01965581.1988.10749540

Kheireddine, M., Ouhssain, M., Claustre, H., Uitz, J., Gentili, B., and Jones, B. H.. (2017). Assessing pigment-based phytoplankton community distributions in the Red Sea. *Front. Mar. Sci.* 4 (MAY). doi: 10.3389/fmars.2017.00132

Kramer, S. J., Siegel, D. A., and Graff, J. R. (2020). Phytoplankton community composition determined from co-variability among phytoplankton pigments from the NAAMES field campaign. *Front. Mar. Sci.* 7 (April). doi: 10.3389/fmars.2020.00215

Kritten, L., Preusker, R., and Fischer, J. (2020). A new retrieval of sun-induced chlorophyll fluorescence in water from ocean colour measurements applied on OLCI L-1b and L-2. *Remote Sens.* 12 (23), 1–24. doi: 10.3390/rs12233949

Kruk, C., Peeters, E. T. H. M., Nes Van Huszar, E. H. V. L. M., Costa, L. S., and Scheffer, M.. (2011). Phytoplankton community composition can be predicted best in terms of morphological groups. *Limnology Oceanography* 56 (1), 110–118. doi: 10.4319/lo.2011.56.1.0110

Kwak, I., and Park, Y. (2020). Food chains and food webs in aquatic ecosystems. *Appl. Sci.* 10 (5012), 1–5. doi: 10.3390/app10145012

Lachkar, Z., and Gruber, N. (2012). A comparative study of biological production in eastern boundary upwelling systems using an artificial neural network. *Biogeosciences* 9, 293–308. doi: 10.5194/bg-9-293-2012

Laiolo, L., Matear, R., Soja-wo, M., Suggett, D. J., Hughes, D. J., Baird, M. E., et al. (2021). Modelling the impact of phytoplankton cell size and abundance on inherent optical properties (IOPs) and a remotely sensed chlorophyll- a product. *J. Mar. Syst.* 213, 1–12. doi: 10.1016/j.jmarsys.2020.103460

Lamont, T., Barlow, R. G., and Brewin, R. J. W. (2019). Long - term trends in phytoplankton chlorophyll a and size structure in the benguela upwelling system. *J. Geophysical Research: Oceans* 51 (10), 1170–1195. doi: 10.1029/2018JC014334

Lamont, T., García-Reyes, M., Bograd, S. J., van der Lingen, C. D., and Sydeman, W. J. (2018). Upwelling indices for comparative ecosystem studies: Variability in the Benguela Upwelling System. *J. Mar. Syst.* 188, 3–16. doi: 10.1016/j.jmarsys.2017.05.007

Lass, H. U., and Mohrholz, V. (2008). On the interaction between the subtropical gyre and the Subtropical Cell on the shelf of the SE Atlantic. *J. Mar. Systems.* 74 (1–2), 1–43. doi: 10.1016/j.jmarsys.2007.09.008

Letelier, R. M., and Abbott, M. R. (1996). An analysis of chlorophyll fluorescence algorithms for the moderate resolution imaging spectrometer (MODIS). *Remote Sens. Environ.* 58 (2), 215–223. doi: 10.1016/S0034-4257(96)00073-9

Lett, C., Veitch, J., van der Lingen, C. D., and Hutchings, L. (2007). Assessment of an environmental barrier to transport of ichthyoplankton from the southern to the northern Benguela ecosystems. *Mar. Ecol. Prog. Ser.* 347, 247–259. doi: 10.3354/meps06982

Lizotte, M., Levasseur, M., Law, C. S., Walker, C. F., Safi, K. A., and Marriner, A. (2017). Dimethylsulfoniopropionate (DMSP) and dimethyl sulfide (DMS) cycling across contrasting biological hotspots of the New Zealand subtropical front. *Ocean Sci.* 13, 961–982. doi: 10.5194/os-13-961-2017

Louw, D. C., Doucette, G. J., and Voges, E. (2017). Annual patterns, distribution and long-term trends of Pseudo-nitzschia species in the northern Benguela upwelling system. *J. Plankton Res.* 39 (1), 35–47. doi: 10.1093/plankt/fbw079

Louw, D. C., Plas, A. K., Van Der Mohrholz, V., Wasmund, N., Junker, T., and Eggert, A.. (2016). Seasonal and interannual phytoplankton dynamics and forcing mechanisms in the Northern Benguela upwelling system. *J. Mar. Systems.* 157, 124–134. doi: 10.1016/j.jmarsys.2016.01.009

Mackey, M. D., Mackey, D. J., Higgins, H. W., and Wright, S. W. (1996). CHEMTAX - A program for estimating class abundances from chemical markers: Application to HPLC measurements of phytoplankton. *Mar. Ecol. Prog. Ser.* 144 (1–3), 265–283. doi: 10.3354/meps144265

Mao, Z., Stuart, V., Pan, D., Chen, J., Gong, F., Huang, H., et al. (2010). Effects of phytoplankton species composition on absorption spectra and modeled hyperspectral reflectance. *Ecol. Informatics.* 5 (5), 359–366. doi: 10.1016/j.ecoinf.2010.04.004

Matlakala, M. L. (2019). *Seasonal characteristics of phytoplankton bloom phenology in the northern Benguela Upwelling System.* (Cape Town, Rondebosch, South Africa: University of Cape Town).

Mayer, K. J., Wang, X., Santander, M. V, Mitts, B. A., Sauer, J. S., Sultana, C. M., et al. (2020). Secondary marine aerosol plays a dominant role over primary sea spray aerosol in cloud formation. *ACS Cent. Sci.* 6 (12), 2259–2266. doi: 10.1021/acscentsci.0c00793

Mcclelland, H. L. O., Barbarin, N., Beaufort, L., Hermoso, M., Ferretti, P., Greaves, M., et al. (2016). Calcification response of a key phytoplankton family to millennial-scale environmental change. *Nat. Sci. Rep. Nat. Publishing Group* 6, 1–11. doi: 10.1038/srep34263

Mohrholz, V., Eggert, A., Junker, T., Nausch, G., Ohde, T., and Schmidt, M.. (2014). Cross shelf hydrographic and hydrochemical conditions and their short term variability at the northern Benguela during a normal upwelling season. *J. Mar. Systems.* 140 (PB), 92–110. doi: 10.1016/j.jmarsys.2014.04.019

Morel, A., Claustre, H., and Gentili, B. (2010). The most oligotrophic subtropical zones of the global ocean: Similarities and differences in terms of chlorophyll and yellow substance. *Biogeosciences* 7 (10), 3139–3151. doi: 10.5194/bg-7-3139-2010

Moutier, W., Thomalla, S. J., Bernard, S., Wind, G., Ryan-keogh, T. J., and Smith, M. E. (2019). Evaluation of chlorophyll-a and POC MODIS aqua products in the southern ocean. *Remote Sens.* 11, 1–18. doi: 10.3390/rs11151793

Ohde, T., and Dadou, I. (2018). Seasonal and annual variability of coastal sulphur plumes in the northern Benguela upwelling system. *PloS One* 13 (2), 1–33. doi: 10.1371/journal.pone.0192140

O'Reilly, J. E., Maritorena, S., Mitchell, B. G., Siegel, D. A., Carder, K. L., Garver, S. A., et al. (1998). Ocean color chlorophyll algorithms for SeaWiFS. *J. Geophysical Res.* 103 (Cll), 24937–24953. doi: 10.1029/98JC02160

O'Reilly, J. (2000). "Ocean Color Chlorophyll-a Algorithm for SeaWiFS, OC2, and OC4: SeaWiFS Postlaunch Technical Report Series,"In: S. B. Hooker and R. Firestone Eds., Volume 11, *SeaWiFS Postlaunch Calibration and Validation Analyses Version 4, Part 3*, NASA Goddard Space Flight Center, Greenbelt, 9–23.

Otero, J., Álvarez-salgado, X. A., and Bode, A. (2020). Phytoplankton diversity effect on ecosystem functioning in a coastal upwelling system. *Front. Mar. Sci.* 7. doi: 10.3389/fmars.2020.592255

Paul, M., Velappan, M. N., Nanappan, U., Gopinath, V., Velloth, R. T., Rajendran, A., et al. (2021). Characterization of phytoplankton size-structure based productivity, pigment complexes (HPLC/CHEMTAX) and species composition in the Cochin estuary (southwest coast of India): special emphasis on diatoms. *Oceanologia.* 63 (4), 463–481. doi: 10.1016/j.oceano.2021.05.004

Pei, S., Laws, E. A., Zhang, H., Ye, S., Yuan, H., and Liu, H. (2017). Patchiness of phytoplankton and primary production in Liaodong Bay, China. *PloS One* 12 (2), 1–14. doi: 10.1371/journal.pone.0173067

Pollard, R. T., Salter, I., Sanders, R. J., Lucas, M. I., Moore, C. M., Mills, R. A., et al. (2009). Southern Ocean deep-water carbon export enhanced by natural iron fertilization. *Nature* 457, 14–18. doi: 10.1038/nature07716

Polonsky, A. B., and Serebrennikov, A. N. (2020). On the change in the sea surface temperature in the Benguela upwelling region: part II. Long-term tendencies. *Atmospheric Ocean Phys.* 56 (9), 970–978. doi: 10.1134/S0001433820090200

Riebesell, U., and Rost, B. (2004). "Coccolithophores and the biological pump: responses to environmental changes," in *Coccolithophores: from molecular processes to global impact.* Eds. J. R. Young and H. R. Thierstein (Berlin: Springer), 99–125.

Rouault, M., Illig, S., Lübbecke, J., and Koungue, R. A. I. (2018). Origin, development and demise of the 2010 – 2011 Benguela Niño. *J. Mar. Systems.* 188 (November 2016), 39–48. doi: 10.1016/j.jmarsys.2017.07.007

Schalles, J. F. (2006). "Optical remote sensing techniques to estimate phytoplankton chlorophyll a concentrations in coastal waters with varying suspended matter and cdom concentrations," in *Remote sensing of aquatic coastal ecosystem processes.* (Dordrecht: Springer), 27–79.

Scheinin, M., and Asmala, E. (2020). Ubiquitous patchiness in chlorophyll a concentration in coastal archipelago of Baltic Sea. *Front. Mar. Sci.* 7 (July). doi: 10.3389/fmars.2020.00563

Shikwambana, L., and Kganyago, M. (2022). Meteorological influence of mineral dust distribution over South-Western Africa deserts using reanalysis and satellite data. *Front. Environ. Sci.* 10 (June). doi: 10.3389/fenvs.2022.856438

Shillington, F., Reason, C. J., Duncombe rae, C., Florenchie, P., and Penven, P. (2006). Large scale physical variability of the benguela current large marine ecosystem (BCLME). *Large Mar. Ecosyst.* 14, 15–30. doi: 10.1016/S1570-0461(06)80009-1

Smetacek, V. (1999). Diatoms and the ocean carbon cycle. *Protist* 150 (1), 25–32. doi: 10.1016/S1434-4610(99)70006-4

Smith, M. E., and Bernard, S. (2020). Satellite ocean color based harmful algal bloom indicators for aquaculture decision support in the Southern Benguela. *Front. Mar. Sci.* 7 (61). doi: 10.3389/fmars.2020.00061

Smith, M. E., Robertson Lain, L., and Bernard, S. (2018). An optimized Chlorophyll a switching algorithm for MERIS and OLCI in phytoplankton-dominated waters. *Remote Sens. Environ.* 215 (January), 217–227. doi: 10.1016/j.rse.2018.06.002

Soja-Wozniak, M., Darecki, M., and Wojtasiewicz, B. (2018). Laboratory measurements of remote sensing reflectance of selected phytoplankton species from the Baltic Sea. *Oceanologia* 60, 86–96. doi: 10.1016/j.oceano.2017.08.001

Soja-Woźniak, M., Laiolo, L., Baird, M. E., Matear, R., Clementson, L., Schroeder, T., et al. (2020). Effect of phytoplankton community size structure on remote-sensing reflectance and chlorophyll a products. *J. Mar. Syst.* 211, 103400. doi: 10.1016/j.jmarsys.2020.103400

Spirig, R., Vogt, R., Larsen, J. A., Feigenwinter, C., Wicki, A., Franceschi, J., et al. (2017). Probing the fog life cycles in the Namib desert. *Bull. Am. Meteorological Soc.* 100 (12), 2491–2508. doi: 10.1175/BAMS-D-18-0142.1

Stefels, J. (2000). Physiological aspects of the production and conversion of DMSP in marine algae and higher plants. *J. Sea Res.* 43 (3–4), 183–197. doi: 10.1016/S1385-1101(00)00030-7

Stock, C. A., John, J. G., Rykaczewski, R. R., Asch, R. G., Cheung, W. W. L., Dunne, J. P., et al. (2017). Reconciling fisheries catch and ocean productivity. *PNAS* 1, 1441–1449. doi: 10.1073/pnas.1610238114

Thuillier, G., Herse, M., Labs, D., Foujols, T., Peetermans, W., Gillotay, D., et al. (2003). The solar spectral irradiance from 200 to 2400 nm as measured by the SOLSPEC spectrometer from the ATLAS and EURECA missions. *Solar Phys.* 214 (1), 1–22. doi: 10.1023/A:1024048429145

Tortell, P. D., Payne, C. D., Li, Y., Trimborn, S., Smith, W. O., Riesselman, C., et al. (2008). CO 2 sensitivity of Southern Ocean phytoplankton. *Geophysical Res. Lett.* 35, 1–5. doi: 10.1029/2007GL032583

Uitz, J., Claustre, H., Morel, A., and Hooker, S. B.. (2006). Vertical distribution of phytoplankton communities in open ocean : An assessment based on surface chlorophyll. *J. Geophysical Res.* 111 (1), 1–23. doi: 10.1029/2005JC003207

Utermöhl, H. (1958). Zur Vervollkommnung der quantitativen Phytoplankton-Methodik. *Mitt. der Internationalen Vereinigung für Theoretische und Angewandte Limnologie* 9 (1), 1–38. doi: 10.1080/05384680.1958.11904091

Vaillancourt, R. D., Brown, C. W., Guillard, R. R. L., and Balch, W. M. (2004). Light backscattering properties of marine phytoplankton : relationships to cell size, chemical composition and taxonomy. *J. Plankton Res.* 26 (2), 191–212. doi: 10.1093/plankt/fbh012

Vidussi, F., Clauster, H., Manca, B. B., Luchetta, A., and Marty, J.-C. (2001). Phytoplankton pigment distribution in relation to upper thermocline circulation in the eastern Mediterranean Sea during winter. *J. Geophysical Res.* 106, 939–956. doi: 10.1029/1999JC000308

Wasmund, N. (2011a). *Chlorophyll pigments from the Namibian upwelling system during Discovery 356, Leibniz Institute for Baltic Sea Research*. doi: 10.1594/PANGAEA.773204

Wasmund, N. (2011b). *Phytoplankton biomass from the Namibian upwelling system during Discovery 356, Leibniz Institute for Baltic Sea Research* (Warnemünde: PANGAEA). doi: 10.1594/PANGAEA.773205

Wasmund, N. (2012). *Phytoplankton measurements from the Namibian upwelling system during the Maria S. Merian cruise MSM 17/3, Leibniz Institute for Baltic Sea Research* (Warnemünde: PANGAEA). doi: 10.1594/PANGAEA.779150

Wasmund, N. (2015a). *Chlorophyll pigments from the Namibian upwelling system during Maria S. Merain cruise MSM17/3* (PANGAEA). doi: 10.1594/PANGAEA.843325

Wasmund, N. (2015b). *Chlorophyll pigments from the Namibian upwelling system during Maria S. Merain cruise MSM18/4* (PANGAEA). doi: 10.1594/PANGAEA.843328

Wasmund, N. (2015c). *Phytoplankton biomass from the Namibian upwelling system during Maria S. Merain cruise MSM18/4* (PANGAEA). doi: 10.1594/PANGAEA.843339

Wasmund, N., Nausch, G., and Hansen, A. (2014). Phytoplankton succession in an isolated upwelled Benguela water body in relation to different initial nutrient conditions. *J. Mar. Systems.* 140 (1), 163–174. doi: 10.1016/j.jmarsys.2014.03.006

Welschmeyer, N. (1994). Fluorometric analysis of chlorophyll a in the presence of chlorophyll b and pheopigments. *Limnology Oceanography* 39 (8), 1985–1992. doi: 10.4319/lo.1994.39.8.1985

Williams, O. J., Beckett, R. E., and Maxwell, D. L. (2016). Marine phytoplankton preservation with Lugol's: a comparison of solutions. *J. Appl. Phycology. J. Appl. Phycology* 28 (3), 1705–1712. doi: 10.1007/s10811-015-0704-4

frontiers | Frontiers in Marine Science

TYPE Original Research
PUBLISHED 20 October 2023
DOI 10.3389/fmars.2023.1249802

Check for updates

OPEN ACCESS

EDITED BY
Gemma Kulk,
Plymouth Marine Laboratory,
United Kingdom

REVIEWED BY
Tomonori Isada,
Hokkaido University, Japan
John Marra,
Brooklyn College (CUNY), United States

*CORRESPONDENCE
Wen Zhou
wenzhou@scsio.ac.cn
Jie Xu
xujiest@um.edu.mo

RECEIVED 29 June 2023
ACCEPTED 04 October 2023
PUBLISHED 20 October 2023

CITATION
Zhao H, Cao W, Deng L, Liao J, Zeng K, Zheng W, Zhang Y, Xu J and Zhou W (2023) Estimation of primary production from the light absorption of phytoplankton and photosynthetically active radiation in the South China Sea.
Front. Mar. Sci. 10:1249802.
doi: 10.3389/fmars.2023.1249802

COPYRIGHT
© 2023 Zhao, Cao, Deng, Liao, Zeng, Zheng, Zhang, Xu and Zhou. This is an open-access article distributed under the terms of the Creative Commons Attribution License (CC BY). The use, distribution or reproduction in other forums is permitted, provided the original author(s) and the copyright owner(s) are credited and that the original publication in this journal is cited, in accordance with accepted academic practice. No use, distribution or reproduction is permitted which does not comply with these terms.

Estimation of primary production from the light absorption of phytoplankton and photosynthetically active radiation in the South China Sea

Hongwuyi Zhao[1,2], Wenxi Cao[1], Lin Deng[3], Jianzu Liao[4], Kai Zeng[5], Wendi Zheng[1], Yuanfang Zhang[1,2], Jie Xu[6]* and Wen Zhou[1]*

[1]State Key Laboratory of Tropical Oceanography (LTO), South China Sea Institute of Oceanology, Chinese Academy of Sciences, Guangzhou, China, [2]College of Oceanography, University of Chinese Academy of Sciences, Beijing, China, [3]School of Marine Sciences, Sun Yat-sen University, Zhuhai, China, [4]Faculty of Chemistry and Environmental Science, Guangdong Ocean University, Zhanjiang, China, [5]Department of Ocean Science and Engineering, Southern University of Science and Technology, Shenzhen, China, [6]Department of Ocean Science and Technology, University of Macau, Macao, Macao SAR, China

A model was constructed to estimate Primary production (PP) and examine the effect of the dominant phytoplankton group on PP, using a dataset collected in 2019 in the South China Sea (SCS) based on phytoplankton absorption coefficient at 443nm [a_{ph}(443)] and photosynthetically active radiation (PAR). There was a significant log-log linear correlation between PP and the product of a_{ph}(443) and PAR (a_{ph}(443)×PAR), with an adjusted R^2 of 0.64. The model was validated using K-fold cross-validation and an *in situ* dataset collected in 2018 in the SCS basin. The results showed that the model had good generalisability and was suitable across marine environments, including basin, coastal, and offshore areas. The model was more sensitive to changes in PAR than changes in a_{ph}(443). Phytoplankton in the diatom-dominant and haptophyte-dominant clusters were in the light-limited stage, and their PP values increased with increasing a_{ph}(443)×PAR. However, *Prochlorococcus*-dominant samples exhibited photoinhibition, and the PP values decreased with increasing a_{ph}(443)×PAR, likely due to their bio-optical characteristics. The model's predictive power was related to the photo-physiological state of dominant phytoplankton, which performs well in light-limited conditions but not in cases of massive photoinhibition. This study provides insight into the development of phytoplankton-specific a_{ph}-based PP models.

KEYWORDS

primary production, phytoplankton absorption coefficient, photosynthetically active radiation, phytoplankton pigments, marine optics

1 Introduction

Marine primary production (PP) refers to the process of assimilation and fixation of inorganic carbon and other inorganic nutrients into organic matter by marine phytoplankton. This process constitutes a major carbon pump and fuels the marine food chain, making it a critical component of ocean biogeochemical cycles that impact climate change (Falkowski et al., 1998). As the annual productivity of the entire ocean is approximately half of the global total (Hemsley et al., 2015), ocean PP remains an essential ecological process deserving of continued research.

The *in vivo* technique with ^{14}C proposed by Steemann Nielsen is the conventional ship-based method used to measure PP (Nielsen, 1952). In recent decades, satellite-based sensors have made remote sampling of the ocean surface possible at large spatial and temporal scales, providing a cost-effective way to study PP at satellite-visible depths (Platt and Sathyendranath, 1988; Hilker et al., 2008). When combined with *in situ* observations, it may be possible to obtain the PP of the entire euphotic zone. Consequently, various models of PP have been or are being proposed (Kahru, 2017) based on products that can be obtained from water-leaving radiance in both open ocean (Campbell et al., 2002) and coastal waters (Saba et al., 2010; Setiawan and Habibi, 2011; Setiawan and Kawamura, 2011). Chlorophyll *a* (Chl *a*), a well-established ocean colour product, is the main pigment at the photochemical reaction centre in most phytoplankton and is often considered an index of phytoplankton biomass (Boyce et al., 2010). Since primary productivity may be simply defined as the product of phytoplankton biomass times the phytoplankton growth rate (Cloern et al., 2014), Chl *a* is frequently involved in modeling primary productivity of the marine surface layer, euphotic layer, or mixed layer (Eppley et al., 1985; Platt and Sathyendranath, 1993; Antoine and Morel, 1996; Ondrusek et al., 2001; Campbell et al., 2002; Platt et al., 2008; Westberry et al., 2008).

PP can also be defined by a combination of the phytoplankton absorption coefficient (a_{ph}) and photosynthetically active radiation (PAR) (Kiefer and Mitchell, 1983; Barnes et al., 2014), both of which are well-established ocean colour products, and a_{ph} can perform better than Chl *a* in estimations of PP (Oliver et al., 2004; Claustre et al., 2005; Hirawake et al., 2011). Credible global gridded $a_{ph}(\lambda)$ data can be retrieved from R_{rs} using semianalytical algorithms (Moore et al., 2009; Sauer et al., 2012; Werdell et al., 2013) such as the generalized inherent optical properties (GIOP) algorithm (Werdell et al., 2013) and quasi-analytical algorithm (QAA) (Lee et al., 2002). As a result, a_{ph} has been considered an alternative bio-optical proxy for estimating PP in both coastal and open ocean waters (Lee et al., 1996; Huot et al., 2007; Marra et al., 2007; Barnes et al., 2014; Silsbe et al., 2016). Different phytoplankton communities have varying bio-optical characteristics and can display different responses to various environmental variables, including light, temperature, nutrients, etc. (Uitz et al., 2010; Barnes et al., 2014; Brewin et al., 2017; Curran et al., 2018). Compared to Chl *a*, $a_{ph}(\lambda)$ contains more information, such as phytoplankton pigment concentration and composition, phytoplankton community, and cell size (Morel and Maritorena, 2001; Ciotti et al., 2002; Bricaud et al., 2004; Uitz et al., 2015). The combined response of the various environmental variables is also reflected in $a_{ph}(\lambda)$ (Marra et al., 2007; Aiken et al., 2008; Brewin et al., 2019). These characteristics extend the application scope of a_{ph}-based models, which have been successfully applied to estimate not only total PP (Lee et al., 1996; Marra et al., 2007; Barnes et al., 2014; Robinson et al., 2017) but also size-fractionated PP (Hirata et al., 2009; Barnes et al., 2014; Brewin et al., 2017; Curran et al., 2018) in different marine environments, including the North Atlantic Ocean (euphotic layer) (Lee et al., 1996), Arabian Sea, Ross Sea, Equatorial Pacific (surface layer) (Marra et al., 2007), English Channel, North Sea (surface layer) (Barnes et al., 2014), Australian Coastal Waters (surface layer) (Robinson et al., 2017), and eastern boundary upwelling systems (Hirata et al., 2009), using *in situ* and remote sensing datasets. However, classifying phytoplankton by size does not provide information on taxonomic structure, and variation in phytoplankton taxonomic structure can affect PP (Jochem et al., 1995; Kameda and Ishizaka, 2005).

One of the primary objectives of this study is to investigate the utility of a_{ph} as a predictor of PP within the euphotic zone of the South China Sea (SCS). A regional a_{ph}-based PP model was built based on an *in situ* dataset collected during 2019 in the SCS. To evaluate the generalization performance of this model, we employed K-fold cross-validation and validated it with an independent *in situ* dataset collected during 2018 in the SCS (Liao et al., 2021). Furthermore, the impact of uncertainties in the two inputs, $a_{ph}(\lambda)$ and PAR, on the relationship was also analyzed. In addition, our study seeks to partition the dataset into clusters dominated by different phytoplankton types derived from pigment composition. This allows us to explore the effect of each cluster on our a_{ph}-based PP model. The model could be applied to autonomous optical sensors and remotely sensed data in coastal, estuarine, offshore, and basin environments of the SCS. This study provides valuable insight into the development of phytoplankton-specific a_{ph}-based PP models.

2 Materials and methods

2.1 Sampling site

Field observations in the western SCS were conducted at 12 stations during two cruises, from 11 June to 15 June and from 29 September to 5 October 2019 (denoted as the 2019 SCS dataset). The sampling stations are depicted in Figure 1, which includes a total of 12 stations denoted by blue dots and covers both coastal (contains estuarine (S1-S7, ≤100 m) and offshore (S8-S12, >100 m) waters. A comprehensive set of variables pertinent to productivity, including PP, $a_{ph}(\lambda)$, PAR, phytoplankton pigments, temperature, and depth, were measured at each station. In addition, we obtained an open dataset collected by Liao et al. at 8 stations in the SCS basin during September 2018 (Liao et al., 2021), denoted as the 2018 SCS dataset (L1-L8, >1500 m), Which is illustrated by orange dots in Figure 1.

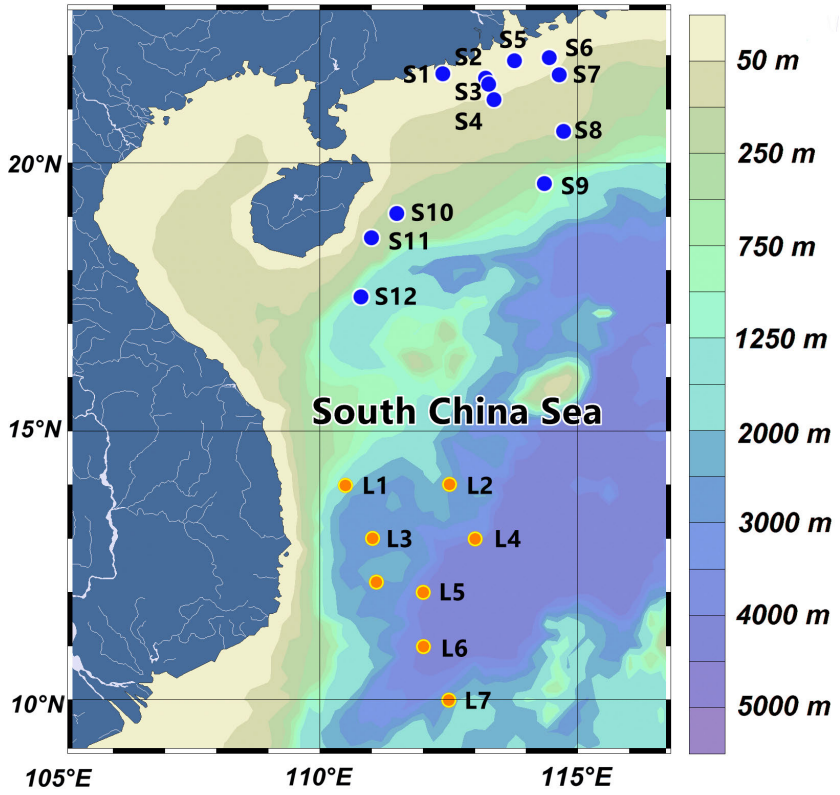


FIGURE 1
Locations of the 2019 SCS dataset (blue dots) and the 2018 SCS dataset (orange dots).

2.2 *In situ* sampling

2.2.1 Primary productivity

PP was determined through on-deck incubation at five light penetration depths (100%, 56%, 22%, 7%, and 1% of the surface PAR) at each station (49 samples in the 2019 SCS dataset and 28 samples in the 2018 SCS dataset) (Liao et al., 2021). Seawater samples were obtained using Niskin bottles connected to a conductivity-temperature-depth (CTD) device (Seabird SBE 911) and were obtained in the morning, prefiltered through a 180-μm mesh to eliminate large zooplankton. These samples were then transferred to acid-clean polycarbonate bottles (Nalgene, USA), with two white bottles and one black bottle collected for each layer. After inoculation with 5-μCi of $NaH^{14}CO_3$, samples were incubated in duplicate at five light levels and in the dark at *in situ* temperature (± 2°C) with a water cooler for 6 h. After incubation, the samples were filtered onto 25-mm GF/F filters (Whatman, USA), and all filters were stored at −20°C until analysis. The filters were fumed with HCl for 12 h to eliminate nonfixed ^{14}C and then immersed in a 5-mL scintillation cocktail (Ultima Gold) in 20-mL scintillation vials. Radioactivity was measured using a Tri-Carb 2810 TR liquid scintillation analyzer (Perkin-Elmer, USA) (Knap et al., 1996). Water samples for dissolved inorganic carbon (DIC) were preserved with $HgCl_2$ in amber glass bottles and analyzed using an AS-C3 DIC analyzer (Apollo SciTech, USA) with an infrared CO_2 detector (Li-7000) following the procedure outlined by Cai et al. (Cai et al., 2004). PP was then calculated using Equation 1, where CPM_L and CPM_D represent the counts per minute for the white and black vial samples, respectively, CPM_{add} is the counts per minute for ^{14}C addition, and T is the incubation time in hours. To harmonize the units of each variable, PP was converted from mg C $m^{-3}h^{-1}$ to mol C $m^{-3}h^{-1}$.

$$PP = DIC \times (CPM_L - CPM_D)/CPM_{add}/T \quad (1)$$

2.2.2 Phytoplankton absorption coefficient

To obtain $a_{ph}(\lambda)$, samples were filtered onto GF/F filters (Whatman, USA), placed in cell dishes, and stored in liquid nitrogen until the laboratory analysis took place. The absorption spectra of the particles $[a_p(\lambda)]$ were measured using the quantitative filter-pad technique by the Transmittance mode (i.e., T mode) with a Lambda 650S ultraviolet–visible spectrophotometer at a 1-nm resolution ranging from 350 to 750 nm (Yentsch, 1962). Before the measurement, a clean GF/F filter was soaked in a 0.2-μm seawater filtrate to obtain a blank. After removing the phytoplankton pigments with methanol, the filters were rescanned to obtain the absorption spectra of nonalgal particles $[a_d(\lambda)]$ (Kishino et al., 1985). The background signal was corrected by subtracting the absorption values at 750 nm from the entire spectrum (Bricaud and Stramski, 1990), and the optical path amplification effect was corrected according to the method of Stramski et al. (Stramski et al., 2015). The obtained difference between $a_p(\lambda)$ and $a_d(\lambda)$ was taken to be $a_{ph}(\lambda)$.

2.2.3 Phytoplankton pigments

The quantification of pigments was accomplished using high-performance liquid chromatography (HPLC), as outlined by Zapata et al. (Manuel et al., 2000). Following filtration onto Whatman GF/F filters and subsequent storage in liquid nitrogen, samples were subjected to an extraction procedure involving 1.5 ml 95% methanol solution at 4°C for 24 hours. A mixture of 1 ml of extract and 200 µl ultrapure water was then prepared for measurement. A Waters 2695 HPLC system was employed, with signals being detected by a Waters 2998 photodiode array detector. As per the methodology of Zapata et al. (Manuel et al., 2000), pigments containing Chlorophyll *a*, Chlorophyll *b*, Chlorophyll $c_{1,2,3}$, Divinyl chlorophyll *a* (DVChl *a*), Divinyl chlorophyll *b*, Peridinin, Fucoxanthin, Lutein, Diadinoxanthin, Diatoxanthin, Antheraxanthin, Violaxanthin, Zeaxanthin, Alloxanthin, 19′-hex-fucoxanthin, 19′-but-fucoxanthin, Neoxanthin, and β-carotene were analyzed. Quantification was confirmed by the standards manufactured by the Danish Hydraulic Institute (DHI) Water and Environment, Hørsholm, Denmark. The dominant phytoplankton within each sample was determined through the characteristic pigment approach (Alvain et al., 2005). To facilitate the analysis of the HPLC pigments in this study, a grouping system was employed, wherein the pigments were categorized into Chlorophyll, photosynthetic carotenoids (PSCs), and photoprotective carotenoids (PPCs) (Frank and Cogdell, 1996; Dall'Osto et al., 2007; Roy et al., 2011). Specifically, PPCs were calculated as the sum of Violaxanthin, Diadinoxanthin, Alloxanthin, Zeaxanthin, Lutein, and β-carotene, whereas PSCs were calculated as the sum of Peridinin, 19′-but-fucoxanthin, 19′-hex-fucoxanthin and Fucoxanthin.

2.2.4 PAR and temperature

A Profiler II underwater spectral profiling instrument (Satlantic, Canada) was used to record the downwelling irradiance [$E_d(\lambda,z)$] of the water column profile during free-fall, employing a range of wavelengths between 350-800 nm and consisting of 136 channels. The original raw data was calibrated using ProSoft 7.7.1.6 (Satlantic, Canada), while PAR was determined by integrating the $E_d(\lambda,z)$ within the 400-700 nm wavelength range. Sampling takes place during clear and cloudless conditions between 12:00 and 13:00 every day, in sync with the PP incubation experiment. In Southeast Asia, between 12:00 and 18:00, PAR shows an almost linear decreasing trend (Rundel et al., 2017; Vongcharoen et al., 2018). Simultaneously, the tropical climate characteristics of the South China Sea and the duration of the voyage (5 and 7 days) imply that during these days, the daily sunlight pattern remains relatively consistent, and the daily PAR changes are relatively stable. Thus, we simply made this assumption, PAR was multiplied by 3600 to convert its unit from umol $m^{-2}s^{-1}$ to mol $m^{-2}h^{-1}$. Here, the calculated hourly PAR only characterizes the relative trend of PAR changes, not the actual value of the hourly PAR. Temperature profiles were established via a CTD device (Seabird SBE 911).

2.3 Basic model

The basic model of the $a_{ph}(\lambda)$-based marine PP algorithm can be simply expressed as Equation 2 (Barnes et al., 2014):

$$\mathrm{PP} = \phi \times a_{ph}(\lambda_0) \times \mathrm{PAR} \tag{2}$$

$a_{ph}(\lambda_0)$ represents the phytoplankton absorption coefficient at a particular wavelength (443 nm being the selected wavelength for this study). PAR is photosynthetic active radiation. The quantum yield, represented by ϕ is given by the slope, which denotes the efficiency of photosynthesis in converting absorbed light energy into organic carbon. Under varying physicochemical conditions or in distinct marine areas, ϕ may exhibit fluctuations concerning light intensity, temperature, phytoplankton community structure, and nutrients (Iluz and Dubinsky, 2013; Zoffoli et al., 2018). If Equation 2 proves to be applicable to the 2019 SCS dataset, the regionalization of ϕ in the SCS can be established.

2.4 Statistics

The statistical analyses were conducted using OriginPro (OriginLab Corporation, USA) and Python 3.8.1. A probability coefficient was employed to assess the statistical significance of the correlation between two variables, with a p-value threshold of 0.05. The regression model was evaluated using several statistical metrics, including the adjusted coefficient of determination (Adj.R^2) (a penalty can be given for adding nonsignificant variables, i.e., adding an arbitrary variable does not necessarily increase the model fit, and Adj.R^2 can be positive or negative), the mean square difference (MSD), root mean square difference (RMSD), and the mean absolute difference (MAD). The standard deviation (σ) was used to measure the dispersion of the data, while bias quantified the difference between the observed and predicted values. All non-integer values, except for the p-value were reported to two significant digits. The mathematical expressions for these statistical metrics are provided below:

$$RMSD = \sqrt{\frac{\sum_{i=1}^{n}(Y_i - y_i)^2}{n}} \tag{3}$$

$$MSD = \frac{\sum_{i=1}^{n}(Y_i - y_i)^2}{n} \tag{4}$$

$$MAD = \frac{\sum_{i=1}^{n}|y_i - m(y)|}{n} \tag{5}$$

$$\sigma = \sqrt{\frac{\sum_{i=1}^{n}(y_i - m(y))^2}{n}} \tag{6}$$

$$\mathrm{Bias} = y_i - Y_i \tag{7}$$

where n is the number of data values, Y_i is the predicted value, y_i is the data value in the set, and $m(y)$ is the average value of the dataset.

2.5 K-fold cross-validation and *in situ* data validation

K-fold cross-validation was employed to test the generalisability of the model (Geisser, 1975), given that the total number of data

points did not exceed 50. This technique is widely utilized to evaluate the overall performance of models (Russell, 2010). Specifically, the dataset was divided into K nearly equal partitions, where K-1 partitions were employed to construct the model, and the remaining sample was used for validation. This process was iterated K times, resulting in K learners, with each fold serving as the validation data (Fushiki, 2011).

The choice of K is an important consideration, as underfitting or overfitting of learners can occur with small or large K values, respectively, which can adversely impact the assessment of general model performance. Although typical K values range between 5 and 10, researchers have suggested other values as well (Jung, 2018). In this study, K values were not arbitrarily chosen, rather, the mean MSD of K learners and the standard deviation of the mean MSD were evaluated over a range of K values, from 2 to 49. With increasing K, the standard deviation of the mean MSD increased, and when K was either less than 10 or greater than 20, the mean MSD exhibited pronounced fluctuations (Figure 2). Therefore, K was set to 10, which resulted in a small standard deviation of the mean MSD and a stable mean MSD across K learners. Accordingly, a 10-fold cross-validation approach was employed in section 3.2.

In addition, the 2018 SCS dataset was used to validate the adaptability of the model in the SCS basin waters.

2.6 Sensitivity analysis

The sensitivity of the model was tested using the Monte Carlo method, a widely adopted statistical technique in simulation studies (Brewin et al., 2017). In essence, a normal distribution was generated through Monte Carlo simulation, with either $a_{ph}(443)$ or PAR serving as the mean value at any given station. To reflect measurement error, we introduced errors of 5% for $a_{ph}(443)$ and 10% and 20% for PAR, based on empirical measurement estimations. Subsequently, the Monte Carlo method was employed to generate numbers, which were then fed into the model to obtain a new set of data. This new set of data was then verified as normally distributed, and the standard deviation was calculated as the index of uncertainty. In alignment with the methodology of Brewin et al., the minimum number of iterations required to produce a stable estimate of standard deviation was determined to be 200 (Brewin et al., 2017).

3 Results

3.1 Model building

Upon applying Equation 2 to the 2019 SCS dataset, PP was significantly correlated with $a_{ph}(443)\times$PAR (Adj.R^2=0.55, p-value <0.01), Nevertheless, a direct linear regression between $a_{ph}(443)\times$PAR and PP suffered from heteroscedasticity. In the 2019 SCS dataset, ϕ was not assumed to be a constant value and thus was neither parameterized nor treated as an independent variable. Instead, it was included in the slope (k) of Equation 8.

To raise the accuracy of a predictive model, a logarithmic transformation of PP and $a_{ph}(443)\times$PAR was conducted. Subsequently, a log-log linear $a_{ph}(\lambda)$-based regression model for PP (hereafter referred to as the 'log-log linear PP model') was built (Equation 8):

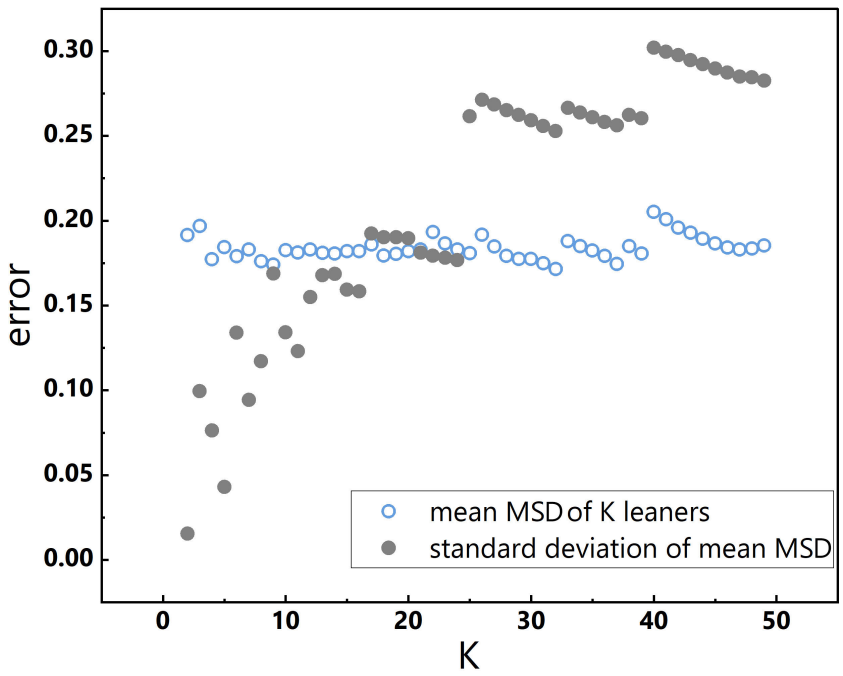


FIGURE 2
Changes in K and corresponding changes in the mean MSD of K learners and the standard deviation of the mean MSD.

$$\log(PP) = k \times \log(a_{ph}(443) \times PAR) + b \quad (8)$$

Figure 3 presents the values of k (slope) and b (intercept) for the log-log linear PP model, which demonstrates a greater aptitude for fitting the data, as indicated by a higher Adj.R^2. Moreover, the residual plot depicted in Figure 3 confirms homoscedasticity as a defining feature of the model.

3.2 K-fold cross-validation and *in situ* data validation in the log-log linear PP model

At K=10, the standard deviation of the mean MSDs is low (0.13), and the mean MSD derived from cross-validation (0.18) approximates that of the 'log-log linear PP model' (0.17). Furthermore, the Adj.R^2 (0.56) of the relationship between the measured and predicted values derived from cross-validation is quite similar to that of the log-log linear PP model (0.64). Collectively, the results of K-fold cross-validation affirm the commendable generalisation performance of the log-log linear PP model.

An Independent dataset of the SCS in 2018 (2018 SCS dataset, including the *in situ* $a_{ph}(443)$, PAR, and PP) was used to verify our model. The logarithmic bias between the predicted and measured PP was approximately 0.077, leading to a deviation of nearly 10% in PP estimates (Figure 4). These results corroborated the model's robustness and effectiveness for data collected in estuarine, coastal, and offshore areas (2019 SCS dataset) and data collected within the SCS basin (2018 SCS dataset).

3.3 Sensitivity analysis of the log-log linear PP model

The inclusion of a 5% standard deviation of $a_{ph}(443)$ caused a 2.9% standard deviation in the predicted PP (Figure 5). Moreover, the incorporation of 10% and 20% standard deviations of PAR resulted in 5.1% and 11% standard deviations in the predicted PP, respectively. This analysis reveals that the log-log linear PP model is more sensitive to alterations in PAR than to changes in $a_{ph}(443)$.

3.4 Identification of dominant phytoplankton clusters

Phytoplankton groups responded differently to environmental variables, such as temperature, light, and nutrient availability, due to their diverse physiological characteristics. Phytoplankton species vary with depths (e.g., sea surface and maximum chlorophyll depth) and marine environments. Therefore, the dominant phytoplankton species were identified to examine their impact on the log-log linear PP model.

Based on the characteristic pigment approach as defined by Alvain et al. (2005), five major phytoplankton species were identified, namely diatoms (Diato), dinoflagellates (Dino), *Prochlorococcus* (Pro), haptophytes (Hapto), and *Synechococcus*-like cyanobacteria (SLC) (Figure 6). However, the SLC-dominant and Dino-dominant clusters, consisting of limited sample sizes (only two and five samples, respectively), are not discussed in this study.

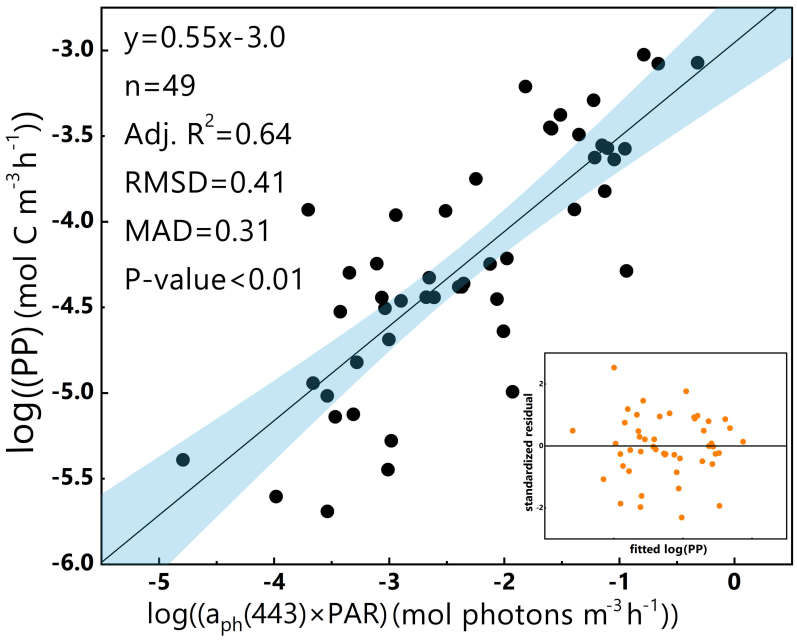


FIGURE 3
Log-log linear regression of PP and $a_{ph}(443)$×PAR in the euphotic zone for the 2019 SCS dataset. The dark line represents the linear regression, and the blue band represents the 95% confidence interval. The residual plot is in the bottom-right corner. The equation, number of data points (n) and some statistical parameters are shown in the upper-left corner.

10.3389/fmars.2023.1249802

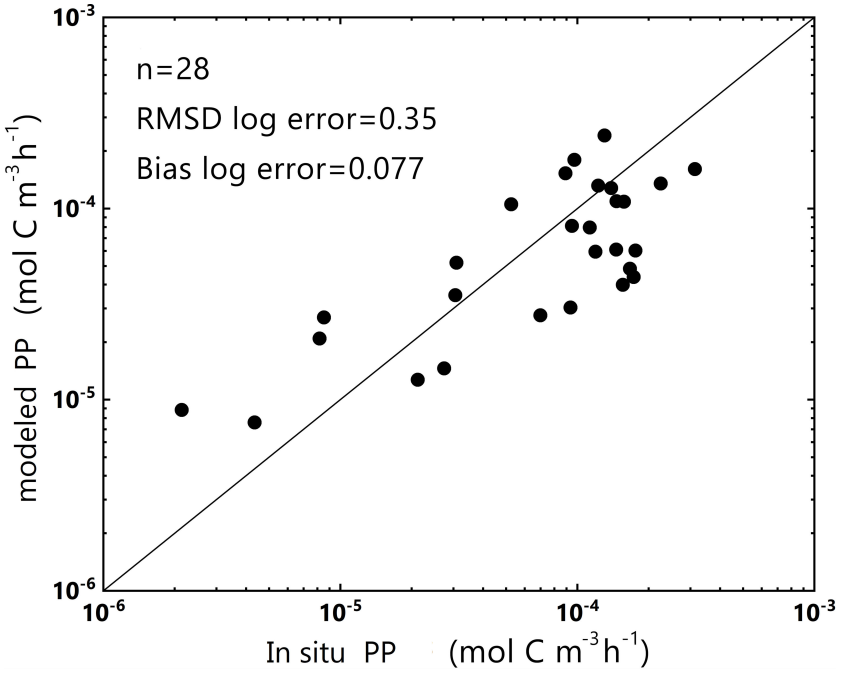


FIGURE 4
Plot of PP obtained from the log-log linear PP model and *in situ* PP from the 2018 SCS dataset (in log-scale). y = x is represented by the dark line. The number of data points (n) and some statistical parameters are shown in the upper-left corner.

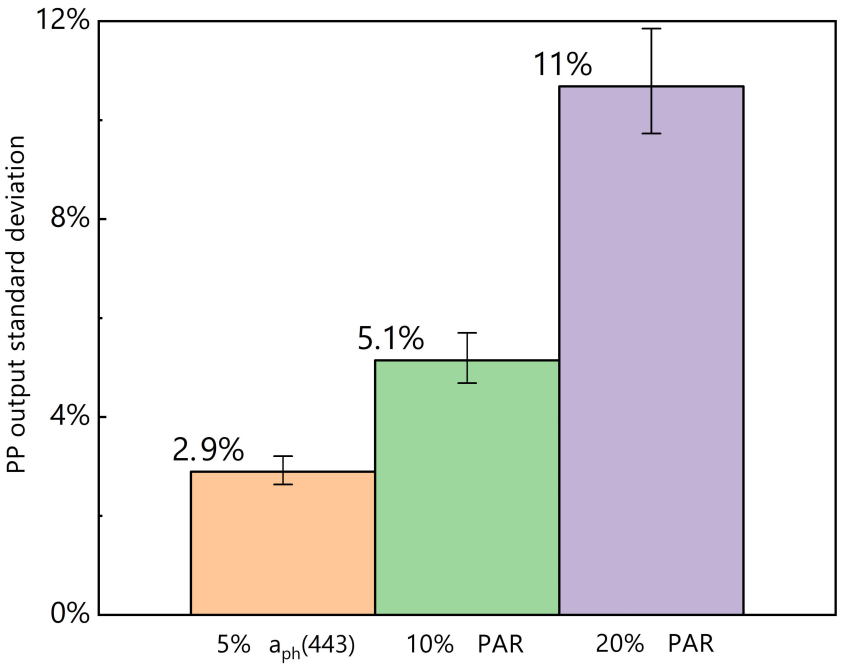


FIGURE 5
Results of the sensitivity analysis; orange = input of 5% $a_{ph}(443)$ standard deviation, green = input of 10% PAR standard deviation, and purple = input of 20% PAR standard deviation.

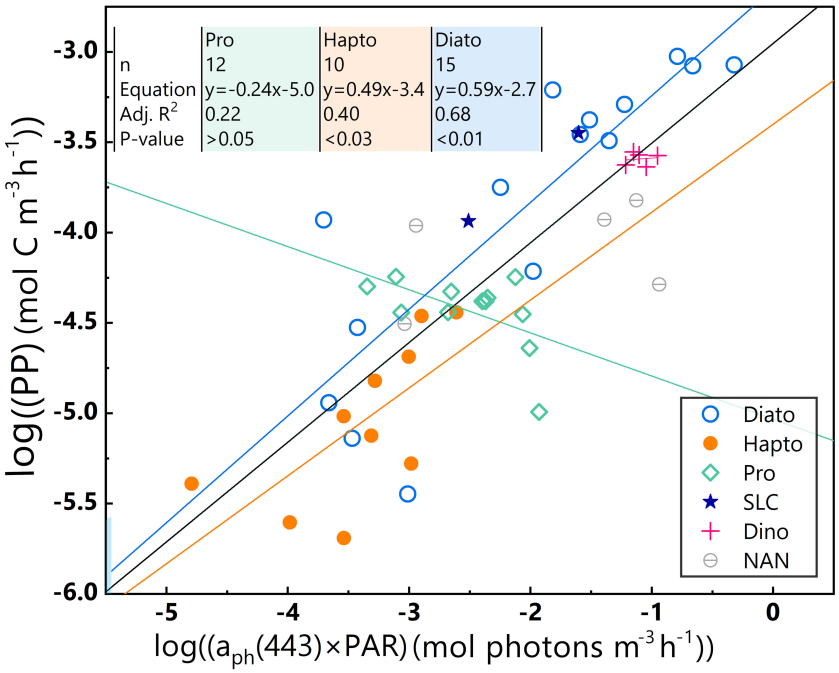


FIGURE 6
Different dominant phytoplankton samples are represented by various colours and shapes. Log-log linear regressions of PP and a_{ph}(443)×PAR of the whole dataset and three phytoplankton-dominant clusters in the euphotic zone for the 2019 SCS dataset; black line = whole dataset, blue line = Diato-dominant cluster, orange line = Hapto-dominant cluster, green line = Pro-dominant cluster. Equations, numbers of data points (n), and some statistical parameters of Pro-, Hapto- and Diato-dominant clusters are shown in the upper-left corner.

4 Discussion

4.1 Bio-optical characteristics of different dominant phytoplankton clusters

Table 1 lists statistical results for the varied bio-optical parameters of Diato-, Hapto-, and Pro-dominant phytoplankton clusters, which exhibit differences in their response to environmental variables and physiological characteristics.

The Diato-dominant cluster has the largest average a_{ph}(443), average PAR, and average PP values, as well as the largest range of variable variations. In contrast, the Pro-dominant cluster has a smaller average PAR value than the Diato-dominant cluster, but the smallest mean a_{ph}(443) value and a limited range of variation, especially for PP. The Hapto-dominant cluster presents the lowest average values for PAR and PP, with a mid-range variability. These distinct bio-optical characteristics of the dominant phytoplankton clusters are reflected in their different distribution patterns as seen in Figure 6, which in turn impacts the statistical properties of the log-log linear PP model. To delve deeper into these effects, a linear regression was performed for each cluster in Figure 6.

To identify the photophysiological state of the dominant phytoplankton, we examined their pigment composition. Pigments play a crucial role in phytoplankton photosynthesis. Roy et al. illustrated that phytoplankton can modify their pigment pool which comprises two functional classes: photosynthetic carotenoids (PSCs) and photoprotective carotenoids (PPCs), in response to variable light intensities (Roy et al., 2011). PPCs primarily dissipate excess light energy in the form of heat and to protect photosynthetic organs, while PSCs mainly transmit light energy. According to previous studies (Frank and Cogdell, 1996; Dall'Osto et al., 2007; Roy et al., 2011), the pigments in this study were categorized into Chlorophyll, PPC and PSC and subsequently normalized to TChl *a* (Table 1).

4.2 Pro-dominant cluster

Figure 6 displays a negative fitting slope for the Pro-dominant cluster, which contrasts with the fitting slope of the whole dataset. To understand this phenomenon, we examined the relationships of a_{ph}(443) with PP (in order to estimate the impact of biomass on PP) and PAR with PP/TChl *a* (in order to estimate the impact of PAR on PP. Additionally, to eliminate the impact of biomass on PP, PP was normalized to TChl *a*) (Figure 7).

a_{ph}(443) does not exhibit a significant relationship with PP (p-value > 0.05) in Figure 7A. However, the ratio of PP/TChl *a* decreases with an increase in PAR (Figure 7B), which is comparable to the relationship between a_{ph}(443)×PAR and PP (Figure 7C).

The Pro-dominant cluster has a significantly higher PPC/TChl *a* and a much lower PSC/TChl *a* than the other two clusters (Table 1), Since most of the samples within the Pro-dominant cluster results from the surface and in the upper layer (shallower than the maximum chlorophyll *a* layer), the negative correlation between PAR and PP/TChl *a* in the Pro-dominant cluster may be attributed to the photoinhibition of phytoplankton.

10.3389/fmars.2023.1249802

TABLE 1 Statistical results for the bio-optical parameters of each dominant phytoplankton cluster.

	Diato-dominant cluster	Hapto-dominant cluster	Pro-dominant cluster
Average PAR (mol m^{-2} h^{-1})	0.86	0.035	0.79
Range of PAR (mol m^{-2} h^{-1})	[0.0062, 3.8]	[0.0019, 0.096]	[0.080, 1.9]
Average a_{ph} (443) (m^{-1})	0.052	0.019	0.0061
Range of a_{ph} (443) (m^{-1})	[0.011, 0.13]	[0.0084, 0.026]	[0.0041, 0.0097]
Average PP (mol C m^{-3} h^{-1})	3.5×10^{-4}	1.4×10^{-5}	4.0×10^{-5}
Range of PP (mol C m^{-3} h^{-1})	[3.6×10^{-6}, 9.4×10^{-4}]	[2.0×10^{-6}, 3.6×10^{-5}]	[1.0×10^{-5}, 5.7×10^{-5}]
Average TChl *a* (mg m^{-3})	1.2	0.40	0.095
Average PPC/TChl *a* (mg m^{-3})	0.20	0.20	0.92
Average PSC/TChl *a* (mg m^{-3})	0.65	0.92	0.34

* TChl a = Chl a+DVChl a; PPC = Violaxanthin+ Diadinoxanthin+ Alloxanthin+ Zeaxanthin+ Lutein+ (β-carotene); PSC = Peridinin+ (19′-but-fucoxanthin)+ (19′-hex-fucoxanthin)+ Fucoxanthin.

For *Prochlorococcus* photosynthesis, Hess et al. suggested that the optimum irradiance is 200 µmol photons m^{-2} s^{-1} for the surface and 30–50 µmol photons m^{-2} s^{-1} for deeper water, respectively (Hess et al., 2001). However, all of the PAR values in our dataset are beyond the suggested optimum irradiance for both at the sea surface and deeper water. Additionally, temperatures in waters with the Pro-dominant cluster were high (28–29°C). The photoinhibition of *Prochlorococcus* is generally more pronounced in high temperature than in low temperature ranges at the same irradiance (Xiao et al., 2019).

Ultraviolet light and high light intensity increase the production of reactive oxygen species, which damages the PSII reaction centre and antenna complexes (Dring et al., 2001; Van De Poll et al., 2001; He and Häder, 2002; Sarvikas et al., 2006; Rastogi et al., 2010; Mella-Flores et al., 2012). PPC/TChl *a* in the Pro-dominant cluster does not exhibit an obvious upward trend with increasing PAR (Figure 8) likely since that *Prochlorococcus* has a limited mechanism for nonphotochemical quenching (NPQ) (Rocap et al., 2003; Xu et al., 2017; Xu et al., 2018). Moreover, the PSII repair capacity of *Prochlorococcus* reaches a maximum of approximately 400 µmol photons m^{-2} s^{-1} (Mella-Flores et al., 2012). Thus, it appears that the Pro-dominant cluster, when exposed to high light intensity, has a constrained ability for self-protection and self-repair, making it more susceptible to photoinhibition.

During photoinhibition, both the quantum efficiency (ϕ) and the maximum photosynthetic efficiency decrease (Cullen and Renger, 1979; Powles, 1984; Lesser et al., 1994; Behrenfeld et al., 1998; Marshall et al., 2000; Andersson and Aro, 2001; Oliver et al., 2003; Ross et al., 2008). As a consequence, PP values also diminish.

4.3 Hapto-dominant cluster and Diato-dominant cluster

The significant positive correlations between a_{ph}(443) ×PAR and PP were observed in both Hapto-dominant cluster (Figure 9C) and Diato-dominant cluster (Figure 10C).

In addition, no significant relationship exists between a_{ph}(443) and PP (p-value>0.05) (Figure 9A), while there is a significant positive correlation between PAR and PP/TChl *a* (Figure 9B), similar to the trend observed between a_{ph}(443) ×PAR and PP (Figure 9C). These results implied that PAR plays a pivotal role in regulating PP in this cluster. Interestingly, the Hapto-dominant cluster exhibits a considerably higher level of PSC/TChl *a* than the other two clusters (Table 1), indicating that phytoplankton in the Hapto-dominant cluster may be light-limited. This suggestion is in agreement with the observation that phytoplankton in this cluster inhabit deeper regions with low light intensity beneath the mixed layer. Therefore, the higher PSC/TChl *a* ratio in the Hapto-dominant cluster may be an adaptive strategy to enhance its light absorption and utilization under conditions of limited light availability.

The Diato-dominant cluster displays positive covariance between a_{ph}(443) and PP (Figure 10A), as well as between PAR

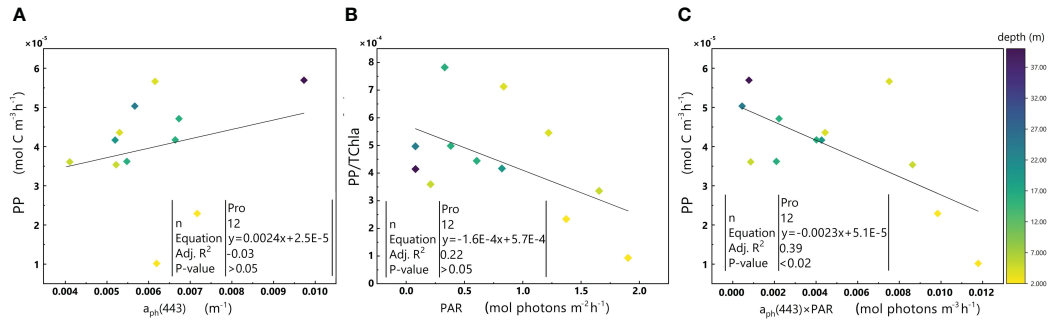


FIGURE 7
Relationships between a_{ph}(443) and PP **(A)**, PAR and PP/TChl *a* **(B)**, and a_{ph}(443)×PAR and PP **(C)** in the euphotic zone for the Pro-dominant cluster in the 2019 SCS dataset. Colorbar represents depth. Equations and some statistical parameters are also shown.

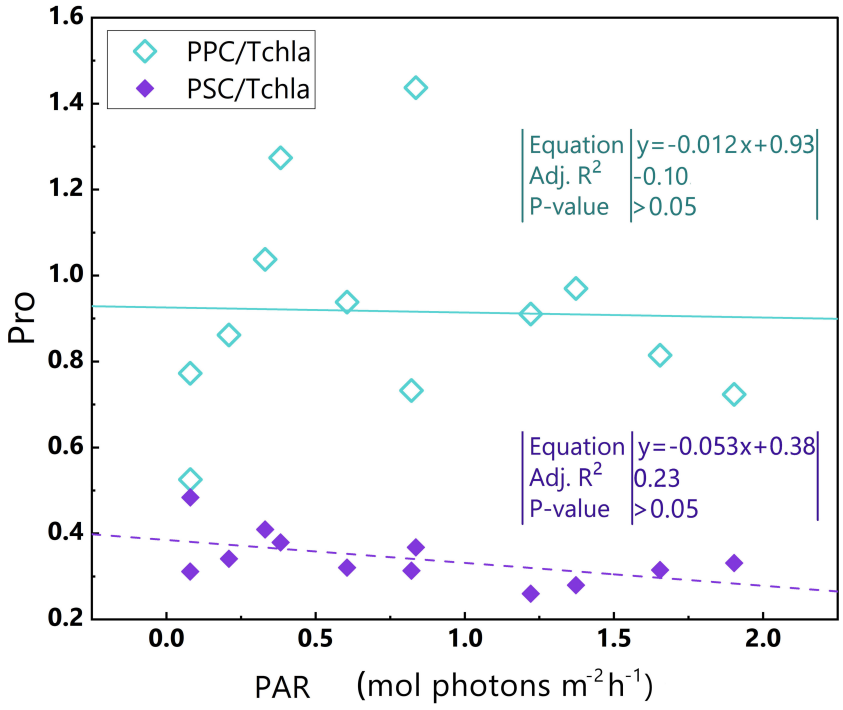


FIGURE 8
Relationships between PAR and PPC/TChl *a*, PAR and PSC/TChl *a* in the euphotic zone for the Pro-dominant cluster in the 2019 SCS dataset. Linear regression for PAR and PSC/TChl *a* (purple dotted line) and linear regression for PAR and PPC/TChl *a* (green line). Equations and some statistical parameters are also shown (green text for green line, purple text for purple dotted line).

and PP/TChl *a* (Figure 10B). These relationships are consistent with the significant correlation observed between $a_{ph}(443)$ ×PAR and PP (Figure 10C).

Phytoplankton within the Diato-dominant cluster mainly appeared at both the surface and in deeper water layers in coastal and estuarine areas. The level of the PPC/TChl *a* of the Diato-dominant cluster is similar to that of the Hapto-dominant cluster, but higher than that of PSC/TChl *a*. It is reasonable to infer that most samples in the Diato-dominant cluster are also in a light-limited stage, with several diatom-dominated samples appearing to be light-saturated. Remarkably, despite some samples in the Diato-dominant cluster being subjected to much stronger light intensities than those in the Pro-dominant cluster, photoinhibition does not occur in this cluster. Unlike the Pro-dominant cluster, the PPC/TChla of the Diato-dominant cluster increases significantly with the enhancement of light intensity (Figure 11), which likely protects it from the damage caused by photoinhibition. Furthermore, the mechanism of small photoregulation movements, the xanthophyll cycle and non-photochemical quenching (NPQ) may also safeguard diatoms from high light intensity to some extent (Prins et al., 2020).

5 Conclusions

A log-log linear primary production (PP) model based on the regional phytoplankton absorption coefficient [$a_{ph}(\lambda)$] was

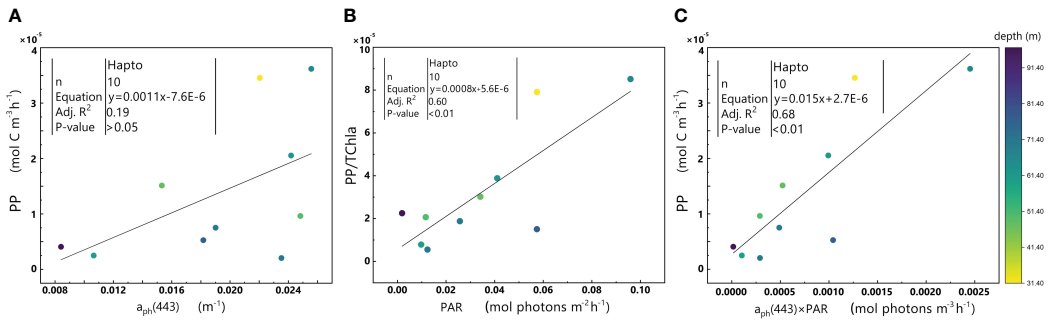


FIGURE 9
Relationships between $a_{ph}(443)$ and PP **(A)**, PAR and PP/TChl *a* **(B)**, and $a_{ph}(443)$×PAR and PP **(C)** in the euphotic zone for the Hapto-dominant cluster in the 2019 SCS dataset. Colorbar represents depth. Equations and some statistical parameters are also shown.

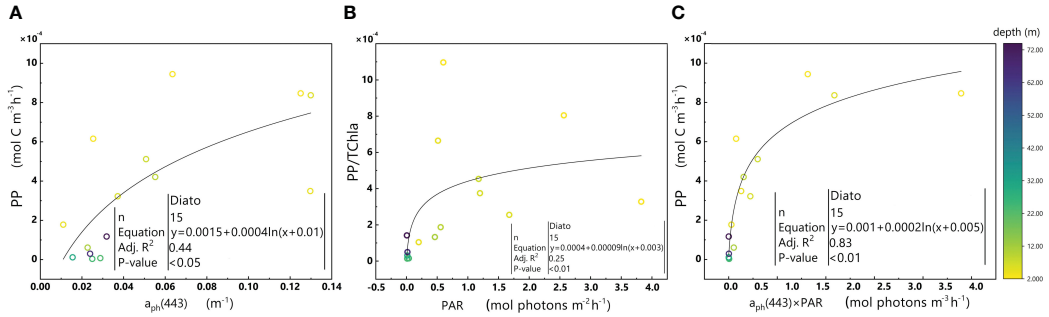


FIGURE 10
Relationships between a_{ph}(443) and PP **(A)**, PAR and PP/TChl *a* **(B)**, and a_{ph}(443)×PAR and PP **(C)** in the euphotic zone for the Diato-dominant cluster in the 2019 SCS dataset. Colorbar represents depth. Equations and some statistical parameters are also shown.

developed for the South China Sea (SCS), using an *in situ* dataset complied from the observation data collected in 2019. The predictive capacity of the model was evaluated by statistical analysis, K-fold cross validation, and *in situ* data validation, indicating that it can well predict PP across marine environment, ranging from estuarine to offshore and basin. The model's response is more sensitive to changes in photosynthetically active radiation (PAR) than to changes in a_{ph}(443).

To account for the bio-optical characteristics of different dominant phytoplankton in the SCS, the dataset was divided into five dominant phytoplankton clusters. The study analyzed the effects of environmental variables and physiological characteristics on the log-log linear PP model for the Diato-dominant, Hapto-dominant, and Pro-dominant clusters. The Diato-dominant and the Hapto-dominant clusters are mostly in the light-limited stage. Although some samples in the Diato-dominant clusters were exposed to extremely high light intensity, diatoms have efficient pigment regulation mechanisms and other ways to adapt to high light intensity. The Hapto-dominant cluster appeared below the mixed layer, where light is undersaturation. As a result, an increase in light levels, as indicated by a_{ph}(443)×PAR, leads to a corresponding increase in PP for both clusters. In contrast, the

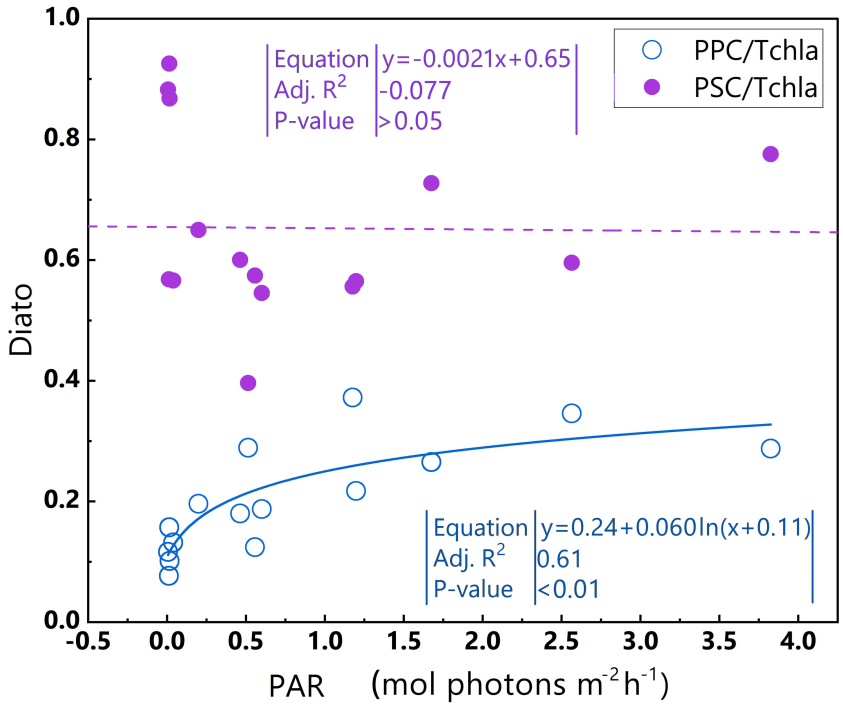


FIGURE 11
Relationships between PAR and PPC/TChl *a* and between PAR and PSC/TChl *a* in the euphotic zone for the Diato-dominant cluster in the 2019 SCS dataset. Linear regression for PAR and PSC/TChl *a* (purple dotted line) and log regression for PAR and PPC/TChl *a* (blue line). Equations and some statistical parameters are also shown (blue text for blue line, purple text for purple dotted line).

Pro-dominant cluster exhibited an opposite trend, suggesting that this cluster undergoes photoinhibition due to samples exposure to extremely high light intensity and the lack of self-protection mechanism.

Therefore, the accuracy of the log-log linear PP model depends on the photo-physiological state of the phytoplankton. In natural marine environment, dominant phytoplankton assemblages may be in different physiological states, varying from light inhibition to light limitation simultaneously. Large-scale photoinhibition may lead to inaccurate PP predictions. However, if phytoplankton are light-limited, the log-log linear PP model can well predict PP. Our findings provide insights into the establishment of phytoplankton-specific primary productivity models in marine environments.

Data availability statement

The datasets presented in this study can be found in online repositories. The names of the repository/repositories and accession number(s) can be found below: https://doi.org/10.5281/zenodo.5709178.

Author contributions

Conceptualization, HZ and WZ. Methodology, HZ, WC, JL, WDZ, WZ, and YZ. Software, HZ and KZ. Validation, HZ, WZ, and WC. Formal Analysis, HZ. Investigation, JL, LD, and KZ. Resources, WZ, WC, and JX. Data Curation, HZ. Writing – Original Draft Preparation, HZ. Writing – Review & Editing, HZ, WZ, WC, KZ, JX, and LD. Visualization, HZ. Supervision, WZ and WC. Project Administration, WZ and WC. Funding Acquisition, WZ and WC. All authors contributed to the article and approved the submitted version.

Funding

The author(s) declare financial support was received for the research, authorship, and/or publication of this article. Financial support for this research was provided by Science & Technology Fundamental Resources Investigation Program (Grant No.2022FY100601); National Natural Science Foundation of China (NSFC) (41976170, 42276181, 41976172, 41976181); Guangdong Basic and Applied Basic Research Foundation (2023A1515011703).

Acknowledgments

The authors would like to thank the co-workers and researchers of R/V Haike 68 and R/V Shiyan 3 supported by NSFC Shiptime Sharing Project. In addition, we would like to thank Dr. Xin Liu for conducting HPLC-CHEMTAX validation work on the classification of dominant phytoplankton clusters.

Conflict of interest

The authors declare that the research was conducted in the absence of any commercial or financial relationships that could be construed as a potential conflict of interest.

Publisher's note

All claims expressed in this article are solely those of the authors and do not necessarily represent those of their affiliated organizations, or those of the publisher, the editors and the reviewers. Any product that may be evaluated in this article, or claim that may be made by its manufacturer, is not guaranteed or endorsed by the publisher.

References

Aiken, J., Hardman-Mountford, N. J., Barlow, R., Fishwick, J., Hirata, T., and Smyth, T. (2008). Functional links between bioenergetics and bio-optical traits of phytoplankton taxonomic groups: an overarching hypothesis with applications for ocean colour remote sensing. *J. Plankton Res.* 30 (2), 165–181. doi: 10.1093/plankt/fbm098

Alvain, S., Moulin, C., Dandonneau, Y., and Bréon, F. M. (2005). Remote sensing of phytoplankton groups in case 1 waters from global SeaWiFS imagery. *Deep Sea Res. Part I: Oceanogr. Res. Papers* 52 (11), 1989–2004. doi: 10.1016/j.dsr.2005.06.015

Andersson, B., and Aro, E.-M. (2001). "Photodamage and D1 protein turnover in photosystem II," in *Regulation of Photosynthesis*. Eds. E.-M. Aro and B. Andersson (Dordrecht: Springer Netherlands), 377–393.

Antoine, D., and Morel, A. (1996). Oceanic primary production: 1. Adaptation of a spectral light-photosynthesis model in view of application to satellite chlorophyll observations. *Global Biogeochem. Cycles* 10 (1), 43–55. doi: 10.1029/95GB02831

Barnes, M. K., Tilstone, G. H., Smyth, T. J., Suggett, D. J., Astoreca, R., Lancelot, C., et al. (2014). Absorption-based algorithm of primary production for total and size-fractionated phytoplankton in coastal waters. *Mar. Ecol. Prog. Ser.* 504, 73–89. doi: 10.3354/meps10751

Behrenfeld, M. J., Prasil, O., Kolber, Z. S., Babin, M., and Falkowski, P. G. (1998). Compensatory changes in Photosystem II electron turnover rates protect photosynthesis from photoinhibition. *Photosynth. Res.* 58 (3), 259–268. doi: 10.1023/A:1006138630573

Boyce, D. G., Lewis, M. R., and Worm, B. (2010). Global phytoplankton decline over the past century. *Nature* 466 (7306), 591–596. doi: 10.1038/nature09268

Brewin, R. J. W., Morán, X. A. G., Raitsos, D. E., Gittings, J. A., Calleja, M. L., Viegas, M., et al. (2019). Factors regulating the relationship between total and size-fractionated chlorophyll-a in coastal waters of the Red Sea. *Front. Microbiol.* 10. doi: 10.3389/fmicb.2019.01964

Brewin, R. J. W., Tilstone, G. H., Jackson, T., Cain, T., Miller, P. I., Lange, P. K., et al. (2017). Modelling size-fractionated primary production in the Atlantic Ocean from remote sensing. *Prog. Oceanogr.* 158, 130–149. doi: 10.1016/j.pocean.2017.02.002

Bricaud, A., Claustre, H., Ras, J., and Oubelkheir, K. (2004). Natural variability of phytoplanktonic absorption in oceanic waters: Influence of the size structure of algal populations. *J. Geophys. Res.: Oceans* 109 (C11). doi: 10.1029/2004JC002419

Bricaud, A., and Stramski, D. (1990). Spectral absorption coefficients of living phytoplankton and nonalgal biogenous matter: A comparison between the Peru upwelling areaand the Sargasso Sea. *Limnol. Oceanogr.* 35 (3), 562–582. doi: 10.4319/lo.1990.35.3.0562

Cai, W.-J., Dai, M., Wang, Y., Zhai, W., Huang, T., Chen, S., et al. (2004). The biogeochemistry of inorganic carbon and nutrients in the Pearl River estuary and the adjacent Northern South China Sea. *Cont. Shelf Res.* 24 (12), 1301–1319. doi: 10.1016/j.csr.2004.04.005

Campbell, J., Antoine, D., Armstrong, R., Arrigo, K., Balch, W., Barber, R., et al. (2002). Comparison of algorithms for estimating ocean primary production from surface chlorophyll, temperature, and irradiance. *Global Biogeochem. Cycles* 16 (3), 9–1-9-15. doi: 10.1029/2001GB001444

Ciotti, Á. M., Lewis, M. R., and Cullen, J. J. (2002). Assessment of the relationships between dominant cell size in natural phytoplankton communities and the spectral shape of the absorption coefficient. *Limnol. Oceanogr.* 47 (2), 404–417. doi: 10.4319/lo.2002.47.2.0404

Claustre, H., Babin, M., Merien, D., Ras, J., Prieur, L., Dallot, S., et al. (2005). Toward a taxon-specific parameterization of bio-optical models of primary production: A case study in the North Atlantic. *J. Geophys. Res.: Oceans* 110 (C7). doi: 10.1029/2004JC002634

Cloern, J. E., Foster, S., and Kleckner, A. (2014). Phytoplankton primary production in the world's estuarine-coastal ecosystems. *Biogeosciences* 11 (9), 2477–2501. doi: 10.5194/bg-11-2477-2014

Cullen, J. J., and Renger, E. H. (1979). Continuous measurement of the DCMU-induced fluorescence response of natural phytoplankton populations. *Mar. Biol.* 53 (1), 13–20. doi: 10.1007/BF00386524

Curran, K., Brewin, R. J. W., Tilstone, G. H., Bouman, H. A., and Hickman, A. (2018). Estimation of size-fractionated primary production from satellite ocean colour in UK shelf seas. *Remote Sens.* 10 (9). doi: 10.3390/rs10091389

Dall'Osto, L., Cazzaniga, S., North, H., Marion-Poll, A., and Bassi, R. (2007). The Arabidopsis aba4-1 Mutant Reveals a Specific Function for Neoxanthin in Protection against Photooxidative Stress. *Plant Cell* 19 (3), 1048–1064. doi: 10.1105/tpc.106.049114

Dring, M. J., Wagner, A., and Lüning, K. (2001). Contribution of the UV component of natural sunlight to photoinhibition of photosynthesis in six species of subtidal brown and red seaweeds. *Plant Cell Environ.* 24 (11), 1153–1164. doi: 10.1046/j.1365-3040.2001.00765.x

Eppley, R. W., Stewart, E., Abbott, M. R., and Heyman, U. (1985). Estimating ocean primary production from satellite chlorophyll. Introduction to regional differences and statistics for the Southern California Bight. *J. Plankton Res.* 7 (1), 57–70. doi: 10.1093/plankt/7.1.57

Falkowski, P. G., Barber, R. T., and Smetacek, V. (1998). Biogeochemical controls and feedbacks on ocean primary production. *Science* 281 (5374), 200–206. doi: 10.1126/science.281.5374.200

Frank, H. A., and Cogdell, R. J. (1996). Carotenoids in photosynthesis. *Photochem. Photobiol.* 63 (3), 257–264. doi: 10.1111/j.1751-1097.1996.tb03022.x

Fushiki, T. (2011). Estimation of prediction error by using K-fold cross-validation. *Stat. Comput.* 21 (2), 137–146. doi: 10.1007/s11222-009-9153-8

Geisser, S. (1975). The predictive sample reuse method with applications. *J. Am. Stat. Assoc.* 70 (350), 320–328. doi: 10.1080/01621459.1975.10479865

He, Y.-Y., and Häder, D.-P. (2002). Reactive oxygen species and UV-B: effect on cyanobacteria. *Photochem. Photobiol. Sci.* 1 (10), 729–736. doi: 10.1039/B110365M

Hemsley, V. S., Smyth, T. J., Martin, A. P., Frajka-Williams, E., Thompson, A. F., Damerell, G., et al. (2015). Estimating oceanic primary production using vertical irradiance and chlorophyll profiles from ocean gliders in the North Atlantic. *Environ. Sci. Technol.* 49 (19), 11612–11621. doi: 10.1021/acs.est.5b00608

Hess, W. R., Rocap, G., Ting, C. S., Larimer, F., Stilwagen, S., Lamerdin, J., et al. (2001). The photosynthetic apparatus of Prochlorococcus: Insights through comparative genomics. *Photosynth. Res.* 70 (1), 53–71. doi: 10.1023/A:1013835924610

Hilker, T., Coops, N. C., Wulder, M. A., Black, T. A., and Guy, R. D. (2008). The use of remote sensing in light use efficiency based models of gross primary production: A review of current status and future requirements. *Sci. Total Environ.* 404 (2), 411–423. doi: 10.1016/j.scitotenv.2007.11.007

Hirata, T., Hardman-Mountford, N. J., Barlow, R., Lamont, T., Brewin, R., Smyth, T., et al. (2009). An inherent optical property approach to the estimation of size-specific photosynthetic rates in eastern boundary upwelling zones from satellite ocean colour: An initial assessment. *Prog. Oceanogr.* 83 (1), 393–397. doi: 10.1016/j.pocean.2009.07.019

Hirawake, T., Takao, S., Horimoto, N., Ishimaru, T., Yamaguchi, Y., and Fukuchi, M. (2011). A phytoplankton absorption-based primary productivity model for remote sensing in the Southern Ocean. *Polar Biol.* 34 (2), 291–302. doi: 10.1007/s00300-010-0949-y

Huot, Y., Babin, M., Bruyant, F., Grob, C., Twardowski, M. S., and Claustre, H. (2007). Relationship between photosynthetic parameters and different proxies of phytoplankton biomass in the subtropical ocean. *Biogeosciences* 4 (5), 853–868. doi: 10.5194/bg-4-853-2007

Iluz, D., and Dubinsky, Z. (2013). "Quantum yields in aquatic photosynthesis," in *Photosynthesis* (Intech Rijeka), 135–158.

Jochem, F. J., Mathot, S., and Quéguiner, B. (1995). Size-fractionated primary production in the open Southern Ocean in austral spring. *Polar Biol.* 15 (6), 381–392. doi: 10.1007/BF00239714

Jung, Y. (2018). Multiple predicting K-fold cross-validation for model selection. *J. Nonparametric Stat.* 30 (1), 197–215. doi: 10.1080/10485252.2017.1404598

Kahru, M. (2017). Ocean productivity from space: Commentary. *Global Biogeochem. Cycles* 31 (1), 214–216. doi: 10.1002/2016GB005582

Kameda, T., and Ishizaka, J. (2005). Size-fractionated primary production estimated by a two-phytoplankton community model applicable to ocean color remote sensing. *J. Oceanogr.* 61 (4), 663–672. doi: 10.1007/s10872-005-0074-7

Kiefer, D. A., and Mitchell, B. G. (1983). A simple, steady state description of phytoplankton growth based on absorption cross section and quantum efficiency1. *Limnol. Oceanogr.* 28 (4), 770–776. doi: 10.4319/lo.1983.28.4.0770

Kishino, M., Takahashi, M., Okami, N., and Ichimura, S. (1985). Estimation of the spectral absorption coefficients of phytoplankton in the sea. *Bull. Mar. Sci.* 37 (2), 634–642.

Knap, A., Michaels, A., Close, A., Ducklow, H., and Dickson, A. (1996). Protocols for the joint global ocean flux study (JGOFS) core measurements. *JGOFS Reprint IOC Manuals Guides No. 29 UNESCO 1994* 19, 111–115. doi: 10.013/epic.27912

Lee, Z., Carder, K. L., and Arnone, R. A. (2002). Deriving inherent optical properties from water color: a multiband quasi-analytical algorithm for optically deep waters. *Appl. Optics* 41 (27), 5755–5772. doi: 10.1364/AO.41.005755

Lee, Z. P., Carder, K. L., Marra, J., Steward, R. G., and Perry, M. J. (1996). Estimating primary production at depth from remote sensing. *Appl. Optics* 35 (3), 463–474. doi: 10.1364/AO.35.000463

Lesser, M. P., Cullen, J. J., and Neale, P. J. (1994). Carbon uptake in A marine diatom during acute exposure to ultraviolet B radiation: relative importance of damage and repair1. *J. Phycol.* 30 (2), 183–192. doi: 10.1111/j.0022-3646.1994.00183.x

Liao, J., Xu, J., Li, R., and Shi, Z. (2021). Photosynthesis-irradiance response in the eddy dipole in the Western South China sea. *J. Geophys. Res.: Oceans* 126 (5), e2020JC016986. doi: 10.1029/2020JC016986

Manuel, Z., Rodríguez, F., and José, L. G. (2000). Separation of chlorophylls and carotenoids from marine phytoplankton: a new HPLC method using a reversed phase C8 column and pyridine-containing mobile phases. *Mar. Ecol. Prog. Ser.* 195, 29–45. doi: 10.3354/meps195029

Marra, J., Trees, C. C., and O'Reilly, J. E. (2007). Phytoplankton pigment absorption: A strong predictor of primary productivity in the surface ocean. *Deep Sea Res. Part I: Oceanogr. Res. Papers* 54 (2), 155–163. doi: 10.1016/j.dsr.2006.12.001

Marshall, H. L., Geider, R. J., and Flynn, K. J. (2000). A mechanistic model of photoinhibition. *New Phytol.* 145 (2), 347–359. doi: 10.1046/j.1469-8137.2000.00575.x

Mella-Flores, D., Six, C., Ratin, M., Partensky, F., Boutte, C., Le Corguillé, G., et al. (2012). Prochlorococcus and synechococcus have evolved different adaptive mechanisms to cope with light and UV stress. *Front. Microbiol.* 3. doi: 10.3389/fmicb.2012.00285

Moore, T. S., Campbell, J. W., and Dowell, M. D. (2009). A class-based approach to characterizing and mapping the uncertainty of the MODIS ocean chlorophyll product. *Remote Sens. Environ.* 113 (11), 2424–2430. doi: 10.1016/j.rse.2009.07.016

Morel, A., and Maritorena, S. (2001). Bio-optical properties of oceanic waters: A reappraisal. *J. Geophys. Res.: Oceans* 106 (C4), 7163–7180. doi: 10.1029/2000JC000319

Nielsen, E. S. (1952). Use of radio-active carbon (/sup 14/C) for measuring organic production in the sea. *ICES J. Mar. Sci.* 18, 2. doi: 10.1093/icesjms/18.2.117

Oliver, M. J., Schofield, O., Bergmann, T., Glenn, S., Orrico, C., and Moline, M. (2004). Deriving *in situ* phytoplankton absorption for bio-optical productivity models in turbid waters. *J. Geophys. Res.: Oceans* 109 (C7). doi: 10.1029/2002JC001627

Oliver, R. L., Whittington, J., Lorenz, Z., and Webster, I. T. (2003). The influence of vertical mixing on the photoinhibition of variable chlorophyll a fluorescence and its inclusion in a model of phytoplankton photosynthesis. *J. Plankton Res.* 25 (9), 1107–1129. doi: 10.1093/plankt/25.9.1107

Ondrusek, M. E., Bidigare, R. R., Waters, K., and Karl, D. M. (2001). A predictive model for estimating rates of primary production in the subtropical North Pacific Ocean. *Deep Sea Res. Part II: Topical Stud. Oceanogr.* 48 (8), 1837–1863. doi: 10.1016/S0967-0645(00)00163-6

Platt, T., and Sathyendranath, S. (1988). Oceanic primary production: estimation by remote sensing at local and regional scales. *Science* 241 (4873), 1613–1620. doi: 10.1126/science.241.4873.1613

Platt, T., and Sathyendranath, S. (1993). Estimators of primary production for interpretation of remotely sensed data on ocean color. *J. Geophys. Res.: Oceans* 98 (C8), 14561–14576. doi: 10.1029/93JC01001

Platt, T., Sathyendranath, S., Forget, M.-H., White, G. N., Caverhill, C., Bouman, H., et al. (2008). Operational estimation of primary production at large geographical scales. *Remote Sens. Environ.* 112 (8), 3437–3448. doi: 10.1016/j.rse.2007.11.018

Powles, S. B. (1984). Photoinhibition of photosynthesis induced by visible light. *Annu. Rev. Plant Physiol.* 35 (1), 15–44. doi: 10.1146/annurev.pp.35.060184.000311

Prins, A., Deleris, P., Hubas, C., and Jesus, B. (2020). Effect of light intensity and light quality on diatom behavioral and physiological photoprotection. *Front. Mar. Sci.* 7. doi: 10.3389/fmars.2020.00203

Rastogi, R. P., Singh, S. P., Häder, D.-P., and Sinha, R. P. (2010). Detection of reactive oxygen species (ROS) by the oxidant-sensing probe 2′,7′-dichlorodihydrofluorescein diacetate in the cyanobacterium Anabaena variabilis PCC 7937. *Biochem. Biophys. Res. Commun.* 397 (3), 603–607. doi: 10.1016/j.bbrc.2010.06.006

Robinson, C. M., Cherukuru, N., Hardman-Mountford, N. J., Everett, J. D., McLaughlin, M. J., Davies, K. P., et al. (2017). Phytoplankton absorption predicts patterns in primary productivity in Australian coastal shelf waters. *Estuarine Coast. Shelf Sci.* 192, 1–16. doi: 10.1016/j.ecss.2017.04.012

Rocap, G., Larimer, F. W., Lamerdin, J., Malfatti, S., Chain, P., Ahlgren, N. A., et al. (2003). Genome divergence in two Prochlorococcus ecotypes reflects oceanic niche differentiation. *Nature* 424 (6952), 1042–1047. doi: 10.1038/nature01947

Ross, O. N., Moore, C. M., Suggett, D. J., MacIntyre, H. L., and Geider, R. J. (2008). A model of photosynthesis and photo-protection based on reaction center damage and repair. *Limnol. Oceanogr.* 53 (5), 1835–1852. doi: 10.4319/lo.2008.53.5.1835

Roy, S., Llewellyn, C. A., Egeland, E. S., and Johnsen, G. (2011). *Phytoplankton pigments: characterization, chemotaxonomy and applications in oceanography* (Cambridge: Cambridge University Press).

Rundel, P. W., Boonpragob, K., and Patterson, M. (2017). Seasonal water relations and leaf temperature in a deciduous dipterocarp forest in Northeastern Thailand. *Forests* 8 (10), 368. doi: 10.3390/f8100368

Russell, S. J. (2010). *Artificial intelligence a modern approach* (New Jersey: Pearson Education, Inc).

Saba, V. S., Friedrichs, M. A. M., Carr, M.-E., Antoine, D., Armstrong, R. A., Asanuma, I., et al. (2010). Challenges of modeling depth-integrated marine primary productivity over multiple decades: A case study at BATS and HOT. *Global Biogeochem. Cycles* 24 (3). doi: 10.1029/2009GB003655

Sarvikas, P., Hakala, M., Pätsikkä, E., Tyystjärvi, T., and Tyystjärvi, E. (2006). Action Spectrum of Photoinhibition in Leaves of Wild Type and npq1-2 and npq4-1 Mutants of Arabidopsis thaliana. *Plant Cell Physiol.* 47 (3), 391–400. doi: 10.1093/pcp/pcj006

Sauer, M. J., Roesler, C. S., Werdell, P. J., and Barnard, A. (2012). Under the hood of satellite empirical chlorophyll a algorithms: revealing the dependencies of maximum band ratio algorithms on inherent optical properties. *Optics Express* 20 (19), 20920–20933. doi: 10.1364/OE.20.020920

Setiawan, R. Y., and Habibi, A. (2011). Satellite detection of summer chlorophyll-a bloom in the Gulf of Tomini. *IEEE J. Selected Topics Appl. Earth Observ. Remote Sens.* 4 (4), 944–948. doi: 10.1109/JSTARS.2011.2163926

Setiawan, R. Y., and Kawamura, H. (2011). Summertime phytoplankton bloom in the South Sulawesi Sea. *IEEE J. Selected Topics Appl. Earth Observ. Remote Sens.* 4 (1), 241–244. doi: 10.1109/JSTARS.2010.2094604

Silsbe, G. M., Behrenfeld, M. J., Halsey, K. H., Milligan, A. J., and Westberry, T. K. (2016). The CAFE model: A net production model for global ocean phytoplankton. *Global Biogeochem. Cycles* 30 (12), 1756–1777. doi: 10.1002/2016GB005521

Stramski, D., Reynolds, R. A., Kaczmarek, S., Uitz, J., and Zheng, G. (2015). Correction of pathlength amplification in the filter-pad technique for measurements of particulate absorption coefficient in the visible spectral region. *Appl. Optics* 54 (22), 6763–6782. doi: 10.1364/AO.54.006763

Uitz, J., Claustre, H., Gentili, B., and Stramski, D. (2010). Phytoplankton class-specific primary production in the world's oceans: Seasonal and interannual variability from satellite observations. *Global Biogeochem. Cycles* 24 (3). doi: 10.1029/2009GB003680

Uitz, J., Stramski, D., Reynolds, R. A., and Dubranna, J. (2015). Assessing phytoplankton community composition from hyperspectral measurements of phytoplankton absorption coefficient and remote-sensing reflectance in open-ocean environments. *Remote Sens. Environ.* 171, 58–74. doi: 10.1016/j.rse.2015.09.027

Van De Poll, W. H., Eggert, A., Buma, A. G. J., and Breeman, A. M. (2001). Effects of Uv-B-induced Dna damage and photoinhibition on growth of temperate marine red macrophytes: habitat-related differences in Uv-B tolerance. *J. Phycol.* 37 (1), 30–38. doi: 10.1046/j.1529-8817.2001.037001030.x

Vongcharoen, K., Santanoo, S., Banterng, P., Jogloy, S., Vorasoot, N., and Theerakulpisut, P. (2018). Seasonal variation in photosynthesis performance of cassava at two different growth stages under irrigated and rain-fed conditions in a tropical savanna climate. *Photosynthetica* 56 (4), 1398–1413. doi: 10.1007/s11099-018-0849-x

Werdell, P. J., Franz, B. A., Bailey, S. W., Feldman, G. C., Boss, E., Brando, V. E., et al. (2013). Generalized ocean color inversion model for retrieving marine inherent optical properties. *Appl. Optics* 52 (10), 2019–2037. doi: 10.1364/AO.52.002019

Westberry, T., Behrenfeld, M. J., Siegel, D. A., and Boss, E. (2008). Carbon-based primary productivity modeling with vertically resolved photoacclimation. *Global Biogeochem. Cycles* 22 (2). doi: 10.1029/2007GB003078

Xiao, W., Laws, E. A., Xie, Y., Wang, L., Liu, X., Chen, J., et al. (2019). Responses of marine phytoplankton communities to environmental changes: New insights from a niche classification scheme. *Water Res.* 166, 115070. doi: 10.1016/j.watres.2019.115070

Xu, K., Grant-Burt, J. L., Donaher, N., and Campbell, D. A. (2017). Connectivity among Photosystem II centers in phytoplankters: Patterns and responses. *Biochim. Biophys. Acta (BBA) - Bioenerget.* 1858 (6), 459–474. doi: 10.1016/j.bbabio.2017.03.003

Xu, K., Lavaud, J., Perkins, R., Austen, E., Bonnanfant, M., and Campbell, D. A. (2018). Phytoplankton σPSII and excitation dissipation; implications for estimates of primary productivity. *Front. Mar. Sci.* 5. doi: 10.3389/fmars.2018.00281

Yentsch, C. S. (1962). Measurement of visible light absorption by particulate matter in the Ocean1. *Limnol. Oceanogr.* 7 (2), 207–217. doi: 10.4319/lo.1962.7.2.0207

Zoffoli, M. L., Lee, Z., and Marra, J. F. (2018). Regionalization and dynamic parameterization of quantum yield of photosynthesis to improve the ocean primary production estimates from remote sensing. *Front. Mar. Sci.* 5. doi: 10.3389/fmars.2018.00446

frontiers | Frontiers in Marine Science

TYPE Original Research
PUBLISHED 08 January 2024
DOI 10.3389/fmars.2023.1197953

Check for updates

OPEN ACCESS

EDITED BY
Victor Martinez-Vicente,
Plymouth Marine Laboratory,
United Kingdom

REVIEWED BY
Martí Galí,
Spanish National Research Council (CSIC),
Spain
Jordon Scott Beckler,
Florida Atlantic University, United States

*CORRESPONDENCE
Daniel Koestner
daniel.koestner.optics@gmail.com

RECEIVED 31 March 2023
ACCEPTED 22 November 2023
PUBLISHED 08 January 2024

CITATION
Koestner D, Stramski D and Reynolds RA (2024) Improved multivariable algorithms for estimating oceanic particulate organic carbon concentration from optical backscattering and chlorophyll-a measurements.
Front. Mar. Sci. 10:1197953.
doi: 10.3389/fmars.2023.1197953

COPYRIGHT
© 2024 Koestner, Stramski and Reynolds. This is an open-access article distributed under the terms of the Creative Commons Attribution License (CC BY). The use, distribution or reproduction in other forums is permitted, provided the original author(s) and the copyright owner(s) are credited and that the original publication in this journal is cited, in accordance with accepted academic practice. No use, distribution or reproduction is permitted which does not comply with these terms.

Improved multivariable algorithms for estimating oceanic particulate organic carbon concentration from optical backscattering and chlorophyll-a measurements

Daniel Koestner[1]*, Dariusz Stramski[2] and Rick A. Reynolds[2]

[1]Department of Physics and Technology, University of Bergen, Bergen, Norway, [2]Marine Physical Laboratory, Scripps Institution of Oceanography, University of California San Diego, La Jolla, CA, United States

The capability to estimate the oceanic particulate organic carbon concentration (POC) from optical measurements is crucial for assessing the dynamics of this carbon reservoir and the capacity of the biological pump to sequester atmospheric carbon dioxide in the deep ocean. Optical approaches are routinely used to estimate oceanic POC from the spectral particulate backscattering coefficient b_{bp}, either directly (e.g., with backscattering sensors on underwater platforms like BGC-Argo floats) or indirectly (e.g., with satellite remote sensing). However, the reliability of algorithms which relate POC to b_{bp} is typically limited due to the complexity of interactions between light and natural assemblages of marine particles, which depend on variations in particle concentration, composition, and size distribution. This study expands on our previous work by analysis of an extended field dataset created with judicious data inclusion criteria with the aim to provide POC algorithms for multiple light wavelengths of measured b_{bp}, which can be useful for applications with *in situ* optical sensors as well as above-water active or passive measurement systems. We describe an improved empirical multivariable approach to estimate POC from simultaneous measurements of b_{bp} and chlorophyll-a concentration (Chla) to better account for the effects of variable particle composition on the relationship between POC and b_{bp}. The multivariable regression models are formulated using a relatively large dataset of coincident measurements of POC, b_{bp}, and Chla, including surface and subsurface data from the Atlantic, Pacific, Arctic, and Southern Oceans. We show that the multivariable algorithm provides reduced uncertainty of estimated POC across diverse marine environments when compared with a traditional univariate algorithm based on only b_{bp}. We also propose an improved formulation of univariate algorithm based on b_{bp} alone. Finally, we examine performance of several algorithms to estimate POC using our dataset as well as a dataset consisting of optical measurements from BGC-Argo floats and traditional POC measurements collected during a coincident research cruise in the Atlantic Ocean.

KEYWORDS

marine optics, bio-optical algorithms, particulate organic carbon, inherent optical properties, backscattering coefficient, chlorophyll-a fluorescence, Biogeochemical-Argo observations, satellite ocean color observations

1 Introduction

The ocean plays a vital role in the global carbon cycle, regulating our climate and sustaining life on Earth through exchanges and transformations of atmospheric CO_2. The fate of carbon in the ocean is driven by several interconnected processes including the biological carbon pump that refers to the biogeochemical processes which transfer dissolved and particulate organic carbon from the surface ocean to the deep ocean. Atmospheric CO_2 levels would be ~50% higher than they are today without the biological carbon pump (Paraekh et al., 2006). However, the magnitude of the global ocean biological carbon pump is poorly constrained because ocean biogeochemical models struggle to accurately simulate distributions of concentration of particulate organic carbon (POC), some of which can serve as long-term storage for atmospheric CO_2 through sinking to the deep ocean (Boyd and Trull, 2007; Brewin et al., 2021). Due to uncertainties in biogeochemical models, the range in the estimated quantity of organic carbon that is exported annually by the biological carbon pump is large, ranging from about 5 to 12 Pg C yr^{-1} (Boyd and Trull, 2007; Middelburg, 2019; Nowicki et al., 2022). To put this range in perspective, it is equivalent to between 50% and over 100% of global anthropogenic emissions of CO_2 in 2022 (Friedlingstein et al., 2022).

Particulate organic carbon in the ocean forms the base of marine food webs and is associated with phytoplankton, heterotrophic organisms, and non-living organic detrital material. Although POC constitutes one of the smallest carbon stocks in the global ocean, it is highly dynamic, experiencing turnover on short timescales with respect to primary production and remineralization (Brewin et al., 2021). A major limiting factor on the development of a better quantitative understanding of the biological carbon pump is the limited number of observations of the spatial and temporal distribution of POC (Siegel et al., 2016; Brewin et al., 2021).

Traditional POC measurements rely on discrete water sampling, which has significant limitations in terms of temporal and spatial scales of observational coverage. The estimation of POC from optical measurements, conducted either remotely from above the ocean or in situ, has the potential to fill this gap in understanding of the global distribution of POC (e.g., Gardner et al., 1993; Bishop, 1999; Claustre et al., 1999; Stramski et al., 1999; Loisel et al., 2002; Stramska and Stramski, 2005; Gardner et al., 2006; Stramski et al., 2008; Balch et al., 2010; Cetinić et al., 2012; Stramski et al., 2022). Optical estimates of POC, however, can be subject to large uncertainties because the interactions between light and marine particles can be influenced by many factors, including the effects of light and nutrient availability on phytoplankton (e.g., Ackleson et al., 1990; Stramski and Morel, 1990; Reynolds et al., 1997; Stramski et al., 2002), particle size distribution (e.g., Morel and Bricaud, 1981; Stramski and Kiefer, 1991; Uitz et al., 2010; Stemmann and Boss, 2012), and particle composition such as the ratio of phytoplankton vs. non-phytoplankton or organic vs. mineral material (e.g., Stramski et al., 2001; Twardowski et al., 2001; Stramski et al., 2007; Neukermans et al., 2012; Woźniak et al., 2022). Knowledge of particle composition can improve estimates of POC from optical measurements (e.g., Woźniak et al., 2010; Reynolds et al., 2016; Koestner et al., 2021).

Recently, Koestner et al. (2022) proposed an advancement in the estimation of POC across diverse environments from a multivariable empirical algorithm that utilizes concurrent measurements of the particulate backscattering coefficient (b_{bp}) and concentration of chlorophyll-a (Chla) as predictor variables. In this multi-component algorithm, the b_{bp} component is considered a measure of particle concentration while the additional components involving both b_{bp} and Chla serve as a proxy for particulate composition to improve estimations of POC. This formulation was proven to be more effective than a univariate b_{bp}-based algorithm by providing reduced uncertainty when examining an independent dataset of contrasting surface and subsurface samples from several major oceanic basins. The use of the multivariable algorithm was demonstrated with data from BGC-Argo floats in the Labrador Sea. Another recent study in the Arctic seas also demonstrated improved estimation of POC using adaptive optical algorithms that account for variability in the particulate composition parameterized in terms of a proxy that represents the contribution of organic vs. mineral particles to the total suspended particulate matter (Stramski et al., 2023).

In the current study we seek to improve the algorithms presented in Koestner et al. (2022) resulting from several important enhancements brought about by the use of an extended field dataset for algorithm development, more considerate inclusion and exclusion criteria applied in the process of compilation of development dataset, and adjustments in the approach to correct for algorithm bias at low POC values. We evaluate performance of newly developed algorithms compared with several other algorithms from the literature. We provide algorithms for several light wavelengths used commonly in observations of optical backscattering (i.e., 470, 532, 550, 660, and 700 nm), and specifically formulated algorithms for application with water column observations using vertically profiling platforms such as BGC-Argo floats or autonomous gliders and also for potential applications of satellite ocean color observations used to derive b_{bp} and Chla (e.g., Loisel and Stramski, 2000; Lee et al., 2002; Loisel et al., 2018; O'Reilly and Werdell, 2019). We also recognize potential for the use of one of the proposed POC algorithms in conjunction with retrievals of near-surface oceanic b_{bp} with air- or shipborne ocean lidar systems (Churnside et al., 1998; Jamet et al., 2019), including ATLAS lidar on ICESat-2 satellite (Lu et al., 2019), and CALIOP lidar on CALIPSO satellite (Getzewich et al., 2018). These lidar systems show promise for providing observations complementary to passive ocean color remote sensing including night sampling, observations through thin clouds, and vertical profiling to estimate b_{bp} and POC (e.g., Behrenfeld et al., 2013; Bisson et al., 2021; Lu et al., 2021; Zhang et al., 2023). Finally, within the context of application of newly proposed algorithms with the global array of BGC-Argo floats, we present a validation exercise with optical data from BGC-Argo floats acquired in the vicinity of traditional POC measurements down to 500 m during the AMT-24 research cruise in the Atlantic Ocean.

2 Methods

A field dataset of concurrent particle and optical measurements was assembled for the formulation and analysis of optical algorithms in this study. Of most relevance to the current study, the post-cruise analyses of discrete water samples provided mass concentration of particulate organic carbon (POC) and total chlorophyll-a (Chla) while the spectral backscattering coefficient b_{bp} was measured *in situ* shortly before or after water sample collection. Note that b_{bp} is dependent on light wavelength λ, however it is often not shown in symbolic representation for brevity. Various methodological details relating to field measurements, data processing, and algorithm development can be found in Koestner et al. (2022). Some details are summarized below for clarity or to describe differences specific to the current study.

2.1 Sampling locations

The final dataset used in the current study was composed from analyses of the total of 407 surface and subsurface water samples from the Arctic, Atlantic, Pacific, and Southern Oceans obtained during 13 research cruises. Sample locations are shown in Figure 1A and Table 1 summarizes information on sampling region, dates, and number of samples. Additional information on these cruises, including citations to relevant literature, can be found in Stramski et al. (2022). The requirement for concurrent measurements of POC, Chla, and spectral b_{bp} utilizing consistent methodology is a major determinant of the size of the dataset. This dataset encompasses many contrasting oceanic particle assemblages in terms of particle and optical properties (Figure 1B; see also Koestner et al., 2022). Following reanalysis of data from the South Pacific BIOSOPE cruise, the current study includes 18 subsurface samples from this cruise which were not included in Koestner et al. (2022). These subsurface samples (11 of which contain POC < 30 mg m^{-3}) importantly expand coverage of very low POC values often found in ultraoligotrophic waters.

In this study, we differentiate sample location using oceanic biomes to indicate that data were collected across diverse water types and also to examine performance within different oceanic biomes (Figure 1). The biomes were defined using the mean biomes described in Fay and McKinley (2014). These biomes represent distinct biogeochemical regions defined by sea surface temperature, spring/summer Chla, ice fraction, and maximum mixed layer depth determined with observational and climatology data from 1998 to 2010. These broadscale biomes are relevant for open ocean regions and address first-order differences in biogeochemistry. The biomes relevant to our study are marginal sea ice (ICE), subpolar seasonally stratified (SPSS), subtropical seasonally stratified (STSS), equatorial (EQU), and subtropical permanently stratified (STPS). Important distinctions are that ICE biomes have at least 50% ice coverage during some of the year, SPSS biomes have strong seasonal upwelling driving higher summer Chla, STSS biomes are areas of downwelling but intermediate Chla and deep winter mixed layer, and STPS biomes are also downwelling areas but with year-round stratification, shallow mixed layer, and low Chla. For the purposes of the current study, we differentiate only the North Pacific (NP) and Southern Ocean (SO) marginal sea ice biomes, while all other biomes are not differentiated by larger oceanic basin. A breakdown of the number of samples from each biome and variability in particle composition characteristics (described below in Section 2.2) is shown in Figure 1B.

The temporal coverage of sampling at given locations is dictated by the cruises comprising our assembled dataset, a common occurrence with compiled field-based datasets. Regarding seasonal coverage of samples, all ICE data originated from sampling during summer months, Atlantic Ocean meridional cruises were during spring and autumn months, and data from Pacific Ocean were collected in spring months (Table 1).

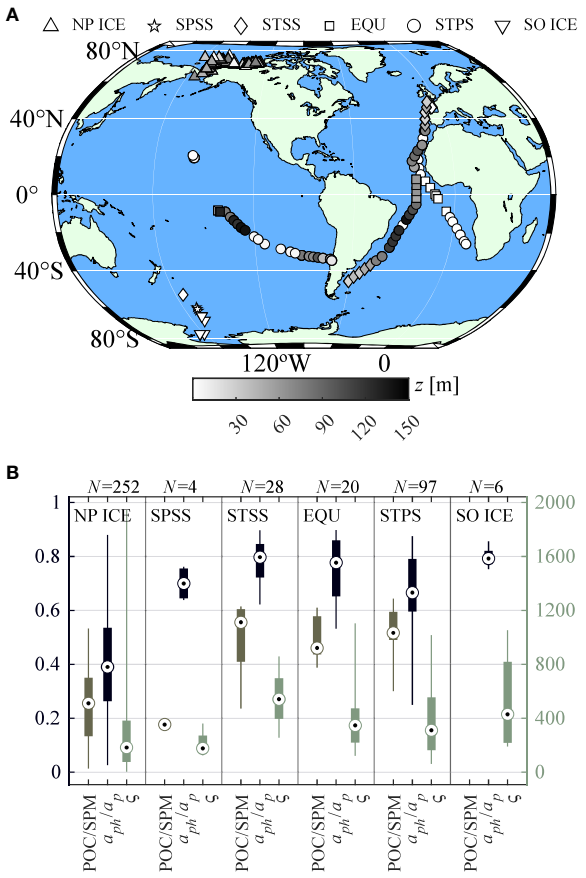


FIGURE 1
Summary of samples utilized in algorithm development. **(A)** Location of stations where samples were collected differentiated by oceanic biome and shaded by depth *z* of any additional subsurface sampling. The biomes are North Pacific and Southern Ocean marginal sea ice (ICE), subpolar seasonally stratified (SPSS), subtropical seasonally stratified (STSS), equatorial (EQU), and subtropical permanently stratified (STPS). **(B)** Non-parametric box plots of three particle composition metrics for samples in each biome. The whiskers represent the entire data range while box represents (from bottom to top), 25th, 50th, and 75th percentile of available data. The first two box plots within each biome refer to proxies of particulate composition representing organic vs. inorganic (i.e., POC/SPM) and phytoplankton vs. non-phytoplankton (i.e., a_{ph}/a_p) content of particles. The third boxplot (light green) refers to the particulate composition proxy ς = Chla/b_{bp}(700) in units [mg m^{-2}]. Number of samples (*N*) in the dataset are displayed above each biome, noting that not all samples had available POC/SPM and a_{ph}/a_p data.

TABLE 1 Summary of cruises.

Ocean	Sub-Location	Cruise(s)	Sampling Dates	*N*
Arctic	Chukchi/Beaufort Seas	HLY1001 HLY1101 MR17-05C	18 Jun. – 16 Jul., 2010 28 Jun. – 24 Jul., 2011 23 Aug. – 2 Oct., 2017	30 94 42
	SE Beaufort Sea	MALINA	31 Jul. – 24 Aug., 2009	75
	S Beaufort Sea	PB18 PB19	8 Sep. – 12 Sep., 2018 11 Aug. – 15 Aug., 2019	5 6
Atlantic	Meridional Transect	ANTXXIII/1 ANTXXVI/4	13 Oct. – 17 Nov., 2005 7 Apr. – 17 May, 2010	25 65
Pacific	Tropical and Subtropical SE Pacific Ocean Tropical N Pacific Ocean	BIOSOPE KM12-10	17 Oct. – 15 Dec., 2004 28 May – 10 Jun., 2012	48 7
Southern	Southern Ocean	NBP97-8 RR-KIWI 8,9	5 Nov. – 13 Dec., 1997 8 Jan. – 19 Mar., 1998	3 7

2.2 Characterization of particulate assemblages

POC and Chla were determined for each water sample through analysis of particulate matter retained on 25 mm diameter Whatman glass fiber filters (GF/F). Sample volumes were filtered at low vacuum (<120 mm Hg) using pre-combusted filters for the determination of POC following standard methodology (Parsons et al., 1984; Intergovernmental Oceanographic Commission, 1994). The determination of POC did not include correction for adsorption of dissolved organic carbon, but rather filtration of appropriately large volumes of seawater for the purposes of relating POC to optical measurements influenced by all suspended material (Stramski et al., 2022), while the measurement of Chla was made using high-performance liquid chromatography (HPLC) analysis. However, 11 samples from coastal Alaska utilized subtraction of a "wet" blank to derive POC with correction for DOC-adsorption (IOCCG Protocol Series, 2021; Koestner et al., 2021) and *in situ* fluorometric measurements of Chla (with appropriate corrections; Roesler et al., 2017). We note that the inclusion of these 11 samples did not meaningfully impact algorithm development. We also note that 45 samples from one Atlantic cruise (ANTXXVI/4) that were used in Koestner et al. (2022) had refinements to Chla as a result of reprocessing of HPLC data. This reprocessing mostly resulted in some reduction of Chla.

For the purpose of POC algorithm formulation, the compositional aspect of particulate matter was quantified with ς = Chla/b_{bp}, the inverse of the chlorophyll-a specific particulate backscattering coefficient and defined for a specific light wavelength. This optical proxy is advantageous as it is retrievable from *in situ* measurements with chlorophyll-a fluorescence and backscattering sensors and serves as a reasonable compositional indicator of the contributions of phytoplankton vs. non-phytoplankton particles (Koestner et al., 2022).

For further characterization of variability in particulate composition in our dataset, Figure 1B also provides information on two additional proxies of particulate composition representing organic vs. inorganic and phytoplankton vs. non-phytoplankton content of particles. Specifically, we present the ratio of POC to the mass concentration of all suspended particulate matter SPM (i.e., POC/SPM) and the ratio of the absorption coefficient of phytoplankton a_{ph} to the absorption coefficient of all particles a_p at light wavelength of 410 nm. These data were obtained from measurements which were made on the samples considered in this study (Koestner et al., 2022).

2.3 Measurements of the spectral backscattering coefficient

More detailed information regarding the acquisition and processing applied to light scattering data can be found in Stramski et al. (2008) and Reynolds et al. (2016). All spectral backscattering measurements were measured *in situ* with HydroScat-6 and a-βeta sensors (HOBI Labs, Inc.) at depths where water samples were collected. These instruments resolve scattering at an angle approximately 140° from the direction of incident light and, depending on the instrument configuration available for each research cruise, typically utilized 6 to 11 wavelengths from about 400 to 850 nm. To derive b_{bp} from these measurements, the contribution of theoretical pure seawater backscattering was removed, a factor of 1.13 was applied to relate backscattering at a single angle to b_{bp}, and adjustments were made for scattering and absorption losses to and from the sample volume. The spectral b_{bp} data were fit using an ordinary least squares linear regression of $\log_{10}(b_{bp})$ vs. $\log_{10}(\lambda)$ to obtain b_{bp} at λ = 470, 532, 550, 660, and 700 nm. We focus on these wavelengths as they are commonly utilized with *in situ* backscattering sensors (e.g., WET Labs Environmental Characterization Optics ECO sensors). There is additional special interest in 532 and 550 nm which approximately correspond to available wavelengths on active and passive satellite observation systems.

2.4 Criteria applied to compilation of final dataset

Although the initial assembly of data from 13 cruises resulted in 475 samples, approximately 15% of samples were excluded from the final algorithm development dataset based on several inclusion and exclusion criteria to better serve the intended purpose of this study. First, to avoid uncertainties related to spectral interpolation of b_{bp}, data were excluded if the spectral slope of the power function of b_{bp} vs. λ was positive (unlikely for natural samples) or if the power function fit of b_{bp} had greater than 30% mean absolute percent difference from the measured b_{bp} for available measurement wavelengths. Samples with particularly high b_{bp} were removed using $b_{bp}(700) > 0.04$ m^{-1} as an exclusion criterion, noting that values higher than about 0.03 m^{-1} are highly unlikely in the global ocean (e.g., Organelli et al., 2017). The accepted POC data were limited to a range of 10–1000 mg m^{-3}, Chla was limited to a range of 0.01–30 mg m^{-3} and ς determined using $b_{bp}(700)$ was limited to not exceed 2000 mg m^{-2}, and we acknowledge that these ranges are reasonable for the surface ocean (e.g., Organelli et al., 2017; Barbieux et al., 2018; Joshi et al., 2023). Finally, the maximum depth of samples was limited to 150 m, which generally encompasses the deepest euphotic zone depths in most oceanic environments depending on criteria used in defining the euphotic zone depth (e.g., Organelli et al., 2017; Wu et al., 2021; Koestner et al., 2022). Overall, the final dataset includes 407 samples from 243 discrete locations, and it was found that the exclusion of the 68 samples from the initial dataset improved algorithm reliability in terms of consistency and statistical significance of algorithm coefficients. We also note that 70% of the excluded samples were from the NP ICE biome which is already sufficiently represented in the dataset (Figure 1).

Figure 2 describes the distribution of sample depths utilized in the current study and we note that all samples were collected within the epipelagic zone with a maximum depth of 150 m. We refer to surface samples as those which were collected within the upper 20 m of the water column corresponding to an approximate limit for above-water remote-sensing observation systems. The number of surface samples in our dataset is 257, and the majority of them were collected from depths shallower than 5 m (Figure 2). Of the 407 samples which were included in data analysis, 150 were collected at subsurface depths (i.e., deeper than 20 m), with only 16 samples from depths between 100 and 150 m (Figure 2).

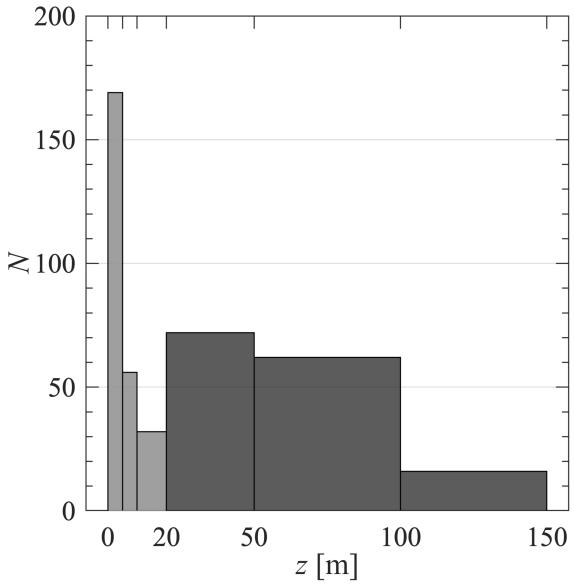


FIGURE 2
Histogram of sample depths z used in algorithm development dataset. Light grey denotes surface samples ($z \leq 20$ m) while dark grey denotes subsurface ($z > 20$ m).

2.5 Algorithm development

In Koestner et al. (2022), we examined several algorithm formulations and here we focus on only the best performing versions. One of the POC algorithms that we investigate is referred to as Model A which is a univariate model with b_{bp} acting as a sole estimator of POC. The general form of Model A is derived from a robust ordinary least squares regression applied to POC vs. b_{bp} data using a power function with $\log_{10}$-transformed b_{bp} and POC.

Another investigated POC algorithm is referred to as Model B which is a multivariable model. The form of Model B is an additive multiple linear regression equation with $\log_{10}$-transformed data and an interaction term: $\log_{10}\text{POC} = k_1 + k_2\log_{10}b_{bp} + k_3\log_{10}\varsigma + k_4 \log_{10}\varsigma \times \log_{10}b_{bp}$, where $\varsigma = \text{Chla}/b_{bp}$ is a composition proxy and k's are model coefficients. In this model, the second term (i.e., k_2b_{bp}) can be assumed to serve primarily as a measure of total particle concentration. The third and fourth terms relate to additional adjustments concerning bulk particulate composition based on the measurement of ς. In Koestner et al. (2022) this version of Model B was found to perform best when tested with an independent dataset. Note that all algorithm coefficients and independent variables are wavelength-dependent. Best-fit coefficients for Models A and B were computed using MATLAB's "regress" function with a robust fitting bisquare weighting function (tuning constant = 4.685).

A bias correction function was included to improve both Model A and Model B estimations for low POC as both models tended to systematically overestimate POC at low values. Two formulations of the bias correction function were determined only for cases in which estimated POC was less than 45 mg m^{-3}. These determinations were made using a Model-II linear regression of observed (measured) vs. algorithm-derived (estimated) POC with and without $\log_{10}$-transformation for power and linear versions. The bias correction function is $\text{POC} = f(\text{POC}^*)$, where superscript * indicates initial algorithm estimation. This correction was only applied if POC* was less than a certain threshold (ε_{min}) to avoid overestimation for POC greater than about 35 mg m^{-3}.

Prediction bounds for new algorithm estimations were computed using the coefficient covariance matrix (S) and mean-square error (MSE) determined from the regression analysis. The

prediction bounds were of the form $y \pm e$, where y is the best-fit model estimate of POC and e is the prediction uncertainty for a specific new estimation determined as $e = t\sqrt{MSE + xSx^T}$. In this equation, t depends on confidence level and can be calculated based on Student's t cumulative distribution function, x is a row vector of the algorithm inputs including a value of 1 in the first element (e.g., $x = [1\ b_{bp}]$ for Model A), and superscript T denotes transpose operation.

The entire dataset was used for deriving model coefficients, rather than randomly splitting the dataset into development and validation datasets as was done in Koestner et al. (2022). This choice was based on the primary goal of optimizing the estimates of model coefficients through the inclusion of all available data. Algorithms were developed and evaluated using either surface samples ($z \leq 20$ m) or the full dataset consisting of samples collected from all depths down to 150 m. Evaluation of algorithms used various statistical metrics to quantify and visualize uncertainty. Assessment metrics included root-mean-square deviation (RMSD), median absolute percent difference (MdAPD), median symmetric accuracy (MdSA), mean bias (MnB), and median ratio (MdR) as defined in Table 2. Coefficients of the Model-II linear regression of algorithm-derived (estimated) vs. observed (measured) POC are considered as an additional measure of algorithm performance and residual plots are also presented for additional examination of performance. A bootstrap resampling approach was also implemented in validation analysis to examine algorithm performance on 1,000 random subsets of the dataset. We utilized a subset size of 135 which was approximately one third of the full dataset and half of the surface dataset. This bootstrap procedure allows for replacement of each sample when randomly drawing a new sample to approximate 1,000 new sample populations or subsets. For each subset, statistical metrics were computed for evaluation of the variability as a function of the number of data subsets. We note that percentiles of most statistical metrics converged between 100 and 1,000 subsets.

TABLE 2 Model-assessment variables.

N or K	Number of samples or model coefficients
O_i or E_i	Observed or algorithm-derived value for sample i of N
$\bar{O}$ or $\bar{E}$	Mean value; $\bar{O} = \frac{1}{N}\sum_{i=1}^{N} O_i$, and likewise for $\bar{E}$
r	Pearson correlation coefficient; $\frac{\sum_{i=1}^{N}(O_i - \bar{O})(E_i - \bar{E})}{\sqrt{\sum_{i=1}^{N}(O_i - \bar{O})^2}\sqrt{\sum_{i=1}^{N}(E_i - \bar{E})^2}}$
Md	Median operator
R^2_{adj}	Adjusted coefficient of determination; $1 - \left(\frac{N-1}{N-K}\right)\frac{\sum_i (O_i - E_i)^2}{\sum_i (O_i - \bar{O})^2}$
RMSD	Root mean square deviation; $\sqrt{\frac{1}{N}\sum_{i=1}^{N}(E_i - O_i)^2}$
MdAPD	Median absolute percent difference; $\mathrm{Md}\left\lvert\frac{E_i - O_i}{O_i}\right\rvert \times 100\%$
MdSA	Median symmetric accuracy; $\left(10^{\mathrm{Md}\left\lvert\log_{10}\frac{E_i}{O_i}\right\rvert} - 1\right) \times 100\%$
MnB	Mean bias; $\frac{1}{N}\sum_{i=1}^{N}(E_i - O_i)$
MdR	Median ratio; $\mathrm{Md}(\frac{E_i}{O_i})$

2.6 BGC-Argo float data

BGC-Argo floats were deployed during the AMT-24 research cruise which surveyed an Atlantic Meridional Transect in the period September 24 – November 1, 2014. This cruise also involved a dedicated effort to evaluate uncertainties in POC throughout the water column down to 500 m (Sandoval et al., 2022). Data from six floats are available with vertical profiles of $b_{bp}(700)$ and Chla (derived from fluorescence measurements) and five of the six floats were programmed to cycle rapidly (approximately daily) after deployment. In total, 53 profiles are available with coincident $b_{bp}(700)$ and Chla that passed quality control efforts and were within the time-window of cruise operations. This results in a total of 19446 individual depth-resolved measurements available for analysis.

Float data were downloaded on September 2, 2023 from the British Oceanographic Data Centre, with the exception of one float (WMO ID 6901437) which was downloaded from the Coriolis data centre. Only adjusted Chla data which had quality control flags of 1, 2, 5, or 8 were used. The so-called "raw" $b_{bp}(700)$ measurements were used, also with the same quality control flags. All data were processed to remove large particle spikes for each profile according to the methodological approach outlined in Briggs et al. (2020). As such, the resulting $b_{bp}(700)$ and Chla refer to the signal from only "small" particles. A background level of $b_{bp}(700)$ and Chla was determined as the 5th percentile of values at 850–900 m from each float. This background is considered mainly as contributions from a pool of scattering or fluorescent material which appear nearly constant in the deep ocean in combination with uncertainties in manufacturer dark-counts (Poteau et al., 2017; Briggs et al., 2020). This background was removed from Chla (0.006 ± 0.003 mg m^{-3}) under the assumption that it is primarily driven by uncertainties in manufacturer dark-counts and any subsequent Chla values that were smaller than this background were set to 0 mg m^{-3}. The background was not removed from $b_{bp}(700)$ under the assumption that it is driven primarily by particulate scattering which should be included in POC. The background for $b_{bp}(700)$ is referred to as b_{bp}^{Δ} and was $2.0 \pm 0.4 \times 10^{-4}$ m^{-1}.

POC was estimated using Model B described in the current study utilizing all surface and subsurface data and referred to as Ko23. An adjustment factor of 0.9 was used to account for differences between HydroScat sensors used in algorithm development and ECO sensors

on floats (discussed further in section 4.3). For individual measurements when the composition term of Model B (ς = Chla/b_{bp}) was 0 mg m^{-2} because Chla was assumed negligible or undetectable, the ς was fixed to the minimum value from the vertical profile. Minimum values of ς were 22 ± 7 mg m^{-2}. An additional approach commonly used with BGC-Argo float data was also implemented as an alternate estimate of POC and is referred to as Ce12 (Cetinić et al., 2012). This approach uses fixed scaling factors to convert b_{bp}(700) to POC within the surface mixed layer (37537 mg C m^{-2}) and below the surface mixed layer (31519 mg C m^{-2}). The Ce12 scaling factors were determined using ECO sensors and over 300 samples collected during the 2008 North Atlantic Bloom Experiment in spring near 61° N, 26° W. One other approach was also used which accounts for vertical variability in the conversion of b_{bp}(700) to POC and is referred to as Ga22 (Galí et al., 2022). In brief, this approach assumes an exponential decrease of scaling factor from below the surface mixed layer based on a reanalysis of Cetinić et al. (2012) data by Bol et al. (2018). The surface value of the scaling factor was set to 58968 mg C m^{-2} based on Stramski et al. (2008) and an asymptote at depth was fixed to 12000 mg C m^{-2}. These values were assumed to be appropriate for the subtropical permanently stratified biomes (Galí et al., 2022). Surface mixed layer depths (MLDs) were determined as the depth corresponding to potential density differing by more than 0.03 kg/m^{-3} of value at 10 dbar. Note that Ga22 estimates in the epipelagic zone are sensitive to MLD methodology and a detailed analysis of such sensitivity is provided in Galí et al. (2022).

All float data were acquired within the subtropical permanently stratified biome (STPS), however additional classification is performed here in accordance with partitioning of data in Sandoval et al. (2022). Floats were spatially differentiated by ecological provinces within the Atlantic Ocean (Longhurst, 2007). The relevant provinces are North Atlantic Subtropical Gyre (NAST), North Atlantic Tropical Gyre (NATL), South Atlantic Gyre (SATL), and South Subtroptical Convergence (SSTC). Further, the water column was partitioned into epipelagic ($z \leq 200$ m) and mesopelagic ($200 < z < 500$ m) zones, again to correspond with depths evaluated in Sandoval et al. (2022).

3 Results

3.1 POC algorithms

Best fit model coefficients for univariate Model A and multivariable Model B are shown in Table 3 for b_{bp} at five wavelengths (i.e., 470, 532, 550, 660, and 700 nm) using only surface samples and separately for the full dataset consisting of samples collected from all depths down to 150 m. Figure 3 presents scatter plots describing Model A and Model B using three example wavelengths: 470, 550, and 700 nm. In Figures 3A, B, E, F, data for b_{bp}(470) and b_{bp}(700) are shown for the full dataset of surface and subsurface samples as these wavelengths are typically used with sensors on BGC-Argo floats and other autonomous platforms providing vertically-resolved water column observations. In Figures 3C, D, data for b_{bp}(550) are shown for only surface samples as 550 nm corresponds to an approximate wavelength commonly used with satellite measurement systems providing ocean color surface observations. Model A reasonably approximates the general trend of increasing POC with increasing b_{bp}, however there is a large scatter around the regression line (Figure 3). This scatter can generally be separated by particulate composition parameter, e.g., most datapoints with the darkest blue colors representing relatively low ς are typically below the regression line while lighter colors are often above the regression line. This can also be seen for the two highlighted cases in each panel referring to samples with similar POC around 100 mg m^{-3}, however one referring to a sample with low ς and another with high ς. There also appear no clear trends regarding region of sampling except generally larger deviations for samples from the NP ICE biome, which also tend to contain the largest contrast in terms of particle composition parameters (Figure 1B). It is worth noting that for the same dataset there is a wider range of b_{bp} for 700 nm compared with 470 nm (Figures 3E vs. 3A) which may provide advantages in terms of algorithm reliability in optically-clear waters. For example, when b_{bp}(470) = 0.0008 m^{-1} there are samples with POC ranging from 10 to 70 mg m^{-3} whereas b_{bp}(700) = 0.0008 m^{-1} corresponds to a smaller range of POC of about 30–70 mg m^{-3}. Model A coefficients decrease with increasing wavelength, with coefficients derived at 700 nm being about 10% lower than coefficients derived with 470 or 532 nm because of increasing backscattering with decreasing wavelength (Table 3). We also can see from Table 3 and Figure 3C that Model A determined with only surface data has notably larger coefficients indicating that for all wavelengths there is on average more POC per unit b_{bp} in samples from the surface compared with samples from all surface and subsurface depths.

Figure 3 also depicts 3-dimensional scatter plots with mesh-grids representing Model B results. The inclusion of an additional independent variable related to particle composition (i.e., ς) results in better representation of the POC data (e.g., R^2_{adj} = 0.79–0.87 for Model B and R^2_{adj} = 0.65–0.74 for Model A; Table 3). The mesh-grids detail steeper slopes of POC vs. b_{bp} for high ς compared with low ς (Figures 3B, D, E). In other words, for samples likely to have relatively high proportions of phytoplankton (high ς), larger values of POC are found for the same amount of particulate backscattering as compared with samples with a lower abundance of phytoplankton. This matches our expectation; non-phytoplankton particles can efficiently backscatter light, especially inorganic material that does not contribute to POC, and, conversely, phytoplankton particles generally contribute significantly to POC while having lower relative contribution to light backscattering. The ability of Model B to account for the variability in particle composition when estimating POC based on particulate backscattering and chlorophyll-a measurements can provide strong advantages for samples which vary in terms of particle composition, as is often the case in natural waters. Similarly, as seen with Model A, the Model B coefficients generally decrease with increasing wavelength and are notably larger when determined with surface samples compared to all samples (Table 3). Interestingly, k_3 for Model B, which refers to the exponent of the composition parameter, varies very little (less than 2%) for Model B determined

TABLE 3 Algorithms for estimating POC.

Model A: $POC^* \ [mg\ m^{-3}] = k_1 b_{bp}{}^{k_2}$							*Bias correction:* $POC = \begin{cases} f(POC^*), POC^* < \varepsilon_{min} \\ POC^*, POC^* \geq \varepsilon_{min} \end{cases}$		
λ	z_{max}	k_1	k_2	k_3	k_4	R^2_{adj}	ε_1	ε_2	ε_{min}
470	20	7148.85	0.7351	–	–	0.67	2.616	−2.565	38.6
470	150	2980.20	0.6160	-	-	0.62	3.040	−3.243	38.9
532	20	7967.85	0.7316	–	–	0.71	2.406	−2.220	38
532	150	3037.17	0.6022	-	-	0.65	2.763	−2.787	38.1
550	20	8202.78	0.7305	–	–	0.72	2.279	−2.018	37.8
550	150	3029.84	0.5975	-	-	0.65	2.691	−2.667	37.8
660	20	7318.58	0.6860	–	–	0.73	1.909	−1.429	37.3
660	150	2820.75	0.5636	-	-	0.67	2.044	−1.656	38.7
700	20	7004.89	0.6713	–	–	0.74	1.772	−1.217	37.7
700	150	2729.94	0.5518	-	-	0.67	1.918	−1.454	38.4
Model B: $POC^* \ [mg\ m^{-3}] = k_1\ b_{bp}{}^{k_2}\ \varsigma^{k_3}\ \varsigma^{k_4 \log b_{bp}}$									
470	20	516.93	0.5978	0.5687	0.0713	0.86	1.613	−0.953	35.8
470	150	98.05	0.2652	0.8448	0.2167	0.79	2.174	−1.843	37.1
532	20	331.11	0.5032	0.6617	0.1117	0.87	1.634	−0.983	35.5
532	150	65.78	0.1798	0.9147	0.2457	0.81	2.078	−1.676	35.8
550	20	295.24	0.4798	0.6855	0.1214	0.87	1.649	−1.003	35
550	150	60.46	0.1622	0.9247	0.2496	0.81	2.044	−1.618	35.4
660	20	191.79	0.3924	0.7402	0.1433	0.87	1.570	−0.878	34.8
660	150	50.59	0.1263	0.9104	0.2393	0.82	1.616	−0.956	35.5
700	20	181.77	0.3815	0.7357	0.1409	0.87	1.513	−0.793	35.2
700	150	52.82	0.1353	0.8849	0.2268	0.82	1.469	−0.734	36.8

Descriptions of Model A and Model B including formula and coefficients (k_1, k_2, k_3, and k_4) determined from regression analysis utilizing b_{bp} data at various light wavelengths λ [nm] and for two maximum depths z_{max} [m] restricting data. Here, surface algorithms correspond to z_{max} = 20 m while algorithms developed with the full dataset of surface and subsurface samples correspond to z_{max} = 150 m. Particulate composition term ς [mg m^{-2}] is calculated as Chla/b_{bp}, where b_{bp} is in units of m^{-1} and Chla is in units of mg m^{-3}. Coefficients for bias corrections are shown on the right for the power formulation described by $f(POC^*) = 10^{\varepsilon_2} \times POC^{*\varepsilon_1}$. Note that Model B is shown here following re-arrangement to remove most logarithms in support of applications.

using all data and light wavelengths of 532, 550, 660, and 700 nm (Table 3). This suggests that the weighting of this composition term in Model B can be quite consistent regardless of wavelength while all other coefficients account for variability associated with wavelength.

A positive bias for Model A and Model B can be observed in Figure 3, particularly when POC is lower than about 40 mg m^{-3}. Koestner et al. (2022) proposed a low-POC bias correction for Model B based on a linear function and we extend this approach to Model A along with two different formulations of the bias correction function. Figure 4 depicts scatter plots of uncorrected algorithm estimates of POC vs. measured POC with two functional fits of the data for bias correction (i.e., linear and power models). In Figure 4, we present results based on the algorithms determined with b_{bp}(550) and the full dataset to demonstrate trends in bias and we extrapolate bias correction functions to measured POC = 3 mg m^{-3} which can be considered a lower limit of detection for conventional POC methodology (Sandoval et al., 2022). Prior to bias-correction, Model B outperforms Model A in terms of accuracy (i.e., RMSD and MdSA) and bias (i.e., MnB and MdR) for POC < 60 mg m^{-3} (Figure 4). However, both models exhibit a positive bias in the range of POC < 60 mg m^{-3} (e.g., in this range MdR is 1.22 and 1.12 for Model A and Model B, respectively). After applying a bias correction, RMSD is quite consistent for both Model A and Model B, however Model A does have reduced MdSA (29% before and around 25% after correction in the range of POC < 60 mg m^{-3}). Of most importance, the positive aggregate bias in terms of MdR for POC < 60 mg m^{-3} is reduced to the ideal value of around 1 after bias correction (Figure 4). Although the differences between the application of linear or power functions for bias correction are minimal, we believe that the power function will be more reliable given that the linear bias correction can result in negative POC after correction if estimated POC is less than the *y*-intercept and the power function is generally more conservative for POC less than

10.3389/fmars.2023.1197953

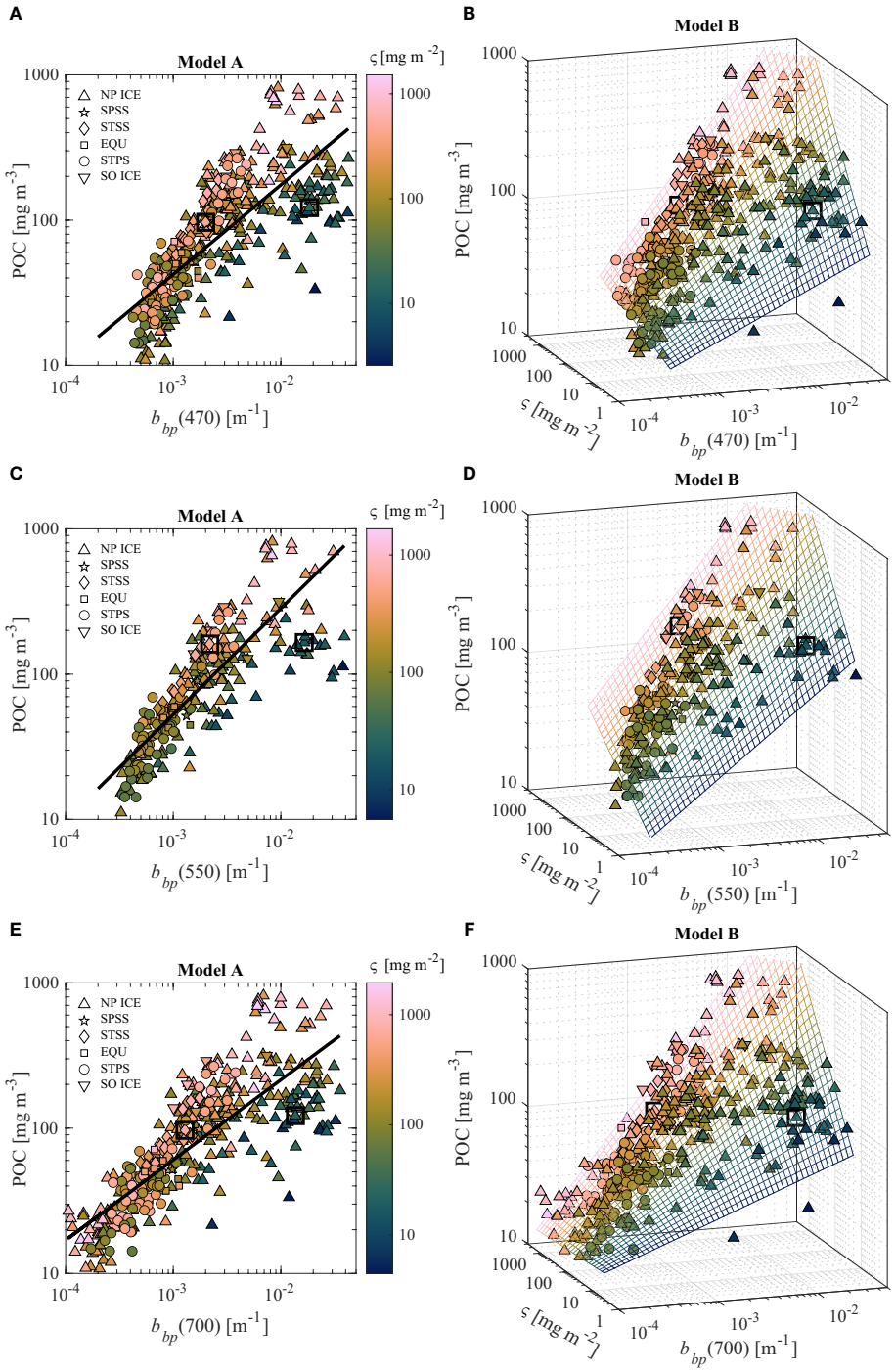


FIGURE 3
Univariate **(A, C, E)** and multivariable **(B, D, F)** algorithms to estimate POC utilizing light wavelength of 470, 550, and 700 nm. Algorithms in **(C, D)** utilize only surface samples for formulation (N = 257) while other algorithms utilize the entire dataset (N = 407). Data are color coded by the value of particle composition parameter ς = Chla/b_{bp}. Two data points which contrast in terms of ς but contain similar levels of POC are marked with a square for discussion purposes.

about 15 mg m^{-3} (Figure 4). Thus, we recommend the power function form for bias correction and accordingly provide model coefficients for this case in Table 3. We note that there are similar trends in terms of bias for other wavelengths except that there are generally smaller bias corrections for longer wavelengths (e.g., Table 3 and Figure 3).

3.2 Validation

In the following figures, we present results from validation exercises based on comparison of measured POC with bias-corrected estimates from Model A and Model B. In Figures 5–7, we describe statistical assessment of the six examples shown in

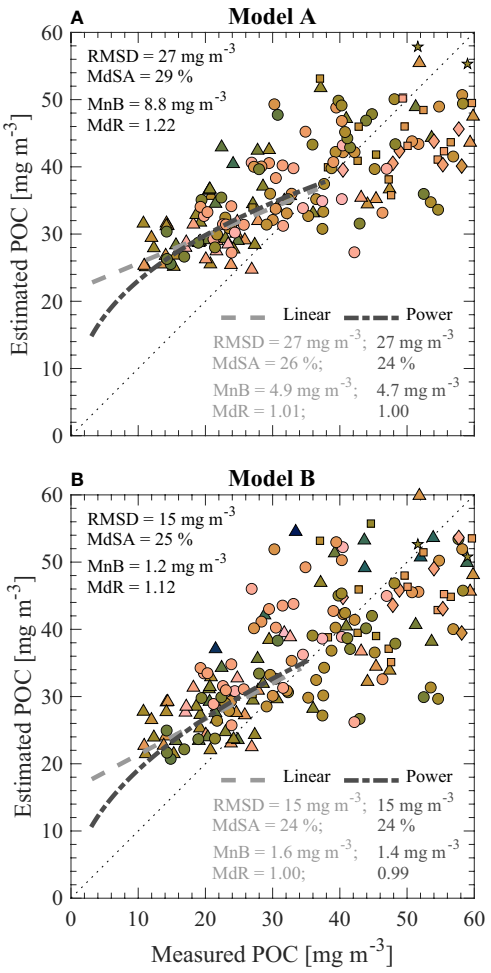


FIGURE 4
Example of algorithm-derived (estimated) vs. observed (measured) POC before any bias-correction for **(A)** Model A and **(B)** Model B developed using $b_{bp}(550)$ and the full dataset (N = 407). Statistical metrics are displayed and computed for measured POC< 60 mg m^{-3} (N = 189). Metrics displayed in top left refer to estimated POC before any bias-correction while numbers in bottom right denote metrics derived after applying the linear (light grey) and power (dark grey) functions for bias-correction. Note that bias correction functions are extrapolated to measured POC = 3 mg m^{-3}, a reasonable lower limit of detection for conventional POC methodology (Sandoval et al., 2022).

Figure 3 through comparison of estimated and measured POC. Next, we present a summary of the bootstrapping validation analysis for all model formulations (Figure 8). Finally, we take advantage of our relatively large dataset to assess other optical approaches for estimating POC found in the literature (Figure 9).

In Figures 5–7, multivariable Model B outperforms univariate Model A in terms of all statistical metrics evaluated over the entire dynamic range of the investigated dataset. This is the case for algorithms developed with the full dataset as well as only surface data (e.g., Figure 6). Although Model A performs reasonably well for POC less than about 100 mg m^{-3}, there is a clear compositional dependence on performance where more algal-dominated (i.e., high ς value) samples tend to be underestimated and nonalgal dominated (i.e., low ς value) samples are overestimated (e.g., Figure 5C). This issue is not as apparent for Model B where there are no clear trends of over- and underestimation in terms of particle composition (e.g., Figure 5D). The major improvements in Model B can also be observed when examining the cluster of samples with low or high ς values from the Arctic which have Model A estimated POC of around 200–300 mg m^{-3} (e.g., Figure 5A). Whereas Model A greatly overestimates the datapoints with low composition values and underestimates the datapoints with high composition values, Model B is able to correctly adjust its estimates of POC much closer along the 1:1 line due to the inclusion of composition-specific independent variable ς (e.g., Figure 5B). Furthermore, the two contrasting samples from completely different oceanic biomes (i.e., Atlantic Ocean STSS and Arctic Ocean NP ICE near Alaska) shown in Figures 5–7 are correctly estimated by Model B (less than about 3% differences from measured POC) while they are incorrectly estimated by Model A (about 30% to over 100% differences from measured POC).

In the current study, our primary emphasis is on optimizing the determination of algorithm coefficients by using a relatively large dataset containing available measurements from diverse oceanic conditions. Thus, we did not split the available dataset into independent subsets of data for algorithm development and validation purposes, as was done in Koestner et al. (2022). In this study, we employed a bootstrap resampling approach to investigate algorithm performance on random subsets of the entire algorithm development dataset. Figure 8 presents a summary of this analysis focusing on the variability in four statistical metrics derived from the 1,000 subsets and using all algorithm formulations in Table 3. Here, we focus on RMSD and MdSA for quantifying magnitude of the random component of uncertainty while MnB and MdR are used to describe bias. Again, Model B has lower uncertainty and less bias for all formulations when compared with Model A for the overwhelming majority of random subsets (Figure 8). In terms of uncertainty magnitude, Model B typically has MdSA of 20–35% and RMSD of about 70–110 mg m^{-3} depending on wavelength and dataset utilized. For example, there are somewhat larger MdSA values (rarely below 25%) for Model B developed and tested with the full dataset while median values of MdSA are around 22% when considering only surface data. Differences associated with wavelength utilized are minor, however when considering Model B formulated with the full dataset, there may be some small advantages in terms of MdR when utilizing λ = 660 or 700 nm (Figure 8). Spectral differences are even smaller when considering surface-only algorithms.

Figure 9 depicts comparisons of measured POC with algorithm-derived (estimated) POC using four other algorithms found in the literature. Two algorithms presented here (i.e., Stramski et al., 1999 and Stramski et al., 2008) were developed using a small portion of the data included in the present study, however, they are tested on the entire dataset of surface samples consolidated for the current study. The Loisel et al. (2002) algorithm combines two approaches: one to estimate the scattering coefficient based on the backscattering coefficient and Chla (Twardowski et al., 2001) and another to relate the scattering coefficient to POC (Claustre et al., 1999). These three algorithms are evaluated for only surface data as they have been proposed as potential candidate algorithms for estimating POC based on remote-sensing reflectance observations (Loisel et al.,

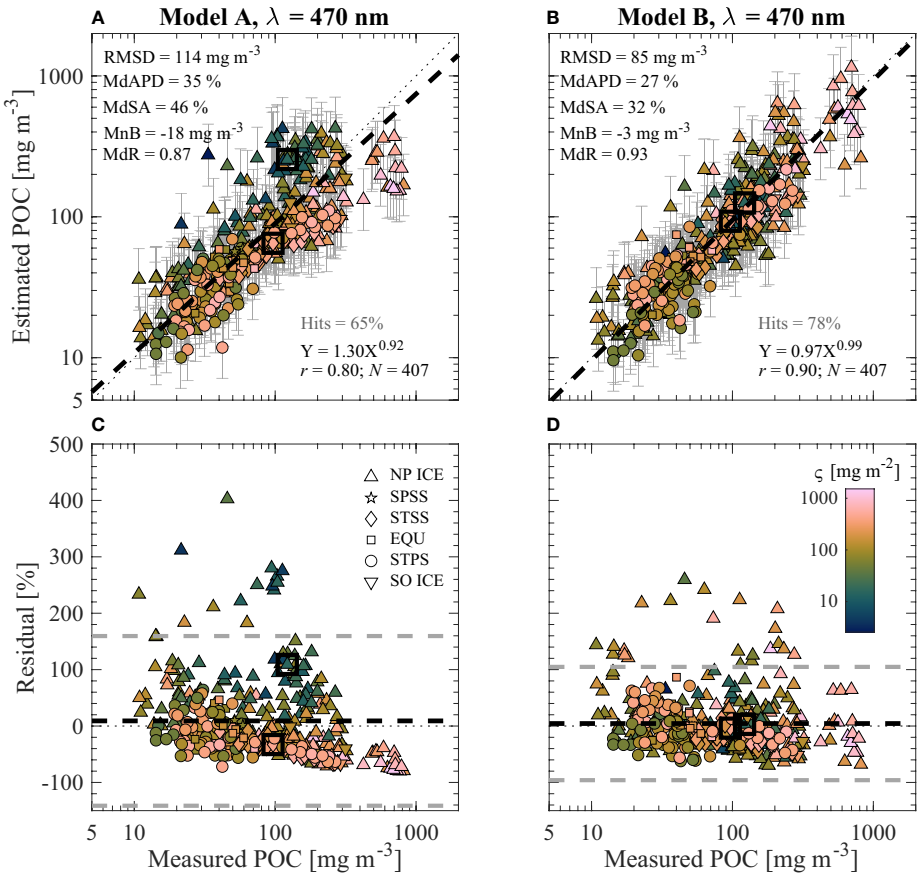


FIGURE 5
Validation of **(A, C)** Model A and **(B, D)** Model B through comparison of algorithm-derived (estimated) and observed (measured) POC for bias-corrected estimates from algorithms utilizing $b_{bp}(470)$ and the full dataset shown in Figures 3A, B. Data are color coded by the particle composition parameter ς described by color bar in **(D)**. Two data points are marked with a square to illustrate effectiveness of Model B with contrasting particle composition. **(A, B)** Algorithm-derived (estimated) vs. observed (measured) POC. Statistical metrics described in Table 2 and derived from this comparison are shown. Model-II linear regressions of $\log_{10}$-transformed data are displayed with a dashed line and equation is shown, where X and Y refer to measured and estimated POC, respectively. A 1:1 dotted line is plotted for reference. Hits describe the percentage of datapoints whose prediction error bars (two-tailed, α = 0.125) contain the measured value. **(C, D)** Residual plots from data in panel above. Percent residuals are defined as 100% × (Estimated POC − Measured POC)/Measured POC. Black dashed line represents mean residual value while grey dashed lines represent approximate 95% confidence limits of residuals (i.e., mean ± 1.96 standard deviations).

2002; Stramski et al., 2008; Evers-King et al., 2017). The fourth algorithm is from Cetinić et al. (2012) and has been commonly used to estimate POC with *in situ* measurements from platforms such as BGC-Argo; thus, we present evaluation based on the full dataset with sample depths down to 150 m. Although all algorithm estimates have some regions of reasonable agreement with POC measured using standard methodology (typically around 100 mg m^{-3}), there are large deviations resulting in relatively high values of some aggregate statistical metrics (Figure 9). These relatively simple approaches may produce reasonably good estimations for water types similar to those used in the algorithm development, however large uncertainties are observed when considering the wide range of contrasting optical and particle properties in our dataset. The advantage of Model B to adapt to a variety of environments can offer useful advantages when examining POC estimates from optical measurements collected across diverse water bodies including large ocean scales.

Finally, we consider comparisons of the 700 nm version of Model B from our previous study (Ko22; Koestner et al., 2022) with the current formulation determined with the larger dataset of surface and subsurface samples. Coefficients from the current study are somewhat different (e.g., k_1 and k_2 are smaller while k_3 and k_4 are larger compared to Ko22). In terms of aggregate statistics based on analysis with the full dataset, there are no appreciable differences between the formulation from Ko22 and the current version (e.g., RMSD = 68 mg m^{-3}, MdAPD = 25%, MdSA = 29%, MnB = −6 mg m^{-3}, and MdR = 1.01 for Ko22; compare with current values in Figure 6B). Generally, the largest differences between the two models relate to about a 10% underestimation of POC for highest composition values and about a 10% overestimation for lowest composition values in the Ko22 model compared with current Model B estimations. There are some additional differences when considering POC < 35 mg m^{-3} which relate more directly to the use of bias correction recalling that Ko22 utilized a linear bias correction function. We expect some of the above-mentioned differences to relate to refinements in Chla data from ANTXXVI/4 cruise as well as the addition of some "new" data and application of several inclusion/exclusion criteria in the

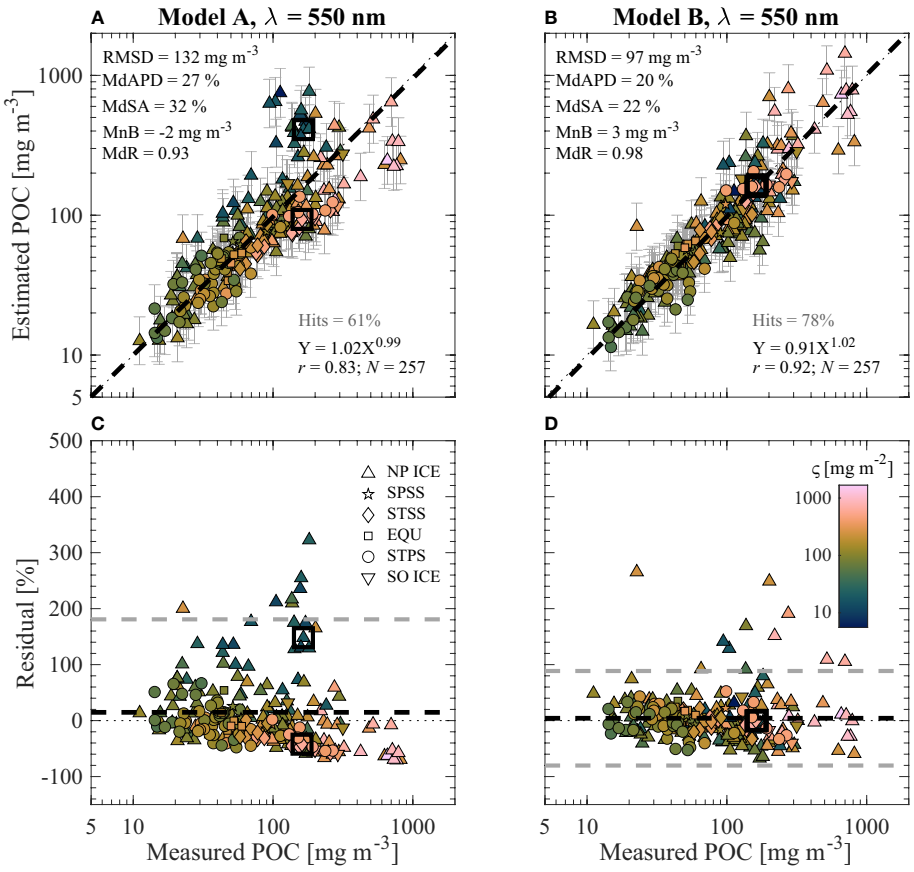


FIGURE 6
Similar to Figure 5 but utilizing algorithms for b_{bp}(550) developed with only surface data shown in Figures 3C, D.

compilation of the dataset for the current study. Additionally, current Model B coefficients all have smaller uncertainty (in terms of 95% confidence intervals) and are more statistically significant (in terms of *p*-value) compared with coefficients in Ko22. For example, current coefficients have confidence intervals which are between 30% and 180% of their best-fit coefficient value and *p*-values less than 10^{-16}, apart from k_2 with a *p*-value of 0.03. For Ko22 coefficients, confidence intervals were nearly twice as large (60–280% of their best-fit coefficient value) and *p*-values were less than 10^{-5} with the exception of k_2 with a *p*-value of 0.06. As a result, we recommend use of the current formulation of Model B.

4 Discussion

4.1 Depth dependencies

As seen in Table 3, there are noticeable differences in algorithm coefficients derived using only surface data compared with the full dataset. We also found that algorithms developed and tested with only surface data generally had improvements in the model performance (Figure 8). It is desirable to apply a single approach when making assessments of the vertical structure of POC with *in situ* measurements; therefore, we examine how well Model A and Model B perform with surface data when developed with the full dataset in Figure 10. Overall, these algorithms perform well when examining only surface data. For example, Model B estimations typically differ by less than about 25% from measured POC in terms of MdAPD and MdSA (Figures 10B, D). Surprisingly, when evaluating the surface data, RMSD is lower for the algorithms developed with the full dataset compared with versions developed with only surface data (e.g., Figures 10A, B vs. 6A, B). We believe this counterintuitive reduction in RMSD illustrates that RMSD is not always a reliable measure of performance as it is not a proportional or symmetric metric because larger magnitude errors are more heavily weighted. Unlike the algorithm versions developed with only surface data, the Model B algorithms presented in Figure 10 display systematic underestimation as seen with MnB of about –20 mg m^{-3} and MdR around 0.82–0.86. Moreover, this underestimation is quite small for lower POC but worsening with increasing POC as illustrated with the linear regression line of estimated vs. measured POC (Figures 10B, D). Importantly, we recall that the majority of the surface samples are from depths less than 5 m (Figure 2), and these biases are likely minor when considering large portions of the water column including the epipelagic layer or deeper. Nonetheless, we generally recommend using the model coefficients derived with only surface samples when the investigation is focused on surface waters, for example with

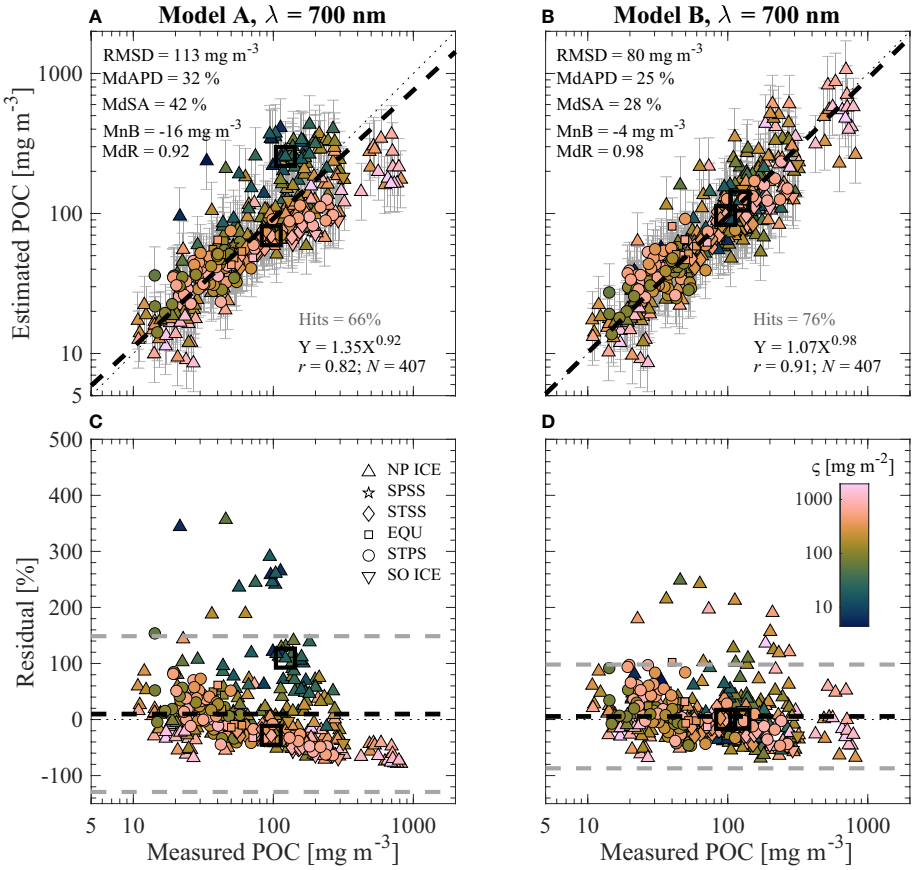


FIGURE 7
Similar to Figure 5 but utilizing algorithms for b_{bp}(700) developed with the full dataset shown in Figures 3E, F.

satellite or other above-water observation systems. When the investigation is focused on vertically-resolved measurements within the water column (for example with BGC-Argo floats or gliders), we recommend using model coefficients derived with the full dataset of surface and subsurface samples.

4.2 Biomes

Our algorithm development dataset is composed of samples collected in 6 oceanic biomes, however samples are not evenly distributed among these biomes and across all seasons (Figure 1B and Table 1). For example, only 4 samples are in the subpolar seasonally stratified biome (3 of which are from the Southern Ocean), and only 6 samples are in the Southern Ocean marginal sea ice biome. A large portion of the data is from the North Pacific marginal sea ice biome which importantly incorporates samples which are not organic-dominated and not algal-dominated into the dataset (Figure 1B). This contributed to a compositionally diverse dataset for algorithm development, however, it may produce some bias when examining other samples in other biomes. Here, we examine the uncertainties in POC estimations within each biome separately using Model A and Model B from the current study, as well as four algorithms from the literature which have already been shown in Figure 9.

Figure 11 depicts the statistical variability in percent difference of algorithm estimates from measured POC. Model B outperforms nearly all algorithms for the four main biomes sampled, with the exception of the subtropical seasonally and permanently stratified biomes (STSS and STPS) where Stramski et al. (2008) and Stramski et al. (1999) algorithms respectively display minor improvements (Figure 11). Of note, Model B performs well in the NP ICE, EQU, and STPS biomes, where median percent differences are less than 5%. Based on this dataset, it appears that Model A and Model B have the largest biases in the STSS and SO ICE biomes in that over 75% of the samples have POC underestimations by more than about 10%. This difference is largest in SO ICE with a median underestimation of 35% for Model B (noting that only 6 samples are available for this analysis). In STSS, median underestimation for Model B is only 14%. The Ce12 algorithm consistently produces large underestimations (>25% for majority of samples and >50% for most biomes). We suspect this result may be associated with differences in POC methodology (IOCCG Protocol Series, 2021; Sandoval et al., 2022) and backscattering instrumentation (e.g., Erickson et al., 2022), and the fact that the Ce12 dataset was collected in the North Atlantic subpolar seasonally stratified (SPSS) biome during spring. Although Model B performs well in the SPSS

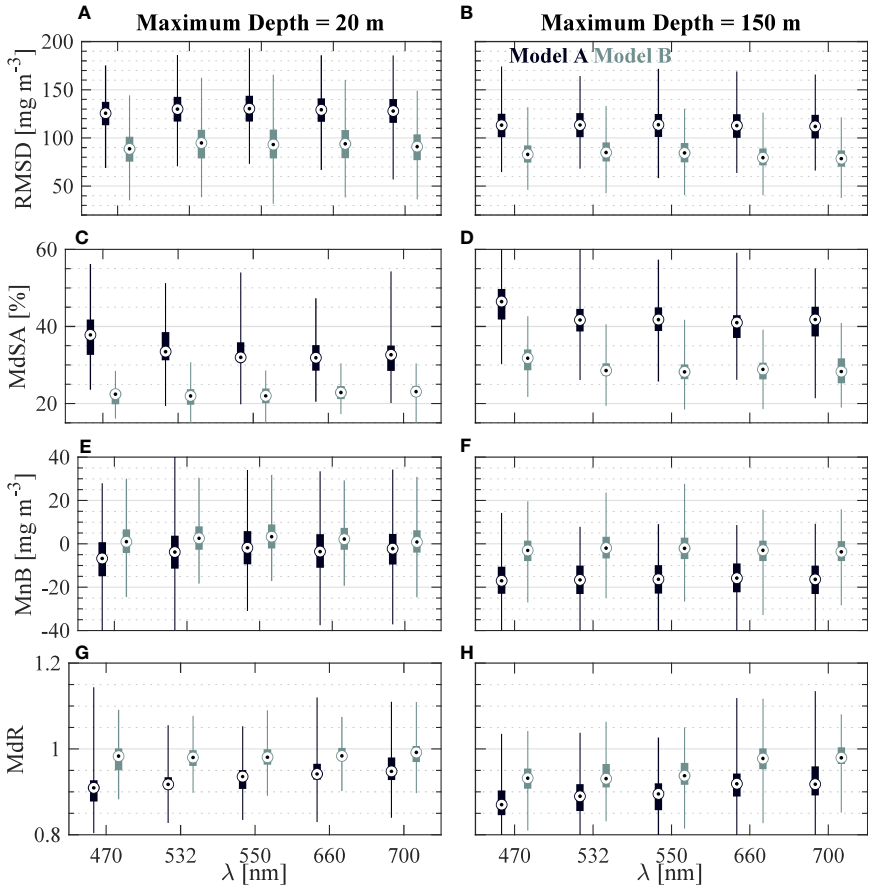


FIGURE 8
Nonparametric box plots summarizing performance of all algorithms using a bootstrap sampling approach for validation statistics. In each box plot, whiskers represent the entire range while the box contains the semi-interquartile range and circles denote median. Box plots are derived based on 1,000 repetitions of random sampling of 135 datapoints with replacement allowed. **(A, C, E, G)** Statistics for the algorithms developed with only surface data. **(B, D, F, H)** Statistics for the algorithms developed with full dataset.

biome (Figure 11), we acknowledge that only 4 samples are available for the current study. Further investigation and inclusion of more data, especially from the SPSS and SO ICE biomes and all biomes during winter months, is highly desirable to support potential refinements of algorithms and more comprehensive validation.

4.3 Uncertainties and implications to applications

The algorithm development dataset mainly utilized Chla derived from HPLC analysis and spectral b_{bp} derived at 6 to 11 wavelengths with HydroScat-6 instruments (HS-6). This was to avoid additional uncertainties and establish reliable algorithms describing the relationships between spectral b_{bp}, particle composition approximated with ς = Chla/b_{bp}, and POC. In most applications, however, Chla will be retrieved from either *in situ* fluorometric measurements or ocean color remote sensing observations and b_{bp} will be retrieved from *in situ* scattering measurements (most likely with different instruments) or satellite observations including lidar or passive ocean color remote sensing. Here, we discuss some of the potential uncertainties associated with different sources of algorithm inputs and how they may impact applications of Model B to estimate POC.

In situ fluorometric estimates of Chla have been shown to contain systematic biases when compared with HPLC-derived Chla and significant efforts have been made to reduce these uncertainties (e.g., Xing et al., 2012; Roesler et al., 2017; Xing et al., 2017). With regards to processing of *in situ* fluorometric data from ECO-series fluorometers on BGC-Argo floats, a community-established bias factor of 2 is often applied, however it has been shown to be as high as 4–6 in various oceanographic regions (Roesler et al., 2017). Routinely implemented algorithms which estimate Chla from current satellite ocean color observations achieve median absolute errors of up to 60–70% based on analysis of over 2000 satellite and *in situ* matchups spanning the global oceans (O'Reilly and Werdell, 2019). For the purposes of illustrating propagation of uncertainty in Chla to Model B estimations of POC, we assume a 65% error for Chla. For this case, the resulting uncertainty in POC estimated from Model B is typically much less than 65%. For example using realistic values for productive ocean surface water of $b_{bp}(700) = 0.001$ m^{-1} and Chla = 0.5 mg m^{-3}, the Model B estimate of POC is about 74 mg m^{-3} with a prediction interval of 46–118 mg m^{-3} (approximately 75% confidence). Assuming that Chla is 65% larger, POC estimation

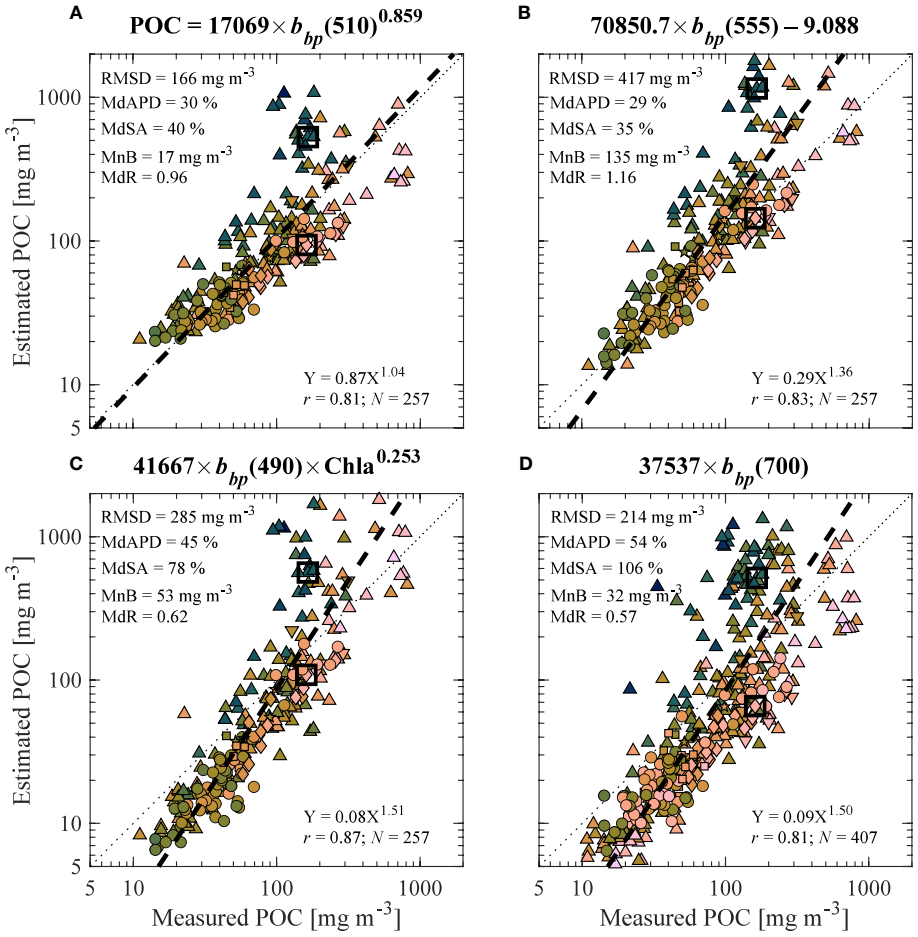


FIGURE 9
Validation results similar to Figures 5A, B comparing algorithm-derived (estimated) and observed (measured) POC using four previously published approaches relating b_{bp} to POC: **(A)** Stramski et al. (1999) using data from Antarctic Polar Front Zone, **(B)** Stramski et al. (2008) using data from the Pacific and Atlantic Oceans and subtraction of backscattering by pure water according to Buiteveld et al. (1994) with additional correction for salinity of pure seawater, **(C)** Loisel et al. (2002), and **(D)** Cetinić et al. (2012) using only the slope of POC vs. b_{bp}(700) for downcast data within the oceanic mixed layer. Equations are shown above each panel and **(D)** includes the full dataset from the present study while the other relationships in **(A–C)** are examined only with surface data from the present study.

only increases by about 11% to 82 mg m^{-3} which is well within the prediction interval. This suggests relatively weak sensitivity of algorithm estimates of POC to uncertainty in Chla.

Regarding b_{bp} uncertainty, a community standard similar to HPLC for Chla does not yet exist. Estimating b_{bp} with single-angle backscattering measurements is expected to result in errors typically less than 10% (Boss and Pegau, 2001; Sullivan et al., 2013). Analysis of over 16,000 BGC-Argo float profiles found approximately 30–50% differences when comparing median values of b_{bp}(700) between 900–950 m from 200 floats which were equipped with one of three sensor types (Poteau et al., 2017). For satellite-based retrievals of b_{bp} from lidar or passive ocean color observations, 20–50% uncertainty is reasonable based on limited comparisons of satellite b_{bp} retrievals and *in situ* measurements (Loisel et al., 2018; Bisson et al., 2021; McKinna et al., 2021). Here we also acknowledge that uncertainties in b_{bp} retrievals from lidar or passive ocean color observations are dependent on wavelength as well as statistical approaches utilized in defining uncertainty and accepted "true" *in situ* b_{bp} values. Nevertheless, if we assume that b_{bp}(700) is 30% higher, POC estimated from Model B using the above example is about 85 mg m^{-3}, an increase of about 15%. Again, this exemplifies the robustness of Model B estimations. Finally, combining 30% and 65% overestimations for b_{bp} and Chla, respectively, we find that Model B estimated POC is about 95 mg m^{-3}, an overestimation of 27% but still within the prediction interval defined above.

We also acknowledge that differences have been observed between HS-6 and other backscattering sensors likely owing to differences in instrument calibration procedures, data processing, and instrument geometries. For example, Erickson et al. (2022) observed lower values by about 30% on average for b_{bp}(700) from HS-6 when compared with ECO sensors (two or three channel sensors formerly produced by WET Labs, currently Sea-Bird Scientific) which are typically deployed on BGC-Argo floats and gliders. This comparison involved intercomparison of several backscattering sensors deployed during the EXPORTS field campaign in the North Pacific Ocean. In contrast, Twardowski et al. (2007) observed good agreement in very clear South Pacific Ocean waters during the BIOSOPE cruise with HS-6 b_{bp}(470) about

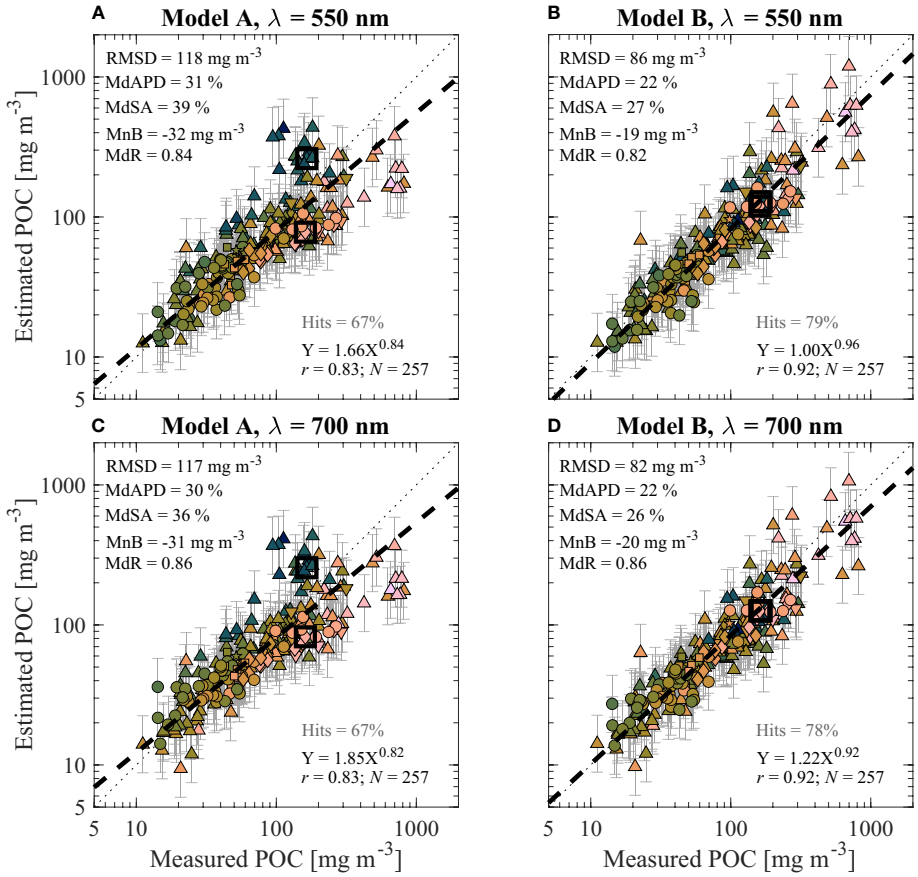


FIGURE 10
Validation results similar to Figures 5A, B comparing algorithm-derived (estimated) and observed (measured) POC for only surface data using algorithms developed with the full dataset. Descriptions regarding algorithm used (i.e., model and wavelength of b_{bp}) are above each panel. **(A)** Model A, λ = 550 nm. **(B)** Model B, λ = 550 nm. **(C)** Model A, λ = 700 nm. **(D)** Model B, λ = 700 nm.

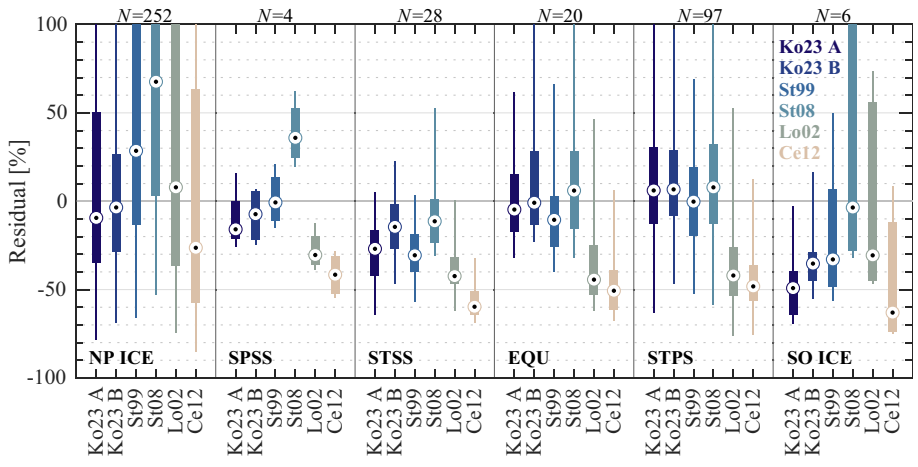


FIGURE 11
Nonparametric box plots summarizing performance of various POC algorithms for available data within each oceanic biome as indicated. In each box plot, whiskers represent the entire range while the box contains the semi-interquartile range and circles denote median. All surface and subsurface data are used to derive percent residuals, defined as 100% x (Estimated POC – Measured POC)/Measured POC. Ko23 A and Ko23 B refer to Model A and Model B from current study utilizing λ = 700 nm and the entire dataset. The four additional algorithms are described in Figure 9 noting that St99 refers to Stramski et al. (1999), St08 refers to Stramski et al. (2008), Lo02 refers to Loisel et al. (2002), and Ce12 refers to Cetinić et al. (2012).

4% lower on average than b_{bp}(462) from an ECO-BB3. Similarly, others found that b_{bp}(530) from an HS-6 was also about 3% lower than the ECO-VSF b_{bp}(532) in very clear waters of Crater Lake Oregon (Boss et al., 2007) and less than 2% lower for coastal shelf waters in the Mid-Atlantic Bight (Boss et al., 2004). Note that the ECO-VSF instrument is somewhat different than other ECO sensors as it measures scattering at three angles from the incident light direction at approximately 104°, 124°, and 151° whereas other ECO sensors typically measure scattering of light at one scattering angle (usually approximately 124° or 142° from incident direction). In our own, but limited, studies we have observed differences for b_{bp}(700) from HS-6 (close to 12% lower on average) compared to an ECO-Triplet deployed on the same optical package for 12 stations in coastal Alaska. We also observed a 1–26% (median of 10%) lower b_{bp}(532) from HS-6 compared with the LISST-VSF (Sequoia Scientific) based on a 40-minute time series of simultaneous measurements off the Scripps Institution of Oceanography Pier in La Jolla, California where LISST-VSF-derived b_{bp}(532) was about 0.0085 m^{-1}. Unlike other scattering instruments, the LISST-VSF measures backscattered light from 90–150° in 1° increments and therefore requires less assumptions about the shape of the angular scattering function than other single or multi-angle sensors (Koestner et al., 2018). We expect the above-mentioned differences in b_{bp} are mainly related to data processing steps including assumptions about angular scattering function, pure water and baseline subtraction, calibration scaling factors, and corrections for losses along path to and from the sample volume. Overall, however, the HS-6 instrument appears to yield systematically lower values of b_{bp} when compared with several different instruments. Therefore, when applying algorithms developed entirely with HS-6 data (such as Model A and Model B from the current study) to b_{bp} measurements from other backscattering sensors, a normalizing factor for b_{bp} can be considered. For example, applying a multiplicative factor of 0.9 to measurements with ECO-like instruments may provide a reasonable average factor accounting for these differences. However, we recommend caution if applying this factor as it will likely depend on data processing, specifics of the sensor, and particulate and optical properties of seawater. Importantly, this will not result in the reduction of POC by the same factor; rather it is often a smaller change in POC dependent on Chla and b_{bp}. For example, using the case described in the previous paragraphs, multiplication of b_{bp} by 0.9 results in POC of about 70 mg m^{-3}, or a reduction of approximately 5%.

There are some additional considerations when applying Model B to measurements in optically clear waters such as deep waters in the mesopelagic zone below 200 m or ultraoligotrophic surface waters often surveyed with BGC-Argo floats. Our algorithm development dataset did not include any samples deeper than 150 m (Figure 2) and mesopelagic POC values are generally expected to be near the lower limit of 10 mg m^{-3} utilized in our algorithm development (e.g., Sandoval et al., 2022). For this reason, we expect the choice of bias correction function will strongly influence algorithm estimations of mesopelagic POC less than about 20 mg m^{-3} (see Figure 4), as will the treatment of data in terms of background subtraction, spike removal, vertical averaging, and inclusion of POC estimates outside of the algorithm development range. Additionally, instrument sensitivity and calibration will also play a more significant role when backscattering signals become very low in the mesopelagic or very clear surface waters. Finally, reliance of the particulate composition term on Chla inherently carries some challenges when considering that mesopelagic waters usually have low ς values regardless of their nature as the composition term is likely poor at distinguishing between nonalgal type, whether it be inorganic and contributing nothing to POC (e.g., calcium carbonate or silica) or organic with no chlorophyll-a content but contributing to POC (e.g., detrital material or heterotrophic bacteria). We recommend fixing ς to some minimum value if Chla is effectively zero (i.e., below detection limit), and when vertical profiles of measurements are available, it is appropriate to use a minimum nonzero value of ς determined from the profile. Furthermore, we also recommend fixing ς to a value of 2000 mg m^{-2} at a maximum because values higher than this are unlikely to be observed in the ocean (e.g., Figure 1B; Barbieux et al., 2018) and can be related to very low signal from both Chla and b_{bp}.

Finally, it is of the utmost importance to recognize that POC is an operationally-defined parameter, whereas b_{bp} is defined more precisely as the backscattering coefficient with contributions of pure water and dissolved salts removed. Operationally, POC is the "particulate" pool of organic carbon usually defined as the mass concentration of organic carbon retained on GF/F filters with a nominal 0.7 µm pore size. Typically, some amount of truly "dissolved" carbon is also included in the POC due to adsorption of dissolved organic carbon (DOC) to the GF/F filters (Moran et al., 1999; Novak et al., 2018). This adsorption effect is typically minimized by (1) filtering a sufficient volume of water so that the "particulate" signal retained on the filter overwhelms the adsorbed "dissolved" signal, and/or (2) subtracting a "wet" blank filter created with GF/F filtrate (IOCCG Protocol Series, 2021). The POC used in the current algorithm development dataset mostly did not include any subtraction of a "wet" blank, but rather filtration of large volumes of seawater which may still introduce some positive bias of POC due to DOC adsorption, likely by at most 10 to 20% (Stramski et al., 2022). Very importantly, however, the correction for DOC adsorption was purposefully not made because the measurement of POC on GF/F filters is missing some portion of carbon from colloidal particles which contributes to *total* POC (e.g., small bacteria and phytoplankton cells, viruses, and other small-sized detrital material). This missing portion of POC, in addition to other sources of negative bias, leads to an underestimation of *total* POC which is expected to largely balance the positive biasing effect due to uncorrected adsorption of truly dissolved DOC. Thus, the resultant estimate of measured POC without correction for DOC-adsorption is expected to provide a closer agreement with *total* POC (including all suspended particles) compared to POC measurement corrected for DOC-adsorption alone (Stramski et al., 2022). This is critical from the standpoint of relating measured POC to measured optical properties. In particular, the measured b_{bp} is, in principle, influenced by *all* particles, including a portion of small colloidal particles not included in POC collected on GF/F filters (Organelli et al., 2018; Stramski et al., 2004; Stramski and Woźniak, 2005; Zhang et al., 2020). It is therefore sensible to correlate the measured b_{bp} associated with *all* particles with the best possible estimate of *total* POC. This distinction is important to consider when comparing

results of Model A or Model B with other estimates of POC, either from measurement results with GF/F filters from other studies or from biogeochemical modeling results (e.g., Galí et al., 2022; Wang and Fennel, 2023), as we consider our algorithms to provide optimal estimates of *total* POC with the currently available methodology of POC determinations on GF/F filters.

4.4 Application to BGC-Argo floats

The AMT-24 research cruise provided a unique opportunity to examine an independent dataset spanning several distinct ecological provinces within the subtropical permanently stratified (STPS) biome of the Atlantic Ocean in late 2014. Here, POC estimates from optical measurements on BGC-Argo floats are compared with POC derived from traditional discrete water sampling to depths of 500 m made during the cruise (Sandoval et al., 2022). Importantly, we note that Sandoval et al. (2022) utilized a DOC-adsorption correction for POC based on the double-filter method which reduced POC by about 10–20% due to presumed adsorption of DOC.

A summary of BGC-Argo floats and the AMT-24 cruise is shown in Figure 12A and corresponding vertical profiles of POC derived from our present Model B (hereafter referred to as Ko23) are shown in Figure 12B. We note that only float profiles within the time-window of cruise operations are examined here. Each ecological province appears to have distinct vertical POC profiles and individual float profiles are generally consistent within each ecological province; however, some differences are observed. For example, the depth associated with maximum POC for the two floats in North Atlantic Tropical Gyre (NATL) vary, while differences are seen for individual profiles within the South Subtropical Convergence (SSTC) province (Figure 12B). We acknowledge that the float in SSTC was on the border of two biomes (i.e., seasonally and permanently stratified subtropical), which may explain some of the extra variability at this location. Nonetheless, these differences are minor when considering the spread of values within the entire epipelagic and mesopelagic zones.

In Figure 13, we present the statistical distributions of POC estimations from float data within the epipelagic and mesopelagic zones of each ecological province. Estimations of POC from BGC-Argo floats using approaches described by Galí et al. (2022), referred to as Ga22, and Cetinić et al. (2012), referred to as Ce12, are also shown. Overall, all three approaches (i.e., Ko23, Ga22, and Ce12) reproduce the general trend of largest POC values in the SSTC (Figure 13A). Most Ko23 estimates in the epipelagic zone are within the values from Sandoval et al. (2022), except for the North and South Atlantic Tropical Gyres (NATL and SATL) where Ko23 tends to provide larger estimates of POC (Figure 13A). Importantly, the SATL province is large spanning approximately 5°–35° S in latitude and POC measurements by Sandoval et al. (2022) are based on only 2–4 discrete depths in the epipelagic zone. In the SATL province, the median POC from Ko23 is 33 mg m^{-3} and we note that similar values (22–28 mg m^{-3}) were observed by Sandoval et al. (2022) near the float locations. Similarly in the NATL province, the highest values reported by Sandoval et al. (2022) were found near the float locations (35–46 mg m^{-3}), which are similar to the 50th to 75th percentile POC values from Ko23 of 37–46 mg m^{-3}. When considering Ga22 and Ce12 results, we find that both estimates are generally in agreement with the data from Sandoval et al. (2022)

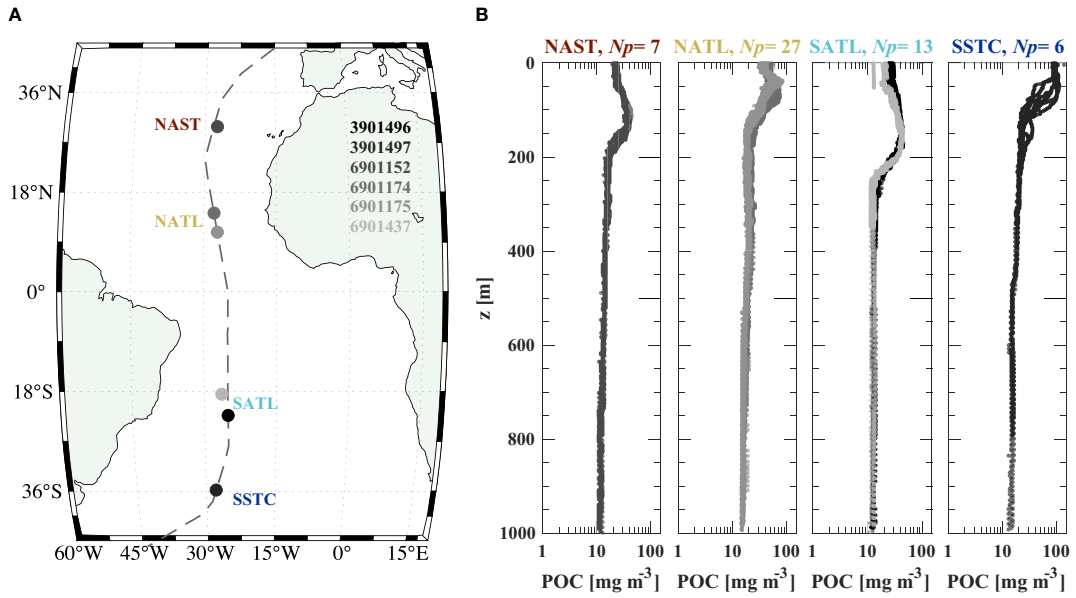


FIGURE 12
(A) Map of BGC-Argo floats (circles) coincident with the AMT-24 cruise (dashed line) for 24 September – 1 November, 2014. World Meteorological Organization IDs of floats are displayed, and ecological provinces are marked; North Atlantic Subtropical Gyre (NAST), North Atlantic Tropical Gyre (NATL), South Atlantic Gyre (SATL), and South Subtropical Convergence (SSTC). **(B)** Vertical profiles of POC estimated from Model B of the current study (Table 3; λ = 700 nm, full dataset of surface and subsurface samples). Profiles are grouped by ecological province and number of profiles (*Np*) is provided.

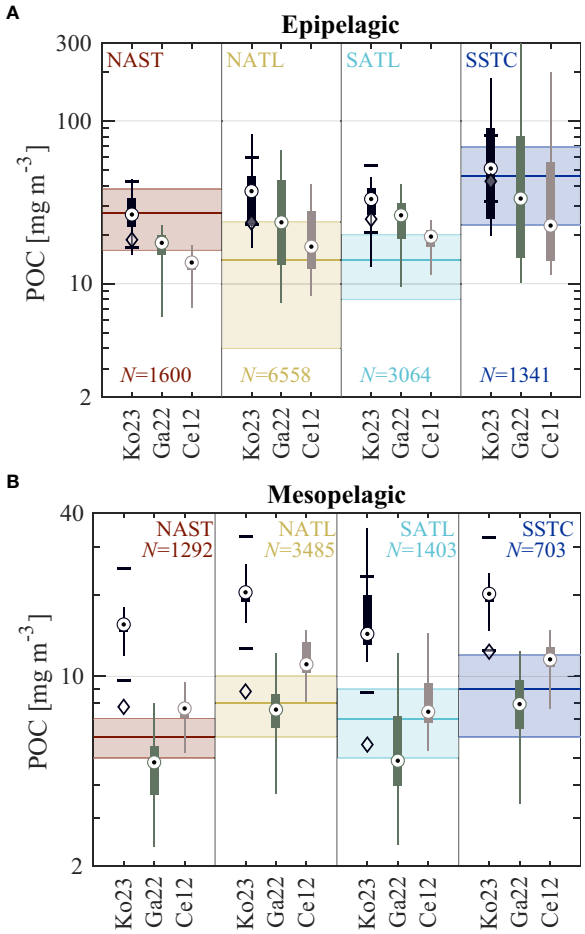


FIGURE 13
Summary of POC values within the **(A)** epipelagic ($z \leq 200$ m) and **(B)** mesopelagic ($200 < z < 500$ m) zones using nonparametric boxplots derived from float data in Figure 12. Lower and upper portions of boxes represent 25th and 75th percentile values while central circles denote median values and whiskers denote range. Results are displayed for the Ko23 algorithm from the current study as well as the Ga22 and Ce12 algorithms from Gali et al. (2022) and Cetinić et al. (2012), respectively (see section 2.6 for more details). Small horizontal black lines are shown for Ko23 data which represent median values of all lower or upper prediction bounds (two-tailed, $\alpha = 0.125$). An additional diamond marker is shown for Ko23 estimates which represents median values after removal of a background signal (i.e., b_{bp}^{Δ}) determined as the 5th percentile of b_{bp} values at a depth of 850–900 m. Reference data are shown for each ecological province using the median value (solid horizontal colored line) ± 1 standard deviation (shaded region) as provided in Sandoval et al. (2022).

(Figure 13A). In summary, all epipelagic estimates of POC from Ko23, Ga22, and Ce12 are 35 ± 13 mg m^{-3}, 22 ± 16 mg m^{-3}, and 17 ± 9 mg m^{-3}, respectively, while reported values from Sandoval et al. (2022) are 18 ± 9 mg m^{-3}. Note that Sandoval et al. (2022) report median ± 1 robust standard deviation determined as half the difference between the 84th and 16th percentiles, and we report the same statistical measures.

In the mesopelagic zone, all approaches also reproduce the general trend of largest POC values in SSTC and second largest values in NATL (Figure 13B). Ko23 estimates are noticeably higher than Sandoval et al. (2022) values by about a factor of two, while Ga22 yields somewhat lower and Ce12 somewhat higher values than the median values of each ecological province reported in Sandoval et al. (2022) (Figure 13B). It is worth noting that the majority of Ga22 estimates are within the measured values from Sandoval et al. (2022). When considering all mesopelagic estimates of POC, Ko23, Ga22, and Ce12 are 19 ± 3.5 mg m^{-3}, 6.7 ± 2.3 mg m^{-3}, and 10 ± 2.9 mg m^{-3}, respectively, while reported values from Sandoval et al. (2022) are 7 ± 2 mg m^{-3}. It is notable that POC values exceeding 10 mg m^{-3} and extending even above 20 mg m^{-3} have been previously measured at mesopelagic depths. For example, during the ANT-XXIII/1 cruise in the Atlantic Ocean described in Stramski et al. (2008), POC measurements for the depth range 200-500 m ranged from 11 to 41 mg m^{-3} with an average of about 18 mg m^{-3}. These data were obtained with the same POC method as our present algorithm development dataset (i.e., no DOC-adsorption correction and filtration of sufficiently large volumes). We also note that these mesopelagic data are not reported in Stramski et al. (2008) but are available through NASA's SeaWiFS Bio-optical Archive and Storage System (SeaBASS, https://seabass.gsfc.nasa.gov/).

Although there are some expected uncertainties from the above analysis (e.g., discrete water measurements lack vertical coverage of BGC-Argo floats and there are no precise match-ups with regards to time of sampling), we found that Ko23 estimates are significantly higher compared with estimates from Sandoval et al. (2022), especially in the mesopelagic zone. Although our algorithm development dataset did not include any mesopelagic samples, we believe that this discrepancy is mostly explainable by a combination of three factors: (1) the influence of DOC adsorption, (2) the influence of backscattering by small colloidal particles, and (3) general uncertainties when particulate signals are very low. Sandoval et al. (2022) applied a DOC-adsorption correction by use of two stacked GF/F filters, where the signal of any material retained on the lower filter is *subtracted* from the upper filter to estimate POC. We note here that it has been shown that Chla-containing particles can be retained on GF/F filters during filtration of GF/F filtrate, suggesting that some material which passes through a GF/F should be *added* back to the first filter for a more accurate representation of total particulate matter (e.g., Taguchi and Laws, 1988; Stramski, 1990). As discussed previously in section 4.3, we intentionally did not include DOC-adsorption subtraction from POC in our algorithm development dataset because b_{bp} is indeed influenced by small-sized colloidal particles which are mostly missed by GF/F filters. For example, Zhang et al. (2020) found that in the very clear North Pacific Ocean, approximately 15–50% of $b_{bp}(517)$ can be attributed to colloids in GF/F filtrate and this proportion of b_{bp} from colloids was highest for subsurface samples deeper than 100 m. Thus, in the mesopelagic zone, it is reasonable to expect that small colloids are an important and, at times, dominant contributor to b_{bp} and this may, at least partly, explain why Ko23 estimates of POC are consistently larger than Sandoval et al. (2022) estimates in the mesopelagic zone (Figure 13B). We reiterate here that we believe that Ko23 estimates are more representative of *total* POC including some contributions from small colloidal material due to the purposeful omission of an attempt at DOC-adsorption correction, whereas Sandoval et al.

(2022) estimates are likely more representative of POC associated with particles retained on GF/F filters.

As an attempt to examine what optically-based POC estimates would be without influence of small-sized colloids, we reprocessed the BGC-Argo data with the removal of a background signal of b_{bp}. This background (referred to as b_{bp}^{Δ}) was determined as the 5th percentile of b_{bp} values at 850–900 m depth from each float and is considered a combination of a quasi-constant backscattering background and uncertainty in manufacturer dark-counts (Poteau et al., 2017; Briggs et al., 2020). For the six floats included in our analysis, b_{bp}^{Δ} was 1.5–2.4 × 10^{-4} m^{-1}. Importantly, we note that b_{bp}^{Δ} is reasonable in comparison to the so-called "background" b_{bp}(517) signal from particles smaller than 0.2 µm and 0.7 µm found by Zhang et al. (2020); 2.3 × 10^{-4} (± 25%) m^{-1} and 3.5 × 10^{-4} (± 26%) m^{-1}, respectively, recalling that b_{bp}^{Δ} in the current study is determined with λ = 700 nm and thus should be somewhat lower. In Figure 13, we also report median values (diamond markers) of Ko23 estimates of POC for each province determined using b_{bp} with the contribution from b_{bp}^{Δ} removed and we believe these adjusted estimates are more representative of POC without the contribution of small colloids and, thus, more similar to POC corrected for DOC-adsorption. With this adjustment, we find overall better agreement of Ko23 estimates with Sandoval et al. (2022) reported values, especially in the mesopelagic zone (Figure 13B). The removal of b_{bp}^{Δ} decreases POC in the mesopelagic zone by about 3–15 mg m^{-3} for Ko23, 3–5 mg m^{-3} for Ga22, and 5–8 mg m^{-3} for Ce12. However, the estimates from Ga22 and Ce12 with removal of b_{bp}^{Δ} would become unrealistically low in the mesopelagic zone. We recall that Ga22 relies on relatively little observational data to generate the expected POC/b_{bp} ratio in the mesopelagic zone, relying on data from Cetinić et al. (2012) which, importantly, did include a DOC-adsorption correction resulting in some negative POC data below 200 m (Bol et al., 2018). The POC/b_{bp} ratios from Ga22 decrease with depth, but typically were 20471 ± 3481 mg C m^{-2} for mesopelagic depths considered (a factor of about 2 lower than the surface), although Bol et al. (2018) showed that these ratios in the mesopelagic zone can be less than 0 mg C m^{-2} to over 40000 mg C m^{-2}. The decrease in POC/b_{bp} with depth could be explained by changes in particle composition and size distribution, as well as the increased influence of colloidal scattering to b_{bp} with minimal increase to POC retained on GF/F filters. In conclusion, we do not recommend removing b_{bp}^{Δ} from b_{bp} in application studies aimed at examining *total* POC estimates from optical measurements, rather we see the influence of small-sized colloids to b_{bp} as a reasonable factor contributing to differences between Ko23 estimates of POC and the DOC-corrected Sandoval et al. (2022) observations in the mesopelagic zone, while we encourage careful consideration of various influences to and definitions of "particulate" signals. There is also a need for consistency in definition and interpretation of POC estimates obtained from measurements and/or modeling.

It must also be recognized that the mesopelagic zone is characterized by generally low values of both POC and particulate backscattering which approach the limits of methodological and instrument sensitivity, and thus both measurements in this depth range are subject to a high risk of large relative uncertainties. For POC values typically observed at mesopelagic depths, measurements reported in different studies will be considerably affected by the POC measurement protocol employed and subject to high relative uncertainties in experimental determination (e.g., Moran et al., 1999; Gardner et al., 2003). In addition, there is a need to develop improvements of POC measurement methodology to provide better estimates of *total* POC associated with all suspended particles, including small colloidal particles which can have a strong contribution to ocean optical properties (Organelli et al., 2018; Stramski and Woźniak, 2005; Zhang et al., 2020). Determinations of the particulate backscattering coefficient in many oceanic environments are also strongly influenced by instrument sensitivity and relatively large contributions of pure water and other background to the measured scattering signal. In Figure 14, we present an analysis of the sources of "background" signal to optical backscattering measured by the BGC-Argo float sensors. In the epipelagic zone, b_{bp}^{Δ} corresponds to roughly 35% ± 16% of b_{bp}, while the backscattering coefficient of seawater b_{bw} and b_{bp}^{Δ} together account for 61% ± 15% of the total backscattering coefficient b_b (Figure 14A). These proportions increase noticeably in the mesopelagic zone where such "background" signals are often over 70% and sometimes over 90% of the backscattering coefficient (Figure 14B). It is important to recognize that investigating particulate backscattering in the mesopelagic zone is often at the sensitivity limit of available instrumentation. Although the types of sensors on BGC-Argo floats typically have resolution of approximately 0.5–3 × 10^{-5} m^{-1} per detector count, dark counts are typically around 30–50 and sufficient signal is required for accuracy. In addition, there are various sources of instrument uncertainty that are important to consider, e.g., factory dark-counts, drift in scale factor, and so-called χ-factor used to estimate b_{bp} from a single backscattering angle (which may vary with large changes in the particle size distribution). We also recall that Poteau et al. (2017) showed that b_{bp}^{Δ} had significant differences for different sensors (e.g., MCOMS vs. ECO-Triplet) and suggest that significant deviation in b_{bp}^{Δ} is expected from extraordinary processes or malfunctioning sensor, which further emphasizes that caution must be taken when investigating such low particulate scattering signals. Further work is needed to examine performance of optical backscattering algorithms to estimate POC in the mesopelagic zone, and with varying sensors, especially those on BGC-Argo floats and gliders.

5 Concluding remarks

In the current study, we revised univariate and multivariable algorithms presented recently in Koestner et al. (2022) for improved estimations of POC from optical backscattering and chlorophyll-a measurements using a relatively large dataset covering various contrasting water types, including surface and subsurface waters from the Atlantic, Pacific, Arctic, and Southern Oceans. We provide useful refinements to the algorithms including improved model coefficients and prediction uncertainty using a larger and updated dataset compared to that in Koestner et al. (2022). We also provide

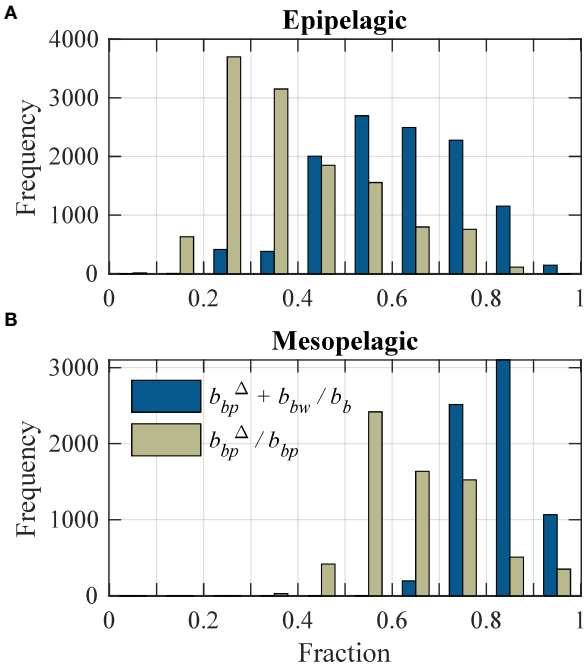


FIGURE 14
Histograms of various sources of background signal to optical backscattering measured by the BGC-Argo floats shown in Figure 12 for the **(A)** epipelagic ($z \leq 200$ m) and **(B)** mesopelagic ($200 < z < 500$ m) zones. The backscattering coefficient of pure water and dissolved salts b_{bw} was determined as a function of salinity and temperature based on Zhang and Hu (2009). The total backscattering coefficient b_b refers to the sum of b_{bp} and b_{bw}. b_{bp}^{Δ} was determined as the 5th percentile of b_{bp} values at a depth of 850–900 m from each float.

algorithms for several wavelengths used commonly in observations to derive b_{bp}, and specifically formulated algorithms for application with near-surface observations. The multivariable algorithm (Model B) can produce reliable estimates of POC across a range of highly contrasting waters in terms of location of sampling and particle and optical properties with noteworthy improvements compared with a typical univariate b_{bp}-based algorithm (Model B). We determined that the multivariable algorithm has limited sensitivity to uncertainties in both b_{bp} and Chla. Finally, we also examined performance of several algorithms to estimate POC using our dataset as well as a dataset consisting of optical measurements from BGC-Argo floats and traditional POC measurements collected during a coincident research cruise in the Atlantic Ocean.

The formulation of algorithms based exclusively on near-surface observations will be useful for satellite applications, especially as capabilities to derive b_{bp} and Chla from ocean color reflectance measurements improve (e.g., Loisel et al., 2018; O'Reilly and Werdell, 2019), as well as b_{bp} more directly from lidar observations (e.g., Lu et al., 2021; Behrenfeld et al., 2022). We expect some challenges for estimating POC using Model B based on the combination of satellite observations of b_{bp} and Chla, e.g., reliability of b_{bp} from lidar or ocean color inversions (Werdell et al., 2018; Behrenfeld et al., 2022). In comparison, POC algorithms which rely on estimation of POC in surface ocean waters directly from satellite-derived ocean reflectance have been recently improved and validated for applications in open-ocean pelagic environments that dominate the global ocean as well as other environments including coastal waters that exhibit bio-optical properties consistent with those found typically in the open ocean (e.g., Stramski et al., 2022; Joshi et al., 2023). There is also potential for further advancements in applications across diverse water bodies including optically-complex waters through development of adaptive POC algorithms which explicitly account for variations in particulate composition in terms of varying proportions of organic vs. mineral particles (Stramski et al., 2023). Nonetheless, one potential advantage of the proposed multivariable approach involving b_{bp} as a predictive variable for POC regards the decoupling of POC estimates from optically-derived Chla estimates. Historically, such coupling has been associated with satellite estimates of POC and Chla retrieved from similar spectral bands of ocean reflectance (e.g., Gordon et al., 1983; Stramski et al., 2008; Evers-King et al., 2017; O'Reilly and Werdell, 2019; Stramski et al., 2022). Although Chla is included as input into our multivariable b_{bp}–based algorithms and there should be some natural correlation between Chla and POC in many oceanic environments, the multivariable Model B can reasonably produce large variability in POC (factors of about 2–10) for the same values of Chla depending on b_{bp} and particle composition. Thus, further exploring application of this multivariable algorithm to remote sensing observations is worthwhile.

Notwithstanding satellite or other above-water remote sensing observations, we consider a main use-case of multivariable model B in conjunction with *in situ* measurements such as from BGC-Argo floats or autonomous gliders which typically make measurements of both b_{bp} and chlorophyll-a fluorescence. We expect that the algorithms can be particularly useful for assessments of temporal and spatial (including vertical) distributions of POC in the ocean (Johnson et al., 2009; Biogeochemical-Argo Planning Group, 2016; Roemmich et al., 2019). We acknowledge, however, that further validation of algorithm performance during various time frames, seasons, and depths outside the algorithm development dataset is desirable. Currently, estimates of POC with BGC-Argo floats rely almost exclusively on univariate b_{bp} algorithms (e.g., Dall'Olmo and Mork, 2014; Johnson et al., 2017; Xing et al., 2020; Wang and Fennel, 2023), or approaches which rely on adjustments to account for vertical and regional variability in the relationship between b_{bp} and POC (Bol et al., 2018; Galí et al., 2022). We also believe that multivariable Model B can be particularly useful for assessments of POC with optical measurements from autonomous gliders in nearshore or coastal waters which are often not surveyed by BGC-Argo floats and are optically-complex containing non-negligible contributions of non-phytoplankton material.

We believe that it is possible to develop relatively robust optical algorithms which can work across diverse environments by incorporating mechanistic aspects of the interactions of light and seawater constituents. The use of particle composition parameter in our multivariable approach of Model B is meant to introduce a mechanistic aspect to the b_{bp}-based POC algorithm which can pave the way for applications across diverse water bodies regardless of regional or seasonal variations in environmental conditions. Although the current multivariable algorithm is expected to

provide reasonable estimates of POC for a variety of water types within the epipelagic zone and extending potentially also to deeper mesopelagic depths (Figure 13), it is important to recognize a need for new sensors and approaches. For example, while targeting POC at deeper depths with no active phytoplankton growth, it will be useful to account for particulate composition that does not just rely on chlorophyll-a fluorescence. In addition, the effects of particle size distribution on optical properties may also be important to consider. The potential new sensors may take advantage of specific polarization and angular scattering properties which are indicative of particle size distribution as well as compositional properties such as the ratio of particulate organic carbon to total suspended particulate matter (Koestner et al., 2020; Koestner et al., 2021). With advancements targeting the improved estimation of POC throughout the ocean water column including the mesopelagic and deeper depths, we expect to better understand the natural ability of the biological carbon pump to sequester carbon in the deep ocean (e.g., Brewin et al., 2021).

Data availability statement

The raw data supporting the conclusions of this article will be made available by the authors, without undue reservation. POC algorithms are available at https://github.com/DanielKoestner/Koestner_2023_POC.

Author contributions

DK, DS, and RR conceptualized the study with DK performing the bulk of the algorithm development and validation. DK wrote the first draft of the manuscript. All authors contributed to the article and approved the submitted version.

Funding

This study was supported by the European Union's Horizon 2020 Framework Programme for Research and Innovation under the Marie Skłodowska-Curie grant agreement No. 101034309. Partial support was provided by the U.S. National Aeronautics and Space Administration (Grants NNX17AI72G, 80NSSC18K0956, and 80NSSC21K0700).

Acknowledgments

POC analysis of seawater samples was done at the Marine Science Institute, University of California Santa Barbara. We express our gratitude to Dr. Paul Lerner for support in the development of BGC-Argo processing codes. Thanks to all science crew and ship operators who facilitated collection of data used in this study. We also thank Dr. Martí Galí and Jordon Scott Beckler for their valuable comments on the manuscript.

Conflict of interest

The authors declare that the research was conducted in the absence of any commercial or financial relationships that could be construed as a potential conflict of interest.

Publisher's note

All claims expressed in this article are solely those of the authors and do not necessarily represent those of their affiliated organizations, or those of the publisher, the editors and the reviewers. Any product that may be evaluated in this article, or claim that may be made by its manufacturer, is not guaranteed or endorsed by the publisher.

References

Ackleson, S. G., Cullen, J. J., Brown, J., and Lesser, M. P. (1990). Some changes in the optical properties of marine phytoplankton in response to high light intensity. *Proc. SPIE 1302, Ocean Optics X*, 238–249. doi: 10.1117/12.21449

Balch, W. M., Bowler, B. C., Drapeau, D. T., Poulton, A. J., and Holligan, P. M. (2010). Biominerals and the vertical flux of particulate organic carbon from the surface ocean. *Geophys. Res. Lett.* 37, L22605. doi: 10.1029/2010GL044640

Barbieux, M., Uitz, J., Bricaud, A., Organelli, E., Poteau, A., Schmechtig,, et al. (2018). Assessing the variability in the relationship between the particulate backscattering coefficient and the chlorophyll a concentration from a global Biogeochemical-Argo database. *J. Geophys. Res.* 123, 1229–1250. doi: 10.1002/2017JC013030

Behrenfeld, M. J., Hu, Y., Bisson, K. M., Lu, X., and Westberry, T. K. (2022). Retrieval of ocean optical and plankton properties with the satellite Cloud-Aerosol Lidar with Orthogonal Polarization (CALIOP) sensor: Background, data processing, and validation status. *Remote Sens. Environ.* 281, 113235. doi: 10.1016/j.rse.2022.113235

Behrenfeld, M. J., Hu, Y., Hostetler, C. A., Dall'Olmo, G., Rodier, S. D., Hair, J. W., et al. (2013). Space-based lidar measurements of global ocean carbon stocks. *Geophys. Res. Lett.* 40, 4355–4360. doi: 10.1002/grl.50816

Biogeochemical-Argo Planning Group. (2016). *The scientific rationale, design and implementation plan for a Biogeochemical-Argo float array*. Eds. K. Johnson and H Claustre. doi: 10.13155/46601

Bishop, J. K. B. (1999). Transmissometer measurement of POC. *Deep-Sea. Res. I.* 46, 353–369. doi: 10.1016/S0967-0637(98)00069-7

Bisson, K. M., Boss, E., Werdell, P. J., Ibrahim, A., and Behrenfeld, M. J. (2021). Particulate backscattering in the global ocean: A comparison of independent assessments. *Geophys. Res. Lett.* 48, e2020GL090909. doi: 10.1029/2020GL090909

Bol, R., Henson, S. A., Rumyantseva, A., and Briggs, N. (2018). High-frequency variability of small-particle carbon export flux in the Northeast Atlantic. *Glob. Biogeochem. Cycles.* 32, 1803–1814. doi: 10.1029/2018GB005963

Boss, E., and Pegau, W. (2001). Relationship of light scattering at an angle in the backward direction to the backscattering coefficient. *Appl. Opt.* 40, 5503–5507. doi: 10.1364/AO.40.005503

Boss, E., Pegau, W. S., Lee, M., Twardowski, M., Shybanov, E., Korotaev, G., et al. (2004). Particulate backscattering ratio at LEO 15 and its use to study particle composition and distribution. *J. Geophys. Res.* 109, C01014. doi: 10.1029/2002JC001514

Boss, E. S., Collier, R., Pegau, W. S., Larson, G., and Fennel, K. (2007). "Measurements of spectral optical properties and their relation to biogeochemical variables and processes in Crater Lake, Crater Lake National Park, OR," in *Long-term Limnological Research and Monitoring at Crater Lake, Oregon. Developments in Hydrobiology*, vol. 191. (Dordrecht: Springer), 149–159. doi: 10.1007/978-1-4020-5824-0_9

Boyd, P. W., and Trull, T. W. (2007). Understanding the export of biogenic particles in oceanic waters: Is there consensus? *Prog. Oceanogr.* 72, 276–312. doi: 10.1016/j.pocean.2006.10.007

Brewin, R. J. W., Sathyendranath, S., Platt, T., Bouman, H., Ciavatta, S., Dall'Olmo, G., et al. (2021). Sensing the ocean biological carbon pump from space: A review of capabilities, concepts, research gaps and future developments. *Earth Sci. Rev.* 217, 103604. doi: 10.1016/j.earscirev.2021.103604

Briggs, N., Dall'Olmo, G., and Claustre, H. (2020). Major role of particle fragmentation in regulating biological sequestration of CO2 by the oceans. *Science* 367, 791–793. doi: 10.1126/science.aay1790

Buiteveld, H., Hakvoort, J. H.M., and Donze, M. (1994). Optical properties of pure water. *Proc. SPIE* 2258, Ocean Optics XII. doi: 10.1117/12.190060

Cetinić, I., Perry, M. J., Briggs, N. T., Kallin, E., D'Asaro, E. A., and Lee, C. M. (2012). Particulate organic carbon and inherent optical properties during 2008 North Atlantic Bloom Experiment. *J. Geophys. Res.* 117, C06028. doi: 10.1029/2011JC007771

Churnside, J. H., Tatarskii, V. V., and Wilson, J. J. (1998). Oceanographic lidar attenuation coefficients and signal fluctuations measured from a ship in the Southern California Bight. *Appl. Opt.* 47, 3105–3112. doi: 10.1364/AO.37.003105

Claustre, H., Morel, A., Babin, M., Cailliau, C., Marie, D., Marty, J.-C., et al. (1999). Variability in particle attenuation and chlorophyll fluorescence in the Tropical Pacific: Scales, patterns, and biogeochemical implications. *J. Geophys. Res.* 104, 3401–3422. doi: 10.1029/98JC01334

Dall'Olmo, G., and Mork, K. J. (2014). Carbon export by small particles in the Norwegian Sea. *Geophys. Res. Lett.* 41, 2921–2927. doi: 10.1002/2014GL059244

Erickson, Z. K., Cetinić, I., Zhang, X., Boss, E., Werdell, P. J., Freeman, S., et al. (2022). Alignment of optical backscatter measurements from the EXPORTS Northeast Pacific Field Deployment. *Elem. Sci. Anth.* 10, 1. doi: 10.1525/elementa.2021.00021

Evers-King, H., Martinez-Vicente, V., Brewin, R. J. W., Dall'Olmo, G., Hickman, A. E., Jackson, T., et al. (2017). Validation and intercomparison of ocean color algorithms for estimating particulate organic carbon in the oceans. *Front. Mar. Sci.* 4, 251. doi: 10.3389/fmars.2017.00251

Fay, A. R., and McKinley, G. A. (2014). Global open-ocean biomes: mean and temporal variability. *Earth System. Sci. Data* 6 (2), 273–284. doi: 10.5194/essd-6-273-2014

Friedlingstein, P., O'Sullivan, M., Jones, M. W., Andrew, R. M., Gregor, L., Hauck, J., et al. (2022). Global carbon budget 2022. *Earth Syst. Sci. Data* 14, 4811–4900. doi: 10.5194/essd-14-4811-2022

Galí, M., Falls, M., Claustre, H., Aumont, O., and Bernardello, R. (2022). Bridging the gaps between particulate backscattering measurements and modeled particulate organic carbon in the ocean. *Biogeosciences* 19, 1245–1275. doi: 10.5194/bg-19-1245-2022

Gardner, W. D., Mishonov, A. V., and Richardson, M. J. (2006). Global POC concentrations from *in-situ* and satellite data. *Deep. Sea. Res. II.* 53, 718–740. doi: 10.1016/j.dsr2.2006.01.029

Gardner, W. D., Richardson, M. J., Carlson, C. A., Hansell, D., and Mishonov, A. V. (2003). Determining true particulate organic carbon: bottles, pumps and methodologies. *Deep. Sea. Res. II.* 50, 655–674. doi: 10.1016/S0967-0645(02)00589-1

Gardner, W. D., Walsh, I. D., and Richardson, M. J. (1993). Biophysical forcing of particle production and distribution during a spring bloom in the North Atlantic. *Deep. Sea. Res. II.* 40, 171–195. doi: 10.1016/0967-0645(93)90012-C

Getzewich, B. J., Vaughan, M. A., Hunt, W. H., Avery, M. A., Powell, K. A., Tackett, J. L., et al. (2018). CALIPSO lidar calibration at 532 nm: Version 4 daytime algorithm. *Atmos. Meas. Tech.* 11, 6309–6326. doi: 10.5194/amt-11-6309-2018

Gordon, H. R., Clark, D. K., Brown, J. W., Brown, O. B., Evans, R. H., and Broenkow, W. W. (1983). Phytoplankton pigment concentrations in the Middle Atlantic Bight: comparison of ship determinations and CZCS estimates. *Appl. Opt.* 22, 20–36. doi: 10.1364/AO.22.000020

Intergovernmental Oceanographic Commission. (1994). *Protocols for the Joint Global Ocean Flux Study (JGOFS) Core Measurements. Intergovernmental Oceanographic Commission, Scientific Committee on Oceanic Research, Manuals and Guides No. 29* (Paris: UNESCO-IOC).

IOCCG Protocol Series. (2021). *Particulate Organic Matter Sampling and Measurement Protocols: Consensus Towards Future Ocean Color Missions*. J. E. Chaves, I. Cetinić, G. Dall'Olmo, M. Estapa, W. Gardner, M. Goñi, et al. *IOCCG Ocean Optics and Biogeochemistry Protocols for Satellite Ocean Colour Sensor Validation* Vol. 6.0 (Dartmouth, NS, Canada: IOCCG).

Jamet, C., Ibrahim, A., Ahmad, Z., Angelini, F., Babin, M., Behrenfeld, M. J., et al. (2019). Going beyond standard ocean color observations: Lidar and polarimetry. *Front. Mar. Sci.* 6, 251. doi: 10.3389/fmars.2019.00251

Johnson, K. S., Berelson, W. M., Boss, E. S., Chase, Z., Claustre, H., Emerson, S. R., et al. (2009). Observing biogeochemical cycles at global scales with profiling floats and gliders: Prospects for a global array. *Oceanography* 22, 216–225. doi: 10.5670/oceanog.2009.81

Johnson, K. S., Plant, J. N., Coletti, L. J., Jannasch, H. W., Sakamoto, C. M., Riser, S. C., et al. (2017). Biogeochemical sensor performance in the SOCCOM profiling float array. *J. Geophys. Res.* 122, 6416–6436. doi: 10.1002/2017jc012838

Joshi, I. D., Stramski, D., Reynolds, R. A., and Robinson, D. H. (2023). Performance assessment and validation of ocean color sensor-specific algorithms for estimating the concentration of particulate organic carbon in oceanic surface waters from satellite observations. *Remote Sens. Environ.* 286, 113417. doi: 10.1016/j.rse.2022.113417

Koestner, D., Stramski, D., and Reynolds, R. A. (2018). Measurements of the volume scattering function and the degree of linear polarization of light scattered by contrasting natural assemblages of marine particles. *Appl. Sci.* 8 (12), 2690. doi: 10.3390/app8122690

Koestner, D., Stramski, D., and Reynolds, R. A. (2020). Polarized light scattering measurements as a means to characterize particle size and composition of natural assemblages of marine particles. *Appl. Opt.* 59, 8314–8334. doi: 10.1364/AO.396709

Koestner, D., Stramski, D., and Reynolds, R. A. (2021). Characterization of suspended particulate matter in contrasting coastal marine environments with angle-resolved polarized light scattering measurements. *Appl. Opt.* 60, 11161–11179. doi: 10.1364/AO.441226

Koestner, D., Stramski, D., and Reynolds, R. A. (2022). A multivariable empirical algorithm for estimating particulate organic carbon concentration in marine environments from optical backscattering and chlorophyll-a measurements. *Front. Mar. Sci.* 9, 941950. doi: 10.3389/fmars.2022.941950

Lee, Z., Carder, K. L., and Arnone, R. A. (2002). Deriving inherent optical properties from water color: a multiband quasi-analytical algorithm for optically deep waters. *Appl. Opt.* 41, 5755–5772. doi: 10.1364/AO.41.005755

Loisel, H., Nicolas, J.-M., Deschamps, P.-Y., and Frouin, R. (2002). Seasonal and inter-annual variability of particulate organic matter in the global ocean. *Geophys. Res. Lett.* 29, 2196. doi: 10.1029/2002GL015948

Loisel, H., and Stramski, D. (2000). Estimation of the inherent optical properties of natural waters from the irradiance attenuation coefficient and reflectance in the presence of Raman scattering. *Appl. Opt.* 39, 3001–3011. doi: 10.1364/AO.39.003001

Loisel, H., Stramski, D., Dessailly, D., Jamet, C., Li, L., and Reynolds, R. A. (2018). An inverse model for estimating the optical absorption and backscattering coefficients of seawater from remote-sensing reflectance over a broad range of oceanic and coastal marine environments. *J. Geophys. Res.* 123, 2141–2171. doi: 10.1002/2017JC013632

Longhurst, A. R. (2007). "Chapter 9 - The Atlantic Ocean," in *Ecological Geography of the Sea, 2nd ed.* Ed. A. R. Longhurst (Burlington: Academic Press), 131–273.

Lu, X., Hu, Y., and Yang, Y. (2019). "Ocean subsurface study from ICESat-2 mission," in *Photonics & Electromagnetics Research Symposium - Fall (PIERS - Fall)*. 910–918(Xiamen, China). doi: 10.1109/PIERS-Fall48861.2019.9021802

Lu, X., Hu, Y., Yang, Y., Neumann, T., Omar, A., Baize, R., et al. (2021). New ocean subsurface optical properties from space lidars: CALIOP/CALIPSO and ATLAS/ICESat-2. *Earth Space. Sci.* 8, e2021EA001839. doi: 10.1029/2021EA001839

McKinna, L. I. W., Cetinić, I., and Werdell, P. J. (2021). Development and validation of an empirical ocean color algorithm with uncertainties: A case study with the particulate backscattering coefficient. *J. Geophys. Res.* 126, e2021JC017231. doi: 10.1029/2021JC017231

Middelburg, J. J. (2019). *Marine Carbon Biogeochemistry: A Primer for Earth System Scientists* (Berlin, Germany: Springer Nature).

Moran, S. B., Charette, M. A., Pike, S. M., and Wicklund, C. A. (1999). Differences in seawater particulate organic carbon concentration in samples collected using small-and large-volume methods: the importance of DOC adsorption to the filter blank. *Mar. Chem.* 67 (1-2), 33–42. doi: 10.1016/S0304-4203(99)00047-X

Morel, A., and Bricaud, A. (1981). Theoretical results concerning light absorption in a discrete medium, and application to specific absorption of phytoplankton. *Deep. Sea. Res.* 28A, 1375–1393. doi: 10.1016/0198-0149(81)90039-X

Neukermans, G., Loisel, H., Meriaux, X., Astoreca, R., and McKee, D. (2012). *In situ* variability of mass-specific beam attenuation and backscattering of marine particles with respect to particle size, density, and composition. *Limnol. Oceanogr.* 57, 124–144. doi: 10.4319/lo.2012.57.1.0124

Novak, M. G., Cetinić, I., Chaves, J. E., and Mannino, A. (2018). The adsorption of dissolved organic carbon onto glass fiber filters and its effect on the measurement of particulate organic carbon: A laboratory and modeling exercise. *Limnol. Oceanogr. Methods* 16 (6), 356–366. doi: 10.1002/lom3.10248

Nowicki, M., DeVries, T., and Siegel, D. A. (2022). Quantifying the carbon export and sequestration pathways of the ocean's biological carbon pump. *Glob. Biogeochem. Cycles.* 36 (3), e2021GB007083. doi: 10.1029/2021GB007083

O'Reilly, J. E., and Werdell, P. J. (2019). Chlorophyll algorithms for ocean color sensors - OC4, OC5 & OC6. *Remote Sens. Environ.* 229, 32–47. doi: 10.1016/j.rse.2019.04.021

Organelli, E., Barbieux, M., Claustre, H., Schmechtig, C., Poteau, A., Bricaud, A., et al. (2017). Two databases derived from BGC-Argo float measurements for marine biogeochemical and bio-optical applications. *Earth Syst. Sci. Data* 9, 861–880. doi: 10.5194/essd-9-861-2017

Organelli, E., Dall'Olmo, G., Brewin, R. J.W., Tarran, G. A., Boss, E., and Bricaud, A. (2018). The open-ocean missing backscattering is in the structural complexity of particles. *Nat. Commun.* 9, 5439. doi: 10.1038/s41467-018-07814-6

Paraekh, P., Dutkiewicz, S., Follows, M. J., and Ito, T. (2006). Atmospheric carbon dioxide in a less dusty world. *Geophys. Res. Lett.* 33, L03610. doi: 10.1029/2005GL025098

Parsons, T. R., Maita, Y., and Lalli, C. M. (1984). *A Manual of Chemical and Biological Methods for Seawater Analysis* (Oxford, England: Pergamon Press).

Poteau, A., Boss, E., and Claustre, H. (2017). Particulate concentration and seasonal dynamics in the mesopelagic ocean based on the backscattering coefficient measured with Biogeochemical-Argo floats. *Geophys. Res. Lett.* 44, 6933–6939. doi: 10.1002/2017GL073949

Reynolds, R. A., Stramski, D., and Kiefer, D. A. (1997). The effect of nitrogen-limitation on the absorption and scattering properties of the marine diatom Thalassiosira pseudonana. *Limnol. Oceanogr.* 42, 881–892. doi: 10.4319/lo.1997.42.5.0881

Reynolds, R. A., Stramski, D., and Neukermans, G. (2016). Optical backscattering by particles in Arctic seawater and relationships to particle mass concentration, size distribution, and bulk composition. *Limnol. Oceanogr.* 61, 1869–1890. doi: 10.1002/lno.10341

Roemmich, D., Alford, M. H., Claustre, H., Johnson, K., King, B., Moum, J., et al. (2019). On the future of Argo: A global, full-depth, multi-disciplinary array. *Front. Mar. Sci.* 6. doi: 10.3389/fmars.2019.00439

Roesler, C., Uitz, J., Claustre, H., Boss, E., Xing, X., Organelli, E., et al. (2017). Recommendations for obtaining unbiased chlorophyll estimates from *in situ* chlorophyll fluorometers: a global analysis of WET Labs ECO sensors. *Limnol. Oceanogr.* 15, 572–585. doi: 10.1002/lom3.10185

Sandoval, P. S., Dall'Olmo, G., Haines, K., Rasse, R., and Ross, J. (2022). Uncertainties of particulate organic carbon concentrations in the mesopelagic zone of the Atlantic Ocean. *Open Res. Europe.* 1, 43. doi: 10.12688/openreseurope.13395.3

Siegel, D. A., Buesseler, K. O., Behrenfeld, M. J., Benitez-Nelson, C. R., Boss, E., Brzezinski, M. A., et al. (2016). Prediction of the export and fate of global ocean net primary production: The EXPORTS science plan. *Front. Mar. Sci.* 3, 22. doi: 10.3389/fmars.2016.00022

Stemmann, L., and Boss, E. (2012). Plankton and particle size and packaging: From determining optical properties to driving the biological pump. *Ann. Rev. Mar. Sci.* 4, 263–290. doi: 10.1146/annurev-marine-120710-100853

Stramska, M., and Stramski, D. (2005). Variability of particulate organic carbon concentration in the north polar Atlantic based on ocean color observations with Sea-viewing Wide Field-of-view Sensor (SeaWiFS). *J. Geophys. Res.* 110, C10018. doi: 10.1029/2004JC002762

Stramski, D. (1990). Artifacts in measuring absorption spectra of phytoplankton collected on a filter. *Limnol. Oceanogr.* 35, 1804–1809. doi: 10.4319/lo.1990.35.8.1804

Stramski, D., Babin, M., and Woźniak, S. B. (2007). Variations in the optical properties of terrigenous mineral-rich particulate matter suspended in seawater. *Limnol. Oceanogr.* 52, 2418–2433. doi: 10.4319/lo.2007.52.6.2418

Stramski, D., Boss, E., Bogucki, D., and Voss, K. J. (2004). The role of seawater constituents in light backscattering in the ocean. *Prog. Oceanogr.* 61 (1), 27–56. doi: 10.1016/j.pocean.2004.07.001

Stramski, D., Bricaud, A., and Morel, A. (2001). Modeling the inherent optical properties of the ocean based on the detailed composition of the planktonic community. *Appl. Opt.* 40, 2929–2945. doi: 10.1364/AO.40.002929

Stramski, D., Constantin, S., and Reynolds, R. A. (2023). Adaptive optical algorithms with differentiation of water bodies based on varying composition of suspended particulate matter: A case study for estimating the particulate organic carbon concentration in the western Arctic seas. *Remote Sens. Environ.* 286, 113360. doi: 10.1016/j.rse.2022.113360

Stramski, D., Joshi, I., and Reynolds, R. A. (2022). Ocean color algorithms to estimate the concentration of particulate organic carbon in surface waters of the global ocean in support of a long-term data record from multiple satellite missions. *Remote Sens. Environ.* 269, 112776. doi: 10.1016/j.rse.2021.112776

Stramski, D., and Kiefer, D. A. (1991). Light scattering by microorganisms in the open ocean. *Prog. Oceanogr.* 28, 343–383. doi: 10.1016/0079-6611(91)90032-H

Stramski, D., and Morel, A. (1990). Optical properties of photosynthetic picoplankton in different physiological states as affected by growth irradiance. *Deep. Sea. Res.* 37, 245–266. doi: 10.1016/0198-0149(90)90126-G

Stramski, D., Reynolds, R. A., Babin, M., Kaczmarek, S., Lewis, M. R., Röttgers, R., et al. (2008). Relationships between the surface concentration of particulate organic carbon and optical properties in the eastern South Pacific and eastern Atlantic Oceans. *Biogeosciences* 5, 171–201. doi: 10.5194/bg-5-171-2008

Stramski, D., Reynolds, R. A., Kahru, M., and Mitchell, B. G. (1999). Estimation of particulate organic carbon in the ocean from satellite remote sensing. *Science* 285, 239–242. doi: 10.1126/science.285.5425.23

Stramski, D., Sciandra, A., and Claustre, H. (2002). Effects of temperature, nitrogen, and light limitation on the optical properties of the marine diatom Thalassiosira pseudonana. *Limnol. Oceanogr.* 47, 392–403. doi: 10.4319/lo.2002.47.2.0392

Stramski, D., and Woźniak, S. B. (2005). On the role of colloidal particles in light scattering in the ocean. *Limnol. Oceanogr.* 50, 1581–1591. doi: 10.4319/lo.2005.50.5.1581

Sullivan, J. M., Twardowski, M. S., Ronald, J., Zaneveld, V., and Moore, C. C. (2013). Measuring optical backscattering in water. *Light Scattering Reviews 7: Radiative Transfer and Optical Properties of Atmosphere and Underlying Surface* (Berlin, Germany: Springer Verlag), 189-224. doi: 10.1007/978-3-642-21907-8_6

Taguchi, S., and Laws, E. A. (1988). On the microparticles which pass through glass-fiber filter type GF/F in coastal and open waters. *J. Plankton. Res.* 10, 999–1008. doi: 10.1093/plankt/10.5.999

Twardowski, M., Boss, E., Macdonald, J., Pegau, W., Barnard, A., and Zaneveld, J. (2001). A model for estimating bulk refractive index from the optical backscattering ratio and the implication for understanding particle composition in Case I and Case II waters. *J. Geophys. Res.* 106, 14129–14142. doi: 10.1029/2000JC000404

Twardowski, M. S., Claustre, H., Freeman, S. A., Stramski, D., and Huot, Y. (2007). Optical backscattering properties of the "clearest" natural waters. *Biogeosciences* 4, 1041–1058. doi: 10.5194/bg-4-1041-2007

Uitz, J., Stramski, D., Baudoux, A.-C., Reynolds, R. A., Wright, V. M., Dubranna, J., et al. (2010). Variations in the optical properties of a particle suspension associated with viral infection of marine bacteria. *Limnol. Oceanogr.* 55, 2317–2330. doi: 10.4319/lo.2010.55.6.2317

Wang, B., and Fennel, K. (2023). An assessment of vertical carbon flux parameterizations using backscatter data from BGC Argo. *Geophys. Res. Lett.* 50, e2022GL101220. doi: 10.1029/2022GL101220

Werdell, P. J., McKinna, L. I., Boss, E., Ackleson, S. G., Craig, S. E.Gregg, et al. (2018). An overview of approaches and challenges for retrieving marine inherent optical properties from ocean color remote sensing. *Progress in Oceanography* 160, 186–212. doi: 10.1016/j.pocean.2018.01.001

Woźniak, S. B., Meler, J., and Stoń-Egiert, J. (2022). Inherent optical properties of suspended particulate matter in the southern Baltic Sea in relation to the concentration, composition and characteristics of the particle size distribution; new forms of multicomponent parameterizations of optical properties. *J. Mar. Sys.* 229, 103720. doi: 10.1016/j.jmarsys.2022.103720

Woźniak, S. B., Stramski, D., Stramska, M., Reynolds, R. A., Wright, V. M., Miksic, E. Y., et al. (2010). Optical variability of seawater in relation to particle concentration, composition, and size distribution in the nearshore marine environment at Imperial Beach, California. *J. Geophys. Res.* 115, C08027. doi: 10.1029/2009JC005554

Wu, J., Lee, Z., Xie, Y., Goes, J., Shang, S., Marra, J. F., et al. (2021). Reconciling between optical and biological determinants of the euphotic zone depth. *J. Geophys. Res.* 126, e2020JC016874. doi: 10.1029/2020JC016874

Xing, X., Claustre, H., Blain, S., D'Ortenzio, F., Antoine, D., Ras, J., et al. (2012). Quenching correction for *in vivo* chlorophyll fluorescence acquired by autonomous platforms: A case study with instrumented elephant seals in the Kerguelen region (Southern Ocean). *Limnol. Oceanogr. Methods* 10, 483–495. doi: 10.4319/lom.2012.10.483

Xing, X., Claustre, H., Boss, E., Roesler, C., Organelli, E., Poteau, A., et al. (2017). Correction of profiles of *in-situ* chlorophyll fluorometry for the contribution of fluorescence originating from non-algal matter. *Limnol. Oceanogr. Methods* 15, 80–93. doi: 10.1002/lom3.10144

Xing, X., Wells, M. L., Chen, S., Lin, S., and Chai, F. (2020). Enhanced winter carbon export observed by BGC-Argo in the Northwest Pacific Ocean. *Geophys. Res. Lett.* 47, e2020GL089847. doi: 10.1029/2020GL089847

Zhang, Z., Chen, P., Zhong, C., Xie, C., Sun, M., Zhang, S., et al. (2023). Chlorophyll and POC in polar regions derived from spaceborne lidar. *Front. Mar. Sci.* 10, 1050087. doi: 10.3389/fmars.2023.1050087

Zhang, X., and Hu, L. (2009). Estimating scattering of pure water from density fluctuation of the refractive index. *Opt. Express.* 17 (3), 1671–1678. doi: 10.1364/OE.17.001671

Zhang, X., Hu, L., Xiong, Y., Huot, Y., and Gray, D. (2020). Experimental estimates of optical backscattering associated with submicron particles in clear oceanic waters. *Geophys. Res. Lett.* 47, e2020GL087100. doi: 10.1029/2020GL087100

frontiers | Frontiers in Marine Science

TYPE Original Research
PUBLISHED 16 January 2024
DOI 10.3389/fmars.2023.1256990

Check for updates

OPEN ACCESS

EDITED BY
Huizeng Liu,
Shenzhen University, China

REVIEWED BY
Zhigang Cao,
Chinese Academy of Sciences (CAS), China
Jamie Shutler,
University of Exeter, United Kingdom

*CORRESPONDENCE
Luis González Vilas
luis.gonzalezvilas@artov.ismar.cnr.it

RECEIVED 11 July 2023
ACCEPTED 22 December 2023
PUBLISHED 16 January 2024

CITATION
González Vilas L, Brando VE, Di Cicco A, Colella S, D'Alimonte D, Kajiyama T, Attila J and Schroeder T (2024) Assessment of ocean color atmospheric correction methods and development of a regional ocean color operational dataset for the Baltic Sea based on Sentinel-3 OLCI.
Front. Mar. Sci. 10:1256990.
doi: 10.3389/fmars.2023.1256990

COPYRIGHT
© 2024 González Vilas, Brando, Di Cicco, Colella, D'Alimonte, Kajiyama, Attila and Schroeder. This is an open-access article distributed under the terms of the Creative Commons Attribution License (CC BY). The use, distribution or reproduction in other forums is permitted, provided the original author(s) and the copyright owner(s) are credited and that the original publication in this journal is cited, in accordance with accepted academic practice. No use, distribution or reproduction is permitted which does not comply with these terms.

Assessment of ocean color atmospheric correction methods and development of a regional ocean color operational dataset for the Baltic Sea based on Sentinel-3 OLCI

Luis González Vilas[1]*, Vittorio Ernesto Brando[1], Annalisa Di Cicco[1], Simone Colella[1], Davide D'Alimonte[2], Tamito Kajiyama[2], Jenni Attila[3] and Thomas Schroeder[4]

[1]CNR-ISMAR, Istituto di Scienze Marine, Consiglio Nazionale delle Ricerche, Rome, Italy, [2]AEQUORA LDA, Lisboa, Portugal, [3]Finnish Environment Institute (SYKE), Helsinki, Finland, [4]Commonwealth Scientific and Industrial Research Organization (CSIRO) Environment, Brisbane, QLD, Australia

The Baltic Sea is characterized by large gradients in salinity, high concentrations of colored dissolved organic matter, and a phytoplankton phenology with two seasonal blooms. Satellite retrievals of chlorophyll-*a* concentration (chl-*a*) are hindered by the optical complexity of this basin and the reduced performance of the atmospheric correction in its highly absorbing waters. Within the development of a regional ocean color operational processing chain for the Baltic Sea based on Sentinel-3 Ocean and Land Colour Instrument (OLCI) full-resolution data, the performance of four atmospheric correction processors for the retrieval of remote-sensing reflectance (*Rrs*) was analyzed. Assessments based on three Aerosol Robotic Network-Ocean Color (AERONET-OC) sites and shipborne hyperspectral radiometers show that POLYMER was the best-performing processor in the visible spectral range, also providing a better spatial coverage compared with the other processors. Hence, OLCI *Rrs* spectra retrieved with POLYMER were chosen as input for a bio-optical ensemble scheme that computes chl-*a* as a weighted sum of different regional multilayer perceptron neural nets. This study also evaluated the operational *Rrs* and chl-*a* datasets for the Baltic Sea based on OC-CCI v.6. The chl-*a* retrievals based on OC-CCI v.6 and OLCI *Rrs*, assessed against *in-situ* chl-*a* measurements, yielded similar results (OC-CCI v.6: R^2 = 0.11, bias = −0.22; OLCI: R^2 = 0.16, bias = −0.03) using a common set of match-ups for the same period. Finally, an overall good agreement was found between chl-*a* retrievals from OLCI and OC-CCI v.6 although differences between *Rrs* were amplified in terms of chl-*a* estimates.

KEYWORDS

ocean color, atmospheric correction, Baltic Sea, Sentinel-3 OLCI, chlorophyll-*a*, optically complex waters

1 Introduction

The Baltic Sea (Figure 1) is a brackish shallow semi-enclosed basin characterized by large inputs of pollutants and nutrients from natural and anthropogenic sources combined with a limited water exchange with the open ocean through the Danish Straits in the southwest, causing large latitudinal gradients of salinity and dissolved organic matter (Omstedt et al., 2004; Leppäranta and Myrberg, 2009). As a consequence of the strong anthropogenic pressure, pollution (HELCOM, 2018), eutrophication episodes (Andersen et al., 2011; Fleming-Lehtinen et al., 2015; Heiskanen et al., 2019), and/or phytoplankton blooms (Wasmund et al., 2011; Kahru et al., 2018; Hjerne et al., 2019) threaten its fragile ecosystems. Growing concern about the basin's health is raised by the Baltic Marine Environment Protection Commission (Helsinki Commission, HELCOM) (HELCOM, 2007). The Baltic Sea is characterized by high concentrations of colored dissolved organic matter (CDOM). Rivers are the main CDOM source, which follows a general dilution gradient from north to south with a large spatiotemporal variability driven by processes such as ice melting, rainfall, phytoplankton blooms, or photodegradation (Berthon and Zibordi, 2010; Ylöstalo et al., 2016; Simis et al., 2017; Kratzer and Moore, 2018).

Two seasonal phytoplankton blooms are usually observed in most areas of the Baltic Sea (Wasmund et al., 2011; Kahru et al., 2018; Brando et al., 2021). Firstly, a strong spring bloom dominated by diatoms and dinoflagellates is responsible for most of the annual primary production in the area (Simis et al., 2017; Zhang et al., 2018). This spring bloom progresses from south to north due to light and nitrogen limitation, and it can cause anoxia and hypoxia events in the bottom layer because of the fast diatom sedimentation (Hjerne et al., 2019). After a minimum production in early summer (May–June), phosphorus excess and increasing surface water temperature lead to the blooming of nitrogen-fixing cyanobacteria, causing extensive and prolongated surface and near-surface accumulations of filamentous species during calm weather periods in July and August (Kahru et al., 1994; Finni et al., 2001; Kahru et al., 2007; Kahru et al., 2018).

Chlorophyll-*a* (chl-*a*) concentration (measured in mg m^{-3}) is one of the most relevant indicators for water quality monitoring within the Baltic Sea Action Plan implemented by HELCOM, as it is useful for assessing the eutrophication status and a good proxy for phytoplankton blooms (HELCOM, 2017; HELCOM, 2019; Ahlman et al., 2020). Compared with chl-*a* data from sampling stations, *in-situ* platforms, or automated ship measurements, chl-*a* maps derived from ocean color (OC) satellite images provide a synoptic view of the phytoplankton spatial distribution. Although data availability in terms of spatial coverage and temporal resolution is limited by the cloud cover, it can be significantly enhanced by merging data from different sensors (Groom et al., 2019; O'Reilly and Werdell, 2019; Sathyendranath et al., 2019).

Accuracy and reliability of chl-*a* retrievals from OC data depend on two related factors: 1) the optical characteristics of the

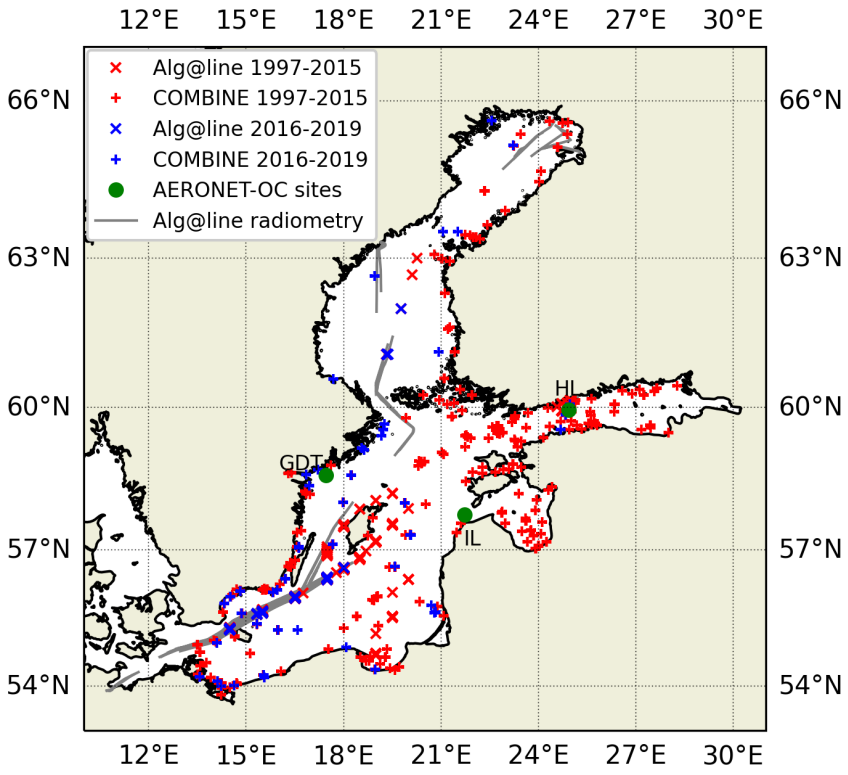


FIGURE 1
Study area showing the location of the *in-situ* measurements. The crosses identify the *in-situ* Alg@line *chl-a* data collected by the SYKE, whereas the pluses are chl-*a* data extracted from the COMBINE database (red points: 1997–2015; blue points: OLCI period from 2016 to 2019) (Section 2.2.2). The green dots mark the location of the AERONET-OC sites (GDT, Gustav Dalen Tower; HL, Helsinki Lighthouse; IL, Irbe Lighthouse; Section 2.2.1). Gray lines show the trajectories of the ships during the collection of the Alg@line shipborne radiometry data by SYKE in 2016 (Section 2.2.1).

water and 2) the performance of the atmospheric correction (AC) algorithms converting the spectral top-of-atmosphere (TOA) radiances measured by the satellite sensors to spectral remote-sensing reflectance (*Rrs*, defined as the ratio of the water-leaving radiance and the downwelling irradiance and measured in sr^{-1}) used as input in chl-*a* estimation algorithms (Brewin et al., 2015; Sathyendranath et al., 2019). Despite the good results in open-ocean and high-scattering coastal areas (Blondeau-Patissier et al., 2014; O'Reilly and Werdell, 2019), retrieval of reliable OC products from high-absorbing waters such as the Baltic Sea is a challenging task. High absorption coefficients related to the high CDOM concentrations (with aCDOM values exceeding 1.0 m^{-1} at 440 nm, Ylöstalo et al., 2016) in combination with relative low sun elevation lead to low *Rrs* values, especially in the blue part of the spectrum. Therefore, AC algorithms show a limited performance producing inaccurate *Rrs* spectra with low and even negative values (Attilla et al., 2013; Beltrán-Abaunza et al., 2014; Alikas et al., 2020; Brando et al., 2021; Tilstone et al., 2022).

Regarding chl-*a* retrieval, standard blue-green band-ratio algorithms have been reported as not suitable for the Baltic Sea because they tend to a significant overestimation (Darecki and Stramski, 2004; Odermatt et al., 2012; D'Alimonte et al., 2016; Pitarch et al., 2016; Ligi et al., 2017; Kratzer and Moore, 2018). Better results have been achieved with regionalized blue-green ratios (Darecki and Stramski, 2004; Attilla et al., 2013; Ligi et al., 2017), red-edge bands (Ligi et al., 2017), or neural network (NN) algorithms based on different sets of *Rrs* values (Kratzer and Vinterhav, 2010; Hieronymi et al., 2017; Toming et al., 2017; Kyryliuk and Kratzer, 2019), although accuracy is still hampered by the optical complexity of the basin and the low performance of the AC processors.

Within the Copernicus Marine Service (CMEMS, Le Traon et al., 2019; von Schuckmann et al., 2022), two operational chl-*a* data streams are available for the Baltic Sea based on OLCI and on merged multisensor time series. These data streams are based on sensor merging to improve the daily spatial coverage at 300 m and 1 km resolutions to support the operational oceanography users and environmental reporting needs (Le Traon et al., 2019; Sathyendranath et al., 2019; von Schuckmann et al., 2022).

Brando et al. (2021) proposed a new ensemble approach based on multilayer perceptron neural network (MLP) bio-optical algorithms (ENS-MLP), with results outperforming those based on other methods reported in the literature. This new approach was implemented in a fully reprocessed multisensor time series of *Rrs* and chl-*a* data at ~1 km spatial resolution (OCEANCOLOUR_BAL_BGC_L3_MY_009_133, 2023).

This work documents the implementation of the new *Rrs* and chl-*a* level-3 datasets for the Baltic Sea based on the complete Sentinel-3 A and B OLCI time series (2016 to present) of OC images at full resolution (300 m), using the same ENS-MLP approach for chl-*a* retrievals. To this aim, the following steps were carried out: 1) the selection of the best AC processor to obtain OLCI level-2 *Rrs* from level-1 data, 2) the assessment of the new OLCI level-3 *Rrs* dataset and comparison with the CMEMS multisensor dataset at 1 km resolution, and 3) the comparative validation analysis of the multisensor and OLCI level-3 chl-*a* datasets based on the ENS-MLP approach. The validation results were based on several *in-situ* data sources: automated radiometry from the Aerosol Robotic Network-Ocean Color (AERONET-OC) sites in the Baltic Sea, shipborne hyperspectral radiometry collected by the Finnish Environment Institute (SYKE), and chl-*a* concentrations from Alg@line and COMBINE datasets.

The remainder of this document is structured as follows: Section 2 introduces the data and methods used in this work, describing the validation exercises; the results presented in Section 3 include a match-up summary, validation results for level-2 OLCI *Rrs*, level-3 *Rrs* and chl-*a*, and a comparison between CMEMS-OLCI level-3 and OC-CCI v.6 datasets. The discussion and concluding remarks are addressed in Sections 4 and 5, respectively.

2 Materials and methods

2.1 Satellite *Rrs*

2.1.1 Level-2 reflectance datasets

OLCI *Rrs* spectra were extracted from Sentinel-3 level-2 products processed by four different atmospheric correction algorithms: OLCI level-2 Water Full Resolution (WFR), POLYMER, Case 2 Regional CoastColour (C2RCC), and S3 FUB-CSIRO Coastal Water Processor (hereafter S3 FUB-CSIRO). All the level-2 products were derived from a set of Sentinel-3 level-1b Full Resolution (FR) images at 300 m resolution acquired over the Baltic Sea for both Sentinel-3A (between April 2016 and September 2022) and Sentinel-3B (between May 2018 and September 2022) missions.

The OLCI WFR products were available from the Ocean Colour baseline collection OL_L2M.003, processed by EUMETSAT using the OLCI L2 processor IPF-OL-2 version 07 (EUMETSAT, 2021; Zibordi et al., 2022). This product provides water-leaving reflectance data at the OLCI spectral bands between 400 nm and 1,020 nm except those bands dedicated to atmospheric measurements (Table 1). It also contains the pixel classification band Water Quality and Science Flags (WQSFs), providing information about invalid and/or suspicious pixels (Table 2).

POLYMER is a coupled ocean–atmosphere algorithm that applies polynomial functions to model the (TOA) spectral reflectance and sun glint, and it applies a forward bio-optical model for the water component. It was originally developed for MERIS from an atmospheric correction processor for case-1 waters that is able to deal with sun glint (Steinmetz et al., 2011; Steinmetz and Ramon, 2018). In this study, we applied POLYMERv.4.14 (https://forum.hygeos.com/viewtopic.php?f=5&t=155), which is already adapted to OLCI, providing fully normalized water-leaving reflectance data for 16 bands between 400 nm and 1,020.5 nm (Table 1), as well as a flag band (bitmask) with pixel classification (Table 2).

C2RCC applies parametrized radiative transfer models based on the successive order of scattering (SOS) technique to obtain a large database of simulated TOA radiances, which is then used as input to train a set of neural networks (NN) for the retrieval of water-leaving reflectance as well as other water products (Doerffer and Schiller, 2007; Brockmann et al., 2016). In this work, we applied C2RCC v.2 (https://c2rcc.org/neural-nets/), providing, among other outputs,

10.3389/fmars.2023.1256990

TABLE 1 Available wavelengths from OLCI level-2 (*: OLCI WFR, C2RCC, and POLYMER) and level-3 products, multisensor OC-CCI products, and AERONET-OC sites.

Satellite bands					AERONET-OC bands	
OLCI-level-2*	S3 FUB-CSIRO	CMEMS-OLCI	OC-CCI v.6	OC-CCI v4.2 (chl-*a*)	2005–2018	2018–2022
400		**400**				**400**
412.5	**412.5**	**412.5**	**412**	412	**412**$^{+}$	**412**
442.5	**442.5**	**442.5**	**443**	443	**443**$^{+}$	**443**
490	**490**	**490**	**490**	490	**490**$^{+}$	**490**
510	**510**	**510**	**510**	510		**510**
					532	
560	**560**	**560**	**560**	555	551 $^{+1}$	**560**
620	**620**	**620**				**620**
665	**665**	**665**	**665**	670	**667**$^{+}$	**667**
673.75		673.75				
681.25		681.25				
708.75	708.75	708.75				
753.75						
778.75		**778.75**				**779**
865		**865**			**870**	**865**
885						
1,020.5					**1,020**	**1,020**

Bands available for validation during the OLCI period using data from AERONET-OC are shown in bold. Bands available for OC-CCI v.6 validation since 2005 until 2016 are indicated with the superscript $^{+}$ ($^{+1}$: 555 nm between 2005 and 2011).

TABLE 2 Flag bands and flag lists implemented for each AC processor.

AC	Flag band	Flag list
WFR	Wqsf	land, coastline, cloud[1], cloud_ambiguous[1], cloud_margin[1], invalid[2], cosmetic, saturated, suspect, hisolzen, highglint[4], snow_ice, ac_fail, whitecaps, adjac, rwneg_o2[5], rwneg_o3[5], rwneg_o4[5], rwneg_o5[5], rwneg_o6[5], rwneg_o7[5], rwneg_o8[5]
C2RCC	c2rcc_flags	tosa_OOR, Rhow_OOR, Cloud_risk[1]
C2RCC S3 FUB-CSIRO	quality_flags	land, coastline, fresh_inland_water, bright[3], straylight_risk, invalid[2], cosmetic, sun_glint_risk[4], dubious, saturated_OaXX (with XX from 01 to 21).
POLYMER	Bitmask	land, cloud_base[1], l1_invalid[2], negative_bb, out_of_bounds[6], exception, thick_aerosol[6], high_air_mass[6], external_mass, inconsistency[6], anomaly_rwmod_blue[6]
IdePix	pixel_classif_flags	land, coastline, invalid[2], cloud[1], cloud_buffer[1], cloud_shadow[1], snow_ice, bright[3], white, mountain_shadow

IdePix was used for all the AC processors as a common flag framework. Subscript numbers indicate the flag lists used for the outputs in Figure 3 ([1]CLOUD; [2]INVALID; [3]BRIGHT; [4]SUNGLINT_RISK; [5]RNEG; [6]POLYMER).

Rrs data for 16 OLCI bands between 400 nm and 1,020.5 nm (Table 1) and two flag bands (c2rcc_flag and quality_flags) with pixel identification information (Table 2).

The S3 FUB-CSIRO Coastal Water Processor is an ensemble neural network inversion trained with extensive coupled ocean–atmosphere radiative transfer simulations (Schroeder et al., 2022). The algorithm was adapted to an approach previously developed by Schroeder et al. (2007); Schroeder et al. (2003) for MERIS. The S3 FUB-CSIRO processor version 1.0.0.0.5.3 used in this study, therefore, does not provide outputs for OLCI bands at 400 nm, 673.75 nm, 681.25 nm, and above 708.75 nm (Table 1). The algorithm performs a pixel-per-pixel direct inversion of the TOA radiance signal into spectral remote sensing reflectance at mean sea level and selected water quality parameters. It also provides per-pixel sensor and inverse model uncertainties, which were not further evaluated in this study. Quality control was applied by using the flag band *quality_flags* for masking (Table 2), which are based on the level-1b flags but not the additional neural network-specific input/output out-of-range flags.

2.1.2 Level-3 reflectance datasets

Within CMEMS, two operational ocean color time series are available for the Baltic Sea: merged OLCI (Sentinel-3A and

Sentinel-3B) at 300 m spatial resolution and merged multisensor at 1 km resolution.

The CMEMS-OLCI level-3 *Rrs* dataset for the Baltic Sea merges OLCI level-2 *Rrs* spectra retrieved from level-1b FR images for both Sentinel-3A and Sentinel-3B missions using POLYMERv.4.14. *Rrs* values are remapped using the "nearest value" interpolation on an equi-rectangular grid at 300 m resolution. As in the EUMETSAT v.3.0.1 reprocessing the System Vicarious Calibration gains that have been implemented by EUMETSAT for both sensors, *Rrs* values are merged without any bias correction. The dataset has been produced operationally by CNR as daily data since April 2016 to present for 11 OLCI bands between 400 nm and 708.74 nm (Table 1) and is available at the Copernicus Marine Service in near real-time (OCEANCOLOUR_BAL_BGC_L3_NRT_009_131, Baltic Sea Ocean Colour Plankton, Reflectances, Transparency and Optics L3 NRT daily observations, 2023) and as a fully reprocessed multiyear time series (OCEANCOLOUR_BAL_BGC_L3_MY_009_133, 2023).

The CMEMS multisensor level-3 *Rrs* dataset for the Baltic Sea is derived from the Ocean Color (OC)-Climate Change Initiative (CCI) v.6 processor (OC-CCI v.6) implemented by Plymouth Marine Laboratory (PML) (Sathyendranath et al., 2019; OC-CCI, 2022; Sathyendranath et al., 2022). Data were obtained from different sensors and processed with specific atmospheric correction algorithms to obtain L2 *Rrs* spectra: NASA standard atmospheric correction was applied to the SeaWiFS NASA R2018.0 reprocessed dataset, while POLYMER was selected for MERIS (ESA 4th reprocessing) MODIS-AQUA and VIIRS (NASA R2018.0, included only until the end of 2019) and both OLCI sensors (EUMETSAT v.3.0.1 reprocessing). *Rrs* output values from each sensor were band-shifted using the inverse and direct application of the Quasi-Analytical Algorithm (QAA) algorithm (Lee et al., 2014; Mélin and Sclep, 2015) to six MERIS bands (Table 1) and then bias-corrected and merged at 1 km resolution, providing a consistent time series from 1997 to 2022.

2.2 *In situ* data for validation

2.2.1 *In situ* automated radiometry

For the validation of satellite-derived *Rrs*, this study relies on two sources of *in-situ* automated above-water radiometry: the AERONET-OC and the Alg@line hyperspectral datasets were collected following the same above-water radiometry approach (Zibordi et al., 2009; Simis and Olsson, 2013).

In-situ radiometry data were available from the automated measurements collected by AERONET-OC at three sites in the Baltic Sea: Gustav Dalen Tower (58.594°N, 17.467°E), with data from 2005 to 2022; Helsinki Lighthouse (59°949°N, 24.925°E), from 2006 to 2019; and Irbe Lighthouse (57.751°N, 21.723°E), from 2018 to 2022. Due to the illumination conditions of the Baltic Sea, data are usually available between May and September, with some single days in March, April, or October. We used level-2 data available from the AERONET-OC web page (https://aeronet.gsfc.nasa.gov), consisting of quality-controlled measurements of normalized water-leaving radiances (L_{wN}) corrected for bidirectional effects and referred to nadir (Zibordi et al., 2009, Zibordi et al., 2020). AERONET-OC provides multispectral data (Table 1): 8 bands between 412 nm and 1,020 nm until 2018 (adapted to MERIS) and 11 bands between 400 nm and 1,020 nm since 2019 when instruments were modified for OLCI validation (Zibordi et al., 2009, 2020).

The Alg@line hyperspectral dataset was collected by SYKE within the BONUS FerryScope project (Simis and Olsson, 2013; Simis et al., 2021) from April to September 2016. Data were acquired every 15 ss using a three-spectroradiometer system mounted approximately 7 m from the sea surface on board the merchant vessels Finnmaid (Finnlines) and Transpaper (Transatlantic). Downwelling irradiance (E_d) was collected using a TriOS RAMSES-ACC unit with a cosine collector, and sky (L_d) and water radiance (L_s) were measured with RAMSES-ARC sensors with a 7° field of view. The dataset was filtered to eliminate measurements with an obstructed view of the sea or affected by underexposure or oversaturation. *Rrs* spectra were derived by correcting for the reflection of sky radiance at the water surface using E_d, L_t, and L_s measurements. More details about data collection, processing, and quality control are available from Simis et al. (2021); Qin et al. (2017), and Warren et al. (2019).

2.2.2 *In situ* chl-*a* datasets

We used two *in-situ* datasets in order to validate the chl-*a* concentrations retrieved from satellite *Rrs* for the Baltic Sea: Alg@line and COMBINE.

The Alg@line dataset is derived from a set of water samples collected by SYKE from 1997 to 2017 using an acquisition system installed on board ferries operating in the Helsinki–Travemünde, Helsinki–Stockholm, and Kemi–Travemünde transects. Water samples (from surface to 5 m depth) were filtered using glass fiber filters (Whatman GF/F, 0.7-µm nominal pore size), chlorophyll-*a* was extracted with ethanol, and concentrations were determined by fluorometry using a Jasco FP-750 spectrofluorometer or a Perkin-Elmer LS2-b fluorometer with an excitation wavelength of 413 nm and emission wavelength of 668 nm (Fleming and Kaitala, 2006; Kaitala et al., 2008).

The COMBINE dataset, available from the International Council for the Exploration of the Sea (ICES) oceanographic database, includes chl-*a* measurements gathered by several institutions from the 1970s to the present within the HELCOM marine monitoring program (HELCOM, 2017; HELCOM, 2019). Chl-*a* concentrations were obtained using different analytical protocols and techniques, from fluorimetry to spectrophotometry and HLPC, but always meeting the quality requirements established by the program. We excluded from the analysis data acquired in the Skagerrak and Kattegat regions since these basins are characterized by physical and optical water properties deemed different from the actual Baltic Sea (Ligi et al., 2017; Simis et al., 2017).

2.3 Chl-*a* retrieval algorithm from satellite *Rrs*

Retrieval of chl-*a* concentrations from satellite *Rrs* in the Baltic Sea was based on the methodological approach proposed by Brando et al. (2021). It builds on a bio-optical ensemble scheme in which chl-*a* concentrations are estimated as a weighted sum of the outputs

of different regional multilayer perceptron neural net (MLP) bio-optical algorithms developed using *in-situ* data available from the JRC/EC BiOMaP program (D'Alimonte et al., 2011; Zibordi et al., 2011). Weights defining the contribution of each individual MLP algorithm are dynamically established through the novelty index (D'Alimonte et al., 2014; Kajiyama et al., 2019; Brando et al., 2021).

Each MLP bio-optical algorithm uses as input *Rrs* values at a different subset of wavelengths, considering all the SeaWiFS bands implemented in the OC-CCI v4.2 product (Table 1): *chl-aMLP6b* (*Rrs* values at 412, 443, 490, 510, 555, and 670 nm), *chl-aMLP_5b* (*Rrs* values at 443, 490, 510, 555, and 670 nm), *chl-aMLP_4b* (*Rrs* values at 490, 510, 555, and 670 nm), and *chl-aMLP_3b* (*Rrs* values at 490, 510, and 555 nm).

Brando et al. (2021) tested two ensemble solutions based on four (*chl-aENS4*: *chl-aMLP_6b*, *chl-aMLP_5b*, *chl-aMLP_4b*, *chl-aMLP_3b*) and three (*chl-aENS3*: *chl-aMLP_5b*, *chl-aMLP_4b*, *chl-aMLP_3b*) MLP algorithms, evaluating their performance through a match-up analysis of chl-*a* retrievals from OC-CCI v4.2 time series against *in-situ* chl-*a* concentrations. Results showed that both ensemble solutions outperformed all the band-ratio regression algorithms based on *Rrs* spectral slopes instead of *Rrs* values at different bands and that *chl-aENS3* outperformed *chl-aENS4*.

In this work, the performance of both *chl-aENS3* and *chl-aENS4* was evaluated through a match-up analysis of chl-*a* retrievals from satellite *Rrs* extracted from the CMEMS-OLCI level-3 *Rrs* dataset and OC-CCI v.6 datasets (see Section 2.1.2), against *in-situ* chl-*a* measurements from Alg@Line and COMBINE datasets (see Section 2.2.2). Only results for the best-performing solution, i.e., *chl-aENS3*, are shown in this document.

Chl-aENS3 was also the selected algorithm for the implementation of the new CMEMS-OLCI level-3 chl-*a* dataset for the Baltic Sea (OCEANCOLOUR_BAL_BGC_L3_MY_009_133, 2023; OCEANCOLOUR_BAL_BGC_L3_NRT_009_131, 2023), in which chl-*a* concentrations are retrieved from the CMEMS-OLCI level-3 *Rrs* dataset merging *Rrs* outputs from POLYMERv.4.14 (see Section 2.2.1). The new dataset was produced by CNR for the complete OLCI time series (from April 2016 to the present).

As *chl-aENS3* was developed considering the SeaWiFS spectral bands available in the OC-CCI v.4.2 product, in this work, chl-*a* retrievals using *Rrs* values from CMEMS-OLCI or OC-CCI v.6 required a previous band shift to the SeaWiFS spectral bands. The band shift was performed through the inverse and direct application of the QAA algorithm (Mélin and Sclep, 2015; Lee et al., 2009) modified to ensure non-negative phytoplankton at any band (Brando et al., 2021).

2.4 Validation exercises

2.4.1 Workflow

Figure 2 summarizes the workflow for the validation exercises carried out in this work, all of them implemented using a Match-up Database File (MDB) infrastructure (EUMETSAT, 2019; González Vilas et al., submitted; González Vilas et al., 2023).

The top panel (Figure 2A) depicts the steps for a round-robin comparison of four AC algorithms (i.e., WFR, C2RCC, POLYMER, and S3 FUB-CSIRO) to select the best processor for deriving OLCI level-2 *Rrs* spectra from level-1 data. *In-situ* radiometry data for this comparative validation exercise were available from both the AERONET-OC and Alg@line hyperspectral datasets. The bottom panel of Figure 2B shows the validation procedure for the *Rrs* and chl-*a* level-3 datasets, comparing the new CMEMS-OLCI and OC-CCI v.6 datasets. In this case, only radiometric data from AERONET-OC were used for *Rrs* validation.

We also run the Identification of Pixels Properties (IdePix) to obtain a common flag band for all the processors. IdePix is a multisensor pixel identification tool available as a plugin for Sentinel Application Platform (SNAP) implementing pixel identification algorithms for different sensors including Sentinel-3 (https://www.brockmann-consult.de/portfolio/idepix/). It classifies pixels certainly or ambiguously affected by clouds and provides also other flags as *white* or *bright* (Table 2).

The main steps are the following ones (note that some steps are common for both analyses):

a) Trimming: With the aim of reducing the AC computational time, level-1b FR images were first trimmed into micrograNules keeping the OLCI data format (SENTINEL-SAFE). In the case of AERONET-OC or chl-*a* measurements, micrograNules cover an area of 2° by 2° around the site location. For shipborne radiometry, granules were trimmed to cover the daily transect. The same protocol was also adopted for trimming the level-2 WFR and level-3 files.

b) Atmospheric correction (Figure 2A): POLYMER, C2RCC, S3 FUB-CSIRO, and IdePix were run on the level-1b micrograNules using default options. POLYMER is available from the HYGEOS website, and it is run directly in Python. C2RCC and IdePix are available as SNAP, while the S3 FUB-CSIRO processor is available as a Python/C plugin for SNAP at https://github.com/s3tbx-fub-csiro/s3tbx-fub-csiro.git. C2RCC, IdePix, and S3 FUB-CSIRO were processed using the SNAP Graph Processing Tool (GPT).

c) Chl-*a* processing (Figure 2B): Satellite chl-*a* was retrieved from level-3 micrograNules using the method proposed by Brando et al. (2021) (Section 2.3).

d) Generation of satellite extract files: Level-2 extract files (Figure 2A) were created for the Sentinel-3A or Sentinel-3B mission and each AC processor (WFR, POLYMER, C2RCC, and S3 FUB-CSIRO) starting from the corresponding output microfiles. Each extract file contains 25 × 25 pixels of satellite data centered at the site location (for AERONET-OC) or transect point(s) (for shipborne radiometry). These files include always *Rrs* for all the available bands, geometry (zenith and azimuth observation and sun angles), the flag band corresponding to the processor (see Section 2.1.1), and the IdePix results. If output values are defined as water-leaving reflectance (WFR and POLYMER), they are converted to *Rrs* by dividing by pi. The satellite overpass time and band wavelengths are also included in the files.

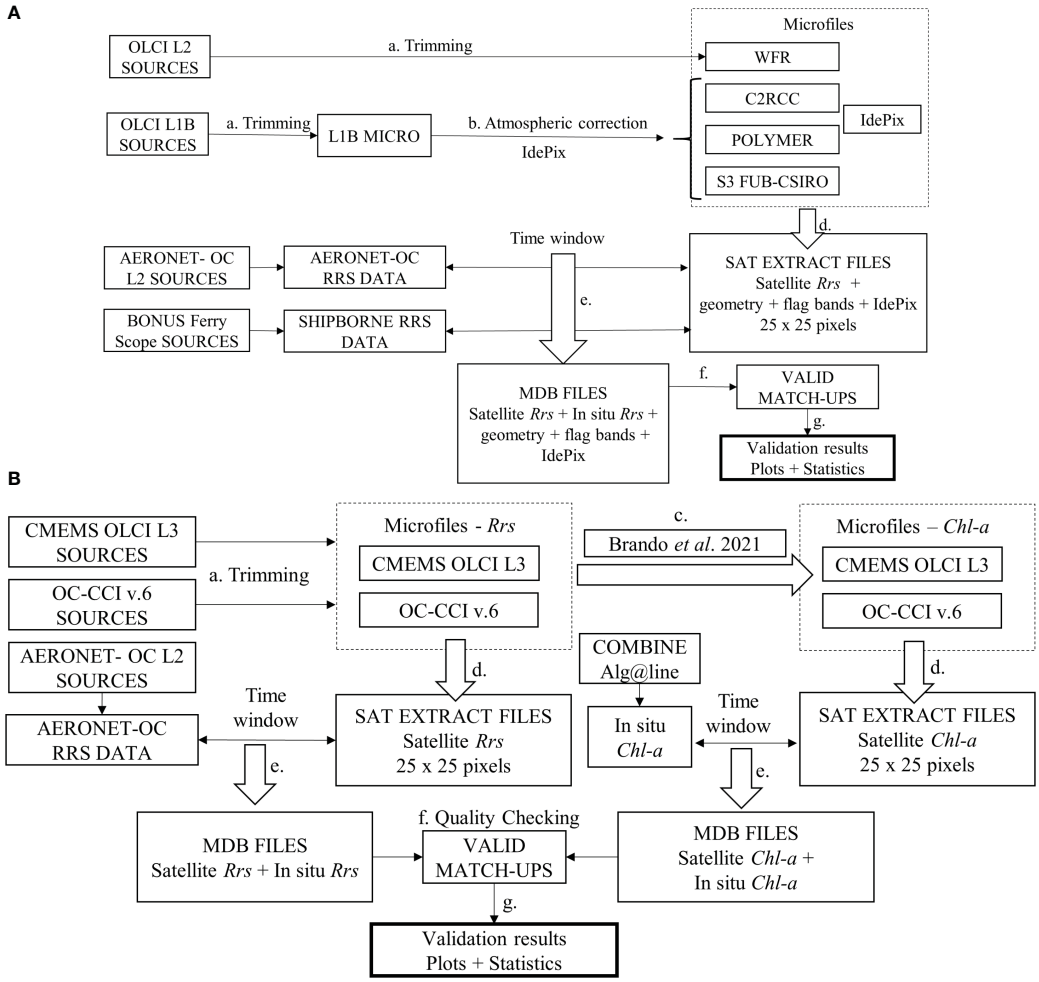


FIGURE 2
(A) Workflow for the comparative validation analysis of the four AC processors from OLCI level-1b to level-2 *Rrs*. **(B)** Workflow for the validation of CMEMS-OLCI and OC-CCI v.6 level-3 *Rrs* and chl-*a* datasets.

In the case of shipborne radiometry, to reduce the number of extracts associated with a single satellite image, extract files were only created if the time difference between the satellite overpass and the transect points within a given central pixel was lower than 15 min.

Level-3 extract files (Figure 2B) produced from level-3 microfiles include a window of 25 × 25 pixels of *Rrs* for all the bands around the AERONET-OC site or chl-*a* concentrations around the measurement location. Unlike level-2 extract files, flag bands are not required since invalid pixels were already masked in the source datasets during the level-3 creation. Moreover, as data with different acquisition times and observation geometries are merged, satellite time is limited to the date, and geometry information is not available.

e) Generation of MDB files: An MDB file is created as a NetCDF file including all the potential match-ups, i.e., spatiotemporal collocations between satellite and *in-situ* data, in this case, *Rrs* spectra or chl-*a* concentrations. MDB files are built by associating the satellite data from each extract file with the corresponding *in-situ* spectra or chl-*a* measurements. For level-3 extracts merging sensors with different acquisition times, satellite time is set to 9:30 UCT, which is approximately the average overpass time in the Baltic Sea considering all the sensors (Brando et al., 2021). By default, the maximum time difference between satellite and *in-situ* acquisitions is set to 3 h for AERONET-OC and chl-*a* measurements and 15 min for shipborne radiometry (see Section 2.4.3). Normalized water-leaving radiances available in the AERONET-OC level-2 source files (see Section 2.2.1) were transformed to *Rrs* by dividing by the extra-solar irradiance spectrum and then band-shifted to the OLCI or OC-CCI v.6 spectral wavelengths using inverse and direct application of the QAA algorithm (Mélin and Sclep, 2015; Lee et al., 2009). Shipborne radiometry data (already available as *Rrs*) and chl-*a* concentrations (in mg m^{-3}) were incorporated directly into the MDB files.

f) Quality checking: Starting from the MDB file with all the potential match-ups, we applied the quality control protocols to obtain valid match-ups for the statistical analysis (details are provided in Sections 2.4.2 and 2.4.3).

g) Statistical analysis: Plot generation and computation of validation metrics (see Section 2.4.4) using the valid match-ups.

2.4.2 Satellite quality control

Satellite quality control was based on the recommendations for OLCI or other medium-resolution satellites (Concha et al., 2021; Cazzaniga et al., 2022; Zibordi et al., 2022).

In this study, we used extraction windows of 3 × 3 pixels centered on the site only with 100% of valid pixels (9 pixels). Satellite *Rrs* for each band or chl-*a* concentrations were computed as the mean excluding outliers, considering a single pixel as an outlier if out of the range defined as the mean ± 1.5 standard deviations (EUMETSAT, 2022).

Pixels were masked according to two flag bands: IdePix and the specific flag band for each atmospheric correction algorithm. IdePix is used as a common framework for obtaining a set of common match-ups, whereas the specific flag band is useful for evaluating the spatial coverage of each AC processor in case of being applied operationally. Flag lists are summarized in Table 2.

Geometry was also considered for validation of level-2 *Rrs*, masking pixels with an observation zenith angle greater than 60° and a sun zenith angle greater than 70°.

We applied a spatial homogeneity test for *Rrs* validation by excluding match-ups with a coefficient variation (CV) at 560 nm higher than 20%. Note that CV is computed after the removal of out-of-range pixels (defined as the mean ± 1.5 standard deviations).

2.4.3 *In situ* quality control

As AERONET-OC systems acquire spectral measurements several times per day (usually every 20 min), MDB files can include up to 30 *in-situ* valid spectra for each satellite acquisition within the default 3-h time window. The validation was based on the closest spectrum in time with respect to the satellite overpass with a maximum time difference of 2 h.

For the Alg@line hyperspectral shipborne radiometry, the number of spectra in the central pixel within the 15-min time window varies from 1 to 3. Validation was also based on the closest spectrum in time.

In the case of chl-*a*, measurements collected between 7:00 UTC and 16 UTC on the same day as the satellite overpass were considered for obtaining valid match-ups.

2.4.4 Validation metrics

As validation metrics, we used the determination coefficient (R^2), the absolute percent differences (APD), the root mean square deviation (RMSD), the relative percent differences (RPD), and the bias parameter between the *in-situ* (x) and satellite measurements (expected y):

$$R^2 = \frac{\sum_{i=1}^{N}(x_i-\bar{x})(y_i-\bar{y})}{\sqrt{\sum_{i=1}^{N}(x_i-\bar{x})^2}\sqrt{\sum_{i=1}^{N}(y_i-\bar{y})^2}}$$

$$RMSD = \sqrt{\frac{\sum_{i=1}^{N}(y_i-x_i)^2}{N}}$$

$$APD = \frac{1}{N}\sum_{i=1}^{N}\frac{|y_i-x_i|}{x_i} \times 100\,\%$$

$$RPD = \frac{1}{N}\sum_{i=1}^{N}\frac{y_i-x_i}{x_i} \times 100\,\%$$

$$bias = \frac{1}{N}\sum_{i=1}^{N} y_i - x_i$$

The determination coefficient R^2 (unitless) assesses the agreement between both variables ranging from 0 (no agreement) to 1 (perfect agreement). The bias (in *Rrs* units: sr^{-1}, or *chl-a* units: mg m^{-3}) is useful for determining if there is overestimation (positive values) or underestimation (negative values). RMSD and APD (%) measure the absolute error in absolute units or percentage, respectively. Likewise, RPD (%) is a measurement of the relative error, but measured in percentage. In the case of chl-*a*, R^2, RMSD, and bias are computed on log-transformed data, whereas RPD and APD are based on non-transformed values. As error measurement, APD is preferred for the chl-*a* because RMSD is more difficult to interpret since it is based on log-transformed data, where RMSD is used for *Rrs* validation.

2.5 Comparison between CMEMS-OLCI level-3 and OC-CCI v.6 datasets

As within CMEMS two operational *Rrs* and chl-*a* datasets are available for the Baltic Sea, the consistency of the times series with spatial resolutions at 300 m and 1 km was assessed. To this aim, the CMEMS-OLCI level-3 and multisensor datasets were compared through the extraction of a set of co-collocated data points. Values were extracted from an image every 10 days from 1 May 2016 to 31 December 2022. These daily images were sampled based on a regular grid of 10 km × 10 km (115 × 119 longitude–latitude points), using the corresponding pixel value for the multisensor 1-km dataset and the mean on a 3 × 3 window for OLCI (only cases with 9 valid values were considered). The extraction was carried out for the five *Rrs* bands involved in the chl-*a* retrieval (i.e., 443 nm, 490 nm, 510 nm, 555 nm, and 670 nm) and for the chl-*a* concentration itself. Then, we obtained the scatter plots and computed the validation metrics (Section 2.4.4).

3 Results

3.1 Match-up summary and flagging analysis

Table 3 shows the number of total and valid match-ups available for the validation of level-2 (OLCI) and level-3

10.3389/fmars.2023.1256990

TABLE 3 Total and valid number of match-ups available for *Rrs* validation of OLCI level-2 and level-3 (CMEMS-OLCI and OC-CCI v.6) datasets.

		OLCI level 2						Level 3				
								CMEMS-OLCI		OC-CCI v.6		
		All	Valid				C.M.	All	Valid	All	Valid	C.M.
			WFR	C2RCC	POL.	S3 FUB-CSIRO						
AERONET	Total	1,161	546	522	773	538	392	706	486	785	561	433
	GDL	564	292	274	404	285	215	338	241	377	266	210
	HLH	185	79	80	117	84	53	141	90	164	122	80
	ILH	412	175	168	252	169	124	227	155	244	173	143
SYKE		348	182	114	207	117	110					

AERONET-OC sites are Gustav Dalen Tower (GDL), Helsinki Lighthouse (HLH), and Irbe Lighthouse (ILH). C.M. indicates the number of common match-ups for both level-2 and level-3 datasets; POL.: POLYMER v.4.14.

(CMEMS-OLCI and OC-CCI v.6) *Rrs* datasets, using both AERONET-OC and SYKE data.

When considering *in-situ* data from AERONET-OC sites, POLYMER is able to generate a higher number of valid match-ups for OLCI level-2 *Rrs* validation as compared with other AC processors (~65% of valid match-ups against ~45%), which show comparable figures. The percentage of valid match-ups is lower using SYKE data, but with a similar pattern: POLYMER shows the highest validity rate (~60%), followed by WFR (~52%) and finally C2RCC and S3 FUB-CSIRO (~35%).

Regarding the level-3 *Rrs* validation, both CMEMS-OLCI and OC-CCI v.6 show similar numbers with percentages of valid match-ups of approximately 70%, as expected considering that both datasets are mainly based on POLYMER.

As for the distribution across the AERONET-OC sites, the number of total (and valid) match-ups reveals the data availability, with more match-ups from Gustav Dalen Tower (data from 2016 to 2022), followed by Irbe Lighthouse (data from 2018 to 2022) and finally Helsinki Lighthouse (data from 2016, 2017, and 2019). Temporally, the number of match-ups has increased since 2018 (e.g., from 45 POLYMER valid match-ups in 2017 to 98 in 2018) with the launch of Sentinel-3B, being 2019 the year with the highest number as *in-situ* spectra were available from the three sites (e.g., 202 valid match-ups using POLYMER). The number of match-ups was also smaller in 2020 because the instruments were operational for a limited period (mainly between July and August) due to the COVID restrictions (56 valid POLYMER match-ups against 150 in 2021 or 171 in 2022).

Validation results shown in the following sections are based on common match-ups, i.e., those valid for all the AC processors in the case of level-2 *Rrs* validation and for both datasets (OLCI and OC-CCI v.6) in the case of level-3 *Rrs* validation.

Figure 3 shows a summary of the potential match-ups classified as invalid because at least one pixel in the 3 × 3 extraction window over the AERONET-OC sites was flagged using IdePix and/or other specific flag bands (Table 2).

The number of match-ups affected by cloud cover varies from 150 to almost 300 match-ups, depending on the flag band specific to each processor (Table 2). As *in-situ* data and potential match-ups are mainly available from April to September, cloud coverage percentage is relatively low (between 10% and 30%) when compared with sites located in mid-latitudes.

Sun glint risk was the most frequent flag based on *quality_flags* (C2RCC and S3 FUB-CSIRO) with more than 330 match-ups, although this number is limited to only 87 match-ups using *wqsf* (WFR).

A common problem in the CDOM-dominated Baltic Sea waters affecting more than 230 potential match-ups is the negative reflectance retrievals (RNEGs), mainly in the blue part of the spectrum, i.e., *rneg_02* (412 nm) and *rneg_03* (443 nm). Note that *rneg_* flags included in *wqsf* (WFR) allow negative values up to a threshold (EUMETSAT, 2021) so that some valid match-ups could include slightly negative reflectance values.

A remarkable number of match-ups were also flagged as *invalid* (42 match-ups in all the flag bands) and *bright* (133 match-ups using IdePix and *quality_flags*). Other flags (not shown in Figure 3) were identified in a small number of match-ups (less than 5), including the *suspect*, *dubious*, *whitecaps*, or *ac_fail* cases.

Approximately 100 match-ups were flagged by one of the flags in POLYMER *bitmask* (*out_of_bounds*, *thick_aerosol*, *high_air_mass*, *external_mass*, *inconsistency*, *anomaly_rwmod_blue*), joining to the match-ups classified as cloud (*cloud_base*) or invalid (*l1_invalid*). However, approximately 74 match-ups flagged as SUNGLINT_RISK or 146 as RNEG are considered valid using *bitmask* or IdePix, explaining the higher number of valid POLYMER match-ups as compared with other AC processors.

3.2 Level-2 *Rrs* validation

This section reports the validation results for OLCI level-2 *Rrs* processed using the four AC processors: WFR (standard AC), C2RCC, POLYMER, and S3 FUB-CSIRO (see Section 2.1.1). Satellite *Rrs* were validated against *in-situ* radiometric data from AERONET-OC (Section 3.2.1) and Alg@line shipborne radiometry (Section 3.2.2) based on common sets of 392 and 100 valid match-ups, respectively (Table 3).

10.3389/fmars.2023.1256990

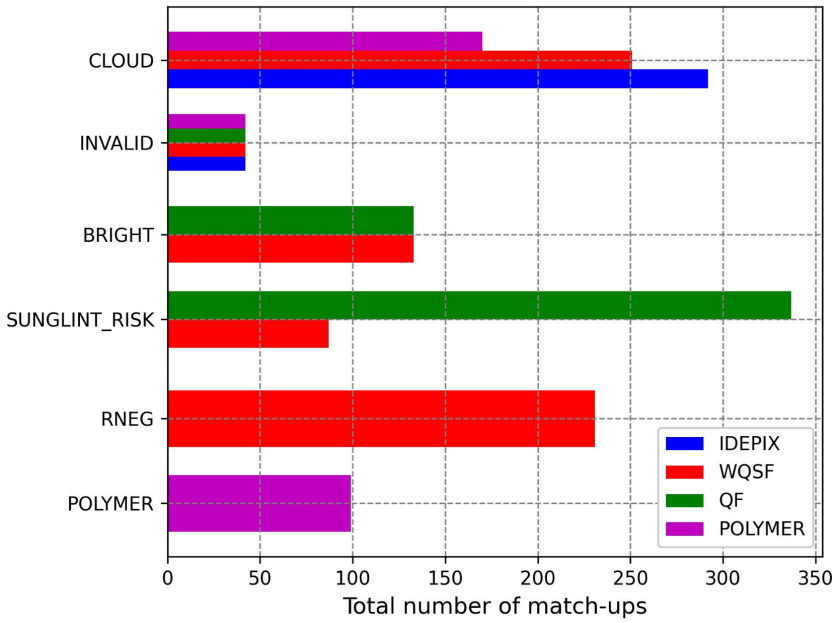


FIGURE 3
Total number of invalid match-ups with at least one pixel flagged in the 3 × 3 extraction window over the AERONET-OC sites. Legend colors indicate specific flag bands (IdePix: *pixel_classif_flag*; WQSF: *wqsf*; QF: *quality_flags*; POLYMER: *bitmask*). Specific flags defining each flag output are indicated according to the subscripts of Table 2 (1: CLOUD; 2: INVALID; 3: BRIGHT; 4: SUNGLINT_RISK; 5: RNEG; 6: POLYMER).

3.2.1 AERONET-OC

Figure 4 shows the comparison between *in-situ Rrs* spectra from AERONET-OC sites and OLCI level-2 *Rrs* spectra processed using the four AC processors. Note that *in-situ* data for OLCI bands between 673.75 nm and 753.75 nm, as well as 885 nm, are not available using the multispectral AERONET-OC radiometers, as we limited the band shifting to a maximum of 5 nm (Table 2). Data for 1,020 nm were also excluded from the analysis because they are affected by high uncertainties in these highly absorbing waters and are not included in the OLCI level-3 dataset.

In the case of WFR, both *in-situ* and satellite median spectra keep a similar shape across the whole range, with a remarkable overlapping of the interquartile areas between 520 nm and 620 nm. In other wavelengths, WFR tends to underestimate, showing high negative deviations and higher variability in the 400–490-nm spectral range. POLYMER also shows similar spectral shapes, although it tends to overestimate across the whole spectra (except at 865 nm), with higher positive deviations between 400 nm and 490 nm. Regarding C2RCC, although satellite and *in-situ Rrs* spectra keep similar shapes, there is a substantial overestimation, even without any overlapping between the interquartile areas at wavelengths lower than 510 nm. Finally, despite the acceptable overlapping, the main problem of S3 FUB-CSIRO is the spectral shape, as it tends to overestimate at wavelengths lower than 510 nm but shows negative deviations in the red part of the spectrum.

The match-up scatter plots between satellite and *in-situ* AERONET-OC *Rrs* for nine OLCI bands (between 400 nm and 778.75 nm) grouped by AC processor are shown in Figure 5. The results include all the available bands for validation using AERONET-OC data except for 865 nm and 1,020 nm (Table 2). The number of valid match-ups is lower for bands 400 nm, 510 nm, 560 nm, 620 nm, and 778.75 nm as *in-situ* data at these spectral bands were only available after 2018 (Table 2). Note also that the S3 FUB-CSIRO reflectance is not available at 400 nm and 778.75 nm.

In the blue bands (i.e., 400, 412.5, and 442.5 nm), POLYMER displays a better agreement with the *in-situ* data than other AC processors, which are affected by a marked deviation of their regression lines from the identity line (1:1). At 490 nm and 510 nm, POLYMER and S3 FUB-CSIRO perform better, whereas C2RCC and WFR tend to over- and underestimate, respectively. A good agreement is obtained at 560 nm using all the ACs except for C2RCC, which shows a positive bias. In the red part of the spectrum (i.e., 620 nm, 665 nm), the POLYMER regression line in agreement with the identity line is better than that of other ACs. Finally, at 778.75 nm, there are higher uncertainties and none of the AC processors seem to perform adequately. Nevertheless, POLYMER seems to give the best results when limiting the match-ups to low *Rrs* values (<0.5 10^{-3} sr^{-1}).

Figure 6 shows the spectral variation of some validation metrics per wavelength and AC algorithm, including also results in the infrared (i.e., 865 nm and 1,020 nm). Metric values confirm the tendencies observed in Figures 4, 5 in the visible spectral range. The WFR performance in the blue spectral region is inadequate with negative bias and RPD values and higher RMSD and lower correlation coefficients compared with other processors. However, statistical figures improve between 510 nm and 778.75 nm, being the best-performing algorithm at 560 nm. Broadly speaking, C2RCC performs worse than other AC algorithms clearly overestimating the *in-situ Rrs* (Figures 4, 5). It shows higher RMSD values, lower determination coefficients, and very high

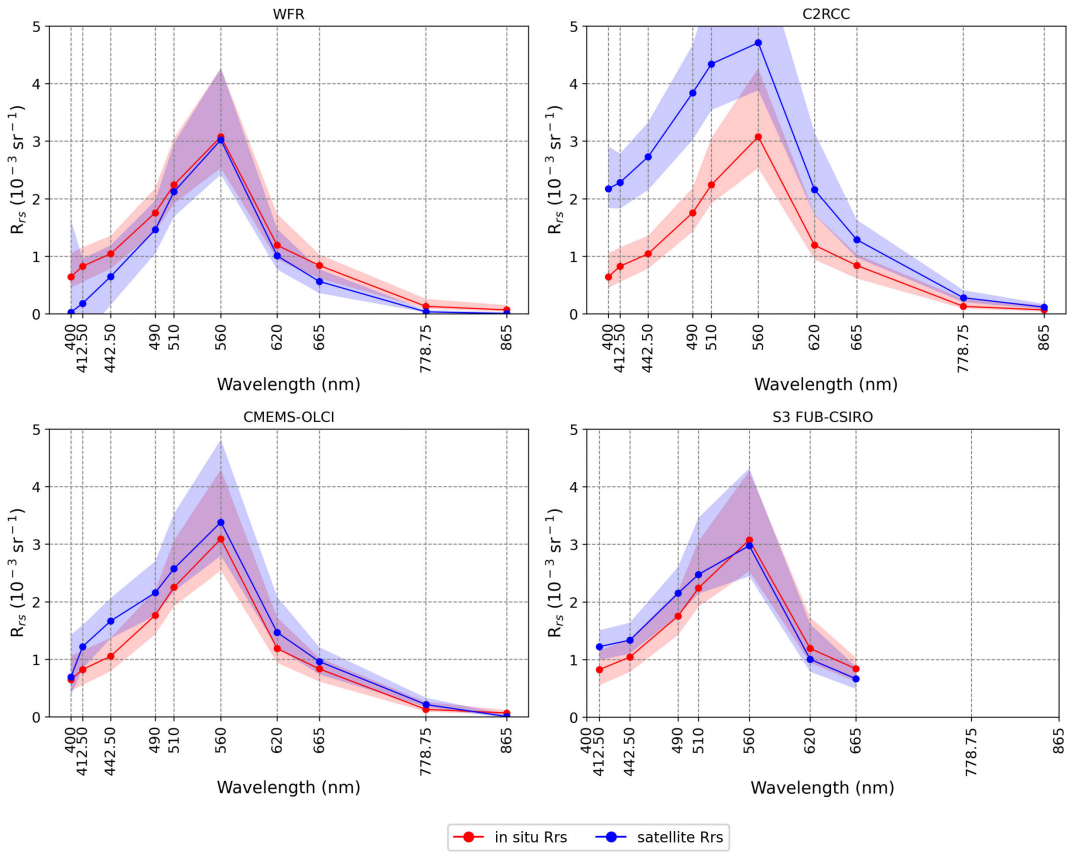


FIGURE 4
Comparison between *in-situ Rrs* from AERONET-OC sites and OLCI level-2 *Rrs* obtained using four AC processors: WFR, C2RCC, POLYMER, and S3 FUB-CSIRO. Distribution is based on the set of common match-ups (N = 392). Lines and shadowed areas represent the median values and the interquartile ranges, respectively.

positive RPD and bias values (up to 0.002 sr^{-1}), especially between 400 nm and 620 nm. On the other hand, POLYMER is the best-performing AC processor: it provides the best fitting (higher R^2) and lower error (RMSD) values (except for 442.5 nm). As observed in Figure 4, its main issue is the overestimation, showing positive RPD and bias values (lower than 0.0005 sr^{-1} except for 442.5 nm) across the visible spectral range. Finally, S3 FUB-CSIRO performs well in terms of error (RMSD) and fitting, with determination coefficients only lower than those obtained using POLYMER. Its main drawback is the spectral shape (Figure 4), with bias and RPD varying from positive to negative values with increasing wavelengths. Overall, metrics in the infrared spectral region are worse in comparison with those obtained for the visible spectral range. At 865 nm, WFR provides better results, whereas C2RCC performs better at 1,020.5 nm.

3.2.2 Shipborne radiometry

A comparison between *in-situ Rrs* spectra from Alg@line shipborne radiometry and OLCI level-2 *Rrs* spectra processed using the four AC processors is shown in Figure 7. In this case, as the shipborne radiometric data are hyperspectral measurements, *in-situ* data are available for all the OLCI bands. Although patterns are similar to those observed in Figure 4, some differences exist.

In detail, WFR can express well the median spectral shape, but with a higher negative bias across the bands and limited overlapping of the interquartile areas between 400 nm and 442 nm. In the case of C2RCC, it also shows extreme positive deviations for all the wavelengths, with hardly any overlapping between both distributions. S3 FUB-CSIRO follows the same pattern with a transition from positive to negative bias toward the red, but with higher uncertainties and less overlapping in the blue part of the spectrum.

Regarding POLYMER, the divergence from the reference data is more pronounced than in Figure 4: it shows negative deviations at 400 nm and 412 nm and an anomalous spectral shape between 673.75 nm and 708 nm in the three bands that are acquired at AERONET-OC sites (and hence not shown in Figure 4). For the remaining bands, they display a spectral shape agreement with a lower positive bias.

Figure 8 shows the match-up scatter plots between satellite and *in-situ* shipborne *Rrs* grouped by AC processor for the same nine OLCI bands between 400 nm and 778.75 nm shown in Figure 5. Overall, the results are worse than those obtained with the AERONET-OC sites, with the regression lines clearly deviating from the identity line (1:1). This behavior could be due to the presence of some *in-situ* spectra with very high *Rrs* values, possibly unflagged glint.

10.3389/fmars.2023.1256990

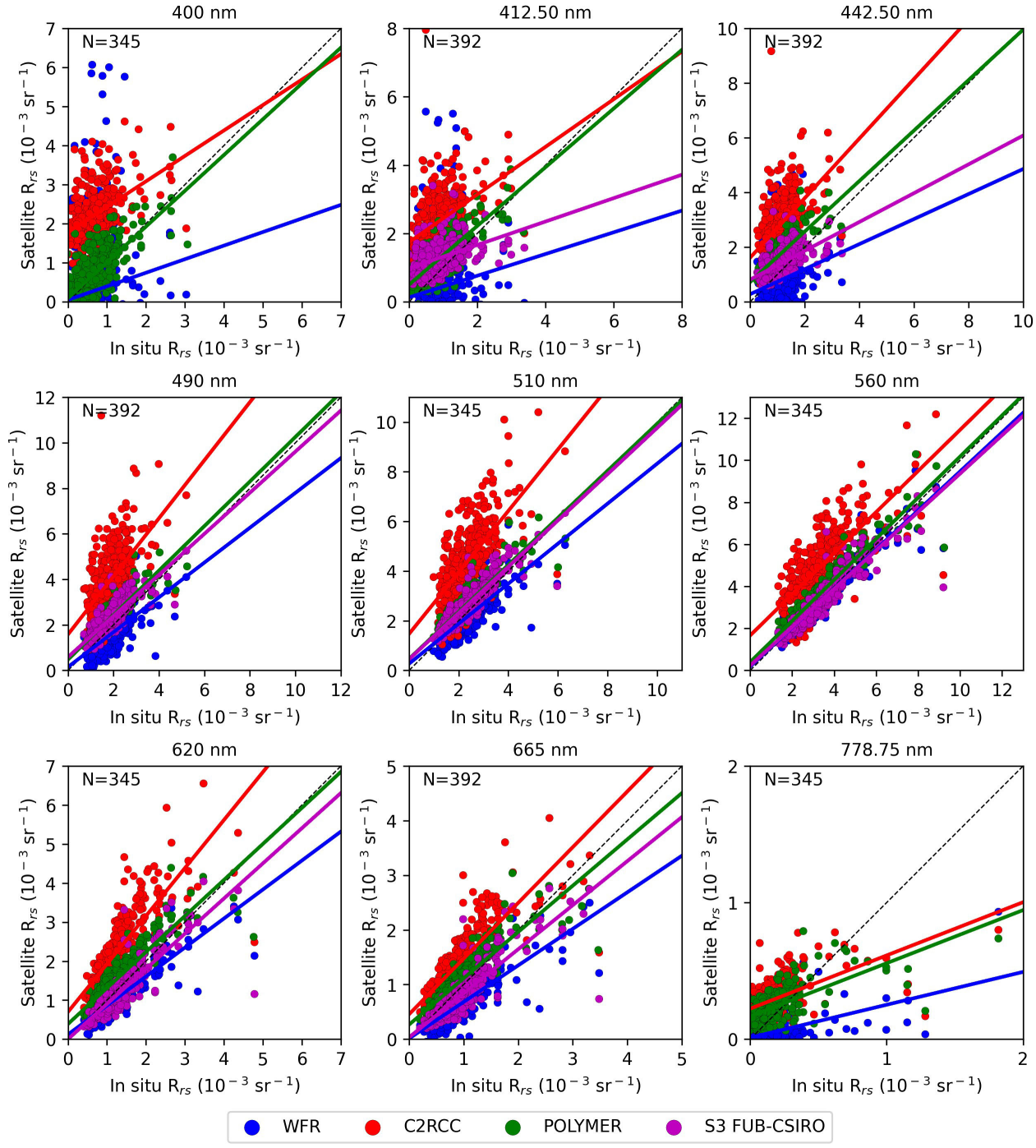


FIGURE 5
Scatter plots of common match-ups between satellite (OLCI level-2) and *in-situ* (AERONET-OC) *Rrs* measurements for nine OLCI bands between 400 and 778.75 nm. Data points and regression lines are color-coded by AC. The dash line represents the identity line (1:1 ratio).

If we consider the distribution of the data points, POLYMER seems to perform better with a higher density over the identity line for all the wavelengths, although S3 FUB-CSIRO also shows good results, especially in the central wavelengths. Like AERONET-OC validation results, and as observed in Figure 7, WFR presents higher variability in the blue (wavelengths lower than 490 nm) and a better agreement in the green and red parts of the spectrum, whereas C2RCC tends to overestimate with high positive deviations across the spectra.

The spectral metrics for each processor (Figure 9) confirm the patterns observed in Figures 7, 8, as well as the validation results based on AERONET-OC *in-situ Rrs*. POLYMER is again the best-performing processor in the visible spectral range in terms of error (RMSD, RPD) and fitness (R^2), showing a positive bias lower than 0.0005 sr^{-1} across the spectra (except for 400 nm). As observed in Figure 7, performance is worse between 673.75 nm and 708.75 nm for the bands not validated using AERONET-OC, with lower R^2 and

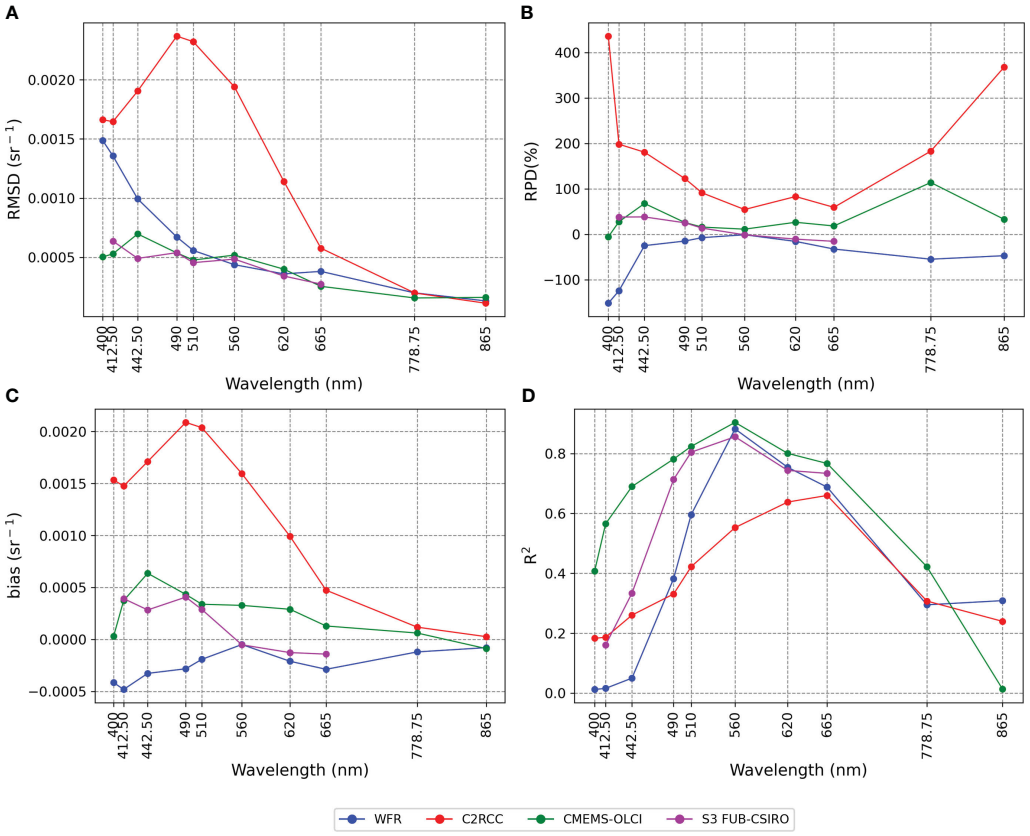


FIGURE 6
Spectral variation of the validation metrics computed for each AC from match-ups of OLCI level-2 and AERONET-OC *in-situ Rrs* data. **(A)** RMSD (in *Rrs* units: sr^{-1}). **(B)** Relative percent differences (%). **(C)** Bias (in *Rrs* units: sr^{-1}). **(D)** Determination coefficient (R^2, unitless).

higher bias values. WFR does not perform well in the blue part of the spectrum, showing higher RMSD values and high negative bias compared with POLYMER or S3 FUB-CSIRO. The S3 FUB-CSIRO shows similar results to POLYMER between 560 nm and 708.75 nm, even with a better agreement (higher R^2 value) at 708.75 nm and a lower RMSD at 560 nm. However, the results are worse in terms of correlation and RMSD with wavelengths lower than 510 nm, and it cannot match the spectral shape as indicated by the decreasing bias (changing from positive to negative values) with increasing wavelengths. C2RCC, as seen in Figures 7, 8, shows a high positive bias across the whole spectra and high RMSD values with wavelengths lower than 620 nm. Overall, it performs worse than other ACs at all the wavelengths and metrics except for its higher determination coefficients between 620 nm and 708 nm. Performance metrics in the infrared (865 nm, 885 nm, and 1,020 nm) are worse than those obtained for the visible range in terms of correlation and RPD, although bias and RMSD show comparable values due to their lower *Rrs* range. WFR appears as the best-performing AC in this spectral range, with higher R^2 and lower RPD values.

3.3 Level-3 *Rrs* validation

The OLCI level-3 *Rrs* dataset was processed by merging OLCI level-2 *Rrs* obtained using POLYMER v.4.14, as it was the best-performing AC algorithm in the Baltic Sea according to the results shown in Section 3.2. In this section, we summarize the validation results of this dataset in comparison with the multisensor level-3 *Rrs* dataset derived from OC-CCI v.6 (see Section 2.1.2) using *in-situ* radiometric measurements from AERONET-OC as reference. In addition to a common set of 433 match-ups acquired between 2016 and 2022, the results were obtained for the complete OC-CCI v.6 time series (2005–2022). Figure 10 shows the comparison between satellite and *in-situ* spectra using all the datasets and including the six bands available in OC-CCI v.6.

Using the complete time series (Figure 10A), OC-CC1 v.6 captures the spectral shape across the complete spectral range with positive deviations for all the bands except for 665 nm. Similar results are observed with data from the OLCI period (Figure 10B), although the bias is close to zero or slightly negative at 560 nm with a larger overlap of the interquartile regions. CMEMS-OLCI level 3 also matches the spectral shape with positive deviations at all the bands (including 665 nm) and a relatively higher bias value at 443 nm.

Scatter plots between satellite and AERONET-OC for the same six bands comparing CMEMS-OLCI and OC-CCI v.6 (complete time series and OLCI period) are shown in Figure 11. Overall, all the datasets perform adequately in terms of fitting, especially between 490 nm and 560 nm.

As observed in Figure 10, all the datasets show positive deviations with respect to the identity line between the 412-nm

10.3389/fmars.2023.1256990

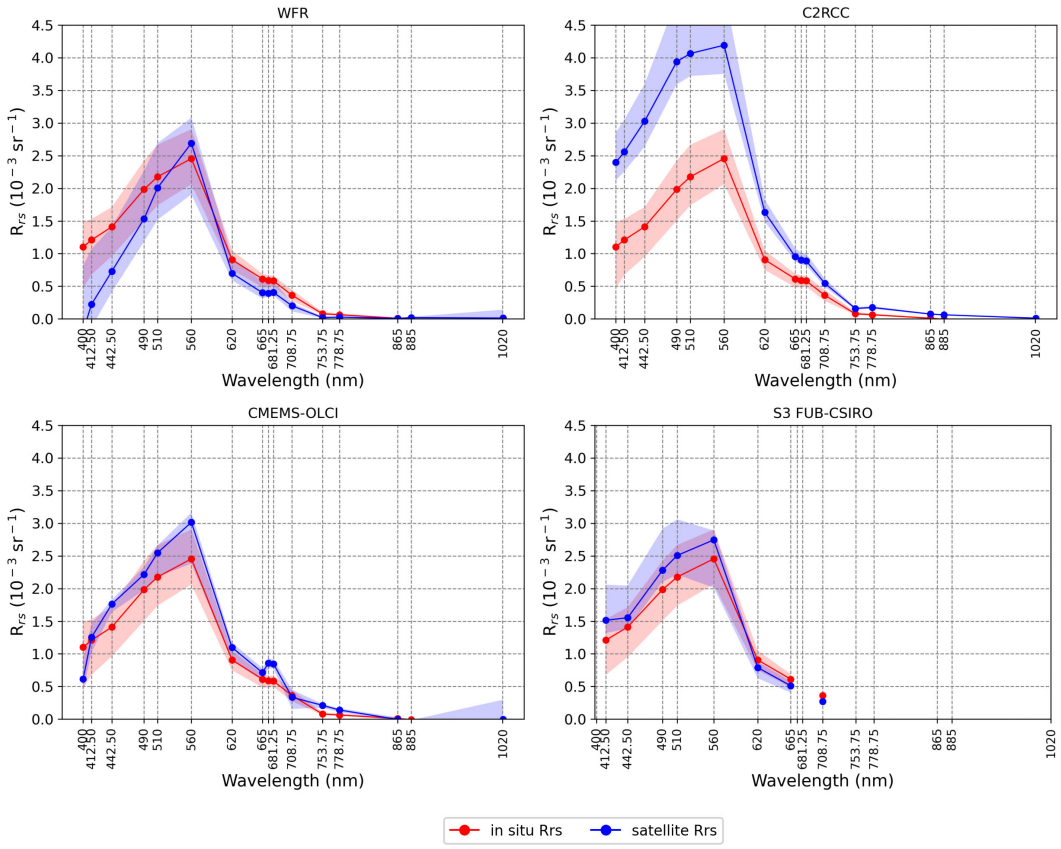


FIGURE 7
Comparison between *in-situ Rrs* from automated shipborne radiometry and OLCI level-2 *Rrs* obtained using four AC processors: WFR, C2RCC, POLYMER, and S3 FUB-CSIRO. Lines and shadowed areas represent the median values and the interquartile ranges, respectively.

and 490-nm spectral range, with an offset more remarkable at 443 nm. Although comparable regression fits were achieved from all the datasets, CMEMS-OLCI seems to perform better at 412 nm and 665 nm.

Figure 12 shows the spectral variation of some metrics computed from the match-ups between satellite level 3 and AERONET-OC *Rrs*.

Overall, all the metrics using the complete time series for OC-CCI v.6 are worse than those obtained only for the OLCI period, and this may be due to the differences in satellite missions being included in the OC-CCI v.6 time series and to differences related to the data availability from the three AERONET-OC sites.

Comparing CMEMS-OLCI and OC-CCI v.6 based on the metric computed with the common set of match-ups between 2016 and 2022, CMEMS-OLCI performs better at 412 nm and OC-CCI v.6 in the 490–665-nm spectral range in terms of RMSD, RPD, and bias, whereas the results are equivalent at 443 nm. In terms of correlation, similar R^2 values were obtained for all the wavelengths except at 665 nm, with a higher R^2 (0.84 vs. 0.77) for OC-CCI v.6. In summary, both level-3 datasets perform adequately in the 490–665-nm spectral range (R^2: 0.75–0.95; RMSD< 0.005) and acceptable results at 443 nm (R^2 ~ 0.75; RMSD< 0.007), whereas higher uncertainties are observed at 412 nm (Figure 12).

3.4 Chl-*a* validation

Chl-*a* concentrations were retrieved using the *chl-aENS3* ensemble approach based on *Rrs* spectra from CMEMS-OLCI and OC-CCI v.6 and validated against co-collocated *in-situ* chl-*a* measurements from COMBINE and Alg@line datasets. Scatter plots and main metrics are shown in Figure 13, including the results from a common set of match-ups (2016–2019) for both satellite datasets and from all the valid match-ups (1997–2019) using the complete OC-CCI v.6 time series.

Our dataset includes a total of 9,035 chl-a *in-situ* measurements from 1997 to 2019 (3,955 from Alg@line, 5,080 from COMBINE). For the OLCI period, only 1,047 measurements (325 from Alg@line, 722 from COMBINE) were available between 2016 and 2019. After applying the quality control (see Section 2.4), the number of valid match-ups for the OC-CCI v.6 (1997–2019) was 1,770, whereas for the OLCI period, validation for both CMEMS-OLCI and OC-CCI v.6 was based on a common set of 55 match-ups.

The results were quite comparable using the common set of match-ups, although, looking in detail, CMEMS-OLCI performs better for all performance metrics. As compared with CMEMS-OLCI, the results from the longer OC-CCI v.6 time series are characterized by a better fitness (R^2 = 0.29) and a lower RPD (5%), but also a higher APD (69%) and a tendency toward underestimation (bias = –0.14). These negative

10.3389/fmars.2023.1256990

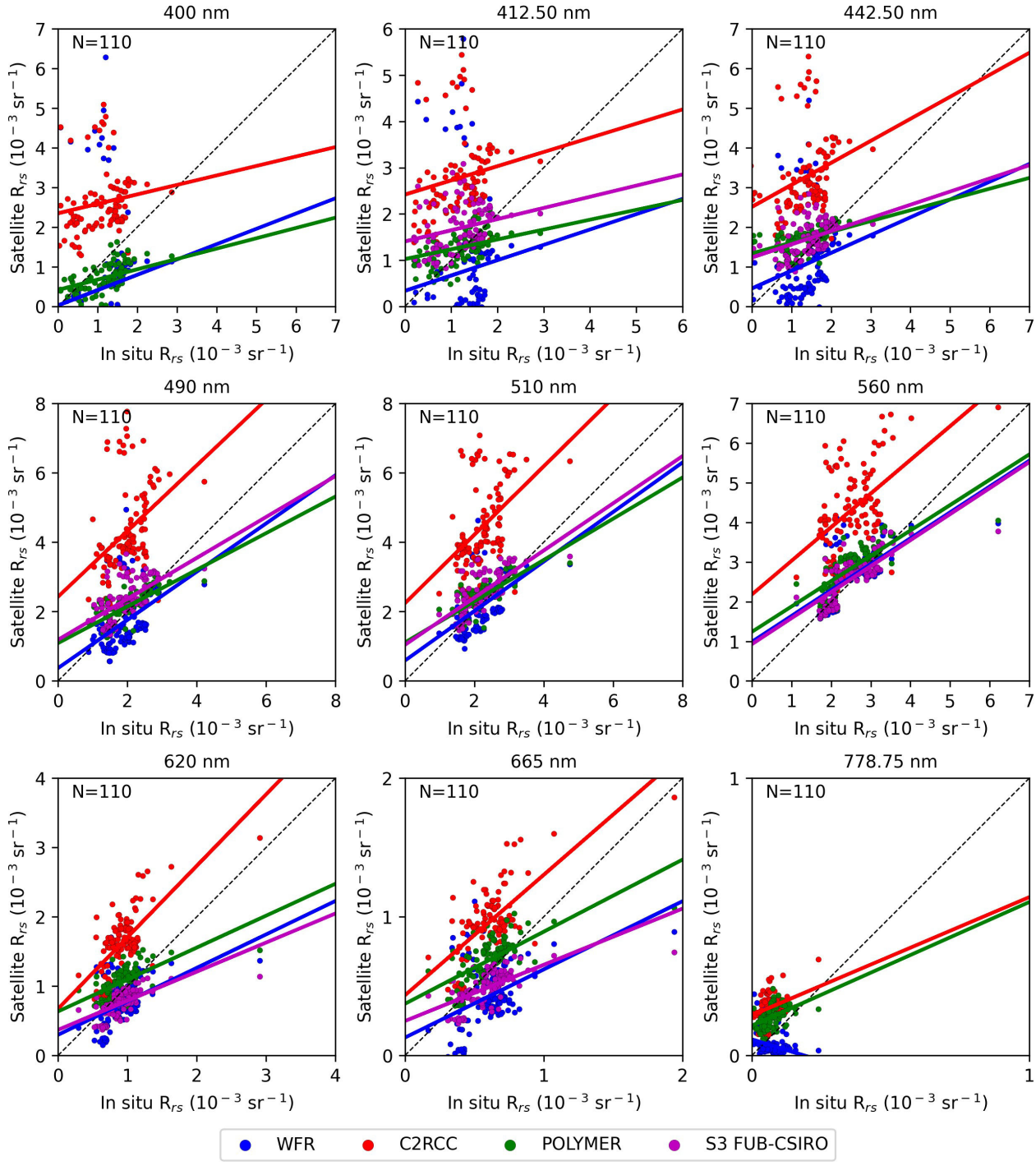


FIGURE 8
Scatter plots of common match-ups between satellite (OLCI level-2) and *in-situ* (shipborne radiometry) *Rrs* measurements, for nine OLCI bands between 400 nm and 778.75 nm. Data points and regression lines are color-coded by AC. The dash line represents the identity line (1:1 ratio).

deviations also appear in the results from the shorter OC-CCI v.6 time series (bias = −0.22) but are not observed in the CMEMS-OLCI dataset (bias = −0.03). Although metrics differences between both datasets could be explained by uncertainties associated with the input *Rrs* spectra, OLCI results should be interpreted with caution considering the lower number of match-ups (55 vs. 1,770) available for the OLCI period (from 2016 to 2019).

3.5 Comparison between CMEMS-OLCI and OC-CCI v.6 datasets

Figure 14 shows the scatter plots between OC-CCI v.6 and CMEMS-OLCI based on a set of co-collocated data points for the five *Rrs* bands involved in the chl-*a* retrieval as well as for the satellite-derived chl-*a* concentration (see Section 2.5).

10.3389/fmars.2023.1256990

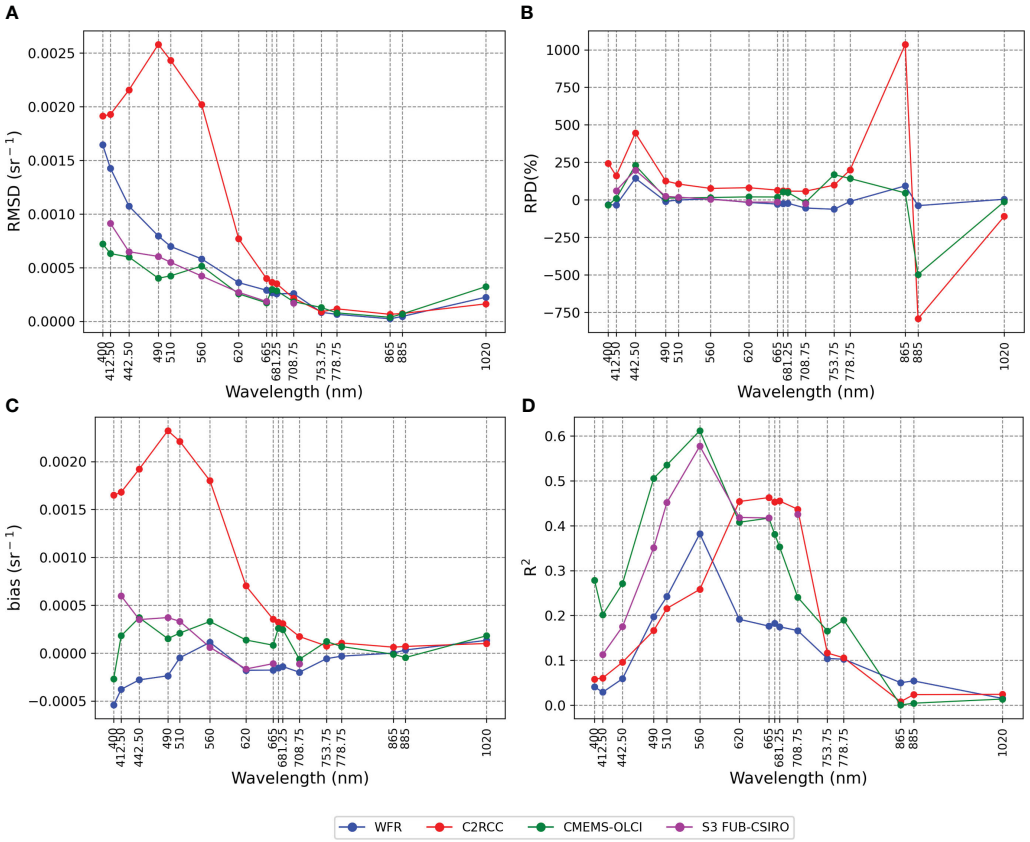


FIGURE 9
Spectral variation of the validation metrics computed for each AC from match-ups of OLCI level-2 and SYKE *in-situ Rrs* data. **(A)** RMSD (in *Rrs* units: sr^{-1}). **(B)** Relative percent differences (%). **(C)** Bias (in *Rrs* units: sr^{-1}). **(D)** Determination coefficient (R^2, unitless).

A good *Rrs* fitting with determination coefficients higher than 0.90 was observed in the 490–670-nm spectral range, whereas a poorer agreement and a higher dispersion, especially with low *Rrs* values (<5 10^{-3} sr^{-1}), were found at 443 nm. Most of the data points fall around the identity line leading to a bias value close to zero (lower than 1.9 10^{-4} sr^{-1}). In terms of percent error (APD and RPD), values were lower than 12% for all the bands except for 670 nm, whereas comparable RMSD values were also found for all the bands (between 2.7 10^{-4} and 7.6 10^{-4}). Note that RMSD depends, to some extent, on the distribution range, so that the maximum was obtained at 443 nm (i.e., with the maximum range) and the minimum at 670 nm (minimum range) despite this band showing the maximum APD.

The scatter plots also show the data points deviating from the expected 1:1 ratio. The greatest deviation of the regression line with respect to the identity line is observed at 443 nm, caused by a significant number of points with low OC-CCI v.6 values (lower than 5 10^{-3} sr^{-1}) but high CMEMS-OLCI *Rrs* (higher than 10 10^{-3} sr^{-1}). Moreover, some erroneous data points with low CMEMS-OLCI *Rrs* (lower than 0.5 10^{-3} sr^{-1}) but OC-CCI v.6 *Rrs* values approximately 5 10^{-3} sr^{-1} are also clearly visible in the scatter plot at 670 nm. These deviations are caused by problems with CMEMS-OLCI.

The chl-*a* concentration yielded an acceptable fitting (R^2 = 0.67) but with a negative bias, meaning that chl-*a* values retrieved from OC-CCI v.6 tend to be lower than those from CMEMS-OLCI. In fact, most of the points are located below the identity line. Similar to *Rrs* at 443 nm and 670 nm, there is also a significant number of data points deviated from the expected 1:1 ratio, with concentrations ranging from 1.5 mg m^{-3} to 15 mg m^{-3} from OC-CCI v.6 but values lower than 0.5 mg m^{-3} when retrieved from CMEMS-OLCI.

4 Discussion

This study presented the introduction within the Copernicus Marine Service of the operational *Rrs* and chl-*a* datasets for the Baltic Sea from OLCI full resolution (300 m). Poor performances have been reported in the assessment of OLCI *Rrs* for the Baltic CDOM-dominated waters using both the EUMETSAT Operational Baseline (Zibordi et al., 2018; Zibordi et al., 2022) and the alternative atmospheric correction processing chain based on CR2CC (Cazzaniga et al., 2022). Hence, the first step was to select the best AC method to retrieve OLCI *Rrs* by comparing the accuracy of four processors using *in-situ* radiometric data from AERONET-OC sites and Alg@line shipborne hyperspectral radiometry as reference.

Our validation results from both *in-situ* sources (fixed platform and shipborne observations) show that POLYMER v.4.14 was the best option for the implementation in the processing chain for the

10.3389/fmars.2023.1256990

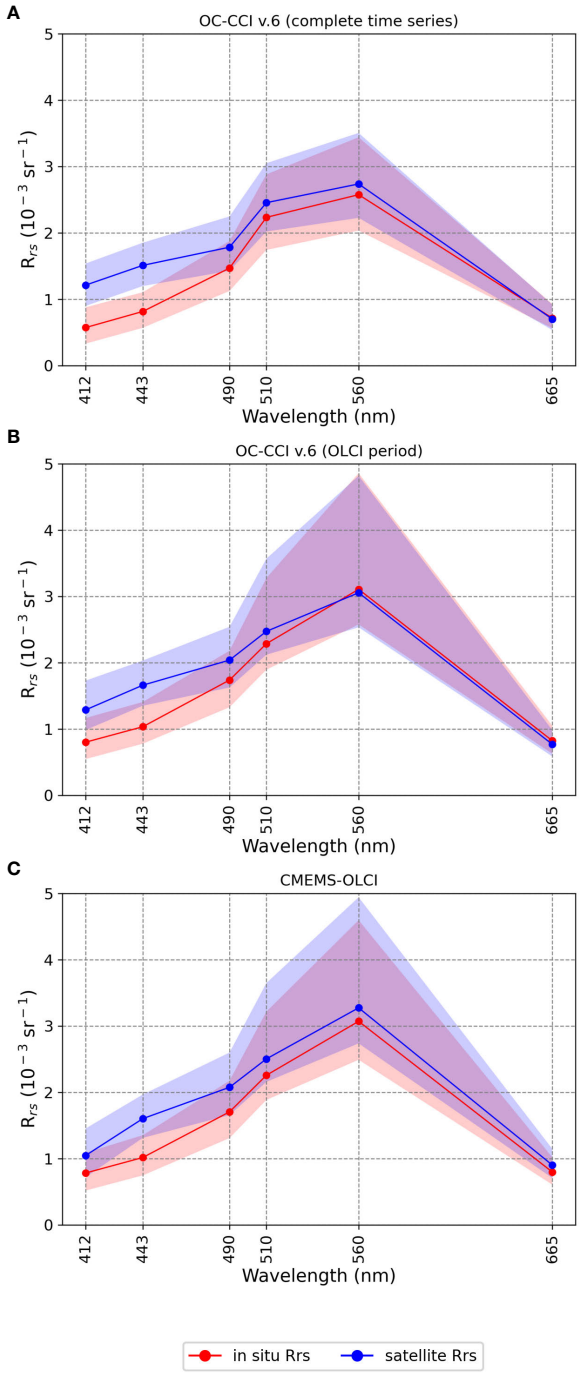


FIGURE 10
Comparison between *in-situ Rrs* from AERONET-OC sites and level-3 *Rrs* datasets. **(A)** OC-CCI v.6 (complete time series: 2005–2022). **(B)** OC-CCI v.6 (OLCI period: 2016–2022). **(C)** CMEMS-OLCI. Lines and shadowed areas represent the median values and the interquartile ranges, respectively.

new level-3 OLCI *Rrs* and chl-*a* datasets (see Section 3.2). In fact, it performs better not only in the 443–665-nm spectral range which includes the relevant bands for chl-*a* retrieval (Table 1), but also at 400 nm, 412.5 nm, and 778.75 nm. A greater variability in the metrics in the 673.75–708.75-nm spectral range (validated only with shipborne radiometry) and at 865 nm hinders the identification of the best-performing AC in this spectral range. Overall, performance differences are more remarkable in the blue spectral region (400–490 nm), especially in terms of correlation (Figures 6, 9). The main drawback for chl-*a* retrieval is the positive bias observed from both sources across the 412.5–665-nm spectral range.

Although validation results from AERONET-OC sites are expected to be more robust and reliable as *in-situ* data come from a stable platform with fewer uncertainties, metrics based on shipborne radiometry collected in 2016 were consistent and show the potential of this method to increase the number of match-ups providing data at other sites with different atmospheric and/or water conditions. According to Tilstone et al. (2022), differences between both *in-situ* sources could be mainly explained by two factors: 1) site differences—Baltic Sea waters are mainly dominated by CDOM, but ship trajectories could be more influenced by increases in chl-*a* concentrations due to phytoplankton blooms, whereas CDOM concentrations are generally higher in AERONET-OC sites; and 2) instruments and data processing—the differences in instruments (TriOS-RAMSES in the case of the hyperspectral shipborne radiometry; CIMEL-SeaPRISM for AERONET-OC) with their specific uncertainties by wavelength may be augmented by the fact that the data are processed with distinct methodologies. Moreover, in our study, shipborne radiometry is only available for validating Sentinel-3A in 2016, as AERONET-OC *in-situ* data extend from 2016 to 2022 enabling the validation of both Sentinel-3A and Sentinel-3B.

In our study, POLYMER results from AERONET-OC as compared with Alg@line in the 442.5–665-nm spectral range were better in terms of correlation (0.41–0.90 vs. 0.19–0.61), but slightly worse considering RMSD (2.6–7.0 10^{-4} sr^{-1} vs. 1.7–6.0 10^{-4} sr^{-1}) or bias (1.3–6.4 10^{-4} sr^{-1} vs. 0.8–3.7 10^{-4} sr^{-1}). As RPD are similar from the two sources (between 10% and 28% except for 442.5 nm), higher RMSD or bias values using AERONET-OC could also be related to its larger *in-situ Rrs* range and maximum values (see *in-situ* distribution in Figures 4, 7). Moreover, overall better results according to all the metrics were derived from AERONET-OC at 400 nm, 412.5 nm, and 778.75 nm (except for RMSD at 412.5 nm). At 400 nm, a negative bias was obtained from Alg@line (−2.7 10^{-4} sr^{-1}) but a positive value (3.2 10^{-5} sr^{-1}) from AERONET-OC, which could be related to differences in optical water characteristics: higher CDOM concentrations leading to lower *Rrs* (and higher bias) in AERONET-OC sites. In fact, only 21% of match-ups from AERONET-OC show *Rrs* greater than 1 10^{-3} sr^{-1} against 55% from the shipborne radiometry.

Another remarkable feature is the high RPD peak at 442 nm from shipborne radiometry, which is present in all the processors. This peak is explained by a small set of match-ups with very high RPD values (>200% with a maximum of approximately 23,000%) from 2 days (9 June 2016 and 28 July 2016). These high RPD values are caused by some outliers in the *in-situ* distribution at 442 nm characterized by very low *Rrs* values (0.06–0.86 10^{-3}), as compared with the interquartile range between 1.25 10^{-3} and 1.75 10^{-3} sr^{-1} (Figure 7). These results evidence that results from shipborne radiometry could be improved by a stricter *in-situ* quality control

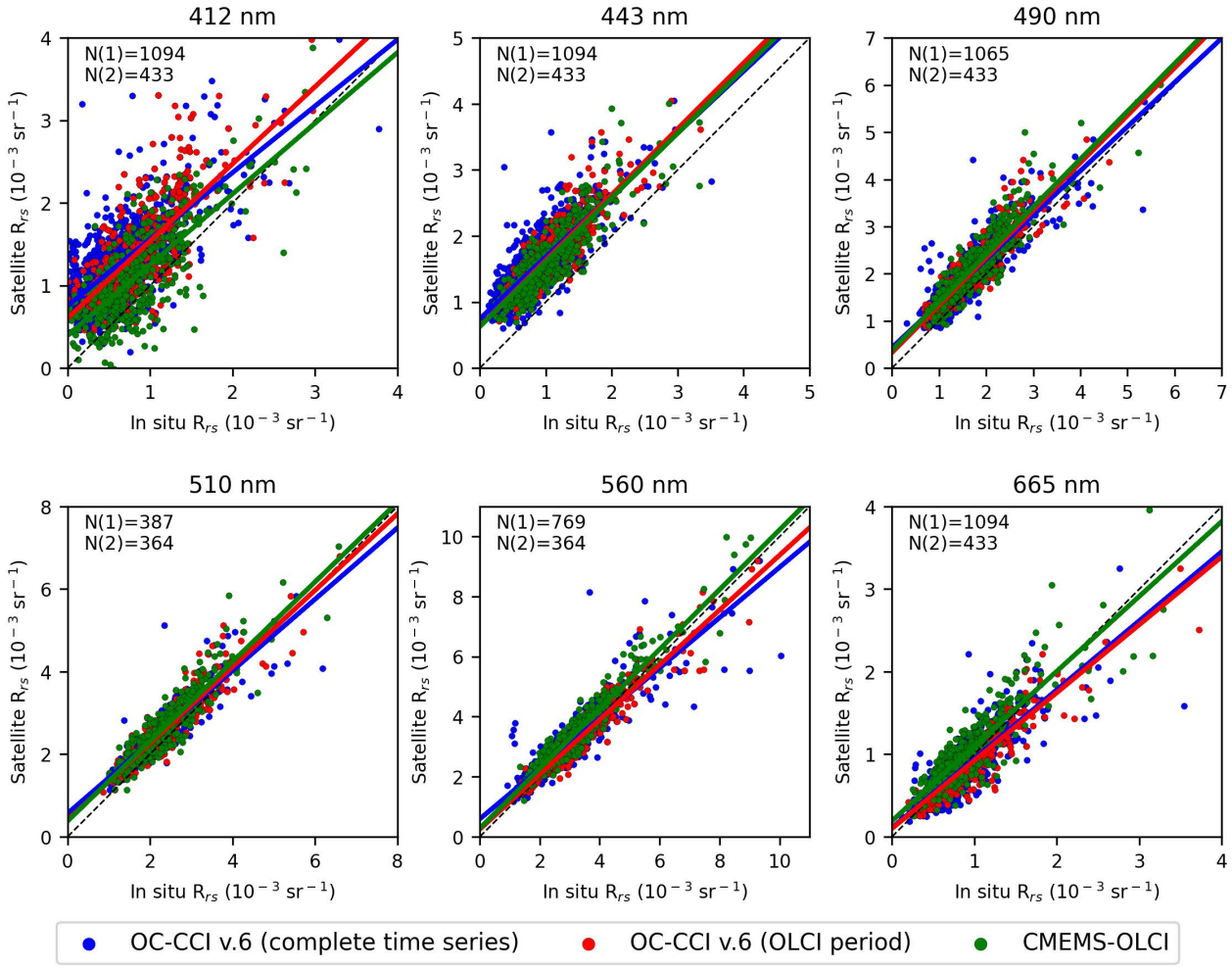


FIGURE 11
Scatter plots of match-ups between satellite level 3 and *in-situ* AERONET-OC *Rrs* measurements for six bands between 412 n and 665 nm. Data points and regression lines are color-coded by level-3 dataset (OC-CCI v.6—complete time series; OC-CCI v.6—OLCI period; CMEMS-OLCI). The dashed line represents the identity line (1:1 ratio). *N*(1) and *N*(2) are the number of match-ups available for the OC-CCI v.6 complete time series and for the OLCI period, respectively.

(e.g., removing spectra with outliers). However, this refinement is out of the scope of this work as we use the dataset as a method to confirm the conclusions based on AERONET-OC data.

POLYMER also shows advantages in terms of coverage in comparison with other AC methods as by design it is able to deal with residual sun glint (Steinmetz and Ramon, 2018). As seen in Table 3, the number of valid match-ups based only on POLYMER flag mask *bitmask* (846 valid match-ups from AERONET-OC) or combining *bitmask* and IdePix (773 valid match-ups from AERONET-OC) is 30% higher than those using other processors. However, yielding more match-ups does not imply a better or worse performance of the validation results. In fact, datasets showed similar distributions, with close ranges and median values across the spectra. Table 4, based on AERONET-OC *in-situ* data, presents comparable values for R^2, RMSD, or bias in the 412.5–665-nm spectral range, whereas expected higher uncertainties were observed at 400 nm or 778.75 nm. Note that bias was consistently lower across the whole spectra using only *bitmask*, especially in the blue, meaning that extra match-ups produced by POLYMER tend to show a lower bias.

Table 4 also shows the differences between the POLYMER validation metrics from Sentinel-3A and Sentinel-3B using *in-situ* data from AERONET-OC. Overall, results from Sentinel-3A are better considering all the metrics across the spectra, except for the bias between 620 nm and 778.75 nm. Differences are expected since match-up datasets do not show the same spatial–temporal coverage leading to different numbers of valid match-ups as Sentinel-3B is only available from 2018.

Our level-2 validation results agree with the findings in other works comparing AC algorithms over the Baltic Sea. Tilstone et al. (2022) assessed Sentinel-3A *Rrs* from WFR (pb 2.23–2.29 and OL_L2M.003), POLYMER v.4.14, and C2RCC using *in-situ* data from Alg@line shipborne radiometry (199 match-ups), Gustav Dalen Tower (5 match-ups), and Helsinki Lighthouse (4 match-ups), all the match-ups for only 2016. They found that POLYMER was the best-performing AC algorithm for six bands (412 nm, 443 nm, 490 nm, 560 nm, 665 nm, and 709 nm). Alikas et al. (2020) validated satellite OLCI *Rrs* from four AC processors (i.e., ALTNN, C2RCC, POLYMER, and WFR) against above-water field

10.3389/fmars.2023.1256990

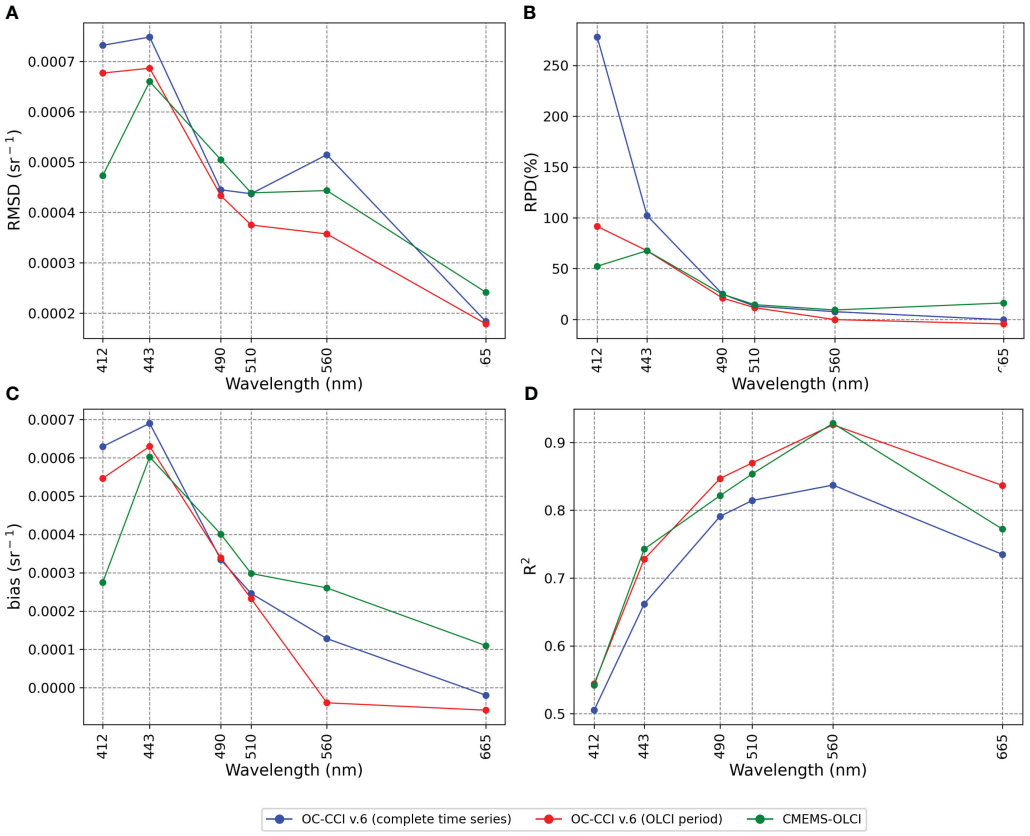


FIGURE 12
Spectral variation of the validation metrics computed from match-ups of level-3 datasets (OC-CCI v.6 complete time series; OC-CCI v.6—OLCI period; CMEMS-OLCI) and AERONET *in-situ Rrs* data. **(A)** RMSD (in *Rrs* units: sr^{-1}). **(B)** Relative percent differences (%). **(C)** Bias (in *Rrs* units: sr^{-1}). **(D)** Determination coefficient (R^2, unitless).

measurements collected from a research vessel over the coast of the Baltic Sea and Estonian Lakes in 2016. With a number of valid match-ups between 15 and 49 depending on the AC processor and filtering level, they reported POLYMER as the best suitable algorithm for all the OLCI bands except for 865 nm.

Since most of the valid match-ups (199 of 208) in Tilstone et al. (2022) are derived from the same dataset based on shipborne radiometry, metric values are expected to be similar to those reported in Section 3.2.2. In fact, RMSD values (2–6 10^{-4} sr^{-1} in this work; 3–7 10^{-4} sr^{-1} in Tilstone et al., 2022) or Pearson correlation coefficients (0.45–0.78 in this work; 0.38–0.6) follow a similar pattern. Differences are mainly observed in the bias, with negative values in Tilstone et al. (2022) (−4 10^{-4} to −1 10^{-4} sr^{-1}) instead of the positive bias found in our work (8 10^{-5} to 4 10^{-4}).

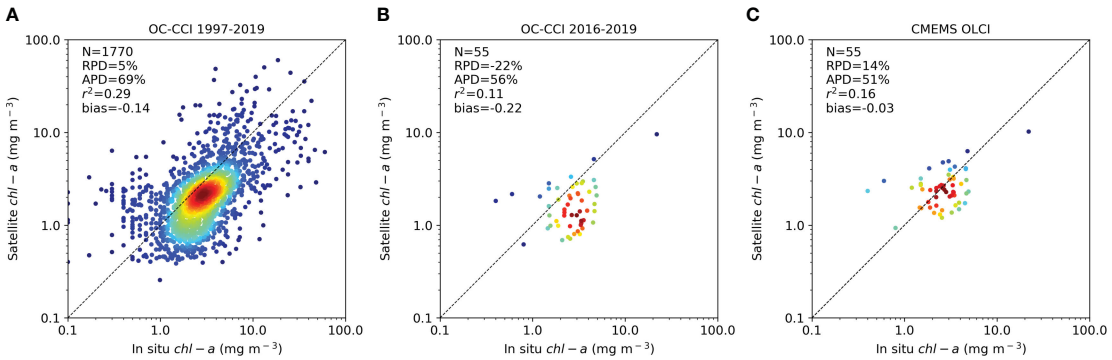


FIGURE 13
Scatter plots of match-ups between satellite-derived and *in-situ* log-transformed chl-*a* measurements. Satellite chl-*a* concentrations were retrieved using *chl-aENS3*. **(A)** all the valid match-ups (1997–2019) from OC-CCI v.6; **(B)** common match-ups (2016–2019) for OC-CCI v.6; and **(C)** CMEMS-OLCI. Data points are colored by density. The continuous line represents the 1:1 ratio.

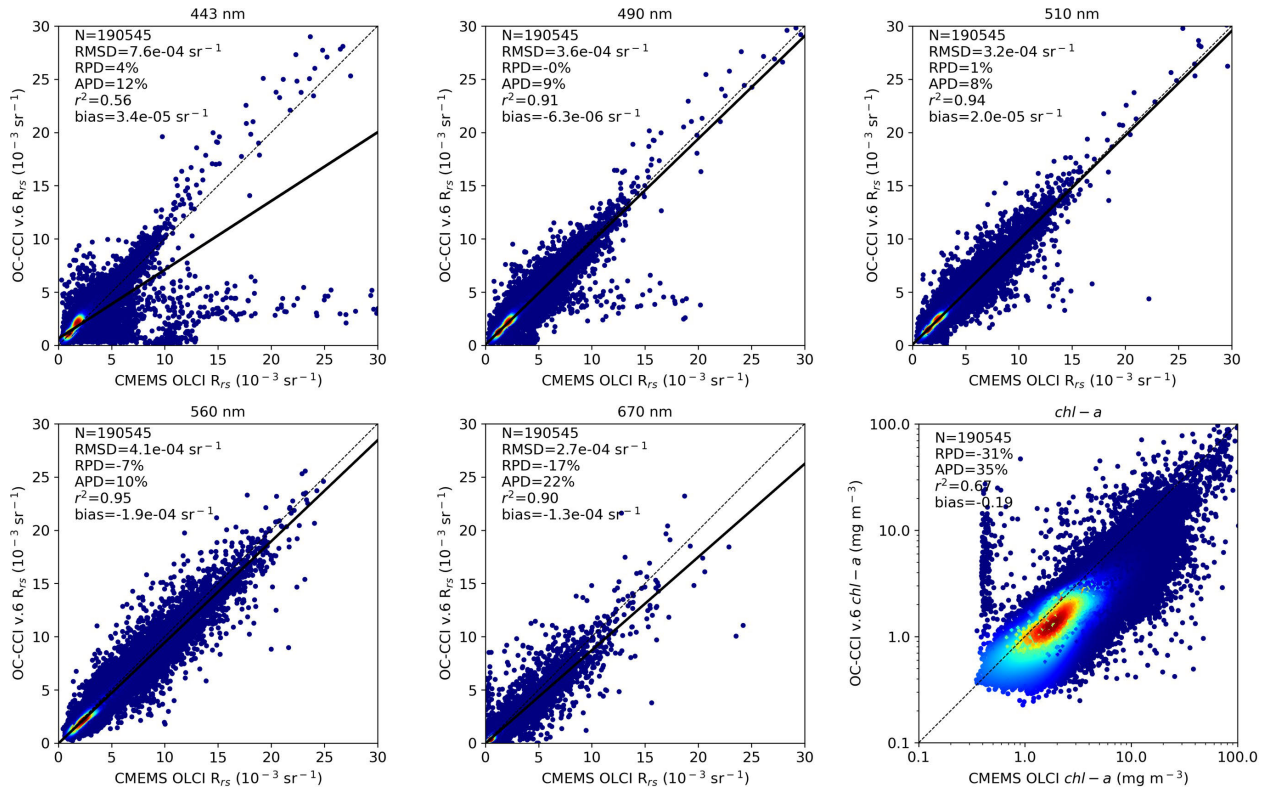


FIGURE 14
Scatter plots of co-collocated data points between OC-CCI v.6 and CMEMS-OLCI data points, including *Rrs* for five bands (443 nm, 490 nm, 510 nm, 560 nm, 670 nm) and chl-*a* concentration.

This disparity could be explained because we applied a stricter validation protocol with results based on a dataset of common match-ups, leading to a considerably lower number of match-ups (107 vs. 199 in Tilstone et al.). Relaxing our protocol using only *bitmask* as flag band, the number of valid match-ups increases until 251 and bias tends to be lower (likewise using the AERONET-OC dataset), so that comparable negative bias values ($-8.9\ 10^{-5}$ to $-1.4\ 10^{-4}$) were found in the 490–665-nm spectral range.

Regarding the level-3 datasets, the *in-situ* distribution for the complete OC-CCI v.6 time series (Figure 10A) is characterized by lower *Rrs* values at 490 and 560 nm in comparison with the OLCI period (Figures 10B, C). Differences are more remarkable at 560 nm, with an upper quartile value approximately $3.5\ 10^{-3}$ sr^{-1} against a peak of almost $5\ 10^{-3}$ sr^{-1}. These discrepancies could be explained by two facts. Firstly, differences in the optical water types related to the data availability from the three AERONET-OC sites: the complete time series include more spectra from Helsinki Lighthouse, whereas *in-situ* data from Irbe Lighthouse (available since 2018) become more predominant during the OLCI period as measurements at the Helsinki Lighthouse ended in 2019. Secondly, the results at 560 nm for the complete time series use *in-situ* data from the AERONET-OC band at 555 nm available between 2005 and 2011, introducing uncertainties associated with the band-shifting process. However, the results for the OLCI period are only based on the AERONET-OC band at 560 nm introduced in 2018 (Table 1).

Using the common set of match-ups, CMEMS-OLCI and multisensor OC-CCI v.6 show equivalent distributions and metrics (with some differences indicated in Section 3.3) notwithstanding the different spatial resolution (300 m vs. 1 km). This similar behavior could be explained because both datasets are based on the same AC processor, i.e., POLYMER (with the exception of SeaWiFS), and that from 2020 onward, OC-CCI v.6 is based only on OLCI from Sentinel-3A and Sentinel-3B, as MODIS-AQUA and VIIRS are included only until the end of 2019 (OC-CCI, 2022). As expected, the metrics from CMEMS-OLCI L3 (Figure 6) are very close to those from POLYMER OLCI L2 (Figure 12).

Our results based on the complete OC-CCI v.6 time series differ from the metrics for OC-CCI v4.2 reported in Brando et al. (2021). OC-CCI v.6 performs better in terms of correlation for the 412–490-nm spectral range, whereas R^2 values are similar for the other bands, with more remarkable differences at 400 nm (0.51 vs. 0.05) and 442.5 nm (0.66 vs. 0.34). However, OC-CCI v4.2 shows lower positive bias values ($0.1\ 10^{-4}$–$0.8\ 10^{-4}$ sr^{-1} against $1.2\ 10^{-4}$–$6.9\ 10^{-4}$ sr^{-1}) and performs better in terms of APD or RPD in the 412–560-nm spectral range. Finally, OC-CCI v.6 shows lower bias, APD, and RPD at 665 nm.

The main differences between both OC-CCI versions explaining these discrepancies are the change of reference sensor from SeaWiFS to MERIS, the introduction of OLCI from Sentinel-3A and Sentinel-3B, and the shift of the green band from 555 nm to 560

10.3389/fmars.2023.1256990

TABLE 4 Validation metrics for eight OLCI wavelengths in the visible spectral range.

	400*	412.5	442.5	490	510*	560*	620*	665	778.75
POLYMER L2 common match-ups (*N* = 392; *N** = 354)									
R^2	0.41	0.57	0.69	0.78	0.82	0.9	0.8	0.77	0.74
RMSD	5.0	5.3	7.0	5.4	4.8	5.2	4.0	2.6	3.5
Bias	0.3	3.8	6.4	4.3	3.4	3.3	2.9	1.3	0.6
POLYMER L2 bitmask (*N* = 846; *N** = 754)									
R^2	0.36	0.53	0.69	0.77	0.81	0.88	0.76	0.7	0.35
RMSD	5.1	5.1	6.9	5.3	4.7	5.2	4.0	2.7	1.6
Bias	0.0	3.3	6.3	4.1	3.1	2.7	2.6	1.0	0.5
POLYMER L2 common match-ups—SENTINEL-3A (*N* = 428; *N** = 342)									
R^2	0.43	0.57	0.74	0.82	0.87	0.93	0.86	0.8	0.46
RMSD	4.6	4.5	6.7	5.1	4.4	4.5	3.7	2.3	1.2
Bias	−0.1	2.8	6.2	4.2	3.3	2.8	2.9	1.2	0.6
POLYMER L2 common match-ups—SENTINEL-3B (*N* = 345; *N** = 345)									
R^2	0.39	0.54	0.66	0.74	0.80	0.86	0.73	0.68	0.36
RMSD	5.1	5.7	7.2	5.6	4.9	5.7	4.3	2.9	1.7
Bias	0.7	4.2	6.5	4.3	3.3	3.0	2.7	1.1	0.5
CMEMS L3—Gustav Dalen Tower (*N* = 241; *N** = 206)									
R^2		0.57	0.74	0.81	0.86	0.91		0.73	
RMSD		4.7	6.9	5.2	4.7	5.2		2.5	
Bias		2.9	6.4	4.3	3.4	3.0		1.1	
CMEMS L3—Helsinki Lighthouse (*N* = 90; *N** = 39)									
R^2		0.51	0.68	0.77	0.84	0.91		0.78	
RMSD		4.2	6.4	5.2	5.7	6.2		2.6	
Bias		2.4	5.8	4.2	4.5	4.2		1.1	
CMEMS L3—Irbe Lighthouse (*N* = 155; *N** = 155)									
R^2		0.36	0.63	0.74	0.80	0.92		0.72	
RMSD		5.2	6.5	4.8	3.9	3.9		2.5	
Bias		2.8	5.7	3.4	1.9	1.4		0.9	

Match-ups based on AERONET-OC in-situ Rrs. *Wavelengths with in-situ data only from 2018. R^2: unitless. RMSD and bias: in 10^{-4} sr^{-1}.

nm. Moreover, the results in Brando et al. (2021) include 680 match-ups from 2005 to 2019, most of them from Gustav Dalen Tower and Helsinki Lighthouse, as the results from v.6 until 2022 introduce more *in-situ* data from Irbe Lighthouse. Note also that a stricter quality control (9 valid pixels in the extractions window instead of 4) was introduced in this work.

Table 4 shows the metrics from CMEMS-OLCI *Rrs* for the three sites. Overall, all of them are characterized by CDOM-dominated waters, and the metrics follow the same spectral pattern. The results from Gustav Dalen Tower and Helsinki Lighthouse lead to similar results, with more match-ups and a better adjustment (R^2) from Gustav Dalen Tower. In the case of Irbe Lighthouse, the results show a poorer agreement at 412.5 nm and lower RMSD and bias in the 490–560-nm spectral range, which could be explained by a lower *Rrs* range.

OC-CCI v.6 chl-*a* retrievals show validation results (R^2 = 0.29; RPD = 5%; APD = 69%; bias = −0.14), consistent with those reported for the previous version of the multisensor level-3 processing chain, i.e., OC-CCI v4.2 (Brando et al., 2021: R^2 = 0.24; RPD = 41%; APD = 90%; bias = −0.78), with a better performance considering all the metrics. Overall, the effect of the positive bias observed in the 412–510-nm spectral range (Figures 12, 13) seems to be adequately handled by the ensemble approach.

Chl-*a* validation results from CMEMS-OLCI are similar to those from OC-CCI v.6 using the common set of match-ups (Figure 13). The most remarkable difference is the lower bias

(−0.03 against −0.22), which is consistent with the bias decrease with the introduction of OLCI in the multisensor level-3 datasets from −0.78 (OC-CCI v.4.2, without OLCI, Brando et al., 2021) to −0.22 (OC-CCI v.6, with OLCI, this work). In any case, further research is required because of the small number of chl-*a* match-ups available for the OLCI period.

Scatter plots of co-collocated OC-CCI v.6 and CMEMS-OLCI data points (Figure 14) show better statistical figures for *Rrs* (except for 443 nm) than chl-*a*. Note that OC-CCI v.6 *Rrs* are derived from different space sensors and AC, whereas CMEMS-OLCI *Rrs* are obtained from Sentinel-A and Sentinel-B images processed with POLYMER v.4.14. With the exclusion of outliers, which are possibly related to the resolution and coverage of both datasets, most *Rrs* differences can be attributed to the specificities of data processing and absolute radiometric accuracy of the reference sensor (MERIS for OC-CCI v.6 and OLCI for CMEMS-OLCI).

An overall good agreement was found in the comparison between chl-*a* retrievals from CMEMS-OLCI and OC-CCI v.6, with a tendency of CMEMS-OLCI toward greater chl-*a* concentrations (Figure 14).

Nevertheless, the differences in *Rrs* are amplified in terms of chl-*a* retrieval. This is probably due to the non-linear nature of the MLP retrievals of chl-*a* and of the weights in the *chl-aENS3* ensemble approach adopted in this study, as well as the underlying relationship between apparent and inherent optical properties in the Baltic Sea.

An issue is the presence of erroneous data points caused by underestimation in the chl-*a* retrievals from CMEMS-OLCI (<0.5 mg m^{-3}) as compared with OC-CCI v.6 (1.5–15 mg m^{-3}) (Figure 14). These wrong retrievals are caused by anomalously high OLCI *Rrs* values with a smaller range at 490 nm (4–5 10^{-3} sr^{-1} in CMEMS-OLCI against 0.01–3.5 10^{-3} sr^{-1} in OC-CCI v.6) and 510 nm (3–3.25 10^{-3} sr^{-1} in CMEMS-OLCI against 0.01–2.5 10^{-3} sr^{-1} in OC-CCI v.6). Note that these points are not clearly visible in the scatter plots in Figure 14.

Potential differences in the validation results between the available datasets (i.e., COMBINE and Alg@line, see Section 2.2.2), as well as differences in the analytical methods and protocols for the chl-*a* concentration estimation, were not considered in this study because of the limited number of match-ups, mainly for the OLCI period. It should be noted that Brando et al. (2021) reported higher uncertainty for the match-ups of their multisensor time series with the COMBINE measurements as compared with Alg@line water samples due to different sampling strategies and dynamic ranges of both data sources.

In our sampling to perform the comparative analysis (a point every 10 km, an image every 10 days, see Section 2.5), only 143 points (of 190,546) from 32 images (of 240) were identified as erroneous. For most of the images, only one erroneous point was found, with a maximum of 28 points on a single image. Despite this low impact, further research with a full sampling is required to evaluate the actual effect of these wrong pixels and to implement a flagging procedure.

Regarding wrong *Rrs* values with a lower impact on the chl-*a* results (e.g., at 442 nm or 670 nm, see Figure 14), the presence in our sampling is limited to a small number of points by image (often only one). For instance, we identified 216 erroneous points in 64 images at 442 nm and only 32 points in 18 images at 660 nm. In any case, likewise chl-*a*, a further masking could improve the mapping results.

5 Conclusions

In this study, the performance of four atmospheric correction processors for the *Rrs* retrieval from Sentinel-3 OLCI was assessed within the development of the regional ocean color processing chain for the Baltic Sea. The validations with the *in-situ* measurements collected at three AERONET-OC sites and those relying on the Alg@line shipborne hyperspectral radiometry show that POLYMER v.4.14 was the best-performing processor in terms of error and fitness in the visible spectral range, as well as spatial coverage. Results also document the relevance of shipborne radiometry to complement *in-situ* measurements from fixed sites, allowing for a larger spatial footprint across all subbasins.

POLYMER-derived *Rrs* spectra were thus employed to retrieve chl-*a* from OLCI full-resolution (300 m) data using the bio-optical ensemble scheme already introduced in the CMEMS processing chain for the Baltic Sea. Additionally, this study evaluated the operational *Rrs* and chl-*a* multiyear time series (from 1997 to 2022) for the Baltic Sea based on OC-CCI v.6.

The chl-*a* values retrieved from OC-CCI v.6 and OLCI *Rrs* using the same regional bio-optical ensemble scheme were compared with the *in-situ* chl-*a* measurements. Results confirm previous analyses undertaken within the CMEMS products assessments, even if the number of OLCI match-ups (2016–2019) was lower. A study extension is planned to include more recent *in-situ* measurements once available.

Finally, an overall good agreement was found in the comparison between chl-*a* retrievals from OLCI and OC-CCI v.6. However, differences between the *Rrs* bands used as input for the bio-optical ensemble scheme were amplified in terms of chl-*a* retrieval. A flagging strategy should be devised to identify and reduce the presence of erroneous data points in both datasets. Furthermore, a sensitivity analysis is then part of the future developments to analyze the response of the bio-optical ensemble by adding synthetic offsets and noise to input *Rrs* spectra and verify how it affects the chl-*a* retrieval.

Our results confirm that the quality of operational ocean color datasets presented in this study is suitable for studies on phytoplankton phenology, bloom occurrence, water quality monitoring, and eutrophication assessment in this threatened ecosystem.

Data availability statement

The datasets presented in this study can be found in online repositories. The names of the repository/repositories and accession number(s) can be found below: E.U. Copernicus Marine Service Information (CMEMS) Marine Data Store (MDS: marine.copernicus.eu): OCEANCOLOUR_BAL_BGC_L3_NRT_009_131 (Baltic Sea Ocean Colour Plankton, Reflectances, Transparency and Optics L3 NRT daily observations). E.U. Copernicus Marine Service Information (CMEMS). Marine Data Store (MDS). DOI: 10.48670/moi-00294 (Accessed on 10-JUL-2023)OCEANCOLOUR_BAL_BGC_L3_MY_009_133 (Baltic Sea Multiyear Ocean Colour Plankton, Reflectances and Transparency L3 daily observations). E.U. Copernicus Marine Service Information (CMEMS). Marine Data Store (MDS). DOI: 10.48670/moi-00296 (Accessed on 10-JUL-2023).

Author contributions

LG: Conceptualization, Data curation, Formal analysis, Software, Validation, Visualization, Writing – original draft. VB: Conceptualization, Formal analysis, Funding acquisition, Methodology, Project administration, Software, Supervision, Validation, Visualization, Writing – original draft. ADC: Data curation, Writing – review & editing. SC: Data curation, Software, Writing – review & editing. DD'A: Conceptualization, Funding acquisition, Methodology, Software, Supervision, Writing – review & editing. TK: Writing – review & editing. JA: Data curation, Writing – review & editing. TS: Writing – review & editing.

Funding

The author(s) declare financial support was received for the research, authorship, and/or publication of this article. This work has been performed in the context of the Ocean Colour Thematic Assembly Centre of the Copernicus Marine Environment and Monitoring Service (contract: 21001L02-COP-TAC OC-2200– Lot 2: Provision of Ocean Colour Observation Products (OC-TAC)) and the HYPERNETS project funded by the European Union's Horizon 2020 research and innovation programme (Grant agreement no 775983).

Acknowledgments

EUMETSAT is acknowledged for the provision of the Copernicus Sentinel-3 full-resolution data. The Plymouth Marine Laboratory made available the OC-CCI v.6 *Rrs* spectra at 1 km resolution produced using the OC-CCI processor within the Ocean Colour Thematic Assembly Centre activities. The AERONET Team is acknowledged for the continuous effort in supporting the AERONET-OC subnetwork. Giuseppe Zibordi, Barbara Bulgarelli, and Frederic Melin from the Joint Research Center of the European Commission are acknowledged for establishing and maintaining the Irbe Lighthouse, Gustav Dalen Tower, and Helsinki Lighthouse AERONET-OC sites. ICES and HELCOM along with all single contributors are thanked for the COMBINE *in-situ* dataset. Scientists and technical personnel at SYKE are thanked for the acquisition of the Alg@line *in-situ* dataset. The ESA Sentinel Application Platform and Sentinel tool-box development teams are thanked for making the SNAP software freely available. We are grateful to Vega Forneris and Flavio Lapadula for maintaining the satellite data processing and the satellite data archive at CNR-ISMAR.

Conflict of interest

The authors declare that the research was conducted in the absence of any commercial or financial relationships that could be construed as a potential conflict of interest.

Publisher's note

All claims expressed in this article are solely those of the authors and do not necessarily represent those of their affiliated organizations, or those of the publisher, the editors and the reviewers. Any product that may be evaluated in this article, or claim that may be made by its manufacturer, is not guaranteed or endorsed by the publisher.

References

Ahlman, M., Alenius, P., Attila, J., Arnkil, A., Arponen, H., Below, A., et al. (2020). *Seurantakäsikirja suomen merenhoitosuunnitelman seurantaohjelmaan vuosille 2020–2026 (Manual for marine monitoring in Finland 2020–2026)* (Helsinki, Finland: Suomen Ympäristökeskus).

Alikas, K., Ansko, I., Vabson, V., Ansper, A., Kangro, K., Uudeberg, K., et al. (2020). Consistency of radiometric satellite data over lakes and coastal waters with local field measurements. *Remote Sens.* 12 (4), 616. doi: 10.3390/rs12040616

Andersen, J. H., Axe, P., Backer, H., Carstensen, J., Claussen, U., Fleming-Lehtinen, V., et al. (2011). Getting the measure of eutrophication in the baltic sea: towards improved assessment principles and methods. *Biogeochemistry* 106, 137–156. doi: 10.1007/s10533-010-9508-4

Attilla, J., Koponen, S., Kallio, K., Lindfors, A., Kaitala, S., and Ylöstalo, P. (2013). MERIS Case II water processor comparison on coastal sites of the northern Baltic Sea. *Remote Sens. Environ.* 128, 138–149. doi: 10.1016/j.rse.2012.07.009

Beltrán-Abaunza, J. M., Kratzer, S., and Brockmann, C. (2014). Evaluation of MERIS products from Baltic Sea coastal waters rich in CDOM. *Ocean Sci.* 10, 377–396. doi: 10.5194/os-10-377-2014

Berthon, J.-F., and Zibordi, G. (2010). Optically black waters in the Northern Baltic Sea. *Geophys. Res. Lett.* 37, L09605. doi: 10.1029/2010GL043227

Blondeau-Patissier, D., Gower, J. F. R., Dekker, A. G., Phinn, S. R., and Brando, V. E. (2014). A review of ocean color remote sensing methods and statistical techniques for the detection, mapping and analysis of phytoplankton blooms in coastal and open oceans. *Prog. Oceanogr.* 123, 123–144. doi: 10.1016/j.pocean.2013.12.008

Brando, V. E., Sammartino, M., Colella, S., Bracaglia, M., Di Cicco, A., D'Alimonte, D., et al. (2021). Phytoplankton bloom dynamics in the baltic sea using a consistently reprocessed time series of multi-sensor reflectance and novel chlorophyll-a retrievals. *Remote Sens.* 13, 3071. doi: 10.3390/rs13163071

Brewin, R. J., Sathyendranath, S., Müller, D., Brockmann, C., Deschamps, P. Y., Devred, E., et al. (2015). The Ocean Colour Climate Change Initiative: III. A round-robin comparison on in-water bio-optical algorithms. *Remote Sens. Environ.* 162, 271–294. doi: 10.1016/j.rse.2013.09.016

Brockmann, C., Doerffer, R., Peters, M., Stelzer, K., Embacher, S., and Ruescas, A. (2016). "Evolution of the C2RCC neural network for sentinel 2 and 3 for the retrieval of ocean colour products in normal and extreme optically complex waters," in *Proc. Living Planet Symposium*. 740, 1–13. (Prague, Czech Republic: ESA).

Cazzaniga, I., Zibordi, G., Mélin, F., Kwiatkowska, E., Talone, M., Dessailly, D., et al. (2022). Evaluation of OLCI neural network radiometric water products. *IEEE Trans. Geosci. Remote Sens.* 19 (1-5), 1503405. doi: 10.1109/LGRS.2021.3136291

Concha, J., Bracaglia, M., and Brando, V. (2021). Assessing the influence of different validation protocols on Ocean Colour match-up analyses. *Remote Sens. Environ.* 259, 112415. doi: 10.1016/j.rse.2021.112415

D'Alimonte, D., Kajiyama, T., and Saptawijaya, A. (2016). Ocean color remote sensing of atypical marine optical cases. *IEEE Trans. Geosci. Remote Sens.* 54, 6574–6586. doi: 10.1109/TGRS.2016.2587106

D'Alimonte, D., Zibordi, G., Berthon, J.-F., Canuti, E., and Kajiyama, T. (2011). *Bio-optical algorithms for european seas: performance and applicability of neural-net inversion schemes* (Luxembourg: Publications Office of the European Union).

D'Alimonte, D., Zibordi, G., Kajiyama, T., and Berthon, J.-F. (2014). Comparison between MERIS and Regional High-Level Products in European Seas. *Remote Sens. Environ.* 140, 378-395.

Darecki, M., and Stramski, D. (2004). An evaluation of MODIS and seaWiFS bio-optical algorithms in the baltic sea. *Remote. Sens. Environ.* 89, 326–350. doi: 10.1016/j.rse.2003.10.012

Doerffer, R., and Schiller, H. (2007). The MERIS Case 2 water algorithm. *Int. J. Remote Sens.* 28, 517–535. doi: 10.1080/01431160600821127

EUMETSAT (2019) *EUMETSAT OCDB user manual. Copyright 2019, copernicus revision 763d8907* (Accessed December 11, 2023).

EUMETSAT (2021) *Sentinel-3 OLCI L2 report for baseline collection OL_L2M_003 - EUM/RSP/REP/21/1211386* (Accessed December 11, 2023).

EUMETSAT (2022) *Recommendations for Sentinel-3 OLCI Ocean Colour product validations in comparison with in situ measurements – Matchup Protocols* (Accessed December 11, 2023).

Finni, T., Kononen, K., Olsonen, R., and Wallström, K. (2001). The history of cyanobacterial blooms in the Baltic Sea. *Ambio* 30, 172–178. doi: 10.1579/0044-7447-30.4.172

Fleming, V., and Kaitala, S. (2006). Phytoplankton spring bloom intensity index for the baltic sea estimated for the years 1992 to 2004. *Hydrobiologia* 554, 57–65. doi: 10.1007/s10750-005-1006-7

Fleming-Lehtinen, V., Andersen, J. H., Carstensen, J., Łysiak-Pastuszak, E., Murray, C., Pyhälä, M., et al. (2015). Recent developments in assessment methodology reveal that the Baltic Sea eutrophication problem is expanding. *Ecol. Indic.* 48, 380–388. doi: 10.1016/j.ecolind.2014.08.022

González Vilas, L., Brando, V. E., Concha, A. J., Dogliotti, A. I., Goyens, C., and Doxaran, D. (2023) *HYPERNETS multi-mission validation of water products V2. Deliverable D7.3, version 1.0, 24/04/2023* (Accessed December 11, 2023).

González Vilas, L., Brando, V. E., Concha, A. J., Goyens, C., Dogliotti, A. I., Doxaran, D., et al (2024). Validation of satellite water products based on Hypernets in situ data using a Match-up Database File (MDB) structure. *Front. Remote Sens.*

Groom, S., Sathyendranath, S., Ban, Y., Bernard, S., Brewi, R., Brotas, V., et al. (2019). Satellite ocean colour: current status and future perspective. *Front. Mar. Sci.* 6, 485. doi: 10.3389/fmars.2019.00485

Heiskanen, A.-S., Bonsdorff, E., and Joas, M. (2019). "Baltic sea: A recovering future from decades of eutrophication," in *Coasts and estuaries* (Amsterdam, The Netherlands: Elsevier), 343–362.

HELCOM (2007). *HELCOM baltic sea action plan* (Helsinki, Finland: HELCOM).

HELCOM (2017). *Manual for marine monitoring in the COMBINE programme of HELCOM* (Helsinki, Finland: HELCOM).

HELCOM (2018). *State of the baltic sea—Second HELCOM holistic assessment 2011–2016* (Helsinki, Finland: HELCOM).

HELCOM (2019). *HELCOM guidelines for monitoring of chlorophyll a* (Helsinki, Finland: HELCOM).

Hieronymi, M., Müller, D., and Doerffer, R. (2017). The OLCI neural network swarm (ONNS): A bio-geo-optical algorithm for open ocean and coastal waters. *Front. Mar. Sci.* 4, 140. doi: 10.3389/fmars.2017.00140

Hjerne, O., Hajdu, S., Larsson, U., Downing, A. S., and Winder, M. (2019). Climate driven changes in timing, composition and magnitude of the Baltic Sea Phytoplankton Spring Bloom. *Front. Mar. Sci.* 6. doi: 10.3389/fmars.2019.00482

Kahru, M., Elmgren, R., Di Lorenzo, E., and Savchuk, O. (2018). Unexplained interannual oscillations of cyanobacterial blooms in the Baltic Sea. *Sci. Rep.* 8, 6365. doi: 10.1038/s41598-018-24829-7

Kahru, M., Horstmann, U., and Rud, O. (1994). Satellite detection of increased cyanobacteria blooms in the Baltic Sea: Natural fluctuation or ecosystem change? *Ambio* 23, 469–472.

Kahru, M., Savchuk, O., and Elmgren, R. (2007). Satellite measurements of cyanobacterial bloom frequency in the Baltic Sea: Interannual and spatial variability. *Mar. Ecol. Prog. Ser.* 343, 15–23. doi: 10.3354/meps06943

Kaitala, S., Zibordi, G., Melin, F., Seppälä, J., and Ylöstalo, P. (2008). Coastal water monitoring and remote sensing products validation using ferrybox and above-water radiometric measurements. *EARSeL eProceedings* 7, 75–80.

Kajiyama, T., D'Alimonte, D., and Zibordi, G. (2019). Algorithms merging for the determination of chlorophyll-a concentration in the black sea. *IEEE Geosci. Remote Sens. Lett.* 16, 677–681. doi: 10.1109/LGRS.2018.2883539

Kratzer, S., and Moore, G. (2018). Inherent optical properties of the Baltic Sea in comparison to other seas and oceans. *Remote. Sens.* 10, 418. doi: 10.3390/rs10030418

Kratzer, S., and Vinterhav, C. (2010). Improvement of MERIS level 2 products in baltic sea coastal areas by applying the improved contrast between ocean and land processor (ICOL)—Data analysis and validation. *Oceanologia* 52, 211–236. doi: 10.5697/oc.52-2.211

Kyryliuk, D., and Kratzer, S. (2019). Evaluation of sentinel-3A OLCI products derived using the case-2 regional coast colour processor over the baltic sea. *Sensors* 19, 3609. doi: 10.3390/s19163609

Lee, Z., Carder, K. L., and Arnone, R. A. (2014). *Update of the quasi-analytical algorithm (QAA_V6)* (Dartmouth, Canada: IOCCG).

Leppäranta, M., and Myrberg, K. (2009). *Physical oceanography of the baltic sea* (Berlin/Heidelberg, Germany: Springer).

Le Traon, P. Y., Reppucci, A., Alvarez Fanjul, E., Aouf, L., Behrens, A., Belmonte, M., et al. (2019). From observation to information and users: the copernicus marine service perspective. *Front. Mar. Sci.* 6, 234. doi: 10.3389/fmars.2019.00234

Ligi, M., Kutser, T., Kallio, K., Attila, J., Koponen, S., Paavel, B., et al. (2017). Testing the performance of empirical remote sensing algorithms in the Baltic Sea waters with modelled and in *situ* reflectance data. *Oceanologia* 59, 57–68. doi: 10.1016/j.oceano.2016.08.002

Mélin, F., and Sclep, G. (2015). Band shifting for ocean color multi-spectral reflectance data. *Opt. Express* 23, 2262. doi: 10.1364/OE.23.002262

OC-CCI (2022) *Ocean colour climate change initiative (OC-CCI) – phase3. Product user guide for v6.0 dataset* (Accessed December 11, 2023).

OCEANCOLOUR_BAL_BGC_L3_MY_009_133 (2023) *E.U. Copernicus marine service information (CMEMS). Marine data store (MDS)* (Accessed July 10, 2023).

OCEANCOLOUR_BAL_BGC_L3_NRT_009_131 (2023) *Marine data store (MDS)* (Accessed July 10, 2023).

Odermatt, D., Gitelson, A., Brando, V. E., and Schaepman, M. (2012). Review of constituent retrieval in optically deep and complex waters from satellite imagery. *Remote Sens. Environ.* 118, 116–126. doi: 10.1016/j.rse.2011.11.013

Omstedt, A., Elken, J., Lehmann, A., and Piechura, J. (2004). Knowledge of the Baltic Sea physics gained during the BALTEX and related programmes. *Prog. Oceanogr.* 63, 1–28. doi: 10.1016/j.pocean.2004.09.001

O'Reilly, J. E., and Werdell, P. J. (2019). Chlorophyll algorithms for ocean color sensors—OC4, OC5 & OC6. *Remote. Sens. Environ.* 229, 32–47. doi: 10.1016/j.rse.2019.04.021

Pitarch, J., Volpe, G., Colella, S., Krasemann, H., and Santoleri, R. (2016). Remote sensing of chlorophyll in the baltic sea at basin scale from 1997 to 2012 using merged multi-sensor data. *Ocean Sci.* 12, 379–389. doi: 10.5194/os-12-379-2016

Qin, P., Simis, S. G. H., and Tilstone, G. H. (2017). Radiometric validation of atmospheric correction for MERIS in the Baltic Sea based on continuous observations from ships and AERONET-OC. *Remote Sens. Environ.* 200, 263–280. doi: 10.1016/j.rse.2017.08.024

Sathyendranath, S., Brewin, R., Brockmann, C., Brotas, V., Calton, B., Chuprin, A., et al. (2019). An ocean-colour time series for use in climate studies: The experience of the ocean-colour climate change initiative (OC-CCI). *Sensors* 19, 4285. doi: 10.3390/s19194285

Sathyendranath, S., Groom, S. B., Jackson, T., Volpe, G., and Calton, B. (2022). *ESA Ocean colour climate change initiative-phase 3 climate assessment report* (Accessed December 11, 2023).

Schroeder, T., Behnert, I., Schaale, M., Fischer, J., and Doerffer, R. (2007). Atmospheric correction algorithm for MERIS above case-2 waters. *Int. J. Remote Sens.* 28, 1469–1486. doi: 10.1080/01431160600962574

Schroeder, T., Fischer, J., Schaale, M., and Fell, F. (2003). "Artificial-neural-network-based atmospheric correction algorithm: application to MERIS data," in *Proc. SPIE 4892, Ocean Remote Sensing and Applications*. doi: 10.1117/12.467293

Schroeder, T., Schaale, M., Lovell, J., and Blondeau-Patissier, D. (2022). An ensemble neural network atmospheric correction for Sentinel-3 OLCI over coastal waters providing inherent model uncertainty estimation and sensor noise propagation. *Remote Sens. Environ.* (SPIE) 270, 112848. doi: 10.1016/j.rse.2021.112848

Simis, S. G. H., and Olsson, J. (2013). Unattended processing of shipborne hyperspectral reflectance measurements. *Remote Sens. Environ.* 135, 202–212. doi: 10.1016/j.rse.2013.04.001

Simis, S., Qin, P., Attila, J., Kervinen, M., Kallio, K., Koponen, S., et al. (2021). *Baltic sea shipborne hyperspectral reflectance data from 2016 (1.0)* (Zenodo), 5572537.

Simis, S. G. H., YloÈstalo, P., Kallio, K. Y., Spilling, K., and Kutser, T. (2017). Contrasting seasonality in optical-biogeochemical properties of the Baltic Sea. *PloS One* 12, e0173357. doi: 10.1371/journal.pone.0173357

Steinmetz, F., Deschamps, P.-Y., and Ramon, D. (2011). Atmospheric correction in presence of sun glint: application to MERIS. *Opt. Express* (SPIE) 19, 9783-9800. doi: 10.1364/OE.19.009783

Steinmetz, F., and Ramon, D. (2018). "Sentinel-2 MSI and Sentinel-3 OLCI consistent ocean colour products using POLYMER," in *Proceedings of the remote sensing of the open and coastal ocean and inland waters*(Honolulu, HI, USA).

Tilstone, G. H., Pardo, S., Simis, S. G. H., Qin, P., Selmes, N., Dessailly, D., et al. (2022). Consistency between satellite ocean colour products under high coloured dissolved organic matter absorption in the baltic sea. *Remote Sens.* 14 (1), 89. doi: 10.3390/rs14010089

Toming, K., Kutser, T., Uiboupin, R., Arikas, A., Vahter, K., and Paavel, B. (2017). Mapping water quality parameters with sentinel-3 ocean and land colour instrument imagery in the baltic sea. *Remote Sens.* 9, 1070. doi: 10.3390/rs9101070

von Schuckmann, K., Le Traon, P.-Y., Smith, N., Pascual, A., Djavidnia, S., Brasseur, P., et al. (2022). Copernicus ocean state report, issue 6. *J. Oper. Oceanogr.* 15, s1–s220. doi: 10.1080/1755876X.2022.2095169

Warren, M. A., Simis, S. G. H., Martinez-Vicente, V., Poser, K., Bresciani, M., Alikas, K., et al. (2019). Assessment of atmospheric correction algorithms for the sentinel-2A multispectral imager over coastal and inland waters. *Remote Sens. Environ.* 225, 267–289. doi: 10.1016/j.rse.2019.03.018

Wasmund, N., Tuimala, J., Suikkanen, S., Vandepitte, L., and Kraberg, A. (2011). Long-term trends in phytoplankton composition in the western and central Baltic Sea. *J. Mar. Syst.* 87 (2), 145–159. doi: 10.1016/j.jmarsys.2011.03.010

Ylöstalo, P., Seppälä, J., Kaitala, S., Maunula, P., and Simis, S. (2016). Loadings of dissolved organic matter and nutrients from the Neva Riverinto the Gulf of Finland–

Biogeochemical composition and spatial distribution within the salinity gradient. *Mar. Chem.* 186, 58–71. doi: 10.1016/j.marchem.2016.07.004

Zhang, D., Lavender, S., Muller, J.-P., Walton, D., Zou, X., and Shi, F. (2018). MERIS observations of phytoplankton phenology in the Baltic Sea. *Sci. Total. Environ.* 642, 447–462. doi: 10.1016/j.scitotenv.2018.06.019

Zibordi, G., Berthon, J.-F., Mélin, F., and D'Alimonte, D. (2011). Cross-site consistent in situ measurements for satellite ocean color applications: the biOMaP radiometric dataset. *Remote Sens. Environ.* 115, 2104–2115. doi: 10.1016/j.rse.2011.04.013

Zibordi, G., Kwiatkowska, E., Mélin, F., Talone, M., Cazzaniga, I., Dessailly, D., et al. (2022). Assessment of OLCI-A and OLCI-B radiometric data products across European seas. *Remote Sens. Environ.* 272, 112911. doi: 10.1016/j.rse.2022.112911

Zibordi, G., Melin, F., and Berthon, J.-F. (2018). A regional assessment of OLCI data products. *IEEE Geosci. Remote Sens. Lett.* 15, 1490–1494. doi: 10.1109/LGRS.2018.2849329

Zibordi, G., Mélin, F., Berthon, J.-F., Holben, B., Slutsker, I., Giles, D., et al. (2009). AERONET-OC: A network for the validation of ocean color primary products. *J. Atmos. Oceanic Technol.* 26, 1634–1651. doi: 10.1175/2009JTECHO654.1

frontiers | Frontiers in Marine Science

TYPE Original Research
PUBLISHED 18 March 2024
DOI 10.3389/fmars.2024.1323271

Check for updates

OPEN ACCESS

EDITED BY
Gemma Kulk,
Plymouth Marine Laboratory, United Kingdom

REVIEWED BY
Yizhen Li,
Woods Hole Oceanographic Institution, United States
Ulrike Löptien,
University of Kiel, Germany
Inia Soto Ramos,
Morgan State University, United States

*CORRESPONDENCE
Bronwyn Cahill
bronwyn.cahill@io-warnemuende.de

RECEIVED 17 October 2023
ACCEPTED 27 February 2024
PUBLISHED 18 March 2024

CITATION
Cahill B, Chrysagi E, Vortmeyer-Kley R and Gräwe U (2024) Deconstructing co-occurring marine heatwave and phytoplankton bloom events in the Arkona Sea in 2018. *Front. Mar. Sci.* 11:1323271. doi: 10.3389/fmars.2024.1323271

COPYRIGHT
© 2024 Cahill, Chrysagi, Vortmeyer-Kley and Gräwe. This is an open-access article distributed under the terms of the Creative Commons Attribution License (CC BY). The use, distribution or reproduction in other forums is permitted, provided the original author(s) and the copyright owner(s) are credited and that the original publication in this journal is cited, in accordance with accepted academic practice. No use, distribution or reproduction is permitted which does not comply with these terms.

Deconstructing co-occurring marine heatwave and phytoplankton bloom events in the Arkona Sea in 2018

Bronwyn Cahill[1]*, Evridiki Chrysagi[1], Rahel Vortmeyer-Kley[2] and Ulf Gräwe[1]

[1]Physical Oceanography and Instrumentation, Leibniz Institute for Baltic Sea Research, Warnemünde, Germany, [2]Institute for Chemistry and Biology of the Marine Environment (ICBM), Carl von Ossietzky Universität Oldenburg, Oldenburg, Germany

Between May and August 2018, two separate marine heatwaves (MHWs) occurred in the Arkona Sea in the western Baltic Sea. These heatwaves bookended an extended period of phytoplankton growth in the region. Data from the Ocean and Land Colour Instrument (OLCI) on board the European Sentinel-3 satellite revealed an eddy-like structure containing high chlorophyll a (Chl-a) concentrations (ca. 25 $mg.m^{-3}$) persisting for several days at the end of May in the Arkona Sea. Combining ocean colour observations, a coupled bio-optical ocean model and a particle tracking model, we examined the three dimensional relationship between these co-occurring MHW and phytoplankton bloom events. We find that the onset of the MHW in May provided the optimal conditions for phytoplankton growth, i.e. sufficient light and nutrients. Wind-driven surface eddy circulation, geostrophic eddy stirring and transient submesoscale dynamics along the edges of the eddy provided a transport path for nutrient fluxes and carbon export, and helped to sustain the phytoplankton bloom. The bloom may have indirectly had an enhancing effect on the MHW, through the impact of water constituent-induced heating rates on air-sea energy fluxes. The subsurface signature of the MHW plays a critical role in de-coupling surface and subsurface dynamics and terminating the phytoplankton bloom. Subsurface temperature anomalies of up to 8°C between 15 and 20 m depth are found to persist up to 15 days after the surface signature of the MHW has disappeared. The study reveals how surface and subsurface dynamics of MHWs and phytoplankton blooms are connected under different environmental conditions. It extends our knowledge on surface layer processes obtained from satellite data.

KEYWORDS

marine heatwaves, phytoplankton blooms, light and nutrient availability, biooptical modelling, ocean colour, mesoscale eddy stirring, submesoscale dynamics

1 Introduction

Satellite and ocean data reveal a marked increase in the Earth's heating rate (Loeb et al., 2021), with the Earth trapping nearly twice as much heat as it did in 2005. This trend is likely to continue in the near term due to global warming and the increase in frequency and magnitude of heat waves (IPCC, 2023). There is also evidence of a growing trend in the frequency and duration of marine heatwaves (MHWs) in the global oceans (Oliver et al., 2018). MHWs, defined as periods where the surface temperature of the ocean exceeds the 90th percentile of the 30 year local mean for longer than 5 days, can have severe and destructive consequences on marine species, ecosystems and biogeochemical processes (Smale et al., 2019). Marginal seas have warmed faster than the global ocean, with the Baltic Sea warming at a rate up to four times the global mean warming rate (Belkin, 2009). As of 2020, the summer of 2018 was the warmest on instrumental record in Europe, and the warmest summer in the past 30 years in the southern Baltic Sea with surface-water temperatures 4-5°C above the 1990-2018 long-term mean (Naumann et al., 2019) and bottom water temperatures of 20.5°C recorded at 32 m at the Tvärminne Zoological Station (TZS) in southern Finland (Humborg et al., 2019).

A recent statistical analysis by Lorenz (2019) of historical sea surface temperature (SST) and surface chlorophyll (Chl-a) satellite data products showed that sea surface temperature (SST) and MHW are meaningful parameters for the initiation and development of phytoplankton spring blooms in the Baltic Sea and North Sea, and that there is a relationship between co-occurring MHWs and bloom events. During the last 20 years, a trend towards an earlier spring bloom start has developed which is significantly stronger in the Baltic Sea (Wasmund et al., 2019a). In addition, there is some evidence of a positive trend in bloom sum and peak, and therefore, magnitude in the Baltic Sea which may be connected to climate variability and eutrophication (Jaanus et al., 2011; Kahru et al, 2016; Lorenz, 2019). Lorenz found significant positive relationships between MHW and bloom indices of magnitude indicating one event may have an enhancing effect on the other by creating a positive feedback.

Spatio-temporal studies of MHW typically examine the response of the sea surface using blended satellite data products (e.g. NOAA OI SST V2, Huang et al., 2021). While these provide the spatial and temporal surface coverage needed to investigate the frequency and duration of MHWs, they do not provide any diagnostic information on the drivers of MHWs or any prognostic information on surface and subsurface processes which may be impacted by MHWs, i.e. stratification, vertical mixing, light and nutrient availability, phytoplankton growth and optically significant water constituent concentrations. A number of recent studies discuss the subsurface response of marginal and shallow shelf seas to MHWs. An observation-based study by Elzahaby and Schaeffer (2019) highlight how MHWs occurring in shallow seas (< 150m), occur predominantly during the stratified season (summer/autumn) in various mesoscale structures (cyclonic, anticyclonic or no eddies). They are characterized by stratified and fresher surface waters and the depth to which they extend is correlated with the SST anomaly. The surface origin is likely a response to air-sea flux forcing whereby anomalous solar radiation and decreased wind stress act on the latent heat-flux to reduce evaporation (Chen et al., 2014; Bond et al., 2015; Chen et al., 2015; Benthuysen et al., 2018). Schaeffer and Roughan (2017) show that MHWs regularly extend over the full depth of the water column in coastal waters off southeastern Australia, and their maximum intensity occurs below the surface and can persist long after the surface signature of the MHW has disappeared. Hayashida et al. (2020) use daily output from a near-global ocean physical-biogeochemical model to explore how background nutrient concentrations determine the response of co-occurring phytoplankton blooms and MHWs in regional seas.

In this paper, we examine two different late spring and mid-summer MHW events which bookmark the evolution and decay of a phytoplankton bloom in the Arkona Sea in the Western Baltic Sea. We use a combination of satellite data, a coupled bio-optical ocean model and a particle tracking model, in order to better understand the full three-dimensional impact MHWs have on bloom dynamics. Our objective is to explore the relationship between co-occurring MHW and phytoplankton bloom events with the following specific questions in mind:

1. How, and under which circumstances, do MHWs contribute to the initiation of phytoplankton blooms?
2. Which dynamics play a role in sustaining the bloom?
3. How deep and for how long is the impact of the MHW felt?
4. What role, if any, do MHWs play in terminating a phytoplankton bloom?
5. Do phytoplankton blooms have an enhancing effect on MHWs by creating a positive feedback from water constituent–induced surface heating?

2 Materials and methods

2.1 Study site

Our study site is the Arkona Sea located in the Western Baltic Sea (Figure 1). This site was selected because two significant MHW events took place here in May and July 2018 (Figure 2B). During the peak surface heating period of the May event, the sea surface temperature (SST) anomaly on 29 May 2018 shows a distinct eddy-like structure of warmer water (up to 6°C) in the Arkona Sea (Figure 3A). Coincident satellite data from the Ocean and Land Colour Instrument (OLCI) on board the European Sentinel-3 series satellites also shows a similar eddy-like structure containing high Chl-a concentrations (c. 25 mg m^{-3}) in the Arkona Sea (Figure 4A). During the July MHW, surface Chl-a concentrations were much lower (c. 3 mg m^{-3}), with no distinct structure visible in the satellite data (Figure 4H). Prevailing winds show weak northeasterly and southeasterly winds converging along 55° N during the May event, with wind speeds on the order of 5 m s^{-1}, while in July, prevailing winds were ca. 2 m s^{-1} with northerly winds west of 13°30' E, and southerly east of 13°30' E (Figures 5A, B). The Arkona Sea is

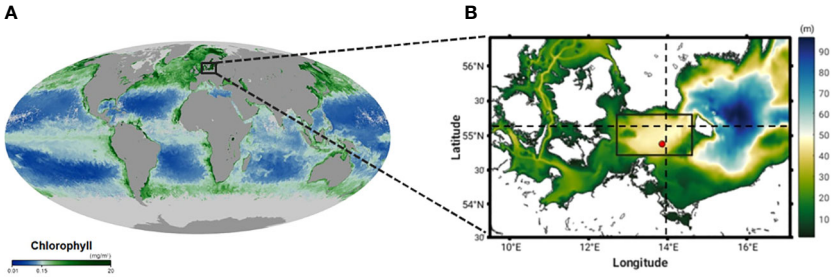


FIGURE 1
(A) Global distribution of chlorophyll-a, as seen by MODIS, May 2018 (source: https://earthobservatory.nasa.gov/global-maps/MY1DMM_CHLORA). Black rectangle indicates location of our study region. **(B)** Western Baltic Sea model domain bathymetry (m). Black rectangle shows the location of the Arkona Sea, the red dot indicates the location of Marnet Arkona Buoy long term mooring site (13°52' E; 54°53' N) and the dashed lines show the location of the transects used in the analysis.

characterized by a basin which covers an area of approximately 18,700 km^2, and has a maximum depth of 47 m. A semi-permanent halocline separates the fresher surface water (6 – 8 PSU) from the more saline deep water (12 – 14 PSU) between 20 and 40 m depth. Large variability in baroclinic circulation caused by the imbalance between filling and emptying the dense bottom water pool results in a range of reported Rossby radii (2.5 to 6 km) and baroclinic phase velocities (0.27 to 0.75 ms^{-1}) for the first baroclinic mode (Fennel et al., 1991; Lass and Mohrholz, 2003). Seasonal hypoxia can also occur. The mean stratification can be disturbed by geostrophic

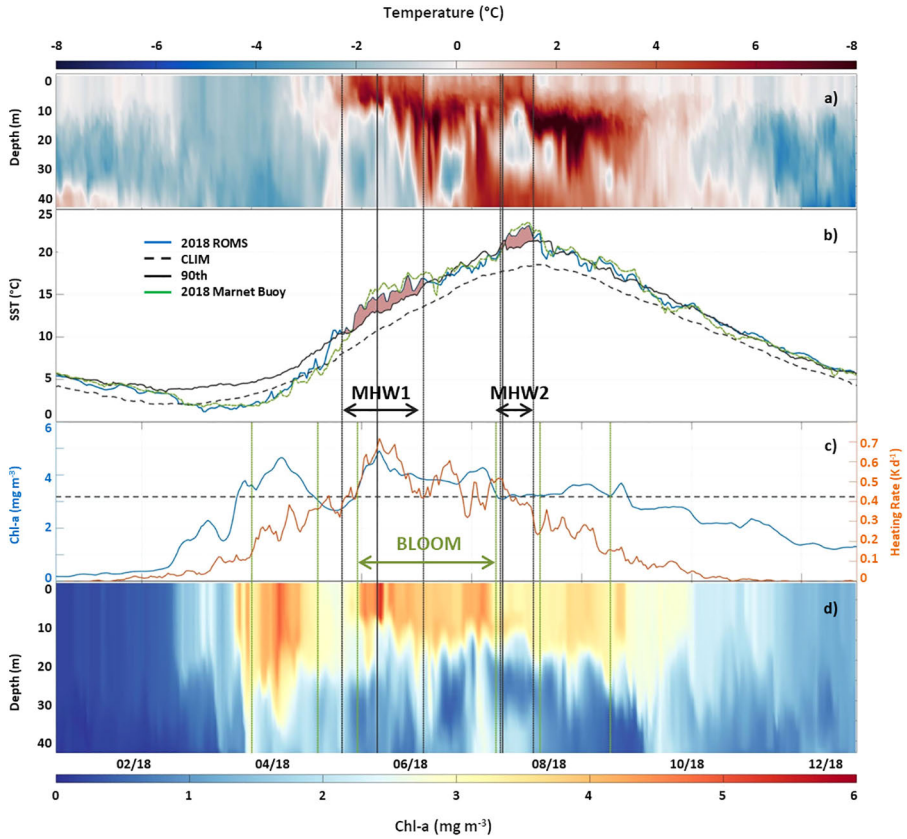


FIGURE 2
(A) modelled 2018 temperature anomaly at Marnet Arkona Buoy location (see Figure 1), 2018 temperature minus 90th percentile 40 year climatology (1979 – 2019); **(B)** surface temperature at Marnet Arkona Buoy location: modelled (2018 ROMS), observed (2018 Marnet Buoy) and 30 year mean climatology (CLIM) and 90th percentile (90th) [using the NOAA OI SST V2 High Resolution Data Set (Huang et al., 2021)] (ROMS vs Marnet Buoy statistics: r^2: 0.99, RMSE: 0.016, BIAS: -0.0010). Pink shaded areas indicate timing of MHW-1 and MHW-2, respectively; **(C)** modelled 2018 surface Chl-a (blue) and optically significant water constituent-induced surface heating rate (orange) at the Marnet Arkona Buoy location (dashed horizontal line indicates threshold value for onset of phytoplankton bloom (see text); **(D)** modelled 2018 water column Chl-a at the Marnet Arkona Buoy location. (grey dashed vertical lines indicate onset and end of MHW events, solid grey vertical line indicates day of detailed analysis during MHW event, green vertical dashed lines indicate start and end of phytoplankton blooms).

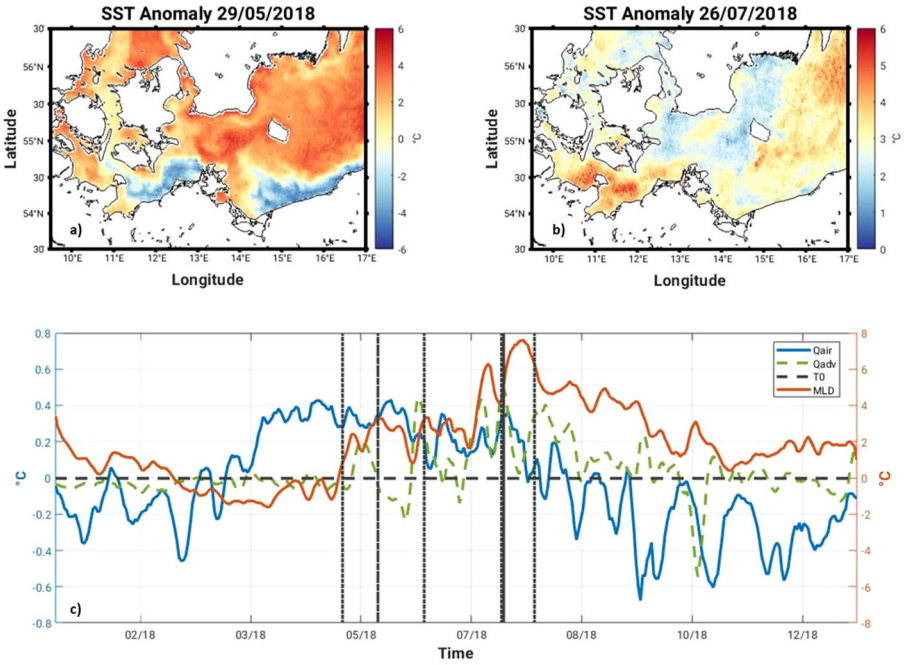


FIGURE 3
SST anomaly on 29 May 2018 **(A)** and 26 July 2018 **(B)** in the Western Baltic Sea; **(C)** cumulative contribution of the air-sea heat flux (blue line), horizontal advection (dashed green line) to the temperature anomaly and the mixed layer depth temperature anomaly (orange line) in the Arkona Sea in 2018. The SST Reanalysis (https://doi.org/10.48670/moi-00156) described in Høyer and She (2007) and Høyer and Karagali (2016) was used to calculate the SST anomalies shown in **(A, B)**, while the Baltic Sea Physics Reanalysis (https://doi.org/10.48670/moi-00013) and the ERA-5 Global Reanalysis (https://doi.org/10.1002/qj.3803) described in Hersbach et al. (2020) were used to calculate the temperature anomalies shown in **(C)**.

eddies with a characteristic radius equal to the first baroclinic Rossby radius and up- and downwelling occurring along the rim of the eddy. Vortmeyer-Kley et al. (2019) found in a modelling case study of the surface velocity field in the Western Baltic Sea from May 1 to October 31, 2010 about 28 000 eddies, while Reißmann (2005) detected in a CTD measurement campaign 5 to 18 eddies as three dimensional isolated anomalies in pressure in the Arkona Basin in October 1999. These structures are found at a mean depth of about 15 - 22 m in Reißmann (2005). In their satellite image study for 2009 - 2011, Karimova and Gade (2016) found the Arkona Basin as region of eddies that might be caused by sharp thermal gradients. Nonlinear eddies are important for biological production because they trap fluid, phytoplankton and nutrients within them (Chelton et al., 2007; Chelton et al., 2011a, Chelton et al., 2011b; McGillicuddy, 2016).

The Arkona Sea is an optically complex and biologically productive region, influenced by significant inputs of terrestrial organic matter from neighbouring rivers, especially colour dissolved organic matter (CDOM) during months of intensive mixing and high riverine discharge, March, April and November (Kowalczuk et al., 2006). In recent years, the growing season of phytoplankton in the Western Baltic Sea has extended from 159 days in the period 1988 to 1992 to 284 days in the period 2014 to 2017 (Wasmund et al., 2019a) in response to climate change. In 2018, Wasmund et al. (2019b) observed a shift in the spring bloom peak in the region to May with a prolonged period of moderate phytoplankton growth in the Arkona Sea primarily dominated by diatoms and dinoflagellates in May and June 2018.

2.2 Modelling the bio-optical ocean state in the Arkona Sea in 2018

We use the Regional Ocean Modelling System, ROMS, which drives the physics and the advection and diffusion of tracers, coupled with the Ecosim/Bio-Optic module (herein referred to as ROMS-BioOptic) which drives the ecosystem and a spectrally-resolved underwater light field. This setup is used to simulate the bio-optical ocean state in the western Baltic Sea for the year 2018 and is described in detail in Cahill et al. (2023) and references therein. Here we summarize important features. ROMS, is widely used for shelf circulation (e.g. Haidvogel et al., 2008; Wilkin et al., 2011) and coupled physical-biological applications (e.g. Fennel et al., 2006; Cahill et al., 2008; Fennel et al., 2008; Fennel and Wilkin, 2009; Cahill et al., 2016, Cahill et al., 2023). Ecosim is a carbon-based, ecological/optical modelling system (Bissett et al., 1999a, Bissett et al., 1999b) which was developed for simulations of carbon cycling and biological productivity. Ecosim simulates up to four phytoplankton functional groups each with a characteristic pigment suite which varies with the group carbon-to-chlorophyll-a ratio, C:Chl-a. Each groups' C:Chl-a ratio varies between some maximum and minimum value, as a function of light or nutrient limitation. The properties of each functional group evolve over time as a function of light and nutrient conditions (i.e. NO_3, NH_4, PO_4, SiO and FeO). The maximum phytoplankton growth is modulated by temperature (Eppley, 1972). Loss processes are represented by grazing and excretion. Grazing accounts for the majority of the biomass sink in the model and is considered the closure term of the

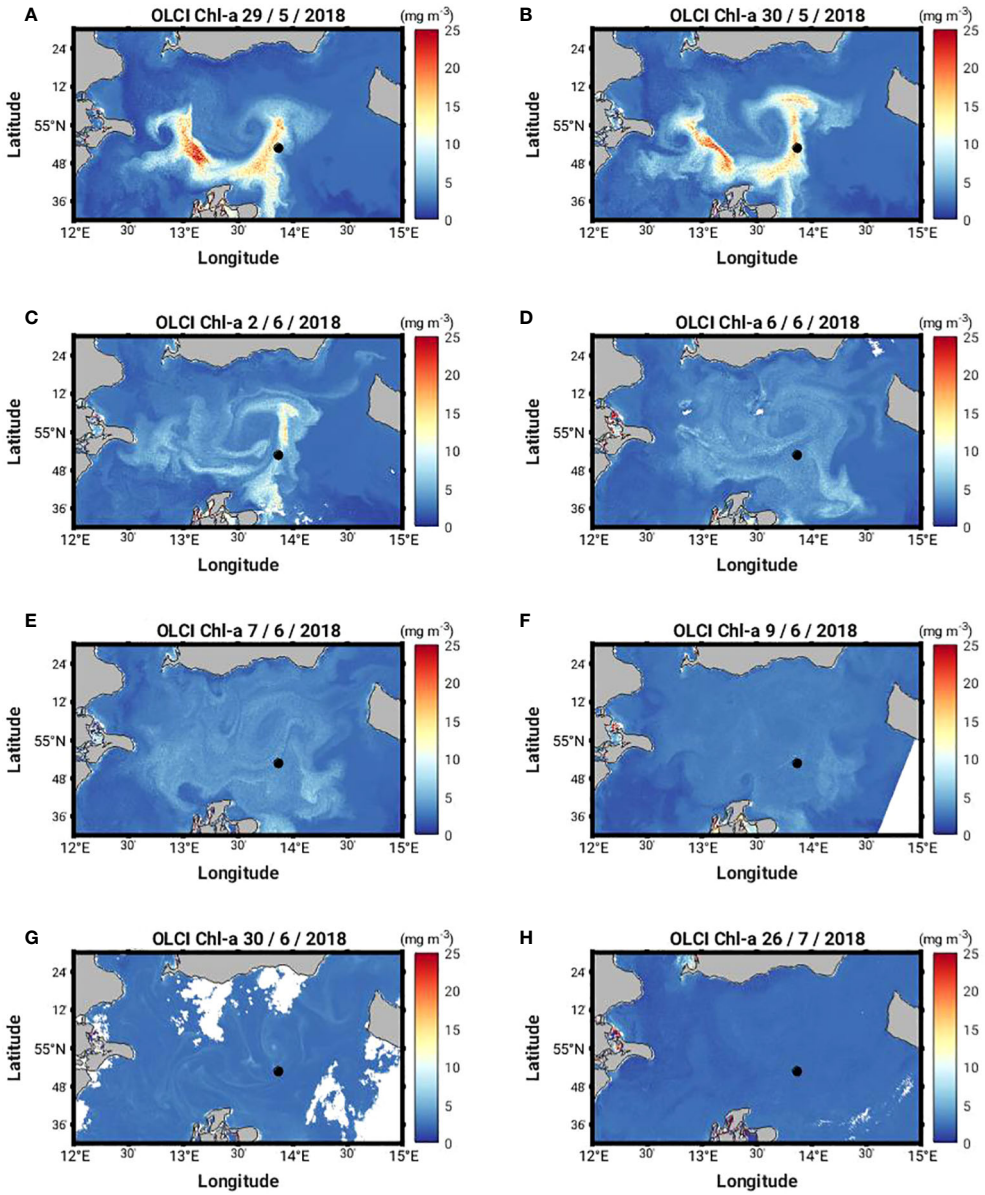


FIGURE 4
Sentinel-3 Ocean Land Cover Instrument (OLCI) L3 300 m resolution Chl-a on selected dates during the study period **(A-H)** 29, 30 May, 2, 6, 7, 9, 30 June, 26 July 2018, respectively). Black dot indicates the location of the Marnet Arkona Buoy long term mooring site.

phytoplankton equations (Steele and Henderson, 1992). It is modelled as a Michaelis-Menten function based on the functional groups' biomass (Bissett et al., 1999a). Marine and riverine sources of dissolved organic carbon (DOC and CDOC) are accounted for and explicitly resolved into labile (e.g. available for biological and photo-degradation) and relict (e.g. available for photo-degradation) forms. Dissolved inorganic carbon (DIC) is also accounted for. Riverine sources of carbon and nutrients are introduced via point sources. The underwater light field is spectrally-resolved at 5nm intervals between 400 and 700 nm. This allows for differential growth of different phytoplankton groups that have unique pigment complements.

Ecosim's daylight module explicitly calculates the in-water spectrally-resolved absorption coefficients for phytoplankton, detritus and CDOM, the scattering and backscattering coefficients for phytoplankton and detritus, the average cosine, downwelling irradiance attenuation coefficient, K_d, in addition to the scalar, E_0, and downward, E_d, irradiance fields following Morel (1988). Cahill et al. (2023) recently updated the K_d formulation following Lee et al., 2005 which accounts for some of the optical complexity found in coastal waters. The spectrally-resolved underwater light field drives the evolution of all the water constituents in the ecosystem model (phytoplankton, detritus and CDOM), while the water constituents in turn determine the evolution of the light field in each layer by absorption and scattering of the light. This means that their contribution to the divergence of the heat flux (Morel, 1988) can be accounted for within the full hydrodynamic solution. Furthermore, water constituent-induced heating rates can be

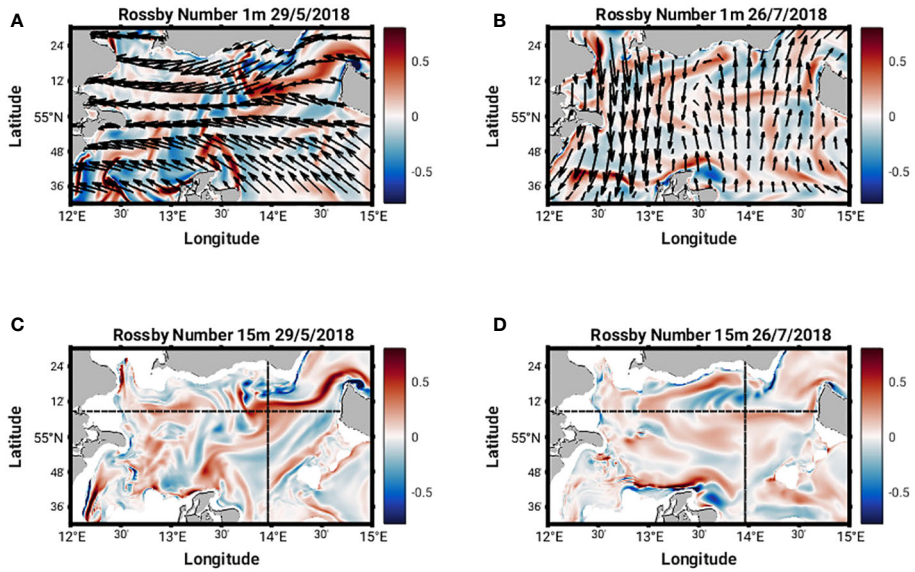


FIGURE 5
Rossby number at 1m and 15m on May 29 and July 26, 2018 **(A–D)**. DWD-ICON 3-hourly surface wind vectors are overlaid on **(A, B)**.

assessed (Cahill et al., 2023) and their impact on the ocean sea surface temperature can be communicated to the bulk flux formulation of the atmosphere in the modelling system.

The ROMS-BioOptic model was configured as described in Cahill et al., 2023 except with a higher resolution 600m horizontal grid in the Western Baltic Sea (see Table 1). A bulk flux atmosphere was forced with DWD-ICON output (Zängl et al., 2015) and river forcing including runoff and biogeochemistry (NO_3, NH_4, PO_4, SiO, DOC, CDOM and DIC) from 9 rivers which influence the region was derived from HELCOM PLC (Pollution Load Compilation) data (Neumann, pers. comm). Open boundaries to the north and east were forced with output from GETM physics using a combination of Chapman/Flather conditions for u and v velocities and transports, and Radiation + Nudging for temperature and salinity. This 3D setup is based on an existing GETM physics setup which has been previously evaluated and published (Gräwe et al., 2015a, Gräwe et al., 2015b). The Ecosim/Bio-Optic module was configured with four phytoplankton functional groups representative of small and large diatoms, large dinoflagellates and cyanobacteria. Initial conditions for the ecosystem model were obtained from previously evaluated and published output from the Ecological Regional Ocean Model (ERGOM) (Neumann et al., 2022). Our simulation period was 1 January to 31 December 2018. Daily averages and snapshots were output for the entire year. Hourly averages and snapshots were output for selected periods during both MHW events.

2.3 Detecting MHW events

Following Hobday et al. (2018), surface temperature data from the BSH (Bundesamt für Seeschifffahrt und Hydrographie) MARNET Arkona Buoy, surface temperature output from our 600m ROMS-BioOptic simulation of the Western Baltic Sea and sea surface temperature data from the NOAA OI SST V2 High Resolution Dataset (Huang et al., 2021) were used to diagnose the May and July 2018 MHW events (Figure 2B; Table 2). The heat budget diagnostic approach summarized in Elzahaby et al. (2021) and based on Chen et al. (2015) and Bowen et al. (2017) was used to diagnose whether the MHWs were atmospheric-driven or oceanic-process driven (Figure 3C). Herein, the respective contributions of advection and air-sea heat flux anomalies to the mixed layer temperature tendency anomaly during each event are used to classify the drivers of MHW drivers. For this purpose, we used the Baltic Sea Physics Reanalysis (https://doi.org/10.48670/moi-00013) and the ERA-5 Global Reanalysis (https://doi.org/10.1002/qj.3803) described in Hersbach et al. (2020) to calculate the temperature anomalies.

2.4 Detecting phytoplankton blooms events

We define a bloom event following a threshold approach as used by Thomalla et al. (2011) and applied by Lorenz (2019) whereby the initiation of the bloom is understood to be the period of the year which registers a relative increase in chlorophyll concentration, irrelevant of the actual value. For our purposes, we define the threshold as the first day that surface Chl-a rises 15% above the annual median as follows:

$$CHL_S = CHL_{MEDIAN} + 0.15 * CHL_{MEDIAN}$$

Thus, the bloom start condition is:

$$CHL_t < CHL_S \text{ and } CHL_t+1 > CHL_S$$

and, the bloom end condition is:

$$CHL_t > CHL_S \text{ and } CHL_{t+1} < CHL_S$$

In the run up to a bloom event, Chl-a tends to pulsate, often exceeding the threshold CHL_S for a short period of time (Racault

TABLE 1 Configuration of ROMS-BioOptic Western Baltic Sea Application.

ROMS-BioOptic	
Application Name	3D Western Baltic Sea
Model Grid	853 x 505 (600 m), 30 sigma levels
Simulation Period	2018
Boundary Conditions	Chapman for zeta, Flather for ubar and vbar; Radiation + Nudging for temperature and salinity
Bulk Flux Atmosphere	DWD-ICON 3-hourly
River Forcing	HELCOM PLC (Pollution Load Compilation), Neumann (pers. comm.)
Initial Conditions	GETM/ERGOM
Time Step	DT = 30s; NDTFAST = 20s
Ecosim	4 phytoplankton groups (small and large diatoms, large dinoflagellates & cyanobacteria)
Spectral Resolution	5 nm intervals between 400 and 700 nm

et al., 2015). Therefore, events which are shorter than 7 days are not considered blooms and blooms which are less than 6 days apart are considered as one event.

2.5 Detecting and tracking eddy-like finite-time coherent structures

Building on the ideas applied by Vortmeyer-Kley et al. (2019), we use our modelled velocity output to search for three dimensional, eddy-like coherent structures in the Arkona Sea during the time of the MHW events. To do this, we apply a particle tracking method combined with the concept of finite-time coherent sets by Froyland and Junge (2018). In general, eddies can be described as separated waterbodies that minimally mix with or leak into their neighbourhood. This links the idea of eddies to the concept of finite-time coherent sets (Froyland and Junge, 2018; Froyland et al., 2019).

Froyland and Junge (2018) and Froyland et al. (2019) formulate the definition of a finite-time coherent set as the solution of the weak eigenproblem of the dynamic Laplacian Equation 1:

$$-\left(\frac{1}{|\tau|}\sum_{t\in\tau} D^t\right)u = \lambda M u \tag{1}$$

with u as set of eigenvectors, whose information correspond to the finite-time coherent set, λ as corresponding eigenvalues, D as the stiffness matrix and M as the mass matrix. The entries in the mass matrix M can be interpreted as the volume of all tetrahedrons built from a three dimensional triangulation from the tracer position in space at time t if the tracers are advected by a flow field for the time period τ. The entries in the stiffness matrix D correspond to the change of the shape of all tetrahedrons (details cf. Froyland and Junge, 2018). The information of the coherent sets in the eigenvectors is often not cleanly represented in the eigenvectors, so we use the SEBA algorithm (Froyland et al., 2019) to disentangle the information and save them into SEBA vectors whose entries represent the coherence level of the finite-time coherent sets.

The backbone of the above mentioned algorithm is a particle tracking that provides the trajectory calculations needed to describe the tracer positions in space in the time period τ properly. Here we use ROMSpath (Hunter et al., 2022; code at https://github.com/imcslatte/ROMSPath/tree/V1.0.0) and integrate massless tracer trajectories on a longitude-latitude-depth grid for 24h starting tracers from the same grid every hour in the period May 27, 2018 00:30am to June 2, 2018 01:30am and July 22, 2018 05:30am to July 29, 2018 11:30pm using the velocity fields from ROMS-BioOptic simulations.

We apply the approach by Froyland and Junge (2018) and Froyland et al. (2019) using their matlab scripts (https://github.com/gaioguy/FEMDL and https://github.com/gfroyland/SEBA) to calculate eddy-like finite-time coherent sets for each hour from the calculated tracer trajectories. We requested 40 eigenvectors and chose the first 25 SEBA vectors to find the largest and most coherent sets. From this assemblage of hourly detected eddy-like coherent sets, we build consecutive tracks of coherent sets by searching in the assemblage for sets of the same type (positive or negative 24h-mean relative vorticity in the centre of the set) that are spatially close to each other in successive time steps. (Spatially close to each other means that their inner product is larger than 0.75.) We define the 0.7 coherence level as the outer shapes of the eddy-like coherent sets in space. We take into account tracks of structures with a lifetime larger than 11 h, to consider only structures that live long enough to have an ecological impact.

TABLE 2 Summary of MHW indices in the Arkona Sea in May and July 2018 (after Hobday et al., 2018).

MHW #	Start	Day	End	Day	# Days	I_{mean}	I_{max}	Category
MHW-1	13/05/2018	133	19/06/2018	170	38	4.0°C	5.3°C	23 days moderate
								15 days strong
MHW-2	25/07/2018	206	09/08/2018	221	16	4.4°C	5.2°C	15 days moderate
								1 day strong

3 Results

3.1 Characteristics of the May and July MHW events

Following the approach described in section 2.3, two MHW events were identified using observations from the Marnet Arkona Buoy in 2018 and the blended NOAA OI SST V2 product from Huang et al. (2021) (Figure 2B). Coincident modelled SST was compared to the Marnet Arkona Buoy data, to ensure the fitness for purpose of the physical model for the analysis of MHW surface and subsurface dynamics. The spatial extent of the MHWs on 29 May and 26 July 2018 was calculated as the SST anomaly using the SST Reanalysis (https://doi.org/10.48670/moi-00156) described in Høyer and She (2007) and Høyer and Karagali (2016) (Figures 3A, B). The MHW events are described in terms of their duration, mean intensity, I_{mean}, maximum intensity, I_{max}, and category (moderate, strong, severe or extreme) (Table 2). The May MHW (herein referred to as MHW-1) lasted 38 days, in which 23 are classified as moderate and 15 as strong. MHW-1 I_{mean} is 4.0°C and I_{max} is 5.3°C. The July MHW (herein referred to as MHW-2) lasted 17 days, in which 15 are classified as moderate and 2 as strong. MHW-2 I_{mean} is 4.4°C and I_{max} is 5.2°C. The heat budget diagnostic (Figure 3C) reveals that MHW-1 is an atmospheric-driven event, while MHW-2 is a mixed atmospheric- and horizontal advection-driven event.

There is very good agreement between our modelled ROMS-BioOptic sea surface temperature at Arkona Sea in 2018 and the observed sea surface temperature in 2018 (r^2 = 0.99, RMSE = 0.016, Bias = -0.001) (Figure 2B). The timing and surface characteristics of both MHW events are also captured very well in the model. This gives us confidence to examine the sub-surface properties of the 2018 modelled temperature anomaly using a 40 year modelled climatology (1979 – 2019) derived from General Estuarine Transport Model (GETM) simulations (Gräwe et al., 2015a) (Figure 2A).

The impact of MHW-1 extends to ca. 15 m during the first half of the event, after which it deepens over the full extent of the water column (Figure 2A). The maximum temperature anomaly (ca. 6°C) occurs a few days after the surface signature of MHW-1 has disappeared at depths between 15 and 25m. This maximum subsurface anomaly persists for about 3 days, after which it relaxes to ca. 4°C, but remains positive until the onset of MHW-2.

The subsurface impact of MHW-2 is much more pronounced compared to MHW-1. MHW-2 extends from the surface to ca. 15 m for the duration of the event with a temperature anomaly of ca. 4° C in the surface layer. Between 15 m and 30 m, a negative temperature anomaly (ca. 2°C) lies over a positive bottom temperature anomaly (ca. 3°C). The maximum temperature anomaly (ca. 8°C) is concentrated between 15 m and 20m for 15 days after the surface signature of MHW-2 has disappeared. Its extent then deepens from 15 m to about 30 m for further 10 days, following which it decays over a period of about 10 days, finally relaxing at the end of September.

3.2 Dynamics of phytoplankton blooms and MHWs

Following the threshold approach described in section 2.4, three distinct phytoplankton bloom periods were identified in the modelled Chl-a in 2018 (Figure 2C). The first bloom developed on 29th March and persisted until 1st May. Peak Chl-a concentration of 4.95 mg m^{-3} occurred on 14th April. A second bloom developed on 20th May, 7 days after the onset of MHW-1. This persisted until 24th July, one day before the onset of MHW-2. Peak Chl-a concentration of 5.4 mg m^{-3} occurred on 29th May and coincided with maximum water constituent-induced surface heating rates (Figure 2C). Modelled phytoplankton, CDOM and detrital absorption at 442 nm show that phytoplankton absorption dominates the diffuse attenuation coefficient at 492 nm during the second bloom event (Figures 6C–F) and thus contributes most to the surface heating rates. A third bloom event developed on 12th August, two days after the end of MHW-2 event and persisted until 14th September. Peak Chl-a concentration of 3.7 mg m^{-3} occurred on 4th September. We focus our attention on the evolution and decay of the 2nd phytoplankton bloom event which is bookended by the MHW-1 and MHW-2.

Our analysis is centered on two separate days within the MHW-1 and MHW-2 events, 29 May and 26 July 2018. These days were selected for a number of reasons: they exhibit different bio-optical and biogeochemical responses to the MHW events; 29 May 2018 coincides with the maximum surface Chl-a concentrations and peak water constituent-induced heating rates during MHW-1 (Figure 2C); 26 July 2018 coincides with the end of the 2nd phytoplankton bloom event, a steady decline in the water constituent-induced surface heating rates and the onset of MHW-2. A sequence of selected cloud-free Chl-a OLCI satellite data (Figure 4) starting from 29 May 2018 show a surface Chl-a signature persisting within the eddy-like structure for at least 10 days. As will be shown below, a similar eddy pattern was found in the model results in the same location at the end of May, although we do not expect the positions of the observed and simulated eddies to agree completely, because trajectories of eddies typically contain a stochastic element.

We evaluated the simulated surface Chl-a with coincident OLCI data. Ocean colour instruments receive most of their in-water signal from the surface down to one optical depth. When we refer to the simulated surface chlorophyll, we actually refer to the mean of the simulated chlorophyll over the first optical depth, rendering such satellite-derived and simulated chlorophyll concentrations comparable. In our area of interest, the OLCI data characterize the diffuse attenuation coefficient at 490 nm, $K_d(490)$, to be about 0.5 m^{-1} on 29 May 2018 and 0.25 m^{-1} on 26 July 2018, resulting in a remotely sensed layer at 490 nm of about 2 m and 4 m, respectively. The evaluation shows that the model captures the surface dynamics of the phytoplankton bloom but highlights the difficulty in capturing the magnitude of the surface bloom event that is seen in the satellite data in May in the model (Supplementary Figures 1A-D). However, we would not expect the model to necessarily reproduce the magnitude of the bloom event observed by OLCI in May as these type of events are very difficult to

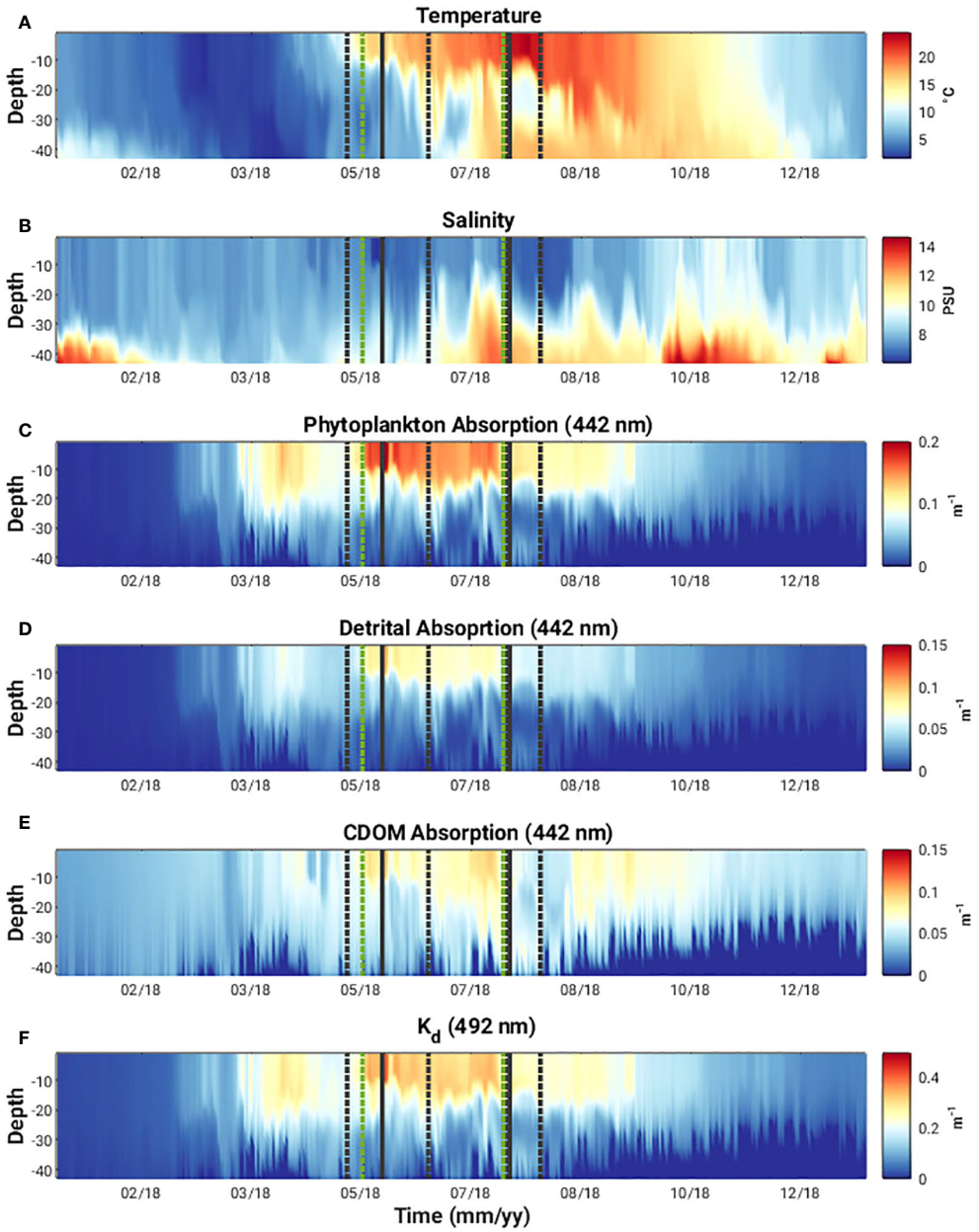


FIGURE 6
(A) Temperature, **(B)** salinity, **(C-E)** phytoplankton, detrital and CDOM absorption at 442 nm, respectively, and **(F)** the diffuse attenuation coefficient at 492 nm [$K_d(492)$] in Arkona Sea 2018. (Grey dashed vertical lines indicate onset and end of two MHW events, solid grey vertical line indicates day of detailed analysis during MHW event, green vertical dashed lines indicate start and end of the prolonged phytoplankton bloom event discussed in the text.).

reproduce in a model without data assimilation. Good agreement is seen between the model and OLCI data in July. Previous evaluations of modelled Chl-a and other water constituents using OLCI data also found good agreement between the model and OLCI data background values in the region (Cahill et al., 2023). The structure of the simulated surface Chl-a concentrations captures the extent of the eddy feature observed by OLCI in May (Supplementary Figure 1A). This supports our application of the model to explore the relationship between co-occurring MHWs and phytoplankton bloom events.

In order to explore the physical differences between the two MHWs further, we examine horizontal cross sections across the area of interest at 1 m and 15 m, and vertical transects across 13°58' E and 55°8' N. We use the Rossby number, Ro (defined as balance between the vertical component of the relative vorticity and planetary vorticity) to situate the flow regime (Figures 5, 7). This will be << 1 in mesoscale regimes, where planetary rotation constrains the flow and vertical stratification dominates, and O(1) in submesoscale flow regimes, where relative vorticity becomes important. Vertical sections of the horizontal (u and v) and

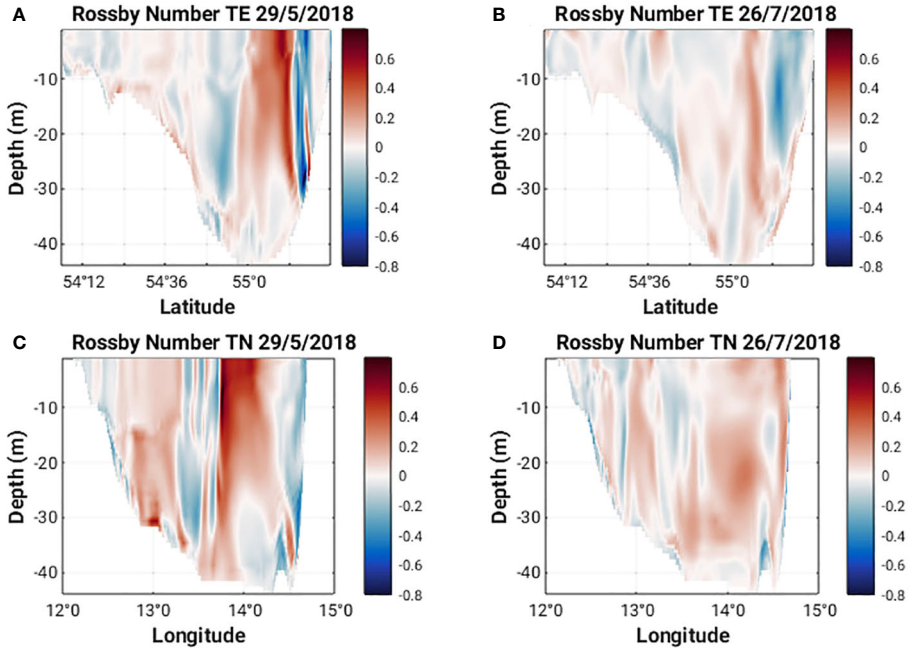


FIGURE 7
Rossby number along 13°58′ E (TE) and 55°8′ N (TN) on May 29 and July 26, 2018 **(A–D)**.

vertical (w) velocity components (Figure 8) provide more information on the structure of the flow.

3.2.1 29th May 2018 (MHW-1)

Horizontal cross sections of Ro at 1 m and 15 m (Figures 5A, C) show a cyclonic eddy structure centered around 13°58' E and 55°8' N present on 29 May 2018. This structure extends from the surface to approximately 27 m depth (Figures 7A, C). The cyclonic nature of the structure is clear in the horizontal velocity components (Figures 8A, C) and relatively strong vertical velocities on the order of 10^{-4} ms^{-1} are seen on the northern and western flanks of the structure (Figures 8E, G) where Ro is +/- 0.8 (Figures 7A, C). The strong vertical velocities coincide with sharp lateral density gradients, a doming of isopycnals and upwelling of cooler subsurface water (Figures 9A, C). Converging north-southeasterly winds prevailed during this time (Figure 5A).

Horizontal cross sections of the diffuse attenuation coefficient at 492 nm, K_d(492) and Chl-a concentration at 1 m and 15 m on 29 May 2018, show higher subsurface values for both quantities compared to the surface values (Figures 10A, C, E, G). A subsurface Chl-a maximum accumulates on the southern flank of the eddy (Figure 9I). Sharp lateral gradients in both quantities also coincide with the sharp lateral density gradients (Figures 9E, G, I, K) and there are strong upward and downward vertical fluxes of Chl-a (ca. 60 mg m^{-2} d^{-1}) along the northern, southern and western flanks of the eddy (Figures 11A, C).

3.2.2 26th July 2018 (MHW-2)

The characteristics of Ro at 1 m and 15 m (Figures 5B, D, 7B, D) on 26th July 2018 are quite different from those seen in May. The values are much smaller (ca. +/- 0.2) and no clear eddy-like structures are evident in the domain. Weaker northerly winds prevail east of 13°58' E while southerly winds prevail west of 13° 58' E (Figure 5B). Along the southern Swedish coast, east of 13°30' E, surface velocities are directed onshore (Figure 8D) and an overturning circulation is evident characterized by downwelling near the coast and upwelling offshore at 55°8' N (Figure 8F). Some doming of isopycnals and upwelling of cooler subsurface water (Figure 9B) can also be seen at 55°12' N. This coincides with a lateral gradient in the diffuse attenuation coefficient at 492nm, K_d (492) (Figure 9F) and Chl-a concentrations (Figure 9J) at this location. Strong downward and upward vertical fluxes of Chl-a (ca. 50 mg m^{-2} d^{-1}) are also seen near the coast and offshore at 55° 12' N, respectively (Figure 11B). Horizontal cross sections of Kd (492) and Chl-a concentration at 1 m and 15 m on 26 July 2018, also reveal higher subsurface values for both quantities compared to surface values (Figures 10B, D, F, H). However, lateral gradients in temperature, Kd(492) and Chl-a values are absent along the 55° 8' N transect (Figures 9D, H, L) and vertical fluxes of Chl-a are weak (Figure 11D).

3.3 Coherent structures found during the MHW events

During MHW-1, a long-living, eddy-like coherent structure according to the methodology described in Section 2.5 is detected below the surface eddy structure visible in the satellite and modelled Chl-a and K_d(490/492) fields (shown in Figures 4A, 10C, G). The structure emerges on May 28, 2018 at 04:30am at 13°55' E and 55°6' N and dies out on June 02, 2018 at 01:30am at 13°47' E and 55°0.6' N, travelling about 13 km (Supplementary Figure 2). The structure

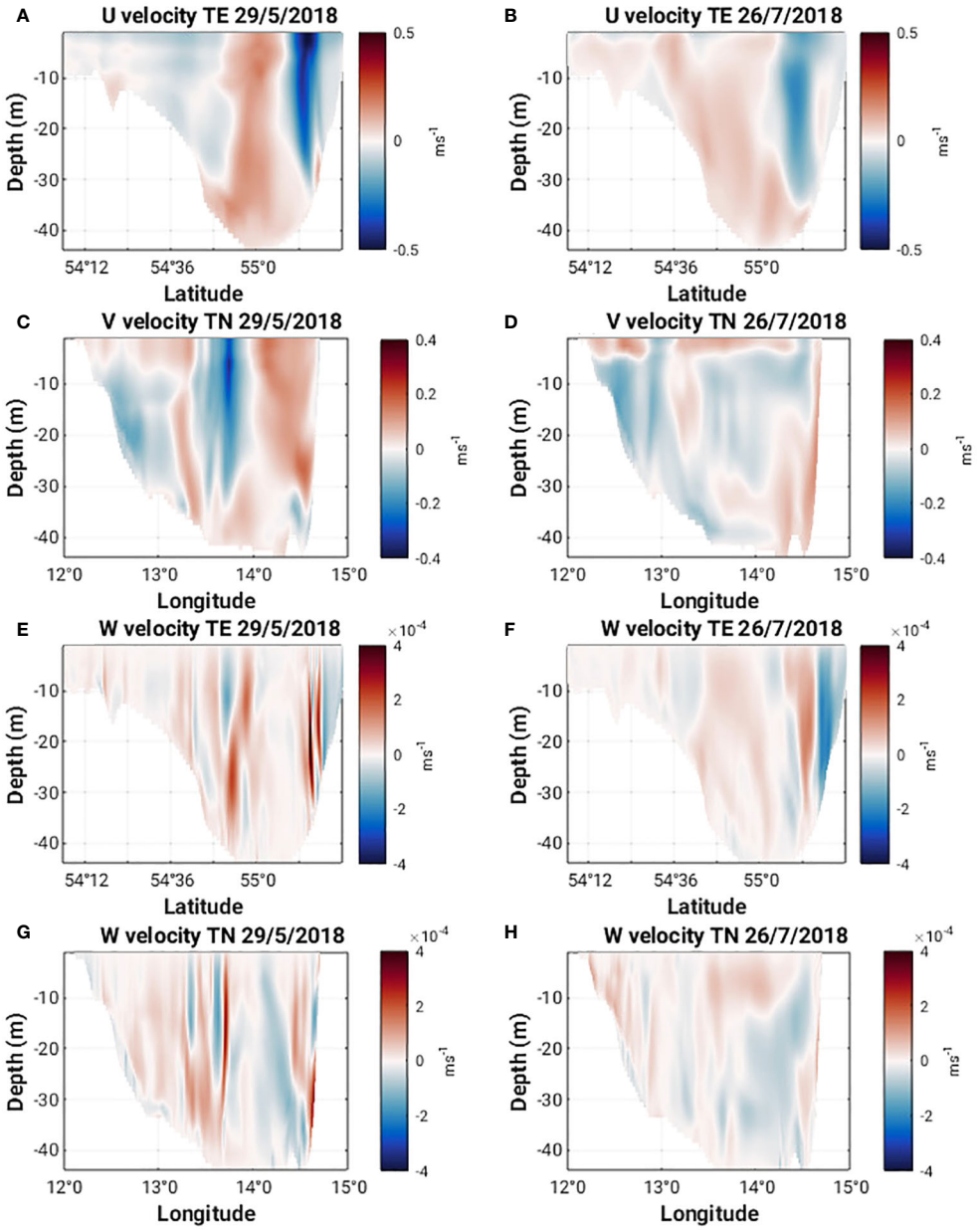


FIGURE 8
U, V, W velocities along 13°58′ E (TE) and 55°8′ N (TN) on May 29 and July 26, 2018.

extends during its life time from about 24 m to about 44 m depth and has a mean volume of 0.4 km^3 (an equivalent diameter of about 4 km if the structure is assumed to be cylindrical). During its lifetime, the tracers inside the structure show tendencies of upward motion (Figures 12A, B) which coincides with a doming of isopycnals above the structure (Figures 9A, C). Tracers seeded along a rectangular slice at 13°58' E and 55°8' N in May 29, 2018 at 11:30am show a strong semi-circular shaped south-eastward displacement after 24h of integration (Figures 12A, B) in the surface layer which correlates with an increase in Chl-a at the eddy boundaries (Supplementary Figure 2). During MHW-2, the tracer displacement starting from the same slice on July 26, 2018 at 11:30am shows a less dynamic displacement into different directions with a small trend towards the north in the surface layers (Figures 12C, D), consistent with the onshore displacement of surface waters and overturning circulation seen earlier in the vertical velocity fields (Figure 8F), and the vertical fluxes of Chl-a (Figure 12B).

Comparing the spatial dynamics of the May coherent structure with the Chl-a content in the water column for May 28 to May 31 (Supplementary Figure 2), we found that the structure correlates with a low Chl-a patch during the whole period of time and weak vertical fluxes of Chl-a. The long lifetime of the deeper coherent structure in May 2018 appears to be linked to the persistence of the eddy in the top 30m and the dynamics of the deeper layers are more coupled to the surface layers during MHW-1. In July, a stronger

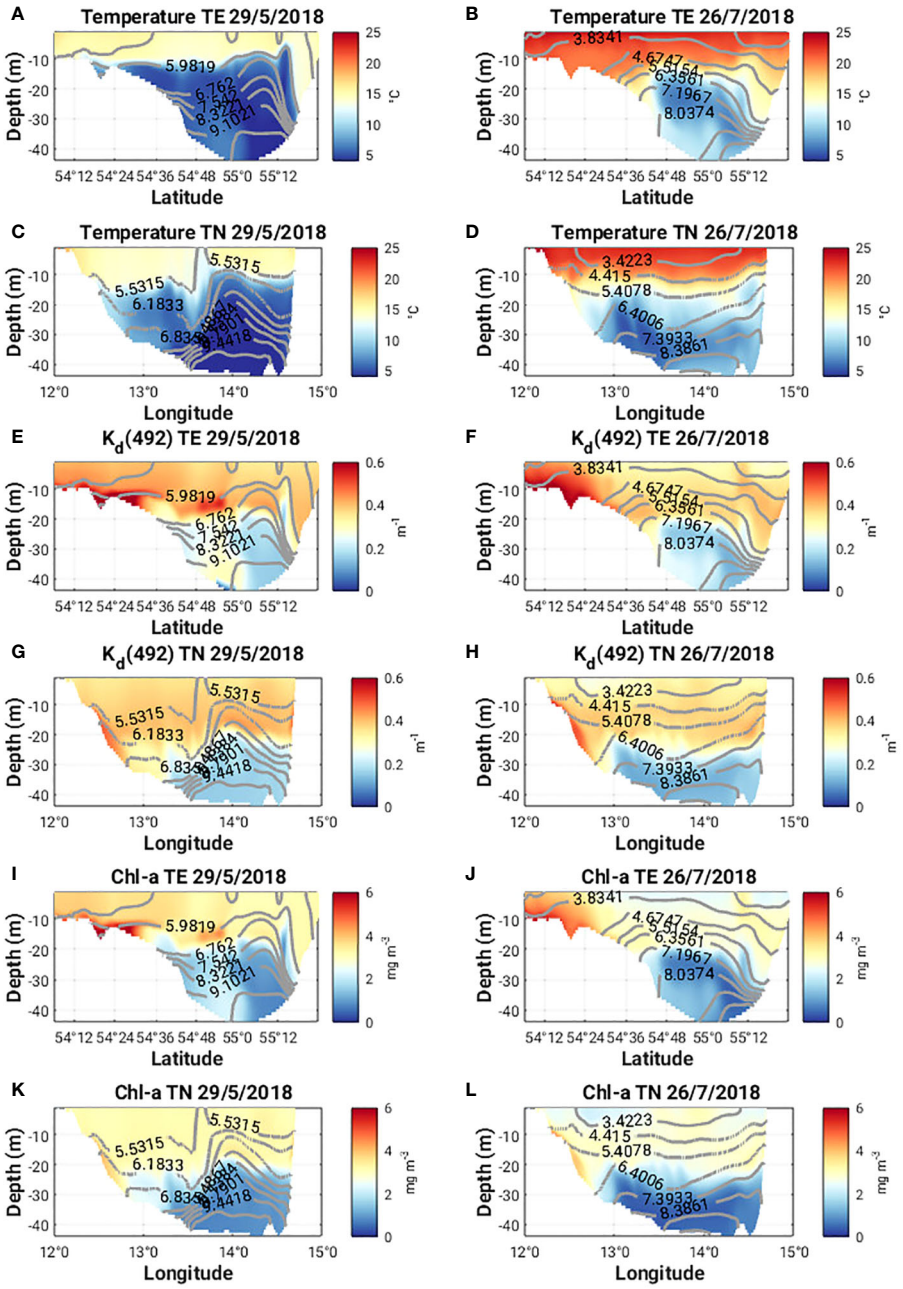


FIGURE 9
(A-D) Temperature (°C), **(E-H)** K_d(492) and **(I-L)** Chl-a along 13°58′ E (TE) and 55°8′ N (TN) on May 29 and July 26, 2018. Density contours are plotted as grey lines.

thermocline de-couples the dynamics between the surface and deeper layers. Combined with onshore winds in July, the tendency is rather to support onshore displacement of surface waters toward the Swedish coast, and a coastal overturning circulation cell.

The high Chl-a patch that bends around the southwestern edge of the eddy in May (Figure 10G) can be interpreted as the impact of a "sticking" (unstable) manifold (Lehahn et al., 2007) on the distribution of particles in the flow. Stable and unstable manifolds act as organizing structures of the flow separating regions of different dynamical behaviour (Prants, 2013). Due to the attracting properties of the unstable manifold, nutrients and plankton are collected along it. This "sticking" manifold is visible as a dark blue singular line in Figure 13A which also correspond to the high K_d and Chl-a patch seen in Figures 10C, G. The manifold extends down into the upper water column, as seen in Figure 13B and provides a three-dimensional transport barrier around the southern, southeastern and eastern edge of the eddy. This mechanism could also explain the surface Chl-a patterns seen in May in the OLCI data (Figure 4).

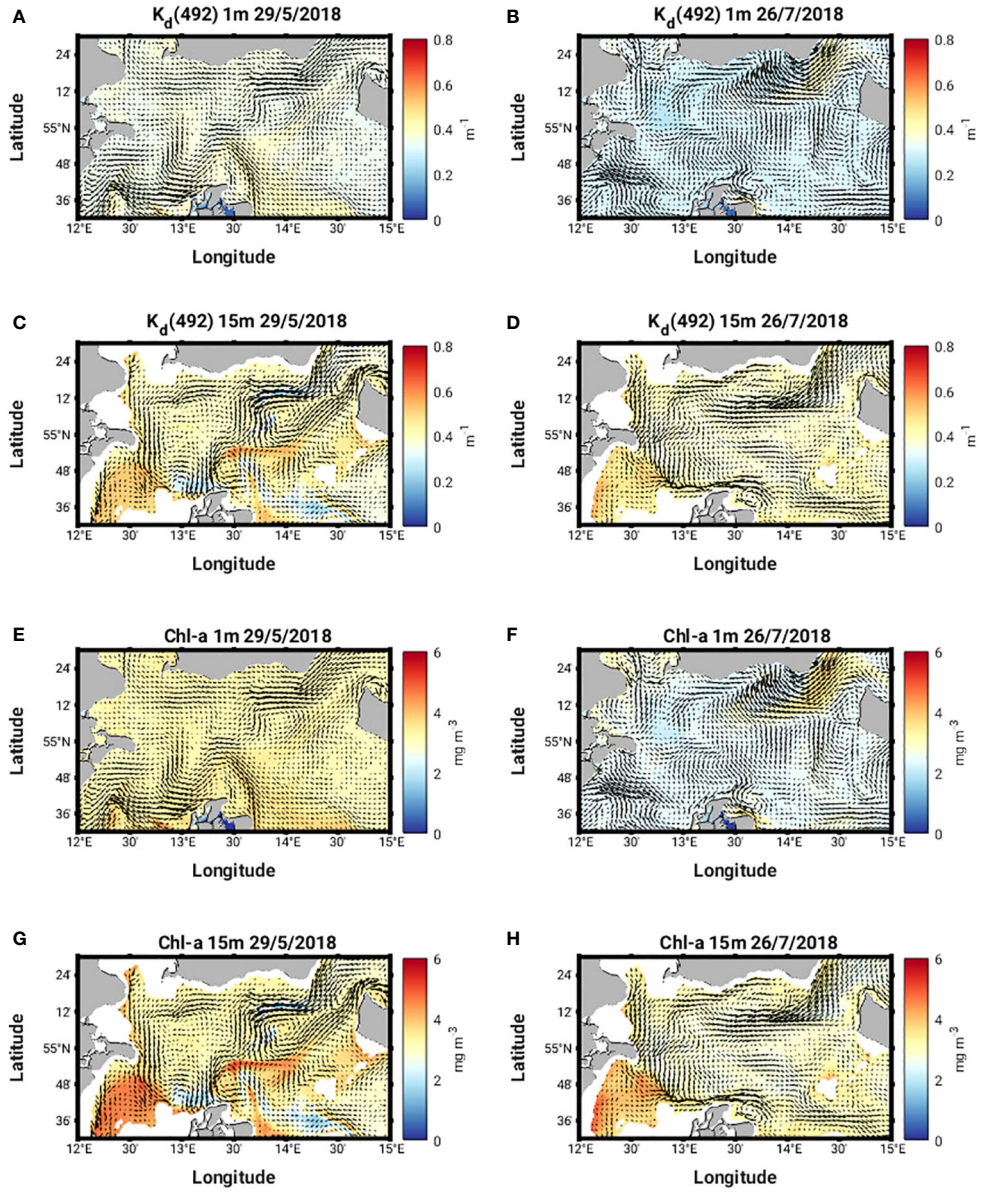


FIGURE 10
(A-D) K_d(492) and **(E-H)** Chl-a at 1m and 15m on May 29 and July 26, 2018.

4 Discussion

We examined two different MHW events in 2018 which bookmark the evolution and decay of a phytoplankton bloom in the Arkona Sea. Our objective was to explore the relationship between co-occurring MHW and phytoplankton bloom events with the following specific questions in mind:

1. How, and under which circumstances, do MHWs contribute to the initiation of phytoplankton blooms?
2. Which dynamics play a role in sustaining the bloom?
3. How deep and for how long is the impact of the MHW felt?
4. What role, if any, do MHWs play in terminating a phytoplankton bloom?
5. Do phytoplankton blooms have an enhancing effect on MHWs by creating a positive feedback from water constituent–induced surface heating?

Marine heatwaves are typically associated with shallower mixed layer depths (Hayashida et al., 2020). Cook et al. (2022) show that atmospheric pressure systems, wind speed and latent heat fluxes are important contributing factors to the generation and decline of MHWs. Surface flux-driven MHWs are shallower and occur predominantly in summer (Elzahaby et al., 2021). MHW-1 develops mid-May in parallel with a strengthening and shoaling of the seasonal thermocline (Figure 6A). The heat budget diagnostic confirms that MHW-1 is an atmospheric-driven event. Surface salinity also decreases during the onset of MHW-1 (Figure 6B), consistent with Elzahaby and Schaeffer (2019) whereby increased

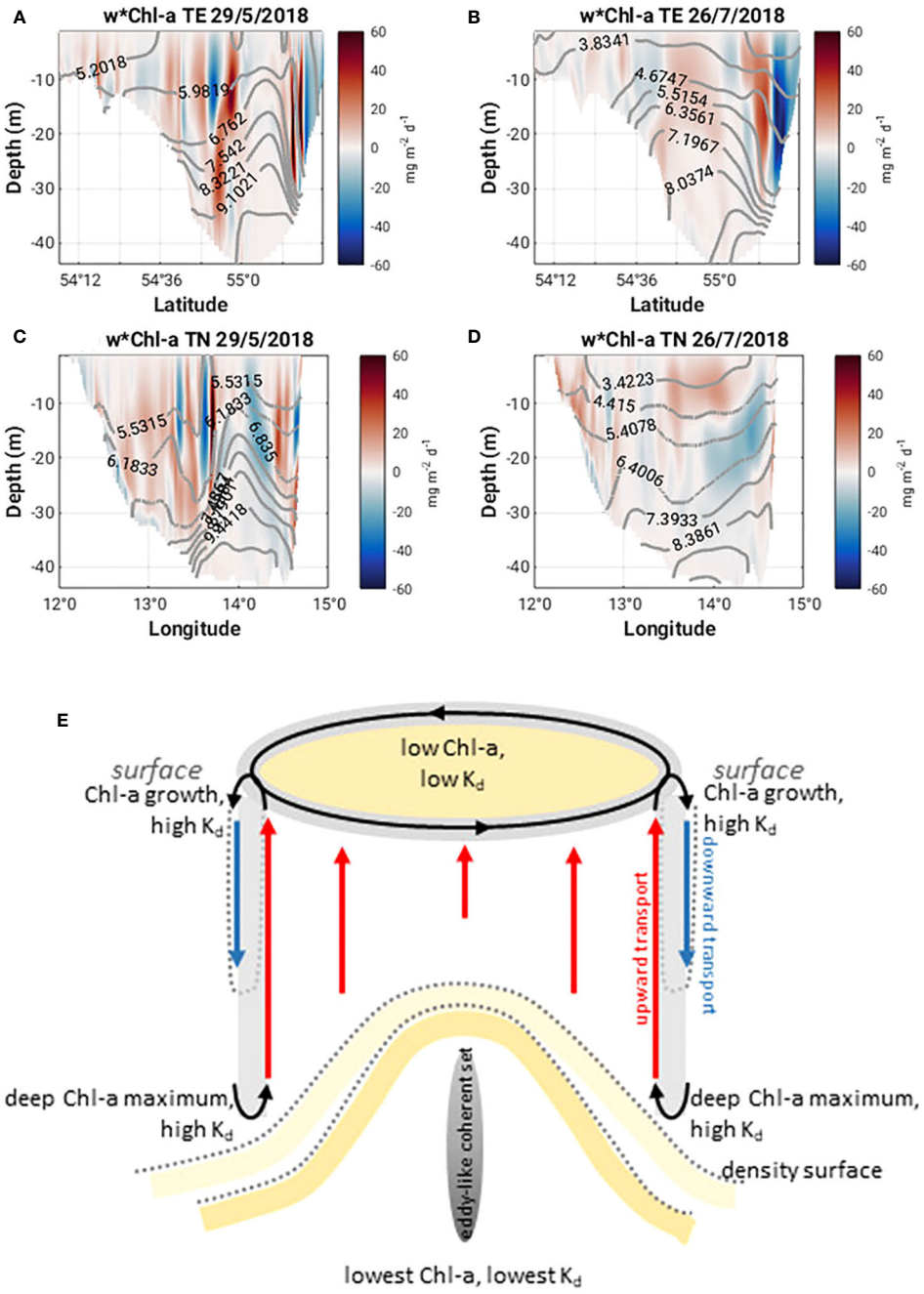


FIGURE 11
Vertical flux of Chl-a (w*Chl-a, mg m^{-2} d^{-1}) along 13°58′ E (TE) and 55°8′ N (TN) on May 29 and July 26, 2018 **(A-D)**. Density contours are plotted as grey lines; **(E)** simplified schematic of coupled surface-deep layer dynamics driven by cyclonic eddy at the peak of MHW-1.

anomalous solar radiation and decreased wind stress act on the latent heat flux to reduce evaporation. Given sufficient light and supply of nutrients, phytoplankton growth will occur. Increased phytoplankton biomass in the surface will increase the surface temperature due to absorption of light by phytoplankton in the surface layer. A thermal structure is established in the water column which will impact the growth, transport and fate of phytoplankton biomass. The availability of light below the productive layer will be strongly reduced. In the absence of other physical transport processes on timescales which are relevant for phytoplankton growth (Kuhn et al., 2019), nutrients will become depleted in the surface layer, the supply of nutrients from deeper waters will be inhibited by the stronger thermocline mid-summer, and phytoplankton growth will be expected to decrease.

A model study by Hayashida et al. (2020) shows that background nutrient conditions will determine the response of phytoplankton blooms co-occurring with MHWs. Generally, they find that in nutrient poor waters, blooms are weaker during MHWs, whereas in nutrient-rich waters, blooms are stronger during MHWs. However, transport dynamics play a critical role in the

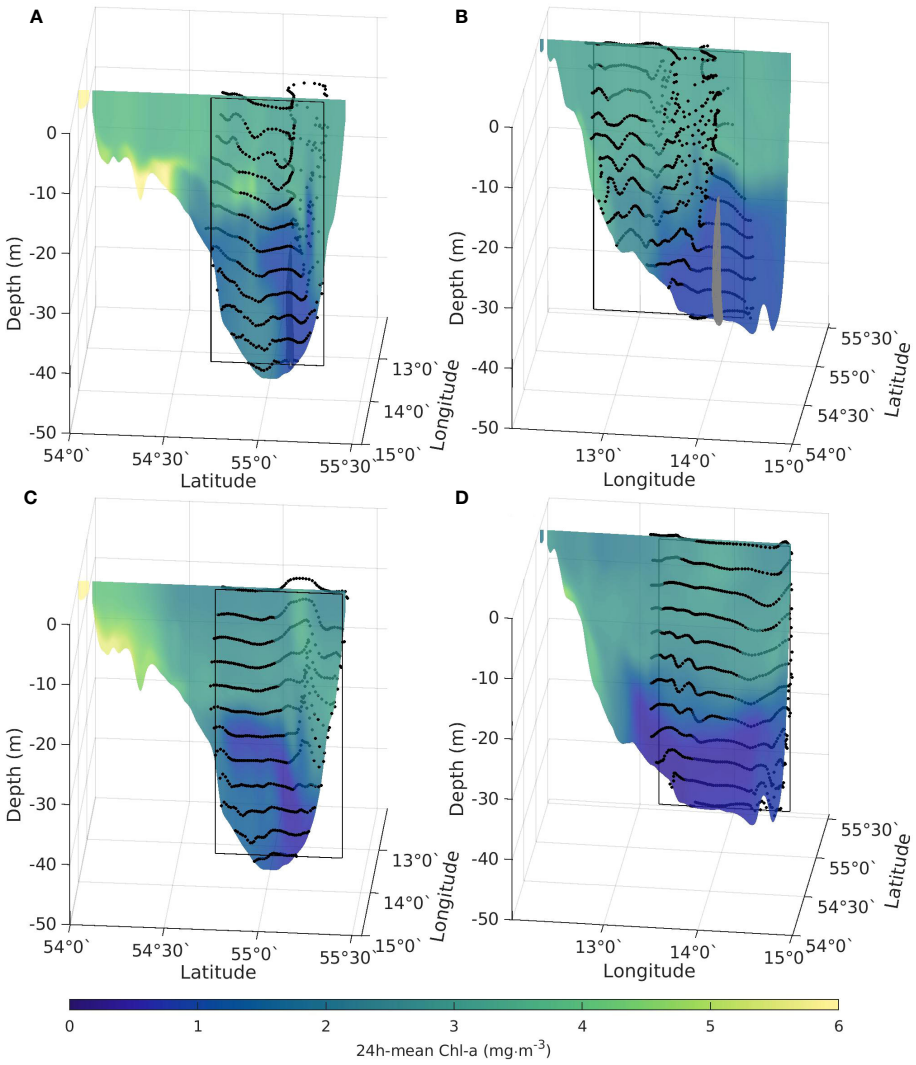


FIGURE 12
(A) 24h-mean chlorophyll along a 13°58′ E slice **(B)** 55°8′ N slice) and the tracer position (black dots) after 24h of particle tracking starting on a grid in the black rectangle at May 29, 2018 11:30am. The gray structure corresponds to the position of the coherent structure at that time. **(C)** 24h-mean chlorophyll along a 13°58′ E slice **(D)** 55°8′ N slice) and the tracer position (black dots) after 24h of particle tracking starting on a grid in the black rectangle at July 26, 2018 11:30am.

supply of nutrients to the surface mixed layer. In our scenario, wind driven surface circulation underpins the development of a series of cyclonic eddies in May and June over the Arkona Basin. The eddy we focus on late May has Ro O(1), an indication that relative vorticity is the same order of magnitude as the Coriolis force, that circulation has departed from geostrophy, and that ephemeral submesoscale dynamics may be at play. Indeed, large vertical velocities (ca. 35 m d^{-1}) along the edges of the eddy are seen, giving rise to upwelling and downwelling along the boundaries of the eddy (Figure 8E, G; Supplementary Figure 2). Vertical fluxes of Chl-a are between 40 and 60 mg m^{-2} d^{-1}, along the north- and south-western boundaries of the eddy (Figures 11A, C). Upwelling vertical fluxes may also transport nutrients to the surface contributing to sustained phytoplankton growth. This potential coupling of surface and subsurface dynamics is illustrated schematically in Figure 11E.

A number of mechanisms relate the role of submesocales and mesoscale eddies and their impact on the horizontal and vertical distribution of Chl-a. Submesoscale phytoplankton patchiness is often visible in satellite images (Lapeyre and Klein, 2006; Levy et al., 2012), whereas in the Baltic Sea intense submesoscale activity has been observed through its imprint on cyanobacteria blooms (McWilliams, 2016). Several dynamical mechanisms that occur in the submesoscale regime, e.g., frontal subduction and submesoscale restratification (Chrysagi et al., 2021), have been proposed to explain not only the surface but also the subsurface biogeochemistry signals (Hosegood et al., 2013; Levy et al., 2018). Eddy stirring which describes the direction of rotational flow of the eddy field, is known to be a source of phytoplankton patchiness (Abraham, 1998; Martin, 2003) and will determine the position of the chlorophyll anomaly and the direction of propagation of the eddy relative to the ambient chlorophyll field (McGillicuddy, 2016). A cyclonic eddy in the northern hemisphere

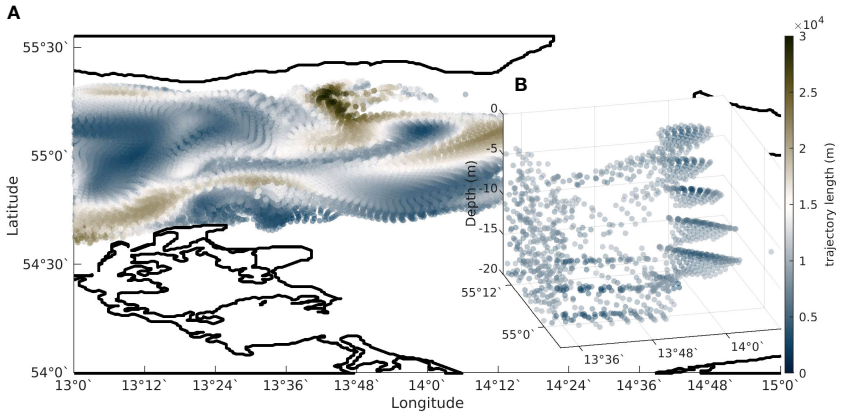


FIGURE 13
Sticking manifold calculated as the trajectory length of backward integrated trajectories of the velocity field (Prants et al., 2011; Prants, 2013; Jimenez Madrid and Mancho, 2009; Mendoza and Mancho, 2010). The values of the trajectory length are assigned to the starting points of the trajectories. All these values make up a three-dimensional map. **(A)** Map of trajectory length of for 24h backward integrated trajectories starting at May 29, 2018 11:30am. The sticking manifold is displayed as the dark blue singular line. **(B)** Three-dimensional view of the sticking manifold.

will result in a positive anomaly in the southwest quadrant, a negative anomaly in the northeast quadrant and westward propagation. We see a Chl-a maximum accumulate on the southern flank of the eddy at about 15 m depth (Figure 9I).

According to Mahadevan (2016), the vertical transport of nutrients into the euphotic zone can be achieved either by the vertical movement of the nutrient-rich isopycnal layers or by an advective flux. The former occurs mainly in the presence of internal waves or within mesoscale eddies but at different timescales. Eddies typically mix properties along isopycnals, and diapycnal mixing is considered to be weak. On the other hand, the advective flux of nutrients dominates in submesoscale features and tends to occur along the vertically tilted isopycnals. Reißmann et al., 2009, show that in the Baltic Sea, mesoscale eddies, known as Beddies may contribute to vertical mixing through different mechanisms. In particular, Beddies can contribute to the diapycnal mixing, inside the permanent halocline region, either through the vertical displacement of water and isopycnals, or through their decay. Another potential yet indirect mechanism through which Beddies may impact the halocline mixing, is through their interaction with internal waves, although this remains to be verified. Nevertheless, the exact dynamical mechanisms by which eddies might affect vertical mixing, are out of the scope of this study, since here we focus mainly on the co-occurence of MHWs and phytoplankton blooms.

We see indications of an unstable "sticking" manifold (Figure 13A), arising from geostrophic eddy stirring, acting as both a horizontal transport barrier for Chl-a and a facilitator of phytoplankton growth mediated by nutrient upwelling, as observed by Lehahn et al. (2007). The manifold extends down into the upper water column (Figure 13B) and provides a three-dimensional transport barrier around the southern, southeastern and eastern edge of the eddy. The emergence of the long-living, eddy-like coherent structure below the surface eddy structure illustrates the role of the surface eddy in isolating a cold, dense, sub-surface, low Chl-a water body below the surface eddy pointing at a coupling of surface and subsurface dynamics (Figures 12A, B; Supplementary Figure 1). Outcropping of isopycnals and upwelling of colder water along the southwestern edge of the eddy (as seen in Figures 9A, C) produce cold sea surface temperature anomalies which would tend to draw heat into the ocean from the atmosphere, further increasing stratification in those features relative to ambient waters. The complexity of eddy-induced transport mechanisms and biophysical interactions is reviewed in depth in McGillicuddy (2016) and references therein).

According to Levy et al. (2018), the combination of the seasonal distribution of light and the vertical supply of nutrients through ephemeral fronts are essential ingredients for sustained phytoplankton growth. The timing of the onset of MHW-1 in May provides optimal light conditions which, given sufficient supply of nutrients, may contribute to the initiation of the phytoplankton bloom. The series of eddies which ensue, support both geostrophic eddy stirring and transient submesoscale dynamics along the edges of the eddies which may in turn provide both an upward and downward transport path for nutrient fluxes and carbon export (Callbeck et al., 2017; Ruiz et al., 2019).

It is important to note that the surface signature of both MHWs, does not represent the deeper signature and impact of the MHWs. Schaeffer and Roughan (2017) suggest that vertical mixing, in combination with downwelling favourable winds, can weaken stratification and enable MHWs to extend deeper than the surface mixed layer, thus homogenizing the water column. We see a deepening of the thermocline take place in MHW-1 (Figure 6A) shortly after the peak in Chl-a concentration and associated water constituent-induced heating rate at the end of May (Figure 4).

Water constituent-induced surface heating increases with the onset the bloom, and peaks in the middle of MHW-1 at 0.7 K d^{-1} (Figure 4). This increase in water constituent-induced surface heating is clearly a response to increases in Chl-a concentration and is directly related to the absorption of light by phytoplankton (Figure 6C) and to a lesser extent, detrital and CDOM absorption (Figures 6D, E). MHW-1 contributes to the initiation of the bloom, which in turn contributes to an increase in water constituent-induced heating rates. A recent study by Cahill et al. (2023)

found that, in 2018, water constituent-induced surface heating rates in the Western Baltic Sea could reach up to 0.4 to 0.8 K d^{-1} during the period April to September. Moreover, this water constituent-induced surface warming resulted in a mean loss of heat (ca. 5 W m^{-2}) from the sea to the atmosphere, primarily in the form of latent and sensible heat fluxes. Thus, the phytoplankton bloom may have an enhancing effect on the MHW as a consequence of its contribution to surface warming but air-sea energy flux exchange plays a role in regulating this.

MHW-2 develops late-July, and coincides with a re-stratification of the water column, a stronger, shallower thermocline and the end of the phytoplankton bloom. The Rossby number is small, indicating that there is no significant submesoscale activity. The end of the phytoplankton bloom is preceded by a period where the temperature anomaly extended the full depth of the water column. Zhan et al (2023) examine the roles of atmospheric forcing-driven and oceanic processes-driven MHWs in driving changes in Chl-a concentrations and phytoplankton biomass. They show that atmospheric forcing-driven MHWs (like MHW-1) tend to increase Chl-a concentrations and phytoplankton biomass, while oceanic processes-driven MHWs tend to decrease Chl-a concentrations and phytoplankton biomass. The heat budget diagnostic shows MHW-2 to be a mixed atmospheric-and horizontal advection-driven event. Indeed, advection of higher salinity, warmer bottom water precedes MHW-2 (Figures 6A, B). Changes in the seasonality of saltwater inflows from the North Sea to the Baltic Sea has been shown to cause exceptional warming trends in the Western Baltic Sea (Barghorn et al., 2023). The stronger thermocline in MHW-2 de-couples the dynamics between the surface and deeper layers and any supply of nutrients to the surface from the deeper waters is cut off. Only along the Swedish coast do we see evidence of some downwelling and upwelling (Figure 8F) and strong vertical fluxes of Chl-a (ca. 40 mg m^{-2} d^{-1}) (Figure 11B).

The persistence (up to 35 days between 15 m and 20 m) of the subsurface maximum temperature anomaly after the surface signature of MHW-2 has disappeared is remarkable. This underscores the importance of considering subsurface hydrography in order to fully understand the impact of MHWs on biological production (Schaeffer and Roughan, 2017). Moreover, the vertical extent of the subsurface temperature anomaly will play a role in the distribution of horizontal gradients in density and intensification of fronts, and thus determine transport pathways for nutrients and carbon.

In summary, we find that in the shallow Arkona Sea, the timing of atmospheric driven MHWs can contribute to the initiation of a phytoplankton bloom by providing the optimal conditions for phytoplankton growth. The vertical component of an eddy-like structure's vorticity balance determines the strength of coupling between the surface and subsurface dynamics, and seems to provide a vertical transport pathway for nutrients. These coupled dynamics might in turn contribute to sustaining phytoplankton growth. Depth-integrated phytoplankton will be restricted within a shallower mixed layer which will in turn increase surface heating. Thus, phytoplankton blooms may have an enhancing effect on MHWs as a consequence of their contribution to surface warming but air-sea energy flux exchange will play a role in regulating this exchange. The subsurface signature of MHWs is often stronger and persists for longer than its surface signature. Moreover, the subsurface signature of the MHW plays a critical role in de-coupling surface and subsurface dynamics and terminating a phytoplankton bloom.

Remotely sensed ocean colour data provides a window into the spatial complexity of optically active constituents in surface waters and how these constituents are transported by surface circulation. Knowledge of coincident surface winds, can provide some clues as to what may be occurring subsurface but used in tandem with 3D biogeochemical ocean models, it is possible to see how surface and subsurface dynamics are really connected and extend our knowledge on surface layer processes obtained from satellite data. In the last decade, ocean colour observations have been recognized as essential climate variables (ECVs) and become an integral part of ocean observing systems. While the volume of this data set increases, it remains underexploited in operational biogeochemical modelling and forecasting. Moreover, the availability of new satellites, automated measurement systems such as Bio-Argo floats, drones, and computational resources presents both a challenge and an opportunity to advance integrated observing systems which combine optical observations, including remotely sensed ocean colour, with biogeochemical models to monitor and predict the impact of extreme events on biogeochemical cycles and ecosystem functioning.

Data availability statement

Publicly available datasets were analyzed in this study. This data can be found here: NOAA OI SST V2 High Resolution Dataset: https://psl.noaa.gov/data/gridded/data.noaa.oisst.v2.highres.html OLCI Level 3 300m Baltic Sea Ocean Colour Plankton, Transparency and Optics NRT daily observations, CMEMS: https://doi.org/10.48670/moi-00294. The ROMS-BioOptic model code can be accessed at https://www.myroms.org. The code of ROMSpath can be found at https://github.com/imcslatte/ROMSPath/tree/V1.0.0. For the calculation of the coherent sets the 3d version of the matlab scripts https://github.com/gaioguy/FEMDL and https://github.com/gfroyland/SEBA were used. Data of the tracer trajectories and the coherent set tracks upon request by RVK.

Author contributions

BC: Writing – review & editing, Writing – original draft, Visualization, Validation, Project administration, Methodology, Investigation, Funding acquisition, Formal analysis, Data curation, Conceptualization. EC: Writing – review & editing, Visualization, Investigation, Conceptualization. RV-K: Writing – review & editing, Visualization, Investigation, Formal analysis, Conceptualization. UG: Writing – review & editing, Resources.

Funding

The author(s) declare financial support was received for the research, authorship, and/or publication of this article. BC was

supported by funding from the German Research Foundation (Grant No. CA 1347/2-1, 2018 to 2021, Temporary Position for Principal Investigator). EC was supported by funding from the CONMAR (CONcepts for conventional MArine Munition Remediation in the German North and Baltic Sea) project. RV-K would like to thank DFG Project VO 2508/1-1 for funding. UG was supported by the Federal Ministry of Education and Research (BMBF, funding code 03F0860H), within the project: ECAS-Baltic project: Strategies of ecosystem-friendly coastal protection and ecosystem-supporting coastal adaptation for the German Baltic Sea Coast. The authors gratefully acknowledge the computing time granted by the Resource Allocation Board and provided on the supercomputer Lise and Emmy at NHR@ZIB and NHR@Göttingen as part of the NHR (North German Supercomputing Alliance) infrastructure. The calculations for this research were conducted with computing resources under the project ID bek00027.

Acknowledgments

BC and RV-K would like to thank John Wilkin, Rutgers University for his advice on setting up the ROMSpath simulations.

Conflict of interest

The authors declare that the research was conducted in the absence of any commercial or financial relationships that could be construed as a potential conflict of interest.

Publisher's note

All claims expressed in this article are solely those of the authors and do not necessarily represent those of their affiliated organizations, or those of the publisher, the editors and the reviewers. Any product that may be evaluated in this article, or claim that may be made by its manufacturer, is not guaranteed or endorsed by the publisher.

Supplementary material

The Supplementary Material for this article can be found online at: https://www.frontiersin.org/articles/10.3389/fmars.2024.1323271/full#supplementary-material

References

Abraham, E. (1998). The generation of plankton patchiness by turbulent stirring. *Nature* 391, 577–580 doi: 10.1038/35361

Barghorn, L., Meier, H. E. M., and Radtke, H. (2023).). Changes in seasonality of saltwater inflows caused by exceptional warming trends in the Western Baltic Sea. *Geophysical Res. Lett.* 50, e2023GL103853doi: 10.1029/2023GL103853

Belkin, I. (2009). Rapid warming of large marine ecosystems. *Prog. Oceanography* 81, 207–213 doi: 10.1016/J.POCEAN.2009.04.011

Benthuysen, J. A., Oliver, E. C. J., Feng, M., and Marshall, A. G. (2018). Extreme marine warming across tropical Australia during austral summer 2015–2016. *J. Geophys. Res. Oceans* 123, 1301–1326 doi: 10.1002/2017JC013326

Bissett, W., Walsh, J., Dieterle, D., and Carder, K. (1999a). Carbon cycling in the upper waters of the Sargasso Sea: I. Numerical simulation of differential carbon and nitrogen fluxes. *Deep Sea Res.* 46, 205–269 doi: 10.1016/S0967-0637(98)00062-4

Bissett, W., Walsh, J., Dieterle, D., and Carder, K. (1999b). Carbon cycling in the upper waters of the Sargasso Sea: II Numerical simulation of apparent and inherent optical properties. *Deep Sea Res.* 46, 271–317 doi: 10.1016/S0967-0637(98)00063-6

Bond, N. A., Cronin, M. F., Freeland, H., and Mantua, N. (2015). Causes and impacts of the 2014 warm anomaly in the NE Pacific. Geophys. *Res. Lett.* 42, 414–420 doi: 10.1002/2015GL063306

Bowen, M., Markham, J., Sutton, P., Zhang, X., Wu, Q., Shears, N. T., et al. (2017). Interannual variability of sea surface temperature in the southwest Pacific and the role of ocean dynamics. *J. Climate*. 30, 7481–7492 doi: 10.1175/JCLI-D-16-0852.1

Cahill, B. E., Kowalczuk, P., Kritten, L., Gräwe, U., Wilkin, J., and Fischer, J. (2023). Estimating the seasonal impact of optically significant water constituents on surface heating rates in the western Baltic Sea. *Biogeosciences* 20, 2743–2768 doi: 10.5194/bg-20-2743-2023

Cahill, B., Schofield, O., Chant, R., Wilkin, J., Hunter, E., Glenn, S., et al. (2008). Dynamics of turbid buoyant plumes and the feedbacks on near-shore biogeochemistry and physics. *Geo. Res. Lett.* 35, 1–6 doi: 10.29/2008GL033595

Cahill, B., Wilkin, J., Fennel, K., Vandemark, D., and Friedrichs, M. (2016). Interannual and seasonal variabilities in air-sea CO2 fluxes along the U.S eastern continental shelf and their sensitivity to increasing air temperatures and variable winds. *J. Geophys. Res.* 121, 295–311 doi: 10.1002/2015JG002939

Callbeck, C. M., Lavik, G., Stramma, L., Kuypers, M. M. M., and Bristow, L. A. (2017). Enhanced nitrogen loss by eddy-induced vertical transport in the offshore Peruvian oxygen minimum zone. *PLoSONE* 12, e0170059doi: 10.1371/journal.pone.0170059

Chelton, D. B., Gaube, P., Schlax, M. G., Early, J. J., and Samelson, R. M. (2011b). The Influence of Nonlinear mesoscale eddies on near-surface oceanic chlorophyll. *Science* 334, 328–332 doi: 10.1126/science.1208897

Chelton, D. B., Schlax, M. G., and Samelson, R. M. (2011a). Global observations of nonlinear mesoscale eddies. *Prog. Oceanography* 91, 167–216 doi: 10.1016/j.pocean.2011.01.002

Chelton, D. B., Schlax, M. G., Samelson, R. M., and de Szoeke, R. A. (2007). Global observations of large oceanic eddies. *Ge. Res. Lett.* 34, L15606doi: 10.1029/2007GL030812

Chen, K., Gawarkiewicz, G., Kwon, Y. O., and Zhang, W. G. (2015). The role of atmospheric forcing versus ocean advection during the extreme warming of the Northeast U.S. continental shelf in 2012. *J. Geophys. Res. Oceans* 120, 4324–4339 doi: 10.1002/2014JC010547

Chen, K., Gawarkiewicz, G. G., Lentz, S. J., and Bane, J. M. (2014). Diagnosing the warming of the Northeastern U.S. Coastal Ocean in 2012: a linkage between the atmospheric jet stream variability and ocean response. *J. Geophys. Res. Oceans* 119, 218–227 doi: 10.1002/2013JC009393

Chrysagi, E., Umlauf, L., Holtermann, P., Klingbeil, K., and Burchard, H. (2021). High-resolution simulations of submesoscale processes in the Baltic Sea: The role of storm events. *J. Geophysical Research: Oceans*, 126. doi: 10.1029/2020JC016411

Cook, F., Smith, R. O., Roughan, M., Cullen, N. J., Shears, N., and Bowen, M. (2022). Marine heatwaves in shallow coastal ecosystems are coupled with the atmosphere: Insights from half a century of daily in *situ* temperature records. *Front. Climate* 4doi: 10.3389/fclim.2022.1012022

Elzahaby, Y., and Schaeffer, A. (2019). Observational insight into the subsurface anomalies of marine heatwaves. *Front. Mar. Sci.* 6doi: 10.3389/fmars.2019.00745

Elzahaby, Y., Schaeffer, A., Roughan, M., and Delaux, S. (2021). Oceanic circulation drives the deepest and longest marine heatwaves in the East Australian Current System. *Geophysical Res. Lett.* 48, e2021GL094785doi: 10.1029/2021GL0947785

Eppley, R. W. (1972). Temperature and phytoplankton growth in the sea, Fish. *Bull.* 70, 1063–1085.

Fennel, W., Seifert, T., and Kayser, B. (1991). Rossby radii and phase speeds in the Baltic Sea. *Continental Shelf Res. 11* 1, 23–236. doi: 10.1016/0278-4343(91)90032-2

Fennel, K., and Wilkin, J. (2009). Quantifying biological carbon export for the northwest North Atlantic continental shelves. *Geo. Res. Lett.* 36doi: 10.1029/2009GL039818

Fennel, K., Wilkin, J., Levin, J., Moisan, J., O'Reilly, J., and Haidvogel, D. (2006). Nitrogen cycling in the Middle Atlantic Bight: Results from a three dimensional model and implications for the North Atlantic nitrogen budget. *Glob. Biogeo. Cycles* 20doi: 10.1029/2005GB002456

Fennel, K., Wilkin, J., Previdi, M., and Najjar, R. (2008). Denitrification effects on air-sea CO_2 flux in the coastal ocean: Simulations for the northwest North Atlantic. *Geo. Res. Lett.* 35doi: 10.1029/2008GL036147

Froyland, G., and Junge, O. (2018). Robust FEM-based extraction of finite-time coherent sets using scattered, sparse, and incomplete trajectories. *SIAM J. Appl. Dynamical Syst. 17* 2, 1891–1924 doi: 10.1137/17M1129738

Froyland, G., Rock, C. P., and Sakellariou, K. (2019). Sparse eigenbasis approximation: Multiple feature extraction across spatiotemporal scales with application to coherent set identification. *Commun. Nonlinear Sci. Numerical Simulation* 77, 81–107 doi: 10.1016/j.cnsns.2019.04.012

Gräwe, U., Holtermann, P., Klingbeil, K., and Burchard, H. (2015a). Advantages of vertically adaptive coordinates in numerical models of stratified shelf seas. *Ocean Model.* 92, 56–68 doi: 10.1016/j.ocemod.2015.05.008

Gräwe, U., Naumann, M., Mohrholz, V., and Burchard, H. (2015b). Anatomizing one of the largest saltwater inflows into the Baltic Sea in December 2014. *J. Geophysical Research: Oceans* 120, 7676–7697 doi: 10.1002/2015JC011269

Haidvogel, D., Arango, H., Budgell, W., Cornuelle, B., Curchitser, E., Lorenzo, E., et al. (2008). Ocean forecasting in terrain-following coordinates: Formulation and skill assessment of the Regional Ocean Modeling System. *J. Comp. Phys.* 227, 3595 3624doi: 10.1016/j.jcp.2007.06.016

Hayashida, H., Matear, R. J., and Strutton, P. G. (2020). Background nutrient concentration determines phytoplankton bloom response to marine heatwaves. *Global Change Biol.* 26, 4800–4811 doi: 10.1111/gcb.15255

Hersbach, H., Bell, B., Berrisford, P., Hirahara, S., Horanyi, A., Munoz-Sabater, J., et al. (2020). The ERA5 global reanalysis. *Q. J. R. Meteorological Soc.* 146, 1999–2049 doi: 10.1002/qj.3803

Hobday, A. J., Oliver, E. C. J., Gupta, A. S., Benthuysen, J. A., Burrows, M. T., Donat, M. G., et al. (2018). Categorizing and naming marine heatwaves. *Oceanography Special Issue Ocean Warming* 31, 162–173. doi: 10.5670/oceanog

Hosegood, P. J., Gregg, M. C., and Alford, M. H. (2013). Wind-driven submesoscale subduction at the north Pacific subtropical front, J. Geophys. *Res. Oceans* 118, 5333–5352 doi: 10.1002/jgrc.20385

Høyer, J. L., and Karagali, I. (2016). Sea surface temperature climate data record for the North Sea and Baltic Sea. *J. Climate* 29, 2529–2541 doi: 10.1175/JCLI-D-15-0663.1

Høyer, J. L., and She, J. (2007). Optimal interpolation of sea surface temperature for the North Sea and Baltic Sea, J. Mar. Sys., Vol 65, 1-4, pp Høyer, J. L. and She, J., Optimal interpolation of sea surface temperature for the North Sea and Baltic Sea. *J. Mar. Sys. Vol* 65, 1–4 doi: 10.1016/j.jmarsys.2005.03.008

Huang, B., Liu, C., Banzon, V., Freeman, E., Graham, G., Hankins, B., et al. (2021). Improvments of the daily optimum interpoaltion sea surface temperature (DOISST) version 2.1. *J. Climate* 348, 2923–2939. doi: 10.1175/JCLI-D-20-0166.1

Humborg, C., Geibel, M. C., Sun, X., McCrackin, M., Mörth, C.-M., Stranne, C., et al. (2019). High emissions of carbon dioxide and methane from the coastal Baltic Sea at the end of a summer heat wave. *Front. Mar. Sci.* 6doi: 10.3389/fmars.2019.00493

Hunter, E., Fuchs, H. L., Wilkin, J. L., Gerbi, G. P., Chant, R. J., and Garwood, J. C. (2022). ROMSPath v1.0: offline particle tracking for the Regional Ocean Modeling System (ROMS). *Geoscientific Model. Dev. 15* 11, 4297–4311 doi: 10.5194/gmd-15-4297-2022

IPCC (2023). "Summary for policymakers. In: climate change 2023: synthesis report. A report of the intergovernmental panel on climate change," in *Contribution of working groups I, II and III to the sixth assessment report of the intergovernmental panel on climate change [CoreWriting team*, vol. 36 . Eds. H. Lee and J. Romero (Switzerland, IPCC, Geneva).

Jaanus, A., Andersson, A., Olenina, I., Toming, K., and Kaljurand, K. (2011). Changes in phytoplankton communities along a north-south gradient in the Baltic Sea between 1990 and 2008. *Boreal Environ. Res.* 16, 191–208.

Jiménez Madrid, J. A., and Mancho, A. M. (2009). Distinguished trajectories in time dependent vector fields. *Chaos 1;* 19, 013111doi: 10.1063/1.3056050

Kahru, M., Elmgren, R., and Sachuk, O. (2016). Changing seasonality of the baltic sea. *Biogeosciences.* 113, 1009–1018 doi: 10.5194/bg-13-1009-2016

Karimova, S., and Gade, M. (2016). Improved statistics of sub-mesoscale eddies in the Baltic Sea retrieved from SAR imagery. *Int. J. Remote Sens.* 37, 2394–2414. doi: 10.1080/01431161.2016.1145367

Kowalczuk, P., Stedmon, C. A., and Markager, S. (2006). Modelling absorption by CDOM in the Baltic Sea from season, salinity and chlorophyll. *Mar. Chem.* 101, 1–11 doi: 10.1016/j.marchem.2005.12.005

Kuhn, A. M., Dutkiewicz, S., Jahn, O., Clayton, S., Rynearson, T. S., Mazloff, M. R., et al. (2019). Temperoal and spatial scales of correlation in marine phytoplankton communities. *J. Geophysical Research: Oceans* 124, 9417–9438 doi: 10.1029/2019JC015331

Lapeyre, G., and Klein, P. (2006). Impact of the small-scale elongated filaments on the ocean vertical pump. *J. Mar. Res.* 64, 835–851. doi: 10.1357/002224006779698369

Lass, H. U., and Mohrholz, V. (2003). On the dynamics and mixing of inflowing saltwater in the Arkona Sea. *J. Geophys. Res.* 108, 3042doi: 10.1029/2002JC001465

Lee, Z., Du, K., and Arnone, R. (2005). A model for the diffuse attenuation coefficient of downwelling irradiance. *J. Geophysical Research Oceans* 110, 1–10 doi: 10.1029/2004JC002275

Lehahn, Y., d'Ovidio, F., Levy, M., and Heifetz, E. (2007). Stirring of the northeast Atlantic spring bloom: A Lagrangian analysis based on multisatellite data. *J. Geophys. Res.* 112, C08005doi: 10.1029/2006JC003927

Levy, M., Ferrari, R., Franks, P. J. S., Martin, A. P., and Rivière, P. (2012). Bringing physics to life at the submesoscale. *Geophys. Res. Lett.* 39, L14602doi: 10.1029/2012GL052756

Levy, M., Franks, P., and Smith, K. (2018). The role of submesoscale currents in structuring marine ecosystems. *Nat. Commununications* 9, 4758doi: 10.1038/s41467-018-07059-3

Loeb, N. G., Johnson, G. C., Thorsen, T. J., Lyman, J. M., Rose, F. G., and Kato, S. (2021). Satellite and ocean data reveal marked increase in Earth's heating rate. *Geophysical Res. Lett.* 48, e2021GL093047doi: 10.1029/2021GL093047

Lorenz, H. (2019). *Marine heatwaves and the phytoplankton spring bloom: a comparative survey of marine heatwaves, spring bloom events and their relationship in the North Sea and Baltic Sea* (University of Potsdam), 86doi: 10.5281/zenodo.10194802

Mahadevan, A. (2016). The impact of submesoscale physics on primary productivity of plankton. *Annu. Rev. Mar. Sci.* 8, 161–184 doi: 10.1146/annurev-marine-010814-015912

Martin, A. P. (2003). Phytoplankton patchiness: the role of lateral stirring and mixing. *Prog. Oceanogr.* 57, 125–174 doi: 10.1016/S0079-6611(03)00085-5

McGillicuddy, D. J. (2016). Mechanisms of physical-biological-biogeochemical interaction at the oceanic mesoscale. *Annu. Rev. Mar. Sci.* 8, 125–159 doi: 10.1146/annurev-marine-010814-015606

McWilliams, J. C. (2016). Submesoscale currents in the ocean. *Proc. R. Soc. A: Mathematical Phys. Eng. Sci.* 472, 20160117doi: 10.1098/rspa.2016.0117

Mendoza, C., and Mancho, A. M. (2010). Hidden geometry of ocean flows. *Phys. Rev. Lett.* 105, 38501doi: 10.1103/PhysRevLett.105.038501

Morel, A. (1988). Optical modelling of the upper ocean in relation to its biogenous matter content (Case I waters). *J. Geophys. Res.* 93, 749–768 doi: 10.1029/JC093iC09p10749

Naumann, M., Gräwe, U., Mohrholz, V., Kuss, J., Siegel, H., Waniek, J. J., et al. (2019). Hydrographic-hydrochemical assessment of the baltic sea 2018. *Meereswiss. Ber. Warnemünde* 110. doi: 10.12754/msr-2019-0110

Neumann, T., Radtke, H., Cahill, B., and Schmidt and G. Rehder, M. (2022). Non-Redfieldian carbon model for the Baltic Sea (ERGOM version 1.2) – implementation and budget estimates. *Geoscientific Model. Dev.* 15, 8473–8540 doi: 10.5194/gmd-15-8473-2022

Oliver, E. C. J., Donat, M. G., Burrows, M. T., Moore, P. J., Smale, D. A., Alexander, L. V., et al. (2018). Longer and more frequent marine heatwaves over the past century. *Nat. Commun.* 9, 1324doi: 10.1038/s41467-018-03732-9

Prants, S. V. (2013). Dynamical systems theory methods to study mixing and transport in the ocean. *Phys. Scr.* 87, 38115doi: 10.1088/0031-8949/87/03/038115

Prants, S. V., Uleysky, M. Y., and Budyansky, M. V. (2011). Numerical simulation of propagation of radioactive pollution in the ocean from the Fukushima Dai-ichi nuclear power plant. *Dokl. Earth Sc.* 439, 1179–1182 doi: 10.1134/S1028334X11080277

Racault, M.-F., Raitsos, D. E., Berumen, M. L., Brewin, R. J. W., Platt, T., Sathyendranath, S., et al. (2015). Phytoplankton phenology indices in coral reef ecosystems: Application to ocean-color observations in the Red Sea. *Remote Sens. Environ.* 160, 222–234 doi: 10.1016/j.rse.2015.01.019

Reißmann, J. H. (2005). An algorithm to detect isolated anomalies in three-dimensional stratified data fields with an application to density fields from four deep basins of the Baltic Sea. *J. Geophysical Research: Oceans* 110doi: 10.1029/2005JC002885

Reißmann, J. H., Burchard, H., Feistel, R., Hagen, E., Lass, H. U., Mohrholz, V., et al. (2009). Vertical mixing in the Baltic Sea and consequences for eutrophication – A review. *Prog. Oceanography* 821, 47–80 doi: 10.1016/j.pocean.2007.10.004

Ruiz, S., Claret, M., Pascual, A., Olita, A., Troupin, C., Capet, A., et al. (2019). Effects of oceanic mesoscale and submesoscale frontal processes on the vertical transport of phytoplankton. *J. Geophysical Research Oceans* 124, 5999–6014 doi: 10.1029/2019JC015034

Schaeffer, A., and Roughan, M. (2017). Subsurface intensification of marine heatwaves off southeastern Australia: the tole of stratification and local winds. *Geophysical Res. Lett.* 44, 5025–5033 doi: 10.1002/2017GL073714

Smale, D. A., Wernberg, T., Oliver, E. C. J., Thomsen, M., Harvey, B. P., Straub, S. C., et al. (2019). Marine heatwaves threaten global biodiversity and the provision of ecosystem services. *Nat. Climate Change.* 9, 206–312 doi: 10.1038/s41558-019-0412-1

Steele, J. H., and Henderson, E. W. (1992). The role of predation in plankton models. *J. Plankton Res.* 14, 157–172 doi: 10.1093/plankt/14.1.157

Thomalla, S. J., Fauchereau, N., Swart, S., and Monteiro, P. M. S. (2011). Regional scale characteristics of the seasonal cycle of chlorophyll in the Southern Ocean. *Biogeosciences* 8, 2849–2866 doi: 10.5194/bg-8-2849-2011

Vortmeyer-Kley, R., Lünsmann, B., Berthold, M., Gräwe, U., and Feudel, U. (2019). Eddies: fluid dynamical niches or transporters?–A case study in the western baltic sea. *Front. Mar. Sci.* 6doi: 10.3389/fmars.2019.00118

Wasmund, N., Dutz, J., Kremp, A., and Zettler, M. L. (2019b). *Biological assessment of the baltic sea 2018* (Warnemuende: Meereswiss. Ber.), 112doi: 10.12754/msr-2019-0112

Wasmund, N., Nausch, G., Gerth, M., Busch, S., Burmeister, C., Hansen, R., et al. (2019a). Extension of the growing season of phytoplankton in the western Baltic Sea in response to climate change. *Mar. Ecol. Prog. Ser.* 622, 1–16 doi: 10.3354/meps12994

Wilkin, J., Zhang, W. G., Cahill, B., and Chant, R. C. (2011). "Integrating coastal models and observations for studies of ocean dynamics, observing systems and forecasting," in *Operational oceanography in the 21st century*. Eds. A. Schiller and Brassington, (Springer)doi: 10.1007/978-94-007-0332-2_19

Zängl, G., Reinert, D., Rípodas, P., and Baldauf, M. (2015). The ICON (ICOsahedral Non-hydrostatic) modelling framework of DWD and MPI-M: Description of the non-hydrostatic dynamical core. *Quar. J. R. Met. Soc.* 141, 563–579 doi: 10.1002/qj.2378

Zhan, W., Zhang, Y., He, Q., and Zhan, H. (2023). Shifting responses of phytoplankton to atmospheric and oceanic forcing in a prolonged marine heatwave. *Limnology Oceanography*. 68, 1821–1834. doi: 10.1002/lno.12388

frontiers | Frontiers in Marine Science

TYPE Original Research
PUBLISHED 24 April 2024
DOI 10.3389/fmars.2024.1309050

Check for updates

OPEN ACCESS

EDITED BY
Donald B. Olson,
University of Miami, United States

REVIEWED BY
Xin Liu,
Xiamen University, China
Shengqiang Wang,
Nanjing University of Information Science and Technology, China

*CORRESPONDENCE
Christina Eunjin Kong
cejkong@gmail.com
Shubha Sathyendranath
ssat@pml.ac.uk

RECEIVED 07 October 2023
ACCEPTED 18 January 2024
PUBLISHED 24 April 2024

CITATION
Kong CE, Sathyendranath S, Jackson T, Stramski D, Brewin RJW, Kulk G, Jönsson BF, Loisel H, Galí M and Le C (2024) Comparison of ocean-colour algorithms for particulate organic carbon in global ocean.
Front. Mar. Sci. 11:1309050.
doi: 10.3389/fmars.2024.1309050

COPYRIGHT
© 2024 Kong, Sathyendranath, Jackson, Stramski, Brewin, Kulk, Jönsson, Loisel, Galí and Le. This is an open-access article distributed under the terms of the Creative Commons Attribution License (CC BY). The use, distribution or reproduction in other forums is permitted, provided the original author(s) and the copyright owner(s) are credited and that the original publication in this journal is cited, in accordance with accepted academic practice. No use, distribution or reproduction is permitted which does not comply with these terms.

Comparison of ocean-colour algorithms for particulate organic carbon in global ocean

Christina Eunjin Kong[1,2]*, Shubha Sathyendranath[2,3]*, Thomas Jackson[4], Dariusz Stramski[5], Robert J. W. Brewin[6], Gemma Kulk[2,3], Bror F. Jönsson[2], Hubert Loisel[7], Martí Galí[8] and Chengfeng Le[9]

[1]Department of Earth, Ocean and Atmospheric Sciences, University of British Columbia, Vancouver, BC, Canada, [2]Earth Observation Science & Applications, Plymouth Marine Laboratory, Plymouth, United Kingdom, [3]National Centre for Earth Observation, Plymouth Marine Laboratory, Plymouth, United Kingdom, [4]EUMETSAT, Darmstadt, Germany, [5]Marine Physical Laboratory, Scripps Institution of Oceanography, University of California San Diego, La Jolla, CA, United States, [6]Centre for Geography and Environmental Science, University of Exeter, Penryn, United Kingdom, [7]Laboratoire d'Océanologie et de Géosciences, Université du Littoral Côte d'Opale, Université Lille, CNRS, UMR 8187, LOG, Wimereux, France, [8]Institut de Ciències del Mar–CSIC, Barcelona, Catalonia, Spain, [9]Ocean College, Zhejiang University, Hangzhou, China

In the oceanic surface layer, particulate organic carbon (POC) constitutes the biggest pool of particulate material of biological origin, encompassing phytoplankton, zooplankton, bacteria, and organic detritus. POC is of general interest in studies of biologically-mediated fluxes of carbon in the ocean, and over the years, several empirical algorithms have been proposed to retrieve POC concentrations from satellite products. These algorithms can be categorised into those that make use of remote-sensing-reflectance data directly, and those that are dependent on chlorophyll concentration and particle backscattering coefficient derived from reflectance values. In this study, a global database of *in situ* measurements of POC is assembled, against which these different types of algorithms are tested using daily matchup data extracted from the Ocean Colour Climate Change Initiative (OC-CCI; version 5). Through analyses of residuals, pixel-by-pixel uncertainties, and validation based on optical water types, areas for POC algorithm improvement are identified, particularly in regions underrepresented in the *in situ* POC data sets, such as coastal and high-latitude waters. We conclude that POC algorithms have reached a state of maturity and further improvements can be sought in blending algorithms for different optical water types when the required *in situ* data becomes available. The best performing band ratio algorithm was tuned to the OC-CCI version 5 product and used to produce a global time series of POC between 1997–2020 that is freely available.

KEYWORDS

particulate organic carbon, ocean carbon cycle, biological carbon pump, essential climate variable, ocean colour remote sensing, ocean colour climate change initiative

Highlights

- Algorithms for retrieval of particulate organic carbon from ocean-colour satellite data are compared, using a database of *in situ* observations matched with concurrent products derived from Ocean Colour Climate Change Initiative data.
- One of the best-performing algorithms is selected to produce a time series of particulate organic carbon at the sea surface from 1997 to 2020.

1 Introduction

Particulate organic carbon (POC) plays a fundamental role in the ocean carbon cycle (Eppley and Peterson, 1979). The POC pool is composed of both living organic carbon (phytoplankton, zooplankton, bacteria, and other marine microorganisms) and organic detritus in particulate form. While the standing stock of POC in the epipelagic zone is relatively small compared with dissolved inorganic and organic carbon pools, it drives large carbon fluxes in the epipelagic ocean owing to its short turnover time. A part of the POC pool can be exported from the epipelagic to the deep pelagic zones through the ocean biological carbon pump, hence playing a crucial role in long-term carbon sequestration (Volk and Hoffert, 1985; CEOS, 2014; Brewin et al., 2021), while serving as vital food for marine microbial communities and also for marine organisms of higher trophic levels, ultimately sustaining deep-sea ecosystems (Eppley and Peterson, 1979; Volk and Hoffert, 1985; Falkowski et al., 1998).

The POC pool in the upper layers of the ocean can be monitored using satellite observations of ocean colour. Various satellite-based algorithms have been proposed to estimate surface POC concentration on a large scale. A recent comparison by Evers-King et al. (2017) has shown relatively good performances of two types of empirical algorithms: (i) those using band ratios of spectral remote sensing reflectances (Stramski et al., 2008); and (ii) those based on chlorophyll-a and particulate backscattering coefficients (Loisel et al., 2002). Since the review by Evers-King et al. (2017), other algorithms have emerged, such as that of (iii) Tran et al. (2019), which has a focus on coastal or optically complex waters, (iv) the colour-index-based algorithm of Le et al. (2018), and (v) the hybrid algorithm of Stramski et al. (2022). In principle, these algorithms can be blended according to their performances in particular regions or optical water types, similar to the approach used to estimate the global satellite-derived chlorophyll-a product in the European Space Agency's Climate Change Initiative (Jackson et al., 2017; Sathyendranath et al., 2019). But this requires that the performance of each algorithm be evaluated for each optical class (or region).

Before selecting a POC algorithm from the different options available, one has to understand its conceptual basis and evaluate the uncertainties associated with each algorithm to determine whether they are appropriate for the applications envisaged. We may anticipate differences when an algorithm developed for a particular satellite sensor is applied to another one. Similarly, an algorithm may also have some dependencies on the atmospheric correction processors, since the water-leaving radiances that underpin all POC algorithms could be a little different, depending on atmospheric-correction algorithms (Müller et al., 2015). Such considerations necessitate that algorithms be re-evaluated for different sensors and atmospheric correction procedures employed, as well as any merging of multiple sensors that might have been implemented before algorithm development and testing. Moreover, when a POC algorithm is applied to satellite products, it not only depends on the quality of the algorithm itself but also the quality of the satellite-derived optical variables that serve as input to the algorithm. For example, the POC algorithm that uses inherent optical properties, such as the backscattering coefficient from satellite observations, may be prone to errors if the retrieval is sensitive to the composition, size distribution, and other characteristics of the POC particles and seawater properties (Loisel et al., 2002; Loisel et al., 2018). It is also important that the *in situ* POC data be representative of the ocean domain over which the algorithm is to be applied, which may not always be the case. However, such a complete evaluation of each of the POC algorithms falls out of the scope of this paper.

In this study, we evaluate seven POC algorithms, when implemented using products from the Ocean Colour - Climate Change Initiative (OC-CCI) (Sathyendranath et al., 2019). These products were developed for applications in climate research and now extend to over two decades. The algorithms selected for the comparison include those that performed well (Stramski et al., 2008; Loisel et al., 2002) in an earlier comparison (Evers-King et al., 2017), as well as promising new algorithms that have emerged since then (Le et al., 2018; Stramski et al., 2022). The uncertainties are evaluated using a large database of near-surface *in situ* POC (0–10m) matched with the OC-CCI products for 1997-2020. The candidate algorithms are evaluated using several quantitative statistical metrics (Section 2.8). An additional evaluation is performed after re-fitting of the original algorithms using the global matchup data, such that all algorithms implemt a common set of *in situ* and satellite observations, and for the same satellite products to which they are to be applied. Recognising the limitations of *in situ* POC and satellite matchup data, such as any potential deficiencies in the representativeness of the matchup data available, differences in spatial scales *in situ* and satellite observations, and incomplete coverage of geographic regions, an indirect mode of validation is also attempted, in which we examine whether the algorithms reproduce faithfully the observed relationships between POC and chlorophyll-a concentration.

2 Data and methods

2.1 *In situ* POC data

In situ POC data (0–10m) compiled by Evers-King et al. (2017) for 1997–2012 were supplemented with 2013–2020 *in situ* POC data from the SeaBASS (Sea-viewing-wide-field-of-view-sensor Bio-optical

Archive and Storage System), providing a more comprehensive spatio-temporal coverage of POC measurements over the last two decades. Most of the data contributors (see source in Table 1) followed the general POC protocol recommended by the Joint Global Ocean Flux Study's international scientific steering committee (Knap et al., 1996). In some cases, however, they modified the protocol or used different instruments to measure *in situ* POC concentrations. Thus, unaccounted uncertainties in the field measurements could persist from differences in methodologies, which are difficult to identify even with the protocol details being provided. Prior to comparisons with satellite-derived POC data, a series of data quality controls (see section 2.5) were carried out, as the assessment of algorithm performance depends on the quality of the *in situ* POC measurements, and on the number of *in situ* POC data matched with satellite observations across diverse oceanic environments.

2.2 Satellite data

Daily OC-CCI version 5 products (Sathyendranath et al., 2021) at 4 km resolution were used for algorithm validation, and monthly composites for indirect validation and for POC time-series product generation (1997–2020). The OC-CCI products were generated based on MERIS (MEdium-Resolution-Imaging-Spectrometer) as the reference sensor. Remote sensing reflectance (R_{rs}) at multiple wavelengths (λ at 443, 490, 510, 560, and 665 nm), chlorophyll-a biomass (B), and backscattering coefficient (b_{bp}) at 490 nm were extracted from the OC-CCI products according to algorithm requirements. As some POC algorithms were initially developed for different sensors and their spectral bands, the $R_{rs}(\lambda)$ retrieved from the OC-CCI products were shifted in reverse to obtain those wavebands (e.g., $R_{rs}(555)$) using the same band-shifting approach that was used when generating the OC-CCI data (Mélin and Sclep, 2015; Jackson et al., 2017; Sathyendranath et al., 2019). The memberships of each optical water class (1–14) (Jackson et al., 2017) were also extracted from the OC-CCI for uncertainty estimation, for mapping per-pixel uncertainties, and for estimating dominant optical water classes.

2.3 *In situ* POC and satellite matchup data

In situ POC data were matched with the OC-CCI products, following the approach of Evers-King et al. (2017) and Jackson et al. (2017). Prior to the matchup process, the *in situ* POC data from the same location and date were averaged over the top 10 m, and over the day of sampling. The satellite pixel containing the same location and date as the *in situ* POC observation was treated as the central pixel for data extraction. When the central pixel was valid, a window of 3 by 3 pixels around the central pixel were also extracted, and their mean, median, and standard deviation were computed for all relevant variables retrieved from the OC-CCI data. The number of valid pixels in the window of 3 by 3 pixels was also noted. The total number of matchup data between the *in situ* POC and OC-CCI data was 5972 (Table 1, whole matchup data). These data were then subjected to quality control and assessment. Only the subset of data (Table 1, validation matchup data) that passed the control and assessment was then used for further analyses, including algorithms validation.

The geographical locations where the *in situ* POC measurements were taken and successfully matched with the OC-CCI products cover a wide range of oceanic environments, including coastal and open oceans (Figure 1). The histogram of the *in situ* POC data showed a bimodal positively-skewed distribution pattern with median and mean of 90.3 and 154 mg m^{-3}, respectively (Figure 2A, blue). The highest peak is associated with a large number of data collected in oligotrophic gyres during the Atlantic Meridional Transect cruises (Rasse et al., 2017; Evers-King et al., 2017). The second peak is associated with data collected from the coastal waters of eastern and western North America.

2.4 Mixed-layer depth

A global, monthly climatology of mixed-layer depth from de Boyer Montegut et al. (2004) was used to estimate the total standing pool of POC in the mixed layer (http://dx.doi:10.1029/2004JC002378).

2.5 Quality control and assessment

Several quality control criteria were applied to the data sets (Table 1, whole matchup data) for removing potentially erroneous *in situ* POC and OC-CCI matchup data. First, all matchup data points pertaining to inland waters were removed. Second, about 2.4% (N = 147) of matchup data that contained less than four valid pixels in the 3 by 3 pixel-box around the central pixel were excluded as adjacency to invalid pixels might indicate potential pixel contamination. Third, a group of some 24 *in situ* POC observations collected from a small geographical area, and close

TABLE 1 Summary of the *in situ* POC data matched with the OC-CCI products (1997-2020).

Data	*N*	Min.	Max.	Mean	Median	S.D.	Source(s)
Whole	5972	2.7	4887	154	90.3	246	SeaBASS; BCO-DMO (Buesseler, 2007; Johnson and Bates, 2023; Perry, 2011; Lomas et al., 2011; Wheeler, 2012); PANGAEA (2020); Thomalla et al. (2017); Martiny and Vrugt (2014); Rasse et al. (2017)
Validation	3287	11.1	2641	99.8	50.7	138	

The number of whole (before QA/QC) and validation (after QA/QC) *in situ* POC and OC-CCI matchup data (N) are provided. The minimum (Min.), maximum (Max.), mean, median, and standard deviation (S.D.) of *in situ* POC data are given in units of mg m^{-3}. The data sources of *in situ* POC are given in the last column. The data sources from the prior compilation are available publicly from the following locations (see acknowledgment section for more detailed information): https://seabass.gsfc.nasa.gov/ (SeaBASS), https://www.bco-dmo.org/ (BCO-DMO), https://www.pangaea.de/ (PANGAEA).

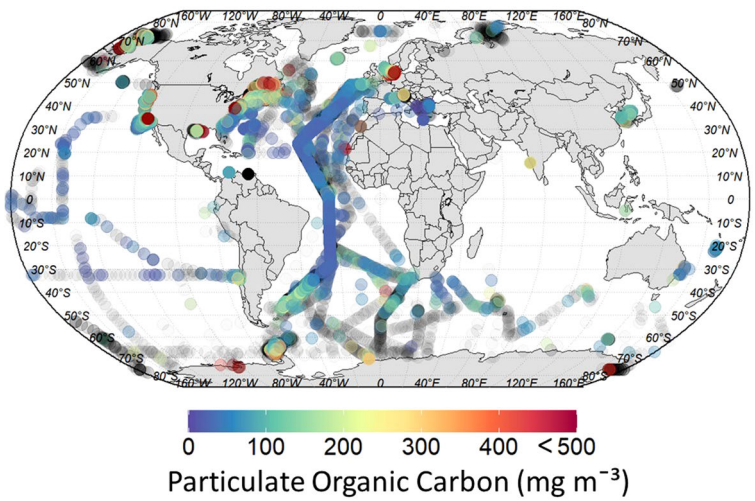


FIGURE 1
Geographical distribution of *in situ* POC data (0–10 m) that matched with valid satellite data for September 1997 to January 2020 (Table 1, whole matchup data). The colour of circles indicate the POC concentration (mg m^{-3}) of *in situ* data. Grey circles indicate the locations of unmatched data point that were excluded in the analysis.

together in time, appeared as outliers when the *in situ* POC data were plotted against corresponding chlorophyll-a data. These stations, with POC concentration less than 10 mg m^{-3} and chlorophyll-a concentration greater than 0.06 mg m^{-3} ($N = 24$), were removed as being potentially erroneous. In addition, a data point with a very high POC concentration (> 4000 mg m^{-3}) was removed. Lastly, OC-CCI variables for which the coefficient of variation (standard deviation divided by the mean) exceeding 0.15 for the valid pixels in the 3 by 3 pixel-box (see Appendix A) were also removed. The high spatial variability surrounding the central pixel could be indicative of

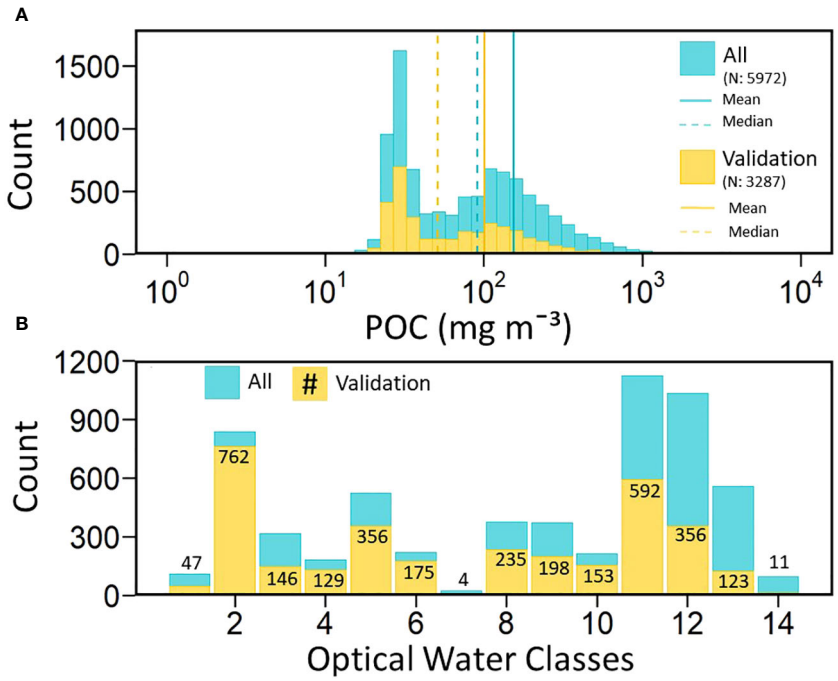


FIGURE 2
(A) Histograms of the *in situ* POC (mg m^{-3}) values for the whole (blue) and validation (yellow) matchup data (1997–2020). The *in situ* POC and OC-CCI matchup data that were retained after quality control and assessment constitute the validation data set (see section 2.5). The dashed and solid lines represent the median and mean values for the whole (blue) and the validation (yellow) matchup data, respectively. **(B)** Frequency distributions of the matchup data per dominant water class (1–14) derived from the OC-CCI products, for the whole (blue) and the validation (yellow) matchup data. The numbers represent the number of validation matchup data per dominant water class. Note that only the validation data set is used in the rest of the work.

locations where uncertainties could be high because of mismatches in time and space between *in situ* POC and satellite observations. The quality control procedure is designed to ensure that the matchup data used in validation and analysis are of high quality, and to eliminate any data with significant bias (Bailey and Werdell, 2006).

After the quality control procedures, 3287 samples, or about 55% of the initial *in situ* POC data matched with the OC-CCI products were retained for use in validation and related analyses (Table 1, validation data). The remaining matchup data of questionable quality were not used in the rest of this work. Though many matchup data were lost during this procedure, with a high proportion of data lost in optically complex waters (Figure 2B, water classes 11–14), the histogram of the validation matchup data (Figure 2A, yellow) show a distribution pattern similar to that of the initial matchup data (Figure 2A, blue), with median and mean of 50.7 and 99.8 mg m^{-3}, respectively. The size of the validation matchup data set of over three thousand observations is one to two orders of magnitude higher than that of the data sets used for the development of the candidate algorithms (see section 2.6). This implies that advantages that any of the algorithms might have, because of the overlap between the data used for development and validation, is likely to be low. The validation matchup data may, however, still contain some potentially low-quality *in situ* POC and satellite-derived products due to a variety of factors, including differences in data collection methods, calibration procedures, and instruments.

2.5.1 Per-pixel uncertainty estimates and optical water classes

Each validation matchup data point (Table 1) was assigned to a dominant optical water class (1–14) associated with its central pixel, estimated from the water class membership values retrieved from the OC-CCI products (Jackson et al., 2017). In general, the lower water classes (1–2) correspond to oligotrophic waters with maximum R_{rs} at the short wavelengths of the visible spectrum, whereas the high water classes (13–14) correspond to turbid waters with relatively higher R_{rs} at longer wavelengths (see Appendix B). The total number of validation matchup data varied across the dominant optical water classes, with water class 2 showing the largest number (N = 762) of data points, followed by water classes 11 and 12 (Figure 2B, yellow). On the other hand, water classes 7 and 14 show very low number of the data points (N = 4 and 11, respectively). The segregation of the validation matchup data into dominant optical water classes served two major purposes: (i) it allowed us to evaluate whether the algorithm performance was linked to the optical complexity of the water represented by the optical class, especially as not all algorithms were originally intended to be used indiscriminately across all types of waters; and (ii) to estimate uncertainties for each water type, which could then be used to map uncertainties on a per-pixel basis (Jackson et al., 2017; Evers-King et al., 2017; Sathyendranath et al., 2019).

2.6 Candidate POC algorithms

Since the first development of an ocean-colour-satellite-based POC algorithm in the late 1990s (Stramski et al., 1999), various algorithms have been proposed to estimate POC concentration from satellite observations in coastal and oceanic waters. These can be categorised into algorithms that use R_{rs} band ratios (Stramski et al., 2008), or a combination of maximum R_{rs} band ratio and band ratio difference index (Stramski et al., 2022), or backscattering and chlorophyll-a (Loisel et al., 2002), or the colour-index (Le et al., 2018). These algorithms were formulated using different types of *in situ* and satellite data sets. For example, while the colour-index algorithm (Le et al., 2018) was formulated using satellite-derived R_{rs} matched with the *in situ* measurements of POC, the other algorithms were formulated using only *in situ* observations. Of these, seven candidate algorithms were selected to be representative of distinct algorithmic types in the analyses presented here, and they are described below in sections 2.6.1–2.6.4. It is important to note that in this paper the validation is carried out over the global ocean, regardless of whether the algorithms were originally intended to be used so broadly. For consistency, all algorithms were evaluated using input variables derived from the same set of satellite products (OC-CCI; version 5) and the same validation data set (Figure 2, yellow).

2.6.1 Band ratio algorithms: S1, S2, S3, and S4

Stramski et al. (2008) developed empirical POC algorithms based on the blue-green band ratio of $R_{rs}(\lambda)$. The band ratio empirical algorithms were developed using *in situ* measurements of R_{rs} matched with *in situ* POC collected from the oligotrophic and upwelling waters of the eastern South Pacific and Atlantic Oceans. In the 53 data points used for the algorithm development, POC ranged from 10–270 mg m^{-3} (Stramski et al., 2008). The band ratio algorithm that uses $R_{rs}(443)$ and $R_{rs}(555)$ (see Equation 1 below) is currently adopted by NASA to generate their standard POC products. While the NASA has adopted the band ratio algorithm to generate global POC products, these algorithms are originally intended to be used for open oceans, where POC is less than 300 mg m^{-3}. Similar band ratio algorithms have been also developed for the Southern Ocean (Allison et al., 2010) and South China Sea (Hu et al., 2016), to improve performance in those regions. Here, we have selected the following four band ratio algorithms (S1–S4; Equations 1–4) from Stramski et al. (2008) that performed well in an earlier evaluation (Evers-King et al., 2017).

$$\hat{C}_p(S1)(\mathrm{mg\,m^{-3}}) = 203.2\left[\frac{R_{rs}(443)}{R_{rs}(555)}\right]^{-1.034}, \quad (1)$$

$$\hat{C}_p(S2)(\mathrm{mg\,m^{-3}}) = 308.3\left[\frac{R_{rs}(490)}{R_{rs}(555)}\right]^{-1.639}, \quad (2)$$

$$\hat{C}_p(S3)(\mathrm{mg\,m^{-3}}) = 423.0\left[\frac{R_{rs}(510)}{R_{rs}(555)}\right]^{-3.075}, \quad (3)$$

$$\hat{C}_p(S4)(\mathrm{mg\,m^{-3}}) = 219.7 \cdot \mathrm{Max}\left(\frac{R_{rs}(443)}{R_{rs}(555)}, \frac{R_{rs}(490)}{R_{rs}(555)}, \frac{R_{rs}(510)}{R_{rs}(555)}\right)^{-1.076}. \quad (4)$$

Here, $\hat{C}_p$ represents satellite-derived POC.

2.6.2 Hybrid algorithm: ST

Stramski et al. (2022) developed ocean color sensor-specific hybrid algorithms based on mechanistic principles to improve satellite-derived POC products across a continuum of water bodies with varying optical properties and particle composition. The hybrid algorithm was

developed using field data sets collected in various water types, with POC ranging 11.9–1022 mg m^{-3} (Stramski et al., 2022). The algorithm uses a blending of maximum band ratio and band ratio difference index: the band ratio difference index component is used for POC less than 15 mg m^{-3}, the maximum band ratio algorithm is used for POC greater than 25 mg m^{-3}, and the weighting approach of these two components is applied for the region of transition (Stramski et al., 2022). In the implementation here, we used the hybrid algorithm (hereafter, labelled ST) developed for the MERIS sensor, since the OC-CCI version 5 products are reported for MERIS wavebands.

2.6.3 Particle backscattering and chlorophyll-a based algorithm: LO

Loisel et al. (2002) developed a semi-analytical algorithm based on the assumption that the particle backscattering (b_{bp}) covaries with POC concentration for oceanic waters (Equation 5). This algorithm (labelled LO here) exploits the relationship between b_{bp}/b_p (where b_p is the particle scattering coefficient) and B developed by Twardowski et al. (2001), which allows the slope of b_{bp} versus POC to vary with tropic status. To take this into account, a fixed mean POC/b_p value of 400 is used in the algorithm (Loisel et al., 2002), leading to the following relationship.

$$\hat{C}_p(LO)(\text{mg m}^{-3}) = 41666.7 \cdot b_{bp}(490) \cdot (B)^{0.253}. \quad (5)$$

The algorithm LO (Equation 5) was initially implemented on POLDER (Polarization-and-Directionality-of-the-Earth's-Reflectances) and SeaWiFS (Sea-viewing-Wide-Field-of-View-Sensor) satellite data. This algorithm was validated using a set of matchup data collected from the North Pacific Subtropical gyres (N = 24) and North Atlantic Central gyre (N = 30) (Loisel et al., 2002). This algorithm performed relatively well in the analyses of Evers-King et al. (2017) that used the *in situ* POC and OC-CCI matchup data. In the implementation here, we used the chlorophyll-a data from the OC-CCI. The b_{bp} at 490 nm was estimated using the algorithm of Loisel et al. (2018), rather than using the b_{bp} data from the OC-CCI, for algorithm consistency.

2.6.4 Colour-index algorithm: LE

Le et al. (2018) developed a POC algorithm based on differences in two pairs of R_{rs} values, known as the colour-index. In contrast to other approaches, this algorithm was developed using satellite-derived R_{rs} and *in situ* POC data. The colour-index algorithm was tested for three satellite sensors: SeaWiFS, MERIS, and MODIS (Moderate-Resolution-Imaging-Spectroradiometer). As for the other algorithms, we chose the MERIS algorithm here (Equations 6, 7):

$$D = R_{rs}(560) - \left(R_{rs}(490) + \frac{(560-490)}{(665-490)} \cdot \left(R_{rs}(665) - R_{rs}(490)\right)\right), \quad (6)$$

where D stands for the colour-index. The D is then used to estimate the concentration of POC using algorithm LE:

$$\begin{aligned} &D < -0.0005 : \log_{10}(\hat{C}_p)(LE)(\text{mg m}^{-3}) = 1.97 + 185.72 \cdot D, \\ &D => -0.0005 : \log_{10}(\hat{C}_p)(LE)(\text{mg m}^{-3}) = 2.1 + 485.19 \cdot D. \end{aligned} \quad (7)$$

2.7 Statistical metrics

Statistical metrics recommended by the algorithm developers and those in general use in the ocean-colour community (Brewin et al., 2015; Evers-King et al., 2017; Seegers et al., 2018; Stramski et al., 2022; Joshi et al., 2023) were used to assess the performance of candidate algorithms. The statistic metrics were applied between the *in situ* POC and satellite-derived POC matchup data (N = 3287): the root-mean-square difference (φ), centred-pattern-root-mean-square difference (Δ), and bias (ψ) for both log-transformed and non-transformed POC matchup data (see Appendix C for the equations used). The Pearson's parametric correlation coefficient (r) was calculated for log-transformed data, and Spearman's correlation coefficient (r_s) was calculated for non-transformed data. The median ratios (δ) and median absolute percentage difference (τ) were estimated for non-transformed data. The median symmetric accuracy (κ) was estimated for log-transformed data. Compared with the other statistics, the κ does not penalize both over-and under-prediction differently (Joshi et al., 2023). The slope (S) and intercept (I) of the linear fit between *in situ* POC and satellite-derived POC matchup data were estimated from the standard major axis of model type II linear regression (Ricker, 1973; Sokal and Rohlf, 1995). Condorcet's pair-wise comparisons of residuals (Seegers et al., 2018; Stramski et al., 2022) were performed for log-transformed and non-transformed data as an additional test.

3 Results

3.1 Performance of the candidate algorithms

The satellite-derived POC data were plotted against the *in situ* POC validation matchup data for each candidate algorithm (S1, S2, S3, S4, ST, LO, and LE) under consideration, along with the fitted linear regression line, for algorithm validation (Figure 3; Table 2). The dominant water classes (1–14) associated with each point are also indicated using colours, to assist assessment of algorithm performance across different optical water classes. It is particularly important to check algorithm performance in those water classes that are poorly represented in the validation matchup data (e.g., water classes 7 and 14). In general, the POC concentration increased with the number of the optical water classes associated with them, as seen from the progression of colours in the scatter plots from blue to red, or from water classes 1 to 14 (Figure 3).

Overall, algorithms S2, S3, and ST performed well, with high r values (0.91–0.92) for the log-transformed matchup data, and with lower uncertainties than the other algorithms (Figure 3; Table 2). Some differences were observed among band ratio algorithms (S1, S2, S3, and S4), especially in water classes 13–14, where algorithm S4 tended to underestimate POC concentrations. Although the differences between these band ratio algorithms are statistically

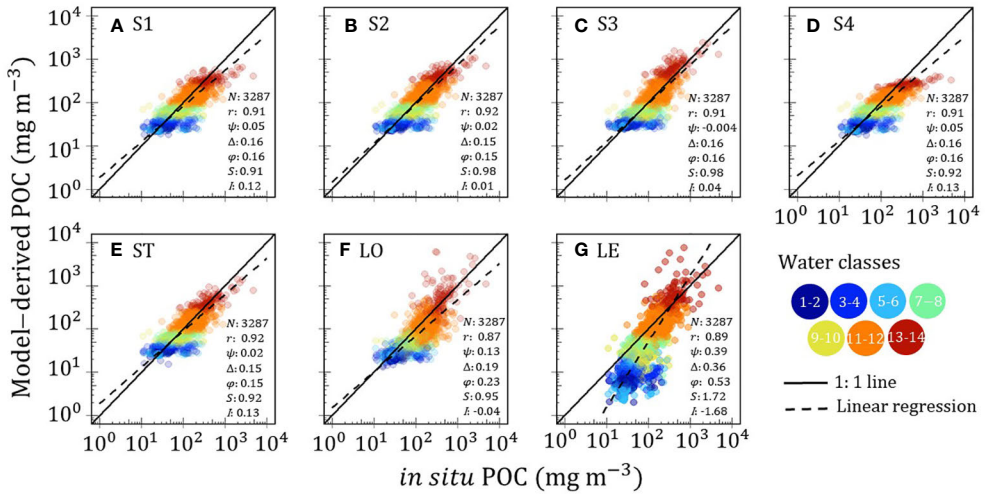


FIGURE 3
Relationships between *in situ* POC and corresponding satellite-derived POC matchup data (mg m^{-3}) estimated from candidate algorithms **(A)** S1, **(B)** S2, **(C)** S3, **(D)** S4, **(E)** ST, **(F)** LO, and **(G)** LE. The solid line is the 1:1 line. The dashed line is the best fit for linear regression. The colour assigned to the data points indicate the corresponding dominant optical water classes (1–14). The number of validation matchup data points (*N*) is shown. The Pearson's parametric correlation coefficient (*r*), root-mean-square difference (φ), centred-pattern-root-mean-square difference (Δ), and bias (ψ), as well as slope (*S*) and intercept (*I*) for the linear fit to log-transformed validation matchup data are shown.

small, algorithm S2 presented the lowest uncertainties over the whole dynamic range of POC concentration for log-transformed matchup data in this analysis, with the fitted regression lying closest to the 1:1 line (Figure 3C). The performance of algorithm S2 is statistically similar to algorithm ST, but with intercept and slope closer to 0 and 1 respectively, for log-transformed matchup data.

The modified Taylor diagram (Taylor, 2001) (Figure 4), which combines information on four key statistical metrics — the Pearson's correlation coefficient, the standard deviation, the centred-pattern-root-mean-square difference (unbiased), and the bias — also conveys the same message: algorithms S2, S3, and ST are clustered together and lie close to the *in situ* observation curve with high correlation coefficient, indicating statistically similar performances, consistent with the results seen in Figure 3. The algorithms S1 and S4 lie close to these algorithms with similar statistical performances for both non-transformed and log-transformed matchup data sets. The algorithm LO also lies close to these algorithms, albeit with higher errors and lower *r* for non-transformed matchup data (Figure 4A). When divided into dominant water classes, the performance of all candidate algorithms were lower than when examined as whole data sets, especially for water classes 1–10 with *r* below 0.5 (see Appendices D, E).

Although the uncertainties associated with algorithm LE were generally relatively high (Figure 4), the spread of data points is most elongated for this algorithm, showing a better separation among the different optical classes (Figure 3). This suggests the algorithm LE has a higher sensitivity, compared with all the other algorithms, especially for low POC concentrations (Figure 3). The main issue with algorithm LE was the deviation of the slope of the regression equation from the 1:1 lime. This could have occurred simply (i) from the differences between the modest set of data that was used initially to develop the algorithms, compared with the data set employed here for testing them; (ii) from implementing the algorithms on different satellite products from the ones used for the development, even though we took care to minimise errors arising from this source; or (iii) from the formulation of the algorithm itself, as it was established with a specific set of satellite-derived R_{rs}. When we applied a linear transformation to each of the algorithm outputs using the slope and intercept of the fitted linear regression for that algorithm, this had the effect of rotating the adjusted outputs to the 1:1 line when re-plotted against the matchup data (which can no longer be considered validation data at this stage). This adjustment (results not shown) had the most positive impact on algorithm LE, bringing it close to the band ratio algorithms on the Taylor diagram for the adjusted outputs, implying that this algorithm has the potential for further improvement.

3.1.1 Analysis of residuals

A detailed analysis of residuals, the differences between *in situ* POC and satellite-derived POC data, was conducted to compare the performances of candidate algorithms (Figure 5). All candidate algorithms presented near-normal distributions of residuals, with a peak near zero (result not shown). The band ratio algorithms (S1, S2, S3, and S4), as well as algorithms LO and ST, showed relatively small residuals compared with the other algorithms, but there was a distinct systematic pattern of change in residuals with the water types (Figure 5). Such water-type-dependent residuals might offer possibilities for further reductions in residuals, especially if algorithm development could be carried out independently for each water type. But such developments must await the availability of sufficient numbers of high-quality matchup data in each water class.

For all candidate algorithms, the highest residuals are associated with water classes 13–14 (Figure 5). Algorithm LE, for example, presented a small number of residuals exceeding 10,000 mg m^{-3} for

10.3389/fmars.2024.1309050

TABLE 2 Summary of statistical performance of the candidate algorithms.

Algorithm(s)	S1	S2	S3	S4	ST	LO	LE
log-transformed matchup data							
N	3287	3287	3287	3287	3287	3287	3287
r	0.91	**0.92**	0.91	0.91	**0.92**	0.87	0.89
ψ	0.05	0.02	**-0.004**	0.05	0.02	0.13	0.39
φ	0.16	**0.15**	0.16	0.16	**0.15**	0.23	0.53
Δ	0.16	**0.15**	0.16	0.16	**0.15**	0.19	0.36
I	0.12	0.01	0.04	0.15	0.13	-0.04	-1.68
S	0.91	0.98	0.98	0.89	0.92	0.95	1.72
Non-transformed matchup data							
N	3287	3287	3287	3287	3287	3287	3287
r_s	**0.89**	**0.89**	0.87	**0.89**	**0.89**	0.86	0.88
ψ	20.1	7.59	**-3.75**	22.8	10.3	17.1	-10.3
φ	94.4	78.3	77.8	102.4	**73.9**	179.1	878.7
Δ	92.2	77.9	77.7	99.8	**73.2**	178.2	878.6
δ	0.65	0.82	0.84	0.58	0.79	0.61	0.76
τ	37.5	29.1	36.4	41.5	27.7	46.2	35.6
I	25.2	18.6	-7.58	31.6	16.2	-81.5	-530.1
S	0.54	0.73	1.11	0.45	0.73	1.65	6.47

The number of validation matchup data points (N), the root-mean-square difference (φ), bias (ψ), centred-pattern-root-mean-square difference (Δ), intercept (I), and slope (S) for both log-transformed and non-transformed validation matchup data are shown. The Pearson's parametric correlation coefficient (r) for the log-transformed and Spearman's correlation coefficient (r_s) for the non-transformed matchup data are shown, accordingly. The median ratios (δ) and median absolute percentage difference (τ) for the non-transformed matchup data are presented. The units for φ, ψ, Δ, and δ are in mg m^{-3} and for τ are in %. The bolded values represent the values that are statistically significant.

these classes, which adversely affected its performance. The residuals were further analysed using Condorcet's pair-wise comparison of residuals (Seegers et al., 2018; Stramski et al., 2022). In this analysis, the residuals of pairs of candidate algorithms were compared, and in each comparison, the algorithm for which the residuals were lower the most number of times is considered as the 'winner'. The final 'winner' is the algorithm with the highest % wins (> 50%) for all pair-wise comparison of residuals. According to this test, algorithm S3 performed the best, followed by algorithms ST, LO, and then S2

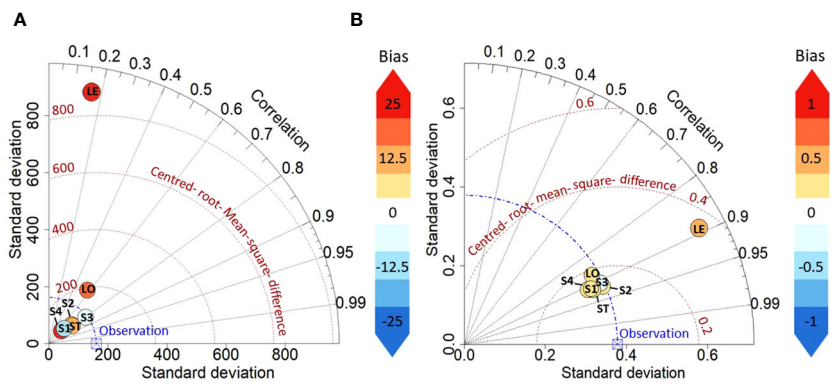


FIGURE 4
Modified Taylor diagrams comparing the **(A)** non-transformed and **(B)** log-transformed satellite-derived POC data estimated from candidate algorithms (S1, S2, S3, S4, ST, LO, and LE) and their relationship to the in situ POC data (blue dotted curve) in terms of the Pearson's parametric correlation coefficient, standard deviation, and centred-pattern-root-mean-square difference (red dotted curves). The colour bar indicates the bias between the in situ POC (mg m^{-3}) and satellite-derived POC data (mg m^{-3}).

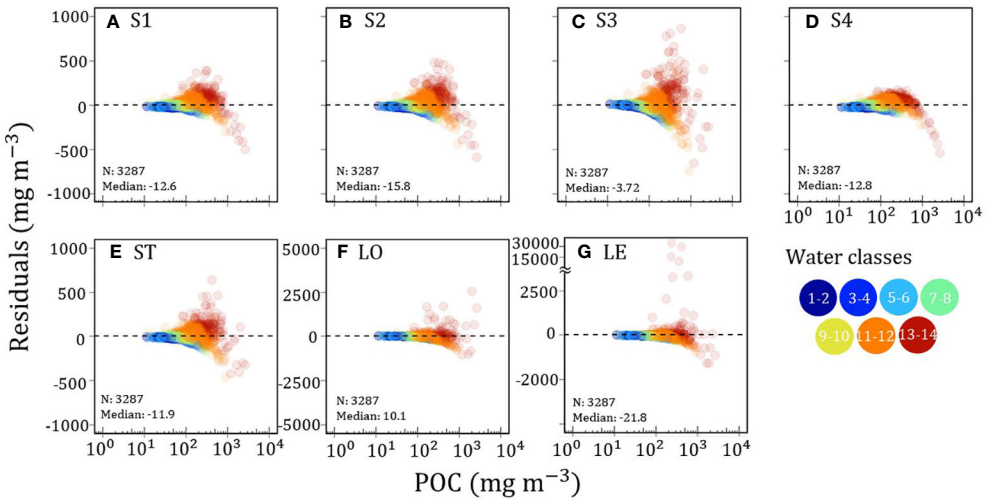


FIGURE 5
Scatter-plots of residuals, computed as the difference between *in situ* POC and satellite-derived POC for candidate algorithms **(A)** S1, **(B)** S2, **(C)** S3, **(D)** S4, **(E)** ST, **(F)** LO, and **(G)** LE, are plotted as a function of *in situ* POC. The colours of the data points indicate the associated dominant water types (1–14) estimated from the OC-CCI products. The dashed line indicates where the residual equals to zero. The units for residuals and *in situ* POC are in mg m^{-3}.

for non-transformed data (Figure 6A), consistent with the results shown in Figure 3. For the log-transformed data, the algorithm ST was the 'winner', but the % win was relatively low except when compared against algorithm LE (Figure 6B).

3.2 Relationship between POC and chlorophyll-a biomass

Comparison of satellite-derived products against *in situ* observations is an essential step in the validation of algorithms, but it is not necessarily a sufficient step. Paucity of matchup data; mismatches in the times of observations (though the matchup criteria are designed to minimise such errors); differences in spatial scales of satellite and *in situ* observations; lack of representative samples from all relevant regions and seasons — all these introduce uncertainties into such validation exercises. Therefore, as a complement to matchup comparisons, we have attempted here an indirect validation by comparing the patterns in the relationship between POC and chlorophyll-a concentration. We examine whether the relationship observed when *in situ* POC is plotted against satellite-derived chlorophyll-a is reproduced when satellite-derived POC is plotted against corresponding chlorophyll-a concentration, as in Evers-King et al. (2017).

In the left panel of Figure 7, the satellite-derived POC is plotted against the corresponding matchup satellite-derived chlorophyll-a. Since the relationship appears to be piece-wise linear with discontinuities at 0.1 and 1 mg m^{-3}, linear regressions were fitted to the data for chlorophyll-a concentration ≤ 0.1 mg m^{-3} (range 1), 1 mg m^{-3} (range 2), and chlorophyll-a ≥ 1 mg m^{-3} (range 3). The *in situ* POC is also shown as a background in grey in all the panels. Ideally, in this comparison, we are looking for algorithms that reproduce the fits and the spread of data around the fits that are observed for the *in situ* matchup data, for all the three chlorophyll-a ranges. The *in situ* POC (grey colour in Figure 7) was poorly correlated with chlorophyll-a in range 1, but the correlation was stronger in ranges 2 and 3. The algorithms S1, S2, S3, S4, ST, and LO (Figure 7) followed a similar pattern to that of the *in situ* relationship. Algorithms LE (Figure 7) showed stronger deviations from the *in situ* relationships, especially for water classes 1 to 10 (range 1 and range 2 of chlorophyll-a concentration).

We also plotted the satellite-derived POC data against the satellite-derived chlorophyll-a for all valid pixels for a randomly selected monthly OC-CCI image (June 2020) (Figures 7H–N), to see whether the satellite-derived POC and chlorophyll-a relationships resembled that of matchup data Figures 7A–G). The regression equations are fitted for the same three ranges of chlorophyll-a, as in the left panel. The regression line of *in situ* POC and chlorophyll-a estimated for the validation matchup data (solid line in left panel of Figure 7) is also reproduced in the middle panel as a common reference line. The number of valid satellite pixels obtained from the monthly image of 9 km resolution was 4,126,389.

In the comparison for the global data (middle panels, (Figures 7H–N), algorithms S1, S2, S3, S4, ST, and LO presented satellite-derived POC and chlorophyll-a relationships that are fairly similar to the matchup results on the left. However, the middle panels revealed some differences among these four algorithms that were not so evident when only the matchup data were plotted in the left panels. For example, the spread of the data points in the vicinity of 1 mg m^{-3}, is high for algorithm S1, whereas such a feature is not seen in the left panel of Figure 7A, and may be related to increased noise in the R_{rs} values at 443nm, as chlorophyll-a concentration increases, and when satellite viewing angles are unfavourable: we found that most of these data points were located in high-latitude waters (40 °S and above) during the southern hemisphere winter

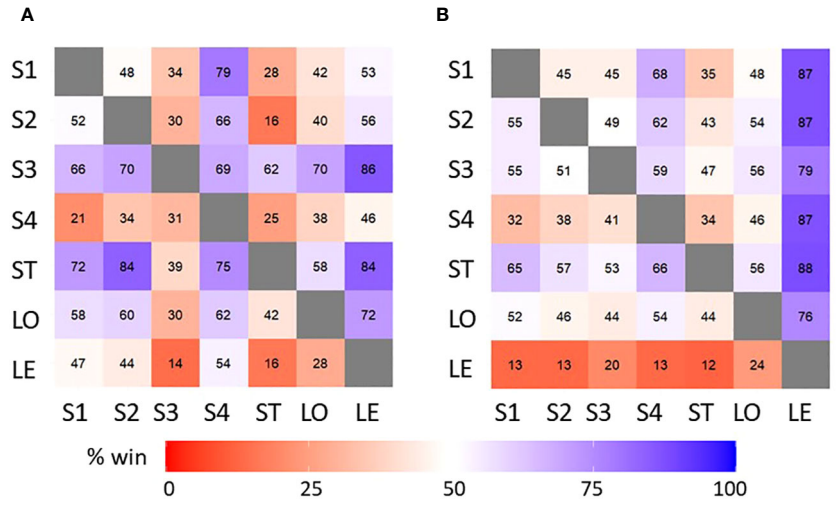


FIGURE 6
Condorcet's pair-wise comparison of residuals between a pair of candidate algorithms (S1, S2, S3, S4, ST, LO, and LE) for **(A)** non-transformed and **(B)** log-transformed POC data. Blue colour represents instances when residuals of an algorithm win over another algorithm. The % win is shown in both colours and numbers. White and red colours represent when the residuals of an algorithm tie or lose against another algorithm, respectively. The magnitude of the wins (>50%) and losses (<50%) are indicated by the intensity of the blue and red colours, respectively. The number of total wins or losses is counted horizontally.

(data not shown). It is also seen that the scatter of points in range 1 is less for algorithms S1 and S4 than for algorithms S2 and S3.

To investigate the performance of candidate algorithms in high-latitude waters from where we lack sufficient *in situ* POC and satellite-derived matchup products for point-by-point comparison, we examined the monthly sea-surface POC concentration in sub-Antarctic waters derived from algorithms ST and S2 (two of the algorithms that performed well in the comparisons) with the POC data derived from BGC-Argo (see Appendix G). The comparison mirrors that carried out by Galí et al. (2022), and is carried out for the Sub-Antarctic region, as defined by them. In Galí et al. (2022), POC was estimated using mixed layer depth and $b_{bp}(700)$ obtained from a monthly climatology from BGC-Argo data (2014-2019). For comparison, we combined monthly POC concentrations (1998-2020) derived from ST and S2 algorithms at each location with mixed-layer depth data (section 2.4) to estimate the POC pool in the layer. Both algorithms, ST and S2, showed values similar to BGC-Argo POC data from April to October. However, the winter average for the area (months 1 and 12 in the figure) overestimates BGC-Argo-based estimates and the model-based estimates of Galí et al. by a factor of two to three, which could reflect the poor sampling of high-latitudes by satellites during the winter months, such that the satellite-based estimates are biased towards the higher POC values at lower (less southern) latitudes. While it is difficult to carry the comparison further, it provides some reassurance that the satellite-derived estimates are not unreasonable in regions from where there are no to little matchup data.

4 Discussion

In this paper, we have compared a number of algorithms that have been proposed for estimating POC from satellite data with the objective of finding the best performing algorithm when used in conjunction with the OC-CCI time series data, for global applications, especially in the context of studying the impact of climate change on the marine environment. In doing this, we have, in some instances, taken some algorithms beyond the specific purposes for which they were designed. For example, some of the algorithms were designed for specific localities. If such algorithms that were tuned for excellence in a particular environment under-performed in the global context, it may not be totally surprising, and it should not be taken as indicative of their value and usefulness when they are used for the application for which they were originally designed. Nevertheless, such comparisons could provide new insights into how the various types of algorithms might be improved further, and where future efforts might be targeted.

Given the objective of applying the algorithm to the OC-CCI version 5 products, which were developed with MERIS as the reference sensor and with R_{rs} values reported for the MERIS wavebands in the visible domain (412, 443, 490, 510, 560, and 670nm), R_{rs} values from the OC-CCI products had to be shifted to the bands used in the initial implementation of the algorithms, which could have added to the differences between algorithms and *in situ* matchup data. In spite of all such problems which made the algorithm-data comparisons difficult, it was algorithms S2 and ST that performed consistently well, though several other algorithms performed almost as well.

POC estimates computed using algorithm S2 have been implemented with OC-CCI data version 4.2, based on its performance in an earlier comparison (Evers-King et al., 2017) and also because of its excellent performance in the comparisons presented here (the data are openly available here (Sathyendranath et al., 2022a): https://catalogue.ceda.ac.uk/uuid/299b1bb28eaa440f9a36e9786adfe398). The global average over the entire time series of POC concentration (1998-2020) estimated from algorithm S2 was

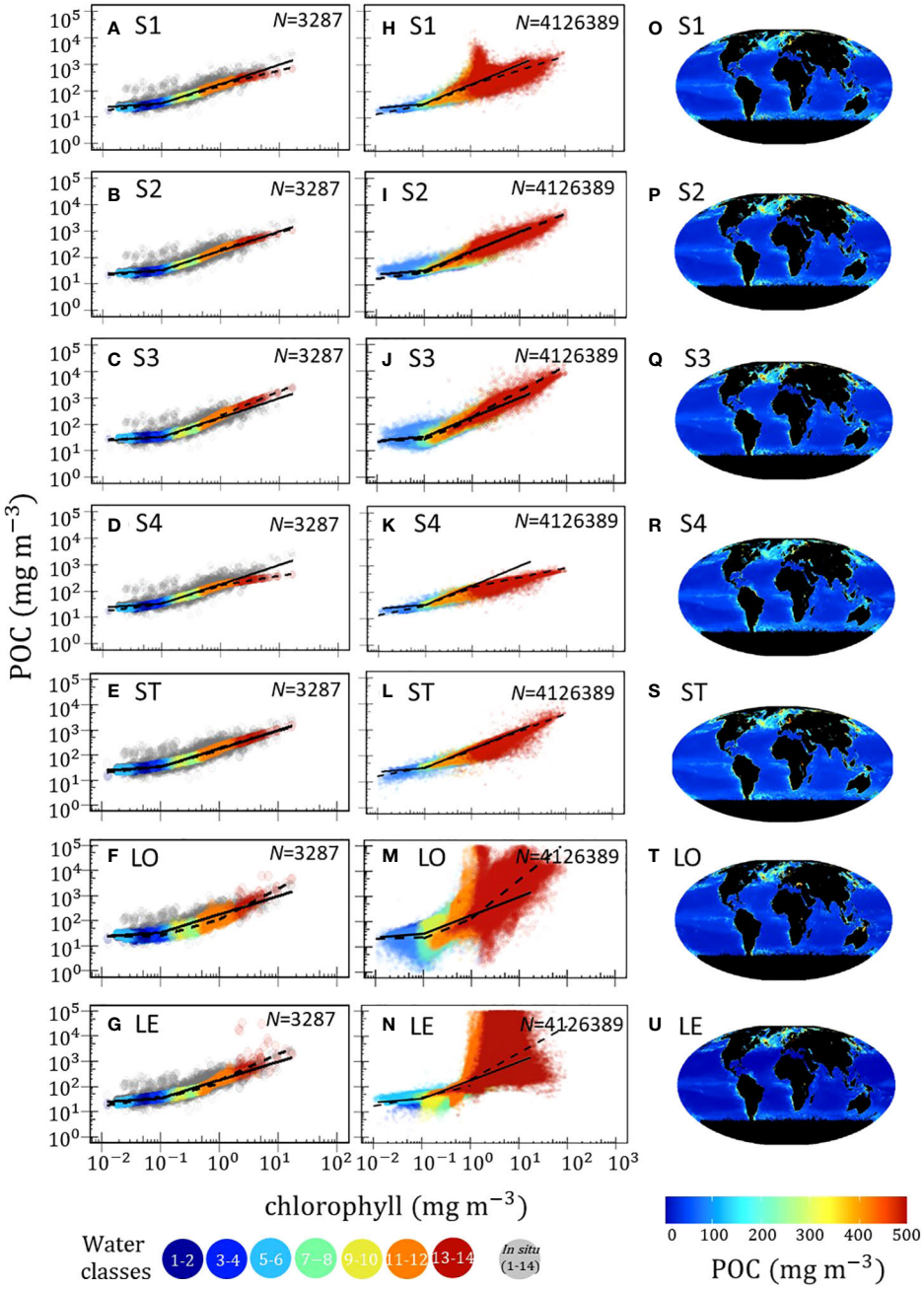


FIGURE 7
Satellite-derived POC estimated from candidate algorithms (S1, S2, S3, S4, ST, LO, and LE) compared with corresponding satellite-derived chlorophyll-a data. The (i) POC and chlorophyll-a relationships from the validation matchup data [left panels, **(A–G)**, (ii) the POC and chlorophyll-a from a sample monthly composite OC-CCI image (June, 2020) (middle panels, **(H–N)**], and (iii) the spatial maps of the POC estimated from the same monthly composite OC-CCI images (right panels, **(O–U)**. The solid lines in the scatter plots (i) and (ii) represent the linear regressions estimated from the *in situ* POC and satellite-derived chlorophyll-a matchup data for three different chlorophyll-a ranges: chlorophyll-a less than or equal to 0.1 mg m^{-3} (range 1), between 0.1 and 1 mg m^{-3} (range 2), and equal to or greater than 1 mg m^{-3} (range 3) (see Appendix F). The dashed lines represent the corresponding linear regressions estimated for the satellite-derived POC and the same satellite-derived chlorophyll-a values.

1.07 ± 0.05 PgC (where the uncertainty is the standard deviation associated with the year-to-year differences). This is similar to estimates from the past inter-comparison study (Evers-King et al., 2017), which lay in the range from 0.77 to 1.3 PgC. Since the original algorithm S2 was developed with a small number of matchup data (of order 100), and also because of the differences in wavebands used for algorithm development and those available on the OC-CCI version 5 products, we used the extensive matchup data sets consisting of *in situ* POC and satellite products assembled here to re-tune the algorithms to the OC-CCI data, before implementation (see Appendix H). The excellent performance of the tuned algorithm, with the low uncertainties associated with the

POC product, gives confidence in its quality, especially for those optical classes for which a large number of matchup data were available (the tuned algorithm S2 data are openly available here (Sathyendranath et al., 2022b): http://dx.doi.org/10.5285/5006f2c553cd4f26a6af0af2ee6d7c94). Our results indicate that algorithm ST also merits to be implemented as a global time series.

The optical classes that are poorly represented in the *in situ* data direct us to areas where future validation exercises should be prioritised. Certainly, the next big challenge is to improve the performance of POC algorithms in coastal waters, for which there is a need for enhancement in the number of observations available from under-represented coastal water classes and from under-represented geographic areas, such as the Indian Ocean and high-latitude waters (Figure 1).

While we consider the needs for a step change in the number of *in situ* observations, and where they are needed, we should also highlight the importance of high-quality data. Empirical POC algorithms depend heavily on the quality of both the Rrs and *in situ* POC data. Most of the *in situ* data assembled in this study were measured following the protocols established during the Joint Global Ocean Flux Study (Knap et al., 1996). Even though the data had been subjected to rigorous quality checking by data providers and by us, some data points with high bias could have gone undetected in the data, which is a compilation of data from various investigators collected from different oceanographic cruises covering a period of over two decades. Residual errors can be difficult to identify, though we were able to spot a small number of outliers on the basis of a comparison with corresponding chlorophyll-a data. The comparison allowed us to identify data with unrealistic carbon-to-chlorophyll ratios. Additional uncertainties are introduced at the matchup step, when discrepancies can stem from differences in temporal and spatial scales of *in situ* and satellite observations. We employed rigorous satellite-matchup criteria to minimise errors from this source. The downside was that it removed over 2000 matchup data points. While the quality control added confidence in the results, it also pointed to the need for consistency in methodology and data management to ensure the high quality of *in situ* POC data. In addition, improvements to methodologies used for *in situ* data collection are also needed, as the works of Novak et al. (2018) and Stramski et al. (2022) indicate.

Given the limitations of direct validation of satellite algorithms, we explored indirect modes of testing the products, by comparing relationships between POC and chlorophyll, similar in approach to that of Evers-King et al. (2017) and by comparing regional estimates of POC in the sub-Antarctic region. These comparisons were helpful in identifying problems not only with the algorithms *per se*, but also in highlighting instances when an increase in uncertainties in satellite products under unfavourable viewing conditions could translate into enhanced errors in the POC product. Whereas such errors are not a limitation of the algorithm itself, it illustrates conditions when such algorithms may not be applicable. They also point to instances where consistent gaps in satellite data (such as in high latitudes) could limit interpretation of data aggregated at large scales.

5 Concluding remarks

The results presented here confirm earlier conclusions that POC algorithms have reached a state of maturity where they meet user requirements (Evers-King et al., 2017). But one could envisage further developments to algorithm performance by blending multiple POC algorithms according to the performance of each algorithm in different optical water types, as is being done in the OC-CCI chlorophyll-a product (Jackson et al., 2017); or as demonstrated by the hybrid algorithm of Stramski et al. (2022). However, we lack sufficient matchup data from many optical water types, especially water classes 1, 7, and 14 (Figure 2B), and development of water-type-based blended algorithms must await a significant increase in matchup data, especially in these optical classes.

Data availability statement

The data sets presented in this study can be found in online repositories. The names of the repository/repositories and accession number(s) can be found below: https://www.bicep-project.org/Deliverables.

Author contributions

CK: Writing – original draft, Writing – review & editing. SS: Writing – original draft, Writing – review & editing. TJ: Data curation, Writing – review & editing. RB: Writing – review & editing. GK: Writing – review & editing. BJ: Data curation, Writing – review & editing. DS: Writing – review & editing. HL: Writing – review & editing. MG: Writing – review & editing. CL: Writing – review & editing.

Funding

The author(s) declare financial support was received for the research, authorship, and/or publication of this article. This work has been carried out as part of the European Space Agency's Biological Pump and Carbon Exchange Processes (BICEP) project and by the Simons Collaboration on Computational Biogeochemical Modeling of Marine Ecosystems (CBIOMES) (549947 SS). The work has been also supported by the National Centre for Earth Observations (NCEO) of the UK. MG has received financial support through the OPERA project (PID2019-107952GA-I00).

Acknowledgments

We would like to thank all BICEP project participants for providing feedback on this work, especially Rio, M. and Concha, J. A. for their support. We would like to give special thanks to Jorge, D. who provided great support in processing the satellite data for

algorithm LO. Special thanks also goes to Aumont, O. for guiding us on how to use the Sub-Antartic data sets and Röttgers, R. for providing essential feedback on the references. Furthermore, we would like to thank all the scientists who measured and collected the *in situ* POC data for this study. This includes, but is not limited to (i) SeaBASS: Balch, W., Larouche, P., Stramska, M., Hooker, S., Chaves, J., Mannino, A., Mulholland, M., Reynolds, R., Arrigo, K., Dijken, G., McClain, C., Neeley, A., Camill, P., Roesler, C., Lichter, J., Freeman, S., Novak, M, etc.; (ii) BCO-DMO: Johnson, R. J., Bates, N., Buesseler, K. O., Perry, M., Lomas, M. W., Dyhrman, S. T., Ammerman, J., Wheeler, P., etc; (iii) PANGAEA: Arístegui Ruiz, J., Doblin, M., Bayrakarov, E., etc; (b) (v) other publications: Martiny, A., Vrugt, J., Rasse, R., Dall'Olmo, G., Graff, J., Westberry, T. K., van Dongen-Vogels, V., Behrenfeld, M. J., Thomalla, S. J., Ogunkoya, A. G., Vichi, M., and Swart, S. Without their dedication, this work would not have been possible. In addition, we would like to thank Evers-King, H. and Dall'Olmo, G. for compiling *in situ* POC data. We would like to express our appreciation to the OC-CCI team for providing satellite products and the National Centre for Earth Observations for funding this study. We sincerely appreciate the valuable feedback and insights of the two reviewers, and we extend our gratitude to our editor, Olson, D. B., for his generous support.

Conflict of interest

The authors declare that the research was conducted in the absence of any commercial or financial relationships that could be construed as a potential conflict of interest.

Publisher's note

All claims expressed in this article are solely those of the authors and do not necessarily represent those of their affiliated organizations, or those of the publisher, the editors and the reviewers. Any product that may be evaluated in this article, or claim that may be made by its manufacturer, is not guaranteed or endorsed by the publisher.

Supplementary material

The Supplementary Material for this article can be found online at: https://www.frontiersin.org/articles/10.3389/fmars.2024.1309050/full#supplementary-material

References

Allison, D. B., Stramski, D., and Mitchell, B. G. (2010). Empirical ocean color algorithms for estimating particulate organic carbon in the Southern Ocean. *J. Geophys. Res.* 115, C10044. doi: 10.1029/2009JC006040

Bailey, S. W., and Werdell, P. J. (2006). A multi-sensor approach for the onorbit validation of ocean color satellite data products. *Remote Sens. Environ.* 102, 12–23. doi: 10.1016/j.rse.2006.01.015

Brewin, R. J. W., Sathyendranath, S., Müller, D., Brockmann, C., Deschamps, P. Y., Devred, E., et al. (2015). The Ocean Colour Climate Change Initiative: III. A round-robin comparison on in-water bio-optical algorithms. *Remote Sens. Environ.* 162, 271–294. doi: 10.1016/j.rse.2013.09.016

Brewin, R. J. W., Sathyendranath, S., Platt, T., Bouman, H., Ciavatta, S., Dall'Olmo, D., et al. (2021). Sinking fux of particulate organic matter in the oceans: Sensitivity to particle characteristics. *Earth-Science Rev.* 217, 103604. doi: 10.1016/j.earscirev.2021.103604

Buesseler, K. O. (2007). Combined water sample data from variety of sampling devices from USCGC Polar Star cruise PS02-2002 in the Southern Ocean, south of New Zealand in 2002 (SOFeX project). *Biol. Chem. Oceanography Data Manage. Office (BCO-DMO)*. doi: lod.bco-dmo.org/id/dataset/2804

CEOS (2014). *CEOS strategy for carbon observations from space. The Committee on Earth Observation Satellites (CEOS) response to the Group on Earth Observations (GEO) carbon strategy* (Tokyo, Japan: JAXA and I & A Corporation).

de Boyer Montégut, C., Madec, G., Fischer, A. S., Lazar, A., and ludicone, D. (2004). Mixed layer depth over the global ocean: An examination of profile data and a profile-based climatology. *J. Geophys. Res.: Oceans* 109 (C12). doi: 10.1029/2004jc002378

Eppley, R. W., and Peterson, B. J. (1979). Particulate organic matter flux and planktonic new production in the deep ocean. *Nature* 282, 667–680. doi: 10.1038/282677a0

Evers-King, H., Martinez-Vicente, V., Brewin, R. J. W., Dall'Olmo, G., Hickman, A. E., Jackson, T., et al. (2017). Validation and inter-comparison of ocean color algorithms for estimating particulate organic carbon in the oceans. *Front. Mar. Sci.* 4, 251. doi: 10.3389/fmars.2017.00251

Falkowski, P. G., Barber, R. T., and Smetacek, V. (1998). Biogeochemical controls and feedbacks on ocean primary production. *Science* 28, 200–206. doi: 10.1126/science.281.5374.200

Galí, M., Falls, M., Claustre, H., Aumont, O., and Bernardello, R. (2022). Bridging the gaps between particulate backscattering measurements and modeled particulate organic carbon in the ocean. *Biogeosci.* 19, 1245–1275. doi: 10.5194/bg-19-1245-2022

Hu, S. B., Cao, W. X., Wang, G. F., Xu, Z. T., Lin, J. F., Zhao, W. J., et al. (2016). Comparison of MERIS, MODIS, SeaWiFS-derived particulate organic carbon, and *in situ* measurements in the South China Sea. *Int. J. Remote Sens* 37, 1585–1600. doi: 10.1080/01431161.2015.1088673

Jackson, T., Sathyendranath, S., and Mélin, F. (2017). An improved optical classification scheme for the ocean colour essential climate variable and its applications. *Remote Sens. Environ.* 203, 152–161. doi: 10.1016/j.rse.2017.03.036

Johnson, R. J., and Bates, N. (2023) *Niskin bottle water samples and CTD measurements at water sample depths collected at Bermuda Atlantic Time-Series sites in the Sargasso Sea ongoing from 1988*. Available online at: http://lod.bcodmo.org/id/dataset/3782.

Joshi, I. D., Stramski, D., Reynolds, R. A., and Robinson, D. H. (2023). Performance assessment and validation of ocean color sensor-specific algorithms for estimating the concentration of particulate organic carbon in oceanic surface waters from satellite observations. *Remote Sens. Environ.* 286, 113417. doi: 10.1016/j.rse.2022.113417

Knap, A. H., Michaels, A., Close, H., Ducklow, H., and Dickson, A. (1996). Protocols for the Joint Global Ocean Flux Study (JGOFS) Core Measurements. *JGOFS Rep.* 19, 1-170. doi: 10.25607/OBP-1409

Le, C., Zhou, X., Hu, C., Lee, Z., Li, L., and Stramski, D. (2018). A Color-Index-Based Empirical Algorithm for Determining Particulate Organic Carbon Concentration in the Ocean From Satellite Observations. *J. Geophys. Res.: Oceans* 123, 7407–7491. doi: 10.1029/2018JC014014

Loisel, H., Nicolas, J. M., Deschamps, P. Y., and Frouin, R. (2002). Seasonal and inter-annual variability of particulate organic matter in the global ocean. *Geophys. Res. Lett.* 29, 491–494. doi: 10.1029/2002GL015948

Loisel, H., Stramski, D., Dessailly, D., Jamet, C., Li, L., and Reynolds, R. A. (2018). An Inverse Model for Estimating the Optical Absorption and Backscattering Coefficients of Seawater From Remote-Sensing Reflectance Over a Broad Range of Oceanic and Coastal Marine Environment. *J. Geophys. Res.: Oceans* 123, 2141–2171. doi: 10.1002/2017JC013632

Lomas, M. W., Dyhrman, S. T., and Ammerman, J. (2011). *Biogeochemistry Data from R/V Atlantic Explorer X0606, X0705, AE0810 in the Western Sargasso Sea roughly 38-20N and 66-43W from 2006-2008 (ATP3 project)* (MA. USA: Biological and Chemical Oceanography Data Management Office (BCO-DMO). Available at: http://lod.bcodmo.org/id/dataset/3354.

Mélin, F., and Sclep, G. (2015). Band shifting for ocean color multi-spectral reflectance data. *Optics Express* 23, 2262–2279. doi: 10.1364/OE.23.002262

Martiny, A., and Vrugt, J. (2014). Concentrations and ratios of particulate organic carbon, nitrogen, and phosphorus in the global ocean. *Sci. Data* 1, 140048. doi: 10.1038/sdata.2014.48

Müller, D., Krasemann, H., Brewin, R. J. W., Brockmann, C., Deschamps, P.-Y., Doerffer, R., et al. (2015). The Ocean Colour Climate Change Initiative: I. A methodology for assessing atmospheric correction processors based on *in-situ* measurements. *Remote Sens. Environ.* 162, 242–256. doi: 10.1016/j.rse.2013.11.026

Novak, M. G., Cetinić, I., Chaves, J. E., and Mannino, A. (2018). The adsorption of dissolved organic carbon onto glass fiber filters and its effect on the measurement of particulate organic carbon: A laboratory and modeling exercise. *Limnol. Oceanogr. Methods* 16, 356-366. doi: 10.1002/lom3.10248

PANGAEA (2020) *Compiled Data of Particulate Organic Carbon Concentrations from Various Sources for 1997 to 2020* (Accessed 03 December 2021).

Perry, M. (2011). *Niskin bottle hydrography from the CTD rosette from cruises KN193-03, B4-2008, B9-2008, and B10-2008 from the subpolar North Atlantic and Iceland Basin in 2008 (NAB 2008 project)* (MA. USA: Biological and Chemical Oceanography Data Management Office (BCO-DMO). Available at: http://lod.bco-dmo.org/id/dataset/3393.

Rasse, R., Dall'Olmo, G., Graff, J., Westberry, T. K., van DongenVogels, V., and Behrenfeld, M. J. (2017). Evaluating optical proxies of particulate organic carbon across the surface Atlantic ocean. *Front. Mar. Sci.* 4. doi: 10.3389/fmars.2017.00367

Ricker, W. E. (1973). Linear regressions in fishery research. *Fish.Res. Board Can.* 30, 409–434. doi: 10.1139/f73-072

Sathyendranath, S., Brewin, R. J. W., Brockmann, C., Brotas, V., Calton, B., Chuprin, A., et al. (2019). An ocean-colour time series for use in climate studies: the experience of the Ocean-Colour Climate Change Initiative (OC-CCI). *Sensors* 19, 4285. doi: 10.3390/s19194285

Sathyendranath, S., Jackson, T., Brockmann, C., Brotas, V., Calton, B., Chuprin, A., et al. (2021). *ESA Ocean Colour Climate Change Initiative: version 5.0 Data* (NERC EDS Centre for Environmental Data Analysis). doi: 10.5285/1dbe7a109c0244aaad713e078fd3059a

Sathyendranath, S., Kong, C. E., and Jackson, T. (2022a). *BICEP/NCEO: Monthly global Particulate Organic Carbon (POC), between 1997–2020 at 4 km resolution (produced from the Ocean Colour Climate Change Initiative v4.2 data set), version 2.* (United Kingdom: NERC EDS Centre for Environmental Data Analysis). doi: 10.5285/299b1bb28eaa440f9a36e9786adfe398

Sathyendranath, S., Kong, C. E., and Jackson, T. (2022b). *BICEP/NCEO: Monthly global Particulate Organic Carbon (POC), between 1997–2020 at 4 km resolution (produced from the Ocean Colour Climate Change Initiative v5.0 data set)* (United Kingdom: NERC EDS Centre for Environmental Data Analysis). doi: 10.5285/5006f2c553cd4f26a6af0af2ee6d7c94

Seegers, B. N., Stumpf, R. P., Schaeffer, B. A., Loftin, K. A., and Werdell, P. J. (2018). Performance metrics for the assessment of satellite data products: an ocean color case study. *J. Optics Express* 26, 7404. doi: 10.1364/OE.26.007404

Sokal, R. R., and Rohlf, F. J. (1995). *Biometry: the Principles and Practice of Statistics in Biological Research. 3rd ed* (NY, USA: W.H.Freeman and Company), 885.

Stramski, D., Joshi, I., and Reynolds, R. A. (2022). Ocean color algorithms to estimate the concentration of particulate organic carbon in surface waters of the global ocean in support of a long-term data record from multiple satellite missions. *Remote Sens. Environ.* 269, 112776. doi: 10.1016/j.rse.2021.112776

Stramski, D., Reynolds, R. A., Babin, M., Kaczmarek, S., Lewis, M. R., Rottgers, R., et al. (2008). Relationships between the surface concentration of particulate organic carbon and optical properties in the eastern South Pacific and eastern Atlantic Oceans. *Biogeosci* 5, 171–201. doi: 10.5194/bg-5-171-2008

Stramski, D., Reynolds, R. A., Kahru, M., and Mitchell, B. G. (1999). Estimation of particulate organic carbon in the ocean from satellite remote sensing. *Science* 285, 239–247. doi: 10.1126/science.285.5425.239

Taylor, K. E. (2001). Summarizing multiple aspects of model performance in a single diagram. *J. Geophys. Res.* 106, 7183–7192. doi: 10.1029/2000JD900719Citations

Thomalla, S. J., Ogunkoya, A. G., Vichi, M., and Swart, S. (2017). Using optical sensors on gliders to estimate phytoplankton carbon concentrations and chlorophyll-to-carbon ratios in the Southern Ocean. *Front. Mar. Sci.* 4. doi: 10.3389/fmars.2017.00034

Tran, T. K., Duforêt-Gaurier, L., Vantrepotte, V., Jorge, D. S. F., Mériaux, X., Cauvin, A., et al (2019). Waters from remote sensing: inter- comparison exercise and development of a maximum band ratio approach. *Remote Sens.* 11, 2849. doi: 10.3390/rs11232849

Twardowski, M. S., Boss, E., Macdonald, J. B., Pegau, W. S., Barnard, A. H., and Zaneveld, J. R. V. (2001). A model for estimating bulk refractive index from optical backscattering ratio and the implications for understanding particle composition in case I and case II waters. *J. Geophys. Res.* 106, 14,129–14,142.

Volk, T., and Hoffert, M. I. (1985). Ocean carbon pumps: Analysis of relative strengths and efficiencies in ocean-driven atmospheric CO2 changes. *Geophy. Mono. Ser.* 10, 99–110. doi: 10.1029/GM032p0099

Wheeler, P. (2012). *Particulate and dissolved organic carbon and nitrogen data from multiple cruises on R/V Wecoma, R/V Atlantis, and R/V New Horizon in the Northeast Pacific from 1997-2004 (GLOBEC NEP)* (MA, USA: Biological and Chemical Oceanography Data Management Office (BCO-DMO). doi: 10.1575/1912/bco-dmo.3643.1

frontiers | Frontiers in Marine Science

TYPE Original Research
PUBLISHED 12 June 2024
DOI 10.3389/fmars.2024.1305050

Check for updates

OPEN ACCESS

EDITED BY
Laura Lorenzoni,
National Aeronautics and Space Administration (NASA), United States

REVIEWED BY
Ishan Joshi,
University of California, San Diego, United States
Cedric Fichot,
Boston University, United States

*CORRESPONDENCE
Marko Laine
marko.laine@fmi.fi

RECEIVED 30 September 2023
ACCEPTED 21 May 2024
PUBLISHED 12 June 2024

CITATION
Laine M, Kulk G, Jönsson BF and Sathyendranath S (2024) A machine learning model-based satellite data record of dissolved organic carbon concentration in surface waters of the global open ocean. *Front. Mar. Sci.* 11:1305050. doi: 10.3389/fmars.2024.1305050

COPYRIGHT
© 2024 Laine, Kulk, Jönsson and Sathyendranath. This is an open-access article distributed under the terms of the Creative Commons Attribution License (CC BY). The use, distribution or reproduction in other forums is permitted, provided the original author(s) and the copyright owner(s) are credited and that the original publication in this journal is cited, in accordance with accepted academic practice. No use, distribution or reproduction is permitted which does not comply with these terms.

A machine learning model-based satellite data record of dissolved organic carbon concentration in surface waters of the global open ocean

Marko Laine[1]*, Gemma Kulk[2,3], Bror F. Jönsson[2] and Shubha Sathyendranath[2,3]

[1]Meteorological Research, Finnish Meteorological Institute, Helsinki, Finland, [2]Earth Observation Science and Applications, Plymouth Marine Laboratory, Plymouth, United Kingdom, [3]National Centre for Earth Observation, Plymouth Marine Laboratory, Plymouth, United Kingdom

Dissolved Organic Carbon (DOC) is the largest organic carbon pool in the ocean. Considering the biotic and abiotic factors controlling DOC processes, indirect satellite methods for open ocean DOC estimation can be developed, using conceptual, empirical or statistical models, driven by multiple satellite products. In this study, we infer a time series of global DOC from data of the European Space Agency's (ESA) Ocean Colour Climate Change Initiative (OC-CCI) in combination with a global database of *in situ* DOC observations. We tested empirical machine learning modelling approaches in which the available *in situ* data are used to train the models and to find empirical relationships between DOC and variables available from remote sensing. Of the tested methods, a random forest regression showed the best results, and the details of this model are further reported here. We present a time series of global open ocean DOC concentrations between 2010–2018 that is made freely available through the archive of the UK Centre for Environmental Data Analysis (CEDA).

KEYWORDS

ocean carbon cycle, dissolved organic carbon, ocean colour, satellite observations, machine learning, random forest

1 Introduction

Dissolved Organic Carbon (DOC) is the largest pool of organic carbon in the ocean at around ~662 Pg C (Hansell and Carlson, 2013). DOC is implicated in the physical transport of carbon from the surface to intermediate or deep waters through circulation, and in the metabolism of heterotrophic organisms. It is possible to classify DOC based on its reactivity as refractory or labile. The labile pool, accounting for ~0.2 Pg C, is biologically available and has a high production rate of ~14–25 Pg C y^{-1} (Hansell and Carlson, 2013).

The refractory pool is the largest pool at ~662 Pg, but has a much lower production rate of 0.043 Pg C y^{-1} and an average turnover time exceeding 1000 years (Williams and Druffel, 1987; Hansell and Carlson, 2013).

Observing DOC from space is challenging because the combined fractions of the DOC pool do not have a strong optical signature. A seasonally and temporally varying part of the DOC pool consisting of chromophoric substances known as Coloured Dissolved Organic Matter (CDOM), which can be directly monitored by ocean-colour remote sensing (Mannino et al., 2008). Satellite-based models of the spectral absorption by CDOM have performed reasonable well in validation studies (Siegel et al., 2013; Loisel et al., 2014; Mannino et al., 2014; Brewin et al., 2015) and their products are routinely produced by space agencies. The total DOC pool can be monitored from satellites by using its empirical relationship with CDOM absorption, which has been found to work well in coastal and shelf seas and the Arctic Ocean, but not in the open ocean where the relationship breaks down (Fichot and Benner, 2012; Nelson and Siegel, 2013; Matsuoka et al., 2017).

Given the various components of DOC, their respective timescales and vertical distribution, photo-bleaching processes, and the influence of biotic and abiotic factors on DOC processes (Hansell et al., 2009; Hansell and Carlson, 2013; Aurin et al., 2018), it is possible to develop indirect methods to estimate open ocean DOC. These methods can be based on conceptual, empirical or statistical relationships, incorporating multiple chemical, physical and biological variables. For example, Roshan and DeVries (2017) used an artificial neural network model to estimate global DOC concentrations using depth, temperature, nutrients, chlorophyll-a and the depth of the euphotic zone as input data. In combination with a data-constrained ocean circulation model, they produced the first observation-based global-scale assessment of DOC production and export. Because many of these physical and biological products are available from remote sensing observations, there is scope for similar satellite-driven approaches to estimate DOC in the global ocean. Recently, Bonelli et al. (2022) used a neural network approach to map DOC in oligotrophic and mesotrophic open ocean waters using sea surface temperature and the absorption of CDOM two weeks prior to the target date; and added chlorophyll-a concentration one week prior to the target date to the DOC model in more productive waters.

In this study, we develop a machine learning regression model to infer a time series of open ocean DOC from satellite-derived quantities and other inputs that are available globally over the ocean. We use the data from the European Space Agency's (ESA) Climate Change Initiative (CCI) in combination with a global *in situ* database of DOC concentrations (Hansell et al., 2021). Several empirical modelling approaches of the machine learning type were tested, in which the available *in situ* data are used to train the models and to find empirical relationships between DOC and variables available from remote sensing. The best performing random forest regression model is used to produce a global data set of open ocean satellite-derived DOC concentrations at 9 km spatial and monthly temporal resolution between 2010–2018. Independent validation is done against time series at two measuring sites: Bermuda Atlantic Time-Series study site (BATS, 31°40'N, 64°10'W) and Hawaii Ocean Time-series Aloha site (HOT, 22°45'N, 158°W).

2 Data and methods

For modelling of DOC using satellite-based remote sensing, we experimented with machine learning regression approaches to map these global observations to *in situ* DOC. The tested methods were 1) multiple linear regression, 2) gradient boosting regression, and 3) random forest regression. The aim was to provide a time series of global, monthly averaged maps of DOC using satellite data only. While the spatial and temporal coverage of *in situ* data that is available for training of the models caused challenges, the results presented here are promising. This study compares and validates the models using cross validation approach.

2.1 Satellite data

As input data to the satellite-based DOC model, we used remote-sensing reflectances at six different wavelengths (412, 443, 490, 510, 555 and 670 nm), phytoplankton primary production and sea surface salinity and temperature (Table 1). In addition, distance-to-shore, bathymetry, and latitude were used as geographical regressors. Remote-sensing reflectances were obtained from the Ocean Colour Climate Change Initiative (OC-CCI) v4.2 (Sathyendranath et al., 2019)[1] for 1997–2019 and the associated global satellite-based primary production data for 1998–2018 was estimated as in Kulk et al. (2020), available from the Centre for Environmental Data Analysis (CEDA)[2]. Sea Surface Salinity was obtained from the Sea Surface Salinity Climate Change Initiative (SSS-CCI) for 2010–2019 (Boutin et al., 2020)[3], and Sea Surface Temperature (SST) data for 2007–2020 were adapted and reprojected from versions of daily 1/25°.

OSTIA foundation SST (UK Met Office, 2005; Fiedler et al., 2019). All data was obtained at ~9 km (1/12°) or better spatial resolution – or reprojected to that resolution – and monthly temporal resolution. Figure 1 shows examples of the global satellite data sets for June 2018.

2.2 *In situ* data

To train the global DOC model, i.e. to calibrate the model parameters, and validate model predictions, *in situ* DOC observations were used (Table 1). The global *in situ* data set from

1 https://catalogue.ceda.ac.uk/uuid/99348189bd33459cbd597a58c30d8d10

2 https://dx.doi.org/10.5285/69b2c9c6c4714517ba10dab3515e4ee6

3 https://catalogue.ceda.ac.uk/uuid/7813eb75a131474a8d908f69c716b031

TABLE 1 Overview of the data sets used in this study.

Data set	Spatial resolution	Temporal coverage	Reference
OC-CCI	1/24°	1997–2019	Sathyendranath et al. (2019)
PP	1/12°	1998–2018	Kulk et al. (2020)
Salinity CCI	1/12°	2010–2019	Boutin et al. (2020)
SST	1/25°	2007–2020	UK Met Office (2005)
In situ		1994–2020	Hansell et al. (2021)

Monthly-averaged data was used, except for the in situ data. Abbreviations as in text.

Hansell et al. (2021) (1994– 2020) was used, which include DOC concentrations and ancillary data from different field campaigns worldwide (Figure 2). From these datasets, we removed any duplicates, and we selected those *in situ* observations where the concentration of DOC was reported and its value was greater than zero. In addition, we chose only near surface measurements, with criteria 'CTD PRESSURE' ≤ 30 dbar, corresponding approximately to 30 metres.

After data selection of near-surface *in situ* DOC, we had a total of 12,910 *in situ* observations available for further analysis. The *in situ* data was matched-up with the satellite data at the time and location of each *in situ* observation and a total of 8,796 data points were available for all regression variables, which forms the maximum size of the training data set for model calibration. However, we further decided to aggregate the *in situ* data to the same spatial and temporal resolutions as our monthly satellite data. After calculating monthly means and means over 1/24° spatial grid, we were left with 1,339 data points. We note that the overlapping period of *in situ* and satellite data is 2010–2018, as this is the time period for which sea surface salinity from CCI and the satellite-based primary production data were available.

2.3 Machine learning models

Linear regression and visual inspection of pair-wise correlation between variables was used to set a baseline for modelling of DOC using other machine learning methods and to make an initial selection of regression variables. The initial multiple linear regression model used here is similar to that of Aurin et al. (2018). We have a total of 13 candidate regressors to predict surface water DOC in μmol kg^{-1}. The regressors, or features in machine learning terminology, are listed in Table 2. As satellite derived quantities, we are using normalised remote-sensing reflectance at wavelength 412, 443, 490, 510, 555 and 670 nm from the OC-CCI as Rrs_{nnn}, primary production from Kulk et al. (2020) as PP. Other globally available regressors include sea surface temperature and salinity. The geographical variables used were water depth and distance to shore. All these regressors are available at the *in situ* locations together with the observed DOC to train the model to be used globally over the open ocean. For satellite-based data we used

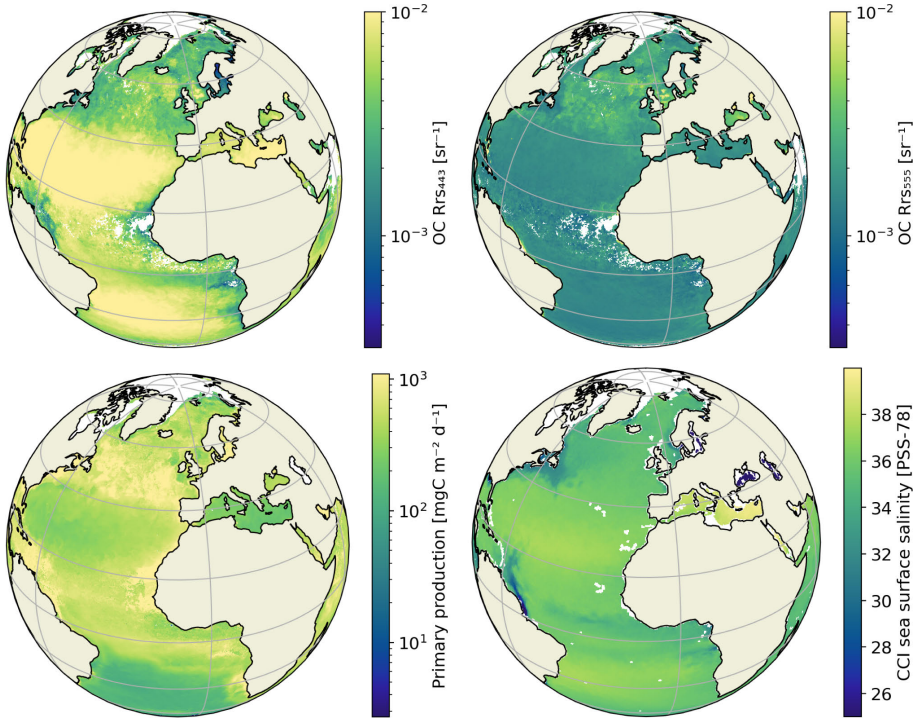


FIGURE 1
Examples of the satellite datasets with. Top left: the remote sensing reflectance (Rrs) at 443 nm. Top right: Rrs at 555 nm. Bottom left: primary production. Bottom right: sea surface salinity. All represent June 2018 mean values. Rrs and primary production are given in log scale. Light grey areas over the oceans are missing data.

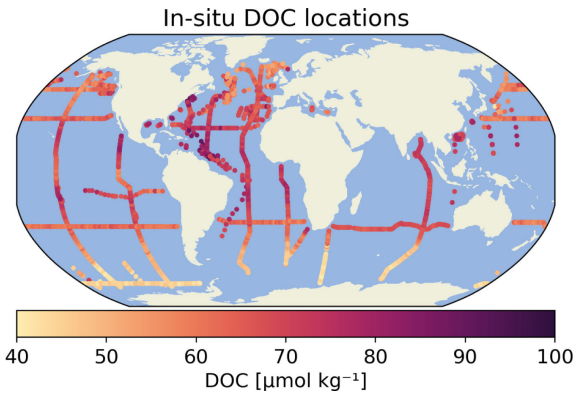


FIGURE 2
Locations of the *in situ* Dissolved Organic Carbon measurements, collected around the world on various field campaigns (Hansell et al., 2021). The original data have been aggregated to monthly means in 1/24° x 1/24° grid boxes.

monthly averages interpolated to the location and time of *in situ* data. Scatter plots of *in situ* DOC vs. various regressors are given in the auxiliary material (Supplementary Figure 1).

For advanced machine learning we use random forest and gradient boosting algorithms. Both are ensemble machine learning methods that use random subsamples of the training data set and builds decision trees or regression models for each sample, with the final model being a combination of the individual models. The book by Murphy (2012) gives an introduction to both methods as well as other similar machine learning approaches. In this study, we have used the Python package scikit-learn (Pedregosa et al., 2011) and its functions LinearRegression, RandomForestRegressor and GradientBoostingRegressor as well as several feature selection and cross validation tools available in the package. To illustrate random forest, Figure 3 shows an example of what an individual decision tree might look like. The actual trees are usually much larger.

2.4 Model and hyper-parameter selection

An important step in model building is the selection of explanatory variables. Including all or too many regressors will make the model perform better for the training data set, but typically causes over-fitting, i.e., the model is not able to predict beyond the data used in training. This is the reason why most machine leaning models use a separate and independent parts of the observational data to evaluate the model's performance. Although there are automatic methods to select explanatory variables, or features, some hand-tuning is necessary. In the case of DOC, the amount of *in situ* data is still limited, both spatially and temporally (Figure 2).

TABLE 2 Regressors used in the models.

feature	
$\sqrt{PP}$	square root of primary production [g C m^{-2} $month^{-1}$]
SST	sea surface temperature [°C]
SSS	sea surface salinity [ppt]
depth	water depth [m]
dts	distance to shore [km]
lat	latitude of the observation [degrees north]
Rrs_{nnn}	remote-sensing reflectance at 6 wavelengths [sr^{-1}]

We ended up comparing 6 models: multiple linear regression with full and reduced set of predictors, and random forest model and gradient boosting model with L2 (least squares) and L1 (least absolute deviation) optimisation criteria. The models use all available regressors given in Table 2, except for the reduced linear model, which used variables SST, $\sqrt{PP}$, Rrs_{443}, Rrs_{510}, Rrs_{490}, and Rrs_{555}, which were receiving largest Lasso scores when using L1 Lasso cross validation feature selection criteria available in the scikit-learn (Pedregosa et al., 2011) package (shown later in Figure 4).

Tuning and verification of the DOC model is challenging due to relative small number of data points for building a global model that depends on seasonally varying covariates. Due to sequential nature of the *in situ* sampling (Figure 2), simple leave-one-out cross validation is not optimal, as even an over-fitted model will easily predict a data points that are very close in time and place to values used in training. Here we decided to do cross-validation and model hyper-parameter tuning by leaving out individual years of the training data and then predicting DOC at the *in situ* location of these left-out years. The main cross validation criteria used for model selection and tuning of the boosting algorithms was R^2 coefficient of determination of the prediction, called Q^2 in the following. Other cross validation criteria used were root mean squared error (RMSE) of prediction and mean absolute error (MAE) of prediction. For random forest and gradient boosting, the cross validation was performed 30 times to calculate the mean Q^2 and other criteria mentioned above. For the multiple linear regression model similar cross validation was performed 100 times. The optimisation was done using package Optuna (Akiba et al., 2019). The both machine learning regression models turned out to be quite robust to overfit. We found out that the best performance was achieved when allowing full model with all available predictors and letting the hyper-parameter optimisation algorithm tune the models using cross validated predictive ability. The three hyper-parameters that were tuned in the process were *max_depth*, *n_estimators*, and *max_features* (Pedregosa et al., 2011). The best performance was achieved by the random forest model and L1 criteria. Table 3 shows the result of model validation and comparison.

In addition to the above cross validation based model tuning, we further evaluated the models using the same year-by-year cross validation as in the tuning, whose results are shown in Table 3. The results for two years, 2010 and 2011, are given in Figure 5, showing estimated vs. observed DOC for the given year with a model that is using all the years as well as cross-validation results where the year has been left out from the training set. Similar figures for all years are given in auxiliary material as Supplementary Figure 5. For the random forest model, the Q^2

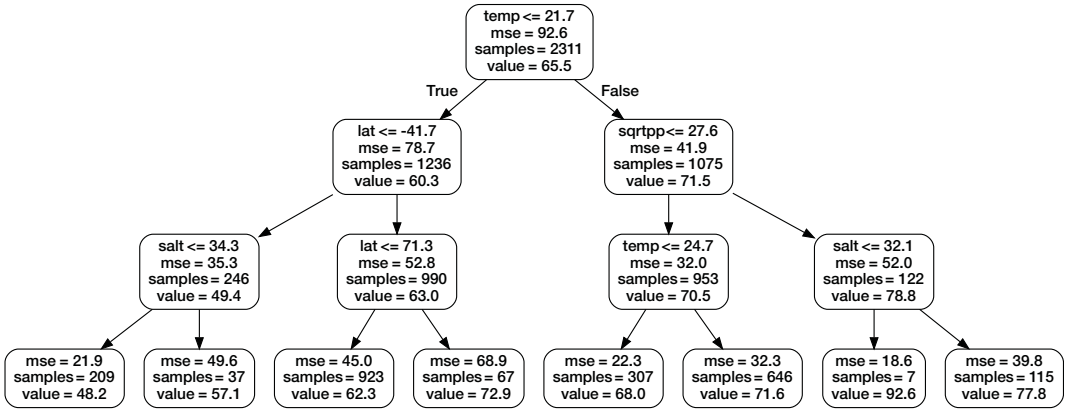


FIGURE 3
A simplified illustration of one random forest decision tree. The actual trees used in the model are much larger. The top line in each box shows branch selection criteria, "mse" is mean squared error in the test data set, "samples" is the size of the sample in the branch, and "value" is the estimated value of DOC.

values for prediction ranged from 20% to 77% for different years. This is an indication that the available training data might not be adequate, or at least that we do need to use all available data to be able to make reasonable predictions. However, the low values for some years in predictive variance explained is not only the property of random forest model. For the multiple linear regression models experimented, the yearly Q^2 values were much worse, also including negative values, which indicate that the linear model is performing worse in predicting new observations than just using the observed average.

2.5 Uncertainty in the predictions

The problem with many machine learning tools is that they do not provide uncertainty estimates for the predicted values. To estimate the predictive ability of the DOC random forest regression model and the uncertainty in predictions, we evaluated model residuals and their dependency on external variables, such as distance-to-shore and SST. In Figure 4 DOC estimations errors, i.e., the difference between *in situ* values and the corresponding model predicted values, are plotted against distance to shore. Panel on left shows absolute errors and panel on right shows relative errors interpolated spatially over the globe using regression kriging. Concentrations of DOC nearshore that are close to river and land discharges will be controlled heavily by factors that do not directly depend on the global variables available from space. For this reason, the data used for the DOC random forest model training include only those data points with distance-to-shore (e.g., variable dts) greater than 300 km. We chose this distance based on model performance and uncertainty analysis as described above. We note that the global predictions of DOC (section 3.2) are

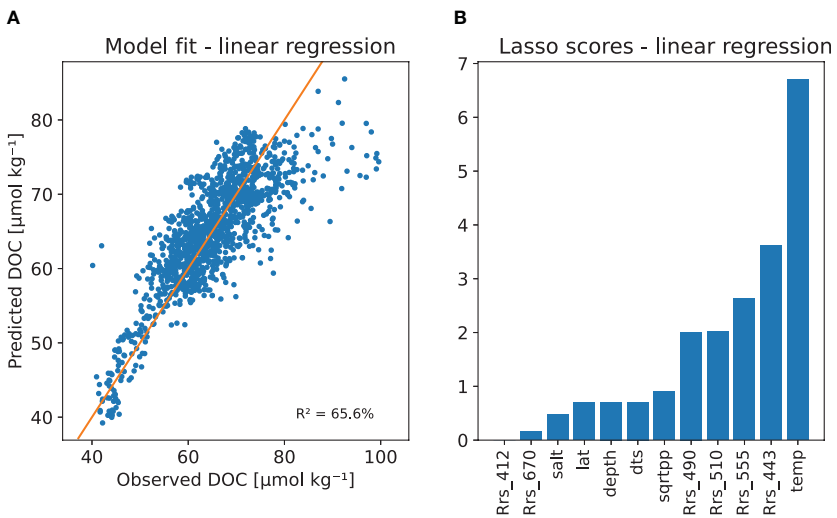


FIGURE 4
DOC multiple linear regression model with **(A)** Predicted versus observed Dissolved Organic Carbon (DOC) concentrations (in µmol kg^{-1}, and **(B)** LassoCV scores for the model parameters.

TABLE 3 Validation of different models using stratified cross validation.

Model	R^2	Q^2	MAE	RMSE	MAPE%
Linear Regression, full	66	57	4.61	6.04	7.02
Linear Regression, reduced	63	61	4.22	5.82	6.41
Random Forest, L1	97	64	4.27	5.66	6.49
Random Forest, L2	97	60	4.29	5.75	6.49
Gradient Boosting, L1	90	62	4.36	5.73	6.67
Gradient Boosting, L2	88	58	4.59	5.99	7.03

The cross validation was repeated at least 30 times to get the mean score. The R^2 statistic is calculated over the whole in situ data set. Other scores are: variance explained in prediction Q^2, mean absolute prediction error MAE, prediction root mean square error, RMSE, and relative mean absolute prediction error MAPE%. For MAE and RMSE the unit is the same as for DOC, µmol kg^{-1}.

calculated also for near shore points where the accuracy is not optimal and only reflects the background DOC not affected by inland fluxes.

2.6 Other machine learning methods

There are other machine learning methods that have been used successfully when predicting natural phenomena. The use of artificial neural networks (ANN) has grown enormously in recent years and they have shown to have good performance in complicated modelling situations. An ANN model is even more dependent on good training data than the machine learning methods experimented here. We did experiment with ANN for DOC estimation, but at least with tests utilising dense network layer structure with different number of layers and layer widths, we were not able to build models that would have enough predictive performance with the Q^2 criteria. The full development of a neural network model, given the rapid development of the field in recent years, would need much more work than was available for this study. We refer to Bonelli et al. (2022) and earlier Roshan and DeVries (2017) for interesting experiments using ANN for modelling DOC.

3 Results

Figures 6, 7 show random forest and gradient boosting models fitted to the whole *in situ* training data set. Both models can provide very good fit to the whole *in situ* data and from the feature importance analysis we can infer that all the regressors used can provide some extra information to the procedure. The most important predictors being sea surface temperature and latitude of the observation. If we compare this to Figure 8 of multiple linear regression and Lasso cross validation based scores we see that the fit is much better and the effect of latitude is not so strong, which is natural as the effect is not linear on the value of the latitude. We could have tried to use different transformations to achieve linearity, so this comparison is not totally fair against a more simple model that only includes linear effects.

As seen in Figure 6A, the random forest DOC model can produce a good fit to the training data with an R^2 and Q^2 values of 97% and 64%, respectively (see Table 3). Variable importance, or feature importance in machine learning terminology, based on a permutation method, is shown in Figure 6B. The SST and latitude being the most important features. From ocean colour the reflectance at 412 nm was the most important, salinity and primary production bringing both about equally amount of predictive power to the model. There is a tendency to over-fit, but still we conclude, that machine learning DOC models provide relatively robust behaviour in cross validation. Supplementary Figure 3 in supplementary shows observed vs. predicted DOC scatter plots for individual years.

We used model residuals and their dependency on external variables to estimate the predictive ability of the model and the uncertainty in predictions. This analysis showed that a rough estimate of the relative uncertainty in the estimated DOC is on average 5% or less when in open ocean waters, i.e., more than 1,000

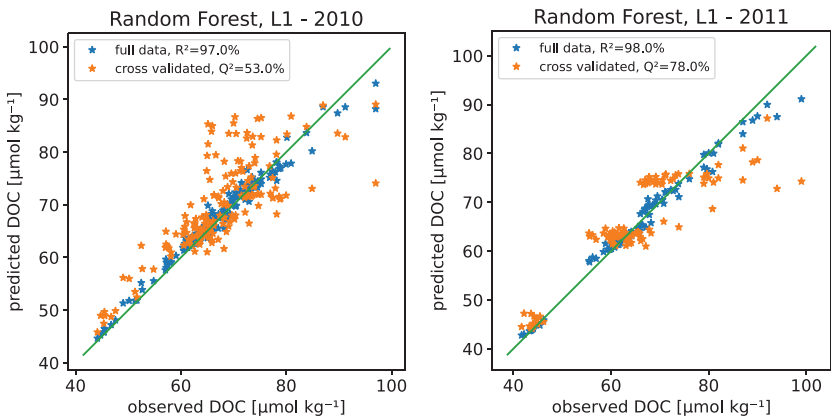


FIGURE 5
Observed versus predicted Dissolved Organic Carbon (DOC) in µmol kg^{-1} from the random forest model in years 2010 and 2011 with the 1:1 line. The panel shows model fitted with all available data as well as the version where the given year has been left out of the training data set. All the estimated years are shown in Supplementary Figure 16 in the Supplementary Material.

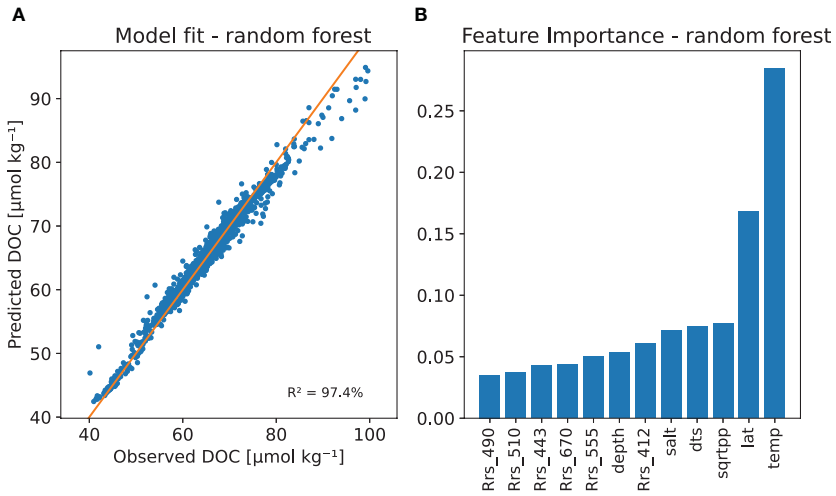


FIGURE 6
The DOC random forest model with **(A)** Model fit with the observed versus predicted DOC and **(B)** The relative importance of the regressor variables based on a permutation method.

km from the shore, and the error stays smaller than 10% when the distance is more than 300 km, see Figure 4.

3.1 Validation against measurement sites

There are few open ocean stations that measure DOC in systematic manner. As an independent validation, we used *in situ* data from two sites. The first time series was obtained at the Hawaii Ocean Time-series HOT-DOGS application[4]. We compared model estimates to the *in situ* measurements from station Aloha (22°45'N, 158°W), which were not part of the data used in the model calibration. Figure 9 shows the estimated DOC with observations. In this case, all our global models show similar seasonal pattern that does not fully match to that in the observations. There is an average bias of 1–3 µmol kg^{-1} for both machine learning models. The multiple linear regression model has larger bias. The seasonal pattern is not so noticeable in the observation, perhaps due to sampling and representation issues. Overall the match is quite good and within the anticipated estimation error.[4]

Figure 10 shows similar time series of data from Bermuda Atlantic Time-Series study (BATS, 31°40'N, 64°10'W) station. This is the same data set as was used by Bonelli et al. (2022), who kindly provided the data they used. We used daily averages of first 30 metres depth, whereas Bonelli et al. (2022) used 50 m. Here the observational data shows much clearer seasonal variability, which is also present in all the models. From year 2014, the variability of the observation changes, again perhaps due to some changes in sampling. The bias in the model results is up to 7% during some years. There were only three observations in Hansell et al. (2021) data set close to BATS that are used to train the model for years 2010–2018. Those are shown separately in the figure.

3.2 Global satellite-based DOC time series

Using our DOC model for open water, we generated a global monthly time series of DOC for 2010– 2018, for which time period, all global input data were available. The output data have a spatial resolution of 9 km (1/12°) in an uniform longitude-latitude grid, and the data contains the estimated monthly DOC concentrations in µmol kg^{-1}. Data were generated only for those locations where remote sensing reflectance, primary production, salinity and SST data were available. We used the open ocean model even for near shore pixels. As examples, Figure 11 shows the mean climatology for years (2010–2018), with more maps provided in the supplementary material (Supplementary Figure 4). The entire data set is freely available online through the UK Centre for Environmental Data Analysis (CEDA).

4 Discussion

Thanks to the comprehensive collections of *in situ* DOC data by (Hansell et al., 2021), it is now possible to apply machine-learning-based methods to estimate DOC in the surface waters of the global ocean. This is, nevertheless, a challenging task (Brewin et al., 2021). The current work explored modelling surface DOC from satellite data using multiple linear regression, gradient boosting and random forest. They are all designed to map the output variable of interest from the input variables in such a way that the model would have some explanatory power on predicting values outside the training data set. Extended validation of the models is still essential to establish confidence in the model predictions. This study shows that there are promising possibilities, but also room for more work.

In this study, we presented a machine learning approach to develop a global time series of DOC from observations of remote-

4 University of Hawai'i at Mānoa. National Science Foundation Award # 1756517
https://hahana.soest.hawaii.edu/hot/hot-dogs/bextraction.html

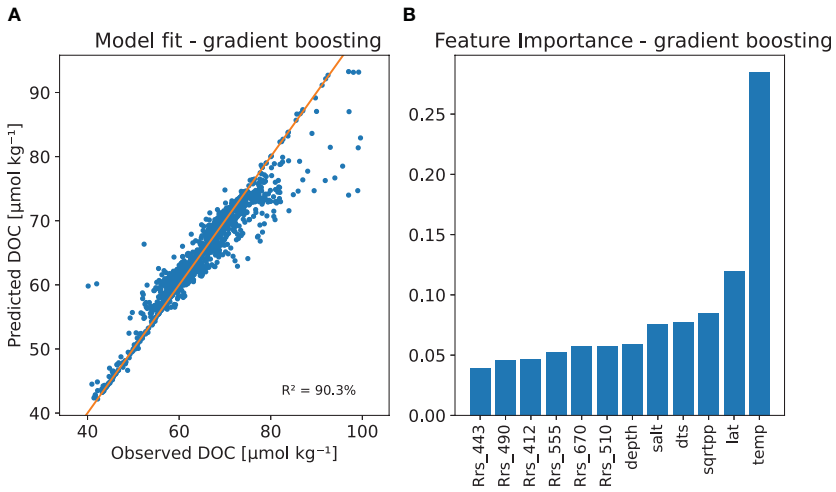


FIGURE 7
The DOC gradient boosting model with **(A)** Model fit with the observed versus predicted DOC and **(B)** The relative importance of the regressor variables based on a permutation method.

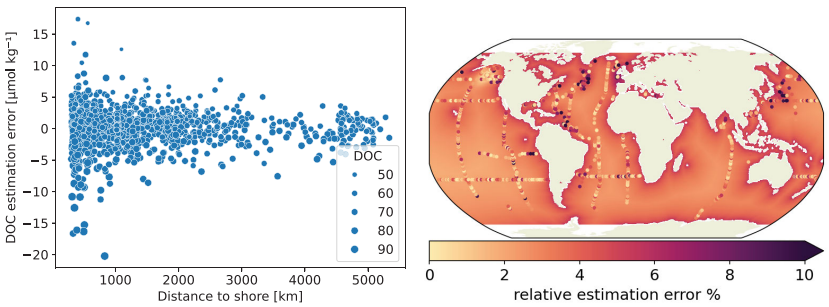


FIGURE 8
Uncertainty in the DOC random forest model. Left: the estimation error in all *in situ* locations compared against distance-to-shore. Right: the relative mean absolute error interpolated globally using regression kriging method and distance to shore as predictor. The dots show relative model residual error at *in situ* locations.

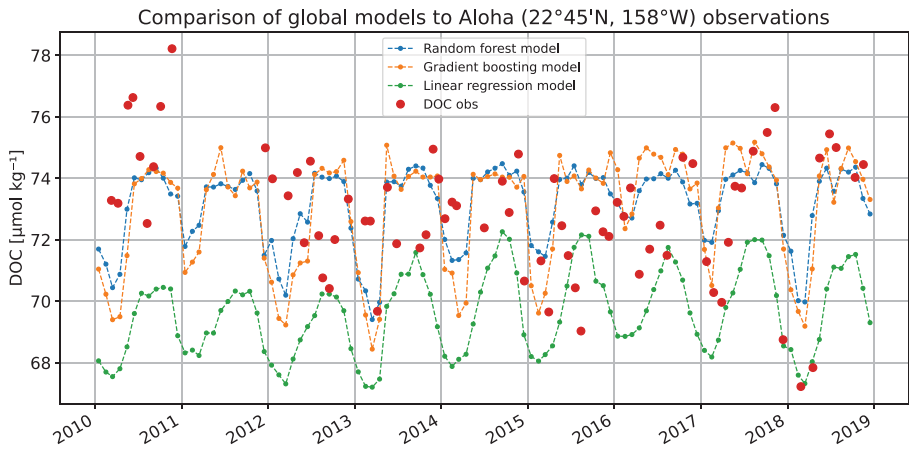


FIGURE 9
Time series from globally estimated DOC with gradient boosting and random forest models (both using L1 error criteria) and reduced linear regression model at a location of Aloha HOT-DOGS station compared to observations available from that stations for 2010–2018.

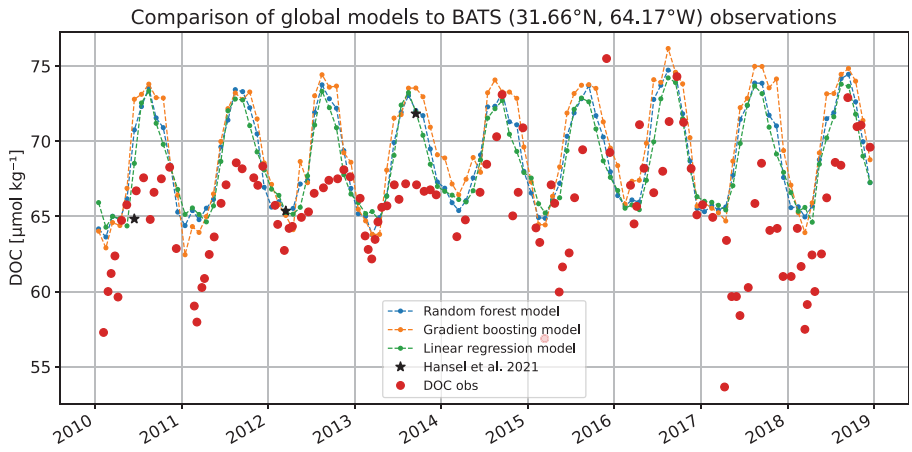


FIGURE 10
Time series from globally estimated DOC with gradient boosting and random forest models (both using L1 error criteria) and reduced linear regression model at a location of BATS station compared to observations available from that stations for 2010–2018.

sensing reflectance values at OC_CCI provided wavelengths (412, 443, 490, 510, 555, and 670 nm) phytoplankton primary production, sea surface temperature and salinity, as well as geographical variables. Other studies have used similar predictor variables, notably sea surface temperature and salinity, but also other variables such as nutrient concentrations and the absorption of Colour Dissolved Organic Matter (a_{CDOM}) (Siegel et al., 2002; Roshan and DeVries, 2017; Aurin et al., 2018; Bonelli et al., 2022). The selection of predictor variables is in part driven by domain-knowledge, but also by the type of data available. We have chosen to use only those predictor variables that are available from remote sensing observations, while other studies have used a combination of data available from *in situ* observations, satellite observations and biogeochemical models (Siegel et al., 2002; Aurin et al., 2018; Bonelli et al., 2022). In the DOC model presented here, sea surface temperature and latitude had the highest relative importance in predicting DOC, followed by primary production, distance to shore, sea surface salinity, and the remote sensing reflectance at 412 nm, (Figure 6). The importance of temperature and salinity in estimating DOC has been demonstrated in other studies: for example, the empirical model of Siegel et al. (2002) is based on relationships between temperature and *in situ* DOC that are parameterised per ocean basin; and the empirical model of Aurin et al. (2018) is based on the relationship between sea surface salinity and satellite-derived a_{CDOM}. While phytoplankton biomass has been used in other global DOC models (Roshan and DeVries, 2017; Bonelli et al., 2022), phytoplankton primary production is not commonly used, maybe in part because *in situ* observations of primary production are not available in sufficient numbers. Here, satellite-based primary production is seen to add to the predictive power of the gradient boosting and random forest models. It is important that internally consistent datasets based on the Ocean Colour Climate Change Initiative (remote sensing reflectances and primary production) were used in this study.

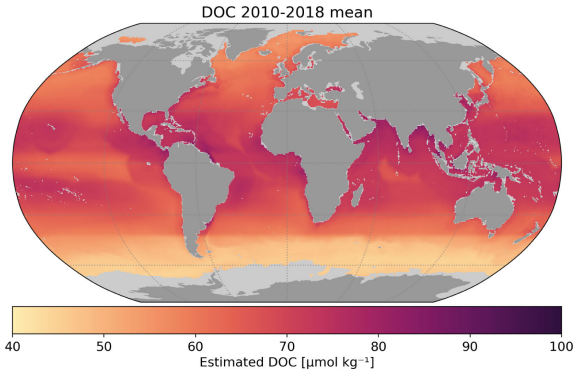


FIGURE 11
Climatology of Dissolved Organic Carbon (DOC) for 2010–2018. The light grey areas represent missing pixels for which input satellite data from CCI was not available. Climatologies of each year in the time series are provided in the Supplementary Material.

The DOC values estimated from our model compared well with *in situ* observations used in training the model (Figure 6). Leave-one-year-out cross validation (Figure 5) showed varying consistency across the years, but still provided reasonable results. Distance from shore (dts) appeared as a key determinant of outliers (Figure 4). Validation against *in-situ* measurements at Station Aloha and at BATS (Section 3.1) revealed biases that were in agreement with the assumed errors, and also showed challenges in reproducing seasonal variability at a local scale. The globally-mapped climatology (Figure 11) can be compared visually with the results of Bonelli et al. (2022), who recently published a 10-year DOC climatology based on a neural network approach that incorporated sea surface temperature, absorption of CDOM and chlorophyll-a. The two models showed a high level of qualitative agreement in spite of the differences in the AI methods employed, and in the satellite input data sets used. Though we did not use absorption by CDOM in our analysis, it is interesting to note that one of the key regressor variables in our study is the remote-sensing reflectance at 412 nm, the wavelength were the absorption by CDOM is the highest, compared with longer wavelengths that were included in the model.

All the tested machine learning models suffer from the tendency to over-fit. Their ability to model and find non-linear relationships between explanatory variables and the variable of interests (DOC in our case) is their strength. At the same time, it can be a weakness, if not enough representative *in situ* and satellite observations are used. The validation of predictions by independent observations is not always possible and the second best option is to cross validate by leaving out a part of the already scarce data. Doing cross validation and studying errors in the predictions can also help on the second problematic feature of many machine learning models, namely the lack of uncertainty estimates in model outputs. The tested approaches showed similar performance. Machine learning models require careful tuning of the parameters of the methods as they are prone to perform well on the data set that is used for training the model, but have worse results on independent new data. The ability to predict new observations and extrapolate spatially and temporally is usually the main reason to use machine learning models. In our case having a single collection of *in situ* observations, the problem of over-fitting is handled by using model scoring based on repeated cross validation by stratified random sampling. The final results will necessarily have some dependency on the choice of model's tuning parameters and other estimation strategies. This is a common feature in advanced machine learning models.

Against the background of the complex biogeochemistry of DOC and in the absence of a clear optical signal that can unequivocally be related to DOC, our study has focused on exploring indirect methods to estimate DOC using proxy variables selected on the basis of our understanding of the biogeochemistry of DOC. Using an *in situ* database and satellite observations of primary production, sea surface temperature and salinity as well as remote sensing reflectances, a series of empirical and machine-learning approaches were tested to map global DOC in open ocean waters. This resulted in the selection of a satellite-based random forest model to map the total pelagic DOC on a monthly basis between 2010–2018. Due to spatially and temporally limited *in situ* data, it is still unclear how well the model can represent the seasonal patterns and trends in the global ocean DOC. One future approach might be to include dynamical processes, such as advection by ocean currents in satellite-based DOC models to improve our understanding of the temporal dynamics and spatial correlation structures of DOC. Undoubtedly, further progress must rely on parallel improvement in our understanding of the biogeochemical processes that underpin DOC dynamics in the ocean, as well as in improvements to the *in situ* data on DOC, with respect to both geographical and seasonal coverage.

Data availability statement

The datasets presented in this study can be found in online repositories. The names of the repository/repositories and accession number(s) can be found below: https://catalogue.ceda.ac.uk/uuid/372375fff81e44428ed62dacd562a5f2.[5] The code used in the analysis is available from https://github.com/mjlaine/ESA-BICEP-DOC which is now public repository.

5 https://catalogue.ceda.ac.uk/uuid/372375fff81e44428ed62dacd562a5f2

Author contributions

ML: Methodology, Software, Visualization, Writing – original draft, Writing – review & editing. GK: Methodology, Visualization, Writing – review & editing. BJ: Conceptualization, Data curation, Software, Writing – review & editing. SS: Conceptualization, Funding acquisition, Project administration, Resources, Supervision, Validation, Writing – review & editing.

Funding

The author(s) declare financial support was received for the research, authorship, and/or publication of this article. This research was funded by European Space Agency's project BICEP - Biological Pump and Carbon Exchange Processes and the Simons Foundation grant Computational Biogeochemical Modeling of Marine Ecosystems (CBIOMES, number 549947, SS). ML was partly supported by Research Council of Finland grant n:o 321890. This work is a contribution to the activities of the National Centre of Earth Observation of the UK.

Acknowledgments

We would like to thank Ana Bonelli for providing details of her analysis of the time series data at BATS, for comparison with the results presented in this study.

Conflict of interest

The authors declare that the research was conducted in the absence of any commercial or financial relationships that could be construed as a potential conflict of interest.

The author(s) declared that they were an editorial board member of Frontiers, at the time of submission. This had no impact on the peer review process and the final decision.

Publisher's note

All claims expressed in this article are solely those of the authors and do not necessarily represent those of their affiliated organizations, or those of the publisher, the editors and the reviewers. Any product that may be evaluated in this article, or claim that may be made by its manufacturer, is not guaranteed or endorsed by the publisher.

Supplementary material

The Supplementary Material for this article can be found online at: https://www.frontiersin.org/articles/10.3389/fmars.2024.1305050/full#supplementary-material

References

Akiba, T., Sano, S., Yanase, T., Ohta, T., and Koyama, M. (2019). "Optuna: A next-generation hyperparameter optimization framework," in *Proceedings of the 25th ACM SIGKDD International Conference on Knowledge Discovery and Data Mining*. (New York, NY, USA: Association for Computing Machinery), 2623–2631. doi: 10.1145/3292500

Aurin, D., Mannino, A., and Lary, D. J. (2018). Remote sensing of CDOM, CDOM spectral slope, and dissolved organic carbon in the global ocean. *Appl. Sci.* 8. doi: 10.3390/app8122687

Bonelli, A. G., Loisel, H., Jorge, D. S. F., and Mangin, A. (2022). Odile Fanton d'Andon, and Vincent Vantrepotte. A new method to estimate the dissolved organic carbon concentration from remote sensing in the global open ocean. *Remote Sens. Environ.* 281, 113227. doi: 10.1016/j.rse.2022.113227

Boutin, J., Vergely, J.-L., Reul, N., Catany, R., Koehler, J., Martin, A., et al. (2020) ESA Sea Surface Salinity Climate Change Initiative (Sea_Surface_Salinity_cci): Monthly sea surface salinity product, v2.31, for 2010 to 2019. Available at: https://catalogue.ceda.ac.uk/uuid/7813eb75a131474a8d908f69c716b031.

Brewin, R. J. W., Sathyendranath, S., Müller, D., Brockmann, C., Deschamps, P. Y., Devred, E., et al. (2015). The ocean colour climate change initiative: Iii. a round-robin comparison on in-water bio-optical algorithms. *Remote Sens. Environ.* 162, 271–294. doi: 10.1016/j.rse.2013.09.016

Brewin, R. J. W., Sathyendranath, S., Platt, T., Bouman, H., Ciavatta, S., Dall'Olmo, G., et al. (2021). Sensing the ocean biological carbon pump from space: A review of capabilities, concepts, research gaps and future developments. *Earth-Science Rev.* 217, 103604. doi: 10.1016/j.earscirev.2021.103604

Fichot, C. G., and Benner, R. (2012). The spectral slope coefficient of chromophoric dissolved organic matter (s275–295) as a tracer of terrigenous dissolved organic carbon in river-influenced ocean margins. *Limnol. Oceanogr.* 57, 453–1466. doi: 10.4319/lo.2012.57.5.1453

Fiedler, E. K., McLaren, A., Banzon, V., Brasnett, B., Ishizaki, S., Kennedy, J., et al. (2019). Intercomparison of long-term sea surface temperature analyses using the GHRSST multi-product ensemble (GMPE) system. *Remote Sens. Environ.* 222, 18–33. doi: 10.1016/j.rse.2018.12.015

Hansell, D. A., and Carlson, C. A. (2013). Localized refractory dissolved organic carbon sinks in the deep ocean. *Global Biogeochemical Cycles* 27, 705–710. doi: 10.1002/gbc.20067

Hansell, D. A., Carlson, C. A., Repeta, D. J., and Schlitzer, R. (2009). Dissolved organic matter in the ocean: A controversy stimulates new insights. *Oceanography* 22, 202–211. doi: 10.5670/oceanog.2009.109

Hansell, D. A., Carlson, R. M.W., Amon, C. A., Álvarez-Salgado, X. Antón, Yamashita, Y., Romera-Castillo, C., et al. (2021). *Compilation of dissolved organic matter (DOM) data obtained from the global ocean surveys from 1994 to 2020 (NCEI accession 0227166)*. doi: 10.25921/s4f4-ye35

Kulk, G., Platt, T., Dingle, J., Jackson, T., Jönsson, B. F., Bouman, H. A., et al. (2020). Primary production, an index of climate change in the ocean: Satellite-based estimates over two decades. *Remote Sens.* 12. doi: 10.3390/rs12050826

Loisel, H., Vantrepotte, V., Dessailly, D., and Meriaux, X. (2014). Assessment of the colored dissolved organic matter in coastal waters from ocean color remote sensing. *Opt. Express* 22, 13109. doi: 10.1364/OE.22.013109

Mannino, A., Novak, M. G., Hooker, S. B., Hyde, K., and Aurin, D. (2014). Algorithm development and validation of cdom properties for estuarine and continental shelf waters along the northeastern us coast. *Remote Senssing Environ.* 152, 567–602. doi: 10.1016/j.rse.2014.06.027

Mannino, A., Russ, M. E., and Hooker, S. B. (2008). Algorithm development and validation for satellite-derived distributions of DOC and CDOM in the U.S. Middle Atlantic Bight. *J. Geophysical Res.: Oceans* 113. doi: 10.1029/2007JC004493

Matsuoka, A., Boss, E., Babin, M., Karp-Boss, L., Hafez, M., Chekalyuk, A., et al. (2017). Pan-arctic optical characteristics of colored dissolved organic matter: Tracing dissolved organiccarboninchangingarcticwatersusingsatelliteoceancolordata. *RemoteSensingofEnvironment* 200, 89–101. doi: 10.1016/J.RSE.2017.08.009

Murphy, K. P. (2012). *Machine Learning A Probabilistic Perspective* (Cambridge, MA: The MIT Press). Available at: https://probml.github.io/pml-book/book0.html.

Nelson, N. B., and Siegel, D. A. (2013). The global distribution and dynamics of chromophoric dissolved organic matter. *Annu. Rev. Mar. Sci.* 5, 20.1–20.3. doi: 10.1146/annurev-marine-120710-100751

Pedregosa, F., Varoquaux, G., Gramfort, A., Michel, V., Thirion, B., Grisel, O., et al. (2011). Scikit-learn: machine learning in python. *J. Mach. Learn. Res.* 12, 2825–2830. Available at: http://jmlr.org/papers/v12/pedregosa11a.html.

Roshan, S., and DeVries, T. (2017). Efficient dissolved organic carbon production and export in the oligotrophic ocean. *Nat. Commun.* 8, 2036. doi: 10.1038/s41467-017-02227-3

Sathyendranath, S., Brewin, R. J. W., Brockmann, C., Brotas, V., Calton, B., Chuprin, A., et al. (2019). An ocean-colour time series for use in climate studies: The experience of the Ocean-Colour Climate Change Initiative (OC-CCI). *Sensors* 19. doi: 10.3390/s19194285

Siegel, D. A., Behrenfeld, M. J., Maritorena, S., McClain, C. R., Antoine, D., Bailey, S. W., et al. (2013). Regional to global assessments of phytoplankton dynamics from the SeaWiFS mission. *Remote Senssing Environ.* 135, 77–91. doi: 10.1016/j.rse.2013.03.025

Siegel, D. A., Maritorena, S., Nelson, N. B., Hansell, D. A., and Lorenzi-Kayser, M. (2002). Global distribution and dynamics of colored dissolved and detrital organic materials. *J. Geophys. Res. Oceans* 107, 1–14. doi: 10.1029/2001JC000965

UK Met Office (2005) GHRSST Level 4 OSTIA global foundation sea surface temperature analysis.doi: 10.5067/GHOST-4FK01.

Williams, P. M., and Druffel, E. R.M. (1987). Radiocarbon in dissolved organic matter in the central North Pacific Ocean. *Nature* 330, 246–248. doi: 10.1038/330246a0

frontiers | Frontiers in Marine Science

TYPE Original Research
PUBLISHED 22 August 2024
DOI 10.3389/fmars.2024.1358899

Check for updates

OPEN ACCESS

EDITED BY
Astrid Bracher,
Alfred Wegener Institute Helmholtz Centre for Polar and Marine Research (AWI), Germany

REVIEWED BY
Ana B. Ruescas,
University of Valencia, Spain
Andrew Banks,
Hellenic Centre for Marine Research (HCMR), Greece

*CORRESPONDENCE
Robert J. W. Brewin
r.brewin@exeter.ac.uk

†PRESENT ADDRESS
Jonathan R. Heath,
School of Ocean Sciences, Bangor University, Menai Bridge, United Kingdom

RECEIVED 20 December 2023
ACCEPTED 29 July 2024
PUBLISHED 22 August 2024

CITATION
Heath JR, Brewin RJW, Pitarch J and Raitsos DE (2024) Detecting centennial changes in the clarity and colour of the Red and Eastern Mediterranean Seas by retracting the "Pola" expeditions.
Front. Mar. Sci. 11:1358899.
doi: 10.3389/fmars.2024.1358899

COPYRIGHT
© 2024 Heath, Brewin, Pitarch and Raitsos. This is an open-access article distributed under the terms of the Creative Commons Attribution License (CC BY). The use, distribution or reproduction in other forums is permitted, provided the original author(s) and the copyright owner(s) are credited and that the original publication in this journal is cited, in accordance with accepted academic practice. No use, distribution or reproduction is permitted which does not comply with these terms.

Detecting centennial changes in the clarity and colour of the Red and Eastern Mediterranean Seas by retracting the "Pola" expeditions

Jonathan R. Heath[1†], Robert J. W. Brewin[2*], Jaime Pitarch[3] and Dionysios E. Raitsos[4]

[1]Centre for Ecology and Conservation, University of Exeter, Penryn, United Kingdom, [2]Centre for Geography and Environmental Science, University of Exeter, Penryn, United Kingdom, [3]Consiglio Nazionale delle Ricerche (CNR), Istituto di Scienze Marine (ISMAR), Rome, Italy, [4]Department of Biology, National and Kapodistrian University of Athens, Athens, Greece

The world's oceans and seas are changing rapidly due to several natural and anthropogenic reasons. Among these, the largest and likely most threatening to marine life being the climate crisis and rising sea temperatures. Studying the dominant primary producers of most marine ecosystems, phytoplankton, and their response to these alterations is challenging, yet essential due to the critical role phytoplankton play in both the oceans and wider biosphere. Satellites are a crucial tool used to study phytoplankton but lack the timespan needed to accurately observe abundance patterns in response to climate change. Historical oceanographic data are increasingly being used to understand changes in the abundance of phytoplankton over the last century. Here, we retrace Secchi depth and Forel-Ule colour scale surveys performed during the "Pola" expeditions between 1890-1898 using contemporary satellite data, to assess changes in water colour and clarity (and by extension phytoplankton abundance) in the Red Sea and the Eastern Mediterranean Sea over the past century. The results show a significant greening of both regions investigated as well as a decrease in water clarity. The Red Sea Forel-Ule colour increased by 0.83 (± 0.08) with an average decrease in Secchi depth of 5.07 m (± 0.44). The Forel-Ule colour in the Eastern Mediterranean increased by 0.50 (± 0.07) and the historic Secchi depth readings were an average of 8.85 m (± 0.47) deeper than present day. Changes in Secchi depth between periods were greater than that which may have been caused by differences in the size of the Secchi disk used on the "Pola" expeditions, estimated using traditional Secchi depth theory. There was no clear change in seasonality of phytoplankton abundance and blooms, although winter months saw many of the largest changes in both measured variables. We discuss potential drivers for this change and the challenges and limitations of combining historical and modern datasets of water clarity and colour.

KEYWORDS

phytoplankton, Forel-Ule colour scale, Secchi disk, ocean colour, climate change

Introduction

Phytoplankton play a crucial role in both the marine environment and the wider biosphere. They contribute to approximately half of global organic net carbon uptake and oxygen production through photosynthesis and are essential for supporting marine life and fisheries (Field et al., 1998; Chassot et al., 2010). Climate change poses a significant threat to life on Earth and has wide ranging impacts in the marine environment (Doney et al., 2012). Human-induced greenhouse gases have been linked to increasing sea surface temperatures and acidity, expansion of oxygen minimum zones and increasing stratification, severely affecting marine life (IPCC, 2019). These changes are projected to continue through the 21st century, with further impacts on marine biomass and the global water cycle (Wilson et al., 2016; Bryndum-Buchholz et al., 2019). Climate change can affect phytoplankton in numerous ways. For example, through changes in the timing and magnitude of spring phytoplankton blooms, shifts in their community composition, both in terms of species and size structures, and changes in geographical and vertical distribution (Winder and Sommer, 2012; Brewin et al., 2022). Recording phytoplankton abundance is crucial for understanding these impacts and their effect on primary production and the marine ecosystem. The total chlorophyll-a concentration (Chl-*a*) is regularly used as an approximation of phytoplankton biomass owing to its ubiquitousness in phytoplankton and that it can be measured in both field and satellite applications (Sathyendranath et al., 2023).

Despite many studies investigating the impact of climate change on marine phytoplankton (e.g., Falkowski and Wilson, 1992; Boyce et al., 2010; Wernand and van der Woerd, 2010a; Wernand et al., 2013a; Henson et al., 2021) there is little consensus among the results. This lack of agreement is likely attributed to variations in data collection and analysis methodologies, as well as differences in spatial and temporal ranges that can result in certain biases (Brewin et al., 2023). An essential requirement for the investigation of phytoplankton biomass and productivity in response to climate change is the presence of a dataset with substantial time length. The time span required to accurately separate anthropogenic climate drivers from natural variability is estimated to be over 40 years (Henson et al., 2010). Although satellites can provide a global dataset of Chl-a measurements, derived from algorithms that relate radiometric measurements to Chl-a empirically or semi-analytically with an uncertainty in the open ocean (relative percentage difference when compared with *in situ* data) of around 30% (Tilstone et al., 2021), their recent employment renders them insufficient to provide the required temporal coverage (Sathyendranath et al., 2019). Thus, a combination of contemporary measurements with historical *in-situ* visual measurements, retrieved as a Chl-a proxy from apparatuses such as the Secchi disk, Forel-Ule colour scale or Continuous Plankton Recorder (Raitsos et al., 2013b; Wernand et al., 2013a), is needed to create a suitably long time series.

Secchi disk depth and Forel-Ule colour scale are two of the longest oceanographic datasets available, following bathymetry and sea surface temperature (Boyer et al., 2018). A Secchi disk is (typically) a 30 cm white disk which is lowered into the water and the depth at which the disk is no longer visible is proportional to the water clarity. This measurement is recorded as the Secchi disk depth (Secchi, 1865; Tyler, 1968; Wernand, 2010; Pitarch, 2020). The Forel-Ule colour scale was devised in the late 19th century by François Forel and amended by Willi Ule (Forel, 1890; Wernand and van der Woerd, 2010b). The scale consists of 21 different indexed colours, ranging from blue through green and yellow to brown. The measurement is recorded as the index of the colour in the scale that best matches that of the water. These historical techniques can provide information on many different components of marine waters and provide important biological information such as Chl-*a* concentrations and the depth of the euphotic zone (Lee et al., 2018; Wang et al., 2019; Ye and Sun, 2022). Specifically, Secchi depth and Forel Ule colour data are significant measurements to the oceanographic community, as they are among only a few techniques that have provided data on optical oceanography that is over a century in length. Furthermore, when the concentration of phytoplankton increases in the ocean, the water turns greener and becomes less transparent. Consequently, visual tools like the Secchi disk and Forel Ule colour scale can be used to estimate the concentration of Chl-*a* in the water.

A large amount of work has been performed to interrogate the effectiveness of these historical techniques and the robustness of the data obtained, for use in modern studies. Overall, studies agree that Secchi depth is a powerful predictor of Chl-*a* concentration, comparable to *in-situ* or satellite derived estimates (Boyce et al., 2012; Lee et al., 2018; Brewin et al., 2023). This is particularly true in open-ocean waters where optical variability is controlled principally by phytoplankton and its covarying material (Morel and Prieur, 1977). However, in more optically complex waters, optical variability is controlled by a variety of components that do not always covary in a predictable manner, such that the relationship between Secchi depth and Chl-*a* becomes more complex. The Forel-Ule colour scale has been examined spectrally and shown to have sufficient variation for capturing seasonal cycles at global scales (Wernand and van der Woerd, 2010b; Novoa et al., 2013), although the introduction of a value of zero for the clearest open oceans such as oligotrophic ocean gyres has been suggested (Pitarch et al., 2019a). This scale is also shown to be closely related to Chl-*a*, for all but the highest values and most complex waters (Pitarch et al., 2019a). These historical variables can be estimated using modern satellite-derived products with a high degree of confidence (uncertainty in Secchi depth of ~20% and Forel-Ule<1 for the dimensionless scale unit) providing a means to bridge historic and modern data (Lee et al., 2015; Pitarch et al., 2019a; Brewin et al., 2023). Together, the different methods provide a crucial, yet currently underutilised, tool for long term oceanographic studies.

Most studies that have used these data have focused on large spatial scales, often encompassing the entire global oceans (Boyce et al., 2010; Wernand et al., 2013a), reporting unclear trends, or differing localised trends within the global trend. This study aims to investigate changes over a smaller spatial scale, aiming to determine clearer local trends in well-sampled seas. The Eastern Mediterranean and Red Sea were two of the first marine regions to be systematically sampled during the 1890s by the Austro-

Hungarian "Pola" expeditions (Luksch, 1901; Wernand, 2010). These marginal seas have warmed at a rapid rate during the last few decades (Nykjaer, 2009; Cantin et al., 2010; Raitsos et al., 2010, 2011; Sisma-Ventura et al., 2014; Chaidez et al., 2017; Mohamed et al., 2019; Pastor et al., 2020; Pisano et al., 2020), however, there is limited work performed on trends in phytoplankton abundance since the 19th century, widely used as the start of anthropogenic climate change. This work therefore provides an important opportunity to investigate potential changes to the base of these ecosystems over the last 120 years.

In this work, we compare the large historic dataset of Secchi depth and Forel-Ule measurements collected in the 1890s on the Austro-Hungarian "Pola" expeditions, with modern measurements derived from remotely sensed satellite data. To minimise differences between the two datasets and optimise data utilisation, samples are matched in space and season. This dataset is used to answer the following two questions: 1) Has the clarity and colour of the water changed in the Eastern Mediterranean and Red Sea over the past century? And 2) Are there any distinct spatial and seasonal shifts in the clarity and colour of these marginal seas?

Methods

Study region

The Red Sea is an elongated basin connected to the open ocean at its southern point, through the Strait of Bab-el-Mandeb, interacting with the Gulf of Aden where seasonal water exchange occurs (Yao et al., 2014). The Red Sea experiences strong stratification in the hot summer months and undergoes increased vertical mixing during the winter months. This change in nutrient availability is a key driver in the seasonal cycles of phytoplankton (Raitsos et al., 2013a). Despite its ecological significance and the presence of threatened habitats and species, the Red Sea remains a largely understudied region of the world's oceans due to challenging environmental and political conditions (Berumen et al., 2013). The Eastern Mediterranean is a highly oligotrophic region, showcasing the lowest Chl-*a* concentrations recorded within the Mediterranean Sea (Simboura et al., 2019). Regardless of its oligotrophic nature, the area is characterized by a high level of species richness and habitat diversity, particularly in the Aegean Sea. Similar to the Red Sea, the seasonal primary productivity cycle is driven by the deepening of the mixed layer depth during winter, bringing nutrients upwards from deeper water into the sunlit layer (Simboura et al., 2019). Both these regions are facing many new and historic anthropogenic pressures, such as ship traffic, large coastal settlements and pollutants (Alahmadi et al., 2019; Simboura et al., 2019).

Measurements (both *in situ* and satellite) were collected from locations across the Eastern Mediterranean and Red Seas, ranging from the Ionian Sea and the coast of Salento to the southern end of the Red Sea (Figure 1).

Data sources

The historical dataset was collected aboard the navy transport vessel "Pola" during its cruises around the Eastern Mediterranean and Red Sea. This expedition was organised as an alternative to a circumnavigation and sampling from a range of waters, to instead focus on the systematic investigation of a particular region (Schefbeck, 1996). The ship was equipped with state-of-the-art

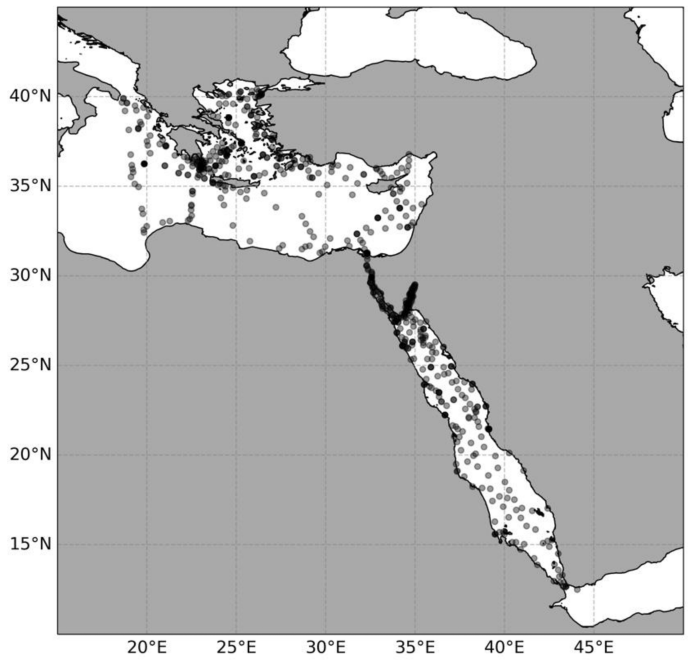


FIGURE 1
A map of all sample sites (black dots) included in the historic dataset, covering the Red Sea and Eastern Mediterranean.

survey equipment with scientists from the Viennese Academy of Sciences onboard, leading multiple oceanographic cruises in the waters of the Eastern Mediterranean between 1890 and 1894. However, following the success of these cruises, the area was expanded to include the Red Sea which was sampled during the years 1895-1898. The ship sampled a range of different oceanographic variables from depth soundings to isotherm and isohaline charts, as well as dredging samples of deep-sea life. The data used for this study were recorded by Josef Luksch, a marine physicist on board the expeditions. The methodology used for obtaining the Secchi Depth differed from the modern standardised method and instrument as standardisation didn't occur until decades after the Pola cruises. As such, the Secchi depths were recorded using a slightly larger disk of 45 cm diameter (with occasional use of a 2 m disk) deployed from the shady side of the ship. To measure ocean colour a scale of coloured liquid vials was created, ranging from 0 to 11, and the water colour was compared to these coloured vials. The recorded vial colour measurements were later compiled and digitised, and Forel-Ule colour values were estimated from the recorded vial numbers by Marcel Wernand. The final dataset covers the period 1890-1898 and comprises the translated Forel-Ule colour scale values, Secchi depth measurements, latitude and longitude coordinates, as well as the year, month, and day for each recorded observation.

Satellite data were obtained from the dataset created by Pitarch et al. (2021), containing monthly averaged maps of Forel-Ule scale and Secchi depth from 1998 to 2018 (Pitarch et al., 2019b). These values were calculated from satellite-obtained remote sensing reflectance with a monthly frequency and projected on a 2.5 arcmin rectangular grid, corresponding to approximately a 4 km spatial resolution at the equator and decreasing towards the poles (Pitarch et al., 2021). Full technical details about the algorithms used for this retrieval are found in van der Woerd and Wernand (2015) and Lee et al. (2015). From this dataset Forel-Ule and Secchi depth values were extracted with the minimum distance to each historical observations' coordinates and from the same month. This process aimed to ensure the closest spatial and temporal match possible, thereby minimising any effect this difference may have on the analysis. This matching was performed using a monthly scale instead of a coarser yearly or finer weekly for several reasons. Firstly, due to the lack of uniform sampling across the expedition a finer temporal scale would have resulted in fewer matched observations (as there are more gaps in satellite data due to clouds and swath coverage at weekly scales) making it more challenging to observe clear trends. Secondly, considering the large temporal difference of around 120 years between the datasets, matching them at any finer time scale than monthly is likely to have limited impact on our analysis.

The year 2008 was chosen for the retrieval of remote sensing data, in order to minimize the effect of other large scale global circumstances that are known to influence the regions, such as the El Niño-Southern Oscillation (ENSO) (Raitsos et al., 2015; Basterretxea et al., 2018). The period in which the original dataset was collected (1890-1899) was during a period of strong La Niña (Wolter and Timlin, 2011), similar to conditions experienced in 2008 (https://psl.noaa.gov/enso/mei/). The year 2008 also had very good satellite spatial coverage, with three ocean colour satellites (SeaWiFS, MERIS and MODIS-Aqua) all running (Yu et al., 2023), maximising potential coverage available in the Ocean Colour Climate Change Initiative (OC-CCI) merged ocean colour product used in Pitarch et al. (2019b). As a confirmation step, the analysis was also replicated on other years between 1998 and 2018, to investigate whether any significant trends observed in 2008 persisted across different years. Additionally, a monthly climatology of the data between 1998 and 2018 was created and analysed as an alternative option to using a single year.

Sun elevation is known to affect Secchi disk measurements in blue waters (Pitarch, 2020), and so to ensure this was not significantly affecting the results, sun angle values were calculated using the time of day and year data. The analysis was repeated by removing any values in blue waters (Forel-Ule< 2) with a sun angle greater than 70 degrees.

Statistical tests

To investigate the differences between the observed historical measurements and remote sensing estimates the following statistical tests were adopted. These tests are commonly used for comparisons between models and *in-situ* data (Brewin et al., 2023), and therefore the satellite data were treated as modelled data, and the historical measurements were treated as *in-situ* data.

The absolute Root Mean Square Difference (RMSD) was calculated according to

$$RMSD = \left[\frac{1}{N}\sum_{i=1}^{N}(X_i^S - X_i^M)^2\right]^{1/2}, \quad (1)$$

where, X is the variable and N is the number of samples. The superscript S denotes the satellite estimated variable and the superscript M denotes the measured historical variable.

The bias (δ) between the satellite estimation and measurement can be expressed according to

$$\delta = \frac{1}{N}\sum_{i=1}^{N}(X_i^S - X_i^M) \quad . \quad (2)$$

The absolute centre-pattern (or unbiased) Root Mean Square Difference ($RMSD_{CP}$) was calculated according to

$$RMSD_{CP} = \left(\frac{1}{N}\sum_{i=1}^{N}\left\{\left[X_i^S - \left(\frac{1}{N}\sum_{j=1}^{N}X_j^S\right)\right] - \left[X_i^M - \left(\frac{1}{N}\sum_{k=1}^{N}X_k^M\right)\right]\right\}^2\right)^{1/2}. \quad (3)$$

This describes the difference of the satellite values with respect to the measured values regardless of the average bias (i.e. the standard deviation). It can also be expressed as $RMSD_{CP} = (RMSD^2 - \delta^2)^{0.5}$.

These statistical tests (Equations 1–3) represent the difference between the two means (δ) and the differences in variability between the two distributions ($RMSD_{CP}$). Together, they provide substantial insights into the similarities between the two distributions.

The historic dataset was also checked for any irregular or unexpected results. Given the previously established inverse

relationship between Secchi depth and Forel-Ule colour (Wernand, 2011; Pitarch et al., 2019a), the presence of this relationship was verified in both the satellite and historical dataset. Paired t-tests were used throughout the study as the datapoints in both the historic and satellite data were obtained from the same location and were being directly compared to one another.

To examine monthly changes in Secchi depth, a climatology was calculated for both datasets, plotting the distribution and mean value for each month. This climatology was created using the total datasets instead of the direct comparisons used for the statistical testing. This was done to avoid losing any historical data from lack of remote sensing data availability. Climatology results are presented in "box and whisker" diagrams, chosen for their simplicity in representing the properties of the datasets investigated. Statistical tests were also run for each month, calculating δ, RMSD, $RMSD_{CP}$ values, as well as performing paired t-tests between the historical and satellite observations. T-tests were used as some months have a low number of samples and the t-test is designed for investigating differences in means between small sample sizes. This process was then repeated for the Forel-Ule colour scale.

Spatial differences were investigated by dividing the datapoints between the Red Sea and the Mediterranean Sea. Any data point recorded at a latitude greater than 31.26° North was treated as being in the Mediterranean Sea as this is the northernmost point of the Suez Canal, and those at a latitude lower than 29.9° North were treated as being in the Red Sea as this is the southern tip of the Suez Canal. Datapoints within the narrow Suez Canal were removed from the analysis due to a lack of satellite coverage ($n = 26$). The distribution of values was plotted on box plots along with the mean value. The statistical values δ, RMSD, $RMSD_{CP}$ were then calculated for each location for both Secchi depth and Forel-Ule scale, alongside paired t-tests. To test the effectiveness of the dataset in describing spatial patterns within the study area, spatially interpolated plots of the data were created (see Supplementary Figures S1, S2).

Analysis of uncertainty

To compute uncertainties in the differences in Secchi depth and Forel-Ule colour between the two historical periods, we first require estimates of uncertainty in the individual data points. Not a trivial task, but we could make some basic decisions on this. For the *in-situ* data (historical), we can estimate uncertainty based on our current understanding of uncertainty when collecting data at the same location by multiple individuals.

- For *in-situ* Secchi depth measurements, we used an uncertainty of 10%. This is based on the average percent deviation among individuals collecting data at locations at a series of stations in the Atlantic Ocean (see Section 2.3.2 of Brewin et al., 2023). This relative error was converted to an absolute error for each *in-situ* measurement.

- For *in-situ* Forel-Ule colour measurements, we used an absolute uncertainty of 1.0 (scale unit). This was based on typical uncertainties in Forel-Ule colour reported in Burggraaff et al. (2021). Though Burggraaff et al. (2021) report uncertainties can be higher than 1.0, this value seems reasonable considering studies quantifying standard deviations in Forel-Ule colour among individuals collecting data at a set location in the ocean, typically report lower values of around 0.5 (Wernand and van der Woerd, 2010b; Brewin et al., 2023b).

For the modern satellite data, we can estimate uncertainty based on satellite validation studies.

- For satellite Secchi depth measurements, we used an uncertainty of 19.3%. This was based on a validation of the Secchi depth algorithm used by Pitarch et al. (2021) in Lee et al. (2015). This relative error was converted to an absolute error for each satellite Secchi depth measurement.

- For satellite Forel-Ule colour measurements, we used an uncertainty of 0.81. This value (0.81) was derived from the root-mean-square-deviation in a comparison of remote-sensing reflectance-based estimates of Forel-Ule colour (using the same method of van der Woerd and Wernand (2015) and Novoa et al. (2014)) with *in-situ* data in the Atlantic. Specifically, we computed this as the square root of the sum of the squared bias (-0.38) and unbiased- root-mean-square-deviation (0.71), reported in Figure 7A of Brewin et al. (2023).

Making these assumptions, we computed the absolute uncertainties for each data point. We then estimated the absolute uncertainty in the difference (ϵ_d) between two corresponding data points at a given location, one historical [*in-situ*, denoted ϵ_h] and one modern [satellite, denoted ϵ_m]), by square rooting the sum of the squared estimates, such that

$$\epsilon_d = \sqrt{\epsilon_h^2 + \epsilon_m^2}\,. \tag{4}$$

Given the uncertainties in the differences (ϵ_d) for individual data point matches, and following the laws of error propagation, we then propagated these uncertainties to the average uncertainty ($\overline{\epsilon_d}$) among a dataset of length n, according to

$$\overline{\epsilon_d} = \sqrt{\frac{\sum_{i=1}^{n} \epsilon_{d,i}^2}{n^2}}\,. \tag{5}$$

Equations 4 and 5 were used to estimate the uncertainty ($\overline{\epsilon_d}$) in the mean differences between the two historical periods, for the two variables (Secchi depth and Forel-Ule colour). It is important to note that this approach assumes that the uncertainties associated with each data point are independent and normally distributed.

Results

Suitability of data

The δ, RMSD and $RMSD_{CP}$ values for Forel-Ule and Secchi depth data were calculated for each year (Table 1) to test whether results from the year 2008 differed from other years (1998-2018). Any value outside the range of 1st quartile - 1.5IQR to the 3rd quartile + 1.5IQR was treated as an outlier. For both Forel-Ule and Secchi depth the result for the year 2008 fall within this range (Secchi depth: 1st quartile = -7.495, median = -7.090, 3rd quartile = -6.611, IQR = 0.884; Forel-Ule: 1st quartile = 0.489, median = 0.564, 3rd quartile = 0.661, IQR = 0.171). Overall, the δ results are tightly distributed suggesting that the results from the comparison were not sensitive to the

selection of reference year (2008) from other years during the recent period (1998-2018). This analysis also shows that the climatology does not differ from the year selected for analysis. Filtered data (removing any values with a sun angle greater than 70 degrees and Forel-Ule< 2) also showed similar trends (Table 1).

Spatially interpolated plots of the data (see Supplementary Figures S1, S2) revealed the presence of known oceanographic features (oligotrophic and mesotrophic biomes) that were consistent with the 2008 climatology. Some unusual finer scale differences were present in the interpolated products, suggesting the spatial coverage of the data was not well suited to make conclusions at sub-basin scales.

Total dataset

After removing datapoints from the Suez Canal, a total of 385 historical Secchi Disk measurements and 723 Forel-Ule colour recordings were present, and a total of 643 satellite estimations for each variable. This enabled a total of 343 comparisons for the Secchi Disk data and 643 for the colour scale. Paired t-tests performed for the whole dataset revealed a significant decrease in Secchi depth and an increase in the Forel-Ule between the historic and modern data (Secchi depth: t=-20.38, d.f. = 342, $p< 0.01$, Forel-Ule: t=15.00, df=642, $p< 0.01$). The total bias for Secchi depth was found to be -7.50 m (uncertainty of ±0.34 m) and the bias for the Forel-Ule scale 0.64 (uncertainty of ±0.05), suggesting a decrease in Secchi depth of approximately 0.06 m y^{-1} and an increase in the Forel-Ule scale of 0.005 y^{-1} over the ~123-year period.

Relationships between Secchi depth and Forel-Ule were investigated separately for the historical data and for the satellite data used in this study, and a log-linear model was found to fit the data closest (R^2 = 0.767 for the historical data, R^2 = 0.940 for the satellite dataset, see Figure 2). The model fits were broadly consistent (similar parameters) between the two datasets, and consistent with those reported in previous works (Figure 2).

TABLE 1 The results of analysis on each year of satellite data, showing the δ, RMSD and $RMSD_{CP}$ for both Secchi depth and the Forel-Ule colour scale.

Secchi Depth					Forel-Ule Scale			
Year	δ	RMSD	$RMSD_{CP}$	Uncertainty in δ	δ	RMSD	$RMSD_{CP}$	Uncertainty in δ
1998	-6.77	9.62	6.83	0.34	0.49	1.13	1.02	0.05
1999	-6.01	9.16	6.91	0.35	0.40	1.09	1.01	0.05
2000	-7.60	10.09	6.63	0.34	0.60	1.22	1.07	0.05
2001	-6.22	9.27	6.87	0.34	0.49	1.14	1.03	0.05
2002	-7.36	10.30	7.21	0.34	0.66	1.33	1.16	0.05
2003	-7.65	10.01	6.46	0.33	0.70	1.31	1.11	0.05
2004	-7.09	9.71	6.63	0.34	0.68	1.33	1.14	0.05
2005	-7.35	9.87	6.58	0.34	0.73	1.34	1.12	0.05
2006	-7.63	10.35	6.99	0.33	0.64	1.25	1.07	0.05
2007	-8.01	10.34	6.53	0.33	0.78	1.40	1.16	0.05
2008	-7.50	10.13	6.82	0.34	0.63	1.29	1.12	0.05
Filtered	-8.26	10.87	7.06	0.39	0.58	1.28	1.14	0.06
2009	-6.90	9.77	6.91	0.34	0.68	1.31	1.12	0.05
2010	-5.84	9.30	7.24	0.35	0.53	1.26	1.14	0.05
2011	-6.57	9.31	6.59	0.35	0.55	1.23	1.09	0.05
2012	-7.72	10.21	6.68	0.34	0.62	1.30	1.14	0.05
2013	-6.61	9.69	7.09	0.35	0.48	1.07	0.96	0.05
2014	-6.49	9.57	7.03	0.35	0.49	1.11	1.00	0.05
2015	-7.38	10.15	6.97	0.34	0.52	1.09	0.96	0.05
2016	-6.94	9.58	6.60	0.35	0.48	1.09	0.97	0.05
2017	-7.25	9.97	6.85	0.34	0.56	1.12	0.97	0.05
2018	-7.03	10.24	7.45	0.38	0.53	1.11	0.98	0.06
Climatology	-6.96	9.54	6.52	0.33	0.64	1.28	1.11	0.05

Also included are the results of analysis on the calculated climatology and the chosen 2008 dataset with data affected by sun angle removed (denoted by row after 2008 named Filtered).

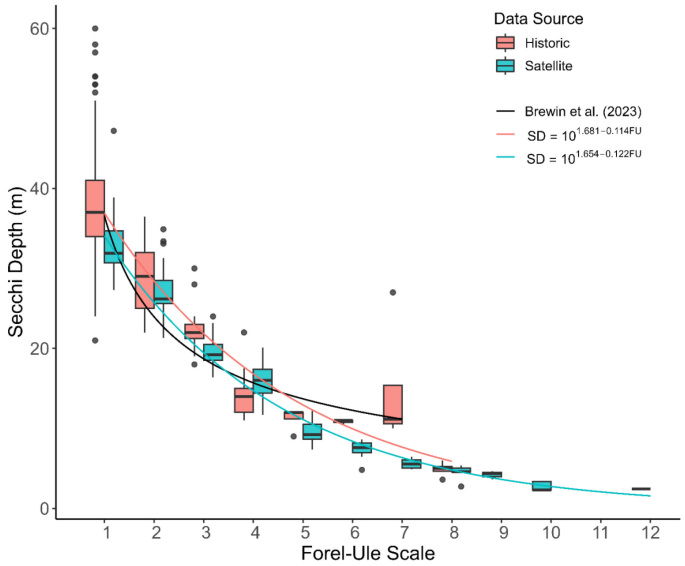


FIGURE 2
The relationship between observed Secchi disk and Forel-Ule scale. Boxes in red represent the historic data, and blue represents the satellite derived data. The relationship calculated by Brewin et al., 2023 is plotted in black (SD = $36.56FU^{-0.61}$ where SD represents Secchi depth and FU represents the Forel-Ule scale score). This relationship was calculated for Forel-Ule values up to 7 and is plotted for this range. Relationships were calculated for both the historical and satellite data used in this study and are plotted in red and blue respectively.

Changes by month

A total of 343 matchups of Secchi Depth were obtained, containing both historical and satellite measurements. Comparisons were possible for every month except May and June due to the lack of historical Secchi depth measurements. The distribution of measurements was uneven throughout the year, with some months having more samples than others (Table 2). The historic Secchi depth measurements were greater for every month measured (Figure 3). The greatest value was recorded in September, and the highest mean was in August. Overall, the trend across the year is similar between the modern and historical measurements, with lower values observed in the early and late months, and greater values in the late summer and early autumn.

Paired t-tests were performed between the datasets for each month, as well as δ, RMSD and $RMSD_{CP}$ calculations (Table 2).

TABLE 2 p – values, t – score, degrees of freedom, bias, lower and upper 95% confidence interval of the bias, RMSD, $RMSD_{CP}$ and uncertainties in the bias calculated for Secchi depths grouped by month.

Month	p	t	d.f.	δ	95% CI	RMSD	$RMSD_{CP}$	Uncertainty in δ
Jan	<0.01	-7.80	11	-11.46	[-8.22, -14.69]	12.45	4.87	1.24
Feb	0.034	-2.32	16	-2.96	[-0.25, -5.67]	5.91	5.11	1.00
Mar	<0.01	-4.21	6	-10.73	[-4.50, -16.96]	12.41	6.24	1.83
Apr	<0.01	-4.58	21	-4.31	[-2.35, -6.26]	6.09	4.31	0.99
May	NA	NA	NA	NA	NA	NA	NA	NA
Jun	NA	NA	NA	NA	NA	NA	NA	NA
Jul	<0.01	-7.26	26	-7.38	[-5.29, -9.47]	9.02	5.19	1.34
Aug	<0.01	-15.31	86	-9.36	[-8.15, -10.58]	10.94	5.67	0.76
Sep	<0.01	-12.44	104	-8.77	[-7.37, -10.17]	11.34	7.19	0.67
Oct	0.044	-2.11	29	-1.90	[-0.06, -3.75]	5.22	4.86	1.00
Nov	0.118	-1.66	15	-3.39	[0.96, -7.74]	8.60	7.91	1.32
Dec	<0.01	-4.45	19	-8.39	[-4.45, -12.34]	11.75	8.22	1.01

Results were calculated from paired t-test, except the bias, RMSD,$RMSD_{CP}$ and uncertainties in the bias. There is a significant difference between the two datasets in every month except November. Negative bias represents a decrease in Secchi depth between the historic and satellite data. NA refers to Not Applicable, d.f represents the number of possible comparisons.

There was a significant negative bias in the Secchi depth between the historic and satellite measurements in every month except November, although a decrease was still present. The greatest bias was observed in January, with historic measurements over 10 m deeper on average than the satellite calculated observations. The greatest $RMSD_{CP}$ values were during December, meaning that these observations had the highest range (widest distribution).

Of the 749 historical measurements of Forel Ule, 650 satellite retrieved estimates were obtained for the modern era. The monthly distribution of these results across a year are plotted in Figure 4. The distribution of Forel-Ule data was more even across the year than with the Secchi depth data. Over 25 comparisons were feasible for all months except May and June. A similar trend is observed over the year for the two datasets, with the variation plotted revealing the same peaks and troughs over the seasons. The months of May and June were poorly sampled due to a low number of historical measurements (n = 4) and no matched satellite sampling (n = 0).

Because of the discrete nature of the Forel-Ule scale, and the extreme positive skewness of the values recorded (2.12 and 2.01 for the historic and satellite results respectively), the bias was less distinct over the year than the Secchi disk results. However, there is still a significantly positive difference present for every month compared except March and November (Table 3). The greatest bias was observed in January, with the latter along with April and December displaying a bias exceeding 1, meaning that the satellite retrieved data was on average at least 1 higher in the historical Forel-Ule scale data.

Overall, similar trends are seen across the year for both the Secchi depth and Forel-Ule scale across the two datasets, with the highest and lowest values seen in the same months for both satellite and historical data. The trends between the two variables are also similar, with the deepest Secchi depths corresponding to lower values in the Forel-Ule scale, observed in the late summer/early autumn.

Changes by location

The comparison between historical and satellite data revealed a significant decrease in Secchi depth recorded in both the Mediterranean and the Red Sea between the historic and satellite data (Med: t=-20.59, df=219, p< 0.01, paired t-test; Red Sea: t=-8.08, df=122, p<0.01, paired t-test) (Figure 5). The mean absolute bias value was greater in the Mediterranean ($|\delta|$ = 8.85 m, uncertainty 0.47 m), indicating that, on average, the decrease in Secchi depth was more pronounced in this region than in the Red Sea ($|\delta|$ = 5.07 m, uncertainty 0.44 m), though both regions indicate a significant reduction in Secchi depth, and by proxy, phytoplankton Chl-a concentration. A wide range of bias scores were recorded for both locations, shown in Figure 5, suggesting increases in Secchi depth varied within the two regions (see also Supplementary Figures S1, S2).

There was a significant increase in the mean Forel-Ule recorded between the two sets of data for both the locations (Med: t=11.23, df=382, p< 0.01, paired t-test; Red Sea: t=9.74, df=266, p<0.01, paired t-test). The mean Forel-Ule values for the Mediterranean were 1.39 and 1.89 for the historical and satellite data respectively. In the Red Sea the mean Forel-Ule values were 2.67 and 3.50 for the historic and satellite data. The calculated bias value was greater for the Red Sea (δ = 0.83, uncertainty ±0.08) compared to the Mediterranean (δ = 0.50, uncertainty ±0.07). The greatest Forel-Ule increase recorded was 10, in the Red Sea, and the greatest decrease in the Forel-Ule scale was -7, in the Mediterranean.

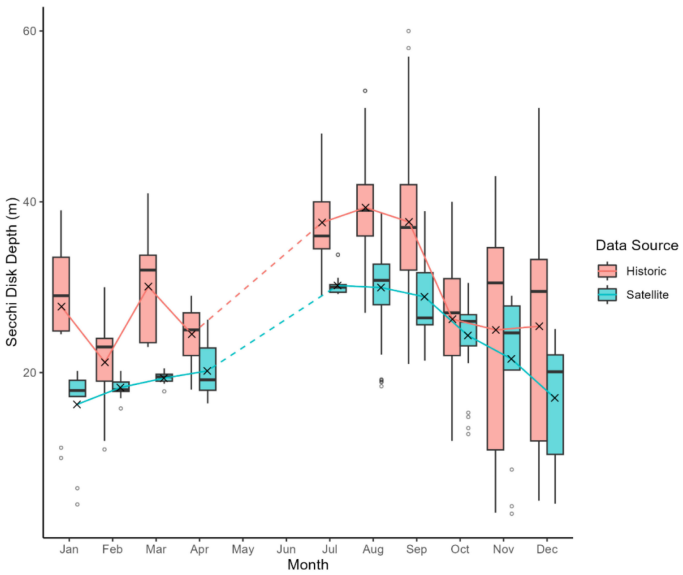


FIGURE 3
Boxplot comparing Secchi depth seasonal distribution between modern satellite data and *in-situ* historical data. Mean values are plotted as crosses on each box plot, and variations between the mean values are represented by coloured lines matching the box fill. Outliers are represented by empty circles above the limits represented by the lines outside the boxes. Dashed trendlines are drawn for months with no data. The mean and trendline are consistently higher in the historic data than in the satellite estimations.

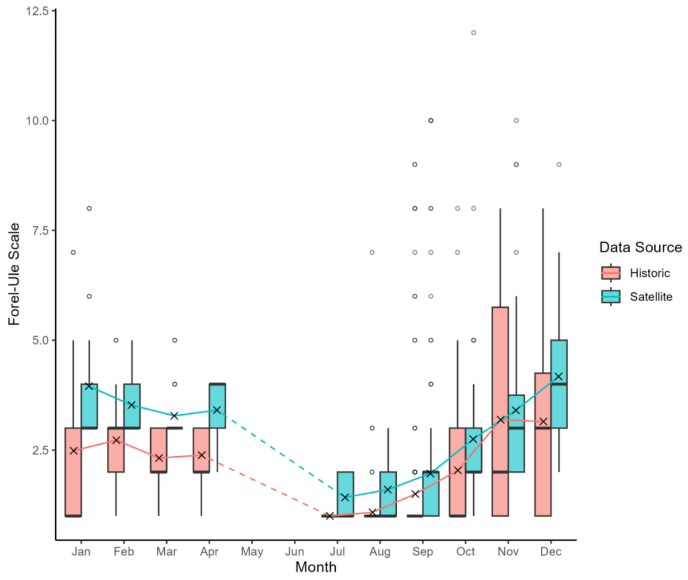


FIGURE 4
The distribution of Forel-Ule colour measurements grouped by month for both datasets. The means for each box are represented by a black cross, variations between the mean values are represented by coloured lines matching the box fill. The means for the satellite data are higher for every month and the highest mean results are recorded in the winter months, peaking in December. The lowest Forel-Ule values were observed during July and August for both datasets.

Discussion

Overall, and considering our estimates of uncertainty, our results suggest a greening of the Mediterranean and Red Sea, in support of previous results (Wernand et al., 2013a), and a decrease in water clarity. This greening, although more pronounced in the Red Sea, was present in both regions. The seasonality in both the colour and clarity of the water was relatively consistent between the historical and modern datasets, as was the relationship between Secchi depth and Forel-Ule (Figure 2). The presence of similar differences between the historical and modern datasets, irrespective of the satellite reference years tested, provides confidence in the veracity of the trends reported.

TABLE 3 p – values, t – score, degrees of freedom, bias, lower and upper 95% confidence interval of the bias, RMSD, $RMSD_{CP}$ and uncertainties in the bias calculated for the Forel-Ule scale grouped by month.

Month	p	t	d.f.	δ	95% CI	RMSD	$RMSD_{CP}$	Uncertainty in δ
Jan	<0.01	6.44	32	1.47	[1.00, 1.93]	1.96	1.29	0.22
Feb	<0.01	4.74	39	0.80	[0.46, 1.14]	1.32	1.05	0.20
Mar	0.07	1.91	25	0.65	[-0.05, 1.36]	1.83	1.71	0.26
Apr	<0.01	6.88	38	1.03	[0.72, 1.33]	1.38	0.92	0.20
May	NA	NA	NA	NA	NA	NA	NA	NA
Jun	NA	NA	NA	NA	NA	NA	NA	NA
Jul	<0.01	5.67	44	0.42	[0.27, 0.57]	0.65	0.49	0.19
Aug	<0.01	7.87	144	0.52	[0.39, 0.65]	0.94	0.79	0.11
Sep	<0.01	7.65	182	0.48	[0.36, 0.60]	0.98	0.85	0.10
Oct	<0.01	3.35	55	0.73	[0.29, 1.17]	1.78	1.62	0.18
Nov	0.45	0.77	41	0.21	[-0.35, 0.78]	1.81	1.79	0.20
Dec	<0.01	6.18	39	1.03	[0.69, 1.36]	1.46	1.04	0.20

d.f. represents the number of possible comparisons.
Results were calculated from paired t-test, except the bias, RMSD, $RMSD_{CP}$ and uncertainty in the bias. A significant difference between the datasets was found for every month except March and November. NA refers to Not Applicable.

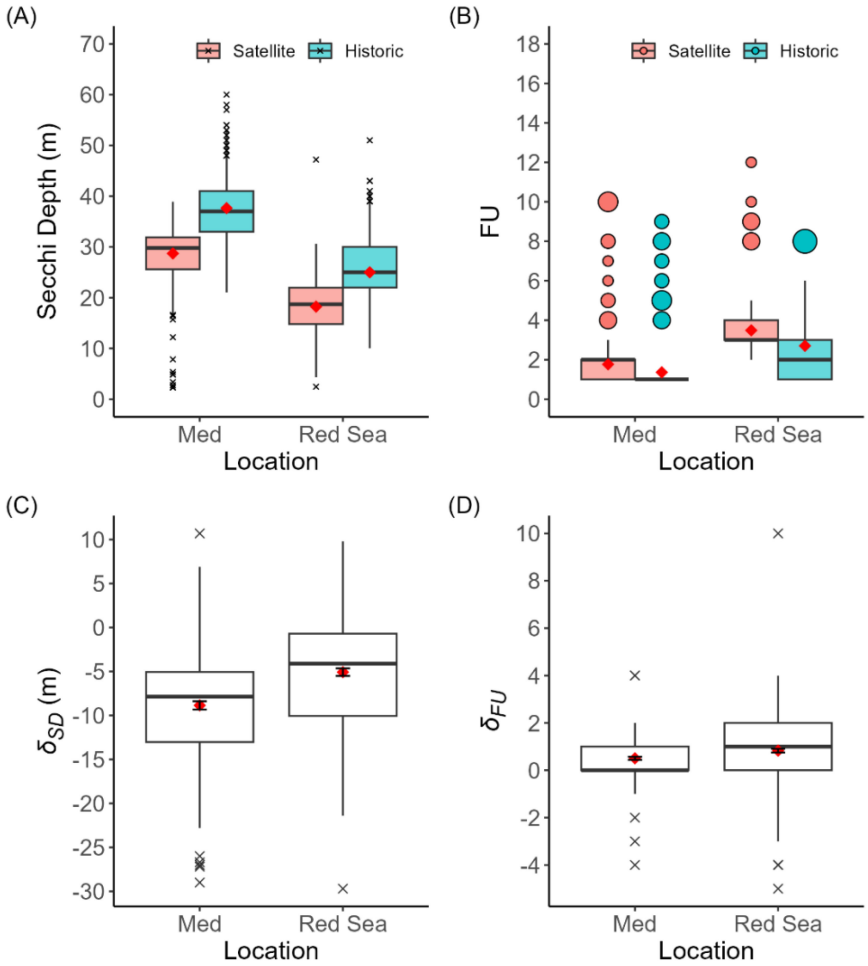


FIGURE 5
Boxplots of the distribution of measurements and biases for the two variables. Plots **(A, B)** display the distribution of measurements of Secchi depth and Forel-Ule scale respectively, with the boxplots grouped by location and subdivided by the data source. Plots **(C, D)** represent the distribution of bias scores for Secchi depth and Forel-Ule respectively. Subscript SD indicates the values displayed are calculated for Secchi depth, and subscript FU represents values calculated for the Forel-Ule scale. Across the plots the red diamond represents the mean of values plotted, and crosses plotted outside the boxes represent outliers excluding plot **(B)**. For plot **(B)** points were used to represent outliers, with the size of the point equivalent to the number of points. This was to avoid not representing any data due to the discrete nature of the Forel-Ule scale. Error bars on plots **(C, D)** represent the uncertainty around the bias calculations.

Changes in colour (Forel-Ule)

The increase in the mean Forel-Ule calculated for the Mediterranean in this study is lower than reported previously in Wernand et al. (2013a). However, this may be due to the strict spatial data filtering process used in their study (samples within 100 km of the coast were excluded) which also included a low amount of data from intermediate years.

Although the absolute increases for the Forel-Ule scale in both locations are small, they can indicate a large change in Chl-*a*. For open, oligotrophic waters with lower Forel-Ule values there is an exponential relationship between the colour scale and Chl-*a* (Wernand et al., 2013b; Pitarch et al., 2019a). Using the equation from Brewin et al. (2023), to convert Forel-Ule to Chl-a, the mean Chl-*a* concentration may have increased on average from 0.24 mg m^{-3} to 0.34 mg m^{-3}. The lack of high Forel-Ule scale values, typically observed in coastal or estuarine regions and shelf seas (Garaba et al., 2015; Li et al., 2021), indicate that phytoplankton are likely the dominate factor driving the change in ocean colour and clarity in our dataset. However, further verification is required to ascertain if such a large increase in Chl-a over this period is real.

Changes in clarity (Secchi depth)

The Secchi depth data broadly supports the trends revealed in the colour scale data. The decrease in water clarity observed in the modern dataset provides further evidence for an increase in optically active components in the water, and, when considered along with the Forel-Ule results, implies an increase in phytoplankton abundance and Chl-*a*. Using a blend of Secchi depth measurements and *in-situ* Chl-*a*, Boyce et al. (2010) reported a decrease in Chl-*a* in the easternmost Mediterranean Levantine Sea and Northern Red Sea, in contrast to our results, and

an increase in the Southern Red Sea and the Aegean Sea. Differences between studies may possibility be caused by differences in the spatial grouping of data, with the Boyce et al. (2010) study including the Gulf of Aden not sampled in our study, as well as differences in the datasets used (their study did not utilise the historical dataset used here). Boyce et al. (2010) also applied one blanket relationship between Secchi depth and Chl-*a* for all the world's seas, when this relationship differs between regions. Later work by Boyce et al. (2012) included Forel-Ule colour scale values, and a larger sample of Secchi depth and Chl-*a* measurements, however, excluded Forel-Ule values below 2 due to the saturation of the scale at this point. This led to the exclusion of a substantial portion of historical data for regions such as the Eastern Mediterranean and Red Sea and so trends were not reported in either region.

Seasonality

We observed no clear evidence for a change in phytoplankton phenology, with both the historical and satellite data following a similar seasonal trend. Both the Red Sea and Eastern Mediterranean experience the highest phytoplankton and Chl-*a* concentrations between December and April (Gittings et al., 2018; Salgado-Hernanz et al., 2019) consistent with the high Forel-Ule values and lower Secchi depths observed in those months. However, the greatest differences between historical and modern datasets were observed in these months, suggesting a possible increase in the magnitude of blooms, disproportionate to the increase seen across the dataset. It is worth considering that studies that have reported a change in timing in phytoplankton blooms report changes in the scale of weeks rather than months (Gittings et al., 2018) and so any change may potentially be masked by the coarser temporal scale used in this study. Furthermore, our uncertainty analysis does not consider uncertainty in seasonal changes in atmospheric properties that could be influencing atmospheric correction and consequently, satellite estimates of Secchi depth and Forel-Ule colour.

Spatial differences

Whilst both the Red Sea and Eastern Mediterranean are known to be oligotrophic, the southern Red Sea is characterised by a higher productivity than the northern area, due to the intrusion of nutrient-rich water masses from the Indian Ocean (Raitsos et al., 2015). Nonetheless, the Secchi depth data from the Mediterranean did include some lower values, suggesting that whilst predominantly unproductive, there are hotspots of productivity. The northern Aegean Sea and southern coastline of the Levantine Basin at the mouth of the Nile Delta are two areas of the Mediterranean sampled that typically have a high Chl-*a* concentration (Tsiaras et al., 2012; Kotta and Kitsou, 2019). The changes between the historic and satellite data for both variables show broadly the same trend, however, the decrease in Secchi depth was found to be greater in the Mediterranean than in the Red Sea, whilst the Forel-Ule score increased slightly more in the Red Sea than the Mediterranean (Figure 5). Finer spatial scale analysis revealed some spatial differences within the two regions (see Supplementary Figures S1, S2) but was limited by lower numbers of observations.

Potential drivers

Both the Red Sea and Eastern Mediterranean Sea are largely oligotrophic systems, highly stratified with plenty of light, meaning phytoplankton abundance at the surface is limited primarily by the availability of nutrients (Krom et al., 1991; Raitsos et al., 2013a), though light limitation can occur during some periods (Bellacicco et al., 2016). As a result of these conditions, an increase in phytoplankton is often associated with an increase in nutrient availability (Marañón et al., 2018). This increase in nutrients can come from several sources, including an increased degree of mixing of the water column by physical forcing, enabling access to nutrient-rich deep water, or horizontal advection of coastal nutrients from eddies (Raitsos et al., 2013a; 2017), or other external inputs on nutrients (Churchill et al., 2014), for example, from aeolian deposition or increased nitrogen fixation. In the Red Sea, a decrease in wind and wave heights have been reported (Langodan et al., 2017) as well as increases in temperature (Raitsos et al., 2011), which are likely to drive further stratification. Thus, increasing vertical mixing is unlikely to be the key driver behind the Forel-Ule increased values in the Red Sea. However, Raitsos et al. (2015) revealed that ENSO positive phases (and its extreme i.e., El Niño) lead to an increase in wind-driven advection of fertile waters from the Indian Ocean into the Red Sea, ultimately showing an increase in phytoplankton biomass during positive ENSO years (usually warmer years). In addition, Cai et al. (2014) reported that greenhouse warming has led to more frequent and abrupt occurrence of extreme El Niño events. Thus, changes in this climate index could potentially provide an explanation for the increase in phytoplankton abundance observed in this study in the Red Sea. Nonetheless, such links with El Niño are speculative and require further substantiation, since the data used in this study is not of sufficient temporal resolution to quantify El Niño related effects.

Another potential mechanism for the increase in nutrient availability in the Eastern Mediterranean is runoff from human activity and coastal settlements and subsequent nutrient enrichment. Additionally, aquaculture in the northern and southern Red Sea has been linked to nutrient enrichment in this area (Loya et al., 2004; Gokul et al., 2020), as have untreated effluent discharges due to inefficient or above capacity treatment plants (Jessen et al., 2013). In nutrient limited systems, this discharge may result in an increase in phytoplankton abundance, and in extreme cases eutrophication. Drivers of this observed change are likely to be similar in the Eastern Mediterranean due to similar oceanographic and nutrient conditions (Siokou-Frangou et al., 2010). In some areas of the sampled Mediterranean, eutrophication has been reported, primarily in coastal areas close to large urban centres (Pavlidou et al., 2015).

Limitations of historical methods

There are limitations in the usage of historic Forel-Ule data. The first is the saturation of the scale at a value of one, which makes it difficult to observe small variations in colour in oligotrophic systems. Recent analysis has recommended the creation and addition of a zero value to the scale (Pitarch et al., 2019a), enabling better identification of trends even in the bluest waters such as the oligotrophic gyres. This is not possible using historical data as we are limited to what was sampled originally. The second factor is the presence of differences when recording the Forel-Ule colour over a Secchi disk (as is often used in historic or *in-situ* measurements), or against the water column alone, as retrieved from satellites (Pitarch, 2017). This is not an issue in this study as the original cruise reports describe comparing the coloured solutions directly to the water column, rather than over a Secchi disk. The historical data used here also contains more observations of the Forel-Ule scale than Secchi depth, confirming that the colour scale is likely to have been observed over the water column directly. Recent optical modelling applied to data from the Atlantic Ocean has suggested that most historical Forel-Ule data were likely collected over the water column alone, and not over a Secchi disk (Brewin et al., 2023).

There may also be systematic differences in the historical methods used in these studies. The Secchi depth collected by Josef Luksch was collected primarily using a disk of 45 cm, as opposed to the standard 30 cm disk used in modern studies (Wernand, 2010). The original cruise performed by Secchi examined differences in visibility of disks measuring 43 cm and 237 cm and revealed that larger disks are visible at deeper depths, particularly in clear waters such as in this study (Secchi, 1865; Pitarch, 2020). Traditional Secchi depth theory (Preisendorfer, 1986) includes the influence of disk size on Secchi depth. Using a standard set of parameters as reported by Preisendorfer (1986), and for a Secchi depth of 24 m using a 30 cm disk (average Secchi depth of satellite data in this study for the modern period) and assuming a solar zenith angle of 10 degrees and wind speed of 10 ms^{-1}, we estimate the Secchi depth to be around 4.2 m deeper using a 45 cm disk (size used on the "Pola" expeditions). Though significant, and certainly accounting for some of the decreasing Secchi depth trend between period, it does not account for the large differences observed (average of 7.7m +/- 0.34). Furthermore, more recent work has suggested the influence of disk size on Secchi depth can be much smaller than traditional theory suggests (Hou et al., 2007). Further work evaluating the difference in visibility of Secchi disks of variable sizes is recommended.

Implications of this study

This study is unique in analysing direct pairs of observations from historic and satellite estimations, by 'resampling' the original locations sampled by Luksch in the 19th century. Whilst this means that less data were used than in studies using spatially grouped means (Boyce et al., 2010; Wernand et al., 2013b) it allowed a more direct comparison by minimising spatial and temporal differences in sampling between historical and modern data. Overall, our analysis provides some evidence for an increase in phytoplankton abundance over the past century in the Red and Eastern Mediterranean Seas.

The observed decrease in Secchi depth has further ecological implications beyond an increase in phytoplankton. This decrease in Secchi depth would mean that light is more concentrated in the upper layer, which may have caused warming and an increase of stratification. Lower water transparency has direct implications for benthic habitats through changes in light availability for photosynthesis. The bodies of water examined contain coral reef systems (Berumen et al., 2013) and seagrass beds which may have been impacted (Simboura et al., 2019). Decreasing light availability, in conjunction with other stressors, such as rising temperatures or anthropogenic disturbances, may inhibit the growth and detrimentally affect the health of these benthic ecosystems (Grech et al., 2012).

Our results suggest changes may have happened to the baseline of the ecosystems of the Red Sea and Eastern Mediterranean over the past century through an increase in productivity. Increased sampling is required to continue monitoring these baselines and allow for effective management decisions to limit negative ecosystem impacts. Satellite sensing is believed to be the future for monitoring large bodies of water, yet studies such as this prove the need for further utilisation of the wealth of historical oceanographic data buried in archives. As such, the discovery, digitisation, and analysis of these historical datasets, alongside the evaluation of their power to estimate crucial variables such as Chl-*a*, including rigorous estimates of measurement uncertainty, may help understand long-term anthropogenic impacts on our seas.

Data availability statement

The original contributions presented in the study are included in the article/Supplementary Material. Further inquiries can be directed to the corresponding author.

Author contributions

JH: Formal analysis, Investigation, Methodology, Software, Validation, Visualization, Writing – original draft, Writing – review & editing. RB: Conceptualization, Formal analysis, Funding acquisition, Investigation, Methodology, Project administration, Resources, Supervision, Writing – review & editing. JP: Conceptualization, Data curation, Funding acquisition, Investigation, Methodology, Resources, Supervision, Writing – review & editing. DR: Funding acquisition, Supervision, Writing – review & editing.

Funding

The author(s) declare financial support was received for the research, authorship, and/or publication of this article. RB is supported by a UKRI Future Leader Fellowship (MR/V022792/1) and by the the Gordon and Betty Moore Foundation (GBMF11171).

JP acknowledges funding by the European Union through the NextGenerationEU Program, Project IR0000032 – ITINERIS - Italian Integrated Environmental Research Infrastructures System - CUP B53C22002150006. DR acknowledges funding by the European Union HORIZON EUROPE program ACTNOW: Advancing understanding of Cumulative Impacts on European marine biodiversity, ecosystem functions and services for human wellbeing (Grant no. 101060072).

Acknowledgments

We acknowledge all those involved in the collection of data used in this study, particularly those involved in the "Pola" expeditions in the late 19th century. We are strongly indebted to early work by Marcel Wernand who pioneered the mining of these historical data allowing us to perform this analysis. This work was supported by a MSci project in Marine Biology at the University of Exeter, Penryn, Cornwall, and we acknowledge all the staff and students on that programme who helped make this work possible. We thank Dionysia Rigatou for reading an early version of our manuscript and providing useful textual edits. We thank the reviewers for insightful comments that helped us improve our paper.

Conflict of interest

The authors declare that the research was conducted in the absence of any commercial or financial relationships that could be construed as a potential conflict of interest.

Publisher's note

All claims expressed in this article are solely those of the authors and do not necessarily represent those of their affiliated organizations, or those of the publisher, the editors and the reviewers. Any product that may be evaluated in this article, or claim that may be made by its manufacturer, is not guaranteed or endorsed by the publisher.

Supplementary material

The Supplementary Material for this article can be found online at: https://www.frontiersin.org/articles/10.3389/fmars.2024.1358899/full#supplementary-material

References

Alahmadi, S., Al-Ahmadi, K., and Almeshari, M. (2019). Spatial variation in the association between NO2 concentrations and shipping emissions in the Red Sea. *Sci. Total Environment* 676, 131–143. doi: 10.1016/j.scitotenv.2019.04.161

Basterretxea, G., Font-Muñoz, J. S., Salgado-Hernanz, P. M., Arrieta, J., and Hernández-Carrasco, I. (2018). Patterns of chlorophyll interannual variability in Mediterranean biogeographical regions. *Remote Sens. Environment* 215, 7–17. doi: 10.1016/j.rse.2018.05.027

Bellacicco, M., Volpe, G., Colella, S., Pitarch, J., and Santoleri, R. (2016). Influence of photoacclimation on the phytoplankton seasonal cycle in the Mediterranean Sea as seen by satellite. *Remote Sens. Environ.* 184, 595–604. doi: 10.1016/j.rse.2016.08.004

Berumen, M. L., Hoey, A. S., Bass, W. H., Bouwmeester, J., Catania, D., Cochram, J. E. M., et al. (2013). The status of coral reef ecology research in the Red Sea. *Coral Reefs* 32, 737–748. doi: 10.1007/s00338-013-1055-8

Boyce, D. G., Lewis, M. R., and Worm, B. (2010). Global phytoplankton decline over the past century. *Nature* 466, 591–596. doi: 10.1038/nature09268

Boyce, D. G., Lewis, M., and Worm, B. (2012). Integrating global chlorophyll data from 1890 to 2010. *Limnol. Oceanogr.: Methods* 10, 840–852. doi: 10.4319/lom.2012.10.840

Boyer, T. P., Baranova, O. K., Coleman, C., Garcia, H. E., Locarnini, R. A., Mishonov, A. V., et al. (2018). *World Ocean Database 2018. A.V. Mishonov, Technical Ed. NOAA Atlas NESDIS 87*. Available online at: https://www.ncei.noaa.gov/sites/default/files/2020-04/wod_intro_0.pdf.

Brewin, R. J. W., Dall'Olmo, G., Gittings, J., Sun, X., Lange, P. K., Raitsos, D. E., et al. (2022). A conceptual approach to partitioning a vertical profile of phytoplankton biomass into contributions from two communities. *J. Geophysical Res.: Oceans* 127, e2021JC018195. doi: 10.1029/2021JC018195

Brewin, R. J. W., Pitarch, J., Dall'Olmo, G., van der Woerd, H. J., Lin, J., Sun, X., et al. (2023). Evaluating historic and modern optical techniques for monitoring phytoplankton biomass in the Atlantic Ocean. *Front. Mar. Sci.* 10. doi: 10.3389/fmars.2023.1111416

Brewin, R. J. W., Pitarch, J., Dall'Olmo, G., van der Woerd, H. J., Lin, J., Sun, X., et al. (2023b). *Modern and traditional optical measurements, and environmental data, collected on four Atlantic Meridional Transect cruises between 2013 and 2018* (NERC EDS British Oceanographic Data Centre NOC). doi: 10.5285/f3198e10-faf3-1525-e053-6c86abc0d2f6

Bryndum-Buchholz, A., Tittensor, D. P., Blanchard, J. L., Cheung, W. W. L., Coll, M., Galbraith, E. D., et al. (2019). Twenty-first-century climate change impacts on marine animal biomass and ecosystem structure across ocean basins. *Glob. Change Biol.* 25, 459–472. doi: 10.1111/gcb.14512

Burggraaff, O., Panchagnula, S., and Snik, F. (2021). Citizen science with colour blindness: A case study on the Forel-Ule scale. *PloS One* 16, e0249755. doi: 10.1371/journal.pone.0249755

Cai, W., Borlace, S., Lengaigne, M., van Rensch, P., Collins, M., Vecchi, G., et al. (2014). Increasing frequency of extreme El Niño events due to greenhouse warming. *Nat. Clim Change* 4, 111–116. doi: 10.1038/nclimate2100

Cantin, N. E., Cohen, A. L., Karnauskas, K. B., Tarrant, A. M., and McCorkle, D. C. (2010). Ocean warming slows coral growth in the central Red Sea. *Science* 329, 322–325. doi: 10.1126/science.1190182

Chaidez, V., Dreano, D., Agusti, S., Duarte, C. M., and Hoteit, I. (2017). Decadal trends in Red Sea maximum surface temperature. *Sci. Rep.* 7, 8144. doi: 10.1038/s41598-017-08146-z

Chassot, E., Bonhommeau, S., Dulvy, N. K., Mé lin, F., Watson, R., Gascuel, D., et al. (2010). Global marine primary production constrains fisheries catches. *Ecol. Lett.* 13, 495–505. doi: 10.1111/j.1461-0248.2010.01443.x

Churchill, J. H., Bower, A. S., McCorkle, D. C., and Abualnaja, Y. (2014). The transport of nutrient-rich Indian Ocean water through the Red Sea and into coastal reef systems. *J. Mar. Res.* 72, 165–181. doi: 10.1357/002224014814901994

Doney, S. C., Ruckelhaus, M., Duffy, J. E., Barry, J. P., Chan, F., English, C. A., et al. (2012). Climate change impacts on marine ecosystems. *Annu. Rev. Mar. Sci.* 4, 11–37. doi: 10.1146/annurev-marine-041911-111611

Falkowski, P., and Wilson, C. (1992). Phytoplankton productivity in the North Pacific Ocean since 1900 and implications for absorption of anthropogenic CO_2. *Nature* 358, 741–743. doi: 10.1038/358741a0

Field, C. B., Behrenfeld, M. J., Randerson, J. T., and Falkowski, P. G. (1998). Primary production of the biosphere: integrating terrestrial and oceanic components. *Science* 281, 237–240. doi: 10.1126/science.281.5374.237

Forel, F. A. (1890). "Une nouvelle forme de la gamme de couleur pour l'étude de l'eau des lacs," in *Archives des Sciences Physiques et Naturelles/Société de Physique et d'Histoire Naturelle de Genève*, vol. 6. , 25.

Garaba, S. P., Voβ, D., and Zielinski, O. (2015). Physical, bio-optical state and correlations in North–Western European shelf seas. *Remote Sensing* 6, 5042–5066. doi: 10.3390/rs6065042

Gittings, J. A., Raitsos, D. E., Krokos, G., and Hoteit, I. (2018). Impacts of warming on phytoplankton abundance and phenology in a typical tropical marine ecosystem. *Sci. Rep.* 8, 2240. doi: 10.1038/s41598-018-20560-5

Gokul, E. A., Raitsos, D. E., Gittings, J. A., and Hoteit, I. (2020). Developing an atlas of harmful algal blooms in the Red Sea: Linkages to local aquaculture. *Remote Sensing* 12, 3695. doi: 10.3390/rs12223695

Grech, A., Chartrand-Miller, K., Erftmeijer, P., Fonseca, M., McKenzie, L., Rasheed, M., et al. (2012). A comparison of threats, vulnerabilities and management approaches in global seagrass bioregions. *Environ. Res. Letters* 7, 24006. doi: 10.1088/1748-9326/7/2/024006

Henson, S. A., Cael, B. B., Allen, S. R., and Dutkiewicz, S. (2021). Future phytoplankton diversity in a changing climate. *Nat. Commun.* 12, 1–8. doi: 10.1038/s41467-021-25699-w

Henson, S. A., Sarmiento, J. L., Dunne, J. P., Bopp, L., Lima, I., Doney, S. C., et al. (2010). Detection of anthropogenic climate change in satellite records of ocean chlorophyll and productivity. *Biogeosciences* 7, 621–640. doi: 10.5194/bg-7-621-2010

Hou, W., Lee, Z., and Weidemann, A. D. (2007). Why does the Secchi disk disappear? An imaging perspective. *Optics Express* 15, 2791–2802. doi: 10.1364/OE.15.002791

IPCC (2019). *IPCC Special Report on the Ocean and Cryosphere in a Changing Climate*. eds. H.-O. Pörtner, D. C. Roberts, V. Masson-Delmotte, P. Zhai, M. Tignor, E. Poloczanska, et al. (Cambridge, UK and New York, NY, USA: Cambridge University Press), 755. doi: 10.1017/9781009157964

Jessen, C., Roder, C., Villa Lizcano, J. F., Voolstra, C. R., and Wild, C. (2013). *In-situ* effects of simulated overfishing and eutrophication on benthic coral reef algae growth, succession, and composition in the central Red Sea. *PloS One* 8, e66992. doi: 10.1371/journal.pone.0066992

Kotta, D., and Kitsou, D. (2019). Chlorophyll in the Eastern Mediterranean sea: correlations with environmental factors and trends. *Environments* 6, 98. doi: 10.3390/environments6080098

Krom, M. D., Kress, N., Brenner, S., and Gordon, L. I. (1991). Phosphorus limitation of primary productivity in the eastern Mediterranean Sea. *Limnol. Oceanogr.* 36, 424–432. doi: 10.4319/lo.1991.36.3.0424

Langodan, S., Cavaleri, L., Vishwanadhapalli, Y., Pomaro, A., Bertotti, L., and Hoteit, I. (2017). The climatology of the Red Sea – part 1: the wind. *Int. J. Climatol.* 37, 4509–4517. doi: 10.1002/joc.5103

Lee, Z., Shang, S., Du, K., and Wei, J. (2018). Resolving the long-standing puzzles about the observed Secchi depth relationships. *Limnol. Oceanogr.* 63, 2321–2336. doi: 10.1002/lno.10940

Lee, Z., Shang, S., Hu, C., Du, K., Weidemann, A., Hou, W., et al. (2015). Secchi disk depth: A new theory and mechanistic model for underwater visibility. *Remote Sens. Environment* 169, 139–149. doi: 10.1016/j.rse.2015.08.002

Li, M., Sun, Y., Li, X., Cui, M., and Huang, C. (2021). An improved eutrophication assessment algorithm of estuaries and coastal waters in Liaodong bay. *Remote Sensing* 13, 3867. doi: 10.3390/rs13193867

Loya, Y., Lubinevsky, H., Rosenfield, M., and Kramarsky-Winter, E. (2004). Nutrient enrichment caused by in *situ* fish farms at Eilat, Red Sea is detrimental to coral reproduction. *Mar. Pollut. Bulletin* 49, 344–353. doi: 10.1016/j.marpolbul.2004.06.011

Luksch, J. (1901). *Expeditionen SM Schiff "Pola im Mittelländischen, Ägäischen und Rothen Meere in den Jahren 1890–1898. Wissenschaftliche Ergebnisse XIX. Untersuchungen über die Transparenz und Farbe de Seewassers. Berichte der Commission für Oceanographische Foeschungen, Collectiv-Ausgabe aus dem LXIX Bande der Denkschriften Kaiserlichen Akademie der Wissenschafte, A. Forschungen im Rothen Meere, B. Forschungen im Östlichen Mittelmeere*, 400–485.

Marañón, E., Lorenzo, M. P., Cermeño, P., and Mouriño-Carballido, B. (2018). Nutrient limitation suppresses the temperature dependence of phytoplankton metabolic rates. *ISME J.* 12, 1836–1845. doi: 10.1038/s41396-018-0105-1

Mohamed, B., Abdallah, A. M., Alam El-Din, K., Nagy, H., and Shaltout, M. (2019). Inter-annual variability and trends of sea level and sea surface temperature in the Mediterranean Sea over the last 25 years. *Pure Appl. Geophysics* 176, 3787–3810. doi: 10.1007/s00024-019-02156-w

Morel, A., and Prieur, L. (1977). Analysis of variations in ocean color. *Limnol. Oceanogr.* 22, 709–722. doi: 10.4319/lo.1977.22.4.0709

Novoa, S., Wernand, M. R., and van der Woerd, H. J. (2013). The Forel-Ule scale revisited spectrally: preparation protocol, transmission measurements and chromaticity. *J. Of Eur. Optical Soc. - Rapid Publications* 8, 13057. doi: 10.2971/jeos.2013.13057

Novoa, S., Wernand, M. R., and van der Woerd, H. J. (2014). The modern Forel-Ule scale: a 'do-it-yourself' colour comparator for water monitoring. *J. Of Eur. Optical Soc. - Rapid Publications* 9, 1–10. doi: 10.2971/jeos.2014.14025

Nykjaer, L. (2009). Mediterranean Sea surface warming 1985–2006. *Climate Res.* 39, 11–17. doi: 10.3354/cr00794

Pastor, F., Valiente, J. A., and Khodayar, S. (2020). A warming Mediterranean: 38 years of increasing sea surface temperature. *Remote Sens.* 12, 2687. doi: 10.3390/rs12172687

Pavlidou, A., Simboura, N., Rousselaki, E., Tsapakis, M., Pagou, K., Drakopoulou, P., et al. (2015). Methods of eutrophication assessment in the context of the water framework directive: Examples from the Eastern Mediterranean coastal areas. *Continental Shelf Res.* 108, 156–168. doi: 10.1016/j.csr.2015.05.013

Pisano, A., Marullo, S., Artale, V., Falcini, F., Yang, C., Leonelli, F. E., et al. (2020). New evidence of Mediterranean climate change and variability from sea surface temperature observations. *Remote Sens.* 12, 132. doi: 10.3390/rs12010132

Pitarch, J. (2017). Biases in ocean color over a Secchi disk. *Optics Express* 25, 1124–1131. doi: 10.1364/OE.25.0A1124

Pitarch, J. (2020). A review of Secchi's contribution to marine optics and the foundation of Secchi disk science. *Oceanography* 33, 26–37. doi: 10.5670/oceanog.2020.301

Pitarch, J., Bellacicco, M., Marullo, S., and van der Woerd, H. J. (2021). Global maps of Forel–Ule index, hue angle and Secchi disk depth derived from 21 years of monthly ESA Ocean Colour Climate Change Initiative data. *Earth Syst. Sci. Data* 13, 481–490. doi: 10.5194/essd-13-481-2021

Pitarch, J., van der Woerd, H. J., Brewin, R. J. W., and Zielinski, O. (2019a). Optical properties of Forel-Ule water types deduced from 15 years of global satellite ocean color observations. *Remote Sens. Environment* 231, 111249. doi: 10.1016/j.rse.2019.111249

Pitarch, J., van der Woerd, H. J., Brewin, R. J. W., and Zielinski, O. (2019b). Twenty years of monthly global maps of Hue angle, Forel-Ule and Secchi disk depth, based on ESA-OC-CCI data. *PANGAEA*. doi: 10.1594/PANGAEA.904266

Preisendorfer, R. W. (1986). Secchi disk science: Visual optics of natural waters. *Limnol. Oceanogr.* 31, 909–926. doi: 10.4319/lo.1986.31.5.0909

Raitsos, D. E., Beaugrand, G., Georgopoulos, D., Zenetos, A., Pancucci-Papadopoulou, M. A., Theocharis, A., et al. (2010). Global climate change amplifies the entry of tropical species into the eastern Mediterranean Sea. *Limnol. Oceanogr.* 55, 1478–1484. doi: 10.4319/lo.2010.55.4.1478

Raitsos, D. E., Brewin, R. J. W., Zhan, P., Dreano, D., Pradhan, Y., Nanninga, G. B., et al. (2017). Sensing coral reef connectivity pathways from space. *Sci. Rep.* 7, 9338. doi: 10.1038/s41598-017-08729-w

Raitsos, D. E., Hoteit, I., Prihartato, P. K., Chronis, T., Triantafyllou, G., and Abualnaja, Y. (2011). Abrupt warming of the red sea. *Geophys. Res. Lett.* 38, L14601. doi: 10.1029/2011GL047984

Raitsos, D. E., Pradhan, Y., Brewin, R. J. W., Stenchikov, G., and Hoteit, I. (2013a). Remote sensing the phytoplankton seasonal succession. *PloS One* 8, e64909. doi: 10.1371/journal.pone.0064909

Raitsos, D. E., Walne, A., Lavender, S. J., Licandro, P., Reid, P. C., and Edwards, M. (2013b). A 60-year ocean colour data set from the continuous plankton recorder. *J. Plankton Res.* 35, 158–164. doi: 10.1093/plankt/fbs079

Raitsos, D. E., Yi, X., Platt, T., Racault, M.-F., Brewin, R. J. W., Pradhan, Y., et al. (2015). Monsoon oscillations regulate fertility of the Red Sea. *Geophysical Res. Letters* 42, 855–862. doi: 10.1002/2014GL062882

Salgado-Hernanz, P. M., Racault, M.-F., Font-Munoz, J. S., and Basterretxea, G. (2019). Trends in phytoplankton phenology in the Mediterranean Sea based on ocean-colour remote sensing. *Remote Sens. Environment* 221, 50–64. doi: 10.1016/j.rse.2018.10.036

Sathyendranath, S., Brewin, R. J. W., Brockmann, C., Brotas, V., Calton, B., Chuprin, A., et al. (2019). An ocean-colour time series for use in climate studies: the experience of the ocean-colour climate change initiative (OC-CCI). *Sensors* 19, 4285. doi: 10.3390/s19194285

Sathyendranath, S., Brewin, R. J. W., Jonsson, B. F., Ciavatta, S., Jackson, T., Kulk, G., et al. (2023). Ocean biology from space. *Survey Geophysics* 44, 1287–1308. doi: 10.1007/s10712-023-09805-9

Schefbeck, G. (1996). "On the pathways of the "Pola" expeditions. The Austro-Hungarian Deep-Sea Expeditions: in *Deep Sea and Extreme Shallow-water Habitats: Affinities and Adaptations. – Biosystematics and Ecology* – 11, 1–27. Available online at: https://www.zobodat.at/pdf/BioEco_11_0001-0027.pdf.

Secchi, P. A. (1865). *Relazione delle esperienze fatte a bordo della pontificia pirocorvetta l'*Immacolata concezione *per determinare la trasparenza del mare; memoria del P. A. Secchi. Il Nuovo Cimento, (1855-1868)*. 20, 205–238. doi: 10.1007/BF02726911

Simboura, N., Maragou, P., Paximadis, G., Kapiris, K., Papadopoulos, V. P., Sakellariou, D., et al. (2019). "Greece," in *World Seas: an Environmental Evaluation, 2nd ed.*, vol. I . Ed. C. Sheppard (Academic Press, Europe, The Americas and West Africa), 227–260.

Siokou-Frangou, I., Christake, U., Mazzochi, M. G., Montresor, M., d'Alcala, M. R., Vaque, D., et al. (2010). Plankton in the open Mediterranean Sea: a review. *Biogeosciences* 7, 1543–1586. doi: 10.5194/bg-7-1543-2010

Sisma-Ventura, G., Yam, R., and Shemesh, A. (2014). Recent unprecedented warming and oligotrophy of the eastern Mediterranean Sea within the last millennium. *Geophysical Res. Lett.* 41, 5158–5166. doi: 10.1002/2014GL060393

Tilstone, G. H., Pardo, S., Dall'Olmo, G., Brewin, R. J., Nencioli, F., Dessailly, D., et al. (2021). Performance of Ocean Colour Chlorophyll a algorithms for Sentinel-3 OLCI, MODIS-Aqua and Suomi-VIIRS in open-ocean waters of the Atlantic. *Remote Sens. Environ.* 260, 112444. doi: 10.1016/j.rse.2021.112444

Tsiaras, K. P., Kourafalou, V. H., Raitsos, D. E., Triantafyllou, G., Petihakis, G., and Korres, G. (2012). Inter-annual productivity variability in the North Aegean Sea: influence of thermohaline circulation during the Eastern Mediterranean Transient. *J. Mar. Syst.* 96-97, 72–78. doi: 10.1016/j.jmarsys.2012.02.003

Tyler, J. E. (1968). THE SECCHI DISC. *Limnol. Oceanogr.* 13, 1–6. doi: 10.4319/lo.1968.13.1.0001

van der Woerd, H. J., and Wernand, M. (2015). True colour classification of natural waters with medium-spectral resolution satellites: Seawifs, MODIS, MERIS and OLCI. *Sensors* 15, 25663–25680. doi: 10.3390/s151025663

Wang, S., Lee, Z., Shang, S., Li, J., Zhang, B., and Lin, G. (2019). Deriving inherent optical properties from classical water color measurements: Forel-Ule index and Secchi disk depth. *Optics Express* 27, 7642–7655. doi: 10.1364/OE.27.007642

Wernand, M. R. (2010). On the history of the Secchi disc. *J. Eur. Optical Soc - Rapid Publications* 5, 10013s. doi: 10.2971/jeos.2010.10013s

Wernand, M. (2011). *Poseidon's paintbox: historical archives of ocean colour in global-change perspective*. (PhD Thesis). Utrecht University, Netherlands.

Wernand, M. R., Hommersom, A., and van der Woerd, H. J. (2013b). MERIS-based ocean colour classification with the discrete Forel–Ule scale. *Ocean Sci.* 9, 477–487. doi: 10.5194/os-9-477-2013

Wernand, M. R., and van der Woerd, H. J. (2010a). Ocean colour changes in the North Pacific since 1930. *J. Eur. Optical Soc - Rapid Publications* 5, 10015s. doi: 10.2971/jeos.2010.10015s

Wernand, M. R., and van der Woerd, H. J. (2010b). Spectral analysis of the Forel-Ule ocean colour comparator scale. *J. Eur. Optical Soc - Rapid Publications* 5, 10014s. doi: 10.2971/jeos.2010.10014s

Wernand, M. R., van der Woerd, H. J., and Gieskes, W. W. C. (2013a). Trends in ocean colour and chlorophyll concentration from 1889 to 2000, worldwide. *PloS One* 8, e63766. doi: 10.1371/journal.pone.0063766

Wilson, L. J., Fulton, C. J., Hogg, A. M., Joyce, K. E., Radford, B. T. M., and Fraser, C. I. (2016). Climate-driven changes to ocean circulation and their inferred impacts on marine dispersal patterns. *Global Ecol. Biogeogr.* 25, 923–939. doi: 10.1111/geb.12456

Winder, M., and Sommer, U. (2012). Phytoplankton response to a changing climate. *Hydrobiologia* 698, 5–16. doi: 10.1007/s10750-012-1149-2

Wolter, K., and Timlin, M. S. (2011). El Niño/Southern Oscillation behaviour since 1871 as diagnosed in an extended multivariate ENSO index (MEI.ext). *Int. J. Climatol.* 31, 1074–1087. doi: 10.1002/joc.2336

Yao, F., Hoteit, I., Pratt, L. J., Bower, A. S., Zhai, P., Köhl, A., et al. (2014). Seasonal overturning circulation in the Red Sea: 1. Model validation and summer circulation. *J. Geophys. Res. Oceans* 119, 2238–2262. doi: 10.1002/2013JC009004

Ye, M., and Sun, Y. (2022). Review of the Forel–Ule Index based on in *situ* and remote sensing methods and application in water quality assessment. *Environ. Sci. pollut. Res.* 29, 13024–13041. doi: 10.1007/s11356-021-18083-0

Yu, S., Bai, Y., He, X., Gong, F., and Li, T. (2023). A new merged dataset of global ocean chlorophyll-a concentration for better trend detection. *Front. Mar. Sci.* 10. doi: 10.3389/fmars.2023.1051619

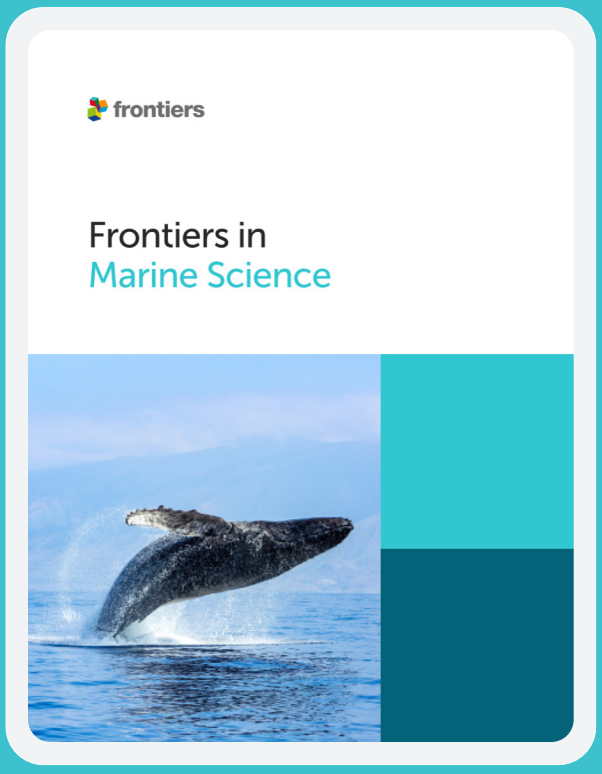
Frontiers in Marine Science

Explores ocean-based solutions for emerging global challenges

The third most-cited marine and freshwater biology journal, advancing our understanding of marine systems and addressing global challenges including overfishing, pollution, and climate change.

Discover the latest Research Topics

See more →



Frontiers

Avenue du Tribunal-Fédéral 34
1005 Lausanne, Switzerland
frontiersin.org

Contact us

+41 (0)21 510 17 00
frontiersin.org/about/contact